Springer Series in Computational Neuroscience

Vassilis Cutsuridis · Bruce P. Graham
Stuart Cobb · Imre Vida *Editors*

Hippocampal Microcircuits

A Computational Modeler's Resource Book

Second Edition

Springer

Springer Series in Computational Neuroscience

Computational Neuroscience gathers monographs and edited volumes on all aspects of computational neuroscience, including theoretical and mathematical neuroscience, biophysics of the brain, models of neurons and neural networks, and methods of data analysis (e.g. information theory). The editors welcome suggestions and projects for inclusion in the series.

About the Editors: Alain Destexhe is Research Director at the Centre National de la Recherche Scientifique (CNRS), France, and Romain Brette is Research Director at the Institut National de la Santé et de la Recherche Médicale (INSERM), France.

More information about this series at http://www.springer.com/series/8164

Vassilis Cutsuridis • Bruce P. Graham
Stuart Cobb • Imre Vida
Editors

Hippocampal Microcircuits

A Computational Modeler's Resource Book

Second Edition

Springer

Editors
Vassilis Cutsuridis
School of Computer Science
University of Lincoln
Lincoln, UK

Stuart Cobb
Centre for Discovery Brain Sciences
University of Edinburgh
Edinburgh, UK

Bruce P. Graham
School of Natural Sciences, Department
of Computing Science and Mathematics
University of Stirling
Stirling, UK

Imre Vida
Institute for Integrative Neuroanatomy
Charité – Universitätsmedizin Berlin
Berlin, Germany

ISSN 2197-1900 ISSN 2197-1919 (electronic)
Springer Series in Computational Neuroscience
ISBN 978-3-319-99102-3 ISBN 978-3-319-99103-0 (eBook)
https://doi.org/10.1007/978-3-319-99103-0

Library of Congress Control Number: 2019930148

This Springer imprint is published by the registered company Springer Nature Switzerland AG.
The registered company address is: Gewerbestrasse 11, 6330 Cham, Switzerland

Introduction

The hippocampus is amongst the most widely studied of mammalian brain regions hypothesized to play a role in the short-term storage of declarative memories. Recent years have witnessed a dramatic accumulation of knowledge about the morphological, physiological and molecular characteristics as well as the connectivity and synaptic properties of the various cell types found in the hippocampus. The microcircuits these cells form exhibit different rhythmic states such as theta (4–7 Hz) and gamma (30–100 Hz) oscillations in different behavioural conditions. This dynamic complexity presumably corresponds to specific functional processing of information. Much work has been devoted to trying to understand the cellular and network properties that generate these and other complex network patterns, but much is still to be done to decipher the function of the detailed microcircuits.

Microcircuits can be thought as functional modules that act as elementary processing units bridging the gap between single-cell activity, network activity and global brain function. Microcircuits can be found in many parts of mammalian nervous systems consisting of a complex architecture involving many different neuronal types connected in feedforward and feedback loops. Synaptic connections may be excitatory or inhibitory and target specific spatial compartments of a neuron. In addition to synaptic input, a neuron and the microcircuit it is a part of are subject to diffuse neuromodulatory signals. Neural synaptic transmission and neuromodulation combine to provide a complex dynamics of neural activity and presumed information processing in a neuronal microcircuit.

This book is the second edition of the 2010 *Hippocampal Microcircuits* and provides an updated snapshot and resumé of the current state of the art of the ongoing research avenues concerning the hippocampal microcircuits. The central aim of the volume is to provide a methodology to anyone interested in developing microcircuit-level models of the hippocampus. The book is divided into two thematic areas: (1) experimental background and (2) computational analysis. In the first thematic area, leading experimental neuroscientists discuss the morphological, physiological and molecular characteristics as well as the connectivity and synaptic

properties of the various cell types found in the hippocampus. Behaviour-related ensemble activity patterns of morphologically identified neurons in anaesthetized and freely moving animals provide insights on the function of the hippocampal areas. In the second thematic area, computational neuroscientists present models of hippocampal microcircuits at various levels of detail (e.g. single-cell level, network level). These models make use of the knowledge presented in the first thematic area to discuss the overall global function of hippocampal microcircuits (in areas CA1, CA3, dentate gyrus and entorhinal cortex). Synaptomics and connectomics models of hippocampal structures are initially discussed. Then, network models of memory, rhythm generation and spatial navigation are presented, followed by abstract and biophysical models of synaptic plasticity. Network models of hippocampal implicated disorders (epilepsy and schizophrenia) are then detailed and how their network topologies, connectivities and activities change in these diseases. Finally, two chapters are dedicated to describing simulator environments of single neurons and networks currently used by computational neuroscientists in developing their models and modelling tools to parametrically constrain them.

This engaging volume is invaluable to experimental and computational neuroscientists, electrical engineers, physicists, mathematicians and others interested in developing microcircuit models of the hippocampus. Graduate-level students and trainees in all of these fields will find this book a significant source of information. The following unique features make this volume distinct:

- It provides concise snapshots of experimental evidence rather than lengthy and detailed descriptions of the morphological, physiological and molecular characteristics as well as the connectivity and synaptic properties of the various cell types found in the hippocampus are presented. This evidence is often provided in either tabular and/or pictorial form.
- In contrast to previous editorial attempts in which main target audience was either the *entire hippocampus neuroscience disciplines*, this volume is targeting experimental and computational neuroscientists interested in *developing microcircuit models of the hippocampus*.
- Aside from presenting up-to-date experimental evidence on the hippocampal microcircuits, this second edition also suggests a didactic methodology approach of modelling microcircuits necessary to all computational neuroscientists interested in bridging the gap between the single-cell level, the network level and the behavioural level.

- All chapters not only discuss the current state of the art of experimental and computational research avenues regarding the hippocampal microcircuits but also provide a section on outstanding questions and areas in need of further clarification that will guide future research to be carried out by young and/or senior computational neuroscientists.

School of Computer Science — Vassilis Cutsuridis
University of Lincoln, Lincoln, UK
Department of Computing Science & Mathematics — Bruce P. Graham
University of Stirling, Stirling, UK
Centre for Discovery Brain Sciences — Stuart Cobb
University of Edinburgh, Edinburgh, UK
Institute for Integrative Neuroanatomy — Imre Vida
Charité – Universitätsmedizin Berlin, Berlin, Germany

Contents

Contributors

Giorgio A. Ascoli Center for Neural Informatics, Structures, & Plasticity, Krasnow Institute for Advanced Study, George Mason University, Fairfax, VA, USA

Marlene Bartos Institute for Physiology I, Albert-Ludwigs University Freiburg, Freiburg, Germany

Lubica Benuskova Department of Applied Informatics, Faculty of Mathematics, Physics and Informatics, Comenius University, Bratislava, Slovakia

Theodore W. Berger Department of Biomedical Engineering, Center for Neural Engineering, Viterbi School of Engineering, University of Southern California, Los Angeles, CA, USA

Justas Birgiolas School of Life Sciences, Arizona State University, Tempe, AZ, USA

Sam A. Booker Centre for Discovery Brain Sciences, University of Edinburgh, Edinburgh, UK

Nicolas Brunel Department of Neurobiology, Duke University, Durham, NC, USA

Daniel Bush UCL Institute of Cognitive Neuroscience, London, UK

UCL Institute of Neurology, London, UK

Stuart Cobb Centre for Discovery Brain Sciences, University of Edinburgh, Edinburgh, UK

Sharon M. Crook School of Mathematical and Statistical Sciences, School of Life Sciences, Arizona State University, Tempe, AZ, USA

Vassilis Cutsuridis School of Computer Science, University of Lincoln, Lincoln, UK

Claudius E. Degro Institute for Integrative Neuroanatomy, Charité – Universitätsmedizin Berlin, Berlin, Germany

Markus Diesmann Institute of Neuroscience and Medicine (INM-6) and Institute for Advanced Simulation (IAS-6) and JARA Institute Brain Structure-Function Relationships (INM-10), Jülich Research Centre, Jülich, Germany

Department of Psychiatry, Psychotherapy and Psychosomatics, Medical Faculty, and Department of Physics, Faculty 1, RWTH Aachen University, Aachen, Germany

Tamar Dugladze Institute of Integrative Neuroanatomy, Charité – Universitätsmedizin Berlin, Berlin, Germany

Howard Eichenbaum Center for Memory and Brain, Boston University, Boston, MA, USA

Gaute T. Einevoll Faculty of Science and Technology, Norwegian University of Life Sciences, Ås, Norway

Department of Physics, University of Oslo, Oslo, Norway

Jörg Frauendiener Mathematics & Statistics, University of Otago, New Zealand

Richard C. Gerkin School of Life Sciences, Arizona State University, Tempe, AZ, USA

Tengis Gloveli Cellular and Network Physiology Lab, Neuroscience Research Center, Charité – Universitätsmedizin Berlin, Berlin, Germany

Bruce P. Graham Department of Computing Science and Mathematics, University of Stirling, Stirling, UK

Michael Graupner Laboratoire de Physiologie Cerebrale – UMR 8118, CNRS, Universite Paris Descartes, Paris, France

Sonja Grün Institute of Neuroscience and Medicine (INM-6) and Institute for Advanced Simulation (IAS-6) and JARA Institute Brain Structure-Function Relationships (INM-10), Jülich Research Centre, Jülich, Germany

Theoretical Systems Neurobiology, RWTH Aachen University, Aachen, Germany

Alexander Hanuschkin Optophysiology Lab, Department of Biology, University of Freiburg, Freiburg, Germany

Phillip J. Hendrickson Department of Biomedical Engineering, Center for Neural Engineering, Viterbi School of Engineering, University of Southern California, Los Angeles, CA, USA

J. Josh Lawrence Department of Pharmacology and Neuroscience, Centre for Translational Neuroscience and Therapeutics, Texas Tech University Health Sciences Centre School of Medicine, Lubbock, TX, USA

Jeeyune Q. Jung Department Physiology and Pharmacology, SUNY Downstate, Brooklyn, NY, USA

Joseph J. Kabariti Department Physiology and Pharmacology, SUNY Downstate, Brooklyn, NY, USA

Nancy Kopell Department of Mathematics, Boston University, Boston, MA, USA

Srinivasa B. Krothapalli Neurophysiology Unit, Department of Neurological Sciences, Christian Medical College, Vellore, India

Ákos Kulik Institute for Physiology II, Albert-Ludwigs University Freiburg, Freiburg, Germany

Szymon Łeşki Department of Neurophysiology, Nencki Institute of Experimental Biology of Polish Academy of Sciences, Warsaw, Poland

Cheng-Chang Lien Institute of Neuroscience, National Yang-Ming University, Taipei, Taiwan

Henrik Lindén Department of Neuroscience, University of Copenhagen, Copenhagen, Denmark

William W. Lytton Department Neurology, Kings County Hospital Center, Brooklyn, NY, USA

Department Physiology and Pharmacology, SUNY Downstate, Brooklyn, NY, USA

Sanjay M. Neurophysiology Unit, Department of Neurological Sciences, Christian Medical College, Vellore, Tamil Nadu, India

Department of Bioengineering, Christian Medical College, Vellore, Tamil Nadu, India

Department of Electrical Engineering, National Institute of Technology Calicut, Kattangal, Kerala, India

Marco Martina Department of Physiology, Northwestern University, Feinberg School of Medicine, Chicago, IL, USA

Jack Mellor Centre for Synaptic Plasticity, School of Physiology, Pharmacology and Neuroscience, University of Bristol, Bristol, UK

Keivan Moradi Center for Neural Informatics, Structures, & Plasticity, Krasnow Institute for Advanced Study, George Mason University, Fairfax, VA, USA

Ahmed A. Moustafa School of Social Sciences and Psychology & Marcs Institute for Brain and Behaviour, Western Sydney University, Sydney, NSW, Australia

Samuel A. Neymotin Department of Neuroscience, Brown University, Providence, RI, USA

Matt Nolan Centre for Integrative Physiology, University of Edinburgh, Edinburgh, UK

Klas H. Pettersen Letten Centre and GliaLab, Department of Molecular Medicine, Institute of Basic Medical Sciences, University of Oslo, Oslo, Norway

Ausra Saudargiene Laboratory of Biophysics and Bioinformatics, Neuroscience Institute, Lithuanian University of Health Sciences, Kaunas, Lithuania

Jonas-Frederic Sauer Institute for Physiology I, Albert-Ludwigs University Freiburg, Freiburg, Germany

Christoph Schmidt-Hieber Neuroscience Department, Institut Pasteur, Paris, France

Vladislav Sekulić Krembil Research Institute, University Health Network, Toronto, ON, Canada

Department of Physiology, University of Toronto, Toronto, ON, Canada

Mohamed A. Sherif Yale University, New Haven, CT, USA

VA Connecticut Healthcare System, West Haven, CT, USA

Department Physiology and Pharmacology, SUNY Downstate, Brooklyn, NY, USA

Azam Shirrafiardekani Department of Computer Science, University of Otago, Dunedin, New Zealand

Frances K. Skinner Krembil Research Institute, University Health Network, Toronto, ON, Canada

Departments of Medicine (Neurology) and Physiology, University of Toronto, Toronto, ON, Canada

Dong Song Department of Biomedical Engineering, Center for Neural Engineering, Viterbi School of Engineering, University of Southern California, Los Angeles, CA, USA

Tom Tetzlaff Institute of Neuroscience and Medicine (INM-6) and Institute for Advanced Simulation (IAS-6) and JARA Institute Brain Structure-Function Relationships (INM-10), Jülich Research Centre, Jülich, Germany

Katalin Tóth CERVO Brain Research Centre, Université Laval, Quebec City, QC, Canada

John J. Tukker Neuroscience Research Center, Charité University Medicine Berlin, Berlin, Germany

Imre Vida Institute for Integrative Neuroanatomy, Charité – Universitätsmedizin Berlin, Berlin, Germany

Menno P. Witter Kavli Institute for Systems Neuroscience, Centre for Neural Computation, and Egil and Pauline Braathen and Fred Kavli Centre for Cortical Microcircuits, NTNU Norwegian University of Science and Technology, Trondheim, Norway

Jakob Wolfart Medizinische Hochschule Brandenburg Theodor Fontane, Neuruppin, Germany

Oscar Langendorff Institute of Physiology, University of Rostock, Rostock, Germany

Man Yi Yim Center for Theoretical and Computational Neuroscience and Department of Neuroscience, The University of Texas at Austin, Austin, TX, USA

Gene J. Yu Department of Biomedical Engineering, Center for Neural Engineering, Viterbi School of Engineering, University of Southern California, Los Angeles, CA, USA

The original version of this book was revised. The correction to this chapter is available at https://doi.org/10.1007/978-3-319-99103-0_26 and https://doi.org/10.1007/978-3-319-99103-0_27

Part I
Experimental Background

Stuart Cobb and Imre Vida

The hippocampus is one of the most intensely studied structures in the brain. It has been investigated at many different levels in an attempt to understand the neurobiology of cognitive functions, including learning and spatial coding. The accumulated knowledge of hippocampal anatomy, physiology, and function provides a rich repository of information that presents enormous opportunity to model different aspects of neuronal signaling and information processing within this structure. As a primary focus in neurobiology over many decades, studies of the hippocampus have also helped reveal elementary properties of neurons, their synapses, and the microcircuits they are embedded.

There are several reasons why the study of the hippocampus has been at the forefront of neurobiology research. These include the involvement of this brain structure in memory processes, spatial navigation, as well as major disease states. Another reason is the ability to readily recognize the hippocampus as well as target it in vivo and isolate it for in vitro investigations. Finally, a major impetus for focusing basic studies of the nervous system on the hippocampus owes to its apparently simple cytoarchitecture and circuitry and thus its tractability as a cortical "model" system.

The hippocampal formation is a highly organized structure and has a striking appearance at the gross anatomical level. The complexity of the system can appear overwhelming at first. Nevertheless, there continues an evolution in our understanding of the constituent cells, their connectivity, their neurochemical and biophysical properties, and the emergent properties of these in terms of hippocampal-dependent behavior. However, many of the details remain to be established, and indeed significant gaps persist in our understanding of some key concepts.

S. Cobb
Centre for Discovery Brain Sciences, University of Edinburgh, Edinburgh, UK

I. Vida
Institute for Integrative Neuroanatomy, Charité – Universitätsmedizin Berlin, Berlin, Germany

In this section, experimental neuroscientists discuss the salient structural and functional properties of the hippocampus. This includes morphological, physiological, and molecular characteristics as well as the connectivity and synaptic properties of the various cell types found in the hippocampus. We provide concise overviews of each aspect of hippocampal structure and function and, where possible, provide quantitative descriptions of the experimental findings. While we believe this will be a valuable summary for all readers interested in the biology of the hippocampus, by conveying often quantitative experimental data from different levels of complexity into a coherent picture, we hope this section will provide a valuable resource for researchers embarking on modeling different aspects of this system. In this second edition of *Hippocampal Microcircuits: A computational Modeler's Resource Book*, we have updated each chapter to reflect the most recent advances in understanding hippocampal cells and circuits.

In the first chapter "Connectivity of the Hippocampus," Menno Witter provides a comprehensive description of the major connectivity of the hippocampal formation. In this, he goes beyond the simplified classical models of anatomical organization to produce an updated and extended connectional scheme that incorporates important new as well as some older but hitherto overlooked details. In the chapter "Morphology of Hippocampal Neurons," Imre Vida and colleagues extend this overview to the microcircuit and single-cell levels. The chapter provides detailed quantitative descriptions of the morphology, major molecular markers, as well as connectivity of hippocampal neuron types. While the most detailed quantitative information is available for principal cells, this chapter provides a comprehensive summary of the major anatomically defined classes of interneurons, a rapidly developing area of hippocampal biology. In the chapter "Physiological Properties of Hippocampal Neurons," Marco Martina and Cheng-Chang Lien provide a detailed overview of the physiological properties of the different classes of hippocampal neurons from a single-cell biophysics perspective. Where possible, they provide detailed quantitative descriptions of the passive and active properties together with a discussion of the significance of these in shaping the electrical behavior of respective cell types. In the chapter "Glutamatergic Neurotransmission in the Hippocampus," Katalin Tóth moves from individual cells to consider excitatory synaptic communication between neurons in the hippocampus. In this, she provides a detailed yet accessible overview of glutamatergic transmission at different synapses in the hippocampus including key qualitative and quantitative differences in the physiology, biophysics, and pharmacology at different synapses and pathways. In the chapter "Fast and Slow GABAergic Transmission in Hippocampal Circuits," Marlene Bartos and colleagues provide an overview of GABAergic transmissions in hippocampal circuits. In this, they introduce a variety of different forms of GABAergic inhibition and discuss functional differences between ionotropic and metabotropic forms of GABAergic inhibition at different inhibitory synapses. In the chapter "Synaptic Plasticity at Hippocampal Synapses – Experimental Background," Jack Mellor reviews the divergent forms of synaptic plasticity that are characteristic of different hippocampal synapses. Ranging from short-term frequency facilitation to more enduring forms of synaptic plasticity, he provides a succinct summary of the experimental background

and highlights key literature in this area, as well as quantitative descriptions of plasticity at some major synapses. In the chapter "Neuromodulation of Hippocampal Cells and Circuits," Stuart Cobb and Josh Lawrence introduce the concept of neuromodulation and the many ways by which hippocampal cells and circuits can be regulated. Thereafter, they provide a detailed yet condensed summary of the main neuromodulator systems ranging from classical modulators (monoamines and acetylcholine) to neuropeptide modulators and paracrine/autocrine substances. In the chapter "Neuronal Activity Patterns During Hippocampal Network Oscillations In Vitro," Tengis Gloveli and colleagues describe the importance and relevance of neuronal activity patterns during hippocampal network oscillations in vitro. He provides a detailed account of the emergent electrical behavior of hippocampal networks including the importance of intrinsic cellular and synaptic properties in their genesis and modulation. In the chapter "Recording Identified Neurons in Awake and Anesthetized Rodents," John Tukker extends the concept of patterned neuronal activities by describing physiological patterns of neuronal activity that occur in vivo under anesthetic and conscious conditions. Under these circumstances, it is possible to observe highly stereotyped patterns of behavior within different morphologically identified principal and interneuronal cell types when viewed with respect to ongoing EEG states. This precise sculpting of neuronal activity in the temporal domain provides important insights into the spatial and temporal processing of synaptic signals during hippocampal activity in the intact network. In the final experimental chapter "Spatial and Behavioral Correlates of Hippocampal Neuronal Activity: A Primer for Computational Analysis," the late Howard Eichenbaum described spatial and behavioral correlates of hippocampal neuronal activity. By providing a succinct overview of the literature, this chapter offers a framework for considering the relationship between behavior, the activity of hippocampal neurons, and how these might be modeled.

Connectivity of the Hippocampus

Menno P. Witter

Abstract The aim of this chapter is to extend the standard simplified diagram of the connectional organization of the hippocampus found in many current textbooks, by adding details on the connectivity of area CA2 and on entorhinal intrinsic wiring. In the chapter, some of the 'traditional wisdoms' on hippocampal connectivity are discussed, emphasizing the need for a more inclusive framework to model the hippocampus. The chapter focusses on intrinsic connections, and many of the well-known extrinsic connections of the hippocampus will not be covered in this chapter, for two reasons. First, the information is already available at a summarized (meta) level, and a new summary would not assist those who need anatomical details to contribute to the explanation of the functional outcome of a study. Second, this chapter is meant to provide a framework of knowledge to support computational modelling of the region, and therefore only the most relevant and quantitative data on the connectivity of the hippocampus are covered.

Overview

In the first edition of this book, I pointed to the increasingly complex intrinsic wiring diagram of the hippocampus and that new data are being added at an increasing speed. With the emergence of cell-specific viral tracing techniques, the potential for a data explosion has become eminent, going hand in hand with an increase of the potential for false-positive or incomplete data. The relevance of interneurons in the local network, as well as the fact that interneurons contribute to long-range projections, has been integrated into current conceptualizations of the 'Connectivity of the Hippocampus'. Several comprehensive reviews have been published to which the reader is referred for many of the connections not covered in this chapter or for

M. P. Witter (✉)
Kavli Institute for Systems Neuroscience, Centre for Neural Computation, and Egil and Pauline Braathen and Fred Kavli Centre for Cortical Microcircuits, NTNU Norwegian University of Science and Technology, Trondheim, Norway
e-mail: menno.witter@ntnu.no

V. Cutsuridis et al. (eds.), *Hippocampal Microcircuits*, Springer Series in Computational Neuroscience, https://doi.org/10.1007/978-3-319-99103-0_1

more details on the connections described here. An excellent, much more detailed resource can be found in a recent book chapter (Cappaert et al. 2015). Several online databases contribute to making this wealth of connectional data accessible as well (see further reading).

In contrast to this ever-expanding connectional knowledge base, many functional papers and reviews still use a simplified diagram of the connectional organization of the hippocampus as their reference, which we will here refer to as the standard view. The aim of this chapter is to extend this standard view, adding details that have been known for some time or have recently been provided, but apparently have not yet been incorporated in the commonly accepted connectional scheme for the region. For example, the increased insights on the connectivity of area CA2 are added in this second edition, as well as many new details on entorhinal intrinsic wiring.

I further aim to reinterpret some of the 'traditional wisdoms' on hippocampal connectivity, potentially pointing to the need of a changed functional framework for the hippocampus. The use will be made of a standardized scheme of connections which hopefully will facilitate easy dissemination of these adapted connectional concepts for the region. Many of the very well-known connections, such as all extrinsic connections of the HF and EC, will not be covered in this chapter, for two reasons. First, the information is already available at a summarized (meta) level, and a new summary would not assist those who need anatomical details to contribute to the explanation of the functional outcome of a study. Second, this chapter is meant to provide a framework of knowledge to support computational modelling of the region, and therefore I have selected what I consider the most relevant new data on the connectivity of the hippocampus, not of the brain.

Microscopical Anatomy and Nomenclature

Throughout the chapter, reference will be made to the hippocampal formation (HF) and the entorhinal cortex (EC) as the two main areas of interest. The HF in turn comprises three distinct subregions (Fig. 1): the dentate gyrus (DG), the hippocampus proper (consisting of CA3, CA2 and CA1) and the subiculum (Sub). The HF is a three-layered cortex that is easily differentiated from the EC, since the latter has more than three layers (see below). The deepest layer of the HF houses basal dendrites of principal cells and a mixture of afferent and efferent fibres and local circuitry – interneurons. Superficial to this polymorph layer is the cell layer, which is composed of principal cells and interneurons. On top, the most superficial layer or molecular layer contains the apical dendrites of the neurons and the large majority of axons that provide inputs. In the dentate gyrus, these layers are, respectively, referred to as the hilus, granular (cell) layer and molecular layer (*stratum moleculare*). In the CA-region, we find the deep polymorph layer (*stratum oriens*), followed by the pyramidal layer (*stratum pyramidale*), topped by the superficial or molecular layer. The latter is subdivided into a number of sub-layers. In CA3, three sub-layers are distinguished: *stratum lucidum*, representing

the mossy fibre input from DG; *stratum radiatum*, i.e. the apical dendrites of the neurons in stratum pyramidale; and, most superficially, the *stratum lacunosum-moleculare* comprising the apical tufts of the apical dendrites. The lamination in CA2 and CA1 is similar to that in CA3, with the exception that the *stratum lucidum* is missing in CA1 and absent or much less evident in CA2. In Sub, the superficial layer is generally referred to as molecular layer, sometimes divided into an outer and inner portion, and the remaining two layers are referred to as the pyramidal (cell) layer (*stratum pyramidale*) and *stratum oriens*. The latter is very thin and quite often not specifically differentiated from the underlying white matter of the brain. The EC, commonly subdivided into a medial (MEC) and a lateral (LEC) part,[1] is generally described as having six layers, a molecular layer (layer I), the superficial cell layer (layer II), the superficial pyramidal cell layer (layer III), a cell-sparse lamina dissecans (layer IV), the deep pyramidal cell layer (layer V) and a polymorph cell layer (layer VI).[2]

In order to understand the anatomical organization, it is relevant to describe the coordinate systems that define position within the HF and PHR (Fig. 1). For the HF, there are three relevant axes: the long axis, the transverse or proximodistal axis, which runs in parallel to the cell layer, starting at the DG; and the radial or superficial-to-deep axis, which is defined perpendicular to the transverse axis. In the EC, a similar superficial-to-deep axis is used in addition to mediolateral (proximodistal) and anteroposterior (rostrocaudal) axes.

[1]The lateral and medial entorhinal cortex or Brodmann's areas 28a and 28b, respectively, have been further subdivided by a large number of authors (for a more detailed description and comparison of different nomenclatures used in the rat and in other species, the reader is referred to a number of reviews (cf. Witter et al., 1989)). In the rat, and likewise in the mouse, a further division into dorsolateral (DLE), dorsal-intermediate (DIE), ventral-intermediate (VIE), caudal (CE) and medial (ME) subdivisions have been proposed (Insausti et al., 1997, Hippocampus 7:146; van Groen et al., 2003, Hippocampus 13: 133–149). In monkeys, humans and in other species in which the entorhinal cortex was described, such as cat, dog, guinea pig and bat (Amaral et al., 1987 J Comp Neurol 264: 326–355; Witter et al., 1989, Progr Neurobiol 33:161–254; Buhl and Dann 1991, Hippocampus 1: 131–152; Insausti et al., 1995, J Comp Neurol 355: 171–198; Uva et al., 2004 J Comp Neurol 474: 289–303; Woznicka et al. 2006, Brain Res Rev. 52: 346–367), comparable partitioning schemes have been proposed. However, in case of most species, there is a tendency to consider the entorhinal cortex as composed of two primary components, the lateral and medial entorhinal cortex, most likely reflecting functional differences (see further Witter et al. 2017a, Front Syst Neurosci 11:46).

[2]Note that some authors have adopted a slightly different nomenclature in which the lamina dissecans is either without number or considered to be the deep part of layer III (layer IIIb), such that layer IV is used to designate the superficial part of layer V, characterized by the presence of rather large pyramidal cells that stain strongly for Nissl substance.

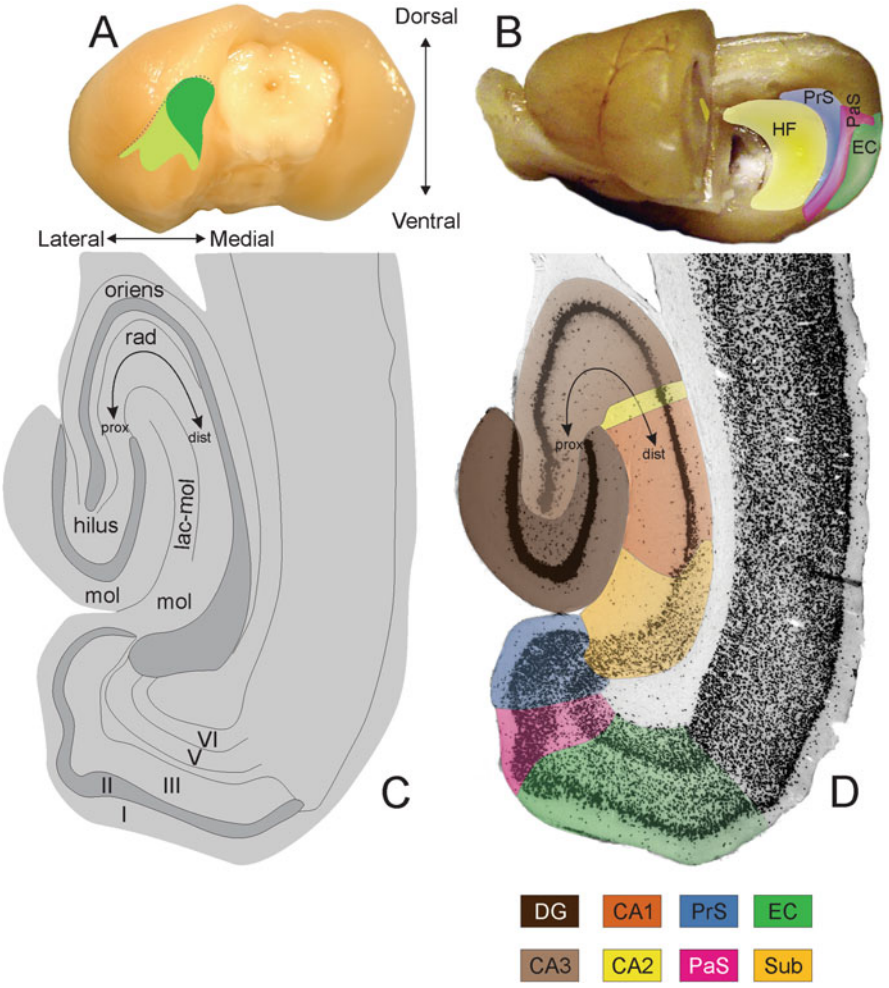

Fig. 1 Schematic representation of the position of the HF and the EC and main topological axes. (**a**) Posterior view of the rat brain showing the position of the LEC (light green) and MEC (dark green; modified with permission from Fyhn et al., 2004, Science 305: 1258–1264. (**b**) Lateral view of a partially dissected brain showing the shape and position of the HF and the longitudinal or dorsoventral axis, as well as the position and extent of the pre- and parasubiculum (PrS and PaS, respectively) and entorhinal cortex (EC) (Modified with permission from Boccara et al. 2010 Nat Neurosci.13:987. (**c**) Schematic drawing of a horizontal section illustrating the main nomenclature. (**d**) Horizontal section stained for the neuronal marker NeuN, illustrating the main subdivisions of HF and the EC

The Standard Connectional View

According to the standard view (Fig. 2), neocortical projections eventually reach the EC, which in turn provides the main source of input to DG of the hippocampal formation. All subregions of the hippocampal formation are sequentially connected by a serial chain of connections. In short, the dentate granule cells give rise to the mossy fibre pathway which targets the CA3. Axons from CA3 neurons form the so-called Schaffer collateral projection, targeting CA1 and lastly, CA1 projects to Sub. Output from the hippocampal formation arises in CA1 and the Sub and is directed to the parahippocampal region, mainly, but not exclusively to the deep layers of the EC. This series of unidirectional connections has also been referred to as the extended trisynaptic circuit. In a more complex version, EC mediates two parallel projection streams by way of LEC and MEC, respectively, that each reflect major input/output differences. The EC is the source of the perforant pathway, which projects to all subregions of the hippocampal formation. Entorhinal layer II projects to the dentate gyrus, CA3 and CA2, whereas layer III projects to CA1 and Sub. CA2 has been added to the circuitry. Whether or not CA2 receives mossy fibre input is still debated, but recent data indicate that species differences might exist. For now, we assume that the mossy fibre projection is a characterizing feature of CA3. In turn, CA2 has strong projections to both CA3 and CA1. The projections to CA1 and subiculum show a complex topographical organization (Fig. 3). In the following sections, each of the connections of the more extended scheme will be reviewed, detailed and

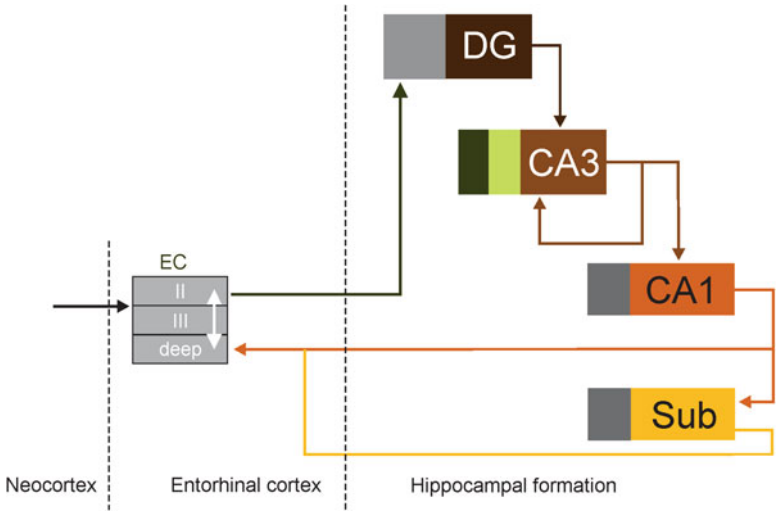

Fig. 2 The standard view of the entorhinal-hippocampal network. Layer II of EC originates the perforant pathway to DG. DG in turn sends the mossy fibre projection to CA3, where neurons originate the autoassociative projection as well as Schaffer collaterals to CA1. CA1 projects to Sub and both of them send return projections back to layer V of EC

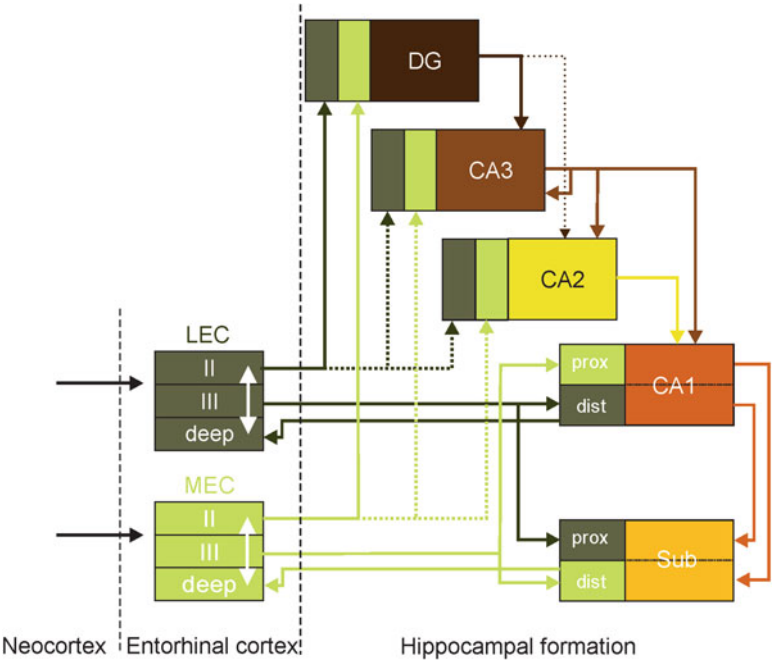

Fig. 3 The extended version of the standard view of the entorhinal-hippocampal network. CA2 was added to the network, as well as additional projections for Layer II of EC to CA3 and CA2 and the layer III projections to CA1 and Sub. The differential distribution of the projections from the LEC and the MEC along the transverse axis of the CA1 and the Sub has been included, as well as the organization of the projections from the CA1 to the Sub and from both back to LEC and MEC. The longitudinal topologies of neither connections are represented

when appropriate appended, starting with the entorhinal projections to the individual subdivisions of the HF.

Entorhinal-Hippocampal Projections

The elaborate Golgi studies of Ramon y Cajal and Lorente de Nó first demonstrated that EC is the origin of an immensely strong projection to HF. The latter became generally known as the perforant path(way). These observations were subsequently corroborated and extended in a seemingly continuous stream of tracing studies that drew attention to the many parallel entry routes for entorhinal inputs to HF, providing us with the contemporary image of EC projections to DG, the hippocampal fields CA1–CA3 and Sub. The total component of fibres was originally

named the perforant (temporo-ammonic) pathway by Cajal,[3] since the axons from EC perforated the pyramidal cell layer of the Sub. In the molecular layer of Sub, axons subsequently travel towards DG, crossing the hippocampal fissure, or course in stratum lacunosum-moleculare of CA1, CA2 and CA3, while making en passant synapses on the pyramidal neurons and interneurons in the CA fields, and continue into the tip of the molecular layer of the DG. There is an additional route for entorhinal fibres to reach targets in the hippocampus, referred to as the temporo-alvear tract. Axons in this pathway, which does not perforate the Sub, travel in the alveus and to some extent in stratum oriens below Sub and CA1–CA3 and will eventually traverse the pyramidal cells layer of the CA fields at specific points and continue to stratum lacunosum-moleculare where they terminate. Note that these axons target basal and apical dendrites of pyramidal cells as well as interneurons in strata oriens, pyramidale and radiatum.[4]

EC Projections to DG, CA3 and CA2

Cells in layer II of EC give rise to projections to DG, CA3 and CA2, and this observation has been made in most if not all species studied, including humans. It is likely that both the projections to DG and CA3 originate as collaterals from the same neuron and that the majority of neurons that project to DG and CA3 express marked levels of the protein Reelin, one of the two main cell markers for neurons in layer II. Details regarding the origin of CA2 projecting cells are unknown, but it is likely that these neurons also belong to the reelin-positive class of neurons. The other neuron class stains positive for the calcium-binding protein calbindin. These neurons give rise to widespread projections to the forebrain, but interestingly, about half of the population of EC layer II calbindin-positive neurons apparently issues local axon collaterals, contributing to an extensive, though yet now well-analysed intrinsic projection system. Only a small percentage of these neurons contribute to the projections to the hippocampus. Although the organization of the EC projection to DG has been described in much more detail than the EC to CA3 projection, the latter appears to follow organization principles like those that govern the projection from entorhinal layer II to DG. Generally, two components are differentiated which have their exclusive origin in LEC or MEC, respectively.

[3] See Witter et al. 2017 Brain Behav Evol 90:15–24 for details on the complex and sometimes confusing terminology used to describe EC-HF projections.

[4] Note that the term temporo-ammonic tract is often used to refer to all of the entorhinal projections to the CA fields but more commonly only to all fibres that reach CA1. In the temporal portion of the hippocampus, most of the entorhinal fibres reach CA1 after perforating the subiculum (classical perforant pathway). At more septal levels, however, the number of entorhinal fibres that take the alvear temporo-ammonic pathway increases. A third route taken by fibres from the entorhinal cortex involves the molecular layers of the entorhinal cortex, para- and presubiculum, continuing into the molecular layer of the subiculum. The latter route has not been given a specific name.

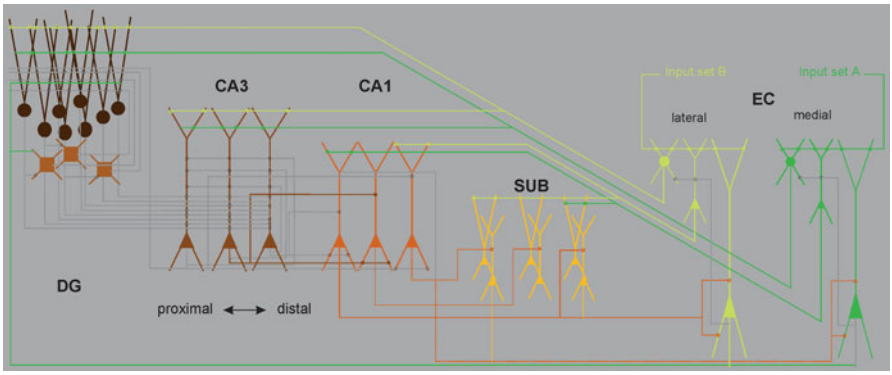

Fig. 4 Wiring diagram, illustrating the organization of the projections from layers II, III and V of the MEC and the LEC to the various subdivisions of the HF. Note the laminar terminal distribution of the layer II component to the DG and the CA3 and the restricted transverse terminal distribution of the layer III projection to the CA1 and the Sub

Projections from LEC terminate in the outer half of the stratum moleculare of DG and the stratum lacunosum-moleculare of CA3 and CA2, whereas those from MEC terminate deep to the lateral fibres (Figs. 3 and 4). In DG, the entorhinal terminal zone occupies the outer two-thirds of the molecular layer, and in CA3/CA2, the entire radial dimension of stratum lacunosum-moleculare contains entorhinal fibres.[5]

There are conflicting papers on the transverse distribution of the layer II perforant path projection. Whereas in some studies no differences were reported, others reported that the lateral perforant pathway preferentially projects to the enclosed blade of the dentate gyrus and the medial component either does not show a preference or predominantly targets the exposed blade. In CA3 no indications have been found for a further transverse organization, although it should be mentioned that the distribution of apical dendrites makes it likely that neurons in the most proximal portion of CA3 are largely devoid of entorhinal input since their dendrites do not reach into the terminal zone in CA3. In the mouse and the monkey, no transverse organization has been described in either the DG or the CA3 projection.

[5]The laminar pattern has been extensively described in the rat and available data in mice, guinea pigs and cats indicate a similar laminar terminal differentiation between the lateral and medial components of the perforant path. In contrast, in the macaque monkey the situation is different in that irrespective of the origin in EC, at all levels of the dentate gyrus, projections have been reported to distribute throughout the extent of the outer two-thirds of the molecular layer and stratum lacunosum –moleculare in CA3. It is important though that in all species information from functionally different entorhinal domains converges onto a single population of dentate and CA3 cells.

EC Projections to CA1 and Sub

Layer III of the EC contributes a second component to the perforant path that selectively targets CA1 and the Sub (Fig. 3). Axons originating from the LEC and the MEC show strikingly different terminal patterns, but unlike the layer II projections, the difference is not along the radial axis but along the transverse axis. The projection that arises from the LEC selectively targets neurons in the distal part of CA1 (the part closest to the Sub) and in the adjacent proximal part of the Sub. In contrast, the projection from the MEC distributes selectively to the proximal CA1 and the distal Sub (Figs. 3, 4).[6] In their respective target domain, entorhinal fibres completely cover the radial extent of stratum lacunosum-moleculare of CA1 and the other portion of the molecular layer of the Sub.

In addition to the main innervations arising from layers II and III in the EC, a projection originating from deep layers has been described as well. In the DG, this deep layer component preferentially distributes to the inner portion of the molecular layer, the granule cell layer as well as the subgranular, hilar zone, where it establishes asymmetrical synapses onto granule cell dendrites as well as on their somata and onto spine-free dendrites in the subgranular zone. The latter most likely represent dendrites of interneurons (Fig. 4). In the other divisions of the HF, details on the distribution of this deep pathway are lacking.

Also, weak inputs from the PrS and PaS reach all hippocampal subfields, where they terminate throughout stratum moleculare/lacunosum-moleculare, overlapping with the inputs from the EC. The CA1 and Sub receive additional inputs from the perirhinal (PER) and postrhinal cortices (POR). The inputs from the PER and POR show a topology along the transverse axis comparable to that seen in case of the projections from the LEC and MEC, respectively. However, both projections have a strong preference for the extremes, such that the PER project to the most distal part of CA1 and the most proximal part of the SUB and the projections from the POR favour the opposite extremes.

Synaptic Organization

In the rat, a majority of the terminals of the perforant path fibres (around 90%) form asymmetric synapses and thus likely are excitatory, and no major differences have been reported between the lateral and medial components of the pathway. Fibres contact most frequently dendritic spines of dentate granule cells or of pyramidal cells in the CA fields and the Sub. A small proportion of the presumed excitatory

[6]In rodents, the layer II components from the LEC and the MEC apparently do not overlap with respect to their respective terminal zone in the molecular layer of the DG and likely the same holds true for CA3. It has not been established whether the same holds true for the respective layer III components, i.e. whether or not they have a zone of overlap in the centre part of CA1 or the Sub.

perforant path fibres terminate on non-spiny dendrites of presumed interneurons. In addition, a small proportion of the perforant path synapses is symmetrical, indicative of their inhibitory nature, and these likely target both interneurons and principal cells alike.

In the DG, entorhinal synapses make up at least 85% of the total synaptic population, and they target mainly apical dendrites of granule cells. Interneurons that are innervated are those positive for parvalbumin, as well as those positive for somatostatin and NPY. No details have been reported for the CA3, but on the basis of quantitative analyses on reconstructed single neurons (Matsuda et al., 2004), one may assume that a large majority of the excitatory entorhinal fibres terminate on spines, i.e. indicating synapses with pyramidal cells, and only a minor percentage terminate on shafts, taken to indicate presumed contacts with interneurons. Although in the stratum lacunosum-moleculare of the CA3 inhibitory terminals make up approximately 10% of the total population, it has not been established whether these all belong to local interneurons or whether part of them have an entorhinal origin. No studies to date have looked into possible interneuron targets for perforant path fibres in the CA3. In stratum lacunosum-moleculare of the CA1, about 15% of the total population of synapses is inhibitory, and the other 85% are excitatory. Unlike the situation in the DG and CA3 where most if not all of the synapses in stratum moleculare/lacunosum-moleculare are of entorhinal origin, in the CA1 the total population of excitatory terminals likely have three different origins, the EC, thalamic midline nuclei such as nucleus reuniens and the amygdala.[7] Regarding entorhinal inputs, over 90% is asymmetrical, i.e. excitatory terminating on spines, and around 5% is excitatory terminating on shafts. Almost no symmetrical, i.e. inhibitory entorhinal fibres have been reported in CA1. The terminals on shafts likely indicate that interneurons are among the targets and recently interneurons that reside at the interface between strata lacunosum-moleculare and radiatum have been identified as recipients of entorhinal input.

In the Sub, the situation in the superficial half of the molecular layer is likely to be comparable to that in stratum lacunosum-moleculare of CA1 with the adding complexity of having even more inputs distributing here, including those from PrS and PER/POR. Of the entorhinal synapses, over 90% is excitatory and 80% terminates on spines and 10% on dendritic shafts, likely of interneurons, including those containing the calcium-binding protein parvalbumin, and the remaining are symmetrical terminals. The postsynaptic targets have not been identified anatomically, but electrophysiological data indicate that pyramidal cells that project back to EC are among the targets, an observation that has not been corroborated by anatomical findings (own unpublished data).

[7] Amygdala inputs reach only the ventral two-thirds of the CA1 and the Sub. The dorsal one-third of both fields is devoid of input from the amygdala.

Projections from CA1 and Subiculum to Entorhinal Cortex

Transverse and Laminar Organization

The dentate gyrus and CA3 field of the hippocampus do not project back to EC. Thus, the recipients of the layer II projection do not have any direct influence over the activities of EC. It is only after the layer II and layer III projection systems are combined in CA1 and Sub that return projections to EC are generated. The return projections mainly terminate in the deep layers (V and VI) although a component ascends into the superficial layers. The main targets of these output projections are in layer V, where likely two or three different subgroups of principal neurons reside. The cells in the deeper part, referred to as layer Vb, stain positive for the transcription factor Ctip 2, whereas those in the superficial layer Va stain for Etv1. Projections from CA1 mainly target neurons in layer Vb, whereas subicular output seems to target both layers. Whereas neurons in Va originate the main extrinsic projection system of EC, those in Vb project preferentially intrinsically, targeting layers Va, III and II (Fig. 5). In case of the projections from the Sub, up to 93% of fibres form asymmetrical, i.e. excitatory synapses onto dendritic spines (68%) and

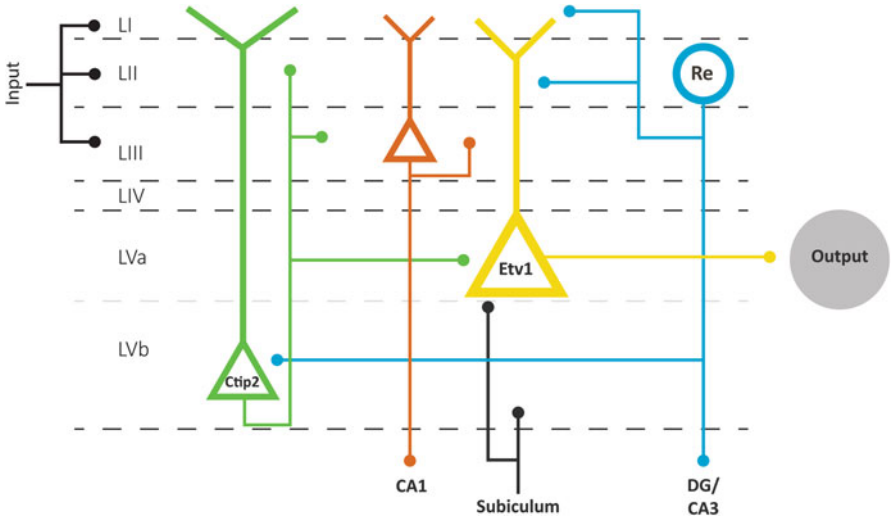

Fig. 5 Wiring diagram of some of the main intrinsic and extrinsic connections of EC. Reelin-positive layer II neurons project to DG, CA3 (and CA2), whereas neurons in layer III project to CA1 (and subiculum). Return projections from CA1 target mainly neurons in layer Vb, whereas those from the subiculum distribute to both Vb and Va. Neurons in layer Vb give rise to strong intrinsic connections to layers Va, III-I. Note that the intrinsic component originating from layer II calbindin-positive neurons is not indicated (Modified with permission from Witter et al. 2017a, Front Syst Neurosci. 11: 46)

onto shafts (23%). A small proportion (7%) forms symmetrical synapses, equally onto dendritic shafts and spines.

In addition, electrophysiological evidence indicates that among the target cells are neurons in layer V that project to layers II and III of the EC (see section on "Entorhinal Associational and Commissural System"). It is relevant to point to the fact that the projections from CA1 and the Sub to the EC show a topology along the transverse or proximodistal axis. The projections from the proximal part of CA1 and the distal part of the Sub distribute exclusively to the MEC, whereas cells located in the distal part of CA1 and the proximal part of the Sub project mainly to the LEC. In this way the return projections thus maintain the topography displayed by the input projections from the MEC and the LEC (Figs. 3 and 4).

Longitudinal Organization

In addition to the radial and transverse organization of the layer II and layer III projections, respectively, as described above, all connections between the EC and the HF show a striking topology along the long axis of the HF. Both the projections from and to the EC follow the same principle in that lateral and posterior parts of the EC are connected to the dorsal portion of the HF, whereas increasingly more medial and anterior parts of the EC are connected to more ventral parts of the HF (Fig. 6). It is relevant to point out that this topographical organization is indeed a gradual one such that a small portion of the EC may distribute axons over up to 25–30% of the long axis of the HF and likewise a small part of CA1 and the Sub may distribute axons to a rather extensive area of the EC.

When taking the transverse and longitudinal organization into account, the important point emerges that these return projections from CA1 and the Sub are

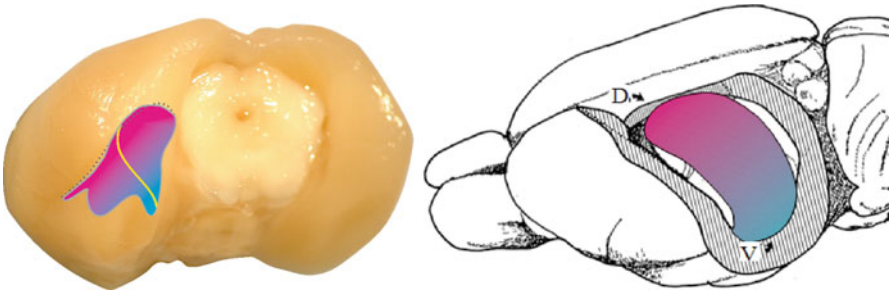

Fig. 6 Longitudinal organization of entorhinal-hippocampal connectivity. A dorsolateral–to–ventromedial gradient in the EC (left-hand side; magenta to blue) corresponds to a dorsal–to–ventral gradient in the HF (right-hand side). Note that the topology in the EC cuts across the MEC-LEC border indicated with the yellow line (left-hand side, modified with permission from Fyhn et al. 2004, Science 305: 1258–1264; right-hand side, modified with permission from Amaral and Witter 1989, Neuroscience 31: 571–591)

exactly in register, i.e. they are point-to-point reciprocal, with the entorhinal inputs to these areas. This remarkable topography confirms the critical role of the EC with respect to the input to, and output from, the HF.

Entorhinal Associational and Commissural System

The EC harbours an extensive, well-developed, yet largely underestimated network of intrinsic connections. There are three prevailing organizational principles that govern the overall organization. First, columnar-like projections emanate from layer Vb pyramidal cells distributing to the superficial layers Va, III-I (Fig. 5). This projection consists mainly of asymmetrical synapses (95%) which target presumed principal neurons and interneurons in almost equal proportions. Second, longitudinal connectivity prevails over transverse connectivity. The longitudinal projections that originate from a particular layer will preferentially innervate more superficial layers and they tend to be stronger from posterior (i.e. MEC) to anterior (i.e. LEC) than those that travel into the reverse direction. These longitudinal connections seem to originate preferentially from layers Vb and the calbindin-positive neurons in layer II. The transverse connections are much more restricted, and mostly confined to the layer of origin. Fairly strong homotopic commissural projections exist that terminate predominantly in layers I and II.

Connections of the Dentate Gyrus

Mossy Fibre Projections to Hilus and CA3

Dentate granule cells issue a massive projection of so-called mossy fibres to the entire transverse or proximodistal extent of CA3. Mossy fibres provide en passant presynaptic terminals that are unique with respect to size, anatomical complexity and the fact that they are correlated with likely complex postsynaptic specializations called thorny excrescences. On their way to field CA3, these fibres contact a fairly large cell type in the hilus called mossy cells. They also give rise to many small collaterals that target a wide variety of presumed interneurons in the hilus (Fig. 7).

The projections from a single neuron or from a small group of neighbouring neurons distribute axons within a fairly limited longitudinal extent that hardly ever covers more than 400–500 μm and coincides with their level of origin. There is however a noticeable exception, in that mossy fibres abruptly change their course from an overall transverse orientation to a longitudinal one, once they reach the distal end of CA3. The extent of the longitudinal component depends on the dorsoventral level of origin in that granule cells at dorsal levels distribute mossy fibres ventrally for about 2 mm. The more ventral the origin, the less the longitudinal

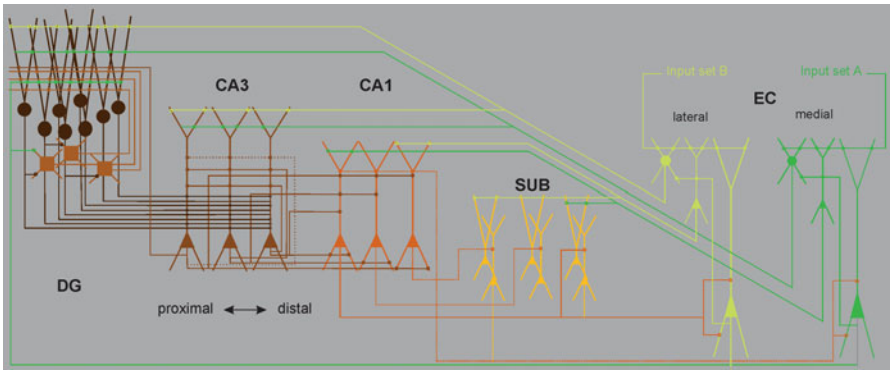

Fig. 7 Wiring diagram, extended version of Fig. 4, illustrating the organization of the intrinsic connections of the HF. Indicated are the mossy fibre projections to the hilus and to the CA3, the return projection from proximal CA3 to the DG and the diminished contribution of proximal CA3 cells to the associate projection (stippled line). Also indicated is the proximodistal organization of the CA1-to-Sub projections as well as the calbindin-positive associative connection in the CA1. Finally, the intrinsic entorhinal connections from layer V to more superficial layers are indicated. (Note that additional associative networks in the CA1 and the Sub have not been indicated; see text for further details)

projection is developed such that granule cells at the ventral DG have little or no longitudinal component. The longitudinal component of the mossy fibre projection appears synaptically indifferent from the transverse component.

The anatomical organization of the mossy fibre projections along the transverse axis indicates that the influence exerted by granule cells on CA3 pyramidals depends on the position along the transverse axis of DG, since the proximal portion of CA3 is innervated preferentially by neurons in the exposed (infrapyramidal) blade, the crest and the adjacent portion of the enclosed (suprapyramidal) blade of the DG. The distal portion of CA3 receives mossy fibre input preferentially from granule cells in the enclosed blade of DG.

Current conceptions of CA3 as having a homogeneously wired architecture are incorrect or at least incomplete. Cells at different transverse positions receive inputs from cells in the DG that in turn are either different in their connectivity or functionally. In addition, at the most distal end of the dorsal part of CA3, a population of CA3 pyramidal cells most likely integrate inputs from the entire dorsal tip of the DG, a feature which is absent at proximal and mid-transverse levels as well as at ventral CA3 levels.

The DG Associational and Commissural System

The mossy cells in turn give rise to axons that bilaterally innervate the inner molecular layer of the DG, thus providing a powerful excitatory input to the

proximal dendrites of the dentate granule cells. Interesting feature of this associational/commissural connection is that it may innervate as much of 65% of the long axis of the DG, but the innervation is weak at the level of origin and increases in density with increasing distance from the origin. Local hilar interneurons provide an inhibitory projection to the outer portions of the molecular layer, and this innervation is largely restricted to the level of origin, thus complimenting the excitatory associational system (see also section on "Neurons, Numbers and Connections").

Connections of CA3

The CA3 to Dentate Projections

In contrast to the well-accepted view that projections within the hippocampal formation are largely if not exclusively unidirectional, implying that CA3 does not project to the DG, there is now substantial evidence to support such projections. These connections have not been described in the initial Golgi and subsequent tracing studies. However, intracellular filling consistently showed that pyramidal cells in the most proximal portion of CA3 embedded within the blades of the dentate granule cell layer issue collaterals that reach the hilar region (Fig. 7). Described as sparse, true at more dorsal levels of the hippocampal formation, at more ventral levels, CA3 neurons actually densely innervate the DG; not only the hilus but numerous CA3 axon collaterals also terminate in the most inner portions of the dentate molecular layer. The increase in density of projections to the DG at ventral levels goes hand in hand with a decreased contribution to the more traditionally known projections to CA1 (see below). Note that also GABAergic projections from CA3 to the DG have been reported.

The CA3 Associational/Commissural System

Local axon collaterals of CA3 axons make preferentially asymmetrical, thus most likely representing excitatory synapses, contacting dendrites of interneurons and importantly also spines of pyramidal cells, thus forming the strong autoassociative network considered to be the characteristic feature of the CA3 network (Fig. 7). The organization of the associational projections from CA3 to CA3 follows a few systematic principles that have been described essentially in two detailed tracing studies using either larger injections of anterogradely transported tracers or intracellular filling of individual CA3 pyramidal cells. Density and extent of local connectivity in CA3 is inversely related to the origin along the proximodistal axis. Irrespective of their dorsoventral position, CA3 pyramidals embedded within the

extent of the DG that, as described contribute to the projection to the DG, do not seem to contribute much to the intrinsic associative system. The associative fibres that do emerge from these CA3 cells are restricted both along the proximodistal axis and along the longitudinal (dorsoventral) axis to the level of the parent cell(s). Cells with an increasingly more distal position in CA3 tend to exhibit increased associational axonal collaterals, extending several hundred microns anterior and posterior to the cell body but restricted along the transverse axis to the region of the parent cell body. The proximodistal origin also apparently relates to the radial distribution of the axons, such that proximal neurons preferentially project to stratum radiatum, whereas axons from increasingly more distal cells distribute more to stratum oriens. To further complicate the connectional matrix, the transverse-radial relation varies along the longitudinal axis.

Single pyramidal cells in CA3 not only distribute axonal branches ipsilaterally but also contralaterally. The detailed topography of the commissural connections has not been as thoroughly investigated as the ipsilateral connections, but it appears an image of the ipsilateral organization for both the projections to CA3 as to CA1 (see below). Also, the synaptic organization of both ipsilateral and commissural projections is quite similar. Note that species differences are present with respect to whether or not the commissural connections are present and if present, how they are organized with respect to their longitudinal and radial distribution.

The CA3 to CA1 System: Schaffer Collaterals

Comparable to the situation in CA3, the postsynaptic targets in CA1 for CA3 fibres comprise both interneurons and pyramidal cells. CA3 projections distribute in stratum radiatum and stratum oriens of CA1, whereas almost no fibres are present in the pyramidal cell layer (Fig. 7). Almost without exception, the longitudinal extent of the projections to CA1 is larger than that of the corresponding associative CA3 projections. Irrespective of the level of origin, projections do extent to levels both dorsal and ventral to the level of origin; however there is a preferential direction of the projections that relates to the transverse level of origin. Neurons with a proximal location, close to or inside the hilus, preferentially project to more dorsal levels, whereas more distal origins result in a shift to more ventral levels. Irrespective of the location of the neuron of origin though, the projections exhibit differences in radial distribution along the long axis of CA1. At more dorsal levels, collaterals tend to be located deeper in stratum radiatum and in stratum oriens, whereas at progressively more ventral levels, the fibres shift towards a more superficial position in stratum radiatum and less dense innervation in stratum oriens. This pattern is thus similar to that described above for the associative CA3-CA3 projections. The transverse position of the parent CA3 neuron does relate, at and around the level of origin to two other features. First, proximal projections tend to distribute somewhat more distally in CA1, and more distal CA3 cells project with some preference to more proximal portions of CA1. Furthermore, proximally originating projections

terminate more superficially in stratum radiatum than distal projections, which distribute deeper in strata radiatum and oriens.

Connections of CA1

The CA1 to CA3 Projection

No excitatory projections from CA1 have been described that systematically target neurons in CA3. All the projections that run counter to the traditional unidirectional view apparently arise from a specific group of long-range GABAergic neurons that are prominently present in CA1. These neurons also provide projections of the DG, the EC and the lateral septum.

The CA1 Associational and Commissural System

Although much weaker than in CA3, there are recurrent connections in CA1. Anterograde tracing and intracellular filling date all consistently show that pyramidal cells in CA1 issue collaterals that distribute throughout strata oriens, pyramidale and radiatum of CA1. Of similar interest are reports on a narrow calbindin-positive bundle of fibres located at the exact border between lacunosum-moleculare and radiatum most likely emerging from calbindin-positive pyramidal cells in the distal part of CA (Fig. 7). The physiological nature and terminal distribution of any of these associational connections need further study before any functional inferences are intelligible.

The CA1 to Subiculum Projection

Principal cells in CA1 give rise to a strong projection to the Sub, terminating on proximal distal and apical dendrites of subicular pyramidal cells, not innervating the outer half of the molecular layer. Both intracellular fills and tracing studies have convincingly shown that this projection shows a marked topology along the transverse axis such that a cell or group of cells in the proximal one-third of CA1 project to the distal one-third of the Sub. Vice versa, cells in the distal CA1 will exclusively target cells in the proximal portion of the Sub, and cells in the centre of CA1 will reach cells in the centre of the Sub. Note that although a single cell will provide a set of axonal collaterals spanning about one-third of the transverse extent of the Sub, a cell with a slightly shifted position will also slightly shift its axonal pattern slightly in the opposite direction (Fig. 7).

The CA1 to Entorhinal Projection

The projection from all parts of the CA1 to the EC and the complex transverse and longitudinal topology have been dealt with already (see section "Projection from CA1 and Subiculum to Entorhinal Cortex"). Also the striking similarities with respect to these topologies with the reciprocal EC-to-CA1 projection have been mentioned (see also below in the next section on "Connections of the Subiculum").

Connections of Subiculum

The Subiculum to CA1 Projection

According to at least two studies, neurons in the pyramidal cell layer of the Sub send axon collaterals into all layers of CA1. The origin of this projection includes superficial pyramidal cells and is likely to form both excitatory and inhibitory terminals on spines and dendritic shafts, respectively. Although no detailed information is available on spread along the transverse or longitudinal axes, the data indicate no marked transverse topography and a restricted longitudinal spread, comparable to the CA1 to CA3 projection.

The Subiculum Associational System

There are at least two types of pyramidal cell types in the Sub that both belong to the group of projection neurons. Both types, the so-called bursters and regular-spiking neurons, contribute to an extensive intrinsic innervation in the Sub. Intracellular filling of electrophysiologically identified bursting cells reveals an axonal distribution that remains within the region circumscribed by their apical dendrites. In contrast, the regular-spiking cells give rise to an axon that shows more widespread distribution along the transverse axis. Since these data have been generated in in vitro slices, it is not known whether similar differences exist with respect to a possible longitudinal spread. The longitudinal spread of the average population of neurons covers approximately 0.5–0.7 mm which is about 7% of the long axis.

The Subiculum to Entorhinal Projection

The projections from the Sub to the EC and the complex transverse and longitudinal topology have been described already (see section "Projection from CA1 and Subiculum to Entorhinal Cortex"). Also the striking similarities with the topological organization of the reciprocal EC-to-Sub projection have been referenced.

Table 1 Quantitative data on principal neurons in the HF and the EC

	# of principal neurons	Dendritic length in μm	% exc and inh synapses	# of synapses/connection
DG Gcl	1.200.000	3.100		
DG hilus	50.000			
CA3	250.000	16.000	88 exc 12 inb	
CA2	12.000 cassell 1980			
CA1	390.000	12.600	95 exc	2.000–3.000 exc EC
			5 inh	12.000 exc CA3
Sub	290.000			
PrS/PaS	700.000			
EC II	110.000			
LEC II	46.000–59.500	Fan 9.300		
	65% fan	Multipol 7.500		
		Pyr 9.800		
MEC II	36.000–66.000			
	67% stellate			
EC III	250.000			
LEC III	153.000	Pyr 11.400		
MEC III	105.000			
EC V and VI	330.000			
LEC V and VI	184.000	Pyr 7.800		
		Hor 8.200		
		Polym 10.900		
MEC V and VI	125.000	Pyr 5.200		
		Hor 7.800		
		Polym 8.300		

Indicated are total number of neurons (# neurons), the average total dendritic length, the percentage of excitatory and inhibitory synapses that impinge on the dendrites and the estimated total number of synapses/input (# synapses/connection)
Sources for information: Amaral et al. (1990), Cameron and McKay (2001), Gatome et al. (2010), Hamam et al. (2000, 2002), Lavenex and Amaral (2007), Matsuda et al. (2004), Megias et al. (2001), Merril et al. (2001), Rapp and Gallagher (1996), Rapp et al. (2002), Rasmussen et al. (1996), Tahvildari and Alonso (2005), West et al. (1991)

Neurons, Numbers and Connections

A number of estimates are available on how many neurons there are in the different areas of the HF and the EC as well as on total dendritic length and number of synapses leading to a number of published attempts addressing questions like how many cells converge on to a single cell and what is the level of divergence for a single cell axons. Although far from complete, in the following section, an attempt is made to summarize those data in rats (Table 1). Note that possible age and strain differences as well as methodological differences are not taken into account.

Numerical estimates have indicated that the population of granule cells may carry a total number of 4.6×10^9 spines of which 77%, i.e. 3.542×10^9, would belong to entorhinal synapses. Taken the total number of entorhinal layer II cells, each of them could potentially contact 32,200 spines. If we would know how many entorhinal inputs target a single granule cell, we would be able to estimate how many granule cells would be innervated by a single layer II cell in the EC, i.e. we should have a numerical estimate of the divergence of this connection. By using published estimations of the number of spines on granular cell dendrites (4600), we could estimate that each granule cell can receive input from maximally 0.77×4600 is 3542 cells in EC or 3542/110.000 is 3.2% of the total layer II population (based on Amaral et al. 1990). Using comparable lines of reasoning, it has been inferred that a single mossy fibre can make as many as 37 synaptic contacts with dendrites of a single CA3 pyramidal cell, a single granule cell may innervate 15 CA3 pyramidal cells, and a single CA3 pyramidal cell may receive convergent input from 72 granule cells. A single CA3 neuron might be innervated by 6000 other CA3 neurons, and a single CA1 cell receives input from 5500 CA3 cells. Details on the Sub and the EC are currently lacking. A final word of caution would be in place since all these numerical estimates assume homogeneity of the network, which most likely will turn out to be a false assumption. For example, it is known that the absolute numbers as well as the percentages of the total population of principal cells and interneurons vary along the long axis of the hippocampus. Also differences in numbers of neurons are obvious for the LEC versus the MEC (Table 1).

A complementary approach would be to look at the overall distribution of the individual connections that make up the region of interest. A single entorhinal neuron may distribute its axon along approximately 25% of the long axis of the HF. It has been estimated that in adult animals, this axis extends for up to 10 mm, so a single axon targets 2.5 mm of the length of the HF. Axons from granular cells are fairly limited in their longitudinal distribution, extending for about 400 μm in CA3c-b but up to 1.5 mm in CA3a. The associational projection from the hilus back into the inner molecular layer extends over 6.5 mm, exhibiting a dramatic drop in density around the level of its origin. Note that some other hilar projections, such as those originating from somatostatin-positive interneurons to the outer portions of the molecular layer, fill that gap. The subsequent projection from CA3 to CA1 shows a longitudinal extent similar to that of the DG association system, whereas the autoassociative connections are slightly more restricted. The projections from a single cell in CA1 to the Sub extend up to 2 mm along the long axis forming a slab-like innervated strip. The associative connections within CA1 apparently are rather restricted along the long axis, whereas currently no data are available for the associational connections in the Sub, be it that they at least extend for 400 μm. Finally the projections from CA1 and the Sub to the EC cover a narrow strip in EC that extends for at least along 60% of the longitudinal extent of either the LEC or the MEC, depending on whether the injection is in proximal or distal part of the Sub, respectively.

Experimental Techniques

Most of what is known today about the pathways that connect neurons in different brain regions has been discovered by using neuroanatomical tract-tracing techniques. Tracers are molecules that are either applied extracellularly or intracellularly. In case of extracellular application, the tracer is taken up by neurons at the injection site and transported or diffused within cells. A tracer substance can be transported anterogradely (e.g. *Phaseolus vulgaris leucoagglutinin*), from the soma towards the axon terminals, retrogradely (e.g. Fast Blue) and from the axon terminals towards the soma, or it can be transported in both directions (e.g. *horseradish peroxidase*). In case of intracellular application, both autofluorescent dyes (e.g. Lucifer yellow, Alexa dyes) and biotin-conjugated dyes are most often used, since they can be easily visualized for fluorescent or transmitted light microscopy (LM). All these methods can be analysed using a variety of microscopical techniques, including to some extent electron microscopy (EM). In the latter case, one quite often combines them with lesions. Small lesions (mechanical, toxins, electrolytic) will result in local degeneration of axon terminals that show up as electron dense material in the EM.

Standard light and confocal techniques, when applied to extracellular tracer deposits, allow the visualization of distribution patterns, including laminar distribution, topologies as well as the identification of likely synaptic relationships. They are poor with respect to quantitative resolution since it is very difficult to control or estimate the number of neurons that take up and transport the tracer. A much more reliable but very time-consuming method is the intracellular filling of single neurons in vivo and the subsequent complete reconstruction of its dendritic and axonal arborizations. This technique can be combined with anterograde or retrograde tracing to identify projection targets and synaptic inputs. A recently added tool is to make use of retrograde labelling with genetically modified viruses that carry the genes for certain fluorescent proteins such that infected cells express the protein throughout their dendritic and sometimes even axonal arborizations. The viral toolkit has expanded enormously and now comprises a number of ways to selectively visualize monosynaptic inputs to identified neurons both at the population and single cell level.

Another powerful approach is to use in vitro slice electrophysiology combined with viral expression of light-sensitive channels. This facilitates the analysis of postsynaptic targets of distant inputs, i.e. those that are difficult, if not impossible to maintain in a slice preparation.

Electron microscopy can be used to visualize whether a presynaptic axon contacts a postsynaptic identified neuron. This is a very accurate but time-consuming method because only small pieces of tissue can be examined at one time. A promising development may be the use of automated systems to do serial reconstructions, at the EM level but also at the LM level, but in all instances, our limited understanding of the mechanisms underlying labelling and transport of tracers seriously hampers our aims to generate quantitative data. The only exception is the high standard of

unbiased methods to count number of cells, synapses and actually any identifiable element in the nervous system, using stereological approaches. But even when applying such sophisticated methods, one has to be aware of differences between strains, effects of age, environment and gender on quantitative estimates. A recent and promising addition is the use of serial EM techniques which have now provided the first very large quantitative datasets on connectivity of small volumes of brain, for example, a recent reconstruction of part of the entorhinal cortex (Schmidt et al. 2017, Nature 549:469).

The Future: Open Questions and How to Address Them

Many conceptual or theoretical accounts and modelling attempts use a rather simple and generalized representation of what we actually know as their starting point. This may eventually lead to disuse of available data, such that these data eventually will be forgotten. Our attempts to understand structure needs to take into account all the subtle differences in topology and densities of projections, the many parallel pathways that are so characteristic of the brain and the many different levels of integration that may occur within the different networks that constitute the HF. It will become relevant to integrate our current insights in the connectional organization of the hippocampus into a new functional framework. To give one example, the current traditional view of the hippocampal network as a unidirectional, sequential series of connections does not credit the wealth of data on parallel EC inputs to all components of HF and the well-established backprojections in the system. The addition of CA2 to the network provides a further complicating factor.

During the last decade, we have learned a lot about EC, the types of principal neurons and their specific connectivity. In addition to data on layer II, more recently data on layer V have become available. Data on layer III are still very sparse as are data on intralaminar interactions. By adding the complexity of the very many specific types of interneurons, our task to describe, to model and to understand EC is still a major challenge. The combination of anatomical and electrophysiological studies, with the use of promising new genetic tools and computational modelling, will provide the foundation for further detailed functional studies in freely behaving animals, which in turn form the ground work to understand the human hippocampus, both when it is healthy and when it starts to break down, as seen in ageing and in several neurodegenerative diseases.

Acknowledgements The revision of this chapter has been supported by the Kavli Foundation, the Centre of Excellence scheme – Centre for Neural Computation and research grant # 191929 and 227769 of the Research Council of Norway and The Egil and Pauline Braathen and Fred Kavli Centre for Cortical Microcircuits.

Resources

http://www.temporal-lobe.com/: online searchable database of hippocampus connectivity and visualization tools
http://www.rbwb.org/: online atlas tools with detailed description of the anatomy of the hippocampal region in the rat
http://neuromorpho.org/index.jsp: index of morphologies of hippocampal neurons

Further Reading

Amaral DG, Witter MP (1989) The three-dimensional organization of the hippocampal formation: a review of anatomical data. Neuroscience 31:571–591
Amaral DG, Ishizuka N, Claiborne B (1990) Neurons, numbers and the hippocampal network. Progr Brain Res 83:1–11
Amaral DG, Scharfman HE, Lavenex P (2007) The dentate gyrus: fundamental neuroanatomical organization (dentate gyrus for dummies). Progr Br Res 163:3–22
Blaabjerg M, Zimmer J (2007) The dentate mossy fibers: structural organization, development and plasticity. Progr Br Res 163:85–107
Cameron HA, McKay RD (2001) Adult neurogenesis produces a large pool of new granule cells in the dentate gyrus. J Comp Neurol 435(4):406–417
Canto CB, Witter MP (2012a) Cellular properties of principal neurons in the rat entorhinal cortex. I The lateral entorhinal cortex. Hippocampus 22:1256–1276
Canto CB, Witter MP (2012b) Cellular properties of principal neurons in the rat entorhinal cortex. II The medial entorhinal cortex. Hippocampus 22:1277–1299
Canto CB, Wouterlood FG, Witter MP (2008) What does the anatomical organization of the entorhinal cortex tell us? Neural Plast 381243
Cappaert NLM, van Strien NM, Witter MP (2015) Hippocampal formation. In: Paxinos G (ed) The rat brain, 4th edn. Elsevier Academic, San Diego/London, pp 511–574
Dudek SM, Alexander GM, Farris S (2016 Feb) Rediscovering area CA2: unique properties and functions. Nat Rev Neurosci 17(2):89–102. https://doi.org/10.1038/nrn.2015.22
Gatome CW et al (2010) Number estimates of neuronal phenotypes in layer II of the medial entorhinal cortex of rat and mouse. Neuroscience 170:156
Hamam BN et al (2000) Morphological and electrophysiological characteristics of layer V neurons of the rat medial entorhinal cortex. J Comp Neurol 418:457
Haman BN et al (2002) Morphological and electrophysiological characteristics of layer V neurons of the rat lateral entorhinal cortex. J Comp Neurol 451:45
Jones MW, McHugh TJ (2011 Oct) Updating hippocampal representations: CA2 joins the circuit. Trends Neurosci 34(10):526–535. https://doi.org/10.1016/j.tins.2011.07.007
Klausberger T, Somogyi P (2008) Neuronal diversity and temporal dynamics: the unity of hippocampal circuit operations. Science 321:53–57
Lavenex P, Amaral DG (2000) Hippocampal-neocortical interaction: a hierarchy of associativity. Hippocampus 10:420
Matsuda S, Kobayashi Y, Ishizuka N (2004) A quantitative analysis of the laminar distribution of synaptic boutons in field CA3 of the rat hippocampus. Neurosci Res 29:241–252
Megias M, Emri ZS, Freund TF, Gulyas AI (2001) Total number and distribution of inhibitory and excitatory synapses on hippocampal CA1 pyramidal cells. Neuroscience 102:527–540
Merril DA, Chiba AA, Tuszynski MH (2001) Conservation of neuronal number and size in the entorhinal cortex in behaviorally characterized aged rats. J Comp Neurol 438:445–456
Rapp PR, Gallagher M (1996) Preserved neuron number in the hippocampus of aged rats with spatial learning deficits. Proc Natl Acad Sci U S A 93:9926–9930

Rapp PR, Deroche PS, Mao Y, Burwell RD (2002) Neuron number in the parahippocampal region is preserved in aged rats with spatial learning deficits. Cer Ctx 12:1171–1179
Rasmussen T, Schliemann T, Sørensen JC, Zimmer J, West MJ (1996) Memory impaired aged rats: no loss of principal hippocampal and subicular neurons. Neurobiol Ageing 17:143–147
Strange B, Witter MP, Moser EI, Lein E (2014) Functional organization of the hippocampal longitudinal axis. Nat Rev Neurosci 15:655–669
Tahvildari B, Alonso A (2005) Morphological and electrophysiological properties of lateral entorhinal cortex layers II and III principal neurons. J Comp Neurol 491:123
Van Strien NM, Cappeart N, Witter MP (2009) The anatomy of memory: an interactive overview of the parahippocampal-hippocampal network. Nat Rev Neurosci 10:272–282
West MJ et al (1991) Unbiased stereological estimation of the total number of neurons in thesubdivisions of the rat hippocampus using the optical fractionator. Anat Rec 231:482
Wickersham IR, Finke S, Conzelmann KK, Callaway EM (2007) Retrograde neuronal tracing with a deletion-mutant rabies virus. Nat Methods 4:47–49
Witter MP (2006) Connections of the subiculum of the rat: topography in relation to columnar and laminar organization. Behav Brain Res 174(2):251–264
Witter MP (2007a) Intrinsic and extrinsic wiring of CA3; indications for connectional heterogeneity. Learn Mem 14:705–713
Witter MP (2007b) The Perforant path. Projections from the entorhinal cortex to the dentate gyrus. Progr Br Res 163:43–61
Witter MP, Groenewegen HJ, Lopes da Silva FH, Lohman AHM (1989) Functional organization of the extrinsic and intrinsic circuitry of the parahippocampal region. Prog Neurobiol 33:161–253
Witter MP, Canto CB, Couey JJ, Koganezawa N, O'Reilly K (2014) Architecture of spatial circuits in the hippocampal region. Phil Trans R Soc B 369:20120515
Witter MP, Doan TP, Jacobsen B, Nilssen ES, Ohara S (2017a) Architecture of the entorhinal cortex. A review of entorhinal anatomy in rodents with some comparative notes. Front Syst Neurosci 11:46. https://doi.org/10.3389/fnsys.2017.00046
Witter MP, Kleven H, Kobro Flatmoen A (2017b) Comparative contemplations on the hippocampus. Brain Behav Evol 90:15–24. https://doi.org/10.1159/000475703
Zhang S-J, Ye J, Couey JJ, Witter MP, Moser EI, Moser M-B (2014) Functional connectivity of the entorhinal-hippocampal space circuit. Phil Trans R Soc B 369:20120516

Morphology of Hippocampal Neurons

Imre Vida, Claudius E. Degro, and Sam A. Booker

Overview

"Form follows function" states the credo of modern architecture, defining how the shape of an object should be determined by its function. While natural objects, such as neurons, have not taken their shape from design boards, the inquisitive observer can nevertheless gain insights about their function by studying morphological features. This teleological mindset was the main driving force behind the early neuroanatomical investigations, which culminated in the work of Cajal and formed the foundation of modern neuroscience. Neuroanatomical analysis remains an essential part of neuroscience research today and computational neuroscientists particularly benefit from the flow of morphological data, with increasing detail and resolution.

Nerve cells or neurons are the structural and functional units of the nervous system and come in various sizes and shapes, conceivably reflecting differences in the functional roles played by them in brain circuits. On the one hand, the distribution of dendrites and axon determines the synaptic inputs and available targets to cells. On the other hand, the three-dimensional structure of neuronal processes constitutes the cable structure in which signals are integrated and processed.

Neurons in cortical areas, including the hippocampus, can be broadly divided into two major classes: principal cells and non-principal cells or interneurons. Principal cells comprise the majority (~80–90%) of the neuronal population with area-specific morphological features. While they are regarded largely homogeneous

I. Vida (✉) · C. E. Degro
Institute for Integrative Neuroanatomy, Charité – Universitätsmedizin Berlin, Berlin, Germany
e-mail: imre.vida@charite.de

S. A. Booker
Centre for Discovery Brain Sciences, University of Edinburgh, Edinburgh, UK

V. Cutsuridis et al. (eds.), *Hippocampal Microcircuits*, Springer Series in Computational Neuroscience, https://doi.org/10.1007/978-3-319-99103-0_2

within an area, there is increasing evidence for position-dependent differences in their properties. Cortical principal cells are excitatory glutamatergic neurons and are considered to be the workhorse of information processing. They send axon collaterals to other brain areas and therefore are also referred to as "projection neurons." Interneurons are inhibitory, GABAergic, cells and are characterized by dense local axonal arbor which enables them to control and coordinate the activity of large populations of local neurons. Although interneurons comprise only a small proportion of the neuronal population (~10–20%), they display a high degree of morphological heterogeneity and can be subdivided into a number of types. The diversity of the interneurons conceivably serves a division of labor in spatiotemporal control of principal cell activity, much like a conductor leading an orchestra.

In this chapter we will review the morphological characteristics and local connectivity of the various neuron types in the hippocampus of rodents. Although due to the possibilities offered by genetically modified organisms and elegant optogenetic approaches, studies more commonly use mice nowadays, the majority of the cellular level data available in the literature are still from the rat hippocampus.

The Data

Anatomical Structure and Nomenclature

The hippocampus is a phylogenetically ancient cortical structure ("archicortex") which evolved from the dorsomedial aspects of the cerebral hemispheres. It consists of two interlocked folds of the cortical mantel, the hippocampus proper and the dentate gyrus (DG; Cajal 1968; Lorente de Nó 1934). Macroscopically the curved structure of the hippocampus bears some resemblance to the horns of a ram, hence the Latin *cornu ammonis* (CA). Its cranial ("septal") pole is located close to the midline in the dorsal part of the hemisphere, below the *corpus callosum*, whereas its caudal ("temporal") pole extends ventrolaterally into the temporal lobes (see Fig. 1 in the chapter "Connectivity of the Hippocampus").

In cross section, the hippocampus proper (CA areas) and the DG form two interlocked "C" shapes (Fig. 1). The hippocampus proper features pyramidal cells and can be cytoarchitecturally divided into the CA1, CA2, and CA3 areas. Lorente de Nó (1934) further subdivided the CA1 and CA3 areas to three zones along the transverse axis: "a" (closer to the subiculum), "b," and "c" (closer to the hilus) on the basis of their anatomical connectivity. In contrast to the CA regions, the DG comprises a population of granule cells (GC) as principal neurons. The interface between the DG and CA areas is called the *hilus* which contains a third population of principal cells, the mossy cells. The *hilus* differs from other parts of the hippocampus in that it shows no clear lamination, and the ratio of principal cells and interneurons is close to equal. It has been a matter of some controversy whether it belongs to the hippocampus proper as a CA4 area (Lorente de Nó 1934) or to the

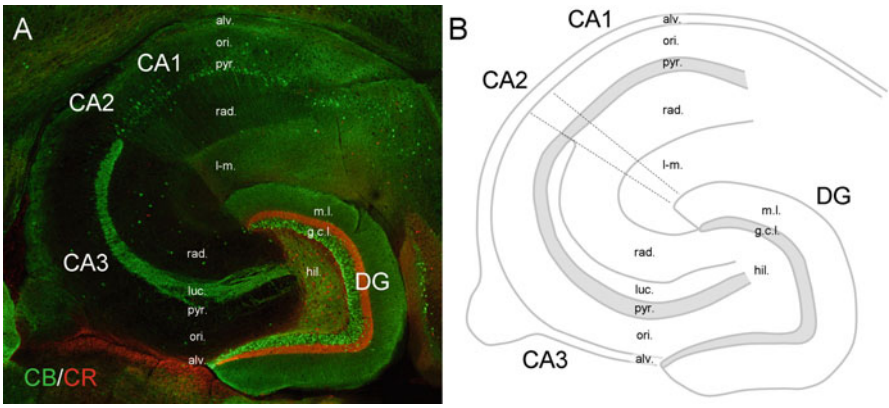

Fig. 1 Areas and layering of the hippocampus. (**a**)Transverse section from the ventral mouse hippocampus immunolabeled for the calcium-binding proteins calbindin (CB, *green*) and calretinin (CR, *red*). CB is expressed by GCs and a subset of CA1 pyramidal cells. Therefore the DG and the CA1 area show labeling of the cell bodies and a homogeneous staining of the dendritic layers. In the CA3 area, the narrow band of GC axons (the mossy fibers) is labeled in the *str. lucidum* (luc.). CR immunostaining labels mossy cells in the hilus (hil.) and delineates the termination of their axon in the inner third of the molecular layer (m.l.) of the mouse hippocampus. In addition to principal cells, a subset of interneurons scattered throughout the hippocampus can be seen labeled by either CB or CR. (**b**) Schematic drawing of the areas and layers of the hippocampus. Abbreviations: alv., alveus; ori., str. oriens; pyr., str. pyramidale; rad., str. radiatum; l-m., str. lacunosum-moleculare; g.c.l., granule cell layer. *Dashed lines* indicate borders between the CA areas

DG as a "polymorphic layer" (Blackstad 1956; Amaral 1978). Because of the tight mutual connectivity, the general consensus seems to favor the latter hypothesis, with the term CA4 no longer used. Nevertheless, the *hilus* is often silently regarded as an area on its own right.

The hippocampus displays a strict laminar structure (Förster et al. 2006; Fig. 1). Principal cells are tightly aligned and their somata form well-defined layers, the *stratum (str.) pyramidale* in the CA areas and the granule cell layer in the DG. The multiple curvatures of the hippocampus mean that the orientation of principal cells depends on their position along the septotemporal and transverse axes. Vertical positions are therefore referenced to the main axis of the principal neurons. The neuropil in the CA areas is subdivided into three major layers (from basal to apical direction): (1) the *str. oriens*, which is below the cell body layer; (2) the *str. radiatum* above the cell body layer; and (3) the *str. lacunosum-moleculare*. The *str. oriens* and *radiatum* are the innervation zones for the ipsilateral associational fibers (including the *Schaffer collaterals*) and the contralateral commissural axons originating in the CA3 areas. The *str. lacunosum-moleculare* is the layer in which the perforant and temporoammonic path axons from the entorhinal cortex terminate. The *str. lacunosum-moleculare* can be further divided into the *str. lacunosum* (being the common location of dendritic bifurcation) and the *str. moleculare* (location of distal dendritic tuft). In the CA3 area, there is an additional narrow layer, the *str. lucidum*,

immediately above the cell body layer where projections from the mossy fibers of the DG terminate (for further details on connectivity, see chapter "Connectivity of the Hippocampus"). Finally, a layer of white matter consisting of afferent and efferent axons, the alveus, is found below *str. oriens*.

In the DG, the neuropil above the granule cell layer forms the molecular layer (ML). Similar to CA3, commissural/associational axons originating primarily from hilar mossy cells terminate proximally in the inner third of the molecular layer (inner molecular layer, iML) and perforant path axons from either lateral or medial entorhinal cortex innervate the middle (mML) and the outer third (oML) of the ML, respectively. As noted above, the area beneath the cell body layer is regarded as the polymorphic layer (or hilus) of the DG; however, GCs have no basal dendrites and only their axons extend into that region.

Principal Cells

Principal cells of the hippocampus include the pyramidal cells of the CA areas, GCs of the DG, and mossy cells of the hilus, each of which is largely homogeneous, but each possesses subtle anatomical, molecular, and genetic variations.

CA1 Pyramidal Cells

Pyramidal cells of the CA1 are one of the most-investigated types of neurons in the brain. The number of pyramidal cells in the rat CA1 has been estimated to be on the order of 3.2–3.5 $\times$ 10^5 (unilateral values from male Wistar rats, Hosseini-Sharifabad and Nyengaard 2007, or Sprague-Dawley rats, Miettinen et al. 2012). These neurons are characterized by a pyramid-shaped or ovoid soma, a large-caliber apical dendrite, and a number of small-caliber basal dendrites (Fig. 2a, b). Cell bodies of CA1 pyramidal cells are typically found in the cell body layer (*str. pyramidale*) or in proximal *str. oriens*. The *str. pyramidale* of the CA1 area has been subdivided in a superficial compact layer with one to two dense rows of pyramidal cells and a deep loosely packed layer of scattered cell bodies (Lorente de Nó 1934; Slomianka et al. 2011). As mentioned above, increasing evidence indicate that CA1 pyramidal cells do not constitute a uniform cell type throughout the region, rather differ remarkably in their physiological characteristics (Graves et al. 2012). Beyond that, superficial and deep cells have been recently found to differ in their internal and external excitatory and inhibitory connectivity as well as their functional properties (Mizuseki et al. 2011; Lee et al. 2014; Masurkar et al. 2017). Moreover, a population of displaced pyramidal cells has been identified in *str. radiatum* (Cajal 1968; Gulyás et al. 1998), which possess certain unique physiological properties and projection patterns (Christie et al. 2000; Bullis et al. 2007).

The cell bodies of CA1 pyramidal cells have a diameter of $\sim$15 μm and a surface area of 465 $\pm$ 50 μm^2 (Megías et al. 2001). The apical dendrites (typically 1,

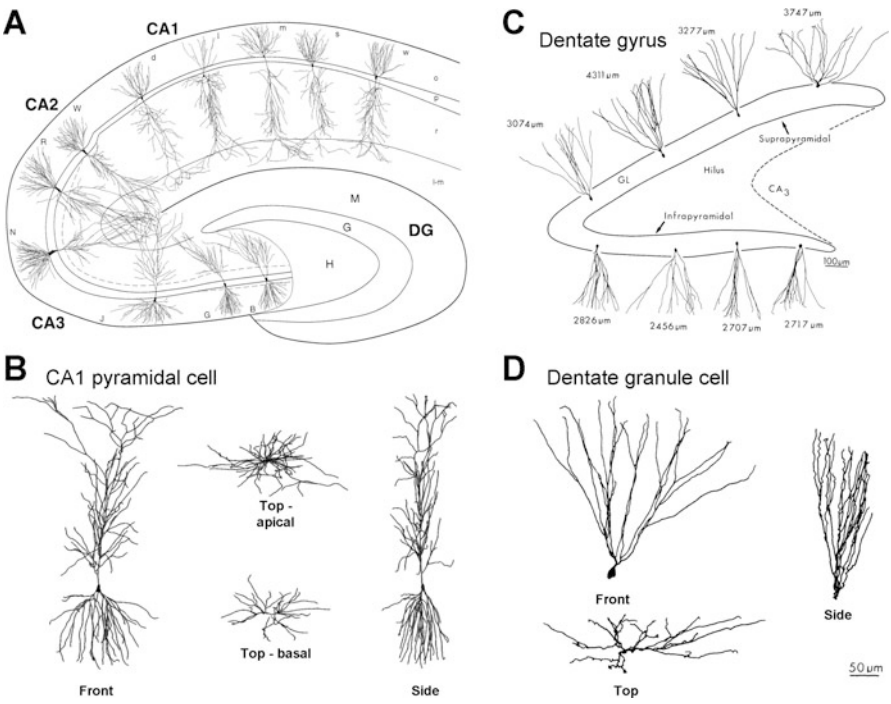

Fig. 2 Morphology of hippocampal principal cells. (**a**) Pyramidal cells of the CA1, CA2, and CA3 area. (**b**) Three-dimensional structure of a CA1 pyramidal cell illustrated from frontal, side, and top views. (**c**) Morphological diversity of DG GCs. Values adjacent to the cells indicate the total dendritic length. Note the difference between the upper (suprapyramidal) and lower (infrapyramidal) blades. (**d**) Three-dimensional structure of a GC illustrated from frontal, side, and top views (**a**, **b** from Ishizuka et al. 1995; **c**, **d** from Claiborne et al. 1990, reproduced with permission. © J. Wiley & Sons)

occasionally 2, or even 3 primary branches) extend into *str. radiatum* with between 9 and 30 oblique side branches in this layer (Bannister and Larkman 1995a). They end with a bifurcation at the border of *str. radiatum* and *str. lacunosum* and form a dendritic tuft in *str. lacunosum-moleculare*. Two to eight basal dendrites emerge from the base of the cell body in the *str. oriens*. These dendrites bifurcate repeatedly close to the soma and the long terminal branches run toward the alveus.

The total dendritic length of CA1 pyramidal cells has been reported to be in the range of 11.5 and 17.5 mm (Table 1). The considerable variability could be due to differences in the strain, sex, and age of the rats, as well as the experimental approach used in the studies (i.e., in vitro vs. in vivo labeling, correction for shrinkage). Corresponding estimates of the somatodendritic surface area are 28,860 and 36,000 μm^2, excluding dendritic spines (Bannister and Larkman 1995b, Cannon et al. 1999; Table 1). However, dendrites of CA1 pyramidal cells are densely covered with spines and they can significantly influence the calculated surface area.

Table 1 Dendritic length and somatodendritic surface area of CA1 pyramidal cells

Layer	Dendritic length (μm)	% of dendrites	Surface area (μm^2)	Reference/rat strain, age
Total	13,424 ± 1061			Ishizuka et al. (1995)
L-M	2531 ± 571	18.8%		Sprague-Dawley, 33–57 days
Rad	6307 ± 975	47.0%		In vitro labeling
Ori	4586 ± 935	34.2%		
Total	16,300 ± 4330			Pyapali et al. (1998)
Apical	11,300 ± 4080	69.5%		Fischer 344, 2 months
Basal	5070 ± 1160	30.5%		In vitro labeling
Total	17,400 ± 3900			Pyapali et al. (1998)
Apical	10,600 ± 2450	60.9%		Sprague-Dawley, 2–8 months
Basal	6890 ± 2110	39.1%		In vivo labeling
Total	11,915 ± 1030		28,860 ±3102	Bannister and Larkman (1995a)
L-M	2259 ± 526	19%		Sprague-Dawley, male 100–150 g
Rad	4118 ± 1203	35%		In vitro labeling
Ori/Pyr	5538 ± 943	47%		
Total	17,400 ± 6200		36,100 ± 17,00	Cannon et al. (1999)

				Sprague-Dawley, 2–8 months In vivo labeling
Total	11,549 ± 2010			Megías et al. (2001)
L-M	2712 ± 873	23.5%		Wistar, male, ~300 g
Rad	4638 ± 1022	40.2%		In vivo labeling
Ori/Pyr	4198 ± 1056	36.3%		
Total	12,808 ± 1541		67,102 ± 10,953	Ambros-Ingerson and Holmes (2005) adapted from Carnevale et al. (1997)
Apical	7943 ± 1526	62%		Sprague-Dawley, 42–368 days
Soma	40 ± 9	0%		In vitro labeling
Basal	4826 ± 995	38%		
Total	14,472 ± 2539			Buckmaster (2012) Sprague-Dawley, adults In vivo labeling
Total	8810 ± 1719		64,208 ± 15,087	Degro et al. (2015) Wistar, 3–4 weeks In vitro labeling

Values are mean ± S.D. Surface area is given without spines

The total number of spines has been estimated to be over 30,000 (Bannister and Larkman 1995b, Megías et al. 2001; see Table 2). Bannister and Larkman (1995b) calculated that spines increase the dendritic surface area by a factor of 0.89 in CA1 pyramidal cells. The distribution of spines is not homogeneous on the dendritic surface: spine density is highest in *str. oriens* and *radiatum* with values between 1.26 and 1.43 μm^{-2} and lower with 0.6 μm^{-2} in *str. lacunosum-moleculare* (Bannister and Larkman 1995b). These surface density values correspond to a linear, length density of 7.5 μm^{-1} on the apical trunk, 2.4–3.2 μm^{-1} on basal and oblique dendrites, and 1.4 μm^{-1} on dendrites of the apical tuft (Bannister and Larkman 1995b); these values are in good agreement with electron microscopic estimates of spine density (Harris et al. 1992). Interestingly, spines in *str. lacunosum-moleculare* are more often contacted by the same presynaptic axon, forming clustered synapses, than for *str. radiatum* spines (Bloss et al. 2018).

Spines serve as postsynaptic targets primarily for glutamatergic terminals; therefore their high numbers indicate a massive excitatory synaptic input to these cells. In fact, in a detailed morphological study, Megías et al. (2001) showed that on average ~30,600 terminals converge and form asymmetrical, putative excitatory synapses onto a single CA1 pyramidal cell in the rat (Table 2), whereas in the mouse, this value is substantially lower on the order of 10,000 (Bloss et al. 2016; Table 3). Over 99% of these asymmetrical synapses are located on dendritic spines, although in the *str. lacunosum-moleculare*, up to 17% of the synapses can be found on dendritic shafts. Somata of pyramidal cells are devoid of excitatory synapses (Fig. 3). Interestingly, superficial and deep pyramidal cells in the mouse differ with respect to the density of spines in s*tr. lacunosum-moleculare:* deep pyramidal cells have 50% fewer spines in CA1a corresponding to fewer medial entorhinal cortex inputs, whereas in CA1c deep pyramidal cells have higher spine density, reflecting a higher incidence of medial entorhinal inputs (Masurkar et al. 2017).

The number of symmetrical, putative inhibitory synapses formed by GABA-immunopositive boutons is much lower. A single neuron receives ~1700 symmetrical synapses, which correspond to only 5.6% of the total number (Megías et al. 2001). In contrast to excitatory synapses, a large proportion (40%) of inhibitory synapses are found in the perisomatic domain, with 7% of the synapses located on the soma and the axon initial segment and 33% on proximal dendrites. In these compartments, inhibitory synapses comprise 50–100% of all synapses. In contrast, on dendrites in the *str. radiatum* and *oriens*, the proportion of these synapses is only 4–5%. Interestingly, on distal apical dendrites in the *str. lacunosum-moleculare*, the proportion increases again to 16% (see Table 2). On the dendrites, almost all (>98%) inhibitory terminals form contacts with shafts. However, as an exception to this rule, in the str. lacunosum-moleculare, 10–20% of the inhibitory synapses have been found on spines (Megías et al. 2001).

The axon of CA1 pyramidal cells with origin at the axon initial segment (AIS) emerges from either the soma or a proximal dendrite, with equal likelihood (Thome et al. 2014). Action potentials are preferentially generated in AIS, with the initiation site localized in the distal half, and backpropagate to the soma and dendrites (Stuart and Sakmann 1994; Palmer and Stuart 2006). If the AIS is found on a dendrite,

Table 2 Laminar distribution of excitatory and inhibitory synapses on CA1 pyramidal cells in the rat

Layer	Spines	% of total	Synapses	GABA(−) synapses	% within layer	GABA(+) synapses	% within layer
Total	30,382 ± 5214		32,351 ± 5486	30,637 ± 5259	94.7%	1713 ± 261	5.3%
L-M	1521 ± 541	5.0%	2110 ± 726	1776 ± 613	84.2%	334 ± 113	15.8%
Rad	16,878 ± 3964	55.6%	17,619 ± 4085	16,878 ± 3964	95.8%	741 ± 126	4.2%
Ori	11,982 ± 3164	39.4%	12,621 ± 3292	11,982 ± 3164	94.9%	639 ± 147	5.1%
Soma	N/A	N/A	92 ± 12	0	0%	92 ± 12	100%
AIS	N/A	N/A	24 ± 2	0	0%	24 ± 2	100%

Percentage values for the spines indicate the proportions found in the different layers; percentages after synapse numbers indicate the proportion of putative excitatory GABA-immunonegative (GABA(−)) and GABA-positive (GABA(+)) synapses. Data from Megías et al. (2001)

Table 3 Laminar distribution of excitatory and inhibitory synapses on CA1 pyramidal cells in the mouse

Layer	Spines	% of total	GABA(+) synapses	% within layer
Total	9537		560	5.3%
L-M	1300	13.6%	287 (51,3%)	51.3%
Rad	4998	52.4%	113 (20,2%)	20.2%
Ori	3239	34.0%	160 (28,6%)	28.6%
Soma	N/A			
AIS	N/A			

Values represent estimated numbers of synapses D. Percentage values for the spines indicate the proportions found in the different layers. Data from Bloss et al. (2016)

action potentials will occur earlier in the "privileged" dendrite than in the soma or other dendrites of the neuron (Thome et al. 2014). The main axon collateral runs in the alveus and is directed toward the fimbria/fornix, forming long-range connections with the subiculum, entorhinal cortex, amygdala, prefrontal cortex, as well as many other cortical regions (see chapter "Connectivity of the Hippocampus"). Although the extent of local arborization is limited, axon collaterals are present in the *str. oriens* and to a lesser degree in the radiatum. These collaterals provide a major excitatory input to interneurons providing feedback inhibition, in particular to somatostatin-immunopositive O-LM interneurons (Blasco-Ibáñez and Freund 1995; Katona et al. 1999a; Csicsvari et al. 1998; Maccaferri et al. 2000) but other interneuron subtypes as well (Ali and Thomson 1998, Takács et al. 2012). Additionally, these collaterals also form synapses onto neighboring pyramidal cells; however this recurrent connectivity in the CA1 area is very low at only ∼1% (Deuchars and Thomson 1996).

Positional Differences in the Anatomical, Molecular, and Functional Properties of CA1 Pyramidal Cells Along the Medio-Distal and Septotemporal Axes

CA1 pyramidal cells were long considered to constitute a largely homogeneous population; however, increasing evidence points to a stronger heterogeneity of these neurons. In particular, position-dependent effects were observed along all three

Fig. 3 (continued) In the *str. lacunosum-moleculare*, three subclasses of dendrites were identified on the basis of diameter and spine density: thick dendrites possessed fewer spines (l-m/thick), intermediate sparsely spinous (l-m/medium), and more distal thin and nearly spine-free dendrites (l-m/thin). For every dendritic subclass, the density of asymmetrical, putative excitatory and symmetrical, putative inhibitory synapses (*boxes*, left and middle numbers, respectively [μm^{-1}]) and the proportion of symmetrical synapses (*boxes*, right number) are shown. Values below the *boxes* indicate total length (mean ± S.D.) and diameter (mean and range in μm) (Modified from Megías et al. 2001 with permission. © Elsevier)

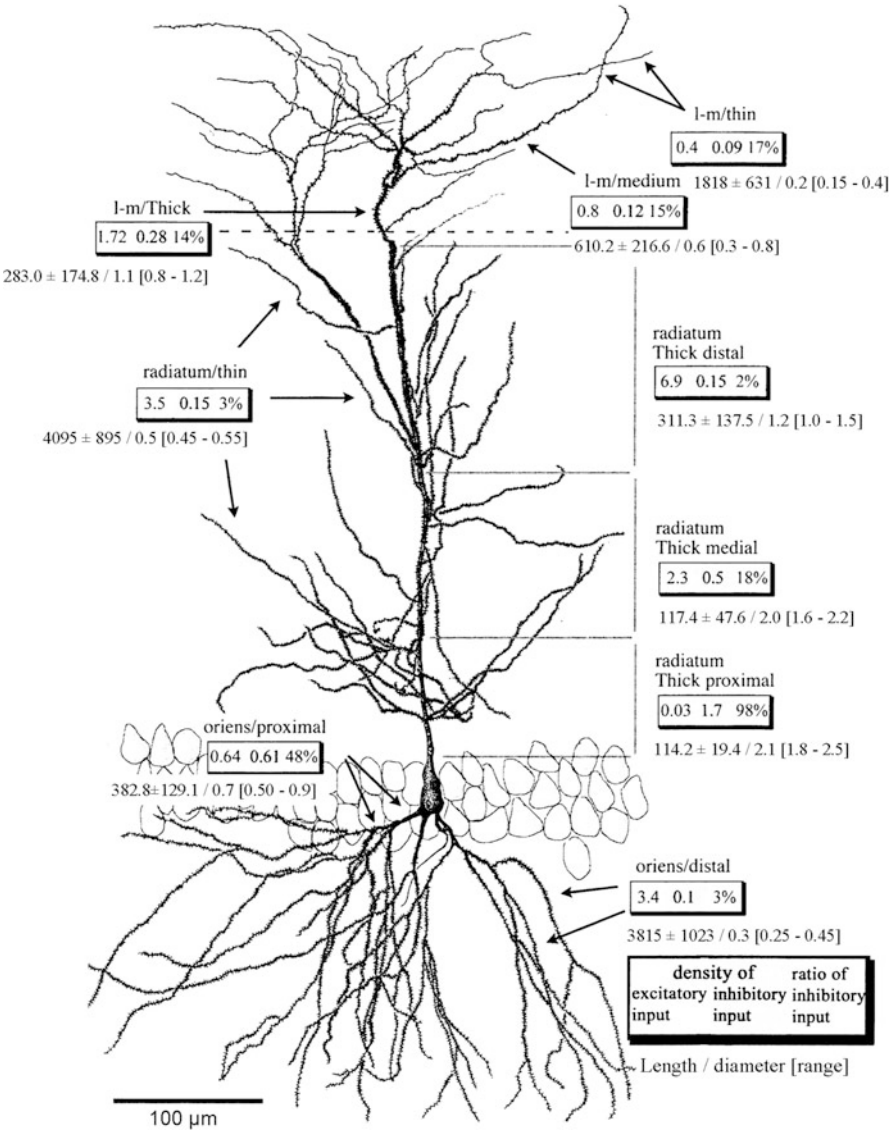

Fig. 3 Distribution of synapses on the dendrites of CA1 pyramidal cells. The drawing illustrates the subclasses of dendrites distinguished in the study by Megías et al. (2001). In the *str. oriens*, two types of dendritic processes were classified: first-order proximal basal dendrites with low spine density (oriens/proximal) and higher-order distal dendrites with high spine density (oriens/distal). In the *str. radiatum*, four subclasses of dendrites were distinguished. The thick apical dendritic trunk was divided into three segments: a proximal part with no spines (radiatum/thick/proximal), a medial sparsely spiny part (radiatum/thick/medial), and a densely spiny distal part (radiatum/thick/distal). The fourth type corresponds to the thin oblique side branches (radiatum/thin).

axes of the CA1 area in terms of anatomical, molecular, and functional properties of pyramidal cells. In fact, Lorente de Nó in his early study of the hippocampus introduced the "a, b, and c" subdivisions of the CA1 area along the transverse axis based on differences in the anatomical connectivity of pyramidal cells (Lorente de Nó 1934; see chapter "Connectivity of the Hippocampus"). More recent in vitro and in vivo electrophysiological studies revealed further divergence in the intrinsic properties, discharge pattern, and place field properties along this axis (Igarashi et al. 2014). Furthermore, as noted above, superficial and deep cells differ in their internal and external excitatory and inhibitory connectivity (Mizuseki et al. 2011; Lee et al. 2014; Masurkar et al. 2017).

Similar but not tightly correlated gradients were observed in neurochemical properties of CA1 pyramidal cells, in particular in the expression of the calcium-binding protein calbindin (CB, see Fig. 1), which labels a subset of CA1 PCs. In proximal CA1 (i.e., the CA1c, closest to CA2), a relatively sparse population of pyramidal cells is labeled, while in distal CA1 (CA1a, closest to subiculum), almost all neurons express CB (Sloviter 1989). The functional ramifications of the CB are yet to be fully understood, but the absence of CB leads to reduced plasticity and impaired synaptic transmission (Jouvenceau et al. 1999). Interestingly, only very few CA2 pyramidal cells are labeled for CB and almost no CA3 neurons either. However, CB strongly labels mature dentate GCs and their axons, suggesting strong calcium sequestration in mossy fiber axons (Dumas et al. 2004).

Genetic analysis, in particular single-cell reverse-transcriptase PCR and RNA sequencing, at the level of the population and single cells, has further revealed a diversity of principal cell populations, with respect to hippocampal position and cell type (Cembrowski et al. 2016a, b; Fig. 4). This approach is redefining our understanding of molecular composition in ways not possible in earlier studies, producing exhaustive lists of neurochemical diversity within and between principal cell types. One notable example is the divergence of CA1 pyramidal cells along the dorsoventral axis of the hippocampus in terms of RNA expression gradients (Fig. 4b), which is also reflected in their physiological and morphological properties (Dougherty et al. 2012, 2013; Cembrowski et al. 2016a; Milior et al. 2016; Ruchi et al. 2016; Fig. 5).

The list of known genes differing between different principal cell types is ever increasing, with the known unique genes and proteins (see Table 4). Despite many of these genes being associated with synaptic and intrinsic physiology, numerous of the alternatively expressed genes are associated with cytoskeletal elements and growth/transcription factors. For example, this genetic anatomical approach, thus, reveals a greater subdivision of hippocampal subregions and helps to define their borders (Thompson et al. 2008), plausibly reflecting functional differences. While the role that these alternative gene expression patterns play in divergent morphology and connectivity of principal cells is yet to be fully understood, they could serve as markers as well as targets for genetic manipulations in future attempts to understand

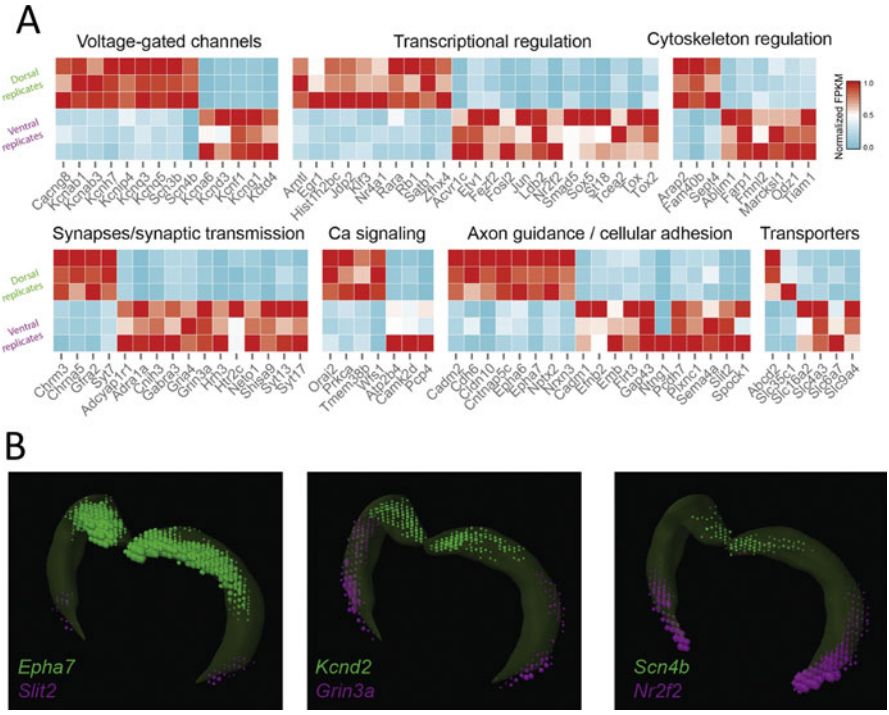

Fig. 4 Differential gene expression patterns along the dorsoventral axis of the CA1 area of the hippocampus. (**a**)**,** A subset of genes enriched in a pole-specific fashion with neuronal relevance. Top and bottom three rows depict dorsal and ventral replicates, respectively. Range is normalized to the highest replicate FPKM on a gene-by-gene basis. (**b**)**,** Regionally restricted gene expression along the dorsoventral axis of the CA1 area from the Allen *Brain* Atlas Brain Explorer. CA1 areas of the left and right hippocampi are shown in green. Genes identified were involved in neurotransmission (Grin3a), transcriptional regulation (Nr2f2), intrinsic excitability (Kcnd2, Scn4b), and axon guidance (Epha7, Slit2). (Adapted from Cembrowski et al. 2016a with permission. © Cell Press)

functional relevance of the identified neurons and the molecules (Cembrowski et al. 2016b; Mikulovic et al. 2015).

CA3 Pyramidal Cells

The number of pyramidal cells of the CA3 area is substantially lower at $1.88 \pm 0.02 \times 10^5$ than that of CA1 neurons (male Wistar rats, Hosseini-Sharifabad and Nyengaard 2007). In their morphology, CA3 pyramidal cells show many similarities to CA1 pyramidal cells; however, there are a number of notable differences. The cell bodies are larger and have a surface area approximately 2–4 times higher than that of CA1 pyramidal cells. The apical dendrites bifurcate closer to *str. pyramidale* and often two or three apical dendrites emerge from the apical pole of the elongated

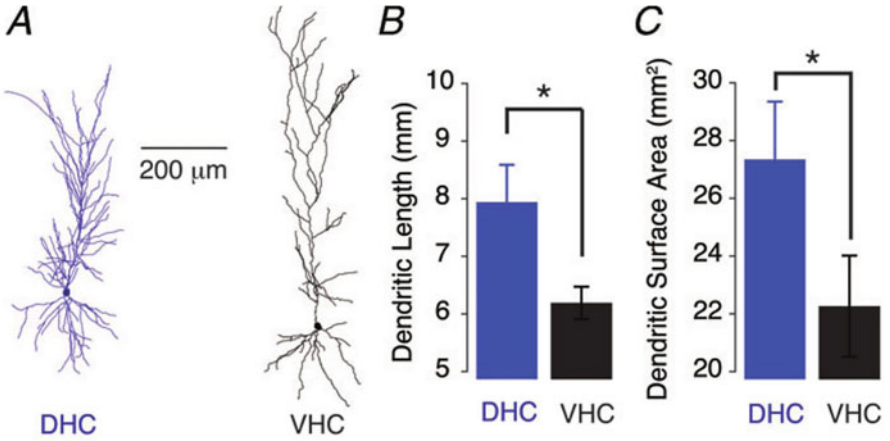

Fig. 5 Morphological differences between CA1 PCs from the dorsal (DHC) and ventral hippocampal (VHC). (**a**)**,** Representative morphological reconstructions of a DHC (left) and a VHC (right) pyramidal neuron. (**b, c**)**,** Summary bar charts of the total dendritic length (**b**) and surface area (**c**) indicate significantly greater dendritic arbor for DHC neurons than VHC neurons (Wilcoxon RS tests, $P < 0.05$). (Reproduced from Dougherty et al. 2012 with permission. © Wiley-Blackwell)

soma. Finally, proximal dendrites of CA3 pyramidal cells bear large complex spines ("thorny excrescences"); these complex spines are the postsynaptic targets of mossy fiber boutons (Blackstad and Kjaerheim 1961; Frotscher et al. 1994; Claiborne et al. 1986; Chicurel and Harris 1992; Acsády et al. 1998).

The total dendritic length of CA3 pyramidal cells (Table 5) is comparable to that in the CA1 area. However, the cell-to-cell variability is higher, partially due to structural differences along the transverse axis of the CA3 (Ishizuka et al. 1995; Turner et al. 1995); estimates of the somatodendritic surface without spines range between 22,033 and 50,400 μm2 (Henze et al. 1996; Cannon et al. 1999). Spines enlarge the dendritic surface by a factor of 0.88 (based on data by Major et al. 1994, Table 5). The density (2.9 $\mu m-1$) and total number (33,200) of spines are also similar to those in the CA1 area (Major et al. 1993).

Complex spines are found in small clusters on the proximal apical dendrite in the *str. lucidum*, corresponding to the termination zone of mossy fibers (Gonzales et al. 2001). In the CA3c, where mossy fibers form an infrapyramidal bundle, spines can also be found on the proximal basal dendrites. Due to limitations of light microscopy, the resolution of individual spines is difficult, but estimates suggest that the number of complex spines on a single CA3 pyramidal cell can be up to 41 (Gonzales et al. 2001). As each complex spine is contacted by a single mossy fiber bouton (Chicurel and Harris 1992; Acsády et al. 1998), this number defines the convergence of GCs onto CA3 pyramidal cells. Although there is only limited information about other excitatory synaptic inputs to CA3 pyramidal cells, the distribution of dendrites and the number of spines suggest that the total

Table 4 A non-exhaustive list of known cell-type specific genes in hippocampal principal cells, organized by broad function

Region	Cytoskeletal	Signaling	References
CA1	*Col5a1*[3] (collagen formation)	*Wfs1*[1,3] (Ca^2+ signaling)	[1]Luuk et al. (2008)
	Dcn[3] (collagen formation)	Calbindin [2] (Ca^{2+} signaling)	[2] Sloviter (1989)
	Matn2[3] (ext. cellular matrix)	*Grp*[3] (neuropeptide)	[3]Dong et al. (2009)
	Fbln2[3] (ext. cellular matrix)	*Lct*[3] (lactase)	
CA2	Alpha actinin 2 (actin cross-linking)	*PCP4* (calmodulin binding)	Botcher et al. (2014)
CA3	*Itga7* (cell adhesion)	*Fmo1* (metabolism)	Thompson et al. (2008)
	Coch (neurite outgrowth)	*Mas1* (7-TM)	
	Loxl1 (ext. cellular matrix)	*Plagl1* (DNA binding)	
		Ptgs2 (mitochondrial)	
Mossy cell	p11 (scaffold and transport)	mGluR2/3 (7-TM)	Scharfman (2016)
	Dysbindin 1C (axon growth)	Calretinin (Ca^{2+} signaling)	
		CGRP (neuropeptide)	
		STEP (tyrosine phosphatase)	
GC	Dysbindin (axon)	Calbindin (Ca^{2+} signaling)	
	Prox1 (maturation)	Glucocorticoid R2 (receptor)	
	Tuj1 (cytoskeleton)	mGluR2/3 (7-TM)	
Adult-born GC	Doublecortin (differentiation)		Seri et al. (2004)
	Reelin (differentiation)		
	NeuroD (differentiation)		

Table 5 Dendritic length and somatodendritic surface area of CA3 and CA2 pyramidal cells

Layer	Dendritic length (μm)	% of dendrites	Surface area (μm^2)	Reference/rat strain, age
CA3c ($n = 4$)				Major et al. (1994)
Total	11,169 ± 878a		59,900 ± 4738	Wistar, 18–21 days
Dendrites			30,600 ± 4700	In vitro labeling
Dendrites with spines			57,600[a]	
Soma			2300 ± 600	
Axon			22,600 ± 3000	
CA3 ($n = 20$)				Ishizuka et al. (1995)
Total	12,482 ± 2999			Sprague-Dawley, 33–57 days
L-M	1983 ± 458	15.9%		In vitro labeling
Rad	4382 ± 975	35.1%		
Luc/Pyr	471 ± 250	3.8%		
Ori	5646 ± 1745	45.2%		
CA3a ($n = 4$)				Turner et al. (1995)
Total	19,800 ± 2030			Sprague-Dawley, 2–8 months
CA3b ($n = 4$)				In vitro labeling
Total	19,100 ± 2330			
CA3c ($n = 4$)				
Total	10,400 ± 720			

CA3b ($n = 8$)				Henze et al. (1996)
Total	11394 ± 1735		22,033 ± 3559	Sprague-Dawley, 28–35 days
Apical	6332 ± 1029	55.6%	12,629 ± 3556	In vitro labeling
Basal	5062 ± 1397	44.4%	9404 ± 4958	
CA3 ($n = 15$)				Cannon et al. (1999)
Total	18,100 ± 8600		50,400 ± 24,000	Sprague-Dawley, 2–8 month, in vivo labeling
CA3 (n=9)				Buckmaster (2012), Sprague-Dawley, adult
Total	8804 ± 2224			In vivo labeling
CA3 (n=5)				Degro et al. (2015)
Total	7730 ± 1791		41,422± 8840	Wistar, 3–4 weeks
				In vitro labeling
CA2 ($n = 14$				Ishizuka et al. (1995)
Total	15,406 ± 950			Sprague-Dawley, 33–57 days
L-M	4672 ± 293	30.3%		In vitro labeling
Rad	4799 ± 732	31.1%		
Pyr	71 ± 34	0.5%		
Ori	5865 ± 491	38.1%		

number of synapses made by commissural/associational and perforant path axons is comparable to the numbers obtained for the pyramidal cells of the CA1 area.

The axon of CA3 pyramidal cells typically emanates from the soma or a proximal dendrite, with 30% of AIS's being found on a dendrite (Thome et al. 2014). Of note, the AIS of CA3 PCs possesses axonal protrusions (similar to dendritic spines), which were contacted by between 1 and 5 inhibitory synapses and occasionally also excitatory synapses (Kosaka 1980). The main axonal projection is to the ipsi- and contralateral hippocampi, forming the commissural/associational pathways to the CA3, CA2, and CA1 areas; the latter is referred to as the "Schaffer collaterals" (Ishizuka et al. 1990; Li et al. 1994). However, there are also collaterals, mostly arising from the CA3c, which are directed to the hilus and the DG (Li et al. 1994; Scharfman 2007). The length of the axon ipsilaterally ranges between 150 and 300 mm and may contact up to 30,000–60,000 postsynaptic neurons (Li et al. 1994). A recent in vivo labeling study found that the total axonal length of a single CA3 pyramidal cell was more than 0.5 m, covering almost two-thirds of the septotemporal extent of the area (Wittner et al. 2007). The majority of target cells (85%) are innervated through a single synaptic contact (Sík et al. 1993; Gulyás et al. 1993b). Axons originating in the CA3a area terminate to a larger degree in the CA3 than in the CA1 area (ratio 3:1), whereas for the CA3c area, the termination pattern is inverse (ratio 1:3, Li et al. 1994). Thus, local targets of a single CA3 pyramidal cell may vary between ~7500 and 45,000 (i.e., 5–30% of the ~150,000 neurons comprising the CA3 population). Postsynaptic targets include feedforward interneurons, such as parvalbumin-containing basket cells, in proportion to their occurrence (Sík et al. 1993; Gulyás et al. 1993b; Wittner et al. 2006).

Similar to the results obtained for the CA1, morphological and genetic analysis of CA3 pyramidal cells reveals divergence along both the medio-distal and the dorsoventral axis of the hippocampus (Ishizuka et al. 1995; Turner et al. 1995; Thompson et al. 2008).

CA2 Pyramidal Cells

CA2 area was defined by Lorente de Nó (1934) as a small, distinct region between the CA1 and CA3 based on its cytoarchitectural features. More recent analyses of gene expression further demonstrated that CA2 area can be reliably identified by selective molecular markers, including Purkinje cell protein 4 (PCP4), regulator of G protein signaling 14 (RGS14), STEP, and MAP3K15, indicating a wider region (~300 μm) than what was cytoarchitecturally defined (~100 μm) (Lein et al. 2005; Lee et al. 2010; Kohara et al. 2014).

CA2 pyramidal cells show morphological features in between those of the CA1 and CA3 areas. Cell bodies of these neurons have similar size as those of CA3 pyramidal cells, and 2–3 times larger than CA1 pyramids, but the cells lack complex spines and their dendritic arborization pattern is more similar to that of CA1 pyramids (Ishizuka et al. 1995; Mercer et al. 2007). Quantitative analysis of the dendrites of in vitro labeled neurons indicates that CA2 pyramidal cells have the

highest total dendritic length compared to CA1 and CA3 pyramidal cells in the same study (Ishizuka et al. 1995; but see Mercer et al. 2007). The difference is primarily due to the higher length of dendrites in the *str. lacunosum-moleculare*, whereas in the *str. radiatum* and *oriens*, values are comparable (Ishizuka et al. 1995; Table 5). In fact, the dendritic arborization pattern of CA2 pyramidal neurons differ from those of CA1 cells, in that the primary apical dendrite divides into several secondary branches relatively close to the soma. The secondary branches give rise to very few oblique branches in *str. radiatum* but extend deep into the *str. lacunosum-moleculare* (Srinivas et al. 2017).

There is little information on the synaptic connectivity of these neurons. Two major excitatory inputs are the commissural/associational fibers and the perforant path with similar termination as in the CA1 and CA3 areas. However, they have over twofold higher spine density, which, combined with a higher total dendritic length, results in a near threefold larger entorhinal input (Srinivas et al. 2017). However, the entorhinal input appears to originate from layer II but not from layer III neurons (Kohara et al. 2014). In addition, the CA2 region receives a strong input from the supramammillary nucleus (Maglóczky et al. 1994; Kohara et al. 2014). Finally, despite their lack of complex spines, CA2 pyramidal cells have excitatory synaptic input from the DG via the mossy fibers (Kohara et al. 2014). Inhibitory innervation of the CA2 area is similar to both CA1 and the CA3 (Mercer et al. 2007); however CA2 contains many more PV and Reelin immunopositive interneurons than either CA1 or CA3 (Botcher et al. 2014). Axons of CA2 pyramidal cells, similar to CA3 pyramids, project to the ipsi- and contralateral CA1–3 areas contributing to the commissural/associational system (Tamamaki et al. 1988; Li et al. 1994; Mercer et al. 2007). The ipsilateral length of axons was measured to be ~150 mm, further indicating that not only the distribution but also the number of postsynaptic targets is comparable to those of CA3 pyramids (Li et al. 1994). In contrast to CA3 pyramidal cells, however, CA2 neurons preferentially project to deep CA1 pyramidal cells (Kohara et al. 2014).

DG Granule Cells

DG possesses a large population of unique principal cell type, the GCs, which markedly differ in their anatomical properties from pyramidal cells of the CA areas. The number of GCs has been estimated to be on the order of 10^6 ($1.08 \pm 0.09 \times 10^6$, unilateral value, male Wistar rats, Hosseini-Sharifabad and Nyengaard 2007). GCs show a moderate diversity, due in part to the fact that GCs are one of only two known populations of adult-born neurons (Cameron et al. 1993, 2001); as a result the population of mature GCs is interspersed with immature GCs with divergent morphologies (Zhao 2006). GCs are characterized by a strictly bipolar morphology: spiny dendrites originate from the upper pole of the soma and an axon emerges from the base (Fig. 2c, d; Seress and Pokorny 1981; Claiborne et al. 1990; Schmidt-Hieber et al. 2007). Mature GCs have small, round, or ovoid cell bodies with a diameter of ~10 μm and are located densely packed in the GC layer most

proximal to the ML. One to four primary dendrites arise from the soma, bifurcating 3–6 times to form a dendritic tuft in the ML. Terminal branches extend mostly to the hippocampal fissure, and the tuft occupies a conical-shaped volume within the ML with a wider transverse (~300 μm) and a narrower (~180 μm) septotemporal extent. Dendrites show a gradual taper with diameters changing from ~1.5 μm on proximal dendrites to 0.7 μm on distal dendrites (Schmidt-Hieber et al. 2007). The total dendritic length ranges between 2324 and 4582 μm, thus, substantially shorter than for pyramidal cells (Claiborne et al. 1990; Table 6). Quantitative differences exist between GCs of the upper and the lower blades, as well as between superficial (near the molecular layer) and deep cells (near the hilus; Claiborne et al. 1990). However other studies have failed to confirm these differences (Beining et al. 2017). Superficial neurons in the upper blade have the highest total dendritic length and the widest arbor, whereas deep neurons in the lower blade have the shortest length and the narrowest transverse extent (Table 6).

Similar to pyramidal cells, mature GC dendrites are densely covered with spines. The total number was calculated to be between 3091 and 6830 on the basis of a light microscopic estimate of spine density ($2.39 \pm 0.06\ \mu m^{-1}$; Schmidt-Hieber et al. 2007). Electron microscopic investigation obtained similar density values and indicated moderate differences between proximal ($3.36 \pm 0.35\ \mu m^{-1}$), mid-distal ($2.88 \pm 0.33\ \mu m^{-1}$), and distal ($2.02 \pm 0.28\ \mu m^{-1}$) dendritic segments (Hama et al. 1989). The differences in the density are largely explained by the decreasing diameter and surface area of proximal to distal dendrites. In fact, the surface density of spines was comparable in the dendritic compartments with values ranging from 0.79 to 0.88 μm^{-2} (Hama et al. 1989). Spine surface contributes by a factor of 0.91–1.05 to the total surface area of the neurons (Schmidt-Hieber et al. 2007; Hama et al. 1989).

There are only limited quantitative data on the synaptic inputs to GCs. The number of excitatory synapses can be estimated on the basis of spine densities. The three main afferent systems, the commissural/associational path, the medial and the lateral perforant path, terminate in a strictly laminated fashion in the inner, middle, and outer molecular layers, respectively. The proportions of the dendrites falling into these layers are ~30, 30, and 40% (Claiborne et al. 1990; Schmidt-Hieber et al. 2007). The corresponding spine numbers on the surface of GCs with a dendritic length of ~3200 μm (Claiborne et al. 1990), calculated using the spine density estimates of Hama et al. (1989; see above), are 3250, 2780, and 2600. Thus, the number of excitatory synapses onto a single GC could be as high as 8630.

The distribution of inhibitory terminals was analyzed in a combined immunocytochemical and electron microscopic study (Halasy and Somogyi 1993a). Results indicate that in the molecular layer, ~7.5% of the synapses are GABA-immunopositive, and these synapses comprise 75% of all inhibitory synapses, with the remaining 25% located in the cell body layer. Therefore, the number of inhibitory synapses onto a single granule cell can be estimated as ~860, with ~650 in the molecular layer and ~190 in the cell body layer. The compartmental distribution of the inhibitory input is broken down to 63–73% dendritic shafts and 27–37% spines in the molecular layer. In the cell body layer, the majority, between

Table 6 Dendritic length and spine numbers of dentate GCs

Dendritic segments	Dendritic length (μm)	Surface (μm^2)[a]	Spine number (density [μm^{-1}])	Region	Reference Rat/Mouse strain, age
29 ± 1	3221 ± 78			Pooled data	Claiborne et al. (1990)
31 ± 1	3484 ± 130			Upper superficial	Sprague-Dawley rat, 35–49 days
30 ± 1	3468 ± 92			Upper, deep	In vitro labeling
28 ± 1	2875 ± 95			Lower, superf.	
25 ± 1	2629 ± 86			Lower, deep	
32 ± 3	2264 ± 133	13,300 ± 900			Schmidt-Hieber et al. (2007) Wistar rat, 2–4 months, in vitro labeling
24 ± 5	1985 ± 160		2254 ± 317 (1.14 ± 0.15)	Pooled	Vuksic et al. (2008)
	362 ± 53		487 ± 121 (1.34 ± 0.12)	iML	Mouse, Thy1-GFP C57BL/6 background male, 3–4 months
	1482 ± 114		1701 ± 145 (1.14 ± 0.11)	oML	

(continued)

Table 6 (continued)

Dendritic segments	Dendritic length (μm)	Surface (μm^2)[a]	Spine number (density [μm^{-1}])	Region	Reference Rat/Mouse strain, age
21 ± 2	1912 ± 90		2272 ± 252 (1.19 ± 0.12)	Dorsal DG	
	357 ± 36		486 ± 104 (1.36 ± 0.18)	iML	
	1475 ± 102		1741 ± 156 (1.18 ± 0.12)	oML	
29 ± 1	2106 ± 197		2233 ± 473 (1.06 ± 0.18)	Ventral DG	
	369 ± 80		488 ± 143 (1.32 ± 0.16)	iML	
	1486 ± 118		1664 ± 143 (1.12 ± 0.11)	oML	
	3337 ± 149			Pooled data	Buckmaster (2012), Sprague-Dawley rats, adults
					In vivo labeling
	3662 ± 88			Pooled data	Desmond and Levy (1982)
	4000 ± 215,7	9010 ± 642,4		Pooled data	Cannon et al. (1999), Sprague-Dawley rats (2–8 months), in vivo labeling
	3152 ± 323	16,271 ± 1501		Pooled data	Degro et al. (2015), Wistar, 3–4 weeks
					In vitro labeling

Values are mean ± S.E.M. Abbreviations: upper/lower, GCs in upper/lower bade; superf./deep, superficial/deep part of the granule cell layer; IML/OML, dendrites in the inner/outer molecular layer

[a]Surface area includes the axon and spines

46 and 60%, are on somata, 25–28% on proximal dendritic shafts, 7–14% on spines, and 7–9% on axon initial segments (Halasy and Somogyi 1993a).

The axons of GCs, the so-called mossy fibers, provide the major output of the DG to the CA3. The unique features of mossy fibers are the 10–18 sparsely spaced large varicosities (4–10 μm) or mossy fiber boutons that form synaptic contacts with complex spines of CA3 pyramidal cells in the *str. lucidum* and mossy cells in the hilus (Claiborne et al. 1986; Frotscher et al. 1994; Acsády et al. 1998; Rollenhagen et al. 2007). Furthermore, mossy fibers innervate a large number of inhibitory interneurons (Blasco-Ibáñez et al. 2000) in both regions through small, en passant boutons (0.5–2 μm) and filopodial extensions emerging from the large boutons, outnumbering of CA3 PCs contacted by 10:1 (Acsády et al. 1998), suggesting that the mossy fiber may predominantly drive net inhibition.

A further subtype of GC was recently described, the so-called semilunar granule cell (SLGC), which is predominantly found within the proximal iML. Despite similar dendritic branching to regular GCs, SLGCs have a greater lateral extent of their dendritic tree (420.3 ± 26.8 for SLGCs compared to 284.9 ± 33.7 μm for GCs). Their often ovoid somata give rise to their name. SLGCs surprisingly have axon collaterals which innervate the iML, forming an average of 1.8 branches in this region, suggesting a role in feedback excitation onto other GCs. SLGCs possess unique intrinsic excitability, as compared to typical GCs, and receive a strong excitatory input from hilar mossy cells (Williams et al. 2007).

Adult-Born GCs

Immature, or adult-born, GCs are found on the border of the hilus and GCL. During the weeks following neurogenesis, their dendrites are growing through the ML (Kempermann et al. 2004), with dendritic lengths of ~300 μm at 2 weeks reaching full penetration of the ML by 3 weeks (Zhao 2006). Spines do not develop on these adult-born GCs until 16 days post-differentiation, and they show strongly reduced glutamatergic inputs from all entorhinal inputs (Dieni et al. 2016), but with a strong input from hilar mossy cells (Vivar et al. 2012). The axon of adult-born GCs has already infiltrated CA3 by 10 days post-differentiation (Zhao 2006) and can drive strong inhibition (Drew et al. 2016).

Hilar Mossy Cells

Mossy cells share some morphological features with CA3 pyramidal cells. In particular, the presence of large complex spines on proximal dendrites and small, simple spines on distal dendrites underpins this resemblance. However, major differences in their morphology, connectivity, and physiological properties demonstrate that mossy cells constitute a discrete cell population (Amaral 1978; Buckmaster et al. 1993; Scharfman 2016).

The somata of the cells are slightly larger than those of CA3 pyramidal cells and have a triangular or ovoid shape. Three to six primary dendrites arise from the soma and bifurcate repeatedly to produce an extensive multipolar dendritic arborization confined to the hilus. Dendrites very rarely invade the granule cell layer or the molecular layer in mature rats (Amaral 1978; Ribak et al. 1985; Buckmaster et al. 1993; Lübke et al. 1998; but see Scharfman 1991). In vitro labeled mossy cells from mice have a total dendritic length of 5392 ± 313 μm (Kowalski et al. 2010), whereas in vivo labeled mossy cells from rats disclose a total dendritic length of 8293± 361 μm (adapted from Buckmaster 2012). Although these values are not directly comparable to those obtained for other types of hippocampal neurons, the extent of mossy cell dendritic arbor appears to lie between GCs and pyramidal cells.

Similarly, only limited quantitative data are available on synaptic inputs to mossy cells. Proximal dendrites and the soma are covered by complex spines reflecting a high degree of convergence of GC inputs onto electrotonically proximal locations (Frotscher et al. 1991; Acsády et al. 1998). Additionally, mossy fibers make synaptic contact with distal, simple dendritic spines (Frotscher et al. 1991). Other excitatory inputs include the hilar collaterals of CA3 pyramidal cells (Scharfman 1994, 2007; Jinde et al. 2013) and mossy cell axons terminating mainly on distal spines. However, data from paired intracellular recordings indicate that the mutual connectivity between mossy cells is very low (∼0.5%; Larimer and Strowbridge 2008). The major source of inhibitory input is from hilar interneurons (Acsády et al. 2000; Larimer and Strowbridge 2008).

The axon of mossy cells forms an extensive arbor in the ipsi- and contralateral hippocampi (Soltész et al. 1993; Buckmaster et al. 1996). While the extent of the dendrites is restricted along the septotemporal axis (<500 μm), the axon can cover 53–61% of the hippocampus (Buckmaster et al. 1996). Thus, mossy cells provide a distributed excitatory feedback to the DG. The ipsilateral length of the axon is between 73 and 96 mm (uncorrected two-dimensional projection, Buckmaster et al. 1996). Most of the axon is in the inner molecular layer (53–56%) and the hilus (23–27%), but collaterals are also found in the granule cell layer, the middle molecular layer, the CA3, and occasionally also the CA1 (Buckmaster et al. 1996). In the molecular layer, the axon forms synapses every ∼2 μm and the large majority of the postsynaptic targets are dendritic spines of GCs (Buckmaster et al. 1996). While numerically low, synaptic contacts onto interneurons have been suggested to play an important role in regulating the excitability of the DG (Ratzliff et al. 2002; Sloviter et al. 2003). In the hilus, interestingly, the density of synapses is five times lower along the axon (0.1 μm^{-1}), and the main targets are smooth dendrites of interneurons (Buckmaster et al. 1996; Larimer and Strowbridge 2008).

GABAergic Interneurons

Morphological Classification of Interneurons

Local inhibitory interneurons are characterized by extensive local axonal arborizations and can thereby provide inhibitory innervation and control the activity of large sets of local neurons. In contrast to the largely uniform population of principal cells, interneurons are extremely heterogeneous with respect to not only their morphological features but also their physiological characteristics and their expression of neurochemical markers and transcription factors. Differences in their properties are thought to reflect the functional diversity of interneurons in the network (Table 7). A key determinant of interneuron types is their origin, i.e., in which ganglionic eminence (either medial or caudal) are the cells formed during early embryonic development. Indeed, unique genetic markers define interneuron type, origin, and fate and their final location within the cerebral cortex (Kepecs and Fishell 2014). The most distinct anatomical feature of interneurons is the layer-specific distribution of their axon (Fig. 6). Correlated light and electron microscopic studies revealed that the axon projection reflects the differential targeting of subcellular compartments (e.g., soma, proximal, or distal dendrites) of the postsynaptic neurons (Han et al. 1993; Gulyás et al. 1993a; Buhl et al. 1994a). Additionally, termination of the axon often parallels afferent pathways leading to co-alignment of excitatory and inhibitory inputs.

However, not only the axon but also dendrites and cell bodies of interneurons show variability in their laminar distribution. While some interneuron types have a dendritic arbor spanning all layers, others have dendrites restricted to one or more layers. The dendritic distribution determines what inputs are available to an interneuron: whether it can be activated by one or more afferent system in a feedforward manner or by recurrent collaterals of principal cells as part of feedback inhibitory microcircuit (Fig. 6).

Thus, the precise localization of the interneurons, their dendrites, and axon within the layered structure of the hippocampus determines their anatomical connectivity. In turn, input and output connections define the functions that the cells can play in the circuitry. Therefore, most classification schemes have considered these anatomical features as defining criteria (Freund and Buzsáki 1996; McBain and Fisahn 2001; Somogyi and Klausberger 2005). Although there is still some debate regarding the terminology and identification of interneuron types (Maccaferri and Lacaille 2003; Petilla Interneuron Nomenclature Group et al. 2008), two main classes of interneurons can be distinguished on the basis of postsynaptic targets: perisomatic and dendritic inhibitory cells (Fig. 6). In addition, a set of interneurons that selectively target other interneurons (interneuron-specific [IS] cells; Acsády et al. 1996a, b; Gulyás et al. 1996; Hájos et al. 1996) and interneurons with long-range projections have been identified (Jinno et al. 2007; Melzer et al. 2012; Katona et al. 2017).

Table 7 Passive membrane parameters of the hippocampal principal cells and interneurons in morphologically and electrophysiologically constrained models

	*R*i (Ω cm)	*R*m (kΩ.cm^2)	*C*m (μF.cm^{-2})	Surface (1000 μm^2)	Reference
CA1 PC[a]	199	85.1	0.7	64.4	Major et al. (1993)
CA1 PC	228 (198–261)	27.2(16.1–39.9)	1.43(1.02–1.86)	42.8	Golding et al. (2005)[f]
CA1 PC	107 ± 10.7		170.1 ± 11.4 pF		Chevaleyre and Siegelbaum (2010)
CA2 PC	76.2 ± 11.1		305.3 ± 20.8 pF		Chevaleyre and Siegelbaum (2010)
CA3 PC	270 (170–340)	170(150–200)	0.75(0.69–0.81)	82.5 ± 5.2	Major et al. (1994)
CA3 PC	200/100[c]	50/1[c]	0.75	54.91	Traub et al. (1994)
CA3 PC	107.5 ± 28.1		150.1 ± 26.1 pF		Chevaleyre and Siegelbaum (2010)
GC	194 ± 24	38.0 ± 2.3	1.01 ± 0.03	13.3 ± 0.9	Schmidt-Hieber et al. (2007)
CA1 BC	296 ± 75	66.2 ± 37.8	1[e]	7.9 ± 0.9	Thurbon et al. (1994)
CA3 INs[b]	189 ± 130	62 ± 34	0.92 ± 0.34		Chitwood et al. (1999)
DG BC	121 ± 21	6.3/30.5[d]	1.1 ± 0.1	9.8/31.2[c]	Nörenberg et al. (2010)[f]

Abbreviations: *PC* pyramidal cell, *IN* interneuron, *Ri* axial resistivity, *Rm* membrane resistivity, *Cm* specific membrane capacitance

[a]Recordings were obtained with sharp microelectrodes and the simulations included a shunt to reproduce the leakage around the electrode

[b]The sample includes various interneuron types

[c]Values indicate somatodendritic/axonal compartments separately

[d]R_m before and after blocking Ih by ZD7288

[e]C_m was set as a constant

[f]Parameters of uniform models. For non-uniform models see original publications

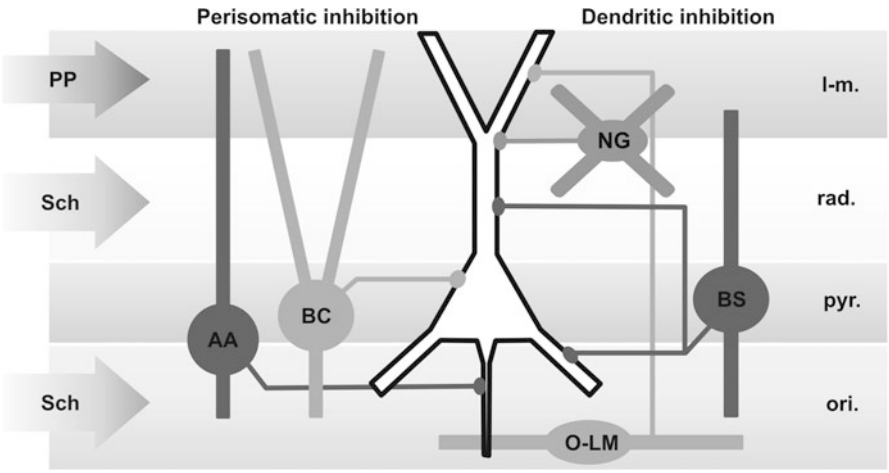

Fig. 6 Schematic representation of major interneuron types of the hippocampal CA1 area. Two main classes can be distinguished on the basis of postsynaptic targets: (1) *perisomatic inhibitory interneurons* include basket cells (BC, targets: soma and proximal dendrites) and axo-axonic cells (AA, targets: axon initial segments). The axon of these interneurons terminates in and near the str. pyramidale (pyr.). (2) *Dendrite-inhibiting interneurons* include many types. Here three well-characterized types are illustrated: (i) bistratified cells (BS) innervate the mid-distal dendrites in the *str. radiatum* (*rad.*) and *oriens* (*ori.*). (ii) Neurogliaform (NG) interneurons are found in the *rad.* or *str. lacunosum-moleculare* (*l-m.*) and inhibit the apical dendrites in the same layers. NG cells are mainly activated by the perforant path (PP) and the Schaffer collaterals (Sch) and therefore provide feedforward inhibition. (iii) O-LM interneurons are found in the *ori.* and innervate the distal apical dendrites in the *l-m*. O-LM cells receive strong recurrent excitation from pyramidal cells and therefore mediate primarily feedback inhibition

Perisomatic inhibitory interneurons innervate soma, proximal dendrites, and axon initial segments of principal cells. They include basket cells (BC) and axo-axonic cells (AAC, also known as *chandelier cells*). The majority of these cells has a vertically oriented dendritic tree and can mediate both feedforward and feedback inhibition.

Dendrite-inhibiting interneurons comprise several distinct types (Fig. 6) which innervate various portions of the dendritic tree of their target cells. The axon of dendrite-inhibiting interneurons is often co-aligned with afferent pathways in the dendritic layers (Han et al. 1993; Gulyás et al. 1993a; Vida et al. 1998; Vida and Frotscher 2000; Booker et al. 2017b). Thus, the various interneuron types can control excitatory postsynaptic responses in an input-specific manner (Miles et al. 1996; Maccaferri and Dingledine 2002). Furthermore, the co-alignment enables mutual presynaptic interactions between glutamatergic and GABAergic axons (Vogt and Nicoll 1999; Guetg et al. 2009; Min et al. 1999; Stafford et al. 2009; Urban-Ciecko et al. 2015). While some dendrite-inhibiting interneurons have dendrites spanning all layers and therefore can mediate feedforward and feedback inhibition, the majority of these cells have dendrites restricted to one or two layers. Interneurons

in the *str. oriens* and the hilus, such as O-LM interneurons, receive over 90% of their excitation from local principal cells and mediate feedback inhibition. In contrast, interneurons in the *str. radiatum* and *lacunosum-moleculare* are activated by the Schaffer collaterals and/or the perforant path and thereby mediate feedforward inhibition.

Neurochemical Classification of Interneurons

Interneuron types differentially express a wide range of molecular markers, including calcium-binding proteins (parvalbumin, PV; calbindin, CB; and calretinin, CR), neuropeptides (somatostatin, SOM; cholecystokinin, CCK; neuropeptide Y, NPY; vasoactive intestinal peptide, VIP), and certain enzymes (NADPH-diaphorase; neuronal nitric oxide synthase, nNOS). While the function of the molecules in these cells is not yet fully understood, detection of the markers by immunocytochemistry, in situ hybridization, single-cell RT-PCR, or RNA-seq investigations have been successfully applied to identify and classify GABAergic neurons (for reviews see Freund and Buzsáki 1996; Somogyi and Klausberger 2005; Jinno and Kosaka 2006; Houser 2007; Klausberger and Somogyi 2008; Pelkey et al. 2017). Importantly, the interneuron types defined on the basis of neurochemical identification converge well with the morphological classification, when the combinatorial expression pattern of multiple markers is considered (Table 8).

Interneurons of the CA1–3 Areas

Most interneuron types can be identified in all areas of the hippocampus on the basis of their salient anatomical properties. However, due to differences in the layering of the areas, some types may differ in certain anatomical properties, whereas a few specific types may exist only in one area. As the structure and layering of the CA1–CA3 areas are almost identical, we discuss interneuron types from these areas together. The classification and descriptions are based on results from the CA1 as this is the best study region of the hippocampus and possibly the whole cortex. But published data from the CA3 (Gulyás et al. 1993a) and the CA2 areas (Mercer et al. 2007; Botcher et al. 2014) confirm that the classification, with some exceptions, can be extrapolated to these regions.

Perisomatic Inhibitory Interneurons

(1) *Fast-spiking parvalbumin-positive basket cells.* PV-BCs form synapses with the somata and proximal dendrites of pyramidal cells as well as other interneurons (Buhl et al. 1994a; Halasy et al. 1996; Cobb et al. 1997; Pawelzik et al. 2002). At the light microscopic level, this interneuron type is characterized by an axon terminating in

Table 8 Divergence of neurochemical markers of hippocampal interneurons

	PV	CB	CR	SOM	CCK	VIP	NPY	CRH	NADPH	nNOS	GABAAα1	CoupTFII	Kv3.1b	Reelin	ErbB4	vGluT3	nAChR4α	mGluR1α	M2	μOR	CB1R	NR2D
Perisomatic inhibitory interneurons																						
PV-BC	++			+/−					++		++		++		++				++	++		++
CCK-BC		+/−			+++	+/−									++	+					++	
PV-AAC	++																		++	++		
Dendritic inhibitory interneurons																						
Bistratified cell	++			+			+												++	++		++
SCA		+			++										++	+/−					++	
PPA		+			++										++	+/−						
LA		?			++										++	+/−					++	
Neurogliaform							++			++	++	++		++						++		
Ivy cell							++			++	++	++								++		
O-LM/HIPP	+			++			+										++	++				++
MFA		++			++																	
Interneuron-specific interneurons																						
IS-I			++			+/−									++							
IS-II			+/−			++	++								++							
IS-III			+			++									++			++				
Long-range projecting interneurons																						
Back-projecting		+		++					++	++								++				
CRH		+	+	+				++														
Double/projection		+		++			+											++	+			

(++) indicates consistent high expression of the marker, (+) indicates low expression and/or expression in a subset, (−) indicates the consistent absence of the marker, when important for distinguishing types. For abbreviations, please see the text

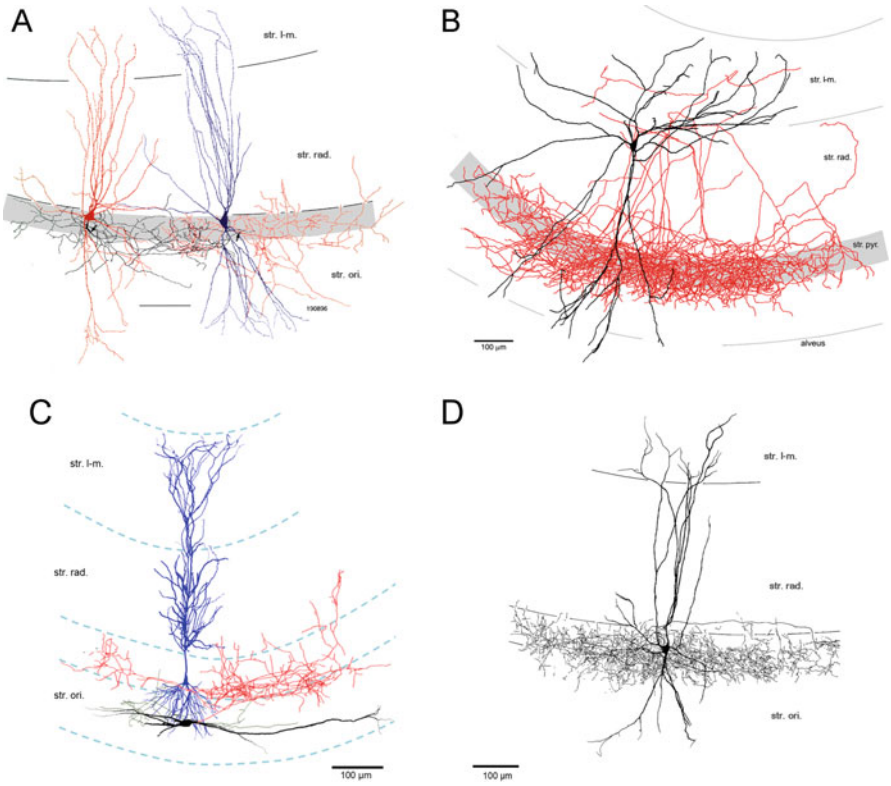

Fig. 7 Morphology of CA1 perisomatic inhibitory interneurons. (**a**) A synaptically coupled fast-spiking putative PV-positive BC-BC pair. The axons of both cells are found mainly in the cell body layer (shaded area, initial segments indicated by *arrows*), whereas their dendrites extend into the dendritic layers. (**b**) A BC with morphological feature of CCK-BCs with soma in the *str. radiatum* (rad.). Note the dense axon (*red*) in and near the cell body layer (str. pyr.). (**c**) A horizontal PV-BC with horizontally oriented dendrites restricted to the *str. oriens* (ori.) but with a typical BC axon arbor in the cell body layer. (**d**) An AAC with a dense axon plexus at the border of the *str. pyr.* and *ori*. Scale bars: 100 µm. (Reproduced with permission: (**a**) from Cobb et al. 1997, © Elsevier; (**b**) from Vida et al. 1998, © Wiley-Blackwell; (**c**), from Booker et al. 2017b, © The authors; (**d**) from Buhl et al. 1994b, © The American Physiological Society)

and near the cell body layer (Fig. 7a). In addition to PV, the cells express high levels of the alpha-1 subunit of $GABA_A$ receptors ($GABA_A$-α1; Table 8) as well as both $GABA_B$ receptor subunits ($GABA_{B1/2}$) and their effector Kir3 channels (Booker et al. 2013). It is estimated that PV-BCs constitute ~60% of all PV-immunoreactive cells and ~12% of all GABAergic interneurons in the CA1 area (Kosaka et al. 1987; Baude et al. 2007).

Cell bodies of PV-BCs are located in the *str. pyramidale* or *oriens*, but a few cells have been found in the *str. radiatum*. The dendrites are radially orientated and span all layers (Buhl et al. 1995, 1996; Halasy et al. 1996). Work published by

Gulyás et al. (1999) analyzed the distribution of dendrites and input synapses of PV-immunoreactive neurons. Although they could not unequivocally identify the cells as BCs, their results conceivably reflect characteristics of this predominant cell type. Their quantitative data revealed that the total length of the dendrites (4348 μm) is substantially shorter than that of pyramidal cells, but their laminar distribution is similar (Table 9). CA2 appears to be the anomaly for PV interneuron dendrites, with both narrow and wide dendritic arbors observed (312 ± 121 μm vs. 570 ± 111 μm lateral spread; Botcher et al. 2014).

The estimated total number of synapses (16,293, Table 9) is also markedly lower than for pyramidal cells, but it is the highest among interneurons (Gulyás et al. 1999); however their synaptic density is considerably higher. The proportion of excitatory (~93.5%) and inhibitory synapses (~6.5%) is comparable to that for pyramidal cells. As the dendrites of BCs lack spines, both excitatory and inhibitory synapses are formed onto dendritic shafts. Inhibitory synapses show a concentration in the perisomatic domain with ~17% of the synapses converging onto the soma, but in contrast to principal cells, the soma also receives a high number of excitatory synapses (Table 9). A large proportion of the inhibitory synapses are PV-immunopositive: ~27.6% on the dendrites and ~70% on the soma (Gulyás et al. 1999; Table 9). Thus, PV-containing interneurons are heavily interconnected by mutual inhibitory synapses (Sík et al. 1995; Fukuda and Kosaka 2000; Bartos et al. 2001, 2002). In addition to the chemical synapses, PV-BCs are also coupled by electric synapses to other PV-containing interneurons (Fukuda and Kosaka 2000, 2003; Bartos et al. 2001; Hormuzdi et al. 2001). Gap junctions are found primarily at dendritic locations with the highest density between basal dendrites at the *str. oriens*-alveus border (Fukuda and Kosaka 2000, 2003). This dual – chemical and electric – connectivity is thought to be important for the synchronization of the interneurons during network activity patterns, such as gamma oscillations (Bartos et al. 2001; Hormuzdi et al. 2001).

The output of BCs has been analyzed in both in vitro and in vivo labeled neurons. The length of the axon of in vivo-labeled BCs ranges between 40.5 and 53.5 mm and terminates in an approximately circular or ellipsoid area of the cell body layer with a diameter between 0.9 and 1.2 mm. It is emerging that BCs in the hippocampus exist with either narrow or wide axonal arbors; in the CA2 region, wide arbor BCs have axon spanning 937 ± 133 μm, whereas narrow arbor BCs span 616 ± 130 μm, suggesting that CA2 BCs project into both CA1 and CA2, suggesting a level of innervation of CA1 and CA3. This phenotype does not appear to exist within CA1 BC populations (Mercer et al. 2007). On the basis of the bouton density of 0.226 ± 0.039 μm^{-1}, the number of total synapses was estimated to be between 9000 and 12,000 (Sík et al. 1995). As unitary IPSCs in pyramidal cells are mediated by multiple, 10–12 synaptic contacts (Buhl et al. 1994a), the number of postsynaptic neurons (*divergence*) is likely to be between 750 and 1200 (Bezaire and Soltész 2013), whereas the number of PV-BCs making synaptic contacts onto a single postsynaptic pyramidal cell (*convergence*) is between 15 and 25 (Bezaire and Soltész 2013), calculated from the total number of synaptic contacts (92–119, Megías et al. 2001; Buhl et al. 1994a) and the number of contacts formed by a single

Table 9 Dendritic length and synaptic inputs of PV-containing interneurons of the CA1 area

			Density of synapses			Estimated number of synapses		
	Dendritic length (μm)	% of dendrites	All	Exc.	Inh.	Exc.	Inh.	PV+
Dendrites	4348 ± 1125					14,825	868	240
L-M	656 ± 255	(15.0%)						
Med	214 ± 124	(4.9%)	171.34	143.44	27.89			
Thin	442 ± 208	(10.1%)	155.72	126.75	28.97			
Rad	2369 ± 786	(54.5%)						
Thick	255 ± 165	(5.8%)	483.81	444.68	39.13			
Med	1713 ± 635	(39.4%)	432.68	416.01	16.67			
Thin	401 ± 219	(9.2%)	145.63	133.50	12.14			
Pyr	248 ± 121	(5.7%)						
Ori	1075 ± 535	(24.7%)						
Thick	21 ± 47	(0.4%)	612.94	568.45	44.49			
Med	686 ± 303	(15.7%)	361.08	344.95	16.13			
Thin	368 ± 243	(8.5%)	348.54	325.08	23.46			
Soma	1006 ± 184 μm^2 (surface area)					413	177	124
AIS						0	10	0
Total						15,238	1055	364

Values are mean ± S.E.M. Percentage values in parentheses indicate the proportion of dendrites within a layer. Density of synapses is per 100 μm. Excitatory (Exc.) and inhibitory (Inhib.) synapses were identified on the basis of postembedding immunolabeling for GABA. Data from Gulyás et al. (1999)

BC onto the soma (5–6, Gulyás et al. 1993a; Buhl et al. 1994a). Examples of PV-BCs with horizontal dendrites exclusively in *str. oriens* have also been described, suggesting divergent dendritic morphologies (Booker et al. 2017a, b; Fig. 7c)

(2) *CCK-expressing basket cells.* Similar to PV-BCs, CCK-BCs form synapses with the somata and proximal dendrites of pyramidal cells as also indicated by the axonal distribution in the *str. pyramidale* and adjacent region of *str. radiatum* and *oriens* (Fig. 7b; Nunzi et al. 1985; Acsády et al. 1996b; Cope et al. 2002; Pawelzik et al. 2002). In addition to CCK, neurochemical markers include VIP, substance P receptor, and vesicular glutamate transporter 3 (VGluT3), but the cells are consistently immunonegative for PV (Table 8; Cope et al. 2002; Pawelzik et al. 2002; Mátyás et al. 2004; Somogyi et al. 2004; Klausberger et al. 2005). Terminals of these interneurons express high levels of cannabinoid CB1 receptor which plays a role in regulating the release of GABA (Katona et al. 1999b). CCK-BCs mostly show regular-spiking discharge pattern, with some exceptions showing a fast-spiking phenotype (Cope et al. 2002; Pawelzik et al. 2002). In contrast to PV-BCs, cell bodies of CCK-BCs can be found in all hippocampal layers. The dendrites run radially and span all layers (Cope et al. 2002; Pawelzik et al. 2002). Mátyás et al. (2004) and Booker et al. (2017a, b) performed a detailed quantitative analysis of the laminar distribution of dendrites and input synapses of CCK-BCs. These analyses show that the total dendritic length of 6338 μm is higher than PV-BCs but markedly lower than pyramidal cells (Table 10). Despite the larger dendritic tree, the estimated total number of afferent synaptic contacts (8147, Table 10) is lower than for PV-BCs. This is due to the fact that the number of excitatory synapses is markedly lower. In contrast, the number of inhibitory synapses is ∼2.6-fold higher (Gulyás et al. 1999; Mátyás et al. 2004). Thus, CCK-BCs have a lower proportion of excitatory (∼64%) and a higher proportion of inhibitory synapses (∼36%) than both PV-BC and pyramidal cells. CCK-BCs are also interconnected by mutual inhibitory synapses. The number of CCK-immunopositive terminals on their surface is ∼350 (Table 10), very close to the number of mutual inhibitory synaptic contacts on PV-BCs. However, the proportion of these synapses among the inhibitory terminals is lower due to the higher overall inhibitory input (Mátyás et al. 2004). Although the PV- and CCK-interneuron networks seem largely independent, there is evidence for the existence of mutual inhibitory synapses and interactions between the two networks (Karson et al. 2009).

While immunocytochemical data at the light and electron microscopic levels demonstrate that terminals of CCK-BCs innervate soma and proximal dendrites of principal cells with a preference proximal to the soma (Földy et al. 2010; Nunzi et al. 1985; Acsády et al. 1996b; Cope et al. 2002; Pawelzik et al. 2002; Klausberger et al. 2005; Booker et al. 2017b), only limited data are available on the divergence or convergence of CCK-BC output. Bezaire and Soltész (2013) postulated a divergence of 1250 cells (1150 pyramidal cells and 100 interneurons) with a convergence of 13 CCK-BCs onto a single pyramidal cell.

(3) *Axo-axonic cells.* AACs provide GABAergic innervation to the axon initial segments of principal cells (Somogyi et al. 1983; Li et al. 1992; Gulyás et al. 1993a; Buhl et al. 1994a), placing them in a unique position to control action potential

Table 10 Dendritic length and synaptic inputs of CCK-BCs of the CA1 area

			Estimated number of synapses		
CCK +	Dendritic length (μm)	All	Excitatory	Inhibitory	CCK+
Dendrites	6338 ± 986	7948 ± 1229	5191 ± 805	2757 ±430	315 ± 55
L-M	1291 ± 456 (20.4%)	1876		759	
Rad/LM	647 ± 575 (10.2%)	798		258	
Rad	2876 ± 211 (45.4%)	3421		1074	
Pyr	111 ± 61	435		271	
Ori	311 ± 118 (4.90%)	1418			
Soma	966 ± 134 (surface area, μm^2)	193 ± 43	34 ± 14	5 ± 2	36 ± 14
AIS		6 ± 2	1 ± 1	5 ± 2	1 ± 2
Total		8147	5266	2921	352

Values are mean ± S.E.M. Values in parentheses indicate percentage of dendrites in a layer. Rad/L-M denotes the broader region of the two layers which contains many horizontally running dendrites. Excitatory (Exc.) and inhibitory (Inhib.) synapses were identified on the basis of postembedding immunolabeling for GABA. Data from Mátyás et al. (2004)

output of the target neurons. Similar to PV-BCs, the termination zone of the axon is mainly in the cell body layer, but it is slightly shifted toward the *str. oriens* (Fig. 7d). Many, but not all, AACs can be distinguished from BCs at the light microscopic level by the presence of vertical rows of synaptic boutons (cartridges), which form contacts with the axon initial segment (AIS). AACs show a fast-spiking discharge pattern and contain high levels of PV, but, in contrast to PV-BCs, they express low level of GABAA-α1 (Katsumaru et al. 1988; Pawelzik et al. 2002). It is estimated that this type constitutes ∼15% of all PV-immunoreactive cells and ∼3% of GABAergic interneurons in the CA1 area (Baude et al. 2007).

Cell bodies of AACs are located in the *str. pyramidale* or *oriens*. The majority has vertically oriented dendrites spanning all layers. In comparison with PV-BCs, the distal apical dendrites often branch and form an extensive tuft in the str. lacunosum-moleculare (Buhl et al. 1994b; Klausberger et al. 2003) indicating a stronger perforant path input to these neurons. A few cells with horizontally oriented dendrites in str. oriens have also been reported (Ganter et al. 2004).

AACs receive input from all major afferent pathways and there is also evidence for recurrent excitatory inputs from pyramidal cells (Li et al. 1992; Buhl et al. 1994b). Regarding the quantitative distribution of input synapses, Gulyás et al. (1999) suggested that their data may apply not only to PV-BCs but also to AACs (see Table 9). However, some disagreement remains regarding the extent of dendrites in the str. lacunosum-moleculare (see above). AACs are thought to be involved in the PV interneuron network coupled by gap junction and also receive inhibitory synapses from this network (Fukuda and Kosaka 2000; Baude et al. 2007). However, AACs themselves do not contribute inhibitory synapses to this network.

The output of AACs is directed exclusively to the AIS of principal cells (Somogyi et al. 1983). The synapses formed onto the AIS can contact the shaft directly or onto membrane protrusions that can receive 1–5 inhibitory synapses, with 25–130

AAC synapses formed per AIS (Kosaka 1980). Morphological analysis of an in vivo labeled CA1 AAC revealed that it can innervate ~1200 pyramidal cells within an area of 600 by 850 μm around the cell (Li et al. 1992). However, in vitro studies indicate that the axon can have a larger extent with values up to 950 μm in the CA1 and 1300 μm in the CA3 area (Gulyás et al. 1993a; Buhl et al. 1994b). The in vivo data further show that the cells form 2–10 synaptic contacts on a single axon initial segment (Li et al. 1992). As the number of synaptic contacts on initial segments is ~24 (Gulyás et al. 1999), 3–12 AACs may converge onto a single pyramidal cell (Bezaire and Soltész 2013).

Dendritic Inhibitory Interneurons

(4) *Bistratified cells (BSC)*. These interneurons are characterized by an axon in the *str. radiatum* and *oriens* co-aligned with the Schaffer collateral pathway (Fig. 8a; Buhl et al. 1994a, 1996). BSCs show a fast-spiking discharge pattern. They contain PV, the neuropeptides SOM, NPY, and high levels of the GABAA-α1 (Pawelzik et al. 2002; Klausberger et al. 2004; Baude et al. 2007). This type constitutes ~25% of all PV-immunopositive cells and ~5% of GABAergic interneurons in the CA1 area (Baude et al. 2007).

Cell bodies of BSCs, similar to other PV interneurons, are found primarily in the *str. pyramidale* or *oriens*. The dendrites show radial orientation and span *str. oriens* and *radiatum* but, in contrast to other PV interneurons, rarely invade the *str. lacunosum-moleculare* (Buhl et al. 1996; Halasy et al. 1996; Klausberger et al. 2004). A few cells with similar axonal arborization but horizontal dendrites have been reported and classified as oriens-BSCs (Maccaferri et al. 2000).

Dendritic distributions and electrophysiological data indicate that the cells are activated primarily by the Schaffer collaterals and can also receive recurrent excitatory input from pyramidal cells in the *str. oriens*, but they generally lack perforant path inputs (Buhl et al. 1996). It remains unclear whether the data on the quantitative distribution of synaptic inputs described for PV interneurons (Gulyás et al. 1999; see Table 9), apart from the lack of perforant path inputs, also apply to BSCs.

The output of BSCs targets shafts (~76–79%) and spines (~11–17%) of small-caliber dendrites and rarely the large-caliber main apical dendrites (~10%) or somata (~4%) of principal cells (Halasy et al. 1996; Klausberger et al. 2004). The proportion of interneuron targets is also low (~3%, Klausberger et al. 2004). Nevertheless, BSCs are thought to be involved in the network of PV interneurons connected by mutual inhibitory synapses and gap junction (Fukuda and Kosaka 2000; Baude et al. 2007). The axon of an in vivo labeled BSC has a total length of 78,800 μm and covers an area of 1860 μm (septotemporal) by 2090 μm (mediolateral axis). The axon of this cell has a bouton density of 0.21 ± 0.06 μm^{-1} and forms ~16,600 boutons. Since BSC-pyramidal cell synapses involve ~6 synaptic contacts (Buhl et al. 1994a), an individual BSC may target over 2500 pyramidal cells. A recent study, calculating 10 synaptic contacts made by a BSC

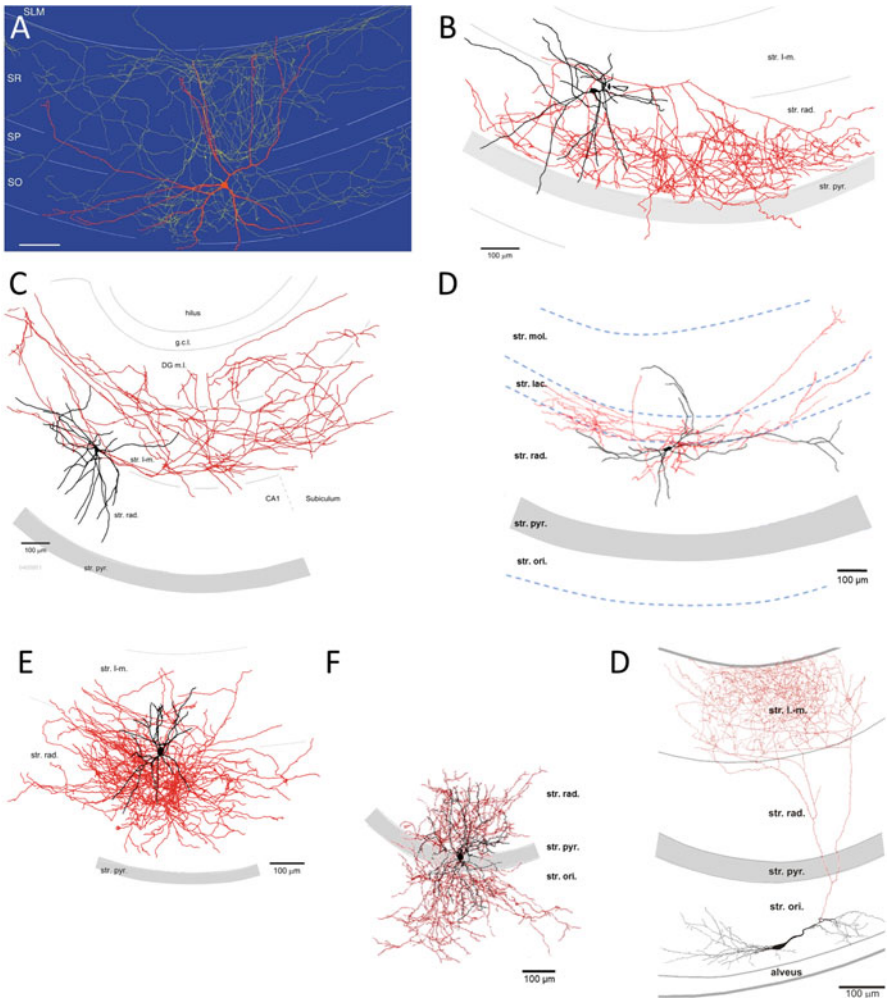

Fig. 8 Dendritic inhibitory interneuron types of the CA1 area. (**a**) A BSC with cell body at the border of *str. pyramidale* (SP) and *oriens* (SO). Dendrites span the str. radiatum (SR) and oriens, but do not extend into the *str. lacunosum-moleculare* (SLM). (**b**) SCA cell with axon (in *red*) in the *str. radiatum* (rad.). (**c**) PPA interneuron. Note the axon terminating in the CA1 *str. lacunosum-moleculare* (l-m.), the subiculum, and the DG molecular layer (m.l.). (**d**) A lacunosum-projecting (LA) interneuron, with axon and the majority of dendrites confined to *str. lacunosum* (lac). (**e**) NGF cell with a compact dendritic tree and a very dense axon in the *str. rad.* and *l-m*. (**f**) An Ivy cell with soma in *str. pyr*. and similarly dense focal axon around the soma. **G** O-LM interneurons have horizontal dendritic tree in the *str. oriens* (ori) and project to the distal apical dendrites of pyramidal cells in the *str. l-m*. (Reproduced with permission: (**a**) from Klausberger et al. 2004, © Nature Publishing Group; (**b, c, e)** from Vida et al. 1998, © Wiley-Blackwell; (**d**) from Booker et al. 2017b, © Oxford University Press; (**f**) from Krook-Magnuson et al. 2011, © The Society for Neuroscience**; G** from Martina et al. 2000, © The American Association for the Advancement of Science)

Table 11 Dendritic length and synaptic inputs of CB interneurons in the CA1 area Estimated number of synapses

	Dendritic length (μm)	All	Exc.	Inhib.
Dendrites	3441 ± 938	3585	2498 ± 666	1087 ± 277
L-M	130 ± 117 (3.8%)			
Rad	2622 ± 827 (76.2%)			
Pyr	197 ± 162 (5.7%)			
Ori	492 ± 300 (14.3%)			
Soma	799 ± 140 (surface area [μm^2])	244	102 ± 10	142 ± 15
AIS		7	0	7 ± 1
Total		3839	2601	1237

Values are mean ± S.E.M. Values in parentheses indicate percentage of dendrites in a layer. Excitatory (Exc.) and inhibitory (Inhib.) synapses were identified on the basis of postembedding immunolabeling for GABA. Data from Gulyás et al. (1999)

synapse, led to a convergence of 10 BSC onto a single pyramidal cell with a divergence to contact 1597 cells in total (Bezaire and Soltész 2013).

(5) *Schaffer collateral-associated (SCA) interneurons.* These interneurons, similar to BSCs, are characterized by an axon in the *str. radiatum* and *oriens* co-aligned with the Schaffer collaterals (Fig. 8b; Vida et al. 1998; Cope et al. 2002, Booker et al. 2017a). They differ, however, in their localization of the soma and dendrites, as well as neurochemical markers. The main markers are CCK and CB (Cope et al. 2002; Pawelzik et al. 2002; Klausberger 2009). Similar to CCK-BCs, SCA interneurons show a regular-spiking discharge pattern.

Somata of SCA cells are predominantly found in *str. radiatum*. Their dendrites run radially, mostly in the *str. radiatum*, but can extend into the str. *lacunosum-moleculare*, *oriens*, and even the alveus (Vida et al. 1998; Pawelzik et al. 2002; Booker et al. 2017a). Although dendritic arbor and synaptic inputs of identified SCA interneurons have not been quantitatively described, Gulyás et al. (1999) provide data on CB-immunoreactive interneurons, a set of dendritic inhibitory interneurons (Gulyás and Freund 1996) which overlap with the SCA type (Cope et al. 2002). The total dendritic length of CB interneurons is 3441 ±938 μm with 76% localized in the *str. radiatum* (Table 11). The excitatory input is relatively weak (~68%) and originates plausibly from the Schaffer collaterals, whereas the inhibitory input is strong (32%). Large part of the inhibitory input may correspond to the mutual inhibitory connections observed between CCK and SCA cells (Ali 2007). In addition to the chemical synapses, SCA cells have been shown to be connected by gap junctions (Ali 2007).

The axon of SCA cells terminates in the *str. radiatum* and to a lesser extent in the *str. oriens*. Output synapses are formed with shafts, but only rarely spines of small-caliber side branches of the pyramidal cells (~80%) and aspiny dendritic shafts of interneurons (~20%; Vida et al. 1998). Synaptic effects in pyramidal cells are mediated by multiple contacts (4–6, light microscopic estimates, Vida et al. 1998;

Pawelzik et al. 2002). The axon of an in vitro labeled SCA interneuron formed ~6000 boutons and may innervate 1000–1500 postsynaptic cells within a 400 μm slice.

(6) *Perforant path-associated (PPA) interneurons.* This cell type has an axon in the str. lacunosum-moleculare co-aligned with the perforant path (Fig. 8c; Vida et al. 1998; Pawelzik et al. 2002). Neurochemical markers of PPA cells include CCK (Pawelzik et al. 2002; Klausberger et al. 2005) and they may also express CB. Cell bodies of PPA cells are in the str. radiatum or lacunosum-moleculare, often at the border of the two layers. Dendrites run radially in these two layers but can also extend into the oriens/alveus (Hájos and Mody 1997; Vida et al. 1998). The dendritic distribution suggests that the cells' input is primarily from the perforant path and Schaffer collaterals, but they may also receive feedback excitation on their distal dendrites in the oriens/alveus.

The axon terminates in the str. lacunosum-moleculare; however, collaterals often spread significantly into the subiculum and, crossing the fissure, into the DG. The postsynaptic targets are primarily principal cells, CA1 pyramidal cells (58–94%), and DG granule cells (0–26%) but also include interneurons (6–11%); the synapses are found mostly on small-caliber dendritic shafts and to a lesser extent (5–7%) dendritic spines (Vida et al. 1998; Klausberger et al. 2005). This cell type provides a convergence of two PPA interneurons onto a single pyramidal cell and can diverge to 1333 neurons (Bezaire and Soltész 2013).

(7) *Lacunosum-associated (LA) cell.* This subtype of interneuron has only recently been described (Fig. 8d, Booker et al. 2017a) and represents a novel dendritic inhibitory subtype. With horizontal somata found in *str. lacunosum*, they have horizontally orientated dendrites and axons. Over 50% of LA cell axon is found within str. lacunosum itself, with dendrites confined to proximal *str. radiatum* and *moleculare.* Of the 5 neurons identified, all are CCK and CB1R immunoreactive and have unique electrophysiological properties (Booker et al. 2017a). The full physiological role of these neurons is yet to be ascertained, but their axonal plexus being found close to CA1 PC primary dendrite bifurcation points suggests a role in branch integration and/or calcium signaling.

(8) *Neurogliaform (NG) cell.* This interneuron type is identified on the basis of a small, stellate dendritic arbor and an extremely dense local axon (Fig. 8e, Vida et al. 1998; Price et al. 2005). NG cells express NPY, NOS, COUP TFII, α-actinin, and reelin as well as high levels of α_1 and δ and $GABA_A$ and μ-opioid receptors, but are consistently negative for PV (Price et al. 2005, Fuentealba et al. 2010; Tricoire et al. 2010; Armstrong et al. 2011, 2012; Krook-Magnuson et al. 2011; Table 8). However, there is a high heterogeneity from cell to cell in their marker expression (Armstrong et al. 2012). The small, round cell body is located in the *str. radiatum* or *lacunosum-moleculare;* within the DG their cell bodies are found at high density at the border with the hippocampal fissure (Armstrong et al. 2011). Several main dendrites emerge from the soma and branch profusely to form a very dense local dendritic arbor. There are no quantitative anatomical data on the input synapses of NG cells. Electrophysiological recordings indicate that the cells receive excitatory input from both the perforant path and the Schaffer collaterals (Price et al. 2005).

Inhibition is mediated by O-LM interneurons (Elfant et al. 2008) and other NGs cells through mutual inhibitory synapses with unique unitary synaptic properties (~70% connectivity, Price et al. 2005). The NG cells are also extensively coupled by gap junctions (~80% connectivity, Price et al. 2005).

The axon forms an extremely dense arbor in the *str. radiatum* and *lacunosum-moleculare* in the vicinity of the cell. An in vitro-labeled NG cell formed almost 13,000 boutons within its termination zone with less than 700 μm diameter along the transverse axis. Postsynaptic targets are mainly pyramidal cell dendritic shafts (~89%) but also spines (11%; Vida et al. 1998). Interestingly, unitary postsynaptic effects of NG-IPSCs are unusually slow and involve not only $GABA_A$ but also $GABA_B$ receptors (Tamás et al. 2003; Szabadics et al. 2007; Price et al. 2008). In fact, postsynaptic response mediated by both these receptor types is elicited in the absence of synaptic contacts through volume transmission plausibly due to the dense and focal axon and the presence of high-affinity extrasynaptic receptors (Szabadics et al. 2007; Oláh et al. 2009). Recent evidence suggests that NG cells in the DG are capable of forming multifarious synapses between both presubiculum, CA1 and the DG, as the axon of some NG cells profusely crosses the hippocampal fissure, with axon varicosities observed on these crossing axons (Armstrong et al. 2011).

(9) *"Ivy" interneurons.* Similar to NG cells, Ivy interneurons can be distinguished by a very dense axonal plexus close to the soma terminating in *str. oriens* and *radiatum* (Fig. 8f, Fuentealba et al. 2008). These cells are immunoreactive for NPY, NOS, COUP TFII, and α-actinin as well as express high levels of α_1 and δ and $GABA_A$ and μ-opioid receptors but are negative for reelin (Fuentealba et al. 2010; Tricoire et al. 2010; Armstrong et al. 2011, 2012; Krook-Magnuson et al. 2011; Table 8). They show a slow-spiking discharge pattern. Ivy cells are more numerous than PV-positive perisomatic inhibitory cells (~1.4-fold higher density, Fuentealba et al. 2008) and may comprise ~20% of all GABAergic interneurons.

Cells bodies of Ivy interneurons are located in the *str. pyramidale* and adjacent regions of the *radiatum*. Dendrites extend radially into the str. oriens and radiatum but rarely reach the str. lacunosum-moleculare. Dendritic distribution and electrophysiological data indicate that these interneurons are activated by the Schaffer collaterals and receive recurrent excitatory input from pyramidal cells, but lack perforant path input, similar to BSCs (Fuentealba et al. 2008).

Postsynaptic targets of Ivy cells are primarily the shafts (81%) of basal dendrites in str. oriens and oblique dendrites in the str. radiatum (Fuentealba et al. 2008). Dendritic spines (13%) and apical dendrites of pyramidal cells (6%) are less frequently targeted. The axon profusely branches close to its point of origin and forms a dense meshwork in the str. oriens and radiatum. In comparison with BSCs labeled under similar conditions, the area covered by axon collaterals is slightly smaller (Ivy, 0.75 ± 0.12 mm [mediolateral] by 1.31 ± 0.11 mm [rostrocaudal], Fuentealba et al. (2008); BSC, 1.15 ± 0.26 mm by 1.53 ± 0.38 mm, Klausberger et al. 2004). However, Ivy cells have a denser axonal plexus, especially in the str. oriens, and representative samples indicate an approximately two times higher total axon length (Fuentealba et al. 2008). Thus, Ivy cells could innervate larger sets

of postsynaptic neurons than BSCs. Indeed, a single Ivy cell can contact up to 1620 cells and on each pyramidal cell a total of 42 Ivy cells converge (Bezaire and Soltész 2013).

(10) *Oriens lacunosum-moleculare-projecting* (O-LM) *interneurons*, as their name indicates, are located in the str. oriens and project to the *str. lacunosum-moleculare* (Fig. 8g; McBain et al. 1994; Sík et al. 1995; Maccaferri et al. 2000). These interneurons are immunopositive for SOM, the metabotropic glutamate receptor mGluR1α, occasionally weakly positive for PV (∼50% of neurons; Booker et al. 2018; Table 8), NPY (Kosaka et al. 1988; Baude et al. 1993; Klausberger et al. 2003), and specifically in CA1 the nicotinic acetylcholine receptor α4 subunits (Leão et al. 2012). SOM interneurons constitute ∼14% of all GABAergic neurons in the hippocampus (Kosaka et al. 1988), but the exact proportion of O-LM cell subset has not yet been established. At the str. oriens/alveus border, approximately 95% of SOM interneurons are of O-LM type, with the remaining 5% being bistratified (Booker et al. 2018)

The soma of O-LM interneurons is located in the *str. oriens*, often at the border to the alveus. The dendritic tree has a horizontal orientation and is restricted to the *str. oriens* and the alveus. In contrast to most other interneurons, the dendrites are densely covered with long, thin spines. Electron microscopic investigations indicate that ∼20% of the afferent synaptic contacts are inhibitory and ∼80% excitatory (Blasco-Ibáñez and Freund 1995). Although the dendritic arbor falls in the termination zone of the Schaffer collateral pathway, degeneration studies revealed that over ∼75% of excitatory synapses originate from the pyramidal cells in the CA1 area (Blasco-Ibáñez and Freund 1995), with direct synaptic contacts being formed from local pyramidal cell (Lacaille et al. 1987). Thus, these interneurons primarily mediate feedback inhibition. CA1 O-LM cells themselves also receive a near homogeneous inhibitory input from CR-containing interneurons (70% of inputs; Tyan et al. 2014). In the CA3 area, the cell bodies and dendrites of this type of interneuron are not restricted to the *str. oriens*, in accordance with the wider distribution of recurrent collaterals seen in this region. A smaller set of interneurons with similar axonal projection and neurochemical profile but with somata located in the *str. pyramidale* (P-LM cells) or *radiatum* (R-LM cells) and dendrites spanning *str. radiatum* and *oriens* have been identified in transgenic "GIN" mice (Oliva Jr et al. 2000).

The axon of O-LM cells originates often from one of the main dendrites (Martina et al. 2000). Major collaterals ascend to the *str. lacunosum-moleculare* (often bifurcating within *str. radiatum)* and form a dense arborization in that layer. Some cells additionally form an axonal arbor, albeit much less extensive, in the *str. oriens*. The axon of an in vivo-labeled O-LM cell has a length of 63,436 μm occupying a relatively small termination field of 500 μm by 840 μm (mediolateral and septotemporal axes; Sík et al. 1995). Interestingly, in vitro-labeled O-LM interneurons in the CA3 show similar restricted axon projection in transverse slices but form multiple innervation fields along the septotemporal axis (Gloveli et al. 2005a). Over 91% of the collaterals are found in the *str. lacunosum-moleculare*, only 7% in the *str. oriens*, and a small proportion invading the subiculum. The

bouton density is $0.27 \pm 0.04\ \mu m^{-1}$ and the number of boutons was calculated to be over 16,800 (Sík et al. 1995). However, electron microscopic analysis of in vitro-labeled neurons showed that the axon can make synaptic contacts without forming varicosities, therefore it is difficult to estimate the total number of output synaptic contacts (Maccaferri et al. 2000). Postsynaptic targets of O-LM cells include dendrites of principal cells and interneurons in proportion to their occurrence (Katona et al. 1999a; Elfant et al. 2008). The synapses are found on dendritic shafts (~70%) and to a lesser degree on spines (~30%; Sík et al. 1995; Katona et al. 1999a; Maccaferri et al. 2000). Briefly, a single O-LM cell can innervate 1457 pyramidal cells and 180 interneurons and 8 O-LM cells converge onto a single principal cell (Bezaire and Soltész 2013).

(11) *Trilaminar (TL) interneurons*. This interneuron type is characterized by an axon distributed to three adjacent layers (hence the name): the *str. radiatum, pyramidale*, and the *oriens* (Sík et al. 1995; Gloveli et al. 2005b; Ferraguti et al. 2005). TL cells express high levels of muscarinic acetylcholine receptor (M2), but other markers are unknown (Hájos et al. 1998; Ferraguti et al. 2005).

The cells show some similarities to O-LM interneurons. Their cell bodies are located in the *str. oriens* and the dendritic trees are restricted to the same layer. The dendrites are sparsely spiny. The cells receive synaptic input from excitatory and inhibitory terminals expressing high levels of mGluR8, indicating a strong glutamatergic modulation of the input (Ferraguti et al. 2005). The cellular origin of the synapses is unknown, but local pyramidal cells are likely to be involved in the excitatory input. A part of the inhibitory terminals shows immunoreactivity for VIP and is likely to originate from a subset of IS interneurons (Ferraguti et al. 2005).

The axon terminates in the *str. radiatum, pyramidale, and oriens* and extends into neighboring areas, i.e., to the subiculum from the CA1 (Ferraguti et al. 2005) or the CA1 from the CA3 (Gloveli et al. 2005b) and may also project to other brain areas as well. The total axon length of an in vivo-labeled TL cell in the CA1 area was 55,913 μm and covers an area of 2600 μm (septotemporal) by 2450 μm (mediolateral) (Sík et al. 1995). Based on bouton density ($0.28 \pm 0.05\ \mu m^{-1}$), the calculated number of boutons is 15,767. Synapses formed by TL cells constitute 10 synaptic contact sites, and a single TL cell can innervate approximately 1544 cells (Bezaire and Soltész 2013). Postsynaptic neurons of TL cells locally include pyramidal cells and an unusually high proportion of interneurons. In the CA1, the targets are interneuron dendrites (44%), interneuron cell bodies (8%), pyramidal cell dendritic shafts (25%), and somata (23%; Ferraguti et al. 2005).

(12) *Mossy fiber-associated (MFA) interneurons.* This interneuron is a specific CA3 type and characterized by an axon plexus in the str. lucidum co-aligned with mossy fibers (Fig. 9; Vida and Frotscher 2000; Losonczy et al. 2004). MFA interneurons express CCK and high levels of CB1 receptor in their synaptic terminals maintaining a very low initial release probability (Losonczy et al. 2004). The small round or ovoid soma of MFA cells is located in or near the *str. lucidum*, and their dendrites extend radially into the str. radiatum and the oriens. The dendritic distribution indicates that the main sources of excitation are ipsi- and contralateral

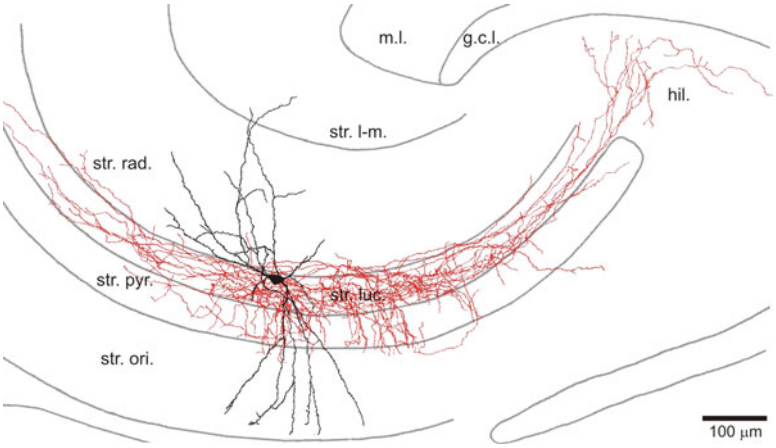

Fig. 9 MFA interneurons of the CA3 area. The axon (*red*) of this interneuron type terminates mainly in the str. lucidum (luc.) but also extends into the hilus displaying a striking association to the mossy fiber projection. The dendrites are found in the *str. radiatum* (rad.) and *oriens* (ori.) but absent from the *str. lacunosum-moleculare* (m-l.), reflecting that the cells receive excitatory input primarily from ipsi- and contralateral CA3 pyramidal cells. (Reproduced from Vida and Frotscher 2000 with permission. © National Academy of Sciences, USA)

CA3 pyramidal cells (i.e., the recurrent collaterals and commissural fibers), but physiological data (Tóth and McBain 1998) further show that the cells also receive mossy fiber input. No or minimal excitatory input arrives to these cells from the perforant path.

The axon forms a dense plexus in the str. lucidum, covering 50–100% of the transverse extent of the CA3 and fanning out into the hilus. Additionally, some collateral extend into the cell body layer. The axonal distribution is strikingly similar to that of the mossy fibers; this cell type best exemplifies the co-alignment of inhibitory interneuron axons and excitatory afferent pathway. Synaptic contacts are located on dendritic shafts (85%), mostly large-caliber proximal dendrites, and to a lesser degree on somata (15%) in the CA3 area. Majority of the targets are pyramidal cells, although ~20% of the postsynaptic profiles belong to GABA-immunoreactive interneurons (Vida and Frotscher 2000). The length of the axon in the in vitro-labeled neurons is 20.3–28.6 mm and forms ~5000–7000 boutons (density, 0.23 – 0.25 μm^{-1}). As the postsynaptic pyramidal cells are innervated by ~4 synaptic contact sites, a single MFA interneuron may target 1300–1700 neurons.

Interneuron-Specific Interneurons

A class of interneuron specialized to innervate other interneurons has been identified by imunohistochemically staining for CR and VIP (Acsády et al. 1996a, b; Gulyás

et al. 1996; Hájos et al. 1996; Table 8). Three types have been distinguished on the basis of the neurochemical markers and synaptic targets (Fig. 10):

(13) *Type I (IS-I) cells* contain CR, the soma of IS-I cells is in *str. oriens, pyramidale*, or *radiatum* and the dendrites span most layers (Acsády et al. 1996a; Gulyás et al. 1996). They target CB-positive dendrite-inhibiting interneurons but avoid PV-expressing BCs and axo-axonic cells. Furthermore, these interneurons form extensive mutual inhibitory connections as well as making dendrodendritic contacts coupled by gap junctions (Gulyás et al. 1996; Fig. 10).

(14) *Type II (IS-II) cells* express VIP and their soma is found in *str. radiatum*, often at its upper border, whereas the dendrites mostly extend into the *str. lacunosum-moleculare* and are densely spiny. These interneurons preferentially innervate CCK/VIP-positive basket cells. Furthermore, they form inhibitory synapses onto CR interneurons, thereby contributing to the mutual inhibitory network of IS-I cells, but receiving no output from this network.

(15) *Type III (IS-III) cells* contain both VIP and CR and have soma located in *str. pyramidale* or *radiatum* with radial dendrites, which show either unipolar or bipolar morphologies spanning most layers and forming a tuft in the str. L-M (Acsády et al. 1996b; Gulyás et al. 1996; Chamberland et al. 2010). IS-III have an axon mostly localized to *str. oriens* and mainly target SOM-positive interneurons in this layer, in particular O-LM cells, with a connection probability of 56%, which is higher than for BCs (10%) or BSCs (16%), but they never contacted CA1 PCs (Tyan et al. 2014). Interestingly, as their main targets, the O-LM cells, IS-IIIs also express mGluR1α on their somatodendritic domains (Ferraguti et al. 2004), and additionally mGluR7 are localized to their axon terminals (Somogyi et al. 2003).

INs with Local and Long-Range Projecting Axons

While interneurons are characterized by an extensive local axon restricted to a given area, it has long been noted that axon collaterals of some types, for example, those localized close to the fissure, such as CA1 PPA cells, crossed boundaries of the area and often extend into the neighboring area, e.g., the ML of the dentate gyrus (Vida et al. 1998). Additionally, interneurons were identified with major axon collaterals forming distinct collateralizations in other hippocampal areas. First and most prominent example was described by Sík et al. (1994) as BP cells found in the str. oriens of the CA1 area (see type 12 above). Finally, a subset of INs possesses both local and long-range projecting axons, targeting retrohippocampal regions or the septum. The latter two group of INs are referred to as projection INs and are believed to synchronize activity across brain regions, allowing coordinated neuronal firing.

(16) *Back-projection (BP) interneurons.* This interneuron type was named for its extensive axon projecting "back" to the CA3 area and the hilus from the CA1 (Sík et al. 1994, 1995). BP cells have been suggested to correspond to a subset of NADPH-diaphorase and NOS-immunoreactive cells (Sík et al. 1994) and were also found to express SOM and CB (Goldin et al. 2007; Gulyás et al. 2003; Table 8). The

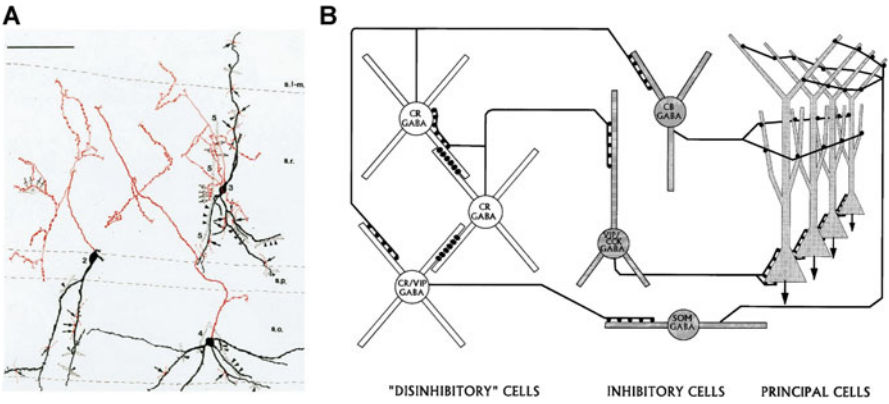

Fig. 10 IS interneurons of the hippocampus. (**a**) Camera lucida drawing of CR-containing interneurons of the CA1 area (cell bodies and dendrites are in black; axons are in *red*). The cells often form dendrodendritic and axodendritic contacts with each other. Synaptic partners are indicated by *dotted outlines*. Arrowheads indicate locations where the dendrites ran parallel in close contact. (**b**) Simplified schematic representation of hippocampal microcircuits including IS interneurons ("disinhibitory cells"). IS cells are interconnected by dendrodendritic (bars on dendrites) and axodendritic contacts which presumably serve their rhythmic and synchronized activity. The cells' output is directed to and controls the activity of several types of inhibitory interneurons including CCK- and VIP-containing BCs (VIP/CCK GABA), O-LM interneurons (SOM GABA), and CB-immunoreactive dendritic inhibitory interneurons (CB GABA). (Reproduced from Gulyás et al. 1996 with permission. © The Society for Neuroscience)

somatodendritic domain of BP cells is bipolar and confined to the *str. oriens* and shows similarities to other horizontal interneuron types of this layer (e.g., O-LM cells) including the presence of long, thin spines. The total length of axon collaterals is 20,642 μm, 59% of which is in the CA1 region and 41% project back to CA3 area innervating the *str. oriens* and *radiatum*. The synaptic connections of these cells have not been studied in detail, but they form synapses on dendrites and somata of pyramidal cells in the CA1 (Sík et al. 1994).

On the basis of their local axonal distribution, these cells may overlap with previously described oriens-BSC and/or TL cells identified morphologically in slice preparation. Furthermore, interneurons with long-range projection to the septum (*double-projections cells*; see below) have similar neurochemical profile and intrahippocampal projection pattern and may overlap, at least partially, with this interneuron type (Gulyás et al. 2003; Goldin et al. 2007).

(17) *Corticotropin-releasing hormone-expressing interneurons.* A recently described CA1 interneuron type, which selectively expresses corticotropin-releasing hormone (CRH) (Yan et al. 1998; Hooper and Maguire 2016). Found within the CA1 *str. pyramidale*, these neurons also express SOM (40% of neurons), CB (27% of neurons), and CR (23% of neurons) and may also express PV and CCK. They

have large ovoid somata and vertically oriented dendritic tree, spanning *str. oriens* and *radiatum,* reminiscent of CA1 PCs. Their axon projects to the *str. pyramidale* of CA3, providing strong inhibition to cell bodies of CA3 PCs (Hooper and Maguire 2016).

(18) *RADI cells* express CB and COUP-TFII and have somata in *str. L-M*, with short dendrites that remain in the same layer (Fuentealba et al. 2010). The axon of RADI cells densely innervates *str. radiatum*, forming synaptic contacts with the dendrites of CA1 PCs and other interneurons, but minimally ramifies in *str. L-M*. In addition, RADI cells send an axon collateral across the hippocampal fissure to *str. granulosum* of the DG, forming BC like synapses with the cell bodies of dentate granule cells (Fuentealba et al. 2010).

(19) *Double-projecting interneurons* are characterized by a long-range axonal projection to the septum and retrohippocampal areas, in addition to its intrahippocampal axon (Jinno et al. 2007; Fig. 11). Similar to many other interneuron types in the oriens/alveus, their somata and dendrites are located in *str. oriens* and they are immunoreactive for SOM, CB, NPY, and MGluR1α (Gulyás et al. 2003; Jinno et al. 2007). Interestingly, in the CA3 interneurons with hippocampo-septal projection also exist and mostly express SOM, but instead of CB they show CR immunoreactivity (Gulyás et al. 2003). In the CA1, they have horizontal

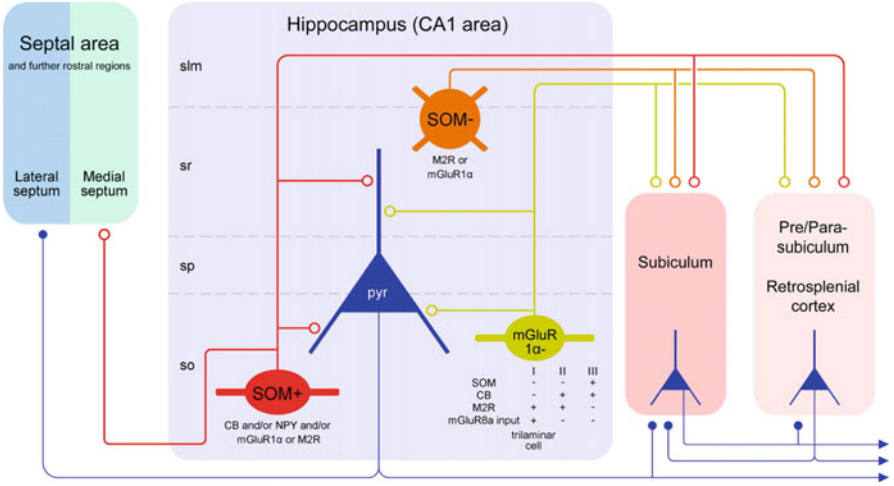

Fig. 11 Long-range projecting interneurons of the hippocampus. The schematic diagram shows the three main subsets of CA1 hippocampal GABAergic neurons projecting to the septal and/or retro-hippocampal areas. The first major population (double-projecting cells, in red) is located in str. oriens and projects to both the retrohippocampal and septal areas. The second population (*oriens/retrohippocampal projection cells, in* green) is less common in str. oriens, projects exclusively to the subicular areas, and shows diverse molecular expression profiles, as indicated below the cell. The third population (*radiatum/retrohippocampal projection cells,* in brown), found in the str. radiatum and lacunosum-moleculare, projects to retrohippocampal areas but not to the septum. (Reproduced from Jinno et al. 2007 with permission. © The Society for Neuroscience)

dendrites restricted to the *str. oriens*; however some multipolar and vertical examples have been observed. Double-projecting neurons have intrahippocampal axonal arborization in the CA3 and DG, in addition to their thick and strongly myelinated long-range retrohippocampal and a septal axon collaterals. The major divergence of double-projecting cells is with respect to their target cells. While some of these interneurons contact spiny principal cell dendrites (Jinno et al. 2007), others have been shown to preferentially contact interneuron dendrites (Gulyás et al. 2003). Therefore it remains ambiguous to what extent these cells are one class or multiple subtypes.

(20) *Oriens/retrohippocampal projection* cells have somata and bipolar, horizontal dendrites confined to *str. oriens,* comparable in morphology to other horizontally oriented *str. oriens/alveus* interneurons. These interneurons are immunoreactive for CB, as well as SOM. Oriens retrohippocampal projection INs possess a dense axon in *str. radiatum* and *oriens* of CA1, where they predominately contact CA1 PC dendrites (Jinno et al. 2007). The myelinated projection axon ramifies in either subiculum or the mEC where, in contrast to the local collaterals, it seems to preferentially form synapses onto INs (Melzer et al. 2012).

(21) *Radiatum/retrohippocampal projection* interneurons have soma located at the *str. radiatum/L-M* border region and radially oriented dendrites spanning these layers. *Their* axon which may form local synapses in the *str. L-M* sends a thick, myelinated axon to the subiculum, presubiculum, retrosplenial cortex, and indusium griseum, where it preferentially forms synapses with GABAergic interneurons dendrites.

Interneurons of the DG and Hilus

The layering of the DG differs markedly from that of the CA areas. Therefore, many of the DG interneuron types show differences in their morphology to their counterparts in those areas. In the following section, we briefly review the main morphological feature and connectivity, whenever known, of the major DG interneuron types.

Perisomatic Inhibitory Interneurons

(1) *Fast-spiking PV-BCs* are the best investigated interneuron type of the DG (Han et al. 1993; Halasy and Somogyi 1993b; Scharfman 1995; Sík et al. 1997; Mott et al. 1997; Bartos et al. 2001, 2002; Doischer et al. 2008; Nörenberg et al. 2010). The somatodendritic morphology is reminiscent of pyramidal cells. The large triangular or ovoid soma is located in the granule cell layer, often at the border to the hilus. Apical dendrites extend into the molecular layer and can receive input from all major afferent pathways. Basal dendrites are found in the hilus and receive recurrent excitatory input from mossy fibers mediated by multiple, 2–4 distributed contacts

(Geiger et al. 1997). The mean surface area of the apical and basal dendrites of in vitro labeled BCs is 7600 and 2200 μm^2, respectively (Nörenberg et al. 2010). The main postsynaptic targets of BCs are GCs (Geiger et al. 1997; Kraushaar and Jonas 2000; Bartos et al. 2002). Similar to the CA areas, DG PV-BCs are also extensively coupled by mutual inhibitory synapses (70–80% connectivity for closely spaced BCs) and gap junctions (~30% connectivity, Bartos et al. 2001, 2002).

(2) *CCK-BCs* were described in the in vivo labeling study by Sík et al. (1997), but no further data have been obtained from identified CCK-BC from the DG.

(3) *AACs* of DG were first described in detail by Han et al. (1993) and Buhl et al. (1994a, b). Somatodendritic morphology of AACs is largely similar to that of BCs. The output is directed exclusively to the axon initial segment of GCs. These synapses involve multiple contact sites; in case of one AAC-GC pair, eight contacts were identified and the number of AACs converging onto the same initial segment was calculated to be five (Buhl et al. 1994a).

Dendritic Inhibitory Interneurons

(4) *Molecular layer perforant path-associated (MOPP) interneurons* are located in the molecular layer and project to the outer two-thirds of this layer co-aligned with the perforant path (Han et al. 1993; Halasy and Somogyi 1993b; Sík et al. 1997). A subset of molecular layer interneurons shows a similar projection in the DG, but many of its axon collaterals cross the hilus and terminate in the CA1 area and/or the subiculum ("OML cells," Ceranik et al. 1997; Hosp et al. 2005). Many features of these interneurons correspond to those of CA1 PPA cells.

(5) *Hilar perforant path-associated (HIPP) interneurons* (Han et al. 1993; Halasy and Somogyi 1993b; Sík et al. 1997; Hosp et al. 2005) correspond to O-LM interneurons of the CA areas. Their soma and dendrites are confined to the hilus and receive recurrent excitation from the mossy fibers. Their axon terminates in the outer two-thirds of the molecular layer parallel to the perforant path. Thus, HIPP interneurons constitute the main feedback dendritic inhibitory cell types of the DG. Similar to O-LM cells, HIPP cells express SOM (Katona et al. 1999a).

(6) *Hilar commissural/associational path-associated (HICAP) interneurons* are characterized by an axon in the inner molecular layer, co-aligned with the commissural/associational path (Han et al. 1993; Halasy and Somogyi 1993b; Sík et al. 1997; Lübke et al. 1998; Hosp et al. 2005). The soma is located in the hilus, and the dendrites are found both in the hilus and in the molecular layer. Therefore, HICAP cells can mediate both feedforward and feedback inhibition.

(7) *Total molecular layer (TML) interneurons* project to the molecular layer, covering vertically the entire layer (Mott et al. 1997; Hosp et al. 2005). The soma is located in the cell body layer and the dendrites extend into both the hilus and the molecular layer. Therefore, TML cells can mediate inhibition to the entire dendritic tree of GCs in both feedforward and feedback manner.

Genetic Diversity of Hippocampal Interneurons

All of the neurochemical classifications of interneurons rely on differential translation of proteins, either calcium-binding, neuropeptides, transmembrane receptors and channels, or transcription factors and enzymes. All of these differentiating factors rely on differential gene expression, through DNA transcription to RNA translation. Recent advances in single-cell reverse-transcriptase PCR (RT-PCR) and RNA sequencing (RNAseq) have allowed detailed characterization of individual genetic markers and classification of inhibitory interneurons in an unbiased manner. Despite the early stage that this form of analysis is, we will highlight several genetic divergences, which partly explain interneuron diversity (Monyer and Markram 2004).

The single greatest form of genetic diversity arises from the location from which interneurons progenitors arise in the brain, the ganglionic eminences. Those neurons which are formed within the medial ganglionic eminence (mGE) are fated to become PV, NPY, and SOM. Meanwhile interneurons formed from the central ganglionic eminence (cGE) contain CCK, Reelin, and VIP. However, there is still some overlap, with nNOS and CR containing interneurons arising from both mGE and cGE (reviewed in Wamsley and Fishell 2017). These fate maps of interneuron development are underlain by precise genetic cues, with mGE expression of *Nkx2.1*, *Lhx6*, *Sox6*, and *Sip1*, the order of which defines the maturation state of these interneurons. cGE VIP neurons meanwhile selectively express *Igf1*, which controls synaptogenesis in these interneurons.

More recent adoption of single-cell RNAseq methods has allowed unbiased characterization of interneuron subtypes. For example, using this technique approximately 16 clustered subtypes of CA1 interneuron have been described (Zeisel et al. 2015). How these subtypes overlap with the 20+ described neurochemical, anatomical, and electrophysiological types remains to be seen. One technique that is approaching is the development of Patch-Seq (Fuzik et al. 2016), whereby electrophysiological recordings can be combined with RNA harvesting and anatomical tracing to determine genetic diversity. This technique, so far only applied to neocortical CCK interneurons, has identified five CCK subtypes, which is near to consistent with the number of putative cell types observed in CA1.

Experimental Techniques

Golgi Silver Staining Method

The first experimental approach that enabled detailed analysis of the morphological features of neurons was the “black reaction” developed by Camillo Golgi in the late nineteenth century. The Golgi method results in the complete labeling of a random set of neurons. The sparse staining pattern enables the examination of the

morphology of individual cells. Many neuroscientists, including Ramon y Cajal, applied this method successfully to investigate the structure and gain insights into the function of neurons in various brain areas, including the hippocampus. Although targeted labeling methods often offer clear advantages, the Golgi method can be still used to label and characterize abundant cell types (e.g., cortical principal cells). A modern version of the Golgi staining method can be observed in some transgenic lines, such as Thy1-GFP mice, in which green fluorescent protein is randomly expressed in a subset of DG GCs (Feng et al. 2000).

Immunocytochemistry

Neurons express a wide variety of molecules which can be detected and visualized using specific antibodies (Freund and Buzsáki 1996; Somogyi and Klausberger 2005; Jinno and Kosaka 2006). Some of these neurochemical markers are evenly distributed in the cytoplasm (e.g., PV, CB, and CR) or on the surface of the plasma membrane (mGluR1a); therefore, the immunostaining can delineate neurons in their entirety. Morphology of cell types with low density can be investigated using this method; however, the analysis is often restricted to the somatodendritic domain, as overlapping axonal arbors cannot be resolved with accuracy.

Targeted Labeling of Single Cells

Microelectrode and whole-cell patch-clamp recordings can be combined with intracellular labeling, using either fluorescent markers (including ion- and voltage-sensitive dyes) or biocytin/neurobiotin-based assay systems (Lacaille et al. 1987; Buhl et al. 1994a). While fluorescent dyes can be directly observed during recording, biocytin needs to be visualized by histological processing of the tissue after the recording session. This combined approach enables the identification and detailed morphological analysis of the recorded neurons to complement the physiological data. Intracellular staining of synaptically coupled neurons has been successfully used to establish the number and location of synaptic contacts. Furthermore, intracellular labeling can be combined with immunostaining to characterize the neurons neurochemically.

In vitro labeling in acute hippocampal slices has been extensively applied and provided much of the information on the structure and function of various hippocampal neurons obtained in the last two decades. However, in vitro labeling has obvious limitations in that the neurons are incomplete; part of the dendritic tree and the axon is removed during the slicing procedure. For this reason, in vivo labeling approaches, despite their lower efficiency and laborious nature, are often preferable.

In Vivo Labeling of Single Cells

In vivo labeling has been performed using microelectrode (Soltész et al. 1993; Sík et al. 1994) and more recently by whole-cell patch-clamp recordings (Lee et al. 2009). These two methods provide high-resolution electrophysiological data but inevitably lead to some degree of damage to the neurons. Alternatively, juxtacellular recordings can be performed (Klausberger et al. 2003). The physiological data, using this approach, are restricted to the discharge pattern of the neurons, but high-quality anatomical data can be obtained for correlated light and electron microscopic investigations.

The Future

Neuroanatomical investigation focusing on hippocampal neurons and networks has been performed for well over a century. These investigations have identified a large number of neuron types and provided a growing body of information on their morphology and synaptic connections. However, despite the extensive research, our knowledge is still rather limited and patchy, as this chapter also reflects.

First, classification of interneurons with atypical morphological features needs further attention. Their classification is difficult while often only one or a few examples exist in the literature. The low numbers conceivably suggest low abundance; however, the recent identification of "Ivy" interneurons (Fuentealba et al. 2008) indicates that there are still significant discoveries to be made. Second, detailed quantitative information about the morphological structure (Emri et al. 2001; Nörenberg et al. 2010) of many cell types is still missing; this would be required to create realistic single-cell models and investigate integrative properties of these neurons. Finally, connectivity of the various types should be systematically mapped (Li et al. 1992; Megías et al. 2001). While synaptic target profiles are mostly well established, divergence and convergence factors in the network have remained often unknown. This information is indispensable for our understanding of how microcircuits and large-scale networks are built and function under normal and pathological conditions.

To achieve these goals, we need to invest, no doubt, hundreds of "man-years" of dedicated and meticulous work. However, recent and future advances in experimental techniques will offer better conditions, higher efficiency, and improved resolution to morphological analysis. Novel, high-resolution imaging techniques in combination with ion- and voltage-sensitive dyes (Rózsa et al. 2004; Homma et al. 2009) and genetically encoded markers (Oliva Jr et al. 2000; Meyer et al. 2002; Livet et al. 2007) will facilitate correlated investigations of activity patterns and structure of hippocampal neurons and networks. Improved transsynaptic viral tools should advance mapping of functional and anatomical connectivity (Boldogkői et al. 2009). In combination with these methods, post hoc electron microscopic ultrastructural

investigations remain important to confirm and extend results obtained at the light microscopic level. While in vitro recording and labeling techniques continue to dominate hippocampal research, especially in the analysis of individual synaptic connections, in vivo approaches, such as juxtacellular and whole-cell patch-clamp recordings (Klausberger et al. 2003; Lee et al. 2009), will become increasingly important not only for the physiological but also for the anatomical characterization of the neurons. Wider use of these methods will help us to create large libraries of neurons and enable us on the one hand to establish general morphological features of the various neuron types and on the other to better appreciate variability of individual cells.

Further Reading

Acsády L, Arabadzisz D, Freund TF (1996a) Correlated morphological and neurochemical features identify different subsets of vasoactive intestinal polypeptide-immunoreactive interneurons in rat hippocampus. Neurosci 73:299–315

Acsády L, Görcs TJ, Freund TF (1996b) Different populations of vasoactive intestinal polypeptide-immunoreactive interneurons are specialized to control pyramidal cells or interneurons in the hippocampus. Neurosci 73:317–334

Acsády L, Kamondi A, Sík A, Freund T, Buzsáki G (1998) GABAergic cells are the major postsynaptic targets of mossy fibers in the rat hippocampus. J Neurosci 18:3386–3403

Acsády L, Katona I, Martınez-Guijarro FJ, Buzsáki G, Freund TF (2000) Unusual target selectivity of perisomatic inhibitory cells in the hilar region of the rat hippocampus. J Neurosci 20:6907–6919

Ali AB (2007) Presynaptic Inhibition of GABAA receptor-mediated unitary IPSPs by cannabinoid receptors at synapses between CCK-positive interneurons in rat hippocampus. J Neurophysiol 98:861–869

Ali AB, Thomson AM (1998) Facilitating pyramid to horizontal oriens-alveus interneurone inputs: dual intracellular recordings in slices of rat hippocampus. J Physiol 507:185–199

Amaral DG (1978) A Golgi study of cell types in the hilar region of the hippocampus in the rat. J Comp Neurol 182:851–914

Ambros-Ingerson J, Holmes WR (2005) Analysis and comparison of morphological reconstructions of hippocampal field CA1 pyramidal cells. Hippocampus 15:302–315

Armstrong C, Szabadics J, Tamás G, Soltész I (2011) Neurogliaform cells in the molecular layer of the dentate gyrus as feed-forward γ-aminobutyric acidergic modulators of entorhinal–hippocampal interplay. J Comp Neurol 519:1476–1491

Armstrong C, Krook-Magnuson E, Soltész I (2012) Neurogliaform and ivy cells: a major family of nNOS expressing GABAergic neurons. Front Neural Circuits 6(May):1–10

Bannister NJ, Larkman AU (1995a) Dendritic morphology of CA1 pyramidal neurones from the rat hippocampus: I. Branching patterns. J Comp Neurol 360:150–160

Bannister NJ, Larkman AU (1995b) Dendritic morphology of CA1 pyramidal neurones from the rat hippocampus: II. Spine distributions. J Comp Neurol 360:161–171

Bartos M, Vida I, Frotscher M, Geiger JRP, Jonas P (2001) Rapid signaling at inhibitory synapses in a dentate gyrus interneuron network. J Neurosci 21:2687–2698

Bartos M, Vida I, Frotscher M, Meyer A, Monyer H, Geiger JRP, Jonas P (2002) Fast synaptic inhibition promotes synchronized gamma oscillations in hippocampal interneuron networks. Proc Natl Acad Sci U S A 99:13222–13227

Baude A, Bleasdale C, Dalezios Y, Somogyi P, Klausberger T (2007) Immunoreactivity for the GABAA receptor alpha1 subunit, somatostatin and Connexin36 distinguishes axoaxonic, basket, and bistratified interneurons of the rat hippocampus. Cereb Cortex 17:2094–2107

Baude A, Nusser Z, Roberts JD, Mulvihill E, McIlhinney RA, Somogyi P (1993) The metabotropic glutamate receptor (mGluR1 alpha) is concentrated at perisynaptic membrane of neuronal subpopulations as detected by immunogold reaction. Neuron 11:771–787

Beining M, Jungenitz T, Radic T, Deller T, Cuntz H, Jedlicka P, Schwarzacher SW (2017) Adult-born dentate granule cells show a critical period of dendritic reorganization and are distinct from developmentally born cells. Brain Struct Funct 222:1427–1446

Bezaire MJ, Soltész I (2013) Quantitative assessment of CA1 local circuits: Knowledge base for interneuron-pyramidal cell connectivity. Hippocampus 23:751–785

Blackstad TW (1956) Commissural connections of the hippocampal region in the rat, with special reference to their mode of termination. J Comp Neurol 105:417–537

Blackstad TW, Kjaerheim A (1961) Special axo-dendritic synapses in the hippocampal cortex: electron and light microscopic studies on the layer of mossy fibers. J Comp Neurol 117:133–159

Blasco-Ibáñez JM, Freund TF (1995) Synaptic input of horizontal interneurons in stratum oriens of the hippocampal CA1 subfield: Structural basis of feed-back activation. Eur J Neurosci 7:2170–2180

Blasco-Ibáñez JM, Martínez-Guijarro F-J, Freund TF (2000) Recurrent mossy fibers preferentially innervate parvalbumin-immunoreactive interneurons in the granule cell layer of the rat dentate gyrus. Neuroreport 11:3219–3225

Bloss EB, Cembrowski MS, Karsh B, Colonell J, Fetter RD, Spruston N (2016) Structured dendritic inhibition supports branch-selective integration in CA1 pyramidal cells. Neuron 89:1016–1030

Bloss EB, Cembrowski MS, Karsh B, Colonell J, Fetter RD, Spruston N (2018) Single excitatory axons form clustered synapses onto CA1 pyramidal cell dendrites. Nature Neurosci 19:1

Boldogkői Z, Bálint K, Awatramani GB, Balya D, Busskamp V, Viney TJ, Lagali PS, Duebel J, Pásti E, Tombácz D, Tóth JS, Takács IF, Scherf BG, Roska B (2009) Genetically timed, activity-sensor and rainbow transsynaptic viral tools. Nat Methods 6:127–130

Booker SA, Gross A, Althof D, Shigemoto R, Bettler B, Frotscher M, Hearing M, Wickman K, Watanabe M, Kulik Á, Vida I (2013) Differential $GABA_B$-receptor-mediated effects in perisomatic- and dendrite-targeting parvalbumin interneurons. J Neurosci 33:7961–7974

Booker SA, Althof D, Degro CE, Watanabe M, Kulik Á, Vida I (2017a) Differential surface density and modulatory effects of presynaptic GABAB receptors in hippocampal cholecystokinin and parvalbumin basket cells. Brain Struct Funct 222:3677–3690

Booker SA, Althof D, Gross A, Loreth D, Müller J, Unger A, Fakler B, Varro A, Watanabe M, Gassmann M, Bettler B, Shigemoto R, Vida I, Kulik Á (2017b) KCTD12 auxiliary proteins modulate kinetics of GABAB receptor-mediated inhibition in cholecystokinin-containing interneurons. Cerebral Cortex (New York, N.Y.: 1991) 27:2318–2334

Booker SA, Loreth D, Gee AL, Watanabe M, Kind PC, Wyllie DJA, Kulik Á, Vida I (2018) Postsynaptic GABABRs inhibit L-type calcium channels and abolish long-term potentiation in hippocampal somatostatin interneurons. Cell Rep 22:36–43

Botcher NA, Falck JE, Thomson AM, Mercer A (2014) Distribution of interneurons in the CA2 region of the rat hippocampus. Front Neuroanatomy 8

Buckmaster PS, Strowbridge BW, Schwartzkroin PA (1993) A comparison of rat hippocampal mossy cells and CA3c pyramidal cells. J Neurophysiol 70:1281–1299

Buckmaster PS, Wenzel HJ, Kunkel DD, Schwartzkroin PA (1996) Axon arbors and synaptic connections of hippocampal mossy cells in the rat in vivo. J Comp Neurol 366:271–292

Buckmaster PS (2012) Mossy cell dendritic structure quantified and compared with other hippocampal neurons labeled in rats in vivo. Epilepsia 53(Suppl. 1):9–17

Buhl EH, Cobb SR, Halasy K, Somogyi P (1995) Properties of unitary IPSPs evoked by anatomically identified basket cells in the rat hippocampus. Eur J Neurosci 7:1989–2004

Buhl EH, Halasy K, Somogyi P (1994a) Diverse sources of hippocampal unitary inhibitory postsynaptic potentials and the number of synaptic release sites. Nature 368:823–828
Buhl EH, Han ZS, Lőrinczi Z, Stezhka VV, Karnup SV, Somogyi P (1994b) Physiological properties of anatomically identified axo-axonic cells in the rat hippocampus. J Neurophysiol 71:1289–1307
Buhl EH, Szilágyi T, Halasy K, Somogyi P (1996) Physiological properties of anatomically identified basket and bistratified cells in the CA1 area of the rat hippocampus in vitro. Hippocampus 6:294–305
Bullis JB, Jones TD, Poolos NP (2007) Reversed somatodendritic Ih gradient in a class of rat hippocampal neurons with pyramidal morphology. J Physiol 579:431–443
Cajal SR (1968) The structure of the Ammon's horn. Charles C. Thomas, Springfield
Cannon RC, Wheal HV, Turner DA (1999) Dendrites of classes of hippocampal neurons differ in structural complexity and branching patterns. J Comp Neurol 413:619–633
Carnevale NT, Tsai KY, Claiborne BJ, Brown TH (1997) Comparative electrotonic analysis of three classes of rat hippocampal neurons. J Neurophysiol 78:703–720
Cembrowski MS, Bachman JL, Wang L, Sugino K, Shields BC, Spruston N (2016a) Spatial gene-expression gradients underlie prominent heterogeneity of CA1 pyramidal neurons. Neuron 89:351–368
Cembrowski MS, Wang L, Sugino K, Shields BC, Spruston N (2016b) Hipposeq: a comprehensive RNA-seq database of gene expression in hippocampal principal neurons. eLife 5
Ceranik K, Bender R, Geiger JR, Monyer H, Jonas P, Frotscher M, Lübke J (1997) A novel type of GABAergic interneuron connecting the input and the output regions of the hippocampus. J Neurosci 17:5380–5394
Chamberland S, Salesse C, Topolnik D, Topolnik L (2010) Synapse-specific inhibitory control of hippocampal feedback inhibitory circuit. Front Cell Neurosci 4 Available at: https://www.frontiersin.org/articles/10.3389/fncel.2010.00130/full
Chevaleyre V, Siegelbaum SA (2010) Strong CA2 pyramidal neuron synapses define a powerful disynaptic cortico-hippocampal loop. Neuron 66:560–572
Chicurel ME, Harris KM (1992) Three-dimensional analysis of the structure and composition of CA3 branched dendritic spines and their synaptic relationships with mossy fiber boutons in the rat hippocampus. J Comp Neurol 325:169–182
Chitwood RA, Hubbard A, Jaffe DB (1999) Passive electrotonic properties of rat hippocampal CA3 interneurones. J Physiol 515:743–756
Christie BR, Franks KM, Seamans JK, Saga K, Sejnowski TJ (2000) Synaptic plasticity in morphologically identified CA1 stratum radiatum interneurons and giant projection cells. Hippocampus 10:673–683
Claiborne BJ, Amaral DG, Cowan WM (1986) A light and electron microscopic analysis of the mossy fibers of the rat dentate gyrus. J Comp Neurol 246:435–458
Claiborne BJ, Amaral DG, Cowan WM (1990) Quantitative, three-dimensional analysis of granule cell dendrites in the rat dentate gyrus. J Comp Neurol 302:206–219
Cobb SR, Halasy K, Vida I, Nyiri G, Tamás G, Buhl EH, Somogyi P (1997) Synaptic effects of identified interneurons innervating both interneurons and pyramidal cells in the rat hippocampus. Neurosci 79:629–648
Cope DW, Maccaferri G, Márton LF, Roberts JD, Cobden PM, Somogyi P (2002) Cholecystokinin-immunopositive basket and Schaffer collateral-associated interneurones target different domains of pyramidal cells in the CA1 area of the rat hippocampus. Neurosci 109:63–80
Csicsvari J, Hirase H, Czurkó A, Buzsáki G (1998) Reliability and state dependence of pyramidal cell-interneuron synapses in the hippocampus: An ensemble approach in the behaving rat. Neuron 21:179–189
Degro CE, Kulik A, Booker SA, Vida I (2015) Compartmental distribution of gabab receptor-mediated currents along the somatodendritic axis of hippocampal principal cells. Front Synaptic Neurosci 7(MAR):1–15
Desmond NL, Levy WB (1982) A quantitative anatomical study of the granule cell dendritic fields of the rat dentate gyrus using a novel probabilistic method. J Comp Neurol 212:131–145

Deuchars J, Thomson AM (1996) CA1 pyramid-pyramid connections in rat hippocampus in vitro: dual intracellular recordings with biocytin filling. Neuroscience 74:1009–1018

Dieni CV, Panichi R, Aimone JB, Kuo CT, Wadiche JI, Overstreet-Wadiche L (2016) Low excitatory innervation balances high intrinsic excitability of immature dentate neurons. Nat Commun 7:11313

Doischer D, Hosp JA, Yanagawa Y, Obata K, Jonas P, Vida I, Bartos M (2008) Postnatal differentiation of basket cells from slow to fast signaling devices. J Neurosci 28:12956–12968

Dong H-W, Swanson LW, Chen L, Fanselow MS, Toga AW (2009) Genomic–anatomic evidence for distinct functional domains in hippocampal field CA1. Proc Natl Acad Sci 106:11794–11799

Dougherty KA, Islam T, Johnston D (2012) Intrinsic excitability of CA1 pyramidal neurones from the rat dorsal and ventral hippocampus. J Physiol 590:5707–5722

Dougherty KA, Nicholson DA, Diaz L, Buss EW, Neuman KM, Chetkovich DM, Johnston D (2013) Differential expression of HCN subunits alters voltage-dependent gating of h-channels in CA1 pyramidal neurons from dorsal and ventral hippocampus. J Neurophysiol 109:1940–1953

Drew LJ, Kheirbek MA, Luna VM, Denny CA, Cloidt MA, Wu MV, Hen R (2016) Activation of local inhibitory circuits in the dentate gyrus by adult-born neurons. Hippocampus 26:763–778

Dumas TC, Powers EC, Tarapore PE, Sapolsky RM (2004) Overexpression of calbindin D28K in dentate gyrus granule cells alters mossy fiber presynaptic function and impairs hippocampal-dependent memory. Hippocampus 14:701–709

Elfant D, Pál BZ, Emptage N, Capogna M (2008) Specific inhibitory synapses shift the balance from feedforward to feedback inhibition of hippocampal CA1 pyramidal cells. Eur J Neurosci 27:104–113

Emri Z, Antal K, Gulyás AI, Megías M, Freund TF (2001) Electrotonic profile and passive propagation of synaptic potentials in three subpopulations of hippocampal CA1 interneurons. Neuroscience 104:1013–1026

Feng G, Mellor RH, Bernstein M, Keller-Peck C, Nguyen QT, Wallace M, Nerbonne JM, Lichtman JW, Sanes JR (2000) Imaging neuronal subsets in transgenic mice expressing multiple spectral variants of GFP. Neuron 28:41–51

Ferraguti F, Cobden P, Pollard M, Cope D, Shigemoto R, Watanabe M et al (2004) Immunolocalization of metabotropic glutamate receptor 1alpha (mGluR1alpha) in distinct classes of interneuron in the CA1 region of the rat hippocampus. Hippocampus 14:193–215

Ferraguti F, Klausberger T, Cobden P, Baude A, Roberts JD, Szucs P, Kinoshita A, Shigemoto R, Somogyi P, Dalezios Y (2005) Metabotropic glutamate receptor 8-expressing nerve terminals target subsets of GABAergic neurons in the hippocampus. J Neurosci 25:10520–10536

Földy C, Lee SH, Morgan RJ, Soltész I (2010) Regulation of fast-spiking basket cell synapses by the chloride channel ClC-2. Nature Neuroscience 13:1047–1049

Förster E, Zhao S, Frotscher M (2006) Laminating the hippocampus. Nat Rev Neurosci 7:259–267

Freund TF, Buzsáki G (1996) Interneurons of the hippocampus. Hippocampus 6:347–470

Frotscher M, Seress L, Schwerdtfeger WK, Buhl E (1991) The mossy cells of the fascia dentata: a comparative study of their fine structure and synaptic connections in rodents and primates. J Comp Neurol 312:145–163

Frotscher M, Soriano E, Misgeld U (1994) Divergence of hippocampal mossy fibers. Synapse 16:148–160

Fuentealba P, Begum R, Capogna M, Jinno S, Márton LF, Csicsvari J, Thomson A, Somogyi P, Klausberger T (2008) Ivy cells: a population of nitric-oxide-producing, slow-spiking GABAergic neurons and their involvement in hippocampal network activity. Neuron 57:917–929

Fuentealba P, Klausberger T, Karayannis T, Suen WY, Huck J, Tomioka R, Rockland K, Capogna M, Studer M, Morales M, Somogyi P (2010) Expression of COUP-TFII nuclear receptor in restricted GABAergic neuronal populations in the adult rat hippocampus. J Neurosci 30:1595–1609

Fukuda T, Kosaka T (2000) Gap junctions linking the dendritic network of GABAergic interneurons in the hippocampus. J Neurosci 20:1519–1528

Fukuda T, Kosaka T (2003) Ultrastructural study of gap junctions between dendrites of parvalbumin-containing GABAergic neurons in various neocortical areas of the adult rat. Neurosci 120:5–20

Fuzik J, Zeisel A, Mate Z, Calvigioni D, Yanagawa Y, Szabo G, Harkany T (2016) Integration of electrophysiological recordings with single-cell RNA-seq data identifies neuronal subtypes. Nat Biotechnol 34:175–183

Ganter P, Szücs P, Paulsen O, Somogyi P (2004) Properties of horizontal axo-axonic cells in stratum oriens of the hippocampal CA1 area of rats in vitro. Hippocampus 14:232–243

Geiger JR, Lübke J, Roth A, Frotscher M, Jonas P (1997) Submillisecond AMPA receptor-mediated signaling at a principal neuron-interneuron synapse. Neuron 18:1009–1023

Gloveli T, Dugladze T, Rotstein HG, Traub RD, Monyer H, Heinemann U, Whittington MA, Kopell NJ (2005a) Orthogonal arrangement of rhythm-generating microcircuits in the hippocampus. Proc Natl Acad Sci U S A 102:13295–13300

Gloveli T, Dugladze T, Saha S, Monyer H, Heinemann U, Traub RD, Whittington MA, Buhl EH (2005b) Differential involvement of oriens/pyramidale interneurones in hippocampal network oscillations in vitro. J Physiol 562:131–147

Goldin M, Epsztein J, Jorquera I, Represa A, Ben-Ari Y, Crépel V, Cossart R (2007) Synaptic Kainate Receptors Tune Oriens-Lacunosum Moleculare Interneurons to Operate at Theta Frequency. J Neurosci 27:60–9572

Golding NL, Mickus TJ, Katz Y, Kath WL, Spruston N (2005) Factors mediating powerful voltage attenuation along CA1 pyramidal neuron dendrites. J Physiol 568:69–82

Gonzales RB, DeLeon Galvan CJ, Rangel YM, Claiborne BJ (2001) Distribution of thorny excrescences on CA3 pyramidal neurons in the rat hippocampus. J Comp Neurol 430:357–368

Graves AR, Moore SJ, Bloss EB, Mensh BD, Kath WL, Spruston N (2012) Hippocampal Pyramidal Neurons Comprise Two Distinct Cell Types that Are Countermodulated by Metabotropic Receptors. Neuron 76:776–789

Guetg N, Seddik R, Vigot R, Turecek R, Gassmann M, Vogt KE, Bräuner-Osborne H, Shigemoto R, Kretz O, Frotscher M, Kulik A, Bettler B (2009) The GABAB1a isoform mediates heterosynaptic depression at hippocampal mossy fiber synapses. J Neurosci 29:1414–1423

Gulyás AI, Freund TF (1996) Pyramidal cell dendrites are the primary targets of calbindin D28k-immunoreactive interneurons in the hippocampus. Hippocampus 6:525–534

Gulyás AI, Hájos N, Freund TF (1996) Interneurons containing calretinin are specialized to control other interneurons in the rat hippocampus. J Neurosci 16:3397–3411

Gulyás AI, Megías M, Emri Z, Freund TF (1999) Total number and ratio of excitatory and inhibitory synapses converging onto single interneurons of different types in the CA1 area of the rat hippocampus. J Neurosci 19:10082–10097

Gulyás AI, Miles R, Hájos N, Freund TF (1993a) Precision and variability in postsynaptic target selection of inhibitory cells in the hippocampal CA3 region. Eur J Neurosci 5:1729–1751

Gulyás AI, Miles R, Sík A, Tóth K, Tamamaki N, Freund TF (1993b) Hippocampal pyramidal cells excite inhibitory neurons through a single release site. Nature 366:683–687

Gulyás AI, Tóth K, McBain CJ, Freund TF (1998) Stratum radiatum giant cells: a type of principal cell in the rat hippocampus. Eur J Neurosci 10:3813–3822

Gulyás AI, Hájos N, Katona I, Freund TF (2003) Interneurons are the local targets of hippocampal inhibitory cells which project to the medial septum. Eur J Neurosci 17:1861–1872

Hájos N, Acsády L, Freund TF (1996) Target selectivity and neurochemical characteristics of VIP-immunoreactive interneurons in the rat dentate gyrus. Eur J Neurosci 8:1415–1431

Hájos N, Mody I (1997) Synaptic communication among hippocampal interneurons: Properties of spontaneous IPSCs in morphologically identified cells. J Neurosci 17:8427–8442

Hájos N, Papp EC, Acsády L, Levey AI, Freund TF (1998) Distinct interneuron types express m2 muscarinic receptor immunoreactivity on their dendrites or axon terminals in the hippocampus. Neuroscience 82:355–376

Halasy K, Buhl EH, Lőrinczi Z, Tamás G, Somogyi P (1996) Synaptic target selectivity and input of GABAergic basket and bistratified interneurons in the CA1 area of the rat hippocampus. Hippocampus 6:306–329

Halasy K, Somogyi P (1993a) Distribution of GABAergic synapses and their targets in the dentate gyrus of rat: a quantitative immunoelectron microscopic analysis. J Hirnforsch 34:299–308

Halasy K, Somogyi P (1993b) Subdivisions in the multiple GABAergic innervation of granule cells in the dentate gyrus of the rat hippocampus. Eur J Neurosci 5:411–429

Hama K, Arii T, Kosaka T (1989) Three-dimensional morphometrical study of dendritic spines of the granule cell in the rat dentate gyrus with HVEM stereo images. J Electron Microsc Tech 12:80–87

Han ZS, Buhl EH, Lőrinczi Z, Somogyi P (1993) A high degree of spatial selectivity in the axonal and dendritic domains of physiologically identified local-circuit neurons in the dentate gyrus of the rat hippocampus. Eur J Neurosci 5:395–410

Harris KM, Jensen FE, Tsao B (1992) Three-dimensional structure of dendritic spines and synapses in rat hippocampus (CA1) at postnatal day 15 and adult ages: Implications for the maturation of synaptic physiology and long-term potentiation. J Neurosci 12:2685–2705

Henze DA, Cameron WE, Barrionuevo G (1996) Dendritic morphology and its effects on the amplitude and rise-time of synaptic signals in hippocampal CA3 pyramidal cells. J Comp Neurol 369:331–344

Homma R, Baker BJ, Jin L, Garaschuk O, Konnerth A, Cohen LB, Bleau CX, Canepari M, Djurisic M, Zecevic D (2009) Wide-field and two-photon imaging of brain activity with voltage- and calcium-sensitive dyes. Methods Mol Biol 489:43–79

Hooper A, Maguire J (2016) Characterization of a novel subtype of hippocampal interneurons that express corticotropin-releasing hormone. Hippocampus 26:41–53

Hormuzdi SG, Pais I, LeBeau FE, Towers SK, Rozov A, Buhl EH, Whittington MA, Monyer H (2001) Impaired electrical signaling disrupts gamma frequency oscillations in connexin 36-deficient mice. Neuron 31:487–495

Hosp JA, Strüber M, Yanagawa Y, Obata K, Vida I, Jonas P et al (2005) Morpho-physiological criteria divide dentate gyrus interneurons into classes. Hippocampus 24:189–203

Hosseini-Sharifabad M, Nyengaard JR (2007) Design-based estimation of neuronal number and individual neuronal volume in the rat hippocampus. J Neurosci Methods 162:206–214

Houser CR (2007) Interneurons of the dentate gyrus: an overview of cell types, terminal fields and neurochemical identity. Prog Brain Res 163:217–232

Igarashi KM, Ito HT, Moser EI, Moser MB (2014) Functional diversity along the transverse axis of hippocampal area CA1. FEBS Lett 588:2470–2476

Ishizuka N, Cowan WM, Amaral DG (1995) A quantitative analysis of the dendritic organization of pyramidal cells in the rat hippocampus. J Comp Neurol 362:17–45

Ishizuka N, Weber J, Amaral DG (1990) Organization of intrahippocampal projections originating from CA3 pyramidal cells in the rat. J Comp Neurol 295:580–623

Jinde S, Zsiros V, Nakazawa K (2013) Hilar mossy cell circuitry controlling dentate granule cell excitability. Front Neural Circuits 7:14

Jinno S, Klausberger T, Marton LF, Dalezios Y, Roberts JD, Fuentealba P, Bushong EA, Henze D, Buzsáki G, Somogyi P (2007) Neuronal diversity in GABAergic long-range projections from the hippocampus. J Neurosci 27:8790–8804

Jinno S, Kosaka T (2006) Cellular architecture of the mouse hippocampus: a quantitative aspect of chemically defined GABAergic neurons with stereology. Neurosci Res 56:229–245

Jouvenceau A, Potier B, Battini R, Ferrari S, Dutar P, Billard JM (1999) Glutamatergic synaptic responses and long-term potentiation are impaired in the CA1 hippocampal area of calbindin D(28K)-deficient mice. Synapse 33:172–180

Karson MA, Tang AH, Milner TA, Alger BE (2009) Synaptic cross talk between perisomatic-targeting interneuron classes expressing cholecystokinin and parvalbumin in hippocampus. J Neurosci 29:4140–4154

Katona I, Acsády L, Freund TF (1999a) Postsynaptic targets of somatostatin-immunoreactive interneurons in the rat hippocampus. Neuroscience 88:37–55

Katona I, Sperlágh B, Sík A, Käfalvi A, Vizi ES, Mackie K, Freund TF (1999b) Presynaptically located CB1 cannabinoid receptors regulate GABA release from axon terminals of specific hippocampal interneurons. J Neurosci 19:4544–4558

Katona L, Micklem B, Borhegyi Z, Swiejkowski DA, Valenti O, Viney TJ, Kotzadimitriou D, Klausberger T, Somogyi P (2017) Behavior-dependent activity patterns of GABAergic long-range projecting neurons in the rat hippocampus. Hippocampus 27:359–377

Katsumaru H, Kosaka T, Heizmann CW, Hama K (1988) Immunocytochemical study of GABAergic neurons containing the calcium-binding protein parvalbumin in the rat hippocampus. Exp Brain Res 72:347–362

Kempermann G, Jessberger S, Steiner B, Kronenberg G (2004) Milestones of neuronal development in the adult hippocampus. Trends Neurosci 27:447–452

Kepecs A, Fishell G (2014) Interneuron cell types are fit to function. Nature 505:318–326

Klausberger T, Magill PJ, Márton LF, Roberts JD, Cobden PM, Buzsáki G, Somogyi P (2003) Brain-state- and cell-type-specific firing of hippocampal interneurons in vivo. Nature 421:844–848

Klausberger T, Márton LF, Baude A, Roberts JD, Magill PJ, Somogyi P (2004) Spike timing of dendrite-targeting bistratified cells during hippocampal network oscillations in vivo. Nat Neurosci 7:41–47

Klausberger T, Marton LF, O'Neill J, Huck JH, Dalezios Y, Fuentealba P, Suen WY, Papp E, Kaneko T, Watanabe M, Csicsvari J, Somogyi P (2005) Complementary roles of cholecystokinin- and parvalbumin-expressing GABAergic neurons in hippocampal network oscillations. J Neurosci 25:9782–9793

Klausberger T, Somogyi P (2008) Neuronal diversity and temporal dynamics: the unity of hippocampal circuit operations. Science 321:53–57

Klausberger T (2009) GABAergic interneurons targeting dendrites of pyramidal cells in the CA1 area of the hippocampus. Eur J Neurosci 30:947–957

Kohara K, Pignatelli M, Rivest AJ, Jung HY, Kitamura T, Suh J, Frank D, Kajikawa K, Mise N, Obata Y, Wickersham IR, Tonegawa S (2014) Cell type-specific genetic and optogenetic tools reveal hippocampal CA2 circuits. Nat Neurosci 17:269–279

Kosaka T (1980) The axon initial segment as a synaptic site: Ultrastructure and synaptology of the initial segment of the pyramidal cell in the rat hippocampus (CA3 region). J Neurocytol 9:861–882

Kosaka T, Katsumaru H, Hama K, Wu JY, Heizmann CW (1987) GABAergic neurons containing the Ca^{2+}-binding protein parvalbumin in the rat hippocampus and dentate gyrus. Brain Res 419:119–130

Kosaka T, Wu JY, Benoit R (1988) GABAergic neurons containing somatostatin-like immunoreactivity in the rat hippocampus and dentate gyrus. Exp Brain Res 71:388–398

Kowalski J, Geuting M, Paul S, Dieni S, Laurens J, Zhao S, Drakew A, Haas CA, Frotscher M, Vida I (2010) Proper layering is important for precisely timed activation of hippocampal mossy cells. Cereb Cortex 20:2043–2054

Kraushaar U, Jonas P (2000) Efficacy and stability of quantal GABA release at a hippocampal interneuron-principal neuron synapse. J Neurosci 20:5594–5607

Krook-Magnuson E, Luu L, Lee S-H, Varga C, Soltész I (2011) Ivy and neurogliaform interneurons are a major target of μ-opioid receptor modulation. J Neurosci 31:14861–14870

Lacaille JC, Mueller AL, Kunkel DD, Schwartzkroin PA (1987) Local circuit interactions between oriens/alveus interneurons and CA1 pyramidal cells in hippocampal slices: electrophysiology and morphology. J Neurosci 7:1979–1993

Larimer P, Strowbridge BW (2008) Non-random local circuits in the dentate gyrus. J Neurosci 28:12212–12223

Leão RN, Mikulovic S, Leão KE, Munguba H, Gezelius H, Enjin A, Patra K, Eriksson A, Loew LM, Tort ABL, Kullander K (2012) OLM interneurons differentially modulate CA3 and entorhinal inputs to hippocampal CA1 neurons. Nat Neurosci 15:1524–1530

Lee AK, Epsztein J, Brecht M (2009) Head-anchored whole-cell recordings in freely moving rats. Nat Protoc 4:385–392

Lee SE, Simons SB, Heldt SA, Zhao M, Schroeder JP, Vellano CP, Cowan DP, Ramineni S, Yates CK, Feng Y, Smith Y, Sweatt JD, Weinshenker D, Ressler KJ, Dudek SM, Hepler JR (2010) RGS14 is a natural suppressor of both synaptic plasticity in CA2 neurons and hippocampal-based learning and memory. Proc Natl Acad Sci U S A 107:16994–16998

Lee SH, Marchionni I, Bezaire M, Varga C, Danielson N, Lovett-Barron M, Losonczy A, Soltész I (2014) Parvalbumin-positive basket cells differentiate among hippocampal pyramidal cells. Neuron 82:1129–1144

Lein ES, Callaway EM, Albright TD, Gage FH (2005) Redefining the boundaries of the hippocampal CA2 subfield in the mouse using gene expression and 3-dimensional reconstruction. J Comp Neurol 485:1–10

Li XG, Somogyi P, Tepper JM, Buzsáki G (1992) Axonal and dendritic arborization of an intracellularly labeled chandelier cell in the CA1 region of rat hippocampus. Exp Brain Res 90:519–525

Li XG, Somogyi P, Ylinen A, Buzsáki G (1994) The hippocampal CA3 network: an in vivo intracellular labeling study. J Comp Neurol 339:181–208

Livet J, Weissman TA, Kang H, Draft RW, Lu J, Bennis RA, Sanes JR, Lichtman JW (2007) Transgenic strategies for combinatorial expression of fluorescent proteins in the nervous system. Nature 450:56–62

Lorente de Nó R (1934) Studies on the structure of the cerebral cortex II: Continuation of the study of the ammonic system. J Psychol Neurol 46:113–177

Losonczy A, Biró AA, Nusser Z (2004) Persistently active cannabinoid receptors mute a subpopulation of hippocampal interneurons. Proc Natl Acad Sci U S A 101:1362–1367

Luuk H, Koks S, Plaas M, Hannibal J, Rehfeld JF, Vasar E (2008) Distribution of Wfs1 protein in the central nervous system of the mouse and its relation to clinical symptoms of the Wolfram syndrome. J Comp Neurol 509:642–660

Lübke J, Frotscher M, Spruston N (1998) Specialized electrophysiological properties of anatomically identified neurons in the hilar region of the rat fascia dentata. J Neurophysiol 79:1518–1534

Maccaferri G, Dingledine R (2002) Control of feedforward dendritic inhibition by NMDA receptor-dependent spike timing in hippocampal interneurons. J Neurosci 22:5462–5472

Maccaferri G, Lacaille JC (2003) Interneuron diversity series: Hippocampal interneuron classifications – making things as simple as possible, not simpler. Trends Neurosci 26:564–571

Maccaferri G, Roberts JD, Szucs P, Cottingham CA, Somogyi P (2000) Cell surface domain specific postsynaptic currents evoked by identified GABAergic neurones in rat hippocampus in vitro. J Physiol 524:91–116

Maglóczky Z, Acsády L, Freund TF (1994) Principal cells are the postsynaptic targets of supramammillary afferents in the hippocampus of the rat. Hippocampus 4:322–334

Major G, Evans JD, Jack JJB (1993) Solutions for transients in arbitrarily branching cables: 1. Voltage recording with a somatic shunt. Biophys J 65:423–449

Major G, Larkman AU, Jonas P, Sakmann B, Jack JJ (1994) Detailed passive cable models of whole-cell recorded CA3 pyramidal neurons in rat hippocampal slices. J Neurosci 14:4613–4638

Masurkar AV, Srinivas KV, Brann DH, Warren R, Lowes DC, Siegelbaum SA (2017) Medial and lateral entorhinal cortex differentially excite deep versus superficial CA1 pyramidal neurons. Cell Rep 18:148–160

Martina M, Vida I, Jonas P (2000) Distal initiation and active propagation of action potentials in interneuron dendrites. Science 287:295–300

Mátyás F, Freund TF, Gulyás AI (2004) Convergence of excitatory and inhibitory inputs onto CCK-containing basket cells in the CA1 area of the rat hippocampus. Eur J Neurosci 19:1243–1256

McBain CJ, DiChiara TJ, Kauer JA (1994) Activation of metabotropic glutamate receptors differentially affects two classes of hippocampal interneurons and potentiates excitatory synaptic transmission. J Neurosci 14:4433–4445

McBain CJ, Fisahn A (2001) Interneurons unbound. Nat Rev Neurosci 2:11–23

Megías M, Emri Z, Freund TF, Gulyás AI (2001) Total number and distribution of inhibitory and excitatory synapses on hippocampal CA1 pyramidal cells. Neurosci 102:527–540

Melzer S, Michael M, Caputi A, Eliava M, Fuchs EC, Whittington MA, Monyer H (2012) Long-range-projecting gabaergic neurons modulate inhibition in hippocampus and entorhinal cortex. Science 335:1506–1510

Mercer A, Trigg HL, Thomson AM (2007) Characterization of neurons in the CA2 subfield of the adult rat hippocampus. J Neurosci 27:7329–7338

Meyer AH, Katona I, Blatow M, Rozov A, Monyer H (2002) In vivo labeling of parvalbumin-positive interneurons and analysis of electrical coupling in identified neurons. J Neurosci 22:7055–7064

Miettinen R, Hajszan T, Riedel A, Szigeti-Buck K, Leranth C (2012) Estimation of the total number of hippocampal CA1 pyramidal neurons: New methodology applied to helpless rats. J Neurosci Methods 205:130–138

Mikulovic S, Restrepo CE, Hilscher MM, Kullander K, Leão RN (2015) Novel markers for OLM interneurons in the hippocampus. Front Cell Neurosci 9:201

Miles R, Tóth K, Gulyás AI, Hájos N, Freund TF (1996) Differences between somatic and dendritic inhibition in the hippocampus. Neuron 16:815–823

Milior G, Di Castro MA, Sciarria LP, Garofalo S, Branchi I, Ragozzino D, Limatola C, Maggi L (2016) Electrophysiological properties of CA1 pyramidal neurons along the longitudinal axis of the mouse hippocampus. Scientific Rep 6:38242

Min MY, Melyan Z, Kullmann DM (1999) Synaptically released glutamate reduces gamma-aminobutyric acid GABAergic inhibition in the hippocampus via kainite receptors. Proc Natl Acad Sci U S A 96:9932–9937

Mizuseki K, Diba K, Pastalkova E, Buzsáki G (2011) Hippocampal CA1 pyramidal cells form functionally distinct sublayers. Nat Neurosci 14:1174–1181

Monyer H, Markram H (2004) Interneuron Diversity series: Molecular and genetic tools to study GABAergic interneuron diversity and function. Trends Neurosci 27:90–97

Mott DD, Turner DA, Okazaki MM, Lewis DV (1997) Interneurons of the dentate-hilus border of the rat dentate gyrus: morphological and electrophysiological heterogeneity. J Neurosci 17:3990–4005

Nörenberg A, Hu H, Vida I, Bartos M, Jonas P (2010) Distinct nonuniform cable properties optimize rapid and efficient activation of fast-spiking GABAergic interneurons. PNAS 107:894–899

Nunzi MG, Gorio A, Milan F, Freund TF, Somogyi P, Smith AD (1985) Cholecystokinin-immunoreactive cells form symmetrical synaptic contacts with pyramidal and nonpyramidal neurons in the hippocampus. J Comp Neurol 237:485–505

Oláh S, Füle M, Komlósi G, Varga C, Báldi R, Barzó P, Tamás G (2009) Regulation of cortical microcircuits by unitary GABA-mediated volume transmission. Nature 461:1278–1281

Oliva AA Jr, Jiang M, Lam T, Smith KL, Swann JW (2000) Novel hippocampal interneuronal subtypes identified using transgenic mice that express green fluorescent protein in GABAergic interneurons. J Neurosci 20:3354–3368

Palmer LM, Stuart GJ (2006) Site of action potential initiation in layer 5 pyramidal neurons. J Neurosci 26:1854–1863

Pawelzik H, Hughes DI, Thomson AM (2002) Physiological and morphological diversity of immunocytochemically defined parvalbumin- and cholecystokinin-positive interneurones in CA1 of the adult rat hippocampus. J Comp Neurol 443:346–367

Pelkey KA, Chittajallu R, Craig MT, Tricoire L, Wester JC, McBain CJ (2017) Hippocampal GABAergic inhibitory interneurons. Physiol Rev 97:1619–1747

Petilla Interneuron Nomenclature Group, Ascoli GA, Alonso-Nanclares L, Anderson SA, Barrionuevo G, Benavides-Piccione R, Burkhalter A, Buzsáki G, Cauli B, Defelipe J, Fairén A, Feldmeyer D, Fishell G, Fregnac Y, Freund TF, Gardner D, Gardner EP, Goldberg JH, Helmstaedter M, Hestrin S, Karube F, Kisvárday ZF, Lambolez B, Lewis DA, Marin O, Markram H, Munoz A, Packer A, Petersen CC, Rockland KS, Rossier J, Rudy B, Somogyi P, Staiger JF, Tamas G, Thomson AM, Toledo-Rodriguez M, Wang Y, West DC, Yuste R (2008)

Petilla terminology: nomenclature of features of GABAergic interneurons of the cerebral cortex. Nat Rev Neurosci 9:557–568
Price CJ, Cauli B, Kovacs ER, Kulik A, Lambolez B, Shigemoto R, Capogna M (2005) Neurogliaform neurons form a novel inhibitory network in the hippocampal CA1 area. J Neurosci 25:6775–6786
Price CJ, Scott R, Rusakov DA, Capogna M (2008) GABA(B) receptor modulation of feedforward inhibition through hippocampal neurogliaform cells. J Neurosci 28:6974–6982
Pyapali GK, Sík A, Penttonen M, Buzsáki G, Turner DA (1998) Dendritic properties of hippocampal CA1 pyramidal neurons in the rat: Intracellular staining in vivo and in vitro. J Comp Neurol 391:335–352
Ratzliff AH, Santhakumar V, Howard A, Soltész I (2002) Mossy cells in epilepsy: Rigor mortis or vigor mortis? Trends Neurosci 25:140–144
Ribak CE, Seress L, Amaral DG (1985) The development, ultrastructure and synaptic connections of the mossy cells of the dentate gyrus. J Neurocytol 14:835–857
Rollenhagen A, Sätzler K, Rodríguez EP, Jonas P, Frotscher M, Lübke JH (2007) Structural determinants of transmission at large hippocampal mossy fiber synapses. J Neurosci 27:10434–10444
Rózsa B, Zelles T, Vizi ES, Lendvai B (2004) Distance-dependent scaling of calcium transients evoked by backpropagating spikes and synaptic activity in dendrites of hippocampal interneurons. J Neurosci 24:661–670
Ruchi M, Ann DK, Komal P, Connor B, Daniel J (2016) Mapping the electrophysiological and morphological properties of CA1 pyramidal neurons along the longitudinal hippocampal axis. Hippocampus 26:341–361
Scharfman HE (1991) Dentate hilar cells with dendrites in the molecular layer have lower thresholds for synaptic activation by perforant path than granule cells. J Neurosci 11:1660–1673
Scharfman HE (1994) Evidence from simultaneous intracellular recordings in rat hippocampal slices that area CA3 pyramidal cells innervate dentate hilar mossy cells. J Neurophysiol 72:2167–2180
Scharfman HE (1995) Electrophysiological diversity of pyramidal-shaped neurons at the granule cell layer/hilus border of the rat dentate gyrus recorded in vitro. Hippocampus 5:287–305
Scharfman HE (2007) The CA3 “backprojection” to the dentate gyrus. Prog Brain Res 163: 627–637
Scharfman HE (2016) The enigmatic mossy cell of the dentate gyrus. Nat Rev Neurosci 17: 562–575
Schmidt-Hieber C, Jonas P, Bischofberger J (2007) Subthreshold dendritic signal processing and coincidence detection in dentate gyrus granule cells. J Neurosci 27:8430–8441
Seress L, Pokorny J (1981) Structure of the granular layer of the rat dentate gyrus. A light microscopic and Golgi study. J Anat 133:181–195
Seri B, García-Verdugo JM, Collado-Morente L, McEwen BS, Alvarez-Buylla A (2004) Cell types, lineage, and architecture of the germinal zone in the adult dentate gyrus. J Comp Neurol 478:359–378
Sík A, Penttonen M, Buzsáki G (1997) Interneurons in the hippocampal dentate gyrus: an in vivo intracellular study. Eur J Neurosci 9:573–588
Sík A, Penttonen M, Ylinen A, Buzsáki G (1995) Hippocampal CA1 interneurons: an in vivo intracellular labeling study. J Neurosci 15:6651–6665
Sík A, Tamamaki N, Freund TF (1993) Complete axon arborization of a single CA3 pyramidal cell in the rat hippocampus, and its relationship with postsynaptic parvalbumin-containing interneurons. Eur J Neurosci 5:1719–1728
Sík A, Ylinen A, Penttonen M, Buzsáki G (1994) Inhibitory CA1–CA3-hilar region feedback in the hippocampus. Science. 265:1722–1724
Slomianka L, Amrein I, Knuesel I, Sørensen JC, Wolfer DP (2011) Hippocampal pyramidal cells: The reemergence of cortical lamination. Brain Struct Funct 216:301–317

Sloviter RS (1989) Calcium-binding protein (calbindin-D28k) and parvalbumin immunocytochemistry: localization in the rat hippocampus with specific reference to the selective vulnerability of hippocampal neurons to seizure activity. J Comp Neurol 280:183–196

Sloviter RS, Zappone CA, Harvey BD, Bumanglag AV, Bender RA, Frotscher M (2003) "Dormant basket cell" hypothesis revisited: relative vulnerabilities of dentate gyrus mossy cells and inhibitory interneurons after hippocampal status epilepticus in the rat. J Comp Neurol 459: 44–76

Soltész I, Bourassa J, Desche^nes M (1993) The behavior of mossy cells of the rat dentate gyrus during theta oscillations in vivo. Neurosci 57:555–564

Somogyi P, Dalezios Y, Lujan R, Roberts JD, Watanabe M, Shigemoto R (2003) High level of mGluR7 in the presynaptic active zones of select populations of GABAergic terminals innervating interneurons in the rat hippocampus. Eur J Neurosci 17:2503–2520

Somogyi J, Baude A, Omori Y, Shimizu H, El Mestikawy S, Fukaya M, Shigemoto R, Watanabe M, Somogyi P (2004) GABAergic basket cells expressing cholecystokinin contain vesicular glutamate transporter type 3 (VGLUT3) in their synaptic terminals in hippocampus and isocortex of the rat. Eur J Neurosci 19:552–569

Somogyi P, Klausberger T (2005) Defined types of cortical interneurone structure space and spike timing in the hippocampus. J Physiol 562:9–26

Somogyi P, Nunzi MG, Gorio A, Smith AD (1983) A new type of specific interneuron in the monkey hippocampus forming synapses exclusively with the axon initial segments of pyramidal cells. Brain Res 259:137–142

Srinivas KV, Buss EW, Sun Q, Santoro B, Takahashi H, Nicholson DA, Siegelbaum SA (2017) The dendrites of CA2 and CA1 pyramidal neurons differentially regulate information flow in the cortico-hippocampal circuit. J Neurosci 37(12):3276–3293

Stafford MM, Brown MN, Mishra P, Stanwood GD, Mathews GC (2009) Glutamate spillover augments GABA synthesis and release from axodendritic synapses in rat hippocampus. Hippocampus 20:134–144

Stuart GJ, Sakmann B (1994) Active propagation of somatic action potentials into neocortical pyramidal cell dendrites. Nature 367:69–72

Szabadics J, Tamás G, Soltész I (2007) Different transmitter transients underlie presynaptic cell type specificity of GABAA,slow and GABAA,fast. Proc Natl Acad Sci U S A 104:14831–14836

Takács VT, Klausberger T, Somogyi P, Freund TF, Gulyás AI (2012) Extrinsic and local glutamatergic inputs of the rat hippocampal CA1 area differentially innervate pyramidal cells and interneurons. Hippocampus 22:1379–1391

Tamamaki N, Abe K, Nojyo Y (1988) Three-dimensional analysis of the whole axonal arbors originating from single CA2 pyramidal neurons in the rat hippocampus with the aid of a computer graphic technique. Brain Res 452:255–272

Tamás G, Lőrincz A, Simon A, Szabadics J (2003) Identified sources and targets of slow inhibition in the neocortex. Science 299:1902–1905

Thome C, Kelly T, Yanez A, Schultz C, Engelhardt M, Cambridge SB, Egorov AV (2014) Axon-carrying dendrites convey privileged synaptic input in hippocampal neurons. Neuron 83: 1418–1430

Thompson CL, Pathak SD, Jeromin A, Ng LL, MacPherson CR, Mortrud MT, Cusick A, Riley ZL, Sunkin SM, Bernard A, Puchalski RB, Gage FH, Jones AR, Bajic VB, Hawrylycz MJ, Lein ES (2008) Genomic anatomy of the hippocampus. Neuron 60:1010–1021

Thurbon D, Field A, Redman S (1994) Electrotonic profiles of interneurons in stratum pyramidale of the CA1 region of rat hippocampus. J Neurophysiol 71:1948–1958

Tóth K, McBain CJ (1998) Afferent-specific innervation of two distinct AMPA receptor subtypes on single hippocampal interneurons. Nat Neurosci 1:572–578

Tricoire L, Pelkey KA, Daw MI, Sousa VH, Miyoshi G, Jeffries B, McBain CJ (2010) Common origins of hippocampal ivy and nitric oxide synthase expressing neurogliaform cells. J Neurosci 30:2165–2176

Traub RD, Jefferys JG, Miles R, Whittington MA, Tóth K (1994) A branching dendritic model of a rodent CA3 pyramidal neurone. J Physiol 481:79–95

Turner DA, Li XG, Pyapali GK, Ylinen A, Buzsáki G (1995) Morphometric and electrical properties of reconstructed hippocampal CA3 neurons recorded in vivo. J Comp Neurol 356:580–594

Tyan L, Chamberland S, Magnin E, Camire O, Francavilla R, David LS, Topolnik L (2014) Dendritic inhibition provided by interneuron-specific cells controls the firing rate and timing of the hippocampal feedback inhibitory circuitry. J Neurosci 34:4534–4547

Urban-Ciecko J, Fanselow EE, Barth AL (2015) Neocortical somatostatin neurons reversibly silence excitatory transmission via GABAb receptors. Curr Biol 25:722–731

Yan X-X, Toth Z, Schultz L, Ribak CE, Baram TZ (1998) Corticotropin-Releasing Hormone (CRH)-containing neurons in the immature rat hippocampal formation: light and electron microscopic features and colocalization with glutamate decarboxylase and parvalbumin. Hippocampus 8:231–243

Vida I, Frotscher M (2000) A hippocampal interneuron associated with the mossy fiber system. Proc Natl Acad Sci U S A 97:1275–1280

Vida I, Halasy K, Szinyei C, Somogyi P, Buhl EH (1998) Unitary IPSPs evoked by interneurons at the stratum radiatum-stratum lacunosum-moleculare border in the CA1 area of the rat hippocampus in vitro. J Physiol 506:755–773

Vivar C, Potter MC, Choi J, Lee JY, Stringer TP, Callaway EM, Gage FH, Suh H, Van Praag H (2012) Monosynaptic inputs to new neurons in the dentate gyrus. Nat Commun 3

Vogt KE, Nicoll RA (1999) Glutamate and gamma-aminobutyric acid mediate a heterosynaptic depression at mossy fiber synapses in the hippocampus. Proc Natl Acad Sci U S A 96:1118–1122

Vuksic M, Del Turco D, Bas Orth C, Burbach GJ, Feng G, Müller CM, Schwarzacher SW, Deller T (2008) 3D-reconstruction and functional properties of GFP-positive and GFP-negative granule cells in the fascia dentata of the Thy1-GFP mouse. Hippocampus 18:364–375

Wamsley B, Fishell G (2017) Genetic and activity-dependent mechanisms underlying interneuron diversity. Nat Rev Neurosci 18:299–309

Williams PA, Larimer P, Gao Y, Strowbridge BW (2007) Semilunar granule cells: glutamatergic neurons in the rat dentate gyrus with axon collaterals in the inner molecular layer. J Neurosci 27:13756–13761

Wittner L, Henze DA, Záborszky L, Buzsáki G (2006) Hippocampal CA3 pyramidal cells selectively innervate aspiny interneurons. Eur J Neurosci 24:1286–1298

Wittner L, Henze DA, Záborszky L, Buzsáki G (2007) Three-dimensional reconstruction of the axon arbor of a CA3 pyramidal cell recorded and filled in vivo. Brain Struct Funct 212:75–83

Zeisel A, Manchado ABM, Codeluppi S, Lonnerberg P, La Manno G, Jureus A, Linnarsson S (2015) Cell types in the mouse cortex and hippocampus revealed by single-cell RNA-seq. Science 347:1138–1142

Zhao C (2006) Distinct morphological stages of dentate granule neuron maturation in the adult mouse hippocampus. J Neurosci 26:3–11

Physiological Properties of Hippocampal Neurons

Marco Martina and Cheng-Chang Lien

Abstract Neurons are the basic computational units of the nervous system. Information processing in the brain is critically dependent on the electrophysiological properties of individual neurons, which are determined by the presence and distribution of many functionally and pharmacologically different ion channels. The parameters that define the functional roles of individual neurons can be grouped into two major groups: on one side are cellular morphology and topology, which dictate the connectivity of each neuron; on the other side are the different electrophysiological properties of each cell type, which are defined by the combined effects of neuronal active and passive properties and shape the integrative function of each individual cell. The type and timing of neuronal responses to synaptic inputs depend on the firing pattern of each neuron, which in turn is set by the interplay of intrinsic and synaptic electrophysiological properties. In recent years it has also become clear that within each individual neuron the electrophysiological properties are not homogeneous but vary in the various cellular compartments. In particular, it has been shown that dendrites, far from being simple cellular antennas that passively conduct synaptic inputs toward the soma and the axon, are very active structures capable of actively boost synaptic inputs and, at least in some neurons, of generating action potentials that effectively propagate to the soma (Llinás and Sugimori, J Physiol 305:197–213, 1980; Stuart and Sakmann, Nature 367:69–72, 1994; Häusser et al., Neuron 15:637–647, 1995; Spruston et al., Science 268:297–300, 1995; Martina et al., Science 287:295–300, 2000). Thus, the different voltage-gated ion channels expressed by each neuron and in each cellular compartment within individual neurons play a fundamental role in shaping the electrical response of individual neurons to synaptic stimulation and ultimately in

M. Martina (✉)
Department of Physiology, Northwestern University, Feinberg School of Medicine, Chicago, IL, USA
e-mail: m-martina@northwestern.edu

C.-C. Lien
Institute of Neuroscience, National Yang-Ming University, Taipei, Taiwan
e-mail: cclien@ym.edu.tw

V. Cutsuridis et al. (eds.), *Hippocampal Microcircuits*, Springer Series in Computational Neuroscience, https://doi.org/10.1007/978-3-319-99103-0_3

dictating the role of each neuron within the hippocampal network. This chapter will focus on the properties and distribution of voltage-gated ion channels in some of the major neuronal types in the hippocampus and dentate gyrus.

The Data

Comprehensive models describing the function of any brain area must take account of the large differences in the electrophysiology of individual neuronal types. Such differences are mainly the result of the properties of the ion channels expressed by each individual cell type. This chapter provides a brief review of the properties and distribution of voltage-gated ion channels in some of the main hippocampal cell types. The hippocampal formation contains three classes of glutamatergic projection neurons (pyramidal neurons of the hippocampus and granule cells and mossy cells of the dentate gyrus) and many different types of GABAergic interneurons (Freund and Buzsáki 1996, Parra et al. 1998; see also chapter "Connectivity of the Hippocampus" of this book). Hippocampal pyramidal neurons are among the most extensively studied neurons in the entire brain. Electrophysiologically, they can be grouped into three major groups, CA1, CA2, and CA3, although a recent study reports a striking heterogeneity in both intrinsic properties and synaptic connectivity along the transverse axis of CA3 (Sun et al. 2017). Furthermore, pyramidal neurons in the subiculum likely constitute a fourth neuronal class with different electrical properties (Jung et al. 2001).

CA1 Pyramidal Neurons

The recorded resting membrane potential of CA1 pyramidal neurons varies in different preparations from −64 mV (recorded in perforated patch configuration at 32 °C, Spruston and Johnston 1992) to −84 mV, inferred from the reversal potential of voltage-gated potassium currents recorded in cell-attached configuration at 34 °C (Fricker et al. 1999). These cell have typically low input resistance (27 KΩ*cm^2, measured in acute rat slices using whole-cell configuration at room temperature, Taverna et al. 2005). The background conductance of CA1 pyramidal neurons is mainly mediated by inward rectifier potassium currents (Takigawa and Alzheimer 2002), voltage-insensitive KCNK potassium currents (largely TASK3 Taverna et al. 2005), and Ih (Maccaferri et al. 1993). The voltage response of CA1 pyramidal neurons is characterized by the presence of voltage sag upon injection of hyperpolarizing current and by action potential frequency accommodation on injection of depolarizing current. About 15% of the neurons show intrinsic bursting (defined as a ratio of <0.1 between the shortest interspike interval and the mean interspike interval; Metz et al. 2005). Spike accommodation mostly depends on the properties of the voltage-gated sodium and potassium currents expressed in these

Table 1 Sodium channels of CA1 pyramidal neurons

	Soma	Dendrites	Axon
Current type	Fast/persistent (Yue et al. 2005)	Fast (Magee and Johnston 1995a, b)	Fast (Colbert and Pan 2002)
Current density	+ (Magee and Johnston 1995a, b)	+ (Magee and Johnston 1995a, b)	++
Channel subunit	Nav1.1, Nav1.2 (Gong et al. 1999) Nav1.3 RNA before p30 (Felts et al. 1997)	Nav1.1, Nav1.2 (Gong et al. 1999)	Nav1.1, Nav1.2 (Gong et al. 1999)

cells. Action potentials are normally initiated close to the soma and backpropagate into dendrites in an activity-dependent manner so that while action potentials early in a train propagate reliably, those occurring later may fail to actively invade the distal dendrites (Spruston et al. 1995). Sodium currents of CA1 pyramidal neurons recover from inactivation with a bi-exponential time course (Martina and Jonas 1997); interestingly, longer lasting depolarizations increase both the relative contribution of the slow component and its time constant (see below). Thus, during a long depolarization, sodium channels undergo cumulative inactivation, which prevents sustained fast firing. Additionally, sustained high-frequency firing is also hindered because most of the voltage-gated potassium currents of these neurons inactivate rapidly (see below), and therefore prolonged depolarizations inactivate the potassium current and interfere with action potential repolarization.

Sodium Currents Voltage-gated sodium currents are expressed in all three functional compartments (soma, axon, dendrites; see Table 1) of pyramidal neurons. The current density appears relatively uniform in the different compartments (Colbert and Pan 2002; Magee and Johnston 1995a, b, Fig. 1), although enrichment in the axon initial segment is also compatible with the experimental data (Colbert and Pan 2002) and would mirror observations in CA3 pyramidal neurons, where sodium channel density peaks in the axon at ~50 μm from the soma (see below). The density of sodium current in CA1 pyramidal cell nucleated patches is ~5 mS/cm^2 (M. Martina, unpublished observations).

The properties of the sodium current slightly differ between soma and dendrites. In particular, dendritic channels appear to undergo stronger cumulative inactivation during repetitive firing (Jung et al. 1997) and to have slower recovery from inactivation compared to somatic channels (Colbert et al. 1997). Recovery from inactivation in pyramidal neurons is described by a double exponential process, with the fast and slow components having time constant of ~2 and ~150 ms and contributing 85% and 15%, respectively, for a 30 ms-long test pulse; for 300 ms-long pulses, the values of the time constants are similar (2.6 and 351 ms, respectively), but the contribution of the slow component increases to 24% (all data were obtained at −120 mV holding potential and 22–24 °C, Martina and Jonas 1997). Abundant expression of two sodium channel subunits (Nav 1.1 and 1.2) has been detected in

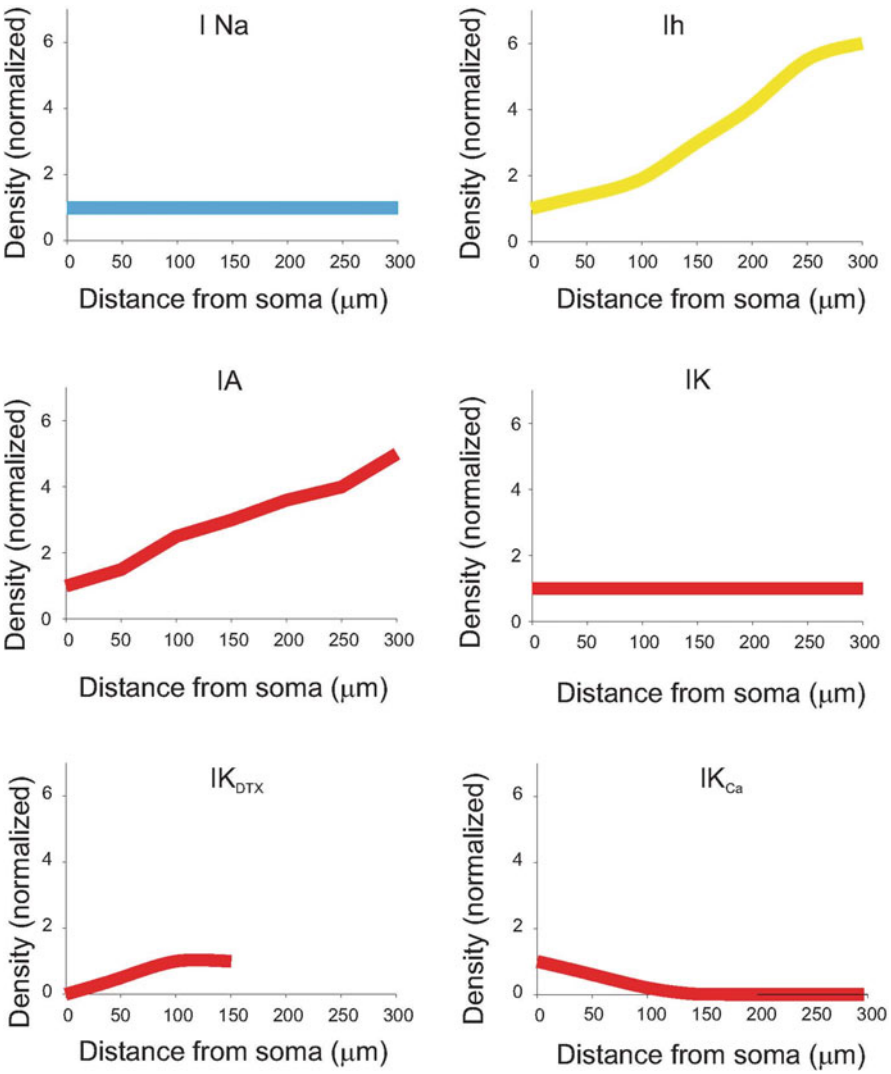

Fig. 1 Ion current density along the somatodendritic axis of CA1 pyramidal neurons. The density of each current type was normalized to its own density at the soma (except for IK_{DTX} in which it was normalized to the value in proximal dendrites). Therefore the figure only depicts the trend for each individual current, and no comparison is possible between the absolute values of the different currents

the hippocampus; type 1 channels appear to account for most of the somatodendritic staining, while type 2 staining is concentrated in the axons (Gong et al. 1999). In hippocampal pyramidal neurons, action potentials are normally initiated in the axon initial segment (Colbert and Johnston 1996). Colbert and Pan (2002) showed that initiation at this site is probably favored by a more negative activation range of

voltage-gated sodium current (sodium channel activation is shifted by ~7 mV in the hyperpolarizing direction). Modulation of Na^+ channel activation is also detected in dendritic channels. Sodium channels in distal dendritic segments have more negative activation range than in proximal dendrites. The midpoint of the activation curve is ~−12 mV for distal dendritic channels and ~−20 mV for proximal channels (Gasparini and Magee 2002), and this difference appears as the result of phosphorylation-dependent modulation since it is reproduced by staurosporine, a nonselective kinase inhibitor (Gasparini and Magee 2002). Yet, in spite of the more negative activation range of sodium channels, dendritic action potential initiation is not common and requires highly synchronized (within 3 ms) activation of ~50 synaptic inputs spread over 100 μm of the apical trunk/tuft (Gasparini et al. 2004). Moreover, the voltage threshold for dendritic action potential initiation is more positive than the somatic one (−48 ± 1 mV in the dendrites vs. -56 ± 1 mV at the soma, Gasparini et al. 2004). This apparent contradiction may be explained by the higher density of A-type potassium current in distal dendrites (Hoffman et al. 1997, Gasparini et al. 2004).

Voltage-Gated Potassium Channels CA1 pyramidal neurons express multiple types of voltage-gated K^+ channels (Storm 1990, Hoffman et al. 1997; Martina et al. 1998, Table 2). Three main components can be identified on the basis of functional and molecular analysis: an A-type current (see Table 3 for the A-type current properties), most likely mediated by Kv4 channels, which contributes ~60% of the total somatic current; a slow delayed rectifier (ID), likely attributable to Kv1 and Kv2 subunits, which contributes ~27% of the total somatic current; and a fast delayed rectifier (IK) mediated by Kv3 channels that contributes ~12% of the somatic current (Martina and Jonas 1997). The relative contribution of these components is different between the somatic and dendritic compartments (See Fig. 1). While the non-inactivating voltage-dependent currents (most likely mediated by Kv2 and Kv3 channels) show relatively constant density in the somatodendritic compartment, A-type current (mediated by Kv4 subunits Martina et al. 1998; Hoffman and Johnston 1998; Kim et al. 2005) progressively increases with distance from the soma (up to fivefold, Hoffman et al. 1997). The A-type potassium current typically activates at relatively hyperpolarized membrane potentials (starting ~−45 mV, Martina et al. 1998). Interestingly, A-type current of pyramidal neurons is highly sensitive to metabolic modulation (Hoffman and Johnston 1998). Such modulation could play an important role in regulating synaptic plasticity, as shown by the change in the threshold for induction of long-term potentiation measured in response to pharmacological blockade of this current (Ramakers and Storm 2002). Expression of dendrotoxin-sensitive (Kv1-mediated) potassium currents is spatially segregated in pyramidal neurons. This current is not expressed in the soma, but it is expressed in proximal dendrites (Fig. 2) where it contributes to the active regulation of the action potential afterdepolarization and therefore of burst firing (Metz et al. 2007).

Calcium-Dependent Potassium Channels Depolarizations produced in CA1 pyramidal neurons by iontophoretically applied glutamate are followed by hyperpolarizations which are mediated by calcium-dependent potassium channels

Table 2 Voltage-gated potassium channels of CA1 pyramidal neurons

	Soma	Dendrites	Axon
Current type	Potassium A-type (Storm 1990, Martina et al. 1998)	Potassium A-type (Hoffman et al. 1997)	Potassium A-type (Kim 2014)
Current density	+	+++	++
Channel subunit	Kv4.2 (++), Kv4.3(++)	Kv4.2, Kv4.3	Kv1.4 (?), Dendrotoxin-sensitive K^+ current (likely Kv1.1, Kv1.2, Kv1.6)
Current type	Potassium fast delayed rectifier (IK)	Potassium fast delayed rectifier (IK)	Potassium fast delayed rectifier (IK)
Current density	+ (Hoffman et al. 1997)	+ (Hoffman et al. 1997)	
Channel subunit	Kv3.1, 3.2	Kv3.1, 3.2	
Current type	Potassium slow rectifier (ID)	Potassium slow rectifier (ID)	Potassium slow rectifier (ID)
Current density	+ − (Martina et al. 1998)	+ (Chen and Johnston 2004; Metz et al. 2007)	
Channel subunit	Kv1.1 (+, Wang et al. 1994, Martina et al. 1998),1.2; Kv2.1,2.2 (Maletic-Savatic et al. 1995; Martina et al. 1998)	Kv1.3(Metz et al. 2007); Kv 1.5 (Maletic-Savatic et al. 1995); Kv2.1 (Maletic-Savatic et al. 1995; Du et al. 2000; Misonou et al. 2006)	Kv1.1; 1.2 (Wang et al. 1994)
Current type	Potassium slow rectifier (ID)	Potassium slow rectifier (ID)	Potassium slow rectifier (ID)
IK_{Ca}	+++	+ (Johnston et al. 2000); but not Slo1 (Misonou et al. 2006)	
M-current (KCNQ)	++ (Hu et al. 2007)	- (Chen and Johnston 2004)	+ Vervaeke et al. 2006
Subunits	KCNQ2; KCNQ5 Shah et al. 2002	KCNQ2; KCNQ5 Shah et al. 2002	KCNQ2 Devaux et al. 2004

Table 3 Properties of inactivating voltage-gated K^+ current in different hippocampal neurons and the MFB

	DG FS (1)	CA1 PC (1)	DGGC (2, 3)	MFB (4)
Act. $V_{1/2}$	−6.2	−3	−7.6 (3)	−26
Act. Slope (mV/e-fold)	5.75*	6.75*	10 (3)	5.2*
Inact. $V_{1/2}$	−75.5	−77.3	−65.1 (3); −67 (2)	−72
Inact. Slope	8.5	7.4	6 (3); 6.3 (2)	9.6
TEA block	No	No	Yes	Yes

In the original papers (1) and (4) activation curves were fitted with a Boltzmann function raised to the fourth power. In order to allow direct comparison with data obtained fitting a simple Boltzmann component (References 2 and 3), the slope factors reported in the papers have been divided by 4 in this table (marked by *)

References 1: Martina et al. (1998), 2: Beck et al. (1992); 3: Riazanski et al. (2001); 4: Geiger and Jonas (2000)

(Nicoll and Alger 1981). Additionally, action potential frequency is also regulated by a Ca^{2+}-dependent potassium current, although the molecular identity of the channels mediating this current remains still unclear (King et al. 2015). Calcium-dependent, charybdotoxin-sensitive potassium channels appear to be unevenly distributed along the somatodendritic axis of CA1 neurons, with channel density decreasing with distance from the soma (Poolos and Johnston 1999) so that the current mediated by these channels is almost completely absent at ∼150 μm from the soma (Johnston et al. 2000, see Fig. 1). This is in stark contrast to the A-type current density, which strongly increases along the dendrites, but also to the non-inactivating currents mediated by voltage-gated channels (most likely by Kv3 and Kv2 subunits), which are expressed at constant density throughout the somatodendritic compartment (Hoffman et al. 1997).

The data presented so far suggest that several different potassium channel subunits are expressed by CA1 pyramidal neurons. Indeed, in situ hybridization, immunostaining, and single-cell RT-PCR show that CA1 pyramidal neurons express many different potassium channel subunits, including Kv1.1, 1.2, 1.4, and 1.5 (Maletic-Savatic et al. 1995, Martina et al. 1998); Kv2.1 and 2.2 and Kv3.1, 3.2, and 3.3 (Martina et al. 1998; Du et al. 2000); and Kv4.2 and 4.3 (Serôdio and Rudy 1998; Martina et al. 1998; Rhodes et al. 2004). It is interesting that although expression of dendrotoxin-sensitive Kv1 subunits is detected in these cells, no effect of dendrotoxin, a Kv1-selective toxin (Grissmer et al. 1994), is detected on potassium currents either in nucleated patches from CA1 pyramidal neurons (Martina et al. 1998) or in focal somatic application of the toxin (Metz et al. 2007). This is consistent with reports showing that Kv1 channels are mainly expressed in presynaptic structures (Monaghan et al. 2001; Sheng et al. 1992). Whole-cell recordings, however, showed an effect of dendrotoxin on action potential initiation (Golding et al. 1999), further suggesting axonal localization of these channels. Finally, dendritic recordings and focal drug application showed that dendrotoxin-sensitive channels are also expressed in apical dendrites, where they modulate the

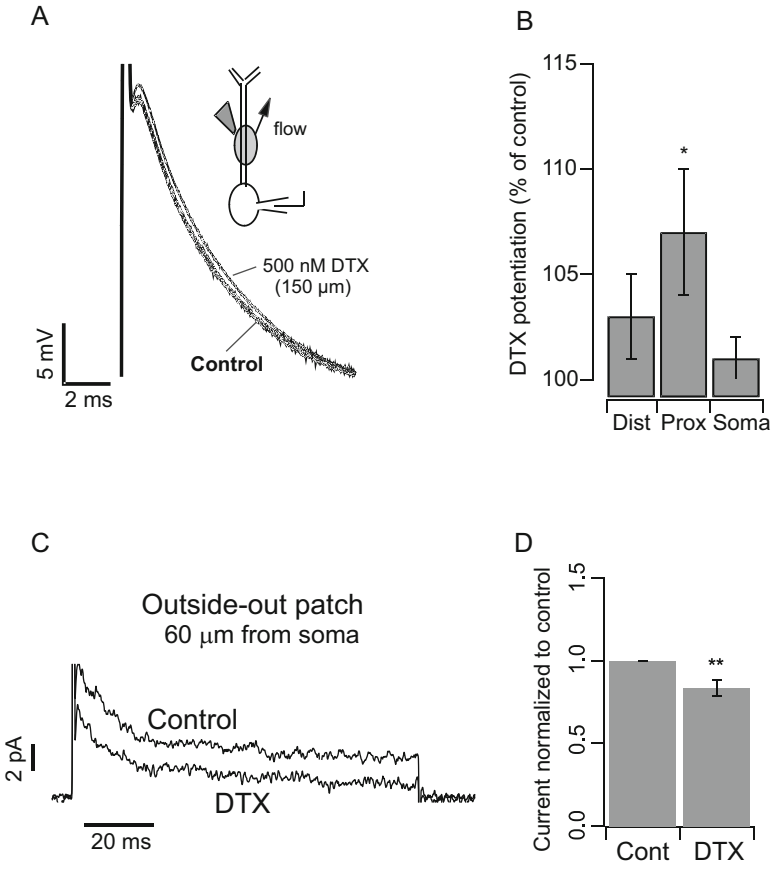

Fig. 2 Dendrotoxin sensitive currents in dendrites of CA1 pyramidal neurons (**a**) Current clamp recording of a somatic afterdepolarization (ADP) recorded in control conditions (thick line) and in the presence of focal dendritic application of dendrotoxin (DTX, thin line). The ADP is increased by DTX. (**b**) Bar chart summarizing the effects of DTX locally applied to the soma, proximal, and distal apical dendrites on the somatic ADP. (**c**) Voltage clamp outside-out dendritic recordings confirm the presence of DTX-sensitive currents in proximal apical dendrites. (**d**) Bar chart summarizing the blocking effect of DTX on dendritic potassium currents. (Figure modified from Metz et al. 2007)

size of the afterdepolarization that underlies burst firing (Metz et al. 2007). These data nicely match those obtained by histological analysis that shows expression of Kv1 subunits in the dendritic arbor of CA1 pyramidal neurons (Park et al. 2001). Thus, Kv1 subunit expression appears to be selectively absent from the soma, while present in both the axon and dendrites of CA1 pyramidal neurons.

M-Current This potassium current is mediated by members of the KCNQ family (Wang et al. 1998; Schroeder et al. 2000). M-current is expressed at very low density in the dendritic compartment of CA1 pyramidal neurons (Chen and Johnston 2004).

However, expression of KCNQ2 and KCNQ3 subunits is high in CA1 pyramidal neurons (Saganich et al. 2001), and M-type current in these neurons effectively controls burst generation (Yue and Yaari 2004). In keeping with these observations, Hu et al. (2007) have shown that M-current in CA1 pyramidal neurons is mainly localized in the perisomatic area. It has been proposed that the interaction between M-current and persistent sodium current mediates a form of theta resonance (M-resonance) in hippocampal CA1 pyramidal neurons (Hu et al. 2002).

Voltage-Gated Calcium Channels Both low- and high-voltage-activated calcium currents have been described in CA1 pyramidal neurons (Table 4). Calcium channels are primarily located at the soma, and their density decreases along the dendrites (Christie et al. 1995), although they are present in dendrites and in dendritic spines (Mills et al. 1994).

The high-voltage-activated current is itself mediated by multiple components. An omega-agatoxin IVA-sensitive (P-type) current contributes about 26% of the somatic high-threshold current (Mintz et al. 1992). N-type channels have also been described in the soma as well as dendrites and spines (Mills et al. 1994) although somatic expression appears more prominent. Nevertheless postsynaptic N-type current has been shown to play an important role in modulation of synaptic strength (Normann et al. 2000). CA1 pyramidal neurons also express large blocker-resistant high-voltage calcium current (R-type). In acutely dissociated cells, this component (defined as the fraction of calcium current available from a holding potential of −50 mV in the presence of the combined application of ω-CgTx GVIA, ω-CgTx MVIIC, ω-AgaTx IVa, and nifedipine) contributes ∼40% of the high-voltage-activated current (Sochivko et al. 2003). Interestingly, a large fraction of the tail current activated by an action potential in nucleated patches is attributable to the R-type (Metz et al. 2005). This current appears to play an important role in the regulation of the afterdepolarization that drives burst firing in CA1 pyramidal neurons. In particular, the calcium influx mediated by this tail current downregulates Kv7 potassium channels, which, when fully available, strongly attenuate the afterdepolarization (Chen and Yaari 2008). R-type currents are present also in dendrites and dendritic spines, where, together with T-type, they provide about 50% of the calcium currents evoked by backpropagated action potentials (Hoogland and Saggau 2004). The R-component in CA1 pyramidal neurons is partly mediated by α1E subunits (Sochivko et al. 2002), although other subunits also contribute as demonstrated by the fact that a current with the functional properties of the R current is still present in α1E knockout mice (Wilson et al. 2000).

The classical dihydropyridine-sensitive L-type current is also present in the soma as well as in the dendrites of pyramidal neurons (Takahashi et al. 1989; Magee and Johnston 1995a, b; Hoogland and Saggau 2004). Dihydropyridine-sensitive channels appear to be open at membrane potential around resting and therefore contribute to the neuronal calcium homeostasis (Magee et al. 1996). This current is expressed in every neuronal compartment although its density appears particularly elevated in the proximal apical dendrites. Activation at negative membrane potential and sensitivity to dihydropyridine suggest that this current is mediated by the α1D

Table 4 Voltage-gated calcium channels of CA1 pyramidal neurons

	Soma	Dendrites	Axon
T-type			
Density	++ (Magee and Johnston 1995a, b)	+ (Magee and Johnston 1995a, b)	
Subunits	Cav3.1; 3.2; 3.3 (McKay et al. 2006)	Cav 3.2; 3.3 (McKay et al. 2006)	Cav3.3 (McKay et al. 2006)
L-type			
Density	++ (Magee and Johnston 1995a, b)	++(Magee and Johnston 1995a, b)	
Subunits	Cav1.2 (Tippens et al. 2008) +++	Cav1.2 (Tippens et al. 2008) ++	Cav1.2 (Tippens et al. 2008) ++
	+ Bowden et al. 2001	++ Bowden et al. 2001	
Subunits	Cav1.3 (Veng and Browning 2002) ++	Cav1.3 (Veng and Browning 2002) ++	Cav1.3(Veng and Browning 2002) + −
	+ Bowden et al. 2001	++ Bowden et al. 2001	
N-type	++ (Christie et al. 1995)	+ − (Christie et al. 1995)	
	But NOT Cav2.2 (Chung et al. 2000)		
Density	++ Magee and Johnston (1995a, b)	+ Mills et al. 1994 (omega-CgTx-sensitive);	
		- Magee and Johnston (1995a, b)	
P/Q-type			
Density	+ (Christie et al. 1995)	+ − (Christie et al. 1995)	
	+ Hillman et al. 1991	+ Hillman et al. 1991	
	++ Stea et al. 1994		
Subunits	Cav2.1 (Day et al. 1996)	+ dendritic shaft	
	But NOT Cav2.2 (Chung et al. 2000)	Bloodgood and Sabatini 2007	
T-type (Cav2.3)	+ Metz et al. 2005	+ Dendritic spines	
	+ Wilson et al. 2000	Bloodgood and Sabatini 2007	
	+ Sochivko et al. 2002		

subunit (Cav1.3, Xu and Lipscombe 2001), which has been shown to be expressed throughout the somatodendritic compartment of CA1 pyramidal neurons (Veng and Browning 2002). However, Radzicki et al. (2013) showed that a large low-threshold nimodipine-sensitive current is still present in CA1 pyramidal neurons of Cav1.3 KO mice. The same authors also showed that Cav1.2 and 1.3 are the only L-type subunits expressed in the CA1 subfield, thus suggesting that Cav1.2 subunits mediate a large fraction of the resting calcium current in these neurons. Low-threshold T-type currents (in CA1 pyramidal cells, these currents start activating ~ -60 mV and reach full amplitude ~ -20 mV; Takahashi et al. 1991) are also present in both the somatic and dendritic compartments (Takahashi et al. 1989; Magee and Johnston 1995a, b). Dendritic T-type currents are activated by subthreshold synaptic events and produce local increases in intracellular calcium, which may be important for the regulation of synaptic strength (Magee et al. 1995). It has been shown that selective potentiation of T-type current occurs in status epilepticus and can transform CA1 pyramidal neurons from regular firing to intrinsically low-threshold bursting cells (Su et al. 2002); it has also been proposed that the increase in T-type current density associated with status epilepticus is limited to, or more prominent, in the apical dendrites where these channels facilitate dendritic depolarization by backpropagating somatic spikes (Yaari et al. 2007).

Hyperpolarization-Activated Current (Ih) The hyperpolarization-activated current is a depolarizing current (the reversal potential is ~ -20 mV) activated by hyperpolarizations more negative than ~ -60 mV and was first described in CA1 pyramidal neurons by Maccaferri et al. (1993). This current is important for regulating firing activity as well as input resistance, and its density sharply increases along the somatodendritic axis (Magee 1998; Fig. 1). It is worth stressing that such gradient in Ih density, although very prominent in CA1 pyramidal neurons as well as in layer 5 cortical pyramidal neurons (Stuart and Spruston 1998), does not appear to constitute a general property of all pyramidal neurons. Bullis et al. (2007) recently described pyramidal-like principal (PLP) neurons, a novel class of hippocampal neurons with pyramidal morphology found in the stratum radiatum. Interestingly, in these neurons the Ih gradient is inverted, showing high somatic density that declines along the dendrites. This finding further supports the notion that, although general rules may regulate ion channel distribution among different neuronal classes, extrapolations should be avoided, and a detailed study is required for each cell type.

CA3 Pyramidal Neurons

The input resistance of CA3 pyramidal neurons is in the range 120–200 KΩ cm^2 (Major et al. 1994). The **sodium currents** are functionally similar to those in CA1 pyramidal cells, although some differences were observed in the voltage-dependent inactivation (Steinhäuser et al. 1990). It was recently shown that in CA3 pyramidal

neurons, sodium channel density is maximal in the axon at 30–50 μm from the soma, which constitutes the location of first action potential generation (Meeks and Mennerick 2007).

Similar to CA1 pyramidal neurons, the voltage-gated **potassium current** of CA3 pyramidal neurons can be classified into three main components: IA, ID, and IK. Of these, the fast-activating ID and IA contribute to the repolarization of the action potential (Mitterdorfer and Bean 2002).

A direct comparison of the potassium currents in CA1 and CA3 pyramidal neurons was performed by Klee et al. (1995). The main difference found was a larger contribution of Ca-dependent current in CA3 cells (20% of total delayed rectifier vs. 10% in CA1). This finding fits well with the observed impact of SK channels on the frequency of intra-burst action potentials in CA3 pyramidal neurons.

One potentially interesting difference is that in CA3 pyramidal neurons, part of the inactivating A-type current is highly 4-AP-sensitive (Bossu et al. 1996), which suggests that channels constituted either by Kv1 subunits associated to beta subunits (which confer rapid A-type inactivation to non-inactivating Kv1 channels; Rettig et al. 1994) or by Kv3.3/3.4 subunits contribute to this current. Relatively abundant expression of Kv3.3 transcript was actually reported in CA3 pyramidal layer (Weiser et al. 1994). A larger contribution of Kv3.3 subunits to the fast transient potassium current of CA3 neurons compared to the current of CA1 neurons (which is almost entirely mediated by Kv4 subunits, see above) may favor the generation of low-threshold bursts because of the more depolarized action potential values required to activate Kv3.3 channels compared to Kv4 (Baldwin et al. 1991; Fernandez et al. 2003). Another potential difference between the potassium current of CA3 and CA1 pyramidal neurons concerns the expression by CA3 cells, at least in organotypic cultures, of a current that is down-modulated by intracellular calcium and is involved in action potential repolarization as well as in the control of synaptic transmission (Saviane et al. 2003). In keeping with this observation, two of the potassium currents of CA3 pyramidal neurons, a voltage-gated current and a Ca-dependent current, are inhibited by activation of an ACPD-sensitive quisqualate receptor (Charpak et al. 1990), suggesting that the local metabolic state influences the size of these currents and therefore the input-output function of CA3 pyramidal neurons. Along this line, Hyun et al. (2013) have shown that a current likely mediated by Kv1.2 channels is downregulated by increased intracellular calcium and causes intrinsic hyperexcitability in response to action potential trains (10 Hz). Interestingly, such potentiation was not detected in CA1 pyramidal neurons.

Similar to CA1, the **calcium current** in CA3 pyramidal neurons is the sum of multiple components (Mogul and Fox 1991). Overall the currents are similar to those of CA1 pyramidal neurons (Thompson and Wong 1991). P-type contribution to the high-threshold currents, however, is smaller in CA3 neurons than in their CA1 counterparts (14% vs. 26% Mintz et al. 1992); a detailed analysis (Avery and Johnston 1996) showed that the main difference between the currents of the two cell types is that in CA3 pyramidal neurons, the low-voltage-activated current actually comprises two different components, one inactivating and nickel sensitive (typical T-type) and one sustained and partly dihydropyridine sensitive (L-type; see

Table 5 Distribution and gating properties of dendritic Na^+ channels in the main glutamatergic cell types of the hippocampus

	DG FS (Hu et al. 2010)	CA1 PC (Magee and Johnston 1995a, b; Kim et al. 2012)	CA3 PC (Kim et al. 2012)
Conductance density vs. distance to soma	Low (+/−)	Constant (++)	Increasing (from ++ to ++++)
Act. $V_{1/2}$	N/A	−30	−37.6
Act. slope (mV/e-fold)	7.2	7.9	
Inact. $V_{1/2}$	−62	−72.9	
Inact. slope	6.9	8.0	

Xu and Lipscombe (2001)). The presence of multiple types of low-voltage-activated calcium channels may contribute to the intrinsic firing of CA3 neurons.

Recent technical advancements, such as confocally guided subcellular patch clamp techniques, have helped advancing our knowledge of the ion conductances in dendrites of CA3 pyramidal neurons (Kim et al. 2012). Interestingly, in these cells dendritic spikes are mediated by voltage-gated Na^+ channels, rather than by Ca^{2+} channels. Conversion of dendritic current density into conductance density revealed that the average ratio of Na^+ to total K^+ conductance density is 0.72. Thus, CA3 pyramidal neuron dendrites show a high Na^+-to-K^+ current ratio in comparison with other types of neurons (Table 5). The density of the different components showed differential distance dependence. For the Na^+ current, the apparent density decreased from the soma to the proximal dendrites and then increased from the proximal to the distal dendrites. In contrast, the dendritic A-type K^+ current density increased continuously from the soma to the distal dendritic region. Finally, the delayed rectifier K^+ current density was not significantly dependent on distance (Kim et al. 2012).

CA2 Pyramidal Neurons

CA2 is a unique region situated between CA3 and CA1. Several recent studies revealed that pyramidal cells in this subfield have distinctive synaptic connectivity, intrinsic membrane properties, and functional roles (Chevaleyre and Siegelbaum 2010; Kohara et al. 2014; Palacio et al. 2017; Srinivas et al. 2017; see review by Robert et al. 2018). The development over the past decade of new tools such as molecular profiling and transgenic mouse lines has enabled the reliable identification of CA2 pyramidal neurons, facilitating the investigation of the functional properties of this cell population. CA2 pyramidal neurons display unique intrinsic electrophysiological properties that are distinct from those of CA1 or CA3 pyramidal neurons. In comparison to CA1 pyramidal neurons, the resting

potential of CA2 pyramidal neurons is more hyperpolarized, with values ranging from −76 mV to −74 mV at 30–36 °C for adult mice (Zhao et al. 2007; Chevaleyre and Siegelbaum 2010; Sun et al. 2014, 2017; Piskorowski et al. 2016; Srinivas et al. 2017). Additionally, the resting potential of CA2 pyramidal neurons appears to become gradually more hyperpolarized along the transverse axis from area CA2 and throughout CA3 (Sun et al. 2017). Similarly, the input resistance exhibits a proximo-distal (from CA3c to CA2) gradient, with the lowest values measured in CA2 pyramidal neurons, ranging from 49 to 86 MΩ (∼15.5–26 KΩ cm^2) at 33–36 °C (Palacio et al. 2017; Chevaleyre and Siegelbaum 2010; Srinivas et al. 2017). The gradients in both resting potential value and input resistance may be mediated, at least in part, by a similar proximo-distal gradient in Ih (see below).

Voltage-Gated Potassium Channels Although molecular profiling studies have identified distinct mRNA expression patterns between CA1 and CA2 (Talley et al. 2001; Lein et al. 2005), the expression of different types of channels in CA2 pyramidal neurons remains largely unexplored. The expression levels of the Kv2 subunit are strikingly different in CA1 and CA2 pyramidal neurons (Palacio et al. 2017). Fluorescence immunohistochemistry in mouse brain has revealed that Kv2.1, Kv2.2, and their auxiliary subunit AMIGO-1 have the highest expression levels in CA1, with a sharp decrease at the CA1-CA2 boundary, and significantly reduced levels in CA2 pyramidal neurons (Palacio et al. 2017). Consistent with this observation, CA2 pyramidal neurons lack the prominent slow afterhyperpolarization seen in CA1 pyramidal neurons (Chevaleyre and Siegelbaum 2010; Palacio et al. 2017), and that has been attributed to Kv2-mediated currents (Liu and Bean 2014).

Hyperpolarization-Activated Current (Ih) The depolarizing membrane "sag" in response to hyperpolarizing current injection, which is caused by Ih activation, is much larger in CA1 than in CA2 pyramidal neurons (Chevaleyre and Siegelbaum 2010). This difference is consistent with the higher expression of the HCN1 subunit in CA1 pyramidal neurons compared to CA2 and CA3 (Notomi and Shigemoto 2004; Santoro et al. 2004; Srinivas et al. 2017). In agreement with the linear gradient in resting potential and input resistance across the transverse axis, CA2 pyramidal neurons exhibit the greatest sag amplitude, followed by CA3a, with CA3c having the smallest sag (Sun et al. 2017).

Dentate Gyrus Granule Neurons

Granule cells are glutamatergic projection neurons conveying information from the dentate gyrus to the CA3 area of the hippocampus. From an electrophysiological perspective, these neurons are particularly interesting among central glutamatergic neurons because the large size of their axonal terminals allows patch clamp characterization of the ion channels in the boutons (Geiger and Jonas 2000; Bischofberger et al. 2002; Engel and Jonas 2005), thus providing a rare opportunity to compare the properties and density of ion channels in the soma and the axon terminal of

Table 6 Gating properties of Na^+ channels in hippocampal neurons

	DG FS Soma (1)	CA1 PC Soma (1)	DGGC Soma (2, 4)	DGGC Bouton (3)
Act. $V_{1/2}$	−25.1	−23.9	−22.6 (2)	−38.4
			−25.8 (4)	
Act. slope (mV/e-fold)	11.5	11.8	5.8 (2); 5.2 (4)	8
Deact. τ (−40 mV)	0.13 ms	0.2 ms		0.17 ms
Inact. $V_{1/2}$	−58.3	−62.9	−56.8	−89.6
Inact. slope	6.7	10.7	6.7	6.4

References 1: Martina and Jonas 1997; 2: Ellerkmann et al. 2001; 3: Engel and Jonas 2005 4: Ellerkmann et al. 2003

an individual neuron. Granule cells have particularly negative membrane potentials (−75 mV at physiologic temperature, Lübke et al. 1998) and relatively low input resistance (38 KΩ* cm^2, Schmidt-Hieber et al. 2007), which suggests abundant expression of background potassium channels.

Sodium Current The density of sodium current in granule cells was determined in acutely dissociated rat neurons (Ellerkmann et al. 2003); thus, these measurements offer an estimate of the density in the somatic compartment. These authors found a density of ∼33 mS cm^{-2} (extrapolated from the reported 1400 pA/pF, assuming a reversal potential of 30 mV, see Fig. 1 in their paper, and a specific capacitance of 0.9 μF cm^{-2} (Gentet et al. 2000)), similar to that in the soma and dendrites of OLM interneurons. These authors also studied the expression profile of the different voltage-gated sodium channel subunits and found co-expression of several subunits in these neurons: in particular, they demonstrated expression of Nav 1.2; 1.3; 1.5; 1.6. The current activation is strongly voltage-dependent (the slope is 5.2 mV/e-fold, Table 6); similar strong voltage dependence characterizes the fast inactivation process of the current, which is half inactivated at −48 mV and has a slope of −5.8 mV/e-fold. The recovery from fast inactivation is best fit by the sum of two exponential functions: a fast component with time constant (at −80 mV) of 6.8 ms (and relative amplitude ∼90%) and a smaller slow component with time constant of 546 ms. The recovery from inactivation in somatic granule cells channels was also analyzed by Engel and Jonas (2005) using outside-out patches. Similar to Ellerkmann et al., they found that the recovery from inactivation is best fit by a double exponential function with the fast component accounting for most of the current (relative amplitude 0.8). The time constants were however faster than in dissociated neurons ($\tau_1 = 4$ ms and $\tau_2 = 65$ ms), possibly suggesting that the recovery from inactivation is actively modulated through intracellular pathways which may be differently affected in whole cell and excised patch recordings.

When long depolarizations are applied (10–300 s at −10 mV, at room temperature), the sodium current of dentate gyrus granule cells undergoes slow inactivation.

The recovery from this inactivated state is described by a bi-exponential process, with fast and slow time constants ranging in the 1–10 and 20–50 seconds, respectively (Ellerkmann et al. 2001). The importance of slow inactivation in physiologic processes remains to be explored; it is interesting, for instance, that status epilepticus deeply affects the properties of fast activation and fast inactivation of granule cells' sodium currents (half maximal activation shifts from −25.8 in control to −28.6 mV and the fast inactivation half point from −48.2 to −43.2 mV; these changes lead to a significant increase of the window current, resulting in higher neuronal excitability), while the slow inactivation appears to be unaffected (Ellerkmann et al. 2003).

The axon terminals of these neurons have been carefully studied. The gating properties of the sodium current in the mossy fiber boutons were compared to those of the somatic component; the main difference was in the inactivation kinetics that in the bouton is almost twofold faster than in somatic patches (Engel and Jonas 2005). The current density in mossy fiber bouton is 49.0 mS cm^{-2} (range: 9–138 mS cm^{-2}), which corresponds to an estimated channel density of 41 channels μm^{-2} in hippocampal MFBs. These density values are comparable to previous estimates in invertebrate axons (120 mS cm^{-2} in squid axons and 40 mS cm^{-2} in Myxicola axons; Hodgkin and Huxley 1952 and Goldman and Schauf 1973). Thus, presynaptic mossy fiber terminals have axon-like properties, expressing voltage-gated Na^+ channels at very high density. Very recently, Schmidt-Hieber et al. (2008) have used dual axo-somatic recordings and computer modeling to obtain an estimate of the sodium current density in mossy fiber axons and found that axonal sodium current density of 100 mS cm^{-2} best fit the experimental data.

Potassium Current Similar to other neurons, the potassium current of granule cells is the sum of at least two components: IA (see Table 3 for the A-type current properties) and IK (Beck et al. 1992).

Contrary to pyramidal neurons, however, the fast inactivating component in granule cells is TEA sensitive and largely mediated by Kv3.4 channels (Riazanski et al. 2001). Interestingly, these authors showed that Kv3.4 expression in granule cells is spatially segregated, showing higher expression around the axon initial segment and lower expression in the somatic compartment more distal from the axon; these data suggest a role for these channels in controlling the generation of action potentials.

The heterogeneous nature of the potassium current in granule neurons is supported by the expression of multiple ion channel subunits, including Kv1.1, 1.2, and 4.2 (Sheng et al. 1994; Tsaur et al. 1992), Kv4.3 (Serôdio et al. 1996), and GIRK1 and GIRK2 (Liao et al. 1996). Kv3.1 RNA expression was also detected in granule neurons, although at low level (Weiser et al. 1995).

The current in the mossy fiber terminal is largely dendrotoxin-sensitive (Geiger and Jonas 2000), in agreement with the prominent expression of Kv1.2 subunits (Sheng et al. 1994). Additionally, specialized voltage-activated K^+ channels of the Kv3 family and calcium-dependent, large conductance, potassium (BK) channels are present at a low density (Alle et al. 2011; but see Misonou et al. 2006). Interestingly, direct bouton recordings show that Kv3 channels efficiently contribute

to the presynaptic AP repolarization, whereas BKCa channels, which are designed and arranged not to interfere with basal AP repolarization, are activated during sustained AP trains and limit AP duration in case of KV3 hypofunction (Alle et al. 2011).

Calcium Current Voltage-gated calcium currents of granule cells include both high- and low-voltage activated currents (Blaxter et al. 1989; Fisher et al. 1990). About 40% of the current is blocked by dihydropyridines (and is therefore L-type), while P/Q-type and N-type current each accounts for about 20% of the total current (Eliot and Johnston 1994). These data suggest that T- and R-type currents account for ~23% of the total current. T-type current was described by Zhang et al. (1993) and contributes to the spike afterdepolarization (ADP). R-type current was estimated to contribute about half of the blocker-resistant current (Sochivko et al. 2002).

Calcium currents have been carefully studied in the mossy fiber bouton (Li et al. 2007). These authors found that a single bouton contains ~2000 voltage-gated calcium channels. The largest current fraction (66%) is mediated by P/Q channels, while N- and R-type contribute 26% and 8% of the total current, respectively.

Dentate Gyrus Mossy Cells

Mossy cells represent the third population of glutamatergic neurons in the hippocampal formation. These large multipolar neurons of the fascia dentata (Frotscher et al. 1991; Lübke et al. 1998) are characterized by relatively slow maximum firing rate (50 Hz at 35–37 °C, Lübke et al. 1998) and by the presence of a prominent membrane sag upon injection of hyperpolarizing currents. The resting membrane potential is between −60 and − 62 mV at 30–37 °C (Jinno et al. 2003; Lübke et al. 1998). The voltage-gated **sodium current** of mossy cells activates at potentials ≥ − 50 mV; fitting the conductance/voltage plot reveals half activation at −31 mV and (Howard et al. 2007).

The **potassium current** of these cells consists of at least three components: an A-type current, a delayed rectifier, and a third component, resistant to both 4-AP (2.5 mM) and TEA (25 mM), characterized by activation kinetics slower than the two other components (Howard et al. 2007). The kinetics and pharmacological properties strongly suggest that the A-type current is mediated by Kv4 subunits. More data are required in order to attribute the two other current components to expression of any individual channel subunit. An interesting difference in intrinsic electrophysiological properties has been reported between dorsal and ventral mossy cells. The majority of the ventral cells show intrinsic bursting, a phenotype that is never observed in dorsal mossy cells (Jinno et al. 2003). Interestingly, Ih expression is similar in bursting and non-bursting neurons; in keeping with these data, it was found that Ih in mossy cells starts activating around −65 mV, so that activation of this current is absent or minimal at resting membrane potential. Thus, in mossy cells Ih does not appear to play a role in intrinsic firing, similarly to what observed

in other neurons in different parts of the CNS (Atherton and Bevan 2005; Russo et al. 2007). Bursting in these neurons appears to depend on a phenytoin-sensitive persistent sodium current that starts activating around −50 mV (Jinno et al. 2003).

Hippocampal Interneurons

DG Basket Cells

Dentate gyrus basket cells are parvalbumin-positive fast-spiking interneurons and can be considered prototypical perisomatic inhibitory interneurons (see chapter "Connectivity of the Hippocampus"). These cells can fire at extremely high frequency (>200 Hz) and have very low input resistance (10 KΩ*cm^2, Bartos et al. 2001).

Sodium Currents Sodium currents of fast-spiking interneurons (see Table 6) are characterized by their very rapid recovery from fast inactivation, which is described (at −120 mV and room temperature) by a single exponential process with a time constant of ∼2 ms. Another typical property of the sodium current of these neurons is the extremely fast deactivation (the time constant at −40 mV and ∼23 °C is 0.13 ms; Martina and Jonas 1997). These two kinetic properties constitute the main difference between the current of basket cells and that of CA1 pyramidal neurons. Whether these differences are attributable to ion channel modulation or to expression of different subunits remains to be investigated. The sodium channel density at the soma is ∼36 mS cm^{-2} and quickly declines along the dendrites with an estimated length constant of 25 μm in basal dendrites (Hu et al. 2010).

Potassium Currents Voltage-gated potassium currents of fast-spiking DG interneurons (putative basket cells) were studied in detail using the nucleated patch technique and single-cell RT-PCR (Martina et al. 1998). Two aspects set the potassium current of these cells apart from that of pyramidal neurons or dentate gyrus granules: (1) the total current density is almost double than in CA1 pyramidal neurons (175 vs. 95 pS/μm^2), and (2) the current is characterized by the almost complete absence of time-dependent inactivation. Functional and pharmacological dissection of the total voltage-gated current shows that, similar to the current of CA1 pyramidal cells, it is composed by three main components: a highly TEA- and 4AP-sensitive fast delayed rectifier (mediated by Kv3 subunits); a slow activating, slowly inactivating component (ID, probably mediated at least in part by Kv2 channels); and an A-type (fast activating and inactivating), TEA-resistant current (mediated by Kv4 subunits, Table 3). Contrary to pyramidal neurons, though, the A-type current only contributes ∼17% of the total current, while the Kv3-like sustained current accounts for 58%. This sustained current appears ideally suited to allow effective repolarization of the fast action potential of these neurons due to extremely fast activation and deactivation kinetics (Fig. 3) and relatively positive activation potential (the activation midpoint is ∼ − 7 mV).

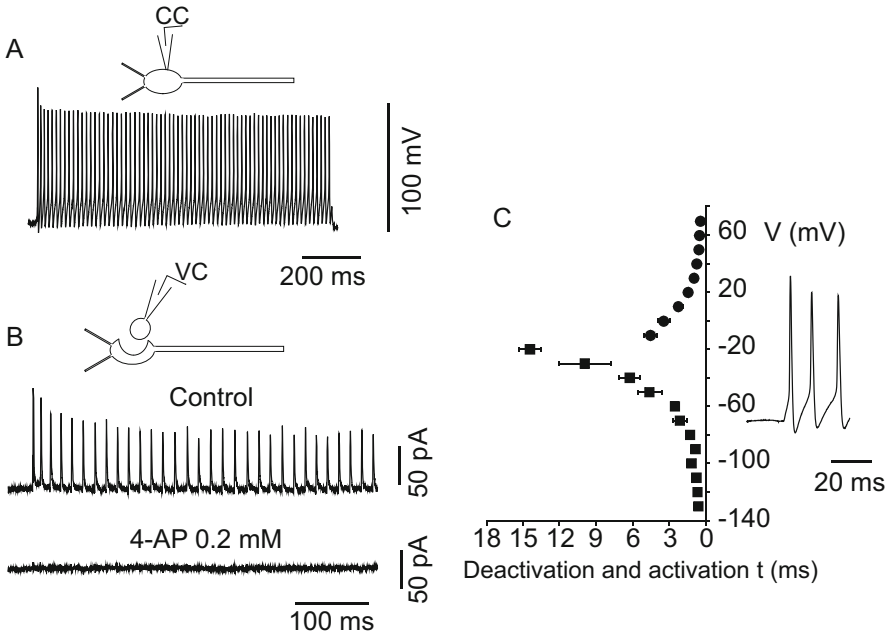

Fig. 3 Kv3 channels mediate action potential repolarization in fast-spiking interneurons of the dentate gyrus. (**a**) Current clamp recording of the firing response of a fast-spiking interneuron to the injection of depolarizing current. (**b**) The membrane potential waveform was then used as voltage stimulus to nucleated patches to study the potassium currents activated by each spike (recordings were performed after blockade of voltage-gated sodium and calcium currents). The potassium current elicited by the high-frequency action potentials was abolished by low concentration of 4-AP. (**c**) Plotting the activation and deactivation time constants of the 4-AP-sensitive current versus the voltage trajectory of the action potentials shows that asymptotic values of activation and deactivation time constants are reached at membrane potentials within the action potential range, allowing fast spike repolarization and minimum refractory period. (Figure modified from Martina et al. 1998)

Recent work has shed further light on the subcellular signaling properties of parvalbumin-positive fast-spiking interneurons (Hu et al. 2010; Table 7). Simultaneous somatodendritic recordings from basket cell dendrites show a high K^+ to Na^+ conductance ratio in BC dendrites. The Na^+ current density is a function of the distance from the soma, with 13.3 ± 2.1 pA/μm^2 (−120 mV to 0 mV) at the soma and steeply declines as a function of distance, with estimated length constants of 87 μm in apical dendrites and 25 μm in basal dendrites. In contrast, in somatic outside-out patches isolated with K^+ internal solution, voltage pulses from −120 mV to 70 mV evoked large voltage-dependent outward currents. Quantitative analysis revealed a K^+ current density of 91.5 ± 21.1 pA/μm^2 at the soma. In apical dendrites, the K^+ current density decays moderately as a function of distance, with an estimated length constant of 763 μm. In contrast, in basal dendrites, the decay is steeper, with a length constant of 57 μm. Consistent with immunocytochemical

Table 7 Gating properties of dendritic K^+ channels of hippocampal neurons

	DG FS (Hu et al. 2010)	CA1 PC (Hoffman et al. 1997)		CA3 PC (Kim et al. 2012)	
Component	Sustained (Kv3-like)	Transient	Sustained	Transient	Sustained
Act. $V_{1/2}$	−10.9 (apical) −12.6 (basal)	−1	13	−9.6	−3.8
Act. slope (mV/e-fold)	10.9 (apical) 8.9 (basal)	15	11	16	10.2
Inact. $V_{1/2}$	N/A	−56	N/A	−65.6	N/A
Inact. slope	N/A	8	N/A	7.1	N/A
TEA block	Yes	Yes	Yes	N/A	Yes
4-AP block	N/A	Yes	Little	Yes	N/A

data, analysis of dendritic K^+ current kinetics suggests that it is mainly mediated by Kv3-type channels. Such a high density of K^+ channels in basket cell dendrites contributes to unique integrative properties, leading to the rapid and temporally precise activation by excitatory inputs (Hu et al. 2010).

Calcium Currents Less is known about the calcium currents in basket cells; it has been recently shown that P/Q calcium channels mediate release at synapses of basket cells (Hefft and Jonas 2005), but a comprehensive study of the calcium currents present in these cells is still missing.

It is also worth mentioning that basket cells also express connexin36, although the strength of the electrical coupling is low and appears to decline with development. In 14-day-old mice, 92% of the cells tested are electrically coupled, although the coupling coefficient is low (0.029). In slices from 42-day-old mice, in contrast, only 30% of the cells are electrically coupled, and the coupling coefficient is further reduced (0.012, Meyer et al. 2002).

Hyperpolarization-Activated Current (Ih) Ih current contributes to the resting membrane potential and background conductance and thus mediates the fast membrane time constant of fast-spiking basket cells (Aponte et al. 2006). Ih channels of basket cells are nonselective cation channels with a slight preference for K^+ over Na^+ ions (P_{Na}/P_K is 0.36), and their activation curve has a midpoint potential (−83.9 mV) similar to other cell types (−90 to −83 mV; Franz et al. 2000). It is important to notice that Ih in basket cells displays several distinct functional properties compared with other types of central neurons. First, Ih channels in basket cells have slower activation as its activation time constant is 190 ms (at −120 mV and 21–24 °C), significantly slower than in hippocampal CA1 pyramidal neurons (64 ms) and neocortical layer 5 pyramidal neurons (84 ms), but faster than in substantia nigra dopaminergic neurons (482 ms) and thalamocortical neurons (602 ms; 22–24 °C; Franz et al. 2000). Second, both ZD7288- and Cs^+-sensitive currents evoked by hyperpolarizing test pulses from a holding potential of −50 mV show a time-dependent current component and an instantaneous component.

Ih channels are expressed in both somatodendritic and axonal domains of basket cells (Aponte et al. 2006). Somatodendritic Ih shapes the input-output relation of basket cells, whereas axonal Ih current contributes to axonal excitability and synaptic output. Ih channels in presynaptic terminals maintain facilitate spontaneous release by maintain the terminals closer to action potential threshold. A recent study (Elgueta et al. 2015) demonstrates that Ih channels enable basket cells to integrate their intrinsic activity over time and can sustain persistent firing mode characterized by the ability to generate long-lasting trains of action potentials at 50 Hz in the absence of additional inputs. Interestingly, computational models suggest that the instantaneous component in the axon may contribute to the sustained firing (Elgueta et al. 2015).

Stratum Oriens Horizontal Interneurons
Horizontal interneurons in the hippocampal CA1 area represent a relatively homogeneous population and are prototypical feedback interneurons (see chapter "Connectivity of the Hippocampus"). Many of these cells are somatostatin-expressing OLM cells (Martina et al. 2000) which are capable of repetitive firing upon injection of depolarizing current, although their maximum frequency does not reach frequencies as high as those of basket cells (Lien and Jonas 2003). These neurons are also functionally easily distinguishable from basket cells because they are often intrinsically firing due to presence of large Ih (Maccaferri and McBain 1996). Ih expression also differentiates the response to hyperpolarizing current injection of these neurons from that of basket cells because the voltage response of OLM cells is characterized by a large voltage sag, which is absent in basket cells. Another interesting difference between OLM neurons and basket cells resides in the value of the input resistance, which in OLM cells is quite high (48 $K\Omega*cm^2$, Taverna et al. 2005), due to relatively low expression of background potassium channels (Taverna et al. 2005; Torborg et al. 2006).

Sodium currents of OLM neurons have properties similar to those of dentate gyrus basket cells; in particular the recovery from fast inactivation can be fit by a single exponential function (time constant 5 ms at −120 mV and 22–23 °C, Martina et al. 2000). An interesting feature of these neurons is the capability of action potentials to undergo reliable and full amplitude backpropagation into the dendrites. In addition, strong focal excitation may also lead to dendritic action potential initiation (Martina et al. 2000). Full amplitude backpropagation is the consequence of high dendritic sodium current density (∼25 mS/cm^2, calculated from data in Martina et al. 2000). Dendritic initiation may also be favored by a ∼8 mV left shift in voltage dependence of the activation curve (midpoint was −37.8 mV for somatic patches and − 45.6 for dendritic patches). Dendritic sodium currents also contribute to boosting of excitatory synaptic inputs. As to the molecular identity of the sodium channels in these cells, recent data from the Catterall laboratory (Tai et al. 2014) suggest that Nav1.1 subunits contribute importantly to this current.

Potassium Currents Voltage-gated potassium currents are expressed at high and constant density throughout the somatodendritic compartment of OLM neurons

(Martina et al. 2000). The current composition is very similar, both in functional and molecular terms, to that of dentate basket cells (Lien et al. 2002). The total current is the sum of three components: a fast delayed rectifier (57% of the total current, mediated by Kv3 channels), an A-type current (19% of the total current, mediated by Kv4 subunits), and a slow delayed rectifier (25% of the total). In these neurons the deactivation of the Kv3 component is slower than in basket cells, most likely because of the more important contribution of the Kv3.2 subunit (Lien et al. 2002). Interestingly, this deactivation velocity appears to be finely tuned to allow the maximum firing frequency in this particular cell type (Lien and Jonas 2003). The potassium currents in OLM dendrites are very similar to the somatic ones with regard to both kinetics and sensitivity to block by broad-spectrum blockers such as TEA (Martina et al. 2000). It has also been suggested that a fraction of the TEA-sensitive current in the somatodendritic compartment of OLM cells appears to be mediated by KCNQ (M-current) channels. Although the size of this conductance is relatively small ($\sim$0.2 mS/cm^2, Lawrence et al. 2006), computer models suggest that this current may regulate the firing frequency of these neurons with minimal impact on the shape of the action potential (Lawrence et al. 2006).

Finally, little is known about voltage-gated **calcium channels** in these neurons. Poncer et al. (1997), however, showed that inhibitory potentials generated by interneurons in the CA3 stratum oriens are mediated by P/Q-type calcium channels.

Interneurons of the Stratum Radiatum-Lacunosum-Moleculare

Interneurons in this area can be classified into several classes. Vida et al. (1998) distinguished four classes: basket (BC), Schaffer associated (SA), perforant-path associated (PA), and neurogliaform (NC); most of these cells however can be classified as feedforward dendritic targeting interneurons. As it is the case in other brain areas, BCs are characterized by lower input resistance (70 MΩ) and more negative resting membrane potential (−60 mV) than the other interneurons (−56 mV, 96 MΩ; -55 mV, 84 MΩ; and − 58 mV, 75 MΩ for SA, PA, and NG, respectively). Although no comprehensive studies of the voltage-gated sodium currents in these cells are available, sensitivity to beta pompilidotoxin, a wasp toxin, shows that the sodium currents differ between radiatum and LM interneurons (Miyawaki et al. 2002), suggesting differential expression of individual subunits.

Contrary to basket cells of the stratum pyramidale and to OLM interneurons, which express Kv3.1b subunits at high level, interneurons in the stratum radiatum-lacunosum-moleculare only seldom express this subunit (21% vs. $\sim$90% of PV-positive basket cells; Sekirnjak et al. 1997). In agreement with this result, voltage-gated potassium currents of cultured interneurons of the stratum lacunosum-moleculare exhibit slow activation kinetics. Similar to other interneurons, the delayed rectifier current represents the sum of two components (a 4-AP sensitive and a 4-AP insensitive); the time to peak of the 4-AP-sensitive component is 4.2 ms at +45 mV (Chikwendu and McBain 1996; by comparison, the 20–80% rise time of Kv3-like currents at 40 mV in basket cells is $\sim$1 ms, Martina et al. 1998). The 4-AP insensitive component has much slower (and voltage-independent) activation

(the time to peak at 30 mV is 46 ms, Chikwendu and McBain 1996). It is likely that at least part of the 4-AP- and TEA-sensitive slow delayed rectifier is mediated by Kv1.1 channels, which are expressed in these cells (Rhodes et al. 1997).

Voltage-clamp recordings were performed to study calcium currents in visually identified interneurons in stratum radiatum, near the border with LM. When held at −80 mV, these cells exhibited a relatively small calcium current (0.4–1 nA in whole-cell configuration) that appeared to include at least three (L, N, and P/Q) calcium current components: the L-type component contributed ∼28% of the current, while the N-type current accounted for ∼23% of the total. The contribution of the P/Q component was more heterogeneous ranging from 0% to 30% (average ∼10%, Lambert and Wilson 1996). It is possible that the different contribution of N-type current in different cells reflected different histological classes of interneurons; this hypothesis however still needs experimental confirmation.

Low-voltage-activated calcium currents were also described in interneurons acutely dissociated from CA1 lacunosum-moleculare (Fraser and MacVicar 1991). The current size was quite small (the peak current, recorded at −30 mV, was 100 ± 7 pA, compared with ∼2 nA of TTX-sensitive sodium currents in the same neurons). This calcium current showed marked voltage-dependent inactivation, being half inactivated at −84 mV and totally inactivated at −60 mV. Less is known about dendritic calcium channels in these cells. Optical measurements however showed that action potential-associated calcium signals backpropagate into the dendrites of these neurons; indeed, backpropagated calcium signals progressively increase in size with distance from the soma (Rozsa et al. 2004). Whether this feature is the result of differential distribution of calcium channels or of other mechanisms (for instance, a different basal calcium level) remains to be investigated. These data however suggest that, similar to OLM interneurons, action potentials actively backpropagate into the dendrites of CA1 SR interneurons.

Experimental Techniques

Although conventional intracellular (sharp electrode) recordings can still provide valuable information about the electrophysiologic properties of neurons, most of the more recent literature (and of the data presented in this chapter) is based on patch clamp recordings. Some basic cellular properties appear quite different when compared using these two techniques. For example, resting membrane potential and input resistance measured with sharp electrodes and patch clamp techniques were directly compared in dentate gyrus basket cells (Staley et al. 1992), and the results obtained with the two techniques were quite different: with sharp pipette recordings, the resting potential was −74 mV and the input resistance was 54 MΩ, while the values obtained with patch clamp recordings were − 85 mV and 228 MΩ, respectively. A potential explanation for these differences is that they are the consequence of a sub-optimal seal around the sharp electrodes that leads to some current leakage and that is not present in patch clamp recordings. Therefore,

patch clamp data were preferentially used for this chapter, except when sharp electrode data were the only available. The patch clamp technique was pioneered in the late 1970s by Erwin Neher and Bert Sakmann (Neher et al. 1978) and was originally developed to allow the measurement of the currents flowing through single ion channels in cellular membranes. Briefly, small tip (~1 μm) pipettes are obtained by pulling glass capillaries, filled with saline and connected to a feedback amplifier. A tight electrical seal (in the GΩ range) is obtained between the pipette tip and the cellular membrane by applying gentle suction to the pipette. This leads to a firm attachment between the tip and the membrane, which allows several manipulations (Hamill et al. 1981) that offer invaluable tools for the study of many electrophysiological properties, varying from the cellular input resistance to the current flowing through single individual channels. The most commonly used configuration is the whole-cell configuration, in which, after obtaining the seal, continuity is obtained between the pipette and the cell interior by rupturing the cell membrane by applying brief negative pressure pulses. As a result, the pipette-cell assembly is well insulated from the bath solution. The intrapipette solution for these recordings is designed to reproduce the physiological intracellular solution (high potassium, low sodium). Whole-cell patch clamp recordings allow the accurate measurement of many basic functional properties such as resting membrane potential, input resistance, action potential threshold, amplitude, and frequency. Moreover, the voltage-clamp configuration allows recording the total ionic current flowing through the entire cell at each moment. Thus, complex voltage protocols and pharmacological tools can be used to isolate the currents mediated by individual channel types.

Although extremely successful on small isolated cells, such as acutely dissociated and cultured neurons, whole-cell voltage-clamp recordings are problematic when obtained from intact neurons having complex morphologies and large axonal and dendritic trees, as is the case for most neurons in brain slices. In this case the quality of voltage clamp is dramatically limited (see Major 1993 for a detailed discussion). Thus, data on current kinetics and voltage dependence are best obtained from excised patches and outside-out patches in particular. This configuration is obtained by pulling the pipettes away from the cell after having achieved the whole-cell mode (Hamill et al. 1981). By doing so, the lipid membrane seals the pipette tip leaving the outer side of the cell membrane exposed to the bath, while the inner side is exposed to the intrapipette solution. This configuration allows ideal voltage control and quick solution exchange, but is not always suitable for the study of channels expressed at low density in the cell membrane because the currents are often very small. An interesting variation of this technique is the nucleated patch (Sather et al. 1992). Similarly to the outside patch, the first step consists in achieving a whole-cell configuration. At this point a light suction is applied to the pipette, and the nucleus is attracted to the pipette tip. The pipette is then slowly withdrawn from the cell to obtain an outside-out patch. Because of the presence of the nucleus, the membrane has to reseal around the nucleus itself, and the result is an almost perfectly spherical outside patch comprising a large membrane area. Thus, the nucleated patch combines the possibility of precise identification of cells

in a slice with the possibility to record macroscopic currents and to obtain in almost ideal voltage-clamp conditions (Martina and Jonas 1997).

A potential pitfall common to intracellular and whole-cell patch clamp recordings is that these types of experiments lead to dialysis of the intracellular content. This fact has two main consequences: (1) it may lead to disappearance of some currents or cell functions ("rundown") due to the loss of diffusible factors into the recording pipette and (2) the intracellular ion concentrations are not the native ones but those imposed by the experimenter: this fact may become critical when examining the functional role of a conductance. A typical example is the $GABA_A$ channel, which is selective for anions and Cl^- ions in particular. Depending on the intracellular $[Cl^-]$, the $GABA_A$ conductance can be either hyperpolarizing or depolarizing. For this type of experiments, it is therefore critical to know the undisturbed cellular $[Cl^-]$. This can be obtained by establishing the electrical connection between the pipette and the cell interior not by rupturing the membrane but by inclusion in the pipette solution of a channel forming substance in the cell-attached mode (Horn and Marty 1988). By using substances that form channels selectively permeant to cations, as gramicidin, it is possible to obtain whole-cell recordings that maintain intact the neuronal chloride gradient. The technique also prevents intracellular dialysis because of the small diameter of the pores (they are only permeant to monovalent cations).

The Future

Although the hippocampus is one of the most thoroughly studied brain areas, much work is still needed to obtain a comprehensive description of the physiological properties of hippocampal neurons. In particular, future work will have to address two important aspects: one concerns the large heterogeneity of hippocampal neurons and interneurons in particular. Clearly, only a thorough study of each cell type will allow understanding of the fine tuning of hippocampal function; thus, detailed studies of the functional properties of anatomically identified neurons will be required for the many types of hippocampal neurons. With the technology of mouse genetic engineering, researchers have been able to create Cre-dependent driver lines that target specific classes of excitatory neurons (Kohara et al. 2014; Hitti and Siegelbaum 2014) as well as major classes and lineages of GABAergic neurons (Taniguchi et al. 2011). For example, using highly cell type-specific transgenic mouse lines for CA2, researchers can identify the CA2 pyramidal cells and characterize their intrinsic properties and ion channels (Kohara et al. 2014; Hitti and Siegelbaum 2014). Similarly, this approach allows reliable identification of GABAergic interneuron subtypes, thereby enabling detailed correlation between cell types and functional properties. At the same time, some technical aspects for functional studies may also require further development. Patch clamp recordings have greatly improved our knowledge of the electrophysiological properties of neurons. This technique, however, is not devoid of weaknesses. Two limitations of the

patch clamp technique are (1) the difficulty of obtaining data from small structures such as small dendrites, axons, and terminals, which results from the physical limitation in the size of the pipette tip as well as in the optical resolution necessary to distinguish such structures, and (2) the fact that the sealing process and, even more, the formation of the whole-cell configuration may cause important changes to the cellular cytoskeleton as well as to the composition of the intracellular milieu. Nowadays, increasing expectation is directed toward the development of low-toxic voltage-sensitive dyes, which may allow studying neuronal electrophysiology in intact cells. The signal to noise ratio of such dyes still represents a problem, but it is quickly improving (Baker et al. 2005). Particularly interesting is a recently developed method that allows filling neurons without the need to patch them to wash in the dye. This technique is the electrical electroporation, which has been extensively used for the delivery of DNA, RNA, and other molecules to the interior of cells. It has been shown that this technique can be effectively used to load neurons with fluorescent calcium indicators in vitro and in vivo (Nevian and Helmchen 2007). The combined use of electroporation and voltage-sensitive dyes may allow recording from cells with intact cytoskeleton and, even more importantly, obtaining detailed functional maps of small local circuitries. Another interesting technique that allows the identification of functional connections in a brain slice is the laser-scanning photostimulation (LSPS) based on glutamate uncaging. This technique allows for rapid imaging of local synaptic circuits by recording synaptic responses from a postsynaptic neuron while stimulating small clusters of presynaptic cells with high spatial resolution (Callaway and Katz 1993). A neuron is recorded in the whole-cell configuration and the slice bathing solution contains a molecularly caged form of glutamate. This molecule is then converted to the active form by submillisecond pulses of ultraviolet irradiation, which can be delivered selectively to small areas (of <100 μm diameter). It has been shown that, in most cases, this technique is selective enough to prevent activation of axons of passage, while the stimulus is sufficient to induce firing in the investigated neurons. Thus, the technique can be effectively used for mapping local circuits.

Optogenetic-assisted circuit mapping is another unprecedented development, which is based on the combination of optogenetics and patch clamp recordings. Optogenetics is a recent technology emerging from basic genetic research on microorganisms that rely on light-responsive opsin proteins to survive (see review by Deisseroth 2010, 2011). Using viral vectors, scientists can insert opsin genes, which encode light-sensitive proteins, in a specific population of neurons and control their activity with the light. Channelrhodopsin-2 (ChR2) is a light-sensitive cationic channel. By expressing ChR2 in the neuronal membrane of a select cell population, scientists can effectively drive the neurons to generate action potentials by shining blue light (470 nm). In contrast, halorhodopsin (HR) is a light-sensitive chloride pump, which transports the chloride into the cells. With a flash of amber light (589 nm), scientists can silence HR-expressing neurons. This technology permits temporally precise, cell type-targeted experiments in ex vivo brain slices as well as in vivo in anesthetized or freely moving animals. Additionally, viral-genetic

tracing allows the investigation of the intrinsic properties neuronal populations with common synaptic input or output.

Further Reading

Alle H, Kubota H, Geiger JR (2011) Sparse but highly efficient Kv3 outpace BKCa channels in action potential repolarization at hippocampal mossy fiber boutons. J Neurosci 31(22):8001–8012

Aponte Y, Lien CC, Reisinger E, Jonas P (2006) Hyperpolarization-activated cation channels in fast-spiking interneurons of rat hippocampus. J Physiol 574(Pt 1):229–243

Atherton JF, Bevan MD (2005) Ionic mechanisms underlying autonomous action potential generation in the somata and dendrites of GABAergic substantia nigra pars reticulata neurons in vitro. J Neurosci 25(36):8272–8281

Avery RB, Johnston D (1996) Multiple channel types contribute to the low-voltage-activated calcium current in hippocampal CA3 pyramidal neurons. J Neurosci 16(18):5567–5582

Baker BJ, Kosmidis EK, Vucinic D, Falk CX, Cohen LB, Djurisic M, Zecevic D (2005) Imaging brain activity with voltage- and calcium-sensitive dyes. Cell Mol Neurobiol 25(2):245–282

Baldwin TJ, Tsaur ML, Lopez GA, Jan YN, Jan LY (1991) Characterization of a mammalian cDNA for an inactivating voltage-sensitive K+ channel. Neuron 7(3):471–483

Bartos M, Vida I, Frotscher M, Geiger JR, Jonas P (2001) Rapid signaling at inhibitory synapses in a dentate gyrus interneuron network. J Neurosci 21(8):2687–2698

Beck H, Ficker E, Heinemann U (1992) Properties of two voltage-activated potassium currents in acutely isolated juvenile rat dentate gyrus granule cells. J Neurophysiol 68(6):2086–2099

Bischofberger J, Geiger JR, Jonas P (2002) Timing and efficacy of Ca2+ channel activation in hippocampal mossy fiber boutons. J Neurosci 22:10593–10602

Blaxter TJ, Carlen PL, Niesen C (1989) Pharmacological and anatomical separation of calcium currents in rat dentate granule neurones in vitro. J Physiol 412:93–112

Bloodgood BL, Sabatini BL (2007) Nonlinear regulation of unitary synaptic signals by CaV(2.3) voltage-sensitive calcium channels located in dendritic spines. Neuron 53(2):249–260

Bossu JL, Capogna M, Debanne D, RA MK, Gähwiler BH (1996) Somatic voltage-gated potassium currents of rat hippocampal pyramidal cells in organotypic slice cultures. J Physiol 495:367–381

Bowden SE, Fletcher S, Loane DJ, Marrion NV (2001) Somatic colocalization of rat SK1 and D class (CA(v)1.2) L-type calcium channels in rat CA1 hippocampal pyramidal neurons. J Neurosci 21(20):RC175

Bullis JB, Jones TD, Poolos NP (2007) Reversed somatodendritic I(h) gradient in a class of rat hippocampal neurons with pyramidal morphology. J Physiol 579(Pt 2):431–443

Callaway EM, Katz LC (1993) Photostimulation using caged glutamate reveals functional circuitry in living brain slices. Proc Natl Acad Sci U S A 90:7661–7665

Charpak S, Gähwiler BH, Do KQ, Knöpfel T (1990) Potassium conductances in hippocampal neurons blocked by excitatory amino-acid transmitters. Nature 347(6295):765–767

Chen X, Johnston D (2004) Properties of single voltage-dependent K+ channels in dendrites of CA1 pyramidal neurones of rat hippocampus. J Physiol 559:187–203

Chen S, Yaari Y (2008) Spike Ca2+ influx upmodulates the spike afterdepolarization and bursting via intracellular inhibition of KV7/M channels. J Physiol 586:1351–1363

Chevaleyre V, Siegelbaum SA (2010) Strong CA2 pyramidal neuron synapses define a powerful disynaptic cortico-hippocampal loop. Neuron 66:560–572

Chikwendu A, McBain CJ (1996) Two temporally overlapping "delayed-rectifiers" determine the voltage-dependent potassium current phenotype in cultured hippocampal interneurons. J Neurophysiol 76:1477–1490

Christie BR, Eliot LS, Ito K, Miyakawa H, Johnston D (1995) Different Ca2+ channels in soma and dendrites of hippocampal pyramidal neurons mediate spike-induced Ca2+ influx. J Neurophysiol 73(6):2553–2557

Chung YH, Shin C, Park KH, Cha CI (2000) Immunohistochemical study on the distribution of the voltage-gated calcium channel alpha(1B) subunit in the mature rat brain. Brain Res 866(1–2):274–280

Colbert CM, Johnston D (1996) Axonal action-potential initiation and Na+ channel densities in the soma and axon initial segment of subicular pyramidal neurons. J Neurosci 16(21):6676–6686

Colbert CM, Pan E (2002) Ion channel properties underlying axonal action potential initiation in pyramidal neurons. Nat Neurosci 5:533–538

Colbert CM, Magee JC, Hoffman DA, Johnston D (1997) Slow recovery from inactivation of Na+ channels underlies the activity-dependent attenuation of dendritic action potentials in hippocampal CA1 pyramidal neurons. J Neurosci 17(17):6512–6521

Day NC, Shaw PJ, AL MC, Craig PJ, Smith W, Beattie R, Williams TL, Ellis SB, Ince PG, Harpold MM, Lodge D, Volsen SG (1996) Distribution of alpha 1A, alpha 1B and alpha 1E voltage-dependent calcium channel subunits in the human hippocampus and parahippocampal gyrus. Neuroscience 71(4):1013–1024

Deisseroth K (2010) Controlling the brain with light. Sci Am 303:48–55

Deisseroth K (2011) Optogenetics. Nat Methods 8:26–29

Devaux JJ, Kleopa KA, Cooper EC, Scherer SS (2004) KCNQ2 is a nodal K^+ channel. J Neurosci 24:1236–1244

Dietrich D, Kirschstein T, Kukley M, Pereverzev A, von der Brelie C, Schneider T, Beck H (2003) Functional specialization of presynaptic Cav2.3 Ca2+ channels. Neuron 39(3):483–496

Du J, Haak LL, Phillips-Tansey E, Russell JT, CJ MB (2000) Frequency-dependent regulation of rat hippocampal somato-dendritic excitability by the K+ channel subunit Kv2.1. J Physiol 522(Pt 1):19–31

Elgueta C, Köhler J, Bartos M (2015) Persistent discharges in dentate gyrus perisoma-inhibiting interneurons require hyperpolarization-activated cyclic nucleotide-gated channel activation. J Neurosci 35(10):4131–4139

Eliot LS, Johnston D (1994) Multiple components of calcium current in acutely dissociated dentate gyrus granule neurons. J Neurophysiol 72(2):762–777

Ellerkmann RK, Riazanski V, Elger CE, Urban BW, Beck H (2001) Slow recovery from inactivation regulates the availability of voltage-dependent Na(+) channels in hippocampal granule cells, hilar neurons and basket cells. J Physiol 532(Pt 2):385–397

Ellerkmann RK, Remy S, Chen J, Sochivko D, Elger CE, Urban BW, Becker A, Beck H (2003) Molecular and functional changes in voltage-dependent Na(+) channels following pilocarpine-induced status epilepticus in rat dentate granule cells. Neuroscience 119(2):323–333

Engel D, Jonas P (2005) Presynaptic action potential amplification by voltage-gated Na+ channels in hippocampal mossy fiber boutons. Neuron 45(3):405–417

Felts PA, Yokoyama S, Dib-Hajj S, Black JA, Waxman SG (1997) Sodium channel alpha-subunit mRNAs I, II, III, NaG, Na6 and hNE (PN1): different expression patterns in developing rat nervous system. Brain Res Mol Brain Res 45:71–82

Fernandez FR, Morales E, Rashid AJ, Dunn RJ, Turner RW (2003) Inactivation of Kv3.3 potassium channels in heterologous expression systems. J Biol Chem 278(42):40890–40898

Fisher RE, Gray R, Johnston D (1990) Properties and distribution of single voltage-gated calcium channels in adult hippocampal neurons. J Neurophysiol 64(1):91–104

Franz O, Liss B, Neu A, Roeper J (2000) Single-cell mRNA expression of HCN1 correlates with a fast gating phenotype of hyperpolarization-activated cyclic nucleotide-gated ion channels (Ih) in central neurons. Eur J Neurosci 12:2685–2693

Fraser DD, MacVicar BA (1991) Low-threshold transient calcium current in rat hippocampal lacunosum-moleculare interneurons: kinetics and modulation by neurotransmitters. J Neurosci 11(9):2812–2820

Freund TF, Buzsáki G (1996) Interneurons of the hippocampus. Hippocampus 6(4):347–470

Fricker D, Verheugen JA, Miles R (1999) Cell-attached measurements of the firing threshold of rat hippocampal neurones. J Physiol 517(Pt 3):791–804

Frotscher M, Seress L, Schwerdtfeger WK, Buhl E (1991) The mossy cells of the fascia dentata: a comparative study of their fine structure and synaptic connections in rodents and primates. J Comp Neurol 312(1):145–163

Gasparini S, Magee JC (2002) Phosphorylation-dependent differences in the activation properties of distal and proximal dendritic Na+ channels in rat CA1 hippocampal neurons. J Physiol 541(Pt 3):665–672

Gasparini S, Migliore M, Magee JC (2004) On the initiation and propagation of dendritic spikes in CA1 pyramidal neurons. J Neurosci 24(49):11046–11056

Geiger JR, Jonas P (2000) Dynamic control of presynaptic Ca(2+) inflow by fast-inactivating K(+) channels in hippocampal mossy fiber boutons. Neuron 28:927–939

Gentet LJ, Stuart GJ, Clements JD (2000) (2000) direct measurement of specific membrane capacitance in neurons. Biophys J 79(1):314–320

Golding NL, Jung HY, Mickus T, Spruston N (1999) Dendritic calcium spike initiation and repolarization are controlled by distinct potassium channel subtypes in CA1 pyramidal neurons. J Neurosci 19(20):8789–8798

Goldman L, Schauf CL (1973) Quantitative description of sodium and potassium currents and computed action potentials in Myxicola giant axons. J Gen Physiol 61:361–384

Gong B, Rhodes KJ, Bekele-Arcuri Z, Trimmer JS (1999) Type I and type II Na(+) channel alpha-subunit polypeptides exhibit distinct spatial and temporal patterning, and association with auxiliary subunits in rat brain. J Comp Neurol 412(2):342–352

Grissmer S, Nguyen AN, Aiyar J, Hanson DC, Mather RJ, Gutman GA, Karmilowicz MJ, Auperin DD, Chandy KG (1994) Pharmacological characterization of five cloned voltage-gated K+ channels, types Kv1.1, 1.2, 1.3, 1.5, and 3.1, stably expressed in mammalian cell lines. Mol Pharmacol 45(6):1227–1234

Gu N, Vervaeke K, Hu H, Storm JF (2005) M-channels (Kv7/KCNQ channels) that regulate synaptic integration, excitability, and spike pattern of CA1 pyramidal cells are located in the perisomatic region. J Physiol 566(Pt 3):689–715

Hamill OP, Marty A, Neher E, Sakmann B, Sigworth FJ (1981) Improved patch-clamp techniques for high-resolution current recording from cells and cell-free membrane patches. Pflugers Arch 391(2):85–100

Häusser M, Stuart G, Racca C, Sakmann B (1995) Axonal initiation and active dendritic propagation of action potentials in substantia nigra neurons. Neuron 15:637–647

Hefft S, Jonas P (2005) Asynchronous GABA release generates long-lasting inhibition at a hippocampal interneuron-principal neuron synapse. Nat Neurosci 8(10):1319–1328

Hillman D, Chen S, Aung TT, Cherksey B, Sugimori M, Llinás RR (1991) Localization of P-type calcium channels in the central nervous system. Proc Natl Acad Sci U S A 88(16):7076–7080

Hitti FL, Siegelbaum SA (2014) The hippocampal CA2 region is essential for social memory. Nature 508(7494):88–92

Hodgkin AL, Huxley AF (1952) A quantitative description of membrane current and its application to conduction and excitation in nerve. J Physiol 117:500–544

Hoffman DA, Johnston D (1998) Downregulation of transient K+ channels in dendrites of hippocampal CA1 pyramidal neurons by activation of PKA and PKC. J Neurosci 18(10):3521–3528

Hoffman DA, Magee JC, Colbert CM, Johnston D (1997) K+ channel regulation of signal propagation in dendrites of hippocampal pyramidal neurons. Nature 387(6636):869–875

Hoogland TM, Saggau P (2004) Facilitation of L-type Ca2+ channels in dendritic spines by activation of beta2 adrenergic receptors. J Neurosci 24(39):8416–8427

Horn R, Marty A (1988) Muscarinic activation of ionic currents measured by a new whole-cell recording method. J Gen Physiol 92:145–159

Howard AL, Neu A, Morgan RJ, Echegoyen JC, Soltesz I (2007) Opposing modifications in intrinsic currents and synaptic inputs in post-traumatic mossy cells: evidence for single-cell homeostasis in a hyperexcitable network. J Neurophysiol 97(3):2394–2409

Hu H, Vervaeke K, Storm JF (2002) Two forms of electrical resonance at theta frequencies, generated by M-current, h-current and persistent Na+ current in rat hippocampal pyramidal cells. J Physiol 545(Pt 3):783–805

Hu H, Vervaeke K, Storm JF (2007) M-channels (Kv7/KCNQ channels) that regulate synaptic integration, excitability, and spike pattern of CA1 pyramidal cells are located in the perisomatic region. J Neurosci 27:1853–1867

Hu H, Martina M, Jonas P (2010) Dendritic mechanisms underlying rapid synaptic activation of fast-spiking hippocampal interneurons. Science 327(5961):52–58

Hyun JH, Eom K, Lee KH, Ho WK, Lee SH (2013) Activity-dependent downregulation of D-type K+ channel subunit Kv1.2 in rat hippocampal CA3pyramidal neurons. J Physiol 591(22):5525–5540

Jinno S, Ishizuka S, Kosaka T (2003) Ionic currents underlying rhythmic bursting of ventral mossy cells in the developing mouse dentate gyrus. Eur J Neurosci 17(7):1338–1354

Johnston D, Hoffman DA, Magee JC, Poolos NP, Watanabe S, Colbert CM, Migliore M (2000) Dendritic potassium channels in hippocampal pyramidal neurons. J Physiol 525(Pt 1):75–81

Jung HY, Mickus T, Spruston N (1997) Prolonged sodium channel inactivation contributes to dendritic action potential attenuation in hippocampal pyramidal neurons. J Neurosci 17(17):6639–6646

Jung HY, Staff NP, Spruston N (2001) Action potential bursting in subicular pyramidal neurons is driven by a calcium tail current. J Neurosci 21(10):3312–3321

Kim J, Wei DS, Hoffman DA (2005) Kv4 potassium channel subunits control action potential repolarization and frequency-dependent broadening in rat hippocampal CA1 pyramidal neurones. J Physiol 569:41–57

Kim S (2014) Action potential modulation in CA1 pyramidal neuron axons facilitates OLM interneuron activation in recurrent inhibitory microcircuits of rat hippocampus. PLoS One 19(11):e113124

Kim S, Guzman SJ, Hu H, Jonas P (2012) Active dendrites support efficient initiation of dendritic spikes in hippocampal CA3 pyramidal neurons. Nat Neurosci 15:600–606

King B, Rizwan AP, Asmara H, Heath NC, Engbers JD, Dykstra S, Bartoletti TM, Hameed S, Zamponi GW, Turner RW (2015) IKCa channels are a critical determinant of the slow AHP in CA1 pyramidal neurons. Cell Rep 11(2):175–182

Klee R, Ficker E, Heinemann U (1995) Comparison of voltage-dependent potassium currents in rat pyramidal neurons acutely isolated from hippocampal regions CA1 and CA3. J Neurophysiol 74(5):1982–1995

Kohara K, Pignatelli M, Rivest AJ, Jung HY, Kitamura T, Suh J, Frank D, Kajikawa K, Mise N, Obata Y, Wickersham IR, Tonegawa S (2014) Cell type-specific genetic and optogenetic tools reveal hippocampal CA2 circuits. Nat Neurosci 17(2):269–279

Lambert NA, Wilson WA (1996) High-threshold Ca2+ currents in rat hippocampal interneurones and their selective inhibition by activation of GABA(B) receptors. J Physiol 492(Pt 1):115–127

Lawrence JJ, Saraga F, Churchill JF, Statland JM, Travis KE, Skinner FK, McBain CJ (2006) Somatodendritic Kv7/KCNQ/M channels control interspike interval in hippocampal interneurons. J Neurosci 26(47):12325–12338

Li L, Bischofberger J, Jonas P (2007) Differential gating and recruitment of P/Q-, N-, and R-type Ca2+ channels in hippocampal mossy fiber boutons. J Neurosci 27(49):13420–13429

Liao YJ, Jan YN, Jan LY (1996) Heteromultimerization of G-protein-gated inwardly rectifying K+ channel proteins GIRK1 and GIRK2 and their altered expression in weaver brain. J Neurosci 16(22):7137–7150

Lien CC, Jonas P (2003) Kv3 potassium conductance is necessary and kinetically optimized for high-frequency action potential generation in hippocampal interneurons. J Neurosci 23(6):2058–2068

Lien CC, Martina M, Schultz JH, Ehmke H, Jonas P (2002) Gating, modulation and subunit composition of voltage-gated K(+) channels in dendritic inhibitory interneurones of rat hippocampus. J Physiol 538(Pt 2):405–419

Lein ES, Callaway EM, Albright TD, Gage FH (2005) Redefining the boundaries of the hippocampal CA2 subfield in the mouse using gene expression and 3-dimensional reconstruction. J Comp Neurol 485:1–10

Liu PW, Bean BP (2014) Kv2 channel regulation of action potential repolarization and firing patterns in superior cervical ganglion neurons and hippocampal CA1 pyramidal neurons. J Neurosci 34:4991–5002

Llinás R, Sugimori M (1980) Electrophysiological properties of in vitro Purkinje cell dendrites in mammalian cerebellar slices. J Physiol 305:197–213

Lübke J, Frotscher M, Spruston N (1998) Specialized electrophysiological properties of anatomically identified neurons in the hilar region of the rat fascia dentata. J Neurophysiol 79(3):1518–1534

Maccaferri G, McBain CJ (1996) The hyperpolarization-activated current (Ih) and its contribution to pacemaker activity in rat CA1 hippocampal stratum oriens-alveus interneurones. J Physiol 497(Pt 1):119–130

Maccaferri G, Mangoni M, Lazzari A, DiFrancesco D (1993) Properties of the hyperpolarization-activated current in rat hippocampal CA1 pyramidal cells. J Neurophysiol 69(6):2129–2136

Magee JC (1998) Dendritic hyperpolarization-activated currents modify the integrative properties of hippocampal CA1 pyramidal neurons. J Neurosci 18(19):7613–7624

Magee JC, Carruth M (1999) Dendritic voltage-gated ion channels regulate the action potential firing mode of hippocampal CA1 pyramidal neurons. J Neurophysiol 82(4):1895–1901

Magee JC, Johnston D (1995a) Characterization of single voltage-gated Na+ and Ca2+ channels in apical dendrites of rat CA1 pyramidal neurons. J Physiol 487:67–90

Magee JC, Johnston D (1995b) Synaptic activation of voltage-gated channels in the dendrites of hippocampal pyramidal neurons. Science 268:301–304

Magee JC, Christofi G, Miyakawa H, Christie B, Lasser-Ross N, Johnston D (1995) Subthreshold synaptic activation of voltage-gated Ca2+ channels mediates a localized Ca2+ influx into the dendrites of hippocampal pyramidal neurons. J Neurophysiol 74(3):1335–1342

Magee JC, Avery RB, Christie BR, Johnston D (1996) Dihydropyridine-sensitive, voltage-gated Ca2+ channels contribute to the resting intracellular Ca2+ concentration of hippocampal CA1 pyramidal neurons. J Neurophysiol 76:3460–3470

Major G (1993) Solutions for transients in arbitrarily branching cables: III. Voltage clamp problems. Biophys J 65:469–491

Major G, Larkman AU, Jonas P, Sakmann B, Jack JJ (1994) Detailed passive cable models of whole-cell recorded CA3 pyramidal neurons in rat hippocampal slices. J Neurosci 14:4613–4638

Maletic-Savatic M, Lenn NJ, Trimmer JS (1995) Differential spatiotemporal expression of K+ channel polypeptides in rat hippocampal neurons developing in situ and in vitro. J Neurosci 15:3840–3851

Martina M, Jonas P (1997) Functional differences in Na+ channel gating between fast-spiking interneurones and principal neurones of rat hippocampus. J Physiol 505:593–603

Martina M, Schultz JH, Ehmke H, Monyer H, Jonas P (1998) Functional and molecular differences between voltage-gated K+ channels of fast-spiking interneurons and pyramidal neurons of rat hippocampus. J Neurosci 18:8111–8125

Martina M, Vida I, Jonas P (2000) Distal initiation and active propagation of action potentials in interneuron dendrites. Science 287:295–300

McKay BE, McRory JE, Molineux ML, Hamid J, Snutch TP, Zamponi GW, Turner RW (2006) Ca(V)3 T-type calcium channel isoforms differentially distribute to somatic and dendritic compartments in rat central neurons. Eur J Neurosci 24:2581–2594

Meeks JP, Mennerick S (2007) Action potential initiation and propagation in CA3 pyramidal axons. J Neurophysiol 97:3460–3472

Metz AE, Jarsky T, Martina M, Spruston N (2005) R-type calcium channels contribute to afterdepolarization and bursting in hippocampal CA1 pyramidal neurons. J Neurosci 25:5763–5773

Metz AE, Spruston N, Martina M (2007) Dendritic D-type potassium currents inhibit the spike afterdepolarization in rat hippocampal CA1 pyramidal neurons. J Physiol 581:175–187

Meyer AH, Katona I, Blatow M, Rozov A, Monyer H (2002) In vivo labeling of parvalbumin-positive interneurons and analysis of electrical coupling in identified neurons. J Neurosci 22:7055–7064

Mills LR, Niesen CE, So AP, Carlen PL, Spigelman I, Jones OT (1994) N-type Ca2+ channels are located on somata, dendrites, and a subpopulation of dendritic spines on live hippocampal pyramidal neurons. J Neurosci 14:6815–6824

Mintz IM, Adams ME, Bean BP (1992) P-type calcium channels in rat central and peripheral neurons. Neuron 9:85–95

Misonou H, Menegola M, Buchwalder L, Park EW, Meredith A, Rhodes KJ, Aldrich RW, Trimmer JS (2006) Immunolocalization of the Ca2+−activated K+ channel Slo1 in axons and nerve terminals of mammalian brain and cultured neurons. J Comp Neurol 496:289–302

Mitterdorfer J, Bean BP (2002) Potassium currents during the action potential of hippocampal CA3 neurons. J Neurosci 22:10106–10115

Miyawaki T, Tsubokawa H, Yokota H, Oguro K, Konno K, Masuzawa T, Kawai N (2002) Differential effects of novel wasp toxin on rat hippocampal interneurons. Neurosci Lett 328:25–28

Mogul DJ, Fox AP (1991) Evidence for multiple types of Ca2+ channels in acutely isolated hippocampal CA3 neurones of the Guinea-pig. J Physiol 433:259–281

Monaghan MM, Trimmer JS, Rhodes KJ (2001) Experimental localization of Kv1 family voltage-gated K+ channel alpha and beta subunits in rat hippocampal formation. J Neurosci 21:5973–5983

Neher E, Sakmann B, Steinbach JH (1978) The extracellular patch clamp: a method for resolving currents through individual open channels in biological membranes. Pflugers Arch 375:219–228

Nevian T, Helmchen F (2007) Calcium indicator loading of neurons using single-cell electroporation. Pflugers Arch 454:675–688

Nicoll RA, Alger BE (1981) Synaptic excitation may activate a calcium-dependent potassium conductance in hippocampal pyramidal cells. Science 212:957–959

Normann C, Peckys D, Schulze CH, Walden J, Jonas P, Bischofberger J (2000) Associative long-term depression in the hippocampus is dependent on postsynaptic N-type Ca2+ channels. J Neurosci 20:8290–8297

Notomi T, Shigemoto R (2004) Immunohistochemical localization of Ih channel subunits, HCN1-4, in the rat brain. J Comp Neurol 471:241–276

Palacio S, Chevaleyre V, Brann DH, Murray KD, Piskorowski RA, Trimmer JS (2017) Heterogeneity in Kv2 channel expression shapes action potential characteristics and firing patterns in CA1 versus CA2 hippocampal pyramidal neurons. eNeuro. 4. pii: ENEURO.0267-17.2017

Park KH, Chung YH, Shin C, Kim MJ, Lee BK, Cho SS, Cha CI (2001) Immunohistochemical study on the distribution of the voltage-gated potassium channels in the gerbil hippocampus. Neurosci Lett 298:29–32

Parra P, Gulyás AI, Miles R (1998) How many subtypes of inhibitory cells in the hippocampus? Neuron 20:983–993

Piskorowski RA, Nasrallah K, Diamantopoulou A, Mukai J, Hassan SI, Siegelbaum SA, Gogos JA, Chevaleyre V (2016) Age-dependent specific changes in area CA2 of the hippocampus and social memory deficit in a mouse model of the 22q11.2 deletion syndrome. Neuron 89:163–176

Poncer JC, McKinney RA, Gähwiler BH, Thompson SM (1997) Either N- or P-type calcium channels mediate GABA release at distinct hippocampal inhibitory synapses. Neuron 18:463–472

Poolos NP, Johnston D (1999) Calcium-activated potassium conductances contribute to action potential repolarization at the soma but not the dendrites of hippocampal CA1 pyramidal neurons. J Neurosci 19:5205–5212

Price CJ, Cauli B, Kovacs ER, Kulik A, Lambolez B, Shigemoto R, Capogna M (2005) Neurogliaform neurons form a novel inhibitory network in the hippocampal CA1 area. J Neurosci 25:6775–6786

Radzicki D, Yau HJ, Pollema-Mays SL, Mlsna L, Cho K, Koh S, Martina M (2013) Temperature-sensitive Cav1.2 calcium channels support intrinsic firing of pyramidal neurons and provide a target for the treatment of febrile seizures. J Neurosci 33:9920–9931

Ramakers GM, Storm JF (2002) A postsynaptic transient K(+) current modulated by arachidonic acid regulates synaptic integration and threshold for LTP induction in hippocampal pyramidal cells. Proc Natl Acad Sci U S A 99:10144–10149

Reckziegel G, Beck H, Schramm J, Elger CE, Urban BW (1998) Electrophysiological characterization of Na+ currents in acutely isolated human hippocampal dentate granule cells. J Physiol 509:139–150

Rettig J, Heinemann SH, Wunder F, Lorra C, Parcej DN, Dolly JO, Pongs O (1994) Inactivation properties of voltage-gated K+ channels altered by presence of beta-subunit. Nature 1994(369):289–294

Rhodes KJ, Strassle BW, Monaghan MM, Bekele-Arcuri Z, Matos MF, Trimmer JS (1997) Association and colocalization of the Kvbeta1 and Kvbeta2 beta-subunits with Kv1 alpha-subunits in mammalian brain K+ channel complexes. J Neurosci 17:8246–8258

Rhodes KJ, Carroll KI, Sung MA, Doliveira LC, Monaghan MM, Burke SL, Strassle BW, Buchwalder L, Menegola M, Cao J, An WF, Trimmer JS (2004) KChIPs and Kv4 alpha subunits as integral components of A-type potassium channels in mammalian brain. J Neurosci 24:7903–7915

Riazanski V, Becker A, Chen J, Sochivko D, Lie A, Wiestler OD, Elger CE, Beck H (2001) Functional and molecular analysis of transient voltage-dependent K+ currents in rat hippocampal granule cells. J Physiol 537:391–406

Robert V, Cassim S, Chevaleyre V, Piskorowski RA (2018) Hippocampal area CA2: properties and contribution to hippocampal function. Cell Tissue Res. https://doi.org/10.1007/s00441-017-2769-7

Rozsa B, Zelles T, Vizi ES, Lendvai B (2004) Distance-dependent scaling of calcium transients evoked by backpropagating spikes and synaptic activity in dendrites of hippocampal interneurons. J Neurosci 24:661–670

Russo MJ, Mugnaini E, Martina M (2007) Intrinsic properties and mechanisms of spontaneous firing in mouse cerebellar unipolar brush cells. J Physiol 581(Pt 2):709–724

Saganich MJ, Machado E, Rudy B (2001) Differential expression of genes encoding subthreshold-operating voltage-gated K+ channels in brain. J Neurosci 21:4609–4624

Santoro B, Wainger BJ, Siegelbaum SA (2004) Regulation of HCN channel surface expression by a novel C-terminal protein-protein interaction. J Neurosci 24:10750–10762

Sather W, Dieudonné S, MacDonald JF, Ascher P (1992) Activation and desensitization of N-methyl-D-aspartate receptors in nucleated outside-out patches from mouse neurones. J Physiol 450:643–672

Saviane C, Mohajerani MH, Cherubini E (2003) An ID-like current that is downregulated by Ca2+ modulates information coding at CA3-CA3 synapses in the rat hippocampus. J Physiol 552:513–524

Schmidt-Hieber C, Jonas P, Bischofberger J (2007) Subthreshold dendritic signal processing and coincidence detection in dentate gyrus granule cells. J Neurosci 27:8430–8441

Schmidt-Hieber C, Jonas P, Bischofberger J (2008) Action potential initiation and propagation in hippocampal mossy fibre axons. J Physiol 586:1849–1857

Schroeder BC, Hechenberger M, Weinreich F, Kubisch C, Jentsch TJ (2000) KCNQ5, a novel potassium channel broadly expressed in brain, mediates M-type currents. J Biol Chem 275:24089–24095

Sekirnjak C, Martone ME, Weiser M, Deerinck T, Bueno E, Rudy B, Ellisman M (1997) Subcellular localization of the K+ channel subunit Kv3.1b in selected rat CNS neurons. Brain Res 766:173–187

Serôdio P, Vega-Saenz de Miera E, Rudy B (1996) Cloning of a novel component of A-type K+ channels operating at subthreshold potentials with unique expression in heart and brain. Neurophysiol 75:2174–2179

Serôdio P, Rudy B (1998) Differential expression of Kv4 K+ channel subunits mediating subthreshold transient K+ (A-type) currents in rat brain. J Neurophysiol 79:1081–1091

Shah M, Mistry M, Marsh SJ, Brown DA, Delmas P (2002) Molecular correlates of the M-current in cultured rat hippocampal neurons. J Physiol 544:29–37

Sheng M, Tsaur ML, Jan YN, LY J (1992) Subcellular segregation of two A-type K+ channel proteins in rat central neurons. Neuron 9:271–284

Sheng M, Tsaur ML, Jan YN, Jan LY (1994) Contrasting subcellular localization of the Kv1.2 K+ channel subunit in different neurons of rat brain. J Neurosci 14:2408–2417

Sochivko D, Pereverzev A, Smyth N, Gissel C, Schneider T, Beck H (2002) The Ca(V)2.3 Ca(2+) channel subunit contributes to R-type Ca(2+) currents in murine hippocampal and neocortical neurones. J Physiol 542:699–710

Sochivko D, Chen J, Becker A, Beck H (2003) Blocker-resistant Ca2+ currents in rat CA1 hippocampal pyramidal neurons. Neuroscience 116:629–638

Spruston N, Johnston D (1992) Perforated patch-clamp analysis of the passive membrane properties of three classes of hippocampal neurons. J Neurophysiol 67:508–529

Spruston N, Schiller Y, Stuart G, Sakmann B (1995) Activity-dependent action potential invasion and calcium influx into hippocampal CA1 dendrites. Science 268:297–300

Srinivas KV, Buss EW, Sun Q, Santoro B, Takahashi H, Nicholson DA, Siegelbaum SA (2017) The dendrites of CA2 and CA1 pyramidal neurons differentially regulate information flow in the cortico-hippocampal circuit. J Neurosci 37:3276–3293

Staley KJ, Otis TS, Mody I (1992) Membrane properties of dentate gyrus granule cells: comparison of sharp microelectrode and whole-cell recordings. J Neurophysiol 67:1346–1358

Stea A, Tomlinson WJ, Soong TW, Bourinet E, Dubel SJ, Vincent SR, Snutch TP (1994) Localization and functional properties of a rat brain alpha 1A calcium channel reflect similarities to neuronal Q- and P-type channels. Proc Natl Acad Sci U S A 91:10576–10580

Steinhäuser C, Tennigkeit M, Matthies H, Gündel J (1990) Properties of the fast sodium channels in pyramidal neurones isolated from the CA1 and CA3 areas of the hippocampus of postnatal rats. Pflugers Arch 415:756–761

Storm JF (1990) Potassium currents in hippocampal pyramidal cells. Prog Brain Res 83:161–187

Stuart GJ, Sakmann B (1994) Active propagation of somatic action potentials into neocortical pyramidal cell dendrites. Nature 367:69–72

Stuart G, Spruston N (1998) Determinants of voltage attenuation in neocortical pyramidal neuron dendrites. J Neurosci 18:3501–3510

Su H, Sochivko D, Becker A, Chen J, Jiang Y, Yaari Y, Beck H (2002) Upregulation of a T-type Ca2+ channel causes a long-lasting modification of neuronal firing mode after status epilepticus. J Neurosci 22:3645–3655

Sun Q, Srinivas KV, Sotayo A, Siegelbaum SA (2014) Dendritic Na^+ spikes enable cortical input to drive action potential output from hippocampal CA2 pyramidal neurons. elife 3. https://doi.org/10.7554/eLife.04551

Sun Q, Sotayo A, Cazzulino AS, Snyder AM, Denny CA, Siegelbaum SA (2017) Proximodistal Heterogeneity of Hippocampal CA3 Pyramidal Neuron Intrinsic Properties, Connectivity, and Reactivation during Memory Recall. Neuron 95:656–672

Tai C, Abe Y, Westenbroek RE, Scheuer T, Catterall WA (2014) Impaired excitability of somatostatin- and parvalbumin-expressing cortical interneurons in a mouse model of Dravet syndrome. Proc Natl Acad Sci U S A 111(30):E3139–E3148

Takahashi K, Wakamori M, Akaike N (1989) Hippocampal CA1 pyramidal cells of rats have four voltage-dependent calcium conductances. Neurosci Lett 104:229–234

Takahashi K, Ueno S, Akaike N (1991) Kinetic properties of T-type Ca2+ currents in isolated rat hippocampal CA1 pyramidal neurons. J Neurophysiol 65:148–155

Takigawa T, Alzheimer C (2002) Phasic and tonic attenuation of EPSPs by inward rectifier K+ channels in rat hippocampal pyramidal cells. J Physiol 539:67–75

Talley EM, Solorzano G, Lei Q, Kim D, Bayliss DA (2001) CNS distribution of members of the two-pore-domain (KCNK) potassium channel family. J Neurosci 21:7491–7505

Taniguchi H, He M, Wu P, Kim S, Paik R, Sugino K, Kvitsiani D, Fu Y, Lu J, Lin Y, Miyoshi G, Shima Y, Fishell G, Nelson SB, Huang ZJ (2011) A resource of Cre driver lines for genetic targeting of GABAergic neurons in cerebral cortex. Neuron 71:995–1013

Taverna S, Tkatch T, Metz AE, Martina M (2005) Differential expression of TASK channels between horizontal interneurons and pyramidal cells of rat hippocampus. J Neurosci 25:9162–9170

Thompson SM, Wong RK (1991) Development of calcium current subtypes in isolated rat hippocampal pyramidal cells. J Physiol 439:671–689

Tippens AL, Pare JF, Langwieser N, Moosmang S, Milner TA, Smith Y, Lee A (2008) Ultrastructural evidence for pre- and postsynaptic localization of Cav1.2 L-type Ca2+ channels in the rat hippocampus. J Comp Neurol 506:569–583

Torborg CL, Berg AP, Jeffries BW, Bayliss DA, McBain CJ (2006) TASK-like conductances are present within hippocampal CA1 stratum oriens interneuron subpopulations. J Neurosci 26:7362–7367

Tsaur ML, Sheng M, Lowenstein DH, Jan YN, Jan LY (1992) Differential expression of K+ channel mRNAs in the rat brain and down-regulation in the hippocampus following seizures. Neuron 8:1055–1067

Tsay D, Dudman JT, Siegelbaum SA (2007) HCN1 channels constrain synaptically evoked Ca2+ spikes in distal dendrites of CA1 pyramidal neurons. Neuron 56:1076–1089

Veng LM, Browning MD (2002) Regionally selective alterations in expression of the alpha(1D) subunit (Ca(v)1.3) of L-type calcium channels in the hippocampus of aged rats. Brain Res Mol Brain Res 107:120–127

Vervaeke K, Gu N, Agdestein C, Hu H, Storm JF (2006) Kv7/KCNQ/M-channels in rat glutamatergic hippocampal axons and their role in regulation of excitability and transmitter release. J Physiol 576:235–256

Vida I, Halasy K, Szinyei C, Somogyi P, Buhl EH (1998) Unitary IPSPs evoked by interneurons at the stratum radiatum-stratum lacunosum-moleculare border in the CA1 area of the rat hippocampus in vitro. J Physiol 506:755–773

Wang H, Kunkel DD, Schwartzkroin PA, Tempel BL (1994) Localization of Kv1.1 and Kv1.2, two K channel proteins, to synaptic terminals, somata, and dendrites in the mouse brain. J Neurosci 14:4588–4599

Wang HS, Pan Z, Shi W, Brown BS, Wymore RS, Cohen IS, Dixon JE, McKinnon D (1998) CNQ2 and KCNQ3 potassium channel subunits: molecular correlates of the M-channel. Science 282:1890–1893

Weiler N, Wood L, Yu J, Solla SA, Shepherd GM (2008) Top-down laminar organization of the excitatory network in motor cortex. Nat Neurosci 11:360–366

Weiser M, Vega-Saenz de Miera E, Kentros C, Moreno H, Franzen L, Hillman D, Baker H, Rudy B (1994) Differential expression of Shaw-related K+ channels in the rat central nervous system. J Neurosci 14:949–972

Weiser M, Bueno E, Sekirnjak C, Martone ME, Baker H, Hillman D, Chen S, Thornhill W, Ellisman M, Rudy B (1995) The potassium channel subunit KV3.1b is localized to somatic and axonal membranes of specific populations of CNS neurons. J Neurosci 15:4298–4314

Wilson SM, Toth PT, Oh SB, Gillard SE, Volsen S, Ren D, Philipson LH, Lee EC, Fletcher CF, Tessarollo L, Copeland NG, Jenkins NA, Miller RJ (2000) The status of voltage-dependent calcium channels in alpha 1E knock-out mice. J Neurosci 20:8566–8571

Xu W, Lipscombe D (2001) Neuronal Ca(V)1.3alpha(1) L-type channels activate at relatively hyperpolarized membrane potentials and are incompletely inhibited by dihydropyridines. J Neurosci 21:5944–5951

Yaari Y, Yue C, Su H (2007) Recruitment of apical dendritic T-type Ca2+ channels by backpropagating spikes underlies de novo intrinsic bursting in hippocampal epileptogenesis. J Physiol 580:435–450

Yue C, Yaari Y (2004) KCNQ/M channels control spike afterdepolarization and burst generation in hippocampal neurons. J Neurosci 24:4614–4624

Yue C, Remy S, Su H, Beck H, Yaari Y (2005) Proximal persistent Na+ channels drive spike afterdepolarizations and associated bursting in adult CA1 pyramidal cells. J Neurosci 25:9704–9720

Zhang L, Valiante TA, Carlen PL (1993) Contribution of the low-threshold T-type calcium current in generating the post-spike depolarizing afterpotential in dentate granule neurons of immature rats. J Neurophysiol 70:223–231

Zhao M, Choi YS, Obrietan K, Dudek SM (2007) Synaptic plasticity (and the lack thereof) in hippocampal CA2 neurons. J Neurosci 27:12025–12032

Glutamatergic Neurotransmission in the Hippocampus

Katalin Tóth

Abstract This chapter will summarize key data about glutamatergic transmission in the hippocampus. Glutamate is the major excitatory neurotransmitter similar to other CNS regions. Biophysical properties of various receptors and channels will be described and functional relevance of these parameters discussed.

The major components of the excitatory synaptic network in the hippocampus form the so-called tri-synaptic circuit. This circuit consists of the perforant pathway input from the entorhinal cortex to the dentate gyrus, mossy fibers projecting from the dentate gyrus to the CA3 area, and Schaffer collaterals, axons of CA3 pyramidal cells innervating the CA1 area. This chapter will focus on the properties of these glutamatergic synapses, highlighting the most distinct features these inputs possess.

Glutamatergic transmission in the hippocampus is known to play a crucial role in learning and memory due to activity-dependent changes in synaptic efficacy. However, this chapter will focus on the basic properties of glutamatergic synapses, and "Synaptic Plasticity at Hippocampal Synapses" chapter will discuss synaptic plasticity in detail.

Introduction

The main excitatory transmitter in the hippocampus is glutamate. Its action is mediated via two main classes of glutamate receptors: ionotropic and metabotropic receptors (Fig. 1).

The ionotropic glutamate receptors are ligand-gated ion channels; they are responsible for the vast majority of fast excitatory neurotransmission in the CNS. In these receptors, glutamate binding causes channel opening, with the resulting predominant Na^+ influx leading to membrane depolarization. Based on their particular pharmacology, ionotropic glutamate receptors fall into three major classes which

K. Tóth (✉)
CERVO Brain Research Centre, Université Laval, Quebec City, QC, Canada
e-mail: katalin.toth@crulrg.ulaval.ca

V. Cutsuridis et al. (eds.), *Hippocampal Microcircuits*, Springer Series in Computational Neuroscience, https://doi.org/10.1007/978-3-319-99103-0_4

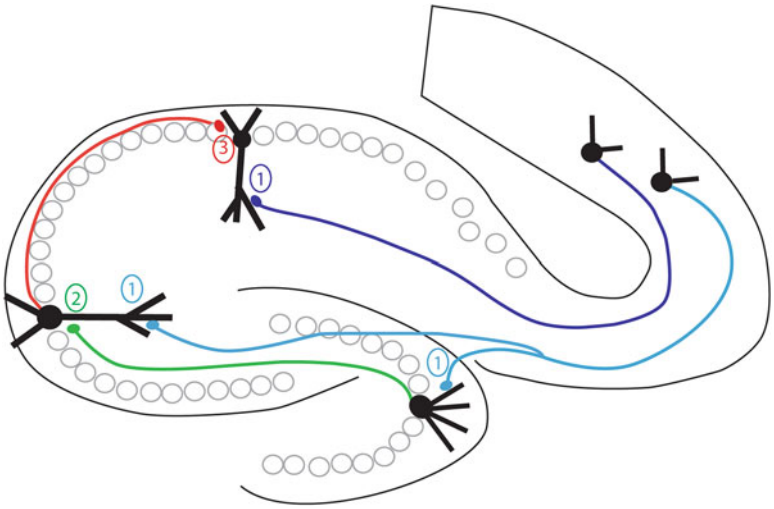

Fig. 1 Major excitatory pathways in the hippocampus. Layer II neurons in the entorhinal cortex project to the dentate gyrus and the CA3 via the perforant pathways (1, blue). Neurons in layer III of the entorhinal cortex send their axons to the CA1 subfield and the subiculum (1, purple). Dentate granule cells innervate the CA3 area via mossy fibers (2, green). Pyramidal cells of the CA3 subregion project to the CA1 area via Schaffer collaterals (3, red)

are named after their selective agonists: AMPA (α-amino-3-hydroxy-5-methyl-4-isoxazolepropionic acid), NMDA (N-methyl-D-aspartate), and kainate receptors. All three receptors types form heteromeric structures consisting of four subunits.

AMPA receptors are composed of a combination of four subunits: GluA1, GluA2, GluA3, and GluA4 (Dingledine et al. 1999). The presence or absence of the GluA2 subunit in the complex will determine several biophysical properties of the receptor. This subunit undergoes posttranscriptional RNA editing at the "Q/R site"; insertion of the edited form into AMPA receptors will result in low-conductance, Ca^{2+}-impermeable channels with linear I-V relationship. In contrast, GluA2-lacking AMPA receptors have higher conductance, are Ca^{2+}-permeable, and show inwardly rectifying I-V relationships due to the block by endogenous polyamine at positive membrane potentials (Bowie and Mayer 1995; Kamboj et al. 1995; Koh et al. 1995). Principal cells in the hippocampus express high levels of GluA2; hence Ca^{2+}-impermeable AMPA receptors dominate synaptic transmission in these cells. Ca^{2+}-permeable AMPA receptors are present on some hippocampal interneurons, and during development, some fetal GluA2 subunits remain unedited. Inward rectification of GluA2-lacking receptors is caused by voltage-dependent block by intracellular polyamines (Bowie and Mayer 1995; Donevan and Rogawski 1995; Kamboj et al. 1995; Koh et al. 1995). Therefore, polyamine toxins, such as philanthotoxin (PhTx), a high-affinity agonist of currents mediated by receptors lacking the GluA2 subunit, can be used to pharmacologically differentiate between Ca^{2+}-permeable and Ca^{2+}-impermeable AMPA receptors (Blaschke et al. 1993; Washburn and Dingledine 1996).

In the hippocampus, NMDA receptors are heteromultimers of GluN1 and GluN2A-D subunits. NMDA receptors have very slow kinetics compared to AMPA or kainate receptors, which is explained by the slow dissociation rate of glutamate. While glutamate is bound, NMDA channels can undergo repeated opening. NMDA receptors activation requires two agonists, glycine and glutamate. The glycine site must be occupied first, followed by glutamate binding. When this occurs, the channel can open and Na^+ and Ca^{2+} enter the cell. However, channel opening can only occur when Mg^{2+} block is removed from NMDA receptors while the membrane is depolarized. At resting membrane potentials, glutamate binding does not lead to channel opening. Ca^{2+} entering the cell via NMDA receptors plays important role in synaptic plasticity.

Kainate receptors are also heteromultimers composed of the combination of GluK1,2,3 and GluK4,5 subunits. GluK4 and GluK5 subunits alone are nonfunctional and are retained in the endoplasmic reticulum but can combine with GluK1–3 to form surface-localized functional receptors. GluK1 and GluK6 subunits undergo alternative splicing similar to the GluA2 subunit of AMPA receptors at the Q/R site. Receptors incorporating edited GluK1 and GluK6 subunits have linear I-V relationship, while insertion of the unedited form of GluK1 or GluK6 results in inward rectification due to intracellular polyamine block at depolarized membrane potentials. Receptors containing solely unedited GluK1 and GluK2 are also weakly permeable to Ca^{2+}. Relationship between rectification, Ca^{2+}-permeability, and subunit composition is more complex than in AMPA receptors because only a portion of GluK1 and GluK6 subunits are edited at the Q/R site. Recombinant kainate receptors have fast kinetics; they rapidly activate and deactivate in the submillisecond range. Interestingly these parameters are markedly different from the relatively slow kinetics of synaptically evoked kainate responses.

The metabotropic glutamate receptors contain seven transmembrane domains, and their actions are mediated via G proteins. Metabotropic receptors fall into three groups based on amino acid homology, signal transduction pathway, and their pharmacological profile.

Group I metabotropic receptors are generally localized postsynaptically, coupled to the Gq signaling pathway, and their activation increases cell excitability. Group II and III receptors are localized on the presynaptic membrane and coupled to adenylyl cyclase via G proteins; in general they are involved in the control of neurotransmitter release. Presynaptically located metabotropic glutamate receptors are generally involved in plastic changes leading to modifications in synaptic strength, while glutamate binding to postsynaptic metabotropic receptors can lead to ion channel opening and closing and the generation of various intracellular messengers (Table 1).

The Perforant Pathway

The hippocampus receives its major cortical input from the entorhinal cortex via the perforant pathway. This pathway originates from layer II and III of the entorhinal

Table 1 Various glutamate receptors in the hippocampus

	Groups	Subunits	Conducting ions	Pharmacology
Ionotropic receptors	AMPA	GluA1, GluA2, GluA3, GluA4	Na^+, K+ (Ca^{2+})	Antagonist: kyuneric acid, CNQX, GYKI53655
	NMDA	GluN1, GluN2A, GluN2B, GluN2C, GluN2D, GluN3A	Na^+, Ca^{2+} K+	Antagonist: kyuneric acid, D-AP5, CPP
	Kainate	GluK1, GluK2, GluK3, GluK4, GluK4	Na^+, (Ca^{2+}) K+	Antagonist: kyuneric acid, CNQX, LY3882884
			Signaling pathway	
Metabotropic receptors	Group I	mGluR1, mGluR5	Phospholipase C	Agonist: DHPG, 1S,3R-ACPD, Antagonist: MCPG
	Group II	mGluR2, mGluR3	Adenylyl cyclase	Agonist: 1S,3R-ACPD, DCG-IV, Antagonist: MCPG, LY341496
	Group III	mGluR4, mGluR6, mGluR7, mGluR8	Adenylyl cyclase	Agonist: L-AP4, Antagonist: MSOP

cortex and provides direct input to all three major areas of the hippocampus. Distal dendrites of dentate granule cells receive input from the lateral entorhinal cortex, while the medial entorhinal cortex innervates the middle third of the molecular layer of the dentate gyrus (Amaral and Witter 1989). In tCA1 region, entorhinal terminals are scattered throughout the stratum lacunosum-moleculare. Projections from the lateral entorhinal cortex innervate the superficial layers of the stratum lacunosum-moleculare, and input from the medial entorhinal area projects to the deep half of this layer (Witter 1993). Medial entorhinal cortical inputs preferentially excite pyramidal cells in the deep pyramidal layer toward the CA2 area, while lateral entorhinal input favors superficial pyramidal cells closer to the subiculum (Masurkar et al. 2017). Direct input to the dentate gyrus and the CA3 originates from layer II of the entorhinal cortex; in contrast distal dendrites in the CA1 area are innervated by axons from layer III. Input from the lateral entorhinal cortex has been shown to play a critical role in episodic memory both in rodents and humans (Wilson et al. 2013; Reagh and Yassa 2014).

Salient Features of Perforant Pathway Synapses:

- Distinct features of medial and lateral perforant pathway inputs.
- Direct input to CA1 plays important role in feed-forward inhibition.
- Input-specific subunit composition of NMDA receptors.
- Complimentary distribution of metabotropic receptors at the medial and lateral perforant pathway.

AMPA Receptors

Stimulation of the perforant pathway from the entorhinal cortex evokes monosynaptic responses in the dentate granule cells. Both the medial and lateral perforant pathways use glutamate as principal transmitter, and accordingly CNQX blocks 80–90% of the synaptic events at resting membrane potential (Lambert and Jones 1990). However, the physiological and pharmacological properties of these inputs are distinct. Topographical separation of the medial and lateral pathway in the dentate gyrus allows their investigation in isolation. In response to repeated stimuli, lateral perforant pathway synapses exhibit marked facilitation, while medial perforant path synapses show less facilitation or even depression using a paired-pulse paradigm (McNaughton 1980). During the course of a longer train of stimulus, the medial perforant path input shows significant depression, while the lateral pathway shows minimal change (McNaughton 1980; Rush et al. 2002). Since the ratio of the EPSP to fiber response is greater in the medial pathway and the observed short-term depression converts to facilitation in lower extracellular [Ca^{2+}], it is very likely that the initial release probability is lower at lateral pathway synapses than at medial perforant input. Discrepancy between the synaptically released quanta sensed by NMDA and AMPA receptors is observed in the lateral, but not in the medial perforant path, indicating that silent synapses are present only at lateral pathway synapses. Consequently, NMDA receptor-mediated recruitment of AMPA receptors to the active zone could play an important role in plastic changes at this synapse (Min et al. 1998). Several presynaptic receptors have different modulatory effects on these two inputs. Carbachol selectively depresses synaptic potentials evoked with the stimulation of the medial perforant pathway, indicating that acetylcholine receptors are selectively involved in the regulation of the glutamatergic responses at the medial but not at the lateral perforant pathway (Kahle and Cotman 1989). Noradrenalin has opposing effects on the long-term plasticity of medial and lateral perforant path inputs (Dahl and Sarvey 1989; Pelletier et al. 1994; Dahl and Sarvey 1989; Pelletier et al. 1994). Glutamatergic input from hilar mossy cells onto granule cells is potently and transiently suppressed by endocannabinoids; similarly the lateral perforant path input is also affected, while the medial performant path does not show similar modulation (Chiu and Castillo 2008; Wang et al. 2016).

Pharmacological and electrophysiological differences between lateral and medial perforant inputs terminating on CA3 pyramidal cells show similar distinct pattern even though synaptic inputs are not spatially segregated here (Berzhanskaya et al. 1998).

The dendritic arborization of certain types of inhibitory cells located in the dentate gyrus indicate that they are receiving the vast majority of their inputs from the perforant pathway (MOPP, molecular layer perforant path-associated cells); the functional role of these cells in the modulation of hippocampal activity still needs to be determined (Han et al. 1993). In the CA3 region, interneurons receiving inputs from the perforant pathway and mossy fibers were suggested to act as coincidence detectors manifesting supralinear EPSP summation (Calixto et al. 2008).

Table 2 Kinetic properties of perforant pathway inputs onto granule cells and GABAergic basket cells in the dentate gyrus (Sambandan et al. 2010)

	Granule cells	Basket cells
EPSC		
EPSC peak amplitude (minimal stimulation)	16.77 ± 3.95 pA	44.47 ± 9.48 pA
Rise time (20–80%) (minimal stimulation)	2.4 ± 0.15 ms	1.33 ± 0.25 ms
EPSC decay time constant (minimal stimulation)	10.94 ± 1.58 ms	7.09 ± 0.90 ms
EPSP		
EPSP peak amplitude (minimal stimulation)	1.15 ± 0.24 mV	2.30 ± 0.43 mV
EPSP rise time (20–80%) (minimal stimulation)	5.31 ± 0.46 ms	2.26 ± 0.13 ms
EPSP decay time constant (minimal stimulation)	25.7 ± 1.57 ms	26.71 ± 3.60 ms

Indicated values are mean ± SEM

Stimulation of the direct perforant path input to the CA1 area evokes a small glutamatergic current in CA1 pyramidal cells. This input is shown to have very little effects on the firing pattern of the postsynaptic cells (Colbert and Levy 1992; Empson and Heinemann 1995b). However, it initiates a powerful feed-forward inhibition and is capable of regulating the probability of Schaffer collateral-evoked CA1 spikes (Empson and Heinemann 1995a; Jarsky et al. 2005; Remondes and Schuman 2002).

Properties of individual perforant pathway inputs onto granule cells and inhibitory cells were investigated using minimal stimulation. While the kinetics of synaptic inputs terminating on inhibitory and excitatory cells are similar, the amplitude of perforant pathway EPSC/Ps is significantly bigger on identified PV basket cells. This difference could stem from larger number of active zones or higher number of AMPA receptors in synapses innervating basket cells (Sambandan et al. 2010) (Table 2).

NMDA Receptors

NMDA receptors significantly contribute to EPSPs evoked by perforant pathway stimulation in dentate granule cells, CNQX blocks 80–90% of the synaptic events at resting membrane potential, and further addition of APV completely abolishes the residual component (Lambert and Jones 1989, 1990). Complete and selective deletion of the GluN1 subunit in granule cells lead to impaired context discrimination in the incremental fear-conditioning paradigm and context-modulated place cell activity in the CA3. However, both of these deficits only manifested in the initial phases of the experiments and were overcome by experience. This indicates that NMDA receptors on granule cells play an important role in the animals' ability to rapidly discriminate between similar contexts (McHugh et al. 2007). Pharmacological blockade of the GluN2B-containing NMDA receptors also leads

to learning difficulties and diminished activity-dependent synaptic plasticity at the medial perforant pathway-granule cell synapses (Valenzuela-Harrington et al. 2007).

In CA1 pyramidal cells, perforant path input forms synapses on distal dendrites in the stratum lacunosum-moleculare; NMDA/AMPA charge ratio of this input is significantly larger than those of the Schaffer collateral inputs. The properties of the NMDA component were also quite different, as the NMDA-mediated current at +60 mV in the perforant pathway input is six times smaller than in the Schaffer collateral input after scaling by the maximal inward current at −20 mV (Otmakhova et al. 2002). Different NMDA receptor properties could contribute to different subunit compositions of the receptors facing the two different inputs. GluN2B subunit contribution to NMDA responses at Schaffer collateral inputs is larger than at perforant pathway inputs on a single CA1 pyramidal cell, indicating that NMDA receptors with distinct subunit composition are segregated in an input-specific manner along the dendritic tree (Arrigoni and Greene 2004). Synaptic plasticity is also expressed in an input-specific manner; performant pathway LTP in the CA1 area of the hippocampus in vivo is only partially affected by NMDAR antagonists and can be sensitive to VGCC antagonists. In contrast, perforant pathways LTP in the CA3 area is NMDAR dependent (Aksoy-Aksel and Manahan-Vaughan 2015).

Metabotropic Glutamate Receptors

In the perforant pathway terminating in the CA3 area and the dentate gyrus, the localization of presynaptic mGluRs, mGluR2, and mGluR8 is complimentary; mGluR2 is present at the medial and mGluR8 at the lateral perforant input (Shigemoto et al. 1997). Differential regulation of the medial and lateral perforant path by different metabotropic receptors has been demonstrated by selective group II and group III agonists and antagonists, indicating that group III metabotropic receptors regulate glutamate release at the lateral perforant pathway, while group II mGluRs serve as autoreceptors at the medial perforant path (Macek et al. 1996). Activation of presynaptic group II mGluRs at the medial perforant pathway reduced synaptic transmission and resulted in a reduction of short-term depression (Kilbride et al. 2001). While short-term depression is not prominent at the lateral perforant input at lower frequencies, it increases with higher stimulus frequencies, and L-AP4, a selective agonist of group III mGluRs, reduced this depression (Rush et al. 2002). In the CA1 area, perforant pathway axons display both group II and group III mGluRs; while mGluR7a and mGluR4 are detected in active zones, mGluR2 can be found in preterminal zones (Shigemoto et al. 1997). Segregation of these mGluRs to different zones of the presynaptic terminal and their different signaling suggest that they could be involved in distinct regulatory roles (Capogna 2004). Similar pattern of mGluR distribution and regulatory function was observed on perforant

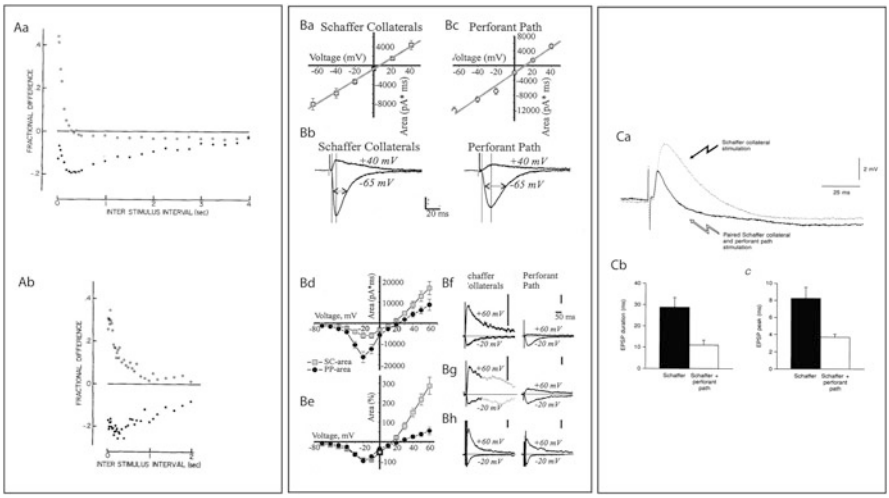

Fig. 2 Properties of the perforant path input. Different properties of short-term plasticity of the medial (filled circles) and lateral (open circles) pathway, demonstrated in vivo (Aa) and in vitro (Ab). Graphs illustrating paired-pulse ratios at various interstimulus intervals (McNaughton 1980). Comparison of current-voltage relationship of AMPA (Ba-Bc) and NMDA (Bd-Bh) responses at Schaffer collateral and perforant path inputs (Otmakhova et al. 2002). Simultaneous activation of Schaffer collaterals and the perforant path (Ca) decreases both EPSP duration (Cb) and amplitude (Cc) by activating strong feed-forward inhibition (Empson and Heinemann 1995b)

path inputs terminating on CA1 interneurons located in the stratum lacunosum-moleculare (Price et al. 2005). II mGluR activation can prevent LTP at perforant pathway synapses in the CA3 area but not in the CA1 (Aksoy-Aksel and Manahan-Vaughan 2015) (Fig. 2).

Mossy Fibers

Dentate granule cells send their axons to the hilus and the CA3 area of the hippocampus. Mossy fibers are unmyelinated axons arborizing in the hilar area and forming a distinctive axon bundle in the stratum lucidum of the CA3 area. They form three distinct types of presynaptic terminals: complex en passant presynaptic terminals called mossy fiber expansions (Amaral and Dent 1981), filopodial extensions of large mossy boutons, and small en passant terminals (Acsády et al. 1998). Large mossy terminals innervate exclusively excitatory cells, mossy cells in the hilus, and pyramidal cells in the CA3 area. In contrast, small filopodial extensions originating from the large terminals and small en passant terminals specifically terminate on GABAergic cells both in the hilus and in the CA3 (Acsády et al. 1998). Complex mossy terminals are large (4–10 μm) and form several (30–40) synaptic contacts (Chicurel and Harris 1992) with a single thorny excrescence on each CA3 pyramidal

neuron or mossy cell. A single granule cell gives rise to 10–18 large mossy terminals (Amaral et al. 1990) innervating 11–15 CA3 pyramidal cells and 7–12 hilar mossy cells. Acsády et al. (1998) elegantly demonstrated that the number of GABAergic targets innervated via small filopodial extensions and en passant terminals is ten times larger than the number of excitatory targets.

Salient Features of Mossy Fiber Synapses:

- Large presynaptic terminal with several release sites.
- Inputs to pyramidal cells and interneurons have distinct features.
- Robust short-term and frequency facilitation.
- NMDA-independent LTP.
- Small amplitude, slow postsynaptic kainate responses.

AMPA Receptors

Mossy Fiber: CA3 Pyramidal Cell Synapses

Investigation of the I-V relationship of mossy fiber inputs onto CA3 pyramidal cells showed that the excitatory connection between granule cells and CA3 pyramidal cells has linear I-V relationship indicating that these receptors are Ca^{2+}-impermeable (Jonas et al. 1993; Koh et al. 1995). Mossy fiber evoked EPSCs were insensitive to PhTx, further supporting the idea that mossy fiber input onto CA3 pyramidal cells is exclusively mediated by GluA2-containing, Ca^{2+}-impermeable AMPA receptors (Toth et al. 2000). However, in a recent study Ho et al. (Ho et al. 2007) demonstrated that while AMPA receptors at mature mossy fiber synapses are Ca^{2+}-impermeable, during the first 3 weeks of postnatal development Ca^{2+}-permeable AMPA receptors contribute to mossy fiber transmission. This transient, developmentally regulated expression of Ca^{2+}-permeable AMPA receptors could play an important role in synapse maturation and various forms of synaptic plasticity.

Unitary EPSCs have fast kinetics with a latency of 2.3–4.2 ms, a 20–80% rise time of 0.6–1.7 ms, a decay time constant of 6.2–9.6 ms, and a maximal peak conductance of 1 nS (Jonas et al. 1993; Tóth and McBain 2000). In these studies, fast kinetics were used as a criterion to ensure that evoked events are purely originating from mossy fibers; hence potential events with slower kinetics were excluded. However, in a study by Henze et al. (Henze et al. 1997), the authors found large presumptive mEPSCs with significantly slower kinetics. Later they also postulated that these events are monoquantal (Henze et al. 2002a). The amplitude of mossy fiber EPSPs can be 2–10 mV, and unitary EPSCs show amplitudes up to 1 nA; these values are severalfold larger than synaptic events evoked with the

stimulation of small glutamatergic synapses. Large unitary EPSCs are the result of a highly synchronized release from multiple release sites. The number of release sites was estimated to be between 8 and 21 in the study by Lawrence et al. (Lawrence et al. 2004); in the same study using variance-mean analysis, the quantal amplitude of mossy fiber events was calculated to be ~30pA. This value is quite different from earlier estimates deriving quantal parameters from amplitude histograms (8 pA) (Jonas et al. 1993; von Kitzing et al. 1994). Interestingly, in the recordings used for variance-mean analysis, in low extracellular Ca^{2+} conditions, smaller (7–12 pA) events could also be resolved. This indicates that quantal size might show high degree of variability among various release sites and potentially help to reconcile findings of these two studies. This possibility is further supported by recent morphological data finding large variability in the size of active zones within the mossy fiber terminal (from 0.07 to 0.17 μm2) (Rollenhagen et al. 2007). The initial release probability at mossy fiber-pyramidal cell synapses is estimated to be between 0.20 and 0.28 (Lawrence et al. 2004; von Kitzing et al. 1994). However, this low release probability is increased dramatically after repeated activation of mossy fibers; frequency-dependent facilitation can lead to up to 600% increase in EPSC amplitude (Salin et al. 1996; Toth et al. 2000). Short-term facilitation can be observed at frequencies as low as 0.1 Hz. The combination of low initial probability and pronounced short-term facilitation leads to increased spike transmission following short trains. Single action potentials initiated in the dentate granule cells in vivo rarely drive their postsynaptic targets, whereas high-frequency trains with short interspike intervals robustly increased spike transmission probability (Henze et al. 2002b). In in vitro experiments, the probability that the initial EPSP in a train elicited action potentials in CA3 pyramidal cells is only 0.28; however this value rapidly increases to 0.76 over the course of 40 Hz stimulation (Lawrence et al. 2004).

The efficacy and timing of transmitter release is largely dependent on the spatiotemporal profile of presynaptic Ca^{2+} transients. Presynaptic Ca^{2+} channels have fast activation and deactivation kinetics, with time constants in the millisecond range; gating of these channels appears to be optimized to generate maximal Ca^{2+} influx during a minimal period of time (Bischofberger et al. 2002; Geiger and Jonas 2000). Presynaptic Ca^{2+} influx is triggered by presynaptic action potentials. The duration of these action potentials is not constant, but they broaden with increased presynaptic stimuli (Geiger and Jonas 2000).

Mossy fibers can follow high-frequency stimuli with high precision and efficacy; this is only possible if the terminal has large enough releasable vesicle pool. Capacitance measurements indicated that sustained Ca^{2+} inflow (30 ms, 0 V) will lead to the release of ~1400 vesicles; this corresponds to ~40 vesicles per active zone (Hallermann et al. 2003). These measurements were closely matched with data stemming from detailed electron microscopic investigation of the mossy fiber terminal (Rollenhagen et al. 2007)103]. During high-frequency stimulation, short-term facilitation is supported by a switch from univesicular to multivesicular release and the subsequent recruitment of additional release sites (Chamberland et al. 2014).

P/Q and N-type calcium channels contribute to short-term facilitation in a distinct fashion. While N-type calcium channels are responsible for calcium increase in the close vicinity of active zones, P/Q-type calcium channels are contributing to increased calcium levels at large segments of the terminal (Chamberland et al. 2017).

Mossy Fiber: Interneuron Synapse

While principal cells express high levels of GluA2, some GABAergic inhibitory interneurons in the hippocampus have inwardly rectifying I-V relationships and are Ca^{2+}-permeable (Geiger et al. 1995; Jonas et al. 1994; Koh et al. 1995; McBain and Dingledine 1993). Mossy fibers innervate GABAergic interneurons via synapses comprised of either Ca^{2+}-permeable or Ca^{2+}-impermeable AMPA receptors. The two different types of AMPA receptors differ in the plastic properties and degree by which they colocalize with NMDA receptors.

The kinetics of mossy fiber-interneuron transmission is significantly faster than the input onto pyramidal cells. The mean 10–90% rise time of EPSCs at both types of synapses was found to be in the submillisecond range, with the time constant for decay between 1 and 4 ms (Geiger et al. 1997). Geiger et al. (1997) have suggested that the kinetics at mossy fiber-interneuron synapses are fast due to the precise timing of glutamate release and the rapid deactivation of AMPA receptors.

Anatomical and physiological data equally suggest that the mossy fiber-interneuron synapse comprises of a small number of release sites (1–2). Variance-mean analysis indicated that the initial release probability at these synapses is significantly higher (0.1–0.5) than at pyramidal cell synapses (Lawrence et al. 2004). High initial release probability contributes to the mild facilitation or depression observed at these synapses during brief stimulus trains.

The unitary quantal amplitude at this synapse was found to be 27 pA (Lawrence et al. 2004); this value was calculated using variance-mean analysis and confirmed with recorded unitary events in the presence of strontium. The average size of the EPSCs evoked in CA3 interneurons is approximately three times smaller than EPSCs recorded from pyramidal cells (88 pA vs. 20 pA) (Lawrence et al. 2004). However, the probability that an EPSC would evoke an action potential in the postsynaptic cell is not significantly different between these cells when only a single stimulus was used. After brief trains of stimulation however, the probability of spike transmission is greater in pyramidal cell synapses. This difference could be explained by the distinct short-term plastic properties expressed by these synapses.

Properties of individual contacts between mossy fiber terminals and GABAergic cells have been elegantly investigated using mossy fiber bouton to interneuron paired recordings (Szabadics and Soltesz 2009). This study demonstrated that the amplitude and transmission probability of these synaptic interactions were largely target cell dependent. Inputs onto fast-spiking basket cells and spiny lucidum cells were small in amplitude and had low transmission probabilities. In contrast,

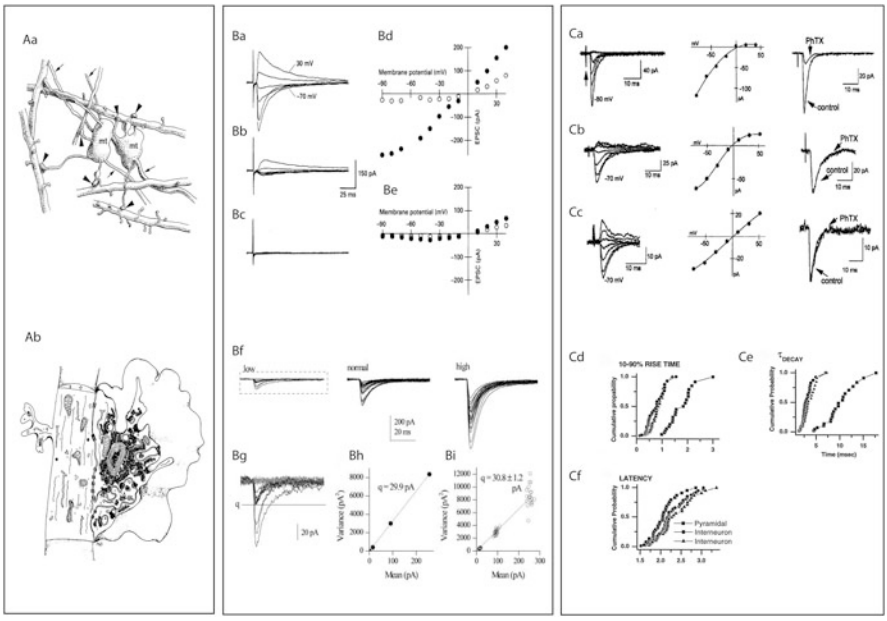

Fig. 3 Anatomical and physiological properties of mossy fiber inputs. Morphological characteristics of mossy fiber terminals: large filopodial extensions originate from the main terminal (Aa) (Acsády et al. 1998); boutons have several (20–30) active zones (Ab) (Amaral and Dent 1981). AMPA/kainate and NMDA receptor-mediated components of mossy fiber inputs (Ba-Be), current-voltage relationship of the peak current (filled circles) and the current measured 50 ms after the peak (open circles) under control conditions (Ba and Bd), in the presence of CNQX alone (Bb and Be) or in the presence of CNQX and APV (Bc) (Jonas et al. 1993). Variance-mean analysis is used to determine quantal parameters at the mossy fiber-CA3 pyramidal cell synapse (Bf-Bi) (Lawrence et al. 2004). Current-voltage relationship of mossy fiber-interneuron synapses, rectification index, and philanthotoxin sensitivity of inputs show high degree of variability (Ca-Cc) (Tóth and McBain 1998). Kinetic properties of mossy fiber inputs terminating on pyramidal cells and on interneurons mediated by calcium-permeable and calcium-impermeable AMPA receptors (Cd-Cf) (Toth et al. 2000)

regular-spiking basket cells and ivy cells received inputs with larger amplitude and transmission probability (Szabadics and Soltesz 2009) (Fig. 3).

NMDA Receptors

NMDA receptors are present at mossy fiber synapses; however mossy fiber synapses are showing lower immunostaining intensity than the Schaffer collateral inputs (Petralia et al. 1994; Takumi et al. 1999; Watanabe et al. 1998). Electrophysiological examination showed that mossy fiber synaptic inputs onto pyramidal cells are partially mediated by NMDA receptors; this component has significantly slower

kinetics than those of the AMPA component (Jonas et al. 1993; Spruston et al. 1995). In a recent study, the activation of postsynaptic NMDA receptors at mossy fiber synapses was shown to influence short-term plasticity of kainate-mediated transmission (Rebola et al. 2007). NMDA receptor-mediated depression of kainate EPSC ($EPSC_{KA}$) was observed, while the AMPA component of the event was not modified, this effect was expressed postsynaptically and was homosynaptic. Unlike in the CA1 area of the hippocampus, mossy fiber LTP is independent of NMDA receptor activation. However, NMDA receptor-mediated synaptic currents at this site are potentiated by high-frequency stimuli (Kwon and Castillo 2008b; Rebola et al. 2007).

At mossy fiber-interneuron synapses, the distribution of different subtypes of NMDA receptors and different subtypes of AMPA receptors is highly correlated. Ca^{2+}-permeable AMPA receptors occur at synapses where NMDA receptors contain the GluN2B subunit, while Ca^{2+}-impermeable AMPA receptors are associated with GluN2B-lacking NMDA receptors (Lei and McBain 2002). This particular distribution pattern leads to Ca^{2+}-permeable synapses possessing smaller NMDA components with slower decay kinetics (Lei and McBain 2002).

Kainate Receptor

Kainate receptors are located on both the pre- and postsynaptic sites at hippocampal mossy fibers. While on the postsynaptic site they generate small but prolonged depolarization, the presynaptic receptors modulate excitatory and inhibitory synaptic transmission.

Postsynaptic Receptors

Kainate-mediated postsynaptic responses were first demonstrated at mossy fiber synapses. Kainate-mediated components of the mossy fiber responses ($EPSC_{KA}$) to a single stimulus are very small, with an amplitude ~10 times smaller than the AMPA component. However, the amplitude largely increases on repetitive stimulation of the mossy fibers. Short high-frequency trains lead to a severalfold increase in kainate responses, but even a moderate increase in presynaptic stimuli (from 0.05 Hz to 0.2 Hz) could almost double the amplitude of the $EPSC_{KA}$. Postsynaptic kainate responses are selectively present at mossy fiber inputs in CA3 pyramidal cells and are absent from the commissural/associational inputs. The mossy fiber $EPSC_{KA}$ has very slow decay kinetics with the time constant approximately ten times slower than that of the AMPA component (~100 ms v. ~10 ms); the rise time (10–90%) of the kainate response is also significantly slower than the AMPA EPSC (7 ms vs. 3 ms). The slow kinetics of the kainate responses could potentially indicate that these receptors are located extrasynaptically; in this case they would not be able to respond to quantal release of glutamate. This question

was addressed by Cossart et al. (Cossart et al. 2002), and their data indicated that kainate receptors are activated by quantal release of glutamate at mossy fiber synapses, as they were able to record pure kainate and mixed AMPA/kainate miniature responses from CA3 pyramidal cells. Frequency analysis showed that 45% of the miniature events involved kainate receptor activation. Morphological data indicates that kainate receptors are localized in postsynaptic densities (Darstein et al. 2003; Petralia et al. 1994a) and the lack of effect of glutamate uptake blockers on the kinetics of kainate responses further strengthen the conclusion that the slow kinetics of EPSCKA are not caused by extrasynaptic localization of these receptors. A recent study by Barberis et al. (2008) rather indicates that slow decay kinetics can be explained by the intrinsic gating properties of GluK2/GluK4 heteromeric receptors. In fact, studies using knockout animals suggest that kainate receptors on CA3 pyramidal cells are composed of these two subunits (GluK2 and GluK4) (Contractor et al. 2003; Mulle et al. 1998).

The slow kinetics and small amplitude of kainate reposes suggest that they might play a role in frequency-dependent synaptic integration (Frerking and Ohliger-Frerking 2002). However short-term and long-term plasticity of $EPSC_{KA}$ is attenuated compared to the AMPA component, hence endowing the AMPA component with a wider dynamic range and limiting the contribution of kainate receptors in the presence of profound increase in presynaptic strength (Ito et al. 2004). Neto1/Neto 2 have been recently identified as auxiliary proteins regulating several functional parameters of kainate receptor function, including binding affinity, kinetics, and synaptic targeting of GluK2/3-containing postsynaptic KARs (Straub et al. 2011; Tang et al. 2011; Wyeth et al. 2014). Neto1 is expressed at high levels and have been shown to contribute the slow kinetics of kainate responses on mossy fiber synapses (Tang et al. 2011).

In addition to the ionotropic function, postsynaptic kainate receptors also show metabotropic activity via the inhibition of the slow Ca^{2+}-activated K^+ current I_{sAHP}, which in turn increases excitability through a G-protein-coupled mechanism (Ruiz et al. 2005; Chamberlain et al. 2013) (Fig. 4).

Presynaptic Receptors

Endogenously applied kainate has a biphasic effect; low doses facilitate mossy fiber transmission, while higher doses depress EPSCs. Endogenous kainate released following a repetitive stimulation of mossy fibers activates presynaptic receptors and facilitates synaptic release (Contractor et al. 2001; Schmitz et al. 2000; Lauri et al. 2001). Enhancement of release via presynaptic kainate receptors was shown to contribute to the robust frequency facilitation observed in mossy fibers (Contractor et al. 2001, 2003; Lauri et al. 2001; Pinheiro et al. 2007; Schmitz et al. 2001, 2003). Presynaptic kainate receptors contributing to frequency facilitation are thought to be calcium-permeable as indicated by their sensitivity to philanthotoxin. Ca^{2+} influx through these receptors is believed to play a crucial role in frequency facilitation (Lauri et al. 2001). The apparent calcium permeability of the receptors can only be

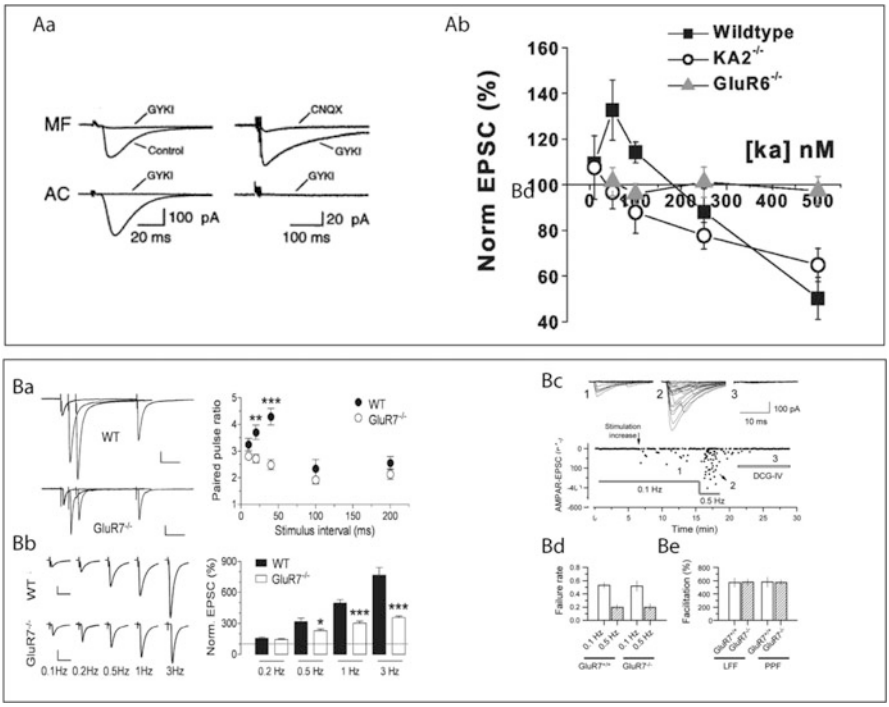

Fig. 4 Properties of kainate neurotransmission at the hippocampal mossy fibers. Kainate-mediated responses (not blocked by GYKI 53655) evoked with repetitive stimulation of the mossy fibers (MF) and are not present at associational/commissional (AC) inputs (Aa) (Castillo et al. 1997). Concentration-dependent, bidirectional modulation of mossy fiber EPSCs by kainate, GluK4 and GluK2 −/− mice shows altered kainate modulation (Ab) (Contractor et al. 2003). Controversy surrounding the role of presynaptic kainate receptors in short-term plasticity of mossy fiber inputs; AMPA receptor-mediated EPSCs from GluK3 −/− mice were shown to be less facilitated by high-frequency stimuli (Ba, Bb) (Pinheiro et al. 2007), having similar properties than their wild-type counterparts (Bc-Be) (Kwon and Castillo 2008a, b)

explained by the presence of unedited forms of kainate receptor subunits; however the mechanism by which these subunits are preferentially inserted into mossy fibers is still unknown. The subunit composition of presynaptic kainate receptors has been a matter of debate; initially the GluK1 subunit was believed to be involved in the presynaptic kainate effect (Lauri et al. 2001). However, these data obtained with pharmacological tools could not be confirmed with the genetic ablation of the GluK1 subunit (Contractor et al. 2001) or in subsequent experiments (Breustedt and Schmitz 2004). In GluK4 and GluK3 knockout animals, frequency facilitation was compromised, pointing to the critical role these subunits play in the short-term plasticity (Contractor et al. 2003; Pinheiro et al. 2007).

Even though a large body of literature is dedicated to the existence and exact functional role of presynaptic kainate receptors at the mossy fibers, Kwon and

Castillo (2008a) question the existence of presynaptic receptors. The authors used GluK1 specific agonist and GluK2 and GluK3 knockout animals and found that presynaptic kainate receptors do not play a significant role in short-term plasticity. They further postulate that the effects generally attributed to presynaptic kainate receptors are mediated by postsynaptic receptors and the activation of recurrent CA3 network activity.

Functionally, both pre- and postsynaptic kainite receptors amplify unitary mossy fiber inputs and act as conditional amplifiers of spike transmission (Sachidhanandam et al. 2009). While presynaptic receptors can effectively modulate the dynamic range of short-term plasticity, activation of postsynaptic kainate receptors during sustained stimulation leads to prolonged depolarization (Sachidhanandam et al. 2009; Pinheiro et al. 2013) (Table 3).

Metabotropic Glutamate Receptors

Presynaptic mossy fiber terminals contain two types of metabotropic glutamate receptors. While group II mGluRs are equally present on synapses opposing pyramidal cells and interneurons (Kamiya et al. 1996; Tóth and McBain 2000), mGluR7 is selectively present in synapses terminating on interneurons. Group II mGluRs depress excitatory transmission at both types of synapses. Interestingly mossy fiber-CA3 pyramidal cell synapses can be blocked completely with the group II mGluR agonist DCG-IV; synaptic inputs onto interneurons are only partially depressed. mGluRs decrease the degree of frequency facilitation observed at mossy fiber-pyramidal cell and mossy fiber-interneuron synapses (Scanziani et al. 1997; Toth et al. 2000). Group III metabotropic glutamate receptor7 (mGluR7) has low affinity for glutamate, and its activation depresses glutamatergic synaptic responses (O'Connor et al. 1999). In the mossy fiber-interneuron synapses, mGluR7 antagonist MSOP did not influence baseline transmission but prevented high-frequency-induced long-term depression, while application of an mGluR7 agonist leads to the development of a chemical LTD at this synapse (Pelkey et al. 2005). Detailed investigation of the plastic properties of this synapse leads to the discovery that mGluR7 goes through activity-dependent internalization and surface expression (Pelkey et al. 2005, 2007), contributing to state-dependent plasticity.

On the postsynaptic site, activation of Group I receptors can evoke a postsynaptic potential which is independent of the G-protein function (Heuss et al. 1999) while inhibiting IAHP through a G-protein-coupled mechanism. Their activation also leads to Ca^{2+} release from intracellular stores, which plays a role in plastic changes (Yeckel et al. 1999).

Schaffer Collaterals

The major input to the CA1 area of the hippocampus arrives from CA3 pyramidal cells via the Schaffer collaterals. Axons of CA3 pyramidal cells heavily innervate

Table 3 Kinetic properties of mossy fiber inputs onto pyramidal cells and interneurons

	MF-P cell	MF-I cell	
Quantal parameters			
Release probability	<0.3	>0.02–0.5	Jonas et al. (1993)
Quantal size	~29 pA	~30 pA	Lawrence et al. (2004) but see Jonas et al. (1993)
Release site/connection	8–35	1–2	Acsády et al. (1998), Lawrence et al. (2004), Rollenhagen et al. (2007)
Probability of action potential generation by the first EPSC	0.28	0.1	Lawrence et al. (2004)
Probability of action potential generation by 40 Hz train EPSC	0.76	0.22	Henze et al. (2002a, b))
AMPA			
Latency	2 ms	2.2 ms	Toth et al. (2000)
Amplitude (at −70 mV)	25–200 pA	2–100 pA	Walker et al. (2002)
Rise time	~1.5 ms	<1 ms	Geiger et al. (1997)
Decay time const.	~10 ms	~ 2.5–4 ms	Toth et al. (2000), Walker et al. (2002)
Channel conductance	10 pS		Jonas et al. (1993)
NMDA			
Rise time	20–30 ms		Spruston et al. (1995), Walker et al. (2002)
Decay time constant (fast)	150–250 ms	58.2 CI (calcium-impermeable), 60.8 CP (calcium-permeable)	Spruston et al. (1995), Walker et al. (2002)
Decay time constant (slow)	~1 s	525 CP, 228 CI	Spruston et al. (1995), Walker et al. (2002)
Channel conductance	46 pS	47 pS	Spruston et al. (1995), Walker et al. (2002)
Kainate			
Amplitude (at −70 mV)	5–70 pA		Castillo et al. (1997)
Rise time	6.8 ms		Castillo et al. (1997)
Decay time constant	103 ms		Castillo et al. (1997)

both the stratum radiatum and the stratum oriens of the CA1 area; proximal postsynaptic dendrites in these layers contain relatively few spines, while distal dendrites are densely spiny, excitatory inputs terminate exclusively on dendritic spines (Megías et al. 2001). A single CA3 pyramidal cell has an extensive axonal arbor and can extend to as much as two-third of the hippocampus and form 30,000–60,000 synapses (Li et al. 1994), while a single CA1 pyramidal cell receives approximately 30,000 excitatory synapses.

Salient Features of Schaffer Collateral Synapses:

- Small terminals with single release site, variable release probability.
- Increased synaptic AMPA, but not NMDA conductances at distal synapses.
- Silent synapses.
- Kainate receptor activation depresses glutamate transmission.
- Wide variety of auxiliary proteins modify receptor function.

AMPA Receptors

Excitatory synaptic inputs are broadly distributed along the dendritic tree of CA1 pyramidal cells. These inputs are integrated at the level of the axon initial segment to determine the output signal of the cell. The distance between the location of the final integration of the cellular outputs and synaptic inputs shows high degree of variety. How does the distance between the soma and the synapse influence the characteristics of synaptic inputs at the level of the soma? In principle, the further the synapse is, their impact on the final inputs should be more and more diminished, due to cable filtering. Interestingly, the local EPSP amplitude increases with distance from the soma, which leads to proximal and distal synaptic inputs producing very similar amplitudes detected at the soma (Magee and Cook 2000) (Fig. 5). Increased synaptic conductance in distal synapses was attributed to an increased AMPA receptor number on the postsynaptic sites, whereas AMPA receptor subunit composition and channel modulation was indistinguishable at proximal and distal synapses (Andrasfalvy and Magee 2001). Presynaptic properties, such as release probability, paired-pulse facilitation, and the size of the readily releasable pool, were also identical at these sites (Smith et al. 2003).

Excitatory synaptic potentials evoked by the stimulation of the Schaffer collaterals are composed of AMPA and NMDA components. However, under certain circumstances, EPSCs lack the AMPA component (Isaac et al. 2007; Kullmann 1994; Liao et al. 1995). The subpopulation of glutamatergic synapses lacking functional AMPA receptors are referred to as “silent synapses”; they have been identified in several brain regions including the CA1 area of the hippocampus.

Fig. 5 The amplitude of synaptically evoked EPSP at the soma does not depend on synapse location. Spontaneously occurring EPSPs in distal and proximal dendrites (d) and at the soma (s) in response to high osmolar external solution. (**A**) Scatterplot of dendritic and simultaneously recorded somatic EPSP amplitude from the cell shown in (**A**). (**B**) Averaged EPSPs simultaneously recorded both at the dendrite and at the soma for the neuron receiving distal and proximal inputs. (**C**) Mean EPSP amplitude for all cells plotted as a function of input distance from the soma. (**D**) Cumulative amplitude histograms showing that the distribution of distal dendritic EPSPs (light solid line) is skewed to the right compared to more proximal dendritic EPSPs (dark solid line). (**E**) (Magee and Cook 2000)

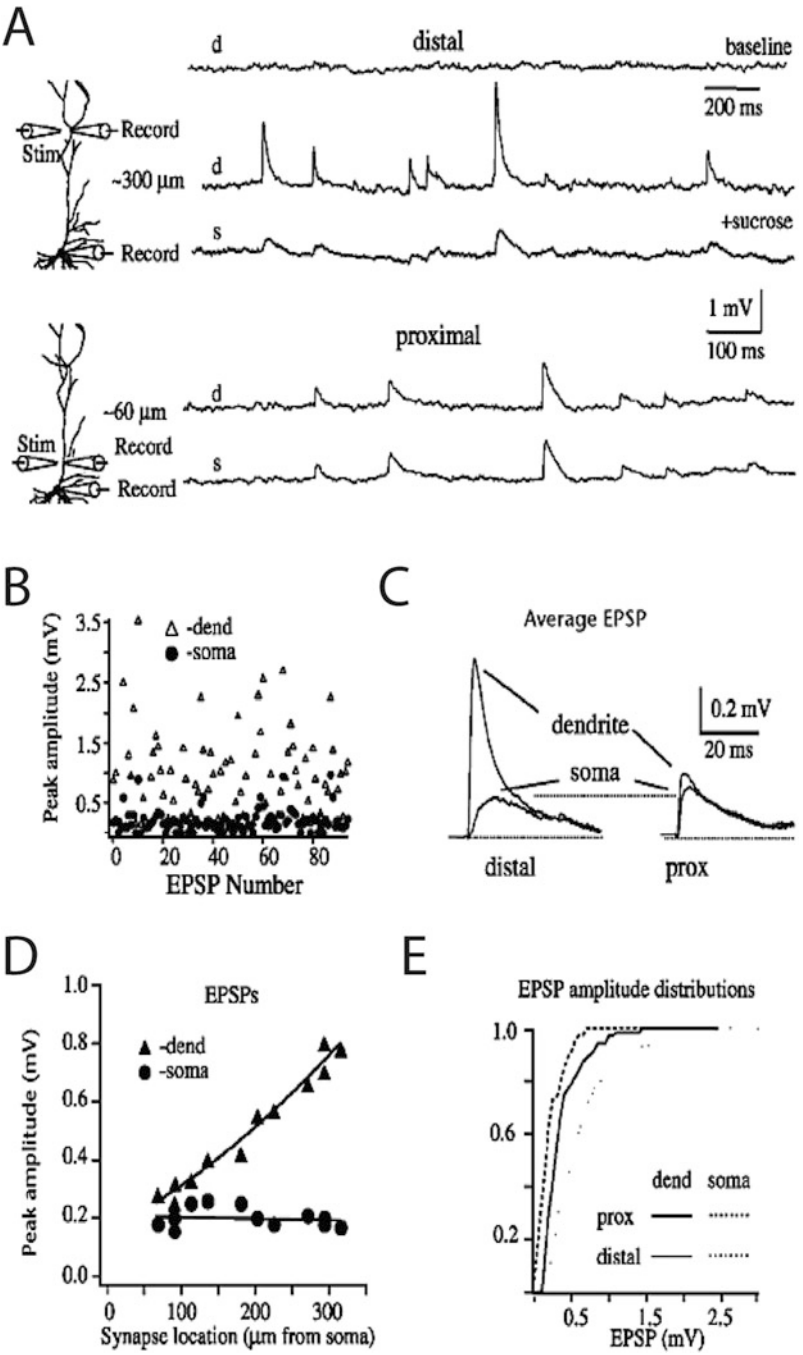

Fig. 5 (continued)

These synapses are not conducting currents at resting membrane potentials. The presence of these receptors is developmentally regulated, and during the first few postnatal days, almost all Schaffer collateral synapses are silent, but by the end of the third week, approximately 50% of them are containing functional AMPA receptors (Durand et al. 1996). Activity-dependent modification at these synapses, such as the expression of LTP, leads to the changes which "unsilence" these synapses.

How do these synapses become functional? Incorporation of AMPA receptors into silent synapse following high-frequency stimulation has been observed either through lateral diffusion (Adesnik et al. 2005) or from AMPA receptor-containing endosomes (Hayashi et al. 2000). However, recent data using optical imaging suggest that AMPA receptor insertion has little influence on synaptic plasticity; the authors rather suggest that LTP is expressed on the presynaptic site in a bidirectional, graded fashion (Enoki et al. 2009).

A novel form of plasticity at synapses with GluA3-containing AMPA receptors has been demonstrated in Schaffer collateral synapses. GluA2/3 subunit-containing receptors are in a low-conductance state but upon a rise in intracellular cAMP levels shift to a high-conductance state and lead to the potentiation of the synapse (Renner et al. 2017).

The majority of Schaffer collateral synapses contains one active zone with several docked vesicles (Harris and Sultan 1995; Schikorski and Stevens 1997). The probability of release at various release sites arising from the same axons is highly variable (Rosenmund et al. 1993). With increased release probability, more glutamate is released to the synaptic cleft; this is possible when more than one vesicle fuses with the presynaptic membrane in response to a single action potential. The probability of multivesicular release increases with release probability (Oertner et al. 2002). Multivesicular release is likely to occur at synapses with higher number of docked vesicles, which is generally observed in larger synapses (Harris and Sultan 1995).

In recent years, several studies showed the diverse effect auxiliary proteins can have on AMPA receptor functions. AMPA receptors can assemble with a wide range of auxiliary subunits belonging to four distinct families: TARP (Jackson and Nicoll 2011), cornichons (Schwenk et al. 2009), shisas (Farrow et al. 2015), and the germ cell-specific gene 1-like protein (Schwenk et al. 2012). The first three can effectively increase the mean channel conductance (Coombs et al. 2012; Jackson et al. 2011; Tomita et al. 2005; Shi et al. 2010), TARPs being the most effective among them. TARPs also influence deactivation kinetics and extra- and intracellular polyamine block of GluA2-lacking AMPA receptors (Jackson et al. 2011; Soto et al. 2009; Cho et al. 2007; Milstein et al. 2007).

NMDA Receptors

receptors are abundantly presentNMDA at excitatory synapses in the CA1 region of the hippocampus, and the number of NMDA receptors in individual synapses shows very little variability (Petralia et al. 1994b; Racca et al. 2000). The number of NMDA receptors activated by synaptic stimulation is small, only 1–5 NMDA

Table 4 Kinetic properties of Schaffer collateral inputs terminating on proximal and distal dendrites of CA1 pyramidal cells

Quantal parameters				
	Release probability	<0.5		Enoki et al. (2009)
	Quantal amplitude	~3 pA, 66–400 μV		Enoki et al. (2009)
AMPA receptors		**Soma**	**Dendrite**	
	EPSP amplitude (locally)	~0.2 mV	~0.6 mV	Larkman et al. (1997)
	EPSC amplitude (locally)	~8 pA	~24 pA	Magee and Cook (2000)
	EPSC amplitude (measured at the soma)	~0.2 mV	~0.2 mV	Magee and Cook (2000)
	20–80% rise time	0.4–0.6 ms	0.4–0.6 ms	Andrasfalvy and Magee (2001)
	10–90% rise time	0.7–3.5 ms	0.7 ms	Larkman et al. (1997)
	Decay time const.	~ 3.5 ms	~ 2.5 ms	Andrasfalvy and Magee (2001)]
	Maximum open probability	~0.8	~0.8	Andrasfalvy and Magee (2001)
	Channel number (calculated using variance-mean analysis)	~450	~1000	Andrasfalvy and Magee (2001)
	Latency	2–3 ms		Larkman et al. (1997)
	Single-channel conductance (γ)	~8–10 pS	10 pS	Andrasfalvy and Magee (2001)
NMDA				
	EPSC amplitude (excised patches, 10 ms, 1 m mGlu)	~70 pA	~ 50 pA	Andrasfalvy and Magee (2001)
	20–80% rise time	~9 ms	~9 ms	Andrasfalvy and Magee 2001)
	Decay time constant tau 1	~250 ms	~250 ms	Andrasfalvy and Magee (2001)
	Decay time constant tau 2	~1.5 sec	~1.5 sec	Andrasfalvy and Magee (2001)
	Single-channel conductance	45 pS		Spruston et al. (1995)

channels open during synaptic transmission at low frequencies, and this value is small enough to render quantal dendritic NMDA responses undetectable at the soma through physiological measurements (Nimchinsky et al. 2004). In contrast to AMPA receptors, the number of NMDA receptors expressed at synapses does not show activity-dependent changes.

Furthermore, dendritic NMDA current amplitudes do not change with distance from the soma, and their kinetics and quantal parameters are very similar in proximal and distal dendrites (Andrasfalvy and Magee 2001) (Table 4).

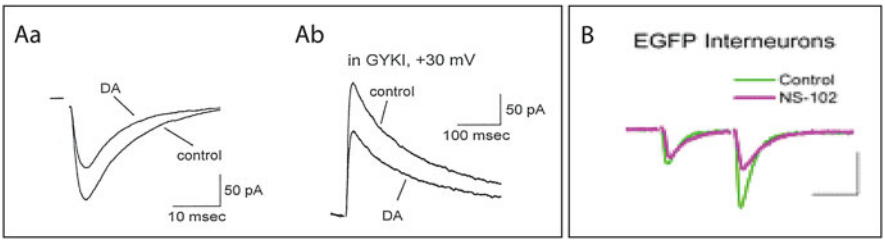

Fig. 6 Kainate responses in the CA1 area of the hippocampus. Kainate activation depresses AMPA (Aa) and NMDA (Ab) (Frerking et al. 2001) receptor-mediated events at the Schaffer collateral synapses. Kainate receptor-specific antagonist reduces facilitation at inputs onto somatostatin-positive interneurons (Sun and Dobrunz 2006)

Kainate Receptors

Kainate receptor activation in the CA1 region leads to the depression of glutamatergic transmission (Chittajallu et al. 1996; Frerking et al. 2001; Kamiya et al. 1996; Vignes et al. 1998). Several mechanisms were suggested to explain this effect: direct action via presynaptic receptors, indirect action via somatodendritic kainate receptors, and also both ionotropic and metabotropic modes of action were postulated. Kainate agonist depresses glutamatergic transmission via a decrease in quantal content; in agreement with this finding, little or no evidence of postsynaptic modulation was observed. Rather, the experimental data indicate that kainate receptors are directly activated on the presynaptic terminal and are coupled to G-proteins (Frerking et al. 2001).

Beside the direct action on pyramidal cells, kainate receptors are also involved in the modulation of network activity via the regulation of inhibitory neurons and their synaptic inputs. Dendritic kainate receptor activation results in the increased activity of inhibitory neurons which provide increased inhibitory input onto pyramidal cells. This postsynaptic effect is mediated by GluK1 subunit-containing receptors (Cossart et al. 1998). Excitatory input onto somatostatin-containing interneurons shows unusually robust short-term facilitation, and the activation of presynaptic kainate receptors contributes to this effect, enabling a target cell-specific mechanism leading to the preferential activation of a subset of interneurons following repeated stimuli (Sun and Dobrunz 2006) (Fig. 6). This effect is mediated by GluK1 and GluK2 subunit-containing, calcium-permeable kainate receptors (Sun et al. 2009). Finally, GABAergic neurotransmission is also regulated by presynaptic kainate receptors. This action mostly affects inhibitory connections between interneurons and may serve to enhance interneuron-interneuron interactions (Cossart et al. 2001).

Metabotropic Glutamate Receptors

Metabotropic receptors have diverse effects in the CA1 area of the hippocampus: they directly excite pyramidal cells (Gereau and Conn 1995) and interneurons

(McBain et al. 1994), they decrease excitatory and inhibitory synaptic transmission, and they influence long-term plasticity (Bortolotto et al. 1999). Direct excitation of pyramidal cells and interneurons is mainly mediated by Group I metabotropic receptors localized postsynaptically on the somato-dendritic membrane (Gereau and Conn 1995; McBain et al. 1994). In interneurons located in the stratum oriens/alveus, activation of mGluR1α leads to Ca^{2+} signals resulting from Ca^{2+} influx through transient potential channels and Ca^{2+} release from intracellular stores. Dendritic Ca^{2+} transients resulting from mGluR5 activation are solely mediated by intracellular Ca^{2+} release. Furthermore, long-term plasticity at oriens/alveus interneurons is influenced by mGluR1- and mGluR5-specific signaling (Le Vasseur et al. 2008; Topolnik et al. 2006).

Glutamate release is suppressed by Group I and Group III metabotropic receptors at Schaffer collateral synapses (Gereau and Conn 1995), while the selective Group II receptors antagonist DCG-IV does not have influence on excitatory neurotransmission (Kamiya et al. 1996). Both Group I and Group III metabotropic receptors are localized presynaptically as evidenced by the effect observed on mEPSC frequency and paired-pulse facilitation (Gereau and Conn 1995), but the two receptors are regulating glutamatergic neurotransmission through different mechanisms. Group II metabotropic receptors are only expressed in granule cells in the adult hippocampus (Tanabe et al. 1992; Tanabe et al. 1993); however activation of group II mGluRs was shown to influence glutamatergic transmission, and this effect is mediated by mGluR3 receptors expressed on glia cells (Winder et al. 1996).

The amplitude of GABA-mediated synaptic events is also reduced by group I mGluR agonist; however this effect can effectively be blocked by the pre-application of CB1 receptor antagonist indicating that mGluR1/5 receptors are not situated directly at the inhibitory presynaptic terminals (Neu et al. 2007). Group III mGluRs are known to present at GABAergic presynaptic terminals (Shigemoto et al. 1997), and activation of these receptors leads to decreased inhibitory transmission among GABAergic cells. These receptors are likely to sense glutamate spillover from neighboring excitatory afferent terminals (Semyanov and Kullmann 2000).

Experimental Techniques

The key techniques used for the investigation of glutamatergic signals are intracellular and patch-clamp recordings. These experimental approaches are described in detail in Chapter X (Marco Martina). Synaptic inputs are evoked with either electric or osmotic stimuli. Alternatively, glutamate can be applied to the tissue by either bath application or focal pressure injection. A more precise approach is the recently developed technique using glutamate uncaging. With the latter approach, synapses on a specific subcellular element can selectively be activated (i.e., dendrite vs. soma). Activation of selected subpopulation of synapses or limited number of synapses can be challenging in in vitro slices, given the complex network connections in the tissue. Under these circumstances, paired recordings can be

used to identify synaptic contacts between individual cells where both the pre- and postsynaptic element can be anatomically identified. Recordings from synaptically connected neuron pairs are harder when the pre- and postsynaptic cells are relatively far away from each other, as the probability of functional connections decreases with distance. In these cases, direct stimulation of presynaptic terminals could provide information about individual synaptic contacts. This is only possible when the presynaptic terminal is large, like the mossy fiber boutons. Optogenetic approaches in combination with two-photon imaging allow the simultaneous activation and imaging of small groups of synapses; however the activation of single synapses with optogenetic tools still remains challenging.

The Future

Recent developments in optogenetics and high-resolution imaging have opened the window to functional questions that are very specific to a group of neurons or receptors and to the combination of these two. With these developments in imaging and genetic techniques, synaptic inputs onto specific subset of cells can be studied in isolation, and target cell specificity of various inputs established. We will see large body of data generated on cell-type and receptor subunit-specific signaling. In addition, using live imaging with high temporal and spatial resolution allows the simultaneous investigation of large population of cells. All this information will require modeling strategies to help better understand the role of a certain type of synapse in network activity and in the control of input/output properties of large population of neurons.

References

Acsády L, Kamondi A, Sík A, Freund T, Buzsáki G (1998) GABAergic cells are the major postsynaptic targets of mossy fibers in the rat hippocampus. J Neurosci 18(9):3386–3403

Adesnik H, Nicoll RA, England PM (2005) Photoinactivation of native AMPA receptors reveals their real-time trafficking. Neuron 48(6):977–985

Aksoy-Aksel A, Manahan-Vaughan D (2015) Synaptic strength at the temporoammonic input to the hippocampal CA1 region in vivo is regulated by NMDA receptors, metabotropic glutamate receptors and voltage-gated calcium channels. Neuroscience 309:191–199

Amaral DG, Dent JA (1981) Development of the mossy fibers of the dentate gyrus: I. A light and electron microscopic study of the mossy fibers and their expansions. J Comp Neurol 195(1):51–86

Amaral DG, Witter MP (1989) The three-dimensional organization of the hippocampal formation: a review of anatomical data. Neuroscience 31(3):571–591

Amaral DG, Ishizuka N, Claiborne B (1990) Neurons, numbers and the hippocampal network. Prog Brain Res 83:1–11

Andrasfalvy BK, Magee JC (2001) Distance-dependent increase in AMPA receptor number in the dendrites of adult hippocampal CA1 pyramidal neurons. J Neurosci 21(23):9151–9159

Arrigoni E, Greene RW (2004) Schaffer collateral and perforant path inputs activate different subtypes of NMDA receptors on the same CA1 pyramidal cell. Br J Pharmacol 142(2):317–322

Barberis A, Sachidhanandam S, Mulle C (2008) GluR6/KA2 kainate receptors mediate slow-deactivating currents. J Neurosci 28(25):6402–6406

Berzhanskaya J, Urban NN, Barrionuevo G (1998) Electrophysiological and pharmacological characterization of the direct perforant path input to hippocampal area CA3. J Neurophysiol 79(4):2111–2118

Bischofberger J, Geiger JR, Jonas P (2002) Timing and efficacy of Ca2+ channel activation in hippocampal mossy fiber boutons. J Neurosci 22(24):10593–10602

Blaschke M, Keller BU, Rivosecchi R, Hollmann M, Heinemann S, Konnerth A (1993) A single amino acid determines the subunit-specific spider toxin block of alpha-amino-3-hydroxy-5-methylisoxazole-4-propionate/kainate receptor channels. Proc Natl Acad Sci U S A 90(14):6528–6532

Bortolotto ZA, Fitzjohn SM, Collingridge GL (1999) Roles of metabotropic glutamate receptors in LTP and LTD in the hippocampus. Curr Opin Neurobiol 9(3):299–304

Bowie D, Mayer ML (1995) Inward rectification of both AMPA and kainate subtype glutamate receptors generated by polyamine-mediated ion channel block. Neuron 15(2):453–462

Breustedt J, Schmitz D (2004) Assessing the role of GLUK5 and GLUK6 at hippocampal mossy fiber synapses. J Neurosci 24(45):10093–10098

Calixto E, Galván EJ, Card JP, Barrionuevo G (2008) Coincidence detection of convergent perforant path and mossy fibre inputs by CA3 interneurons. J Physiol 586(11):2695–2712

Capogna M (2004) Distinct properties of presynaptic group II and III metabotropic glutamate receptor-mediated inhibition of perforant pathway-CA1 EPSCs. Eur J Neurosci 19(10):2847–2858

Castillo PE, Malenka RC, Nicoll RA (1997) Kainate receptors mediate a slow postsynaptic current in hippocampal CA3 neurons. Nature 388(6638):182–186

Chamberlain SE, Sadowski JH, Teles-Grilo Ruivo LM, Atherton LA, Mellor JR (2013) Long-term depression of synaptic kainate receptors reduces excitability by relieving inhibition of the slow afterhyperpolarization. J Neurosci 33(22):9536–9545

Chamberland S, Evstratova A, Tóth K (2014) Interplay between synchronization of multivesicular release and recruitment of additional release sites support short-term facilitation at hippocampal mossy fiber to CA3 pyramidal cells synapses. J Neurosci 34(33):11032–11047

Chamberland S, Evstratova A, Tóth K (2017) Short-term facilitation at a detonator synapse requires the distinct contribution of multiple types of voltage-gated calcium channels. J Neurosci 37(19):4913–4927

Chicurel ME, Harris KM (1992) Three-dimensional analysis of the structure and composition of CA3 branched dendritic spines and their synaptic relationships with mossy fiber boutons in the rat hippocampus. J Comp Neurol 325(2):169–182

Chittajallu R, Vignes M, Dev KK, Barnes JM, Collingridge GL, Henley JM (1996) Regulation of glutamate release by presynaptic kainate receptors in the hippocampus. Nature 379(6560):78–81

Chiu CQ, Castillo PE (2008) Input-specific plasticity at excitatory synapses mediated by endocannabinoids in the dentate gyrus. Neuropharmacology 54(1):68–78

Cho CH, St-Gelais F, Zhang W, Tomita S, Howe JR (2007) Two families of TARP isoforms that have distinct effects on the kinetic properties of AMPA receptors and synaptic currents. Neuron 55(6):890–904

Colbert CM, Levy WB (1992) Electrophysiological and pharmacological characterization of perforant path synapses in CA1: mediation by glutamate receptors. J Neurophysiol 68(1):1–8

Contractor A, Swanson G, Heinemann SF (2001) Kainate receptors are involved in short- and long-term plasticity at mossy fiber synapses in the hippocampus. Neuron 29(1):209–216

Contractor A, Sailer AW, Darstein M, Maron C, Xu J, Swanson GT et al (2003) Loss of kainate receptor-mediated heterosynaptic facilitation of mossy-fiber synapses in KA2−/− mice. J Neurosci 23(2):422–429

Coombs ID, Soto D, Zonouzi M, Renzi M, Shelley C, Farrant M et al (2012) Cornichons modify channel properties of recombinant and glial AMPA receptors. J Neurosci 32(29):9796–9804

Cossart R, Esclapez M, Hirsch JC, Bernard C, Ben-Ari Y (1998) GluR5 kainate receptor activation in interneurons increases tonic inhibition of pyramidal cells. Nat Neurosci 1(6):470–478

Cossart R, Tyzio R, Dinocourt C, Esclapez M, Hirsch JC, Ben-Ari Y et al (2001) Presynaptic kainate receptors that enhance the release of GABA on CA1 hippocampal interneurons. Neuron 29(2):497–508

Cossart R, Epsztein J, Tyzio R, Becq H, Hirsch J, Ben-Ari Y et al (2002) Quantal release of glutamate generates pure kainate and mixed AMPA/kainate EPSCs in hippocampal neurons. Neuron 35(1):147–159

Dahl D, Sarvey JM (1989) Norepinephrine induces pathway-specific long-lasting potentiation and depression in the hippocampal dentate gyrus. Proc Natl Acad Sci U S A 86(12):4776–4780

Darstein M, Petralia RS, Swanson GT, Wenthold RJ, Heinemann SF (2003) Distribution of kainate receptor subunits at hippocampal mossy fiber synapses. J Neurosci 23(22):8013–8019

Dingledine R, Borges K, Bowie D, Traynelis SF (1999) The glutamate receptor ion channels. Pharmacol Rev 51(1):7–61

Donevan SD, Rogawski MA (1995) Intracellular polyamines mediate inward rectification of ca(2+)-permeable alpha-amino-3-hydroxy-5-methyl-4-isoxazolepropionic acid receptors. Proc Natl Acad Sci U S A 92(20):9298–9302

Durand GM, Kovalchuk Y, Konnerth A (1996) Long-term potentiation and functional synapse induction in developing hippocampus. Nature 381(6577):71–75

Empson RM, Heinemann U (1995a) Perforant path connections to area CA1 are predominantly inhibitory in the rat hippocampal-entorhinal cortex combined slice preparation. Hippocampus 5(2):104–107

Empson RM, Heinemann U (1995b) The perforant path projection to hippocampal area CA1 in the rat hippocampal-entorhinal cortex combined slice. J Physiol 484(Pt 3):707–720

Enoki R, Hu YL, Hamilton D, Fine A (2009) Expression of long-term plasticity at individual synapses in hippocampus is graded, bidirectional, and mainly presynaptic: optical quantal analysis. Neuron 62(2):242–253

Farrow P, Khodosevich K, Sapir Y, Schulmann A, Aslam M, Stern-Bach Y et al (2015) Auxiliary subunits of the CKAMP family differentially modulate AMPA receptor properties. elife 4:e09693

Frerking M, Ohliger-Frerking P (2002) AMPA receptors and kainate receptors encode different features of afferent activity. J Neurosci 22(17):7434–7443

Frerking M, Schmitz D, Zhou Q, Johansen J, Nicoll RA (2001) Kainate receptors depress excitatory synaptic transmission at CA3–>CA1 synapses in the hippocampus via a direct presynaptic action. J Neurosci 21(9):2958–2966

Geiger JR, Jonas P (2000) Dynamic control of presynaptic Ca(2+) inflow by fast-inactivating K(+) channels in hippocampal mossy fiber boutons. Neuron 28(3):927–939

Geiger JR, Melcher T, Koh DS, Sakmann B, Seeburg PH, Jonas P et al (1995) Relative abundance of subunit mRNAs determines gating and Ca2+ permeability of AMPA receptors in principal neurons and interneurons in rat CNS. Neuron 15(1):193–204

Geiger JR, Lübke J, Roth A, Frotscher M, Jonas P (1997) Submillisecond AMPA receptor-mediated signaling at a principal neuron-interneuron synapse. Neuron 18(6):1009–1023

Gereau RW, Conn PJ (1995) Multiple presynaptic metabotropic glutamate receptors modulate excitatory and inhibitory synaptic transmission in hippocampal area CA1. J Neurosci 15(10):6879–6889

Hallermann S, Pawlu C, Jonas P, Heckmann M (2003) A large pool of releasable vesicles in a cortical glutamatergic synapse. Proc Natl Acad Sci U S A 100(15):8975–8980

Han ZS, Buhl EH, Lörinczi Z, Somogyi P (1993) A high degree of spatial selectivity in the axonal and dendritic domains of physiologically identified local-circuit neurons in the dentate gyrus of the rat hippocampus. Eur J Neurosci 5:395–410

Harris KM, Sultan P (1995) Variation in the number, location and size of synaptic vesicles provides an anatomical basis for the nonuniform probability of release at hippocampal CA1 synapses. Neuropharmacology 34(11):1387–1395

Hayashi Y, Shi SH, Esteban JA, Piccini A, Poncer JC, Malinow R (2000) Driving AMPA receptors into synapses by LTP and CaMKII: requirement for GluR1 and PDZ domain interaction. Science 287(5461):2262–2267

Henze DA, Card JP, Barrionuevo G, Ben-Ari Y (1997) Large amplitude miniature excitatory postsynaptic currents in hippocampal CA3 pyramidal neurons are of mossy fiber origin. J Neurophysiol 77(3):1075–1086

Henze DA, McMahon DB, Harris KM, Barrionuevo G (2002a) Giant miniature EPSCs at the hippocampal mossy fiber to CA3 pyramidal cell synapse are monoquantal. J Neurophysiol 87(1):15–29

Henze DA, Wittner L, Buzsáki G (2002b) Single granule cells reliably discharge targets in the hippocampal CA3 network in vivo. Nat Neurosci 5(8):790–795

Heuss C, Scanziani M, Gähwiler BH, Gerber U (1999) G-protein-independent signaling mediated by metabotropic glutamate receptors. Nat Neurosci 2(12):1070–1077

Ho MT, Pelkey KA, Topolnik L, Petralia RS, Takamiya K, Xia J et al (2007) Developmental expression of Ca2+−permeable AMPA receptors underlies depolarization-induced long-term depression at mossy fiber CA3 pyramid synapses. J Neurosci 27(43):11651–11662

Isaac JT, Ashby MC, McBain CJ (2007) The role of the GluR2 subunit in AMPA receptor function and synaptic plasticity. Neuron 54(6):859–871

Ito K, Contractor A, Swanson GT (2004) Attenuated plasticity of postsynaptic kainate receptors in hippocampal CA3 pyramidal neurons. J Neurosci 24(27):6228–6236

Jackson AC, Nicoll RA (2011) The expanding social network of ionotropic glutamate receptors: TARPs and other transmembrane auxiliary subunits. Neuron 70(2):178–199

Jackson AC, Milstein AD, Soto D, Farrant M, Cull-Candy SG, Nicoll RA (2011) Probing TARP modulation of AMPA receptor conductance with polyamine toxins. J Neurosci 31(20):7511–7520

Jarsky T, Roxin A, Kath WL, Spruston N (2005) Conditional dendritic spike propagation following distal synaptic activation of hippocampal CA1 pyramidal neurons. Nat Neurosci 8(12):1667–1676

Jonas P, Major G, Sakmann B (1993) Quantal components of unitary EPSCs at the mossy fibre synapse on CA3 pyramidal cells of rat hippocampus. J Physiol 472:615–663

Jonas P, Racca C, Sakmann B, Seeburg PH, Monyer H (1994) Differences in Ca2+ permeability of AMPA-type glutamate receptor channels in neocortical neurons caused by differential GluR-B subunit expression. Neuron 12(6):1281–1289

Kahle JS, Cotman CW (1989) Carbachol depresses synaptic responses in the medial but not the lateral perforant path. Brain Res 482(1):159–163

Kamboj SK, Swanson GT, Cull-Candy SG (1995) Intracellular spermine confers rectification on rat calcium-permeable AMPA and kainate receptors. J Physiol 486(Pt 2):297–303

Kamiya H, Shinozaki H, Yamamoto C (1996) Activation of metabotropic glutamate receptor type 2/3 suppresses transmission at rat hippocampal mossy fibre synapses. J Physiol 493(Pt 2):447–455

Kilbride J, Rush AM, Rowan MJ, Anwyl R (2001) Presynaptic group II mGluR inhibition of short-term depression in the medial perforant path of the dentate gyrus in vitro. J Neurophysiol 85(6):2509–2515

Koh DS, Burnashev N, Jonas P (1995) Block of native Ca(2+)-permeable AMPA receptors in rat brain by intracellular polyamines generates double rectification. J Physiol 486(Pt 2):305–312

Kullmann DM (1994) Amplitude fluctuations of dual-component EPSCs in hippocampal pyramidal cells: implications for long-term potentiation. Neuron 12(5):1111–1120

Kwon HB, Castillo PE (2008a) Role of glutamate autoreceptors at hippocampal mossy fiber synapses. Neuron 60(6):1082–1094

Kwon HB, Castillo PE (2008b) Long-term potentiation selectively expressed by NMDA receptors at hippocampal mossy fiber synapses. Neuron 57(1):108–120

Lambert JD, Jones RS (1989) Activation of N-methyl-D-aspartate receptors contributes to the EPSP at perforant path synapses in the rat dentate gyrus in vitro. Neurosci Lett 97(3):323–328

Lambert JD, Jones RS (1990) A reevaluation of excitatory amino acid-mediated synaptic transmission in rat dentate gyrus. J Neurophysiol 64(1):119–132
Larkman AU, Jack JJ, Stratford KJ (1997) Quantal analysis of excitatory synapses in rat hippocampal CA1 in vitro during low-frequency depression. J Physiol 505(Pt 2):457–471
Lauri SE, Bortolotto ZA, Bleakman D, Ornstein PL, Lodge D, Isaac JT et al (2001) A critical role of a facilitatory presynaptic kainate receptor in mossy fiber LTP. Neuron 32(4):697–709
Lawrence JJ, Grinspan ZM, McBain CJ (2004) Quantal transmission at mossy fibre targets in the CA3 region of the rat hippocampus. J Physiol 554(Pt 1):175–193
Le Vasseur M, Ran I, Lacaille JC (2008) Selective induction of metabotropic glutamate receptor 1- and metabotropic glutamate receptor 5-dependent chemical long-term potentiation at oriens/alveus interneuron synapses of mouse hippocampus. Neuroscience 151(1):28–42
Lei S, McBain CJ (2002) Distinct NMDA receptors provide differential modes of transmission at mossy fiber-interneuron synapses. Neuron 33(6):921–933
Li XG, Somogyi P, Ylinen A, Buzsáki G (1994) The hippocampal CA3 network: an in vivo intracellular labeling study. J Comp Neurol 339(2):181–208
Liao D, Hessler NA, Malinow R (1995) Activation of postsynaptically silent synapses during pairing-induced LTP in CA1 region of hippocampal slice. Nature 375(6530):400–404
Macek TA, Winder DG, Gereau RW, Ladd CO, Conn PJ (1996) Differential involvement of group II and group III mGluRs as autoreceptors at lateral and medial perforant path synapses. J Neurophysiol 76(6):3798–3806
Magee JC, Cook EP (2000) Somatic EPSP amplitude is independent of synapse location in hippocampal pyramidal neurons. Nat Neurosci 3(9):895–903
Masurkar AV, Srinivas KV, Brann DH, Warren R, Lowes DC, Siegelbaum SA (2017) Medial and lateral entorhinal cortex differentially excite deep versus superficial CA1 pyramidal neurons. Cell Rep 18(1):148–160
McBain CJ, Dingledine R (1993) Heterogeneity of synaptic glutamate receptors on CA3 stratum radiatum interneurones of rat hippocampus. J Physiol 462:373–392
McBain CJ, DiChiara TJ, Kauer JA (1994) Activation of metabotropic glutamate receptors differentially affects two classes of hippocampal interneurons and potentiates excitatory synaptic transmission. J Neurosci 14(7):4433–4445
McHugh TJ, Jones MW, Quinn JJ, Balthasar N, Coppari R, Elmquist JK et al (2007) Dentate gyrus NMDA receptors mediate rapid pattern separation in the hippocampal network. Science 317(5834):94–99
McNaughton BL (1980) Evidence for two physiologically distinct perforant pathways to the fascia dentata. Brain Res 199(1):1–19
Megías M, Emri Z, Freund TF, Gulyás AI (2001) Total number and distribution of inhibitory and excitatory synapses on hippocampal CA1 pyramidal cells. Neuroscience 102(3):527–540
Milstein AD, Zhou W, Karimzadegan S, Bredt DS, Nicoll RA (2007) TARP subtypes differentially and dose-dependently control synaptic AMPA receptor gating. Neuron 55(6):905–918
Min MY, Asztely F, Kokaia M, Kullmann DM (1998) Long-term potentiation and dual-component quantal signaling in the dentate gyrus. Proc Natl Acad Sci U S A 95(8):4702–4707
Mulle C, Sailer A, Pérez-Otaño I, Dickinson-Anson H, Castillo PE, Bureau I et al (1998) Altered synaptic physiology and reduced susceptibility to kainate-induced seizures in GluR6-deficient mice. Nature 392(6676):601–605
Neu A, Földy C, Soltesz I (2007) Postsynaptic origin of CB1-dependent tonic inhibition of GABA release at cholecystokinin-positive basket cell to pyramidal cell synapses in the CA1 region of the rat hippocampus. J Physiol 578(Pt 1):233–247
Nimchinsky EA, Yasuda R, Oertner TG, Svoboda K (2004) The number of glutamate receptors opened by synaptic stimulation in single hippocampal spines. J Neurosci 24(8):2054–2064
O'Connor V, El Far O, Bofill-Cardona E, Nanoff C, Freissmuth M, Karschin A et al (1999) Calmodulin dependence of presynaptic metabotropic glutamate receptor signaling. Science 286(5442):1180–1184
Oertner TG, Sabatini BL, Nimchinsky EA, Svoboda K (2002) Facilitation at single synapses probed with optical quantal analysis. Nat Neurosci 5(7):657–664

Otmakhova NA, Otmakhov N, Lisman JE (2002) Pathway-specific properties of AMPA and NMDA-mediated transmission in CA1 hippocampal pyramidal cells. J Neurosci 22(4):1199–1207

Pelkey KA, Lavezzari G, Racca C, Roche KW, McBain CJ (2005) mGluR7 is a metaplastic switch controlling bidirectional plasticity of feedforward inhibition. Neuron 46(1):89–102

Pelkey KA, Yuan X, Lavezzari G, Roche KW, McBain CJ (2007) mGluR7 undergoes rapid internalization in response to activation by the allosteric agonist AMN082. Neuropharmacology 52(1):108–117

Pelletier MR, Kirkby RD, Jones SJ, Corcoran ME (1994) Pathway specificity of noradrenergic plasticity in the dentate gyrus. Hippocampus 4(2):181–188

Petralia RS, Yokotani N, Wenthold RJ (1994) Light and electron microscope distribution of the NMDA receptor subunit NMDAR1 in the rat nervous system using a selective anti-peptide antibody. J Neurosci 14(2):667–696

Petralia RS, Wang YX, Wenthold RJ (1994a) Histological and ultrastructural localization of the kainate receptor subunits, KA2 and GluR6/7, in the rat nervous system using selective antipeptide antibodies. J Comp Neurol 349(1):85–110

Petralia RS, Wang YX, Wenthold RJ (1994b) The NMDA receptor subunits NR2A and NR2B show histological and ultrastructural localization patterns similar to those of NR1. J Neurosci 14(10):6102–6120

Pinheiro PS, Perrais D, Coussen F, Barhanin J, Bettler B, Mann JR et al (2007) GluR7 is an essential subunit of presynaptic kainate autoreceptors at hippocampal mossy fiber synapses. Proc Natl Acad Sci U S A 104(29):12181–12186

Pinheiro PS, Lanore F, Veran J, Artinian J, Blanchet C, Crépel V et al (2013) Selective block of postsynaptic kainate receptors reveals their function at hippocampal mossy fiber synapses. Cereb Cortex 23(2):323–331

Price CJ, Karayannis T, Pál BZ, Capogna M (2005) Group II and III mGluRs-mediated presynaptic inhibition of EPSCs recorded from hippocampal interneurons of CA1 stratum lacunosum moleculare. Neuropharmacology 49(Suppl 1):45–56

Racca C, Stephenson FA, Streit P, Roberts JD, Somogyi P (2000) NMDA receptor content of synapses in stratum radiatum of the hippocampal CA1 area. J Neurosci 20(7):2512–2522

Reagh ZM, Yassa MA (2014) Object and spatial mnemonic interference differentially engage lateral and medial entorhinal cortex in humans. Proc Natl Acad Sci U S A 111(40):E4264–E4273

Rebola N, Sachidhanandam S, Perrais D, Cunha RA, Mulle C (2007) Short-term plasticity of kainate receptor-mediated EPSCs induced by NMDA receptors at hippocampal mossy fiber synapses. J Neurosci 27(15):3987–3993

Remondes M, Schuman EM (2002) Direct cortical input modulates plasticity and spiking in CA1 pyramidal neurons. Nature 416(6882):736–740

Renner MC, Albers EH, Gutierrez-Castellanos N, Reinders NR, van Huijstee AN, Xiong H et al (2017) Synaptic plasticity through activation of GluA3-containing AMPA-receptors. elife 6

Rollenhagen A, Sätzler K, Rodríguez EP, Jonas P, Frotscher M, Lübke JH (2007) Structural determinants of transmission at large hippocampal mossy fiber synapses. J Neurosci 27(39):10434–10444

Rosenmund C, Clements JD, Westbrook GL (1993) Nonuniform probability of glutamate release at a hippocampal synapse. Science 262(5134):754–757

Ruiz A, Sachidhanandam S, Utvik JK, Coussen F, Mulle C (2005) Distinct subunits in heteromeric kainate receptors mediate ionotropic and metabotropic function at hippocampal mossy fiber synapses. J Neurosci 25(50):11710–11718

Rush AM, Kilbride J, Rowan MJ, Anwyl R (2002) Presynaptic group III mGluR modulation of short-term plasticity in the lateral perforant path of the dentate gyrus in vitro. Brain Res 952(1):38–43

Sachidhanandam S, Blanchet C, Jeantet Y, Cho YH, Mulle C (2009) Kainate receptors act as conditional amplifiers of spike transmission at hippocampal mossy fiber synapses. J Neurosci 29(15):5000–5008

Salin PA, Scanziani M, Malenka RC, Nicoll RA (1996) Distinct short-term plasticity at two excitatory synapses in the hippocampus. Proc Natl Acad Sci U S A 93(23):13304–13309

Sambandan S, Sauer JF, Vida I, Bartos M (2010) Associative plasticity at excitatory synapses facilitates recruitment of fast-spiking interneurons in the dentate gyrus. J Neurosci 30(35):11826–11837

Scanziani M, Salin PA, Vogt KE, Malenka RC, Nicoll RA (1997) Use-dependent increases in glutamate concentration activate presynaptic metabotropic glutamate receptors. Nature 385(6617):630–634

Schikorski T, Stevens CF (1997) Quantitative ultrastructural analysis of hippocampal excitatory synapses. J Neurosci 17(15):5858–5867

Schmitz D, Frerking M, Nicoll RA (2000) Synaptic activation of presynaptic kainate receptors on hippocampal mossy fiber synapses. Neuron 27(2):327–338

Schmitz D, Mellor J, Nicoll RA (2001) Presynaptic kainate receptor mediation of frequency facilitation at hippocampal mossy fiber synapses. Science 291(5510):1972–1976

Schmitz D, Mellor J, Breustedt J, Nicoll RA (2003) Presynaptic kainate receptors impart an associative property to hippocampal mossy fiber long-term potentiation. Nat Neurosci 6(10):1058–1063

Schwenk J, Harmel N, Zolles G, Bildl W, Kulik A, Heimrich B et al (2009) Functional proteomics identify cornichon proteins as auxiliary subunits of AMPA receptors. Science 323(5919):1313–1319

Schwenk J, Harmel N, Brechet A, Zolles G, Berkefeld H, Müller CS et al (2012) High-resolution proteomics unravel architecture and molecular diversity of native AMPA receptor complexes. Neuron 74(4):621–633

Semyanov A, Kullmann DM (2000) Modulation of GABAergic signaling among interneurons by metabotropic glutamate receptors. Neuron 25(3):663–672

Shi Y, Suh YH, Milstein AD, Isozaki K, Schmid SM, Roche KW et al (2010) Functional comparison of the effects of TARPs and cornichons on AMPA receptor trafficking and gating. Proc Natl Acad Sci U S A 107(37):16315–16319

Shigemoto R, Kinoshita A, Wada E, Nomura S, Ohishi H, Takada M et al (1997) Differential presynaptic localization of metabotropic glutamate receptor subtypes in the rat hippocampus. J Neurosci 17(19):7503–7522

Smith MA, Ellis-Davies GC, Magee JC (2003) Mechanism of the distance-dependent scaling of Schaffer collateral synapses in rat CA1 pyramidal neurons. J Physiol 548(Pt 1):245–258

Soto D, Coombs ID, Renzi M, Zonouzi M, Farrant M, Cull-Candy SG (2009) Selective regulation of long-form calcium-permeable AMPA receptors by an atypical TARP, gamma-5. Nat Neurosci 12(3):277–285

Spruston N, Jonas P, Sakmann B (1995) Dendritic glutamate receptor channels in rat hippocampal CA3 and CA1 pyramidal neurons. J Physiol 482(Pt 2):325–352

Straub C, Hunt DL, Yamasaki M, Kim KS, Watanabe M, Castillo PE et al (2011) Distinct functions of kainate receptors in the brain are determined by the auxiliary subunit Neto1. Nat Neurosci 14(7):866–873

Sun HY, Dobrunz LE (2006) Presynaptic kainate receptor activation is a novel mechanism for target cell-specific short-term facilitation at Schaffer collateral synapses. J Neurosci 26(42):10796–10807

Sun HY, Bartley AF, Dobrunz LE (2009) Calcium-permeable presynaptic kainate receptors involved in excitatory short-term facilitation onto somatostatin interneurons during natural stimulus patterns. J Neurophysiol 101(2):1043–1055

Szabadics J, Soltesz I (2009) Functional specificity of mossy fiber innervation of GABAergic cells in the hippocampus. J Neurosci 29(13):4239–4251

Takumi Y, Ramírez-León V, Laake P, Rinvik E, Ottersen OP (1999) Different modes of expression of AMPA and NMDA receptors in hippocampal synapses. Nat Neurosci 2(7):618–624

Tanabe Y, Masu M, Ishii T, Shigemoto R, Nakanishi S (1992) A family of metabotropic glutamate receptors. Neuron 8(1):169–179

Tanabe Y, Nomura A, Masu M, Shigemoto R, Mizuno N, Nakanishi S (1993) Signal transduction, pharmacological properties, and expression patterns of two rat metabotropic glutamate receptors, mGluR3 and mGluR4. J Neurosci 13(4):1372–1378

Tang M, Pelkey KA, Ng D, Ivakine E, McBain CJ, Salter MW et al (2011) Neto1 is an auxiliary subunit of native synaptic kainate receptors. J Neurosci 31(27):10009–10018

Tomita S, Adesnik H, Sekiguchi M, Zhang W, Wada K, Howe JR et al (2005) Stargazin modulates AMPA receptor gating and trafficking by distinct domains. Nature 435(7045):1052–1058

Topolnik L, Azzi M, Morin F, Kougioumoutzakis A, Lacaille JC (2006) mGluR1/5 subtype-specific calcium signalling and induction of long-term potentiation in rat hippocampal oriens/alveus interneurones. J Physiol 575(Pt 1):115–131

Tóth K, McBain CJ (1998) Afferent-specific innervation of two distinct AMPA receptor subtypes on single hippocampal interneurons. Nat Neurosci 1(7):572–578

Tóth K, McBain CJ (2000) Target-specific expression of pre- and postsynaptic mechanisms. J Physiol 525(Pt 1):41–51

Toth K, Suares G, Lawrence JJ, Philips-Tansey E, McBain CJ (2000) Differential mechanisms of transmission at three types of mossy fiber synapse. J Neurosci 20(22):8279–8289

Valenzuela-Harrington M, Gruart A, Delgado-García JM (2007) Contribution of NMDA receptor NR2B subunit to synaptic plasticity during associative learning in behaving rats. Eur J Neurosci 25(3):830–836

Vignes M, Clarke VR, Parry MJ, Bleakman D, Lodge D, Ornstein PL et al (1998) The GluR5 subtype of kainate receptor regulates excitatory synaptic transmission in areas CA1 and CA3 of the rat hippocampus. Neuropharmacology 37(10–11):1269–1277

von Kitzing E, Jonas P, Sakmann B (1994) Quantal analysis of excitatory postsynaptic currents at the hippocampal mossy fiber-CA3 pyramidal cell synapse. Adv Second Messenger Phosphoprotein Res 29:235–260

Walker HC, Lawrence JJ, McBain CJ (2002) Activation of kinetically distinct synaptic conductances on inhibitory interneurons by electrotonically overlapping afferents. Neuron 35(1):161–171

Wang W, Trieu BH, Palmer LC, Jia Y, Pham DT, Jung KM et al (2016) A primary cortical input to Hippocampus expresses a pathway-specific and endocannabinoid-dependent form of long-term potentiation. eNeuro 3(4)

Washburn MS, Dingledine R (1996) Block of alpha-amino-3-hydroxy-5-methyl-4-isoxazolepropionic acid (AMPA) receptors by polyamines and polyamine toxins. J Pharmacol Exp Ther 278(2):669–678

Watanabe M, Fukaya M, Sakimura K, Manabe T, Mishina M, Inoue Y (1998) Selective scarcity of NMDA receptor channel subunits in the stratum lucidum (mossy fibre-recipient layer) of the mouse hippocampal CA3 subfield. Eur J Neurosci 10(2):478–487

Wilson DI, Watanabe S, Milner H, Ainge JA (2013) Lateral entorhinal cortex is necessary for associative but not nonassociative recognition memory. Hippocampus 23(12):1280–1290

Winder DG, Ritch PS, Gereau RW, Conn PJ (1996) Novel glial-neuronal signalling by coactivation of metabotropic glutamate and beta-adrenergic receptors in rat hippocampus. J Physiol 494(Pt 3):743–755

Witter MP (1993) Organization of the entorhinal-hippocampal system: a review of current anatomical data. Hippocampus, 3 Spec No, 33–44

Wyeth MS, Pelkey KA, Petralia RS, Salter MW, McInnes RR, McBain CJ (2014) Neto auxiliary protein interactions regulate kainate and NMDA receptor subunit localization at mossy fiber-CA3 pyramidal cell synapses. J Neurosci 34(2):622–628

Yeckel MF, Kapur A, Johnston D (1999) Multiple forms of LTP in hippocampal CA3 neurons use a common postsynaptic mechanism. Nat Neurosci 2(7):625–633

Fast and Slow GABAergic Transmission in Hippocampal Circuits

Marlene Bartos, Jonas-Frederic Sauer, Imre Vida, and Ákos Kulik

Overview

Cortical neuronal networks consist of excitatory glutamatergic principal cells (PCs) and GABAergic inhibitory interneurons (INs). Although INs form a minority of the cortical neuron population, they control key aspects of cortical network function by providing feedforward and feedback inhibition, controlling the formation of PC assemblies, defining the excitability of neuronal networks and the timing of the activation of PCs, and promoting synchrony of fast neuronal network oscillations (Freund and Buzsáki 1996; McBain and Fisahn 2001; Klausberger and Somogyi 2008; Sohal 2016; Strüber et al. 2017). INs are highly diverse and can be subdivided into several types on the basis of various criteria, such as intrinsic physiological properties, neurochemical marker content, morphological features, including the laminar distribution of the axon, and finally the postsynaptic target profile of their output (Freund and Buzsáki 1996; Hosp et al. 2014; Savanthrapadian et al. 2014; Yuan et al. 2017). On the basis of synaptic targets, INs have been classified into two major groups, perisomatic- and dendrite-targeting cells.

Transmission at perisomatic GABAergic synapses is characterized by fast time course and large peak amplitudes (Bartos et al. 2001, 2002; Strüber et al. 2015). Fast $GABA_A$ receptor ($GABA_AR$)-mediated perisomatic inhibition can precisely

M. Bartos (✉) · J.-F. Sauer
Institute for Physiology I, Albert-Ludwigs University Freiburg, Freiburg, Germany
e-mail: marlene.bartos@physiologie.uni-freiburg.de

I. Vida
Institute for Integrative Neuroanatomy, Charité – Universitätsmedizin Berlin, Berlin, Germany
e-mail: imre.vida@charite.de

Á. Kulik
Institute for Physiology II, Albert-Ludwigs University Freiburg, Freiburg, Germany

V. Cutsuridis et al. (eds.), *Hippocampal Microcircuits*, Springer Series in Computational Neuroscience, https://doi.org/10.1007/978-3-319-99103-0_5

determine the timing and the frequency of action potential discharge in PCs (Cobb et al. 1995; Miles et al. 1996; Pouille and Scanziani 2001). In contrast, inhibitory signaling mediated by dendritic GABAergic contacts has slower time course and shows high degree of diversity (Pearce 1993; Miles et al. 1996; Vida et al. 1998; Banks et al. 1998; Szabadics et al. 2007; Savanthrapadian et al. 2014). The slower time course of dendritic inhibitory (DI) signals is partially due to electrotonic attenuation, when examined in somatic recordings; however, differences in the kinetics of the underlying conductance, as a consequence of differential $GABA_AR$ expression, are likely to contribute significantly. Dendritic inhibition plays a major role in regulating local linear or nonlinear integration of excitatory synaptic inputs, activation of dendritic voltage-gated conductances, synaptic plasticity, and dendritic spike generation (Miles et al. 1996; Makara et al. 2009; Müller et al. 2012). Indeed, recent in vivo examinations show that dendritic inhibition is involved in shaping the activity of hippocampal place cells important for spatial navigation (Royer et al. 2012) and certain forms of learning (Lovett-Barron et al. 2014).

In addition to $GABA_ARs$, metabotropic $GABA_BRs$ mediate a slower form of inhibition by synaptically released GABA (Solís and Nicoll 1992; Isaacson et al. 1993; Scanziani 2000; Booker et al. 2013, 2017b). Activation of $GABA_BRs$ generates a slow inhibitory postsynaptic potential (IPSP) postsynaptically and inhibits transmitter release from the axon terminals presynaptically. Finally, besides these forms of phasic inhibition, extrasynaptic GABA receptors mediate "tonic" inhibition (Nusser and Mody 2002; Scimemi et al. 2005; Glykys and Mody 2006). Tonic inhibition controls the excitability of the cell and the gain in the input-output relationship during synaptic excitation as a function of ambient GABA levels.

In this chapter we review characteristics of $GABA_AR$-mediated inhibitory transmission at perisomatic and dendritic synapses, as well as $GABA_BR$-mediated pre- and postsynaptic inhibition in hippocampal networks.

$GABA_AR$-Mediated Synaptic Inhibition in Hippocampal Circuits

$GABA_AR$-Mediated Perisomatic Inhibition

A major factor which determines the influence of a given IN on its target cell is the location of the synapses on the surface of the target cell. Inhibitory synapses located close to the soma have a large impact on the generation of action potentials at the output of neurons (Miles et al. 1996; Jonas et al. 2004). These synapses therefore can precisely control timing and frequency of action potentials. Consequently, soma-near "phasic" inhibition underlies important cortical network functions such as the synchronization of neuronal activity and the generation of neuronal network oscillations (Cobb et al. 1995; Pouille and Scanziani 2001; Mann et al. 2005; Mittmann et al. 2005; Vida et al. 2006; Doischer et al. 2008). The primary sources of perisomatic

inhibition are basket cells (BCs). These INs show characteristic physiological, pharmacological, and immunohistochemical properties (Freund and Buzsáki 1996; Freund 2003; see also chapter "Morphology of Hippocampal Neurons"). On the basis of the expression profile of Ca^{2+}-binding proteins and neuropeptides, two types of soma-inhibiting cells have been distinguished: parvalbumin (PV)- and cholecystokinin (CCK)-expressing cells (Freund and Buzsáki 1996; Hefft and Jonas 2005; Elgueta et al. 2015). Another IN type, the so-called chandelier or axo-axonic (AA) cells, innervate the axon initial segment of PCs (Somogyi et al. 1985; Soriano et al. 1990; Buhl et al. 1994, 1995), and therefore these INs are in an optimal position to control the initiation of action potentials in their postsynaptic targets. While BCs form synaptic contacts onto both pyramidal cells (PyCs) and other INs, including BCs (Bartos et al. 2001, 2002), AA cells selectively target PCs (Buhl et al. 1994, 1995). The contribution of PV-expressing INs (PV-INs) in neuronal network synchronization has been broadly accepted on the basis of single-unit recordings of PV-INs during spatial exploration demonstrating their strong phase relationship of individual action potentials to single gamma cycles in anesthetized (Tukker et al. 2007; Klausberger and Somogyi 2008) and freely moving rodents (Katona et al. 2014). Moreover, optogenetic approaches allowing light-mediated recruitment of PV-INs or their presynaptic PCs in cortical networks showed that gamma power increased upon PV-IN activation (Cardin et al. 2009; Sohal et al. 2009; Cardin 2016).

PV-BCs GABAergic transmission at PV-BC output synapses is characterized by rapid time course, large peak conductance, and high reliability of transmitter release (Fig. 1; Kraushaar and Jonas 2000; Bartos et al. 2001, 2002; Glickfeld and Scanziani 2006; Glickfeld et al. 2008; Savanthrapadian et al. 2014). Paired whole-cell patch-clamp recordings from presynaptic PV-expressing BCs and postsynaptic PCs in acute hippocampal slices revealed that the time course of unitary $GABA_A$R-mediated inhibitory postsynaptic currents (IPSCs) is extremely fast in all hippocampal areas. In dentate gyrus granule cells (GCs), the rise time (20–80%) is 0.2–0.3 ms, and decay time constant is 3.2–3.5 ms at near-physiological temperatures (Bartos et al. 2002; Table 1).

Highly specialized pre- and postsynaptic mechanisms underlie the rapid time course of unitary IPSCs at PV-BC output synapses. Presynaptically, GABA release is initiated by a brief and precisely timed Ca^{2+} transient. This is reflected by the highly synchronous time course of GABA release at BC-GC synapses (Hefft and Jonas 2005). The high level of synchrony is further realized by the tight coupling of the Ca^{2+} source (P/Q - type Ca^{2+} channels) and the sensor (Bucurenciu et al. 2008). Postsynaptically, fast inhibitory signaling at PV-BC synapses is largely mediated by α1 subunit-containing $GABA_A$Rs as revealed by postembedding immunogold-labeling studies (Nyíri et al. 2001; Klausberger et al. 2002). Analysis of recombinant $GABA_A$Rs showed that α1β1γ2 channels deactivate faster than α2β1γ2 channels (Lavoie et al. 1997). Consistent with these findings, bath application of the benzodiazepine type I receptor agonist zolpidem, which has a high affinity to $GABA_A$Rs containing the α1 subunit (Thomson et al. 2000; Cope et al. 2005), results in a

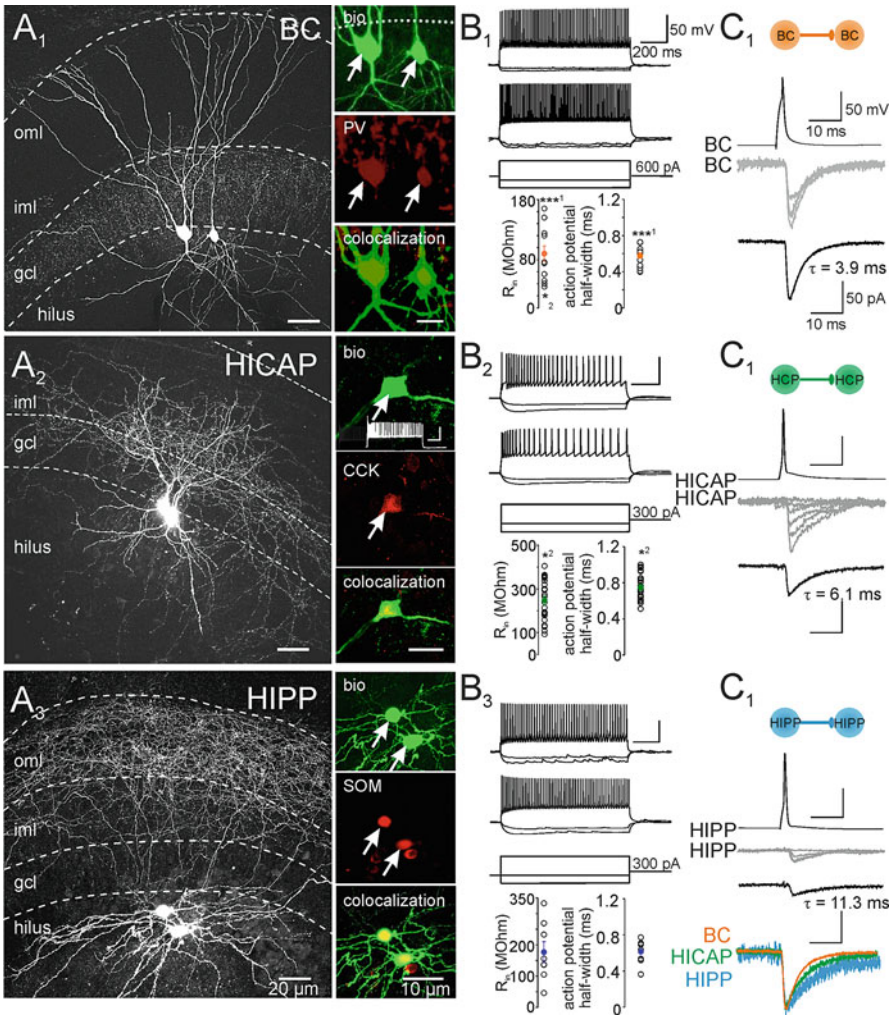

Fig. 1 Morphological, physiological, and synaptic characteristics of perisomatic and dendritic INs in rodent dentate gyrus. (**A**) *left*, confocal image stacks of pairs of synaptically connected GABAergic INs intracellularly labeled with biocytin and visualized with streptavidin conjugated with Alexa Fluor 647 (white labeling). (A_1) perisomatic INs with axon in the granule cell layer (gcl). *Right*, basket cells (BCs) are parvalbumin (PV)-positive as revealed by antibody labeling. From top to bottom, green, biocytin labeling, arrows point to both somata; red, PV expression; colocalization of both markers. (A_2) commissural-associational path cells (HICAPs) with axon collaterals mainly located in the inner molecular layer (iml). *Right*, a single intracellularly labeled HICAP identified as cholecystokinin (CCK)-positive. Inset, characteristic discharge pattern of the HICAP cell (0.7 nA, 1 s; scale bars, 200 ms, 50 mV). (A_3) hilar perforant path-associated cells (HIPPs) with axon located predominantly in the outer molecular layer (oml). *Right*, both neurons co-express somatostatin (SOM; arrows). (**B**) passive and active membrane properties of identified BCs (B_1), HICAPs (B_2), and HIPPs (B_3). Top traces in *B1–B3,* voltage trajectories of cell pairs shown in *A* (1 s, −100, −50, 300–800 pA). Summary graphs in B_1–B_3 show *left* the input resistance

marked prolongation of the decay time constant of PV-BCs IPSCs (Thomson et al. 2000; Doischer et al. 2008).

The peak amplitude of the inhibitory conductance at PV-BC output synapses shows considerable variability across hippocampal areas (Table 1). Nevertheless, peak amplitudes are generally high (up to 9.5 nS), which can be explained by the large number of synaptic contact sites between the coupled neurons. In the CA1 area, for example, the number of contacts per unitary connection is between 10 and 12 (Buhl et al. 1995). Consistent with the high number of contact sites, the failure rate of transmission is low (Hefft and Jonas 2005; Doischer et al. 2008; Table 1). The reliable transmission at BC output synapses is further supported by the high initial probability of transmitter release, estimated to be 0.79 in the dentate gyrus (Kraushaar and Jonas 2000).

BC synapses display differences in kinetic properties depending on the identity of the postsynaptic target (Bartos et al. 2001, 2002; Doischer et al. 2008). In particular, the decay time constant was found to be by a factor of ~2 faster in postsynaptic BCs than in PCs. The mean value of the decay time constant at BC-BC pairs in the dentate gyrus, CA1, and CA3 are 2.5, 1.7, and 1.2 ms, respectively (Bartos et al. 2001, 2002; Table 1). These target cell-specific differences in the hippocampus (Bartos et al. 2002; Glickfeld et al. 2008) could be explained by the expression of distinct postsynaptic $GABA_A$Rs. PV-BCs express α1 $GABA_A$R subunits at higher levels than PCs (Gao and Fritschy 1994; Fritschy and Möhler 1995; Klausberger et al. 2002). Interestingly, however, other parameters of the synapses, including the rise time, the peak amplitude of the inhibitory conductance, and the failure rate of synaptic transmission, show no differences between BC-BC and PV-BC-PC synapses (Bartos et al. 2001 2002; Table 1).

Previous paired recordings have been performed between two closely spaced neurons due to the high connectivity among closely spaced cells. Recent investigations, however, indicate that the amplitude and time course of perisomatic inhibition depends on the axonal distance between the pre- and postsynaptic neuron (Strüber et al. 2015, 2017). In particular in the dentate gyrus, PV-INs effectively control the activity of large neuron populations by their wide axonal arborization. Here, synaptic signals become weaker with axonal distance between presynaptic BC and its target GC due to lower contact numbers. The decay of uIPSCs also declines more slowly with distance, resulting from changes in $GABA_A$R subunit

Fig. 1 (continued) (R_{in}) of the recorded cell types and *right* the half duration of single action potentials. Each circle represents a single data point, and colored circles with lines represent mean values ± SEM. **C**, unitary IPSCs (uIPSCs) recorded at pairs shown in *A*. A presynaptic action potential (top) evokes uIPSCs in the postsynaptic cell. Single uIPSCs (6 traces) are shown superimposed (middle), and the average uIPSC (30 traces) at −70 mV is depicted below. Schematic illustration represents the recoded neuron types; In *C_3bottom*, average uIPSCs shown in *C1–C3* were peak normalized and superimposed. ***$p \leq 0.001$, **$p \leq 0.01$, * $p \leq 0.05$; 1, significantly different to HICAP; 2, different to HIPP. (Adapted from Savanthrapadian et al. 2014; with permission, © The Society for Neuroscience)

Table 1 Kinetic properties of perisomatic inhibition

Postsynaptic cell type	Rise time (ms)	Decay τ (ms)	Peak conductance (nS)	Failure rate (%)	Paired recording configuration	Publication
DG						
GC	0.2–0.3[a]/0.5[ad]	3.4–6.5/14–22[d]	2.0–6.8/1.7[cd]	<7		
	0.2 ± 0.03[a]	3.4 ± 0.4	2.0[c]	5.5 ± 4.0	PV+ BC-GC	Bartos et al. (2002)
		5.2			BC-GC	Bartos et al. (2001)
	0.26 ± 0.01[a]	6.5	6.8[c]	6.5 ± 1.0	BC-GC	Kraushaar and Jonas (2000)
	0.53 ± 0.04[ad]	20.0 ± 1.1[d]		0.5 ± 0.3[d]	BC-GC	Hefft and Jonas (2005)
		4.4 ± 0.5	3.7[c]	2 ± 2	BC-GC	Doischer et al. (2008)
	0.46 ± 0.03[ad]	13.6 ± 0.8[d]			Fast-spiking IN-GC	Liu et al. (2014)
GC	**0.87**	**20.1[d]**		**18.6[d]**		
	0.87 ± 0.08[d]	20.1 ± 0.8[d]		18.6 ± 6.3[d]	CCK-IN-GC	Hefft and Jonas (2005)
BC	**0.3–0.4[a]**	**2.5–3.9**	**2.3–3.5[c]**	**2–11**		
	0.3 ± 0.02[a]	2.5 ± 0.2		10.5 ± 5.5	BC-BC	Bartos et al. (2001)
	0.3 ± 0.03[a]	2.5 ± 0.4	2.29[c]	5 ± 3	PV+ BC-BC	Bartos et al. (2002)
		2.0 ± 0.2	2.5[c]	4.5 ± 3	BC-BC	Doischer et al. (2008)
	0.4 ± 0.06[a]	3.9 ± 0.2	3.5[c]	1.7 ± 1.7	BC-BC	Savanthrapadian et al. 2014
DI cell	**0.2**	**4.0**	**3.1**	**11**		
	0.23 ± 0.04	3.95 ± 0.75	3.06	10.8 ± 6.3	BC-DI	M. Bartos unpublished

CA3						
PC	**1.1–0.3[a]**	**3.3–4.6**	**2–8[c]**	**<17**		
	0.3 ± 0.02[a]	3.3 ± 0.1	5.27[c]	0	PV+ BC-PC	Bartos et al. (2002)
	1.2 ± 0.1[b]		5.2[c]	5.6 ± 2.5	Fast-spiking BC-PC	Szabó et al. (2010)
	1.1 ± 0.1[b]	11.0 ± 0.6[d]	8.8[c]	1.6 ± 1.1	Axo-axonic-PC	Szabó et al. (2010)
	1.8 ± 0.3[b]		2[c]	16.8 ± 2.9	Regular spiking BC-PC	Szabó et al. (2010)
BC	**0.25[a]**	**1.2**	**3.9[c]**	**10**		
	0.25 ± 0.02[a]	1.2 ± 0.02	3.94[c]	10 ± 10	PV+ BC-BC	Bartos et al. (2002)
CA1						
PC	**0.3–0.7[a]0.66–0.86[b]**	**3.5–8.3**	**1.6–9.5**	**3–35**		
	0.3 ± 0.02[a]	3.5 ± 0.5	9.53[c]	3 ± 2	PV+ BC-PC	Bartos et al. (2002)
	0.66 ± 0.06[b]	7.03 ± 1.03	2.07		Fast-spiking BC-PC	Glickfeld et al. (2008) and Glickfeld and Scanziani (2006)
	0.86 ± 0.09[b]	8.3 ± 1.22	1.61		Regular spiking BC-PC	Glickfeld et al. (2008) and Glickfeld and Scanziani (2006)
	0.73 ± 0.05[b]	6.8 ± 0.2	3.12[c]	35 ± 7	CCK+ BC-PC	Neu et al. (2007)
	0.7 ± 0.2	7.1 ± 1.2			CCK+ BC-PC	Tyan et al. (2014)
BC	**0.3[a]**	**1.7**	**5.1[c]**	**4**		
	0.27 ± 0.02[a]	1.7 ± 0.1	5.12[c]	4 ± 3	PV-GFP+ BC-BC	Bartos et al. (2002)

Abbreviations: *PC* pyramidal cell, *PV* parvalbumin, *BC* basket cell, *CCK* cholecystokinin, *MFA* mossy fiber-associated cell, *DI cell* dendrite-inhibiting cell
[a]20–80% rise time, [b]10–90% rise time, [c]calculated from peak IPSC and estimated Cl^- reversal potential, [d]recorded at room temperature (22 ± 2°C)

composition (Strüber et al. 2015). Indeed, antibody labeling revealed that closely spaced GCs are contacted by BC-mediated GABAergic synapses expressing less α2 subunits postsynaptically, whereas the α2 content increases at more distant target GC (Strüber et al. 2015). Interestingly, this form of distance-dependent perisomatic inhibition was independent of the target cell and observed at both postsynaptic GCs as well as PV-INs (Strüber et al. 2017).

Morphological analysis revealed that many BC-IN synapses are on proximal apical dendrites because the cell body of these cells is often located below the somatic layer. The dendritic position of the synapses leads to attenuation and deceleration of the synaptic current (Johnston and Brown 1983; Rall and Segev 1985; Major et al. 1993; Doischer et al. 2008). Therefore, to determine the real-time course of the inhibitory conductance, rise and decay time constants of the inhibitory postsynaptic conductance were estimated using passive cable models of reconstructed BC-IN pairs (Bartos et al. 2001). In these simulations, the mean value for the 20–80% rise time was found to be 0.17 ± 0.04 ms and the decay time constant 1.8 ± 0.6 ms (Bartos et al. 2001). These values were by a factor of 1.8 and 1.4 faster than the experimentally obtained ones, indicating a considerable electrotonic deceleration of the evoked IPSCs for these proximally positioned dendritic synapses.

CCK-BCs Information on kinetic properties, synaptic strength, and precision in transmitter release at CCK-BC inhibitory output synapses is limited (Table 1). Paired whole-cell patch-clamp recordings showed that uIPSCs at CCK-BC to PC synapses in CA1 have a 10–90% rise time of 0.73 ± 0.05 ms and a decay time constant of 6.8 ± 0.2 ms (Neu et al. 2007), indicating that synaptic inhibition at CCK-BC output synapses might be slower than at PV-BC output synapses (Bartos et al. 2002). Furthermore, paired recordings at CCK-BC to GC synapses in the dentate gyrus revealed average uIPSCs with slow 20–80% rise times and decay time constants (∼0.9 ms and ∼22 ms, respectively; Table 1; Harney and Jones 2002; Hefft and Jonas 2005). However, these recordings have been performed at room temperature (20–22 °C) and therefore cannot be directly compared with data obtained at PV-BC output synapses measured at near-physiological temperatures (Bartos et al. 2002). While PV-BCs display a fast-spiking (FS) discharge pattern, CCK-BCs have been shown to be regular-spiking (RS) (Freund 2003). Whole-cell recordings of presynaptic RS-BCs and postsynaptic PCs in CA1 revealed uIPSCs with moderately fast time course with a 10–90% rise time of 0.86 ± 0.09 ms and a decay time constant of 8.3 ± 1.22 ms (Table 1; Glickfeld and Scanziani 2006, Glickfeld et al. 2008). These values were, however, not significantly different to the ones obtained at FS-BC to PCs synapses with a 10–90% rise time of 0.66 ± 0.06 ms and a decay time constant of 7.03 ± 1.03 ms in the same experiments (Table 1; Glickfeld and Scanziani 2006; Glickfeld et al. 2008). Although the time course of IPSCs at FS and RS output synapses are not significantly different, they seem to be mediated by different postsynaptic $GABA_AR$ subunits. Putative CCK/vasoactive intestinal polypeptide (VIP)-immunopositive BC synapses show several-fold lower α1, but higher α2 subunit content than PV-positive synapses (Nyíri et al. 2001;

Klausberger et al. 2002). Finally, CCK-IN to GC synapses show a higher level of transmission failures than PV-BC to GC synapses, pointing to major differences in the release probability among the two BC types (Table 1).

In addition to differences in the kinetics, strength, reliability, and transmitter release at CCK-IN output synapses are characterized by a marked asynchrony (Maccaferri et al. 2000; Hefft and Jonas 2005; M. Bartos, unpublished observation). The less precisely timed GABA release results in a slow rise time of unitary IPSCs observed at CCK-IN to principal cell synapses in the dentate gyrus and CA1 (Maccaferri et al. 2000; Hefft and Jonas 2005). The standard deviation of the first latency distribution, which can be used as a measure for synchrony of release, is significantly larger at CCK-IN to GC than at PV-BC to GC synapses (CCK-INs: 0.95 ± 0.3 ms versus 0.26 ± 0.06 ms). In summary, the properties of the inhibitory output differ markedly between CCK- and PV-BCs. While PV-BC output synapses are characterized by fast, strong, precisely timed transmission, CCK-BC synapses are slower, are weaker, and show asynchronous signaling.

Similar to PV-BCs, CCK-BCs do also target other INs including CCK-BCs. While neuroanatomical studies indicate that the mutual connectivity is comparable to that of PV-BCs, and the total inhibitory input is stronger (Mátyás et al. 2004), functionally, perisomatic inhibition appears to be weaker in CCK-INs. Recordings from the two types in the CA1 area revealed that IPSCs evoked by minimal stimulation in the cell body layer had large peak amplitudes in PV-immunopositive cells, but small in CCK-BCs (Glickfeld et al. 2008). In comparison to ISPCs recorded simultaneously in PyCs, the ratio of the amplitudes was close to 1 in PV- but only 0.14 ± 0.05 in CCK-BCs, pointing to a target cell-dependent difference in the strength perisomatic inhibition (Glickfeld et al. 2008).

Although HICAPs of the dentate gyrus do not have the classical axonal arbors as BCs located in the GC layer, they are CCK-positive (Savanthrapadian et al. 2014), giving rise to the hypothesis that dentate gyrus CCK-expressing BCs are homologous to HICAP cells.

Chandelier or Axo-Axonic (AA) Cells In contrast to PV-BCs, information on the functional properties at AAs output synapses is scarce. Data from paired recordings in the dentate gyrus showed that these INs evoke fast $GABA_AR$-mediated IPSPs in GCs (Buhl et al. 1994). Properties of the currents underlying the effect of AAs were examined in paired whole-cell patch-clamp recordings in the CA3 area. Results showed that unitary AA ISPCs have larger amplitude (463.3 ± 61.8 pA) and a moderately fast time course (rise time, 1.1 ± 0.1 ms; decay time constant 11.0 ± 0.6 ms at room temperature; Szabó et al. 2010). Recordings from neocortical AA cells and synaptically coupled PyCs suggested that the effect of this IN type is not inhibitory but excitatory (Szabadics et al. 2006). Results from the hippocampus, however, indicate that AA cells predominantly mediate hyperpolarization in the postsynaptic PC population (Glickfeld et al. 2009). Indeed, a hyperpolarizing effect of GABAergic synapses located at the AA segment controls ectopic backpropagation of action potentials in PC axons and thereby lowers the invasion of the soma by

antidromic action potentials to maintain the functional polarization of PCs during network oscillations (Dugladze et al. 2012).

Dynamic Properties of Perisomatic Inhibition When two action potentials are elicited in the presynaptic BC in short succession, the amplitude of the second IPSC elicited in the postsynaptic cell is smaller than that of the first. This phenomenon is called paired-pulse depression (PPD) (Kraushaar and Jonas 2000; Bartos et al. 2001 2002). Coefficient of variation analysis (Malinow and Tsien 1990) suggests a presynaptic locus for PPD (Bartos et al. 2001). In fact, PPD is independent of the identity of the postsynaptic neuron: the extent of PPD of PV-BCs evoked ISPCs was found to be similar at in PV-BC and PCs (∼31 % and ∼33 %, respectively; Bartos et al. 2002). Under conditions of prolonged activity, synaptic transmission at BC-BC and BC-GC synapses show rapid and marked initial depression but subsequently stabilize at a lower level (Kraushaar and Jonas 2000; Bartos et al. 2001) demonstrating that GABAergic transmission is extremely stable at BC output synapses.

CCK-BC output synapses express PPD to a similar extent as PV-BCs in the dentate gyrus (Hefft and Jonas 2005). During repetitive stimulation (10 action potentials, 50 Hz), however, the onset of depression was slower at CCK-INs than at PV-BCs (Hefft and Jonas 2005). Interestingly, in the CA3 and CA1 area high-frequency trains elicited in CCK-BCs result in facilitation of IPSCs in PCs (Losonczy et al. 2004; Földy et al. 2006; Neu et al. 2007). Release at these synapses is tightly controlled by endocannabinoids through CB1 receptors resulting in a low release probability when the cells are quiescent (Földy et al. 2006).

Dendritic $GABA_AR$-Mediated Inhibition

Dendritic inhibition is mediated by a highly heterogeneous population of INs. Some of these INs, such as neurogliaform cells (NGFCs), perforant path- and Schaffer collateral-associated INs of the CA1 area, or MOPP cells of the dentate gyrus, mediate exclusively feedforward inhibition (Vida et al. 1998; Price et al. 2008; Elfant et al. 2008); others, such as O-ML and HIPP INs, provide feedback inhibition (Han et al. 1993; Blasco-Ibáñez and Freund 1995); and yet another group, such as CA1 bistratified cells, are involved in both types of inhibitory microcircuits. Dendritic inhibition controls excitation of cells by glutamatergic inputs, voltage-dependent activation of NMDA receptors, and synaptic plasticity (Staley and Mody 1992; Davies et al. 1991; Mott and Lewis 1991; Miles et al. 1996). Furthermore, dendritic inhibition modulates the activation of voltage-gated channels, the generation of slow Ca^{2+} spikes, and the backpropagation of action potentials (Miles et al. 1996; Buzsáki 1996).

The large electrotonic distance between synapse location and the site of somatic action potential generation, as well as the low-pass filtering properties of passive membranes will result in attenuation of synaptically evoked IPSCs (Johnston and

Brown 1983; Rall and Segev 1985; Major et al. 1993; Häusser and Roth 1997). Dendritic inhibition will thereby have a slower, tonic rather than fast, "phasic" inhibitory effect at the soma. Thus, in contrast to perisomatic inhibition which determines spike timing and synchronizes the activity of PCs, dendritic inhibition may offset the input-output relation of postsynaptic target cells (Mitchell and Silver 2003).

Information on the functional properties of GABAergic transmission of identified DIs is limited. The following section summarizes data on properties of $GABA_AR$-mediated transmission at the output synapses of morphologically-identified DIs from the CA1 and the dentate gyrus available in the literature (Hosp et al. 2014; Savanthrapadian et al. 2014).

Neurogliaform Cells NGFCs form a dense axonal plexus in the *stratum (str.) lacunosum-moleculare* of CA1 (Vida et al. 1998; Price et al. 2005, 2008) and the molecular layer (Armstrong et al. 2011). $GABA_AR$-mediated inhibitory signaling at NG output synapses is characterized by slow time course and small peak amplitude (Price et al. 2005, 2008; Szabadics et al. 2007; Armstrong et al. 2011). Paired whole-cell patch-clamp recordings of presynaptic NGFCs and postsynaptic PCs in acute hippocampal slice preparations at near-physiological temperature (30–34 °C) revealed a decay time constant of the unitary IPSCs of 50 ± 4.9 ms and an underlying peak conductance of ~0.48 nS (Table 2; Price et al. 2008). Similarly, paired recordings of synaptically interconnected NGFCs showed slow kinetics with an average decay time constant of 42.05 ± 21.03 ms (Table 2; Price et al. 2005). NGFCs additionally communicate with other types of INs, thereby forming networks of synaptically connected GABAergic cells. Inhibition at these NGFC to non-NGFC synapses is also characterized by a long decay time constant (37.4 ± 11.86 ms; Table 2; Price et al. 2005). In the dentate gyrus, faster kinetics have been observed at NGFCs targeting GCs, but they were still slower than at BC-GC synapses with a rise time (10–90%) of 5.8 ± 1.1 ms, an amplitude of 8.01 ± 1.22 pA (V_{hold} −50 mV), and a decay time constant of 14.7 ± 3.6 ms (Armstrong et al. 2011). Thus, synaptic inhibition by NGFCs has a very slow time course, independent of the nature of the target cell, suggesting that this neuron type is the source of the slow dendritic inhibition observed in earlier studies (Pearce 1993; Banks et al. 1998). The slow time course of the inhibitory conductance stems from several structural and functional characteristics, including spillover of GABA from the synapses formed by the dense axonal arbor and the properties of the GABA receptors on the postsynaptic membrane (Szabadics et al. 2007).

The dynamic properties of GABAergic transmission at NGFC output synapses during repetitive presynaptic activation were characterized by a marked depression (5 Hz trains of 4 presynaptic action potentials). The peak amplitude of the second IPSC in such a train of presynaptic activity was reduced by ~40% at NGFC to PyC synapses (Price et al. 2008) and by ~25% at NGFC-NGFC synapses (Price et al. 2005). Thus, GABA release at NGFC output synapses is strongly depressing.

Table 2 Kinetic properties of dendritic inhibition

Postsynaptic Cell type	20–80 % rise time (ms)	Decay τ (ms)	Peak conductance (nS)	Failure rate (%)	Paired recording configuration	Publication
DG						
GC	**0.6/0.9–1.1[a]**	**6.1/20.1–25.4[a]**	**1.5/1.1[a]**	**32/19–65[a]**		
	0.56 ± 0.13	6.1 ± 1.7	1.50	31.5 ± 8.3	DI-GC	M. Bartos (unpublished)
		24.0 ± 1.0[a]	1.12[a]	65 ± 5[a]	HICAP-GC	Harney and Jones (2002)
	0.87 ± 0.08[a]	20.1 ± 0.8[a]		18.6 ± 6.3[a]	HICAP-GC	Hefft and Jonas (2005)
	1.11 ± 0.08[a]	25.4 ± 2.1[a]			Non fast-spiking cells-GC	Liu et al. (2014)
BC	**0.7**	**5.5**	**0.6–1.5**	**48**		
	0.70 ± 0.15	5.9 ± 1.7	0.84	40.5 ± 10.7	DI-BC	M. Bartos (unpublished)
	0.69 ± 0.06	5.5 ± 0.3	0.61[b]	48.3 ± 5.3	HICAP-BC	Savanthrapadian et al. (2014)
	0.7 ± 0.1	5.5 ± 0.6	1.54[b]		HIPP-BC	Savanthrapadian et al. (2014)
HICAP	**0.7**	**6.4**	**0.32**	**57**		
	0.4 ± 0.18	5.3 ± 1.01	0.46		HICAP-HICAP	M. Bartos (unpublished)
	0.7 ± 0.09	6.4 ± 0.8	0.32[b]	57.2 ± 6.5	HICAP-HICAP	Savanthrapadian et al. (2014)
HIPP	0.5	10.9	0.62	50		
	0.5 ± 0.08	10.9 ± 1.9	0.62[b]	50.4 ± 6.1	HIPP-HIPP	Savanthrapadian et al. (2014)
NG	**5.8; 10–90%**	**14.7**	**8.01**	**50**		
	5.8 ± 1.1	14.7 ± 3.6	8.01 ± 1.22[b]	–	NG-GC	Armstrong et al. (2011)

CA1						
PC		**50**	**0.11**[b]			
		50 ± 4.9	0.11[b]		NG-PC	Price et al. (2008)
NG		**42**	**0.48**[b]			
		42.05 ± 21.03	0.48[b]		NG-NG	Price et al. (2005)
		37.4 ± 11.86			NG- to non-NG	Price et al. (2005)
SO-IN	**1.3–6.2**	**9–23**	**0.43–1.3**	**5–60**		
		23.0 ± 5.0	1.34	5 ± 4	O-LM-IN to SL-IN	Elfant et al. (2008)
	6.2 ± 0.6	20.8 ± 1.7	0.43		O-LM-IN to PC	Maccaferri et al. (2000)
	1.3 ± 0.1	9.0 ± 0.7		59.7 ± 6.0	IS3 to O-LM	Tyan et al. (2014)
SLM-IN		**10**				
		10.2 ± 6.6			SLM-IN to NG	Price et al. (2005)
CA3						
MFA-IN	**0.3–0.9**	**4.7**	**5.0**	**36–100**		
	0.28 ± 0.08	4.6 ± 1.2	4.97[b]		MFA-IN-PC	Vida and Frotscher (2000)
	0.9 ± 0.08	4.8 ± 0.3		96–100/0.2 Hz	MFA-IN-PC	Losonczy et al. (2004)
				36 ± 5/25 Hz		

Abbreviations: *PC* pyramidal cell, *NGC* neurogliaform cell, *SL* stratum lucidum, *IN* interneuron, *DI cell* dendrite-inhibiting cell
[a]Recorded at room temperature (21–24°C); [b]Calculated from peak IPSC and estimated Cl^- reversal potential

Stratum Oriens Interneurons (SO-IN) Functional synaptic communication has been identified between CA1 INs with their somata and dendrites in *str. oriens* and postsynaptic PCs. SO-INs are highly diverse, but one of the most abundant types is the so-called oriens lacunosum-moleculare (O-LM) IN with axonal projection to the *str. lacunosum-moleculare* (Maccaferri et al. 2000). Electron microscopy revealed that the axon terminals of O-LM cells form symmetrical synapses with the distal apical dendrites, mainly shaft, but also dendritic spines, of PyCs and other INs (Gulyás et al. 1993; Sik et al. 1995; Katona et al. 1999). Unitary IPSCs originating from O-LM cells and recorded at the soma of postsynaptic PCs at near-physiological temperature (~30 °C) have small peak amplitudes (~0.43 nS) and slow time courses with a 10–90% rise time of 6.2 ± 0.6 ms and a decay time constant of 20.8 ± 1.7 ms (Table 2; Maccaferri et al. 2000). These dendritic inputs are markedly slower than perisomatic inhibitory synapses, but considerably faster than "slow" dendritic inhibition mediated by NGFCs.

Similarly to O-LM to PC connections, $GABA_AR$-mediated inhibition between presynaptic O-LM and postsynaptic SL-INs is slow and weak with a decay time constant of 23 ± 5 ms and a peak conductance of 1.34 nS (Table 2, Elfant et al. 2008). Short-term plasticity was characterized by ~40% PPD at 100 ms inter-spike intervals. Finally, paired-pulse modulation resulted always in synaptic depression independent of the type of the postsynaptic IN (Elfant et al. 2008). In contrast, similar activity patterns failed to influence the second IPSC in PyCs (93 ± 4%; Maccaferri et al. 2000), raising the possibility of target cell-specific differences in presynaptic properties of these synapses.

Interneuron-Specific Cells (IS-3) IS-3 cells co-express the VIP and calretinin in the hippocampal area CA1 and are located with their soma in the *str. oriens/alveus* (O/A). They innervate several O/A INs including O-LM, bistratified cells, BCs, and oriens-oriens INs with preferential innervation of O-LM cells through dendritic synapses (Tyan et al. 2014). The amplitude of uIPSCs was small and the time course slow with low release probability (Table 2), which was reflected in a high failure rate (59.7%). An O-LM cell was contacted by an IS-3 cell via multiple contact sites. Recruitment of converging inhibitory inputs from IS-3 cells onto target O-LM neurons controlled their firing rate and the timing of action potential generation, indicating that dendritic inhibition provided by IS-3 cells is required for precise activity-dependent recruitment of O-LM cells and thus feedback inhibition in the network.

Mossy Fiber-Associated Interneurons (MFA) MFA INs have dense axonal arborization co-aligned with mossy fibers (MFs) in the *str. lucidum* of CA3 and the hilus (Vida and Frotscher 2000). Their dendrites are located in the *strata radiatum and oriens*, indicating that these INs are innervated by associational and commissural fibers and thus primarily mediate feedback inhibition. Output synapses of MFA INs are found on proximal dendritic shafts and to a lesser degree on somata of PyCs. IPSCs recorded at postsynaptic PCs had fast 20–80% rise times of 0.28 ± 0.08 ms and decay time constants of 4.6 ± 1.2 ms (Vida and Frotscher 2000; Losonczy

et al. 2004; Table 2). The unitary peak conductance was high with an estimated 5 nS. Thus, in comparison to other DIs, GABAergic transmission at MFA output synapses is characterized by fast time courses and high strength. Dynamic properties of MFA synapses are similar to CCK-BCs in that they have a low initial release probability, show a remarkable frequency-dependent facilitation, and transmit with high reliability during high-frequency trains (Vida and Frotscher 2000; Losonczy et al. 2004).

Dendritic Inhibitory Interneurons in the Dentate Gyrus The dense layer-specific axonal distribution of the various DI cells indicates the formation of GABAergic synapses located on the entire somato-dendritic domain of INs and PCs in the dentate gyrus (Han et al. 1993; M. Bartos, unpublished data). Unitary inhibitory events elicited by the activation of DI cells recorded at the soma of GCs and INs are slower and weaker than perisomatic inhibition (Fig. 1; Savanthrapadian et al. 2014). The difference is in part due to electrotonic attenuation of the synaptic events, but properties of postsynaptic $GABA_A$Rs are likely to be of different subunit composition (Table 2). Paired recordings of presynaptic DIs and postsynaptic target cells at near-physiological temperature (32–34 °C) revealed unitary IPSCs with the following parameters:

uIPSCs at HICAP-HICAP synapses were induced after a 1.8-fold longer synaptic latency (2.2 ± 0.1 ms) with a 10.9-fold smaller peak amplitude (12.9 ± 3.9 pA vs. BC-BC in mice 140.2 ± 30.8 pA) and slower time course (rise time 0.7 ± 0.09 ms, decay 6.4 ± 0.8 ms). The coefficient of variation (CV) in the synaptic latency was three times higher at HICAP-HICAP than BC-BC synapses (0.43 ± 0.08 vs. 0.14 ± 0.007). However, the decay time constant of the unitary IPSCs is slower (3.95 ± 0.75 ms) than at BC-BC synapses (2.5 ± 0.2 ms). Similarities in the functional synaptic properties are also evident between BC-BC and HIPP-HIPP connections. Inhibitory signals at HIPP-HIPP synapses are evoked after a similar mean synaptic latency (1.5 ± 0.16 ms) with a low CV (0.2 ± 0.04). The rise time of uIPSCs is also short (0.5 ± 0.08 ms) similar to BC-BC paired recordings, indicating a highly synchronous GABA release. Some differences in the synaptic signaling are also apparent. First, the percentage of failures is 29.7-fold higher than at BC-BC synapses (50.4 ± 6.1%). Second, the amplitude of uIPSCs was 5.6 times smaller (25.0 ± 11.3 pA) than at BC-BC synapses. Finally, the decay is 2.8-fold slower (10.9 ± 1.9 ms).

Although HIPP cells project their main axonal arbors to the outer molecular layer of the dentate gyrus, some axon fibers are located in the hilus. Indeed, the short latency at HIPP-HIPP signaling can be explained by the synapse location close to the soma of the target cell as revealed by single-cell reconstructions (Savanthrapadian et al. 2014). HICAP-HICAP pairs with axon collaterals in the inner molecular layer form their contact sites at apical dendrites (Savanthrapadian et al. 2014). During trains of 10 action potentials at 50 Hz, HICAP-HICAP synapses express multiple-pulse facilitation (MPF) with a mean $uIPSC_{10}/uIPSC_1$ ratio of 1.6 ± 0.4. Signals at HIPP-HIPP synapses have a biphasic response with an initial

strongly facilitating phase ($uIPSC_5/uIPSC_1$ ratio 2.4 ± 0.3) followed by a second phase characterized by a decline in subsequent uIPSC size ($uIPSC_{10}/uIPSC_1$ ratio 1.4 ± 0.5; Savanthrapadian et al. 2014).

Reversal Potential (E_{syn}) of Synaptically Evoked IPSCs

Several lines of evidence indicate that $GABA_A$R-mediated synaptic inhibition on mature INs is not hyperpolarizing as previously assumed but "shunting" (Alger and Nicoll 1979; Andersen et al. 1980; Martina et al. 2001; Chavas and Marty 2003; Vida et al. 2006). Shunting inhibition is defined as an inhibitory effect, which only minimally affects the membrane potential, but counteracts excitation by short-circuiting the underlying currents. In this scenario, the reversal potential of synaptically evoked IPSCs (E_{syn}) is close to the resting membrane potential (V_{rest}), e.g., in the voltage range between V_{rest} and the threshold for action potential generation (Bartos et al. 2007; Sauer et al. 2012). To determine E_{syn}, whole-cell recordings from BCs were performed in the perforated-patch configuration in the dentate gyrus of rats and PV-EGFP-expressing mice (Vida et al. 2006). The ionophore gramicidin preserves the intracellular Cl^- concentration during recording, thus allowing a realistic assessment of E_{syn} (Kyrozis and Reichling 1995). To determine E_{syn}, IPSCs were evoked by extracellular stimulation in the PC layer at varying holding potentials. Synaptically evoked IPSCs reversed on average at −52 ± 1.9 mV (Vida et al. 2006). This value was more positive than the corresponding V_{rest} of −58.4 ± 1.4 mV, but more negative than the threshold potential (Table 3), indicating that inhibition is shunting in BCs. Similarly, perforated-patch recordings from CA3 *str. pyramidale*, *str. oriens*, and *str. lucidum* INs revealed that $GABA_A$R-mediated synaptic inhibition is shunting or slightly hyperpolarizing with average E_{syn} values 4–5 mV more positive than the corresponding V_{rest} (Table 3; Lamsa and Taira 2003; Banke and McBain 2006). These results have been further confirmed in CA1 *str. radiatum* INs by using cell-attached recordings of $GABA_A$R-mediated effects (E_{syn}: −69.1 ± 1 mV; V_{rest}: −66 ± 1 mV; Tyzio et al. 2008).

In contrast to INs, E_{syn} of synaptically evoked IPSCs in PCs seems to be diverse (Table 3). Synaptic inhibition in GCs is shunting with an E_{syn} ∼1–10 mV more positive than the resting membrane potential (Table 3, Overstreet-Wadiche et al. 2005; Sauer et al. 2012). Noninvasive recording of unitary field potentials which reflect the postsynaptic effect of GABA release from an identified presynaptic BC confirmed the shunting nature of perisomatic inhibition in the dentate gyrus (Sauer et al. 2012). Importantly, these results did not depend on the age of the animal, excluding a late developmental change in E_{syn} at this synapse (Sauer et al. 2012). Synaptically evoked IPSCs in CA3 PCs reverse at ∼−73 mV, which is ∼10 mV more negative than the corresponding V_{rest} of ∼−63 mV (Table 3), reflecting hyperpolarizing inhibition in these neurons (Banke and McBain 2006; Lamsa and Taira 2003). In contrast, somatic cell-attached recordings from CA3 PyCs reveal shunting or even depolarizing inhibition with an E_{syn} of −75.3 ± 0.9 mV and a

Table 3 Reversal potential of GABAergic responses

Cell type	E_{syn} (mV)	V_{rest} (mV)	Gramicidin perforated-patch recording technique	Publication
DG				
GC	**−72/−74–82**[a]	**−75**[a]		
	−71.9 ± 1.9		Synaptic stimulation	Kraushaar and Jonas (2000)
	−74 ± 7[a]	75[a]	Synaptic stimulation	Overstreet-Wadiche et al. (2005)
	−81.6 ± 2.2[a]		GABA bath application	Tozuka et al. (2005)
	−64.5 ± 2.4	−75.8 ± 1.1	Synaptic stimulation	Sauer et al. (2012)
BC	**−57/−52[a]**	**−64/−58[a]**		
	−52.3 ± 1.9[a]	−58.4 ± 1.4[a]	Synaptic stimulation	Vida et al. (2006)
CA3				
PC	**−73–75**	**−63–78**		
	−72.7 ± 0.9	−64.6 ± 0.8	Synaptic stimulation	Lamsa and Taira (2003)
	−73 ± 3.8	−62.8 ± 4.4	Synaptic stimulation	Banke and McBain (2006)
	−75.3 ± 0.9	−78 ± 2	Cell-attached GABA application[b]	Tyzio et al. (2008)
STR- and STP/STO INs	**−65–69**	**−61–66**		
	−69.1 ± 1.0	−66.0 ± 1.0	Cell-attached GABA application[b]	Tyzio et al. (2008)
	−65.3 ± 1.0	−60.5 ± 0.7	Synaptic stimulation	Lamsa and Taira (2003)
SL-INs	**−78**	**−75**		
	−78.1 ± 3.7	−75.4 ± 2.5	Synaptic stimulation	Banke and McBain (2006)
CA1				
PC	**−69**	**−66**		
	−69 ± 4	−66.0 ± 0.5	Synaptic stimulation	Riekki et al. (2008)
	−67.8 ± 2.3	−63.2 ± 1.0	Synaptic stimulation	Sauer et al. (2012)

Abbreviations: *GC* granule cell, *BC* basket cell, *PC* pyramidal cell, *STR* stratum lucidum, *STP* stratum pyramidale, *STO* stratum oriens, *SL* stratum lucidum
[a]Recorded at room temperature; [b]GABA receptor reversal potential depicted from cell-attached recordings of individual GABA channels

corresponding V_{rest} of -78 ± 2 mV (Table 3; Tyzio et al. 2008). Similarly, in CA1, some discrepancy persists about the nature of GABAergic inhibition. Perforated-patch recordings from CA1 PyCs indicated shunting or slightly hyperpolarizing inhibition (Table 3, Riekki et al. 2008). In contrast, unitary field recording with distinct IN types including BCs, AA, O-LM, and bistratified cells as the presynaptic neuron was always hyperpolarizing (Glickfeld et al. 2009; Sauer et al. 2012). Differences in the excitation state of the recorded cells (Lamsa and Taira 2003), modulation of Cl^- transporters (Woodin et al. 2003) or differences in membrane properties between neurons in different brain areas might explain the variability in the obtained E_{syn} values.

In summary, synaptic $GABA_A$R-mediated synaptic inhibition onto INs is largely shunting, independent of the nature of the recorded IN type or the hippocampal area. However, synaptic inhibition in PCs is diverse and varies from hyperpolarizing to shunting and even depolarizing inhibition.

$GABA_B$R-Mediated Inhibition in Hippocampal Circuits

Early electrophysiological and pharmacological studies demonstrated that, in addition to fast ionotropic $GABA_A$Rs, slow-acting metabotropic $GABA_B$Rs are also involved in the mediation of the effects of GABA in the hippocampus. In CA1 PyCs, extracellular stimulation in the *str. radiatum* elicits a biphasic IPSP consisting of a fast and a slow component (Newberry and Nicoll 1984; Dutar and Nicoll 1988b). While the fast component of the compound IPSP is blocked by the $GABA_A$R antagonist bicuculline, the slow component persists under bicuculline application (Newberry and Nicoll 1984; Dutar and Nicoll 1988b) and can be blocked by the $GABA_B$R antagonist CGP35348 (Fig. 2a; Solís and Nicoll 1992). Similarly, stimulation in dendritic layers elicits slow $GABA_B$R-mediated inhibitory responses in CA3 PyCs, dentate gyrus GCs, and various types of INs (Thompson and Gähwiler 1992; Otis et al. 1993; Khazipov et al. 1995; Mott et al. 1999; Booker et al. 2013, 2017b). Results of these studies, thus, indicate a widespread and abundant postsynaptic localization of $GABA_B$Rs in the dendrites of PCs and INs (Sibbe and Kulik 2017; Kulik et al. 2017).

$GABA_B$Rs are also expressed presynaptically where they modulate release of various neurotransmitters and neuromodulators (Sibbe and Kulik 2017; Kulik et al. 2017). Presynaptic receptors are commonly subdivided into autoreceptors and heteroreceptors (Bettler et al. 2004) depending on whether they control the release of GABA from inhibitory terminals (Booker et al. 2013, 2017a) in a feedback manner (Davies et al. 1991) or act at the axon terminals of other transmitter systems (e.g., glutamatergic axons; Vogt and Nicoll 1999; Kulik et al. 2002, 2003; Guetg et al. 2009; Oláh et al. 2009).

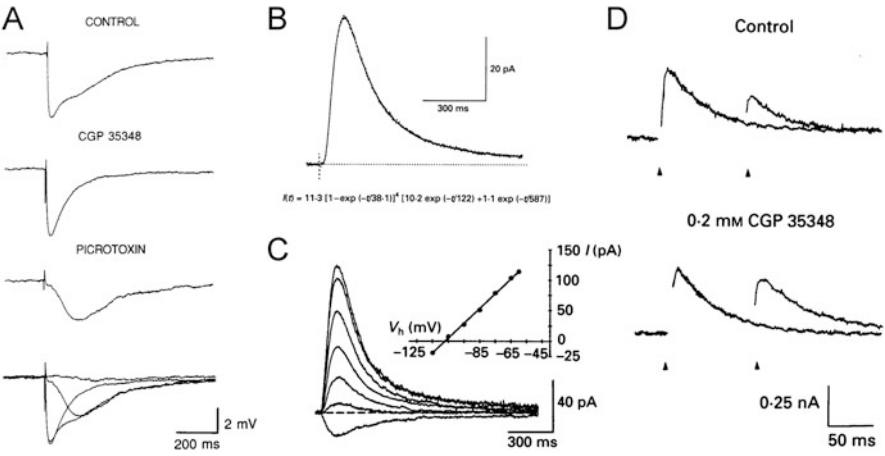

Fig. 2 $GABA_B$R-mediated effects in hippocampal neurons. (**a**) Pharmacological dissection of the monosynaptic IPSP reveals the fast $GABA_A$ and the slow $GABA_B$R-mediated IPSP components in a CA1 PyC. B,C Kinetics (**b**) and reversal potential (**c**) of the $GABA_B$R-mediated slow IPSC in dentate gyrus GCs. (**d**) Activation of $GABA_B$ autoreceptors contribute to depression of IPSCs in response to paired stimuli (top trace, arrow). CGP 35348, a $GABA_B$ receptor antagonist relieves presynaptic inhibition and increases the amplitude of the second response (bottom trace, arrow). (**a** adapted from Solís and Nicoll 1992; **b** and **c** adapted from Otis et al. 1993; **d** adapted from Davies and Collingridge 1993 with permission, © The Society for Neuroscience and The Physiological Society)

Structure and Signaling Through Metabotropic $GABA_B$Rs

$GABA_B$Rs belong to the family of seven transmembrane domain G protein-coupled receptors (GPCRs) (Kaupmann et al. 1997). Two different genes, encoding the $GABA_{B1}$ – which occurs in alternatively spliced forms designated $GABA_{B1a-n}$ – and the $GABA_{B2}$, subunits have so far been identified (Kaupmann et al. 1997; Isomoto et al. 1998; Pfaff et al. 1999; Schwarz et al. 2000; Wei et al. 2001; Lee et al. 2010). As regards $GABA_{B1}$, the $GABA_{B1a}$ and $GABA_{B1b}$ transcripts are the most abundant throughout the central nervous system (CNS), exhibiting differences in the extracellular NH_2-terminal domain (Kaupmann et al. 1997). Although there are indications that splice variants exist for $GABA_{B2}$ ($GABA_{B2a-c}$) (Billinton et al. 2001), more recent results suggest that $GABA_{B2b}$ and $GABA_{B2c}$ transcripts may represent artifacts arising during cDNA synthesis and/or PCR amplification (Bettler et al. 2004).

For their surface localization, efficient coupling to the physiological effectors and formation of fully functional receptors, assembly of heterodimeric complexes made up of $GABA_{B1}$ and $GABA_{B2}$ subunit isoforms is required (Jones et al. 1998; White et al. 1998; Kaupmann et al. 1998a; Marshall et al. 1999; Kuner et al. 1999; Bettler

et al. 2004; Pin and Bettler 2016). The independently regulated $GABA_{B(1a;2)}$ and $GABA_{B(1b;2)}$ receptor subtypes differentially compartmentalize and fulfill distinct pre- vs. postsynaptic functions, respectively, in cortical PCs and INs (Pérez-Garci et al. 2006; Vigot et al. 2006; Shaban et al. 2006; Guetg et al. 2009). In the heterodimers, the $GABA_{B1}$ protein contains the ligand-binding domain, whereas the $GABA_{B2}$ subunit interacts with G proteins (Kaupmann et al. 1998a).

Recent biochemical and electrophysiological studies, prompted by the diversity in properties and characteristics of $GABA_BR$ responses, provided compelling evidence that a further variety of molecularly and functionally distinct types of $GABA_BRs$ exist (Schwenk et al. 2016; Bettler and Fakler 2017; Fritzius et al. 2017). The diversity of the native $GABA_BRs$ originates from the co-assembly of the $GABA_BR$ subunits with numerous types of auxiliary proteins (Gassmann and Bettler 2012; Schwenk et al. 2016). One of the most abundant and best studied constituents of the $GABA_BR$ macromolecular complex is the K^+ channels tetramerization domain-containing (KCTD) family of proteins (Schwenk et al. 2010; Bartoi et al. 2010; Metz et al. 2011; Turecek et al. 2014). Four KCTD proteins, designated KCTD8, KCTD12, KCTD12b, and KCTD16, associate with the $GABA_{B2}$ subunit and determine the kinetics and pharmacology, including agonist potency and G protein signaling, as well as the desensitization of the receptor response in both dendritic and axonal compartments of the cells (Schwenk et al. 2010; Adelfinger et al. 2014; Rajalu et al. 2015; Booker et al. 2017b). Two recent elegant pharmacological studies provided direct evidence for the involvement of both KCTD12 and KCTD16 in determining phenotypes of behavioral activity, emotionality, as well as neuronal excitability (Cathomas et al. 2015, 2017). Furthermore, high-resolution functional proteomics more precisely identified the building blocks of $GABA_BRs$: the receptor core is assembled from $GABA_{B1}$, $GABA_{B2}$, KCTD proteins, and a distinct set of G protein subunits, whereas the periphery of the receptor's nanoenvironment is formed by transmembrane proteins (Schwenk et al. 2016). These peripheral constituents can operate as effectors (Schwenk et al. 2016); can be, via interaction with sushi domains, mediators of cellular processes that direct the trafficking of $GABA_{B(1a;2)}$ receptors into the appropriate compartment of neurons (Tiao et al. 2008); or may represent linkers between $GABA_BRs$ and cellular signaling processes (Sakaba and Neher 2003; Pettem et al. 2013).

As GPCRs, effects of $GABA_BR$ complexes are mediated by second messenger cascades regulating the activity of adenylyl cyclase and phospholipase A_2, as well as effector channels such as G protein-coupled inwardly rectifying K^+ (Kir3) channels or low and high-voltage-activated Ca^{2+} (Ca_v) channels (Marshall et al. 1999; Pérez-Garci et al. 2006; Gassmann and Bettler 2012; Sibbe and Kulik 2017; Kulik et al. 2017; Booker et al. 2018). Accordingly, application of pertussis toxin, an adenosyl transferase, which inactivates several types of G_i proteins, or GDPβ-S, a structural analog of GDP, which competes with GTP for the G protein-binding site, abolishes both pre- and postsynaptic effects of $GABA_BRs$ in hippocampal PyCs (Andrade et al. 1986; Dutar and Nicoll 1988b; Thompson and Gähwiler 1992; Sodickson and Bean 1996).

Postsynaptic Slow Inhibition Mediated by $GABA_BRs$

Functional properties of postsynaptic $GABA_BR$-mediated responses are markedly different from those of fast $GABA_AR$-dependent signaling. First, $GABA_B$ IPSCs have a much slower time course (Fig. 2b). Pharmacologically isolated slow IPSCs have a long onset latency (~12–20 ms, Otis et al. 1993; Table 4), reflecting the multiple steps leading up to the activation of the receptors and their G protein-mediated coupling to the effectors. Furthermore, $GABA_B$ IPSCs have very slow rise and decay. In dentate gyrus GCs, the rise of the IPSC could be described by a fourth-order exponential with an activation time constant of ~45 ms and the decay by a biexponential function with time constants of ~110 and ~516 ms (Otis et al. 1993; Fig. 2b; Table 4). Similarly slow kinetics of $GABA_B$ IPSCs have been reported in CA1 PyCs (Davies et al. 1990; Ling and Benardo 1994; Degro et al. 2015) and in various types of INs (Khazipov et al. 1995; Mott et al. 1999; Booker et al. 2013, 2017b; Table 4).

Second, ionic mechanisms of $GABA_BR$-mediated postsynaptic effects are also different from those of $GABA_ARs$. Slow IPSPs and baclofen-induced currents reverse close to the estimated equilibrium potential of K^+ ions, in the range between −90 and −100 (Fig. 2c and Table 4), indicating that $GABA_BRs$ activate a K^+-selective conductance (Gähwiler and Brown 1985; Davies et al. 1990; Thompson and Gähwiler 1992; Ehrengruber et al. 1997; Booker et al. 2013; Degro et al. 2015). Furthermore, application of Ba^{2+}, an inhibitor of inwardly rectifying K^+ (Kir) channels, abolishes these effects (Gähwiler and Brown 1985; Thompson and Gähwiler 1992; Sodickson and Bean 1996). In fact, the channels mediating the $GABA_B$ responses have been identified as the Kir3 channel subfamily (Lüscher et al. 1997; Kaupmann et al. 1998b). Kir3 channels comprise four subunits (Kir3.1-3-4; Dascal 1997) and form homotetrameric or heterotetrameric complexes (Krapivinsky et al. 1995; Inanobe et al. 1995; Kofuji et al. 1995; Spauschus et al. 1996; Slesinger et al. 1996; Liao et al. 1996; Wischmeyer et al. 1997). In the hippocampus, Kir3 channels are thought to be mainly composed of the Kir3.1 and Kir3.2 subunits (Lesage et al. 1995; Duprat et al. 1995; Leaney 2003). The Kir3.2 subunit is an essential part of the functional channel, determining its assembly and surface localization (Inanobe et al. 1999; Ma et al. 2002; Lujan et al. 2009), whereas Kir3.3 protein contains a lysosomal-targeting motif that reduces its surface expression and accumulation (Ma et al. 2002). In Kir3.2 knockout animals, expression of Kir3.1 is reduced, and slow inhibitory postsynaptic responses are abolished (Liao et al. 1996; Signorini et al. 1997; Lüscher et al. 1997). In good agreement with the proposed coupling of $GABA_BRs$ and Kir3 channels, immunocytochemical investigations revealed robust colocalization of the two proteins in dendrites of CA PyCs and various types of INs (Kulik et al. 2006; Booker et al. 2013; Degro et al. 2015; Booker et al. 2017b).

In addition to regulating Kir3 channels, dendritic $GABA_BRs$ have been shown to inhibit Kir2 channels (Rossi et al. 2006) and modulate Ca_v channels in cortical PCs and INs. Recent studies provided evidence that $GABA_BRs$ can inhibit $Ca_v1.2$ (L-

Table 4 Properties of $GABA_B$ receptor-dependent IPSCs

Cell type	Onset latency (ms)	Rise[a] (ms)	Decay[b] (ms)	Peak conductance (nS)	Reversal potential (mV)	Publication
DG GCs	12–20	$\tau = 45 \pm 1$	$\tau1 = 110 \pm 7$	1.52 ± 0.16	-98 ± 2	Otis et al. (1993)
			$\tau2 = 516 \pm 53$			
	27 ± 3	$T_{peak} = 162 \pm 15$	$\tau1 = 133 \pm 11$	1.31 ± 0.23	-95 ± 2	Mott et al. (1999)
			$\tau2 = 649 \pm 65$			
	53.5 ± 7.3	$T_{rise} = 86.8 \pm 7.0$	$T_{decay} = 428.1 \pm 89.6$	1.82 ± 0.18^c	-98.3 ± 5.8^c	Degro et al. (2015)
DG INs	31 ± 2	$T_{peak} = 154 \pm 6$	$\tau = 261 \pm 28$	0.75 ± 0.12	-97 ± 2	Mott et al. (1999)
BC/HICAP				1.25		
HIPP/TML				0.36		
CA1 PCs	29 ± 2	$T_{rise} = 110$	$T_{IPSC} = 723 \pm 135$		-93 ± 2	Davies et al. (1990)
	62 ± 11	$T = 74 \pm 5$	$\tau1 = 46 \pm 6$	0.94 ± 0.28	-86 ± 2	Ling and Benardo (1994)
			$\tau2 = 247 \pm 32$			
	58.6 ± 4.6	$T_{rise} = 55.3 \pm 5.3$	$\tau = 200.5 \pm 37.7$	2.46 ± 0.37^c	-101 ± 5^c	Booker et al. (2013)
CA1 Ins						
CA1 str. rad. INs		$T_{rise} = 118 \pm 6$	$T_{decay} = 185 \pm 14$	0.79 ± 0.18	-94 ± 8	Khazipov et al. (1995)
CA1 PV BC	78.1 ± 10.7	$T_{rise} = 80.7 \pm 7.9$	$T_{decay} = 152.9 \pm 24.3$	3.56 ± 0.61^c	-95 ± 12^c	Booker et al. (2013)
CA1 PV Bistratified				0.38 ± 0.24^c		Booker et al. (2013)
CA1 CCK BC	56.3 ± 3.0	$T_{rise} = 73.0 \pm 2.5$	$T_{decay} = 141.4 \pm 5.2$	2.31 ± 0.14^c		Booker et al. (2017b)
CA1 CCK SCA				0.80 ± 0.04^c		Booker et al. (2017b)
CA1 CCK PPA				0.88 ± 0.20^c		Booker et al. (2017b)

Abbreviations: *BC* basket cell, *HICAP* hilar commissural-associational pathway-associated cell, *HIPP* hilar perforant pathway-related cell, *TML* total molecular layer cell, *SCA* Schaffer-collateral-associated cells, *PPA* perforant path-associated cells

[a]Values indicate either the time constant (τ) of fitted fourth-power exponential function, peak latency (T_{peak}), or rise time (T_{rise}) measured from onset to peak

[b]Values indicate the time constants of mono-(τ) or biexponential ($\tau1$, $\tau2$) functions fitted to the decay, the full duration (T_{IPSC}) or the decay half-time (T_{decay})

[c]Baclofen-induced whole-cell currents; reversal potential determined using voltage-ramps from –20 to –120 mV (1 s duration); in CCK INs a reversal potential of –95 mV was assumed

type), $Ca_v2.1$ (P/Q-type), $Ca_v2.2$ (N-type), and $Ca_v2.3$ (R-type) channel-mediated dendritic spikes in prefrontal cortical neurons (Chalifoux and Carter 2011) and in layers 2/3 and 5 somatosensory neocortical PyCs (Pérez-Garci et al. 2006, 2013; Larkum et al. 2007). $GABA_BRs$ have also been shown to inhibit $Ca_v1.2$ channels in dendrites of hippocampal somatostatin-expressing INs (SOM-INs) and abolish thereby the induction of long-term potentiation (LTP) at their excitatory input synapses (Booker et al. 2018).

Presynaptic Inhibition of Synaptic Transmission by $GABA_BRs$

Presynaptic $GABA_BRs$ play an important role in regulating synaptic transmission at both excitatory and inhibitory synapses. At excitatory synapses, their activation results in depression of glutamatergic synaptic responses (Lei and McBain 2003). Evidence for presynaptic effects of GABA has been obtained at various hippocampal afferent pathways including the hippocampal CA3-CA1 and MF-CA3 PyC synapses (Vogt and Nicoll 1999; Vigot et al. 2006; Guetg et al. 2009). At these synapses, it has been shown that synaptically released GABA suppresses Schaffer collateral and MF responses through $GABA_BRs$, predominantly via $GABA_{B(1a;2)}$ receptors (Vigot et al. 2006; Guetg et al. 2009). Thus, GABA spilling over from local inhibitory synapses can regulate glutamatergic transmission by heterosynaptic inhibition at various cortical synapses (Vogt and Nicoll 1999; Oláh et al. 2009; Urban-Ciecko et al. 2015). As many DI cells have axons co-aligned with afferent pathways (Gulyás et al. 1993; Han et al. 1993; Vida et al. 1998; Vida and Frotscher 2000; see chapter "Morphology of Hippocampal Neurons"), this mechanism enables INs to provide input-specific presynaptic control through heterosynaptic inhibition to the main afferent systems to the hippocampal areas (Sohal and Hasselmo 1998).

Presynaptic action of $GABA_BRs$ is primarily dependent on G protein-mediated inhibition of the Ca^{2+} conductance (Bettler et al. 2004). Paired recordings from calyx of Held terminals and postsynaptic neurons in the medial nucleus of the trapezoid body provided direct evidence that activation of the receptors by baclofen has no effect on presynaptic K^+ conductances but inhibits Ca^{2+} currents in these terminals (Takahashi et al. 1998). It has been further demonstrated that the presynaptic effect of baclofen is also blocked by GDPβ-S (Takahasi et al. 1998). In the hippocampus, direct patch-clamp recordings from presynaptic elements cannot be routinely performed, with the exception of the large MF terminals on CA3 PyCs (e.g., Geiger and Jonas 2000). Nevertheless, overwhelming evidences suggest that the main mechanisms underlying presynaptic $GABA_BR$ responses at hippocampal synapses also involve Ca_v channels (Bettler et al. 2004; Ulrich and Bettler 2007; Laviv et al. 2011; Vertkin et al. 2015). Presynaptic depression of EPSPs by baclofen is unaffected by Ba^{2+} in cultured hippocampal PyCs (Thompson and Gähwiler 1992), and remains also unchanged in slices from Kir3.2 (GIRK2) knockout mice (Lüscher et al. 1997). In contrast, Ca^{2+} currents evoked in cultured PyCs and INs are highly sensitive to baclofen (Scholz and Miller 1991). Most

compellingly, the inhibitory effects of baclofen on fast presynaptic Ca^{2+} transients and field EPSPs show similar time course in CA1 PyCs (Wu and Saggau 1995). Thus, presynaptic inhibition of excitatory transmission by $GABA_BRs$ depends on reduction in Ca^{2+} conductance rather than activation of K^+ currents in the hippocampus (Gassmann and Bettler 2012). However, the involved Ca^{2+} channel types seem to differ at the various synapses. In CA1 PyCs $GABA_BR$-mediated presynaptic inhibition is occluded by the application of ω-conotoxin, a selective $Ca_v2.2$ Ca^{2+} channel blocker, but not affected by ω-agatoxin, a blocker of $Ca_v2.1$ channels (Wu and Saggau 1995). In contrast, in CA3 *str. radiatum* INs ω-conotoxin and ω-agatoxin occlude presynaptic inhibitory effects of baclofen on miniature EPSCs to an equal degree (Lei and McBain 2003). However, evidence exists that the control of transmitter release by $GABA_BR$ not only acts through Ca^{2+} channels reducing presynaptic release itself but may also lead to altered short-term plasticity independent of the change in release probability (Lei and McBain 2003; Booker et al. 2017a), pointing to more direct interactions with the release machinery.

At hippocampal GABAergic synapses, activation of presynaptic $GABA_BRs$, both $GABA_{B(1a;2)}$ and $GABA_{B(1b;2)}$ receptor types (Vigot et al. 2006), results in reduced inhibitory transmission (Doze et al. 1995; Poncer et al. 2000; Booker et al. 2017a). Consequently, repetitive stimulation leads to the attenuation of IPSCs ("autoinhibition," Davies et al. 1991; Mott and Lewis 1991; Fig. 2d). This dynamic modulation of inhibitory transmission has an important function in regulating the induction of LTP in the hippocampus (Davies et al. 1991; Mott and Lewis 1991). The molecular mechanism of $GABA_BR$-dependent presynaptic inhibition in GABAergic terminals has extensively been investigated. In an early study, effects of baclofen on unitary IPSPs in synaptically coupled pairs of cultured hippocampal neurons were not affected by pre-treatment with pertussis toxin (Harrison 1990). Others have reported that pertussis toxin abolished the baclofen-induced depression of IPSPs in cultured CA3 PyCs (Thompson and Gähwiler 1992). Similarly, findings about the ionic mechanism of presynaptic $GABA_BRs$ have remained somewhat controversial. Thompson and Gähwiler (1992) have shown that extracellular Ba^{2+} reduces presynaptic depression of IPSPs by baclofen in cultured CA3 PyCs, suggesting a contribution of K^+ channels, plausibly of the Kir3 type. Furthermore, baclofen decreases the frequency of both spontaneous IPSCs and action potential- and Ca^{2+}-independent miniature IPSCs recorded in the presence of tetrodotoxin (Lei and McBain 2003). Increased frequency of miniature IPSCs by elevated levels of extracellular KCl is blocked by Cd^{2+}, and the additional application of baclofen leads to a further reduction in the IPSC frequency (Lei and McBain 2003). Thus, in GABAergic terminals the coupling of presynaptic $GABA_BRs$ may, at least partially, utilize pertussis toxin-insensitive G proteins and activate K^+ channels or directly affect the synaptic release machinery in addition to the inhibition of Ca_v channels. Furthermore, there is also evidence that the modulation of K^+ and Ca_v channels is not the only mechanism by which GABA can regulate transmitter release: whole-cell recordings from CA1 PyCs demonstrated that inhibition of GABA release by $GABA_BRs$ is reduced by an activator of protein kinase C (PKC) (Jarolimek and Misgeld 1997).

Cellular and Subcellular Localization of Postsynaptic $GABA_BRs$

Consistent with the physiological and pharmacological data, in situ hybridization (Kaupmann et al. 1998a; Bischoff et al. 1999) and autoradiography (Bowery et al. 1987; Chu et al. 1990) confirmed the abundant expression of $GABA_BR$ subunits in hippocampal PCs and INs. Subsequent immunocytochemical studies (Fritschy et al. 1999; Sloviter et al. 1999; Margeta-Mitrovic et al. 1999; Kulik et al. 2002, 2003) further revealed the cellular and subcellular distribution and localization of the $GABA_BR$ subunits. At the light microscopic level, the immunostaining for the two subunits, $GABA_{B1}$ and $GABA_{B2}$, showed very similar patterns of distribution in the hippocampus (Fig. 3a, b). In the CA areas and the dentate gyrus, immunoreactivity was most intense over the dendritic layers. The *str. lacunosum-moleculare* of CA3 showed the strongest labeling for the proteins, whereas in CA1 the immunoreactivity for the receptor subunits was generally weak to moderate. In the dentate gyrus, the immunolabeling was weak in the hilus and moderate in the molecular layer (Fritschy et al. 1999; Margeta-Mitrovic et al. 1999; Kulik et al. 2003).

At the subcellular level, the immunolabeling for both $GABA_{B1}$ and $GABA_{B2}$ was observed in postsynaptic and, to a lesser extent, presynaptic compartments of PCs (Fig. 3c–e). Postsynaptically, the majority of the receptor subunits were localized to the extrasynaptic plasma membrane of dendritic spines and shafts of PyCs and dentate GCs (Kulik et al. 2003). Quantitative analysis further revealed an enrichment of $GABA_BRs$ around excitatory synapses on dendritic spines, and an even distribution on dendritic shafts of PyCs contacted by GABAergic axon terminals (Fig. 3f, g; Kulik et al. 2003). Interestingly, the effector Kir3 channels displayed a very similar cellular and subcellular distribution (Koyrakh et al. 2005; Kulik et al. 2006). Moreover, $GABA_BRs$ and Kir3 channels were found to be co-clustered around excitatory synapses on dendritic spines of PyCs (Fig. 3g; Kulik et al. 2006) indicating the functional association of these two proteins in this subcellular compartment. The enrichment of the $GABA_BR$-Kir3 channel complexes in spines implies their intimate involvement in the control of synaptic integration and plasticity. Indeed, $GABA_BR$-mediated inhibition has been shown to act as a break on NMDA receptor-mediated responses and thereby reduced synaptic plasticity in PyCs (Otmakhova and Lisman 2004; Malenka and Bear 2004). Conversely, activation of NMDA receptors and Ca^{2+}/calmodulin-dependent protein kinase II (CaMKII), as well as rise in postsynaptic Ca^{2+} results in LTP of the $GABA_BR$-Kir3 channel-mediated slow IPSPs, which parallel the time course of LTP of excitatory transmission (Huang et al. 2005). The functional significance of this IPSC potentiation is to sharpen the coincidence detection of synchronous excitatory inputs (Huang et al. 2005), a hallmark for learning and memory. Moreover, activation of NMDA receptors along with CaMKII can regulate the surface expression and function of $GABA_BRs$: prolonged activation of glutamate receptors results in endocytosis and subsequent degradation of $GABA_BRs$ (Terunuma et al. 2010; Guetg et al. 2010).

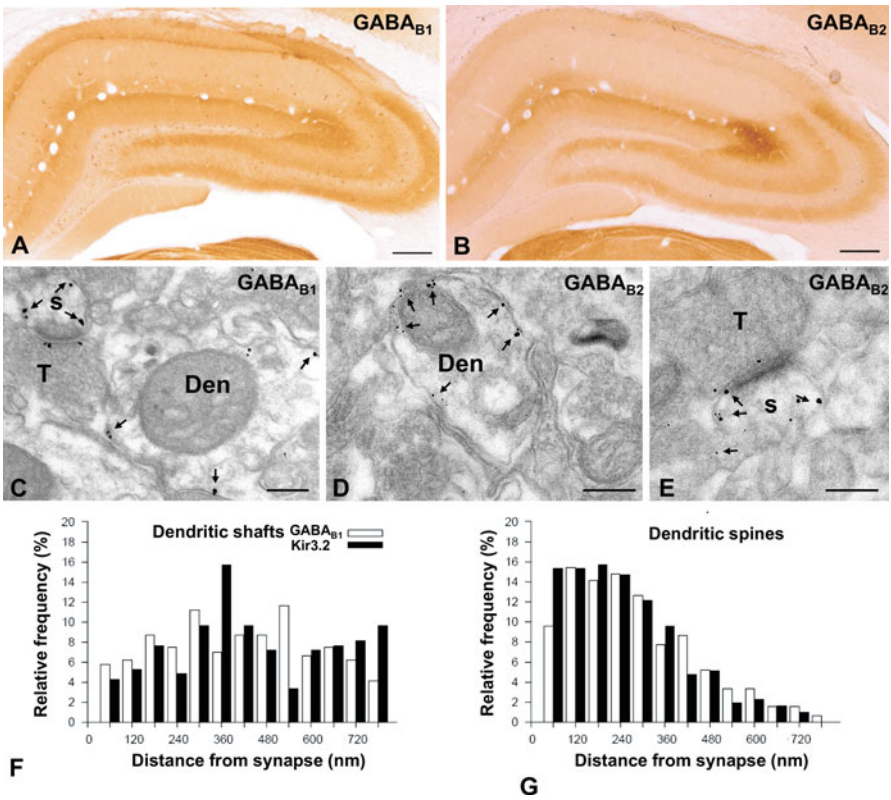

Fig. 3 Cellular and subcellular distribution of $GABA_BRs$ in the hippocampus. (**a** and **b**) Light micrographs show the distribution of immunoreactivity for $GABA_{B1}$ and $GABA_{B2}$ in the hippocampus. Strong labeling for the subunits was observed in dendritic layers of CA areas and dentate gyrus. Strong immunoreactivity for $GABA_{B1}$, but not for $GABA_{B2}$, was detected in somata of CA1 pyramidal cells and INs. (**c**–**e**), Electron micrographs show pre-embedding immunogold labeling for the receptor subunits in pre- and postsynaptic compartments of pyramidal cells. Immunogold particles for $GABA_{B1}$ and $GABA_{B2}$ were detected on the synaptic membranes (arrowheads in **c** and **e**) of the axon terminals (T), as well as on the extrasynaptic membranes (arrows in **c**–**e**) of dendritic spines (s) and dendritic shafts (Den) of pyramidal cells. (**f** and **g**) Histograms illustrate the distribution of immunoparticles for $GABA_{B1}$ and Kir3.2 relative to symmetrical and asymmetrical synapses on dendrites of CA1 pyramidal cells. Note the enrichment of both molecules in the vicinity of asymmetrical, putative glutamatergic synapses on dendritic spines (**g**), but not around symmetrical, putative inhibitory synapses on shafts (**f**). Scale bars: **a** and **b**, 200 μm; **c**–**e**, 0.2 μm (**a** adapted from Kulik et al. 2003; **f** and **g** adapted from Kulik et al. 2006 with permission, © Society for Neuroscience)

Presynaptically, the immunolabeling for $GABA_BRs$ is substantially weaker. Nevertheless, immunoreactivity has been consistently found in glutamatergic axon terminals forming asymmetrical synaptic contacts (Kulik et al. 2003). The labeling intensity was higher in these boutons than in putative inhibitory terminals making symmetrical synapses (see below). The receptor subunits were mainly detected

at the extrasynaptic plasma membrane and occasionally over the presynaptic membrane specialization (Fig. 3c, e; Kulik et al. 2003). Recent results further showed that, while postsynaptic receptors are mainly composed of the $GABA_{B1b}$ and $GABA_{B2}$ subunits ($GABA_{B(1b;2)}$ receptors), terminals of excitatory afferents, including the Schaffer collaterals and the MFs, preferentially contain receptors made up of $GABA_{B1a}$ and $GABA_{B2}$ subunits ($GABA_{B(1a;2)}$ receptors, Vigot et al. 2006; Guetg et al. 2009). Interestingly, receptors with the latter subunit composition have a higher sensitivity for baclofen and GABA and can mediate heterosynaptic inhibition of glutamatergic transmission by synaptically released GABA (Guetg et al. 2009).

Functional $GABA_BRs$ in Hippocampal Inhibitory Interneurons

In addition to labeling in PCs, immunoreactivity for $GABA_BR$ subunits was also found in various subpopulations of INs. At the light microscopic level, strong immunostaining for the $GABA_{B1}$ subunit, but not for the $GABA_{B2}$ subunit, is present in cell bodies of a subset of GABAergic INs scattered throughout the hippocampus (Fritschy et al. 1999; Margeta-Mitrovic et al. 1999; Sloviter et al. 1999; Kulik et al. 2003). Electron microscopic investigation demonstrated that the strong somatic immunoreactivity for $GABA_{B1}$ can be ascribed to the abundance of the protein in the endoplasmic reticulum (Kulik et al. 2003), conceivably reflecting a reserve pool of the receptor subunit. Fluorescence colocalization studies showed that INs with high somatic $GABA_{B1}$ include PV-, CCK-, SOM-, neuropeptide Y-, calbindin-, and calretinin-containing cells (Sloviter et al. 1999; Booker et al. 2013, 2017b). Ultrastructural analysis further demonstrated that immunoreactivity for $GABA_BRs$ is present postsynaptically along the extrasynaptic plasma membrane of dendritic shafts of NGFCs, PV-, CCK-, and SOM-expressing cells (Fig. 4a, b, f, g; Price et al. 2005; Booker et al. 2013, 2017b, 2018). Postsynaptic $GABA_BRs$ were found to activate Kir3 channels in PV- and CCK-expressing BCs producing substantial slow IPSCs (Fig. 4c, d, h; Booker et al. 2013, 2017b), consistent with the expression of both the receptor and Kir3 channels on their dendritic membrane surface. Interestingly, in DI PV- and CCK-positive INs slow $GABA_BR$ IPSCs were consistently smaller than in BCs suggesting IN type-specific expression of the functional receptors (Fig. 4e, h, i). Indeed, on archetypal dendrite-inhibiting SOM-INs postsynaptic $GABA_BRs$ failed to produce substantial inhibitory currents, despite the presence of immunolabeling for both the channel and the receptor on the dendrites of these INs. Instead, in SOM-INs $GABA_BR$ activation selectively inhibited $Ca_v1.2$ channels, leading to reduced Ca^{2+} influx and loss of LTP at excitatory synapses onto these INs (Booker et al. 2018).

Presynaptic $GABA_BRs$ were also observed in GABAergic axon terminals, albeit at lower levels than in excitatory boutons (Kulik et al. 2003). Similar to glutamatergic terminals, the labeling was mainly found on the extrasynaptic and, to a lower degree, on synaptic membrane segments of inhibitory boutons. IN type specific data is scarce, however, in two recent studies PV- and CCK-positive

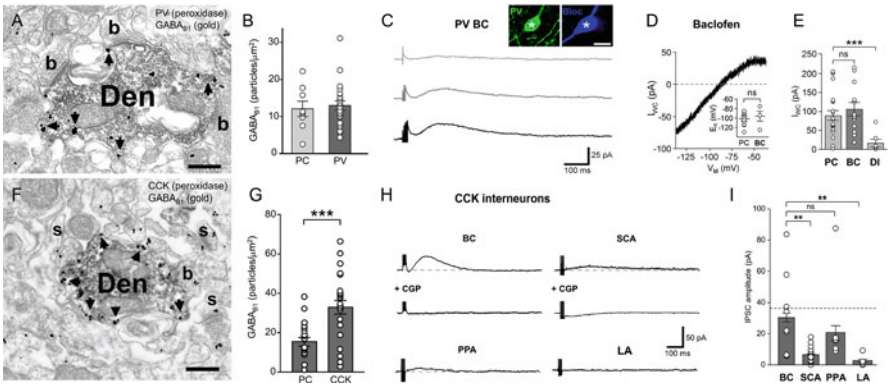

Fig. 4 Postsynaptic dendritic localization and effects of $GABA_BRs$ in hippocampal PV- and CCK-expressing INs. (**a** and **f**) Electron micrographs showing immunoreactivity for $GABA_{B1}$ (immunoparticles, arrows) in dendritic shafts (Den) of PV- (**a**, peroxidase reaction end product) and CCK-positive INs (**f**, peroxidase) contacted by presynaptic boutons (b) in the CA1 str. radiatum. (**b** and **g**), Summary bar charts of the surface density of immunoparticles in dendrites of principal cells (PC), PV- (**b**) and CCK-positive INs (**g**). (**c**) Pharmacologically isolated slow $GABA_BR$ IPSCs in a PV BC evoked by a single stimulus (top trace) or trains of 3 (middle) and 5 stimuli (bottom) elicited via an extracellular electrode. Inset shows the PV immunolabeling (left, green pseudocolor) in the biocytin-filled cell body (right, in blue). (**d**) Inwardly rectifying voltage dependence of the baclofen-induced current (I_{WC}) in a PV BC. Inset, summary of the reversal potential (E_R) of the baclofen-induced currents for PCs and BCs. (**e**) Summary chart of the baclofen-induced I_{WC} measured in PCs, PV-positive BCs and dendritic inhibitory (DI) INs. (**h**) Slow $GABA_BR$/Kir3-mediated IPSC in CCK-expressing INs elicited by 200 Hz train of 5 stimuli applied via an extracellular electrode. Slow IPSCs were recorded from a BC and a DI Schaffer collateral-associated cell (SCA), a perforant path-associated cell (PPA) and a lacunosum projecting cell (LA). The selective $GABA_BR$ antagonist CGP fully blocked the IPSCs in BC and SCA cells (bottom traces). (**i**) Summary bar chart of the $GABA_BR$-mediated IPSC amplitudes recorded from CCK IN types. Bar charts show mean ± SEM overlain by data from individual cells (open circles). Note that the mean IPSC in both PV and CCK DI cells was significantly smaller than in BCs. Scale bars: 0.2 μm (**a**–**e** from Booker et al. 2013, **f**–**J** from Booker et al. 2017b. Reproduced with permission, © Society for Neuroscience and Wiley-Blackwell)

putative BC terminals in the *str. pyramidale* of the CA1 area were investigated comparatively (Booker et al. 2013, 2017a). Results obtained from quantitative SDS-digested freeze-fracture replica (SDS-FRL) immunoelectron microscopic analysis demonstrated a differential expression in these two bouton populations, while $GABA_BRs$ were present at high densities on virtually all CB1-positive putative CCK terminals (Fig. 5a, b, e, f), they showed markedly lower densities and were expressed by only 40% of M2-positive putative PV boutons (Fig. 5c–f; Booker et al. 2017a). This expression pattern was in good agreement with the differential strength of presynaptic inhibition at these synapses: GABA release was dramatically (80–90%) inhibited by the receptor activation at CCK BC synapses, whereas it was reduced only moderately (~50%) at PV BC synapses (Fig. 5g–i).

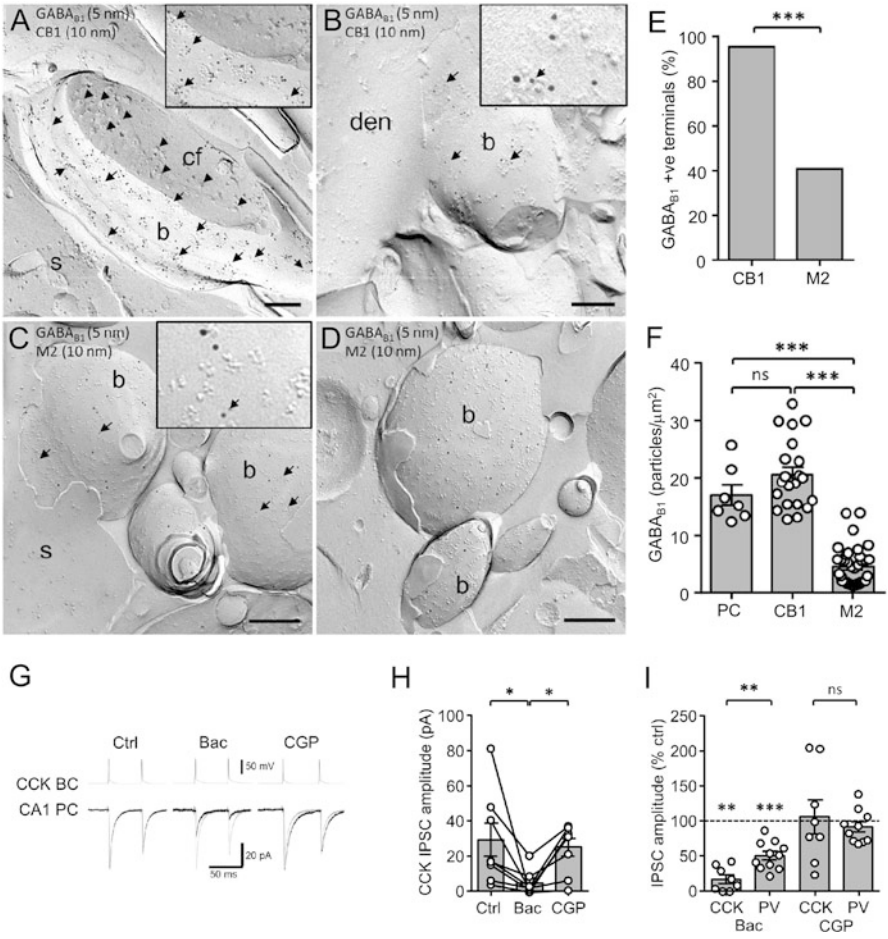

Fig. 5 Presynaptic axonal localization and effects of $GABA_BRs$ in hippocampal CCK- and PV-positive INs. (**a**–**d**) Electron micrographs of freeze-fracture replicas showing the surface distribution of $GABA_{B1}$ (5 nm particles, arrows) in CB1-positive (10 nm particles) putative CCK (**a** and **b**) and M2-positive (10 nm particles) putative PV boutons (*b*; **c** and **d**). (**e**) Summary bar chart of the proportion of $GABA_{B1}$ on double-labeled CB1 receptor – or M2 receptor – containing the axon terminals. (**f**) Quantification of the density of immunoparticles for $GABA_{B1}$ on CB1 receptor- and M2 receptor-positive axon terminals in comparison to PC dendrites. Statistics shown: *** $P < 0.0001$, Fisher's exact test and 1-way ANOVA with multiple comparisons. (**g**) Action potentials elicited in the CCK BC (upper traces) evoked unitary IPSCs in the PC (lower traces) under control conditions (Ctrl, left panel), during bath application of the $GABA_BR$ agonist baclofen (10 μM, middle) and the antagonist CGP (10 μM, right). (**h**) Summary chart of the IPSC amplitudes under control conditions, during baclofen and CGP application. (**i**) Summary bar chart of the normalized IPSC amplitudes for a comparison of baclofen-induced inhibition at CCK and PV BC synapses; recovery in CGP is shown for both types on the right. Statistics: ns $P \geq 0.05$, * $P \leq 0.05$, ** $P \leq 0.01$, *** $P \leq 0.001$. Abbreviations: cf, cross-fractured; S, soma; den, dendritic shaft. Scale bars, 0.2 μm. (Reproduced from Booker et al. 2017a, © The Authors)

Activation of $GABA_BRs$ by Spillover of GABA from Inhibitory Synapses

Conditions for the activation of $GABA_BRs$ differ dramatically from those of $GABA_ARs$ (Farrant and Nusser 2005; Kulik et al. 2017). Whereas $GABA_AR$-mediated responses are readily observed at low-stimulus intensities and in paired recordings of synaptically coupled neurons, strong and/or repetitive stimulation is required to elicit $GABA_BR$-mediated postsynaptic effects (Newberry and Nicoll 1985; Isaacson et al. 1993), indicating that recruitment of a number of GABAergic neurons and the release of larger amount of GABA is necessary for the activation of the receptors. It was estimated that the simultaneous recruitment of ~2–20 INs is required to induce slow $GABA_B$ IPSPs (Scanziani 2000).

These differences between the two receptor types appear to contradict the fact that the affinity of $GABA_BRs$ for GABA is ~16-fold higher than that of $GABA_ARs$. Sodickson and Bean (1996) showed that the EC_{50} for the activation of $GABA_BR$-mediated potassium conductance by GABA is much lower (1.6 mM) than for the activation of $GABA_AR$-mediated chloride conductance (25 mM). However, this apparent discrepancy can be explained by the differential localization of the two types: while $GABA_ARs$ are clustered primarily in synapses opposite to the GABA release sites (Nusser and Somogyi 1997; Farrant and Nusser 2005), $GABA_BRs$ are preferentially localized to the extrasynaptic membrane at some distance from GABAergic synapses (Kulik et al. 2003; Fig. 6). Thus, for the

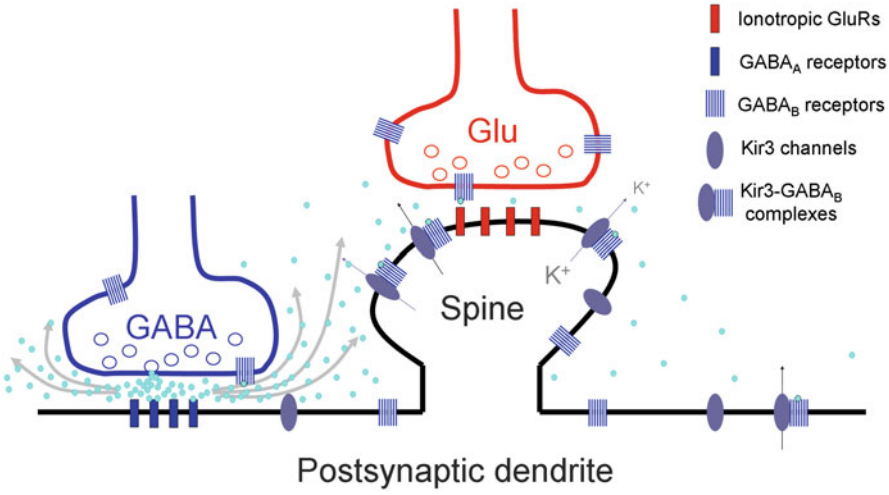

Fig. 6 Activation of the pre- and postsynaptic $GABA_BRs$ by GABA spillover from inhibitory terminals. Abbreviations: GABA – GABAergic terminal, Glu – glutamatergic terminals, blue circles represent GABA molecules released from the inhibitory terminal. (Modified from Kulik et al. 2003 with permission, © Society for Neuroscience)

activation of $GABA_BRs$ GABA needs to flow out from the inhibitory synapses and diffuses through the extracellular space before it can reach the receptors ("spillover hypothesis," Isaacson et al. 1993). In order to achieve sufficiently high concentration of GABA at the location of the receptors, release from larger number of GABAergic terminals is required in a given volume (Newberry and Nicoll 1985; Dutar and Nicoll 1988a; Otis et al. 1993; Brown et al. 2007). Recent studies have, however, provided evidence that single NGFCs can produce activation of $GABA_BRs$ in hippocampal and neocortical PCs (Tamás et al. 2003; Price et al. 2005, 2008; Oláh et al. 2009). A plausible explanation for this observation is that the highly dense focal axonal arbor of NGFCs enables this IN type to produce substantial volume transmission and evoke "unitary" $GABA_BR$-mediated responses in neighboring PyCs and other INs. Indeed, another study provides further evidence that GABA can spillover from synapses of NGFCs and activate extrasynaptic $GABA_ARs$ and plausibly also $GABA_BRs$ (Szabadics et al. 2007). However, in the presence of GABA uptake blockers, other IN types can also elicit $GABA_BR$-mediated currents in PCs and INs (Scanziani 2000; Booker et al. 2013), indicating that under physiological conditions efficient uptake mechanisms control activation of metabotropic GABA receptors in cortical networks.

In summary, under physiological conditions, $GABA_BR$-mediated responses are evoked upon concerted high activity of GABAergic INs. Such synchronous activity of large sets of INs occurs during network oscillations (see chapter "Cell Type-Specific Activity During Hippocampal Network Oscillations In Vitro") and can, indeed, lead to the activation of $GABA_BRs$ (Scanziani 2000). Conversely, $GABA_BR$-mediated effects can dynamically influence the frequency of the oscillations (Scanziani 2000; Booker et al. 2013). Thus, $GABA_BRs$ can serve an important regulatory mechanism during rhythmic oscillatory and other population patterns in vivo. Such a role was further substantiated in recent set of experiments using in vitro models of cortical Up and Down state population activity: in these models activation of $GABA_BRs$ promoted the termination of Up states recorded in the entorhinal cortex (Mann et al. 2009). This function of the receptors was contrasted by the role of $GABA_AR$-mediated inhibition, which was necessary for balancing persistent Up state activity (Mann et al. 2009). Interestingly, both pre- and postsynaptic $GABA_BRs$ were involved in the termination of Up states, but in a differential manner: while presynaptic receptors containing the $GABA_{B1a}$ subunit contributed to spontaneous ending of Up states (Craig et al. 2013), postsynaptic $GABA_BRs$ containing the $GABA_{B1b}$ subunit were found to be essential for afferent input-dependent active termination of Up states (Craig et al. 2013).

Future Perspectives

Although our understanding of the functional and dynamic properties of synaptic ionotropic $GABA_AR$- and the extrasynaptic, predominantly dendritic metabotropic $GABA_BR$-mediated signaling and the underlying mechanisms increased substan-

tially, several fundamental questions remained unanswered. What are the functional and dynamic characteristics of dendritically located GABAergic synapses? How does dendritic inhibition influence local integration of excitatory afferent inputs and thereby the input-output relation of target cells? How does dendritic inhibition contribute to neuronal network function such as information processing and network synchronization? Which other IN types express $GABA_BRs$ and how do they contribute to signaling at the level of the individual neurons and the network? What are the additional constituents of the pre- and postsynaptic $GABA_BR$ nanoenvironment? How dynamic is the functional and structural interaction of $GABA_BRs$ with auxiliary proteins, neurotransmitter receptors, and effector ion channels?

Answering these questions is challenging and requires new experimental strategies and concepts. First, paired whole-cell patch-clamp recordings from synaptically connected INs in combination with light and electron microscopic analyses are required to determine synaptic properties, identity of recorded IN types, as well as the number and location of inhibitory synapses. Second, voltage-sensitive dye imaging in combination with whole-cell recordings are needed to examine dendritic integration of inhibitory and excitatory inputs. Third, in vivo whole-cell recordings from IN types together with biochemical and high-resolution quantitative immunoelectron microscopy would be useful to examine the kinetic and dynamic characteristics of synaptic inputs and receptor-associated network in dependence on the activity state of cortical circuits. Finally, a combined experimental and computational approach based on optogenetic analysis of synaptic and intrinsic physiological properties would be important to model integrative properties of the various IN types and to develop complex networks in order to identify the functional contribution of individual cell types and their synapses to network activity and information processing and network synchronization.

References

Adelfinger L, Turecek R, Ivankova K, Jensen AA, Moss SJ, Gassmann M, Bettler B (2014) $GABA_B$ receptor phosphorylation regulates KCTD12-induced K^+ current desensitization. Biochem Pharmacol 91:369–379

Alger BE, Nicoll RA (1979) GABA-mediated biphasic inhibitory responses in hippocampus. Nature 281:315–317

Andersen P, Dingledine R, Gjerstad L, Langmoen IA, Laursen AM (1980) Two different responses of hippocampal pyramidal cells to application of gamma-amino butyric acid. J Physiol (Lond) 305:279–296

Andrade R, Malenka RC, Nicoll RA (1986) A G protein couples serotonin and $GABA_B$ receptors to the same channels in hippocampus. Science 234:1261–1265

Armstrong C, Szabadics J, Tamás G, Soltesz I (2011) Neurogliaform cells in the molecular layer of the dentate gyrus as feed-forward gamma-aminobutyric acidetic modulators of entorhinal-hippocampal interplay. J Comp Neurol 519:1476–1491

Banke TG, McBain CJ (2006) GABAergic input onto CA3 hippocampal interneurons remains shunting throughout development. J Neurosci 26:11720–11725

Banks MI, Li TB, Pearce RA (1998) The synaptic basis of $GABA_A$,slow. J Neurosci 18:1305–1317

Bartoi T, Rigbolt KT, Du D, Köhr G, Blagoev B, Kornau HC (2010) GABA receptor constituents revealed by tandem affinity purification from transgenic mice. J Biol Chem 285:20625–20633

Bartos M, Vida I, Frotscher M, Geiger JRP, Jonas P (2001) Rapid signaling at inhibitory synapses in a dentate gyrus interneuron network. J Neurosci 21:2687–2698

Bartos M, Vida I, Frotscher M, Meyer A, Monyer H, Geiger JRP, Jonas P (2002) Fast synaptic inhibition promotes synchronized gamma oscillations in hippocampal interneuron networks. Proc Natl Acad Sci U S A 99:13222–13227

Bartos M, Vida I, Jonas P (2007) Synaptic mechanisms of synchronized gamma oscillations in inhibitory interneuron networks. Nat Rev Neurosci 8:45–56

Bettler B, Fakler B (2017) Ionotropic AMPA-type glutamate and metabotropic $GABA_B$ receptors: determining cellular physiology by proteomes. Curr Opin Neurobiol 45:16–23

Bettler B, Kaupmann K, Mosbacher J, Gassmann M (2004) Molecular structure and physiological functions of GABA(B) receptors. Physiol Rev 84:835–867

Billinton A, Ige AO, Bolam JP, White JH, Marshall FH, Emson PC (2001) Advances in the molecular understanding of $GABA_B$ receptors. Trends Neurosci 24:277–282

Bischoff S, Leonhard S, Reymann N, Schuler V, Shigemoto R, Kaupmann K, Bettler B (1999) Spatial distribution of GABA(B)R1 receptor mRNA and binding sites in the rat brain. J Comp Neurol 412:1–16

Blasco-Ibáñez JM, Freund TF (1995) Synaptic input of horizontal interneurons in stratum oriens of the hippocampal CA1 subfield: structural basis of feed-back activation. Eur J Neurosci 7:2170–2180

Booker SA, Gross A, Althof D, Shigemoto R, Bettler B, Frotscher M, Hearing M, Wickman K, Watanabe M, Kulik Á, Vida I (2013) Differential $GABA_B$-receptor-mediated effects in perisomatic- and dendrite-targeting parvalbumin interneurons. J Neurosci 33:7961–7974

Booker SA, Althof D, Degro CE, Watanabe M, Kulik A, Vida I (2017a) Differential surface density and modulatory effects of presynaptic $GABA_B$ receptors in hippocampal cholecystokinin and parvalbumin basket cells. Brain Struct Funct 222:3677–3690

Booker SA, Althof D, Gross A, Loreth D, Müller J, Unger A, Fakler B, Varro A, Watanabe M, Gassmann M, Bettler B, Shigemoto R, Vida I, Kulik A (2017b) KCTD12 auxiliary proteins modulate kinetics of $GABA_B$ receptor-mediated inhibition in cholecystokinin-containing interneurons. Cereb Cortex 27:2318–2334

Booker SA, Loreth D, Gee AL, Watanabe M, Kind PC, Wyllie DJA, Kulik A, Vida I (2018) Postsynaptic $GABA_B$Rs inhibit L-type calcium channels and abolish long-term potentiation in hippocampal somatostatin interneurons. Cell Rep 22:36–43

Bowery NG, Hudson AL, Price GW (1987) $GABA_A$ and $GABA_B$ receptor site distribution in the rat central nervous system. Neuroscience 20:365–383

Brown JT, Davis CH, Randall AD (2007) Synaptic activation of $GABA_B$ receptors regulates neuronal network activity and entrainment. Eur J Neurosci 25:2982–2990

Bucurenciu I, Kulik A, Schwaller B, Frotscher M, Jonas P (2008) Nanodomain coupling between Ca^{2+} channels and Ca^{2+} sensors promotes fast and efficient transmitter release at a cortical GABAergic synapse. Neuron 57:536–545

Buhl EH, Halasy K, Somogyi P (1994) Diverse sources of hippocampal unitary inhibitory postsynaptic potentials and the number of synaptic release sites. Nature 368:823–828

Buhl EH, Cobb SR, Halasy K, Somogyi P (1995) Properties of unitary IPSPs evoked by anatomically identified basket cells in the rat hippocampus. Eur J Neurosci 7:1989–2004

Buzsáki G (1996) The hippocampo-neocortical dialogue. Cereb Cortex 6:81–92

Cardin JA (2016) Snapshots of the brain in action: local circuit operations through the lens of gamma-oscillations. J Neurosci 36:10496–10504

Cardin JA, Carlén M, Meletis K, Knoblich U, Zhang F, Deisseroth K, Tsai LH, Moore CI (2009) Driving fast-spiking cells induces gamma rhythm and controls sensory responses. Nature 459:663–667

Cathomas F, Stegen M, Sigrist H, Schmid L, Seifritz E, Gassmann M, Bettler B, Pryce CR (2015) Altered emotionality and neuronal excitability in mice lacking KCTD12, an auxiliary subunit of $GABA_B$ receptors associated with mood disorders. Transl Psychiatry 5:e510

Cathomas F, Sigrist H, Schmid L, Seifritz E, Gassmann M, Bettler B, Pryce CR (2017) Behavioural endophenotypes in mice lacking the auxiliary $GABA_B$ receptor subunit KCTD16. Behav Brain Res 317:393–400

Chalifoux JR, Carter AG (2011) $GABA_B$ receptor modulation of voltage-sensitive calcium channels in spines and dendrites. J Neurosci 31:4221–4232

Chavas J, Marty A (2003) Coexistence of excitatory and inhibitory GABA synapses in the cerebellar interneuron network. J Neurosci 23:2019–2031

Chu DCM, Albin RL, Young AB, Penney JB (1990) Distribution and kinetics of $GABA_B$ binding sites in rat central nervous system: a quantitative autoradiographic study. Neuroscience 34:341–357

Cobb SR, Buhl EH, Halasy K, Paulsen O, Somogyi P (1995) Synchronization of neuronal activity in hippocampus by individual GABAergic interneurons. Nature 378:75–78

Cope DW, Halbsguth C, Karayannis T, Wulff P, Ferraguti F, Hoeger H, Leppä E, Linden AM, Oberto A, Ogris W, Korpi ER, Sieghart W, Somogyi P, Wisden W, Capogna M (2005) Loss of zolpidem efficacy in the hippocampus of mice with the $GABA_A$ receptor gamma2 F77I point mutation. Eur J Neurosci 21:3002–3016

Craig MT, Mayne EW, Bettler B, Paulsen O, McBain CJ (2013) Distinct roles of $GABA_{B1a}$- and $GABA_{B1b}$-containing $GABA_B$ receptors in spontaneous and evoked termination of persistent cortical activity. J Physiol 591:835–843

Dascal N (1997) Signalling via the G protein-activated K^+ channels. Cell Signal 9:551–573

Davies CH, Collingridge GL (1993) The physiological regulation of synaptic inhibition by $GABA_B$ autoreceptors in rat hippocampus. J Physiol 472:245–265

Davies CH, Davies SN, Collingridge GL (1990) Paired-pulse depression of monosynaptic GABA-mediated inhibitory postsynaptic responses in rat hippocampus. J Physiol 424:513–531

Davies CH, Starkey SJ, Pozza MF, Collingridge GL (1991) GABA autoreceptors regulate the induction of LTP. Nature 349:609–611

Degro CE, Kulik A, Booker SA, Vida I (2015) Compartmental distribution of $GABA_B$ receptor-mediated currents along the somatodendritic axis of hippocampal principal cells. Front Synaptic Neurosci 7:6

Doischer D, Hosp JA, Yanagawa Y, Obata K, Jonas P, Vida I, Bartos M (2008) Postnatal differentiation of basket cells from slow to fast signaling devices. J Neurosci 28:12956–12968

Doze VA, Cohen GA, Madison DV (1995) Calcium channel involvement in $GABA_B$ receptor-mediated inhibition of GABA release in area CA1 of the rat hippocampus. J Neurophysiol 74:43–53

Dugladze T, Schmitz D, Whittington MA, Vida I, Gloveli T (2012) Segregation of axonal and somatic activity during fast network oscillations. Science 336:1458–1461

Duprat F, Lesage F, Guillemare E, Fink M, Hugnot J-P, Bigay J, Lazdunski M, Romey G, Barhanin J (1995) Heterologous multimeric assembly is essential for K^+ channel activity of neuronal and cardiac G-protein-activated inward rectifiers. Biochem Biophys Res Commun 212:657–663

Dutar P, Nicoll RA (1988a) A physiological role for $GABA_B$ receptors in the central nervous system. Nature 332:156–158

Dutar P, Nicoll RA (1988b) Pre- and postsynaptic $GABA_B$ receptors in the hippocampus have different pharmacological properties. Neuron 1:585–591

Ehrengruber MU, Doupnik CA, Xu Y, Garvey J, Jasek MC, Lester HA, Davidson N (1997) Activation of heteromeric G protein-gated inward rectifier K^+ channels overexpressed by adenovirus gene transfer inhibits the excitability of hippocampal neurons. Proc Natl Acad Sci U S A 94:7070–7075

Elfant D, Pál BZ, Emptage N, Capogna M (2008) Specific inhibitory synapses shift the balance from feedforward to feedback inhibition of hippocampal CA1 pyramidal cells. Eur J Neurosci 27:104–113

Elgueta C, Köhler J, Bartos M (2015) Persistent discharges in dentate gyrus perisoma-inhibiting interneurons require hyperpolarization-activated cyclic nucleotide-gated channel activation. J Neurosci 35:4131–4139

Farrant M, Nusser Z (2005) Variations on an inhibitory theme: phasic and tonic activation of $GABA_A$ receptors. Nat Rev Neurosci 6:215–229

Földy C, Neu A, Jones MV, Soltesz I (2006) Presynaptic, activity-dependent modulation of cannabinoid type 1 receptor-mediated inhibition of GABA release. J Neurosci 26:1465–1469

Freund TF (2003) Interneuron diversity series: rhythm and mood in perisomatic inhibition. Trends Neurosci 26:489–495

Freund TF, Buzsáki G (1996) Interneurons of the hippocampus. Hippocampus 6:347–470

Fritschy J-M, Möhler H (1995) $GABA_A$-receptor heterogeneity in the adult rat brain: differential regional and cellular distribution of seven major subunits. J Comp Neurol 359:154–194

Fritschy J-M, Meskenaite V, Weinmann O, Honer M, Benke D, Möhler H (1999) $GABA_B$-receptor splice variants GB1a and GB1b in rat brain: developmental regulation, cellular distribution and extrasynaptic localization. Eur J Neurosci 11:761–768

Fritzius T, Turecek R, Seddik R, Kobayashi H, Tiao J, Rem PD, Metz M, Kralikova M, Bouvier M, Gassmann M, Bettler B (2017) KCTD hetero-oligomers confer unique kinetic properties on hippocampal $GABA_B$ receptor-induced K^+ currents. J Neurosci 37:1162–1175

Gähwiler BH, Brown DA (1985) $GABA_B$-receptor-activated K^+ current in voltage-clamped CA3 pyramidal cells in hippocampal cultures. Proc Natl Acad Sci U S A 82:1558–1562

Gao B, Fritschy J-M (1994) Selective allocation of $GABA_A$ receptors containing the alpha 1 subunit to neurochemically distinct subpopulations of rat hippocampal interneurons. Eur J Neurosci 6:837–853

Gassmann M, Bettler B (2012) Regulation of neuronal $GABA_B$ receptor functions by subunit composition. Nat Rev Neurosci 13:380–394

Geiger JR, Jonas P (2000) Dynamic control of presynaptic Ca^{2+} inflow by fast-activating K^+ channels in hippocampal mossy fiber boutons. Neuron 28:927–939

Glickfeld LL, Scanziani M (2006) Distinct timing in the activity of cannabinoid-sensitive and cannabinoid-insensitive basket cells. Nat Neurosci 9:807–815

Glickfeld LL, Atallah BV, Scanziani M (2008) Complementary modulation of somatic inhibition by opioids and cannabinoids. J Neurosci 28:1824–1832

Glickfeld LL, Roberts JD, Somogyi P, Scanziani M (2009) Interneurons hyperpolarize pyramidal cells along their entire somatodendritic axis. Nat Neurosci 12:21–23

Glykys J, Mody I (2006) Hippocampal network hyperactivity after selective reduction of tonic inhibition in GABA A receptor apha5 subunit-deficient mice. J Neurophysiol 95:2796–2807

Guetg N, Seddik R, Vigot R, Turecek R, Gassmann M, Vogt KE, Bräuner-Osborne H, Shigemoto R, Kretz O, Frotscher M, Kulik A, Bettler B (2009) The $GABA_{B1a}$ isoform mediates heterosynaptic depression at hippocampal mossy fiber synapses. J Neurosci 29:1414–1423

Guetg N, Aziz SA, Holbro N, Turecek R, Rose T, Seddik R, Gassmann M, Moes S, Jenoe P, Oertner TG, Casanova E, Bettler B (2010) NMDA receptor-dependent $GABA_B$ receptor internalization via CaMKII phosphorylation of serine 867 in $GABA_{B1}$. Proc Natl Acad Sci U S A 107:13924–13929

Gulyás AI, Miles R, Hájos N, Freund TF (1993) Precision and variability in postsynaptic target selection of inhibitory cells in the hippocampal CA3 region. Eur J Neurosci 5:1729–1751

Han Z, Buhl E, Lörinczi Z, Somogyi P (1993) A high degree of spatial selectivity in the axonal and dendritic domains of physiologically identified local-circuit neurons in the dentate gyrus of the rat hippocampus. Eur J Neurosci 5:396–410

Harney SC, Jones MV (2002) Pre- and postsynaptic properties of somatic and dendritic inhibition in dentate gyrus. Neuropharmacology 43:584–594

Harrison NL (1990) On the presynaptic action of baclofen at inhibitory synapses between cultured rat hippocampal neurones. J Physiol 422:433–446

Häusser M, Roth A (1997) Estimating the time course of the excitatory synaptic conductance in neocortical pyramidal cells using a novel voltage jump method. J Neurosci 17:7606–7625

Hefft S, Jonas P (2005) Asynchronous GABA release generates long-lasting inhibition at a hippocampal interneuron-principal neuron synapse. Nat Neurosci 8:1319–1328

Hosp JA, Strüber M, Yanagawa Y, Obata K, Vida I, Jonas P, Bartos M (2014) Morpho-physiological criteria divide dentate gyrus interneurons into classes. Hippocampus 24:189–203

Huang CS, Shi S-H, Ule J, Ruggiu M, Barker LA, Darnell RB, Jan YN, Jan LY (2005) Common molecular pathways mediate long-term potentation of synaptic excitation and slow synaptic inhibition. Cell 123:105–118

Inanobe A, Ito H, Ito M, Hosoya Y, Kurachi Y (1995) Immunological and physical characterization of the brain G protein-gated muscarinic potassium channel. Biochem Biophys Res Commun 217:1238–1244

Inanobe A, Yoshimoto Y, Horio Y, Morishige K-I, Hibino H, Matsumoto S, Tokunaga Y, Maeda T, Hata Y, Takai Y, Kurachi Y (1999) Characterization of G-protein-gated K^+ channels composed of Kir3.2 subunits in dopaminergic neurons of the substantia nigra. J Neurosci 19:1006–1013

Isaacson JS, Solís JM, Nicoll RA (1993) Local and diffuse synaptic actions of GABA in the hippocampus. Neuron 10:165–175

Isomoto S, Kaibara M, Sakurai-Yamashita Y, Nagayama Y, Uezono Y, Yano K, Taniyama K (1998) Cloning and tissue distribution of novel splice variants of the rat $GABA_B$ receptor. Biochem Biophys Res Commun 253:10–15

Jarolimek W, Misgeld U (1997) $GABA_B$ receptor-mediated inhibition of tetrodotoxin-resistant GABA release in rodent hippocampal CA1 pyramidal cells. J Neurosci 17:1025–1032

Johnston D, Brown TH (1983) Interpretation of voltage-clamp measurements in hippocampal neurons. J Neurophysiol 50:464–486

Jonas P, Bischofberger J, Fricker D, Miles R (2004) Interneuron diversity series: fast in, fast out – temporal and spatial signal processing in hippocampal interneurons. Trends Neurosci 27:30–40

Jones KA, Borowsky B, Tamm JA, Craig DA, Durkin MM, Dai M, Yao WJ, Johnson M, Gunwaldsen C, Huang LY, Tang C, Shen Q, Salon JA, Morse K, Laz T, Smith KE, Nagarathnam D, Noble SA, Branchek TA, Gerald C (1998) GABA(B) receptors function as a heteromeric assembly of the subunits GABA(B)R1 and GABA(B)R2. Nature 396:674–679

Katona I, Acsády L, Freund TF (1999) Postsynaptic targets of somatostatin-immunoreactive interneurons in the rat hippocampus. Neuroscience 88:37–55

Katona I, Lapray D, Viney TJ, Oulhaj A, Borhegyi Z, Micklem BR, Klausberger T, Somogyi P (2014) Sleep and movement differentiates actions of two types of somatostatin-expressing GABAergic interneuron in rat hippocampus. Neuron 82:872–886

Kaupmann K, Huggel K, Heid J, Flor PJ, Bischoff S, Mickel SJ, McMaster G, Angst C, Bittiger H, Froestl W, Bettler B (1997) Expression cloning of GABA(B) receptors uncovers similarity to metabotropic glutamate receptors. Nature 386:239–246

Kaupmann K, Malitschek B, Schuler V, Heid J, Froestl W, Beck P, Mosbacher J, Bischoff S, Kulik A, Shigemoto R, Karschin A, Bettler B (1998a) GABA(B)-receptor subtypes assemble into functional heteromeric complexes. Nature 396:683–687

Kaupmann K, Schuler V, Mosbacher J, Bischoff S, Bittiger H, Heid J, Froestl W, Leonhard S, Pfaff T, Karschin A, Bettler B (1998b) Human gamma-aminobutyric acid type B receptors are differentially expressed and regulate inwardly rectifying K^+ channels. Proc Natl Acad Sci U S A 95:14991–14996

Khazipov R, Congar P, Ben-Ari Y (1995) Hippocampal CA1 lacunosum-moleculare interneurons: modulation of monosynaptic GABAergic IPSCs by presynaptic $GABA_B$ receptors. J Neurophysiol 74:2126–2137

Klausberger T, Somogyi P (2008) Neuronal diversity and temporal dynamics: the unity of hippocampal circuit operations. Science 321:53–57

Klausberger T, David J, Roberts B, Somogyi P (2002) Cell type- and input-specific differences in the number and subtypes of synaptic $GABA_A$ receptors in the hippocampus. J Neurosci 22:2513–2521

Kofuji P, Davidson N, Lester HA (1995) Evidence that neuronal G-protein-gated inwardly rectifying K^+ channels are activated by G beta gamma subunits and function as heteromultimers. Proc Natl Acad Sci U S A 92:6542–6546

Koyrakh L, Luján R, Colón J, Karschin C, Kurachi Y, Karschin A, Wickman K (2005) Molecular and cellular diversity of neuronal G-protein-gated potassium channels. J Neurosci 25:11468–11478

Krapivinsky G, Gordon EA, Wickman K, Velimirović B, Krapivinsky L, Clapham DE (1995) The G-protein-gated atrial K^+ channel IKACh is a heteromultimer of two inwardly rectifying K(+)-channel proteins. Nature 374:135–141

Kraushaar U, Jonas P (2000) Efficacy and stability of quantal GABA release at a hippocampal interneuron-principal neuron synapse. J Neurosci 20:5594–5607

Kulik A, Nakadate K, Nyíri G, Notomi T, Malitschek B, Bettler B, Shigemoto R (2002) Distinct localization of GABA(B) receptors relative to synaptic sites in the rat cerebellum and ventrobasal thalamus. Eur J Neurosci 15:291–307

Kulik A, Vida I, Luján R, Haas CA, López-Bendito G, Shigemoto R, Frotscher M (2003) Subcellular localization of metabotropic $GABA_B$ receptor subunits $GABA_{B1a/b}$ and $GABA_{B2}$ in the rat hippocampus. J Neurosci 23:11026–11035

Kulik A, Vida I, Fukazawa Y, Guetg N, Kasugai Y, Marker CL, Rigato F, Bettler B, Wickman K, Frotscher M, Shigemoto R (2006) Compartment-dependent colocalization of Kir3.2-containing K^+ channels and $GABA_B$ receptors in hippocampal pyramidal cells. J Neurosci 26:4289–4297

Kulik A, Booker SA, Vida I (2017) Differential distribution and function of $GABA_B$Rs in somato-dendritic and axonal compartments of principal cells and interneurons in cortical circuits. Neuropharmacology 136:80–91. https://doi.org/10.1016/j.neuropharm.2017.10.018 pii: S0028-3908(17)30485-9

Kuner R, Köhr G, Grünewald S, Eisenhardt G, Bach A, Kornau HC (1999) Role of heteromer formation in $GABA_B$ receptor function. Science 283:74–77

Kyrozis A, Reichling DB (1995) Perforated-patch recording with gramicidin avoids artifactual changes in intracellular chloride concentration. J Neurosci Methods 57:27–35

Lamsa K, Taira T (2003) Use-dependent shift from inhibitory to excitatory $GABA_A$ receptor action in SP-O interneurons in the rat hippocampal CA3 area. J Neurophysiol 90:1983–1995

Larkum ME, Waters J, Sakmann B, Helmchen F (2007) Dendritic spikes in apical dendrites of neocortical layer 2/3 pyramidal neurons. J Neurosci 27:8999–9008

Laviv T, Vertkin I, Berdichevsky Y, Fogel H, Riven I, Bettler B, Slesinger PA, Slutsky I (2011) Compartmentalization of the $GABA_B$ receptor signaling complex is required for presynaptic inhibition at hippocampal synepses. J Neurosci 31:12523–12532

Lavoie AM, Tingey JJ, Harrison NL, Pritchett DB, Twyman RE (1997) Activation and deactivation rates of recombinant $GABA_A$ receptor channels are dependent on alpha-subunit isoform. Biophys J 73:2518–2526

Leaney JL (2003) Contribution of Kir3.1, Kir3.2A and Kir3.2C subunits to native G protein-gated inwardly rectifying potassium currents in cultured hippocampal neurons. Eur J Neurosci 18:2110–2118

Lee C, Mayfield RD, Harris RA (2010) Intron 4 containing novel $GABA_{B1}$ isoforms impair $GABA_B$ receptor function. PLoS One 5:e14044

Lei S, McBain CJ (2003) $GABA_B$ receptor modulation of excitatory and inhibitory synaptic transmission onto rat CA3 hippocampal interneurons. J Physiol 546:439–453

Lesage F, Guillemare E, Fink M, Duprat F, Heurteaux C, Fosset M, Roemy G, Barhanin J, Lazdunski M (1995) Molecular properties of neuronal G-protein-activated inwardly rectifying K^+ channels. J Biol Chem 270:28660–28667

Liao YJ, Jan YN, Jan LY (1996) Heteromultimerization of G-protein-gated inwardly rectifying K^+ channel proteins GIRK1 and GIRK2 and their altered expression in *weaver* brain. J Neurosci 16:7137–7150

Ling DS, Benardo LS (1994) Properties of isolated $GABA_B$-mediated inhibitory postsynaptic currents in hippocampal pyramidal cells. Neuroscience 63:937–944

Liu YC, Cheng JK, Lien CC (2014) Rapid dynamic changes of dendritic inhibition in the dentate gyrus by presynaptic activity patterns. J Neurosci 34:1344–1357

Losonczy A, Biró AA, Nusser Z (2004) Persistently active cannabinoid receptors mute a subpopulation of hippocampal interneurons. Proc Natl Acad Sci U S A 101:1362–1367

Lovett-Barron BV, Kaifosh P, Kheirbek MA, Danielsaon N, Zaremba JD, Readron TR, Turi GF, Hen R, Zemelman BV, Losonczy A (2014) Dendritic inhibition in the hippocampus supports fear learning. Science 343:857–863

Lujan R, Maylie J, Adelman JP (2009) New sites of action for GIRK and SK channels. Nat Rev Neurosci 10:475–480

Lüscher C, Jan LY, Stoffel M, Malenka RC, Nicoll RA (1997) G protein-coupled inwardly rectifying K^+ channels (GIRKs) mediate postsynaptic but not presynaptic transmitter actions in hippocampal neurons. Neuron 19:687–695

Ma D, Zerrangue N, Raab-Graham K, Fried SR, Jan YN, Jan LY (2002) Diverse trafficking patterns due to multiple traffic motifs in G protein-activated inwardly rectifying potassium channels from brain and heart. Neuron 33:715–729

Maccaferri G, Roberts JD, Szucs P, Cottingham CA, Somogyi P (2000) Cell surface domain specific postsynaptic currents evoked by identified GABAergic neurones in rat hippocampus *in vitro*. J Physiol 524:91–116

Major G, Evans JD, Jack JJB (1993) Solutions for transients in arbitrarily branching cables: II. Voltage clamp theory. Biophys J 65:450–468

Makara JK, Losonczy A, Wen Q, Magee JC (2009) Experience-dependent compartmentalized dendritic plasticity in rat hippocampal CA1 pyramidal neurons. Nat Neurosci 12:1485–1487

Malenka RC, Bear MF (2004) LTP and LTD: an embarrassment of riches. Neuron 44:5–21

Malinow R, Tsien RW (1990) Presynaptic enhancement shown by whole-cell recordings of long-term potentiation in hippocampal slices. Nature 346:177–180

Mann EO, Suckling JM, Hajos N, Greenfield SA, Paulsen O (2005) Perisomatic feedback inhibition underlies cholinergically induced fast network oscillations in the rat hippocampus *in vitro*. Neuron 45:105–117

Mann EO, Kohl MM, Paulsen O (2009) Distinct roles of GABA(A) and GABA(B) receptors in balancing and terminating persistent cortical activity. J Neurosci 29:7513–7518

Margeta-Mitrovic M, Mitrovic I, Riley RC, Jan LY, Basbaum AI (1999) Immunohistochemical localization of GABA(B) receptors in the rat central nervous system. J Comp Neurol 405:299–321

Marshall FH, White J, Main M, Green A, Wise A (1999) GABA(B) receptors function as heterodimers. Biochem Soc Trans 27:530–535

Martina M, Royer S, Paré D (2001) Cell-type-specific GABA responses and chloride homeostasis in the cortex and amygdala. J Neurophysiol 86:2887–2895

Mátyás F, Freund TF, Gulyás AI (2004) Immunocytochemically defined interneuron populations in the hippocampus of mouse strains used in transgenic technology. Hippocampus 14:460–481

McBain CJ, Fisahn A (2001) Interneurons unbound. Nat Rev Neurosci 2:11–23

Metz M, Gassmann M, Fakler B, Schaeren-Wiemers N, Bettler B (2011) Distribution of the auxiliary $GABA_B$ receptor subunits KCTD8, 12, 12b, and 16 in the mouse brain. J Comp Neurol 519:1435–1454

Miles R, Tóth K, Gulyás AI, Hájos N, Freund TF (1996) Differences between somatic and dendritic inhibition in the hippocampus. Neuron 16:815–823

Mitchell SJ, Silver RA (2003) Shunting inhibition modulates neuronal gain during synaptic excitation. Neuron 38:433–445

Mittmann W, Koch U, Häusser M (2005) Feed-forward inhibition shapes the spike output of cerebellar Purkinje cells. J Physiol 563:369–378

Mott DD, Lewis DV (1991) Facilitation of the induction of long-term potentiation by $GABA_B$ receptors. Science 252:1718–1720

Mott DD, Li Q, Okazaki MM, Turner DA, Lewis DV (1999) $GABA_B$-receptor-mediated currents in interneurons of the dentate-hilus border. J Neurophysiol 82:1438–1450

Müller C, Beck H, Coulter D, Remy S (2012) Inhibitory control of linear and supralinear dendritic excitation in CA1 pyramidal neurons. Neuron. 75:851–864

Neu A, Földy C, Soltesz I (2007) Postsynaptic origin of CB1-dependent tonic inhibition of GABA release at cholecystokinin-positive basket cell to pyramidal cell synapses in the CA1 region of the rat hippocampus. J Physiol 578:233–247

Newberry NR, Nicoll RA (1984) Direct hyperpolarizing action of baclofen on hippocampal pyramidal cells. Nature 308:450–452

Newberry NR, Nicoll RA (1985) Comparison of the action of baclofen with γ-aminobutyric acid on rat hippocampal pyramidal cells *in vitro*. J Physiol 360:161–185

Nusser Z, Mody I (2002) Selective modulation of tonic and phasic inhibitions in dentate gyrus granule cells. J Neurophysiol 87:2624–2628

Nusser Z, Somogyi P (1997) Compartmentalised distribution of $GABA_A$ and glutamate receptors in relation to transmitter release sites on the surface of cerebellar neurones. Prog Brain Res 114:109–127

Nyíri G, Freund TF, Somogyi P (2001) Input-dependent synaptic targeting of alpha(2)-subunit-containing GABA(A) receptors in synapses of hippocampal pyramidal cells of the rat. Eur J Neurosci 13:428–442

Oláh S, Füle M, Komlósi G, Varga C, Báldi R, Barzó P, Tamás G (2009) Regulation of cortical microcircuits by unitary GABA-mediated volume transmission. Nature 461:1278–1281

Otis TS, De Koninck Y, Mody I (1993) Characterization of synaptically elicited $GABA_B$ responses using patch-clamp recordings in rat hippocampal slices. J Physiol 463:391–407

Otmakhova NA, Lisman JE (2004) Contribution of I_h and $GABA_B$ to synaptically induced afterhyperpolarizations in CA1: a brake on the NMDA response. J Neurophysiol 92:2027–2039

Overstreet-Wadiche L, Bromberg DA, Bensen AL, Westbrook GL (2005) GABAergic signaling to newborn neurons in dentate gyrus. J Neurophysiol 94:4528–4532

Pearce RA (1993) Physiological evidence for two distinct $GABA_A$ responses in rat hippocampus. Neuron 10:189–200

Pérez-Garci E, Gassmann M, Bettler B, Larkum ME (2006) The $GABA_{B1b}$ isoform mediates long-lasting inhibition of dendritic Ca^{2+} spikes in layer 5 somato-sensory pyramidal neurons. Neuron 50:603–616

Pérez-Garci E, Larkum ME, Nevian T (2013) Inhibition of dendritic Ca^{2+} spikes by $GABA_B$ receptors in cortical pyramidal neurons is mediated by a direct $G_{i/o}$-β-subunit interaction with Ca_v1 channels. J Physiol 591:1599–1612

Pettem KL, Yokomaku D, Luo L, Linhoff MW, Prasad T, Connor SA, Siddiqui TJ, Kawabe H, Chen F, Zhang L, Rudenko G, Wang YT, Brose N, Craig AM (2013) The specific α-neuroxin interactor calsyntenin-3 promotes excitatory and inhibitory synapses development. Neuron 80:113–128

Pfaff T, Malitschek B, Kaupmann K, Prézeau L, Pin JP, Bettler B, Karschin A (1999) Alternative splicing generates a novel isoform of the rat metabotropic GABA(B)R1 receptor. Eur J Neurosci 11:2874–2882

Pin JP, Bettler B (2016) Organization and functions of mGlu and $GABA_B$ receptor complexes. Nature 540:60–68

Poncer JC, McKinney RA, Gähwiler BH, Thompson SM (2000) Differential control of GABA release at synapses from distinct interneurons in rat hippocampus. J Physiol 1:123–130

Pouille F, Scanziani M (2001) Enforcement of temporal fidelity in pyramidal cells by somatic feed-forward inhibition. Science 293:1159–1163

Price CJ, Cauli B, Kovacs ER, Kulik A, Lambolez B, Shigemoto R, Capogna M (2005) Neurogliaform neurons form a novel inhibitory network in the hippocampal CA1 area. J Neurosci 25:6775–6786

Price CJ, Scott R, Rusakov DA, Capogna M (2008) $GABA_B$ receptor modulation of feedforward inhibition through hippocampal neurogliaform cells. J Neurosci 28:6974–6982

Rajalu M, Fritzius T, Adelfinger L, Jacquier V, Besseyrias V, Gassmann M, Bettler B (2015) Pharmacological characterization of $GABA_B$ receptors with auxiliary KCTD subunits. Neuropharmacology 88:145–154

Rall W, Segev I (1985) Space-clamp problems when voltage clamping branched neurons with intracellular microelectrodes. In: Smith TG Jr, Lecar H, Redman SJ, Gage P (eds) Voltage and patch clamping with microelectrodes. American Physiological Society, Bethesda, pp 191–215

Riekki R, Pavlov I, Tornberg J, Lauri SE, Airaksinen MS, Taira T (2008) Altered synaptic dynamics and hippocampal excitability but normal long-term plasticity in mice lacking hyperpolarizing $GABA_A$ receptor-mediated inhibition in CA1 pyramidal neurons. J Neurophysiol 99:3075–3089

Rossi P, Mapelli L, Roggeri L, Gall D, de Kerchove d'Exaerde A, Schiffmann SN, Taglietti V, D'Angelo E (2006) Inhibition of constitutive inward rectifier currents in cerebellar granule cells by pharmacological and synaptic activation of GABA receptors. Eur J Neurosci 24:419–432

Royer S, Zemelman BV, Losonczy A, Kim J, Chance F, Magee JC, Buzsáki G (2012) Control of timing, rate and bursts of hippocampal place cells by dendritic and somatic inhibition. Nat Neurosci 15:769–775

Sakaba T, Neher E (2003) Direct modulation of synaptic vesicle priming by $GABA_B$ receptor activation at a glutamatergic synapse. Nature 424:775–778

Sauer JF, Strüber M, Bartos M (2012) Interneurons provide circuit-specific depolarization and hyperpolarization. J Neurosci 32:4224–4229

Savanthrapadian S, Meyer T, Elgueta C, Booker SA, Vida I, Bartos M (2014) Synaptic properties of SOM- and CCK-expressing cells in dentate gyrus interneuron networks. J Neurosci 34:8197–8209

Scanziani M (2000) GABA spillover activates postsynaptic $GABA_B$ receptors to control rhythmic hippocampal activity. Neuron 25:673–681

Scholz KP, Miller RJ (1991) $GABA_B$ receptor-mediated inhibition of Ca^{2+} currents and synaptic transmission in cultured rat hippocampal neurones. J Physiol 444:669–686

Schwarz DA, Barry G, Eliasof SD, Petroski RE, Conlon PJ, Maki RA (2000) Characterization of γ-aminobutyric acid receptor GABAB(1e), a GABAB(1) splice variant encoding a truncated receptor. J Biol Chem 275:32174–32181

Schwenk J, Metz M, Zolles G, Turecek R, Fritzius T, Bildl W, Tarusawa E, Kulik A, Unger A, Ivankova K, Seddik R, Tiao JY, Rajalu M, Trojanova J, Rohde V, Gassmann M, Schulte U, Fakler B, Bettler B (2010) Native $GABA_B$ receptors are heteromultimers with a family of auxiliary subunits. Nature 465:231–235

Schwenk J, Pérez-Garci E, Schneider A, Kollewe A, Gauthier-Kemper A, Fritzius T, Raveh A, Dinamarca MC, Hanuschkin A, Bildl W, Klingauf J, Gassmann M, Schulte U, Bettler B, Fakler B (2016) Modular composition and dynamics of native $GABA_B$ receptors identified by high-resolution proteomics. Nat Neurosci 19:233–242

Scimemi A, Semyanov A, Sperk G, Kullmann DM, Walker MC (2005) Multiple and plastic receptors mediate tonic $GABA_A$ receptor currents in the hippocampus. J Neurosci 25:10016–10024

Shaban H, Humeau Y, Herry C, Cassasus G, Shigemoto R, Ciocchi S, Barbieri S, van der Putten H, Kaupmann K, Bettler B, Lüthi A (2006) Generalization of amygdala LTP and conditioned fear in the absence of presynaptic inhibition. Nat Neurosci 9:1028–1035

Sibbe M, Kulik A (2017) GABAergic regulation of adult hippocampal neurogenesis. Mol Neurobiol 54:5497–5510

Signorini S, Liao YJ, Duncan SA, Jan LY, Stoffel M (1997) Normal cerebellar development but susceptibility to seizures in mice lacking G protein-coupled, inwardly rectifying K^+ channel GIRK2. Proc Natl Acad Sci U S A 94:923–927

Sik A, Penttonen M, Ylinen A, Buzsáki G (1995) Hippocampal CA1 interneurons: an *in vivo* intracellular labeling study. J Neurosci 15:6651–6665

Slesinger PA, Patil N, Liao J, Jan YN, Jan LY, Cox DR (1996) Functional effects of the mouse *weaver* mutation on G protein-gated inwardly rectifying K^+ channels. Neuron 16:321–331

Sloviter RS, Ali-Akbarian L, Elliott RC, Bowery BJ, Bowery NG (1999) Localization of GABA(B) (R1) receptors in the rat hippocampus by immunocytochemistry and high resolution autoradiography, with specific reference to its localization in identified hippocampal interneuron subpopulations. Neuropharmacology 38:1707–1721

Sodickson DL, Bean BP (1996) $GABA_B$ receptor-activated inwardly rectifying potassium current in dissociated hippocampal CA3 neurons. J Neurosci 16:6374–6385

Sohal VS (2016) How close are we to understanding what (if anything) γ oscillations do in cortical circuits? J Neurosci 36:10489–10495

Sohal VS, Hasselmo ME (1998) $GABA_B$ modulation improves sequence disambiguation in computational models of hippocampal region CA3. Hippocampus 8:171–193

Sohal VS, Zhang F, Yizhar O, Deisseroth K (2009) Parvalbumin neurons and gamma rhythms enhance cortical circuit performance. Nature 459:698–702

Solís JM, Nicoll RA (1992) Pharmacological characterization of $GABA_B$-mediated responses in the CA1 region of the rat hippocampal slice. J Neurosci 12:3466–3472

Somogyi P, Freund TF, Hodgson AJ, Somogyi J, Beroukas D, Chubb IW (1985) Identified axo-axonic cells are immunoreactive for GABA in the hippocampus and visual cortex of cat. Brain Res 332:143–149

Soriano E, Nitsch R, Frotscher M (1990) Axo-axonic chandelier cells in the rat fascia dentata: Golgi-electron microscopy and immunocytochemical studies. J Comp Neurol 293:1–25

Spauschus A, Lentes KU, Wischmeyer E, Dissmann E, Karschin C, Karschin A (1996) A G-protein-activated inwardly rectifying K^+ channel (GIRK4) from human hippocampus associates with other GIRK channels. J Neurosci 16:930–938

Staley KJ, Mody I (1992) Shunting of excitatory input to dentate gyrus granule cells by a depolarizing $GABA_A$ receptor-mediated postsynaptic conductance. J Neurophysiol 68:197–212

Strüber M, Jonas P, Bartos M (2015) Strength and duration of perisomatic GABAergic inhibition depend on distance between synaptically connected cells. Proc Natl Acad Sci U S A 112:1220–1225

Strüber M, Sauer JF, Jonas P, Bartos M (2017) Distance-dependent inhibition facilitates focality of gamma oscillations in the dentate gyrus. Nat Commun 8:758

Szabadics J, Varga C, Molnár G, Oláh S, Barzó P, Tamás G (2006) Excitatory effect of GABAergic axo-axonic cells in cortical microcircuits. Science 311:233–235

Szabadics J, Tamás G, Soltesz I (2007) Different transmitter transients underlie presynaptic cell type specificity of $GABA_A$,slow and $GABA_A$,fast. Proc Natl Acad Sci U S A 104:14831–14836

Szabó GG, Holderith N, Gulyás AI, Freund TF, Hájos N (2010) Distinct synaptic properties of perisomatic inhibitory cell types and their different modulation by cholinergic receptor activation in the CA3 region of the mouse hippocampus. Eur J Neurosci 31:2234–2246

Takahashi T, Kajikawa Y, Tsujimoto T (1998) G-protein-coupled modulation of presynaptic calcium currents and transmitter release by a $GABA_B$ receptor. J Neurosci 18:3138–3146

Tamás G, Lörincz A, Simon A, Szabadics J (2003) Identified sources and targets of slow inhibition in the neocortex. Science 299:1902–1905

Terunuma M, Vargas KJ, Wilkins ME, Ramirez OA, Jaureguiberry-Bravo M, Pangalos MN, Smart TG, Moss SJ, Couve A (2010) Prolonged activation of NMDA receptors promotes dephosphorylation and alters postendocytic sorting of $GABA_B$ receptors. Proc Natl Acad Sci U S A 107:13918–13923

Thompson SM, Gähwiler BH (1992) Comparison of the actions of baclofen at pre- and postsynaptic receptors in the rat hippocampus *in vitro*. J Physiol 451:329–345

Thomson AM, Bannister AP, Hughes DI, Pawelzik H (2000) Differential sensitivity to zolpidem of IPSPs activated by morphologically identified CA1 interneurons in slices of rat hippocampus. Eur J Neurosci 12:425–436

Tiao JY, Bradaia A, Biermann B, Kaupmann K, Metz M, Haller C, Rolink AG, Pless E, Barlow PN, Gassmann M, Bettler B (2008) The sushi domains of secreted $GABA_{B1}$ isoforms selectively impair $GABA_B$ heteroreceptor function. J Biol Chem 283:31005–31011

Tozuka Y, Fukuda S, Namba T, Seki T, Hisatsune T (2005) GABAergic excitation promotes neuronal differentiation in adult hippocampal progenitor cells. Neuron 47:803–815

Tukker JJ, Fuentealba P, Hartwich K, Somogyi P, Klausberger T (2007) Cell type-specific tuning of hippocampal interneuron firing during gamma oscillations in vivo. J Neurosci 27:8184–8189

Turecek R, Schwenk J, Fritzius T, Ivankova K, Zolles G, Adelfinger L, Jacquier V, Besseyrias V, Gassmann M, Schulte U, Fakler B, Bettler B (2014) Auxiliary $GABA_B$ receptor subunits uncouple G protein βγ subunits from effector channels to induce desensitization. Neuron 82:1032–1044

Tyan L, Chamberland S, Magnin E, Camiré O, Francavilla R, David LS, Deisseroth K, Topolnik L (2014) Dendritic inhibition provided by interneuron-specific cells controls the firing rate and timing of the hippocampal feedback inhibitory circuitry. J Neurosci 34:4534–4547

Tyzio R, Minlebaev M, Rheims S, Ivanov A, Jorquera I, Holmes GL, Zilberter Y, Ben-Ari Y, Khazipov R (2008) Postnatal changes in somatic γ-aminobutyric acid signalling in the rat hippocampus. Eur J Neurosci 27:2515–2528

Ulrich D, Bettler B (2007) $GABA_B$ receptors: synaptic functions and mechanisms of diversity. Curr Opin Neurobiol 17:298–303

Urban-Ciecko J, Fanselow EE, Barth AL (2015) Neocortical somatostatin neurons reversibly silence excitatory transmission via GABAb receptors. Curr Biol 25:722–731

Vertkin I, Styr B, Slomowitz E, Ofir N, Shapira I, Berner D, Fedorova T, Laviv T, Barak-Broner N, Greitzer-Antes D, Gassmann M, Bettler B, Lotan I, Slutsky I (2015) $GABA_B$ receptor deficiency causes failure of neuronal homeostasis in hippocampal network. Proc Natl Acad Sci U S A 112:3291–3299

Vida I, Frotscher M (2000) A hippocampal interneuron associated with the mossy fiber system. Proc Natl Acad Sci U S A 97:1275–1280

Vida I, Halasy K, Szinyei C, Somogyi P, Buhl EH (1998) Unitary IPSPs evoked by interneurons at the stratum radiatum-stratum lacunosum-moleculare border in the CA1 area of the rat hippocampus in vitro. J Physiol 506:755–773

Vida I, Bartos M, Jonas P (2006) Shunting inhibition improves robustness of gamma oscillations in hippocampal interneuron networks by homogenizing firing rates. Neuron 49:107–117

Vigot R, Barbieri S, Bräuner-Osborne H, Turecek R, Shigemoto R, Zhang YP, Luján R, Jacobson LH, Biermann B, Fritschy JM, Vacher CM, Müller M, Sansig G, Guetg N, Cryan JF, Kaupmann K, Gassmann M, Oertner TG, Bettler B (2006) Differential compartmentalization and distinct functions of $GABA_B$ receptor variants. Neuron 50:589–601

Vogt KE, Nicoll RA (1999) Glutamate and γ-aminobutyric acid mediate a heterosynaptic depression at mossy fiber synapses in the hippocampus. Proc Natl Acad Sci U S A 96:1118–1122

Wei K, Jia Z, Wang YT, Yang J, Liu CC, Snead OC III (2001) Cloning and characterization of a novel variant of rat GABA-BR1 with a truncated C-terminus. Brain Res 89:103–110

White JH, Wise A, Main MJ, Green A, Fraser NJ, Disney GH, Barnes AA, Emson P, Foord SM, Marshall FH (1998) Heterodimerization is required for the formation of a functional $GABA_B$ receptor. Nature 396:679–682

Wischmeyer E, Döring F, Wischmeyer E, Spauschus A, Thomzig A, Veh R, Karschin A (1997) Subunit interactions in the assembly of neuronal Kir3.0 inwardly rectifying K^+ channels. Mol Cell Neurosci 9:194–206

Woodin MA, Ganguly K, Poo MM (2003) Coincident pre- and postsynaptic activity modifies GABAergic synapses by postsynaptic changes in Cl^- transporter activity. Neuron 39:807–820

Wu LG, Saggau P (1995) $GABA_B$ receptor-mediated presynaptic inhibition in guinea-pig hippocampus is caused by reduction of presynaptic Ca^{2+} influx. J Physiol 485:649–657

Yuan M, Meyer T, Benkowitz C, Svanthrapadian S, Ansel-Bollepalli L, Foggetti A, Wulff P, Alcami P, Elgueta C, Bartos M (2017) Somatostatin-positive interneurons in the dentate gyrus of mice provide local- and long-range septal synaptic inhibition. Elife 6:e21105. https://doi.org/10.7554/eLife.21105

Synaptic Plasticity at Hippocampal Synapses: Experimental Background

Jack Mellor

Abstract Glutamatergic synapses in the hippocampus undergo activity-dependent bidirectional persistent changes in synaptic strength known as long-term potentiation (LTP) and long-term depression (LTD). This bidirectionality is important for the maintenance of equilibrium within a neuronal network, and distinct activity patterns need to be sensed by the synapse to initiate either LTP or LTD. Donald Hebb originally proposed that coincident firing of inputs onto a neuron or coincident firing of the presynaptic and postsynaptic neurons would strengthen synaptic connections. This theory is broadly correct for associative or Hebbian LTP and has been modified to include a description of LTD induction by uncorrelated firing patterns. However, it does not apply to non-associative or non-Hebbian synaptic plasticity which requires activity in only one neuron. In addition, these theories do not incorporate the role of homeostatic or heterosynaptic plasticity. Glutamatergic synapses in the hippocampus also undergo transient changes in synaptic strength known as short-term potentiation (STP) and short-term depression (STD), which operate on timescales of generally less than a second. Short-term changes in synaptic strength are important for the processing of information in the hippocampus, although their role in learning and memory may be primarily through their impact on long-term forms of synaptic plasticity.

Overview

This chapter discusses what is currently known about synaptic plasticity at synapses in the hippocampus. Hippocampal synaptic plasticity is potentially a vast topic with many thousands of research papers published in the field. However, this chapter does not delve into the detailed molecular mechanisms underlying synaptic plasticity and instead concentrates on the precise activity patterns required to induce synaptic

J. Mellor (✉)
Centre for Synaptic Plasticity, School of Physiology, Pharmacology and Neuroscience, University of Bristol, Bristol, UK
e-mail: Jack.Mellor@bristol.ac.uk

V. Cutsuridis et al. (eds.), *Hippocampal Microcircuits*, Springer Series in Computational Neuroscience, https://doi.org/10.1007/978-3-319-99103-0_6

plasticity. This includes the contribution of presynaptic and postsynaptic spiking and the importance of subthreshold postsynaptic depolarisation. Also, this chapter relates a variety of protocols used to induce synaptic plasticity to known in vivo patterns of neuronal activity.

All glutamatergic synapses in the hippocampus are plastic and can undergo activity-dependent bidirectional persistent changes in synaptic strength known as long-term potentiation (LTP) and long-term depression (LTD). This is important since a neuronal network cannot be functional if synaptic strength can only ever change in one direction. Therefore, distinct activity patterns need to be sensed by the synapse to initiate either LTP or LTD. A general principle for synaptic plasticity originally described by Donald Hebb stated that coincident firing of inputs onto a neuron or coincident firing of the presynaptic and postsynaptic neurons would strengthen synaptic connections (Hebb 1949). This theory is broadly correct for associative or Hebbian LTP and has been modified to include a description of LTD induction by uncorrelated firing patterns (Bienenstock et al. 1982). However, it does not apply to non-associative or non-Hebbian synaptic plasticity which requires activity in only one neuron (see below). In addition, these theories do not incorporate the role of homeostatic or heterosynaptic plasticity (see below).

All synapses in the hippocampus also undergo transient changes in synaptic strength known as short-term potentiation (STP) and short-term depression (STD), which operate on timescales of generally less than a second. Short-term changes in synaptic strength are clearly important for the processing of information in the hippocampus, although their role in learning and memory may be primarily through their impact on long-term forms of synaptic plasticity.

For the purposes of this book, the key questions are:

1. What patterns of activity are required to induce LTP and LTD?
2. How do these relate to patterns of activity found in vivo?
3. What are the functional consequences of long-term synaptic plasticity?

The answers to these questions will need to be incorporated into any model for how the hippocampus functions as a centre for learning within the brain.

The Data

The Different Forms of Hippocampal Synaptic Plasticity

Short-term synaptic plasticity is found at all synapses in the hippocampus and is believed to result from a combination of presynaptic vesicle depletion, presynaptic Ca^{2+} accumulation, changes to presynaptic action potential duration and postsynaptic receptor desensitisation (Geiger and Jonas 2000; Zucker and Regehr 2002). In general, synapses with a high initial probability of release will exhibit STD and those with a low initial probability of release STP, indicating the dominance of

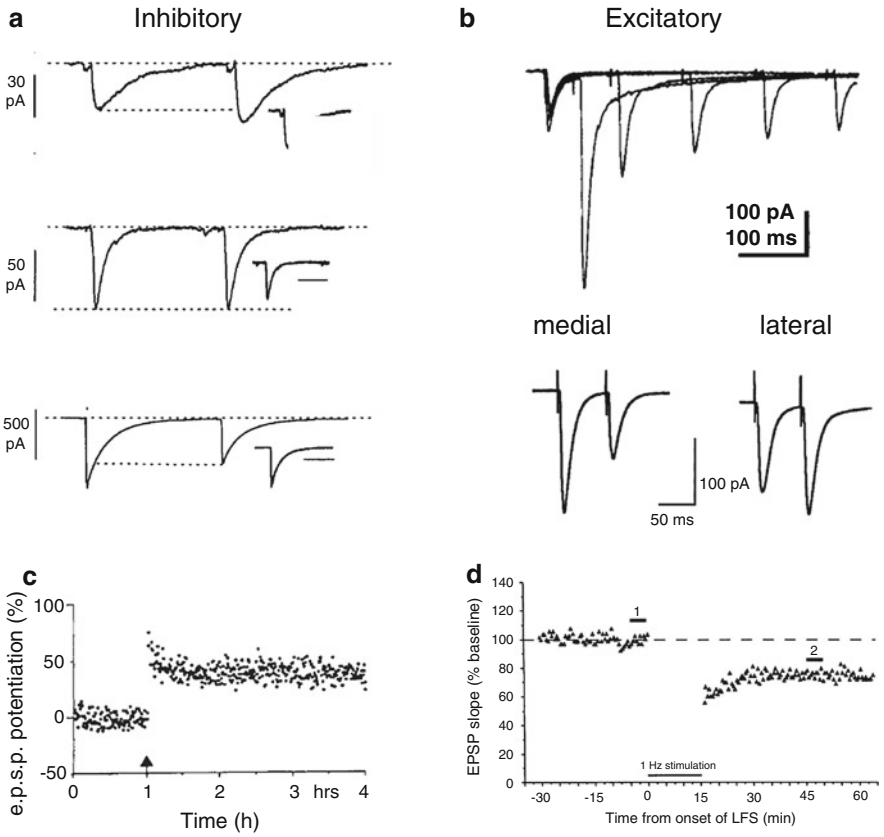

Fig. 1 Examples of synaptic plasticity. (**a**) Three examples of short-term plasticity at inhibitory synapses measured with pairs of stimuli given 100 ms apart (From Maccaferri et al. 2000). (**b**) Top shows STP measured with pairs of stimuli at varying intervals at the mossy fibre synapse (From Salin et al. 1996). Bottom shows STD or STP in the dentate gyrus measured with pairs of stimuli given to the medial or lateral perforant path (From Langmead et al. 2008). (**c**) Example of LTP experiment performed at the perforant path synapse in the dentate gyrus in vivo plotting the evoked EPSP amplitude with time. The arrow represents stimulation at 250 Hz for 200 ms (From Bliss and Collingridge, 1993). (**d**) Example of LTD experiment where LTD is induced by 900 stimuli at 1 Hz. (From Dudek and Bear 1992)

probability of release in defining short-term plasticity. The majority of GABAergic synapses exhibit STD, whereas glutamatergic synapses generally exhibit either STP or STD. Short-term synaptic plasticity can be measured by giving pairs of synaptic stimuli separated by a short interval (∼100 ms) to determine if the second stimulus results in a larger (STP) or smaller (STD) response. The time window for short-term plasticity is generally within a second but may be extended to several seconds (e.g. mossy fibre synapses) with a maximum plasticity found with interstimulus intervals of <100 ms. Some examples of short-term plasticity are shown in Fig. 1.

An interesting and well-characterised example of short-term synaptic plasticity occurs at mossy fibre synapses between dentate gyrus granule cells and CA3 pyramidal cells. At these synapses, the initial probability of release is extremely low but increases dramatically under repeated stimulation endowing the synapses with a very large facilitation in the probability of release and therefore strength of transmission, in some cases up to 1000%.

In general, LTP can be induced by short, high-frequency stimulation, whereas LTD can be induced by prolonged low-frequency stimulation (Fig. 1), and both can be induced at all the major excitatory synapses within the hippocampus but with varying properties (Fig. 2). LTP and LTD may also be expressed at GABAergic synapses and glutamatergic synapses onto interneurons in the hippocampus. In all cases the key mediator of long-term synaptic change is intracellular Ca^{2+}.

Ca^{2+} as a Trigger for the Induction of LTP and LTD

It is widely accepted that the critical trigger for the induction of associative synaptic plasticity is a rise in intracellular Ca^{2+} concentration within the postsynaptic dendrite (Lisman 1989). For many years, the magnitude and duration of the Ca^{2+} increase were thought to determine the direction of plasticity (Bear et al. 1987; Hansel et al. 1996). As a general rule, it was proposed that short, large-magnitude increases in intracellular Ca^{2+} concentration lead to synaptic potentiation, whereas prolonged, small-magnitude increases lead to synaptic depression (Cho et al. 2001; Cormier et al. 2001; Gall et al. 2005; Hansel et al. 1997; Ismailov et al. 2004) (Fig. 3).

Thus, sustained dendritic concentrations of Ca^{2+} between approximately 300 nM and 600 nM induce LTD, and shorter duration concentrations above 600 nM induce LTP. However, recent evidence has questioned this simple model and proposed rules that depend on the timing (Nevian and Sakmann 2006), source and microdomain of the Ca^{2+} concentration increase (Karmarkar and Buonomano 2002; Keller et al. 2008; Nevian and Sakmann 2006; Tigaret et al. 2016). Since the majority of these data come from experiments performed on neocortical synapses from immature rodents, the most relevant data for the purposes of this chapter can be found in Tigaret et al. In this study the magnitude of dendritic spine Ca^{2+} concentration increase did not predict LTP in hippocampal slices from mature rodents suggesting that the timing and localisation of Ca^{2+} to microdomains within the spine are crucial for LTP induction. These findings have important implications for Ca^{2+}-based models of synaptic plasticity.

Non-associative synaptic plasticity (see below) also requires a Ca^{2+} signal but in this case in the presynaptic terminal. Again it is believed that prolonged small-magnitude increases in Ca^{2+} (~100–200 nM) result in LTD, whereas short large-magnitude increases in Ca^{2+} (~500–1000 nM) result in LTP (Castillo et al. 1994; Kobayashi et al. 1999; Regehr and Tank 1991).

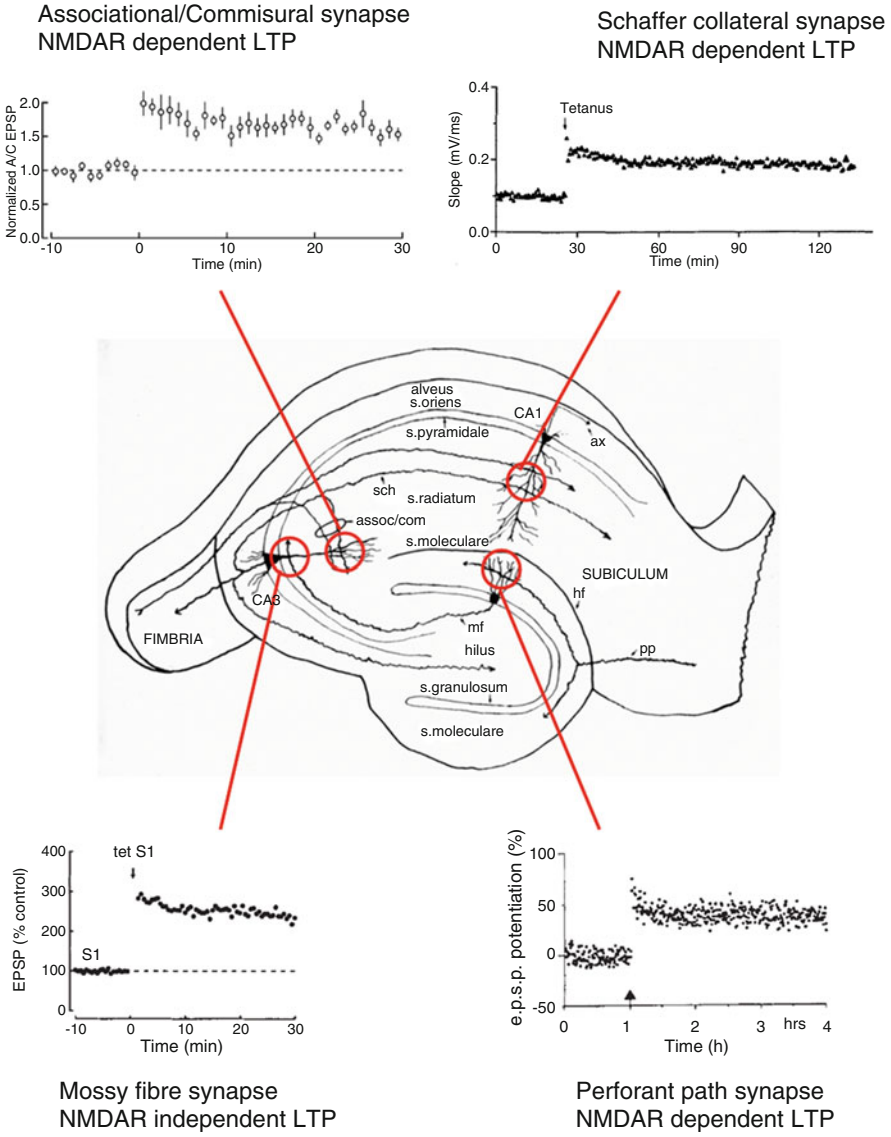

Fig. 2 Examples of four different forms of LTP at the major excitatory synapses in the hippocampus. (From top left, clockwise Kobayashi and Poo 2004; Nicoll et al. 1988; Bliss and Collingridge 1993; Weisskopf et al. 1993)

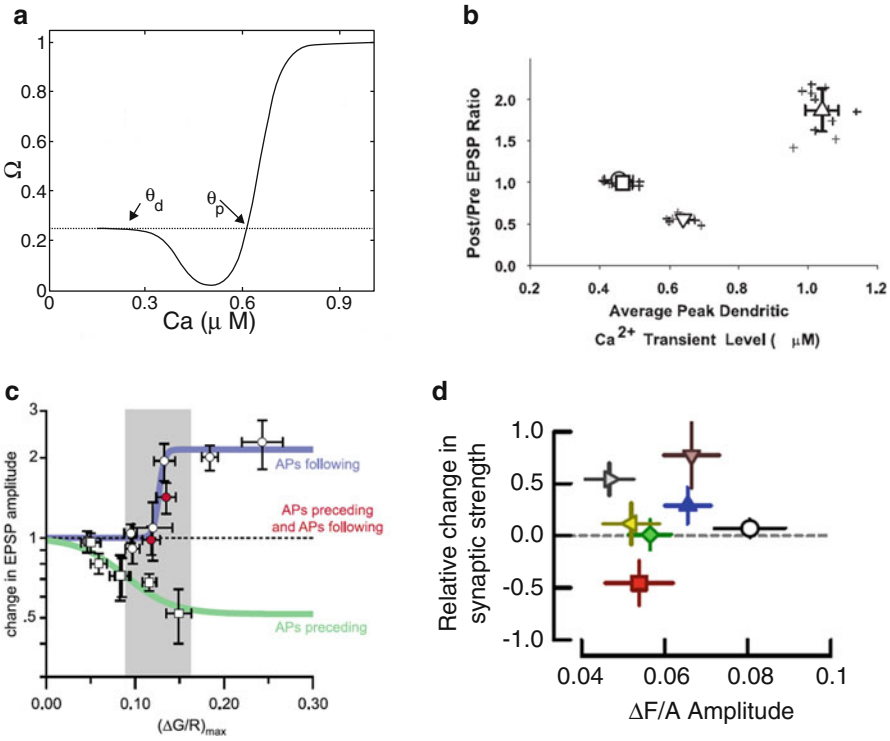

Fig. 3 (**a**) Theoretical relationship between dendritic calcium concentration and direction of synaptic plasticity (Ω) as originally proposed in the Bienenstock-Cooper-Munro (BCM) model (Bienenstock et al. 1982) and subsequently modified by Shouval and Kalantzis (2005). Dendritic calcium concentrations below value θ_d cause no change in synaptic strength. Between values θ_d and θ_p, LTD is induced and above θ_p LTP is induced (From Shouval and Kalantzis 2005). (**b**) Experimentally determined relationship between Ca^{2+} and synaptic plasticity in cortical slices during pairing of pre- and postsynaptic activity (From Ismailov et al. 2004). (**c**) Experimentally determined relationship between Ca^{2+} and synaptic plasticity in neocortical slices during pairing of pre- and postsynaptic spikes (From Nevian and Sakmann 2006). (**d**) Experimentally determined relationship between Ca^{2+} and synaptic plasticity in hippocampal slices during pairing of pre- and postsynaptic spikes. (From Tigaret et al. 2016)

NMDA Receptors Are Coincidence Detectors

The increase in intracellular Ca^{2+} can arise from a number of sources including voltage-dependent Ca^{2+} channels and intracellular Ca^{2+} stores, but the most important source for associative synaptic plasticity is through *N*-methyl-D-aspartate receptors (NMDARs). These glutamate-gated ion channels are permeable to K^+, Na^+ and Ca^{2+}, but at the resting membrane potential, their pore is blocked by Mg^{2+}. Depolarisation of the membrane potential removes the Mg^{2+} block which confers a voltage dependence on the NMDAR (Fig. 4). This makes this receptor ideally

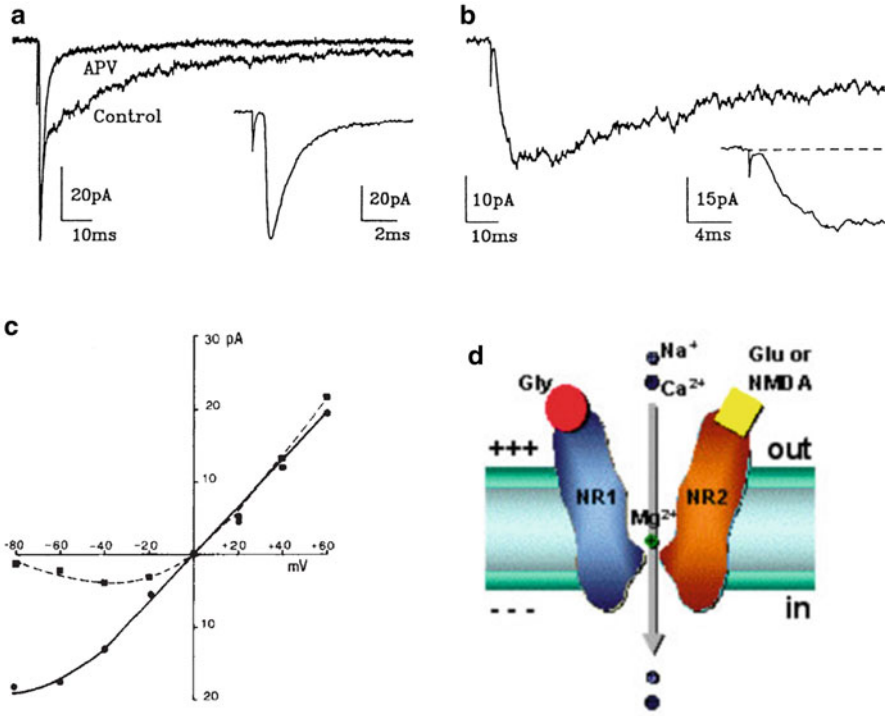

Fig. 4 (**a**) Excitatory postsynaptic currents (EPSCs) recorded from a cerebellar granule cell in the absence of Mg^{2+} before and during application of the NMDA receptor antagonist APV. Inset: rapid AMPAR-mediated component of the EPSC at a faster time scale. (**b**) NMDAR-mediated EPSCs recorded in isolation, following block of AMPARs by CNQX. Note prolonged decay and slow rise time (inset) compared with AMPAR EPSCs (From Silver et al. 1992). (**c**) Voltage dependence of NMDA receptor-mediated currents in 0 Mg^{2+} (solid line) and 0.5 mM Mg^{2+} (dashed line). The current-voltage relationship is approximately linear in the absence of Mg^{2+}, but currents are reduced at negative potentials in the presence of Mg^{2+} (From Nowak et al. 1984). Depiction of the NMDAR illustrating the requirement for glutamate (Glu) and glycine (Gly) binding and the removal of the Mg^{2+} block for channel opening

placed to detect coincident activity in presynaptic and postsynaptic neurons since to open it requires both the release of glutamate from the presynaptic terminal and postsynaptic depolarisation. Activation of NMDARs allows influx of Ca^{2+} to the postsynaptic cell, and the resultant rise in intracellular Ca^{2+} concentration initiates signalling pathways for LTP or LTD expression.

Since NMDARs control the induction of synaptic plasticity, the time course of NMDAR activation is thought to be critical for determining the window for plasticity induction by coincident pre- and postsynaptic activity. NMDARs bind glutamate with a high affinity ($EC_{50} \sim 2\ \mu M$) (Patneau and Mayer 1990) and remain bound long after glutamate has been cleared from the synaptic cleft (time constant of decay ~100 ms) (Jahr and Stevens 1990; McBain and Mayer 1994;

Silver et al. 1992). The precise decay kinetics are dependent on the NMDAR subunit complement that can be developmentally regulated and ranges from 100 ms to 5 s (Monyer et al. 1994). Typical NMDAR-mediated currents are long-lasting in comparison to AMPARs (Fig. 4), and this produces a long time window during which presynaptic and postsynaptic spikes may be considered coincident for the purposes of NMDAR activation. However, depolarisation becomes increasingly less effective at removing the Mg^{2+} block and activating NMDARs the longer the interval after glutamate binding (Kampa et al. 2004).

The postsynaptic depolarisation required for NMDAR activation can arise from different sources. Back-propagating action potentials initiated at the soma provide one source of depolarisation. These potentials are mostly passively propagating, and their amplitude attenuates as they travel away from the soma along the dendrites and through branch points. The rate of attenuation varies depending on neuronal morphology and frequency of action potentials, but it is likely that back-propagating action potentials are attenuated by >50% in the distal dendrites of pyramidal neurons (>200 μm from the soma) (Golding et al. 2005; Spruston et al. 1995). An alternative source of depolarisation is from local synaptic activation within dendrites and spines. The activation of multiple spatially co-localised synapses can produce sufficient depolarisation to activate NMDARs and create local dendritic spikes in membrane potential and Ca^{2+} (Golding et al. 2002; Losonczy and Magee 2006). In addition, estimates for the depolarisation within single spines in response to glutamate release range from 13 mV to 25 mV (Harnett et al. 2012; Palmer and Stuart 2009), which are sufficient for substantial NMDAR activation and Ca^{2+} influx to spines (Tigaret et al. 2016). Spine neck resistance is highly variable and plastic (Tonnesen et al. 2014) and determines spine depolarisation in response to currents generated both inside and outside the spine ensuring that the most relevant source of depolarisation for NMDAR activation will vary from spine to spine.

Other receptors and mechanisms have also been proposed to act as coincidence detectors either on their own or in combination with NMDARs. Synaptic activation of metabotropic glutamate receptors (mGluRs) has been shown to induce LTD or to modulate the induction of LTP at a number of synapses (Bashir et al. 1993; Kemp et al. 2000; Malenka and Bear 2004; Tigaret et al. 2016), and it is clear that there is interaction between the signalling pathways initiated by mGluR and NMDAR activation (Kemp et al. 2000). It has been proposed that the coincident activation of mGluRs and postsynaptic voltage-activated calcium channels is sufficient for the induction of LTD and can override the induction of LTP (Nevian and Sakmann 2006). At hippocampal synapses, postsynaptic calcium transients produced by synaptic stimulation and postsynaptic action potentials arise from multiple sources including NMDARs and voltage-activated calcium channels (Bloodgood and Sabatini 2007).

Hebbian Synaptic Plasticity

NMDAR-dependent LTP and LTD are often termed associative or Hebbian synaptic plasticity because they require coincident activity in the presynaptic and postsynaptic neurons. All of the synaptic connections between glutamatergic neurons in the hippocampus exhibit associative long-term synaptic plasticity with one exception (see next section), but the best studied and characterised in vitro are the Schaffer collateral synapses between CA3 pyramidal cells and CA1 pyramidal cells. Evidence suggests that Hebbian synaptic plasticity at glutamatergic synapses on other hippocampal neurones has similar properties and therefore the properties characterised for the Schaffer collateral synapses are often generalised (see Fig. 2).

However, there are variations which need to be accounted for. The most similar synapses to Schaffer collaterals are the CA3 recurrent collaterals with no major differences reported although it is suggested that inter-hemispheric commissural synapses between CA3 and CA1 pyramidal cells do not exhibit NMDAR-dependent LTP (Kohl et al. 2011). Perforant path/temporoammonic inputs from entorhinal cortex to CA3 or CA1 pyramidal cells do show different induction properties largely because back-propagating action potentials do not reach these synapses due to their distance from the soma (Golding et al. 2002). This means that the postsynaptic depolarisation required to activate NMDARs must come from other sources such as other synapses and/or dendritic Ca^{2+} spikes (Golding et al. 2002). Perforant path synapses onto dentate gyrus granule cells are divided into the medial and lateral synapses corresponding to inputs from layer IV and layer V pyramidal cells of the entorhinal cortex, respectively. These two pathways have similar rules for synaptic plasticity induction, but the lateral pathway has a higher threshold for LTP induction. Pairing of presynaptic stimulation with postsynaptic depolarisation requires a higher rate of stimulation for the lateral pathway (1–4 Hz) compared to the medial pathway (0.5 Hz) (Colino and Malenka 1993). In the subiculum, synapses from CA1 inputs undergo NMDAR-dependent LTP that is expressed presynaptically or postsynaptically depending on the subtype of pyramidal cell (Wozny et al. 2008). The afferent and efferent synapses of CA2 remain largely uncharacterised, but initial evidence suggests that inputs from entorhinal cortex can undergo LTP, whereas those from CA3 do not (Chevaleyre and Siegelbaum 2010).

Activity at spatially distant synapses can also alter the threshold for LTP or LTD induction. The original description of this effect is found at the medial and lateral perforant path synapses in the dentate gyrus where activity in one pathway lowers the threshold for the induction of plasticity in the other (Levy and Steward 1979; McNaughton et al. 1978). Since then the mossy fibre synapse in CA3 has been shown to transform subthreshold activity at CA3 associational/commissural synapses into suprathreshold activity for LTP induction (Kobayashi and Poo 2004) (but not vice versa), and a similar effect is seen in CA1 where perforant path synapses influence Schaffer collateral LTP (Dudman et al. 2007).

Non-Hebbian Synaptic Plasticity

Mossy fibre synapses connecting dentate gyrus granule cells with CA3 pyramidal cells are the only instance of glutamatergic synapses exhibiting non-Hebbian synaptic plasticity in the hippocampus. Non-Hebbian LTP at mossy fibre synapses is induced by a high-frequency train of action potentials in the presynaptic granule cells that cause Ca^{2+} influx into the presynaptic terminals (Harris and Cotman 1986; Zalutsky and Nicoll 1990). Conversely, LTD at these synapses is induced by low-frequency presynaptic stimulation (Kobayashi et al. 1996; Tzounopoulos et al. 1998). Although this model has no requirement for postsynaptic activity, some reports support a postsynaptic role (Carta et al. 2014; Contractor et al. 2002; Yeckel et al. 1999), but see Mellor and Nicoll 2001. In addition there are also Hebbian forms of synaptic plasticity present at these synapses. Short bursts of high-frequency stimulation (24 stimuli at 25 Hz) can potentiate NMDAR-mediated synaptic transmission (Kwon and Castillo 2008; Rebola et al. 2008) enabling subsequent NMDAR-dependent synaptic plasticity (Rebola et al. 2011), and low-frequency stimulation (0.33 Hz) paired with postsynaptic depolarisation can depress AMPAR-mediated synaptic transmission (Lei et al. 2003).

Non-Hebbian synaptic plasticity will clearly have a very different function to Hebbian synaptic plasticity since it is non-associative and requires only firing in a single neuron. If a granule cell fires a high-frequency burst of action potentials above a threshold (approximately 12 action potentials at 25 Hz (Mistry et al. 2011; Schmitz et al. 2003)), then LTP will be induced. The threshold for LTD is not precisely characterised, but generally 900 stimuli at 1 Hz are sufficient (Kobayashi et al. 1996).

Homeostatic Synaptic Regulation, Metaplasticity and Heterosynaptic Plasticity

Synaptic regulation that is not synapse specific and therefore not induced by the activation of individual synapses is known as homeostatic synaptic plasticity. By increasing or decreasing the strength of all the synapses on its dendrites, a neuron can regulate its overall excitability and keep its response to synaptic activity within an efficient and dynamic range. Mechanisms exist to globally decrease the strength of synaptic connections if the postsynaptic neuron experiences hyperactivity and conversely can increase global synaptic strength in conditions of low neuronal activity (Burrone et al. 2002; O'Brien et al. 1998; Turrigiano et al. 1998). These mechanisms occur over a period of days and can lead to twofold increases or decreases in the density of synapses. Homeostatic synaptic regulation thus allows a neuron to normalise its inputs in a range that allows an optimal signal-to-noise ratio (Miller 1996) and ensures network stability (Golowasch et al. 1999). However, since most experiments on homeostatic synaptic plasticity in the hippocampus use

cells in dissociated culture, with induction protocols that last for hours or days, and furthermore do not record the activity that occurs during that period, it is hard to specify the precise conditions that are required to induce this plasticity and relate them to potential in vivo situations although this is more feasible in neocortical circuits (Keck et al. 2013). Homeostatic synaptic regulation also predicts that LTP of specific synapses will result in synaptic depression at other synapses on the neuron and vice versa (Miller 1996), otherwise known as heterosynaptic plasticity.

LTP induction at specific synapses on a single cell can induce heterosynaptic LTD at other synapses (Abraham et al. 1994; Doyere et al. 1997; Levy and Steward 1979). This has been found between the medial and lateral perforant pathways in the dentate gyrus and between Schaffer collateral pathways in CA1 (Daw et al. 2000). In these instances, an LTP of 50% in one synaptic pathway can induce a 20% LTD in the other pathway. This could be an important mechanism to increase synaptic signal-to-noise ratio, and it occurs over the same time frame as LTP or LTD. However, heterosynaptic LTD is not consistently observed, so it is hard to predict what stimuli will reliably induce it.

The ability of prior activity to modify the threshold for subsequent synaptic plasticity induction is termed metaplasticity and has been shown for Schaffer collateral synapses in CA1 and perforant path synapses in the dentate gyrus. Metaplasticity can occur through NMDAR or mGluR-mediated mechanisms. Prior NMDAR activation increases the threshold for LTP induction (Huang et al. 1992) and decreases the threshold for LTD induction (Christie and Abraham, 1992), but, conversely, prior mGluR activation decreases the LTP threshold in CA1 (Cohen and Abraham 1996) although it increases the threshold in the dentate gyrus (Gisabella et al. 2003). It is not known how these two opposing mechanisms interact, but a general rule along similar lines to homeostatic plasticity would indicate that prior LTP induction enhances the subsequent probability of LTD induction and vice versa. The inconsistency of metaplastic effects once again makes it hard to predict the precise patterns of stimuli that will reliably induce it in vivo.

Role of Inhibition in the Induction of LTP

Inhibitory inputs onto the postsynaptic neuron decrease the degree of depolarisation and therefore limit the activation of NMDARs and the induction of associative synaptic plasticity. The timecourse of synaptic $GABA_A$ receptor responses is very similar to synaptic NMDAR responses and therefore effectively counteracts NMDAR activation. This predicts that pharmacological blockade of $GABA_A$ receptors lowers the threshold for LTP induction and this is indeed the case (Meredith et al. 2003; Wigstrom and Gustafsson 1983). The situation with $GABA_B$ receptor activation is somewhat more complex since $GABA_B$ receptors have both pre- and postsynaptic effects. Presynaptically, they inhibit the release of GABA from inhibitory terminals at both feedforward and feedback interneurons. The suppression of GABA release then facilitates LTP induction at glutamatergic synapses

(Davies et al. 1991). Postsynaptically, however, $GABA_B$ receptors on excitatory neurons suppress the induction of LTP by hyperpolarising the dendrite and reducing NMDAR activity. For these reasons, many synaptic plasticity experiments have been performed with pharmacological blockade of $GABA_A$ and/or $GABA_B$ receptors.

During rhythmic oscillatory activity, hippocampal interneurons fire in specific phases providing a powerful inhibitory drive (see Glovelli and Vida chapters) that regulates the induction of LTP. During the theta rhythm (~5–10 Hz), LTP can only be induced at the peak of the cycle, and the same induction protocol induces LTD in the trough (Huerta and Lisman 1993, 1995; Kwag and Paulsen, 2009). Similarly, theta burst stimulation protocols to induce LTP or LTD are thought to be effective because $GABA_B$ receptor-mediated inhibition of GABA release is maximal ~200 ms after the initial GABA release (Davies et al. 1991). Gamma rhythms (~30–100 Hz) are often found nested within theta rhythms with inhibitory drive also tuned to gamma cycles, thereby regulating the induction of LTP on this faster timescale. Similarly, transient high-frequency sharp-wave ripple oscillations (~100–200 Hz) also tune inhibitory drive which may regulate the induction of LTP (Sadowski et al. 2016). Each oscillation frequency engages different inhibitory interneurons that synapse onto distinct sections of the dendrites and soma (see Glovelli and Vida chapters) and therefore will differentially regulate synaptic plasticity.

Plasticity of Inhibition

Inhibitory inputs can also undergo plasticity either at the glutamatergic synapses onto interneurons (Lamsa et al. 2005) or at GABAergic synapses (Chevaleyre and Castillo 2003; Woodin et al. 2003).

At glutamatergic synapses, the induction of LTP or LTD requires a rise in postsynaptic Ca^{2+} through either NMDARs or Ca^{2+}-permeable AMPARs (Laezza et al. 1999; Lamsa et al. 2005; Lei and McBain, 2002). These involve different postsynaptic activity patterns since NMDARs require postsynaptic depolarisation, whereas Ca^{2+}-permeable AMPARs are blocked at depolarised potentials (Lamsa et al. 2007). High-frequency presynaptic stimulation induces LTD at mossy fibre inputs onto CA3 interneurons and LTP at mossy fibre inputs onto dentate gyrus interneurons (Alle et al. 2001; Laezza et al. 1999; Maccaferri et al. 1998). It also induces LTP and LTD at feedforward and feedback interneurons in CA1 (Lamsa et al. 2005; Lamsa et al. 2007; McMahon and Kauer, 1997) where the feedforward interneuron synapses exhibit NMDAR-dependent LTP and the feedback synapses Ca^{2+}-permeable AMPAR-dependent LTP (Lamsa et al. 2005; Lamsa et al. 2007).

At GABAergic synapses, LTD is induced by a rise in intracellular Ca^{2+} in either the postsynaptic interneuron (Woodin et al. 2003) or a nearby CA1 pyramidal cell (Chevaleyre and Castillo, 2003). LTP is also induced by high-frequency stimulation (Caillard et al. 1999; Shew et al. 2000).

Synaptic $GABA_B$ receptors have also recently been shown to undergo synaptic plasticity. Potentiation of synaptic $GABA_B$ receptors was seen after pairing 3 Hz stimulation with postsynaptic depolarisation (Langmead et al. 2008).

Induction of LTP and LTD by Artificial Induction Protocols

The proposed scheme, whereby short, large-magnitude increases in intracellular Ca^{2+} concentration lead to synaptic potentiation, whereas prolonged, small-magnitude increases lead to synaptic depression (Bienenstock et al. 1982), has been reinforced by the use of short high-frequency presynaptic stimulation to induce LTP and long low-frequency presynaptic stimulation to induce LTD. Typical frequencies used to induce LTP sit in the range 10–250 Hz and contain 20–100 stimuli with trains of stimuli often given multiple times. For LTD induction, frequencies range from 1 to 3 Hz, and the number of stimuli is generally much greater at 100–900 stimuli (Dudek and Bear, 1993; Dunwiddie and Lynch, 1978). However, LTD is only easily induced, and therefore almost exclusively studied, in immature preparations. In adult preparations, LTD is difficult to induce reliably, whereas LTP is readily induced.

An alternative method to activate NMDARs by correlating presynaptic glutamate release with postsynaptic depolarisation uses intracellular recordings to depolarise the postsynaptic neuron whilst stimulating presynaptic release (Isaac et al. 1995). Using this technique presynaptic stimulation frequency is kept similar for LTP or LTD induction, but the degree of depolarisation is greater for LTP induction. Typically this is −10 mV to 0 mV for LTP and −40 mV to −30 mV for LTD (Daw et al. 2000; Isaac et al. 1995). Again this reinforces the idea that more NMDAR activation is required for LTP induction resulting in higher intracellular Ca^{2+} concentrations. The number of stimuli given is again generally greater for LTD induction.

Induction of LTP and LTD by Theta Burst Stimulation

In the hippocampus, states during which learning is thought to occur are characterised by pronounced population activity at the theta frequency (∼5–10 Hz). The principal glutamatergic neurons of the hippocampus fire action potentials in bursts on the peak of every theta cycle and are largely silent during the rest of the cycle. This is thought to be due to the activity in the interneuron population that inhibits glutamatergic neuron firing during other phases of the cycle. This observation led to the development of theta burst stimulation (TBS) protocols for synaptic plasticity induction (Larson et al. 1986; Rose and Dunwiddie 1986) (Fig. 5). The progressive increase in synaptic strength after TBS is in contrast to the generally stable or decreasing synaptic strength caused by artificial LTP induction protocols such as

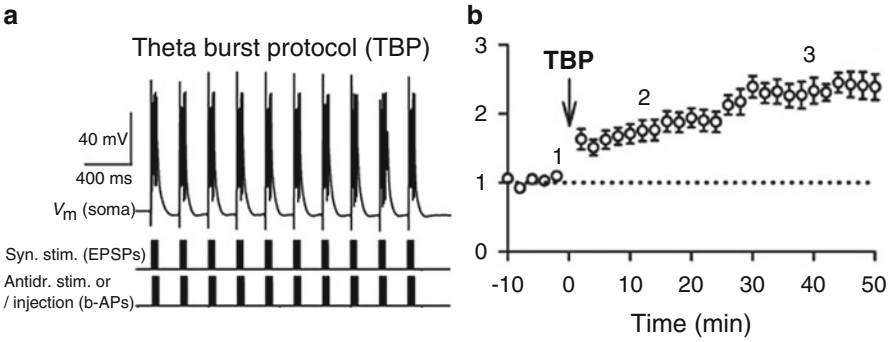

Fig. 5 (**a**) Theta burst stimulation (TBS) protocol showing the pattern of pre- and postsynaptic stimulation used to induce LTP. The upper trace illustrates the cellular response to a train of TBS. Lower traces represent the stimulation given to the presynaptic axons (upper) and postsynaptic cell to induce back-propagating action potentials (b-APs, lower). (**b**) TBS induces LTP. (From Frick et al. 2004; Mulkey and Malenka 1992)

high-frequency stimulation or pairing (see Fig. 2). TBS induces LTP when pre- and postsynaptic entities are stimulated in synchrony but induces LTD when pre- and postsynaptic entities are noncoincident (Huerta and Lisman 1995). Therefore, if presynaptic bursts of activity occur at the peak of the theta cycle, then LTP will be induced, but if they occur in the trough, then LTD results (Huerta and Lisman 1995).

Spike-Timing-Dependent Synaptic Plasticity

Another method of activating NMDARs is to directly pair pre- and postsynaptic action potentials so they coincide at the synapse. In this way the presynaptic action potential causes the release of glutamate, and the postsynaptic action potential back-propagates along the dendrite to depolarise the spine. This method induces LTP in both neocortical and hippocampal slices (Magee and Johnston 1997; Markram et al. 1997). In the neocortical slice, it was also shown that the temporal precision of the pre- and postsynaptic action potentials was critical. If the presynaptic action potential occurred before the postsynaptic action potential, then LTP was induced, but LTD was induced if the timings were reversed (Markram et al. 1997). This temporal specificity has been termed spike-timing-dependent plasticity (STDP) and was subsequently demonstrated in hippocampal dissociated cultures (Bi and Poo 1998), slice cultures (Debanne et al. 1998) and acute slices (Nishiyama et al. 2000). However, the bidirectional nature of STDP appears to be dependent on the frequency of pairings (Wittenberg and Wang 2006), and in acute slices from mature rodents, bidirectional STDP is not evident. LTP can be induced by causal spike pairings, but no LTD results from anticausal pairings (Buchanan and Mellor 2007; Tigaret et al.

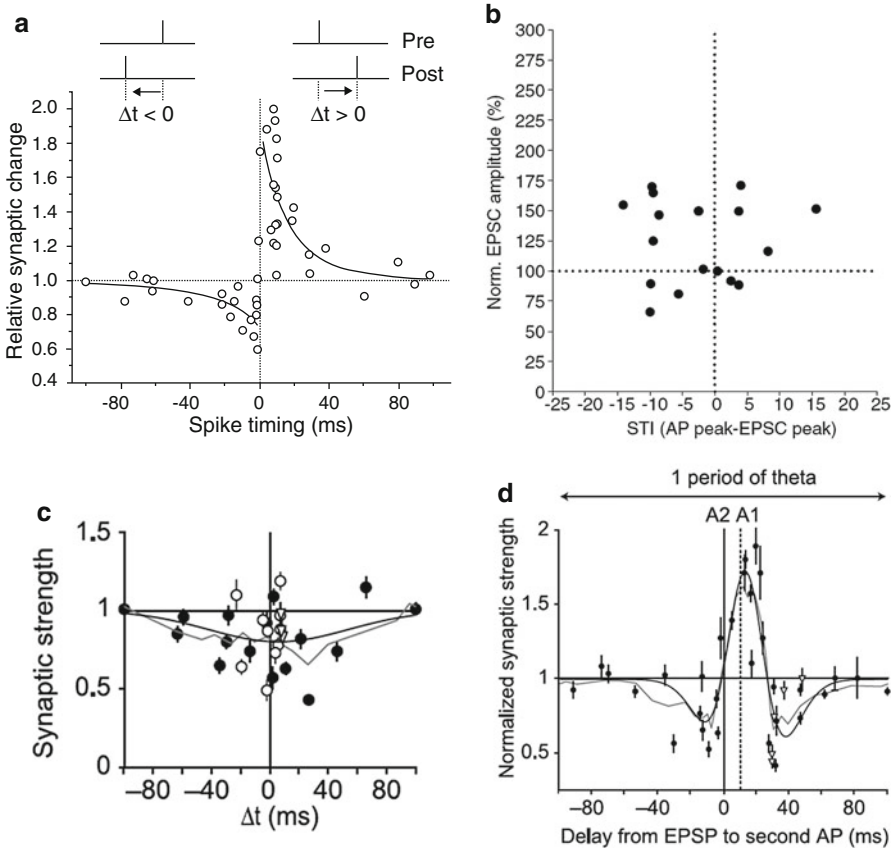

Fig. 6 Relationships between relative spike timing of pre- and postsynaptic spikes in a pair and the synaptic plasticity induced from different studies. (**a**) From Bi and Poo 1998. (**b**) From Buchanan and Mellor 2007. (**c**) From Wittenberg and Wang 2006. Open circles indicate pairings delivered at frequencies from 0.1 to 0.5 Hz and filled circles at 5 Hz. (**d**) The STDP relationship shown in C changes when two postsynaptic stimuli are given for each pre- and postsynaptic pairing. Dashed line indicates the time of the first postsynaptic action potential in most experiments. (From Wittenberg and Wang 2006)

2016). Figure 6 illustrates some examples for STDP relationships at hippocampal synapses.

There is a marked variability in the relationships deduced from the experiments, and this highlights the need for caution when using such data to model synaptic plasticity in the hippocampus. It is becoming clear that multiple postsynaptic spikes, or bursts, are required to induce STDP in the hippocampus (Fig. 6d) (Buchanan and Mellor 2007; Pike et al. 1999; Tigaret et al. 2016; Wittenberg and Wang 2006). The temporal requirements for burst firing have yet to be fully elucidated, but these will impact synaptic plasticity induced by naturally occurring spike patterns (Sadowski

et al. 2016). In contrast, the evidence from neocortical slice experiments consistently indicates a strong temporal dependence for the direction of plasticity (Froemke et al. 2006; Nevian and Sakmann 2006; Sjostrom and Nelson 2002; Sjostrom et al. 2001) that varies slightly between synapses (Letzkus et al. 2006; Sjostrom and Hausser 2006) and can be altered by neuromodulators (Seol et al. 2007; Sjostrom et al. 2003). The temporal specificity of STDP in the neocortex is also affected by multiple postsynaptic spikes (Froemke et al. 2006; Nevian and Sakmann 2006).

Induction of LTP and LTD by Natural Stimulus Patterns

Surprisingly few studies have attempted to induce long-term synaptic plasticity using naturally occurring patterns of activity recorded from cells in vivo. This is possibly because it is difficult to know precisely what activity is present in both the pre- and postsynaptic cells. In the visual cortex, spike patterns from individual cells responding to overlapping visual receptive fields induce STDP when replayed into synaptically coupled cells in a cortical slice (Froemke and Dan 2002). In the hippocampus, place cell firing patterns have been used to induce LTP by stimulating a population of Schaffer collateral axons and recording the change in fEPSP (Dobrunz and Stevens 1999). Furthermore, spike patterns from pairs of place cells with overlapping place fields induce LTP when replayed into synaptically coupled pyramidal cells in a hippocampal slice (Isaac et al. 2009). In addition, replay of place cell activity that occurs during sharp-wave ripples on a compressed timescale can induce LTP when reconstructed in a hippocampal slice (Sadowski et al. 2016). These experiments are perhaps most relevant to this chapter since they demonstrate the patterns of activity that induce synaptic plasticity in the hippocampus in vivo.

Functional Significance of Synaptic Plasticity

Synaptic plasticity increases or decreases the amplitude and initial slope of the EPSP or IPSP leading to changes in the ability of a specific synaptic input to influence the spike output of the postsynaptic neuron (Bliss and Lomo 1973). For excitatory synapses, this changes the probability that an individual synaptic input will cause the postsynaptic neuron to fire an action potential and the latency of postsynaptic spike firing. However, the probability of postsynaptic firing never equals 1 for single presynaptic stimuli and only at the very powerful mossy fibre synapses in CA3 does it approach 1 if multiple EPSPs from a single input summate temporally (Henze et al. 2002). In this case, increasing the presynaptic firing frequency increases the probability of inducing a postsynaptic action potential ($\sim$0.1 at 10 Hz rising to $\sim$0.8

at 100 Hz). However, it is not clear if mossy fibre LTP will change the probability of inducing a postsynaptic action potential since it reduces the pronounced short-term facilitation exhibited at this synapse (Gundlfinger et al. 2007; Mistry et al. 2011). For other excitatory synapses, postsynaptic action potentials are dependent on the temporal and spatial summation of additional synaptic inputs to the neuron. The majority of data addressing the effects of synaptic plasticity on the probability of a postsynaptic action potential use bulk stimulation of presynaptic axons that reveal an increase in spike probability for LTP and a decrease for LTD. However, the use of bulk stimulation necessarily diminishes the ability to make conclusions about the effects of synapse-specific plasticity. This is because the recording of single synaptic inputs requires the recording of synaptically coupled pairs of neurons that is technically challenging in the hippocampus. Technical advances to achieve single synaptic recording are discussed in the final section of this chapter. Data regarding the summation of synaptic inputs can be found in other chapters.

Recordings of CA1 pyramidal cell activity in vivo show that plasticity of dendritic and cellular activity, assumed to be caused by synaptic plasticity, defines the feature selectivity of pyramidal cells which in the case of place cells is measured by their place fields (Bittner et al. 2015; Sheffield and Dombeck 2015). Furthermore, the long-term association of information that forms the basis for learning is shown to be encoded by synaptic plasticity at hippocampal synapses (Gruart et al. 2006; Whitlock et al. 2006).

Experimental Techniques

The study of synaptic plasticity has largely been performed by electrophysiological recording of synaptic strength. In the hippocampus this can be done in a variety of hippocampal preparations listed below together with a description of their strengths and weaknesses (Table 1).

There are also a number of different recording techniques both electrophysiological and non-electrophysiological that can be used to measure synaptic strength (Table 2). Whilst the non-electrophysiological techniques do not directly measure the electrical input from a synapse, in the majority of cases, they have been shown to be positively correlated with electrophysiological measurements. Here, three types of imaging technique are assessed. Ca^{2+} imaging can be used at pre- or postsynaptic sites using intracellular loading of Ca^{2+} indicators. Voltage imaging can also be used at pre- or postsynaptic sites by intracellular loading of membrane voltage indicators. Morphological imaging of presynaptic terminals or postsynaptic spines uses intracellular fluorescent markers such as GFP or actin-bound GFP.

Table 1 Comparison of experimental systems used to investigate synaptic plasticity

System	Uses	Limitations
Dissociated culture	Easy to isolate the pre- and postsynaptic cells and therefore to perform paired intracellular recordings. This has enabled the study of synaptic plasticity at unitary connections between neurons	Synapses and networks have regrown in culture and exhibit very different properties to those found in the intact hippocampus. For example, connections between pairs of neurons have many more synapses, and LTP is hard to induce by conventional high-frequency activity
Acute slices	Retains many of the network connections found in vivo. Easy to make intra- or extracellular recordings	Many connections from other brain areas are cut. The slicing procedure introduces acute trauma to the tissue that alters synaptic properties. Very hard to make paired recordings
Cultured slices	Retains many of the network connections found in vivo. Easy to make intracellular recordings. Connectivity between neurons is high, thus enabling paired recordings	Many connections from other brain areas are cut. The slicing procedure introduces acute trauma to the tissue that alters synaptic properties. New synaptic connections that are not found in vivo are formed during culture
In vivo	Most physiological system	Technically challenging especially intracellular recordings that are difficult to maintain for extended periods. Easier to perform experiments on anaesthetised animals but this reduces the physiological relevance. Technology not currently available to make paired recordings

The Future

It is increasingly apparent that the rules that apply to the induction of synaptic plasticity in vivo are not necessarily the same as those found in in vitro preparations. It is also clear that the patterns of activity that might induce synaptic plasticity in vivo are not the same as those used to induce plasticity in vitro.

Historically, the measurement of synaptic plasticity has necessitated a trade-off between the ease of data acquisition and the physiological relevance of the system and technique. Thus recordings in dissociated culture are easier than slices are easier than in vivo, but the proximity of the experimental system to the situation in a behaving animal goes in the opposite direction. The major factors that limit the applicability of in vitro data to the in vivo system are inhibitory inputs, neuromodulators and the pattern of excitatory synaptic activity. Each of these factors

Table 2 Comparison of approaches used to measure synaptic plasticity

Technique	Strengths	Weaknesses
Field recording	The laminar structure of the hippocampus lends itself to extracellular field recording. Recordings are stable for long periods (several hours in vitro, and several days in vivo). Non-invasive	Large populations of synapses are recorded so difficult to assign synapse specificity. No control of postsynaptic neuronal activity
Whole-cell recording	Control over postsynaptic somatic membrane potential. Paired recordings from two synaptically coupled neurons are possible	Invasive. Endogenous intracellular constituents are progressively washed out of the cell during recordings leading to loss of LTP
Perforated patch recording	Control over postsynaptic somatic membrane potential. Non-invasive intracellular recording	Perforation takes time to stabilise access resistance (up to 1 h)
Ca^{2+} imaging	Measures the critical trigger for the induction of synaptic plasticity. Pinpoints the spatial location of the synapses stimulated. Activity at single synapses can be monitored	Ca^{2+} indicators buffer rises in intracellular Ca^{2+}. Ca^{2+} rises are not linearly related to the amplitude of synaptic transmission. Images lose sensitivity and resolution in deep tissue
Membrane potential imaging	Measures the spatial location of fast membrane voltage changes. Combines the strengths of both electrophysiology and imaging. Non-invasive	Low sensitivity restricts imaging to relatively large voltage changes. Images lose sensitivity and resolution in deep tissue
Morphological imaging	Pinpoints the spatial location of stimulated synapses. Non-invasive	Morphological changes are not linearly related to the amplitude of synaptic transmission. Images lose sensitivity and resolution in deep tissue

plays a crucial role in regulating the induction of LTP and LTD, but they have each proved difficult to accurately replicate in vitro.

The reasons for this are twofold. Firstly, information on the activity patterns of excitatory, inhibitory and neuromodulatory neurons that occurs in vivo is limited, and secondly, it is experimentally challenging to replicate the activity of these separate systems in vitro. Recent technical advances have reduced these barriers to progress. Principally, the ability to label genetically defined cells enables the recording and stimulation of specific components of hippocampal circuits and inputs. From these methods it is anticipated that a wealth of information on the activity of subtypes of inhibitory interneurons, neuromodulator inputs and excitatory neurons will come from recordings made during awake behaviour (e.g. Hangya et al. 2015; Lovett-Barron et al. 2014). Similarly, recapitulation of these activity patterns in vitro can be achieved by control and stimulation of anatomically

and genetically defined populations of neurons (e.g. Basu et al. 2016; Kohl et al. 2011).

An alternative approach is to measure and interfere with the induction of hippocampal synaptic plasticity in vivo, ideally at individual identified synapses. Advances in electrophysiological and imaging techniques make this goal increasingly obtainable. Intracellular electrophysiological recordings from hippocampal neurons in vivo are achievable and can be made from anaesthetised animals (e.g. Henze et al. 2002) or awake animals either head fixed (e.g. Bittner et al. 2015) or freely moving (e.g. Lee et al. 2006). It is hoped that these technologies will become increasingly more widespread. Imaging of excitatory (but not inhibitory) synapse strength in vivo by measurement of morphology, membrane voltage or intracellular Ca^{2+} potentially provides benefits over electrophysiology since they enable the localisation of activated synapses. In particular, voltage-sensitive dyes offer the promise of measuring fast voltage changes at high spatial resolution combining the best aspects of electrophysiology and imaging techniques (e.g. Hochbaum et al. 2014). Progress in optimising resolution and sensitivity suggests that these imaging techniques will become more useful for measuring synaptic plasticity both in vitro and in vivo.

At the same time, methods for intervention in synaptic plasticity processes to determine the role of synaptic plasticity at specific synapses in hippocampal-dependent learning and memory have advanced from blocking plasticity with intra-hippocampal infusion of pharmacological agents that block LTP (Morris et al. 1986; Pastalkova et al. 2006) to genetically targeting synaptic plasticity at specific synapses and specific times. These include deletion of the NR1 subunit of NMDARs from granule cells, CA3 pyramidal cells or CA1 pyramidal cells to reveal the contribution made by NMDAR-dependent synaptic plasticity in each cell type (McHugh et al. 1996; McHugh et al. 2007; Nakazawa et al. 2002). It is expected that highly selective manipulation of plasticity processes in genetically defined neuronal populations will enable further interrogation of the role of synaptic plasticity in hippocampal function.

Acknowledgements Thank you to Tim Bliss for critical reading and comments.

References

Abraham WC, Christie BR, Logan B, Lawlor P, Dragunow M (1994) Immediate early gene expression associated with the persistence of heterosynaptic long-term depression in the hippocampus. Proc Natl Acad Sci U S A 91:10049–10053

Alle H, Jonas P, Geiger JR (2001) PTP and LTP at a hippocampal mossy fiber-interneuron synapse. Proc Natl Acad Sci U S A 98:14708–14713

Bashir ZI, Bortolotto ZA, Davies CH, Berretta N, Irving AJ, Seal AJ, Henley JM, Jane DE, Watkins JC, Collingridge GL (1993) Induction of LTP in the hippocampus needs synaptic activation of glutamate metabotropic receptors. Nature 363:347–350

Basu J, Zaremba JD, Cheung SK, Hitti FL, Zemelman BV, Losonczy A, Siegelbaum SA (2016) Gating of hippocampal activity, plasticity, and memory by entorhinal cortex long-range inhibition. Science 351:aaa5694

Bear MF, Cooper LN, Ebner FF (1987) A physiological-basis for a theory of synapse modification. Science 237:42–48

Bi GQ, Poo MM (1998) Synaptic modifications in cultured hippocampal neurons: dependence on spike timing, synaptic strength, and postsynaptic cell type. J Neurosci 18:10464–10472

Bienenstock EL, Cooper LN, Munro PW (1982) Theory for the development of neuron selectivity – orientation specificity and binocular interaction in visual-cortex. J Neurosci 2:32–48

Bittner KC, Grienberger C, Vaidya SP, Milstein AD, Macklin JJ, Suh J, Tonegawa S, Magee JC (2015) Conjunctive input processing drives feature selectivity in hippocampal CA1 neurons. Nat Neurosci 18:1133–1142

Bliss TV, Collingridge GL (1993) A synaptic model of memory: long-term potentiation in the hippocampus. Nature 361:31–39

Bliss TV, Lomo T (1973) Long-lasting potentiation of synaptic transmission in the dentate area of the anaesthetized rabbit following stimulation of the perforant path. J Physiol 232:331–356

Bloodgood BL, Sabatini BL (2007) Nonlinear regulation of unitary synaptic signals by CaV(2.3) voltage-sensitive calcium channels located in dendritic spines. Neuron 53:249–260

Buchanan KA, Mellor JR (2007) The development of synaptic plasticity induction rules and the requirement for postsynaptic spikes in rat hippocampal CA1 pyramidal neurones. J Physiol Lond 585:429–445

Burrone J, O'Byrne M, Murthy VN (2002) Multiple forms of synaptic plasticity triggered by selective suppression of activity in individual neurons. Nature 420:414–418

Caillard O, Ben-Ari Y, Gaiarsa JL (1999) Long-term potentiation of GABAergic synaptic transmission in neonatal rat hippocampus. J Physiol 518(Pt 1):109–119

Carta M, Lanore F, Rebola N, Szabo Z, Da Silva SV, Lourenco J, Verraes A, Nadler A, Schultz C, Blanchet C, Mulle C (2014) Membrane lipids tune synaptic transmission by direct modulation of presynaptic potassium channels. Neuron 81:787–799

Castillo PE, Weisskopf MG, Nicoll RA (1994) The role of Ca2+ channels in hippocampal mossy fiber synaptic transmission and long-term potentiation. Neuron 12:261–269

Chevaleyre V, Castillo PE (2003) Heterosynaptic LTD of hippocampal GABAergic synapses: a novel role of endocannabinoids in regulating excitability. Neuron 38:997–997, pg 461

Chevaleyre V, Siegelbaum SA (2010) Strong CA2 pyramidal neuron synapses define a powerful disynaptic cortico-hippocampal loop. Neuron 66:560–572

Cho K, Aggleton JP, Brown MW, Bashir ZI (2001) An experimental test of the role of postsynaptic calcium levels in determining synaptic strength using perirhinal cortex of rat. J Physiol Lond 532:459–466

Christie BR, Abraham WC (1992) Priming of associative long-term depression in the dentate gyrus by theta frequency synaptic activity. Neuron 9:79–84

Cohen AS, Abraham WC (1996) Facilitation of long-term potentiation by prior activation of metabotropic glutamate receptors. J Neurophysiol 76:953–962

Colino A, Malenka RC (1993) Mechanisms underlying induction of long-term potentiation in rat medial and lateral perforant paths in vitro. J Neurophysiol 69:1150–1159

Contractor A, Rogers C, Maron C, Henkemeyer M, Swanson GT, Heinemann SF (2002) Trans-synaptic Eph receptor-ephrin signaling in hippocampal mossy fiber LTP. Science 296:1864–1869

Cormier RJ, Greenwood AC, Connor JA (2001) Bidirectional synaptic plasticity correlated with the magnitude of dendritic calcium transients above a threshold. J Neurophysiol 85:399–406

Davies CH, Starkey SJ, Pozza MF, Collingridge GL (1991) GABA autoreceptors regulate the induction of LTP. Nature 349:609–611

Daw MI, Chittajallu R, Bortolotto ZA, Dev KK, Duprat F, Henley JM, Collingridge GL, Isaac JTR (2000) PDZ proteins interacting with C-terminal GluR2/3 are involved in a PKC-dependent regulation of AMPA receptors at hippocampal synapses. Neuron 28:873–886

Debanne D, Gahwiler BH, Thompson SM (1998) Long-term synaptic plasticity between pairs of individual CA3 pyramidal cells in rat hippocampal slice cultures. J Physiol Lond 507:237–247
Dobrunz LE, Stevens CF (1999) Response of hippocampal synapses to natural stimulation patterns. Neuron 22:157–166
Doyere V, Srebro B, Laroche S (1997) Heterosynaptic LTD and depotentiation in the medial perforant path of the dentate gyrus in the freely moving rat. J Neurophysiol 77:571–578
Dudek SM, Bear MF (1992) Homosynaptic long-term depression in area CA1 of hippocampus and effects of N-methyl-D-aspartate receptor blockade. Proc Natl Acad Sci U S A 89:4363–4367
Dudek SM, Bear MF (1993) Bidirectional long-term modification of synaptic effectiveness in the adult and immature Hippocampus. J Neurosci 13:2910–2918
Dudman JT, Tsay D, Siegelbaum SA (2007) A role for synaptic inputs at distal dendrites: instructive signals for hippocampal long-term plasticity. Neuron 56:866–879
Dunwiddie T, Lynch G (1978) Long-term potentiation and depression of synaptic responses in the rat hippocampus: localization and frequency dependency. J Physiol 276:353–367
Frick A, Magee J, Johnston D (2004) LTP is accompanied by an enhanced local excitability of pyramidal neuron dendrites. Nat Neurosci 7:126–135
Froemke RC, Dan Y (2002) Spike-timing-dependent synaptic modification induced by natural spike trains. Nature 416:433–438
Froemke RC, Tsay IA, Raad M, Long JD, Dan Y (2006) Contribution of individual spikes in burst-induced long-term synaptic modification. J Neurophysiol 95:1620–1629
Gall D, Prestori F, Sola E, D'Errico A, Roussel C, Forti L, Rossi P, D'Angelo E (2005) Intracellular calcium regulation by burst discharge determines bidirectional long-term synaptic plasticity at the cerebellum input stage. J Neurosci 25:4813–4822
Geiger JRP, Jonas P (2000) Dynamic control of presynaptic Ca^{2+} inflow by fast-inactivating K^+ channels in hippocampal mossy fiber boutons. Neuron 28:927–939
Gisabella B, Rowan MJ, Anwyl R (2003) Mechanisms underlying the inhibition of long-term potentiation by preconditioning stimulation in the hippocampus in vitro. Neuroscience 121:297–305
Golding NL, Staff NP, Spruston N (2002) Dendritic spikes as a mechanism for cooperative long-term potentiation. Nature 418:326–331
Golding NL, Mickus TJ, Katz Y, Kath WL, Spruston N (2005) Factors mediating powerful voltage attenuation along CA1 pyramidal neuron dendrites. J Physiol 568:69–82
Golowasch J, Casey M, Abbott LF, Marder E (1999) Network stability from activity-dependent regulation of neuronal conductances. Neural Comput 11:1079–1096
Gruart A, Munoz MD, Delgado-Garcia JM (2006) Involvement of the CA3-CA1 synapse in the acquisition of associative learning in behaving mice. J Neurosci 26:1077–1087
Gundlfinger A, Leibold C, Gebert K, Moisel M, Schmitz D, Kempter R (2007) Differential modulation of short-term synaptic dynamics by long-term potentiation at mouse hippocampal mossy fibre synapses. J Physiol 585:853–865
Hangya B, Ranade SP, Lorenc M, Kepecs A (2015) Central cholinergic neurons are rapidly recruited by reinforcement feedback. Cell 162:1155–1168
Hansel C, Artola A, Singer W (1996) Different threshold levels of postsynaptic [Ca2+]i have to be reached to induce LTP and LTD in neocortical pyramidal cells. J Physiol Paris 90:317–319
Hansel C, Artola A, Singer W (1997) Relation between dendritic Ca2+ levels and the polarity of synaptic long-term modifications in rat visual cortex neurons. Eur J Neurosci 9:2309–2322
Harnett MT, Makara JK, Spruston N, Kath WL, Magee JC (2012) Synaptic amplification by dendritic spines enhances input cooperativity. Nature 491:599–602
Harris EW, Cotman CW (1986) Long-term potentiation of Guinea pig mossy fiber responses is not blocked by N-methyl D-aspartate antagonists. Neurosci Lett 70:132–137
Hebb D (1949) The organisation of behaviour. Wiley, New York
Henze DA, Wittner L, Buzsaki G (2002) Single granule cells reliably discharge targets in the hippocampal CA3 network in vivo. Nat Neurosci 5:790–795

Hochbaum DR, Zhao Y, Farhi SL, Klapoetke N, Werley CA, Kapoor V, Zou P, Kralj JM, Maclaurin D, Smedemark-Margulies N et al (2014) All-optical electrophysiology in mammalian neurons using engineered microbial rhodopsins. Nat Methods 11:825–833

Huang YY, Colino A, Selig DK, Malenka RC (1992) The influence of prior synaptic activity on the induction of long-term potentiation. Science 255:730–733

Huerta PT, Lisman JE (1993) Heightened synaptic plasticity of hippocampal Ca1 neurons during a cholinergically induced rhythmic state. Nature 364:723–725

Huerta PT, Lisman JE (1995) Bidirectional synaptic plasticity induced by a single burst during cholinergic Theta-oscillation in Ca1 in-vitro. Neuron 15:1053–1063

Isaac JT, Nicoll RA, Malenka RC (1995) Evidence for silent synapses: implications for the expression of LTP. Neuron 15:427–434

Isaac JT, Buchanan KA, Muller RU, Mellor JR (2009) Hippocampal place cell firing patterns can induce long-term synaptic plasticity in vitro. J Neurosci 29:6840–6850

Ismailov I, Kalikulov D, Inoue T, Friedlander MJ (2004) The kinetic profile of intracellular calcium predicts long-term potentiation and long-term depression. J Neurosci 24:9847–9861

Jahr CE, Stevens CF (1990) A quantitative description of NMDA receptor-channel kinetic behavior. J Neurosci 10:1830–1837

Kampa BM, Clements J, Jonas P, Stuart GJ (2004) Kinetics of Mg2+ unblock of NMDA receptors: implications for spike-timing dependent synaptic plasticity. J Physiol 556:337–345

Karmarkar UR, Buonomano DV (2002) A model of spike-timing dependent plasticity: one or two coincidence detectors? J Neurophysiol 88:507–513

Keck T, Keller GB, Jacobsen RI, Eysel UT, Bonhoeffer T, Hubener M (2013) Synaptic scaling and homeostatic plasticity in the mouse visual cortex in vivo. Neuron 80:327–334

Keller DX, Franks KM, Bartol TM Jr, Sejnowski TJ (2008) Calmodulin activation by calcium transients in the postsynaptic density of dendritic spines. PLoS One 3:e2045

Kemp N, McQueen J, Faulkes S, Bashir ZI (2000) Different forms of LTD in the CA1 region of the hippocampus: role of age and stimulus protocol. Eur J Neurosci 12:360–366

Kobayashi K, Poo MM (2004) Spike train timing-dependent associative modification of hippocampal CA3 recurrent synapses by mossy fibers. Neuron 41:445–454

Kobayashi K, Manabe T, Takahashi T (1996) Presynaptic long-term depression at the hippocampal mossy fiber-CA3 synapse. Science 273:648–650

Kobayashi K, Manabe T, Takahashi T (1999) Calcium-dependent mechanisms involved in presynaptic long-term depression at the hippocampal mossy fibre-CA3 synapse. Eur J Neurosci 11:1633–1638

Kohl MM, Shipton OA, Deacon RM, Rawlins JN, Deisseroth K, Paulsen O (2011) Hemisphere-specific optogenetic stimulation reveals left-right asymmetry of hippocampal plasticity. Nat Neurosci 14:1413–1415

Kwag J, Paulsen O (2009) The timing of external input controls the sign of plasticity at local synapses. Nat Neurosci 12:1219–1221

Kwon HB, Castillo PE (2008) Long-term potentiation selectively expressed by NMDA receptors at hippocampal mossy fiber synapses. Neuron 57:108–120

Laezza F, Doherty JJ, Dingledine R (1999) Long-term depression in hippocampal interneurons: joint requirement for pre- and postsynaptic events. Science 285:1411–1414

Lamsa K, Heeroma JH, Kullmann DM (2005) Hebbian LTP in feed-forward inhibitory interneurons and the temporal fidelity of input discrimination. Nat Neurosci 8:916–924

Lamsa KP, Heeroma JH, Somogyi P, Rusakov DA, Kullmann DM (2007) Anti-Hebbian long-term potentiation in the hippocampal feedback inhibitory circuit. Science 315:1262–1266

Langmead CJ, Austin NE, Branch CL, Brown JT, Buchanan KA, Davies CH, Forbes IT, Fry VA, Hagan JJ, Herdon HJ et al (2008) Characterization of a CNS penetrant, selective M1 muscarinic receptor agonist, 77-LH-28-1. Br J Pharmacol 154:1104–1115

Larson J, Wong D, Lynch G (1986) Patterned stimulation at the theta-frequency is optimal for the induction of hippocampal long-term potentiation. Brain Res 368:347–350

Lee AK, Manns ID, Sakmann B, Brecht M (2006) Whole-cell recordings in freely moving rats. Neuron 51:399–407

Lei S, McBain CJ (2002) Distinct NMDA receptors provide differential modes of transmission at mossy fiber-interneuron synapses. Neuron 33:921–933
Lei S, Pelkey KA, Topolnik L, Congar P, Lacaille JC, McBain CJ (2003) Depolarization-induced long-term depression at hippocampal mossy fiber-CA3 pyramidal neuron synapses. J Neurosci 23:9786–9795
Letzkus JJ, Kampa BM, Stuart GJ (2006) Learning rules for spike timing-dependent plasticity depend on dendritic synapse location. J Neurosci 26:10420–10429
Levy WB, Steward O (1979) Synapses as associative memory elements in the hippocampal formation. Brain Res 175:233–245
Lisman J (1989) A mechanism for the Hebb and the anti-Hebb processes underlying learning and memory. Proc Natl Acad Sci U S A 86:9574–9578
Losonczy A, Magee JC (2006) Integrative properties of radial oblique dendrites in hippocampal CA1 pyramidal neurons. Neuron 50:291–307
Lovett-Barron M, Kaifosh P, Kheirbek MA, Danielson N, Zaremba JD, Reardon TR, Turi GF, Hen R, Zemelman BV, Losonczy A (2014) Dendritic inhibition in the hippocampus supports fear learning. Science 343:857–863
Maccaferri G, Toth K, McBain CJ (1998) Target-specific expression of presynaptic mossy fiber plasticity. Science 279:1368–1370
Maccaferri G, Roberts JD, Szucs P, Cottingham CA, Somogyi P (2000) Cell surface domain specific postsynaptic currents evoked by identified GABAergic neurones in rat hippocampus in vitro. J Physiol 524(Pt 1):91–116
Magee JC, Johnston D (1997) A synaptically controlled, associative signal for Hebbian plasticity in hippocampal neurons. Science 275:209–213
Malenka RC, Bear MF (2004) LTP and LTD: an embarrassment of riches. Neuron 44:5–21
Markram H, Lubke J, Frotscher M, Sakmann B (1997) Regulation of synaptic efficacy by coincidence of postsynaptic APs and EPSPs. Science 275:213–215
McBain CJ, Mayer ML (1994) N-methyl-D-aspartic acid receptor structure and function. Physiol Rev 74:723–760
McHugh TJ, Blum KI, Tsien JZ, Tonegawa S, Wilson MA (1996) Impaired hippocampal representation of space in CA1-specific NMDAR1 knockout mice. Cell 87:1339–1349
McHugh TJ, Jones MW, Quinn JJ, Balthasar N, Coppari R, Elmquist JK, Lowell BB, Fanselow MS, Wilson MA, Tonegawa S (2007) Dentate gyrus NMDA receptors mediate rapid pattern separation in the hippocampal network. Science 317:94–99
McMahon LL, Kauer JA (1997) Hippocampal interneurons express a novel form of synaptic plasticity. Neuron 18:295–305
McNaughton BL, Douglas RM, Goddard GV (1978) Synaptic enhancement in fascia dentata: cooperativity among coactive afferents. Brain Res 157:277–293
Mellor J, Nicoll RA (2001) Hippocampal mossy fiber LTP is independent of postsynaptic calcium. Nat Neurosci 4:125–126
Meredith RM, Floyer-Lea AM, Paulsen O (2003) Maturation of long-term potentiation induction rules in rodent hippocampus: role of GABAergic inhibition. J Neurosci 23:11142–11146
Miller KD (1996) Synaptic economics: competition and cooperation in synaptic plasticity. Neuron 17:371–374
Mistry R, Dennis S, Frerking M, Mellor JR (2011) Dentate gyrus granule cell firing patterns can induce mossy fiber long-term potentiation in vitro. Hippocampus 21:1157–1168
Monyer H, Burnashev N, Laurie DJ, Sakmann B, Seeburg PH (1994) Developmental and regional expression in the rat brain and functional properties of four NMDA receptors. Neuron 12:529–540
Morris RGM, Anderson E, Lynch GS, Baudry M (1986) Selective impairment of learning and blockade of long-term potentiation by an N-methyl-D-aspartate receptor antagonist, Ap5. Nature 319:774–776
Mulkey RM, Malenka RC (1992) Mechanisms underlying induction of homosynaptic long-term depression in area CA1 of the hippocampus. Neuron 9:967–975

Nakazawa K, Quirk MC, Chitwood RA, Watanabe M, Yeckel MF, Sun LD, Kato A, Carr CA, Johnston D, Wilson MA, Tonegawa S (2002) Requirement for hippocampal CA3 NMDA receptors in associative memory recall. Science 297:211–218

Nevian T, Sakmann B (2006) Spine Ca2+ signaling in spike-timing-dependent plasticity. J Neurosci 26:11001–11013

Nicoll RA, Kauer JA, Malenka RC (1988) The current excitement in long-term potentiation. Neuron 1:97–103

Nishiyama M, Hong K, Mikoshiba K, Poo M, Kato K (2000) Calcium stores regulate the polarity and input specificity of synaptic modification. Nature 408:584–588

Nowak L, Bregestovski P, Ascher P, Herbet A, Prochiantz A (1984) Magnesium gates glutamate-activated channels in mouse central neurons. Nature 307:462–465

O'Brien RJ, Kamboj S, Ehlers MD, Rosen KR, Fischbach GD, Huganir RL (1998) Activity-dependent modulation of synaptic AMPA receptor accumulation. Neuron 21:1067–1078

Palmer LM, Stuart GJ (2009) Membrane potential changes in dendritic spines during action potentials and synaptic input. J Neurosci 29:6897–6903

Pastalkova E, Serrano P, Pinkhasova D, Wallace E, Fenton AA, Sacktor TC (2006) Storage of spatial information by the maintenance mechanism of LTP. Science 313:1141–1144

Patneau DK, Mayer ML (1990) Structure-activity relationships for amino acid transmitter candidates acting at N-methyl-D-aspartate and quisqualate receptors. J Neurosci 10:2385–2399

Pike FG, Meredith RM, Olding AWA, Paulsen O (1999) Postsynaptic bursting is essential for 'Hebbian' induction of associative long-term potentiation at excitatory synapses in rat hippocampus. J Physiol Lond 518:571–576

Rebola N, Lujan R, Cunha RA, Mulle C (2008) Adenosine A2A receptors are essential for long-term potentiation of NMDA-EPSCs at hippocampal mossy fiber synapses. Neuron 57:121–134

Rebola N, Carta M, Lanore F, Blanchet C, Mulle C (2011) NMDA receptor-dependent metaplasticity at hippocampal mossy fiber synapses. Nat Neurosci 14:691–693

Regehr WG, Tank DW (1991) The maintenance of LTP at hippocampal mossy fiber synapses is independent of sustained presynaptic calcium. Neuron 7:451–459

Rose GM, Dunwiddie TV (1986) Induction of hippocampal long-term potentiation using physiologically patterned stimulation. Neurosci Lett 69:244–248

Sadowski JH, Jones MW, Mellor JR (2016) Sharp-wave ripples orchestrate the induction of synaptic plasticity during reactivation of place cell firing patterns in the hippocampus. Cell Rep 14:1916–1929

Salin PA, Scanziani M, Malenka RC, Nicoll RA (1996) Distinct short-term plasticity at two excitatory synapses in the hippocampus. Proc Natl Acad Sci U S A 93:13304–13309

Schmitz D, Mellor J, Breustedt J, Nicoll RA (2003) Presynaptic kainate receptors impart an associative property to hippocampal mossy fiber long-term potentiation. Nat Neurosci 6:1058–1063

Seol GH, Ziburkus J, Huang S, Song L, Kim IT, Takamiya K, Huganir RL, Lee HK, Kirkwood A (2007) Neuromodulators control the polarity of spike-timing-dependent synaptic plasticity. Neuron 55:919–929

Sheffield ME, Dombeck DA (2015) Calcium transient prevalence across the dendritic arbour predicts place field properties. Nature 517:200–204

Shew T, Yip S, Sastry BR (2000) Mechanisms involved in tetanus-induced potentiation of fast IPSCs in rat hippocampal CA1 neurons. J Neurophysiol 83:3388–3401

Shouval HZ, Kalantzis G (2005) Stochastic properties of synaptic transmission affect the shape of spike time-dependent plasticity curves. J Neurophysiol 93:1069–1073

Silver RA, Traynelis SF, Cull-Candy SG (1992) Rapid-time-course miniature and evoked excitatory currents at cerebellar synapses in situ. Nature 355:163–166

Sjostrom PJ, Hausser M (2006) A cooperative switch determines the sign of synaptic plasticity in distal dendrites of neocortical pyramidal neurons. Neuron 51:227–238

Sjostrom PJ, Nelson SB (2002) Spike timing, calcium signals and synaptic plasticity. Curr Opin Neurobiol 12:305–314

Sjostrom PJ, Turrigiano GG, Nelson SB (2001) Rate, timing, and cooperativity jointly determine cortical synaptic plasticity. Neuron 32:1149–1164
Sjostrom PJ, Turrigiano GG, Nelson SB (2003) Neocortical LTD via coincident activation of presynaptic NMDA and cannabinoid receptors. Neuron 39:641–654
Spruston N, Schiller Y, Stuart G, Sakmann B (1995) Activity-dependent action-potential invasion and calcium influx into hippocampal Ca1 dendrites. Science 268:297–300
Tigaret CM, Olivo V, Sadowski JH, Ashby MC, Mellor JR (2016) Coordinated activation of distinct Ca(2+) sources and metabotropic glutamate receptors encodes Hebbian synaptic plasticity. Nat Commun 7:10289
Tonnesen J, Katona G, Rozsa B, Nagerl UV (2014) Spine neck plasticity regulates compartmentalization of synapses. Nat Neurosci 17:678–685
Turrigiano GG, Leslie KR, Desai NS, Rutherford LC, Nelson SB (1998) Activity-dependent scaling of quantal amplitude in neocortical neurons. Nature 391:892–896
Tzounopoulos T, Janz R, Südhof TC, Nicoll RA, Malenka RC (1998) A role for cAMP in long-term depression at hippocampal mossy fiber synapses. Neuron 21:837–845
Weisskopf MG, Zalutsky RA, Nicoll RA (1993) The opioid peptide dynorphin mediates heterosynaptic depression of hippocampal mossy fibre synapses and modulates long-term potentiation. Nature 365:188
Whitlock JR, Heynen AJ, Shuler MG, Bear MF (2006) Learning induces long-term potentiation in the hippocampus. Science 313:1093–1097
Wigstrom H, Gustafsson B (1983) Facilitated induction of hippocampal long-lasting potentiation during blockade of inhibition. Nature 301:603–604
Wittenberg GM, Wang SSH (2006) Malleability of spike-timing-dependent plasticity at the CA3-CA1 synapse. J Neurosci 26:6610–6617
Woodin MA, Ganguly K, Poo MM (2003) Coincident pre- and postsynaptic activity modifies GABAergic synapses by postsynaptic changes in Cl- transporter activity. Neuron 39:807–820
Wozny C, Maier N, Schmitz D, Behr J (2008) Two different forms of long-term potentiation at CA1-subiculum synapses. J Physiol 586:2725–2734
Yeckel MF, Kapur A, Johnston D (1999) Multiple forms of LTP in hippocampal CA3 neurons use a common postsynaptic mechanism. Nat Neurosci 2:625–633
Zalutsky RA, Nicoll RA (1990) Comparison of two forms of long-term potentiation in single hippocampal neurons. Science 248:1619–1624
Zucker RS, Regehr WG (2002) Short-term synaptic plasticity. Annu Rev Physiol 64:355–405

Neuromodulation of Hippocampal Cells and Circuits

J. Josh Lawrence and Stuart Cobb

Abstract The hippocampus is a major brain centre for information processing, where subcortical neuromodulatory circuits interface with intrinsic learning circuits to assign salience to sensory information relevant to behavioural state. Glutamatergic principal cells (PCs) of the dentate gyrus (DG), CA3 and CA1 regions comprise the classic trisynaptic circuit, which compare patterns of incoming sensory stimuli with internal representations, enabling the detection of novelty. Within the trisynaptic circuitry, distinct feedforward and feedback inhibitory circuits spatiotemporally constrain the timing of PC excitability, which, together with disinhibitory circuits, synchronize PC ensembles to generate network rhythms. Neuromodulation alters network rhythms and synaptic plasticity by releasing neurotransmitters and neuropeptides onto diverse receptor subtypes, often expressed in a cell type- and circuit-specific manner. Moreover, extrinsic neuromodulation can induce the secondary release of intrinsic neuromodulators. For each neurotransmitter system, we review the structural organization and target specificity of afferent innervation, receptor subtype distribution and, where known, their functional effects on hippocampal cells and circuits. Despite the complexity involved and evident gaps in scientific knowledge, general principles of neuromodulation are emerging. With the development of next-generation technologies, the vision of understanding how neuromodulatory mechanisms engage circuit elements to regulate hippocampal memory encoding and recall is coming into sharper focus.

J. Josh Lawrence (✉)
Department of Pharmacology and Neuroscience, Centre for Translational Neuroscience and Therapeutics, Texas Tech University Health Sciences Centre School of Medicine, Lubbock, TX, USA
e-mail: john.lawrence@ttuhsc.edu

S. Cobb (✉)
Centre for Discovery Brain Sciences, University of Edinburgh, Edinburgh, UK
e-mail: stuart.cobb@ed.ac.uk

V. Cutsuridis et al. (eds.), *Hippocampal Microcircuits*, Springer Series in Computational Neuroscience, https://doi.org/10.1007/978-3-319-99103-0_7

Overview

Neuromodulation is the processes by which the properties of neurons and synapses are altered by neuroactive substances termed neuromodulators. The distinction between neuromodulation and classical neurotransmission can be fuzzy, but, in general, neuromodulation is more diffuse and less targeted and acts over a longer time course than classical fast neurotransmission. Often the same neurochemical may have rapid neurotransmitter-like effects followed by more sustained modulator-like actions. What makes neuromodulation an important consideration is that it appears to be a fundamental process in modifying all aspects of neural network functioning and information processing. Neural networks are not hard-wired, but plastic, and the neuromodulation of its components yields distinct activity patterns that are associated with behavioural state, allowing the same neural circuit to have added computational power. These components include the modification of neuronal excitability, integrative properties of neurons, synaptic transmission and synaptic plasticity. Neuromodulators often have more than one cellular or synaptic consequence. Moreover, not all cellular or synaptic targets of neuromodulation produce the same effects. Due the omnipotent control of the user over parameter space, computational modelling is a powerful tool for gaining insight into how cellular and synaptic targets of neuromodulation alter the functional output of neuronal populations and the processing of synaptic signals within networks. Beyond the acute effects of neuromodulation on cellular and synaptic excitability are longer-term changes in gene expression and neuronal architecture that are essential in regulating developmental processes and structural plasticity. This chapter circumscribes the acute cellular and synaptic effects of neuromodulation on cellular targets within the hippocampal formation. Whilst necessary to constrain the scope of this chapter, the multi-faceted parameter space involved in neuromodulation is so complex that it invites, if not demands, computational modelling to validate specific neuromodulatory mechanisms at work.

The Data

Introduction

The hippocampus receives input from a multitude of neuromodulatory substances, the release of which is often associated with external factors or dependent upon particular behavioural states. This chapter summarizes some of the primary neuromodulators including those that arise from sources extrinsic to the hippocampus (mainly subcortical nuclei) as well as those originating from cells intrinsic to the hippocampal formation. There may be important functional distinctions between intrinsic and extrinsic forms of neuromodulation (Katz and Frost 1996; Marder 2012) with the most obvious being that extrinsic neuromodulation is usually inde-

pendent of ongoing activity within the circuits being modulated, whereas cells or synapses undergoing intrinsic modulation often do so as a result of ongoing activity within those same circuits. However, the extensive reciprocal interconnectivity from the hippocampus to cortex (Melzer et al. 2012), hypothalamus (Jimenez et al. 2018) and subcortical neuromodulatory nuclei (Mattis et al. 2014; Yuan et al. 2017) makes this distinction somewhat superficial (Caputi et al. 2013). As discussed in earlier chapters, glutamate and GABA have multiple modes of action, which still provide important foundational principles upon which to understand other neurotransmitter systems. In addition to ligand-gated ion channels for rapid transmission, slower, often intrinsic neuromodulatory actions are also produced through metabotropic signalling. Many of the 'classical' neuromodulators presented here act in a similar manner and generally provide extrinsic neuromodulation as their sources of input are derived predominantly from subcortical nuclei. Although some modulators, such as acetylcholine and serotonin, appear to possess machinery for fast, point-to-point transmission, 'volume transmission', in which neurotransmitters are released at non-synaptic varicosities, diffuses to high-affinity metabotropic receptors and appears to be a major mode of transmission. It is possible, due to differences in the proximity of neuromodulatory release sites and postsynaptic composition of receptors, that specific cellular targets may employ point-to-point, volume or both modes of transmission. Along the lines of how views of GABAergic transmission have evolved (Farrant and Nusser 2005), one may view these modes of synaptic transmission along a continuum, in that any given hippocampal postsynaptic neuronal cell type may possess a different ratio of point-to-point and volume transmission. Furthermore, this ratio may change dynamically depending on firing frequency of the presynaptic neuromodulatory neurons, magnitude of the neurotransmitter concentration transient, short-term plasticity dynamics of neurotransmitter release, state of occupancy of postsynaptic receptors and neurotransmitter transporters and pooling in the extracellular space. Optogenetic strategies that allow for stimulation of specific neurochemically restricted synapse types are leading to a better understanding of the spatiotemporal dynamics of synaptic neurotransmission (Lorincz and Adamantidis 2017). As with $GABA_A$ receptors, it may soon be possible to categorize neuromodulatory receptors as synaptic ('phasic'), perisynaptic ('spillover' or 'augmented transmission') and tonically active, high-affinity receptors (Farrant and Nusser 2005). Therefore, it is important to recognize that classic pharmacological manipulations, such as bath application of a fixed agonist concentration, may not necessarily mimic volume transmission. Indeed, it is increasingly likely that populations of 'extrasynaptic' receptors can be stimulated by bath application of exogenous agonists but are simply too far away from release sites to be activated by the spatiotemporal concentration transient of endogenous neurotransmitter release. Artificial, pathological or therapeutic interventions may dynamically alter spatiotemporal concentration transients, effectively redefining which neurotransmitter receptors can be classified as synaptic receptors. Whilst extrasynaptic receptors that are not normally activated under physiological circumstances may be considered irrelevant, or even confounding, in understanding synaptic transmission from a 'purist' biophysical perspective, their existence becomes important in understanding

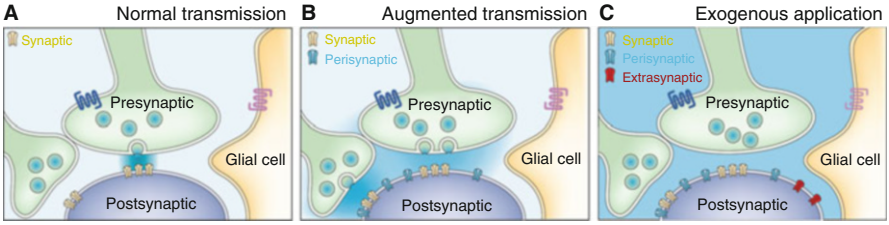

Fig. 1 Different types of neuromodulatory receptors. (**a**) Synaptic receptors (yellow) localized in the immediate vicinity of neurotransmitter release sites are activated. (**b**) Both perisynaptic (blue) and synaptic receptors are activated when multiple simultaneously active synaptic terminals induce 'spillover' from delayed neurotransmitter clearance or when neurotransmitter transport is compromised. (**c**) Exogenous application of neurotransmitter or a non-specific receptor agonist will activate synaptic, perisynaptic and extrasynaptic (red) receptors. In addition, if extrasynaptic receptors are tonically active, application of an antagonist will block these receptors. (Modified from Farrant et al. 2005, with permission)

roles that some neurotransmitters play in setting the 'tone' of transmission. Moreover, pharmacological and therapeutic interventions, such as the use of specific neurotransmitter receptor agonists, allosteric modulators and antagonists, may ultimately change cellular excitability by altering these extrasynaptic receptors. It is therefore important not only to understand how specific neuromodulatory afferents interact with their associated postsynaptic receptors but also to understand the receptor distribution on postsynaptic neurons independent of its relationship to the endogenous neurotransmitter (Fig. 1).

In addition to classical neuromodulatory transmitters, many neuropeptides exert effects in the hippocampus that originate from extrinsic sources, but also from local hippocampal circuits, to provide additional layers of intrinsic modulation. Other modulators including endocannabinoids and nitric oxide have an even more localized autocrine/paracrine modulatory action and are thought to mediate exclusively intrinsic modulation. In some cases, extrinsic neuromodulation by classical neurotransmitters induces secondary effects mediated by intrinsic modulation, as demonstrated by the capacity of metabotropic receptor activation or elevated intracellular calcium to induce release of endocannabinoids. However, whether the modulation is driven by extrinsic or intrinsic sources, the loci of action is an essential factor and can include modification of (1) the properties of presynaptic neurotransmitter release, (2) the modification of postsynaptic responsiveness/receptor signalling and/or (3) the modulation of the postsynaptic intrinsic electrical and biochemical properties or gene regulation. Understanding the overall actions of a neuromodulator that occur on multiple timescales is thus especially challenging. The challenge is even greater if one considers that receptors, intracellular signalling pathways and effectors all could be independently expressed in a cell type-specific manner. The most significant obstacle is that neuromodulators do not simply excite or inhibit neurons in the classical sense. Rather, they usually signal through intracellular messenger cascades to modulate not one but a range of effectors.

This may include the gating of ion channels that orchestrate the response to classical neurotransmitters. That is, they change the way neurons respond to signals arising from other neurons whether that be due to altered intrinsic properties of the receptive neuron or to altered postsynaptic responsiveness or as a result of altered properties of the presynaptic neuron such as action potential patterns and/or neurotransmitter release probability. As a consequence, what an experimenter sees following manipulation of neurotransmitter/modulator mechanisms depends upon how the cell or system is investigated. As pointed out by Surmeier (Surmeier 2007), different questions produce different answers!

Modulation of Intrinsic Properties

Neuromodulators can regulate a diverse range of ion channels and other effectors that modify the active and passive properties of hippocampal neurons. The excitability of cells can be altered in three different ways. (1) Neuromodulation can alter the resting membrane potential, in the form of depolarization or hyperpolarization. This action has several consequences. First, it will bring the cell closer or farther away from the threshold for action potential initiation. This makes a given excitatory synaptic input more or less effective. Secondly, alteration in the resting membrane potential may be associated with a different set of cellular conductances, which themselves could influence the intrinsic membrane properties of the neuron. (2) Neuromodulation also can directly alter the passive properties of the cell, including the cell input resistance and membrane time constant. This is done through neuromodulation of the conductances involved at a given resting potential, such as leak conductances or steady-state conductance. This effect changes the computational properties of the neuron. For example, an increase in the membrane time constant will broaden the excitatory postsynaptic potential (EPSP) so that fewer EPSPs are required to summate to action potential threshold. Another consequence of increasing the input resistance and membrane time constant is to alter the RC filtering characteristics of the cell, thereby impacting the ability of the cell to follow frequency-specific input. (3) Active conductances may also undergo neuromodulation. Depending on the kinetics of activation of the conductances modulated, the action potential waveform, various afterhyperpolarizing potentials and/or action potential discharge patterns are altered by neuromodulation. Some of these effects are summarized in Table 1 and described under the individual neuromodulator headings.

Different neuromodulatory substances often converge onto common effectors to produce similar actions. For example, activation of metabotropic $GABA_B$ receptors, adenosine A1 receptors and serotonin 5-HT_{1A} receptors in CA1 pyramidal cells all increase a common potassium conductance (Nicoll et al. 1990; Sodickson and Bean 1998), thereby providing several redundant and/or synergistic cellular mechanisms for reducing cellular excitability. However, whilst some generalizations may be made, the situation often is far more complex. As seen in the earlier chapters, different hippocampal neurons are endowed with different channels and

Table 1 Summary of key neuromodulator actions

Modulator	Pyramidal cells	postsynaptic	Interneurons	postsynaptic
		presynaptic		presynaptic
Acetylcholine	Depolarization, ↓adaptation, phasic inhibition ↑ I_h, I_{CAT}; ↓ I_M, I_{AHP}, I_{Kleak} (m), ↑$_{IK(Ca)}$		Depolarization, ↓adaptation or hyperpolarization (m / n) I_{CAT}; ↓ I_M, I_{AHP}, ↑ I_{Kir}	
	↓ glutamate release (m), ↑(n)		↓ GABA release (m), ↑ (n)	
Norepinephrine	↓ sAHP; ↓ adaptation (β)		↓K conductance (α); ↑ *I*h (β)	
Dopamine	Hyperpolarization, ↓adaptation, ↓AHP, ↓ Ca^{++} activated *I*k		ND	
	↓ glutamate release (most pathways), ↑ transmitter release (mossy fibers)		↓ GABA release (D_3)	
Serotonin	Hyperpolarization, ↓adaptation ↓I_h (5HT1A); ↑I_h, ↓I_{AHP} ($5HT_7$, $5HT_4$)		$5HT_2$ is excitatory	
	↓ glutamate release, ↓ induction of LTP		↑ GABA release ($5HT_{2+3}$)	
Histamine	Depolarization (dominant, H_2) or hyperpolarization (H_1)		Depolarization (H_2) ↓*I*Kv3.2	
	↓ glutamate release, direction action on NMDA receptors		ND	
Adenosine	Hyperpolarization (A_1, A_{2A}), ↑gK		ND	
	↓ glutamate release, ↓ induction of LTP		Little effect	
ATP	Fast inward current (P2X), ↑gK		ND	
	Contribute to fast EPSP/C (P2X), regulate LTP/LTD		ND	
Endocannabinoids	Modest depolarization, ↓I_M		Little effect	
	↓ glutamate release, DSE		↓ GABA release, DSI	
Nitric oxide	None		None	
	↑LTP		May contribute to DSI	
Neuropeptides	See table 7			

Arrows indicate direction of change. White and grey boxes represent postsynaptic and presynaptic actions, respectively (for more detail and other actions, see text below). Parentheses show receptor subtypes where known

Abbreviations: *ND* not determined, I_{AHP} afterhyperpolarization current, I_{CAT} cation current, I_h hyperpolarization-activated current, I_M M current

neurotransmitter receptor subtypes. For any given modulatory substance in any given cell, the exact channels modulated will depend upon the presence and spatial localization of particular subtype(s) of receptors, together with the presence and spatial localization of coupled ion channels and other effectors. Intracellular signalling is another major determinant of the response, and despite its ubiquity, studies suggest that signalling can be very specific and targeted to specific loci or subcellular compartments within a cell (Kulik et al. 2006; Shigemoto et al. 1996). Moreover, if release of calcium from internal stores is involved, the response will also depend on the history of action potential activity, since intracellular calcium stores can be depleted unless replenished through activation of voltage-gated calcium channels (Gulledge and Kawaguchi 2007; Gulledge et al. 2009). It is through calcium imaging (Grienberger and Konnerth 2012), voltage-sensitive dye imaging (Acker et al. 2011) and the introduction of molecular biosensors and other transduction processes (Sanford and Palmer 2017) that we are beginning to learn how modulation can be restricted to localized microdomains or compartments yet have profound effects on output.

Modulation of Excitatory Synaptic Transmission

The laminar structure of the hippocampal formation lends itself to the study of excitatory pathways. It has long been observed that a wide range of neuromodulatory substances can affect glutamatergic neurotransmission. Whilst many modulators have general actions across very many synapses, such as the suppressant actions of adenosine, others appear to have very precise synapse-specific actions. One of the best examples of synapse-specific effects is the suppression of transmission by activation of group II mGluRs at the mossy fibre (MF)-to-CA3 pyramidal cell synapse but not at Schaeffer collateral (SC) synapses onto the same neuron (Toth and McBain 1998, 2000) (see Chapter 3). Conversely, the same glutamatergic axon can generate different responses depending on the postsynaptic neuron subtype (Maccaferri et al. 1998; Toth and McBain 2000). These examples, amongst others, have made the concept of a generic glutamatergic synapse essentially obsolete. Several other examples of synapse-specific neuromodulation at different hippocampal glutamatergic synapses are illustrated in this chapter. Finally, neuromodulators are known to modulate synaptic plasticity, including activity-dependent changes in the efficacy of glutamatergic transmission, called long-term potentiation (LTP) and long-term depression (LTD).

Modulation of Inhibitory Synaptic Transmission

As described in earlier chapters, GABAergic cells and circuits show great diversity in terms of their neurochemistry, morphology, connectivity and expression of neurotransmitter receptors. Similarly, the neuromodulation of GABAergic circuits appears to be complex, yet general principles are emerging even as the number

of interneuron subtypes is growing. This stems in part from issues that arise from attempting to classify GABAergic interneurons into defined subtypes (Maccaferri and Lacaille 2003; Klausberger and Somogyi 2008; Petilla Interneuron Nomenclature Group et al. 2008). However, it is also complicated by the findings that application of the same neuromodulator to what are considered anatomically discrete cell types can often give rise to variable and unpredictable responses even when considering a simple question such as whether a modulator is excitatory or inhibitory (Parra et al. 1998; Widmer et al. 2006). From this muddle, some patterns are starting to emerge, and we are beginning to understand principles by which neurochemically and functionally distinct interneuron subtypes are differentially recruited, suppressed or modified in a coordinated manner to orchestrate the flow of information in hippocampal circuits (Lawrence 2008; Madison and McQuiston 2006). As has been shown in the neocortex (Bacci et al. 2005; Kawaguchi 1997; Porter et al. 1999; Xiang et al. 1998), one important factor is the neurochemical identity of the hippocampal interneuron subtype (Cea-del Rio et al. 2010; Freund and Katona 2007; Glickfeld et al. 2008; Glickfeld and Scanziani 2006; Lawrence 2008; Lawrence et al. 2006c; McQuiston 2014a). Synaptic plasticity, including LTP and LTD, can also occur in inhibitory circuits, which is dependent on neurochemical identity (Monday and Castillo 2017; Monday et al. 2018). Important clues to interneuron diversity have been revealed by investigating the lineage of interneuron subtypes (Kepecs and Fishell 2014; Rudy et al. 2011). Understanding exactly how the neuromodulatory specializations of each neurochemically distinct interneuron subtype contribute to the modulation of the frequency and magnitude of network oscillations continues to remain a major challenge.

'Classical' Modulators

Many of the classical modulators have an established role in mediating synaptic transmission/neuromodulation, and indeed their discovery as such significantly predates the discovery of glutamate and GABA as neurotransmitter substances. Despite this however, our knowledge of the precise action of classical modulators on hippocampal cells and circuits remains rather disjointed and incomplete. It is with acetylcholine that most progress towards a systematic understanding of its multitude of actions has been achieved and we therefore start with a detailed account of the current state of knowledge with this system. Thereafter, we provide an overview of other classical neuromodulators, highlighting their key features as well as the significant gaps in our current knowledge.

Acetylcholine

Acetylcholine (ACh) is a key neuromodulator that plays a key role in arousal (Jones 2004; Lee et al. 2005), attention (Sarter et al. 2005), assigning salience (Hangya et al. 2015; Raza et al. 2017), spatial navigation (Dannenberg et al. 2016) and learning (Dannenberg et al. 2017; Haam and Yakel 2017; Hasselmo 2006). Cholinergically induced oscillatory activity in the hippocampus (Dannenberg et al. 2015; Vandecasteele et al. 2014) correlates with these behavioural states (Lee et al. 1994). Despite major advances in understanding the cell type-specific (Cobb and Davies 2005; Lawrence 2008; McQuiston 2014a) and subcellular (Lawrence et al. 2015; Szabo et al. 2010) targets of cholinergic modulation, large knowledge gaps remain at cellular and synaptic levels. Although some insights have been gained through computational modelling (Hummos and Nair 2017), knowledge gaps still exist in understanding how cholinergic neuromodulation coordinates the activation of diverse hippocampal circuit elements to give rise to large-scale cholinergically induced population-level oscillatory dynamics (Vijayaraghavan and Sharma 2015). However, the recent discovery of the role of astrocytes in the cholinergic modulation of hippocampal dentate granule cells (Pabst et al. 2016) suggests that the inventory of circuit elements capable of undergoing cholinergic modulation is not even complete.

Origin and Structural Organization of Cholinergic Afferents

The medial septum/diagonal band of Broca (MS-DBB) provides the major source of cholinergic innervation to the hippocampus (Dutar et al. 1995; Gielow and Zaborszky 2017; Lucas-Meunier et al. 2003; Swanson et al. 1987; Woolf 1991) and presents a direct synaptic input to both principal neurones and interneurons (Deller et al. 1999; Frotscher and Leranth 1985; Leranth and Frotscher 1987). The MS-DBB also contains septohippocampal GABAergic (Freund 1989; Freund and Antal 1988; Toth et al. 1997) and glutamatergic (Huh et al. 2010) projection neurons, which serve distinct but complementary roles in cognition (Dannenberg et al. 2015; Muller and Remy 2017). MS-DBB cholinergic neurons are rhythmically active during waking and quiescent during sleep (Lee et al. 2005). Cholinergic axons ramify extensively throughout all regions of the hippocampal formation and in all layers (Aznavour et al. 2002; Aznavour et al. 2005; Leranth and Frotscher 1987). At the ultrastructural level, a significant proportion of cholinergic boutons are not associated with distinct postsynaptic specializations (Vizi and Kiss 1998; Vizi et al. 2004). These observations support two forms of cholinergic transmission: precise synaptic transmission, involving highly localized ACh transients onto low-affinity nAChRs, and volume-mediated cholinergic transmission, where ACh is released into the extracellular space, diffusing to high-affinity receptors at some distance from the synaptic terminal (Vizi and Kiss 1998; Vizi et al. 2004).

A recent study has shown that GABA is co-released with ACh (Takacs et al. 2018), as has been shown at cortical neurons receiving input (Granger et al. 2016; Saunders et al. 2015). Whilst co-transmission of acetylcholine with other classical neurotransmitters, such as glutamate (Allen et al. 2006), also has not been shown directly, MS-DBB cholinergic neurons appear to possess the appropriate cellular machinery for co-release of glutamate or GABA with acetylcholine (Sotty et al. 2003; Takacs et al. 2018).

Laminar and Target Specificity of Cholinergic Afferents

The effects of ACh on hippocampal function first commence with where ACh is released, which relates to the specific pattern of cholinergic afferent innervation in the hippocampus. There are differences in the pattern of innervation across DG, CA3 and CA1, as well as within specific layers (termed lamina). Stratum oriens and stratum pyramidale receive a higher density of cholinergic terminals than in other layers (Aznavour et al. 2002). In addition to this laminar specificity, there are several lines of evidence that suggest that cholinergic septohippocampal fibres preferentially target specific hippocampal cell types. Given that nAChRs cluster under cholinergic terminals (Zago et al. 2006), it is possible that a high expression level of postsynaptic nAChRs may indicate a higher level of cholinergic terminal contacts relative to interneuron subtypes associated with lower nAChR expression. Consistent with this idea, we recently used a statistical approach to demonstrate that the density of cholinergic terminals onto hippocampal GAD65-GFP inhibitory neurons is non-random, implying synaptic targeting mechanisms at work (Smith et al. 2015). In the dentate gyrus, cholinergic afferents appear to exhibit some target selectivity, preferentially innervating NPY- over PV-containing neurons (Dougherty and Milner 1999). Moreover, using vesicular acetylcholine transporter (vAChT) labelling in combination with anterograde labelling of basal forebrain afferents, Jones and colleagues found that cholinergic terminals more closely appose calbindin-positive than PV-positive interneurons (Henny and Jones 2008). These observations are consistent with the demonstration of fast α7 nAChR-mediated synaptic responses in stratum radiatum (SR) interneurons (Alkondon et al. 1998; Chang and Fischbach 2006; Frazier et al. 1998a, b), which likely correspond to CCK-/CB-positive interneurons. Several studies have confirmed that electrical stimulation can evoke α7 nAChR-mediated synaptic responses (Alkondon et al. 1998; Chang and Fischbach 2006; Frazier et al. 1998a, b). Recent optogenetic experiments also have shown that α7 nAChR-mediated synaptic responses can be evoked, but it is more rarely observed than through electrical stimulation (McQuiston 2014b), raising the question as to whether α7 nAChRs are truly synaptically localized (Bell et al. 2011; Bell et al. 2015a; McQuiston 2014a). Finally, cholinergic afferents may target precise spatial locations relative to other afferents. The overlap of cholinergic and GABAergic terminal specializations (Henny and Jones 2008; Zago et al. 2006), combined with the demonstrated crosstalk between nAChRs and $GABA_A$ receptors

(Wanaverbecq et al. 2007; Zhang and Berg 2007), suggests that cholinergic afferents target GABAergic synapses.

Intrinsic Cholinergic Interneurons of the Hippocampus

In addition to the extrinsic cholinergic input, the hippocampus possesses a numerically sparse population of cholinergic interneurons (Frotscher et al. 1986, 2000). Recent studies have used transgenic mouse technology to visualize cholinergic circuit elements by driving expression of fluorescent proteins under the control of the choline acetyltransferase (ChAT) promoter, encountering populations of fluorescently labelled hippocampal neurons (Blusztajn and Rinnofner 2016; Grybko et al. 2011; von Engelhardt et al. 2007; Yi et al. 2015). Monyer and colleagues recorded from ChAT-GFP cells in the neocortex (von Engelhardt et al. 2007). Although evoked nicotinic EPSPs onto postsynaptic targets were not observed, a modest enhancement in spontaneous glutamatergic transmission was detected, suggesting that ACh release from these neurons may spill over to presynaptic nAChRs located on glutamatergic terminals (von Engelhardt et al. 2007). In the cortex, ChAT-GFP cells co-express VIP (von Engelhardt et al. 2007) and possess a high density of nAChRs (Porter et al. 1999), raising the possibility that ACh itself may promote cortical ACh release through a feedforward excitatory cholinergic circuit (Tricoire and Cea-Del Rio 2007). In a recent study in the hippocampus, only a minority of ChAT-GFP or ChAT-CRE/YFP cells expressed VIP but were excited by ACh (Yi et al. 2015). Optogenetic stimulation of ChAT-CRE cells in the hippocampus surprisingly evoked a glutamatergic synaptic current, which may be attributable to a special class of CA3 pyramidal cells that either ectopically or developmentally express ChAT (Yi et al. 2015). ChAT-GFP and ChAT-CRE/YFP cells also were encountered in CA1 (Yi et al. 2015), consistent with earlier studies (Frotscher et al. 2000). However, the unambiguous determination of the neurotransmitter phenotype of ChAT-GFP cells in CA1 awaits future studies.

Acetylcholine Receptors

To complement their rich cholinergic input, hippocampal neurons express a broad range of acetylcholine receptors (Buckley et al. 1988; Lebois et al. 2017; Levey 1996; Levey et al. 1995; Rouse et al. 1999). Cholinergic neuromodulation has complex effects on both glutamatergic and GABAergic neurons in the hippocampus, which occur by the binding of ACh to ionotropic nicotinic receptors (nAChR) and metabotropic muscarinic receptors (mAChRs) at pre- and postsynaptic locations (Cobb and Davies 2005; Dannenberg et al. 2017; Giocomo and Hasselmo 2007). Many of the effects are mediated through metabotropic muscarinic acetylcholine receptors (mAChRs, M1-5). Early studies suggested M1 and M3 receptor proteins being mainly expressed in principal neurones and M2 and M4 receptors predominantly expressed on interneurons (Levey et al. 1995). Within glutamatergic circuits

of the hippocampal formation, there is extreme variability in mAChR immunoreactivity between subfields and laminae (Rouse et al. 1999). The termination zones of the perforant path differentially express presynaptic M2, M3 and M4 receptors.

The septohippocampal pathway is also thought to activate nicotinic acetylcholine receptors (nAChRs). The exact expression of nAChR subunits with respect to the afferent cholinergic input is not fully established, but binding studies suggest that populations of interneurons that are suspected to receive direct septohippocampal innervation bind the nAChR ligand α-bungarotoxin (Freedman et al. 1993), implying the expression of α7 nAChRs. Immunocytochemical studies have demonstrated the α7 AChR subunit to be highly expressed across multiple cell types and multiple cellular and synaptic compartments, including somata, dendrites, spines, axon fibres, glutamatergic axon terminals and GABAergic axon terminals (Fabian-Fine et al. 2001).

Action of Acetylcholine on Intrinsic Properties of Hippocampal Neurones

Pyramidal Cells

ACh has been known for many years to excite hippocampal pyramidal cells (Cobb and Davies 2005; Cole and Nicoll 1983, 1984a, b; Dodd et al. 1981), and the ionic basis of such effects has now been elucidated in some detail. Through mAChRs, ACh is known to modulate a large number of conductances and second messenger cascades in pyramidal neurones. These include I_M, the Kv7/KCNQ-mediated K^+ current; I_{AHP}, the slow Ca^{2+}-activated K^+ current responsible for the slowing of action potential discharges; I_{leak}, the ohmic leak current responsible in large part for the resting membrane potential (Halliwell and Adams 1982; Madison et al. 1987; Halliwell 1990); and I_{Kir}, an inwardly rectifying potassium conductance (Seeger and Alzheimer 2001). mAChR activation also potentiates two mixed cation currents (I_h, the hyperpolarization-activated non-specific cation current; I_{cat}, Ca^{2+}-dependent non-specific cation current) (Brown and Adams 1980; Colino and Halliwell 1993; Fisahn et al. 2002; Halliwell and Adams 1982) as well as modulates a voltage-dependent Ca^{2+} current (Toselli et al. 1989). The action of exogenously applied ACh on hippocampal pyramidal cells is that of a pronounced membrane potential depolarization and increase in cell membrane resistance (Cole and Nicoll 1984a, b; Fraser and MacVicar 1996). Through mAChR knockout mice (Dasari and Gulledge 2011; Fisahn et al. 2002) and pharmacological manipulation (Thorn et al. 2017), M1 mAChRs are largely responsible for ACh effects on the intrinsic excitability of hippocampal pyramidal cells (Dennis et al. 2016). Puff application of mAChR agonists to soma/proximal dendritic regions of principal cells induces a transient hyperpolarization caused by mAChR-induced release of calcium from internal stores, which then activates Ca^{2+}-dependent SK channels (a component of I_{AHP}) (Dasari and Gulledge 2011; Dasari et al. 2017; Gulledge and Kawaguchi 2007). Using electrical stimulation of cholinergic afferents, Power and Sah demonstrated

that synaptic activation of mAChRs leads to propagating calcium signals within the somatodendritic axis of pyramidal cells (Power and Sah 2002).

Despite difficulties in interpreting nAChR pharmacology from early studies using cultured hippocampal neurones, in acute native tissues, pharmacological activation of nAChRs is generally reported to produce either no a or barely detectable response in principal cells (Frazier et al. 1998a, b; McQuiston and Madison 1999c; Reece and Schwartzkroin 1991). There are some reports that nAChRs are detected postsynaptically in principal cells (Hefft et al. 1999) where they facilitate the induction of LTP (Ge and Dani 2005; Gu and Yakel 2011) through enhanced cellular excitability (Szabo et al. 2008). However, with the hippocampal circuit intact, the effect may be minor, since bath application of nicotine reduces the excitability of pyramidal cells through activation of non-desensitizing α2-containing nAChR-containing O-LM interneurons (Jia et al. 2009).

Inhibitory Neurons

In the majority of GABAergic interneurons, pharmacological activation of mAChRs results in a similar membrane depolarization to that seen in pyramidal cells but with a less prominent change in cell input resistance (Lawrence et al. 2006c; McQuiston and Madison 1999a, b; Parra et al. 1998), confirming earlier studies (Benardo and Prince 1982a; Benardo and Prince 1982b, e; Reece and Schwartzkroin 1991). GABAergic interneurons represent a highly heterogeneous population of neurone with respect to their connectivity and neurochemistry (Freund and Buzsaki 1996; Klausberger and Somogyi 2008), and there is wide variation in their response to activation of mAChRs compared to that seen in the relatively homogeneous population of principal neurones (McQuiston and Madison 1999a; Parra et al. 1998; Widmer et al. 2006). In contrast to the slow sustained mAChR-mediated modulation of both pyramidal cells and interneurons, activation of nAChRs produces a more transient response. Similar to neocortical interneurons (Couey et al. 2007; Gulledge and Kawaguchi 2007; Porter et al. 1999; Xiang et al. 1998), there is evidence for cell type specificity in postsynaptic expression of nAChRs in hippocampal interneurons (Bell et al. 2015a).

Oriens-Lacunosum Moleculare (O-LM) Cells

O-LM cells exhibit a highly reproducible response to bath application of acetylcholine, mAChR agonist or nAChR agonist activation (Jia et al. 2009; Lawrence et al. 2006c), similar to neocortical Martinotti cells, another somatostatin-positive interneuron subtype (Fanselow et al. 2008; Kawaguchi 1997). When induced to fire in the presence of mAChR agonists, O-LM cells exhibit an acceleration in firing frequency that is accompanied by a prominent suprathreshold afterdepolarization (ADP) (Lawrence et al. 2006c; McQuiston and Madison 1999b). The ADP, mediated by M1/M3 mAChR activation, is associated with the activation of a non-selective cationic current (I_{CAT}) and the inhibition of both M- (I_M) and

slow afterhyperpolarization K+ currents (I_{AHP}) (Lawrence et al. 2006c). mAChR modulation of O-LM cells enhances their intrinsic oscillatory properties to theta-specific input (Lawrence et al. 2006a), which is mimicked by inhibition of I_M (Lawrence et al. 2006b) and a shift in the voltage dependence of HCN channels in O-LM multicompartmental models (Lawrence 2008; Lawrence et al. 2006b; Sekulic and Skinner 2017). In vivo, pirenzepine-sensitive activation of calcium signalling in O-LM cells by MS-DBB cholinergic afferents occurs during fear learning (Lovett-Barron et al. 2014) via a mechanism consistent with M1/M3 mAChR activation (Lawrence et al. 2006c).

In stratum oriens (SO), a mixed fast α7-mediated and slow non-α7 nAChR-mediated response is consistently observed in oriens-lacunosum moleculare (O-LM) cells (Alkondon et al. 1998; Buhler and Dunwiddie 2001; McQuiston and Madison 1999c). O-LM cells exist as two distinct subpopulations, a PV-positive, 5-HT_3 receptor-lacking population derived from the medial ganglionic eminence (MGE) and a PV-lacking, 5-HT_3R-expressing population derived from the caudal ganglionic eminence (CGE) (Chittajallu et al. 2013). Both populations express α7 nAChRs. O-LM cells that express α2 nAChRs (Jia et al. 2009; Leao et al. 2012; Mikulovic et al. 2015) lack PV and are therefore most likely derived from CGE. Cholinergic inputs onto α2 nAChR-expressing O-LM cells have been shown to evoke a nicotinic EPSC, which is blocked by α7-and non-α7 nAChR antagonists (Leao et al. 2012). Due to their non-desensitizing response upon activation with nicotine, α2 nAChRs may play a role in the activation of O-LM cells by exogenous nicotine (Jia et al. 2009).

M2 mAChR-Positive Trilaminar Cells

There are populations of GABAergic interneuron in stratum oriens that are hyperpolarized in response to mAChR activation (Lawrence et al. 2006c; McQuiston and Madison 1999a; Parra et al. 1998). The neurochemical identity of ADP-lacking SO interneurons is less clear, but likely comprises M2 mAChR-expressing trilaminar cells (Ferraguti et al. 2005; Hajos et al. 1998; Klausberger 2009) and horizontally oriented PV+ BCs (Lawrence et al. 2006c; Maccaferri 2005; Widmer et al. 2006). Immunocytochemical studies showing that mGluR1a-positive and M2-positive SO interneurons are distinct cell types (Ferraguti et al. 2005), which likely correspond to O-LM and trilaminar cells (Gloveli et al. 2005), strengthen the evidence that SO interneuron subtypes possess a different complement of postsynaptic mAChRs. Trilaminar cells are CGE-derived (Craig and McBain 2015) and therefore are likely to possess both nAChR and 5-HT_3 receptors (Chittajallu et al. 2013). The most likely consequence of cholinergic activation in these cells is an initial hyperpolarization and reduction in cellular excitability (Lawrence et al. 2006c), possibly mediated through $G_{i/o}$-coupled M2 and/or M4 mAChRs (McQuiston and Madison 1999a; Seeger and Alzheimer 2001). It is also possible that a biphasic response could be generated, but it is not clear whether trilaminar cells possess G_q-coupled M1/M3 receptors that could mediate a late depolarizing response.

Parvalbumin-Positive (PV) Basket Cells

Fast-spiking basket cells, corresponding to PV BCs, do not express high levels of nAChRs in the neocortex (Gulledge and Kawaguchi 2007; Kawaguchi 1997; Xiang et al. 1998) or hippocampus (McQuiston and Madison 1999c; Buhler and Dunwiddie 2001) but do express mAChRs (van der Zee et al. 1991). With the use of transgenic mice that allows the visualization of PV interneuron circuits (Hippenmeyer et al. 2005; Kaiser et al. 2016), CA1 PV BCs can be specifically targeted (Cea-del Rio et al. 2010; Lawrence et al. 2015; Yi et al. 2014). In response to bath application of 10 μM muscarine, PV BCs strongly depolarize, increase in firing frequency and exhibit a loss of an afterhyperpolarization, all of which do not occur in PV BCs lacking the M1 mAChR subtype (Cea-del Rio et al. 2010; Yi et al. 2014). This depolarizing response profile is consistent with that observed previously in a subset of morphologically defined BCs (McQuiston and Madison 1999a; Widmer et al. 2006). Fast-spiking interneurons in the dentate gyrus, corresponding to PV BCs, also depolarize strongly to bath application of ACh or muscarine and are most likely mediated by M1 mAChRs (Chiang et al. 2010). Interneurons that are insensitive to nAChR activation are encountered predominantly in stratum pyramidale (SP) (McQuiston and Madison 1999a) and tend to be fast spiking, a hallmark of PV BCs (Buhler and Dunwiddie 2001).

Consistent with earlier experiments using electrical stimulation to evoke ACh release (Widmer et al. 2006), recent experiments using optogenetic stimulation of ACh release induce a range of atropine-sensitive response profiles in PV BCs, including depolarizing only, hyperpolarizing only and biphasic hyperpolarizing-depolarizing responses (Bell et al. 2013, 2015b; McQuiston 2014a). The hyperpolarizing response is likely mediated by activation of inward-rectifying potassium channels (McQuiston and Madison 1999a; Seeger and Alzheimer 2001) through $G_{i/o}$-coupled M2 (Hajos et al. 1998) and/or M4 mAChRs (Bell et al. 2013), whereas depolarization most likely occurs through G_q-coupled M1 mAChRs (Cea-del Rio et al. 2010; Yi et al. 2014). The capability of synaptically released ACh to activate different mAChR subtypes on PV BCs likely reflects differences in spatiotemporal dynamics of ACh release from cell to cell or possibly differences in synaptic localization of mAChR subtypes. PV BCs in CA1 (Lawrence et al. 2015) and CA3 (Szabo et al. 2010) also undergo presynaptic cholinergic modulation, which reduces synaptic depression. In a mathematical model of short-term synaptic depression, presynaptic cholinergic modulation can be explained by inhibition of presynaptic calcium channels (Lawrence et al. 2015; Stone et al. 2014) through presynaptic M2 and/or M4 mAChRs (Bell et al. 2013; Cea-del Rio et al. 2010; Hajos et al. 1998).

CCK-Positive Basket Cells

Cholinergic neuromodulation of CCK BCs was investigated with the use of a GAD65 GFP transgenic mouse line in which GFP is expressed in non-PV-positive cells (Cea-del Rio et al. 2010; Cea-del Rio et al. 2012; Daw et al. 2009; Lopez-Bendito et al. 2004). CCK BCs show characteristics of cholinergic neuromodulation

differently than PV BCs (Cea-del Rio et al. 2010; Cea-del Rio et al. 2012). First, a prominent mAChR-induced ADP is observed in these cells, with a time course slower than seen in O-LM cells, and is sometimes briefly interrupted by a mAChR-insensitive fast afterhyperpolarization (AHP) that occurs after the offset of a suprathreshold current step (Cea-del Rio et al. 2010). Hyperpolarization followed by depolarization is often observed, consistent with biphasic response profiles of a subset of basket cells reported previously (McQuiston and Madison 1999a; Widmer et al. 2006). This biphasic response is also seen upon optogenetic stimulation (Bell et al. 2013; McQuiston 2014a). One interesting feature of CCK BCs is that M3 mAChRs appear to control mAChR-induced changes in firing but both M1 and M3 mAChRs control the emergence of the mAChR-induced ADP (Cea-del Rio et al. 2010, 2012). Therefore, the expression of M3 mAChRs and its differential coupling to mAChR-sensitive conductances distinguishes CCK BCs from PV BCs (Cea-del Rio et al. 2010, 2012).

There are two types of CCK BCs, identified based on their expression of vasoactive intestinal peptide (VIP) or vesicular glutamate transporter 3 (vGluT3) (Klausberger and Somogyi 2008). VIP-containing CCK BCs are consistently depolarized upon optogenetic stimulation of ACh release (Bell et al. 2015b), consistent with the relative absence of M2/M4 mAChRs on CCK BCs (Freund and Katona 2007). This observation reinforces the existence of principles governing cell type-specific cholinergic neuromodulation in the hippocampus (Lawrence 2008; Madison and McQuiston 2006; McQuiston 2014a). Consistent with a higher sensitivity of CCK BCs than PV BCs to mAChR stimulation (Cea-del Rio et al. 2010, 2012), inhibitory postsynaptic currents evoked by optogenetic ACh release are sensitive to depolarization-induced suppression of inhibition (DSI), a mechanism mediated by endocannabinoids acting at presynaptic CB1 receptors on CCK interneurons (Nagode et al. 2011; Alger et al. 2014).

CCK is highly co-localized with α7 nAChR mRNA transcripts (Morales et al. 2008) and protein (Freedman et al. 1993). In this context, SR interneurons, which likely comprise CCK interneuron subtypes, exhibit only fast, presumably α7-mediated responses upon puff application of ACh (McQuiston and Madison 1999c), suggesting cell type specificity of nAChR receptor subtypes compared relatively to additional nAChR subtypes found in O-LM interneurons. However, optogenetically evoked ACh responses mediated solely by α7 nAChRs are rare (McQuiston 2014b).

CCK-Positive Schaeffer Collateral-Associated (SCA) Interneurons

CCK SCA interneurons are similar to CCK BCs in that they exhibit a similar mAChR-induced ADP (Cea-del Rio et al. 2010; Cea-del Rio et al. 2011; Cea-del Rio et al. 2012). The presence of M4 mAChR mRNA transcripts in a subset of CCK SCA and CCK BCs (Cea-del Rio et al. 2010, 2011, 2012) may explain the often biphasic hyperpolarizing-depolarizing phenotype of the mAChR-mediated response in CCK SCA cells, observed with bath application of mAChR agonists (Parra et al. 1998; Cea-del Rio et al. 2011, 2012), electrical stimulation (Widmer et al. 2006) and optogenetic stimulation (Bell et al. 2013). The M4-positive allosteric modulator

potentiates the hyperpolarizing component of the biphasic response, consistent with expression of M4 mAChRs on these cells (Bell et al. 2013), in contrast to the absence of a hyperpolarizing component onto VIP CCK BC subtypes (Bell et al. 2015b). mAChR activation boosted its response to oscillatory input in CCK SCAs (Cea-del Rio et al. 2011, 2012). Like CCK BCs, this cell type is likely to be modulated by endocannabinoids through presynaptic CB1 receptors (Nagode et al. 2011; Alger et al. 2014) and therefore unlikely to possess presynaptic M2/M4 receptors, as presynaptic CB1 and M2/M4 receptors are thought to be from mutually exclusive presynaptic terminal populations (Freund and Katona 2007; Armstrong and Soltesz 2012).

CCK-Positive Perforant Path-Associated (PPA) Interneurons

Although likely comprising more than one neurochemically distinct interneuron population (Freund and Buzsaki 1996; Bowser and Khakh 2004; Klausberger 2009), interneurons located at the stratum radiatum/stratum lacunosum moleculare (SR/SLM) border are depolarized by mAChR activation and exhibit intrinsic subthreshold membrane potential oscillations (Chapman and Lacaille 1999a, b). Approximately half of these interneurons exhibit a mAChR-induced transient hyperpolarization that precedes mAChR-induced depolarization (Chapman and Lacaille 1999a), similar to responses observed in CCK BCs and CCK SCAs (Cea-del Rio et al. 2010, 2011, 2012). There are likely common cellular mechanisms across CCK interneuron subtypes; M2/M4 mAChRs mediate the transient hyperpolarizing response, whilst M1/M3 mAChRs mediate the late depolarizing response (Cea-del Rio et al. 2010, 2011, 2012; Bell et al. 2013, 2015b).

SR/SLM interneuron populations also express functional nAChRs (Reece and Schwartzkroin 1991; Jones and Yakel 1997; McQuiston and Madison 1999c). Activation typically induces brief depolarization or inward current which tends to desensitize rapidly. The kinetics and pharmacology of the response vary, but fast depolarization by α7 subunit-containing nAChRs is the predominant response seen in interneurons. The nAChRs expressed on SR/SLM interneurons can also be synaptically activated (Frazier et al. 1998a). Unlike agonist-activated responses, optogenetically activated nAChRs are rarely mediated by α7 subunit-containing nAChRs (Bell et al. 2011; McQuiston 2014b). The reason for this discrepancy is unclear.

VIP/Calretinin-Expressing Interneuron-Selective Interneurons

VIP- and calretinin-expressing neurons form local 'disinhibition circuits', interneuron subtypes that are specialized to inhibit other inhibitory neurons (Acsady et al. 1996a; Francavilla et al. 2015; Tyan et al. 2014). These cells are negative for M2 mAChRs (Tyan et al. 2014). A recent study by McQuiston and colleagues found that VIP-positive interneurons are synaptically activated by α4/β2-containing nAChRs (Bell et al. 2015a), consistent with the enrichment of nAChRs on VIP interneuron

subtypes in cortex (Porter et al. 1999). A subset of these VIP/calretinin interneurons co-express ChAT, which are excited by bath application of ACh (Yi et al. 2015).

Other Hippocampal Interneuron Subtypes

Since publication of the previous edition of this chapter, much knowledge has been gained, greatly increasing our understanding of cholinergic modulation of specific circuit elements and demonstrating general principles in cell type-specific cholinergic neuromodulation in the hippocampus (Lawrence 2008; Madison and McQuiston 2006; McQuiston 2014a). Despite these advances, of the 21 specific interneuron subtypes in the hippocampus (Klausberger and Somogyi 2008), cholinergic modulation has been systematically explored in only a third (8/21). Of the remaining subtypes to be explored, long-range GABAergic projection neurons, such as the hippocamposeptal (HS) neurons (Caputi et al. 2013; Mattis et al. 2014; Melzer et al. 2012) are a major class. Finally, the neurochemical identity of inhibitory interneurons that are totally nonresponsive to cholinergic neuromodulation, which apparently lack both mAChRs and nAChRs, is not clear (McQuiston and Madison 1999a; Parra et al. 1998).

Clearly, the activity of the cholinergic septohippocampal afferents excites the hippocampal network generally and differentially gates inhibitory circuits through both nAChR- and mAChR-mediated mechanisms. This has been proposed to result in switches in inhibition between perisomatic and pathway-specific dendritic domains (Gulyas et al. 1999). A major challenge for the future is to understand how different patterns of cholinergic afferent input can differentially recruit different receptor populations and cell types. McQuiston and colleagues have shown that a single stimulation of cholinergic fibres can be effective at evoking nAChR-mediated postsynaptic potentials in interneurons and that additional stimuli will evoke both mAChR-mediated hyperpolarizing and depolarizing responses. In contrast, trains of stimuli delivered at 10–20 Hz, within the range at which most putative septal cholinergic cells discharge (Brazhnik and Fox 1999; Lee et al. 2005), result in a robust mAChR-mediated synaptic response whilst at the same time depressing nAChR-mediated responses (Morton and Davies 1997). During more sustained ACh release, it is also possible that mAChR activation induces postsynaptic depression of nAChR responses (Shen et al. 2009).

Action of Acetylcholine on Defined Excitatory Synapses

Presynaptic Muscarinic Receptors Located on Defined Excitatory Synapses

ACh depresses Schaffer collateral (SC) afferents onto CA1 pyramidal cells through a presynaptic mechanism involving mAChR activation (Valentino and Dingledine 1981) and presynaptic N-type calcium channels (Qian and Saggau 1997). The nAChR antagonist hexamethonium does not block the action of ACh, suggesting that nAChRs are absent from presynaptic SC afferents (Valentino and Dingledine

1981). mAChR activation also inhibits glutamatergic transmission of CA3 collateral glutamatergic transmission (Vogt and Regehr 2001; Kremin and Hasselmo 2007). The mAChRs involved in presynaptic inhibition of SCs are most likely M2 mAChRs (Seeger and Alzheimer 2001) but possibly include M4 mAChRs (Sanchez et al. 2009). Whilst ACh generally suppresses glutamatergic neurotransmission at most excitatory synapses tested (Valentino and Dingledine 1981), mAChR modulation has a greater effect at SC synapses than on perforant path (PP) synapses in both CA1 (Hasselmo and Schnell 1994) and CA3 (Kremin and Hasselmo 2007). Similarly, in the dentate gyrus, cholinergic suppression of transmitter release differs between medial and lateral pathway (Kahle and Cotman 1989). mAChRs are not present at MF glutamatergic synapses, but bath application of muscarine enhances GABA release from local interneurons, which then inhibits MF transmission indirectly through activation of $GABA_B$ receptors (Vogt and Regehr 2001). This same indirect effect on presynaptic $GABA_B$ receptors, however, is not present at SC synapses (Kremin et al. 2006). This differential effect of cholinergic neuromodulation on specific glutamatergic circuits has been suggested to amplify the impact of sensory input arriving to hippocampus, whereby mAChR activation shifts the weight of glutamatergic input in favour of external (entorhinal cortical) influences over internal (intrahippocampal pathways) activity such as recall from internal CA3 recurrent collaterals upon cholinergic modulation (Giocomo and Hasselmo 2007). This synaptic 'heightening' of sensory awareness has interesting implications for the behavioural manifestation of attention (Giocomo and Hasselmo 2007; Sarter et al. 2005).

Concomitant with acute mAChR-induced presynaptic inhibition of glutamate release discussed above, the action of ACh can induce synaptic plasticity at SC synapses, including long-term potentiation (Auerbach and Segal 1994, 1996; Dennis et al. 2016; Fernandez de Sevilla et al. 2008; Shinoe et al. 2005) and, usually at higher concentrations of cholinergic agonist, long-term depression (Auerbach and Segal 1996; Scheiderer et al. 2006, 2008). Release of ACh by stimulation of the medial septum reproduces this effect on synaptic plasticity (Fernandez de Sevilla et al. 2008; Habib and Dringenberg 2009). The underlying mechanisms appear to be an enhancement in the NMDA receptor component of the excitatory postsynaptic event (Markram and Segal 1990a, b). More recently, Fernandez de Sevilla and colleagues have discovered a postsynaptic mechanism that involves enhanced surface trafficking of AMPA receptors (Fernandez de Sevilla et al. 2008). Presumably through a convergence underlying synaptic, intrinsic and network mechanisms, LTP is preferentially induced at synapses firing on the positive phase of the θ rhythm during cholinergically induced theta oscillations in the hippocampus in vitro and in vivo (Pavlides et al. 1988; Huerta and Lisman 1993; Holscher et al. 1997; Hyman et al. 2003).

Presynaptic Nicotinic Receptors Located on Hippocampal Glutamatergic Terminals

Nicotine application increases the frequency of miniature glutamatergic EPSCs in tissue culture from hippocampus (Radcliffe and Dani 1998), strongly suggesting that presynaptic nAChRs exist. Several lines of evidence support the presence of nAChRs on CA3 MF terminals, where calcium influx through α7 nAChRs induces concerted release of multiple quanta (Gray et al. 1996; Sharma and Vijayaraghavan 2003; Sharma et al. 2008). Nicotine selectively depresses PP but not SC glutamatergic transmission in CA3 (Giocomo and Hasselmo 2005), but this effect is accounted for by an indirect effect on inhibitory interneurons (Giocomo and Hasselmo 2005), possibly related to tonic activation of O-LM interneurons by nicotine (Jia et al. 2009). Similar indirect effects of ACh at MF synapses are also likely (Vogt and Regehr 2001).

Action of Acetylcholine on Defined Inhibitory Synapses

As demonstrated by the early work of Pitler and Alger (Pitler and Alger 1992a), as well as other laboratories (Behrends and ten Bruggencate 1993), the actions of ACh on GABAergic interneurons not only include direct excitation but also presynaptic inhibition. Pharmacological activation of mAChRs directly increases the frequency and amplitude of spontaneous IPSCs whilst at the same time depressing monosynaptically evoked IPSCs and reducing the frequency of miniature IPSCs (Pitler and Alger 1992a; Behrends and ten Bruggencate 1993). In a landmark study demonstrating the differential expression of mAChRs on hippocampal interneurons, Hajos and colleagues found that M2 receptors (M2Rs) were expressed on the presynaptic axon terminals of PV+ basket cells (Hajos et al. 1998). Consistent with M2-mediated inhibition of GABAergic transmission evoked in the pyramidal cell layer (Seeger et al. 2004), mAChR activation reduces GABA release from PV-positive BC terminals (Lawrence et al. 2015). Whether presynaptic mAChRs are present on other hippocampal interneuron subtypes still remains an open question. Interestingly, Soltesz and colleagues demonstrated that mAChR activation inhibits GABA release from identified CCK BCs (Neu et al. 2007). Here, mAChR modulation was indirect (Fukudome et al. 2004), occurring via postsynaptic release of endocannabinoids from pyramidal cells and subsequent activation of presynaptic CB1 receptors (Lawrence 2007; Neu et al. 2007) (Fig. 2). Therefore, mAChR-induced modulation of GABA transmission from PV BCs likely involves direct activation of presynaptic M2 receptors, whilst mAChR-induced modulation of GABA transmission from CCK BCs is indirect, involving endocannabinoid signalling (Freund and Katona 2007). Finally, in addition to mAChR-mediated presynaptic inhibition of GABA release, calcium-permeable nAChRs also regulate GABAergic inhibition through postsynaptic intracellular signalling pathways (Wanaverbecq et al. 2007; Zhang and Berg 2007). Therefore, cholinergic neuromodulation can alter the efficacy of GABAergic transmission through both pre- and postsynaptic mechanisms (Fig. 3).

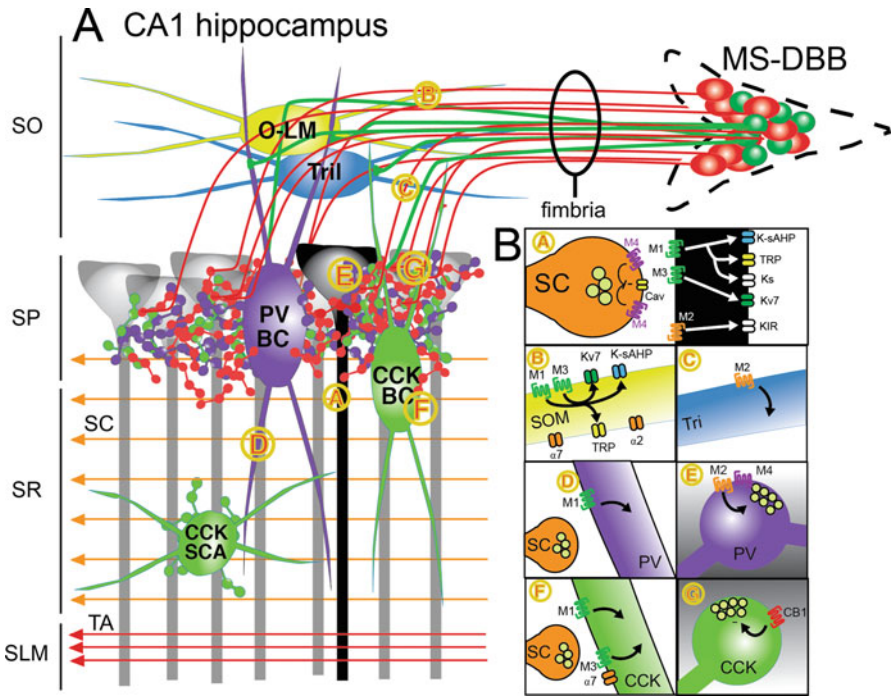

Fig. 2 The medial septal-diagonal band of Broca (MS-DBB) projection to defined cellular and synaptic targets of the CA1 hippocampus. (**a**) The MS-DBB is composed of cholinergic (red) and GABAergic (green) neurons that project via the fimbria to hippocampal regions. Cholinergic projection fibres (red) pass through stratum oriens (SO), where the somatostatin (SOM)-positive oriens-lacunosum moleculare (O-LM) neurons (yellow) and trilaminar (blue) interneurons are located, and arborize in a dense network within stratum pyramidale (SP) with CA1 pyramidal cells (black), CCK BCs and PV BCs (cholinergic terminals in stratum oriens and stratum radiatum (SR) omitted for clarity). MS-DBB GABAergic neurons (*A*, green cells) are thought to innervate exclusively hippocampal interneurons. Areas of interest, denoted by circled numbers in *A*, are expanded in *B*. Known cellular and synaptic targets, denoted by circled numbers, are shown. These are (*A*) the dendrites of pyramidal cells, acting at M1, M2 and M3 mAChRs and presynaptic terminals of Schaffer collaterals (orange) acting at M2 mAChRs (*B*) somatodendritic regions of O-LM cells acting at M1 and M3 mAChRs, α7 nAChRs and non-α7 nAChRs, (*C*) somatodendritic regions of trilaminar interneurons acting at M2 mAChRs, (*D*) somatodendritic regions of PV BCs acting at M1 mAChRs, (*E*) presynaptic terminals of PV BCs acting on M2 mAChRs, (*F*) somatodendritic regions of CCK BCs acting on M1 and M3 mAChRs and α7 nAChRs and (*G*) presynaptic terminals of CCK BCs acting indirectly through presynaptic CB1 mAChRs

Presynaptic Modulation of ACh Release

M2 mAChRs additionally occur at septohippocampal cholinergic terminals where they are thought to have an autoregulatory role (Rouse et al. 1999). Other studies have shown more directly that whilst ACh auto-feedback can regulate, the activation of a range of other transmitters can suppress evoked cholinergic responses including

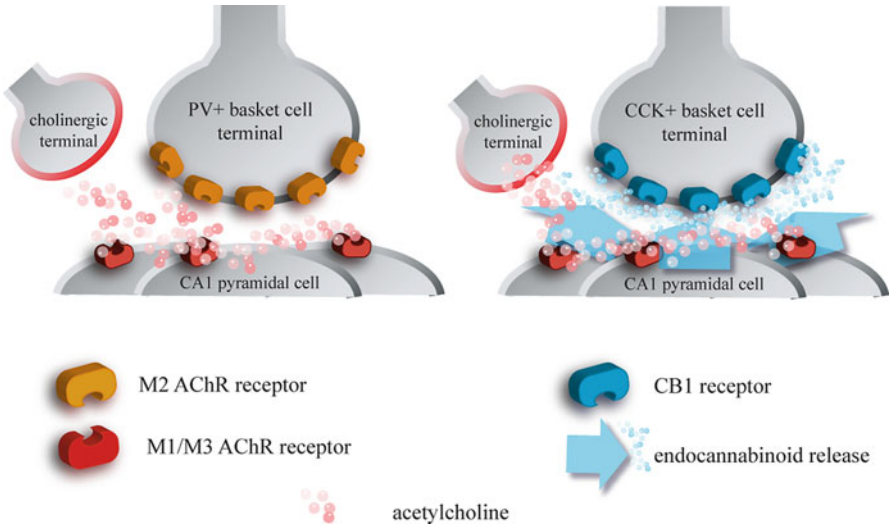

Fig. 3 Cholinergic modulation of GABA release from PV and CCK BC terminals through direct and indirect mechanisms. There is evidence that mAChRs can regulate GABA release through both direct and indirect mechanisms (Freund and Katona 2007). The direct mechanism involves binding of ACh to presynaptic M2 mAChRs (Lawrence et al. 2015; Szabo et al. 2010). The indirect mechanism involves postsynaptic M1/M3 mAChR activation and release of endocannabinoids onto CB1 R-expressing terminals of CCK+ BCs (Neu et al. 2007). (Reproduced from Lawrence 2007, with permission)

A1 adenosine receptors (Morton and Davies 1997), opiate receptors (Kearns et al. 2001) and $GABA_B$ receptors (Morton et al. 2001). The inhibition of ACh release occurs through a common mechanism, where presynaptic $G_{i/o}$ receptor activation converges to reduce calcium influx through presynaptic calcium channels. This mechanism has recently been supported by the observation that optogenetically induced nAChR-mediated EPSCs are potentiated by atropine, consistent with block of presynaptic $G_{i/o}$-coupled mAChRs on cholinergic terminals (Bell et al. 2011).

Dopamine

Dopamine (DA) is considered to play an important role in hippocampal-dependent learning by enhancing the saliency of relevant stimuli and is released into the hippocampus when animals are exposed to a novel environment (Ihalainen et al. 1999; Lisman and Grace 2005; Muzzio et al. 2009). Lesions of the dopaminergic system impair learning and memory (El-Ghundi et al. 1999; Gasbarri et al. 1996) and dysfunction of the DA system have been implicated in neurological disease (Seeman and Van Tol 1994). At the cellular and network levels, the action of DA is complex, involving neuromodulation of intrinsic membrane properties, synaptic

receptors and feedforward inhibition, which collectively act to lower the threshold for spike timing-dependent plasticity, thereby facilitating synaptic plasticity and memory storage.

Origin and Structural Organization of Dopaminergic Afferents

Early histological microdialysis studies have reported that the hippocampal formation receives dopaminergic projections from A9 (substantia nigra) and A10 (ventral tegmental area or VTA) cell groups (Scatton et al. 1980; Swanson et al. 1987). The VTA projects heavily to the subiculum and CA1 and to a lesser extent to the CA3 and dentate gyrus (Gasbarri et al. 1994, 1997). However, through retrograde tracing study, only a small percentage (10–18%) of these fibres are positive for tyrosine hydroxylase (TH) (Gasbarri et al. 1994). Interestingly, there has been a growing appreciation that the VTA is not the only source of DA to the hippocampus (McNamara and Dupret 2017; Smith and Greene 2012). Recent tract tracing in transgenic mice has confirmed that the VTA projection to dorsal hippocampus is sparse, whereas there is a high density of TH-positive fibres originating from locus coeruleus (LC) (Takeuchi et al. 2016). A sophisticated set of optogenetic experiments revealed that novelty-induced memory enhancement is primarily due to the activation of D1/D5 receptors from LC, which is largely independent of VTA (Kempadoo et al. 2016; Takeuchi et al. 2016). Moreover, DA transporter (DAT) expression, an indicator of DA terminals, is relatively absent from the hippocampus (Ermine et al. 2016; Smith and Greene 2012). Finally, retrograde labelling of fibres innervating the dentate gyrus revealed that the origin of TH-positive fibres is in LC, not midbrain DA neurons in SN or VTA (Ermine et al. 2016). Despite the very strong evidence that LC, not VTA, is the primary source of DA, loss of VTA neurons in Alzheimer's disease mice is associated with reduced DA outflow to hippocampus, whereas norepinephrine levels stay the same (Nobili et al. 2017).

Dopamine Receptors

All five DA receptors (DARs) are expressed in the hippocampus with G_s-coupled D1/5 and G_i-coupled D2-4 receptors being positively and negatively coupled to adenylyl cyclase, respectively. The expression pattern of DARs at the level of single cells remains relatively poorly defined, but DARs have been shown to display both presynaptic and postsynaptic localization (Bergson et al. 1995) and to be expressed both in principal cells and interneuronal populations (Mrzljak et al. 1996). There is often a mismatch between the expression patterns of particular DARs and the innervation pattern (Goldsmith and Joyce 1994). This has led some authors to hypothesize that it is the distribution of the DARs and not of dopaminergic fibres that determines the neuronal systems influencing dopaminergic afferent activation.

Through immunocytochemical analysis in D1-GFP mice, D1 receptors have recently been shown to be exclusively expressed on inhibitory interneurons and are

particularly enriched on SR interneurons (Puighermanal et al. 2017). The Drd1a-EGFP-positive neurons were not positive for PV and enriched in stratum oriens and radiatum, suggesting that D1 Rs are present on 5-HT_3 R- and SST-containing interneurons (Gangarossa et al. 2012). With the development of improved transgenic mouse technology, D2 R expression has similarly evolved from initially what was thought to be widespread hippocampal expression to, recently, very limited expression primarily in inhibitory interneurons and hilar neurons (Puighermanal et al. 2015, 2017). D_3 R level is lower than any other dopamine receptor subtype in the hippocampus (Andersson et al. 2012a) but has been detected immunocytochemically in the neuropil of stratum oriens and radiatum (Khan et al. 1998). D_4 Rs are expressed in GABAergic neurons (Mrzljak et al. 1996), specifically PV interneurons (Andersson et al. 2012a). D_4 R activation reduces an outward potassium current in fast-spiking hippocampal interneurons (Andersson et al. 2012b). This observation is counterintuitive given that the D_4 R is a $G_{i/o}$-coupled receptor and expected to increase potassium conductance.

Because DA, serotonin and norepinephrine all have similar structures (are monoamines), DA can activate some receptors that are not the classic D_1-D_5 receptors. DA has low affinity for 5-HT_3 Rs (Solt et al. 2007) and α_1 adrenergic receptors (Cilz et al. 2014).

Action of Dopamine on Intrinsic Properties

Principal Cells

DA has been reported to produce a range of actions, which are largely attributed to the activation of D1-like (D1/5) and D2-like (D2-4) Rs, respectively (Table 2). The effects of DA on intrinsic properties have historically been examined through bath application of DA and/or DAR agonists. In CA1 pyramidal neurons, bath application of DA produces a pronounced hyperpolarization and elevation of action potential threshold (Benardo and Prince 1982c) coupled with a suppression of the I_{AHP} and inhibition of spike frequency adaptation (Malenka and Nicoll 1986; Pedarzani and Storm 1995). This is mainly attributed to suppression of the activation of Ca^{2+}-sensitive potassium channels (Benardo and Prince 1982c, d; Bernardi et al. 1984; Stanzione et al. 1984). Activation of the selective D2 R agonist quinpirole was shown to increase the cellular excitability of hilar mossy cells (Etter and Krezel 2014). However, it is important to keep in mind that bath application of DAR agonists may not be comparable to the actions of synaptically released DA. Indeed, optogenetically stimulated synaptic release of DA fails to substantially alter passive membrane properties (Rosen et al. 2015).

Table 2 Summary of D1-like and D2-like receptors and their actions

Receptor family	D1-like receptors		D2-like receptors		
Subtype	D1	D5	D2	D3	D4
Expression in the hippocampus	Mainly SR interneurons	Pyramidal cell dendrites	Interneurons and hilar cells	Low expression (SO and SR neuropil)	Mainly PV interneurons
Signalling	G_s		G_i		
Gross effect of dopamine on: intrinsic properties	Hyperpolarization, ↑AP threshold, ↓AHP, ↓accommodation (but see text above)				
Synaptic transmission	↓ perforant path signalling, ↑mossy fibre signalling		↓ perforant path signalling		
Network	Modulation of gamma oscillations				

Inhibitory Neurons

Much of what is known about the effects of DA on inhibitory neurons has been studied in cortex (Gorelova et al. 2002; Towers and Hestrin 2008; Zhou and Hablitz 1999) (see (Tritsch and Sabatini 2012) for review). In cortical GABAergic interneurons, D_1 R activation induces a depolarization, accompanied by an increase in input resistance (Zhou and Hablitz 1999; Towers and Hestrin 2008), consistent with the expected actions of G_s-coupled receptors (Nicoll 1988). In the hippocampus, PV-positive interneurons possess D_4 Rs (Andersson et al. 2012a; Mrzljak et al. 1996), which control feedforward excitation of Shaffer collateral inputs onto CA1 pyramidal cells (Rosen et al. 2015). However, effects of DA on intrinsic membrane properties of other neurochemically defined hippocampal interneuron subtypes have not been systematically investigated.

Action of Dopamine on Defined Excitatory Synapses

The actions of DA on excitatory synaptic transmission are generally suppressant in nature (Hsu 1996). However, in parallel with other modulators, certain excitatory pathways are more profoundly affected than others. For instance, DA together with noradrenaline and serotonin produces a strong (30–50%) acute suppression of the PP input to CA1 pyramidal cells in comparison to no or very minimal change in SC input to the same cells (Otmakhova and Lisman 2000). This is consistent with the SLM having an especially high concentration of DARs. The action of DA is thought to involve both D_1 (Noriyama et al. 2006)- and possibly D_2 (Otmakhova and Lisman 1999)-type Rs and induce presynaptic suppression of glutamate release. A similar acute suppressant action is reported in the subiculum (Behr et al. 2000). Conversely, in area CA3, DA produces a pronounced synaptic potentiation of the MF inputs but no effect on associational/commissural synapses onto CA3 pyramidal cells (Kobayashi and Suzuki 2007).

Another important aspect is the temporal aspect of dopaminergic modulation. Many reports describe a biphasic action whereby an initial acute action (e.g. suppression) of synaptic transmission is followed by a long-lasting enhancement of the evoked synaptic response (Gribkoff and Ashe 1984). In this context, DA is considered an important modulator of synaptic plasticity whereby it enhances long-term potentiation (LTP) (Frey et al. 1993; Huang and Kandel 1995; Otmakhova and Lisman 1996; Thompson et al. 2005) and inhibits depotentiation (Otmakhova and Lisman 1998). During exposure to a novel environment, the threshold for LTP is reduced transiently (absent in animals exploring a familiar environment), and this facilitation is suggested to be dependent upon DA acting via D1/5 receptors (Li et al. 2003). In agreement with this observation, D_1 R knockout mice display deficits in hippocampal-dependent spatial learning (El-Ghundi et al. 1999). Moreover, amphetamine, which induces release of endogenous DA, enhances hippocampal-dependent memory tasks (Packard et al. 1994).

There appear to be several mechanisms by which DA may induce synaptic plasticity. These include increased surface expression of AMPA receptors through both direct phosphorylation of AMPA receptors and through the stimulation of local dendritic protein synthesis (Gao and Goldman-Rakic 2003; Smith et al. 2005; Wolf et al. 2003; Yang 2000). Also, DA may enhance NMDA receptor expression (Yang 2000). Interestingly, depending on the GluN2A/GluN2B subunit composition, synaptic NMDA receptor-mediated currents are differentially modulated by D_1/D_5 R agonists (Varela et al. 2009). SC synapses, which contain abundant GluN2B NMDA receptor subunits, are potentiated by D_1/D_5 R activation, whereas GluN2A-rich PP synapses are depressed (Varela et al. 2009). DA may gate synaptic transmission and plasticity in a frequency and synapse-specific manner, which includes modulation of excitatory synapses onto hippocampal interneurons (Ito and Schuman 2007).

Recently, optogenetic release of dopamine has been shown to enhance feed-forward inhibition by increasing the magnitude of the SC EPSP onto PV-positive neurons (Rosen et al. 2015). D_4 Rs have been demonstrated on PV interneurons in the CA1 hippocampus (Rosen et al. 2015; Andersson et al. 2012a, b). In response to SC stimulation, activation of D_4 Rs on PV interneurons increases the AMPA receptor-mediated EPSP, likely due to increased expression and stabilization of AMPA receptors (Rosen et al. 2015). The enhancement of gamma oscillations by D_4 R stimulation is consistent with this mechanism (Andersson et al. 2012a). This mechanism at least partly accounts for DA-induced suppression of SC EPSPs in CA1 pyramidal cells (Rosen et al. 2015). The action of haloperidol, a D_2 R antagonist, on inhibitory transmission, reinforces the idea that DA modulates GABAergic inhibition in the hippocampus (Brady et al. 2016).

Action of Dopamine on Inhibitory Synapses

As optogenetically released DA does not change the amplitude of directly stimulated IPSCs across all hippocampal layers (Rosen et al. 2015), it is unlikely that presynaptic DA heteroreceptors, if present, are modulated by synaptically released DA on any of the major classes of inhibitory neurons in the hippocampus. A detailed understanding of DA effects on hippocampal interneurons and modulation of GABAergic synaptic transmission is extremely sparse, though some analogous systematic studies have been conducted in cortex (Gao and Goldman-Rakic 2003; Gao et al. 2003; Gonzalez-Burgos et al. 2005; Gorelova et al. 2002; Kroner et al. 2007; Towers and Hestrin 2008). In the hippocampus, activation of D_3 Rs can modulate GABAergic transmission in area CA1, suppressing evoked IPSCs in SR but not in SO (Hammad and Wagner 2006). This laminar-specific action has been reported to be due to dopamine (via D_3 Rs) modulating postsynaptic $GABA_A$ receptor endocytosis in apical dendrites of CA1 pyramidal cells and has been postulated to be a significant postsynaptic means of modulating inhibitory synaptic transmission (Swant et al. 2008). Because D_3 R agonists did not alter paired-pulse ratio of GABAergic IPSCs, presynaptic D_3 Rs on GABAergic neurons are unlikely

(Swant et al. 2008). Such a mechanism of D_3 R-mediated inhibition of IPSCs may contribute to a reduction in gamma oscillations by D_3 R agonists (Lemercier et al. 2015).

Additional indirect evidence suggests that DA may also modulate feedforward inhibition of the PP input to the DG and hippocampal area CA1 through D_4 R signalling (Romo-Parra et al. 2005).

Further indirect evidence for DA regulation of hippocampal inhibitory networks comes from the finding that DA depresses cholinergically generated gamma band oscillatory activity in the hippocampus (Weiss et al. 2003; Wojtowicz et al. 2009). Gamma oscillations are increasingly appreciated to involve fast-spiking PV-positive interneurons (Bartos et al. 2007; Sohal et al. 2009). However, DA enhances stimulus-evoked gamma oscillations (Wojtowicz et al. 2009), which may be consistent with the notion that DA increases neuronal synchrony (Muzzio et al. 2009) mediated by its depolarizing action on fast-spiking, PV-positive basket cells (Bartos et al. 2007; Sohal et al. 2009; Towers and Hestrin 2008). Finally, the connectivity and GABAergic levels of PV interneurons, termed PV plasticity, are regulated by D_1/D_5 Rs and are important for memory consolidation (Karunakaran et al. 2016).

Norepinephrine

Norepinephrine (NE) is a major monoamine neuromodulator, and its actions in the hippocampus appear complex and sometimes paradoxical. Through multiple actions on intrinsic excitability and synaptic transmission, NE is considered to be important in learning and memory processes (Gibbs and Summers 2002; Murchison et al. 2004). More recent studies have found a role of astrocytes in mediating effects of NE (Bazargani and Attwell 2017; Paukert et al. 2014).

Origin and Laminar Specificity of Central Adrenergic Afferents

The hippocampus receives dense input from the locus coeruleus (LC), terminating heavily in the polymorph layer of the DG, stratum lucidum (SL) of area CA3 and SLM in area CA1 (Loy et al. 1980; Oleskevich et al. 1989; Swanson et al. 1987). The total NE bouton density varies across hippocampal regions but is estimated to be about twice as high as in cortex (Oleskevich et al. 1989). In the DG, it has been estimated that two-thirds of NA boutons form synaptic specializations with the remainder forming no specialized synaptic profiles and presumably mediating volume transmission (Milner and Bacon 1989a). GABAergic interneurons are often the targets of NA boutons forming synaptic specializations (Milner and Bacon 1989b). More recently, several studies have shown that the LC is a major source of DA to the hippocampus, particularly in dorsal hippocampus (Kempadoo et al. 2016; McNamara and Dupret 2017; Smith and Greene 2012).

Cell Type-Specific Expression of Adrenoceptors

NE acts on a range of adrenoceptors with both alpha and beta classes being widely expressed on both dendritic and axonal elements (Harley 2007; Nicholas et al. 1996). The α1d receptor appears to be the predominant α-receptor in all areas, with the exception of the hilus where α1a R appears to be the dominant subtype (Day et al. 1997). The α2a R appears to be located mainly presynaptically (Milner et al. 1998) but, like many other adrenoceptor subtypes, show dramatic changes in expression level during development. β-Adrenoceptors show laminar-specific differences and are mainly expressed postsynaptically on both principal cells and interneurons (Cox et al. 2008; Milner et al. 2000). Studies that utilize neurochemically defined interneuron subtypes indicate that the expression of both α (Hillman et al. 2005)- and β (Cox et al. 2008)-adrenoceptor subunits is cell type-specific. However, they can also be found on presynaptic profiles. In terms of signalling, all adrenoceptors are G-protein-coupled receptors with α1 being coupled to G_q, β2 being coupled to $G_{i/o}$ and the β-family receptors being coupled to G_s (Harley 2007; Nicholas et al. 1996).

Action of Norepinephrine on Intrinsic Properties

Principal Cells

NE is reported to produce a wide and sometimes contradictory range of effects in principal cells. These include hyperpolarization and reduced excitability in some cells to a depolarization, increased input resistance (Lacaille and Schwartzkroin 1988; Madison and Nicoll 1986; Ul Haq et al. 2012), reduction of afterhyperpolarizing potentials and loss of action potential accommodation (Madison and Nicoll 1982) in cells of the same class (see Table 3). Pharmacological studies suggest that these inhibitory versus excitatory actions may, in part, be due to a differential recruitment of α- versus β-subclasses of adrenoceptors (Bijak 1989; Harley 2007; Lacaille and Schwartzkroin 1988). Activation of β-adrenoceptors reduces resting K^+ conductances (Lacaille and Schwartzkroin 1988), whereas α2 receptor activation strongly suppresses cellular excitability in CA1 pyramidal cells (Otmakhova et al. 2005), most likely through postsynaptic activation of K_{ir} potassium channels (Luscher et al. 1997; Sodickson and Bean 1998). Studies investigating hilar neurons suggest that the dominant response in putative GABAergic cells is depolarization and loss of a slow AHP. In contrast, the dominant response in putative mossy cells was a loss of spike frequency adaptation (Bijak and Misgeld 1995).

The underlying ion mechanisms for the change in intrinsic properties are thought to be a reduction in a Ca^{2+}-activated K conductance leading to an inhibition of the slow AHP and a reduction in spike frequency adaptation (Haas and Rose 1987; Lacaille and Schwartzkroin 1988; Madison and Nicoll 1982; Pedarzani and Storm 1996). In DG granule cells, β1 receptors are also reported to enhance the voltage-dependent Ca^{2+} currents (Gray and Johnston 1987).

Table 3 Primary actions of norepinephrine on hippocampal neurons

Cell Type	Cellular effects	Ion channels effects
Pyramidal	Hyperpolarization,	↓ A-type current (α receptors)
	↑ increased input resistance	
	or	
	Depolarization,	↓ Ca^{++} activated K^+/I_{AHP} (β1 receptors)
	↓ input resistance,	
	↓ AHP,	
	↓ spike frequency adaptation	
	or	
	Hyperpolarization followed by depolarization	Both above (α and β1)
Granule	As above	As above
		Activation of L type current (via β receptor) leading to ↓gK^+

Inhibitory Neurons

In addition to its action on principal neurons, NE is also known to depolarize specific subsets of hippocampal interneurons (Bergles et al. 1996; Hillman et al. 2009; Papay et al. 2006). The effect is primarily due to an α1 receptor-mediated decrease in potassium conductance, though a modest β-receptor component is also sometimes apparent, especially in interneurons displaying a pronounced time-dependent inward rectification (see chapter 'Physiological Properties of Hippocampal Neurons'). Though not tested systematically, NE appears to produce these potent depolarizing actions across multiple classes of interneurons including BCs located outside of the pyramidal cell layer (Bergles et al. 1996) and interneurons located in SO (Bergles et al. 1996; Papay et al. 2006). Depolarizing actions of NE are blocked by the α1AR antagonist (Bergles et al. 1996) and resemble responses to other G_q-mediated GPCRs (Parra et al. 1998). The β AR agonist isoprenaline increases spontaneous firing in O-LM cells through a mechanism consistent with a shift in the activation curve for the hyperpolarization-activated cationic current I_h (Maccaferri and McBain 1996). Consistent with these observations, SO interneurons that contain somatostatin (SOM) mRNA transcripts also possess mRNA transcripts for both α1a and α1b receptors, in striking contrast to the complete absence of α1a and α1b receptors in SR interneurons that contain CCK mRNA transcript (Hillman et al. 2005). A smaller subpopulation of hippocampal interneurons located in SR or SLM exhibit hyperpolarization or reduced excitability to NE application (Bergles et al. 1996; Parra et al. 1998), although the neurochemical identity of these cells is not clear.

Action of Norepinephrine on Excitatory Synapses

NE has a general suppressant action on hippocampal excitatory pathways. The PP input to CA1 is profoundly suppressed by NE (~55%) (Otmakhova et al. 2005), whereas the SC pathway is more weakly (10–15%) suppressed (Otmakhova and Lisman 2000). Studies in acute brain slices provide evidence for α2 receptor-mediated postsynaptic mechanisms (Otmakhova et al. 2005). However, detailed studies in culture systems provide evidence for a presynaptic mode of inhibition of excitatory transmission via α1 (Scanziani et al. 1993) and α2 receptors (Boehm 1999).

In terms of synaptic plasticity, β adrenoceptors enhance both early and late phases of LTP in area CA1 as well as the DG (Hopkins and Johnston 1984, 1988; Huang and Kandel 1996; Gelinas and Nguyen 2005). NE has been shown to regulate AMPA-receptor trafficking (Hu et al. 2007), whilst early studies show that NE modulated glutamate release in the DG (Lynch and Bliss 1986). PKA activation following β-adrenoceptor activation is essential for both MF-mediated and SC-mediated LTP (Huang and Kandel 1996; Gelinas and Nguyen 2005; Gelinas et al. 2008). It is possible that these processes involve the phosphorylation of vesicular proteins including synapsin 1 and 2 (Parfitt et al. 1991, 1992). More recent studies suggest that NE may also trigger long-lasting synaptic potentiation through transcriptional regulation (Maity et al. 2015, 2016).

Action of Norepinephrine on Inhibitory Synapses

Information on the regulation of inhibitory synaptic transmission by NE is relatively sparse. Intracellular studies have shown NE to produce a marked (~50%) suppression of evoked inhibitory synaptic potentials recorded in CA1 pyramidal cells (Madison and Nicoll 1988b). Subsequent studies have suggested this effect to be independent of a direct action of NE on interneuron soma or axon terminals and instead be due to decreased excitatory input to the interneurons (Doze et al. 1991). However, more recent whole-cell recording has demonstrated a subpopulation of CA1 interneurons that are excited by α1a R activation (Hillman et al. 2009). NE, like other transmitters, is also reported to facilitate depolarization-induced suppression of inhibition (DSI) (Martin et al. 2001) (see cannabinoids below). Finally, NE may also influence hippocampal network behaviour through the modulation of electrical coupling of GABAergic circuits in SLM (Zsiros and Maccaferri 2008). Overall, there remains a paucity of data on the selective modulation of discrete inhibitory hippocampal cells and circuits by this modulator.

Serotonin

Serotonin (5-hydroxytryptamine or 5-HT) is an important modulator of hippocampal-dependent behaviours and cognitive performance (Richter-Levin and

Segal 1996). In general terms, 5-HT plays a role in the regulation of mood, anger and aggression. By its association with other limbic structures, more recent studies implicate roles of 5-HT and the hippocampus in fear learning (Balazsfi et al. 2017; Bauer 2015), assigning emotional salience (Mlinar and Corradetti 2017), encoding of reward signals (Li et al. 2016) and memory consolidation (Wang et al. 2015). Transgenic mice have revealed important insights into the function of 5-HT and its receptors in behaviour (Gardier 2009). Cells providing serotonergic input show an interesting dichotomy with one population of cells displaying state-dependent fluctuations in activity across the sleep-wake cycle whilst another population is tightly regulated to the hippocampal theta rhythm (Kocsis et al. 2006). These findings suggest that ascending serotonergic projections regulate both fast, dynamical information processing and slow, state-dependent transitions.

Origin and Structural Organization of Serotonergic Afferents

The serotonergic projection of the hippocampus originates in the dorsal raphe nucleus (DRN) and ramifies extensively throughout the hippocampal formation (Miettinen and Freund 1992; Varga et al. 2009; Vertes et al. 1999). A subset of DRN neurons project only to the medial septum, implying that serotonin transmission can impact hippocampal function both directly and indirectly through the medial septum (Acsady et al. 1996b). The DRN is neurochemically heterogeneous, containing neurons that express 5-HT, glutamate, 5-HT/glutamate and GABA (Domonkos et al. 2016; Gras et al. 2002; Hioki et al. 2010; Sos et al. 2017). DRN fibres innervating the hippocampus co-localize with the vesicular monoamine transporter VMAT2 and the vesicular glutamate transporter vGluT3 (Amilhon et al. 2010; Varga et al. 2009). Consistent with the co-release of both 5-HT and glutamate from DRN fibres, optogenetic activation of DRN afferents evokes synaptic currents onto hippocampal neurons that are mediated by both glutamate receptors and 5-HT_3 receptors (Varga et al. 2009). Similar co-transmission has been observed in the amygdala (Sengupta et al. 2017).

Within the rodent hippocampus, serotonergic afferents exhibit exquisite laminar specificity, with dense innervation at the SR/SLM border in areas CA3 and CA1, and a secondary, lower density in SO (Ihara et al. 1988; Lidov et al. 1980; Miettinen and Freund 1992; Varga et al. 2009; Vertes et al. 1999). This laminar specificity has been confirmed with quantitative autoradiography (Moore and Halaris 1975; Oleskevich and Descarries 1990). The majority of DRN axon varicosities do not make direct synaptic contacts with target neurons, implying that volume transmission is a primary mode of serotonergic transmission (Oleskevich et al. 1991). As a result of the differential laminar localization of 5-HT afferents, interneurons located in SR/SLM, such as calbindin-positive and NPY-positive interneurons, are major cellular targets (Freund et al. 1990; Gulyas et al. 1999; Miettinen and Freund 1992; Varga et al. 2009). The exact anatomical identity of these interneurons is not explicitly known but likely includes dendritically projecting neurons such as CCK/5HT_3-positive SCA and PP-associated interneurons (Klausberger 2009; Varga

et al. 2009) and neurogliaform cells (Overstreet-Wadiche and McBain 2015). The density of 5-HT innervation in principal cell layers is much lower; therefore, PV-positive interneurons embedded in the principal cell layers receive less innervation.

Cell Type-Specific Expression of 5-HT Receptors

There are many different 5-HT R subtypes expressed in the hippocampus, and these have been linked to an array of neurophysiological responses (reviewed by Andrade (1998); Barnes and Sharp (1999); Dale et al. (2016); Fig. 4). There are diverse expression patterns across the dorsoventral axis (Mlinar and Corradetti 2017; Tanaka et al. 2012), between hippocampal cell types (Dale et al. 2016) and even between subcellular neuronal compartments (Fink and Gothert 2007) (Table 4). For instance, in CA1 pyramidal cells, 5-HT_{1A} and 5-HT_4 receptors mediate the

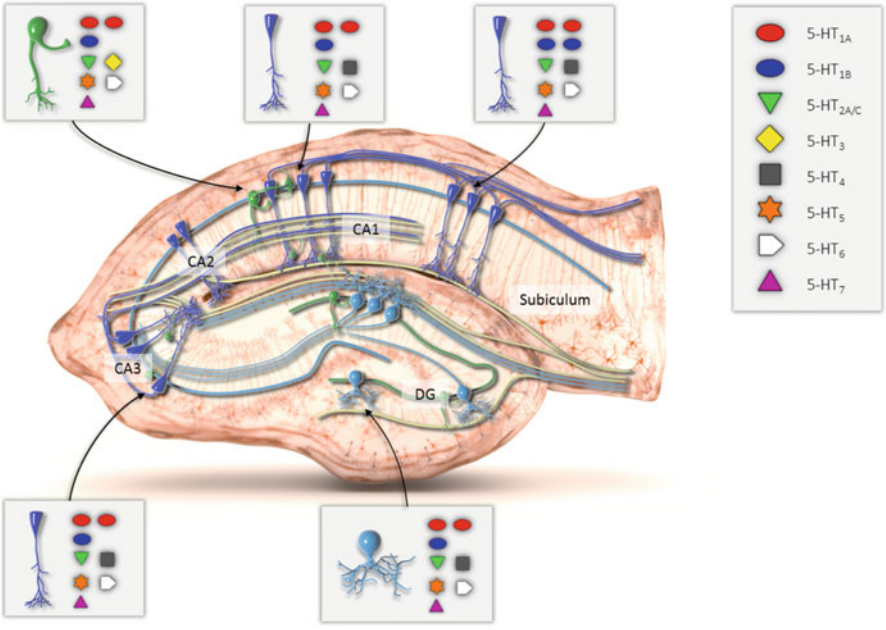

Fig. 4 Schematic illustration of the hippocampal circuit with 5-HT receptor localization. The main areas of the hippocampus together with primary synaptic connections are indicated. Principal (granule and pyramidal) cells are shown in blue, and interneurons are shown in green. Expression of 5-HT receptor subtypes on hippocampal CA1 and CA3 pyramidal cells, granule cells and interneurons is shown. Note that the 5-HT_{1A} heteroreceptor is expressed at high levels throughout the hippocampus. The 5-HT_{1B} receptor is found at highest levels in the subiculum. Based on histology data, the 5-HT_3 receptor is only expressed on the interneurons, and the 5-HT_4 receptor is only expressed on pyramidal cells. Other 5-HT receptor subtypes are found on both principal cells and interneurons (Reproduced from Dale et al. 2016, with permission)

Table 4 Summary of serotonin receptors in the hippocampus

Receptor family	5HT1a	5HT2A	5HT3	5HT4	5HT5	5HT6	5HT7
Expression in the hippocampus	5HT1a,b,f widespread $5HT1_c$ strong in CA3	CA1 SR/SLM interneurons	Strong in SLM and interneurons	Widespread, dendritic and axonal (mf)	5HT5a widespread, 5HT5B restricted to CA1	Widespread	Strongest in CA3
Signalling	$G_{i/o}$	$G_{q/11}$	Cation channel	G_s	G_i	G_s	G_s
Gross effect	Hyperpolarization, secondary depolarization, ↓accommodation, ↓EPSPs	depolarization	Fast depolarization of SR interneurons and DG basket cells; strong negative slope conductance, effect very depended upon MP	↓AHP	?	?	Increased Ih
References	Pompeiano et al. (1992) and Wright et al. (1995)	Weber and Andrade (2010) and Wyskiel and Andrade (2016)	Tecott et al. (1993)	Vilaro et al. (2005), Compan et al. (2004) and Waeber et al. (1996)	Matthes et al. (1993)	Ruat et al. (1993) and Ward et al. (1995)	Gustafson et al. (1996) and Bonaventure et al. (2002)

main postsynaptic actions, whereas $5HT_{1B}$ receptors, considered to be expressed at presynaptic terminals, regulate neurotransmitter release (Dale et al. 2016).

In CA1 hippocampus and DG principal cells, 5-HT_{1A} receptor mRNA is highly expressed, correlating with dense autoradiographic binding of 5-HT_{1A} in these areas (Chalmers and Watson 1991; Pompeiano et al. 1992). The CA3 region exhibits less 5-HT_{1A} mRNA and binding (Pompeiano et al. 1992). The mismatch between mRNA localization and autoradiographic binding in the CA1 region led to the conclusion that 5-HT_{1B} Rs are mainly presynaptic (Boschert et al. 1994). However, functional studies support that 5-HT_{1B} receptors are dendritically localized (Cai et al. 2013). The localization of 5-HT Rs has improved with the generation of GFP mice driven by 5-HT R-specific promoters. Although dense immunocytochemical staining of 5-HT_{2A} receptors in principal cells of CA1, CA3 and DG has been previously reported (i.e. Cornea-Hebert et al. (1999); Li et al. (2004)), the recent use of a 5-HT_{2A}-GFP mouse, combined with a 5-HT_{2A} antibody validated against a 5-HT_{2A} knockout mouse, has demonstrated a total absence of 5-HT_{2A} expression in CA1 pyramidal cells (Weber and Andrade 2010). A recent in situ hybridization study corroborates that 5-HT_{2A} R mRNA expression is not detectable in CA1 pyramidal cells (Tanaka et al. 2012). However, 5-HT_{2A} R mRNA is present in CA3 (Tanaka et al. 2012). $5HT_3$ Rs are preferentially expressed on a specific subclass of hippocampal interneurons (Chameau and van Hooft 2006; Morales et al. 1996; Morales and Bloom 1997; Tecott et al. 1993). 5-HT_4 R mRNA and binding is present in the principal neurons of the hippocampus (Vilaro et al. 2005; Waeber et al. 1996), which has been validated in a 5-HT4 R knockout mouse (Compan et al. 2004).

Action of Serotonin on Intrinsic Properties

Principal Cells

The release of serotonin can activate several different types of receptors on hippocampal neurons. In hippocampal CA1 principal cells, activation of somato-dendritic $5HT_{1A}$ Rs leads to the activation of $K_{ir3.2}$ inward-rectifying potassium channels through a membrane-delimited $G_{i/o}$-coupled pathway (Andrade 1998; Luscher et al. 1997). The consequence is membrane hyperpolarization and a decrease in cellular input resistance (Andrade et al. 1986; Andrade and Nicoll 1987; Andrade and Chaput 1991; Jahnsen 1980; Segal 1980; Behr et al. 1997; Luscher et al. 1997). The same $K_{ir3.2}$ channel conductance mediates both $GABA_B$ and 5-HT_{1A} receptor activation (Andrade et al. 1986; Andrade and Nicoll 1987; Booker et al. 2018; Colino and Halliwell 1987; Degro et al. 2015). A similar 5-HT_{1A}-mediated mechanism exists in CA3 pyramidal cells (Beck and Choi 1991; Beck et al. 1992; Corradetti et al. 1998; Johnston et al. 2014; Okuhara and Beck 1994; Sodickson and Bean 1998) and DG granule cells (Baskys et al. 1989; Ghadimi et al. 1994; Nozaki et al. 2016; Piguet and Galvan 1994). Although this mechanism has not yet been demonstrated to occur in response to DRN afferent stimulation, the

abundant expression of 5-HT_{1A} Rs in DG cells (Samuels et al. 2015; Tanaka et al. 2012) and K_{ir} responses to synaptic $GABA_B$ R activation (Otis et al. 1993) suggests that 5-HT_{1A} R-mediated $K_{ir3.2}$ responses can be evoked in DG cells. Interestingly, deletion of 5-HT_{1A} Rs from adult DG cells eliminates the antidepressant effect of the selective serotonin reuptake inhibitor fluoxetine, implying a critical role of 5-HT_{1A} receptors on mature DG cells in the regulation of mood and anxiety (Samuels et al. 2015).

Consistent with the virtual absence of mRNA transcripts and protein expression for G_q-coupled 5-HT_{2A}, 5-HT_{2B} and 5-HT_{2C} Rs (Tanaka et al. 2012), there are no published studies that attribute activation of these receptors to alterations in CA1 pyramidal cell excitability. However, in subicular neurons, 5-HT_{2C} R activation inhibits T-type calcium channels, which reduces burst firing (Petersen et al. 2017).

Expression and activation of 5-HT_3 Rs are thought to occur exclusively in hippocampal interneurons (Kepecs and Fishell 2014; Rudy et al. 2011; Tremblay et al. 2016). However, the absence of 5-HT_3 R expression has not been confirmed functionally in all hippocampal principal cell types (Kawa 1994).

Activation of G_s-coupled 5-HT_4 Rs increases cellular excitability by modulating at least three different channel conductances in CA1 pyramidal cells. First, 5-HT_4 R activation reduces afterhyperpolarization (AHP) potentials by increasing cAMP, leading to the activation of PKA, inhibition of Ca^{2+}-induced Ca^{2+} release and reduction in a Ca^{2+}-activated potassium channel current ($I_{K(Ca)}$) (Andrade and Chaput 1991; Torres et al. 1995; Torres et al. 1996). The likely underlying molecular mechanism is the inhibition of $K_{Ca3.1}$, a Ca^{2+}-activated potassium channel modulated by G_s-coupled receptors (Andrade et al. 2012) and expressed in hippocampal CA1 pyramidal cells (King et al. 2015). Secondly, activation of 5-HT_4 Rs induces a long-lasting inhibition of a barium-sensitive K_{ir} current (I_{Kir}), which is likely the same $K_{ir3.2}$ that is activated by $G_{i/o}$-coupled 5-HT_{1A} Rs (Mlinar et al. 2006). Activation of 5-HT_4 Rs increases hyperpolarization-activated cyclic nucleotide-gated channel-mediated currents (I_h), whereas activation of 5-HT_{1A} Rs decreases them (Bickmeyer et al. 2002). These findings are consistent with opposing roles of $G_{i/o}$-coupled 5-HT_{1A} Rs and G_s-coupled 5-HT_4 Rs in modulating $I_{K(Ca)}$, I_{Kir} and I_h.

CA3 pyramidal cells also express 5-HT4 Rs (Tanaka et al. 2012). AHP potentials are reduced by G_s-coupled 5-HT_7 Rs, probably via similar mechanisms (Bacon and Beck 2000).

Inhibitory Neurons

Early studies found that bath application of 5-HT increases the frequency of spontaneous GABAergic potentials in the hippocampus in the presence of glutamate receptor blockers (Ropert and Guy 1991). This depolarizing action was blocked by a 5-HT_3 R antagonist, largely accounting for the 5-HT-induced increase in depolarizing drive onto GABAergic interneurons (Ropert and Guy 1991).

Cortical interneurons expressing 5-HT_3Rs are now recognized as a major class of interneurons, which have led to a reorganization in the way that interneurons are classified (Kepecs and Fishell 2014; Rudy et al. 2011; Tremblay et al. 2016). Interneurons expressing 5-HT_3Rs are derived from the caudal ganglionic eminence (CGE) that co-express calretinin, VIP, CCK, NPY and reelin. In contrast, the 5-HT_3R-expressing interneurons exhibit minimal overlap with PV- and SST-containing populations that are derived from the medial ganglionic eminence (MGE). Consistent with this governing principle, cortical VIP interneurons, which are a subtype of CCK interneurons, exhibit enriched expression of 5-HT_3 Rs in cortex (Ferezou et al. 2002). On the basis of this reasoning, this governing principle likely applies to the hippocampus as well (Chittajallu et al. 2013). These observations align reasonably well with previous studies of 5-HT_3 R-positive responses in SR/SLM interneurons (McMahon and Kauer 1997; Sudweeks et al. 2002), in DG BCs (Kawa 1994) and in CA1 BCs, which are most likely to comprise CCK+ interneuron subtypes co-expressing presynaptic CB1 receptors (Ferezou et al. 2002; Freund and Katona 2007; Kepecs and Fishell 2014; Morales and Backman 2002; Rudy et al. 2011; Tremblay et al. 2016).

Synaptic activation mediated by 5-HT_3 Rs has been demonstrated in amygdala (Sugita et al. 1992) and cortex (Ferezou et al. 2002; Roerig et al. 1997). Optogenetic activation of DRN elicits a strong fast excitation of hippocampal interneurons mediated by co-release of 5-HT and glutamate onto 5-HT_3 and glutamatergic receptors, respectively (Varga et al. 2009).

In addition to 5-HT_3 R expression in hippocampal interneurons derived from the CGE, there is evidence that several other types of 5-HT Rs are expressed in distinct hippocampal interneuron subpopulations. In the presence of a 5-HT_3R antagonist, 5-HT_2 R agonists enhance the frequency and amplitude of spontaneous inhibitory postsynaptic currents in CA1 pyramidal cells, indicating that 5-HT_2 receptors are expressed on a population of inhibitory neuron populations (Shen and Andrade 1998). Consistent with this mechanism, 5-HT-mediated enhancement of GABAergic signalling requires 5-HT_{2A} receptors and involves the inhibition of TASK-3 type potassium channels (Deng and Lei 2008).

5-HT responses that resemble 5-HT_2 responses have been anecdotally reported previously in hippocampal interneurons (McMahon and Kauer 1997; Parra et al. 1998). More recently, the use of 5-$HT2_A$-GFP mice have revealed that this interneuron population is located at the SR/SLM border (Wyskiel and Andrade 2016), overlapping strongly with the 5-HT_{3A}-GFP population (Chittajallu et al. 2013). SR/SLM interneurons expressing 5-HT_{2A} Rs strongly depolarize in response to bath application of 5-HT, which is almost completely blocked by the specific 5-HT_{2A} R antagonist MDL 100,907 (Wyskiel and Andrade 2016). In a subset of SR interneurons, the 5-HT response includes a hyperpolarization that precedes the depolarization, suggesting co-expression of 5-HT_{1a} Rs, 5-HT_3 Rs and 5-HT_{2A} Rs (Aznar et al. 2003; Dale et al. 2017). The anatomical and physiological characteristics of 5-HT_{2A}-expressing interneurons are consistent with CCK/5-HT_3 R-containing SCA and PPA interneuron subtypes (Wyskiel and Andrade 2016).

Within the CA1 SO layer, several subpopulations of SOM-positive interneurons are present that express 5-HT Rs. These include 5-HT_3 R-expressing O-LM cells derived from CGE (Chittajallu et al. 2013). In addition, a subset of SO interneurons express 5-HT_{2A} Rs (Wyskiel and Andrade 2016), though it is currently not clear whether this is the same O-LM cell population that co-expresses 5-HT_3 Rs. The majority of SO interneurons are depolarized by 5-HT_2 agonists (Lee et al. 1999b). A subset of SO interneurons hyperpolarize in response to 5-HT, which have axon arborizations that suggest O-LM or basket cells (Parra et al. 1998), and may therefore represent 5-HT_3 R-lacking cells derived from MGE (Chittajallu et al. 2013). The activation of $GABA_B$ Rs was shown to induce substantial $K_{ir3.2}$ channel-mediated currents in CA1 PV interneurons (Booker et al. 2013) but not O-LM cells (Booker et al. 2018). Because 5-HT_{1a} and $GABA_B$ receptors share common $G_{i/o}$ signalling mechanisms (Andrade et al. 1986; Andrade and Nicoll 1987; Colino and Halliwell 1987; Degro et al. 2015), it is possible that $5HT_{1A}$ R activation is more likely to induce a K_{ir3}-mediated hyperpolarization in perisomatically targeted interneurons than dendritically targeted interneurons. However, visually identified PV interneurons in CA3 do not consistently hyperpolarize, on average, in response to bath application of 5-HT (Johnston et al. 2014). In the basolateral amygdala, 5-HT_{1A} Rs are expressed in fast-spiking, presumably PV, interneurons and activated in response to optogenetic stimulation of DRN afferents (Sengupta et al. 2017). Although theoretically plausible, the question of whether 5-HT afferents are localized close enough to hippocampal PV interneurons to sufficiently activate synaptic 5-HT_{1A} Rs remains to be determined.

Action of Serotonin on Excitatory Synapses

Serotonin is known to regulate neurotransmission at a wide range of synapses in the brain (Fink and Gothert 2007). Because diverse 5-HT R subtypes in the hippocampus are expressed in a cell type- and pathway-specific manner, synaptic release of 5-HT has complex pre- and postsynaptic actions that occur on multiple time scales. The diverse ways that 5-HT can modulate glutamatergic transmission could lead to plausible treatment strategies for disorders involving dysfunction of glutamatergic transmission, such as depression (Dale et al. 2016; Pehrson and Sanchez 2014).

Some of the effects of 5-HT at excitatory synapses can be explained by a purely postsynaptic action via alteration of intrinsic membrane properties. For example, the 5-HT_{1A} R-mediated reduction of EPSP amplitude by SC input onto CA1 pyramidal cells can be explained by the postsynaptic dendritic activation of $K_{ir3.2}$ channels, leading to reduced input resistance, effectively shunting glutamatergic EPSPs (Pugliese et al. 1998). A similar mechanism is likely present in DG granule cells (Nozaki et al. 2016). Conversely, dendritic 5-HT_4 R activation increases cellular input resistance by inhibiting $K_{ir3.2}$ channels, which increases cellular excitability, enhancing the ability of EPSPs to generate action potentials (Mlinar et al. 2006). Consistent with this postsynaptic mechanism, SC-stimulated population spikes are

enhanced in vivo by 5-HT_4 R agonists (Matsumoto et al. 2002). Conversely, with 5-HT_{1A} Rs inhibited, fluvoxamine-induced enhancement of SC-stimulated population spikes is blocked by a 5-HT_4 R antagonist (Matsumoto et al. 2002).

In addition to modulating postsynaptic EPSPs by altering the intrinsic membrane properties of postsynaptic neurons, there is strong evidence that 5-HT R activation can alter presynaptic release and postsynaptic neurotransmitter receptor function within the CA1 hippocampus. At SC synapses, 5-HT_{1A} R activation reduces EPSC amplitude, increases paired-pulse ratio and reduces mEPSC frequency, consistent with the presynaptic expression of 5-HT_{1A} and/or 5-HT_{1B} Rs on glutamatergic SC terminals (Costa et al. 2012). Postsynaptically, activation of 5-HT_{1A} Rs reduces the amplitude of AMPA R-mediated EPSCs, whereas activation of 5-HT_7 Rs potentiates AMPA R-mediated EPSCs (Costa et al. 2012). Thus, postsynaptic $G_{i/o}$ and G_s signalling bidirectionally modulates cAMP levels, enabling bidirectional modulation of the phosphorylation state of synaptic AMPA receptors (Andreetta et al. 2016; Costa et al. 2012). Endogenous 5-HT release, induced by administration of the selective 5-HT reuptake inhibitor fluvoxamine, depresses SC evoked CA1 population spikes in vivo through a 5-HT_{1A}-dependent mechanism (Matsumoto et al. 2002).

The CA1 region is proposed to compute novelty signals by comparing PP input encoding ongoing sensory input with SC input encoding stored predictive information (Lisman and Grace 2005). DRN neurons are active during novelty and reward (Kobayashi et al. 2008; Li et al. 2016), and their axons densely innervate the CA1 SLM layer where PP synapses are localized (Ihara et al. 1988; Lidov et al. 1980; Miettinen and Freund 1992; Varga et al. 2009; Vertes et al. 1999). Early studies found that 5-HT more effectively suppressed field EPSPs arising from PP than SC synapses (Otmakhova and Lisman 2000; Otmakhova et al. 2005; Schmitz et al. 1995; Segal 1980). In these studies, paired-pulse ratio was unaffected by 5-HT R activation at PP synapses, implying a postsynaptic mechanism of 5-HT R action (Otmakhova et al. 2005). The underlying mechanism involves the differential postsynaptic expression of 5-HT_{1B} Rs at PP but not SC synapses (Cai et al. 2013; Peddie et al. 2008). In these studies, activation of 5-HT_{1B} Rs potentiates AMPA R-mediated EPSCs at CA1 PP synapses but not at SC synapses (Cai et al. 2013). In this case, postsynaptic 5-HT_{1B} R activation causes the activation of Ca^{2+}/calmodulin-dependent protein kinase (CaMK), which then phosphorylates AMPA Rs, thereby accounting for the pathway-specific potentiation of AMPA R-mediated EPSCs (Cai et al. 2013).

Serotonin also appears to have synapse-specific effects at SC synapses innervating different hippocampal interneuron subtypes. Activation of presynaptic 5-HT_{1B} Rs on SC terminals inhibits feedback excitation onto CCK-expressing interneurons but not PV-expressing interneurons (Winterer et al. 2011). The underlying presynaptic mechanism of presynaptic 5-HT_{1B} R modulation presumably occurs through $G_{i/o}$-induced inhibition of presynaptic Ca^{2+} channels (Winterer et al. 2011). A similar presynaptic mechanism occurs at glutamatergic synapses onto O-LM cells, but in this case 5-HT_{1A} receptors mediate the presynaptic effect (Bohm et al. 2015).

Dense binding sites for 5-HT_4 are found in the CA3 SL layer within MF termination zones (Vilaro et al. 2005). Bath application of serotonin potentiates MF transmission, reduces paired-pulse facilitation and is partially occluded by the adenylate cyclase activator forskolin, consistent with the presynaptic localization of 5-HT_4 receptors on MF terminals (Kobayashi et al. 2008). In DG, 5-HT has differential effects between EPSPs arising from medial and lateral PP synapses in DG granule cells, which may be due to differences in the shunting of these EPSPs by 5-HT_{1A} Rs (Nozaki et al. 2016). However, in anesthetized animals, the 5-HT uptake inhibitor fenfluramine causes enhanced population spikes in the DG, implying the existence of additional indirect mechanisms (Levkovitz and Segal 1997).

Serotonin is also an important modulator of synaptic plasticity at glutamatergic synapses. Postsynaptic activation of 5-HT_{1A} Rs inhibits induction of LTP (Corradetti et al. 1992; Kojima et al. 2003; Shakesby et al. 2002), which could occur by either hyperpolarization and/or shunting of EPSPs (Pugliese et al. 1998) and/or cAMP-dependent dephosphorylation of AMPA receptors (Andreetta et al. 2016; Costa et al. 2012). Serotonin also inhibits LTP at SC synapses in CA3 probably via a similar mechanism (Villani and Johnston 1993). However, $5HT_2$ antagonism enhances NMDA receptor-mediated currents, facilitating LTP induction (Wang and Arvanov 1998).

As revealed by a $5HT_3$ R antagonist, activation of 5-HT_3 Rs suppresses LTP (Staubli and Xu 1995), presumably through an indirection action involving activation of inhibitory interneurons. Similarly, the $5HT_3$ receptor-mediated suppression of MF-CA3 LTP by 5-HT may be due to indirect actions through enhanced activation of 5-HT_3 R-containing GABAergic interneurons (Maeda et al. 1994). Unlike other receptors, $5HT_4$ R activation is reported to enhance glutamatergic transmission (Matsumoto et al. 2002).

Action of Serotonin on Inhibitory Synapses

In addition to the capability of 5-HT to alter cellular excitability through somatodendritic 5-HT R activation and effects on glutamatergic drive onto GABAergic neurons, there is also evidence that 5-HT R activation can alter GABAergic transmission by the activation of presynaptic 5-HT Rs. Consistent with a presynaptic 5-HT_3 Rs, an increase in the frequency of miniature IPSCs is observed upon application of 5-HT or a 5-HT_3 agonist (Choi et al. 2007; Dorostkar and Boehm 2007; Turner et al. 2004). Additional evidence for the activation of presynaptic 5-HT Rs has been shown in a preparation that allows a single GABAergic presynaptic terminal to be stimulated (Katsurabayashi et al. 2003). Two separate populations of GABAergic terminals were discovered. One population expressed only presynaptic 5-HT_{1A} Rs, which reduced release probability, most likely through inhibition of presynaptic calcium channels (Katsurabayashi et al. 2003). A second population co-expressed presynaptic 5-HT_3 and 5-HT_{1A} Rs. Presynaptic 5-HT_3 Rs increases release probability by causing calcium influx directly through the presynaptic 5-HT_3 channels and does not appear to require the activation of presynaptic voltage-

gated calcium channels (Turner et al. 2004). These distinct presynaptic GABAergic populations of 5-HT_3 R-containing and 5-HT_3 R-lacking GABAergic terminals likely arise from two different populations of inhibitory interneuron subtypes. However, presynaptic 5-HT R activation was not detected at CCK basket cell to pyramidal cell synapses (Neu et al. 2007). Therefore, it remains to be determined which hippocampal interneuron subtypes possess presynaptic 5-HT_3 Rs.

Histamine

Histaminergic neurons comprise a small cluster of cells in the tuberomammillary nucleus (TMN) that project to most brain areas, including the hippocampus. As with other neuromodulatory systems associated with the reticular activating system, the activity of histaminergic neurons innervating the hippocampus is strongly modulated across the sleep-wake cycle (Haas et al. 2008). The histamine (HA) system is considered to be important in a number of central nervous system functions, including wakefulness and sleep, cognition, learning, feeding and stress-related behaviours (Alvarez 2009; Brown et al. 2001; Panula and Nuutinen 2013). The histaminergic system operates synergistically with the cholinergic system to modulate hippocampal function (Blandina et al. 2004; Mochizuki et al. 1994; Passani et al. 2007). Histamine receptor (HAR) activation can excite septohippocampal cholinergic and GABAergic neurons (Xu et al. 2004), increasing ACh release in the hippocampus (Bacciottini et al. 2002). In basal forebrain cholinergic neurons (Zant et al. 2012), the mechanism occurs through H1R-mediated inhibition of a leak potassium channel (Vu et al. 2015). However, because TMN afferents also project to the hippocampus, HA can play a direct role in hippocampal learning and retrieval (Fabbri et al. 2016).

Origin and Structural Organization of Histaminergic Afferents

All histaminergic neurons originate in the TMN of the hypothalamus (Haas and Panula 2003; Haas et al. 2008; Panula et al. 1984). TMN neurons send projections to most parts of the brain, including the hippocampus (Watanabe et al. 1984). Within the hippocampus, TMN inputs terminate in all areas but are particularly pronounced in the subiculum and DG, with sparser innervation of hippocampal areas CA1 and CA3 (Barbin et al. 1976; Brown et al. 2001; Inagaki et al. 1988; Panula et al. 1989). Principal neurons of the hippocampus are the major postsynaptic targets of TMN afferents and do not exhibit preference for postsynaptic inhibitory neurons (Magloczky et al. 1994). Like other aminergic modulators, histaminergic axons form varicosities with very few synaptic specializations consistent with a volume transmission mode of action (Takagi et al. 1986). Recently, TMN neurons were shown to optogenetically co-release GABA in cortex and striatum (Yu et al. 2015). Therefore, TMN neurons innervating the hippocampus likely also co-release both

HA and GABA. Whether histaminergic afferents exhibit laminar and/or cell type specificity has not been systematically examined in the hippocampus.

Histamine Receptors

The HAR family is comprised of G-protein-coupled H1-H4 Rs (H1-H4Rs) (Panula et al. 2015). H1Rs have been detected throughout the hippocampus in both in situ hybridization (Andersson et al. 2017) and autoradiographic binding (Bouthenet et al. 1988; Martinez-Mir et al. 1990; Palacios et al. 1981) studies (Haas and Panula 2003; Panula et al. 2015). H1R mRNA is expressed at the highest densities in the CA3 pyramidal cell layer (Andersson et al. 2017). H2R mRNA and autoradiographic ligand binding has also been detected in the hippocampus (Vizuete et al. 1997). H3Rs are most prominent in the subiculum and DG (Pillot et al. 2002; Pollard et al. 1993) and are thought to be autoreceptors at presynaptic terminals (Arrang et al. 1983; Nieto-Alamilla et al. 2016). H4Rs do not appear to be expressed in the hippocampus (Andersson et al. 2017; Schneider and Seifert 2016).

In terms of signalling mechanisms leading to cellular changes in excitability, HA can cause myriad cellular effects due to divergent G-protein-mediated signalling pathways involved (reviewed by (Brown et al. 2001; Haas and Panula 2003)). H1Rs are G_q-coupled receptors, which can reduce a K_{leak} conductance. Recently, in cholinergic neurons, the HA-sensitive leak conductance has been determined to be mediated by the TWIK-like acid-sensitive K+ channel (Vu et al. 2015). G_q signalling activates phospholipase C, generating IP_3 and DAG, PKC activation, Ca^{2+} release from intracellular stores and downstream modulation of numerous conductances, such as a cationic conductance (Haas and Panula 2003). TRP channels remain the leading molecular candidates in underlying H1R-activated cationic conductances, yet no study has yet definitively linked H1Rs to TRP channel activation. Through PKC signalling, H1R activation can lead to phosphorylation of ligand-gated ion channels, including NMDA receptors. However, HA is also reported to directly potentiate NMDA receptor-mediated currents in a process distinct from classical HA receptors (Bekkers 1993; Vorobjev et al. 1993). This action is due to binding of HA to a site distinct from the polyamine site of the NMDA receptor (Burban et al. 2010). Other downstream signalling cascades likely activated by H1Rs include generation of nitric oxide and the modulation of expression of various proteins including gap junctions (Brown et al. 2001). Given the effectiveness of multiple types of G_q-coupled receptors in causing endocannabinoid release (Alger et al. 2014), it is possible that H1Rs also can cause endocannabinoid release. In contrast, H2Rs are G_s-coupled, causing increasing cAMP production and PKA activation. Like other G_s-coupled receptors, H2R activation is associated with the reduction a Ca^{2+}-activated potassium conductance (Greene and Haas 1990; Haas and Konnerth 1983) and shifting the activation threshold of HCN-mediated conductances (McCormick and Williamson 1991; Zhang et al. 2016). H3Rs are $G_{i/o}$-coupled, and their presynaptic activation leads to inhibition of high-threshold voltage-gated Ca^{2+} channels (Takeshita et al. 1998), a mechanism most likely to

underlie histaminergic suppression of neurotransmitter release (Nieto-Alamilla et al. 2016).

H1 and H2 knockout mice exhibit cognitive and/or learning impairment (Ambree et al. 2014; Dai et al. 2007), implicating hippocampal localization of H1Rs and H2Rs. As expected by their function as autoreceptors in regulating histaminergic release, H3 knockout mice exhibit increased histaminergic transmission and increased wakefulness (Gondard et al. 2013). H4 knockout mice appear normal in hippocampal-dependent tasks (Sanna et al. 2017), consistent with a relative absence of H4Rs from the hippocampus (Andersson et al. 2017).

Action of Histamine on Intrinsic Properties

Pyramidal Cells

HA is a powerful modulator of cellular excitability in the hippocampus. In principal cells (Haas and Konnerth 1983; Haas and Greene 1986; Pedarzani and Storm 1993; Selbach et al. 1997; Yanovsky and Haas 1998) and DG granule cells (Greene and Haas 1990), HA decreases a Ca^{2+}-activated potassium conductance, through G_s-coupled H2Rs. Selective activation of H1Rs can however result in a reduction in firing frequency (Selbach et al. 1997). The dominant depolarizing action is caused by enhancing HCN conductance and reducing the Ca^{2+}-activated potassium conductance responsible for the slow AHP and action potential accommodation (Brown et al. 2001; Haas and Konnerth 1983; Pedarzani and Storm 1993, 1995). Intracellular studies show HA to promote burst discharge patterns in CA3 pyramidal cells (Yanovsky and Haas 1998).

Interneurons

HA is reported to regulate interneuronal excitability, as indicated by an increase in spontaneous inhibitory synaptic potentials in the DG (Greene and Haas 1990), CA1 hippocampus (Haas and Greene 1986) and entorhinal cortex (Cilz and Lei 2017). Although effects of HA on neurochemically identified interneuron types have not been systematically investigated, several interneuron populations have been examined in various hippocampal regions. In CA3, bath application of HA enhances the cellular excitability of fast-spiking interneurons (most likely PV interneurons) primarily through H1R-mediated inhibition of Kv7 potassium channels (Andersson et al. 2017). Such a mechanism implies a convergence with postsynaptic M1/M3 mAChR-mediated signalling mechanisms (Lawrence et al. 2006b; Lawrence et al. 2006c). In the layer 3 medial entorhinal cortex (MEC), HA depolarizes Type I and Type II inhibitory neurons through both H1R- and H2R-mediated mechanisms (Cilz and Lei 2017). The conductances modulated involve the activation of a TRP-like cationic conductance and reduction in a K_{ir} conductance (Cilz and Lei 2017). Histaminergic modulation of interneurons in the DG molecular layer occurs

via H2R-mediated inhibition of Kv3.2 channels involved in rapid action potential repolarization (Atzori et al. 2000). HARs are in putative O-LM interneurons confirm an enhanced firing activity in response to HA (Brown et al. 2001).

Action of Histamine on Excitatory Synapses

HA depresses EPSPs from PP stimulation of the DG through H3R-mediated reduction in glutamate release in vitro (Brown and Haas 1999) and in vivo (Chang et al. 1998). The action of HA on evoked synaptic responses at the SC to CA1 pyramidal cell synapse is an enhanced population spike (Segal 1981; Yanovsky and Haas 1998) but modest reduction (~10%) in the excitatory synaptic potential (Brown et al. 1995). These data are consistent with HA suppressing transmitter release but with the enhanced postsynaptic excitability dominating the response. HA is also known to potentiate NMDA-mediated synaptic transmission and enhance LTP through a direct action on the NMDA receptor (Bekkers 1993; Brown et al. 1995) (Fig. 5).

Action of Histamine on Inhibitory Synapses

Early studies using paired-pulse stimulation provided early evidence that HA may modulate inhibitory synaptic transmission in the hippocampus (Springfield and

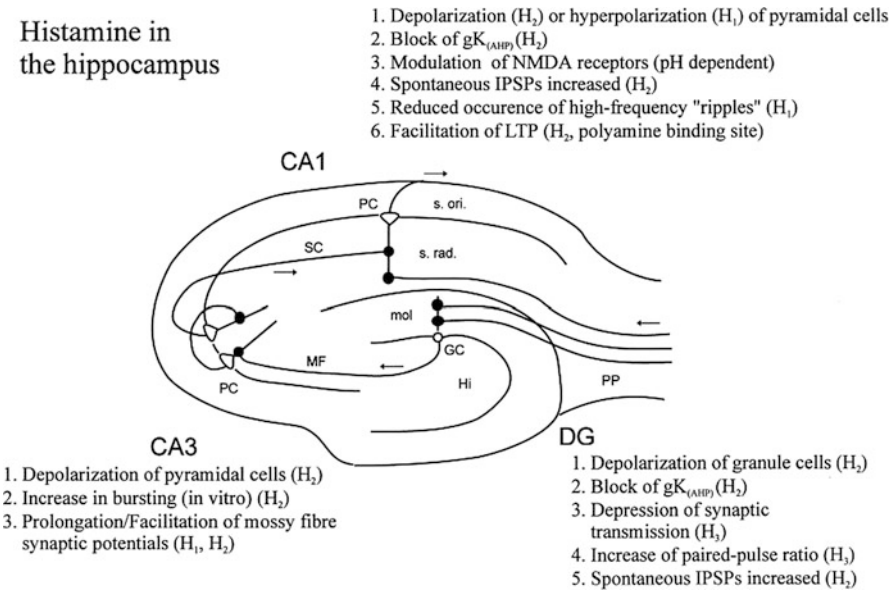

Fig. 5 Primary actions of histamine in the hippocampal formation. (From Brown et al. 2001, with permission)

Geller 1988). HA may modulate inhibitory synaptic transmission indirectly by modulating the action potential frequency and short-term plasticity of GABAergic transmission (Atzori et al. 2000). However, a detailed understanding of how HA modulates GABAergic transmission and the specific interneuron subtypes that express HARs remains to be systematically investigated.

Purines

Production and Release of Purine Transmitters

Adenosine, adenosine triphosphase (ATP) and other purine nucleotides (UTP, UDP etc.) are important cellular metabolites but also are released as modulatory substances in the central nervous system where they display a range of actions. ATP is often stored with other transmitters including GABA and glutamate but can also be released independently. It has been suggested that in the hippocampus, ATP is stored and released from distinct pools of vesicles independent of GABA and glutamate (Pankratov et al. 2006). ATP may be transmitted through gap junctions and other channels. It may also be the source of adenosine, especially when released from astrocytes (Pascual et al. 2005). A component of adenosine release in the hippocampus arises from the extracellular metabolism of ATP released from astrocytes (Wall and Dale 2013). In contrast to ATP, the release of adenosine is more enigmatic. It is not stored in vesicles, and in general the level of adenosine rises with increasing neuronal activity as well as in disease conditions such as epileptic seizures and hypoxia. Recent evidence suggests that adenosine release can be stimulated by glutamate receptor activation via equilibrative nucleoside transporters (Wall and Dale 2013). Despite not being released by exocytosis, adenosine is nevertheless a powerful homeostatic modulator of neuronal excitability and synaptic transmission (Dunwiddie and Masino 2001; Fredholm and Dunwiddie 1988; Rombo et al. 2016b).

Purine Receptors

Separate receptors exist for adenosine (P1 receptors) and ATP (P2 receptors). The latter is broadly divided into ion channel receptors (P2X) and metabotropic receptors (P2Y). Overall, the purine receptors are widely expressed and mediate a number of actions as summarized in Table 5.

Action on Intrinsic Properties

Adenosine causes a hyperpolarization of all hippocampal neurons (Thompson et al. 1992) that has been attributed to the activation of inwardly rectifying K^+

Table 5 Summary of purine receptors, signalling and primary actions

Receptor	Adenosine ($A_{1,\ 2A,\ 2B,\ 3}$)	P2X	P2Y
Family		($P2X_{1\text{-}7}$)	($P2Y_{1,2,4\text{-}6,\ 8\text{-}14}$)
Expression in the hippocampus	A1, widespread	Widespread	Widespread
	A2A, A2B, widespread		
	A3, presynaptic		
Signalling	A_1, $G_{i/o}$; $A_{2A/B,}$ G_s; A_3, $G_{i/o}$	Cation channels (subunits confer biophysics, some have very high Ca^{++} permeability)	$P2Y_{1,2,4,6,14}$ $G_{q/11}$
			$P2Y_{4,\ 12,\ 13}$ G_i
			$P2Y_{11}$ $G_{Q/11}$ and G_s
Gross effect	A_1 (high-affinity) hyperpolarization (↑GIRK), suppression of synaptic transmission (↓VDCCs)	Depolarization, can contribute to evoked EPSPs	Poorly defined
	A2A Depolarization, ↑ synaptic transmission/plasticity		
	A2B		
	A3		
References	Dunwiddie and Masino (2001) and Rombo et al. (2016b)	Pankratov et al. (1998) and Abbracchio et al. (2009)	Abbracchio et al. (2009)

(GIRK) channels (Dunwiddie and Masino 2001). The postsynaptic actions of ATP are mediated through both P2X and P2Y receptors as well as indirectly via P1 receptors when metabolized to adenosine. P2X receptors mediate a fast inward current that is reported to contribute to the EPSC recorded upon afferent fibre (e.g. SC) stimulation (Pankratov et al. 1998). It is proposed that ATP is co-released with glutamate at associational fibres but not MF synapses (Mori et al. 2001). The cationic current associated with P2X-mediated signalling is generally modest (typically 50–100 pA). However, it has often a significant Ca^{2+} component which can in turn give rise to activation of Ca^{2+}-dependent potassium conductances (Illes et al. 1996). Little is known about the action of P2Y receptors in regulating hippocampal primary neurons. Studies in cultured hippocampal neurons report the activation of an outwardly rectifying K^+ current (Ikeuchi et al. 1996) or inhibition of the I_M (Filippov et al. 2006). In contrast to principal cells, hippocampal interneurons in stratum radiatum, identified as calbindin- and calretinin-positive interneurons, are excited by ATP (Bowser and Khakh 2004). This depolarization is associated with a reduction of potassium conductances and activation of non-selective cationic conductances mediated by P2Y1 receptor activation (Bowser and Khakh 2004; Kawamura et al. 2004).

Action of Purines on Excitatory Synapses

The primary action of adenosine is to profoundly (up to ~75–100%) suppress glutamatergic transmission at all hippocampal synapses tested (Dunwiddie and Hoffer 1980; Thompson et al. 1992). This may be mediated by multiple mechanisms, but principal amongst these is a profound suppression of terminal calcium currents by A1 Rs (Fredholm and Dunwiddie 1988; Wu and Saggau 1994, 1997). The exact role of A2A receptors in regulating transmission is complex, but it may counteract the suppression of glutamatergic transmission by A1 Rs (Lopes et al. 2002) and involve the enhancement of glutamate receptor expression and AMPA R-mediated currents (Dias et al. 2012). A2A receptors also facilitate the release of other transmitters in the hippocampus, notably ACh (Cunha et al. 1994). In line with this modulatory action, adenosine is also reported to depress the induction of LTP at a range of synapses (Alzheimer et al. 1991). However, the situation is complex in that low-frequency plasticity induction paradigms are more sensitive to adenosine than higher-frequency patterns which appear to overcome the effect of adenosine (Mitchell et al. 1993). A number of more recent studies point to the fact that adenosine may serve a pivotal role in modulating plasticity (reviewed by (Dias et al. 2013).

As mentioned above, ATP appears to act as a classical neurotransmitter by mediating fast excitatory synaptic reposes through P2X receptors. However, it may also modulate excitatory synaptic transmission and plasticity although the precise mechanistic detail remains unclear (Inoue et al. 1999; Pankratov et al. 2009). Despite this, it has been shown that ATP can induce LTP and LTD in its own right depending on the level of Ca^{++} influx associated with the ATP

current (Yamazaki et al. 2003). ATP can also regulate plasticity induced by classical induction methods (Pankratov et al. 2002). P2X channel-mediated modulation may show some selectivity between different synapses in the hippocampus. For instance, presynaptic P2X2 channels are reported to facilitate excitatory synapses onto SR interneurons in area CA1 but not CA1 pyramidal neurons (Khakh et al. 2003; Khakh 2009). Relatively little is known concerning the possible role of P2Y receptors in regulating synaptic transmission and plasticity in the hippocampus (Guzman and Gerevich 2016). However, a recent report suggests a requirement of P2Y receptor activation in a form of heterosynaptic LTD (Chen et al. 2013).

Action of Purines on Inhibitory Synapses

The actions of adenosine on GABAergic signalling are poorly defined. Early studies suggested that adenosine could suppress GABA release in cortical tissues (Hollins and Stone 1980). However, similar experiments in hippocampal slices failed to find an effect of adenosine on GABA release (Burke and Nadler 1988). Electrophysiological studies using cultured neurons (Yoon and Rothman 1991) and in slices have failed to show a direct suppressant action of adenosine A1 Rs on action potential-dependent GABA release (Rombo et al. 2016b). However, adenosine A1 Rs appear to modulate tonic GABA current (resulting from extrasynaptic $GABA_A$ receptors) (Rombo et al. 2016a) and are known to strongly modulate disynaptic inhibition in the hippocampus through actions on glutamatergic transmission (Lambert and Teyler 1991). A detailed overview of the actions on adenosine A1 and A2A Rs on select GABAergic circuits has recently been described (Rombo et al. 2016b). The actions of ATP via P2X and P2Y classes of receptor on GABAergic signalling remain to be defined.

Paracrine/Autocrine Modulators

Endocannabinoids

Production and Release of Endocannabinoids

Cannabinoids are a group of related lipid-derived modulators that regulate hippocampal circuits through activation of specific cannabinoid receptors (Kano et al. 2009; Castillo et al. 2012). Some endocannabinoids (eCBs) such as anandamide can also signal through TRPV1 receptors and thus also mediate endovanilloid actions (Castillo et al. 2012). Anandamide and other major cannabinoids including 2-AG (2-arachidonyl glycerol) are not stored but synthesized and released tonically on demand in response to neuronal and synaptic activity (Stella et al. 1997; Castillo et al. 2012). The primary action of eCBs is to mediate retrograde signalling and in particular induce various forms of presynaptic inhibition. Common forms of

eCB-mediated STD are driven by postsynaptic depolarization, Ca^{2+} influx through NMDA receptors or via mAChR-mediated activation (Kano et al. 2009). However, the most significant trigger for eCB release and subsequent suppression of synaptic transmission is activation of metabotropic glutamate receptors (Varma et al. 2001).

Endocannabinoid Receptors

The two major forms of cannabinoid receptors (CB1 and CB2 Rs) are both metabotropic receptors with the CB1 being the archetypal 'brain' form. CB2 Rs, once thought to be mainly restricted to immune cells including microglia, recently have been shown to be expressed in the hippocampus (Stempel et al. 2016). The orphan receptor GPR55 is activated by anandamide (Ryberg et al. 2007) and L-α-lyso-phosphatidylinositol (LPI) (Oka et al. 2007) and widely expressed in the hippocampus (Henstridge et al. 2009; Hurst et al. 2017). CB1 Rs are highly abundant but most strongly expressed in CCK interneurons (Freund and Katona 2007). Hippocampal pyramidal cells and DG granule cells are lightly immunopositive for CB1 receptors but are surrounded by a dense plexus of CB1 R-positive GABAergic terminals (Tsou et al. 1998). However, low but significant levels of CB1 mRNA are expressed in principal cells suggesting low levels of CB1 R-mediated signalling in these cells (Marsicano and Lutz 1999). Within the GABAergic cell population, it appears that CB1 receptors are preferentially expressed in the terminals of perisomatically terminating BCs. The two main classes of BCs are PV- and CCK-expressing cells, and it is striking that over 95% of CCK-positive cells express CB1 Rs, which contrasts with PV cells for which only ∼5% of cells are CB1 immunoreactive (Katona et al. 1999). However, CB1 Rs are also expressed at glutamatergic terminals (Katona et al. 2006) (Table 6).

Action of Endocannabinoids on Intrinsic Properties

Most of the actions of eCBs are attributed to their influence on synaptic transmission. Studies addressing the actions of eCBs on hippocampal neuronal excitability are very limited (Kirby et al. 2000), but the primary postsynaptic action of eCB appears to be a modest increased excitability that is mediated through a reduction (∼45%) in I_M (Schweitzer 2000). More detailed studies in somatosensory cortex suggest that low-threshold spiking-type interneurons can exhibit a long-lasting form of action potential suppression whereby activity-dependent release of endocannabinoids causes an autocrine-like enhancement of potassium conductances, consistent with $G_{i/o}$-mediated activation of a K_{ir} conductance (Bacci et al. 2004). Whilst a similar postsynaptic mechanism is yet to be described in the hippocampus, an activity-dependent, autocrine-like, endocannabinoid-mediated hyperpolarization was recently described in CA3 pyramidal cells (Stempel et al. 2016). This hyperpolarization is mediated by endogenous release of 2-AG and postsynaptic activation

Table 6 Summary of cannabinoid signalling in the hippocampus

Receptor	CB1	CB2	GPR55
Expression in the hippocampus	Strongly expressed in interneurons (esp. CCK basket cells)	Highly expressed in non-neuronal cell types (e.g. microglia), weak neuronal expression	Widely expressed
Signalling	Gi and others, ↑A-type K^+, ↓N & P/Q Ca^{2+}, ↓M and D type K^+; ↑ Ih	Gi and others	Gq, Gα13 and others
Gross effect	Decrease GABA release (main effect) and other transmitters, decrease in dendritic excitability	Hyperpolarization of CA3 pyramidal cells	Increases release probability at glutamatergic synapses, enhances LTP
References	Kano et al. (2009), Pagotto et al. (2006) and Maroso et al. (2016)	Onaivi et al. (2006) and Stempel et al. (2016)	Henstridge et al. (2009), Lauckner et al. (2008), Ryberg et al. (2007) and Hurst et al. (2017)

of CB2 Rs (Stempel et al. 2016). Surprisingly, the effect was not mediated by K_{ir}, but by a sodium-dependent bicarbonate transporter (Stempel et al. 2016). GPR55 activation, through G_q-mediated release of calcium from internal stores, has been shown to inhibit I_M in expression systems (Lauckner et al. 2008), but it is not clear whether this is a common postsynaptic mechanism shared with CB1 Rs (Schweitzer 2000). Finally, CB1 receptors have recently been shown to enhance tonic I_h in a subset of CA1 pyramidal cells, which impairs dendritic integration of EPSCs and reduces LTP (Maroso et al. 2016; Vargish and McBain 2016).

Action of Endocannabinoids on Excitatory Synapses

Pharmacological activation of CB1 receptors has been shown to cause a profound (~86%) suppression of EPSCs in cultured neurons (Shen et al. 1996), and this effect is consistent with a presynaptic reduction in glutamate release. In terms of functional control of synaptic transmission, endocannabinoids have been shown to act as a retrograde messenger at glutamatergic synapses to produce a suppression glutamate release (Ohno-Shosaku et al. 2002). This is an activity-dependent depolarization-induced suppression of excitatory transmission (DSE) and is analogous to the more rigorously characterized suppression seen at inhibitory synapses (below). However, the CB1-mediated suppression of excitatory and inhibitory transmission differs in certain respects. Firstly, a more pronounced depolarization (~10 sec) is necessary to induce DSE than to cause suppression at inhibitory synapses (Ohno-Shosaku

et al. 2002). Secondly, the excitatory terminals themselves are less sensitive to cannabinoid receptor activation (Ohno-Shosaku et al. 2002). Activation of GPR55 has recently been shown to increase release probability at SC synapses through the mobilization of internal presynaptic calcium stores (Sylantyev et al. 2013) and enhance LTP (Hurst et al. 2017).

Action of Endocannabinoids on Inhibitory Synapses

Early reports by Pitler and Alger first described a phenomenon known as depolarization-induced suppression of inhibition (DSI) in CA1 pyramidal cells (Pitler and Alger 1992b). This phenomenon has subsequently been demonstrated in CA3 pyramidal cells, DG cells, mossy cells, CCK-positive interneurons (Kano et al. 2009) as well as other brain areas, notably the cerebellum. DSI is a transient but profound suppression of inhibition (spontaneous or evoked inhibitory postsynaptic events) that follows activity (e.g. depolarization and action potentials) in the postsynaptic cell. Studies in brain slices and cultured hippocampal neurons later confirmed that postsynaptic depolarization and resultant increase in intracellular free Ca^{2+} to cause a transient suppression of IPSCs and that this suppression was due to retrograde cannabinoid signalling-mediated reduction of GABA release (Ohno-Shosaku et al. 2002; Wilson and Nicoll 2001). It is now widely accepted that retrograde signalling by CB1 receptors is an important process in the dynamic regulation of GABAergic transmission (Castillo et al. 2012) (Fig. 6a). However, there is considerable evidence that cannabinoid signalling is not ubiquitous but preferentially regulates specific interneuronal connections (Younts and Castillo 2014). For instance, the output of major classes of basket cell is proposed to be differentially sensitive to cannabinoid regulation with the PV-containing basket cells being insensitive to CB1R activation, whereas GABA released from CCK-containing population are exquisitely sensitive (Freund and Katona 2007; Glickfeld and Scanziani 2006). However, the nature of the suppression of release is complex with evidence for both presynaptic and postsynaptic loci of action (Foldy et al. 2006; Neu et al. 2007).

The actions of eCBs at inhibitory synapses highlight the need to view neuromodulation as complex network phenomena. In addition to classical DSI, cannabinoids are known to mediate activity-dependent long-lasting heterosynaptic LTD at GABAergic synapses (Castillo et al. 2012) (Fig. 6b). This mechanism is initially triggered by the synaptic release of glutamate and activation of group 1 mGluRs on CA1 pyramidal cells. In turn, release of endocannabinoids is triggered which then initiates LTD of GABA release (Chevaleyre and Castillo 2003; Castillo et al. 2012) with the ultimate effect being a long-lasting increase in pyramidal cell excitability.

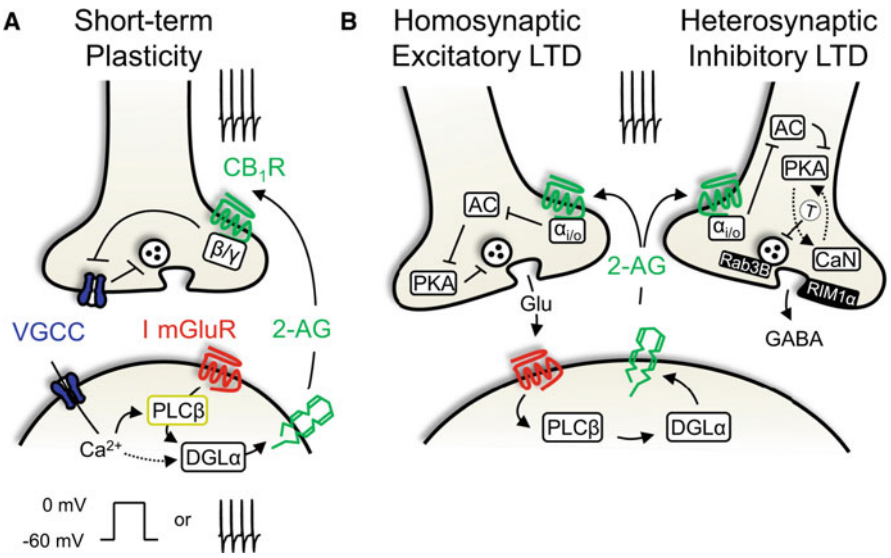

Fig. 6 Molecular mechanisms underlying endocannabinoid-mediated short- and long-term synaptic plasticity. (**a**) In endocannabinoid-mediated short-term plasticity, voltage-gated calcium channels (VGCC) or G_q-coupled receptors (i.e. Type 1 mGluRs) increase postsynaptic intracellular activities of diacylglycerol lipase (DGLα), causing the retrograde diffusion of eCBs to presynaptic CB1Rs. Activation of presynaptic CB1Rs inhibits VGCCs, which reduces neurotransmitter release. (**b**) Presynaptic activity activates postsynaptic mGluRs, inducing release of eCBs and presynaptic activation of CB1Rs at glutamatergic or GABAergic presynaptic terminals. At glutamatergic synapses, CB1-mediated $G_{i/o}$ signalling reduces cAMP levels and PKA activity, causing a LTD of glutamate release. At inhibitory synapses, a similar presynaptic mechanism activates calcineurin (CaN), which induces LTD of GABA release. (From Castillo et al. 2012, with permission)

Nitric Oxide

Production and Release of Nitric Oxide

Nitric oxide (NO) is synthesized de novo by a series of enzymes known as NO synthases (NOS) (Zhou and Zhu 2009). All three forms of NO synthase are expressed in the hippocampus. Original studies suggested pyramidal cells to express high levels of the endothelial form of NOS, whereas the neuronal form of the protein was restricted to diffuse populations of interneurons (Dinerman et al. 1994). However, more recent evidence has shown principal cells and selected interneurons to express the neuronal form with the endothelial form being restricted to vascular endothelium (Blackshaw et al. 2003). As NO is not stored and is a highly membrane-permeable molecule, the wide distribution of the enzymes in dendrites, soma and axon is likely to reflect the nature of its dispersal and suggested primary role as a retrograde transmitter. The prototypical activator of NOS is postsynaptic Ca^{2+} entry via the NMDA receptor leading Ca^{2+}/calmodulin interaction and NO production (Garthwaite 2008). NO may be released from presynaptic nerves by action potential-dependent activation of voltage-gated Ca^{2+} channels. Reports also suggest that

calcium-permeable AMPA receptors are an important regulator of NO production (Frade et al. 2008). Once produced, NO gas is itself is highly soluble, rapidly diffusible, highly membrane permeant but also highly labile (Garthwaite 2016).

Nitric Oxide Effectors

Nitric oxide acts through the regulation of soluble guanylyl cyclase. Within the context of neurons, guanylyl cyclase (the nitric oxide 'receptor') occurs in various isoforms and is often associated with the postsynaptic density in both principal cells and interneurons (Szabadits et al. 2007, 2011). However, other forms of the receptor may be transported to the membrane by signals including cannabinoids (Jones et al. 2008). The resultant production of cGMP regulates a range of cyclic nucleotide-gated channels as well as regulating multiple effectors (Maroso et al. 2016; Garthwaite 2016).

Action of Nitric Oxide on Intrinsic Properties

Despite abundant literature on the role of nitric oxide in regulating synaptic transmission, the action of NO on intrinsic postsynaptic properties of hippocampal neurons is sparse. However, a recent study provided evidence that CB1 R activation generated NO, which increased tonic dendritic I_h in CA1 pyramidal cells (Maroso et al. 2016; Vargish and McBain 2016).

Action of Nitric Oxide on Excitatory Synapses

There exists a significant body of evidence suggesting that certain forms of hippocampal LTP are dependent upon the action of NO as a diffusible retrograde messenger (Feil and Kleppisch 2008; Garthwaite and Boulton 1995; Schuman and Madison 1991, 1994). Blockade of NO signalling prevents LTP, whereas application of NO donors promotes the development of LTP (Schuman and Madison 1991; Arancio et al. 1996). However, the significance of NO in regulating synaptic plasticity seems to vary between species and between synapses. For instance, in areas CA1, NO-mediated/NO-regulated LTP is more prominent at apical dendrites than at synapses targeting basal dendrites (Haley et al. 1996; Son et al. 1996). In terms of the action of NO on basal synaptic transmission, there is evidence to suggest that NO may also produce an enhancement of glutamatergic transmission distinct from the enduring forms of potentiation such as LTP (Bon and Garthwaite 2001). However, studies have shown that NO may also transiently suppress glutamatergic transmission (Boulton et al. 1994). This may in part be mediated through triggering the release of adenosine (Arrigoni and Rosenberg 2006). A recently described mechanism is that CB1 activation on CA1 pyramidal cell dendrites generates NO, which activates I_h, reduces dendritic integration and impairs LTP (Maroso et al. 2016; Vargish and McBain 2016).

Action of Nitric Oxide on Inhibitory Synapses

Whilst morphological studies suggest that hippocampal GABAergic synapses are endowed with the molecular machinery for NO signalling, functional studies to assess the significance of nitric oxide in regulating inhibitory transmission are rather limited (Szabadits et al. 2007; Szabadits et al. 2011). However, recent evidence suggests that NO signalling may be an important mediator in depolarization-induced suppression of inhibition (Makara et al. 2007). The CCK BCs in CA1 and CA3, but not in DG, appear to be the major interneuron subtypes that increase cGMP signalling in response to NO donors (Szabadits et al. 2011). Hippocampal neurogliaform and ivy cells express NOS, but the function of NO within these interneuron circuits is not yet clear (Armstrong et al. 2012; Overstreet-Wadiche and McBain 2015).

Neuropeptides

Production and Release of Neuropeptides

The hippocampal formation is modulated by a diverse array of neuroactive peptides. Some of these are released from neurons intrinsic to the hippocampus (mainly interneurons but also principal cells), whereas others are supplied by inputs from diverse brain regions (Baraban and Tallent 2004). In general, neuropeptides are synthesized and stored for action potential-dependent release. The levels of neuropeptides and their receptors are often dynamically regulated, especially in association with plasticity processes and disease states. The neuropeptides represent a major category of modulator, and a detailed description of their expression, signalling and actions at different hippocampal cells and circuits is beyond the scope of this chapter. Whilst some actions of peptide modulators are rather ubiquitous, other effects can be highly cell type- or synapse-specific. Although much knowledge has been gained on neuropeptide expression and function in the hippocampus, for brevity, the table below summarizes some of the major peptide systems and their primary mechanisms of modulation in the hippocampus.

Action of Neuropeptides on Intrinsic Properties (Table 7)

Miscellaneous Neuromodulators

This chapter has aimed to provide a primer to the concept of neuromodulation by reviewing some of the major neuromodulator systems. However, it should be noted that there are likely to be very many other systems that may be significant regulators of hippocampal cells and circuits. Most of these are activators of metabotropic receptors. Examples here would include sphingolipids (Kajimoto et al. 2007),

Table 7 Summary of neuropeptide transmitter actions in the hippocampus

Neuropeptide	Expression	Receptors	Signalling	Modulation of intrinsic properties	Modulation of synaptic transmission	References
NPY	Neurogliaform cells. Various interneurons (bistratified cells), small amounts in principal cells. Strongest in dentate gyrus. NB. Important species differences in expression between human and rodent brain	$Y_{1\text{-}5}$	Y1	↓ N-type Ca^{++} currents (Y1 and Y2) but little overt postsynaptic action	↓glutamatergic transmission (Y2), ↓ LTP induction and short-term facilitation; ↓IPSC frequency	Haas et al. (1987), Klapstein and Colmers (1993), Ledri et al. (2011), Li et al. (2017), McQuiston et al. (1996), Overstreet-Wadiche and McBain (2015), Sperk et al. (2007) and Whittaker et al. (1999)
		Y1 mainly postsynaptic on principal cell dendrites in areas CA1 and CA3; Y2 postsynaptic on principal cells (DG) and on presynaptic mossy terminals	Y2			
Substance P	Various interneurons and granule cells as well as extrinsic projections (e.g. supramammillary)	$NK_{1\text{-}3}$	Most actions mediated by NK1	Depolarization on pyramidal cells and interneurons	↓EPSP (∼30%) and IPSP amplitude in pyramidal cells, ↑IPSPs between interneurons; ↑ excitability of interneurons	Borhegyi and Leranth (1997), Davies and Kohler (1985), Dreifuss and Raggenbass (1986), Kouznetsova and Nistri (1998), Ogier and Raggenbass (2003), Ogier et al. (2008) and Zaninetti and Raggenbass (2000)

(continued)

Table 7 (continued)

Neuropeptide	Expression	Receptors	Signalling	Modulation of intrinsic properties	Modulation of synaptic transmission	References
CCK	Various interneurons (basket, Schaffer-associated, PP-associated), released mainly as CCK8	Mainly CCK_2 (CCK_B)	CCK_2	Depolarization, $\downarrow K_{leak}$, $\downarrow Ca^{++}$ activated K^+ currents; signalling through endo-cannabinoid pathway; increase tonic inhibition through depolarization of interneurons – non-selective cationic conductance in PV+ basket cells	↓glutamatergic transmission (Schaffer collateral), ↑or↓ GABAergic transmission depending on interneuronal class	Boden and Hill (1988), Bohme et al. (1988), Dodd and Kelly (1979), Foldy et al. (2007), Lee et al. (2011), Karson et al. (2008), MacVicar et al. (1987), Miller et al. (1997) and Shinohara and Kawasaki (1997)

Opioids	Widely distributed	μ, δ, κ	Various	Hyperpolarization of interneurons – PV+ve basket cells, ivy and neurogliaform cells, mixed action on principal cells	↓glutamatergic transmission, ↓LTP, ↓GABAergic transmission	Glickfeld et al. (2008), Krook-Magnuson et al. (2011), Madison and Nicoll (1988a), McDermott and Schrader (2011), Moore et al. (1994), Rezai et al. (2013), Wagner et al. (1993), Weisskopf et al. (1993) and Zieglgansberger et al. (1979)
CGRP	Widely distributed but important species differences, some (CA2) pyramidal cells and strongly expressed in specific interneurons; hilar mossy cells and CA3c pyramidal cells	$CGPR_1$	cAMP	$\downarrow Ca^{++}$ activated K^+ current I(sAHP)	↓LTP	Freund et al. (1997) and Sakurai and Kosaka (2007)
Leptin	Synthesized in adipocytes and transported into brain, local biosynthesis	$Ob\text{-}R_{a\text{-}f}$	Cytokine receptor, JAK2	Hyperpolarization, ↑BK channel activity	Modulation of LTP and LTD;↑ GABAergic transmission	Durakoglugil et al. (2005), Guimond et al. (2014), Harvey (2007), Irving and Harvey (2014), Luo et al. (2015), Mercer et al. (1996), and Shanley et al. (2001)

(continued)

Table 7 (continued)

Neuropeptide	Expression	Receptors	Signalling	Modulation of intrinsic properties	Modulation of synaptic transmission	References
Somatostatin	Various interneurons (e.g. bistratified, O-LM cells)	$SST_{1\text{-}5}$	↓N-type Ca++ currents, ↑M current, ↑K_{leak}	Hyperpolarization of pyramidal cells, modulation of various K^+ channels	↓glutamatergic transmission, suppress PP-GC LTP	Baratta et al. (2002), Moore et al. (1988), Pittman and Siggins (1981), Qiu et al. (2008), Schweitzer et al. (1990), Tallent and Siggins (1997) and Tallent and Qiu (2008)
VIP	Various interneurons (basket cells, interneuron targeting cells)	$VPAC_1$ and $VPAC_2$	Various inc. I_{SAHP}	Depolarization of pyramidal cells, ↑ NMDA currents	Enhance GABAergic and glutamatergic transmission (may be indirect)	Cunha-Reis et al. (2004), Cunha-Reis et al. (2005), Haas and Gahwiler (1992), Haug and Storm (2000) and Yang et al. (2009)
Oxytocin	Produced in hypothalamo-neurohypophyseal cells as well as neurons terminating throughout CA1, CA3 and DG	OXTR	Multiple	No direct effect on pyramidal cells. Depolarize subset of interneurons (important species differences)	Suppress PP-DG LTP; ↑ SC-CA1 LTP; alter chloride transporter expression to regulate polarity of inhibition, use-dependent ↓IPSC	Dubrovsky et al. (2002), Lin et al. (2012), Owen et al. (2013), Raggenbass (2001), Tyzio et al. (2006) and Zaninetti and Raggenbass (2000)

Vasopressin	As above	AVPR1A, AVPR1B are major brain forms		Depolarize subset of interneurons	Conflicting reports showing ↑and ↓ LTP	Chafai et al. (2012), Chen et al. (1993), Dubrovsky et al. (2002), Hallbeck et al. (1999), Muhlethaler et al. (1984) and Ramanathan et al. (2012)
Cortistatin	Hippocampal interneurons, partially co-localized with somatostatin-positive cells	SST_{1-5}		↑Ih	↓ LTP	de Lecea and Sutcliffe (1996), de Lecea et al. (1997), Schweitzer et al. (2003) and Tallent et al. (2005)
Bombesin (neurmedin B and gastrin-releasing peptide)	Widely expressed	BB1 and BB2		Depolarize subset of interneurons (BB2)	↑EPSC amplitude (GRP)	Battey and Wada (1991), Dreifuss and Raggenbass (1986), Lee et al. (1999a) and Yang et al. (2017)
TRH	Widespread expression of hormone mRNA and receptors	TRHR	IP3 and PKC pathways	Hyperpolarization, regulation of various K^+ channels in CA1 pyramidal cells	↓PP-GC LTP, ↑Mossy fibre-CA3 LTP, ↓IPSPs	Deng et al. (2006), Ebihara and Akaike (1993), Ishihara et al. (1992), Manaker et al. (1985) and Stocca and Nistri (1996)
Melanocortin	ACTH and other related peptides released systemically	MC1R-MC5R			↑LTP (MC4R)	Shen et al. (2013)

Abbreviation: *ND* not determined

neurosteroids (Belelli and Lambert 2005), and various orphan and recently deorphanized receptors. Moreover, it is possible that other forms of neuromodulation may be brought about by less orthodox forms of signalling such as the proteolytic cleavage of protease activated receptors (Bushell et al. 2006; Gingrich et al. 2000). In addition to metabotropic receptor signalling, there are many additional modulators that act through direct orthosteric modulation of channels and receptors. One of the best characterized forms of such modulation is neurosteroids which are widely distributed and which produce an orthosteric modulation of the $GABA_A$ receptor. Whilst they do not overtly affect postsynaptic excitability, they exert a powerful potentiation of GABAergic transmission within hippocampal circuits (Belelli and Lambert 2005; Fester and Rune 2015).

Experimental Techniques

Most of the functional data concerning the action of neuromodulators on cellular and synaptic properties is obtained from electrophysiological experiments conducted in vitro either in brain slices experiments or using hippocampal neuronal cultures as described in earlier chapters. Classically this has been extracellular, intracellular (sharp) and more recently patch-clamp recordings. Clearly in vitro hippocampal preparations enable detailed scrutiny of the action of neuromodulators on active and passive intrinsic properties as well as synaptic transmission. They also permit detailed pharmacological investigation as drugs can be applied directly to the cells at a precise concentration. However, as mentioned earlier, optogenetic strategies are filling a niche as a more physiological means of activating specific synaptic neuromodulatory receptors with spatiotemporal precision (Lorincz and Adamantidis 2017; Spangler and Bruchas 2017), though this strategy still has some caveats and limitations, particularly at the synaptic level (Jackman et al. 2014). In contrast, the majority of in vivo recordings (multiunit recording or evoked field potentials) provide less mechanistic cellular/synaptic information, and pharmacological studies are limited by the difficulty in directing drugs to the site of action at a known concentration. Studies in vivo are typically limited to detecting changes in action potential discharge rate to when specific drugs/modulators are applied. However, in vivo studies are often valuable in determining the endogenous action of neuromodulators within the context of behavioural states. Moreover, in vivo recording can be used to relate the activity of neuromodulator sources (e.g. specific subcortical nuclei) with activity within hippocampal circuits. The introduction of the juxtacellular recording technique (Pinault 1996) has permitted the labelling of recorded neurons so that it is possible to relate the activity and modulation of recorded cells with their morphological characteristics and connectivity (Klausberger et al. 2003; Klausberger and Somogyi 2008). Moreover, patch-clamp recording from neurons in vivo (Ferster and Jagadeesh 1992; Jagadeesh et al. 1992) has undergone recent technical advances so that it is now not only possible to record from fine structures such as presynaptic boutons (Rancz et al. 2007; Geiger and Jonas 2000) but also to visualize and target

individual neurons in vivo (Kitamura et al. 2008; Pernia-Andrade and Jonas 2014). Finally, the introduction of optical (Deisseroth et al. 2006; Zhang et al. 2007) and genetic (Gong et al. 2007; Miyoshi and Fishell 2006) techniques to selectively excite or silence specific cells and circuits has already begun to address precise roles of specific cell types in behaviourally relevant network activity (Sohal et al. 2009; Lorincz and Adamantidis 2017). Finally, voltage-sensitive dyes are coming of age, which provide greater access to fine neuronal structures (Rowan and Christie 2017), and their use in conjunction with calcium indicators would prove particularly powerful. Aided by computational modelling, such correlated physiological, pharmacological, transgenic and morphological studies will be essential for the future understanding of how hippocampal cells and circuits are modulated at the whole organism level.

The Future

As has been apparent from the content this chapter, compared with previous chapters, the field of hippocampal neuromodulation is still at a nascent stage, with many unresolved questions remaining for the years ahead. Even for the most well-characterized classical modulators, there are still many unresolved questions, particularly in the context of how neuromodulators couple to specific channels across discrete neuronal subtypes. Questions also remain regarding the magnitude and time course of concentration transients reached by neuromodulatory receptors. The development of low-affinity antagonists for neuromodulatory receptors, in combination with optogenetic stimulation, would be particularly useful in this regard. The cellular and synaptic specificity of many neuromodulators demands molecular tools for systematic targeting of discrete afferents and cell types. Whilst one could argue that the increasing availability of these resources as one of the major technological developments over the last decade, research at the frontier in neuronal classification has shown that next-generation molecular tools are needed to differentiate between an increasing number of distinct cell types. Combining electrophysiological, genetic, molecular, pharmacological and anatomical techniques have revealed striking differences in cell type specificity of cholinergic neuromodulation (Cea-del Rio et al. 2010), which is likely to reveal cell type-specific differences with additional neuromodulators. The availability for genetic manipulation in transgenic animals is already proving very useful, especially in defining the importance of receptor subtypes in specific circuits where specific pharmacological tools may not be useful or available. The increasing use of Cre-loxP systems whereby specific modulator systems can be modified in a cell type-specific manner shows great potential over conventional pharmacological or global knockout strategies in resolving the precise functions of neuromodulators in specific cell types (i.e. Yi et al. 2014). At the level of neurochemically and anatomically defined hippocampal cell types, we are still far from gaining detailed knowledge of the repertoire of neuromodulator receptors expressed and localized.

Some progress is being made in this direction using techniques such as single-cell RT-PCR (Monyer and Markram 2004; Toledo-Rodriguez and Markram 2007) in which it is possible to fully characterize the expression profile of specific receptor classes in neurochemically defined cell types (Hillman et al. 2005; Cea-del Rio et al. 2010). With the availability of large-scale single-cell RNA sequencing, however, the goal of knowing all possible neuromodulatory receptor subtypes within a single-cell type may soon be achievable (Cadwell et al. 2017; Foldy et al. 2016; Zeisel et al. 2015). However, a single-cell transcriptomics approach does not allow the visualization and precise spatial localization of neuromodulatory receptors and their effectors with respect to cellular and synaptic domains (Triller and Choquet 2008). The widespread use of genetically encoded epitope-tagged receptors and channels would facilitate subcellular localization studies even if classic immunocytochemical approaches are not practical or possible.

Whilst the current chapter has focused on individual neuromodulator systems and receptors essentially in isolation, it is important to be mindful that a single neuromodulator can often induce secondary effects that are mediated through different neuromodulators. For example, mAChR activation can induce endocannabinoid release, resulting in CB1-dependent presynaptic depression of GABAergic transmission (Fukudome et al. 2004; Kim et al. 2002; Neu et al. 2007; Alger et al. 2014; Nagode et al. 2011). An additional complication is that multiple neuromodulators may be present in the in vivo milieu in any given point in time; substantial crosstalk across multiple neuromodulatory systems is probably a common occurrence, with both synergistic and antagonistic interactions possible. Behavioural states, rather than discrete neuromodulatory systems turning on and off, are probably comprised of alterations of many different neuromodulatory systems that occur across a broad range of activity levels. At the level of the postsynaptic cell, the dimerization and oligomerization of different G-protein-coupled receptors (Milligan 2007) and neuromodulatory channels (van Hooft et al. 1998) might create novel interactions between different neuromodulators. These interactions and their modulation in hippocampal cells and circuits remain to be fully explored.

Finally, the synaptic and cellular architecture places important spatial constraints on the physiological functions of neuromodulators. Experiments in which receptors are activated exogenously will yield very different results from studies in which endogenous transmitter is released in a naturalistic fashion from endogenous sources within spatially restricted microdomains. The physiological significance of neuromodulation will be greatly assisted by understanding the in vivo activity of neuromodulatory neurons during learning behaviours, short-term plasticity of neurotransmitter release, neurotransmitter receptor kinetics, brain slice preparations that preserve neuromodulatory pathways (Manseau et al. 2008; Widmer et al. 2006) and new molecular or transgenic strategies to optically target neuromodulatory centres or afferents (Deisseroth et al. 2006; Zhang et al. 2007; Lorincz and Adamantidis 2017). It is only by adopting a range of these approaches that it will be possible to fully understand the action of neuromodulators on hippocampal circuitry.

References

Abbracchio MP, Burnstock G, Verkhratsky A, Zimmermann H (2009) Purinergic signalling in the nervous system: an overview. Trends Neurosci 32(1):19–29. https://doi.org/10.1016/j.tins.2008.10.001

Acker CD, Yan P, Loew LM (2011) Single-voxel recording of voltage transients in dendritic spines. Biophys J 101(2):L11–L13. https://doi.org/10.1016/j.bpj.2011.06.021

Acsady L, Arabadzisz D, Freund TF (1996a) Correlated morphological and neurochemical features identify different subsets of vasoactive intestinal polypeptide-immunoreactive interneurons in rat hippocampus. Neuroscience 73(2):299–315

Acsady L, Arabadzisz D, Katona I, Freund TF (1996b) Topographic distribution of dorsal and median raphe neurons with hippocampal, septal and dual projection. Acta Biol Hung 47(1-4):9–19

Alger BE, Nagode DA, Tang AH (2014) Muscarinic cholinergic receptors modulate inhibitory synaptic rhythms in hippocampus and neocortex. Front Synaptic Neurosci 6:18. https://doi.org/10.3389/fnsyn.2014.00018

Alkondon M, Pereira EF, Albuquerque EX (1998) Alpha-bungarotoxin- and methyllycaconitine-sensitive nicotinic receptors mediate fast synaptic transmission in interneurons of rat hippocampal slices. Brain Res 810(1-2):257–263. https://doi.org/10.1016/s0006-8993(98)00880-4

Allen TG, Abogadie FC, Brown DA (2006) Simultaneous release of glutamate and acetylcholine from single magnocellular "cholinergic" basal forebrain neurons. J Neurosci 26(5):1588–1595. https://doi.org/10.1523/JNEUROSCI.3979-05.2006

Alvarez EO (2009) The role of histamine on cognition. Behav Brain Res 199(2):183–189. https://doi.org/10.1016/j.bbr.2008.12.010

Alzheimer C, Rohrenbeck J, ten Bruggencate G (1991) Adenosine depresses induction of LTP at the mossy fiber-CA3 synapse in vitro. Brain Res 543(1):163–165

Ambree O, Buschert J, Zhang W, Arolt V, Dere E, Zlomuzica A (2014) Impaired spatial learning and reduced adult hippocampal neurogenesis in histamine H1-receptor knockout mice. Eur Neuropsychopharmacol 24(8):1394–1404. https://doi.org/10.1016/j.euroneuro.2014.04.006

Amilhon B, Lepicard E, Renoir T, Mongeau R, Popa D, Poirel O, Miot S, Gras C, Gardier AM, Gallego J, Hamon M, Lanfumey L, Gasnier B, Giros B, El Mestikawy S (2010) VGLUT3 (vesicular glutamate transporter type 3) contribution to the regulation of serotonergic transmission and anxiety. J Neurosci 30(6):2198–2210. https://doi.org/10.1523/JNEUROSCI.5196-09.2010

Andersson R, Johnston A, Fisahn A (2012a) Dopamine D4 receptor activation increases hippocampal gamma oscillations by enhancing synchronization of fast-spiking interneurons. PLoS One 7(7):e40906. https://doi.org/10.1371/journal.pone.0040906

Andersson RH, Johnston A, Herman PA, Winzer-Serhan UH, Karavanova I, Vullhorst D, Fisahn A, Buonanno A (2012b) Neuregulin and dopamine modulation of hippocampal gamma oscillations is dependent on dopamine D4 receptors. Proc Natl Acad Sci U S A 109(32):13118–13123. https://doi.org/10.1073/pnas.1201011109

Andersson R, Galter D, Papadia D, Fisahn A (2017) Histamine induces KCNQ channel-dependent gamma oscillations in rat hippocampus via activation of the H1 receptor. Neuropharmacology 118:13–25. https://doi.org/10.1016/j.neuropharm.2017.03.003

Andrade R (1998) Regulation of membrane excitability in the central nervous system by serotonin receptor subtypes. Ann N Y Acad Sci 861:190–203

Andrade R, Chaput Y (1991) 5-Hydroxytryptamine4-like receptors mediate the slow excitatory response to serotonin in the rat hippocampus. J Pharmacol Exp Ther 257(3):930–937

Andrade R, Nicoll RA (1987) Pharmacologically distinct actions of serotonin on single pyramidal neurones of the rat hippocampus recorded in vitro. J Physiol 394:99–124

Andrade R, Malenka RC, Nicoll RA (1986) A G protein couples serotonin and GABAB receptors to the same channels in hippocampus. Science 234(4781):1261–1265

Andrade R, Foehring RC, Tzingounis AV (2012) The calcium-activated slow AHP: cutting through the Gordian knot. Front Cell Neurosci 6:47. https://doi.org/10.3389/fncel.2012.00047

Andreetta F, Carboni L, Grafton G, Jeggo R, Whyment AD, van den Top M, Hoyer D, Spanswick D, Barnes NM (2016) Hippocampal 5-HT7 receptors signal phosphorylation of the GluA1 subunit to facilitate AMPA receptor mediated-neurotransmission in vitro and in vivo. Br J Pharmacol 173(9):1438–1451. https://doi.org/10.1111/bph.13432

Arancio O, Kiebler M, Lee CJ, Lev-Ram V, Tsien RY, Kandel ER, Hawkins RD (1996) Nitric oxide acts directly in the presynaptic neuron to produce long-term potentiation in cultured hippocampal neurons. Cell 87(6):1025–1035

Armstrong C, Soltesz I (2012) Basket cell dichotomy in microcircuit function. J Physiol 590(4):683–694. https://doi.org/10.1113/jphysiol.2011.223669

Armstrong C, Krook-Magnuson E, Soltesz I (2012) Neurogliaform and Ivy Cells: A Major Family of nNOS Expressing GABAergic Neurons. Front Neural Circuits 6:23. https://doi.org/10.3389/fncir.2012.00023

Arrang JM, Garbarg M, Schwartz JC (1983) Auto-inhibition of brain histamine release mediated by a novel class (H3) of histamine receptor. Nature 302(5911):832–837

Arrigoni E, Rosenberg PA (2006) Nitric oxide-induced adenosine inhibition of hippocampal synaptic transmission depends on adenosine kinase inhibition and is cyclic GMP independent. Eur J Neurosci 24(9):2471–2480

Atzori M, Lau D, Tansey EP, Chow A, Ozaita A, Rudy B, McBain CJ (2000) H2 histamine receptor-phosphorylation of Kv3.2 modulates interneuron fast spiking. Nat Neurosci 3(8):791–798. https://doi.org/10.1038/77693

Auerbach JM, Segal M (1994) A novel cholinergic induction of long-term potentiation in rat hippocampus. J Neurophysiol 72(4):2034–2040. https://doi.org/10.1152/jn.1994.72.4.2034

Auerbach JM, Segal M (1996) Muscarinic receptors mediating depression and long-term potentiation in rat hippocampus. J Physiol 492(Pt 2):479–493

Aznar S, Qian Z, Shah R, Rahbek B, Knudsen GM (2003) The 5-HT1A serotonin receptor is located on calbindin- and parvalbumin-containing neurons in the rat brain. Brain Res 959(1):58–67

Aznavour N, Mechawar N, Descarries L (2002) Comparative analysis of cholinergic innervation in the dorsal hippocampus of adult mouse and rat: a quantitative immunocytochemical study. Hippocampus 12(2):206–217. https://doi.org/10.1002/hipo.1108

Aznavour N, Watkins KC, Descarries L (2005) Postnatal development of the cholinergic innervation in the dorsal hippocampus of rat: Quantitative light and electron microscopic immunocytochemical study. J Comp Neurol 486(1):61–75. https://doi.org/10.1002/cne.20501

Bacci A, Huguenard JR, Prince DA (2004) Long-lasting self-inhibition of neocortical interneurons mediated by endocannabinoids. Nature 431(7006):312–316

Bacci A, Huguenard JR, Prince DA (2005) Modulation of neocortical interneurons: extrinsic influences and exercises in self-control. Trends Neurosci 28(11):602–610. https://doi.org/10.1016/j.tins.2005.08.007

Bacciottini L, Passani MB, Giovannelli L, Cangioli I, Mannaioni PF, Schunack W, Blandina P (2002) Endogenous histamine in the medial septum-diagonal band complex increases the release of acetylcholine from the hippocampus: a dual-probe microdialysis study in the freely moving rat. Eur J Neurosci 15(10):1669–1680

Bacon WL, Beck SG (2000) 5-Hydroxytryptamine(7) receptor activation decreases slow after-hyperpolarization amplitude in CA3 hippocampal pyramidal cells. J Pharmacol Exp Ther 294(2):672–679

Balazsfi DG, Zelena D, Farkas L, Demeter K, Barna I, Cserep C, Takacs VT, Nyiri G, Goloncser F, Sperlagh B, Freund TF, Haller J (2017) Median raphe region stimulation alone generates remote, but not recent fear memory traces. PLoS One 12(7):e0181264. https://doi.org/10.1371/journal.pone.0181264

Baraban SC, Tallent MK (2004) Interneuron Diversity series: interneuronal neuropeptides – endogenous regulators of neuronal excitability. Trends Neurosci 27(3):135–142

Baratta MV, Lamp T, Tallent MK (2002) Somatostatin depresses long-term potentiation and Ca2+ signaling in mouse dentate gyrus. J Neurophysiol 88(6):3078–3086. https://doi.org/10.1152/jn.00398.2002

Barbin G, Garbarg M, Schwartz JC, Storm-Mathisen J (1976) Histamine synthesizing afferents to the hippocampal region. J Neurochem 26(2):259–263
Barnes NM, Sharp T (1999) A review of central 5-HT receptors and their function. Neuropharmacology 38(8):1083–1152
Bartos M, Vida I, Jonas P (2007) Synaptic mechanisms of synchronized gamma oscillations in inhibitory interneuron networks. Nat Rev Neurosci 8(1):45–56. https://doi.org/10.1038/nrn2044
Baskys A, Niesen CE, Davies MF, Carlen PL (1989) Modulatory actions of serotonin on ionic conductances of hippocampal dentate granule cells. Neuroscience 29(2):443–451
Battey J, Wada E (1991) Two distinct receptor subtypes for mammalian bombesin-like peptides. Trends Neurosci 14(12):524–528
Bauer EP (2015) Serotonin in fear conditioning processes. Behav Brain Res 277:68–77. https://doi.org/10.1016/j.bbr.2014.07.028
Bazargani N, Attwell D (2017) Amines, astrocytes, and arousal. Neuron 94(2):228–231. https://doi.org/10.1016/j.neuron.2017.03.035
Beck SG, Choi KC (1991) 5-Hydroxytryptamine hyperpolarizes CA3 hippocampal pyramidal cells through an increase in potassium conductance. Neurosci Lett 133(1):93–96
Beck SG, Choi KC, List TJ (1992) Comparison of 5-hydroxytryptamine1A-mediated hyperpolarization in CA1 and CA3 hippocampal pyramidal cells. J Pharmacol Exp Ther 263(1):350–359
Behr J, Empson RM, Schmitz D, Gloveli T, Heinemann U (1997) Effects of serotonin on synaptic and intrinsic properties of rat subicular neurons in vitro. Brain Res 773(1–2):217–222
Behr J, Gloveli T, Schmitz D, Heinemann U (2000) Dopamine depresses excitatory synaptic transmission onto rat subicular neurons via presynaptic D1-like dopamine receptors. J Neurophysiol 84(1):112–119. https://doi.org/10.1152/jn.2000.84.1.112
Behrends JC, ten Bruggencate G (1993) Cholinergic modulation of synaptic inhibition in the guinea pig hippocampus in vitro: excitation of GABAergic interneurons and inhibition of GABA-release. J Neurophysiol 69(2):626–629. https://doi.org/10.1152/jn.1993.69.2.626
Bekkers JM (1993) Enhancement by histamine of NMDA-mediated synaptic transmission in the hippocampus. Science 261(5117):104–106
Belelli D, Lambert JJ (2005) Neurosteroids: endogenous regulators of the GABA(A) receptor. Nat Rev Neurosci 6(7):565–575
Bell KA, Shim H, Chen CK, McQuiston AR (2011) Nicotinic excitatory postsynaptic potentials in hippocampal CA1 interneurons are predominantly mediated by nicotinic receptors that contain alpha4 and beta2 subunits. Neuropharmacology 61(8):1379–1388. https://doi.org/10.1016/j.neuropharm.2011.08.024
Bell LA, Bell KA, McQuiston AR (2013) Synaptic muscarinic response types in hippocampal CA1 interneurons depend on different levels of presynaptic activity and different muscarinic receptor subtypes. Neuropharmacology 73:160–173. https://doi.org/10.1016/j.neuropharm.2013.05.026
Bell LA, Bell KA, McQuiston AR (2015a) Acetylcholine release in mouse hippocampal CA1 preferentially activates inhibitory-selective interneurons via alpha4beta2* nicotinic receptor activation. Front Cell Neurosci 9:115. https://doi.org/10.3389/fncel.2015.00115
Bell LA, Bell KA, McQuiston AR (2015b) Activation of muscarinic receptors by ACh release in hippocampal CA1 depolarizes VIP but has varying effects on parvalbumin-expressing basket cells. J Physiol 593(1):197–215. https://doi.org/10.1113/jphysiol.2014.277814
Benardo LS, Prince DA (1982a) Cholinergic excitation of mammalian hippocampal pyramidal cells. Brain Res 249(2):315–331. https://doi.org/10.1016/0006-8993(82)90066-x
Benardo LS, Prince DA (1982b) Cholinergic pharmacology of mammalian hippocampal pyramidal cells. Neuroscience 7(7):1703–1712. https://doi.org/10.1016/0306-4522(82)90028-8
Benardo LS, Prince DA (1982c) Dopamine action on hippocampal pyramidal cells. J Neurosci 2(4):415–423
Benardo LS, Prince DA (1982d) Dopamine modulates a Ca2+-activated potassium conductance in mammalian hippocampal pyramidal cells. Nature 297(5861):76–79

Benardo LS, Prince DA (1982e) Ionic mechanisms of cholinergic excitation in mammalian hippocampal pyramidal cells. Brain Res 249(2):333–344. https://doi.org/10.1016/0006-8993(82)90067-1

Bergles DE, Doze VA, Madison DV, Smith SJ (1996) Excitatory actions of norepinephrine on multiple classes of hippocampal CA1 interneurons. J Neurosci 16(2):572–585

Bergson C, Mrzljak L, Smiley JF, Pappy M, Levenson R, Goldman-Rakic PS (1995) Regional, cellular, and subcellular variations in the distribution of D1 and D5 dopamine receptors in primate brain. J Neurosci 15(12):7821–7836

Bernardi G, Calabresi P, Mercuri N, Stanzione P (1984) Effect of dopamine on the threshold of the voltage-dependent ionic channels in the rat brain. Ann Ist Super Sanita 20(1):1–4

Bickmeyer U, Heine M, Manzke T, Richter DW (2002) Differential modulation of I(h) by 5-HT receptors in mouse CA1 hippocampal neurons. Eur J Neurosci 16(2):209–218

Bijak M (1989) Antidepressant drugs potentiate the alpha 1-adrenoceptor effect in hippocampal slices. Eur J Pharmacol 166(2):183–191

Bijak M, Misgeld U (1995) Adrenergic modulation of hilar neuron activity and granule cell inhibition in the guinea-pig hippocampal slice. Neuroscience 67(3):541–550

Blackshaw S, Eliasson MJ, Sawa A, Watkins CC, Krug D, Gupta A, Arai T, Ferrante RJ, Snyder SH (2003) Species, strain and developmental variations in hippocampal neuronal and endothelial nitric oxide synthase clarify discrepancies in nitric oxide-dependent synaptic plasticity. Neuroscience 119(4):979–990

Blandina P, Efoudebe M, Cenni G, Mannaioni P, Passani MB (2004) Acetylcholine, histamine, and cognition: two sides of the same coin. Learn Mem 11(1):1–8. https://doi.org/10.1101/lm.68004

Blusztajn JK, Rinnofner J (2016) Intrinsic cholinergic neurons in the hippocampus: fact or artifact? Front Synaptic Neurosci 8:6. https://doi.org/10.3389/fnsyn.2016.00006

Boden PR, Hill RG (1988) Effects of cholecystokinin and pentagastrin on rat hippocampal neurones maintained in vitro. Neuropeptides 12(2):95–103

Boehm S (1999) Presynaptic alpha2-adrenoceptors control excitatory, but not inhibitory, transmission at rat hippocampal synapses. J Physiol 519(Pt 2):439–449

Bohm C, Pangalos M, Schmitz D, Winterer J (2015) Serotonin attenuates feedback excitation onto O-LM interneurons. Cereb Cortex 25(11):4572–4583. https://doi.org/10.1093/cercor/bhv098

Bohme GA, Stutzmann JM, Blanchard JC (1988) Excitatory effects of cholecystokinin in rat hippocampus: pharmacological response compatible with 'central'- or B-type CCK receptors. Brain Res 451(1–2):309–318

Bon CL, Garthwaite J (2001) Exogenous nitric oxide causes potentiation of hippocampal synaptic transmission during low-frequency stimulation via the endogenous nitric oxide-cGMP pathway. Eur J Neurosci 14(4):585–594

Bonaventure P, Nepomuceno D, Kwok A, Chai W, Langlois X, Hen R, Stark K, Carruthers N, Lovenberg TW (2002) Reconsideration of 5-hydroxytryptamine (5-HT)(7) receptor distribution using [(3)H]5-carboxamidotryptamine and [(3)H]8-hydroxy-2-(di-n-propylamino)tetraline: analysis in brain of 5-HT(1A) knockout and 5-HT(1A/1B) double-knockout mice. J Pharmacol Exp Ther 302(1):240–248

Booker SA, Gross A, Althof D, Shigemoto R, Bettler B, Frotscher M, Hearing M, Wickman K, Watanabe M, Kulik A, Vida I (2013) Differential GABAB-receptor-mediated effects in perisomatic- and dendrite-targeting parvalbumin interneurons. J Neurosci 33(18):7961–7974. https://doi.org/10.1523/JNEUROSCI.1186-12.2013

Booker SA, Loreth D, Gee AL, Watanabe M, Kind PC, Wyllie DJA, Kulik A, Vida I (2018) Postsynaptic GABABRs inhibit L-type calcium channels and abolish long-term potentiation in hippocampal somatostatin interneurons. Cell Rep 22(1):36–43. https://doi.org/10.1016/j.celrep.2017.12.021

Borhegyi Z, Leranth C (1997) Substance P innervation of the rat hippocampal formation. J Comp Neurol 384(1):41–58

Boschert U, Amara DA, Segu L, Hen R (1994) The mouse 5-hydroxytryptamine1B receptor is localized predominantly on axon terminals. Neuroscience 58(1):167–182

Boulton CL, Irving AJ, Southam E, Potier B, Garthwaite J, Collingridge GL (1994) The nitric oxide – cyclic GMP pathway and synaptic depression in rat hippocampal slices. Eur J Neurosci 6(10):1528–1535

Bouthenet ML, Ruat M, Sales N, Garbarg M, Schwartz JC (1988) A detailed mapping of histamine H1-receptors in guinea-pig central nervous system established by autoradiography with [125I]iodobolpyramine. Neuroscience 26(2):553–600

Bowser DN, Khakh BS (2004) ATP excites interneurons and astrocytes to increase synaptic inhibition in neuronal networks. J Neurosci 24(39):8606–8620. https://doi.org/10.1523/JNEUROSCI.2660-04.2004

Brady LJ, Bartley AF, Li Q, McMeekin LJ, Hablitz JJ, Cowell RM, Dobrunz LE (2016) Transcriptional dysregulation causes altered modulation of inhibition by haloperidol. Neuropharmacology 111:304–313. https://doi.org/10.1016/j.neuropharm.2016.07.034

Brazhnik ES, Fox SE (1999) Action potentials and relations to the theta rhythm of medial septal neurons in vivo. Exp Brain Res 127(3):244–258

Brown DA, Adams PR (1980) Muscarinic suppression of a novel voltage-sensitive K+ current in a vertebrate neurone. Nature 283(5748):673–676

Brown RE, Haas HL (1999) On the mechanism of histaminergic inhibition of glutamate release in the rat dentate gyrus. J Physiol 515(Pt 3):777–786

Brown RE, Fedorov NB, Haas HL, Reymann KG (1995) Histaminergic modulation of synaptic plasticity in area CA1 of rat hippocampal slices. Neuropharmacology 34(2):181–190

Brown RE, Stevens DR, Haas HL (2001) The physiology of brain histamine. Prog Neurobiol 63(6):637–672

Buckley NJ, Bonner TI, Brann MR (1988) Localization of a family of muscarinic receptor mRNAs in rat brain. J Neurosci 8(12):4646–4652

Buhler AV, Dunwiddie TV (2001) Regulation of the activity of hippocampal stratum oriens interneurons by alpha7 nicotinic acetylcholine receptors. Neuroscience 106(1):55–67

Burban A, Faucard R, Armand V, Bayard C, Vorobjev V, Arrang JM (2010) Histamine potentiates N-methyl-D-aspartate receptors by interacting with an allosteric site distinct from the polyamine binding site. J Pharmacol Exp Ther 332(3):912–921. https://doi.org/10.1124/jpet.109.158543

Burke SP, Nadler JV (1988) Regulation of glutamate and aspartate release from slices of the hippocampal CA1 area: effects of adenosine and baclofen. J Neurochem 51(5):1541–1551

Bushell TJ, Plevin R, Cobb S, Irving AJ (2006) Characterization of proteinase-activated receptor 2 signalling and expression in rat hippocampal neurons and astrocytes. Neuropharmacology 50(6):714–725

Cadwell CR, Scala F, Li S, Livrizzi G, Shen S, Sandberg R, Jiang X, Tolias AS (2017) Multimodal profiling of single-cell morphology, electrophysiology, and gene expression using patch-seq. Nat Protoc 12(12):2531–2553

Cai X, Kallarackal AJ, Kvarta MD, Goluskin S, Gaylor K, Bailey AM, Lee HK, Huganir RL, Thompson SM (2013) Local potentiation of excitatory synapses by serotonin and its alteration in rodent models of depression. Nat Neurosci 16(4):464–472. https://doi.org/10.1038/nn.3355

Caputi A, Melzer S, Michael M, Monyer H (2013) The long and short of GABAergic neurons. Curr Opin Neurobiol 23(2):179–186. https://doi.org/10.1016/j.conb.2013.01.021

Castillo PE, Younts TJ, Chavez AE, Hashimotodani Y (2012) Endocannabinoid signaling and synaptic function. Neuron 76(1):70–81. https://doi.org/10.1016/j.neuron.2012.09.020

Cea-del Rio CA, Lawrence JJ, Tricoire L, Erdelyi F, Szabo G, McBain CJ (2010) M3 muscarinic acetylcholine receptor expression confers differential cholinergic modulation to neurochemically distinct hippocampal basket cell subtypes. J Neurosci 30(17):6011–6024. https://doi.org/10.1523/JNEUROSCI.5040-09.2010

Cea-del Rio CA, Lawrence JJ, Erdelyi F, Szabo G, McBain CJ (2011) Cholinergic modulation amplifies the intrinsic oscillatory properties of CA1 hippocampal cholecystokinin-positive interneurons. J Physiol 589(Pt 3):609–627. https://doi.org/10.1113/jphysiol.2010.199422

Cea-del Rio CA, McBain CJ, Pelkey KA (2012) An update on cholinergic regulation of cholecystokinin-expressing basket cells. J Physiol 590(4):695–702. https://doi.org/10.1113/jphysiol.2011.225342

Chafai M, Corbani M, Guillon G, Desarmenien MG (2012) Vasopressin inhibits LTP in the CA2 mouse hippocampal area. PLoS One 7(12):e49708. https://doi.org/10.1371/journal.pone.0049708

Chalmers DT, Watson SJ (1991) Comparative anatomical distribution of 5-HT1A receptor mRNA and 5-HT1A binding in rat brain – a combined in situ hybridisation/in vitro receptor autoradiographic study. Brain Res 561(1):51–60

Chameau P, van Hooft JA (2006) Serotonin 5-HT(3) receptors in the central nervous system. Cell Tissue Res 326(2):573–581. https://doi.org/10.1007/s00441-006-0255-8

Chang Q, Fischbach GD (2006) An acute effect of neuregulin 1 beta to suppress alpha 7-containing nicotinic acetylcholine receptors in hippocampal interneurons. J Neurosci 26(44):11295–11303. https://doi.org/10.1523/JNEUROSCI.1794-06.2006

Chang M, Saito H, Abe K (1998) Histamine H3 receptor-mediated inhibition of excitatory synaptic transmission in the rat dentate gyrus in vivo. Jpn J Pharmacol 77(3):251–255

Chapman CA, Lacaille JC (1999a) Cholinergic induction of theta-frequency oscillations in hippocampal inhibitory interneurons and pacing of pyramidal cell firing. J Neurosci 19(19):8637–8645

Chapman CA, Lacaille JC (1999b) Intrinsic theta-frequency membrane potential oscillations in hippocampal CA1 interneurons of stratum lacunosum-moleculare. J Neurophysiol 81(3):1296–1307. https://doi.org/10.1152/jn.1999.81.3.1296

Chen C, Diaz Brinton RD, Shors TJ, Thompson RF (1993) Vasopressin induction of long-lasting potentiation of synaptic transmission in the dentate gyrus. Hippocampus 3(2):193–203

Chen J, Tan Z, Zeng L, Zhang X, He Y, Gao W, Wu X, Li Y, Bu B, Wang W, Duan S (2013) Heterosynaptic long-term depression mediated by ATP released from astrocytes. Glia 61(2):178–191. https://doi.org/10.1002/glia.22425

Chevaleyre V, Castillo PE (2003) Heterosynaptic LTD of hippocampal GABAergic synapses: a novel role of endocannabinoids in regulating excitability. Neuron 38(3):461–472

Chiang PH, Yeh WC, Lee CT, Weng JY, Huang YY, Lien CC (2010) M(1)-like muscarinic acetylcholine receptors regulate fast-spiking interneuron excitability in rat dentate gyrus. Neuroscience 169(1):39–51. https://doi.org/10.1016/j.neuroscience.2010.04.051

Chittajallu R, Craig MT, McFarland A, Yuan X, Gerfen S, Tricoire L, Erkkila B, Barron SC, Lopez CM, Liang BJ, Jeffries BW, Pelkey KA, McBain CJ (2013) Dual origins of functionally distinct O-LM interneurons revealed by differential 5-HT(3A)R expression. Nat Neurosci 16(11):1598–1607. https://doi.org/10.1038/nn.3538

Choi IS, Cho JH, Kim JT, Park EJ, Lee MG, Shin HI, Choi BJ, Jang IS (2007) Serotoninergic modulation of GABAergic synaptic transmission in developing rat CA3 pyramidal neurons. J Neurochem 103(6):2342–2353. https://doi.org/10.1111/j.1471-4159.2007.04945.x

Cilz NI, Lei S (2017) Histamine facilitates GABAergic transmission in the rat entorhinal cortex: roles of H1 and H2 receptors, Na(+) -permeable cation channels, and inward rectifier K(+) channels. Hippocampus 27(5):613–631. https://doi.org/10.1002/hipo.22718

Cilz NI, Kurada L, Hu B, Lei S (2014) Dopaminergic modulation of GABAergic transmission in the entorhinal cortex: concerted roles of alpha1 adrenoreceptors, inward rectifier K(+), and T-type Ca(2)(+) channels. Cereb Cortex 24(12):3195–3208. https://doi.org/10.1093/cercor/bht177

Cobb SR, Davies CH (2005) Cholinergic modulation of hippocampal cells and circuits. J Physiol 562(Pt 1):81–88. https://doi.org/10.1113/jphysiol.2004.076539

Cole AE, Nicoll RA (1983) Acetylcholine mediates a slow synaptic potential in hippocampal pyramidal cells. Science 221(4617):1299–1301

Cole AE, Nicoll RA (1984a) Characterization of a slow cholinergic post-synaptic potential recorded in vitro from rat hippocampal pyramidal cells. J Physiol 352:173–188

Cole AE, Nicoll RA (1984b) The pharmacology of cholinergic excitatory responses in hippocampal pyramidal cells. Brain Res 305(2):283–290

Colino A, Halliwell JV (1987) Differential modulation of three separate K-conductances in hippocampal CA1 neurons by serotonin. Nature 328(6125):73–77. https://doi.org/10.1038/328073a0

Colino A, Halliwell JV (1993) Carbachol potentiates Q current and activates a calcium-dependent non-specific conductance in rat hippocampus in vitro. Eur J Neurosci 5(9):1198–1209

Compan V, Zhou M, Grailhe R, Gazzara RA, Martin R, Gingrich J, Dumuis A, Brunner D, Bockaert J, Hen R (2004) Attenuated response to stress and novelty and hypersensitivity to seizures in 5-HT4 receptor knock-out mice. J Neurosci 24(2):412–419. https://doi.org/10.1523/JNEUROSCI.2806-03.2004

Cornea-Hebert V, Riad M, Wu C, Singh SK, Descarries L (1999) Cellular and subcellular distribution of the serotonin 5-HT2A receptor in the central nervous system of adult rat. J Comp Neurol 409(2):187–209

Corradetti R, Ballerini L, Pugliese AM, Pepeu G (1992) Serotonin blocks the long-term potentiation induced by primed burst stimulation in the CA1 region of rat hippocampal slices. Neuroscience 46(3):511–518

Corradetti R, Laaris N, Hanoun N, Laporte AM, Le Poul E, Hamon M, Lanfumey L (1998) Antagonist properties of (-)-pindolol and WAY 100635 at somatodendritic and postsynaptic 5-HT1A receptors in the rat brain. Br J Pharmacol 123(3):449–462. https://doi.org/10.1038/sj.bjp.0701632

Costa L, Trovato C, Musumeci SA, Catania MV, Ciranna L (2012) 5-HT(1A) and 5-HT(7) receptors differently modulate AMPA receptor-mediated hippocampal synaptic transmission. Hippocampus 22(4):790–801. https://doi.org/10.1002/hipo.20940

Couey JJ, Meredith RM, Spijker S, Poorthuis RB, Smit AB, Brussaard AB, Mansvelder HD (2007) Distributed network actions by nicotine increase the threshold for spike-timing-dependent plasticity in prefrontal cortex. Neuron 54(1):73–87. https://doi.org/10.1016/j.neuron.2007.03.006

Cox DJ, Racca C, LeBeau FE (2008) Beta-adrenergic receptors are differentially expressed in distinct interneuron subtypes in the rat hippocampus. J Comp Neurol 509(6):551–565. https://doi.org/10.1002/cne.21758

Craig MT, McBain CJ (2015) Fast gamma oscillations are generated intrinsically in CA1 without the involvement of fast-spiking basket cells. J Neurosci 35(8):3616–3624. https://doi.org/10.1523/JNEUROSCI.4166-14.2015

Cunha RA, Milusheva E, Vizi ES, Ribeiro JA, Sebastiao AM (1994) Excitatory and inhibitory effects of A1 and A2A adenosine receptor activation on the electrically evoked [3H]acetylcholine release from different areas of the rat hippocampus. J Neurochem 63(1):207–214

Cunha-Reis D, Sebastiao AM, Wirkner K, Illes P, Ribeiro JA (2004) VIP enhances both pre- and postsynaptic GABAergic transmission to hippocampal interneurons leading to increased excitatory synaptic transmission to CA1 pyramidal cells. Br J Pharmacol 143(6):733–744. https://doi.org/10.1038/sj.bjp.0705989 sj.bjp.0705989 [pii]

Cunha-Reis D, Ribeiro JA, Sebastiao AM (2005) VIP enhances synaptic transmission to hippocampal CA1 pyramidal cells through activation of both VPAC1 and VPAC2 receptors. Brain Res 1049(1):52–60. https://doi.org/10.1016/j.brainres.2005.04.077 S0006-8993(05)00685-2 [pii]

Dai H, Kaneko K, Kato H, Fujii S, Jing Y, Xu A, Sakurai E, Kato M, Okamura N, Kuramasu A, Yanai K (2007) Selective cognitive dysfunction in mice lacking histamine H1 and H2 receptors. Neurosci Res 57(2):306–313. https://doi.org/10.1016/j.neures.2006.10.020

Dale E, Pehrson AL, Jeyarajah T, Li Y, Leiser SC, Smagin G, Olsen CK, Sanchez C (2016) Effects of serotonin in the hippocampus: how SSRIs and multimodal antidepressants might regulate pyramidal cell function. CNS Spectr 21(2):143–161. https://doi.org/10.1017/S1092852915000425

Dale E, Grunnet M, Pehrson AL, Frederiksen K, Larsen PH, Nielsen J, Stensbol TB, Ebert B, Yin H, Lu D, Liu H, Jensen TN, Yang CR, Sanchez C (2017) The multimodal antidepressant vortioxetine may facilitate pyramidal cell firing by inhibition of 5-HT3 receptor expressing interneurons: an in vitro study in rat hippocampus slices. Brain Res. https://doi.org/10.1016/j.brainres.2017.12.025

Dannenberg H, Pabst M, Braganza O, Schoch S, Niediek J, Bayraktar M, Mormann F, Beck H (2015) Synergy of direct and indirect cholinergic septo-hippocampal pathways coordinates firing in hippocampal networks. J Neurosci 35(22):8394–8410. https://doi.org/10.1523/JNEUROSCI.4460-14.2015

Dannenberg H, Hinman JR, Hasselmo ME (2016) Potential roles of cholinergic modulation in the neural coding of location and movement speed. J Physiol Paris 110(1-2):52–64. https://doi.org/10.1016/j.jphysparis.2016.09.002

Dannenberg H, Young K, Hasselmo M (2017) Modulation of hippocampal circuits by muscarinic and nicotinic receptors. Front Neural Circuits 11:102. https://doi.org/10.3389/fncir.2017.00102

Dasari S, Gulledge AT (2011) M1 and M4 receptors modulate hippocampal pyramidal neurons. J Neurophysiol 105(2):779–792. https://doi.org/10.1152/jn.00686.2010

Dasari S, Hill C, Gulledge AT (2017) A unifying hypothesis for M1 muscarinic receptor signalling in pyramidal neurons. J Physiol 595(5):1711–1723. https://doi.org/10.1113/JP273627

Davies S, Kohler C (1985) The substance P innervation of the rat hippocampal region. Anat Embryol (Berl) 173(1):45–52

Daw MI, Tricoire L, Erdelyi F, Szabo G, McBain CJ (2009) Asynchronous transmitter release from cholecystokinin-containing inhibitory interneurons is widespread and target-cell independent. J Neurosci 29(36):11112–11122. https://doi.org/10.1523/JNEUROSCI.5760-08.2009

Day HE, Campeau S, Watson SJ Jr, Akil H (1997) Distribution of alpha 1a-, alpha 1b- and alpha 1d-adrenergic receptor mRNA in the rat brain and spinal cord. J Chem Neuroanat 13(2):115–139

de Lecea L, Sutcliffe JG (1996) Peptides, sleep and cortistatin. Mol Psychiatry 1(5):349–351

de Lecea L, del Rio JA, Criado JR, Alcantara S, Morales M, Danielson PE, Henriksen SJ, Soriano E, Sutcliffe JG (1997) Cortistatin is expressed in a distinct subset of cortical interneurons. J Neurosci 17(15):5868–5880

Degro CE, Kulik A, Booker SA, Vida I (2015) Compartmental distribution of GABAB receptor-mediated currents along the somatodendritic axis of hippocampal principal cells. Front Synaptic Neurosci 7:6. https://doi.org/10.3389/fnsyn.2015.00006

Deisseroth K, Feng G, Majewska AK, Miesenbock G, Ting A, Schnitzer MJ (2006) Next-generation optical technologies for illuminating genetically targeted brain circuits. J Neurosci 26(41):10380–10386. https://doi.org/10.1523/JNEUROSCI.3863-06.2006 26/41/10380 [pii]

Deller T, Katona I, Cozzari C, Frotscher M, Freund TF (1999) Cholinergic innervation of mossy cells in the rat fascia dentata. Hippocampus 9(3):314–320. https://doi.org/10.1002/(SICI)1098-1063(1999)9:3<314::AID-HIPO10>3.0.CO;2-7

Deng PY, Lei S (2008) Serotonin increases GABA release in rat entorhinal cortex by inhibiting interneuron TASK-3 K+ channels. Mol Cell Neurosci 39(2):273–284. https://doi.org/10.1016/j.mcn.2008.07.005

Deng PY, Porter JE, Shin HS, Lei S (2006) Thyrotropin-releasing hormone increases GABA release in rat hippocampus. J Physiol 577(Pt 2):497–511

Dennis SH, Pasqui F, Colvin EM, Sanger H, Mogg AJ, Felder CC, Broad LM, Fitzjohn SM, Isaac JT, Mellor JR (2016) Activation of muscarinic M1 acetylcholine receptors induces long-term potentiation in the hippocampus. Cereb Cortex 26(1):414–426. https://doi.org/10.1093/cercor/bhv227

Dias RB, Ribeiro JA, Sebastiao AM (2012) Enhancement of AMPA currents and GluR1 membrane expression through PKA-coupled adenosine A(2A) receptors. Hippocampus 22(2):276–291. https://doi.org/10.1002/hipo.20894

Dias RB, Rombo DM, Ribeiro JA, Henley JM, Sebastiao AM (2013) Adenosine: setting the stage for plasticity. Trends Neurosci 36(4):248–257. https://doi.org/10.1016/j.tins.2012.12.003

Dinerman JL, Dawson TM, Schell MJ, Snowman A, Snyder SH (1994) Endothelial nitric oxide synthase localized to hippocampal pyramidal cells: implications for synaptic plasticity. Proc Natl Acad Sci U S A 91(10):4214–4218

Dodd J, Kelly JS (1979) Excitation of CA1 pyramidal neurones of the hippocampus by the tetra- and octapeptide C-terminal fragments of cholecystokinin [proceedings]. J Physiol 295:61P–62P

Dodd J, Dingledine R, Kelly JS (1981) The excitatory action of acetylcholine on hippocampal neurones of the guinea pig and rat maintained in vitro. Brain Res 207(1):109–127

Domonkos A, Nikitidou Ledri L, Laszlovszky T, Cserep C, Borhegyi Z, Papp E, Nyiri G, Freund TF, Varga V (2016) Divergent in vivo activity of non-serotonergic and serotonergic VGluT3-neurones in the median raphe region. J Physiol 594(13):3775–3790. https://doi.org/10.1113/JP272036

Dorostkar MM, Boehm S (2007) Opposite effects of presynaptic 5-HT3 receptor activation on spontaneous and action potential-evoked GABA release at hippocampal synapses. J Neurochem 100(2):395–405. https://doi.org/10.1111/j.1471-4159.2006.04218.x

Dougherty KD, Milner TA (1999) Cholinergic septal afferent terminals preferentially contact neuropeptide Y-containing interneurons compared to parvalbumin-containing interneurons in the rat dentate gyrus. J Neurosci 19(22):10140–10152

Doze VA, Cohen GA, Madison DV (1991) Synaptic localization of adrenergic disinhibition in the rat hippocampus. Neuron 6(6):889–900

Dreifuss JJ, Raggenbass M (1986) Tachykinins and bombesin excite non-pyramidal neurones in rat hippocampus. J Physiol 379:417–428

Dubrovsky B, Harris J, Gijsbers K, Tatarinov A (2002) Oxytocin induces long-term depression on the rat dentate gyrus: possible ATPase and ectoprotein kinase mediation. Brain Res Bull 58(2):141–147

Dunwiddie TV, Hoffer BJ (1980) Adenine nucleotides and synaptic transmission in the in vitro rat hippocampus. Br J Pharmacol 69(1):59–68

Dunwiddie TV, Masino SA (2001) The role and regulation of adenosine in the central nervous system. Annu Rev Neurosci 24:31–55. https://doi.org/10.1146/annurev.neuro.24.1.31

Durakoglugil M, Irving AJ, Harvey J (2005) Leptin induces a novel form of NMDA receptor-dependent long-term depression. J Neurochem 95(2):396–405. https://doi.org/10.1111/j.1471-4159.2005.03375.x

Dutar P, Bassant MH, Senut MC, Lamour Y (1995) The septohippocampal pathway: structure and function of a central cholinergic system. Physiol Rev 75(2):393–427. https://doi.org/10.1152/physrev.1995.75.2.393

Ebihara S, Akaike N (1993) Potassium currents operated by thyrotrophin-releasing hormone in dissociated CA1 pyramidal neurones of rat hippocampus. J Physiol 472:689–710

El-Ghundi M, Fletcher PJ, Drago J, Sibley DR, O'Dowd BF, George SR (1999) Spatial learning deficit in dopamine D(1) receptor knockout mice. Eur J Pharmacol 383(2):95–106

Ermine CM, Wright JL, Parish CL, Stanic D, Thompson LH (2016) Combined immunohistochemical and retrograde tracing reveals little evidence of innervation of the rat dentate gyrus by midbrain dopamine neurons. Front Biol. https://doi.org/10.1007/s11515-016-1404-4

Etter G, Krezel W (2014) Dopamine D2 receptor controls hilar mossy cells excitability. Hippocampus 24(7):725–732. https://doi.org/10.1002/hipo.22280

Fabbri R, Furini CR, Passani MB, Provensi G, Baldi E, Bucherelli C, Izquierdo I, de Carvalho MJ, Blandina P (2016) Memory retrieval of inhibitory avoidance requires histamine H1 receptor activation in the hippocampus. Proc Natl Acad Sci U S A 113(19):E2714–E2720. https://doi.org/10.1073/pnas.1604841113

Fabian-Fine R, Skehel P, Errington ML, Davies HA, Sher E, Stewart MG, Fine A (2001) Ultrastructural distribution of the alpha7 nicotinic acetylcholine receptor subunit in rat hippocampus. J Neurosci 21(20):7993–8003

Fanselow EE, Richardson KA, Connors BW (2008) Selective, state-dependent activation of somatostatin-expressing inhibitory interneurons in mouse neocortex. J Neurophysiol 100(5):2640–2652. https://doi.org/10.1152/jn.90691.2008

Farrant M, Nusser Z (2005) Variations on an inhibitory theme: phasic and tonic activation of GABA(A) receptors. Nat Rev Neurosci 6(3):215–229. https://doi.org/10.1038/nrn1625

Feil R, Kleppisch T (2008) NO/cGMP-dependent modulation of synaptic transmission. Handb Exp Pharmacol 184:529–560

Ferezou I, Cauli B, Hill EL, Rossier J, Hamel E, Lambolez B (2002) 5-HT3 receptors mediate serotonergic fast synaptic excitation of neocortical vasoactive intestinal peptide/cholecystokinin interneurons. J Neurosci 22(17):7389–7397

Fernandez de Sevilla D, Nunez A, Borde M, Malinow R, Buno W (2008) Cholinergic-mediated IP3-receptor activation induces long-lasting synaptic enhancement in CA1 pyramidal neurons. J Neurosci 28(6):1469–1478. https://doi.org/10.1523/JNEUROSCI.2723-07.2008

Ferraguti F, Klausberger T, Cobden P, Baude A, Roberts JD, Szucs P, Kinoshita A, Shigemoto R, Somogyi P, Dalezios Y (2005) Metabotropic glutamate receptor 8-expressing nerve terminals target subsets of GABAergic neurons in the hippocampus. J Neurosci 25(45):10520–10536. https://doi.org/10.1523/JNEUROSCI.2547-05.2005

Ferster D, Jagadeesh B (1992) EPSP-IPSP interactions in cat visual cortex studied with in vivo whole-cell patch recording. J Neurosci 12(4):1262–1274

Fester L, Rune GM (2015) Sexual neurosteroids and synaptic plasticity in the hippocampus. Brain Res 1621:162–169. https://doi.org/10.1016/j.brainres.2014.10.033

Filippov AK, Choi RC, Simon J, Barnard EA, Brown DA (2006) Activation of P2Y1 nucleotide receptors induces inhibition of the M-type K+ current in rat hippocampal pyramidal neurons. J Neurosci 26(36):9340–9348. https://doi.org/10.1523/JNEUROSCI.2635-06.2006

Fink KB, Gothert M (2007) 5-HT receptor regulation of neurotransmitter release. Pharmacol Rev 59(4):360–417. https://doi.org/10.1124/pr.107.07103

Fisahn A, Yamada M, Duttaroy A, Gan JW, Deng CX, McBain CJ, Wess J (2002) Muscarinic induction of hippocampal gamma oscillations requires coupling of the M1 receptor to two mixed cation currents. Neuron 33(4):615–624

Foldy C, Neu A, Jones MV, Soltesz I (2006) Presynaptic, activity-dependent modulation of cannabinoid type 1 receptor-mediated inhibition of GABA release. J Neurosci 26(5):1465–1469

Foldy C, Lee SY, Szabadics J, Neu A, Soltesz I (2007) Cell type-specific gating of perisomatic inhibition by cholecystokinin. Nat Neurosci 10(9):1128–1130. https://doi.org/10.1038/nn1952 nn1952 [pii]

Foldy C, Darmanis S, Aoto J, Malenka RC, Quake SR, Sudhof TC (2016) Single-cell RNAseq reveals cell adhesion molecule profiles in electrophysiologically defined neurons. Proc Natl Acad Sci U S A 113(35):E5222–E5231

Frade JG, Barbosa RM, Laranjinha J (2008) Stimulation of NMDA and AMPA glutamate receptors elicits distinct concentration dynamics of nitric oxide in rat hippocampal slices. Hippocampus 19(7):603–611

Francavilla R, Luo X, Magnin E, Tyan L, Topolnik L (2015) Coordination of dendritic inhibition through local disinhibitory circuits. Front Synaptic Neurosci 7:5. https://doi.org/10.3389/fnsyn.2015.00005

Fraser DD, MacVicar BA (1996) Cholinergic-dependent plateau potential in hippocampal CA1 pyramidal neurons. J Neurosci 16(13):4113–4128

Frazier CJ, Buhler AV, Weiner JL, Dunwiddie TV (1998a) Synaptic potentials mediated via alpha-bungarotoxin-sensitive nicotinic acetylcholine receptors in rat hippocampal interneurons. J Neurosci 18(20):8228–8235

Frazier CJ, Rollins YD, Breese CR, Leonard S, Freedman R, Dunwiddie TV (1998b) Acetylcholine activates an alpha-bungarotoxin-sensitive nicotinic current in rat hippocampal interneurons, but not pyramidal cells. J Neurosci 18(4):1187–1195

Fredholm BB, Dunwiddie TV (1988) How does adenosine inhibit transmitter release? Trends Pharmacol Sci 9(4):130–134

Freedman R, Wetmore C, Stromberg I, Leonard S, Olson L (1993) Alpha-bungarotoxin binding to hippocampal interneurons: immunocytochemical characterization and effects on growth factor expression. J Neurosci 13(5):1965–1975

Freund TF (1989) GABAergic septohippocampal neurons contain parvalbumin. Brain Res 478(2):375–381. https://doi.org/10.1016/0006-8993(89)91520-5

Freund TF, Antal M (1988) GABA-containing neurons in the septum control inhibitory interneurons in the hippocampus. Nature 336(6195):170–173. https://doi.org/10.1038/336170a0

Freund TF, Buzsaki G (1996) Interneurons of the hippocampus. Hippocampus 6(4):347–470. https://doi.org/10.1002/(SICI)1098-1063(1996)6:4<347::AID-HIPO1>3.0.CO;2-I

Freund TF, Katona I (2007) Perisomatic inhibition. Neuron 56(1):33–42. https://doi.org/10.1016/j.neuron.2007.09.012

Freund TF, Gulyas AI, Acsady L, Gorcs T, Toth K (1990) Serotonergic control of the hippocampus via local inhibitory interneurons. Proc Natl Acad Sci U S A 87(21):8501–8505

Freund TF, Hajos N, Acsady L, Gorcs TJ, Katona I (1997) Mossy cells of the rat dentate gyrus are immunoreactive for calcitonin gene-related peptide (CGRP). Eur J Neurosci 9(9):1815–1830

Frey U, Huang YY, Kandel ER (1993) Effects of cAMP simulate a late stage of LTP in hippocampal CA1 neurons. Science 260(5114):1661–1664

Frotscher M, Leranth C (1985) Cholinergic innervation of the rat hippocampus as revealed by choline acetyltransferase immunocytochemistry: a combined light and electron microscopic study. J Comp Neurol 239(2):237–246. https://doi.org/10.1002/cne.902390210

Frotscher M, Schlander M, Leranth C (1986) Cholinergic neurons in the hippocampus. A combined light- and electron-microscopic immunocytochemical study in the rat. Cell Tissue Res 246(2):293–301. https://doi.org/10.1007/bf00215891

Frotscher M, Vida I, Bender R (2000) Evidence for the existence of non-GABAergic, cholinergic interneurons in the rodent hippocampus. Neuroscience 96(1):27–31. https://doi.org/10.1016/s0306-4522(99)00525-4

Fukudome Y, Ohno-Shosaku T, Matsui M, Omori Y, Fukaya M, Tsubokawa H, Taketo MM, Watanabe M, Manabe T, Kano M (2004) Two distinct classes of muscarinic action on hippocampal inhibitory synapses: M2-mediated direct suppression and M1/M3-mediated indirect suppression through endocannabinoid signalling. Eur J Neurosci 19(10):2682–2692. https://doi.org/10.1111/j.0953-816X.2004.03384.x

Gangarossa G, Longueville S, De Bundel D, Perroy J, Herve D, Girault JA, Valjent E (2012) Characterization of dopamine D1 and D2 receptor-expressing neurons in the mouse hippocampus. Hippocampus 22(12):2199–2207. https://doi.org/10.1002/hipo.22044

Gao WJ, Goldman-Rakic PS (2003) Selective modulation of excitatory and inhibitory microcircuits by dopamine. Proc Natl Acad Sci U S A 100(5):2836–2841. https://doi.org/10.1073/pnas.262796399

Gao WJ, Wang Y, Goldman-Rakic PS (2003) Dopamine modulation of perisomatic and peridendritic inhibition in prefrontal cortex. J Neurosci 23(5):1622–1630

Gardier AM (2009) Mutant mouse models and antidepressant drug research: focus on serotonin and brain-derived neurotrophic factor. Behav Pharmacol 20(1):18–32. https://doi.org/10.1097/FBP.0b013e3283243fcd

Garthwaite J (2008) Concepts of neural nitric oxide-mediated transmission. Eur J Neurosci 27(11):2783–2802

Garthwaite J (2016) From synaptically localized to volume transmission by nitric oxide. J Physiol 594(1):9–18. https://doi.org/10.1113/JP270297

Garthwaite J, Boulton CL (1995) Nitric oxide signaling in the central nervous system. Annu Rev Physiol 57:683–706

Gasbarri A, Packard MG, Campana E, Pacitti C (1994) Anterograde and retrograde tracing of projections from the ventral tegmental area to the hippocampal formation in the rat. Brain Res Bull 33(4):445–452

Gasbarri A, Sulli A, Innocenzi R, Pacitti C, Brioni JD (1996) Spatial memory impairment induced by lesion of the mesohippocampal dopaminergic system in the rat. Neuroscience 74(4):1037–1044

Gasbarri A, Sulli A, Packard MG (1997) The dopaminergic mesencephalic projections to the hippocampal formation in the rat. Prog Neuropsychopharmacol Biol Psychiatry 21(1):1–22

Ge S, Dani JA (2005) Nicotinic acetylcholine receptors at glutamate synapses facilitate long-term depression or potentiation. J Neurosci 25(26):6084–6091. https://doi.org/10.1523/JNEUROSCI.0542-05.2005

Geiger JR, Jonas P (2000) Dynamic control of presynaptic Ca(2+) inflow by fast-inactivating K(+) channels in hippocampal mossy fiber boutons. Neuron 28(3):927–939

Gelinas JN, Nguyen PV (2005) Beta-adrenergic receptor activation facilitates induction of a protein synthesis-dependent late phase of long-term potentiation. J Neurosci 25(13):3294–3303. https://doi.org/10.1523/JNEUROSCI.4175-04.2005

Gelinas JN, Tenorio G, Lemon N, Abel T, Nguyen PV (2008) Beta-adrenergic receptor activation during distinct patterns of stimulation critically modulates the PKA-dependence of LTP in the mouse hippocampus. Learn Mem 15(5):281–289. https://doi.org/10.1101/lm.829208

Ghadimi BM, Jarolimek W, Misgeld U (1994) Effects of serotonin on hilar neurons and granule cell inhibition in the guinea pig hippocampal slice. Brain Res 633(1-2):27–32

Gibbs ME, Summers RJ (2002) Role of adrenoceptor subtypes in memory consolidation. Prog Neurobiol 67(5):345–391

Gielow MR, Zaborszky L (2017) The input-output relationship of the cholinergic basal forebrain. Cell Rep 18(7):1817–1830. https://doi.org/10.1016/j.celrep.2017.01.060

Gingrich MB, Junge CE, Lyuboslavsky P, Traynelis SF (2000) Potentiation of NMDA receptor function by the serine protease thrombin. J Neurosci 20(12):4582–4595

Giocomo LM, Hasselmo ME (2005) Nicotinic modulation of glutamatergic synaptic transmission in region CA3 of the hippocampus. Eur J Neurosci 22(6):1349–1356. https://doi.org/10.1111/j.1460-9568.2005.04316.x

Giocomo LM, Hasselmo ME (2007) Neuromodulation by glutamate and acetylcholine can change circuit dynamics by regulating the relative influence of afferent input and excitatory feedback. Mol Neurobiol 36(2):184–200. https://doi.org/10.1007/s12035-007-0032-z

Glickfeld LL, Scanziani M (2006) Distinct timing in the activity of cannabinoid-sensitive and cannabinoid-insensitive basket cells. Nat Neurosci 9(6):807–815. https://doi.org/10.1038/nn1688

Glickfeld LL, Atallah BV, Scanziani M (2008) Complementary modulation of somatic inhibition by opioids and cannabinoids. J Neurosci 28(8):1824–1832. https://doi.org/10.1523/JNEUROSCI.4700-07.2008

Gloveli T, Dugladze T, Saha S, Monyer H, Heinemann U, Traub RD, Whittington MA, Buhl EH (2005) Differential involvement of oriens/pyramidale interneurones in hippocampal network oscillations in vitro. J Physiol 562(Pt 1):131–147. https://doi.org/10.1113/jphysiol.2004.073007

Goldsmith SK, Joyce JN (1994) Dopamine D2 receptor expression in hippocampus and parahippocampal cortex of rat, cat, and human in relation to tyrosine hydroxylase-immunoreactive fibers. Hippocampus 4(3):354–373. https://doi.org/10.1002/hipo.450040318

Gondard E, Anaclet C, Akaoka H, Guo RX, Zhang M, Buda C, Franco P, Kotani H, Lin JS (2013) Enhanced histaminergic neurotransmission and sleep-wake alterations, a study in histamine H3-receptor knock-out mice. Neuropsychopharmacology 38(6):1015–1031. https://doi.org/10.1038/npp.2012.266

Gong S, Doughty M, Harbaugh CR, Cummins A, Hatten ME, Heintz N, Gerfen CR (2007) Targeting Cre recombinase to specific neuron populations with bacterial artificial chromosome constructs. J Neurosci 27(37):9817–9823. https://doi.org/10.1523/JNEUROSCI.2707-07.2007 27/37/9817 [pii]

Gonzalez-Burgos G, Kroener S, Seamans JK, Lewis DA, Barrionuevo G (2005) Dopaminergic modulation of short-term synaptic plasticity in fast-spiking interneurons of primate dorsolateral prefrontal cortex. J Neurophysiol 94(6):4168–4177. https://doi.org/10.1152/jn.00698.2005

Gorelova N, Seamans JK, Yang CR (2002) Mechanisms of dopamine activation of fast-spiking interneurons that exert inhibition in rat prefrontal cortex. J Neurophysiol 88(6):3150–3166. https://doi.org/10.1152/jn.00335.2002

Granger AJ, Mulder N, Saunders A, Sabatini BL (2016) Cotransmission of acetylcholine and GABA. Neuropharmacology 100:40–46. https://doi.org/10.1016/j.neuropharm.2015.07.031

Gras C, Herzog E, Bellenchi GC, Bernard V, Ravassard P, Pohl M, Gasnier B, Giros B, El Mestikawy S (2002) A third vesicular glutamate transporter expressed by cholinergic and serotoninergic neurons. J Neurosci 22(13):5442–5451

Gray R, Johnston D (1987) Noradrenaline and beta-adrenoceptor agonists increase activity of voltage-dependent calcium channels in hippocampal neurons. Nature 327(6123):620–622. https://doi.org/10.1038/327620a0

Gray R, Rajan AS, Radcliffe KA, Yakehiro M, Dani JA (1996) Hippocampal synaptic transmission enhanced by low concentrations of nicotine. Nature 383(6602):713–716. https://doi.org/10.1038/383713a0

Greene RW, Haas HL (1990) Effects of histamine on dentate granule cells in vitro. Neuroscience 34(2):299–303

Gribkoff VK, Ashe JH (1984) Modulation by dopamine of population responses and cell membrane properties of hippocampal CA1 neurons in vitro. Brain Res 292(2):327–338

Grienberger C, Konnerth A (2012) Imaging calcium in neurons. Neuron 73(5):862–885. https://doi.org/10.1016/j.neuron.2012.02.011

Grybko MJ, Hahm ET, Perrine W, Parnes JA, Chick WS, Sharma G, Finger TE, Vijayaraghavan S (2011) A transgenic mouse model reveals fast nicotinic transmission in hippocampal pyramidal neurons. Eur J Neurosci 33(10):1786–1798. https://doi.org/10.1111/j.1460-9568.2011.07671.x

Gu Z, Yakel JL (2011) Timing-dependent septal cholinergic induction of dynamic hippocampal synaptic plasticity. Neuron 71(1):155–165. https://doi.org/10.1016/j.neuron.2011.04.026

Guimond D, Diabira D, Porcher C, Bader F, Ferrand N, Zhu M, Appleyard SM, Wayman GA, Gaiarsa JL (2014) Leptin potentiates GABAergic synaptic transmission in the developing rodent hippocampus. Front Cell Neurosci 8:235. https://doi.org/10.3389/fncel.2014.00235

Gulledge AT, Kawaguchi Y (2007) Phasic cholinergic signaling in the hippocampus: functional homology with the neocortex? Hippocampus 17(5):327–332. https://doi.org/10.1002/hipo.20279

Gulledge AT, Bucci DJ, Zhang SS, Matsui M, Yeh HH (2009) M1 receptors mediate cholinergic modulation of excitability in neocortical pyramidal neurons. J Neurosci 29(31):9888–9902. https://doi.org/10.1523/JNEUROSCI.1366-09.2009

Gulyas AI, Acsady L, Freund TF (1999) Structural basis of the cholinergic and serotonergic modulation of GABAergic neurons in the hippocampus. Neurochem Int 34(5):359–372

Gustafson EL, Durkin MM, Bard JA, Zgombick J, Branchek TA (1996) A receptor autoradiographic and in situ hybridization analysis of the distribution of the 5-ht7 receptor in rat brain. Br J Pharmacol 117(4):657–666

Guzman SJ, Gerevich Z (2016) P2Y receptors in synaptic transmission and plasticity: therapeutic potential in cognitive dysfunction. Neural Plast 2016:1207393. https://doi.org/10.1155/2016/1207393

Haam J, Yakel JL (2017) Cholinergic modulation of the hippocampal region and memory function. J Neurochem 142(Suppl 2):111–121. https://doi.org/10.1111/jnc.14052

Haas HL, Gahwiler BH (1992) Vasoactive intestinal polypeptide modulates neuronal excitability in hippocampal slices of the rat. Neuroscience 47(2):273–277 0306-4522(92)90243-U [pii]

Haas HL, Greene RW (1986) Effects of histamine on hippocampal pyramidal cells of the rat in vitro. Exp Brain Res 62(1):123–130

Haas HL, Konnerth A (1983) Histamine and noradrenaline decrease calcium-activated potassium conductance in hippocampal pyramidal cells. Nature 302(5907):432–434

Haas H, Panula P (2003) The role of histamine and the tuberomamillary nucleus in the nervous system. Nat Rev Neurosci 4(2):121–130. https://doi.org/10.1038/nrn1034

Haas HL, Rose GM (1987) Noradrenaline blocks potassium conductance in rat dentate granule cells in vitro. Neurosci Lett 78(2):171–174

Haas HL, Hermann A, Greene RW, Chan-Palay V (1987) Action and location of neuropeptide tyrosine (Y) on hippocampal neurons of the rat in slice preparations. J Comp Neurol 257(2):208–215

Haas HL, Sergeeva OA, Selbach O (2008) Histamine in the nervous system. Physiol Rev 88(3):1183–1241. https://doi.org/10.1152/physrev.00043.2007

Habib D, Dringenberg HC (2009) Alternating low frequency stimulation of medial septal and commissural fibers induces NMDA-dependent, long-lasting potentiation

of hippocampal synapses in urethane-anesthetized rats. Hippocampus 19(3):299–307. https://doi.org/10.1002/hipo.20507
Hajos N, Papp EC, Acsady L, Levey AI, Freund TF (1998) Distinct interneuron types express m2 muscarinic receptor immunoreactivity on their dendrites or axon terminals in the hippocampus. Neuroscience 82(2):355–376
Haley JE, Schaible E, Pavlidis P, Murdock A, Madison DV (1996) Basal and apical synapses of CA1 pyramidal cells employ different LTP induction mechanisms. Learn Mem 3(4):289–295
Hallbeck M, Hermanson O, Blomqvist A (1999) Distribution of preprovasopressin mRNA in the rat central nervous system. J Comp Neurol 411(2):181–200
Halliwell JV (1990) Physiological mechanisms of cholinergic action in the hippocampus. Prog Brain Res 84:255–272
Halliwell JV, Adams PR (1982) Voltage-clamp analysis of muscarinic excitation in hippocampal neurons. Brain Res 250(1):71–92
Hammad H, Wagner JJ (2006) Dopamine-mediated disinhibition in the CA1 region of rat hippocampus via D3 receptor activation. J Pharmacol Exp Ther 316(1):113–120. https://doi.org/10.1124/jpet.105.091579
Hangya B, Ranade SP, Lorenc M, Kepecs A (2015) Central cholinergic neurons are rapidly recruited by reinforcement feedback. Cell 162(5):1155–1168. https://doi.org/10.1016/j.cell.2015.07.057
Harley CW (2007) Norepinephrine and the dentate gyrus. Prog Brain Res 163:299–318. https://doi.org/10.1016/S0079-6123(07)63018-0
Harvey J (2007) Leptin: a diverse regulator of neuronal function. J Neurochem 100(2):307–313
Hasselmo ME (2006) The role of acetylcholine in learning and memory. Curr Opin Neurobiol 16(6):710–715. https://doi.org/10.1016/j.conb.2006.09.002
Hasselmo ME, Schnell E (1994) Laminar selectivity of the cholinergic suppression of synaptic transmission in rat hippocampal region CA1: computational modeling and brain slice physiology. J Neurosci 14(6):3898–3914
Haug T, Storm JF (2000) Protein kinase A mediates the modulation of the slow Ca(2+)-dependent K(+) current, I(sAHP), by the neuropeptides CRF, VIP, and CGRP in hippocampal pyramidal neurons. J Neurophysiol 83(4):2071–2079
Hefft S, Hulo S, Bertrand D, Muller D (1999) Synaptic transmission at nicotinic acetylcholine receptors in rat hippocampal organotypic cultures and slices. J Physiol Lond 515(3):769–776. https://doi.org/10.1111/j.1469-7793.1999.769ab.x
Henny P, Jones BE (2008) Projections from basal forebrain to prefrontal cortex comprise cholinergic, GABAergic and glutamatergic inputs to pyramidal cells or interneurons. Eur J Neurosci 27(3):654–670. https://doi.org/10.1111/j.1460-9568.2008.06029.x
Henstridge CM, Balenga NA, Ford LA, Ross RA, Waldhoer M, Irving AJ (2009) The GPR55 ligand L-alpha-lysophosphatidylinositol promotes RhoA-dependent Ca2+ signaling and NFAT activation. FASEB J 23(1):183–193
Hillman KL, Knudson CA, Carr PA, Doze VA, Porter JE (2005) Adrenergic receptor characterization of CA1 hippocampal neurons using real time single cell RT-PCR. Brain Res Mol Brain Res 139(2):267–276. https://doi.org/10.1016/j.molbrainres.2005.05.033
Hillman KL, Lei S, Doze VA, Porter JE (2009) Alpha-1A adrenergic receptor activation increases inhibitory tone in CA1 hippocampus. Epilepsy Res 84(2-3):97–109. https://doi.org/10.1016/j.eplepsyres.2008.12.007
Hioki H, Nakamura H, Ma YF, Konno M, Hayakawa T, Nakamura KC, Fujiyama F, Kaneko T (2010) Vesicular glutamate transporter 3-expressing nonserotonergic projection neurons constitute a subregion in the rat midbrain raphe nuclei. J Comp Neurol 518(5):668–686. https://doi.org/10.1002/cne.22237
Hippenmeyer S, Vrieseling E, Sigrist M, Portmann T, Laengle C, Ladle DR, Arber S (2005) A developmental switch in the response of DRG neurons to ETS transcription factor signaling. PLoS Biol 3(5):e159. https://doi.org/10.1371/journal.pbio.0030159
Hollins C, Stone TW (1980) Adenosine inhibition of gamma-aminobutyric acid release from slices of rat cerebral cortex. Br J Pharmacol 69(1):107–112

Holscher C, Anwyl R, Rowan MJ (1997) Stimulation on the positive phase of hippocampal theta rhythm induces long-term potentiation that can be depotentiated by stimulation on the negative phase in area CA1 in vivo. J Neurosci 17(16):6470–6477

Hopkins WF, Johnston D (1984) Frequency-dependent noradrenergic modulation of long-term potentiation in the hippocampus. Science 226(4672):350–352

Hopkins WF, Johnston D (1988) Noradrenergic enhancement of long-term potentiation at mossy fiber synapses in the hippocampus. J Neurophysiol 59(2):667–687. https://doi.org/10.1152/jn.1988.59.2.667

Hsu KS (1996) Characterization of dopamine receptors mediating inhibition of excitatory synaptic transmission in the rat hippocampal slice. J Neurophysiol 76(3):1887–1895. https://doi.org/10.1152/jn.1996.76.3.1887

Hu H, Real E, Takamiya K, Kang MG, Ledoux J, Huganir RL, Malinow R (2007) Emotion enhances learning via norepinephrine regulation of AMPA-receptor trafficking. Cell 131(1):160–173. https://doi.org/10.1016/j.cell.2007.09.017

Huang YY, Kandel ER (1995) D1/D5 receptor agonists induce a protein synthesis-dependent late potentiation in the CA1 region of the hippocampus. Proc Natl Acad Sci U S A 92(7):2446–2450

Huang YY, Kandel ER (1996) Modulation of both the early and the late phase of mossy fiber LTP by the activation of beta-adrenergic receptors. Neuron 16(3):611–617

Huerta PT, Lisman JE (1993) Heightened synaptic plasticity of hippocampal CA1 neurons during a cholinergically induced rhythmic state. Nature 364(6439):723–725. https://doi.org/10.1038/364723a0

Huh CY, Goutagny R, Williams S (2010) Glutamatergic neurons of the mouse medial septum and diagonal band of Broca synaptically drive hippocampal pyramidal cells: relevance for hippocampal theta rhythm. J Neurosci 30(47):15951–15961. https://doi.org/10.1523/JNEUROSCI.3663-10.2010

Hummos A, Nair SS (2017) An integrative model of the intrinsic hippocampal theta rhythm. PLoS One 12(8):e0182648. https://doi.org/10.1371/journal.pone.0182648

Hurst K, Badgley C, Ellsworth T, Bell S, Friend L, Prince B, Welch J, Cowan Z, Williamson R, Lyon C, Anderson B, Poole B, Christensen M, McNeil M, Call J, Edwards JG (2017) A putative lysophosphatidylinositol receptor GPR55 modulates hippocampal synaptic plasticity. Hippocampus 27(9):985–998. https://doi.org/10.1002/hipo.22747

Hyman JM, Wyble BP, Goyal V, Rossi CA, Hasselmo ME (2003) Stimulation in hippocampal region CA1 in behaving rats yields long-term potentiation when delivered to the peak of theta and long-term depression when delivered to the trough. J Neurosci 23(37):11725–11731

Ihalainen JA, Riekkinen P Jr, Feenstra MG (1999) Comparison of dopamine and noradrenaline release in mouse prefrontal cortex, striatum and hippocampus using microdialysis. Neurosci Lett 277(2):71–74

Ihara N, Ueda S, Kawata M, Sano Y (1988) Immunohistochemical demonstration of serotonin-containing nerve fibers in the mammalian hippocampal formation. Acta Anat (Basel) 132(4):335–346

Ikeuchi Y, Nishizaki T, Okada Y (1996) Repetitive applications of ATP potentiate potassium current by Ca2+/calmodulin kinase in cultured rat hippocampal neurons. Neurosci Lett 203(2):115–118

Illes P, Nieber K, Norenberg W (1996) Electrophysiological effects of ATP on brain neurones. J Auton Pharmacol 16(6):407–411

Inagaki N, Yamatodani A, Ando-Yamamoto M, Tohyama M, Watanabe T, Wada H (1988) Organization of histaminergic fibers in the rat brain. J Comp Neurol 273(3):283–300. https://doi.org/10.1002/cne.902730302

Inoue K, Koizumi S, Ueno S, Kita A, Tsuda M (1999) The functions of ATP receptors in the synaptic transmission in the hippocampus. Prog Brain Res 120:193–206

Irving AJ, Harvey J (2014) Leptin regulation of hippocampal synaptic function in health and disease. Philos Trans R Soc Lond B Biol Sci 369(1633):20130155. https://doi.org/10.1098/rstb.2013.0155

Ishihara K, Katsuki H, Sugimura M, Satoh M (1992) YM-14673, a new thyrotropin-releasing hormone analog, augments long-term potentiation in the mossy fiber-CA3 system of guinea pig hippocampal slices. J Pharmacobiodyn 15(2):75–78

Ito HT, Schuman EM (2007) Frequency-dependent gating of synaptic transmission and plasticity by dopamine. Front Neural Circuits 1:1. https://doi.org/10.3389/neuro.04.001.2007

Jackman SL, Beneduce BM, Drew IR, Regehr WG (2014) Achieving high-frequency optical control of synaptic transmission. J Neurosci 34(22):7704–7714. https://doi.org/10.1523/JNEUROSCI.4694-13.2014

Jagadeesh B, Gray CM, Ferster D (1992) Visually evoked oscillations of membrane potential in cells of cat visual cortex. Science 257(5069):552–554

Jahnsen H (1980) The action of 5-hydroxytryptamine on neuronal membranes and synaptic transmission in area CA1 of the hippocampus in vitro. Brain Res 197(1):83–94

Jia Y, Yamazaki Y, Nakauchi S, Sumikawa K (2009) Alpha2 nicotine receptors function as a molecular switch to continuously excite a subset of interneurons in rat hippocampal circuits. Eur J Neurosci 29(8):1588–1603. https://doi.org/10.1111/j.1460-9568.2009.06706.x

Jimenez JC, Su K, Goldberg AR, Luna VM, Biane JS, Ordek G, Zhou P, Ong SK, Wright MA, Zweifel L, Paninski L, Hen R, Kheirbek MA (2018) Anxiety cells in a hippocampal-hypothalamic circuit. Neuron 97(3):670–683e676. https://doi.org/10.1016/j.neuron.2018.01.016

Johnston A, McBain CJ, Fisahn A (2014) 5-Hydroxytryptamine1A receptor-activation hyperpolarizes pyramidal cells and suppresses hippocampal gamma oscillations via Kir3 channel activation. J Physiol 592(19):4187–4199. https://doi.org/10.1113/jphysiol.2014.279083

Jones BE (2004) Activity, modulation and role of basal forebrain cholinergic neurons innervating the cerebral cortex. In: Acetylcholine in the cerebral cortex. Progress in Brain Research, pp 157–169. https://doi.org/10.1016/s0079-6123(03)45011-5

Jones S, Yakel JL (1997) Functional nicotinic ACh receptors on interneurones in the rat hippocampus. J Physiol 504(Pt 3):603–610

Jones JD, Carney ST, Vrana KE, Norford DC, Howlett AC (2008) Cannabinoid receptor-mediated translocation of NO-sensitive guanylyl cyclase and production of cyclic GMP in neuronal cells. Neuropharmacology 54(1):23–30

Kahle JS, Cotman CW (1989) Carbachol depresses synaptic responses in the medial but not the lateral perforant path. Brain Res 482(1):159–163

Kaiser T, Ting JT, Monteiro P, Feng G (2016) Transgenic labeling of parvalbumin-expressing neurons with tdTomato. Neuroscience 321:236–245. https://doi.org/10.1016/j.neuroscience.2015.08.036

Kajimoto T, Okada T, Yu H, Goparaju SK, Jahangeer S, Nakamura S (2007) Involvement of sphingosine-1-phosphate in glutamate secretion in hippocampal neurons. Mol Cell Biol 27(9):3429–3440

Kano M, Ohno-Shosaku T, Hashimotodani Y, Uchigashima M, Watanabe M (2009) Endocannabinoid-mediated control of synaptic transmission. Physiol Rev 89(1):309–380

Karson MA, Whittington KC, Alger BE (2008) Cholecystokinin inhibits endocannabinoid-sensitive hippocampal IPSPs and stimulates others. Neuropharmacology 54(1):117–128

Karunakaran S, Chowdhury A, Donato F, Quairiaux C, Michel CM, Caroni P (2016) PV plasticity sustained through D1/5 dopamine signaling required for long-term memory consolidation. Nat Neurosci 19(3):454–464. https://doi.org/10.1038/nn.4231

Katona I, Sperlagh B, Sik A, Kafalvi A, Vizi ES, Mackie K, Freund TF (1999) Presynaptically located CB1 cannabinoid receptors regulate GABA release from axon terminals of specific hippocampal interneurons. J Neurosci 19(11):4544–4558

Katona I, Urban GM, Wallace M, Ledent C, Jung KM, Piomelli D, Mackie K, Freund TF (2006) Molecular composition of the endocannabinoid system at glutamatergic synapses. J Neurosci 26(21):5628–5637

Katsurabayashi S, Kubota H, Tokutomi N, Akaike N (2003) A distinct distribution of functional presynaptic 5-HT receptor subtypes on GABAergic nerve terminals projecting to single hippocampal CA1 pyramidal neurons. Neuropharmacology 44(8):1022–1030

Katz PS, Frost WN (1996) Intrinsic neuromodulation: altering neuronal circuits from within. Trends Neurosci 19(2):54–61. https://doi.org/10.1016/0166-2236(96)89621-4

Kawa K (1994) Distribution and functional properties of 5-HT3 receptors in the rat hippocampal dentate gyrus: a patch-clamp study. J Neurophysiol 71(5):1935–1947. https://doi.org/10.1152/jn.1994.71.5.1935

Kawaguchi Y (1997) Selective cholinergic modulation of cortical GABAergic cell subtypes. J Neurophysiol 78(3):1743–1747. https://doi.org/10.1152/jn.1997.78.3.1743

Kawamura M, Gachet C, Inoue K, Kato F (2004) Direct excitation of inhibitory interneurons by extracellular ATP mediated by P2Y1 receptors in the hippocampal slice. J Neurosci 24(48):10835–10845. https://doi.org/10.1523/JNEUROSCI.3028-04.2004

Kearns IR, Morton RA, Bulters DO, Davies CH (2001) Opioid receptor regulation of muscarinic acetylcholine receptor-mediated synaptic responses in the hippocampus. Neuropharmacology 41(5):565–573

Kempadoo KA, Mosharov EV, Choi SJ, Sulzer D, Kandel ER (2016) Dopamine release from the locus coeruleus to the dorsal hippocampus promotes spatial learning and memory. Proc Natl Acad Sci U S A 113(51):14835–14840. https://doi.org/10.1073/pnas.1616515114

Kepecs A, Fishell G (2014) Interneuron cell types are fit to function. Nature 505(7483):318–326. https://doi.org/10.1038/nature12983

Khakh BS (2009) ATP-gated P2X receptors on excitatory nerve terminals onto interneurons initiate a form of asynchronous glutamate release. Neuropharmacology 56(1):216–222

Khakh BS, Gittermann D, Cockayne DA, Jones A (2003) ATP modulation of excitatory synapses onto interneurons. J Neurosci 23(19):7426–7437

Khan ZU, Gutierrez A, Martin R, Penafiel A, Rivera A, De La Calle A (1998) Differential regional and cellular distribution of dopamine D2-like receptors: an immunocytochemical study of subtype-specific antibodies in rat and human brain. J Comp Neurol 402(3):353–371

Kim J, Isokawa M, Ledent C, Alger BE (2002) Activation of muscarinic acetylcholine receptors enhances the release of endogenous cannabinoids in the hippocampus. J Neurosci 22(23):10182–10191

King B, Rizwan AP, Asmara H, Heath NC, Engbers JD, Dykstra S, Bartoletti TM, Hameed S, Zamponi GW, Turner RW (2015) IKCa channels are a critical determinant of the slow AHP in CA1 pyramidal neurons. Cell Rep 11(2):175–182. https://doi.org/10.1016/j.celrep.2015.03.026

Kirby MT, Hampson RE, Deadwyler SA (2000) Cannabinoid receptor activation in CA1 pyramidal cells in adult rat hippocampus. Brain Res 863(1-2):120–131

Kitamura K, Judkewitz B, Kano M, Denk W, Hausser M (2008) Targeted patch-clamp recordings and single-cell electroporation of unlabeled neurons in vivo. Nat Methods 5(1):61–67. https://doi.org/10.1038/nmeth1150 nmeth1150 [pii]

Klapstein GJ, Colmers WF (1993) On the sites of presynaptic inhibition by neuropeptide Y in rat hippocampus in vitro. Hippocampus 3(1):103–111

Klausberger T (2009) GABAergic interneurons targeting dendrites of pyramidal cells in the CA1 area of the hippocampus. Eur J Neurosci 30(6):947–957. https://doi.org/10.1111/j.1460-9568.2009.06913.x

Klausberger T, Somogyi P (2008) Neuronal diversity and temporal dynamics: the unity of hippocampal circuit operations. Science 321(5885):53–57. https://doi.org/10.1126/science.1149381

Klausberger T, Magill PJ, Marton LF, Roberts JD, Cobden PM, Buzsaki G, Somogyi P (2003) Brain-state- and cell-type-specific firing of hippocampal interneurons in vivo. Nature 421(6925):844–848

Kobayashi K, Suzuki H (2007) Dopamine selectively potentiates hippocampal mossy fiber to CA3 synaptic transmission. Neuropharmacology 52(2):552–561. https://doi.org/10.1016/j.neuropharm.2006.08.026

Kobayashi K, Ikeda Y, Haneda E, Suzuki H (2008) Chronic fluoxetine bidirectionally modulates potentiating effects of serotonin on the hippocampal mossy fiber synaptic transmission. J Neurosci 28(24):6272–6280. https://doi.org/10.1523/JNEUROSCI.1656-08.2008

Kocsis B, Varga V, Dahan L, Sik A (2006) Serotonergic neuron diversity: identification of raphe neurons with discharges time-locked to the hippocampal theta rhythm. Proc Natl Acad Sci U S A 103(4):1059–1064. https://doi.org/10.1073/pnas.0508360103

Kojima T, Matsumoto M, Togashi H, Tachibana K, Kemmotsu O, Yoshioka M (2003) Fluvoxamine suppresses the long-term potentiation in the hippocampal CA1 field of anesthetized rats: an effect mediated via 5-HT1A receptors. Brain Res 959(1):165–168

Kouznetsova M, Nistri A (1998) Modulation by substance P of synaptic transmission in the mouse hippocampal slice. Eur J Neurosci 10(10):3076–3084

Kremin T, Hasselmo ME (2007) Cholinergic suppression of glutamatergic synaptic transmission in hippocampal region CA3 exhibits laminar selectivity: implication for hippocampal network dynamics. Neuroscience 149(4):760–767. https://doi.org/10.1016/j.neuroscience.2007.07.007

Kremin T, Gerber D, Giocomo LM, Huang SY, Tonegawa S, Hasselmo ME (2006) Muscarinic suppression in stratum radiatum of CA1 shows dependence on presynaptic M1 receptors and is not dependent on effects at GABA(B) receptors. Neurobiol Learn Mem 85(2):153–163. https://doi.org/10.1016/j.nlm.2005.09.005

Kroner S, Krimer LS, Lewis DA, Barrionuevo G (2007) Dopamine increases inhibition in the monkey dorsolateral prefrontal cortex through cell type-specific modulation of interneurons. Cereb Cortex 17(5):1020–1032. https://doi.org/10.1093/cercor/bhl012

Krook-Magnuson E, Luu L, Lee SH, Varga C, Soltesz I (2011) Ivy and neurogliaform interneurons are a major target of mu-opioid receptor modulation. J Neurosci 31(42):14861–14870. https://doi.org/10.1523/JNEUROSCI.2269-11.2011

Kulik A, Vida I, Fukazawa Y, Guetg N, Kasugai Y, Marker CL, Rigato F, Bettler B, Wickman K, Frotscher M, Shigemoto R (2006) Compartment-dependent colocalization of Kir3.2-containing K+ channels and GABAB receptors in hippocampal pyramidal cells. J Neurosci 26(16):4289–4297. https://doi.org/10.1523/JNEUROSCI.4178-05.2006

Lacaille JC, Schwartzkroin PA (1988) Intracellular responses of rat hippocampal granule cells in vitro to discrete applications of norepinephrine. Neurosci Lett 89(2):176–181

Lambert NA, Teyler TJ (1991) Adenosine depresses excitatory but not fast inhibitory synaptic transmission in area CA1 of the rat hippocampus. Neurosci Lett 122(1):50–52

Lauckner JE, Jensen JB, Chen HY, Lu HC, Hille B, Mackie K (2008) GPR55 is a cannabinoid receptor that increases intracellular calcium and inhibits M current. Proc Natl Acad Sci U S A 105(7):2699–2704

Lawrence JJ (2007) Homosynaptic and heterosynaptic modes of endocannabinoid action at hippocampal CCK+ basket cell synapses. J Physiol 578(Pt 1):3–4. https://doi.org/10.1113/jphysiol.2006.123802

Lawrence JJ (2008) Cholinergic control of GABA release: emerging parallels between neocortex and hippocampus. Trends Neurosci 31(7):317–327. https://doi.org/10.1016/j.tins.2008.03.008

Lawrence JJ, Grinspan ZM, Statland JM, McBain CJ (2006a) Muscarinic receptor activation tunes mouse stratum oriens interneurones to amplify spike reliability. J Physiol 571(Pt 3):555–562. https://doi.org/10.1113/jphysiol.2005.103218

Lawrence JJ, Saraga F, Churchill JF, Statland JM, Travis KE, Skinner FK, McBain CJ (2006b) Somatodendritic Kv7/KCNQ/M channels control interspike interval in hippocampal interneurons. J Neurosci 26(47):12325–12338. https://doi.org/10.1523/JNEUROSCI.3521-06.2006

Lawrence JJ, Statland JM, Grinspan ZM, McBain CJ (2006c) Cell type-specific dependence of muscarinic signalling in mouse hippocampal stratum oriens interneurones. J Physiol 570(Pt 3):595–610. https://doi.org/10.1113/jphysiol.2005.100875

Lawrence JJ, Haario H, Stone EF (2015) Presynaptic cholinergic neuromodulation alters the temporal dynamics of short-term depression at parvalbumin-positive basket cell synapses from juvenile CA1 mouse hippocampus. J Neurophysiol 113(7):2408–2419. https://doi.org/10.1152/jn.00167.2014

Leao RN, Mikulovic S, Leao KE, Munguba H, Gezelius H, Enjin A, Patra K, Eriksson A, Loew LM, Tort AB, Kullander K (2012) OLM interneurons differentially modulate CA3 and entorhinal inputs to hippocampal CA1 neurons. Nat Neurosci 15(11):1524–1530. https://doi.org/10.1038/nn.3235

Lebois EP, Thorn C, Edgerton JR, Popiolek M, Xi S (2017) Muscarinic receptor subtype distribution in the central nervous system and relevance to aging and Alzheimer's disease. Neuropharmacology. https://doi.org/10.1016/j.neuropharm.2017.11.018

Ledri M, Sorensen AT, Erdelyi F, Szabo G, Kokaia M (2011) Tuning afferent synapses of hippocampal interneurons by neuropeptide Y. Hippocampus 21(2):198–211. https://doi.org/10.1002/hipo.20740

Lee MG, Chrobak JJ, Sik A, Wiley RG, Buzsaki G (1994) Hippocampal theta activity following selective lesion of the septal cholinergic system. Neuroscience 62(4):1033–1047. https://doi.org/10.1016/0306-4522(94)90341-7

Lee K, Dixon AK, Gonzalez I, Stevens EB, McNulty S, Oles R, Richardson PJ, Pinnock RD, Singh L (1999a) Bombesin-like peptides depolarize rat hippocampal interneurones through interaction with subtype 2 bombesin receptors. J Physiol 518(Pt 3):791–802

Lee K, Dixon AK, Pinnock RD (1999b) Serotonin depolarizes hippocampal interneurones in the rat stratum oriens by interaction with 5HT2 receptors. Neurosci Lett 270(1):56–58

Lee MG, Hassani OK, Alonso A, Jones BE (2005) Cholinergic basal forebrain neurons burst with theta during waking and paradoxical sleep. J Neurosci 25(17):4365–4369. https://doi.org/10.1523/JNEUROSCI.0178-05.2005

Lee SY, Foldy C, Szabadics J, Soltesz I (2011) Cell-type-specific CCK2 receptor signaling underlies the cholecystokinin-mediated selective excitation of hippocampal parvalbumin-positive fast-spiking basket cells. J Neurosci 31(30):10993–11002. https://doi.org/10.1523/JNEUROSCI.1970-11.2011

Lemercier CE, Schulz SB, Heidmann KE, Kovacs R, Gerevich Z (2015) Dopamine D3 receptors inhibit hippocampal gamma oscillations by disturbing CA3 pyramidal cell firing synchrony. Front Pharmacol 6:297. https://doi.org/10.3389/fphar.2015.00297

Leranth C, Frotscher M (1987) Cholinergic innervation of hippocampal GAD- and somatostatin-immunoreactive commissural neurons. J Comp Neurol 261(1):33–47. https://doi.org/10.1002/cne.902610104

Levey AI (1996) Muscarinic acetylcholine receptor expression in memory circuits: implications for treatment of Alzheimer disease. Proc Natl Acad Sci 93(24):13541–13546. https://doi.org/10.1073/pnas.93.24.13541

Levey AI, Edmunds SM, Koliatsos V, Wiley RG, Heilman CJ (1995) Expression of m1-m4 muscarinic acetylcholine receptor proteins in rat hippocampus and regulation by cholinergic innervation. J Neurosci 15(5 Pt 2):4077–4092

Levkovitz Y, Segal M (1997) Serotonin 5-HT1A receptors modulate hippocampal reactivity to afferent stimulation. J Neurosci 17(14):5591–5598

Li S, Cullen WK, Anwyl R, Rowan MJ (2003) Dopamine-dependent facilitation of LTP induction in hippocampal CA1 by exposure to spatial novelty. Nat Neurosci 6(5):526–531. https://doi.org/10.1038/nn1049

Li QH, Nakadate K, Tanaka-Nakadate S, Nakatsuka D, Cui Y, Watanabe Y (2004) Unique expression patterns of 5-HT2A and 5-HT2C receptors in the rat brain during postnatal development: Western blot and immunohistochemical analyses. J Comp Neurol 469(1):128–140. https://doi.org/10.1002/cne.11004

Li Y, Zhong W, Wang D, Feng Q, Liu Z, Zhou J, Jia C, Hu F, Zeng J, Guo Q, Fu L, Luo M (2016) Serotonin neurons in the dorsal raphe nucleus encode reward signals. Nat Commun 7:10503. https://doi.org/10.1038/ncomms10503

Li Q, Bartley AF, Dobrunz LE (2017) Endogenously released neuropeptide Y suppresses hippocampal short-term facilitation and is impaired by stress-induced anxiety. J Neurosci 37(1):23–37. https://doi.org/10.1523/JNEUROSCI.2599-16.2016

Lidov HG, Grzanna R, Molliver ME (1980) The serotonin innervation of the cerebral cortex in the rat – an immunohistochemical analysis. Neuroscience 5(2):207–227

Lin YT, Huang CC, Hsu KS (2012) Oxytocin promotes long-term potentiation by enhancing epidermal growth factor receptor-mediated local translation of protein kinase Mzeta. J Neurosci 32(44):15476–15488. https://doi.org/10.1523/JNEUROSCI.2429-12.2012

Lisman JE, Grace AA (2005) The hippocampal-VTA loop: controlling the entry of information into long-term memory. Neuron 46(5):703–713. https://doi.org/10.1016/j.neuron.2005.05.002
Lopes LV, Cunha RA, Kull B, Fredholm BB, Ribeiro JA (2002) Adenosine A(2A) receptor facilitation of hippocampal synaptic transmission is dependent on tonic A(1) receptor inhibition. Neuroscience 112(2):319–329
Lopez-Bendito G, Sturgess K, Erdelyi F, Szabo G, Molnar Z, Paulsen O (2004) Preferential origin and layer destination of GAD65-GFP cortical interneurons. Cereb Cortex 14(10):1122–1133. https://doi.org/10.1093/cercor/bhh072
Lorincz ML, Adamantidis AR (2017) Monoaminergic control of brain states and sensory processing: existing knowledge and recent insights obtained with optogenetics. Prog Neurobiol 151:237–253. https://doi.org/10.1016/j.pneurobio.2016.09.003
Lovett-Barron M, Kaifosh P, Kheirbek MA, Danielson N, Zaremba JD, Reardon TR, Turi GF, Hen R, Zemelman BV, Losonczy A (2014) Dendritic inhibition in the hippocampus supports fear learning. Science 343(6173):857–863. https://doi.org/10.1126/science.1247485
Loy R, Koziell DA, Lindsey JD, Moore RY (1980) Noradrenergic innervation of the adult rat hippocampal formation. J Comp Neurol 189(4):699–710. https://doi.org/10.1002/cne.901890406
Lucas-Meunier E, Fossier P, Baux G, Amar M (2003) Cholinergic modulation of the cortical neuronal network. Pflugers Arch 446(1):17–29. https://doi.org/10.1007/s00424-002-0999-2
Luo X, McGregor G, Irving AJ, Harvey J (2015) Leptin induces a novel form of NMDA receptor-dependent LTP at hippocampal temporoammonic-CA1 synapses. eNeuro 2(3). https://doi.org/10.1523/ENEURO.0007-15.2015
Luscher C, Jan LY, Stoffel M, Malenka RC, Nicoll RA (1997) G protein-coupled inwardly rectifying K+ channels (GIRKs) mediate postsynaptic but not presynaptic transmitter actions in hippocampal neurons. Neuron 19(3):687–695
Lynch MA, Bliss TV (1986) Noradrenaline modulates the release of [14C]glutamate from dentate but not from CA1/CA3 slices of rat hippocampus. Neuropharmacology 25(5):493–498
Maccaferri G (2005) Stratum oriens horizontal interneurone diversity and hippocampal network dynamics. J Physiol 562(Pt 1):73–80. https://doi.org/10.1113/jphysiol.2004.077081
Maccaferri G, Lacaille JC (2003) Interneuron diversity series: hippocampal interneuron classifications – making things as simple as possible, not simpler. Trends Neurosci 26(10):564–571. https://doi.org/10.1016/j.tins.2003.08.002
Maccaferri G, McBain CJ (1996) The hyperpolarization-activated current (Ih) and its contribution to pacemaker activity in rat CA1 hippocampal stratum oriens-alveus interneurones. J Physiol 497(Pt 1):119–130
Maccaferri G, Toth K, McBain CJ (1998) Target-specific expression of presynaptic mossy fiber plasticity. Science 279(5355):1368–1370. https://doi.org/10.1126/science.279.5355.1368
MacVicar BA, Kerrin JP, Davison JS (1987) Inhibition of synaptic transmission in the hippocampus by cholecystokinin (CCK) and its antagonism by a CCK analog (CCK27-33). Brain Res 406(1-2):130–135
Madison DV, McQuiston AR (2006) Toward a unified hypothesis of interneuronal modulation. J Physiol 570(Pt 3):435. https://doi.org/10.1113/jphysiol.2005.103937
Madison DV, Nicoll RA (1982) Noradrenaline blocks accommodation of pyramidal cell discharge in the hippocampus. Nature 299(5884):636–638
Madison DV, Nicoll RA (1986) Actions of noradrenaline recorded intracellularly in rat hippocampal CA1 pyramidal neurones, in vitro. J Physiol 372:221–244
Madison DV, Nicoll RA (1988a) Enkephalin hyperpolarizes interneurones in the rat hippocampus. J Physiol 398:123–130
Madison DV, Nicoll RA (1988b) Norepinephrine decreases synaptic inhibition in the rat hippocampus. Brain Res 442(1):131–138
Madison DV, Lancaster B, Nicoll RA (1987) Voltage clamp analysis of cholinergic action in the hippocampus. J Neurosci 7(3):733–741
Maeda T, Kaneko S, Satoh M (1994) Inhibitory influence via 5-HT3 receptors on the induction of LTP in mossy fiber-CA3 system of guinea-pig hippocampal slices. Neurosci Res 18(4):277–282

Magloczky Z, Acsady L, Freund TF (1994) Principal cells are the postsynaptic targets of supramammillary afferents in the hippocampus of the rat. Hippocampus 4(3):322–334. https://doi.org/10.1002/hipo.450040316

Maity S, Rah S, Sonenberg N, Gkogkas CG, Nguyen PV (2015) Norepinephrine triggers metaplasticity of LTP by increasing translation of specific mRNAs. Learn Mem 22(10):499–508. https://doi.org/10.1101/lm.039222.115

Maity S, Jarome TJ, Blair J, Lubin FD, Nguyen PV (2016) Noradrenaline goes nuclear: epigenetic modifications during long-lasting synaptic potentiation triggered by activation of beta-adrenergic receptors. J Physiol 594(4):863–881. https://doi.org/10.1113/JP271432

Makara JK, Katona I, Nyiri G, Nemeth B, Ledent C, Watanabe M, de Vente J, Freund TF, Hajos N (2007) Involvement of nitric oxide in depolarization-induced suppression of inhibition in hippocampal pyramidal cells during activation of cholinergic receptors. J Neurosci 27(38):10211–10222

Malenka RC, Nicoll RA (1986) Dopamine decreases the calcium-activated afterhyperpolarization in hippocampal CA1 pyramidal cells. Brain Res 379(2):210–215

Manaker S, Winokur A, Rostene WH, Rainbow TC (1985) Autoradiographic localization of thyrotropin-releasing hormone receptors in the rat central nervous system. J Neurosci 5(1):167–174

Manseau F, Goutagny R, Danik M, Williams S (2008) The hippocamposeptal pathway generates rhythmic firing of GABAergic neurons in the medial septum and diagonal bands: an investigation using a complete septohippocampal preparation in vitro. J Neurosci 28(15):4096–4107. https://doi.org/10.1523/JNEUROSCI.0247-08.2008

Marder E (2012) Neuromodulation of neuronal circuits: back to the future. Neuron 76(1):1–11. https://doi.org/10.1016/j.neuron.2012.09.010

Markram H, Segal M (1990a) Acetylcholine potentiates responses to N-methyl-D-aspartate in the rat hippocampus. Neurosci Lett 113(1):62–65

Markram H, Segal M (1990b) Long-lasting facilitation of excitatory postsynaptic potentials in the rat hippocampus by acetylcholine. J Physiol 427:381–393

Maroso M, Szabo GG, Kim HK, Alexander A, Bui AD, Lee SH, Lutz B, Soltesz I (2016) Cannabinoid control of learning and memory through HCN channels. Neuron 89(5):1059–1073. https://doi.org/10.1016/j.neuron.2016.01.023

Marsicano G, Lutz B (1999) Expression of the cannabinoid receptor CB1 in distinct neuronal subpopulations in the adult mouse forebrain. Eur J Neurosci 11(12):4213–4225

Martin LA, Wei DS, Alger BE (2001) Heterogeneous susceptibility of GABA(A) receptor-mediated IPSCs to depolarization-induced suppression of inhibition in rat hippocampus. J Physiol 532(Pt 3):685–700

Martinez-Mir MI, Pollard H, Moreau J, Arrang JM, Ruat M, Traiffort E, Schwartz JC, Palacios JM (1990) Three histamine receptors (H1, H2 and H3) visualized in the brain of human and non-human primates. Brain Res 526(2):322–327

Matsumoto M, Kojima T, Togashi H, Mori K, Ohashi S, Ueno K, Yoshioka M (2002) Differential characteristics of endogenous serotonin-mediated synaptic transmission in the hippocampal CA1 and CA3 fields of anaesthetized rats. Naunyn Schmiedebergs Arch Pharmacol 366(6):570–577. https://doi.org/10.1007/s00210-002-0634-y

Matthes H, Boschert U, Amlaiky N, Grailhe R, Plassat JL, Muscatelli F, Mattei MG, Hen R (1993) Mouse 5-hydroxytryptamine5A and 5-hydroxytryptamine5B receptors define a new family of serotonin receptors: cloning, functional expression, and chromosomal localization. Mol Pharmacol 43(3):313–319

Mattis J, Brill J, Evans S, Lerner TN, Davidson TJ, Hyun M, Ramakrishnan C, Deisseroth K, Huguenard JR (2014) Frequency-dependent, cell type-divergent signaling in the hippocamposeptal projection. J Neurosci 34(35):11769–11780. https://doi.org/10.1523/JNEUROSCI.5188-13.2014

McCormick DA, Williamson A (1991) Modulation of neuronal firing mode in cat and guinea pig LGNd by histamine: possible cellular mechanisms of histaminergic control of arousal. J Neurosci 11(10):3188–3199

McDermott CM, Schrader LA (2011) Activation of kappa opioid receptors increases intrinsic excitability of dentate gyrus granule cells. J Physiol 589(Pt 14):3517–3532. https://doi.org/10.1113/jphysiol.2011.211623

McMahon LL, Kauer JA (1997) Hippocampal interneurons are excited via serotonin-gated ion channels. J Neurophysiol 78(5):2493–2502. https://doi.org/10.1152/jn.1997.78.5.2493

McNamara CG, Dupret D (2017) Two sources of dopamine for the hippocampus. Trends Neurosci 40(7):383–384. https://doi.org/10.1016/j.tins.2017.05.005

McQuiston AR (2014a) Acetylcholine release and inhibitory interneuron activity in hippocampal CA1. Front Synaptic Neurosci 6:20. https://doi.org/10.3389/fnsyn.2014.00020

McQuiston AR (2014b) Slow synaptic transmission in the central nervous system. In: Nicotinic receptors. pp 201–215. https://doi.org/10.1007/978-1-4939-1167-7_10

McQuiston AR, Madison DV (1999a) Muscarinic receptor activity has multiple effects on the resting membrane potentials of CA1 hippocampal interneurons. J Neurosci 19(14):5693–5702

McQuiston AR, Madison DV (1999b) Muscarinic receptor activity induces an afterdepolarization in a subpopulation of hippocampal CA1 interneurons. J Neurosci 19(14):5703–5710

McQuiston AR, Madison DV (1999c) Nicotinic receptor activation excites distinct subtypes of interneurons in the rat hippocampus. J Neurosci 19(8):2887–2896

McQuiston AR, Petrozzino JJ, Connor JA, Colmers WF (1996) Neuropeptide Y1 receptors inhibit N-type calcium currents and reduce transient calcium increases in rat dentate granule cells. J Neurosci 16(4):1422–1429

Melzer S, Michael M, Caputi A, Eliava M, Fuchs EC, Whittington MA, Monyer H (2012) Long-range-projecting GABAergic neurons modulate inhibition in hippocampus and entorhinal cortex. Science 335(6075):1506–1510. https://doi.org/10.1126/science.1217139

Mercer JG, Hoggard N, Williams LM, Lawrence CB, Hannah LT, Trayhurn P (1996) Localization of leptin receptor mRNA and the long form splice variant (Ob-Rb) in mouse hypothalamus and adjacent brain regions by in situ hybridization. FEBS Lett 387(2-3):113–116

Miettinen R, Freund TF (1992) Neuropeptide Y-containing interneurons in the hippocampus receive synaptic input from median raphe and GABAergic septal afferents. Neuropeptides 22(3):185–193

Mikulovic S, Restrepo CE, Hilscher MM, Kullander K, Leao RN (2015) Novel markers for OLM interneurons in the hippocampus. Front Cell Neurosci 9:201. https://doi.org/10.3389/fncel.2015.00201

Miller KK, Hoffer A, Svoboda KR, Lupica CR (1997) Cholecystokinin increases GABA release by inhibiting a resting K+ conductance in hippocampal interneurons. J Neurosci 17(13):4994–5003

Milligan G (2007) G protein-coupled receptor dimerisation: molecular basis and relevance to function. Biochim Biophys Acta 1768(4):825–835. https://doi.org/10.1016/j.bbamem.2006.09.021

Milner TA, Bacon CE (1989a) GABAergic neurons in the rat hippocampal formation: ultrastructure and synaptic relationships with catecholaminergic terminals. J Neurosci 9(10):3410–3427

Milner TA, Bacon CE (1989b) Ultrastructural localization of tyrosine hydroxylase-like immunoreactivity in the rat hippocampal formation. J Comp Neurol 281(3):479–495. https://doi.org/10.1002/cne.902810311

Milner TA, Lee A, Aicher SA, Rosin DL (1998) Hippocampal alpha2a-adrenergic receptors are located predominantly presynaptically but are also found postsynaptically and in selective astrocytes. J Comp Neurol 395(3):310–327

Milner TA, Shah P, Pierce JP (2000) beta-adrenergic receptors primarily are located on the dendrites of granule cells and interneurons but also are found on astrocytes and a few presynaptic profiles in the rat dentate gyrus. Synapse 36(3):178–193. https://doi.org/10.1002/(SICI)1098-2396(20000601)36:3<178::AID-SYN3>3.0.CO;2-6

Mitchell JB, Miller K, Dunwiddie TV (1993) Adenosine-induced suppression of synaptic responses and the initiation and expression of long-term potentiation in the CA1 region of the hippocampus. Hippocampus 3(1):77–86. https://doi.org/10.1002/hipo.450030108

Miyoshi G, Fishell G (2006) Directing neuron-specific transgene expression in the mouse CNS. Curr Opin Neurobiol 16(5):577–584. https://doi.org/10.1016/j.conb.2006.08.013 S0959-4388(06)00118-8 [pii]

Mlinar B, Corradetti R (2017) Differential modulation of CA1 impulse flow by endogenous serotonin along the hippocampal longitudinal axis. Hippocampus 28:217–225. https://doi.org/10.1002/hipo.22825

Mlinar B, Mascalchi S, Mannaioni G, Morini R, Corradetti R (2006) 5-HT4 receptor activation induces long-lasting EPSP-spike potentiation in CA1 pyramidal neurons. Eur J Neurosci 24(3):719–731. https://doi.org/10.1111/j.1460-9568.2006.04949.x

Mochizuki T, Okakura-Mochizuki K, Horii A, Yamamoto Y, Yamatodani A (1994) Histaminergic modulation of hippocampal acetylcholine release in vivo. J Neurochem 62(6):2275–2282

Monday HR, Castillo PE (2017) Closing the gap: long-term presynaptic plasticity in brain function and disease. Curr Opin Neurobiol 45:106–112. https://doi.org/10.1016/j.conb.2017.05.011

Monday HR, Younts TJ, Castillo PE (2018) Long-term plasticity of neurotransmitter release: emerging mechanisms and contributions to brain function and disease. Annu Rev Neurosci 41:299–322. https://doi.org/10.1146/annurev-neuro-080317-062155

Monyer H, Markram H (2004) Interneuron diversity series: molecular and genetic tools to study GABAergic interneuron diversity and function. Trends Neurosci 27(2):90–97. https://doi.org/10.1016/j.tins.2003.12.008

Moore RY, Halaris AE (1975) Hippocampal innervation by serotonin neurons of the midbrain raphe in the rat. J Comp Neurol 164(2):171–183. https://doi.org/10.1002/cne.901640203

Moore SD, Madamba SG, Joels M, Siggins GR (1988) Somatostatin augments the M-current in hippocampal neurons. Science 239(4837):278–280

Moore SD, Madamba SG, Schweitzer P, Siggins GR (1994) Voltage-dependent effects of opioid peptides on hippocampal CA3 pyramidal neurons in vitro. J Neurosci 14(2):809–820

Morales M, Backman C (2002) Coexistence of serotonin 3 (5-HT3) and CB1 cannabinoid receptors in interneurons of hippocampus and dentate gyrus. Hippocampus 12(6):756–764. https://doi.org/10.1002/hipo.10025

Morales M, Bloom FE (1997) The 5-HT3 receptor is present in different subpopulations of GABAergic neurons in the rat telencephalon. J Neurosci 17(9):3157–3167

Morales M, Battenberg E, de Lecea L, Bloom FE (1996) The type 3 serotonin receptor is expressed in a subpopulation of GABAergic neurons in the rat neocortex and hippocampus. Brain Res 731(1–2):199–202

Morales M, Hein K, Vogel Z (2008) Hippocampal interneurons co-express transcripts encoding the alpha7 nicotinic receptor subunit and the cannabinoid receptor 1. Neuroscience 152(1):70–81. https://doi.org/10.1016/j.neuroscience.2007.12.019

Mori M, Heuss C, Gahwiler BH, Gerber U (2001) Fast synaptic transmission mediated by P2X receptors in CA3 pyramidal cells of rat hippocampal slice cultures. J Physiol 535(Pt 1):115–123

Morton RA, Davies CH (1997) Regulation of muscarinic acetylcholine receptor-mediated synaptic responses by adenosine receptors in the rat hippocampus. J Physiol 502(Pt 1):75–90

Morton RA, Manuel NA, Bulters DO, Cobb SR, Davies CH (2001) Regulation of muscarinic acetylcholine receptor-mediated synaptic responses by GABA(B) receptors in the rat hippocampus. J Physiol 535(Pt 3):757–766

Mrzljak L, Bergson C, Pappy M, Huff R, Levenson R, Goldman-Rakic PS (1996) Localization of dopamine D4 receptors in GABAergic neurons of the primate brain. Nature 381(6579):245–248. https://doi.org/10.1038/381245a0

Muhlethaler M, Charpak S, Dreifuss JJ (1984) Contrasting effects of neurohypophysial peptides on pyramidal and non-pyramidal neurones in the rat hippocampus. Brain Res 308(1):97–107

Muller C, Remy S (2017) Septo-hippocampal interaction. Cell Tissue Res. https://doi.org/10.1007/s00441-017-2745-2

Murchison CF, Zhang XY, Zhang WP, Ouyang M, Lee A, Thomas SA (2004) A distinct role for norepinephrine in memory retrieval. Cell 117(1):131–143

Muzzio IA, Kentros C, Kandel E (2009) What is remembered? Role of attention on the encoding and retrieval of hippocampal representations. J Physiol 587(Pt 12):2837–2854. https://doi.org/10.1113/jphysiol.2009.172445

Nagode DA, Tang AH, Karson MA, Klugmann M, Alger BE (2011) Optogenetic release of ACh induces rhythmic bursts of perisomatic IPSCs in hippocampus. PLoS One 6(11):e27691. https://doi.org/10.1371/journal.pone.0027691

Neu A, Foldy C, Soltesz I (2007) Postsynaptic origin of CB1-dependent tonic inhibition of GABA release at cholecystokinin-positive basket cell to pyramidal cell synapses in the CA1 region of the rat hippocampus. J Physiol 578(Pt 1):233–247. https://doi.org/10.1113/jphysiol.2006.115691

Nicholas AP, Hokfelt T, Pieribone VA (1996) The distribution and significance of CNS adrenoceptors examined with in situ hybridization. Trends Pharmacol Sci 17(7):245–255

Nicoll RA (1988) The coupling of neurotransmitter receptors to ion channels in the brain. Science 241(4865):545–551

Nicoll RA, Malenka RC, Kauer JA (1990) Functional comparison of neurotransmitter receptor subtypes in mammalian central nervous system. Physiol Rev 70(2):513–565. https://doi.org/10.1152/physrev.1990.70.2.513

Nieto-Alamilla G, Marquez-Gomez R, Garcia-Galvez AM, Morales-Figueroa GE, Arias-Montano JA (2016) The Histamine H3 receptor: structure, pharmacology, and function. Mol Pharmacol 90(5):649–673. https://doi.org/10.1124/mol.116.104752

Nobili A, Latagliata EC, Viscomi MT, Cavallucci V, Cutuli D, Giacovazzo G, Krashia P, Rizzo FR, Marino R, Federici M, De Bartolo P, Aversa D, Dell'Acqua MC, Cordella A, Sancandi M, Keller F, Petrosini L, Puglisi-Allegra S, Mercuri NB, Coccurello R, Berretta N, D'Amelio M (2017) Dopamine neuronal loss contributes to memory and reward dysfunction in a model of Alzheimer's disease. Nat Commun 8:14727. https://doi.org/10.1038/ncomms14727

Noriyama Y, Ogawa Y, Yoshino H, Yamashita M, Kishimoto T (2006) Dopamine profoundly suppresses excitatory transmission in neonatal rat hippocampus via phosphatidylinositol-linked D1-like receptor. Neuroscience 138(2):475–485. https://doi.org/10.1016/j.neuroscience.2005.11.032

Nozaki K, Kubo R, Furukawa Y (2016) Serotonin modulates the excitatory synaptic transmission in the dentate granule cells. J Neurophysiol 115(6):2997–3007. https://doi.org/10.1152/jn.00064.2016

Ogier R, Raggenbass M (2003) Action of tachykinins in the rat hippocampus: modulation of inhibitory synaptic transmission. Eur J Neurosci 17(12):2639–2647

Ogier R, Wrobel LJ, Raggenbass M (2008) Action of tachykinins in the hippocampus: facilitation of inhibitory drive to GABAergic interneurons. Neuroscience 156(3):527–536. https://doi.org/10.1016/j.neuroscience.2008.08.001

Ohno-Shosaku T, Tsubokawa H, Mizushima I, Yoneda N, Zimmer A, Kano M (2002) Presynaptic cannabinoid sensitivity is a major determinant of depolarization-induced retrograde suppression at hippocampal synapses. J Neurosci 22(10):3864–3872

Oka S, Nakajima K, Yamashita A, Kishimoto S, Sugiura T (2007) Identification of GPR55 as a lysophosphatidylinositol receptor. Biochem Biophys Res Commun 362(4):928–934. https://doi.org/10.1016/j.bbrc.2007.08.078

Okuhara DY, Beck SG (1994) 5-HT1A receptor linked to inward-rectifying potassium current in hippocampal CA3 pyramidal cells. J Neurophysiol 71(6):2161–2167. https://doi.org/10.1152/jn.1994.71.6.2161

Oleskevich S, Descarries L (1990) Quantified distribution of the serotonin innervation in adult rat hippocampus. Neuroscience 34(1):19–33

Oleskevich S, Descarries L, Lacaille JC (1989) Quantified distribution of the noradrenaline innervation in the hippocampus of adult rat. J Neurosci 9(11):3803–3815

Oleskevich S, Descarries L, Watkins KC, Seguela P, Daszuta A (1991) Ultrastructural features of the serotonin innervation in adult rat hippocampus: an immunocytochemical description in single and serial thin sections. Neuroscience 42(3):777–791

Onaivi ES, Ishiguro H, Gong JP, Patel S, Perchuk A, Meozzi PA, Myers L, Mora Z, Tagliaferro P, Gardner E, Brusco A, Akinshola BE, Liu QR, Hope B, Iwasaki S, Arinami T, Teasenfitz L, Uhl GR (2006) Discovery of the presence and functional expression of cannabinoid CB2 receptors in brain. Ann N Y Acad Sci 1074:514–536

Otis TS, De Koninck Y, Mody I (1993) Characterization of synaptically elicited GABAB responses using patch-clamp recordings in rat hippocampal slices. J Physiol 463:391–407

Otmakhova NA, Lisman JE (1996) D1/D5 dopamine receptor activation increases the magnitude of early long-term potentiation at CA1 hippocampal synapses. J Neurosci 16(23):7478–7486

Otmakhova NA, Lisman JE (1998) D1/D5 dopamine receptors inhibit depotentiation at CA1 synapses via cAMP-dependent mechanism. J Neurosci 18(4):1270–1279

Otmakhova NA, Lisman JE (1999) Dopamine selectively inhibits the direct cortical pathway to the CA1 hippocampal region. J Neurosci 19(4):1437–1445

Otmakhova NA, Lisman JE (2000) Dopamine, serotonin, and noradrenaline strongly inhibit the direct perforant path-CA1 synaptic input, but have little effect on the Schaffer collateral input. Ann N Y Acad Sci 911:462–464

Otmakhova NA, Lewey J, Asrican B, Lisman JE (2005) Inhibition of perforant path input to the CA1 region by serotonin and noradrenaline. J Neurophysiol 94(2):1413–1422. https://doi.org/10.1152/jn.00217.2005

Overstreet-Wadiche L, McBain CJ (2015) Neurogliaform cells in cortical circuits. Nat Rev Neurosci 16(8):458–468. https://doi.org/10.1038/nrn3969

Owen SF, Tuncdemir SN, Bader PL, Tirko NN, Fishell G, Tsien RW (2013) Oxytocin enhances hippocampal spike transmission by modulating fast-spiking interneurons. Nature 500(7463):458–462. https://doi.org/10.1038/nature12330

Pabst M, Braganza O, Dannenberg H, Hu W, Pothmann L, Rosen J, Mody I, van Loo K, Deisseroth K, Becker AJ, Schoch S, Beck H (2016) Astrocyte intermediaries of septal cholinergic modulation in the hippocampus. Neuron 90(4):853–865. https://doi.org/10.1016/j.neuron.2016.04.003

Packard MG, Cahill L, McGaugh JL (1994) Amygdala modulation of hippocampal-dependent and caudate nucleus-dependent memory processes. Proc Natl Acad Sci U S A 91(18):8477–8481

Pagotto U, Marsicano G, Cota D, Lutz B, Pasquali R (2006) The emerging role of the endocannabinoid system in endocrine regulation and energy balance. Endocr Rev 27(1):73–100

Palacios JM, Wamsley JK, Kuhar MJ (1981) The distribution of histamine H1-receptors in the rat brain: an autoradiographic study. Neuroscience 6(1):15–37

Pankratov Y, Castro E, Miras-Portugal MT, Krishtal O (1998) A purinergic component of the excitatory postsynaptic current mediated by P2X receptors in the CA1 neurons of the rat hippocampus. Eur J Neurosci 10(12):3898–3902

Pankratov YV, Lalo UV, Krishtal OA (2002) Role for P2X receptors in long-term potentiation. J Neurosci 22(19):8363–8369

Pankratov Y, Lalo U, Verkhratsky A, North RA (2006) Vesicular release of ATP at central synapses. Pflugers Arch 452(5):589–597. https://doi.org/10.1007/s00424-006-0061-x

Pankratov Y, Lalo U, Krishtal OA, Verkhratsky A (2009) P2X receptors and synaptic plasticity. Neuroscience 158(1):137–148. https://doi.org/10.1016/j.neuroscience.2008.03.076

Panula P, Nuutinen S (2013) The histaminergic network in the brain: basic organization and role in disease. Nat Rev Neurosci 14(7):472–487. https://doi.org/10.1038/nrn3526

Panula P, Yang HY, Costa E (1984) Histamine-containing neurons in the rat hypothalamus. Proc Natl Acad Sci U S A 81(8):2572–2576

Panula P, Pirvola U, Auvinen S, Airaksinen MS (1989) Histamine-immunoreactive nerve fibers in the rat brain. Neuroscience 28(3):585–610

Panula P, Chazot PL, Cowart M, Gutzmer R, Leurs R, Liu WL, Stark H, Thurmond RL, Haas HL (2015) International Union of Basic and Clinical Pharmacology. XCVIII. Histamine Receptors. Pharmacol Rev 67(3):601–655. https://doi.org/10.1124/pr.114.010249

Papay R, Gaivin R, Jha A, McCune DF, McGrath JC, Rodrigo MC, Simpson PC, Doze VA, Perez DM (2006) Localization of the mouse alpha1A-adrenergic receptor (AR) in the brain: alpha1AAR is expressed in neurons, GABAergic interneurons, and NG2 oligodendrocyte progenitors. J Comp Neurol 497(2):209–222. https://doi.org/10.1002/cne.20992

Parfitt KD, Hoffer BJ, Browning MD (1991) Norepinephrine and isoproterenol increase the phosphorylation of synapsin I and synapsin II in dentate slices of young but not aged Fisher 344 rats. Proc Natl Acad Sci U S A 88(6):2361–2365

Parfitt KD, Doze VA, Madison DV, Browning MD (1992) Isoproterenol increases the phosphorylation of the synapsins and increases synaptic transmission in dentate gyrus, but not in area CA1, of the hippocampus. Hippocampus 2(1):59–64. https://doi.org/10.1002/hipo.450020108

Parra P, Gulyás AI, Miles R (1998) How many subtypes of inhibitory cells in the hippocampus? Neuron 20(5):983–993. https://doi.org/10.1016/s0896-6273(00)80479-1

Pascual O, Casper KB, Kubera C, Zhang J, Revilla-Sanchez R, Sul JY, Takano H, Moss SJ, McCarthy K, Haydon PG (2005) Astrocytic purinergic signaling coordinates synaptic networks. Science 310(5745):113–116. https://doi.org/10.1126/science.1116916

Passani MB, Giannoni P, Bucherelli C, Baldi E, Blandina P (2007) Histamine in the brain: beyond sleep and memory. Biochem Pharmacol 73(8):1113–1122. https://doi.org/10.1016/j.bcp.2006.12.002

Paukert M, Agarwal A, Cha J, Doze VA, Kang JU, Bergles DE (2014) Norepinephrine controls astroglial responsiveness to local circuit activity. Neuron 82(6):1263–1270. https://doi.org/10.1016/j.neuron.2014.04.038

Pavlides C, Greenstein YJ, Grudman M, Winson J (1988) Long-term potentiation in the dentate gyrus is induced preferentially on the positive phase of theta-rhythm. Brain Res 439(1–2):383–387

Pedarzani P, Storm JF (1993) PKA mediates the effects of monoamine transmitters on the K+ current underlying the slow spike frequency adaptation in hippocampal neurons. Neuron 11(6):1023–1035

Pedarzani P, Storm JF (1995) Dopamine modulates the slow Ca(2+)-activated K+ current IAHP via cyclic AMP-dependent protein kinase in hippocampal neurons. J Neurophysiol 74(6):2749–2753. https://doi.org/10.1152/jn.1995.74.6.2749

Pedarzani P, Storm JF (1996) Interaction between alpha- and beta-adrenergic receptor agonists modulating the slow Ca(2+)-activated K+ current IAHP in hippocampal neurons. Eur J Neurosci 8(10):2098–2110

Peddie CJ, Davies HA, Colyer FM, Stewart MG, Rodriguez JJ (2008) Dendritic colocalisation of serotonin1B receptors and the glutamate NMDA receptor subunit NR1 within the hippocampal dentate gyrus: an ultrastructural study. J Chem Neuroanat 36(1):17–26. https://doi.org/10.1016/j.jchemneu.2008.05.001

Pehrson AL, Sanchez C (2014) Serotonergic modulation of glutamate neurotransmission as a strategy for treating depression and cognitive dysfunction. CNS Spectr 19(2):121–133. https://doi.org/10.1017/S1092852913000540

Pernia-Andrade AJ, Jonas P (2014) Theta-gamma-modulated synaptic currents in hippocampal granule cells in vivo define a mechanism for network oscillations. Neuron 81(1):140–152. https://doi.org/10.1016/j.neuron.2013.09.046

Petersen AV, Jensen CS, Crepel V, Falkerslev M, Perrier JF (2017) Serotonin regulates the firing of principal cells of the subiculum by inhibiting a T-type Ca(2+) current. Front Cell Neurosci 11:60. https://doi.org/10.3389/fncel.2017.00060

Petilla Interneuron Nomenclature Group, Ascoli GA, Alonso-Nanclares L, Anderson SA, Barrionuevo G, Benavides-Piccione R, Burkhalter A, Buzsaki G, Cauli B, Defelipe J, Fairen A, Feldmeyer D, Fishell G, Fregnac Y, Freund TF, Gardner D, Gardner EP, Goldberg JH, Helmstaedter M, Hestrin S, Karube F, Kisvarday ZF, Lambolez B, Lewis DA, Marin O, Markram H, Munoz A, Packer A, Petersen CC, Rockland KS, Rossier J, Rudy B, Somogyi P, Staiger JF, Tamas G, Thomson AM, Toledo-Rodriguez M, Wang Y, West DC, Yuste R (2008) Petilla terminology: nomenclature of features of GABAergic interneurons of the cerebral cortex. Nat Rev Neurosci 9(7):557–568. https://doi.org/10.1038/nrn2402

Piguet P, Galvan M (1994) Transient and long-lasting actions of 5-HT on rat dentate gyrus neurones in vitro. J Physiol 481(Pt 3):629–639

Pillot C, Heron A, Cochois V, Tardivel-Lacombe J, Ligneau X, Schwartz JC, Arrang JM (2002) A detailed mapping of the histamine H(3) receptor and its gene transcripts in rat brain. Neuroscience 114(1):173–193

Pinault D (1996) A novel single-cell staining procedure performed in vivo under electrophysiological control: morpho-functional features of juxtacellularly labeled thalamic cells and other central neurons with biocytin or Neurobiotin. J Neurosci Methods 65(2):113–136 0165027095001441 [pii]

Pitler TA, Alger BE (1992a) Cholinergic excitation of GABAergic interneurons in the rat hippocampal slice. J Physiol 450:127–142

Pitler TA, Alger BE (1992b) Postsynaptic spike firing reduces synaptic GABAA responses in hippocampal pyramidal cells. J Neurosci 12(10):4122–4132

Pittman QJ, Siggins GR (1981) Somatostatin hyperpolarizes hippocampal pyramidal cells in vitro. Brain Res 221(2):402–408 0006-8993(81)90791-5 [pii]

Pollard H, Moreau J, Arrang JM, Schwartz JC (1993) A detailed autoradiographic mapping of histamine H3 receptors in rat brain areas. Neuroscience 52(1):169–189

Pompeiano M, Palacios JM, Mengod G (1992) Distribution and cellular localization of mRNA coding for 5-HT1A receptor in the rat brain: correlation with receptor binding. J Neurosci 12(2):440–453

Porter JT, Cauli B, Tsuzuki K, Lambolez B, Rossier J, Audinat E (1999) Selective excitation of subtypes of neocortical interneurons by nicotinic receptors. J Neurosci 19(13):5228–5235

Power JM, Sah P (2002) Nuclear calcium signaling evoked by cholinergic stimulation in hippocampal CA1 pyramidal neurons. J Neurosci 22(9):3454–3462 20026335

Pugliese AM, Passani MB, Corradetti R (1998) Effect of the selective 5-HT1A receptor antagonist WAY 100635 on the inhibition of e.p.s.ps produced by 5-HT in the CA1 region of rat hippocampal slices. Br J Pharmacol 124(1):93–100. https://doi.org/10.1038/sj.bjp.0701807

Puighermanal E, Biever A, Espallergues J, Gangarossa G, De Bundel D, Valjent E (2015) drd2-cre:ribotag mouse line unravels the possible diversity of dopamine d2 receptor-expressing cells of the dorsal mouse hippocampus. Hippocampus 25(7):858–875. https://doi.org/10.1002/hipo.22408

Puighermanal E, Cutando L, Boubaker-Vitre J, Honore E, Longueville S, Herve D, Valjent E (2017) Anatomical and molecular characterization of dopamine D1 receptor-expressing neurons of the mouse CA1 dorsal hippocampus. Brain Struct Funct 222(4):1897–1911. https://doi.org/10.1007/s00429-016-1314-x

Qian J, Saggau P (1997) Presynaptic inhibition of synaptic transmission in the rat hippocampus by activation of muscarinic receptors: involvement of presynaptic calcium influx. Br J Pharmacol 122(3):511–519. https://doi.org/10.1038/sj.bjp.0701400

Qiu C, Zeyda T, Johnson B, Hochgeschwender U, de Lecea L, Tallent MK (2008) Somatostatin receptor subtype 4 couples to the M-current to regulate seizures. J Neurosci 28(14):3567–3576. https://doi.org/10.1523/JNEUROSCI.4679-07.2008

Radcliffe KA, Dani JA (1998) Nicotinic stimulation produces multiple forms of increased glutamatergic synaptic transmission. J Neurosci 18(18):7075–7083

Raggenbass M (2001) Vasopressin- and oxytocin-induced activity in the central nervous system: electrophysiological studies using in-vitro systems. Prog Neurobiol 64(3):307–326

Ramanathan G, Cilz NI, Kurada L, Hu B, Wang X, Lei S (2012) Vasopressin facilitates GABAergic transmission in rat hippocampus via activation of V(1A) receptors. Neuropharmacology 63(7):1218–1226. https://doi.org/10.1016/j.neuropharm.2012.07.043

Rancz EA, Ishikawa T, Duguid I, Chadderton P, Mahon S, Hausser M (2007) High-fidelity transmission of sensory information by single cerebellar mossy fibre boutons. Nature 450(7173):1245–1248. https://doi.org/10.1038/nature05995 nature05995 [pii]

Raza SA, Albrecht A, Caliskan G, Muller B, Demiray YE, Ludewig S, Meis S, Faber N, Hartig R, Schraven B, Lessmann V, Schwegler H, Stork O (2017) HIPP neurons in the dentate gyrus mediate the cholinergic modulation of background context memory salience. Nat Commun 8(1):189. https://doi.org/10.1038/s41467-017-00205-3

Reece LJ, Schwartzkroin PA (1991) Effects of cholinergic agonists on two non-pyramidal cell types in rat hippocampal slices. Brain Res 566(1–2):115–126

Rezai X, Kieffer BL, Roux MJ, Massotte D (2013) Delta opioid receptors regulate temporoammonic-activated feedforward inhibition to the mouse CA1 hippocampus. PLoS One 8(11):e79081. https://doi.org/10.1371/journal.pone.0079081

Richter-Levin G, Segal M (1996) Serotonin, aging and cognitive functions of the hippocampus. Rev Neurosci 7(2):103–113

Roerig B, Nelson DA, Katz LC (1997) Fast synaptic signaling by nicotinic acetylcholine and serotonin 5-HT3 receptors in developing visual cortex. J Neurosci 17(21):8353–8362

Rombo DM, Dias RB, Duarte ST, Ribeiro JA, Lamsa KP, Sebastiao AM (2016a) Adenosine A1 receptor suppresses Tonic GABAA receptor currents in hippocampal pyramidal cells and in a defined subpopulation of interneurons. Cereb Cortex 26(3):1081–1095. https://doi.org/10.1093/cercor/bhu288

Rombo DM, Ribeiro JA, Sebastiao AM (2016b) Hippocampal GABAergic transmission: a new target for adenosine control of excitability. J Neurochem 139(6):1056–1070. https://doi.org/10.1111/jnc.13872

Romo-Parra H, Aceves J, Gutierrez R (2005) Tonic modulation of inhibition by dopamine D4 receptors in the rat hippocampus. Hippocampus 15(2):254–259. https://doi.org/10.1002/hipo.20049

Ropert N, Guy N (1991) Serotonin facilitates GABAergic transmission in the CA1 region of rat hippocampus in vitro. J Physiol 441:121–136

Rosen ZB, Cheung S, Siegelbaum SA (2015) Midbrain dopamine neurons bidirectionally regulate CA3-CA1 synaptic drive. Nat Neurosci 18(12):1763–1771. https://doi.org/10.1038/nn.4152

Rouse ST, Marino MJ, Potter LT, Conn PJ, Levey AI (1999) Muscarinic receptor subtypes involved in hippocampal circuits. Life Sci 64(6-7):501–509. https://doi.org/10.1016/s0024-3205(98)00594-3

Rowan MJM, Christie JM (2017) Rapid state-dependent alteration in Kv3 channel availability drives flexible synaptic signaling dependent on somatic subthreshold depolarization. Cell Rep 18(8):2018–2029. https://doi.org/10.1016/j.celrep.2017.01.068

Ruat M, Traiffort E, Arrang JM, Tardivel-Lacombe J, Diaz J, Leurs R, Schwartz JC (1993) A novel rat serotonin (5-HT6) receptor: molecular cloning, localization and stimulation of cAMP accumulation. Biochem Biophys Res Commun 193(1):268–276

Rudy B, Fishell G, Lee S, Hjerling-Leffler J (2011) Three groups of interneurons account for nearly 100% of neocortical GABAergic neurons. Dev Neurobiol 71(1):45–61. https://doi.org/10.1002/dneu.20853

Ryberg E, Larsson N, Sjogren S, Hjorth S, Hermansson NO, Leonova J, Elebring T, Nilsson K, Drmota T, Greasley PJ (2007) The orphan receptor GPR55 is a novel cannabinoid receptor. Br J Pharmacol 152(7):1092–1101

Sakurai O, Kosaka T (2007) Nonprincipal neurons and CA2 pyramidal cells, but not mossy cells are immunoreactive for calcitonin gene-related peptide in the mouse hippocampus. Brain Res 1186:129–143

Samuels BA, Anacker C, Hu A, Levinstein MR, Pickenhagen A, Tsetsenis T, Madronal N, Donaldson ZR, Drew LJ, Dranovsky A, Gross CT, Tanaka KF, Hen R (2015) 5-HT1A receptors on mature dentate gyrus granule cells are critical for the antidepressant response. Nat Neurosci 18(11):1606–1616. https://doi.org/10.1038/nn.4116

Sanchez G, Alvares Lde O, Oberholzer MV, Genro B, Quillfeldt J, da Costa JC, Cervenansky C, Jerusalinsky D, Kornisiuk E (2009) M4 muscarinic receptors are involved in modulation of neurotransmission at synapses of Schaffer collaterals on CA1 hippocampal neurons in rats. J Neurosci Res 87(3):691–700. https://doi.org/10.1002/jnr.21876

Sanford L, Palmer A (2017) Recent advances in development of genetically encoded fluorescent sensors. Methods Enzymol 589:1–49. https://doi.org/10.1016/bs.mie.2017.01.019

Sanna MD, Ghelardini C, Thurmond RL, Masini E, Galeotti N (2017) Behavioural phenotype of histamine H4 receptor knockout mice: focus on central neuronal functions. Neuropharmacology 114:48–57. https://doi.org/10.1016/j.neuropharm.2016.11.023

Sarter M, Hasselmo ME, Bruno JP, Givens B (2005) Unraveling the attentional functions of cortical cholinergic inputs: interactions between signal-driven and cognitive modulation of signal detection. Brain Res Brain Res Rev 48(1):98–111. https://doi.org/10.1016/j.brainresrev.2004.08.006

Saunders A, Granger AJ, Sabatini BL (2015) Corelease of acetylcholine and GABA from cholinergic forebrain neurons. Elife 4. https://doi.org/10.7554/eLife.06412

Scanziani M, Gahwiler BH, Thompson SM (1993) Presynaptic inhibition of excitatory synaptic transmission mediated by alpha adrenergic receptors in area CA3 of the rat hippocampus in vitro. J Neurosci 13(12):5393–5401

Scatton B, Simon H, Le Moal M, Bischoff S (1980) Origin of dopaminergic innervation of the rat hippocampal formation. Neurosci Lett 18(2):125–131

Scheiderer CL, McCutchen E, Thacker EE, Kolasa K, Ward MK, Parsons D, Harrell LE, Dobrunz LE, McMahon LL (2006) Sympathetic sprouting drives hippocampal cholinergic reinnervation that prevents loss of a muscarinic receptor-dependent long-term depression at CA3-CA1 synapses. J Neurosci 26(14):3745–3756. https://doi.org/10.1523/JNEUROSCI.5507-05.2006

Scheiderer CL, Smith CC, McCutchen E, McCoy PA, Thacker EE, Kolasa K, Dobrunz LE, McMahon LL (2008) Coactivation of M(1) muscarinic and alpha1 adrenergic receptors stimulates extracellular signal-regulated protein kinase and induces long-term depression at CA3-CA1 synapses in rat hippocampus. J Neurosci 28(20):5350–5358. https://doi.org/10.1523/JNEUROSCI.5058-06.2008

Schmitz D, Empson RM, Heinemann U (1995) Serotonin and 8-OH-DPAT reduce excitatory transmission in rat hippocampal area CA1 via reduction in presumed presynaptic Ca2+ entry. Brain Res 701(1–2):249–254 0006-8993(95)01005-5 [pii]

Schneider EH, Seifert R (2016) The histamine H4-receptor and the central and peripheral nervous system: a critical analysis of the literature. Neuropharmacology 106:116–128. https://doi.org/10.1016/j.neuropharm.2015.05.004

Schuman EM, Madison DV (1991) A requirement for the intercellular messenger nitric oxide in long-term potentiation. Science 254(5037):1503–1506

Schuman EM, Madison DV (1994) Nitric oxide and synaptic function. Annu Rev Neurosci 17:153–183

Schweitzer P (2000) Cannabinoids decrease the K(+) M-current in hippocampal CA1 neurons. J Neurosci 20(1):51–58

Schweitzer P, Madamba S, Siggins GR (1990) Arachidonic acid metabolites as mediators of somatostatin-induced increase of neuronal M-current. Nature 346(6283):464–467. https://doi.org/10.1038/346464a0

Schweitzer P, Madamba SG, Siggins GR (2003) The sleep-modulating peptide cortistatin augments the h-current in hippocampal neurons. J Neurosci 23(34):10884–10891

Seeger T, Alzheimer C (2001) Muscarinic activation of inwardly rectifying K(+) conductance reduces EPSPs in rat hippocampal CA1 pyramidal cells. J Physiol 535(Pt 2):383–396

Seeger T, Fedorova I, Zheng F, Miyakawa T, Koustova E, Gomeza J, Basile AS, Alzheimer C, Wess J (2004) M2 muscarinic acetylcholine receptor knock-out mice show deficits in behavioral flexibility, working memory, and hippocampal plasticity. J Neurosci 24(45):10117–10127. https://doi.org/10.1523/JNEUROSCI.3581-04.2004

Seeman P, Van Tol HH (1994) Dopamine receptor pharmacology. Trends Pharmacol Sci 15(7):264–270

Segal M (1980) The action of serotonin in the rat hippocampal slice preparation. J Physiol 303:423–439

Segal M (1981) Histamine modulates reactivity of hippocampal CA3 neurons to afferent stimulation in vitro. Brain Res 213(2):443–448

Sekulic V, Skinner FK (2017) Computational models of O-LM cells are recruited by low or high theta frequency inputs depending on h-channel distributions. Elife:6. https://doi.org/10.7554/eLife.22962

Selbach O, Brown RE, Haas HL (1997) Long-term increase of hippocampal excitability by histamine and cyclic AMP. Neuropharmacology 36(11–12):1539–1548

Sengupta A, Bocchio M, Bannerman DM, Sharp T, Capogna M (2017) Control of amygdala circuits by 5-HT neurons via 5-HT and glutamate cotransmission. J Neurosci 37(7):1785–1796. https://doi.org/10.1523/JNEUROSCI.2238-16.2016

Shakesby AC, Anwyl R, Rowan MJ (2002) Overcoming the effects of stress on synaptic plasticity in the intact hippocampus: rapid actions of serotonergic and antidepressant agents. J Neurosci 22(9):3638–3644

Shanley LJ, Irving AJ, Harvey J (2001) Leptin enhances NMDA receptor function and modulates hippocampal synaptic plasticity. J Neurosci 21(24):RC186

Sharma G, Vijayaraghavan S (2003) Modulation of presynaptic store calcium induces release of glutamate and postsynaptic firing. Neuron 38(6):929–939

Sharma G, Grybko M, Vijayaraghavan S (2008) Action potential-independent and nicotinic receptor-mediated concerted release of multiple quanta at hippocampal CA3-mossy fiber synapses. J Neurosci 28(10):2563–2575. https://doi.org/10.1523/JNEUROSCI.5407-07.2008

Shen RY, Andrade R (1998) 5-Hydroxytryptamine2 receptor facilitates GABAergic neurotransmission in rat hippocampus. J Pharmacol Exp Ther 285(2):805–812

Shen M, Piser TM, Seybold VS, Thayer SA (1996) Cannabinoid receptor agonists inhibit glutamatergic synaptic transmission in rat hippocampal cultures. J Neurosci 16(14):4322–4334

Shen JX, Tu B, Yakel JL (2009) Inhibition of alpha 7-containing nicotinic ACh receptors by muscarinic M1 ACh receptors in rat hippocampal CA1 interneurones in slices. J Physiol 587(Pt 5):1033–1042. https://doi.org/10.1113/jphysiol.2008.167593

Shen Y, Fu WY, Cheng EY, Fu AK, Ip NY (2013) Melanocortin-4 receptor regulates hippocampal synaptic plasticity through a protein kinase A-dependent mechanism. J Neurosci 33(2):464–472. https://doi.org/10.1523/JNEUROSCI.3282-12.2013

Shigemoto R, Kulik A, Roberts JD, Ohishi H, Nusser Z, Kaneko T, Somogyi P (1996) Target-cell-specific concentration of a metabotropic glutamate receptor in the presynaptic active zone. Nature 381(6582):523–525. https://doi.org/10.1038/381523a0

Shinoe T, Matsui M, Taketo MM, Manabe T (2005) Modulation of synaptic plasticity by physiological activation of M1 muscarinic acetylcholine receptors in the mouse hippocampus. J Neurosci 25(48):11194–11200. https://doi.org/10.1523/JNEUROSCI.2338-05.2005

Shinohara S, Kawasaki K (1997) Electrophysiological changes in rat hippocampal pyramidal neurons produced by cholecystokinin octapeptide. Neuroscience 78(4):1005–1016

Smith CC, Greene RW (2012) CNS dopamine transmission mediated by noradrenergic innervation. J Neurosci 32(18):6072–6080. https://doi.org/10.1523/JNEUROSCI.6486-11.2012

Smith WB, Starck SR, Roberts RW, Schuman EM (2005) Dopaminergic stimulation of local protein synthesis enhances surface expression of GluR1 and synaptic transmission in hippocampal neurons. Neuron 45(5):765–779. https://doi.org/10.1016/j.neuron.2005.01.015

Smith MO, Ball J, Holloway BB, Erdelyi F, Szabo G, Stone E, Graham J, Lawrence JJ (2015) Measuring aggregation of events about a mass using spatial point pattern methods. Spat Stat 13:76–89. https://doi.org/10.1016/j.spasta.2015.05.004

Sodickson DL, Bean BP (1998) Neurotransmitter activation of inwardly rectifying potassium current in dissociated hippocampal CA3 neurons: interactions among multiple receptors. J Neurosci 18(20):8153–8162

Sohal VS, Zhang F, Yizhar O, Deisseroth K (2009) Parvalbumin neurons and gamma rhythms enhance cortical circuit performance. Nature 459(7247):698–702. https://doi.org/10.1038/nature07991

Solt K, Ruesch D, Forman SA, Davies PA, Raines DE (2007) Differential effects of serotonin and dopamine on human 5-HT3A receptor kinetics: interpretation within an allosteric kinetic model. J Neurosci 27(48):13151–13160. https://doi.org/10.1523/JNEUROSCI.3772-07.2007

Son H, Hawkins RD, Martin K, Kiebler M, Huang PL, Fishman MC, Kandel ER (1996) Long-term potentiation is reduced in mice that are doubly mutant in endothelial and neuronal nitric oxide synthase. Cell 87(6):1015–1023

Sos KE, Mayer MI, Cserep C, Takacs FS, Szonyi A, Freund TF, Nyiri G (2017) Cellular architecture and transmitter phenotypes of neurons of the mouse median raphe region. Brain Struct Funct 222(1):287–299. https://doi.org/10.1007/s00429-016-1217-x

Sotty F, Danik M, Manseau F, Laplante F, Quirion R, Williams S (2003) Distinct electrophysiological properties of glutamatergic, cholinergic and GABAergic rat septohippocampal neurons: novel implications for hippocampal rhythmicity. J Physiol 551(Pt 3):927–943. https://doi.org/10.1113/jphysiol.2003.046847

Spangler SM, Bruchas MR (2017) Optogenetic approaches for dissecting neuromodulation and GPCR signaling in neural circuits. Curr Opin Pharmacol 32:56–70. https://doi.org/10.1016/j.coph.2016.11.001

Sperk G, Hamilton T, Colmers WF (2007) Neuropeptide Y in the dentate gyrus. Prog Brain Res 163:285–297

Springfield SA, Geller HM (1988) Histamine modulates local inhibition in the rat hippocampal slice. Cell Mol Neurobiol 8(4):431–445

Stanzione P, Calabresi P, Mercuri N, Bernardi G (1984) Dopamine modulates CA1 hippocampal neurons by elevating the threshold for spike generation: an in vitro study. Neuroscience 13(4):1105–1116

Staubli U, Xu FB (1995) Effects of 5-HT3 receptor antagonism on hippocampal theta rhythm, memory, and LTP induction in the freely moving rat. J Neurosci 15(3 Pt 2):2445–2452

Stella N, Schweitzer P, Piomelli D (1997) A second endogenous cannabinoid that modulates long-term potentiation. Nature 388(6644):773–778

Stempel AV, Stumpf A, Zhang HY, Ozdogan T, Pannasch U, Theis AK, Otte DM, Wojtalla A, Racz I, Ponomarenko A, Xi ZX, Zimmer A, Schmitz D (2016) Cannabinoid type 2 receptors mediate a cell type-specific plasticity in the hippocampus. Neuron 90(4):795–809. https://doi.org/10.1016/j.neuron.2016.03.034

Stocca G, Nistri A (1996) The neuropeptide thyrotropin-releasing hormone modulates GABAergic synaptic transmission on pyramidal neurones of the rat hippocampal slice. Peptides 17(7):1197–1202

Stone E, Haario H, Lawrence JJ (2014) A kinetic model for the frequency dependence of cholinergic modulation at hippocampal GABAergic synapses. Math Biosci 258:162–175. https://doi.org/10.1016/j.mbs.2014.09.013

Sudweeks SN, Hooft JA, Yakel JL (2002) Serotonin 5-HT(3) receptors in rat CA1 hippocampal interneurons: functional and molecular characterization. J Physiol 544(Pt 3):715–726

Sugita S, Shen KZ, North RA (1992) 5-hydroxytryptamine is a fast excitatory transmitter at 5-HT3 receptors in rat amygdala. Neuron 8(1):199–203

Surmeier DJ (2007) Dopamine and working memory mechanisms in prefrontal cortex. J Physiol 581(Pt 3):885. https://doi.org/10.1113/jphysiol.2007.134502

Swanson LW, Köhler C, Björklund A (1987) The limbic region, I: the septohippocampal system. In: Björklund A, Hökfelt T, Swanson LW (eds) Handbook of chemical neuroanatomy, integrated systems of the CNS, vol 5. Elsevier, Amsterdam, pp 125–277

Swant J, Stramiello M, Wagner JJ (2008) Postsynaptic dopamine D3 receptor modulation of evoked IPSCs via GABA(A) receptor endocytosis in rat hippocampus. Hippocampus 18(5):492–502. https://doi.org/10.1002/hipo.20408

Sylantyev S, Jensen TP, Ross RA, Rusakov DA (2013) Cannabinoid- and lysophosphatidylinositol-sensitive receptor GPR55 boosts neurotransmitter release at central synapses. Proc Natl Acad Sci U S A 110(13):5193–5198. https://doi.org/10.1073/pnas.1211204110

Szabadits E, Cserep C, Ludanyi A, Katona I, Gracia-Llanes J, Freund TF, Nyiri G (2007) Hippocampal GABAergic synapses possess the molecular machinery for retrograde nitric oxide signaling. J Neurosci 27(30):8101–8111

Szabadits E, Cserep C, Szonyi A, Fukazawa Y, Shigemoto R, Watanabe M, Itohara S, Freund TF, Nyiri G (2011) NMDA receptors in hippocampal GABAergic synapses and their role in nitric oxide signaling. J Neurosci 31(16):5893–5904. https://doi.org/10.1523/JNEUROSCI.5938-10.2011

Szabo SI, Zelles T, Vizi ES, Lendvai B (2008) The effect of nicotine on spiking activity and Ca2+ dynamics of dendritic spines in rat CA1 pyramidal neurons. Hippocampus 18(4):376–385. https://doi.org/10.1002/hipo.20401

Szabo GG, Holderith N, Gulyas AI, Freund TF, Hajos N (2010) Distinct synaptic properties of perisomatic inhibitory cell types and their different modulation by cholinergic receptor activation in the CA3 region of the mouse hippocampus. Eur J Neurosci 31(12):2234–2246. https://doi.org/10.1111/j.1460-9568.2010.07292.x

Takagi H, Morishima Y, Matsuyama T, Hayashi H, Watanabe T, Wada H (1986) Histaminergic axons in the neostriatum and cerebral cortex of the rat: a correlated light and electron microscopic immunocytochemical study using histidine decarboxylase as a marker. Brain Res 364(1):114–123

Takacs VT, Cserep C, Schlingloff D, Posfai B, Szonyi A, Sos KE, Kornyei Z, Denes A, Gulyas AI, Freund TF, Nyiri G (2018) Co-transmission of acetylcholine and GABA regulates hippocampal states. Nat Commun 9(1):2848

Takeshita Y, Watanabe T, Sakata T, Munakata M, Ishibashi H, Akaike N (1998) Histamine modulates high-voltage-activated calcium channels in neurons dissociated from the rat tuberomammillary nucleus. Neuroscience 87(4):797–805

Takeuchi T, Duszkiewicz AJ, Sonneborn A, Spooner PA, Yamasaki M, Watanabe M, Smith CC, Fernandez G, Deisseroth K, Greene RW, Morris RG (2016) Locus coeruleus and dopaminergic consolidation of everyday memory. Nature 537(7620):357–362. https://doi.org/10.1038/nature19325

Tallent MK, Qiu C (2008) Somatostatin: an endogenous antiepileptic. Mol Cell Endocrinol 286(1–2):96–103. https://doi.org/10.1016/j.mce.2007.12.004 S0303-7207(07)00452-2 [pii]

Tallent MK, Siggins GR (1997) Somatostatin depresses excitatory but not inhibitory neurotransmission in rat CA1 hippocampus. J Neurophysiol 78(6):3008–3018

Tallent MK, Fabre V, Qiu C, Calbet M, Lamp T, Baratta MV, Suzuki C, Levy CL, Siggins GR, Henriksen SJ, Criado JR, Roberts A, de Lecea L (2005) Cortistatin overexpression in transgenic mice produces deficits in synaptic plasticity and learning. Mol Cell Neurosci 30(3):465–475. https://doi.org/10.1016/j.mcn.2005.08.010

Tanaka KF, Samuels BA, Hen R (2012) Serotonin receptor expression along the dorsal-ventral axis of mouse hippocampus. Philos Trans R Soc Lond B Biol Sci 367(1601):2395–2401. https://doi.org/10.1098/rstb.2012.0038

Tecott LH, Maricq AV, Julius D (1993) Nervous system distribution of the serotonin 5-HT3 receptor mRNA. Proc Natl Acad Sci U S A 90(4):1430–1434

Thompson SM, Haas HL, Gahwiler BH (1992) Comparison of the actions of adenosine at pre- and postsynaptic receptors in the rat hippocampus in vitro. J Physiol 451:347–363

Thompson AM, Swant J, Wagner JJ (2005) Cocaine-induced modulation of long-term potentiation in the CA1 region of rat hippocampus. Neuropharmacology 49(2):185–194. https://doi.org/10.1016/j.neuropharm.2005.03.005

Thorn CA, Popiolek M, Stark E, Edgerton JR (2017) Effects of M1 and M4 activation on excitatory synaptic transmission in CA1. Hippocampus 27(7):794–810. https://doi.org/10.1002/hipo.22732

Toledo-Rodriguez M, Markram H (2007) Single-cell RT-PCR, a technique to decipher the electrical, anatomical, and genetic determinants of neuronal diversity. Methods Mol Biol 403:123–139. https://doi.org/10.1007/978-1-59745-529-9_8

Torres GE, Chaput Y, Andrade R (1995) Cyclic AMP and protein kinase A mediate 5-hydroxytryptamine type 4 receptor regulation of calcium-activated potassium current in adult hippocampal neurons. Mol Pharmacol 47(1):191–197

Torres GE, Arfken CL, Andrade R (1996) 5-Hydroxytryptamine4 receptors reduce afterhyperpolarization in hippocampus by inhibiting calcium-induced calcium release. Mol Pharmacol 50(5):1316–1322

Toselli M, Lang J, Costa T, Lux HD (1989) Direct modulation of voltage-dependent calcium channels by muscarinic activation of a pertussis toxin-sensitive G-protein in hippocampal neurons. Pflugers Arch 415(3):255–261

Toth K, McBain CJ (1998) Afferent-specific innervation of two distinct AMPA receptor subtypes on single hippocampal interneurons. Nat Neurosci 1(7):572–578. https://doi.org/10.1038/2807

Toth K, McBain CJ (2000) Target-specific expression of pre- and postsynaptic mechanisms. J Physiol 525(Pt 1):41–51. https://doi.org/10.1111/j.1469-7793.2000.00041.x

Toth K, Freund TF, Miles R (1997) Disinhibition of rat hippocampal pyramidal cells by GABAergic afferents from the septum. J Physiol 500(Pt 2):463–474. https://doi.org/10.1113/jphysiol.1997.sp022033

Towers SK, Hestrin S (2008) D1-like dopamine receptor activation modulates GABAergic inhibition but not electrical coupling between neocortical fast-spiking interneurons. J Neurosci 28(10):2633–2641. https://doi.org/10.1523/JNEUROSCI.5079-07.2008

Tremblay R, Lee S, Rudy B (2016) GABAergic interneurons in the neocortex: from cellular properties to circuits. Neuron 91(2):260–292. https://doi.org/10.1016/j.neuron.2016.06.033

Tricoire L, Cea-Del Rio CA (2007) Illuminating cholinergic microcircuits in the neocortex. J Neurosci 27(45):12119–12120. https://doi.org/10.1523/JNEUROSCI.3856-07.2007

Triller A, Choquet D (2008) New concepts in synaptic biology derived from single-molecule imaging. Neuron 59(3):359–374. https://doi.org/10.1016/j.neuron.2008.06.022

Tritsch NX, Sabatini BL (2012) Dopaminergic modulation of synaptic transmission in cortex and striatum. Neuron 76(1):33–50. https://doi.org/10.1016/j.neuron.2012.09.023

Tsou K, Brown S, Sanudo-Pena MC, Mackie K, Walker JM (1998) Immunohistochemical distribution of cannabinoid CB1 receptors in the rat central nervous system. Neuroscience 83(2):393–411

Turner TJ, Mokler DJ, Luebke JI (2004) Calcium influx through presynaptic 5-HT3 receptors facilitates GABA release in the hippocampus: in vitro slice and synaptosome studies. Neuroscience 129(3):703–718. https://doi.org/10.1016/j.neuroscience.2004.08.020

Tyan L, Chamberland S, Magnin E, Camire O, Francavilla R, David LS, Deisseroth K, Topolnik L (2014) Dendritic inhibition provided by interneuron-specific cells controls the firing rate and timing of the hippocampal feedback inhibitory circuitry. J Neurosci 34(13):4534–4547. https://doi.org/10.1523/JNEUROSCI.3813-13.2014

Tyzio R, Cossart R, Khalilov I, Minlebaev M, Hubner CA, Represa A, Ben-Ari Y, Khazipov R (2006) Maternal oxytocin triggers a transient inhibitory switch in GABA signaling in the fetal brain during delivery. Science 314(5806):1788–1792. https://doi.org/10.1126/science.1133212

Ul Haq R, Liotta A, Kovacs R, Rosler A, Jarosch MJ, Heinemann U, Behrens CJ (2012) Adrenergic modulation of sharp wave-ripple activity in rat hippocampal slices. Hippocampus 22(3):516–533. https://doi.org/10.1002/hipo.20918

Valentino RJ, Dingledine R (1981) Presynaptic inhibitory effect of acetylcholine in the hippocampus. J Neurosci 1(7):784–792

van der Zee EA, de Jong GI, Strosberg AD, Luiten PG (1991) Parvalbumin-positive neurons in rat dorsal hippocampus contain muscarinic acetylcholine receptors. Brain Res Bull 27(5):697–700

van Hooft JA, Spier AD, Yakel JL, Lummis SC, Vijverberg HP (1998) Promiscuous coassembly of serotonin 5-HT3 and nicotinic alpha4 receptor subunits into Ca(2+)-permeable ion channels. Proc Natl Acad Sci U S A 95(19):11456–11461

Vandecasteele M, Varga V, Berenyi A, Papp E, Bartho P, Venance L, Freund TF, Buzsaki G (2014) Optogenetic activation of septal cholinergic neurons suppresses sharp wave ripples and enhances theta oscillations in the hippocampus. Proc Natl Acad Sci U S A 111(37):13535–13540. https://doi.org/10.1073/pnas.1411233111

Varela JA, Hirsch SJ, Chapman D, Leverich LS, Greene RW (2009) D1/D5 modulation of synaptic NMDA receptor currents. J Neurosci 29(10):3109–3119. https://doi.org/10.1523/JNEUROSCI.4746-08.2009

Varga V, Losonczy A, Zemelman BV, Borhegyi Z, Nyiri G, Domonkos A, Hangya B, Holderith N, Magee JC, Freund TF (2009) Fast synaptic subcortical control of hippocampal circuits. Science 326(5951):449–453. https://doi.org/10.1126/science.1178307

Vargish GA, McBain CJ (2016) The hyperpolarization-activated cation current Ih: the missing link connecting cannabinoids to cognition. Neuron 89(5):889–891. https://doi.org/10.1016/j.neuron.2016.02.027

Varma N, Carlson GC, Ledent C, Alger BE (2001) Metabotropic glutamate receptors drive the endocannabinoid system in hippocampus. J Neurosci 21(24):RC188

Vertes RP, Fortin WJ, Crane AM (1999) Projections of the median raphe nucleus in the rat. J Comp Neurol 407(4):555–582

Vijayaraghavan S, Sharma G (2015) Editorial: brain cholinergic mechanisms. Front Synaptic Neurosci 7:14. https://doi.org/10.3389/fnsyn.2015.00014

Vilaro MT, Cortes R, Mengod G (2005) Serotonin 5-HT4 receptors and their mRNAs in rat and guinea pig brain: distribution and effects of neurotoxic lesions. J Comp Neurol 484(4):418–439. https://doi.org/10.1002/cne.20447

Villani F, Johnston D (1993) Serotonin inhibits induction of long-term potentiation at commissural synapses in hippocampus. Brain Res 606(2):304–308

Vizi ES, Kiss JP (1998) Neurochemistry and pharmacology of the major hippocampal transmitter systems: synaptic and nonsynaptic interactions. Hippocampus 8(6):566–607. https://doi.org/10.1002/(SICI)1098-1063(1998)8:6<566::AID-HIPO2>3.0.CO;2-W

Vizi ES, Kiss JP, Lendvai B (2004) Nonsynaptic communication in the central nervous system. Neurochem Int 45(4):443–451. https://doi.org/10.1016/j.neuint.2003.11.016

Vizuete ML, Traiffort E, Bouthenet ML, Ruat M, Souil E, Tardivel-Lacombe J, Schwartz JC (1997) Detailed mapping of the histamine H2 receptor and its gene transcripts in guinea-pig brain. Neuroscience 80(2):321–343

Vogt KE, Regehr WG (2001) Cholinergic modulation of excitatory synaptic transmission in the CA3 area of the hippocampus. J Neurosci 21(1):75–83

von Engelhardt J, Eliava M, Meyer AH, Rozov A, Monyer H (2007) Functional characterization of intrinsic cholinergic interneurons in the cortex. J Neurosci 27(21):5633–5642. https://doi.org/10.1523/JNEUROSCI.4647-06.2007

Vorobjev VS, Sharonova IN, Walsh IB, Haas HL (1993) Histamine potentiates N-methyl-D-aspartate responses in acutely isolated hippocampal neurons. Neuron 11(5):837–844

Vu MT, Du G, Bayliss DA, Horner RL (2015) TASK channels on basal forebrain cholinergic neurons modulate electrocortical signatures of arousal by histamine. J Neurosci 35(40):13555–13567. https://doi.org/10.1523/JNEUROSCI.1445-15.2015

Waeber C, Sebben M, Bockaert J, Dumuis A (1996) Regional distribution and ontogeny of 5-HT4 binding sites in rat brain. Behav Brain Res 73(1–2):259–262

Wagner JJ, Terman GW, Chavkin C (1993) Endogenous dynorphins inhibit excitatory neurotransmission and block LTP induction in the hippocampus. Nature 363(6428):451–454

Wall MJ, Dale N (2013) Neuronal transporter and astrocytic ATP exocytosis underlie activity-dependent adenosine release in the hippocampus. J Physiol 591(16):3853–3871. https://doi.org/10.1113/jphysiol.2013.253450

Wanaverbecq N, Semyanov A, Pavlov I, Walker MC, Kullmann DM (2007) Cholinergic axons modulate GABAergic signaling among hippocampal interneurons via postsynaptic alpha 7 nicotinic receptors. J Neurosci 27(21):5683–5693. https://doi.org/10.1523/JNEUROSCI.1732-07.2007

Wang RY, Arvanov VL (1998) M100907, a highly selective 5-HT2A receptor antagonist and a potential atypical antipsychotic drug, facilitates induction of long-term potentiation in area CA1 of the rat hippocampal slice. Brain Res 779(1-2):309–313

Wang DV, Yau HJ, Broker CJ, Tsou JH, Bonci A, Ikemoto S (2015) Mesopontine median raphe regulates hippocampal ripple oscillation and memory consolidation. Nat Neurosci 18(5):728–735. https://doi.org/10.1038/nn.3998

Ward RP, Hamblin MW, Lachowicz JE, Hoffman BJ, Sibley DR, Dorsa DM (1995) Localization of serotonin subtype 6 receptor messenger RNA in the rat brain by in situ hybridization histochemistry. Neuroscience 64(4):1105–1111

Watanabe T, Taguchi Y, Shiosaka S, Tanaka J, Kubota H, Terano Y, Tohyama M, Wada H (1984) Distribution of the histaminergic neuron system in the central nervous system of rats; a fluorescent immunohistochemical analysis with histidine decarboxylase as a marker. Brain Res 295(1):13–25

Weber ET, Andrade R (2010) Htr2a gene and 5-HT(2A) receptor expression in the cerebral cortex studied using genetically modified mice. Front Neurosci 4. https://doi.org/10.3389/fnins.2010.00036

Weiss T, Veh RW, Heinemann U (2003) Dopamine depresses cholinergic oscillatory network activity in rat hippocampus. Eur J Neurosci 18(9):2573–2580

Weisskopf MG, Zalutsky RA, Nicoll RA (1993) The opioid peptide dynorphin mediates heterosynaptic depression of hippocampal mossy fibre synapses and modulates long-term potentiation. Nature 365(6442):188

Whittaker E, Vereker E, Lynch MA (1999) Neuropeptide Y inhibits glutamate release and long-term potentiation in rat dentate gyrus. Brain Res 827(1-2):229–233

Widmer H, Ferrigan L, Davies CH, Cobb SR (2006) Evoked slow muscarinic acetylcholinergic synaptic potentials in rat hippocampal interneurons. Hippocampus 16(7):617–628. https://doi.org/10.1002/hipo.20191

Wilson RI, Nicoll RA (2001) Endogenous cannabinoids mediate retrograde signalling at hippocampal synapses. Nature 410(6828):588–592

Winterer J, Stempel AV, Dugladze T, Foldy C, Maziashvili N, Zivkovic AR, Priller J, Soltesz I, Gloveli T, Schmitz D (2011) Cell-type-specific modulation of feedback inhibition by serotonin in the hippocampus. J Neurosci 31(23):8464–8475. https://doi.org/10.1523/JNEUROSCI.6382-10.2011

Wojtowicz AM, van den Boom L, Chakrabarty A, Maggio N, Haq RU, Behrens CJ, Heinemann U (2009) Monoamines block kainate- and carbachol-induced gamma-oscillations but augment stimulus-induced gamma-oscillations in rat hippocampus in vitro. Hippocampus 19(3):273–288. https://doi.org/10.1002/hipo.20508

Wolf ME, Mangiavacchi S, Sun X (2003) Mechanisms by which dopamine receptors may influence synaptic plasticity. Ann N Y Acad Sci 1003:241–249

Woolf NJ (1991) Cholinergic systems in mammalian brain and spinal cord. Prog Neurobiol 37(6):475–524. https://doi.org/10.1016/0301-0082(91)90006-m

Wright DE, Seroogy KB, Lundgren KH, Davis BM, Jennes L (1995) Comparative localization of serotonin1A, 1C, and 2 receptor subtype mRNAs in rat brain. J Comp Neurol 351(3):357–373. https://doi.org/10.1002/cne.903510304

Wu LG, Saggau P (1994) Adenosine inhibits evoked synaptic transmission primarily by reducing presynaptic calcium influx in area CA1 of hippocampus. Neuron 12(5):1139–1148

Wu LG, Saggau P (1997) Presynaptic inhibition of elicited neurotransmitter release. Trends Neurosci 20(5):204–212

Wyskiel DR, Andrade R (2016) Serotonin excites hippocampal CA1 GABAergic interneurons at the stratum radiatum-stratum lacunosum moleculare border. Hippocampus 26(9):1107–1114. https://doi.org/10.1002/hipo.22611

Xiang ZX, Huguenard JR, Prince DA (1998) Cholinergic switching within neocortical inhibitory networks. Science 281(5379):985–988

Xu C, Michelsen KA, Wu M, Morozova E, Panula P, Alreja M (2004) Histamine innervation and activation of septohippocampal GABAergic neurones: involvement of local ACh release. J Physiol 561(Pt 3):657–670. https://doi.org/10.1113/jphysiol.2004.071712

Yamazaki Y, Kaneko K, Fujii S, Kato H, Ito K (2003) Long-term potentiation and long-term depression induced by local application of ATP to hippocampal CA1 neurons of the guinea pig. Hippocampus 13(1):81–92. https://doi.org/10.1002/hipo.7999

Yang SN (2000) Sustained enhancement of AMPA receptor- and NMDA receptor-mediated currents induced by dopamine D1/D5 receptor activation in the hippocampus: an essential role of postsynaptic Ca2+. Hippocampus 10(1):57–63. https://doi.org/10.1002/(SICI)1098-1063(2000)10:1<57::AID-HIPO6>3.0.CO;2-0

Yang K, Trepanier CH, Li H, Beazely MA, Lerner EA, Jackson MF, MacDonald JF (2009) Vasoactive intestinal peptide acts via multiple signal pathways to regulate hippocampal NMDA receptors and synaptic transmission. Hippocampus 19(9):779–789. https://doi.org/10.1002/hipo.20559

Yang J, Yao Y, Wang L, Yang C, Wang F, Guo J, Wang Z, Yang Z, Ming D (2017) Gastrin-releasing peptide facilitates glutamatergic transmission in the hippocampus and effectively prevents vascular dementia induced cognitive and synaptic plasticity deficits. Exp Neurol 287(Pt 1):75–83. https://doi.org/10.1016/j.expneurol.2016.08.008

Yanovsky Y, Haas HL (1998) Histamine increases the bursting activity of pyramidal cells in the CA3 region of mouse hippocampus. Neurosci Lett 240(2):110–112

Yi F, Ball J, Stoll KE, Satpute VC, Mitchell SM, Pauli JL, Holloway BB, Johnston AD, Nathanson NM, Deisseroth K, Gerber DJ, Tonegawa S, Lawrence JJ (2014) Direct excitation of parvalbumin-positive interneurons by M1 muscarinic acetylcholine receptors: roles in cellular excitability, inhibitory transmission and cognition. J Physiol 592(16):3463–3494. https://doi.org/10.1113/jphysiol.2014.275453

Yi F, Catudio-Garrett E, Gabriel R, Wilhelm M, Erdelyi F, Szabo G, Deisseroth K, Lawrence J (2015) Hippocampal "cholinergic interneurons" visualized with the choline acetyltransferase promoter: anatomical distribution, intrinsic membrane properties, neurochemical characteristics, and capacity for cholinergic modulation. Front Synaptic Neurosci 7:4. https://doi.org/10.3389/fnsyn.2015.00004

Yoon KW, Rothman SM (1991) Adenosine inhibits excitatory but not inhibitory synaptic transmission in the hippocampus. J Neurosci 11(5):1375–1380

Younts TJ, Castillo PE (2014) Endogenous cannabinoid signaling at inhibitory interneurons. Curr Opin Neurobiol 26:42–50. https://doi.org/10.1016/j.conb.2013.12.006

Yu X, Ye Z, Houston CM, Zecharia AY, Ma Y, Zhang Z, Uygun DS, Parker S, Vyssotski AL, Yustos R, Franks NP, Brickley SG, Wisden W (2015) Wakefulness is governed by GABA and histamine cotransmission. Neuron 87(1):164–178. https://doi.org/10.1016/j.neuron.2015.06.003

Yuan M, Meyer T, Benkowitz C, Savanthrapadian S, Ansel-Bollepalli L, Foggetti A, Wulff P, Alcami P, Elgueta C, Bartos M (2017) Somatostatin-positive interneurons in the dentate gyrus of mice provide local- and long-range septal synaptic inhibition. Elife 6. https://doi.org/10.7554/eLife.21105

Zago WM, Massey KA, Berg DK (2006) Nicotinic activity stabilizes convergence of nicotinic and GABAergic synapses on filopodia of hippocampal interneurons. Mol Cell Neurosci 31(3):549–559. https://doi.org/10.1016/j.mcn.2005.11.009

Zaninetti M, Raggenbass M (2000) Oxytocin receptor agonists enhance inhibitory synaptic transmission in the rat hippocampus by activating interneurons in stratum pyramidale. Eur J Neurosci 12(11):3975–3984

Zant JC, Rozov S, Wigren HK, Panula P, Porkka-Heiskanen T (2012) Histamine release in the basal forebrain mediates cortical activation through cholinergic neurons. J Neurosci 32(38):13244–13254. https://doi.org/10.1523/JNEUROSCI.5933-11.2012

Zeisel A, Munoz-Manchado AB, Codeluppi S, Lonnerberg P, La Manno G, Jureus A, Marques S, Munguba H, He L, Betsholtz C, Rolny C, Castelo-Branco G, Hjerling-Leffler J, Linnarsson S (2015) Brain structure. Cell types in the mouse cortex and hippocampus revealed by single-cell RNA-seq. Science 347(6226):1138–1142. https://doi.org/10.1126/science.aaa1934

Zhang J, Berg DK (2007) Reversible inhibition of GABAA receptors by alpha7-containing nicotinic receptors on the vertebrate postsynaptic neurons. J Physiol 579(Pt 3):753–763. https://doi.org/10.1113/jphysiol.2006.124578

Zhang F, Wang LP, Brauner M, Liewald JF, Kay K, Watzke N, Wood PG, Bamberg E, Nagel G, Gottschalk A, Deisseroth K (2007) Multimodal fast optical interrogation of neural circuitry. Nature 446(7136):633–639. nature05744 [pii]. https://doi.org/10.1038/nature05744

Zhang J, Zhuang QX, Li B, Wu GY, Yung WH, Zhu JN, Wang JJ (2016) Selective modulation of histaminergic inputs on projection neurons of cerebellum rapidly promotes motor coordination via HCN channels. Mol Neurobiol 53(2):1386–1401. https://doi.org/10.1007/s12035-015-9096-3

Zhou FM, Hablitz JJ (1999) Dopamine modulation of membrane and synaptic properties of interneurons in rat cerebral cortex. J Neurophysiol 81(3):967–976. https://doi.org/10.1152/jn.1999.81.3.967

Zhou L, Zhu DY (2009) Neuronal nitric oxide synthase: structure, subcellular localization, regulation, and clinical implications. Nitric Oxide 20(4):223–230. https://doi.org/10.1016/j.niox.2009.03.001

Zieglgansberger W, French ED, Siggins GR, Bloom FE (1979) Opioid peptides may excite hippocampal pyramidal neurons by inhibiting adjacent inhibitory interneurons. Science 205(4404):415–417

Zsiros V, Maccaferri G (2008) Noradrenergic modulation of electrical coupling in GABAergic networks of the hippocampus. J Neurosci 28(8):1804–1815. https://doi.org/10.1523/JNEUROSCI.4616-07.2008

Cell Type-Specific Activity During Hippocampal Network Oscillations In Vitro

Tengis Gloveli, Sam A. Booker, Nancy Kopell, and Tamar Dugladze

Overview

Neurons form transient functionally specialized assemblies by coordinating their activity within networks. Assembly activity is important for coding and information processing in the brain; oscillations are assumed to entrain and provide temporal structure to this. Recent work from different laboratories has uncovered cell type-specific activity patterns during network oscillations, indicating that the cells may differentially contribute to the generation of oscillation and thereby the coordination of cell assemblies. The purpose of this chapter is to summarize recent findings from these works in in vitro preparations highlighting the importance of different neuronal activity patterns of hippocampal principal cells and different subtypes of interneurons. Special attention will be paid to the role of the firing properties of hippocampal interneurons on the network oscillatory activity at the theta and gamma frequency range. Models based on these ideas are found in Kopell et al. chapter of this book.

T. Gloveli (✉)
Cellular and Network Physiology Lab, Neuroscience Research Center,
Charité – Universitätsmedizin Berlin, Berlin, Germany
e-mail: tengis.gloveli@charite.de

S. A. Booker
Centre for Discovery Brain Sciences, University of Edinburgh, Edinburgh, UK
e-mail: sbooker@exseed.ed.ac.uk

N. Kopell
Department of Mathematics, Boston University, Boston, MA, USA
e-mail: nk@bu.edu

T. Dugladze (✉)
Institute of Integrative Neuroanatomy, Charité – Universitätsmedizin Berlin, Berlin, Germany
e-mail: tamar.dugladze@charite.de

V. Cutsuridis et al. (eds.), *Hippocampal Microcircuits*, Springer Series
in Computational Neuroscience, https://doi.org/10.1007/978-3-319-99103-0_8

In Vitro Models of Network Oscillations

Hippocampal Population Activity Patterns In Vivo and In Vitro

Hippocampal networks show rhythmic oscillations in various frequency ranges in a behavior-dependent manner (Singer 1999; Buzsáki and Draguhn 2004). In the freely moving rat, three types of hippocampal oscillatory activity have been observed (Leung et al. 1982), which are broadly termed theta (4–12 Hz)-, gamma (30–90 Hz)-, and sharp-wave ripples (100–300 Hz). Theta and gamma frequency rhythms are observed in the rat during exploration and rapid eye movement sleep (Fig. 1A). The frequency range of both rhythms is described differently in different studies. These two rhythms often coexist but can also occur separately [Fig. 1A, for review see Whittington and Traub (2003)]. Gamma and theta rhythms also occur throughout the neocortex in vivo and have been proposed to constitute a fundamental mechanism underlying cognitive tasks such as feature recognition, associative learning, and content- and context-sensitive processing of sensory information. In addition, intermittent population bursts, sharp-wave-associated field ripples, are present in the CA3-CA1-subiculum-entorhinal cortex axis during awake

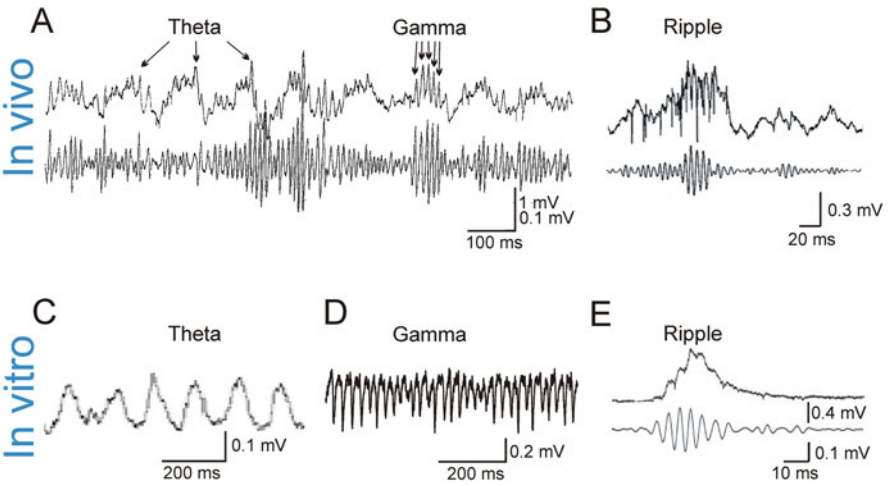

Fig. 1 Hippocampal network oscillations in vivo (**A**, **B**) and in vitro (**C–E**). (**A**) Theta- and gamma-related modulation of the field in the dentate gyrus (hilar region) during exploratory walking. (**B**) Sharp-wave-associated field ripples in CA1 area during slow-wave sleep. Upper traces, wideband recording, lower traces, band bath (40–150 Hz, **A**; 150–250 Hz, **B**) filtered gamma and ripple activity. (**C**) Metabotropic glutamate receptor activation under conditions of reduced AMPA receptor activation generates in CA1 area theta population activity. (**D**) Kainate receptor activation induces network oscillations at the gamma frequency range in CA3 area. (**E**) Spontaneously occurring sharp-wave-associated ripple oscillation in CA1 area in vitro. Upper trace, wideband recording, lower trace, ripple band-pass (140–320 Hz) filtered activity. Panels are adapted from (**A**) Bragin et al. (1995), (**B**) Csicsvari et al. (1999), (**c**) Gillies et al. (2002), (**D**) Gloveli et al. (2005b) and (**E**) Both et al. (2008)

immobility, consummatory behaviors, and slow-wave sleep (Fig. 1B, Vanderwolf 1969; Buzsáki et al. 1983; Bland 1986; Chrobak and Buzsáki 1996, Csicsvari et al. 1999).

Various in vitro models have been developed to gain insight into the cellular and synaptic mechanisms of theta, gamma, and ripple oscillations (Fig. 1C–E). In vitro models of network oscillations, such as the carbachol (Fisahn et al. 1998; Buhl et al. 1998), the kainate (Buhl et al. 1998), the metabotropic glutamate receptor activation (Gilles et al. 2002), and the tetanically induced (Whittington et al. 1997) gamma activity models, reproduce salient features of oscillatory activity in slice preparations maintained in "interface" slice chamber. It has been shown that using an intact hippocampus, and very high flow rates, intrinsic theta and gamma oscillations are maintained without the need for pharmacological intervention (Goutagny et al. 2009). To determine activity pattern of individual neurons, sharp microelectrode or blind whole-cell patch-clamp recordings have been obtained from principal cells or putative interneurons. In addition, an in vivo model, the juxtacellular recording technique, was developed to conjointly record action potential series from single neurons and the extracellular field potential during different forms of network activity in anesthetized animals (Pinault 1996; Klausberger et al. 2003, 2004; see also chapter by Tukker in this book). These in vitro and in vivo methods have some clear advantages in studying network activity. However, the sparse distribution of interneurons makes them unlikely targets for these blind approaches. Therefore, these investigations are very inefficient in mapping neuronal activity patterns. Whole-cell patch-clamp recordings using infrared differential contrast videomicroscopy (Dodt and Zieglgänsberger 1994) have greatly facilitated selection and recordings from interneuron. However, this approach has been hampered by the difficulty of generating population activity in the submerged-type slice chambers. Technical modification of the pharmacological paradigms: brief pressure ejection of kainate (Gloveli et al. 2005a, b) or bath application of kainate (Dugladze et al. 2007, 2012; Zarnadze et al. 2016) and carbachol (Hájos et al. 2004) permitted the reproduction of the network oscillatory activity in submerged slices. The increased use of fluorescent protein expressing reporter lines (i.e., GFP, YFP, td-Tomato, etc.) under the genetic promotion of different unique markers of interneurons and pyramidal cells (PCs) alike (Giepmans et al. 2006) has enabled targeted whole-cell recording from neurochemically defined cells. Furthermore, the use of increasingly more rapid genetically encoded receptors, opsins, and calcium sensors (DREADD, channelrhodopsin, GCaMP6F) has allowed the manipulation of cellular activity to more comprehensively assess their function in the context of network oscillations. Using these approaches, it is possible to record from visually identified pyramidal cells and interneurons during gamma and theta frequency network oscillation in vitro.

Cell Types Involved in Rhythms

Morphological and physiological properties discriminate hippocampal PCs from inhibitory interneurons. In addition, further distinctions exist within both PCs and

interneurons. It is reasonable to postulate that hippocampal neurons with different structural features are also likely to have different functions in the network.

Pyramidal Cells Despite the morphological similarities (pyramid-shaped somata, apical and basal dendritic trees), PCs in CA1 and CA3 areas display some important differences such as the existence of excitatory recurrent collaterals. The latter is considered to be the hallmark of the CA3 but not the CA1 area. PCs of the CA3 area themselves are not homogeneous. Whereas most axon collaterals of the CA3a and CA3b neurons give rise to extensive recurrent collaterals that are confined to the CA3 region, PCs in CA3c subregion are mostly projection cells, with most of their axon collaterals terminating in the ipsi- and contralateral CA1 regions (Li et al. 1994; Wittner et al. 2007). It was hypothesized (Csicsvari et al. 2003) that intrahippocampal gamma oscillations emerge in the recurrent collateral-rich CA3a,b subregions; their activity recruits CA3c subregion, which, in turn, entrains CA1 cells. A further level of complication is added when one considers the less well-studied CA2 PCs, which receive strong theta-modulated input from the supramammillary region (Pan and McNaughton 2002), and they themselves are more preferentially excited by entorhinal cortex inputs than CA3 or CA1 PCs (Chevaleyre and Siegelbaum 2010). While the role of CA2 PCs in the control of oscillatory patterning remains unclear, they may contribute significantly to the timing of theta oscillations.

Interneuron Types In contrast to glutamatergic principal cells, GABAergic interneurons of the hippocampus exhibit substantial diversity. In the CA1 area, for instance, at least 21 classes of interneurons were described (for review see Klausberger and Somogyi (2008) [see Vida chapter of this book]). In contrast to principal cells, the vast majority of interneurons have locally restricted axons and lack spines. Interneurons can be broadly classified into several classes on the basis of different criteria, such as action potential firing properties, somato-dendritic architecture and axonal ramification pattern, neurochemical content, voltage and ligand-gated conductances as well as plastic changes in excitatory synaptic transmission [for reviews see Freund and Buzsáki (1996), McBain and Fisahn (2001), and Klausberger and Somogyi (2008)]. Functionally, at least four main GABAergic cell classes coexist in hippocampal networks: (1) perisomatic inhibitory neurons, (2) dendritic inhibitory interneurons, (3) GABAergic cells specifically innervating other inhibitory interneurons, and (4) projection interneurons which cross hippocampal subfields (Miles et al. 1996; Klausberger and Somogyi, 2008; Booker and Vida 2018). The most striking morpho-functional dichotomy in the population of cortical interneurons is the targeting of the dendritic *versus* the perisomatic domain of principal cells. Dendritic inhibition is likely to control the efficacy and plasticity of excitatory synaptic inputs of principal cells, whereas perisomatic inhibition is ideally suited to control output and the generation of action potentials and can synchronize the firing of large groups of principal cells (Cobb et al. 1995; Miles et al. 1996; Freund and Buzsáki 1996). Further distinctions exist within the same classes of interneurons. Thus, different types *of perisomatic targeting* parvalbumin (PV)-expressing interneurons innervate distinct subcellular

domains of principal cells. Axo-axonic cells (AACs) innervate exclusively the axon initial segment of PCs; in contrast basket cells (BCs) innervate the somata and proximal apical dendrites. In addition, two distinct populations of basket cells – PV-expressing and cholecystokinin (CCK)-expressing interneurons – could be defined on the basis of their neurochemical content [see Vida chapter of this book]. Dendrite-targeting interneurons could be further subdivided into distal (such as oriens lacunosum-moleculare, O-LM, or radiatum lacunosum-moleculare, R-LM, cells) and proximal dendrite-targeting cells (such as bistratified or trilaminar cells). Interneurons belonging to distinct classes defined by their axonal target domain on the PC have clearly different intrinsic, synaptic, and firing properties.

As an example of this diversity, Fig. 2 illustrates the morphology and the physiological properties of two types of interneurons: non-fast-spiking distal dendrite-targeting O-LM cells, which present one of the best studied interneuron classes in the hippocampus, and fast-spiking proximal dendrite-targeting trilaminar cells. These cells differ in their morphology, neurochemical marker contents, and intrinsic membrane properties (see Fig. 2A, B). Clear differences were also detected in spontaneous EPSCs properties between these two subtypes of interneurons – with slower kinetics in O-LM than those in trilaminar interneurons (Fig. 2B). Furthermore, while the excitatory input displayed a late-persistent firing in O-LM cells, fast-spiking trilaminar interneurons displayed an onset-transient firing in response to stimulation of CA1 axons in the alveus (Fig. 2B; Pouille and Scanziani 2004).

These differences in morphological and electrophysiological properties of interneurons indicate that they are likely to have specific roles in the network. In fact, analysis of their spike timing during the oscillations suggests that a division of labor exist among interneurons subtypes involved in hippocampal network oscillations (see sections "Firing Patterns in Gamma Oscillations" and "Firing Patterns in Theta Oscillations").

Gamma Oscillations

Two forms of local network gamma frequency oscillations can be induced in vitro in hippocampal slices (Table 1). Transient forms of gamma frequency oscillations (lasting for a few seconds or minutes) can be evoked in vitro by tetanic stimulation (Whittington et al. 1997) or through pressure ejection of glutamate (Pöschel et al. 2002) and high molarities of locally applied kainate (Gloveli et al. 2005a, b; Craig and McBain 2015) or potassium (LeBeau et al. 2002; Towers et al. 2002) (Table 1).

Another model of gamma frequency oscillations is known as "persistent gamma" (lasting for hours). This kind of oscillation can be induced in the hippocampal CA3 area in vitro by bath application of agonists of muscarinic acetylcholine (mAChR) (Fisahn et al. 1998; Fellous and Sejnowski 2000; Shimono et al. 2000; Fisahn et al. 2002) and kainite receptors (KAR) (Fisahn et al. 2004; Gloveli et al.

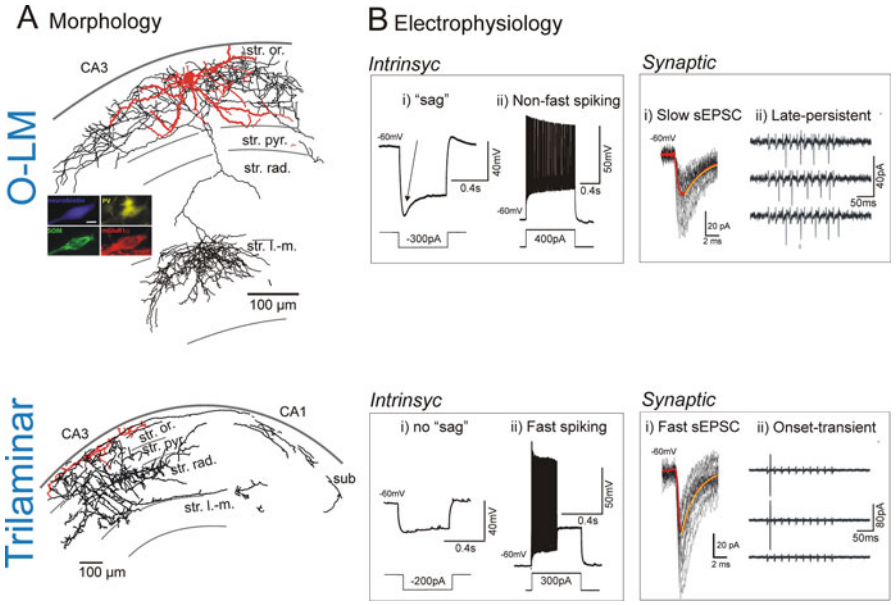

Fig. 2 Properties of distal (O-LM) and proximal (trilaminar) dendrite-targeting interneurons. (**A**) Morphology of O-LM and trilaminar cells. Somata and dendrites are drawn in red; axons are in black. The somata of O-LM cells are located in stratum oriens and have mainly horizontally running dendrites. The main axon of these cells crosses strata pyramidale and radiatum and branches in stratum lacunosum-moleculare. O-LM cells innervate the distal dendrites of PCs which are co-aligned with the entorhinal input (Sik et al. 1995; Maccaferri et al. 2000). (**A**), inset, O-LM cells are immunopositive for the metabotropic glutamate receptor (mGluR1α) and the neuropeptide somatostatin (SOM, Tukker et al. 2007) and express low levels of calcium-binding protein PV (Maccaferri et al. 2000; Klausberger et al. 2003). The trilaminar cells have similar horizontally distributed dendrites in stratum oriens but are clearly different from O-LM cells in respect of axonal arborization (Sik et al. 1995). Sub, subiculum; str.or, stratum oriens; str.pyr., stratum pyramidale; str. rad., stratum radiatum; str. l-m., stratum lacunosum-moleculare. B *Intrinsic*, intrinsic membrane (i) and firing properties (ii) of O-LM and trilaminar cells during hyperpolarizing and depolarizing current injection. O-LM cells demonstrate clear "sag" potential and non-fast-spiking pattern in marked contrast to trilaminar cells showing no "sag" and fast spiking character upon hyperpolarizing and depolarizing pulses. (**B**) *Synaptic* (i) – spontaneous EPSC (sEPSC) in O-LM and trilaminar interneurons. Forty individual traces are black and superimposed averaged currents are red. (**B**) *Synaptic* (ii), Cell-attached responses from an O-LM and trilaminar cells. Current deflections indicate action potential firing in response to the stimulation of CA1 axons in the alveus (indicated by the vertical arrows). (Panels **A** and **B**, *Intrinsic* (i,ii) and *Synaptic* (i), are from Gloveli et al. 2005a; panels **B** *Synaptic* (ii) are from Pouille and Scanziani (2004); Insert (**A**, O-LM) is from Tukker et al. (2007))

2005a, b; Dugladze et al. 2012; Zarnadze et al. 2016) (Table 1). mAChR agonist (carbachol)- and kainate-induced fast network oscillations provide a useful model to explore the mechanisms underlying physiological gamma frequency oscillations for the following reasons. The hippocampus receives a dense cholinergic projection from the medial septum/diagonal band of Broca, which plays an important role in

Table 1 Properties of in vitro models of theta and gamma oscillations

Oscillation type	Activated by	Blocked by	Region	Mean freq. (rec. temp)	Main references
Persistent θ	mGlutR	NMDAR, $GABA_AR$	CA1	7 Hz (35°C)	Gillies et al. (2002)
	mAChR	NMDAR. $GABA_AR$	CA1	9 Hz (35°C)	Gillies et al. (2002)
	mGlutR, mAChR	AMPA	CA3	8 Hz (33°C)	Cobb et al. (2000), Konopacki et al. (1992)
	KAR. long. slice	N.T.	CA3	8 Hz (29°C)	Gloveli et al. (2005b)
Transient θ	Puff KA, long. slice	$GABA_AR$	CA3	8 Hz (29°C)	Gloveli et al. (2005b)
Persistent γ	KAR	$GABA_AR$	CA3	35 Hz (35°C)	Fisahn et al. (2004)
				37 Hz (34°C)	Gloveli et al. (2005b)
	mAChR	AMPAR, $GABA_AR$	CA3	32 Hz(30°C)	Pálhalmi et al. (2004)
			CA3	39 Hz (34°C)	Fisahn et al. (1998)
					Hájos et al. (2004)
	mGluR	AMPAR, $GABA_AR$	CA3	41 Hz (30°C)	Pálhalmi et al. (2004)
Transient γ	Puff Glut.	$GABA_AR$	CA1/DG	42/64 Hz (36°C)	Pöschel et al. (2002)
	Puff KA	$GABA_AR$	CA3	33 Hz (29°C)	Gloveli et al. (2005a)
		N.T.	CA1/CA3	63/52 Hz (33°C)	Craig and McBain (2015)
	Puff K^+	$GABA_AR$	DG	67 Hz (34°C)	Towers et al. (2002)
		AMPA, $GABA_AR$	CA1	63 Hz (34°C)	LeBeau et al. (2002)

Abbreviations: *R* receptor, *m* metabotropic, *KAR* kainate R, *long*. longitudinal, *Puff* pressure jection, *N.T*. not tested

the generation of hippocampal network activity (Leung 1985). In addition, kainate receptors are expressed by both principal cells and interneurons of the hippocampus (Cossart et al. 1998; Frerking et al. 1998; for review see Lerma (2003)). These oscillations in vitro share many of the features of intrahippocampal gamma oscillations in vivo, including the firing of pyramidal neurons at low frequencies (<5 Hz) phase-locked to the oscillation and the generation of oscillations in CA3 and their subsequent propagating to CA1 (Fisahn et al. 1998; Gloveli et al. 2005a). Finally, in vivo and in vitro cholinergically induced oscillations have similar current source density profiles, and the gamma phase relationship between PCs and perisomatic-innervating interneurons is comparable (Csicsvari et al. 2003; Mann et al. 2005; Oren et al. 2006).

Both persistent and transient gamma oscillations can be evoked in different hippocampal areas, including CA3, CA1, and DG (Table 1, Towers et al. 2002; Pöschel et al. 2002; Gloveli et al. 2005a). However, there are regional differences

in frequency and power of the oscillations, suggesting the existence of different rhythm-generating networks in the hippocampus. In line with this suggestion, both persistent and transient forms of kainate-induced gamma oscillations demonstrate faster gamma frequency oscillations in isolated CA1 area than those in CA3 area (N. Maziashvili and T. Gloveli, unpublished observation, Middleton et al. 2008; Craig and McBain 2015). However, gamma oscillations in the same area (e.g., the CA3 area) induced by different pharmacological drugs (carbachol and DHPG) also show significant differences in their properties (the peak frequencies, maximal power, and spectral width, Table 1, Pálhalmi et al. 2004), suggesting involvement of different network mechanisms, such as the recruitment of distinct types of interneurons. In addition, the gamma oscillations evoked under different conditions differ in their dependence on excitation and inhibition (Table 1). Thus, one form of transient oscillation, "interneuronal network gamma" (ING) (Whittington et al. 1995), is based on mutual inhibition between the interneurons [for computational models, see Wang and Buzsáki (1996), White et al. (1998), and Vida et al. (2006)], whereas "pyramidal-interneuronal network gamma" (PING) (Whittington et al. 1997) is based on reciprocal interneuron-PC interaction. Furthermore, fast gamma oscillations in CA1 induced by kainate puff application are independent of CA1 PC firing, as evidenced by optogenetic silencing of them, further reinforcing the idea that local interneurons may be a key determinant of this form of gamma oscillation (Craig and McBain 2015). It seems likely that all of these forms are relevant in vivo, possibly reflecting region and state dependence of mechanisms underlying hippocampal gamma oscillations.

Firing Patterns in Gamma Oscillations

A key requirement for the generation of network oscillations is rhythmic and synchronized activity of large sets of neurons. An important step in understanding the role of hippocampal neurons in network oscillations is to examine their spike patterns during these oscillations.

Principal Cells Analysis of firing properties of electrophysiologically and morphologically identified PCs in CA3 area has been performed in vitro for KAR (Gloveli et al. 2005a, b) and mAChR (Fisahn et al. 1998; Hájos et al. 2004) agonist-induced gamma frequency oscillations. Both KAR and mAChR activation (by kainate and carbachol, respectively) revealed low frequency, <5 Hz, firing of PCs (Table 2, Fisahn et al. 1998; Hájos et al. 2004; Gloveli et al. 2005a). These results are in agreement with in vivo observations demonstrating similar low-frequency firing of PCs (Csicsvari et al. 2003). Moreover, PC firing is phase-locked to the field oscillations (Table 2). In carbachol-induced gamma oscillations, PCs fired action potentials around the negative peak of the field recorded in the PC layer (Fig. 3A, D, Hájos et al. 2004). Both in vivo and in vitro observations suggest that during gamma frequency oscillations, PCs of CA3 area drive local interneurons in a feedback manner (Fisahn et al. 1998; Csicsvari et al. 2003; Pálhalmi et al. 2004; Hájos

Table 2 Firing properties of some hippocampal neurons during gamma frequency oscillations in vitro

Neuron type	Activated by	Mean firing frequency (Hz)	Spikes/gamma cycle	Angle of spikes relative of the field	Main references
Pyramidal	KAR	3.5 ± 0.6	0.18 ± 0.05	N.T.	Gloveli et al. (2005a)
	mAChR	2.82 ± 0.7	0.09 ± 0.02	58.1 ± 5.3°	Hájos et al. (2004)
					Fisahn et al. (1998)
O-LM	KAR	8.3 ± 2.1	0.26 ± 0.04	N.T.	Gloveli et al. (2005a)
	mAChR	12.9 ± 1.8	0.4 ± 0.07	88.1 ± 6.1°	Hájos et al. (2004)
Trilaminar	KAR	32.1 ± 2.8	1.82 ± 0.07	N.T.	Gloveli et al. (2005a)
	mAChR	18.2 ± 2.7	0.6 ± 0.09	96.8 ± 2.2°	Hajos et al. (2004)
Bistratified	KAR	35.0 ± 2.5	1.04 ± 0.08	N.T.	Gloveli et al. (2005a)
Basket	KAR	33.6 ± 2.6	1.28 ± 0.06	N.T.	Gloveli et al. (2005a)
	mAChR	18.1 ± 2.7	0.62 ± 0.09	93 ± 2.1°	Hájos et al. (2004)
R-LM	mAChR	13.2 ± 3.9	N.T.		Hájos et al. (2004)
Radiatum	mAChR	2.3 ± 0.6	0.07 ± 0.02	128.4 ± 12.4°	Hájos et al. (2004)

Abbreviations: *O-LM* oriens lacunosum-moleculare, *R-LM* radiatum lacunosum-moleculare, *N.T.* Not tested

et al. 2004). If PC-interneuron interactions generate gamma oscillations, the firing of PCs should precede interneuron discharge so that PC can recruit interneuron activity in the next gamma cycle (Oren et al. 2006). Consistent with this suggestion, interneuron responses were indeed preceded by PC firing (Fig. 3D, Hájos et al. 2004).

During in vitro gamma frequency oscillations induced by kainate, the interneurons receive a high-frequency barrage of compound EPSPs, modulated at gamma frequency, which are temporally correlated with extracellular population activity (Gloveli et al. 2005a). Since the slice is de-afferented, it is likely that the action potential-dependent excitatory events are mediated by local excitatory input from neighboring pyramidal neurons. Given the relatively low PC somatic spike rate with respect to the frequency of EPSPs invading interneurons, the question remains as to how PCs generate these rhythmic burst of events and reliably discharge interneurons. Interneurons may receive a rhythmic barrage of gamma frequency EPSPs, for the following reasons. First, in the active network, multiple PCs are likely to fire on any given oscillatory cycle. Due to the convergence of numerous PC axons onto a single postsynaptic interneuron it follows that each interneuron is also likely to receive multiple unitary excitatory inputs on each successive gamma wave. Second, there are suggestions that activity in PC axons may orthodromically excite interneurons, without PC somata necessarily firing (Traub et al. 2003). Computational models of carbachol (Traub et al. 2000)- and kainate-induced gamma oscillations (Fisahn et al. 2004) emphasize the importance of ectopic axonal action potentials for the generation of hippocampal gamma oscillations. The coexistence of phasic, high-frequency oscillations in principal cell axon populations and field

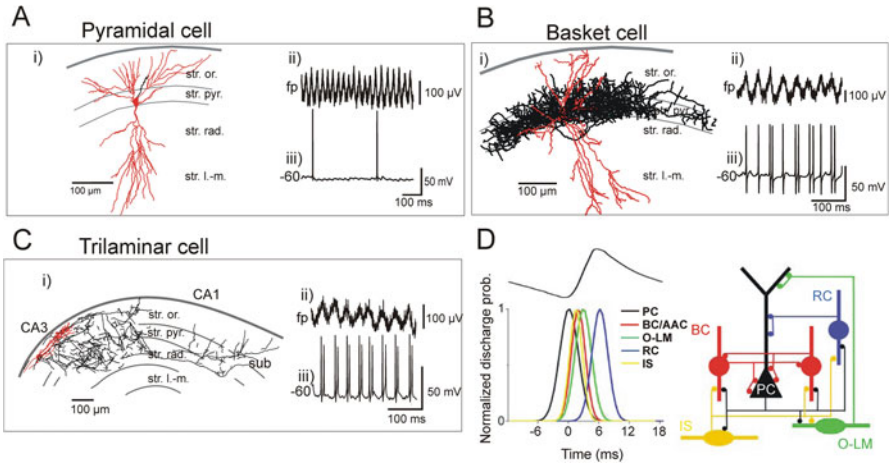

Fig. 3 Morphological and firing properties of hippocampal neurons during pharmacologically induced gamma oscillations. Reconstructions of representative biocytin-filled pyramidal (**A**i), PV-positive basket (**B**i) and trilaminar (**C**i) cells. The soma and dendrites are drawn in red, whereas the axons are in black. CA3, CA3 area; str. or., stratum oriens; str. pyr., stratum pyramidale; str. rad., stratum radiatum; str. l.-m., stratum lacunosum-moleculare. During kainate-induced field oscillatory activity (**A**ii; **B**ii), PCs fire sporadically (**A**iii), whereas basket cells discharged with single spikes interrupted by irregularly occurring doublets of action potentials, phase-locked to the field gamma activity (**B**iii). Trilaminar cell produced spike doublets (**C**iii) on every gamma cycle (**C**ii). (**D**) (left), Time sequence of firing of different neuron types during carbachol-induced oscillatory cycle (top trace). PCs fired at the negative peak of the oscillation followed by the interneurons. Gaussian functions were fitted to the spike time distribution for each type of neuron, and the average mean and SD were used to represent each cell class as a Gaussian function. (**D**) (right), Schematic diagram of the connectivity among phase-coupled neuron types in the CA3 hippocampal circuitry taking part in the gamma oscillation. (Panels **A**–**C** are adapted from Gloveli et al. (2005a); **D** is adapted from Hájos et al. (2004))

potential gamma frequency oscillations was demonstrated in kainate model (Traub et al. 2003).

Interneuron Types During gamma frequency oscillation in vivo and in vitro, the different classes of interneurons fire action potentials at different times and inhibit distinct subcellular domains of PCs (Figs. 2, 3, 4). During pharmacologically induced gamma frequency oscillations in vitro, perisomatic-targeting *PV-expressing basket* cells generate a predominantly gamma frequency output (Fig. 3B, Gloveli et al. 2005a; Hájos et al. 2004). Moreover, the firing of perisomatic basket cells is tightly coupled to the oscillation (Fig. 3B, D). The anatomical and physiological properties make these neurons ideally suited for generating local gamma rhythms, and indeed selective inhibition of PV basket cells' output synapses abolished carbachol-induced gamma oscillations in CA1 (Gulyás et al. 2010). Meanwhile, in kainate-induced gamma oscillations, there was no correlation of putative PV basket cells with the gamma oscillation (Craig and McBain 2015), suggesting that different interneuron mechanisms underlie the different paradigms employed. In

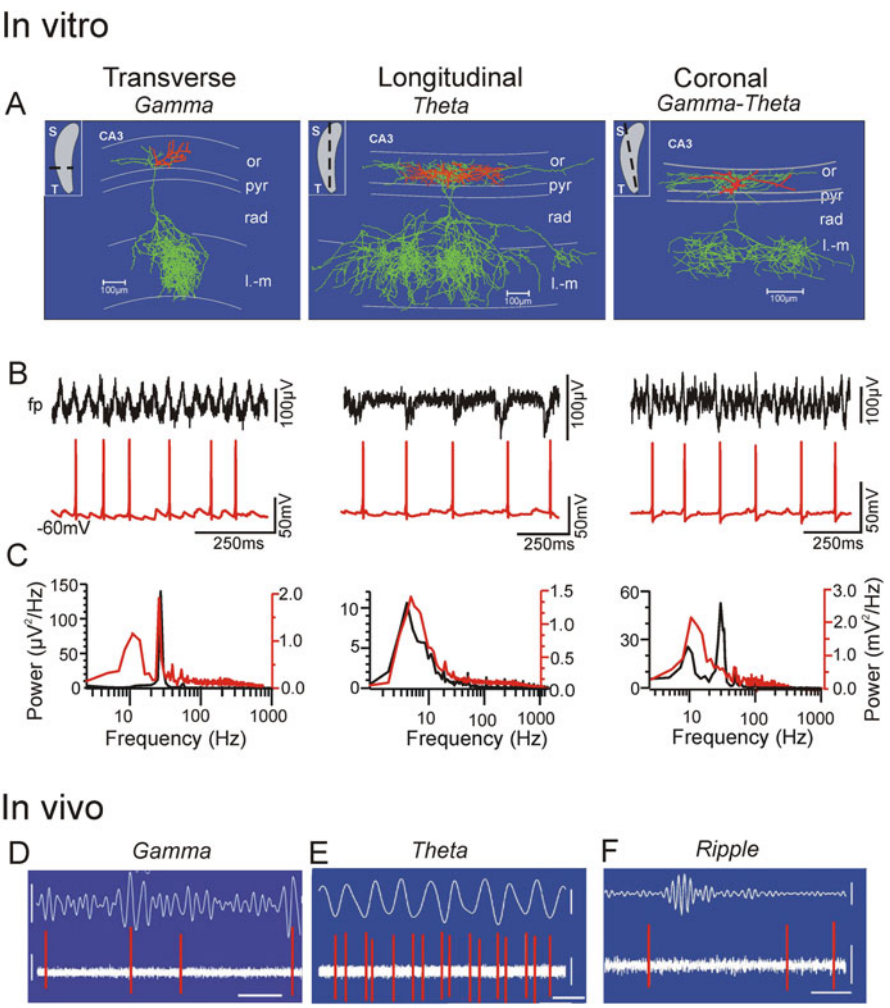

Fig. 4 Morphological and firing properties of O-LM interneurons. (**A**) Neurolucida reconstructed of biocytin-filled O-LM cell in area CA3 from transverse, longitudinal, and coronal slices. The soma and dendrites are drawn in red, whereas the axon is in green. Note different axonal ramification pattern in stratum lacunosum-moleculare in different slice preparation. Hippocampal layers are depicted schematically. CA3, CA3 area; str. or., stratum oriens; str. pyr., stratum pyramidale; str. rad., stratum radiatum; str. l.-m., stratum lacunosum-moleculare. (**B**) Typical example of extracellular field potential (fp) and concomitant current clamp (−60 mV) recordings in an O-LM cell after induction of oscillatory activity with kainate in different slices. (**C**) Corresponding power spectra (60-s epoch) from field (black) and current clamp (red) recordings. (**D**–**F**), O-LM firing in vivo is specifically associated with different types of brain state and network activity. Filtered extracellular network oscillations (top) and extracellularly recorded action potentials (bottom). Note that the O-LM cell firing is not phase-coupled to gamma cycle but fired rhythmically on the trough of theta oscillations and was silent during sharp-wave-associated ripples. Calibrations: (**D**) 0.1 mV (upper trace); 0.2 mV (lower trace) and 0.1 s; E,F, 0.3 mV (lower traces), 0.2 mV (upper theta trace), 0.05 mV (upper sharp-wave trace), and 300 ms (theta), 50 ms (sharp wave). (Adapted from panels **A** to **C** from Gloveli et al. (2005a, b), Dugladze et al. (2007), and Tort et al. (2007); panels **D** to **F** from Klausberger et al. (2003); and panel **F** from Tukker et al. (2007))

contrast, spiking of other PV-expressing perisomatic-targeting interneurons, *axo-axonic* cells was found to be only moderately coupled to the field gamma in anesthetized animals (Tukker et al. 2007), and their GABA release is not critical for the generation of carbachol-induced gamma field oscillations (Gulyás et al. 2010). However, inhibition mediated by axo-axonic cell can separate axonal and somatic activity, maintaining the functional polarization of PCs during gamma oscillations by preventing action potential spread across the axon initial segment (Dugladze et al. 2012).

There is no in vitro data available on the activity of identified *CCK-expressing basket* cells. However, recordings from central ganglionic eminence (CGE)-derived basket cells, which are mostly CCK-expressing, showed minimal spiking in response to kainate-evoked gamma oscillations, with a mean firing probability of 0.069 ± 0.027 (Craig and McBain 2015), much lower than for PV-expressing BCs. In vivo results confirm that, in contrast to PV-expressing BCs, these interneurons fire earlier than PCs and out of phase with PV-expressing interneurons, during the gamma oscillations in anesthetized animals (Tukker et al. 2007). Therefore, CCK-expressing basket cells are likely to interfere with gamma synchronicity (Freund and Katona 2007; Galarreta et al. 2008).

While PV-expressing perisomatic inhibitory interneurons are thought to play a major role in gamma oscillations (Hájos et al. 2004; Gloveli et al. 2005a), other classes of fast-spiking interneurons, such as bistratified and trilaminar cells, may also be important for this rhythm (Gloveli et al. 2005a). *Bistratified cells* were so named because the axonal arbor is found in two strata: oriens and radiatum (Buhl et al. 1994). In addition to PCs, they also innervate interneurons including basket cells (Halasy et al. 1996). During the gamma oscillations in vitro, bistratified cells discharge at high frequency, phase-locked to the field gamma (Gloveli et al. 2005a; Hájos et al. 2004; Tukker et al. 2007). Therefore, they are also likely to be involved in the generation of the gamma oscillatory activity. Interestingly, the most prominent interneuron output seen during pharmacologically induced gamma oscillations in vitro was associated with *trilaminar* interneurons (Gloveli et al. 2005a; Hájos et al. 2004; Craig and McBain 2015). These fast-spiking cells project to three dendritic layers of CA3 and CA1 areas, with axons densely innervating strata oriens, pyramidale and radiatum. Additionally, axon collaterals of CA3 trilaminar cells were seen projecting to area CA1 and into the subiculum and possibly to other brain areas as well (Somogyi and Klausberger 2005). These cells generated highly regular, short latency spike doublets (Fig. 3C, Gloveli et al. 2005a). Their axonal arborization indicates that these interneurons innervate somatic and dendritic compartments of PCs locally as well as distant regions. Thus, via these cells, gamma rhythms generated locally in area CA3 could be efficiently transmitted to distal sites "downstream" in the hippocampal processing pathway.

Interneuron located in the stratum *radiatum* (with both the dendrites and axonal arborization localized in the stratum radiatum) have the lowest firing rate among all dendrite-targeting interneurons with weak coupling to the gamma oscillations in vitro (Table 2, Hájos et al. 2004). Although *R-LM* cells (with dendritic tree

in stratum radiatum and axon restricted to stratum lacunosum-moleculare) fire at higher frequency than other radiatum cells, they also do not show significant phase-related firing (Hájos et al. 2004).

Stratum oriens O-LM cells, as described above (Fig. 2), are the archetypal feedback inhibitory interneuron and are more commonly associated with oscillations at lower frequencies (i.e., theta frequency; see below). However, they can also show preferential firing during in vitro generation of gamma oscillations (Chittajallu et al. 2013). Two populations of O-LM cells are observed following kainate puff-induced gamma activity, those which derive from the medial ganglionic eminence, which had a mean firing probability of 0.158 ± 0.029 during each gamma cycle, much higher than CGE-derived 5-HT3a containing O-LM cells which had a firing probability of 0.033 ± 0.008 for each cycle of gamma (Chittajallu et al. 2013). This serves to demonstrate that while both subtypes of O-LM cell are morphologically similar and express somatostatin, they are differentially recruited to local network activity.

Interestingly, projection interneurons, such as back-projecting CA1 interneurons, are very strongly modulated to gamma oscillations (Craig and McBain 2015), suggesting that these cells may serve to coordinate PC firing at these frequencies across subregions of the hippocampus.

Theta Oscillations

A prominent network pattern in the hippocampus of all mammals studied to date, including humans (Arnolds et al. 1980; Tesche and Karhu 2000), is a slow oscillation in the theta frequency band (4–12 Hz). Theta oscillations are most consistently present during various types of locomotor activities (Vanderwolf 1969) and rapid eye movement (REM) sleep (Jouvet 1969). In general, theta waves are absent in the immobile animal (Bland 1986; for review see Buzsáki (2002)). To explain the generation of these oscillations, various external pacemakers have been proposed [for review see Buzsáki (2002)]. One classical hypothesis is that cholinergic excitation from the septum and the diagonal band of Broca activates inhibitory interneurons, which in turn induce rhythmic IPSPs on the soma of depolarized PCs (Petsche et al. 1962). Indeed, this was elegantly demonstrated in organotypic hippocampal slice cultures, where the medial septum was cultured alongside, leading to the emergence of spontaneous theta oscillations (Fischer et al. 1999). Alternatively, the entorhinal cortex may entrain hippocampal areas at theta frequency. In rodents, hippocampal theta activity has maximal power in the CA1 region, and the synaptic currents underlying these oscillations are mainly generated by the entorhinal input [for review see Buzsáki (2002)]. However, recent in vitro experimental data and computational analysis indicate that theta activity can be generated intrinsically in the CA1 (Gillies et al. 2002; Rotstein et al. 2005) and CA3 (Gloveli et al. 2005b) areas, or the hippocampus as a whole (Goutagny et al. 2009). In fact, Cobb et al. (1995) demonstrated that individual GABAergic interneurons can effectively phase subthreshold membrane potential oscillations

and spontaneous firing in PCs at theta frequencies. Alternating inhibition and post-inhibitory "rebound" activation underlies the entrainment of PCs (Cobb et al. 1995). Intrinsic GABAergic mechanisms are thus sufficient to generate theta activity in cortical networks. Somewhat unexpectedly, the entrainment of local PV and SOM interneurons to theta oscillation is entirely dependent on CA1 recurrent collaterals, with little involvement of CA3 inputs (Huh et al. 2016.).

Various in vitro models of the theta oscillatory activity have been developed, based on either mAChR (Konopacki et al. 1992; Fisahn et al. 1998), metabotropic glutamatergic (mGluR) (Gillies et al. 2002), or kainate receptor activation (Gloveli et al. 2005a, b). Coactivation of mGluRs and metabotropic cholinergic receptors has also been reported to generate robust theta frequency oscillations in the hippocampus in vitro (Cobb et al. 2000).

Metabotropic GluR activation generates prominent, inhibition-based, atropine-resistant theta population oscillations under conditions of reduced AMPA receptor activation in the hippocampal CA1 area (Gillies et al. 2002). This field oscillation was independent of muscarinic cholinergic receptor drive but strongly dependent on NMDA receptor and $GABA_A$ receptor activity (Table 1, Gillies et al. 2002). The mechanism of generation of theta frequency population activity in this model appeared to involve intrinsic theta frequency membrane potential oscillations in a subset of stratum oriens interneurons. The blockade of AMPA receptors was a critical requirement of the experimental conditions needed to see this population theta activity. Many of the properties of theta frequency oscillations in this reduced model match those seen in area CA1 in vivo (Gillies et al. 2002). In particular, the resulting population theta rhythm resembled atropine-resistant theta oscillations recorded in vivo (Buzsáki et al. 1986) and may be generated by a subset of stratum oriens interneurons displaying intrinsic membrane potential oscillations at theta frequency (Gillies et al. 2002). In addition, the coherent theta oscillations may come from the interaction of other GABAergic interneurons with the O-LM cells.

In the CA3 area, theta oscillations can be induced by application of kainate. A necessary prerequisite to ensure precisely synchronized theta activity was specific orientation of the slices: theta frequency population activity was detected predominantly in longitudinal hippocampal slice preparation (Gloveli et al. 2005b). These data demonstrate that theta activity can be generated intrinsically both in the CA1 and the CA3 areas of the hippocampus. In an intact hippocampus, theta activity is capable of spreading in the CA3 -> CA1 direction but also in the alternative direction, dependent on subiculum inputs (Jackson et al. 2014), which contradicts elements of the classic intrinsic theta generation. While there are several differences between these models, a common feature is their dependence on GABAergic inhibition (Table 1).

Firing Patterns in Theta Oscillations

Principal Cells In a model of atropine-resistant theta oscillations following mGluR activation, with AMPA receptor activation blocked, PC somatic firing was seen in

only few cells recorded but could be elicited with injection of tonic depolarizing current (0.1–0.2 nA). In these conditions, PCs fired one spike per field theta (7 Hz) cycle during the trough of the field oscillation (Gillies et al. 2002). Consistent with this finding, pyramidal neurons in the CA1 region showed subthreshold resonance and firing preference at theta frequencies (range 2–7 Hz) (Pike et al. 2000). Recent data has shown that CA1 PC spiking is sparse during intrinsically generated theta oscillations, and its timing is highly dependent on local inhibition (Huh et al. 2016)

Interneuron Types Ample evidence supports the critical involvement of hippocampal interneurons in theta oscillations. The best documented is involvement of stratum oriens distal dendrite-targeting *O-LM* interneurons (Fig. 2, Fig. 4A) in generation of theta rhythm. This cell type was found to participate in hippocampal theta activity both in vivo (Buzsáki 2002; Klausberger et al. 2003) and in vitro (Pike et al. 2000; Gillies et al. 2002; Hájos et al. 2004; Gloveli et al. 2005a, b, Huh et al. 2016), with a small subpopulation that are not phase-locked to theta (Huh et al. 2016). In particular, involvement of O-LM cells was investigated in vitro in kainate- and mAChR-mediated network oscillatory activity. In kainate-induced oscillations, O-LM cells fired in the theta frequency range during both theta and gamma population activity (Fig. 4B, Gloveli et al. 2005b). O-LM cells show prominent membrane potential oscillations in the theta frequency range (Maccaferri and McBain 1996). By contrast, hippocampal fast-spiking cells preferentially resonate in the gamma range (Pike et al. 2000). Furthermore, O-LM cells have longer membrane time constants than the gamma-preferring interneurons and a considerably longer afterhyperpolarization (AHP). Changes in AHP profiles in interneurons have been shown to have dramatic effects on firing patterns (e.g., see Savić et al. (2001)). Thus, O-LM cells and gamma-preferring interneurons discharge at different frequencies and participate preferentially in theta or gamma activity, respectively (Gloveli et al. 2005a). The theta frequency discharge of O-LM interneurons (Fig. 4B, C, Gloveli et al. 2005b) will provide a robust theta frequency rhythmic inhibitory output to the apical dendrites of PCs.

There is a growing body of evidence that PV-expressing basket cells are critical for the generation and maintenance of theta oscillations in vitro (Korotkova et al. 2010; Amilhon et al. 2015; Huh et al. 2016). Indeed, PV basket cells show very strong phase-locking to the peak of theta oscillations, with a spike probability of one per theta cycle (Huh et al. 2016). Indeed, the specific timing of intrinsic theta oscillations are controlled by PV-expressing interneurons, with increasing activity through optogenetic stimulation resulting in increased theta oscillation frequencies (Amilhon et al. 2015).

The dendrite domains of principal cells are innervated by other dendritic inhibitory interneurons, whose involvement in the hippocampal oscillations has not been addressed in vitro. This includes, for example, recently described interneuron type in CA1 area in anesthetized animal, *Ivy* cells, expressing neuropeptide Y (NPY) and the neuronal nitric oxide (NO). The soma of these cells is located in stratum pyramidale, and axonal collaterals innervate two strata: oriens and radiatum. Ivy cells discharge at low frequency during theta as well as gamma

and ripple oscillations in anesthetized animals (Fuentealba et al. 2008). Another GABAergic interneuron type, *neurogliaform* cell that shares many similarities with Ivy cells, such as dense axonal fields, low-frequency discharge, and slow synaptic transmission (Vida et al. 1998; Price et al. 2005; Szabadics et al. 2007), is located in stratum lacunosum-moleculare and innervates the apical dendritic tuft of CA1 PCs co-aligned with the entorhinal input (Price et al. 2005). This cell type provides both fast $GABA_A$ receptor-mediated and slow $GABA_B$ receptor-mediated (Price et al. 2005; Szabadics et al. 2007) inhibition and therefore represents a potential candidate to be involved in both theta and gamma frequency oscillations. However, there is very little information about the activity pattern of this interneuron type and their role in network oscillations.

Nested Theta and Gamma Oscillations

Theta and gamma oscillations often occur simultaneously and show interaction. Amplitude of gamma oscillations is modulated with the phase of the theta rhythm. In addition, the frequencies of the two oscillations are also correlated, providing additional evidence of their interrelated function (Bragin et al. 1995). The coordinated nature of the two rhythms, and the observation that gamma power is stronger during theta-associated behavior (Leung et al. 1982; Bragin et al. 1995), implies that the neuronal generators of the two rhythms interact (and may be also overlap). This nested activity pattern is hypothesized to play a critical role in memory encoding and retrieval (Lisman and Idiart 1995; Lisman 2005).

Combined anatomical and physiological studies have provided evidence that in vitro gamma and theta rhythms are supported by neuronal circuits arranged orthogonally along the transverse and longitudinal axes, respectively (Table 1, Gloveli et al. 2005b). In hippocampal coronal slice preparation with intermediate orientations (between the transverse and longitudinal axis) both theta and gamma population rhythms were manifested (Fig. 4B and C, Gloveli et al. 2005b). The reason for that is a differential preservation of rhythm-generating microcircuits in transverse, longitudinal, and coronal slice preparation. Analysis of the three-dimensional axonal arborization patterns of different hippocampal CA3 interneurons recorded in transverse slices show that PV-expressing perisomatic targeting interneurons, along with trilaminar and bistratified cells, show a clear tendency to arborize widely within the transverse plane (Gloveli et al. 2005a, b). Indeed, mutual inhibition between PV-expressing interneurons produces strong nesting of gamma oscillations to theta cycles (Wulff et al. 2009), likely due to the high theta phase discharge of PV interneurons themselves (Huh et al. 2016). In contrast, distal dendrite-targeting O-LM cells arborized most extensively in the longitudinal plane forming two or three clusters in this direction (see Fig. 4A and Gloveli et al. (2005b)). In longitudinal slices, the preservation of these projections facilitated the generation of theta rhythms (Fig. 4B, C) with robust coherence over large distances (Gloveli et al. 2005b; Tort et al. 2007). Thus, orthogonal arrangement of rhythm-generating

microcircuits alongside the longitudinal and transverse axis, and distinct firing patterns of certain classes of interneurons during the theta and gamma frequency oscillations (Gloveli et al. 2005b; Tort et al. 2007), enables the hippocampus to produce different (solely or combined) population activity.

Sharp-Wave Ripple Activity

The high-frequency oscillations termed ripples (100–300 Hz) are typically associated with sharp-wave activity (Buzsáki et al. 1992; Wilson and McNaughton 1994; O'Neill et al. 2006). The hippocampal sharp-wave ripple (SWR) complex is thought to play an important role in synaptic plasticity and the transfer of new memory trace from the hippocampus to the neocortex (Buzsáki 1989).

The mechanisms of these fast oscillatory patterns in the hippocampus and neocortex are not fully understood (Buzsáki et al. 1992; Ylinen et al. 1995; Draguhn et al. 1998). Both in vivo and in vitro studies suggest that SWRs arise in the recurrent collateral system of the CA3 area (similar to gamma oscillations), propagate toward CA1, and leave the hippocampal formation via the subiculum and the EC (Chrobak and Buzsáki 1996; Csicsvari et al. 2000; Maier et al. 2003, Both et al. 2008). During this state, the hippocampus seems to be less controlled by input from the EC; rather, it generates output signals itself (Chrobak and Buzsáki 1996). Data from the rodent hippocampus showed that GABAergic interneurons, in particular, parvalbumin (PV)-expressing fast-spiking basket cells, play a crucial role in SWR generation in vivo (Schlingloff et al. 2014; Stark et al. 2014).

SWR complex can be induced in vitro by electrical stimulation, pharmacologically, or can occur spontaneously with similar properties to the events seen in vivo (Maier et al. 2003; Nimmrich et al. 2005; Behrens et al. 2005; Hájos et al. 2009; HájosEller et al. 2015; Zarnadze et al. 2016). Several local network mechanisms underlying these patterns have been identified within CA1, including strong inhibition of nonparticipating PCs during SWR (Ylinen et al. 1995; Maier et al. 2003) and electrical coupling of CA1 PCs (Draguhn et al. 1998; Schmitz et al. 2001; Nimmrich et al. 2005). Concomitant extracellular and intracellular recordings of SWR complexes show that PCs display EPSP-IPSP sequences, IPSP-EPSP sequences, and prominent IPSPs, but never isolated EPSPs (Behrens et al. 2005). These results suggest that inhibitory inputs are strong during the development of ripple complexes. Consistent with this finding, fast-spiking basket and bistratified interneurons strongly increase their firing rate during ripple oscillations in vivo (Ylinen et al. 1995; Klausberger et al. 2004). Another fast-spiking cell type, axo-axonic interneurons, fires before the ripple episode but is silenced during and after (Klausberger et al. 2003). In contrast, non-fast-spiking O-LM cell firing is suppressed during ripples in vivo (Klausberger et al. 2003), however 50% of O-LM cells show phase-locking to the end of ripples in vitro (Pangalos et al. 2013). This suggests that although they do not fire during ripples, they may contribute to the subsequent refractory period. Gap junctions also seem to be important for ripples,

since the blockade of gap junctions with carbenoxolone attenuated ripple occurrence (Behrens et al. 2005, LeBeau et al. 2003). Interestingly, SWR can be induced with stimulation protocols known to induce LTP, a model of learning and memory, suggesting that this pattern is associated with changes in functional connectivity (Behrens et al. 2005).

The Interdependence of Gamma Oscillations and Sharp-Wave Ripples

Gamma oscillations and SWRs, involved in memory encoding (Jutras and Buffalo 2010) and consolidation (Buzsáki 1989; Girardeau et al. 2009; Jadhav et al. 2012), respectively, appear to be interlinked in the course of memory processing. These two rhythms reflect two "competing," mutually exclusive network states in vitro (Eller et al. 2015; Zarnadze et al. 2016, Fig. 5): spontaneously occurring SWRs disappear shortly after onset of gamma rhythms induced by bath application of kainic acid (KA, 400 nM) and reappear within a few minutes after KA washout. However, transient slow gamma synchrony may synergistically interact with SWRs and promote hippocampal memory replay (Carr et al. 2012). Thus the two network patterns are not fully independent. Indeed, in an in vitro model, it was found that plastic changes initiated in the network by means of persistent gamma activity altered the subsequent SWR pattern (Fig. 5). Comparison of SWRs before the oscillatory gamma episode with post-gamma SWRs (p-SWR) reveals a significantly increased p-SWR area. In good agreement with this data, gamma oscillations induced by bath application of carbachol (20 μM), an alternative drug to trigger persistent gamma oscillations based on a different network mechanisms (Fisahn et al. 1998, 2002; Hájos et al. 2004), also result in a significant increase in SWR area (Zarnadze et al. 2016). This indicates that gamma activity itself, and not the pharmacological agent, is responsible for network alteration. Moreover, the intervening gamma episode also has an enhancing effect on subsequent gamma oscillations (Fig. 5E and F). Together, these results demonstrate that a gamma frequency episode significantly affects subsequent network activities. These effects are independent of the pharmacological agent used for the induction, but correlate with the presence and the power of gamma oscillations, highlighting the general potential of gamma rhythms to alter network activity. This form of plasticity is impaired by mGluR5 and NMDAR antagonists (Fig. 5D) suggesting that in the hippocampal area, CA3 gamma frequency oscillations influence the subsequent network activity through mGluR5- and NMDAR-dependent mechanisms.

In parallel to this facilitating network effect, the excitability of CA3 PCs following gamma rhythms is also enhanced. In contrast to this excitatory neurons, the excitability of two types of perisomatic targeting inhibitory interneurons, PV-expressing and CCK-expressing basket cells, displayed opposing effects (Zarnadze et al. 2016). In particular, fast-spiking PV-expressing cells, mediating rapid inhi-

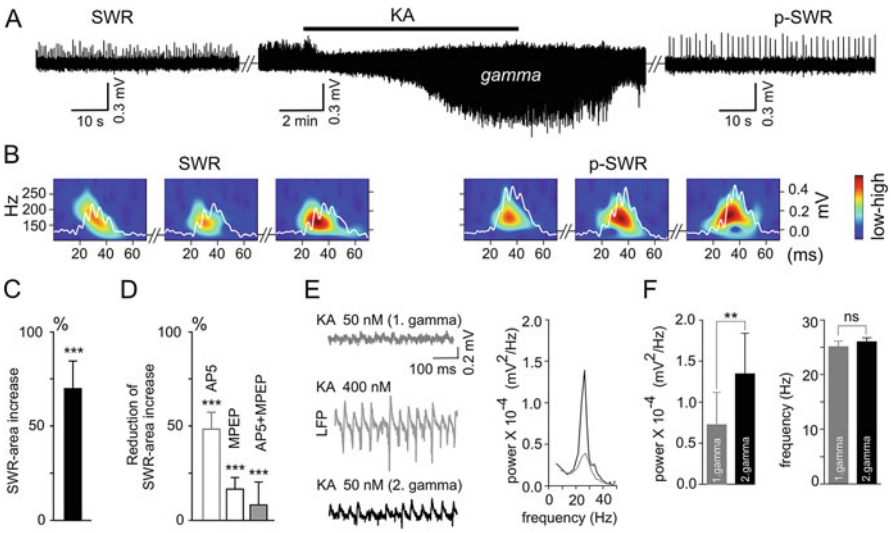

Fig. 5 Gamma oscillations promote long-lasting alterations in the network activity. (**A**) SWRs recorded in the stratum pyramidale of the CA3 region occurred spontaneously (left), disappeared shortly after bath application of KA (middle), and reappeared with a significantly higher amplitude after KA washout (right, p-SWR). Note the persistent gamma network oscillation after KA washout. (**B**) Example of the wavelet transform (color-coded power spectral density) for three consecutive highlighted SWRs (white trace) before (SWR) and after (p-SWR) intermediate gamma oscillations. (**C**) Gamma oscillation induces a significant SWR area increase. (**D**) Gamma oscillation-induced SWR area increase is significantly reduced by administration of AP5 (gray open bar), MPEP (black open bar), and MPEP+AP5 (black bar with gray filling). (**E**) Brief "weak" field gamma episodes were induced by bath application of 50 nM KA (left, top). After this test period, "conventional" gamma frequency oscillations were induced by 400 nM KA application (left middle), followed by KA washout achieving a complete cessation of oscillatory gamma activity. In a third step, the network behavior was tested again with the same low KA concentration as applied in the first step (left, bottom). The spectral analysis of the 1st and 2nd "weak" gamma oscillation reveals a strengthening effect of the intervening "conventional" gamma episode. (**F**), Summary bar charts of peak power (left) and frequency (right) obtained before (1st "weak" gamma) and after "conventional" gamma (2nd "weak" gamma). (Panels **A**–**F** are adapted from Zarnadze et al. (2016))

bition and contributing to the precise timing of neuronal synchronization and emergence of network oscillation (Cobb et al. 1995; Gloveli et al. 2005a; Sohal et al. 2009; Schlingloff et al. 2014), exhibit enhanced activation, while regular firing CCK-expressing cells, mediating slower inhibition (Hefft and Jonas 2005; Daw et al. 2009), show reduced excitability (Zarnadze et al. 2016). In this cell type-specific, differential plasticity of the two major GABAergic interneuron types, in turn, may underlie enhanced network excitability and thus promote synaptic plasticity. These results also emphasize the pivotal role of network gamma oscillations as a tool to investigate synaptic plasticity in the network.

Cellular, Synaptic, and Axonal Mechanisms Involved in Oscillations

Intrinsic Properties The voltage-gated ion channels strongly contribute to **PC** excitability. These channels influence intrinsic properties of the neuron, such as the action potential threshold, spike AHP and afterdepolarization (ADP), and action potential firing mode. Na^+ and A-type K^+ channels are expressed in both CA1 and CA3 PCs, whereas hyperpolarization-activated cation channels (HCN channels) are expressed in CA1 PCs but are almost absent from CA3 PCs (for review see Spruston (2008)). The HCN channels in PCs have important influences also on synaptic integration. Deactivation of these channels reduces EPSP duration and results in a slight hyperpolarization following EPSPs (Magee 1999). Conversely, activation of HCN channels reduces IPSP duration and produces a slight depolarization following the IPSP (Williams and Stuart 2003; for review see Spruston (2008)). This interaction of HCN channels and synaptic conductance may represent elementary mechanisms for rhythmogenesis at the cellular and subcellular levels.

Another feature relevant for the firing pattern of PCs in the hippocampus is their ability to generate subthreshold membrane potential oscillations (MPOs) in the theta frequency range and their resonance properties (Leung and Yu 1998; Pike et al. 2000). These properties of hippocampal PCs are likely to contribute to theta activity (Leung and Yu 1998). In hippocampal PCs the electrical resonance at theta frequencies is generated by M-current, h-current, and persistent Na^+ current (Hu et al. 2002).

How the different firing patterns of certain **GABAergic interneurons** are generated remains largely unknown. Intrinsic membrane properties of these cells may be important for hippocampal network oscillations. For instance, O-LM cells have a longer membrane time constant and a considerably longer (five- to tenfold slower) AHP than the gamma-preferring interneurons (Gloveli et al. 2005a), restricting their firing to low, theta frequencies (see Savić et al. (2001)). In addition, O-LM cells show prominent slow subthreshold membrane potential oscillations and the resonance properties in the theta frequency range (Maccaferri and McBain 1996; Pike et al. 2000).

Hyperpolarization-activated cationic currents (I_h) and I_A currents which have been detected in hippocampal interneurons may not only influence the intrinsic and firing properties but also their synchronization. I_h currents are activated at voltages close to rest (Gu et al. 2005). Different subunit composition (HCN1-4) that is coexpressed in hippocampal GABAergic interneurons (Notomi and Shigemoto 2004) influences not only the kinetics but also the voltage dependency of I_h activation [see Chen et al. (2002)]. Besides O-LM and other types of non-fast-spiking interneurons, I_h channels are expressed in the somato-dendritic region, axon, and presynaptic elements of fast-spiking basket cell in the hippocampus (Aponte et al. 2006). In contrast, hippocampal lacunosum-moleculare and radiatum interneurons display subthreshold MPOs generated by an interplay of Na^+ and

4-AP-sensitive A-type K^+ currents, independent of I_h currents and muscarine-sensitive K^+ currents, I_M (Bourdeau et al. 2007).

Synaptic Properties The properties of excitatory events discriminate hippocampal principal cells from inhibitory neurons (Miles 1990; Jonas et al. 1993; Geiger et al. 1997; Toth et al. 2000). It appears that excitatory synapses onto interneurons not only tend to have a larger number of AMPA receptors (Nusser et al. 1998), thereby increasing the quantal amplitude, but the postsynaptic receptors also appear to have a different molecular composition (Geiger et al. 1995), which, in turn, endows them with faster kinetics (Geiger et al. 1997). Further discrimination in the properties of excitatory input was found between different interneuron types. Different classes of hippocampal interneurons with distinct axonal ramification patterns and efferent target profiles show clear differences in both amplitude and kinetics of EPSCs/Ps during gamma frequency network oscillations (Gloveli et al. 2005a). For instance, the amplitudes of excitatory drive are considerably larger in fast-spiking BCs and trilaminar cells than in O-LM cells (Fig. 2B), suggesting the intensity of synaptic drive may play a role in generating their different outputs (Gloveli et al. 2005a).

Similar to the kinetics of excitatory postsynaptic currents at PC-BC, unitary inhibitory postsynaptic currents at BC-BC synapses demonstrated very fast kinetics (Bartos et al. 2001, 2002). In addition to IPSCs with fast kinetic properties ($GABA_{A,fast}$) mediated by perisomatic synapses, IPSCs with slowly rising and decaying kinetic ($GABA_{A,slow}$) mediated by dendritic synapses were also detected in CA1 area (Banks et al. 2000). Interplay of CA1 interneurons, mediating $GABA_{A,slow}$ and $GABA_{A,fast}$ may contribute to theta and gamma rhythms occurring separately or as a nested gamma/theta rhythm (Banks et al. 2000). Furthermore, $GABA_B$ receptors contribute to the maintenance and modulation of gamma oscillations, as evidenced by the selective agonist acting at presynaptic receptors strengthening gamma power, while activation of pre- and postsynaptic receptors reduces gamma power (Dugladze et al. 2013). Theta oscillations are strongly inhibited by presynaptic $GABA_B$ receptor activation (Booker et al., unpublished observations). Further, it has been shown through modeling of PV BC networks that postsynaptic $GABA_B$ receptor activity on those interneurons has the potential to give rise to theta/gamma nesting (Booker et al. 2013). Finally, activation of $GABA_B$ receptors strongly suppresses the occurrence of sharp-wave ripples in CA3 (Hollnagel et al. 2014).

Thus, different intrinsic membrane properties together with different kinetics of excitatory and inhibitory inputs govern the specific roles of hippocampal cells in shaping distinct network oscillatory activity.

Axonal Properties In central neurons, action potentials (APs) are generated close to the soma, at the axon initial segment (AIS), and propagate along the axon to downstream neurons. The impact of the PCs in network oscillations is typically evaluated from intrasomatic recordings. However, PC axonal activity may arise independently under certain conditions and itself undergo activity-dependent modifications which in turn may affect the network properties and activity. In line with this, a novel form

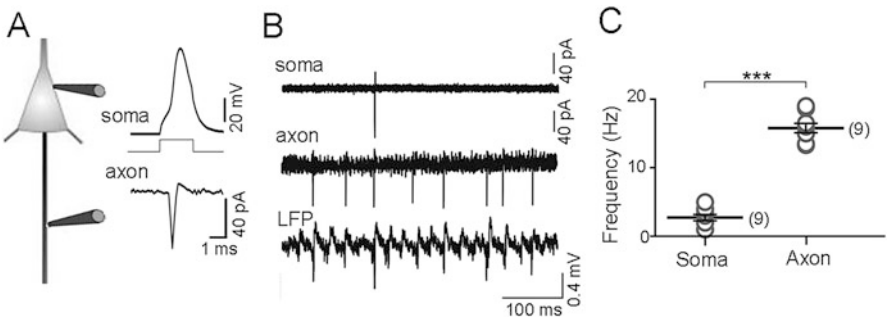

Fig. 6 High-frequency discharge of the axon but not the soma of hippocampal CA3 PCs during gamma frequency oscillations in vitro. (**A**) Scheme of dual somatic and axonal recording configuration. APs evoked in whole-cell configuration by brief depolarizing current injection into the soma (800 pA, inset) reliably induced ACs in the axon, confirming that recordings are made from two compartments of the same cell. (**B**) Dual somatic and axonal cell-attached recoding directly demonstrate that high-frequency axonal spikes ("axon") fail to invade the soma ("soma") during gamma frequency oscillations ("LFP"). (**C**) Summary plot shows the highly significant difference in the discharge frequency observed at the soma and proximal axon in dual recordings (n = 9 cells) during network oscillations. (Panels **A**–**C** are adapted from Dugladze et al. (2012))

of activity-dependent plasticity in a subclass of cortical interneurons was recently reported (Sheffield et al. 2011). During persistent firing (at beta/gamma frequencies of 20–40 Hz), APs are generated in the distal axon and persists for tens of seconds to minutes. The increased frequency of presynaptic firing as result of altered intrinsic properties of axons may enhance the reliability of signal transmission and affect the network properties [see Ganguly et al. (2000)]. Many different types of sodium and potassium channels, as well as calcium transients and hyperpolarization-activated inward currents have been described in axons [for review see Debanne et al. (2011) and Ruiz and Kullmann (2013)]. The complex time and voltage dependence resulting from the properties of ion channels can lead to activity-dependent changes in resting membrane properties, such as a membrane potential, lowering thereby the threshold of ectopic (axonal) spike initiation. Importantly, the changes in AP threshold were shown to be dependent on local protein synthesis and the long-term changes in axon excitability can occur in response to relatively brief changes in activity [see Bucher and Goaillard (2011)]. In addition, a growing number of studies show that the axon can express receptors to glutamate, GABA, acetylcholine, or biogenic amines, changing the relative contribution of some channels to axonal excitability [for review see Debanne et al. (2011), Bucher and Goaillard (2011), and Ruiz and Kullmann (2013)].

Recently developed techniques that allowed to record simultaneously from axons and soma of single PCs (Dugladze et al. 2012; Sasaki et al. 2012) revealed highly unexpected properties of the axon of CA3 PCs during gamma frequency oscillations (Dugladze et al. 2012, Fig. 6). In particular, it was found that (1) under physiological condition AP are initiated also in the distal part of CA3 PCs, (2) the frequency of

APs in axons recorded >600 μm from the soma was four- to fivefold higher, and (3) dual somatic and axonal cell-attached recordings from individual cells demonstrate that distal axonal spikes achieve the proximal axons but fail to invade the soma (Dugladze et al. 2012).

These findings have wider implication for the understanding of signal processing in the hippocampus. First, they provide direct and unequivocal evidence that APs could be initiated independently in axonal and somato-dendritic compartments of PCs during network oscillations. Second, the axonal spikes are generated at high frequency in the active network, and these axonal properties may participate in experimentally observed high-frequency excitatory input to both PCs and interneurons in the active network (Gloveli et al. 2005a). Finally, hippocampal principal cells require an additional mechanism to efficiently control the backpropagation of AP to the somato-dendritic compartments. Indeed, it was found that inhibition at the AIS caused by PV-positive axo-axonic cells underlies the suppression of ectopic AP invasion to the parent PC soma. In particular, shunting inhibition rather than membrane potential hyperpolarization prevents the backpropagation of ectopic APs across the AIS (Dugladze et al. 2012).

Neuromodulatory Control of In Vitro Oscillations

Sources of neuromodulators in the brain are the four aminergic systems: the dopaminergic, histaminergic, serotonergic, and noradrenergic systems. All four of the associated modulators (dopamine, histamine, serotonin, and noradrenalin) are released from small groups of neurons, which have projection patterns to most of the brain, including the hippocampus. Effects of these neuromodulators have been tested in vitro on theta and gamma oscillatory activity.

The hippocampus receives dopaminergic input from the ventral tegmental area. Activation of D1-like **dopamin**e receptors strongly depresses cholinergic gamma oscillations in area CA3 of rat hippocampus, and this effect is most likely mediated via impairment of interneurons involved in generation and maintenance of the carbachol-induced network rhythm (Weiss et al. 2003). Conversely, D4 receptor activation strongly enhances gamma oscillation power (Andersson et al. 2012).

Histamine 3 (H3) receptors seems likely to play an important role in regulation of hippocampal theta oscillation. Systemic administration of the H3 receptor antagonists (ciproxifan and thioperamide) enhances the power of spontaneous theta in anesthetized rats. Since H3 receptors are located at axon terminals of histamine-containing neurons and function as autoreceptors (Arrang et al. 1983), their blockade could enhance histamine release and subsequently promote hippocampal theta oscillation. Regulation of hippocampal theta oscillations by H3 receptors may represent one of the probable mechanisms involved in histamine-induced modulation of higher brain functions, such as attention and learning (Hajós et al. 2008).

Serotonergic neurons of the midbrain raphe have been implicated in the control of affective and cognitive functions and in modulating the neural activities of networks across the sleep–wake cycle. The midbrain raphe nuclei form a strong serotonergic projection to the hippocampus. Recent in vivo finding suggests that a subpopulation of raphe neurons discharged action potentials that were phase-locked to the hippocampal theta rhythm (Kocsis et al. 2006). Hippocampal PCs and interneurons show different expression of metabotropic 5-HT receptor subtypes, such as 5-HT_{1A}, 5-HT_{1B}, and 5-HT_2 (Ropert and Guy 1991; Schmitz et al. 1995; Shen and Andrade 1998), which may result in a differential modulation of intrinsic and synaptic properties of these cells in response to serotonin [for review see Schmitz et al. (1998)]. Serotonin input may influence the hippocampal network also via ionotropic 5-HT_3 receptors, which are expressed by several classes of GABAergic interneurons (Tecott et al. 1993; Ropert and Guy 1991; Morales et al. 1998). These cells include CCK-containing basket cells, an interneuron type that has been proposed to hamper the gamma rhythm (see section "Firing Patterns in Gamma Oscillations," Freund and Katona 2007; Galarreta et al. 2008), as well as calbindin- and calretinin-containing GABAergic cells (Morales and Bloom 1997). In contrast, serotonergic fibers do not contact the PV-containing GABAergic basket cells, which are responsible for some gamma frequency oscillations (see section "Firing Patterns in Gamma Oscillations"). Therefore, the rhythmic serotonergic input may modulate, but not drive, hippocampal network oscillations at gamma frequency range.

The brain **noradrenergic** (NE) neurons, located in the pontine nucleus of locus coeruleus (LC), are presumed to play a role in regulation of the circadian sleep-wake cycle and alertness (Aston-Jones and Cohen 2005). Several experimental findings suggest involvement of this neuromodulators on the hippocampal network activity. Local injection of glutamate in the LC results in multiple actions on the hippocampus, which include an increase in theta rhythm (Brown et al. 2005). Activation of LC-NE neurons by local application of a cholinergic agonist (bethanechol) induces theta oscillation of MS/DB neurons and theta-wave oscillation of hippocampal EEG in anesthetized rats (Berridge and Foote 1991). Furthermore, the selective NE reuptake inhibitor reboxetine modulates hippocampal theta activity in a state-dependent manner, i.e., can either increase or decrease theta amplitude depending on the behavioral state of the animal (Kocsis et al. 2007).

Pharmacological agents which are used with in vitro models of oscillation, such as KAR, mGluR, and mAChR agonist, also have a direct modulatory effect on hippocampal neurons in a manner that is remarkably cell specific. Various types of interneurons express **KARs** (Cossart et al. 1998, 2002; Frerking et al. 1998; Mulle et al. 2000; Lerma 2003). Kinetics of KA-mediated EPSCs is slower than that of AMPAR (Frerking et al. 1998; Cossart et al. 2002), which could enable these two receptor types to generate oscillations with different dominating frequencies (Frerking and Ohliger-Frerking 2002). Consistent with this, O-LM interneurons, which receive a large input mediated by KARs (Cossart et al. 2002), show postsynaptic KAR-mediated action potential firing at 10 Hz during theta stimulations, in contrast to perisomatic, bistratified, or septum/back-projecting cells (Goldin et al. 2007). Activation of **mGluRs** in the hippocampus has a range of effects (Anwyl

1999) which include decreases in I_m and I_{AHP} currents. Therefore, activation of these receptors increases the excitability of hippocampal cells. mGluRs subtypes are differentially expressed in specific hippocampal interneurons resulting in their different responsiveness to agonists. Thus, O-LM cells express a large number of group I mGluRs and are very sensitive to agonists, in marked contrast to other stratum oriens interneurons, including basket cells that express only small number of this receptor subtype and are less sensitive (van Hooft et al. 2000). Also **mAChR** agonists may act on different GABAergic inhibitory interneurons that possess the muscarinic receptors (Pitler and Alger 1992). Activation of these receptors may increase the excitability of interneuronal activity. In particular, muscarinic receptor agonist-carbachol blocks several potassium conductances, including I_{AHP} and I_M in a concentration-dependent manner (Madison et al. 1987). This depolarizes the PCs, unmasking subthreshold membrane potential oscillations in the theta frequency range (Leung and Yim 1986; Fellous and Sejnowski 2000). In addition, muscarinic receptor activation consistently enhanced firing frequency and produced large, sustained ADPs of O-LM but not other stratum oriens interneurons (Lawrence et al. 2006).

In summary, the effects of state-dependent activation of different neuromodulators can be markedly different on hippocampal network activity and depend on the expression and distribution of receptors across the cellular components of the network.

Oscillations in Disease

Schizophrenia

A number of studies have shown changes in gamma frequency EEG activity in schizophrenia. Reduced gamma activity was found in stimulus-dependent responses in the auditory and visual cortices of schizophrenic patients [for review see Kehrer et al. (2008)], and there is also evidence for a change in neuronal synchrony during high-frequency oscillations (Spencer et al. 2004). Interestingly, the amounts of RNA and immunoreactivity for PV are reduced in postmortem tissue from the frontal cortex and the hippocampus pointing to a reduction in perisomatic inhibitory interneuron population (Zhang and Reynolds 2002). The loss of these interneurons could directly explain the observed changes in gamma oscillations (Lewis et al. 2005; Vierling-Claassen et al. 2008). Although most clinical studies have found reductions in gamma band activity in schizophrenic patients [e.g., Slewa-Younan et al. (2001)], there appears to be a symptom-specific pattern in the alterations in gamma activity indicating that increases in amplitude and power are associated with positive symptoms, particularly hallucinations and reality distortions, whereas negative symptoms such as psychomotoric deficits are linked to decreased gamma activity (Baldeweg et al. 1998; Bucci et al. 2007). Similar to clinical observations, in in vitro NMDA-hypofunction models of schizophrenia, both increased (Kehrer et

al. 2007; Pinault 2008) and decreased gamma activities (Cunningham et al. 2006) have been demonstrated [for review see Kehrer et al. (2008) and Roopun et al. (2008)]. Recently it been shown that the acute effects of NMDA-hypofunction result in increased gamma but decreased theta, while chronic administration of NMDA receptor inhibitors results in both decreased gamma and theta oscillation power (Kittelberger et al. 2012).

Alterations of cortical interneurons in schizophrenia, especially parvalbumin- and somatostatin-containing interneurons, are well documented. These alterations are likely to have significant effects on the network oscillatory activity and therefore on cognitive processes (Gonzalez-Burgos and Lewis 2008; Morris et al. 2008). The axo-axonic subclass of GABAergic interneurons containing the calcium-binding protein parvalbumin have attracted the most scrutiny in studies of schizophrenia (Howard Behrens et al. 2007; Sakai et al. 2008; Wang et al. 2008). Although the altered network activities were reported in vivo and in vitro [see, e.g., Cunningham et al. (2006); Behrens et al. (2007); Braun et al. (2007); Gonzalez-Burgos and Lewis (2008), and Spencer (2008)], further investigation needs to be undertaken to address possible model- and region-specific alterations in the gamma network oscillatory activity in different animal models of schizophrenia. Establishing the contingencies of increased versus decreased gamma band activity is of high importance since aberrant network oscillatory activity may underlie the cognitive decline observed in schizophrenic patients and offer vital clues to the relationship between positive and negative symptoms in schizophrenia at a network levels (Cho et al. 2006; Bucci et al. 2007; Ford et al. 2007).

Mesial Temporal Lobe Epilepsy (mTLE)

Epileptic seizures are less frequent in conditions during which theta frequency occurs (e.g., wakefulness or REM sleep, Montplaisir et al. 1987), and thus the theta rhythm appears to indicate a hippocampal functional state in which generation of seizures is hindered (Colom et al. 2006).

In epileptic mice, the power of low-frequency theta oscillations has been reported to be reduced (Arabadzisz et al. 2005; Dugladze et al. 2007). Apart from suppression of the theta oscillatory activity, as a potential anticonvulsant factor (Colom et al. 2006), a strong enhancement of the gamma activity (Dugladze et al. 2007) may underlie emergence of epileptiform activity. Observations in humans support this scenario: spatially localized increase in the power of gamma frequency oscillations have been observed preceding seizures in human TLE patients (Fisher et al. 1992). In addition, gamma oscillatory activity and increases in firing rate of the interneuronal network have been suggested as mechanisms of seizure occurrence in patients with drug-resistant TLE (Bragin et al. 2007). Consistent with this suggestion, intracellular recordings in kainate model of mTLE reveal an increased firing frequency of both PCs and dendrite-inhibiting interneurons in the ventral hippocampal CA3 area of epileptic mice (Dugladze et al. 2007). The involvement of the perisomatic targeting interneurons remains, however, to be investigated. In fact, recent evidence suggests that $GABA_B$ receptor-mediated presynaptic control

of the inhibitory output of parvalbumin- and CCK-expressing basket cells are differentially affected (Dugladze et al. 2013). A cell type-specific upregulation of presynaptic $GABA_B$ receptor expression and consequently enhanced presynaptic inhibition in CCK basket cells promotes aberrant high-frequency oscillations and hyperexcitability in hippocampal networks of chronic epileptic mice (Dugladze et al. 2013).

The epileptic tissue may also generate a specific rhythm, transient high-frequency oscillations (HFOs) in the 200–600 Hz frequency band known as fast ripple (Bragin et al. 1999). In fact, fast ripples may represent a specific marker for the area of the brain in which seizures begin [Bragin et al. 2002; for review see Jacobs et al. (2012) and Frauscher et al. (2017)]. The frequency of these oscillations is about twice as fast as the maximum rate at which most neurons in the hippocampus can fire action potentials. This fact raises the question how these oscillations are generated. Analysis of the firing properties of hippocampal neurons during HFOs in vitro low-Mg^{2+} model of epileptiform activity showed that the PCs fired at the rising phase of the highest frequency portion of the field oscillation. In addition, distal dendrite-targeting interneurons (R-LM cells) fired at the start of the epileptiform bursts (on average 140 Hz) but stopped firing before its end (Spampanato and Mody 2007). However, neither the principal cells nor the distal dendrite-targeting interneurons (R-LM and O-LM cell) fired action potentials at high frequencies (200–600 Hz) seen in the field oscillations (Spampanato and Mody 2007). Another study (Foffani et al. 2007) suggested that these synchronous population oscillations could be generated as a consequence of the out-of-phase activities of two independent oscillators, each operating at half the frequency of the ensemble. In line with this suggestion, it was found that hippocampal PCs fired short bursts of action potentials at frequencies up to 300 Hz (Kandel and Spencer 1961), and some interneurons could sustain frequencies of 400 Hz (Foffani et al. 2007). It is currently hypothesized that the temporary uncontrolled firing of principal cells due to a brief functional collapse of perisomatic inhibition generates fast ripples (Gulyás and Freund 2015).

Thus, numerous studies suggest that alterations in inhibition-based network oscillations may underlie the pathophysiology in schizophrenia and mTLE, which are associated with impaired information processes.

Perspectives

The spatiotemporal patterns of activity during network oscillations would ideally be explored in vivo (Bragin et al. 1995; Penttonen et al. 1998; Csicsvari et al. 2003; Buzsáki et al. 2003). However, it is also reasonable to use relevant in vitro models to test hypotheses for the basic mechanisms involved. The replication of an endogenous brain pattern in vitro allows for the investigation of a number of important cellular and synaptic mechanisms that are difficult or even impossible to explore in vivo. In addition, using transgenic, fluorescent EGFP-expressing mice under the control of different gene promoters (Oliva et al. 2000; Meyer et al. 2002)

enables the identification and selection of different interneurons in the acute slice preparation. The firing properties of single cells in the active network, and the contribution of excitation and inhibition to the generation of network oscillatory activity, can be systematically examined in different models of in vitro oscillations (Table 1), which may reflect region and state dependence of mechanisms underlying network oscillations in vivo. Although there are some differences between the data obtained from in vitro and in vivo observation, these observations show substantial homology. The development of new transgenic methods for activating, inactivating, and labeling neurons and synapses (Marek and Davis 2003; Polleux 2005) has led to important new insights and will certainly further facilitate progress in this area. Furthermore, several in vitro methods may help to overcome the limitations in vivo. These include simultaneous patch-clamp recording from several cells in a brain slice (Miles and Poncer 1996; Markram et al. 1997; Peng et al. 2017), recording of sufficiently large numbers of cells at once using optical methods, and stimulation/suppression of different cellular compartments using uncaging of different substance or optically activated channels (Callaway 2002; Boyden et al. 2005; Deisseroth et al. 2006; Zhang et al. 2007; Deisseroth and Hegemann 2017).

References

Amilhon B, Huh CY, Manseau F, Ducharme G, Nichol H, Adamantidis A, Williams S (2015) Parvalbumin interneurons of hippocampus tune population activity at theta frequency. Neuron 5:1277–1289

Andersson RH, Johnston A, Herman PA, Winzer-Serhan UH, Karavanova I, Vullhorst D, Fisahn A, Buonanno A (2012) Neuregulin and dopamine modulation of hippocampal gamma oscillations is dependent on dopamine D4 receptors. Proc Natl Acad Sci U S A 109:13118–13123

Anwyl R (1999) Metabotropic glutamate receptors: electrophysiological properties and role in plasticity. Brain Res Rev 29:83–120

Aponte Y, Lien CC, Reisinger E, Jonas P (2006) Hyperpolarization-activated cation channels in fast-spiking interneurons of rat hippocampus. J Physiol 574:229–243

Arabadzisz D, Antal K, Parpan F, Emri Z, Fritschy JM (2005) Epileptogenesis and chronic seizures in a mouse model of temporal lobe epilepsy are associated with distinct EEG patterns and selective neurochemical alterations in the contralateral hippocampus. Exp Neurol 194:76–90

Arnolds DE, Lopes da Silva FH, Aitink JW, Kamp A, Boeijinga P (1980) The spectral properties of hippocampal EEG related to behaviour in man. Electroencephalogr Clin Neurophysiol 50:324–328

Arrang JM, Garbarg M, Schwartz JC (1983) Auto-inhibition of brain histamine release mediated by a novel class (H3) of histamine receptor. Nature (Lond) 302:832–837

Aston-Jones G, Cohen JD (2005) An integrative theory of locus coeruleus-norepinephrine function: adaptive gain and optimal performance. Annu Rev Neurosci 28:403–450

Baldeweg T, Spence S, Hirsch SR, Gruzelier J (1998) Gamma-band electroencephalographic oscillations in a patient with somatic hallucinations. Lancet 352:620–621

Banks MI, White JA, Pearce RA (2000) Interactions between distinct GABA(A) circuits in hippocampus. Neuron 25:449–457

Bartos M, Vida I, Frotscher M, Geiger JR, Jonas P (2001) Rapid signaling at inhibitory synapses in a dentate gyrus interneuron network. J Neurosci 21:2687–2698

Bartos M, Vida I, Frotscher M, Meyer A, Monyer H, Geiger JR, Jonas P (2002) Fast synaptic inhibition promotes synchronized gamma oscillations in hippocampal interneuron networks. Proc Natl Acad Sci U S A 99:13222–13227

Behrens CJ, van den Boom LP, de Hoz L, Friedman A, Heinemann U (2005) Induction of sharp wave-ripple complexes in vitro and reorganization of hippocampal networks. Nat Neurosci 8:1560–1567

Behrens MM, Ali SS, Dao DN, Lucero J, Shekhtman G, Quick KL, Dugan LL (2007) Ketamine-induced loss of phenotype of fast-spiking interneurons is mediated by NADPH-oxidase. Science 318:1645–1647

Berridge CW, Foote SL (1991) Effects of locus coeruleus activation on electroencephalographic activity in neocortex and hippocampus. J Neurosci 11:3135–3145

Bland BH (1986) Physiology and pharmacology of hippocampal formation theta rhythms. Prog Neurobiol 26:1–54

Booker SA, Vida I (2018) Morphological diversity and connectivity of hippocampal interneurons. Cell Tissue Res 373:619–641

Booker SA, Gross A, Althof D, Shigemoto R, Bettler B, Frotscher M, Hearing M, Wickman K, Watanabe M, Kulik Á, Vida I (2013) Differential GABAB-receptor-mediated effects in perisomatic-and dendrite-targeting parvalbumin interneurons. J Neurosci 18:7961–7974

Both M, Bähner F, von Bohlen und Halbach O, Draguhn A (2008) Propagation of specific network patterns through the mouse hippocampus. Hippocampus 18:899–908

Bourdeau ML, Morin F, Laurent CE, Azzi M, Lacaille JC (2007) Kv4.3-mediated A-type K+ currents underlie rhythmic activity in hippocampal interneurons. J Neurosci 27:1942–1953

Boyden ES, Zhang F, Bamberg E, Nagel G, Deisseroth K (2005) Millisecond-timescale, genetically targeted optical control of neural activity. Nat Neurosci 8:1263–1268

Bragin A, Jandó G, Nádasdy Z, Hetke J, Wise K, Buzsáki G (1995) Gamma (40–100 Hz) oscillation in the hippocampus of the behaving rat. J Neurosci 15:47–60

Bragin A, Engel J Jr, Wilson CL, Fried I, Mathern GW (1999) Hippocampal and entorhinal cortex high-frequency oscillations (100–500 Hz) in human epileptic brain and in kainic acid–treated rats with chronic seizures. Epilepsia 40:127–137

Bragin A, Mody I, Wilson CL, Engel J Jr (2002) Local generation of fast ripples in epileptic brain. J Neurosci 22:2012–2021

Bragin A, Claeys P, Vonck K, Van Roost D, Wilson C, Boon P, Engel J Jr (2007) Analysis of initial slow waves (ISWs) at the seizure onset in patients with drug resistant temporal lobe epilepsy. Epilepsia 48:1883–1894

Braun I, Genius J, Grunze H, Bender A, Möller HJ, Rujescu D (2007) Alterations of hippocampal and prefrontal GABAergic interneurons in an animal model of psychosis induced by NMDA receptor antagonism. Schizophr Res 97:254–263

Brown RA, Walling SG, Milway JS, Harley CW (2005) Locus ceruleus activation suppresses feedforward interneurons and reduces β-γ electroencephalogram frequencies while it enhances theta frequencies in rat dentate gyrus. J Neurosci 25:1985–1991

Bucci P, Mucci A, Merlotti E, Volpe U, Galderisi S (2007) Induced gamma activity and event-related coherence in schizophrenia. Clin EEG Neurosci 38:96–104

Bucher D, Goaillard JM (2011) Beyond faithful conduction: short-term dynamics, neuromodulation, and long-term regulation of spike propagation in the axon. Prog Neurobiol 94:307–346

Buhl EH, Halasy K, Somogyi P (1994) Diverse sources of hippocampal unitary inhibitory postsynaptic potentials and the number of synaptic release sites. Nature 368:823–828

Buhl EH, Tamás G, Fisahn A (1998) Cholinergic activation and tonic excitation induce persistent gamma oscillations in mouse somatosensory cortex in vitro. J Physiol 513:117–126

Buzsáki G (1989) Two-stage model of memory trace formation: a role for "noisy" brain states. Neuroscience 31:551–570

Buzsáki G (2002) Theta oscillations in the hippocampus. Neuron 33:325–340

Buzsáki G, Buhl DL, Harris KD, Csicsvari J, Czéh B, Morozov A (2003) Hippocampal network patterns of activity in the mouse. Neuroscience 116:201–211

Buzsáki G, Draguhn A (2004) Neuronal oscillations in cortical networks. Science 304:1926–1929

Buzsáki G, Leung LW, Vanderwolf CH (1983) Cellular bases of hippocampal EEG in the behaving rat. Brain Res 287:139–171

Buzsáki G, Czopf J, Kondakor J, Kellenyi L (1986) Laminar distribution of hippocampal rhythmic slow activity (RSA) in the behaving rat; current source density analysis, effects of urethane and atropine. Brain Res 365:125–137

Buzsáki G, Horvath Z, Urioste R, Hetke J, Wise K (1992) High-frequency network oscillation in the hippocampus. Science 256:1025–1027

Callaway EM (2002) Cell type specificity of local cortical connections. J Neurocytol 31:231–237

Carr MF, Karlsson MP, Frank LM (2012) Transient slow gamma synchrony underlies hippocampal memory replay. Neuron 75:700–713

Chen K, Aradi I, Santhakumar V, Soltesz I (2002) H-channels in epilepsy: new targets for seizure control? Trends Pharmacol Sci 23:552–557

Chevaleyre V, Siegelbaum SA (2010) Strong CA2 pyramidal neuron synapses define a powerful disynaptic cortico-hippocampal loop. Neuron 66:560–572

Chittajallu R, Craig MT, McFarland A, Yuan X, Gerfen S, Tricoire L, Erkkila B, Barron SC, Lopez CM, Liang BJ, Jeffries BW, Pelkey KA, McBain CJ (2013) Dual origins of functionally distinct O-LM interneurons revealed by differential 5-HT 3A R expression. Nat Neurosci 11:1598–1607

Cho RY, Konecky RO, Carter CS (2006) Impairments in frontal cortical gamma synchrony and cognitive control in schizophrenia. Proc Natl Acad Sci U S A 103:19878–19883

Chrobak JJ, Buzsáki G (1996) High-frequency oscillations in the output networks of the hippocampal-entorhinal axis of the freely behaving rat. J Neurosci 16:3056–3066

Cobb SR, Buhl EH, Halasy K, Paulsen O, Somogyi P (1995) Synchronisation of neuronal activity in hippocampus by individual GABAergic interneurons. Nature 378:75–78

Cobb SR, Butlers DO, Davies CH (2000) Coincident activation of mGluRs and MachRs imposes theta frequency patterning on synchronised network activity in the hippocampal CA3 region. Neuropharmacology 23:1933–1942

Colom LV, Garcia-Hernandez A, Castaneda MT, Perez-Cordova MG, Garrido-Sanabria ER (2006) Septo-hippocampal networks in chronically epileptic rats: potential antiepileptic effects of theta rhythm generation. J Neurophysiol 95:3645–3653

Cossart R, Esclapez M, Hirsch JC, Bernard C, Ben-Ari Y (1998) GluR5 kainate receptor activation in interneurons increases tonic inhibition of pyramidal cells. Nat Neurosci 1:470–478

Cossart R, Epsztein J, Tyzio R, Becq H, Hirsch J, Ben-Ari Y, Crépel V (2002) Quantal release of glutamate generates pure kainate and mixed AMPA/kainate EPSCs in hippocampal neurons. Neuron 35:147–159

Craig MT, McBain CJ (2015) Fast gamma oscillations are generated intrinsically in CA1 without the involvement of fast-spiking basket cells. J Neurosci 35:3616–3624

Csicsvari J, Hirase H, Czurko´ A, Mamiya A, Buzsáki G (1999) Oscillatory coupling of hippocampal pyramidal cells and interneurons in the behaving rat. J Neurosci 19:274–287

Csicsvari J, Hirase H, Mamiya A, Buzsáki G (2000) Ensemble patterns of hippocampal CA3-CA1 neurons during sharp wave-associated population events. Neuron 28:585–594

Csicsvari J, Jamieson B, Wise KD, Buzsáki G (2003) Mechanisms of gamma oscillations in the hippocampus of the behaving rat. Neuron 37:311–322

Cunningham MO, Hunt J, Middleton S, FE LB, Gillies MJ, Davies CH, Maycox PR, Whittington MA, Racca C (2006) Region-specific reduction in entorhinal gamma oscillations and parvalbumin-immunoreactive neurons in animal models of psychiatric illness. J Neurosci 26:2767–2776

Daw MI, Tricoire L, Erdelyi F, Daw MI, Tricoire L, Erdelyi F, Szabo G, McBain CJ (2009) Asynchronous transmitter release from cholecystokinin-containing inhibitory interneurons is widespread and target-cell independent. J Neurosci 29:11112–11122

Debanne D, Campanac E, Bialowas A, Carlier E, Alcaraz G (2011) Axon physiology. Physiol Rev 91:555–602

Deisseroth K, Hegemann P (2017) The form and function of channelrhodopsin. Science 357:eaan5544

Deisseroth K, Feng G, Majewska AK, Miesenböck G, Ting A, Schnitzer MJ (2006) Next-generation optical technologies for illuminating genetically targeted brain circuits. J Neurosci 26:10380–10386

Dodt HU, Zieglgänsberger W (1994) Infrared videomicroscopy: a new look at neuronal structure and function. Trends Neurosci 17:453–458

Draguhn A, Traub RD, Schmitz D, Jefferys JG (1998) Electrical coupling underlies high-frequency oscillations in the hippocampus in vitro. Nature 394:189–192

Dugladze T, Vida I, Tort AB, Gross A, Otahal J, Heinemann U, Kopell NJ, Gloveli T (2007) Impaired hippocampal rhythmogenesis in a mouse model of mesial temporal lobe epilepsy. Proc Natl Acad Sci U S A 104:17530–17535

Dugladze T, Schmitz D, Whittington MA, Vida I, Gloveli T (2012) Segregation of axonal and somatic activity during fast network oscillations. Science 336:1458–1461

Dugladze T, Maziashvili N, Börgers C, Gurgenidze S, Häussler U, Winkelmann A, Haas CA, Meier JC, Vida I, Kopell NJ (2013) GABAB autoreceptor-mediated cell type-specific reduction of inhibition in epileptic mice. Proc Natl Acad Sci U S A 110(37):15073–15078

Eller J, Zarnadze S, Bäuerle P, Dugladze T, Gloveli T (2015) Cell type-specific separation of subicular principal neurons during network activities. PLoS One 10(4):e0123636

Fellous JM, Sejnowski TJ (2000) Cholinergic induction of oscillations in the hippocampal slice in the slow bands (0.5–2 Hz), theta (5–12 Hz), and gamma (35–70 Hz). Hippocampus 10:187–197

Fisahn A, Pike FG, Buhl EH, Paulsen O (1998) Cholinergic induction of network oscillations at 40 Hz in the hippocampus in vitro. Nature 394:186–189

Fisahn A, Yamada M, Duttaroy A, Gan JW, Deng CX, McBain CJ, Wess J (2002) Muscarinic induction of hippocampal gamma oscillations requires coupling of the M1 receptor to two mixed cation currents. Neuron 33:615–624

Fisahn A, Contractor A, Traub RD, Buhl EH, Heinemann SF, McBain CJ (2004) Distinct roles for the kainate receptor subunits GluR5 and GluR6 in kainate-induced hippocampal gamma oscillations. J Neurosci 24:9658–9668

Fischer Y, Gähwiler BH, Thompson SM (1999) Activation of intrinsic hippocampal theta oscillations by acetylcholine in rat septo-hippocampal cocultures. J Physiol 519:405–413

Fisher RS, Webber WR, Lesser RP, Arroyo S, Uematsu S (1992) High-frequency EEG activity at the start of seizures. J Clin Neurophysiol 9:441–448

Foffani G, Uzcategui YG, Gal B, Menendez de la Prida L (2007) Reduced spike-timing reliability correlates with the emergence of fast ripples in the rat epileptic hippocampus. Neuron 55:930–941

Ford JM, Krystal JH, Mathalon DH (2007) Neural synchrony in schizophrenia: from networks to new treatments. Schizophr Bull 33:848–852

Frauscher B, Bartolomei F, Kobayashi K, Cimbalnik J, van 't Klooster MA, Rampp S, Otsubo H, Höller Y, Wu JY, Asano E, Engel J Jr, Kahane P, Jacobs J, Gotman J (2017) High-frequency oscillations: The state of clinical research. Epilepsia 58:1316–1329

Frerking M, Ohliger-Frerking P (2002) AMPA receptors and kainate receptors encode different features of afferent activity. J Neurosci 22:7434–7443

Frerking M, Malenka RC, Nicoll RA (1998) Synaptic activation of kainate receptors on hippocampal interneurons. Nat Neurosci 1:479–486

Freund TF, Buzsáki G (1996) Interneurons of the hippocampus. Hippocampus 6:347–470

Freund TF, Katona I (2007) Perisomatic inhibition. Neuron 56:33–42

Fuentealba P, Begum R, Capogna M, Jinno S, Márton LF, Csicsvari J, Thomson A, Somogyi P, Klausberger T (2008) Ivy cells: a population of nitric-oxide-producing, slow-spiking GABAergic neurons and their involvement in hippocampal network activity. Neuron 57:917–929

Galarreta M, Erdélyi F, Szabó G, Hestrin S (2008) Cannabinoid sensitivity and synaptic properties of 2 GABAergic networks in the neocortex. Cereb Cortex 18:2296–2305

Ganguly K, Kiss L, Poo M (2000) Enhancement of presynaptic neuronal excitability by correlated presynaptic and postsynaptic spiking. Nat Neurosci 3:1018–1026

Geiger JR, Melcher T, Koh DS, Sakmann B, Seeburg PH, Jonas P, Monyer H (1995) Relative abundance of subunit mRNAs determines gating and Ca2+ permeability of AMPA receptors in principal neurons and interneurons in rat CNS. Neuron 15:193–204

Geiger JR, Lübke J, Roth A, Frotscher M, Jonas P (1997) Submillisecond AMPA receptor-mediated signaling at a principal neuron-interneuron synapse. Neuron 18:1009–1023

Giepmans BN, Adams SR, Ellisman MH, Tsien RY (2006) The fluorescent toolbox for assessing protein location and function. Science 312:217–224

Gillies MJ, Traub RD, LeBeau FE, Davies CH, Gloveli T, Buhl EH, Whittington MA (2002) A model of atropine-resistant theta oscillations in rat hippocampal area CA1. J Physiol (Lond) 543:779–793

Girardeau G, Benchenane K, Wiener SI, Buzsáki G, Zugaro MB (2009) Selective suppression of hippocampal ripples impairs spatial memory. Nat Neurosci 12:1222–1223

Gloveli T, Dugladze T, Saha S, Monyer H, Heinemann U, Traub RD, Whittington MA, Buhl EH (2005a) Differential involvement of oriens/pyramidale interneurones in hippocampal network oscillations in vitro. J Physiol 562:131–147

Gloveli T, Dugladze T, Rotstein HG, Traub RD, Monyer H, Heinemann U, Whittington MA, Kopell NJ (2005b) Orthogonal arrangement of rhythm-generating microcircuits in the hippocampus. Proc Natl Acad Sci U S A 102:13295–13300

Goldin M, Epsztein J, Jorquera I, Represa A, Ben-Ari Y, Crépel V, Cossart R (2007) Synaptic kainate receptors tune oriens-lacunosum moleculare interneurons to operate at theta frequency. J Neurosci 27:9560–9572

Gonzalez-Burgos G, Lewis DA (2008) GABA Neurons and the Mechanisms of Network Oscillations: Implications for Understanding Cortical Dysfunction in Schizophrenia. Schizophr Bull 34:944–961

Goutagny R, Jackson J, Williams S (2009) Self-generated theta oscillations in the hippocampus. Nat Neurosci 12:1491–1493

Gu N, Vervaeke K, Hu H, Storm JF (2005) Kv7/KCNQ/M and HCN/h, but not KCa2/SK channels, contribute to the somatic medium after-hyperpolarization and excitability control in CA1 hippocampal pyramidal cells. J Physiol 566:689–715

Gulyás AI, Freund TT (2015) Generation of physiological and pathological highfrequency oscillations: the role of perisomatic inhibition in sharp-wave rippleand interictal spike generation. Curr Opin Neurobiol 31:26–32

Gulyás AI, Szabó GG, Ulbert I, Holderith N, Monyer H, Erdélyi F, Szabó G, Freund TF, Hájos N (2010) Parvalbumin-containing fast-spiking basket cells generate the field potential oscillations induced by cholinergic receptor activation in the hippocampus. J Neurosci 30:15134–15145

Hájos N, Pálhalmi J, Mann EO, Németh B, Paulsen O, Freund TF (2004) Spike timing of distinct types of GABAergic interneuron during hippocampal gamma oscillations in vitro. J Neurosci 24:9127–9137

Hajós M, Siok CJ, Hoffmann WE, Li S, Kocsis B (2008) Modulation of hippocampal theta oscillation by histamine H3 receptors. J Pharmacol Exp Ther 324:391–398

Hájos N, Ellender TJ, Zemankovics R, Mann EO, Exley R, Cragg SJ, Freund TF, Paulsen O (2009) Maintaining network activity in submerged hippocampal slices: importance of oxygen supply. Eur J Neurosci 29:319–327

Halasy K, Buhl EH, Lörinczi Z, Tamás G, Somogyi P (1996) Synaptic target selectivity and input of GABAergic basket and bistratified interneurons in the CA1 area of the rat hippocampus. Hippocampus 6:306–329

Hefft S, Jonas P (2005) Asynchronous GABA release generates long-lasting inhibition at a hippocampal interneuron-principal neuron synapse. Nat Neurosci 8:1319–1328

Hollnagel JO, Maslarova A, Haq RU, Heinemann U (2014) GABAB receptor dependent modulation of sharp wave-ripple complexes in the rat hippocampus in vitro. Neurosci Lett 574:15–20

Hu H, Vervaeke K, Storm JF (2002) Two forms of electrical resonance at theta frequencies, generated by M-current, h-current and persistent Na+ current in rat hippocampal pyramidal cells. J Physiol 545:783–805

Huh CY, Amilhon B, Ferguson KA, Manseau F, Torres-Platas SG, Peach JP, Scodras S, Mechawar N, Skinner FK, Williams S (2016) Excitatory inputs determine phase-locking strength and spike-timing of CA1 stratum oriens/alveus parvalbumin and somatostatin interneurons during intrinsically generated hippocampal theta rhythm. J Neurosci 36:6605–6622

Jackson J, Amilhon B, Goutagny R, Bott J-B, Manseau F, Kortleven C, Bressler SL, Williams S (2014) Reversal of theta rhythm flow through intact hippocampal circuits. Nat Neurosci 17:1362–1370

Jacobs J, Staba R, Asano E, Otsubo H, Wu JY, Zijlmans M, Mohamed I, Kahane P, Dubeau F, Navarro V, Gotman J (2012) High-frequency oscillations (HFOs) in clinical epilepsy. Prog Neurobiol 98:302–315

Jadhav SP, Kemere C, German PW, Frank LM (2012) Awake hippocampal sharp-wave ripples support spatial memory. Science 336:1454–1458

Jonas P, Major G, Sakmann B (1993) Quantal components of unitary EPSCs at the mossy fibre synapse on CA3 pyramidal cells of rat hippocampus. J Physiol 472:615–663

Jouvet M (1969) Biogenic amines and the states of sleep. Science 163:32–41

Jutras MJ, Buffalo EA (2010) Synchronous neural activity and memory formation. Curr Opin Neurobiol 20:150–155

Kandel ER, Spencer WA (1961) Electrophysiology of hippocampal neurons. II. After-potentials and repetitive firing. J Neurophysiol 24:243–259

Kehrer C, Dugladze T, Maziashvili N, Wójtowicz A, Schmitz D, Heinemann U, Gloveli T (2007) Increased inhibitory input to CA1 pyramidal cells alters hippocampal gamma frequency oscillations in the MK-801 model of acute psychosis. Neurobiol Dis 25:545–552

Kehrer C, Maziashvili N, Dugladze T, Gloveli T (2008) Altered excitatory-inhibitory balance in the NMDA-hypofunction model of schizophrenia. Front Mol Neurosci 1:6

Kittelberger K, Hur EE, Sazegar S, Keshavan V, Kocsis B (2012) Comparison of the effects of acute and chronic administration of ketamine on hippocampal oscillations: relevance for the NMDA receptor hypofunction model of schizophrenia. Brain Struct Funct 217:395–409

Klausberger T, Somogyi P (2008) Neuronal diversity and temporal dynamics: the unity of hippocampal circuit operations. Science 321:53–57

Klausberger T, Magill PJ, Márton LF, Roberts JD, Cobden PM, Buzsáki G, Somogyi P (2003) Brain-state- and cell-type-specific firing of hippocampal interneurons in vivo. Nature 421:844–848

Klausberger T, Márton LF, Baude A, Roberts JD, Magill PJ, Somogyi P (2004) Spike timing of dendrite-targeting bistratified cells during hippocampal network oscillations in vivo. Nat Neurosci 7:41–47

Kocsis B, Varga V, Dahan L, Sik A (2006) Serotonergic neuron diversity: identification of raphe neurons with discharges time-locked to the hippocampal theta rhythm. Proc Natl Acad Sci U S A 103:1059–1064

Kocsis B, Li S, Hajos M (2007) Behavior-dependent modulation of hippocampal EEG activity by the selective norepinephrine reuptake inhibitor reboxetine in rats. Hippocampus 17:627–633

Konopacki J, Gołebiewski H, Eckersdorf B (1992) Carbachol-induced rhythmic slow activity (theta) in cat hippocampal formation slices. Brain Res 578:13–16

Korotkova T, Fuchs EC, Ponomarenko A, von Engelhardt J, Monyer H (2010) NMDA receptor ablation on parvalbumin-positive interneurons impairs hippocampal synchrony, spatial representations, and working memory. Neuron 68:557–569

Lawrence JJ, Statland JM, Grinspan ZM, McBain CJ (2006) Cell type-specific dependence of muscarinic signalling in mouse hippocampal stratum oriens interneurones. J Physiol 570:595–610

LeBeau FEN, Towers SK, Traub RD, Whittington MA, Buhl EH (2002) Fast network oscillations induced by potassium transients in the rat hippocampus in vitro. J Physiol 542:167–179

LeBeau FE, Traub RD, Monyer H, Whittington MA, Buhl EH (2003) The role of electrical signaling via gap junctions in the generation of fast network oscillations. Brain Res Bull 62:3–13

Lerma J (2003) Roles and rules of kainate receptors in synaptic transmission. Nat Rev Neurosci 4:481–495
Leung LW (1985) Spectral analysis of hippocampal EEG in the freely moving rat effects of centrally active drugs and relations to evoked potentials. Electroencephalogr Clin Neurophysiol 60:65–77
Leung LS, Yim CY (1986) Intracellular records of theta rhythm in hippocampal CA1 cells of the rat. Brain Res 367:323–327
Leung LS, Yu HW (1998) Theta-frequency resonance in hippocampal CA1 neurons in vitro demonstrated by sinusoidal current injection. J Neurophysiol 79:1592–1596
Leung LS, Lopes da Silva F, Wadman WJ (1982) Spectral characteristics of the hippocampal EEG in the freely moving rat. Clin Neurophysiol 54:203–219
Lewis DA, Hashimoto T, Volk DW (2005) Cortical inhibitory neurons and schizophrenia. Nat Rev Neurosci 6:312–324
Li XG, Somogyi P, Ylinen A, Buzsáki G (1994) The hippocampal CA3 network: an in vivo intracellular labeling study. J Comp Neurol 339:181–208
Lisman JE (2005) The theta/gamma discrete phase code occurring during the hippocampal phase precession may be a more general brain coding scheme. Hippocampus 15:913–922
Lisman JE, Idiart MAP (1995) Storage of 7+- 2 short term memories in oscillatory subcycles. Science 267:1512–1515
Maccaferri G, McBain CJ (1996) The hyperpolarization-activated current (Ih) and its contribution to pacemaker activity in rat CA1 hippocampal stratum oriens-alveus interneurones. J Physiol 497:119–130
Maccaferri G, Roberts JD, Szucs P, Cottingham CA, Somogyi P (2000) Cell surface domain specific postsynaptic currents evoked by identified GABAergic neurones in rat hippocampus in vitro. J Physiol 524:91–116
Madison DV, Lancaster B, Nicoll RA (1987) Voltage clamp analysis of cholinergic action in the hippocampus. J Neurosci 7:733–741
Magee JC (1999) Dendritic hyperpolarization-activated currents modify the integrative properties of hippocampal CA1 pyramidal neurons. J Neurosci 18:7613–7624
Maier N, Nimmrich V, Draguhn A (2003) Cellular and network mechanisms underlying spontaneous sharp wave-ripple complexes in mouse hippocampal slices. J Physiol 550:873–887
Mann EO, Suckling JM, Hájos N, Greenfield SA, Paulsen O (2005) Perisomatic feedback inhibition underlies cholinergically induced fast network oscillations in the rat hippocampus in vitro. Neuron 45:105–117
Marek KW, Davis GW (2003) Controlling the active properties of excitable cells. Curr Opin Neurobiol 13:607–611
Markram H, Lubke J, Frotscher M, Roth A, Sakmann B (1997) Physiology and anatomy of synaptic connections between thick tufted pyramidal neurones in the developing rat neocortex. J Physiol 500:409–440
McBain CJ, Fisahn A (2001) Interneurons unbound. Nat Rev Neurosci 2:11–23
Meyer AH, Katona I, Blatow M, Rozov A, Monyer H (2002) In vivo labeling of parvalbumin-positive interneurons and analysis of electrical coupling in identified neurons. J Neurosci 22:7055–7064
Middleton S, Jalics J, Kispersky T, Lebeau FE, Roopun AK, Kopell NJ, Whittington MA, Cunningham MO (2008) NMDA receptor-dependent switching between different gamma rhythm-generating microcircuits in entorhinal cortex. Proc Natl Acad Sci U S A 105:18572–18577
Miles R (1990) Synaptic excitation of inhibitory cells by single CA3 hippocampal pyramidal cells of the guinea-pig in vitro. J Physiol 428:61–77
Miles R, Poncer JC (1996) Paired recordings from neurones. Curr Opin Neurobiol 6:387–394
Miles R, Tóth K, Gulyás AI, Hájos N, Freund TF (1996) Differences between somatic and dendritic inhibition in the hippocampus. Neuron 16:815–823
Montplaisir J, Laverdiere M, Saint-Hilaire JM, Rouleau I (1987) Nocturnal sleep recording in partial epilepsy: a study with depth electrodes. J Clin Neurophysiol 4:383–388

Morales M, Bloom FE (1997) The 5-HT3 receptor is present in different subpopulations of GABAergic neurons in the rat telencephalon. J Neurosci 17:3157–3167

Morales M, Battenberg E, Bloom F (1998) Distribution of neurons expressing immunoreactivity for the 5HT3 receptor subtype in the rat brain and spinal cord. J Comp Neurol 402:385–401

Morris HM, Hashimoto T, Lewis DA (2008) Alterations in somatostatin mRNA expression in the dorsolateral prefrontal cortex of subjects with schizophrenia or schizoaffective disorder. Cereb Cortex 18:1575–1587

Mulle C, Sailer A, Swanson GT, Brana C, O'Gorman S, Bettler B, Heinemann SF (2000) Subunit composition of kainate receptors in hippocampal interneurons. Neuron 28:475–484

Nimmrich V, Maier N, Schmitz D, Draguhn A (2005) Induced sharp wave-ripple complexes in the absence of synaptic inhibition in mouse hippocampal slices. J Physiol 563:663–670

Notomi T, Shigemoto R (2004) Immunohistochemical localization of Ih channel subunits, HCN1-4, in the rat brain. J Comp Neurol 471:241–276

Nusser Z, Lujan R, Laube G, Roberts JD, Molnar E, Somogyi P (1998) Cell type and pathway dependence of synaptic AMPA receptor number and variability in the hippocampus. Neuron 21:545–559

Oliva AA Jr, Jiang M, Lam T, Smith KL, Swann JW (2000) Novel hippocampal interneuronal subtypes identified using transgenic mice that express green fluorescent protein in GABAergic interneurons. J Neurosci 20:3354–3368

O'Neill J, Senior T, Csicsvari J (2006) Place-selective firing of CA1 pyramidal cells during sharp wave/ripple network patterns in exploratory behavior. Neuron 49:143–155

Oren I, Mann EO, Paulsen O, Hájos N (2006) Synaptic currents in anatomically identified CA3 neurons during hippocampal gamma oscillations in vitro. J Neurosci 26:9923–9934

Pálhalmi J, Paulsen O, Freund TF, Hájos N (2004) Distinct properties of carbachol- and DHPG-induced network oscillations in hippocampal slices. Neuropharmacology 47:381–289

Pan WX, McNaughton N (2002) The role of the medial supramammillary nucleus in the control of hippocampal theta activity and behaviour in rats. Eur J Neurosci 16:1797–1809

Pangalos M, Donoso JR, Winterer J, Zivkovic AR, Kempter R, Maier N, Schmitz D (2013) Recruitment of oriens-lacunosum-moleculare interneurons during hippocampal ripples. Proc Natl Acad Sci U S A 110:4398–4403

Peng Y, Barreda Tomás FJ, Klisch C, Vida I, Geiger JRP (2017) Layer-Specific Organization of Local Excitatory and Inhibitory Synaptic Connectivity in the Rat Presubiculum. Cereb Cortex 27:2435–2452

Penttonen M, Kamondi A, Acsády L, Buzsáki G (1998) Gamma frequency oscillation in the hippocampus of the rat: intracellular analysis in vivo. Eur J Neurosci 10:718–728

Petsche H, Stumpf C, Gogolák G (1962) The significance of the rabbit's septum as a relay station between midbrain and the hippocampus: I. The control of hippocampus arousal activity by the septum cells. Electroencephalogr Clin Neurophysiol 14:202–211

Pike FG, Goddard RS, Suckling JM, Ganter P, Kasthuri N, Paulsen O (2000) Distinct frequency preferences of different types of rat hippocampal neurones in response to oscillatory input currents. J Physiol 529:205–213

Pinault D (1996) A novel single-cell staining procedure performed in vivo under electrophysiological control: Morpho-functional features of juxtacellularly labeled thalamic cells and other central neurons with biocytin or neurobiotin. J Neurosci Methods 65:113–136

Pinault D (2008) N-methyl d-aspartate receptor antagonists ketamine and MK-801 induce wake-related aberrant gamma oscillations in the rat neocortex. Biol Psychiatry 63:730–735

Pitler TA, Alger BE (1992) Cholinergic excitation of GABAergic interneurons in the rat hippocampal slice. J Physiol 450:127–142

Polleux F (2005) Genetic mechanisms specifying cortical connectivity: let's make some projections together. Neuron 46:395–400

Pöschel B, Draguhn A, Heinemann U (2002) Glutamate-induced gamma oscillations in the dentate gyrus of rat hippocampal slices. Brain Res 938:22–28

Pouille F, Scanziani M (2004) Routing of spike series by dynamic circuits in the hippocampus. Nature 429:717–723

Price CJ, Cauli B, Kovacs ER, Kulik A, Lambolez B, Shigemoto R, Capogna M (2005) Neurogliaform neurons form a novel inhibitory network in the hippocampal CA1 area. J Neurosci 25:6775–6786

Roopun AK, Cunningham MO, Racca C, Alter K, Traub RD, Whittington MA (2008) Region-specific changes in gamma and beta2 rhythms in NMDA receptor dysfunction models of schizophrenia. Schizophr Bull 34:962–973

Ropert N, Guy N (1991) Serotonin facilitates GABAergic transmission in the CA1 region of rat hippocampus in vitro. J Physiol (Lond) 441:121–136

Rotstein HG, Pervouchine DD, Acker CD, Gillies MJ, White JA, Buhl EH, Whittington MA, Kopell N (2005) Slow and fast inhibition and an H-current interact to create a theta rhythm in a model of CA1 interneuron network. J Neurophysiol 94:1509–1518

Ruiz AJ, Kullmann DM (2013) Ionotropic receptors at hippocampal mossy fibers: roles in axonal excitability, synaptic transmission, and plasticity. Front Neural Circ 6:1–12

Sakai T, Oshima A, Nozaki Y, Ida I, Haga C, Akiyama H, Nakazato Y, Mikuni M (2008) Changes in density of calcium-binding-protein-immunoreactive GABAergic neurons in prefrontal cortex in schizophrenia and bipolar disorder. Neuropathology 28:143–150

Sasaki T, Matsuki N, Ikegaya Y (2012) Targeted axon-attached recording with fluorescent patch-clamp pipettes in brain slices. Nat Protoc 7:1228–1234

Savić N, Pedarzani P, Sciancalepore M (2001) Medium afterhyperpolarization and firing pattern modulation in interneurons of stratum radiatum in the CA3 hippocampal region. J Neurophysiol 85:1986–1997

Schlingloff D, Káli S, Freund TF, Hájos N, Gulyás AI (2014) Mechanisms of sharp wave initiation and ripple generation. J Neurosci. 34:11385–11398

Schmitz D, Empson RM, Heinemann U (1995) Serotonin reduces inhibition via 5-HT1A receptors in area CA1 of rat hippocampal slices in vitro. J Neurosci 15:7217–7225

Schmitz D, Gloveli T, Empson RM, Heinemann U (1998) Comparison of the effects of serotonin in the hippocampus and the entorhinal cortex. Mol Neurobiol 17:59–72

Schmitz D, Schuchmann S, Fisahn A, Draguhn A, Buhl EH, Petrasch-Parwez E, Dermietzel R, Heinemann U, Traub RD (2001) Axo-axonal coupling. A novel mechanism for ultrafast neuronal communication. Neuron 31:831–840

Sheffield ME, Best TK, Mensh BD, Kath WL, Spruston N (2011) Slow integration leads to persistent action potential firing in distal axons of coupled interneurons. Nat Neurosci 14:200–207

Shen RY, Andrade R (1998) 5-Hydroxytryptamine2 receptor facilitates GABAergic neurotransmission in rat hippocampus. J Pharmacol Exp Ther 285:805–812

Shimono K, Brucher F, Granger R, Lynch G, Taketani M (2000) Origins and distribution of cholinergically induced beta rhythms in hippocampal slices. J Neurosci 20:8462–8473

Sik A, Penttonen M, Ylinen A, Buzsáki G (1995) Hippocampal CA1 interneurons: an in vivo intracellular labeling study. J Neurosci 15:6651–6665

Singer W (1999) Neuronal synchrony: a versatile code for the definition of relations? Neuron 24:49–65

Slewa-Younan S, Gordon E, Williams L, Haig AR, Goldberg E (2001) Sex differences, gamma activity and schizophrenia. Int J Neurosci 107:131–144

Sohal VS, Zhang F, Yizhar O, Deisseroth K (2009) Parvalbumin neurons and gamma rhythms enhance cortical circuit performance. Nature 459:698–702

Somogyi P, Klausberger T (2005) Defined types of cortical interneurone structure space and spike timing in the hippocampus. J Physiol (Lond) 562:9–26

Spampanato J, Mody I (2007) Spike timing of lacunosom-moleculare targeting interneurons and CA3 pyramidal cells during high-frequency network oscillations in vitro. J Neurophysiol 98:96–104

Spencer KM (2008) Visual gamma oscillations in schizophrenia: implications for understanding neural circuitry abnormalities. Clin EEG Neurosci 39:65–68

Spencer KM, Nestor PG, Perlmutter R, Niznikiewicz MA, Klump MC, Frumin M, Shenton ME, McCarley RW (2004) Neural synchrony indexes disordered perception and cognition in schizophrenia. Proc Natl Acad Sci U S A 101:17288–11793

Spruston N (2008) Pyramidal neurons: dendritic structure and synaptic integration. Nat Rev Neurosci 9:206–221

Stark E, Roux L, Eichler R, Senzai Y, Royer S, Buzsáki G (2014) Pyramidal cell-interneuron interactions underlie hippocampal ripple oscillations. Neuron 83:467–480

Szabadics J, Tamas G, Soltesz I (2007) Different transmitter transients underlie presynaptic cell type specificity of GABAA, slow and GABAA, fast. Proc Natl Acad Sci U S A 104:14831–14836

Tecott LH, Maricq AV, Julius D (1993) Nervous system distribution of the serotonin 5-HT3 receptor mRNA. Proc Natl Acad Sci U S A 90:1430–1434

Tesche CD, Karhu J (2000) Theta oscillations index human hippocampal activation during a working memory task. Proc Natl Acad Sci USA 97:919–924

Tort AB, Rotstein HG, Dugladze T, Gloveli T, Kopell NJ (2007) On the formation of gamma-coherent cell assemblies by oriens lacunosum-moleculare interneurons in the hippocampus. Proc Natl Acad Sci U S A 104:13490–13495

Toth K, Suares G, Lawrence JJ, Philips-Tansey E, McBain CJ (2000) Differential mechanisms of transmission at three types of mossy fiber synapse. J Neurosci 20:8279–8289

Towers SK, LeBeau FE, Gloveli T, Traub RD, Whittington MA, Buhl EH (2002) Fast network oscillations in the rat dentate gyrus in vitro. J Neurophysiol 87:1165–1168

Traub RD, Bibbig A, Fisahn A, LeBeau FE, Whittington MA, Buhl EH (2000) A model of gamma-frequency network oscillations induced in the rat CA3 region by carbachol in vitro. Eur J Neurosci 12:4093–4106

Traub RD, Cunningham MO, Gloveli T, LeBeau FE, Bibbig A, Buhl EH, Whittington MA (2003) GABA-enhanced collective behavior in neuronal axons underlies persistent gamma-frequency oscillations. Proc Natl Acad Sci U S A 100:11047–11052

Tukker JJ, Fuentealba P, Hartwich K, Somogyi P, Klausberger T (2007) Cell type-specific tuning of hippocampal interneuron firing during gamma oscillations in vivo. J Neurosci 27:8184–8189

van Hooft JA, Giuffrida R, Blatow M, Monyer H (2000) Differential expression of group I metabotropic glutamate receptors in functionally distinct hippocampal interneurons. J Neurosci 20:3544–3551

Vanderwolf CH (1969) Hippocampal electrical activity and voluntary movement in the rat. Electroencephalogr Clin Neurophysiol 26:407–418

Vida I, Halasy K, Szinyei C, Somogyi P, Buhl EH (1998) Unitary IPSPs evoked by interneurons at the stratum radiatum-stratum lacunosum-moleculare border in the CA1 area of the rat hippocampus in vitro. J Physiol 506:755–773

Vida I, Bartos M, Jonas P (2006) Shunting inhibition improves robustness of gamma oscillations in hippocampal interneuron networks by homogenizing firing rates. Neuron 49:107–117

Vierling-Claassen D, Siekmeier P, Stufflebeam S, Kopell N (2008) Modeling GABA alterations in schizophrenia: a link between impaired inhibition and altered gamma and beta range auditory entrainment. J Neurophysiol 99:2656–2671

Wang X-J, Buzsáki G (1996) Gamma oscillation by synaptic inhibition in a hippocampal interneuronal network model. J Neurosci 16:6402–6413

Wang CZ, Yang SF, Xia Y, Johnson KM (2008) Postnatal Phencyclidine Administration Selectively Reduces Adult Cortical Parvalbumin-Containing Interneurons. Neuropsychopharmacology 33:2442–2455

Weiss T, Veh RW, Heinemann U (2003) Dopamine depresses cholinergic oscillatory network activity in rat hippocampus. Eur J Neurosci 18:2573–2580

White JA, Chow CC, Ritt J, Soto-Treviño C, Kopell N (1998) Synchronization and oscillatory dynamics in heterogeneous, mutually inhibited neurons. J Comput Neurosci 5:5–16

Whittington MA, Traub RD (2003) Interneuron diversity series: inhibitory interneurons and network oscillations in vitro. Trends Neurosci 26:676–682

Whittington MA, Traub RD, Jefferys JGR (1995) Synchronized oscillations in interneuron networks driven by metabotropic glutamate receptor activation. Nature 373:612–615

Whittington MA, Stanford IM, Colling SB, Jefferys JG, Traub RD (1997) Spatiotemporal patterns of gamma frequency oscillations tetanically induced in the rat hippocampal slice. J Physiol 502:591–607

Williams SR, Stuart GJ (2003) Voltage- and site-dependent control of the somatic impact of dendritic IPSPs. J Neurosci 23:7358–7367

Wilson MA, McNaughton BL (1994) Reactivation of hippocampal ensemble memories during sleep. Science 265:676–679

Wittner L, Henze DA, Záborszky L, Buzsáki G (2007) Three-dimensional reconstruction of the axon arbor of a CA3 pyramidal cell recorded and filled in vivo. Brain Struct Funct 212:75–83

Wulff P, Ponomarenko AA, Bartos M, Korotkova TM, Fuchs EC, Bähner F, Both M, Tort AB, Kopell NJ, Wisden W, Monyer H (2009) Hippocampal theta rhythm and its coupling with gamma oscillations require fast inhibition onto parvalbumin-positive interneurons. Proc Natl Acad Sci U S A 106:3561–3566

Ylinen A, Bragin A, Nadasdy Z, Jando G, Szabo I, Sik A, Buzsáki G (1995) Sharp wave-associated high-frequency oscillation (200 Hz) in the intact hippocampus: Network and intracellular mechanisms. J Neurosci 15:30–46

Zarnadze S, Bäuerle P, Santos-Torres J, Böhm C, Schmitz D, Geiger JR, Dugladze T, Gloveli T (2016) Cell-specific synaptic plasticity induced by network oscillations. Elife 5:pii: e14912

Zhang ZJ, Reynolds GP (2002) A selective decrease in the relative density of parvalbumin-immunoreactive neurons in the hippocampus in schizophrenia. Schizophr Res 55:1–10

Zhang F, Wang LP, Brauner M, Liewald JF, Kay K, Watzke N, Wood PG, Bamberg E, Nagel G, Gottschalk A, Deisseroth K (2007) Multimodal fast optical interrogation of neural circuitry. Nature 446:633–639

Recording Identified Neurons in Awake and Anesthetized Rodents

John J. Tukker

Abstract A deeper understanding of the brain is likely to require detailed, quantitative descriptions at several levels, ranging from the molecular to the behavioral, as well as an understanding of the relations among these levels. Taking the single neuron as the basic building block, I will here outline recent progress in linking different levels of description, including anatomical and molecular properties on the one hand ("structure") and electrochemical activity on the other ("function"), whereby these properties are always considered to be interdependent on the activity of other neurons in the network and the behavior of the organism as a whole.

One key methodological advance has been the ability to both record activity from single neurons and observe their structural properties, in intact animals during specific brain states and/or behaviors. In this chapter, I will describe such methods in some detail, and illustrate with some key examples how observations on single-cell physiological and anatomical properties (membrane potential fluctuations and associated currents, morphology, molecular expression profile), in combination with network and behavioral properties (specifically focusing on navigation and the representation of space), can provide unique insights into hippocampal function.

Overview

Although "understanding the brain" is a stated ultimate goal for many neuroscientists, it remains unclear what such an understanding would entail for a structure whose defining characteristic is perhaps its complexity. In this chapter, I assume it would require, for a start, a detailed description of the brain at several levels, ranging from the molecular to the behavioral (Fig. 1). The challenge will be to not only describe each of these levels in greater detail but to reveal how they are connected. Following the classic "neuron doctrine" and taking the single neuron as

J. J. Tukker (✉)
Neuroscience Research Center, Charité University Medicine Berlin, Berlin, Germany
e-mail: john.tukker@charite.de

V. Cutsuridis et al. (eds.), *Hippocampal Microcircuits*, Springer Series in Computational Neuroscience, https://doi.org/10.1007/978-3-319-99103-0_9

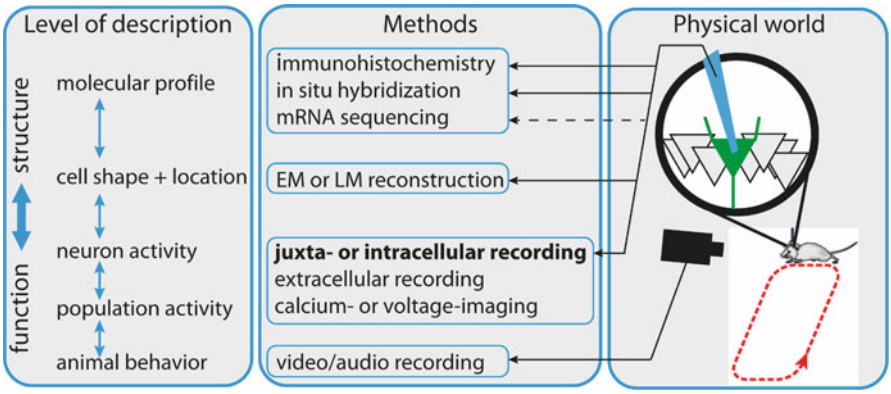

Fig. 1 *Multilevel description of neural circuits underlying behavior*. *Left panel*: Structure and function interact (blue arrows), in the sense that structure underlies function, and function shapes structure in the brain (plasticity).In a similar manner, each of the displayed levels of description is linked to other levels of description (blue arrows; note that additional arrows have been left out for clarity). *Middle panel*: For each level of description in the left panel, different methods are presented. Juxta- or intracellular recording (highlighted), which forms the focus of this chapter, is merely one part of an array of methods that can ideally be deployed in concert to allow observations at several levels of description simultaneously. *Right panel*: For each method in the middle panel, the interface with the physical world is depicted – the use of a glass pipette (shown in blue) allows juxta- or intracellular recording (black arrow); the pipette also enables filling of a single cell (green; gray triangles represent other neurons), which can then be further analyzed by the methods indicated by arrows (dashed arrow for mRNA sequencing indicates a potential application only; this method has not been used in vivo for hippocampal recordings, nor with drug-free mice). Note that although both imaging and extracellular electrophysiology methods typically are used as readouts of neuronal population activity, they do of course also enable observation of single neuron activity, albeit with lower temporal (imaging) or spatial (extracellular) resolution than juxta- or intracellular recordings. The latter methods are most easily combined with methods to describe structure, allowing one to span all included levels of description in a single experiment, including behavior (depicted on bottom right by a camera (black) and a rat running along an oval track (red stippled arrow))

the basic building block (ignoring for the moment the role of non-neuronal cells), an immediate task is therefore to describe neurons in terms of their anatomical and molecular properties on the one hand ("structure") and their electrochemical activity on the other ("function"). As Fig. 1 illustrates, neuronal activity not only depends on the underlying structure of the neuron but also on the activity of other neurons in the network and, eventually, the behavior of the organism (taken here to mean any interaction of the organism with its environment). Importantly, these connections can all be bidirectional. For example, even the firing of a single neuron can, by influencing a population of neurons, change the behavior of an animal (Brecht et al. 2004). Equally, the firing of a single neuron can change its anatomical shape, as well as its molecular expression profile.

This chapter will outline progress that has been made toward recording the activity of single neurons in intact animals. I will particularly focus on relatively

new methods and methodologies that allow us to combine observations on single-cell physiological and anatomical properties (membrane potential fluctuations and associated currents, morphology, molecular expression profile) with synaptic properties (connectivity and plasticity), network properties (oscillatory patterns at different spatial and temporal scales), and behavioral properties (specifically focusing on navigation and the representation of space).

Clearly, this chapter can only give a glimpse of recent advances, but I hope to convey some of the excitement of the field based on the huge possibilities provided by novel technology. On a practical level, these possibilities will also provide a major challenge in the coming years as the accompanying "big data" thinking and technology is incorporated into neuroscience (Sejnowski et al. 2014). The deeper insights we will gain will enable us to intervene ever more effectively, making it possible to ultimately develop more effective treatments for a wide range of devastating neurological and psychiatric disorders. However, the brain is not like other organs, in the sense that it is deeply tied up to what we are as humans. This is what makes our field so fascinating, but it also reminds us of our responsibility to consider potential ethical and societal implications in the face of growing possibilities.

I will not dwell on these aspects but will provide an overview of the techniques presently available, focusing on methods to record "identified" cells in living rodents. In the first section of this chapter, I will provide some examples of data gathered with these techniques, linking anatomical and functional parameters. I will touch upon work related to place cells, grid cells, head-direction cells, and interneurons (categories which need not be mutually exclusive). In the second section, I will describe the techniques in more detail. Finally, I will present a brief outlook on future developments.

Although work done in other organisms ranging from invertebrates to primates (including humans) has also provided great insights, this chapter will focus on research performed in the *rodent* hippocampal region, including parahippocampal areas such as the pre- and parasubiculum and the entorhinal cortex.

Introduction

There are three main factors that make recording from identified cells difficult. The first is the thorny issue of what exactly constitutes "identification." Simply put, it means being able to identify a particular cell as belonging to a certain class. The difficulty is that there are many different levels at which a class can be defined and many different parameters that can be used. Such parameters can include molecular data, such as a cell's protein or mRNA expression profiles (Fig. 2a–b), or anatomical data related to its overall shape or location (Fig. 2c). Parameters based on electrophysiological characterization can include responses to current injection (Fig. 2d) or a combination of spike shape and firing rate/pattern. In the latter case, firing patterns can, for example, be described in terms of their phase locking to local field

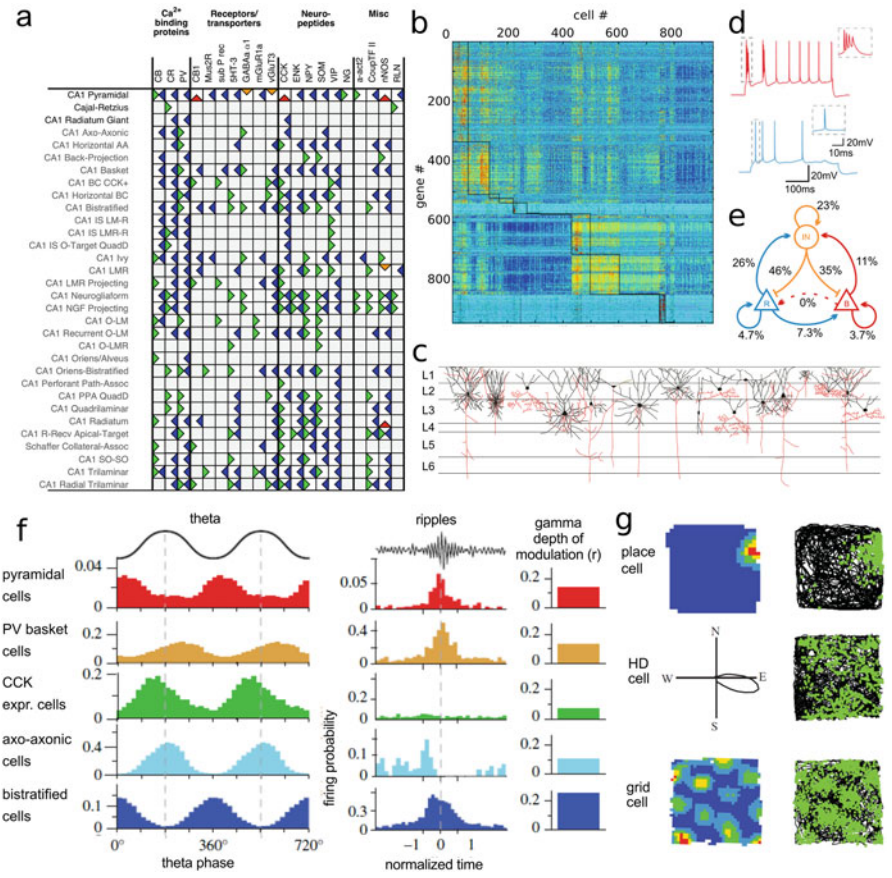

Fig. 2 *Cell types in the hippocampal formation*. (**a**). Expression of 20 common biomarkers for a subset of cell types in the hippocampal area CA1 based on literature mining (green is positive expression, blue is negative, orange is mixed expression based on different experimental protocols, red is unresolved mixed expression). (**b**)ThemRNA-based molecular profile of hippocampal area CA1 pyramidal cells shows distinct clusters (black rectangles) of gene expression (colors represent expression mRNA level for each gene (y-axis) for each analyzed cell (x-axis)). (**c**) Morphology of cell types defined in the superficial layers of the MEC. Black, dendrites and somata; red, axons. *Ln* layer n, *Ld* lamina dissecans. (**d**) Responses to current injection in awake mice for two pyramidal cell types in the subiculum, with either a bursty (top) or regular (bottom) firing pattern. (**e**) The two cell types shown in D (same color scheme) have different local connectivity profiles relative to each other and to PV-expressing interneurons (yellow), based on recording and stimulation in vitro from up to eight cells in parallel. (**f**) Firing patterns of several cell types recorded in area CA1 in anesthetized rats, in relation to different locally recorded cortical oscillations. (**g**) Spatial firing patterns of three common functionally defined cell types in the hippocampal formation: place cells (top row), HD cells (middle row), and grid cells (bottom row). Rate maps (left top, bottom) show color-coded firing rate as a function of location; a polar plot (left middle)shows HD cell firing rate as a function of the direction in which the animal's head is facing (letters denote four cardinal directions). Plots on the right show AP firing locations (green dots) and paths traveled by the animal (black lines). (Figures taken and adapted with permission: (**a**) from Wheeler et al. 2015; (**b**) from Zeisel et al. 2015, (**c**) from Canto et al. 2008, (**d**–**e**) from Böhm et al. 2015, (**f**) from Somogyi et al. 2014; (**g**) from Hartley et al. 2014)

potential (LFP) oscillations (Fig. 2f) and their relationship to behavioral parameters (Fig. 2g) such as the location of the animal or the orientation of its head (defining place cells and head-direction cells, respectively). Finally, both physiological and anatomical methods have recently been developed to study connectivity (Fig. 2e). Decades of research have shown that many of these parameters are often correlated. Although single parameters might appear as a graded continuum, and there is still much debate regarding exactly what constitutes a "cell type" (Bota and Swanson 2007; Battaglia et al. 2013; Seung and Sümbül 2014; Armañanzas and Ascoli 2015), the fact that clusters can be identified in this high-dimensional parameter space gives some justification to the idea that discrete "cell types" exist. Even if the number of cell types in any one area may be quite large (in the range of tens, see, e.g., Klausberger and Somogyi 2008), the identification of such discrete "building blocks" is extremely helpful in the quest to understand the microcircuitry of the brain.

Assuming we can come up with a plan on how exactly to identify a cell type, the second issue to consider is how to collect the required parameters for such an identification (Fig. 1). One way is to record a single cell in the intact brain as an animal performs a behavioral task and then use the recording pipette to selectively "tag" the recorded cell by filling it with a dye (usually biocytin or neurobiotin). After the brain is removed from the skull and processed, the recorded cell can then be recovered and further analyzed. Contact with a target cell is usually established "blindly," typically based on monitoring the resistance at the pipette tip (Zhu and Connors 1999; Margrie et al. 2002). More recently, single-cell recordings have also been combined with imaging, allowing a neuron to be targeted under visual control, either via a genetically defined fluorescent marker (Margrie et al. 2003) or based on the absence of fluorescence relative to a locally injected dye background (so-called shadow-patching (Kitamura et al. 2008)). The latter method was even used to record from dendrites in vivo under visual control. Although the limited penetration of light makes such imaging-dependent methods difficult to apply to deeper-lying structures such as the hippocampus, it has been done (Grienberger et al. 2014) by removal of the overlying cortical areas (Mizrahi et al. 2004; Dombeck et al. 2010).

Another possibility is to "tag" not just a single cell but rather a specific population of cells, by using genetics to induce expression of a protein based on a particular promoter. Besides using promoters for known cell types, an "ensemble" of active cells can be labeled by making use of the so-called immediate early genes such as c-Fos, whose expression can be rapidly induced by neuronal activity (Guzowski et al. 2005; Reijmers et al. 2007; Tonegawa et al. 2015). Finally, expression can be limited to a subpopulation of cells in a particular area or with particular connections by using viral stereotactic injections. All of these methods can be used to drive expression of fluorescent proteins or, perhaps more interestingly, calcium- or voltage indicators which allow imaging of the activity of the transfected neurons (Looger and Griesbeck 2012). It is even possible to extract and further process the imaged volume, enabling, e.g., post hoc immunohistochemistry or even full reconstruction of optically recorded cells with electron microscopy (Bock et al. 2011; Briggman et al. 2011; Langer and Helmchen 2012). Alternatively, the expression of light-

dependent channels such as channelrhodopsin can be used to enable light-induced activity in transfected neurons. Such activity can then be used to identify transfected cells in extracellular recordings (Lima et al. 2009) and can even enable the generation of "false memories" (Ramirez et al. 2013). However, both extracellular and optical recordings have limitations in terms of describing neuronal activity (see "Readouts of Neuronal Function" below), and detailed anatomical analysis of imaged cells is still relatively difficult and limited to small volumes. Therefore, single-cell approaches, as described in this chapter, arguably provide the greatest amount of combined anatomical and functional information per recorded cell.

One way to exponentially increase the amount of anatomical information one can derive from a particular cell, albeit at the cost of destroying the cell's morphology, is to use a glass pipette not to fill the recorded cell but rather to "harvest" material from it and isolate mRNA for further analysis (Lambolez et al. 1992; Martina et al. 1998). Progress in this field means that it is now possible in principle to obtain the "full" transcriptome from a single cell (at least from the soma), as recently published for mouse hippocampal and neocortical neurons (Zeisel et al. 2015; Tasic et al. 2016); this can even be combined with patch-clamp recordings in anesthetized animals (Cadwell et al. 2016). However, the level of technical and biological noise in the acquired data precludes the detection of low-abundance transcripts, making this method still prone to false negatives, depending on the amount of transcripts that can be collected (Okaty et al. 2011). Because cleanly harvesting mRNA material from single recorded cells in intact awake animals is not possible so far, post hoc immunohistochemistry and in situ hybridization (ISH) are still the most commonly used methods to determine molecular expression profiles. Sensitivity and specificity can be an issue for these methods, depending on the available probe/antibody. Since these methods depend on the discriminability of different markers, the spectral overlap of various fluorescent markers typically limits analysis to four different molecules per tissue sample. Usually, the brain is cut into thin sections such that a single labeled cell typically extends over many sections, making the overall number of testable molecules still relatively large, particularly for markers present on the cell's extensive axonal or dendritic trees (see, e.g., Lasztóczi et al. 2011; Viney et al. 2013). However, it is clear that any such analysis can only ever reveal a snapshot of a cell's full genetic expression profile and is limited by prior knowledge of which markers to test for.

The final challenge related to in vivo recording of identified cells is achieving recordings that are stable over sufficiently long time scales to achieve electrophysiological or behaviorally related characterization of the recorded cell. Recording stability always appears to involve some kind of trade-off. For instance, one can achieve stable long-term recordings from freely moving animals, even over many days, using extracellular methods based on tetrodes or silicone probes (Buzsáki et al. 2015) or recently developed imaging methods (Helmchen et al. 2013; Ziv et al. 2013). Such methods can offer access to relatively large populations of cells over long time scales. The trade-off is that the identity of the recorded cells remains largely unknown. Although genetically encoded calcium sensors or light-sensitive channels can give some information on the identity of the recorded cells, and

have thus provided a major boost to our understanding of neural circuits, such methods still typically rely on a single promoter or a single injection site (in the case of virally induced expression), thus severely limiting the amount of available anatomical information. Unique genetic markers identifying single-cell types are likely to be rare. For imaging methods, post hoc identification of the imaged area can provide detailed anatomical information, as mentioned above, but these methods are still quite cost- and labor-intensive and limited to small volumes, which can be problematic particularly in the case of axonal trees which often extend over large distances.

In this chapter, I will focus on whole-cell patch-clamp and juxtacellular recordings of single cells in vivo. These methods allow high temporal resolution recordings (including, for patch-clamp recordings, subthreshold membrane potential fluctuations) from single cells, together with post hoc analysis of both the morphology and molecular expression profile of the recorded cell. The trade-off is that the number of cells one can record with such methods tends to be very small (often just one cell per animal), and recording duration is limited to the timescale of minutes (or hours, in exceptional cases). To achieve stable recordings, researchers have either recorded from anesthetized animals (Fig. 3a; Kitai et al. 1976; Pinault 1996; Margrie et al. 2002; Klausberger et al. 2003), performed head fixation to record from drug-free animals (Fig. 3b; Harvey et al. 2009; Domnisoru et al. 2013; Schmidt-Hieber and Häusser 2013), or used other methods to record single identified cells from freely moving animals (Fig. 3c; Lee et al. 2006, 2014a; Long et al. 2010; Herfst et al. 2012; Tang et al. 2014a). I will address these three different preparations and the abovementioned techniques for recording single neurons in more detail in the two Experimental Techniques sections below, but first I will summarize some recent results obtained with these methods.

Cell Types: Linking Anatomical and Functional/Behavioral Classification

I will here focus on the link, provided by in vivo single-cell recording studies, between "anatomical" and "functional" cell types. The former, extensively classified in vitro, includes, for instance, stellate and pyramidal cells, but also many types of interneurons, whereas the latter category, identified in often classic chronic extracellular recordings, includes place cells (O'Keefe and Dostrovsky 1971; O'Keefe 1976), grid cells (Hafting et al. 2005), and head-direction cells (Taube et al. 1990), among others (Cacucci et al. 2004; Solstad et al. 2008; Krupic et al. 2012; Kropff et al. 2015). We are now finally starting to bring together these two major classification systems, although clearly there are many open questions remaining.

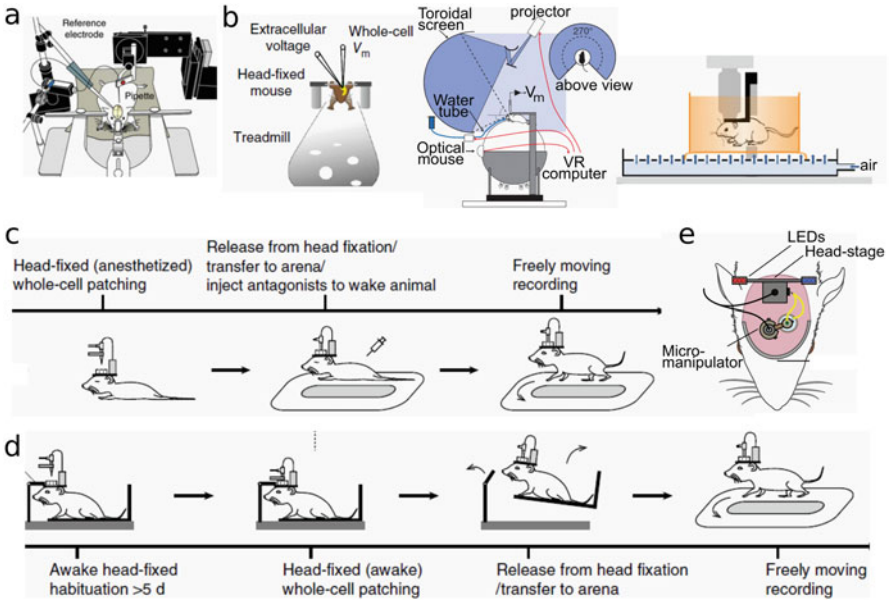

Fig. 3 *Single-cell recordings in vivo.* (**a**) Anesthetized rat in stereotaxic frame. (**b**) Methods to record from awake head-fixed rodents. Left: A mouse running on a treadmill. Two pipettes are shown for simultaneous intracellular (whole-cell patch-clamp) membrane potential (Vm) recording and extracellular recording of the LFP. Middle: A mouse running on an airlifted ball whose movements drive a virtual reality (VR) stimulation, which is projected onto a toroidal screen largely surrounding the mouse (inset shows top view). Note the presence of a water tube to deliver water rewards for motivation. *AAM* angular amplification mirror, *RM* reflecting mirror. Right: Mouse running on an air-lifted platform (orange), providing 3D stimulation. (**c**) Method to record from freely moving rodents by patching a single cell under anesthesia and then injecting antagonists to quickly wake the animal. (**d**) Similar method, except that recording is performed in awake mice after habituation to head fixation. (**e**) A miniaturized drive (micromanipulator) with pipette holder implanted onto the head of a rat, allowing the search for and recording of cells to take place in freely moving animals. Note this method has mainly been applied for juxtacellular recordings. (Figures taken and adapted with permission: (**a**) from Moore et al. 2014; (**b**) left panel from Bittner et al. 2015, middle panel from Harvey et al. 2009, right panel from Kislin et al. 2014; (**c**–**d**) from Lee et al. 2014a; (**e**) from Tang et al. 2014a)

Place Cells

Place cells, firing selectively when an animal is at a particular position (the cell's place field), have long been considered to be pyramidal cells based on electrophysiological parameters. However, it is becoming increasingly clear that pyramidal cells are not a homogeneous population. Recent reports suggest there are two main classes of pyramidal cells in hippocampal area CA1, mostly based on anatomical position within the stratum pyramidale, but also related to the innervation by PV cells and expression of calbindin (Slomianka et al. 2011; Lee

et al. 2014b). Both classes can be place cells, but the sublayer position of recorded cell somata correlates to several functional parameters, including the likelihood of place cell firing, both in freely moving and head-fixed animals (Mizuseki et al. 2011; Danielson et al. 2016). Others have described differences between pyramidal cells based on morphology, intrinsic firing patterns (bursting versus more regular firing), and the expression of metabotropic glutamate expression (Graves et al. 2012). The relation of the latter groups with the abovementioned functional parameters remains unclear, because the functional parameters were thus far only measured in vivo with calcium imaging and extracellular recordings, methods that make further anatomical analysis of the recorded cells in those studies either difficult or impossible.

Beyond the question of anatomical identity, whole-cell recordings in freely moving and head-fixed animals have revealed a great deal about the mechanisms underlying place-specific firing (Fig. 4). As the animal approaches a cell's place field, a ramp-like membrane depolarization and an increase in the amplitude of intracellular theta oscillations were recorded from CA1 pyramidal cells in head-fixed mice (Fig. 4a–b; Harvey et al. 2009). Whole-cell recordings from freely moving animals showed a similar ramp-like depolarization in place cells (Fig. 4c), in contrast to the conspicuously flat membrane potentials of silent cells; furthermore, place cells were shown to have a lower spike threshold than non-place-modulated silent cells (see Table 1) and were intrinsically more "bursty," even when these same cells were recorded under anesthesia prior to any exploration (Epsztein et al. 2011; see Experimental Techniques, section "Freely Moving Animals"). Interestingly, despite these differences, many silent cells can be induced to display place-specific firing by injecting a small constant depolarizing current (Fig. 4d–e; Lee et al. 2012). This suggests that all CA1 pyramidal cells may be receiving spatially modulated inputs at their dendrites. The presence of spikelets was also modulated by the animal's location (Epsztein et al. 2010), suggesting possible axonal interaction among pyramidal cells encoding similar locations. Finally, a recently published seminal paper (Bittner et al. 2015) used head-fixed mice running on a linear track treadmill to show that dendritic plateau potentials drive the previously described somatic ramp-like membrane depolarization and complex burst firing of place cells (Fig. 4f). These plateau potentials were shown to depend on coincident input from entorhinal cortex and CA3. Furthermore, using intracellular induction of plateau potentials, the authors were able to rapidly induce place-selective firing at the location the animal was at when the induction took place (Fig. 4g). This place-selective firing is likely due to plateau potential-mediated enhancement of the amplitude of spatially modulated EPSPs (Fig. 4h). Thus, it appears that not only does each pyramidal cell in CA1 receive spatially tuned input, but it receives spatially tuned input for all potential locations, and the convergence of input from the entorhinal cortex and CA3 determines which particular cell codes for which location (Table 2).

It should be noted that place cells have been recorded not only in CA1 but in all hippocampal subfields including the dentate gyrus and subiculum. It is beyond the scope of this chapter to compare the properties of place cells across subfields, but notable differences do exist both at the single cell and ensemble level (Lee et al. 2004; Mizuseki et al. 2012), consistent with anatomical differences in terms

Table 1 CA1 place cells, in vivo patch-clamp recordings

	Harvey et al. (2009)	Harvey et al. (2009)	Bittner et al. (2015)	Epsztein et al. (2011)
	Mouse VR HF tetrodes	Mouse VR HF patch	Mouse treadmill HF patch	Rat freely moving patch
	Means ± SD	Means ± SD	Means ± SEM	Means ± SEM
FR overall (Hz)	1.0 ± 0.3	2.2 ± 0.4		4.1 ± 1.3[b]
				0.3 ± 0.1[c]
FR in-field/peak (Hz)	4.7 ± 2.6	7.3 ± 1.4	14.3 ± 1.5	
FR out-of-field (Hz)	0.6 ± 0.2	1.5 ± 0.4		
% place cells		36 (8/22)		44 (4/9)
Depolarizing ramp (mV)		5.7 ± 2.9	7.9 ± 1.0	13 ± 3[b]
				2.9 ± 0.3[c]
Field MPO theta ampl change		1.75 ± 0.6[a]	2.8 ± 0.26[f]	
Plateau potential ampl (mV)		~10–25	41 ± 0.3	~20–40
Plateau potential duration (ms)		50–100	56 ± 4	~100–600
RMP (mV)		−67 ± 4		−64 ± 3[b,d]
				−65 ± 2[c,d]
				−66 ± 2[b,e]
				−59 ± 2[c,e]

AP threshold rel to RMP (mV)				13 ± 3^{b}
				2.9 ± 0.3^{c}
AP threshold (mV)				$-48 \pm 2^{b,d}$
				$-44 \pm 2^{c,d}$
				$-55 \pm 2^{b,e}$
				$-46 \pm 2^{c,e}$
Rin (MΩ)		98 ± 23	69.5 ± 2.8	$48 \pm 10^{b,d}$
				$33 \pm 3^{c,d}$
				$41 \pm 9^{b,e}$
				$41 \pm 2^{c,e}$
Recording duration (min)		7.7 ± 3.8	$>15.1 \pm 1.8$	7.0 ± 2.3
			($> 39 \pm 7$ laps)	

[a]Ratio 6–10 Hz power in-field/out-of-field; numbers estimated from Figure S8b
[b]Place cells
[c]Silent cells
[d]Initial anesthetized recordings
[e]Post-anesthesia awake recordings
[f]In-field versus out-of-field difference in theta (4–11 Hz) envelope amplitude (mV)

Table 2 Mouse MEC L2 grid cells, in vivo patch-clamp recordings

	Domnisoru et al. (2013)	Domnisoru et al. (2013)	Schmidt-Hieber and Häusser (2013)	Tsuno et al. (2015)
	VR extracellular	VR HF patch	VR HF patch	Ket/xyl patch
	Means ± SD	Means ± SD	Means ± SEM	Means ± SD
FR overall(Hz)			0.3 ± 0.1[f,h]	5.7 ± 5.5
			3.8 ± 0.6[g,h]	0.4 ± 1.0[9]
Peak FR (Hz)	12 ± 6[a]	13 ± 10[a]	10 ± 2[f]	
Grid field size (cm)	40 ± 11	~36 ± 9[a]	20 ± 2[f]	
LFP theta phase-position correlation	−0.21 ± 0.09		−0.14	
% grid cells		64 (27/42)		
Grid field Δ ramp (mV)		2.9 ± 0.3	5.0 ± 1.0[f]	
Grid field Δ MPO Theta ampl (mV)		0.72 ± 0.12	2.0 ± 0.2[f]	
RMP (mV)		−71 ± 3[b]	−62 ± 1[f, h]	−68.9 ± 5.2
		−73 ± 3[c]	−63 ± 1[g, h]	−73.8 ± 7.2[i]
Rin (MΩ)		77 (median)[d]	34 ± 3[f, h]	~90[j]
		32 (median)[e]	109 ± 4[g, h]	
Rs (MΩ)			25–70 (max 100)	
Recording duration (min)		10.3 ± 8.9	~5 (max ~30)	26.4 ± 9.8

[a]Numbers estimated from Figure
[b]L2 "large θ grid cells," out-of-field RMP after spike removal
[c]L2 "small θ grid cells," out-of-field RMP after spike removal
[d]L2 "large θ cells" (including grid, non-grid, unassigned cells)
[e]L2 "small θ cells" (including grid, non-grid, unassigned cells)
[f]L2 stellate cells, identified by electrophysiological properties (8/26 confirmed morphologically)
[g]Putative pyramidal cells (6/111 confirmed morphologically)
[h]Computed in recordings where mouse was resting
[i]With negative tonic current injection (103 ± 56 pA)
[j]Estimated median from publication Fig. 4b

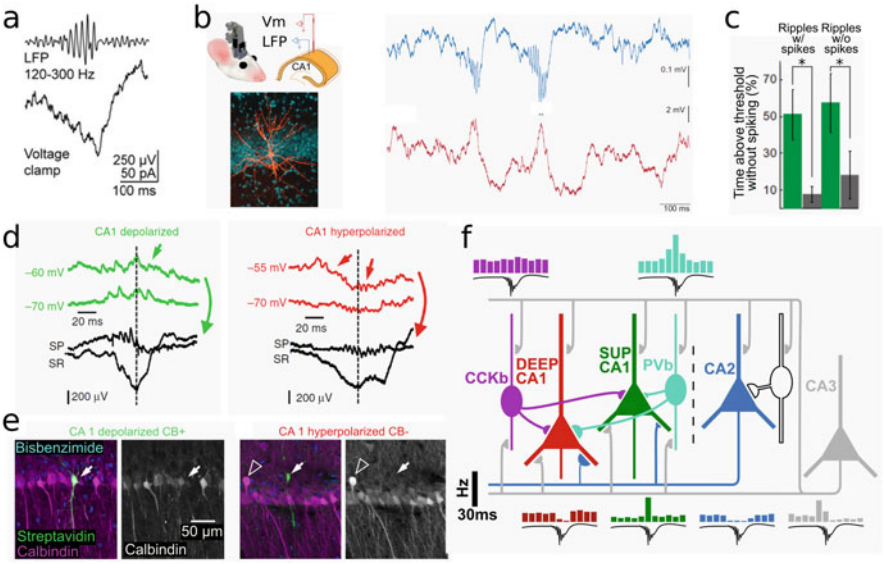

Fig. 4 *Place cell mechanisms revealed by intracellular recordings from CA1 pyramidal cells.* (**a**) Intracellular recording from head-fixed mouse in VR, showing a depolarizing ramp in the membrane potential of a place cell (top trace), and plateau potentials underlying burst firing (bottom trace) when a mouse crosses a place field (outlined in gray). (**b**) Depolarizing ramps (top) and increased theta power were observed as mice crossed virtual place fields. (**c**) In recordings from *freely moving* mice, a similar firing pattern was found when animals crossed the place field (traces as in **a**). (**d**) Injecting depolarizing current (83 pA in this example, left panel) can cause spatial firing to appear in previously silent cells (0 pA, right panel). (**e**) Spatially selective depolarizing ramp (red) induced by depolarizing current. (**f**) Recordings from head-fixed mice running on a treadmill also found that place-field firing (top right) was associated with a depolarizing ramp and plateau potentials (bottom right). (**g**) Inducing a plateau potential at any particular position could induce long-term place-selective firing at this location. (**h**) Input amplitude potentiation was suggested by an increase in Vm residuals (Vm – mean Vm) after place field (PF) induction. (Figures taken and adapted with permission: (**a**) from Long and Lee 2012, adapted from Harvey et al. 2009; (**b**) from Harvey et al. 2009; (**c**) top panel from Lee et al. 2014a, middle and lower panels from Long and Lee 2012, adapted from Epsztein et al. 2011; (**d**–**e**) from Lee et al. 2012; (**f**–**h**) from Bittner et al. 2015)

of inputs and local microcircuits. For instance, granule cells tend to have several place fields (Jung and McNaughton 1993), whereas CA1 and CA3 place cells are classically thought to have one place field, although this depends on the size of the environment (Fenton et al. 2008; Rich et al. 2014).

Grid Cells

Grid cells fire when the animal is at specific locations spaced in a periodic manner such that they form a regular lattice extending over the entire environment (Hafting et al. 2005). The anatomical substrate of grid cells, particularly in MEC layer 2

(L2) where most "pure" grid cells have been reported based on tetrode recordings in rat (Sargolini et al. 2006), remains an unresolved issue. MEC L2 has classically been described as containing two main types of principal cells: pyramidal cells, expressing calbindin and Wfs1 and projecting to the contralateral MEC (Varga et al. 2010) and CA1 stratum lacunosum moleculare (Kitamura et al. 2014), and stellate cells, selectively projecting to the dentate gyrus and CA3 (Varga et al. 2010). In fact, a recent in vitro study challenged this ontology, instead finding four distinct types based on electrophysiological and morphological parameters; importantly, these types also showed distinct (local) connectivity patterns (Fuchs et al. 2016; but see also Winterer et al. 2017). The possible misclassification of intermediate cell types in older reports may be one reason why there have been quite different results regarding the question of whether grid cells in MEC L2 are stellate or pyramidal cells.

Whole-cell patch-clamp recordings show that grid cells can be recorded in head-fixed mice navigating a VR environment (Domnisoru et al. 2013; Schmidt-Hieber and Häusser 2013), but due to the technical difficulties of these experiments, the number of recovered cells was low in these studies. Only one of the reports included a characterization of the spatial firing properties of pyramidal cells, finding that most (6/9) recovered grid cells in L2 were stellate cells (Domnisoru et al. 2013). Other work based on juxtacellular recordings suggested that grid cells in layer 2 include a disproportionate number of calbindin-positive pyramidal cells, which are also significantly more theta-rhythmic than reelin-positive stellate cells (Ray et al. 2014; Tang et al. 2014b). Finally, a third report based on calcium imaging and the marker Wfs1 to delineate pyramidal cells suggests there is an equal proportion of grid cells among pyramidal and stellate cells (Sun et al. 2015). This brief overview highlights the complexities of even answering such a basic question as the anatomical identity of grid cells. This may be due to differences between rats and mice, as well as methodological differences: VR versus freely moving conditions, long versus short recordings, chronic versus acute conditions (and potential differences in behavior), the precision of anatomical localization, and the probability of isolating the activity of single cells (particularly difficult in extracellular recordings where neighboring cells display coincident firing, as may be the case in MEC L2 (Heys et al. 2014)).

Head-Direction Cells

Head-direction (HD) cells fire only when an animal's head is facing a particular direction relative to the environment (Taube et al. 1990). Based on juxtacellular recordings from freely moving rats, it was recently found that all recovered HD cells in the presubiculum (PrS), a major input area of the MEC, were pyramidal neurons (Tukker et al. 2015), with spiny dendrites extending across all layers, mostly including apical tufts in layer 1 that suggest these cells are likely to receive input from the thalamus, another area known to contain a large proportion of HD cells (for review, see Taube 2007). Interestingly, very weak HD tuning was also found in both putative and identified fast-spiking interneurons. Another recent study was able

to record HD cells in head-fixed rats by placing them on a rotating platform, thus taking advantage of the improved success and recovery rates associated with head fixation while at the same time generating the vestibular input necessary for HD cell firing (Preston-Ferrer et al. 2016). In this report, juxtacellular recording and labeling were used to show that long-range axonal projections of PrS HD cells targeted layer 3 of the MEC. These two studies together showed the presence of HD-tuned, non-theta-rhythmic pyramidal cells in PrS providing inputs to MEC layer 3, supporting the idea that grid cells in this layer are likely to receive excitatory HD-tuned inputs.

Virtually all models of grid cells require some directionally selective input, although the anatomical origin of such input is not usually explicitly mentioned. Although the aforementioned studies suggest the PrS input may supply this input, it remains to be shown that indeed grid cells are among the targets of the HD PrS inputs. Interestingly, other studies have also shown that there may be "masked" HD tuning in grid cells (Brandon et al. 2011; Bonnevie et al. 2013), as well as a large proportion of HD cells and conjunctive grid x HD cells (Sargolini et al. 2006) specifically in layer 3 of the MEC. In apparent contrast, a report based on juxtacellularly filled cells as well as tetrode recordings (Tang et al. 2015) recently reported rather weak HD tuning in this layer. This could be partially due to differences in the recording and/or training methods, but it seems likely that other factors such as the precise definition of HD cells and the anatomical localization of recordings may also explain the divergent results. The latter point is related to the fact that there is a gradient of HD tuning in layer 3, with many of the strong HD cells located in the most dorsal part of MEC (Giocomo et al. 2014). Based on recent genetic and anatomical work, this dorsal region may correspond to some extent to the parasubiculum (Ramsden et al. 2015), which contains a much higher proportion of HD cells (Tang et al. 2016). This example emphasizes the importance of precise anatomical localization, which is generally more limited in extracellular recordings, but also reminds us that macroanatomical definitions of brain areas may need to be adapted as we acquire new insights on the basis of molecular markers or connectivity (Boccara et al. 2015; Ramsden et al. 2015; Ishihara and Fukuda 2016).

HD cells, like most functionally defined cell types, are typically defined based on a somewhat arbitrary cutoff within a wider distribution of tuning strengths. In fact, a quantification of the extent to which particular functional parameters could explain the variance in unit firing rate, based on extracellular recordings in several hippocampal areas, found that many cells tend to code for several parameters, to different extents (Sharp 1996; see also Sargolini et al. 2006; Hardcastle et al. 2017). This contrasts to some extent with the often clearer categorization of anatomical or neurochemical cell types, e.g., based on the presence or absence of a particular marker. It may therefore not be feasible to find an anatomical substrate for each functional cell type, and instead we may find certain functional tuning parameters correlating to a greater or lesser extent with particular anatomical parameters. Certainly it is important to keep in mind that functional cell type classifications are often a shorthand for a more complex reality. Furthermore, the precise definitions of functional cell types often vary between studies, and these differences matter.

Interneurons

Historically, the question of the anatomical identity of functional cell types has mostly been limited to principal cells; this is partly because many extracellular electrophysiology studies, where functional cell types have been discovered, have excluded "fast-spiking" units and partly because principal cells are, as the name implies, the majority. In principle, there is no reason any particular functional cell type could not include interneurons, and in fact it is likely that many GABAergic interneurons display some form of functional tuning (Kepecs and Fishell 2014). Thus, depending on how "inclusive" the criteria are, interneurons can either be included as, e.g., HD cells, or excluded. However, in terms of understanding a cortical circuit, it seems clear that GABAergic HD cells can have quite different functions than glutamatergic HD cells. Therefore, it makes sense to treat interneurons as a separate category and ask the complementary question, i.e., what is the function of anatomically identified interneuron cell types?

This question was briefly touched upon in the paragraph on HD cells; for the PrS, so far little is known beyond the fact that fast-spiking interneurons, including at least some PV neurons, show weak but significant HD tuning (Tukker et al. 2015). In general, there is a large body of work showing a similar trend: relatively weak tuning in interneurons has been found in visual cortex, hippocampus, and many other brain areas (Kubie et al. 1990; Maurer et al. 2006; Ego-Stengel and Wilson 2007; Kerlin et al. 2010). In the MEC, a study combining extracellular recordings with optogenetics recently showed that PV cells, although not displaying any HD or grid-like spatial coding, do encode some spatial information (Buetfering et al. 2014). This study is also one of the first to tackle the question of how functionally and anatomically defined cell types are connected with each other, a crucial issue that mostly still remains in the realm of modeling. They showed that PV cells receive inputs from many nonaligned grids, thus explaining their lack of "gridness."

Another recent study from the same laboratory used visually guided intracellular patch-clamp recordings in ketamine-/xylazine-anesthetized mice to show odor-evoked firing in four out of four GAD67 neurons in the lateral entorhinal cortex (LEC; Leitner et al. 2016); although all these cells had dense axonal arborization in the superficial layers, their electrophysiological properties were very heterogeneous. Of course, more cells need to be recorded, preferably in drug-free conditions, and additional knowledge of the molecular expression profile of these cells would also be very informative, but even this small sample suggests that several types of GABAergic interneuron respond to odor in the LEC.

Unfortunately, there are many different classes of PV cells in the MEC, and even more classes of GAD67 cells in the LEC, which could not be discerned in these studies and could explain some of the reported variability. Indeed, most reports of interneuron functional tuning reported thus far are either based on spike shape and firing pattern, as in the case of the classic "theta cells" in the hippocampus (Fox and Ranck 1975; Kubie et al. 1990) or, more recently, based on the expression of one of a small set of genetic markers (e.g., Royer et al. 2012). Although such studies are

insightful, GABAergic interneurons form an incredibly heterogeneous population (Canto et al. 2008; Klausberger and Somogyi 2008; Somogyi et al. 2014; Nassar et al. 2015; Ferrante et al. 2017), and no electrophysiological or single genetic marker can suffice to discern the various types that have been described thus far. For instance, PV cells in the hippocampus include preferentially *soma*-targeting basket cells, axon initial segment-targeting axo-axonic cells (also known as chandelier cells), *proximal dendrite*-targeting bistratified cells, and *distal dendrite*-targeting oriens-lacunosum moleculare (O-LM) cells (Klausberger et al. 2003, 2004). Each of these cell types can have its own connectivity, plasticity, and expression patterns (including neuropeptides, receptors, channels, etc.). Considering the recent use of genetic methods, it should also be mentioned that protein expression patterns are regulated developmentally, and thus the expression of, e.g., Cre recombinase under the control of a particular promoter may not necessarily reflect protein expression in the adult. This was recently shown for neurons in the hippocampus expressing both Cre and Flp recombinases under the control of parvalbumin and somatostatin promoters, respectively; surprisingly, a majority of these neurons were found to be immuno*negative* for PV (Fenno et al. 2014). Based on their morphologies, these cells were identified as mostly O-LM interneurons, a cell type originally described as PV-expressing in rat (Klausberger et al. 2003) but recently reported to be PV-immunonegative in mice (Varga et al. 2012).

Interestingly, although O-LM cells and bistratified cells both express PV and SOM, a recent study showed that they play very different roles in the circuit during fear learning (Lovett-Barron et al. 2014). Since O-LM cells target almost exclusively the stratum lacunosum moleculare, whereas bistratified cells target the neighboring stratum radiatum, calcium imaging of SOM axons restricted to these layers could be used to selectively image putative O-LM and bistratified cells. A contextual fear conditioning task in head-fixed mice running on a treadmill was used to reveal that O-LM but not bistratified or other PV cells responded to aversive stimuli. This was mediated by a cholinergic input signal from the medial septum, which the O-LM cells can respond to because they express cholinergic receptors. The response of SOM expressing putative O-LM cells to aversive air puff stimuli was also shown via visually guided juxtacellular recordings in head-fixed mice (Schmid et al. 2016). This same paper used calcium imaging and pharmacology to reveal that this response was acetylcholine-dependent and impaired in a mouse model of Alzheimer's disease (AD). The deficit in the AD mouse was linked to a reduced number of presynaptic cholinergic cells in the medial septum and an acetylcholine-dependent fear conditioning deficit in these animals. Thus, O-LM cells may be a potential target for cholinergic drugs that could compensate the well-known degeneration of cholinergic neurons in AD: by targeting cholinergic receptors on O-LM cells, future therapeutics could potentially reverse learning deficits by repairing the O-LM cell-mediated modulation of the entorhinal input onto CA1 pyramidal cells. This example serves to illustrate the importance of knowing, e.g., which other cell types also express acetylcholine receptors, and what their synaptic targets may be. For instance, SOM cells in the hippocampus have also been shown to

include long-range interneurons projecting to the MEC (Melzer et al. 2012), which presumably have very different functions from O-LM cells.

A full description of hippocampal interneuronal heterogeneity is beyond the scope of this chapter (see also chapter "Fast and Slow GABAergic Transmission in Hippocampal Circuits"). It is clear, however, that the large diversity of these cells makes the precise identification of cells both important and difficult, particularly in combination with behavior. Earlier intracellular and juxtacellular recordings from anesthetized rats have shown that specific subtypes of GABAergic interneuron play specific roles in the generation of various oscillations of the local field potential (LFP) related to particular behavioral states (Ylinen et al. 1995b; Klausberger et al. 2003, 2004, 2005; Jinno et al. 2007; Tukker et al. 2007; Fuentealba et al. 2008; Lasztóczi et al. 2011). Many, but not all, of these findings were confirmed in juxtacellular recordings in freely moving rats (Lapray et al. 2012; Viney et al. 2013; Katona et al. 2014) and head-fixed mice (Varga et al. 2012, 2014). For the future, it will be important to investigate to what extent the functional tuning of different interneuron classes differs and to relate this to connectivity either directly (e.g., using viral tracing methods in combination with whole-cell recordings in head-fixed mice (Rancz et al. 2011; Vélez-Fort et al. 2014; Wertz et al. 2015)) or based on in vitro results (Couey et al. 2013; Böhm et al. 2015; Fuchs et al. 2016), particularly if those in vitro results can include more extensive cell type classifications, e.g., based on morphology (Jiang et al. 2013, 2015).

What Have We Learned? An Example

It is very difficult, at this stage, to already draw major conclusions based on the previously described work. We are only just beginning to have some overview of the roles of different cells in behavior and in driving network phenomena like cortical oscillations. A major challenge will be to bring together the results of in vivo single-cell studies as described here with in vitro work on the one hand and extracellular, imaging, and behavioral studies on the other, to form a unified picture of hippocampal microcircuits.

Our most advanced understanding is perhaps related to hippocampal place cells (Fig. 4), whose place-specific firing was recently reported to rely on dendritic plateau potentials and convergent inputs from CA3 and layer 3 of the EC, as described above (Bittner et al. 2015). However, there are still many open questions even for this most studied "cell type," including the nature of the specific input provided by layer 3 of the EC (Sargolini et al. 2006; Suh et al. 2011; Tang et al. 2015) and the role of specific types of interneurons in CA1. As one specific example, consider the role of bistratified cells in the hippocampus (Fig. 5; for a more detailed review, see Müller and Remy 2014). Paired recordings in hippocampal area CA1 in vitro, combined with LM reconstructions and EM analysis (Buhl et al. 1994), first showed these cells, which express PV, neuropeptide Y (NPY), and SOM (Klausberger et al. 2004), to selectively innervate pyramidal cell dendrites

co-aligned with Schaffer collateral input from CA3 in strata radiatum and oriens. Bistratified cells receive direct inputs from PV basket cells (Cobb et al. 1997), such that somatic and dendritic inhibition can be coordinated in a complementary manner (Lovett-Barron et al. 2012). The latter in vitro study also showed that direct inputs from CA3 pyramidal cells onto bistratified cells may help these cells to regulate the impact of inputs from CA3 onto CA1 pyramidal cells. Such a role is consistent with recordings from CA1 in urethane-anesthetized rats suggesting that these cells are among the most strongly phase-locked to gamma oscillations (Tukker et al. 2007), which are likely generated in CA3 (Csicsvari et al. 2003). Thus, bistratified cells may ensure that the dendrites of CA1 pyramidal cells can effectively process the gamma-rhythmic inputs from CA3 cell assemblies; alternatively, they may also block transfer of information during certain brain states, for instance, by releasing NPY or SOM in response to high-frequency firing, which bistratified cells display both during movement and sleep (Katona et al. 2014). The latter authors speculated that this slow peptide release may be one mechanism for the termination of SWRs, during which identified bistratified cells have been shown to strongly increase their firing rates in anesthetized (Klausberger et al. 2004), head-fixed (Varga et al. 2014), and freely moving (Katona et al. 2014) rodents. Interestingly, the firing rate increase in bistratified cells appeared to be different depending on the extent of its dendritic tree in stratum radiatum (Varga et al. 2014), raising the question whether bistratified cells should be further subdivided into two separate cell types or not. Like gamma oscillations, SWRs are also generated in CA3; in fact, gamma oscillation power and synchrony across CA3 and CA1 were recently shown to increase during SWRs, in a manner that was predictive of the quality of "replay" of past experiences (Carr et al. 2012).

In general, it seems plausible that bistratified cells are involved in gating the transfer of information from CA3 to CA1 during sharp-wave ripple events as well as gamma oscillations (Buzsaki 2006). One possible way in which this gating might be regulated is via bistratified cell-mediated inhibition of dendritically generated plateau potentials (Lovett-Barron et al. 2012), which were recently shown, as mentioned above (Fig. 4f–g), to be important for the generation of burst firing in pyramidal cells underlying place selectivity (Bittner et al. 2015). In contrast, bistratified cells did not appear to be involved in fear conditioning (Lovett-Barron et al. 2014). Like many other interneuron types in the hippocampus, bistratified cells also show theta-modulated firing (Fig. 5; Klausberger et al. 2004; Katona et al. 2014; Varga et al. 2014), at a similar phase as O-LM cells but different from other interneuron types. Although both theta and gamma oscillations have been linked to the coding of an animal's movement speed, there is unfortunately no report on the speed dependence of bistratified cell firing. Furthermore, recent reports have shown two or even three types of gamma oscillations in CA1, with different underlying mechanisms, which could all be relevant for place cell firing and spatial navigation (Lasztóczi and Klausberger 2014, 2016; Colgin 2015). The relation of these oscillations with bistratified cells, or indeed any other specific interneuron type recorded in awake animals, remains unknown (except PV basket cells; Lasztóczi and Klausberger 2014).

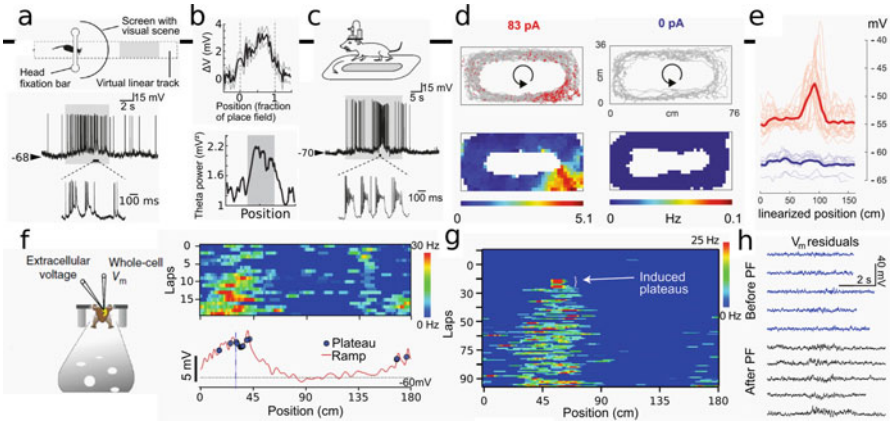

Fig. 5 *Hippocampal bistratified interneurons characterized via in vivo juxtacellular recordings in different rodent preparations.* (**a**) LFP recording (top) and simultaneously recorded APs from a single cell recorded in urethane plus ketamine-xylazine anesthesia. Scale bars: horizontal 0.1 s; vertical 0.2 mV; (**b**) firing probability of seven different bistratified cells (gray is average) at different phases of simultaneously recorded theta oscillations, showing that bistratified cells preferably fire at the trough of the theta cycle. (**c**) Bistratified cells were filled with neurobiotin (blue) and shown to be immunopositive for parvalbumin (green, bottom left), somatostatin (red), and neuropeptide Y (green, bottom right). Scale bar, 20 μm. (**d**) LFP recording (top) and simultaneously recorded APs from a bistratified cell recorded in a head-fixed mouse running on an air-lifted ball; bottom trace shows theta-filtered (5–10 Hz) LFP. (**e**) Theta modulation strength for eight recorded bistratified cells (green), showing that these cell preferentially fired at the trough of theta. Note that other recorded cell types (PV basket cells, red, and axo-axonic cells, blue) were more strongly modulated and fired at earlier theta phases. (**f**) Example filled bistratified cell (axon blue, dendrites red) which was filled with neurobiotin (inset, red) and immunopositive for somatostatin (inset, green). (**g**) LFP recording (top) and simultaneously recorded APs (bottom) from a bistratified cell recorded from a freely moving mouse; inset shows autocorrelogram illustrating theta-rhythmic firing of the recorded cell during periods when the animal was moving. (**h**) Polar plot showing average firing rate as a function of theta phase for five recorded bistratified cells (red), with preferred phase for each cell individually shown as red circles. O-LM cells are shown in green. (**i**) Cell recorded in **g** (axon black, dendrites red) filled with neurobiotin (inset, red), immunopositive for PV both in axon (yellow arrow) and dendrite (yellow arrowhead). (Figures taken and adapted with permission: (**a**) from Somogyi et al. 2014; (**b–c**) from Klausberger et al. 2004; (**d–f**) from Varga et al. 2014; (**g–i**) from Katona et al. 2014)

The work presented here on bistratified cells serves as an example to illustrate the insights that can be gained from recording identified cell types in the hippocampus (based on anatomical and molecular characterization). There are still very few studies directly relating the activity of bistratified cells to navigational function, which may be partly due to the fact that simply very few studies have been done in freely moving or head-fixed animals engaged in spatial tasks, and most of those studies have focused on first understanding place-specific activity of CA1 pyramidal cells (Harvey et al. 2009; Epsztein et al. 2010, 2011; Lee et al. 2012; Bittner et al. 2015). It is indeed still challenging to achieve long and mechanically stable recordings in moving animals, even if they are head-fixed, and to recover

recorded cells such that one can perform the necessary anatomical and molecular characterization to robustly identify neuron types. For interneurons specifically, the presence of many relatively small populations of specific cell types poses further challenges. Bistratified cells, for instance, comprise just 6% of all interneurons (Bezaire and Soltesz 2013), which themselves are estimated to comprise just ~10% of all hippocampal neurons. However,even such relatively small populations have been shown to perform important roles within the hippocampal microcircuit. Comparing the activity of bistratified cells with other interneuron types, including other SOM- or PV-expressing cells, supports the idea that different cell types have specific roles within the neural circuitry underlying hippocampal function (Somogyi et al. 2014).

Experimental Techniques: Rodent Preparations

Anesthetized Animals

Urethane has been a very commonly used (non-recovery) anesthetic for several decades. It has a broad spectrum of actions, including potentiation of GABA-A, nicotinic acetylcholine, and glycine receptors, while inhibiting NMDA- and AMPA-type glutamate receptors (Hara and Harris 2002); furthermore, it has been shown to inhibit glutamate release (Moroni et al. 1981), and LFPs recorded in the hippocampus of urethane-anesthetized animals are similar to those observed during entorhinal lesion (Ylinen et al. 1995b). Although it has pronounced effects on LFP and unit firing (Buzsáki et al. 1983, 1986), the overall network appears relatively intact, and in fact urethane can induce a regularly cycling series or brain states reminiscent of sleep, both in rats (Clement et al. 2008) and mice (Pagliardini et al. 2013). As with all anesthetics, the dosage is a crucial determinant of the effects.

Because of the irreversible nature of its effects, and the fact that urethane is highly carcinogenic, in many situations other anesthetics are preferred. Ketamine, an NMDA antagonist, is often used as an alternative. Its action is relatively short-lasting and on its own it generally provides insufficient anesthetic effect. Therefore it is typically combined with an adrenergic receptor type $\alpha 2$ agonist such as xylazine or medetomidine. This way, a surgical depth of anesthesia can be reached, and the recovery can be aided by an antagonist (e.g., atipamezole). Often, ketamine-xylazine is combined with a relatively low concentration of urethane; by giving top-ups at specific intervals, the experimenter can then have finer control over the depth of anesthesia (Klausberger et al. 2003). At lighter planes of anesthesia, brain state can be additionally influenced by external stimuli such as a foot- or tail-pinch, which can be used to elicit theta oscillations in the hippocampus or entorhinal area (Dickson et al. 1994; Klausberger et al. 2003). Importantly, anesthetized animals can still respond to sensory stimuli, as evidenced by neuronal responses in sensory cortices (Stosiek et al. 2003; Ohki et al. 2005).

In situations where fast recovery is essential, such as when a whole-cell patch-clamp recording established during anesthesia needs to be maintained as the animal wakes up (Lee et al. 2006), a cocktail of drugs including medetomidine, midazolam, and fentanyl has been used. These drugs were selected because administration of atipamezole, flumazenil, and naloxone could be used to end the anesthesia such that behavior could recover within 1–5 min.

For many applications, isoflurane has proven a convenient anesthetic. It is an inhalant that works, as least in part, by reducing transmitter release (Hemmings et al. 2005), particularly at glutamatergic synapses (Westphalen and Hemmings 2006). A recent paper showed that different brain states could be elicited, depending on the concentration: at low doses, exploratory or REM-like brain waves could be detected in the hippocampus, whereas at higher doses, isoflurane elicited slower oscillations more akin to quiet resting or slow-wave sleep (Lustig et al. 2016). One advantage of this method is that one can directly adapt the concentration in response to behavioral signs, resulting in a more reliable stable level of anesthesia. Injections, particularly intraperitoneal injections, can sometimes be misdirected depending on the experience and skill of the experimenter; this can result in unstable anesthesia or even death. Particularly for drugs that often require repeated injections (e.g., ketamine-xylazine), the instability and loss of animals can be serious issues, especially when working with mice.

The exact effects and mechanisms of anesthesia are not always well understood, and certainly a full discussion (including other commonly used anesthetics) is beyond the scope of this chapter. However, it is important to emphasize that anesthetics can and typically do have substantial effects on neuronal activity. For instance, dendritic calcium spikes (measured in vitro) can be differentially affected by urethane versus ketamine-xylazine (Potez and Larkum 2008). Firing rates, spike bursting, and neuronal synchrony have all been shown to be affected by (a relatively high dose of) urethane anesthesia (Greenberg et al. 2008). As a final example, a relatively brief exposure to isoflurane was recently found to affect the phosphorylation state of a wide range of proteins (Kohtala et al. 2016), which may in turn affect neuronal activity. However, as stated above, the overall network often seems relatively intact, and thus indeed many findings from anesthetized animals have been confirmed in awake animals, and the anesthetized animal remains a convenient preparation for in vivo investigations. In particular, the increased mechanical stability achievable in anesthetized animals allows much longer recording times compared to awake animals. The overall time the animal can be used in an experiment also tends to be much longer under anesthesia, allowing more recordings per animal compared to awake conditions, where session times are more limited. Furthermore, these recordings do not require training or habituation of the animals. Thus, it is time efficient and the model of choice for the first implementary steps of a new technique. Finally, anesthetized preparations allow a broad spectrum of profound surgical intervention which might be problematic in the light of animal welfare in awake in vivo preparations.

Head-Fixed Awake Animals

Clearly, the goal of many studies is to establish a link between neuronal activity and behavior. For single-cell recordings, head-fixed animals in many cases provide the best compromise between recording stability on the one hand and a relatively rich behavioral repertoire on the other (for recent reviews, see Minderer et al. 2016; Thurley and Ayaz 2017).

Although head fixation does limit the behavioral repertoire, animals can nevertheless be trained, for example, to press a lever (Guo et al. 2014), lick (Houweling and Brecht 2008), or whisk (Gao et al. 2003) in response to a stimulus. In fact, head fixation can be an advantage since stimuli can be presented in a very controlled manner (O'Connor et al. 2009). By adding the possibility for animals to move all their limbs on an air-cushioned Styrofoam ball (Dombeck et al. 2007; Fuhrmann et al. 2015) or cylinder (Domnisoru et al. 2013), one can increase the behavioral possibilities of the animal. These options are also the most relevant for the study of navigation and spatial memory. Running is often accompanied by brain movement, also in head-fixed animals, and this can be an issue: one study reported motion limited to 5 μm in the head-fixed mouse, being greatest in the rostrocaudal axis (Dombeck et al. 2007); another study reported cranial movement up to 40 μm in the head-fixed rat along the axis of the pipette (Fee 2000). The latter study was able to move the pipette with a piezo device to compensate for measured motion, thus enabling longer intracellular recordings even in moving animals. Of course, brain and/or residual cranial motion may be variable depending on the area recorded from, as well as the precise methods used for head fixation, but overall it seems that in terms of stability mice may provide an advantage over larger, stronger rats.

In terms of stimuli, allowing the animals to run provides additional proprioceptive input, which can be crucial for certain types of navigational processes such as path integration. Furthermore, linear treadmills (Royer et al. 2012) and movable platforms (Kislin et al. 2014; Nashaat et al. 2016) can offer a relatively wide range of somatosensory and visual stimulation. Spherical treadmills have also been combined with moveable walls to provide a "tactile virtual reality" system (Sofroniew et al. 2014); this same study also showed that mouse behavior on the ball resembled natural behavior in terms of running speed and stride and whisking frequencies. However, most studies combine the spherical treadmill with a visually presented virtual reality (VR), either via an array of screens or a toroidal projection system (Harvey et al. 2009). Rats can navigate in VR as long as the visual stimuli extend over a sufficient angle (Hölscher et al. 2005) and can even be trained to lick to indicate recognition of a previously learned location (Cushman et al. 2013). Mice can also perform spatial memory tasks, as shown in a one-dimensional VR environment using just a single widescreen LCD monitor (Youngstrom and Strowbridge 2012), and have been successfully trained to perform a VR T-maze decision task (Harvey et al. 2012). Thus, head fixation, particularly in combination with VR, allows one to employ a relatively wide range of stimuli and tasks relevant

for studying hippocampal microcircuitry, ranging from simple running along a one-dimensional corridor to complex tasks in two dimensions.

However, some caveats are in order. First of all, head fixation does limit the animal's motion; for instance, rearing (Lever et al. 2006) is obviously not possible nor are orienting head movements (Monaco et al. 2014). Secondly, the sensory input tends to be limited: visual cues are all relatively distal, and local somatosensory cues tend to be non-informative. These issues can be resolved to some extent by using a treadmill (Royer et al. 2012) or moveable platform (Kislin et al. 2014; Nashaat et al. 2016) with physical objects on it. However, for any head-fixed system, the lack of vestibular inputs is unavoidable and should be carefully considered particularly in light of its potential importance for certain aspects of navigational function. For instance, place cells could not be detected when rats navigated a virtual 2D environment (Aghajan et al. 2015), suggesting that the spatial maps generated in the more commonly used one-dimensional VR environments may be more related to internal mechanisms keeping track of self-motion than external cues, although there is likely to be heterogeneity among place cells (Chen et al. 2013). The importance of vestibular input was underlined by another recent study which found that in body-tethered rats, which were free to move their head and thus generate intact vestibular inputs, grid, place, and border cells could all be recorded in a 2D VR environment (Aronov and Tank 2014).

A reported lack of correlation between theta oscillations and speed in VR, which clearly differs from real-world results (Ravassard et al. 2013), is also consistent with a role for vestibular inputs in the mechanisms underlying theta oscillations (Russell et al. 2006; Jacob et al. 2014). Interestingly, the absence of speed-dependent theta oscillations did not abolish theta phase precession (Ravassard et al. 2013), a form of temporal coding whereby place cells fire at progressively earlier phases of the theta cycle as an animal crosses a place field (O'Keefe and Recce 1993). The fact that theta phase precession was also intact in a 2D environment (Aghajan et al. 2015), where no place cells could be detected, suggests that theta phase precession may be independent of both speed-dependent theta oscillations and representations of the current location, in support of a recent model positing that theta phase precession represents "mind travel" related to imagined movement rather than actual movement (Sanders et al. 2015).

More generally, the limitations of the virtual reality system in terms of ecological behavior are offset by greater control over different modalities and over the relationship between, e.g., animal motion and the generated visual flow. This has been used successfully to disentangle the relevance of particular inputs to the hippocampal representation of space (Chen et al. 2013; Ravassard et al. 2013; Acharya et al. 2016).

A final point to consider is that time and effort are required to get animals to habituate to head fixation and perform tasks (Schwarz et al. 2010; Guo et al. 2014). Training typically relies on positive feedback (usually water), whereby the animals undergo food or water restriction. The severity of the restriction regime depends on the difficulty of the task to be performed; for relatively simple tasks, such as running on a ball, it may even be sufficient to provide sugar-water to unrestricted animals

(Schmidt-Hieber and Häusser 2013), although this is atypical. With appropriate training, rats will even initiate head fixation voluntarily and remain head-fixed for relatively short durations (Scott et al. 2013), potentially enabling high-throughput automated approaches.

Freely Moving Animals

Extracellular recordings have been possible from freely moving animals for many decades (see also chapter "Spatial, Temporal, and Behavioral Correlates of Hippocampal Neuronal Activity: A Primer for Computational Analysis"), and recently the advent of optogenetics has allowed the use of optrodes in freely moving animals to record from genetically identified populations of cells or populations of cells with specific anatomical targets (Buzsáki et al. 2015; Grosenick et al. 2015; Wu et al. 2015). In addition, various miniaturized microscopes have been developed (Helmchen et al. 2001; Ferezou et al. 2006; Flusberg et al. 2008; Sawinski et al. 2009), which can also be used to image genetically and/or anatomically identified populations of cells in freely moving animals, even in deeper-lying brain regions such as the hippocampus (Ziv et al. 2013). Via targeted light stimulation, one can even selectively manipulate cells (Packer et al. 2015). These are important developments that are, however, outside the scope of this chapter. Electrophysiological tools still have the advantage of being able to directly record and manipulate membrane potentials and spiking activity at high temporal resolution. In head-fixed and particularly anesthetized applications, single-cell electrophysiology is also relatively cheap and easy to implement and enables relatively straightforward labeling and recovery of recorded cells. In freely moving animals, however, it is still a challenging and relatively rarely used technique. The technique has been made possible in part by the development of lightweight, miniature recording equipment that can be implanted on the head, including miniature headstages but also microdrives and holders for glass pipettes (Lee et al. 2006; Long et al. 2010; Herfst et al. 2012; Tang et al. 2014a).

One approach has been to search for cells (using current pulses and monitoring resistance at the pipette tip) under anesthesia, when the brain is relatively stable, and then waking up the animal after a successful recording has been initiated and the pipette has been "anchored" in place (Lee et al. 2006; Tang et al. 2014a). This method has been used with some success to perform whole-cell patch-clamp recordings of CA1 hippocampal pyramidal cells (Lee et al. 2009, 2012; Epsztein et al. 2010, 2011) and has also been applied to perform juxtacellular recordings in the medial entorhinal cortex and hippocampal area CA1 (Burgalossi et al. 2011; Herfst et al. 2012). Refinements of this "anchoring" method have recently enabled whole-cell patch-clamp recordings from drug-free animals (Lee et al. 2014a).

By using a microdrive implanted on the head, it is also possible to search for cells and perform single-cell recordings in fully drug-free animals (Long et al. 2010; Tang et al. 2014a). This method was used to perform intracellular recordings with sharp

electrodes from CA1 pyramidal cells in mice (English et al. 2014) and has also been successfully used to perform juxtacellular recordings in the hippocampus (Lapray et al. 2012; Viney et al. 2013; Katona et al. 2014; Diamantaki et al. 2016a, 2016b), medial entorhinal cortex (Ray et al. 2014; Tang et al. 2014b), presubiculum (Tukker et al. 2015), and parasubiculum (Tang et al. 2016) of freely moving rats.

Experimental Techniques: Readouts of Neuronal Function

Intracellular Recordings

For decades, intracellular recordings with sharp electrodes have been performed in vivo (see Long and Lee 2012, for review), but more recently the whole-cell patch-clamp approach has also been adapted for intracellular recording in vivo (Zhu and Connors 1999; Margrie et al. 2002). The key advantage of the latter approach is that patch-clamp pipette tips are considerably larger, providing lower resistance and thus better electrical access to the inside of the cell. In vivo, these recordings are usually performed blindly, particularly in deep tissues such as the hippocampus. The probability of recording from a particular cell type or layer may therefore be limited. Overall, success rates depend on a thoroughly prepared brain surface and possibly on a slow approach of the pipette through the tissue. Also taking the welfare of the animal into account, which sets practical limits to the recording time in awake animals (particularly when head-fixed), it can be challenging to achieve a successful recording. Newer techniques allow visual guidance (Kitamura et al. 2008) or, for deeper-lying brain structures, the use of optogenetic tools to pre-identify target neurons for intracellular recording and labeling (Muñoz et al. 2014). Even for a deep-lying structure such as the hippocampus, whole-cell recordings have been combined with calcium imaging (Grienberger et al. 2014), revealing the nature of burst firing in CA1 pyramidal cells in head-fixed mice under light isoflurane anesthesia.

Whole-cell patch-clamp recordings offer a number of benefits compared to extracellular recordings and/or calcium-imaging approaches. First of all, subthreshold activity can be measured at high temporal resolution. Although in vivo access resistance is often relatively high, limiting access to compartments further from the soma, it is possible to differentiate inhibitory and excitatory inputs to some extent either by clamping the membrane potential or by extracting putative excitatory and inhibitory synaptic potentials from the recorded voltage traces (Tao et al. 2015). Another possibility is to use pharmacological manipulation to isolate particular synaptic inputs. One limitation of the aforementioned methods is that it can be difficult or impossible to simultaneously observe temporally overlapping inhibition and excitation.

A series of papers has used intracellular recordings to elucidate the roles of excitation and inhibition in the generation of so-called sharp-wave-associated

ripples (SWRs; Fig. 6). SWRs are fast oscillations (~100–200 Hz) thought to play a role in the replay of previously experienced events, linked to memory consolidation, as well as the possible planning of future events (Buzsáki 2015). Early intracellular recordings from urethane- and ketamine-anesthetized mice showed the presence of ripple-frequency membrane oscillations in vivo and suggested a main role for perisomatic inhibition (Ylinen et al. 1995a). A later study combining in vitro experiments with recordings from awake head-fixed mice first showed that SWRs were also coupled to phasic excitation, which preceded hyperpolarization (Maier et al. 2011; see also Hulse et al. 2016; Fig. 6a). More recently, sharp recordings from freely moving mice showed that action potential firing of CA1 pyramidal cells was often suppressed during simultaneously recorded SWRs despite a large (threshold-exceeding) membrane depolarization, indicating the presence of shunting inhibition (English et al. 2014; Fig. 6b–c). Finally, there is also a reported variability among principal cells in terms of the role of inhibitory versus excitatory drive during SWRs. In CA1, intracellular recordings from urethane-anesthetized rats, as well as juxtacellular recordings from freely moving rats, showed that deep-lying pyramidal cells were more inhibited, while more superficial cells were more excited during SWRs, a finding that correlated to calbindin immunoreactivity (Valero et al. 2015; Fig. 6d–f). In the subiculum, both intracellular and juxtacellular recordings in awake head-fixed mice showed that burst-firing cells were more depolarized, whereas regular firing cells were more hyperpolarized during SWRs (Böhm et al. 2015); interestingly, these cells also had different connectivity within the network as shown in vitro by simultaneous intracellular recordings of up to eight cells (Fig. 2e). Both of these reports suggest the presence of different principal cell types playing different roles in the generation of SWRs, whereby recorded firing rates and membrane potential were correlated to either a molecular marker and precise anatomical location (Valero et al. 2015) or to intrinsic electrophysiological properties and connectivity (Böhm et al. 2015).

In general, the ability to record subthreshold oscillations or ramps and their voltage dependence is an important advantage of intracellular recordings, particularly if they can be related to the behavior of the animal (e.g., its location or speed; see below). It is even possible to record signatures of dendritic spiking (Kamondi et al. 1998; Harvey et al. 2009; Epsztein et al. 2011; Grienberger et al. 2014; Bittner et al. 2015) and of axonal events (Epsztein et al. 2010; Chorev and Brecht 2012; Apostolides et al. 2016). Importantly, this recording method also allows cells to be labeled and recovered, enabling further classification to be performed post hoc based on precise anatomical localization as well as morphological, immunohistochemical, and/or ISH characterization. Even complete filling of axonal arbors is possible, which can enable tracking of long-range projections over several millimeters (Oberlaender et al. 2012). Besides filling cells based on the injection of a dye, cells can also be labeled by infusing a plasmid that then drives the expression of a fluorescent protein; this method has been used to transfect single intracellularly recorded cells in the visual cortex not only with a fluorescent protein but also with a receptor allowing selective infection by a rabies mutant (injected 2 days later)

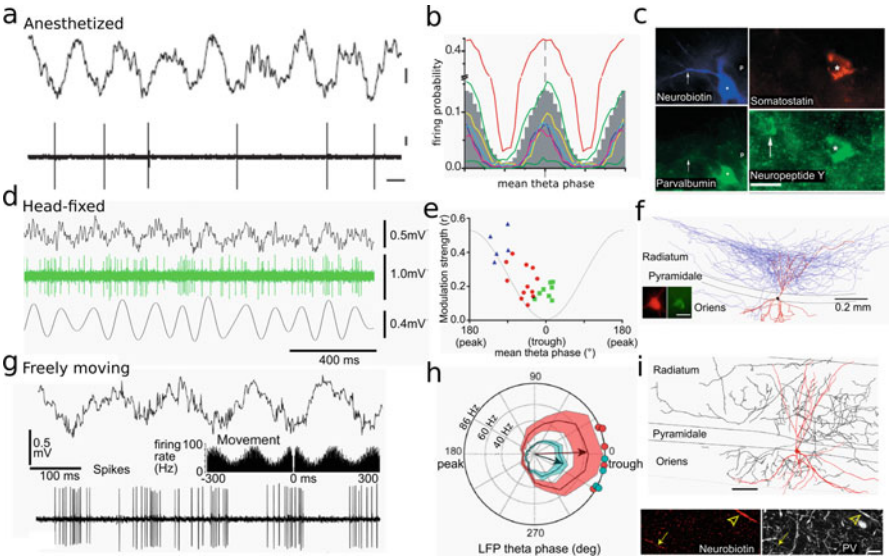

Fig. 6 *Mechanisms underlying SWR generation in CA1.* (**a**) Whole-cell patch-clamp recordings of CA1 pyramidal cells in awake head-fixed mice reveal phasic excitatory currents (bottom trace) coincident with SWRs detected in the LFP recorded with a separate electrode(top trace). (**b**) Intracellular recordings of a CA1 pyramidal cell (left inset) from a freely moving mouse also showed a membrane potential depolarization (bottom trace, V_m) during SWRs (top trace, LFP) followed by a relatively long-lasting after hyperpolarization (AHP). (**c**) These recordings also revealed that during SWRs (green) action potential firing was reduced despite cells being depolarized above threshold. This was not the case during pre-ripple control intervals (gray). (**d**) Intracellular recordings from anesthetized rats revealed that during SWRs, CA1 pyramidal cells could be either predominantly depolarized (green) or hyperpolarized (red). Simultaneously recorded LFPs are shown in black. (**e**) These firing patterns were found in more superficial calbindin-immunopositive (CB+) and deeper-lying calbindin-immunonegative (CB-) cells, respectively. (**f**). Scheme showing hippocampal connectivity related to firing patterns of different cell types during SWRs. (Figures taken and adapted with permission: (**a**) from Maier et al. 2011; (**b–c**) from English et al. 2014; (**d–f**) from Valero et al. 2015)

which retrogradely labels monosynaptically connected presynaptic cells (Rancz et al. 2011).

One caveat is that the washout of cytosol can be an issue for certain markers, e.g., calbindin (Müller et al. 2005), particularly for longer whole-cell patch-clamp recordings (less so for sharp electrodes). It should also be noted that labeling is typically worse for recordings from freely moving animals, particularly for longer axons. The reduced recovery rate is likely due to the fact that cells recorded from freely moving animals are often lost due to mechanical disturbance, rather than being actively terminated via slow withdrawal of the pipette, as typically done in anesthetized animals (Rancz et al. 2011).

In contrast to extracellular recording methods, which rely on unit isolation algorithms that are biased for cells with high firing rates (Pedreira et al. 2012) and

are likely to miss many cells in any particular brain volume (Henze et al. 2000; Shoham et al. 2006; Wolfe et al. 2010), the single-cell recording approach has no bias for cells firing at high rates and can also be used to record silent cells (Margrie et al. 2002; Epsztein et al. 2011). This is not to say this approach cannot have a bias: there may be unknown factors that make some cells more "patchable" than others.

Another advantage of this method is that one can manipulate single cells' membrane potential and spiking activity with high precision. Surprisingly, eliciting action potentials during whole-cell patch-clamp recordings of a single pyramidal cell in vibrissae motor cortex was able to induce whisker movement, both in ketamine-/xylazine-anesthetized and awake rats (Brecht et al. 2004). In the hippocampus, silent cells stimulated can be suddenly, and reversibly, turned into place cells (Lee et al. 2012; Bittner et al. 2015).

There are also a few clear disadvantages that should be considered. First, one can only record a small number of cells per animal. This is due partly to the difficulty in achieving and maintaining a high-quality stable recording and partly to the fact that one must avoid confusing the identity of possibly labeled cells. In theory, this confusion could be avoided by labeling different cells with different colors, but in practice this turns out to be difficult, and labeling still mostly depends on neurobiotin or biocytin. Second, recording times are short. This places limits on, e.g., the extent of space that can be covered by an exploring rodent during a recording. This is important, for example, when recording grid cells, where a grid-like firing pattern only gradually becomes apparent as the animal moves throughout the arena. Third, it is still very difficult to do paired intracellular recordings in vivo, so that it remains difficult to make statements about functional connectivity or synchrony between identified cells. However, it has been achieved in some brain areas, using either sharp electrode (Lampl et al. 1999; Crochet et al. 2005) or patch-clamp recordings (Poulet and Petersen 2008; Jiang et al. 2013; Jouhanneau et al. 2015). Perhaps in the future, automated intracellular recordings will make it feasible to record from larger number of cells in parallel; good automated performance on single cells was recently demonstrated in both in anesthetized (Kodandaramaiah et al. 2012) and awake head-fixed animals (Desai et al. 2015).

Finally, combining intracellular recordings with extracellular (Bruno and Sakmann 2006; Quilichini et al. 2010) or optogenetic approaches (Muñoz et al. 2014; Pala and Petersen 2015) is likely to give many more insights into connectivity in the behaving animal. Antidromic stimulation, applied either optogenetically (Ciocchi et al. 2015) or electrically (e.g., Long et al. 2010), can also be used to obtain information regarding the synaptic targets of a recorded cell.

Juxtacellular Recordings

Juxtacellular recordings, also known by the more precise term of juxtasomatic recordings, are essentially cell-attached recordings, which can be used to record spiking activity with a high signal-to-noise ratio and to inject (charged) dye into

the recorded cell (Pinault 1996). This method shares many of the advantages and disadvantages of whole-cell patch-clamp recordings, with some important differences, the most important one being that one cannot access subthreshold activity with juxtacellular recordings, i.e., this method only provides a physiological readout of a cell's outputs.

However, it is considerably simpler to perform than whole-cell recording. It is also less invasive, so that there is no washout of the cytosol, leading to a perhaps more physiological state of the cell. This method still retains many of the same advantages as described above for whole-cell recordings. There is no clear bias for cells with a higher firing rate, as silent cells can also be recorded and identified (Burgalossi et al. 2011; Herfst et al. 2012; Diamantaki et al. 2016a), although there could be an unknown bias regarding which cells are more easily labeled with this method. In fact, the pipettes used, e.g., for interneuron recordings in the Klausberger and Somogyi labs have a much smaller tip and higher impedance (Klausberger et al. 2003; Lapray et al. 2012), possibly because this configuration is more successful for recording and/or labeling interneurons. However, this has not been shown systematically, and also larger "patch" pipette tips have been used to successfully record and label interneurons both in the presubiculum and medial entorhinal cortex (Tukker et al. 2015), although indeed the proportion of successfully labeled cells may be lower.

In general, the recovery of recorded cells and anatomical characterization is a key advantage of this method. This has proven particularly useful for distinguishing differences among parvalbumin-positive (PV) interneurons in the hippocampus (Klausberger et al. 2003, 2004; Tukker et al. 2007, 2013; Lapray et al. 2012; Varga et al. 2012, 2014; Viney et al. 2013), although many other cell types have also been successfully characterized with this method. With long waiting times after the labeling procedure, even axons over many millimeters can be traced (Jinno et al. 2007; Viney et al. 2013; Arszovszki et al. 2014; Preston-Ferrer et al. 2016).

Finally, manipulation of cell firing is possible with a relatively high degree of control. This has been combined with a behavioral readout in head-fixed animals to show that, surprisingly, manipulation of activity in single cells can modulate behavior (Houweling and Brecht 2008; Doron et al. 2014). A more recent report demonstrated that in the dentate gyrus, juxtacellular stimulation of a silent granule cell in a freely moving rat can induce that "primed" cell to selectively fire again when the rat subsequently revisits the priming location (Diamantaki et al. 2016b).

The Future

Identifying cell types in the future will ideally be done in vivo, based on one or a very small number of easily identifiable "markers." At the moment, we are still in the process of determining which cell types may exist in various parts of the brain, and this endeavor is likely to continue for some time. While methods to describe neurons at any single level (anatomical, molecular, physiological, functional) are

increasingly "scaled up," as will be outlined in this section, the relatively sparse data obtained by single-cell experiments, spanning multiple levels, offers the opportunity to directly study how these levels are related to each other. In the near future we are likely to see the combination of single-cell methods as described in this chapter with more extensive analysis methods at the anatomical and molecular level. In parallel, it is becoming increasingly feasible to combine extensive, high-resolution "structure" descriptions (anatomy and genetics) with quantitative descriptions of behavior and large-scale electrophysiological readouts, e.g., via calcium- or voltage-sensitive dyes (Bock et al. 2011; Begemann and Galic 2016). In all these approaches, one crucial step to dealing with the complexity of such large datasets will be a dimensionality reduction, which is offered by the concept of cell types. Although limited in scale, research so far indicates that indeed there exist tendencies of particular combinations of properties to co-occur, and identifying these cell types will be a major focus for the coming years.

New methods are being developed for more sophisticated, "data-driven" ways to define cell types (Armañanzas and Ascoli 2015), for example, based on fuzzy set theory (Battaglia et al. 2013) or nonparametric Bayesian inference techniques (Jonas and Kording 2015), or to at least improve the consistency of cell identification within the community (DeFelipe et al. 2013). In order to derive potential cell types from the wealth of previously collected data, a number of efforts are under way to collate data from published reports into more formalized database-like structures (Bota et al. 2003; Ascoli et al. 2007; Wheeler et al. 2015), in order to make this data more readily available (and searchable). These initiatives are also likely to help the adoption of a more standardized nomenclature for describing properties of cell types (Ascoli et al. 2008) and cell types themselves (Hamilton et al. 2016). More generally, neuroscientific data is becoming ever more digital and quantitative (Helmstaedter et al. 2013; Budd et al. 2015), enabling data sets to be shared and compared more easily (Ascoli 2015; Teeters et al. 2015). Although such sharing is becoming more common, its usefulness will depend to some extent on the adoption of some standard data formats including more formalized representations of "metadata" (Garcia et al. 2014; Zehl et al. 2016). The adoption of common standards may be helped by large-scale initiatives such as the European Human Brain Project, the American BRAIN initiative, as well as institutions such as the Allen Brain Institute, all of which have cell type classification as one of their primary aims.

Although many experiments are already using, e.g., genetic markers to identify cell types in vivo, at present such experiments still entail considerable compromises. By limiting "identity" to a single promoter (e.g., parvalbumin to delineate fast-spiking interneurons in the cortex), one risks confounding several different cell types with potentially very different functional properties and roles. One solution to this is via "intersectional" approaches, where genetics can be based on several promoters (Fenno et al. 2014; Madisen et al. 2015). However, such approaches still depend on the identification of a very small number of genes that uniquely identify a particular cell type. The development of improved mRNA sequencing methods will certainly

help in the quest for unique markers (Zeisel et al. 2015; Cadwell et al. 2016; Fuzik et al. 2016; Tasic et al. 2016), but they may not necessarily exist for every cell type.

The anatomical analysis of labeled cells is also advancing, particularly through the use of new viral tracing (Nassi et al. 2015) and tissue-processing (Chung and Deisseroth 2013) methods in combination with modern imaging approaches to map out long-range circuits throughout the brain (Ragan et al. 2012; Osten and Margrie 2013; Niedworok et al. 2016). Novel ISH techniques in combination with such imaging approaches are also likely to advance our understanding greatly (Sylwestrak et al. 2016). Expanding ISH and immunohistochemical methods with improved fluorophores with sharp emission spectra (Resch-Genger et al. 2008) would greatly improve the resolution with which cell types can be studied, by increasing the amount of molecules that can be tested for any particular tissue sample. The sequencing of mRNA material from single cells is also likely to improve, together with the quantitative techniques for finding clusters in such datasets; it may soon become routine to extract the complete transcriptome for any single recorded cell and read out the cell type unambiguously.

Another advance related to anatomical analysis is likely to come from the increased availability of EM reconstructions of ever-larger volumes of brain tissue (Plaza et al. 2014; Seung and Sümbül 2014; Swanson and Lichtman 2016). As recently shown in a series of studies focusing on the retina (Helmstaedter et al. 2013; Kim et al. 2014; Sümbül et al. 2014), these methods have the potential to greatly improve the resolution of anatomical data both with regard to morphology and synaptic connectivity. It is in principle already possible to functionally characterize and label a single neuron in vivo (e.g., a grid cell), via methods illustrated in this chapter, and reconstruct a sizeable portion of tissue around this cell in EM. One could theoretically identify all synaptically connected cells in this volume by their reconstructed morphology. This assumes that cell types can indeed be recognized by morphology alone, as in the retina (Helmstaedter et al. 2013). Future work will have to show to what extent this is also the case in the cortex. At the moment, the scale of EM reconstructed volumes in the cortex is still rather limited (Berning et al. 2015; Kasthuri et al. 2015), and the process remains slow and expensive (Marblestone et al. 2014). Dealing with the immense data sets such an endeavor will produce, eventually including, e.g., an entire mouse brain (Mikula and Denk 2015) will also pose new challenges, which may in part be solved by machine learning approaches (Lichtman et al. 2014; Helmstaedter 2015).

Readouts of neuronal activity are also rapidly developing. On the one hand, extracellular recordings from freely moving animals can be made with ever-increasing numbers of channels at ever-higher densities, making it possible to sample large populations of neurons from one or several brain areas (Buzsáki et al. 2015) during a wide range of behaviors. Similarly, miniaturization and improvement of calcium- and voltage-sensitive imaging approaches are also enabling optical recordings from deep-lying brain structures in freely moving animals at increasing temporal and spatial resolution and scale (Ziv and Ghosh 2015; Kim et al. 2016; Lin and Schnitzer 2016). For both optical and electrophysiological methods, novel wireless technology and more advanced ways of stimulating cells are also likely to

increase possibilities to manipulate and record neurons from freely moving animals engaging in natural behaviors such as social interaction (Hasegawa et al. 2015; Kale et al. 2015; Park et al. 2015).

Combining these population-scale methods with opto- or chemogenetics, based on novel viral and genetic methods, will allow future investigators to record from and manipulate large numbers of anatomically and/or genetically defined populations (Grosenick et al. 2015). The caveat here is again that the "cell-type resolution" of such methods is likely to remain limited, as long as our understanding of cell types in the brain remains incomplete. Thus, it is important that the development of single-cell patch-clamp and juxtacellular recordings from behaving animals is also continuing.

Although relatively few laboratories are using these methods in freely moving animals, recent advances have made this method ever more feasible (Lee et al. 2014a; Tang et al. 2014a; Wang et al. 2016). Clearly, for many complex behaviors where one does not know all variables driving neural activity, it is preferable to record from animals engaging in behaviors as close to "natural" as possible. However, for understanding many "simpler" tasks, VR is an increasingly popular option which makes both imaging and single-cell recordings much simpler in awake animals. To what extent navigation can be studied effectively in VR is still a debated issue (Minderer et al. 2016), but since practical considerations also constrain most spatial navigation studies in humans to VR paradigms, the use of VR in rodents may actually be beneficial for allowing a cross-species comparison of neural circuits underlying spatial navigation. Such translatability may be particularly important for studies on animal models of diseases such as Alzheimer's disease, where difficulties in navigation are very common (Lithfous et al. 2013). The fact that VR enables strong experimental control over both the animal's behavior and the stimuli it is exposed to may help to unravel the roles of vestibular, auditory, visual, somatosensory, motor, and higher-order (path-integration) systems in navigation and other tasks (Chen et al. 2013; Cushman et al. 2013; Ravassard et al. 2013; Aronov and Tank 2014; Acharya et al. 2016; Kautzky and Thurley 2016). The question of how the hippocampal system generates an abstract higher-level representation of space based on such inputs is very much unsolved, but the combination of VR with modern viral, genetic, and large-scale recording and imaging tools in head-fixed animals gives us a good chance of addressing this question at the necessary level of detail.

Finally, the complexity of behavior itself may remain the biggest challenge. In Drosophila, a pioneering paper has recently correlated automatically detected behavioral modules ("behaviotypes") with neuronal function from over a thousand neuron lines (Vogelstein et al. 2014). The first steps have also been made toward automated, non-biased analyses of behavior in mice (Wiltschko et al. 2015). Clearly, there is huge potential in this field to look at more complex relationships between stimuli and behavior, and at how such relationships may change over time through plastic processes in the brain. It will be interesting to see how, in the future, the combination of advanced behavioral analysis with other approaches described above will shed new light on the fundamental functioning of neural circuits, both in health and disease.

Acknowledgments The author wishes to thank Andrea Burgalossi, Constance Holman, Nikolaus Maier, and Peter Somogyi for helpful comments on earlier versions of this chapter and Linda Hahn-Tukker for help with the figures.

References

Acharya L, Aghajan ZM, Vuong C, Moore JJ, Mehta MR (2016) Causal influence of visual cues on hippocampal directional selectivity. Cell 164:197–207

Aghajan ZM, Acharya L, Moore JJ, Cushman JD, Vuong C, Mehta MR (2015) Impaired spatial selectivity and intact phase precession in two-dimensional virtual reality. Nat Neurosci 18:121–128

Apostolides PF, Milstein AD, Grienberger C, Bittner KC, Magee JC (2016) Axonal filtering allows reliable output during dendritic plateau-driven complex spiking in CA1 neurons. Neuron 89:770–783

Armañanzas R, Ascoli GA (2015) Towards the automatic classification of neurons. Trends Neurosci 38:307–318

Aronov D, Tank DW (2014) Engagement of neural circuits underlying 2D spatial navigation in a rodent virtual reality system. Neuron 84:442–456

Arszovszki A, Borhegyi Z, Klausberger T (2014) Three axonal projection routes of individual pyramidal cells in the ventral CA1 hippocampus. Front Neuroanat 8:53

Ascoli GA et al (2008) Petilla terminology: nomenclature of features of GABAergic interneurons of the cerebral cortex. Nat Rev Neurosci 9:557–568

Ascoli GA (2015) Sharing neuron data: carrots, sticks, and digital records. PLoS Biol 13:e1002275

Ascoli GA, Donohue DE, Halavi M (2007) NeuroMorpho.Org: a central resource for neuronal morphologies. J Neurosci 27:9247–9251

Battaglia D, Karagiannis A, Gallopin T, Gutch HW, Cauli B (2013) Beyond the frontiers of neuronal types. Front Neural Circuits 7:13

Begemann I, Galic M (2016) Correlative light electron microscopy: connecting synaptic structure and function. Front Synap Neurosci 28

Berning M, Boergens KM, Helmstaedter M (2015) SegEM: efficient image analysis for high-resolution connectomics. Neuron 87:1193–1206

Bezaire MJ, Soltesz I (2013) Quantitative assessment of CA1 local circuits: knowledge base for interneuron-pyramidal cell connectivity. Hippocampus 23:751–785

Bittner KC, Grienberger C, Vaidya SP, Milstein AD, Macklin JJ, Suh J, Tonegawa S, Magee JC (2015) Conjunctive input processing drives feature selectivity in hippocampal CA1 neurons. Nat Neurosci 18:1133–1142

Boccara CN, Kjonigsen LJ, Hammer IM, Bjaalie JG, Leergaard TB, Witter MP (2015) A three-plane architectonic atlas of the rat hippocampal region. Hippocampus 25:838–857

Bock DD, Lee W-CA, Kerlin AM, Andermann ML, Hood G, Wetzel AW, Yurgenson S, Soucy ER, Kim HS, Reid RC (2011) Network anatomy and in vivo physiology of visual cortical neurons. Nature 471:177–182

Böhm C, Peng Y, Maier N, Winterer J, Poulet JFA, Geiger JRP, Schmitz D (2015) Functional diversity of subicular principal cells during hippocampal ripples. J Neurosci 35:13608–13618

Bonnevie T, Dunn B, Fyhn M, Hafting T, Derdikman D, Kubie JL, Roudi Y, Moser EI, Moser M-B (2013) Grid cells require excitatory drive from the hippocampus. Nat Neurosci 16:309–317

Bota M, Dong H-W, Swanson LW (2003) From gene networks to brain networks. Nat Neurosci 6:795–799

Bota M, Swanson LW (2007) The neuron classification problem. Brain Res Rev 56:79–88

Brandon MP, Bogaard AR, Libby CP, Connerney MA, Gupta K, Hasselmo ME (2011) Reduction of theta rhythm dissociates grid cell spatial periodicity from directional tuning. Science 332:595–599

Brecht M, Schneider M, Sakmann B, Margrie TW (2004) Whisker movements evoked by stimulation of single pyramidal cells in rat motor cortex. Nature 427:704–710
Briggman KL, Helmstaedter M, Denk W (2011) Wiring specificity in the direction-selectivity circuit of the retina. Nature 471:183–188
Bruno RM, Sakmann B (2006) Cortex is driven by weak but synchronously active thalamocortical synapses. Science 312:1622–1627
Budd JML, Cuntz H, Eglen SJ, Krieger P (2015) Editorial: quantitative analysis of neuroanatomy. Front Neuroanat 9:143
Buetfering C, Allen K, Monyer H (2014) Parvalbumin interneurons provide grid cell-driven recurrent inhibition in the medial entorhinal cortex. Nat Neurosci 17:710–718
Buhl EH, Halasy K, Somogyi P (1994) Diverse sources of hippocampal unitary inhibitory postsynaptic potentials and the number of synaptic release sites. Nature 368:823–828
Burgalossi A, Herfst L, von Heimendahl M, Förste H, Haskic K, Schmidt M, Brecht M (2011) Microcircuits of functionally identified neurons in the rat medial entorhinal cortex. Neuron 70:773–786
Buzsaki G (2006) Rhythms of the brain, 1st edn. Oxford University Press, New York
Buzsáki G (2015) Hippocampal sharp wave-ripple: a cognitive biomarker for episodic memory and planning. Hippocampus 25:1073–1188
Buzsáki G, Leung LW, Vanderwolf CH (1983) Cellular bases of hippocampal EEG in the behaving rat. Brain Res 287:139–171
Buzsáki G, Czopf J, Kondákor I, Kellényi L (1986) Laminar distribution of hippocampal rhythmic slow activity (RSA) in the behaving rat: current-source density analysis, effects of urethane and atropine. Brain Res 365:125–137
Buzsáki G, Stark E, Berényi A, Khodagholy D, Kipke DR, Yoon E, Wise KD (2015) Tools for probing local circuits: high-density silicon probes combined with optogenetics. Neuron 86:92–105
Cacucci F, Lever C, Wills TJ, Burgess N, O'Keefe J (2004) Theta-modulated place-by-direction cells in the hippocampal formation in the rat. J Neurosci 24:8265–8277
Cadwell CR, Palasantza A, Jiang X, Berens P, Deng Q, Yilmaz M, Reimer J, Shen S, Bethge M, Tolias KF, Sandberg R, Tolias AS (2016) Electrophysiological, transcriptomic and morphologic profiling of single neurons using Patch-seq. Nat Biotechnol 34:199–203
Canto CB, Wouterlood FG, Witter MP (2008) What does the anatomical organization of the entorhinal cortex tell us? Neural Plast 2008:381243
Carr MF, Karlsson MP, Frank LM (2012) Transient slow gamma synchrony underlies hippocampal memory replay. Neuron 75:700–713
Chen G, King JA, Burgess N, O'Keefe J (2013) How vision and movement combine in the hippocampal place code. Proc Natl Acad Sci U S A 110:378–383
Chorev E, Brecht M (2012) In vivo dual intra- and extracellular recordings suggest bidirectional coupling between CA1 pyramidal neurons. J Neurophysiol 108:1584–1593
Chung K, Deisseroth K (2013) CLARITY for mapping the nervous system. Nat Methods 10:508–513
Ciocchi S, Passecker J, Malagon-Vina H, Mikus N, Klausberger T (2015) Brain computation. Selective information routing by ventral hippocampal CA1 projection neurons. Science 348:560–563
Clement EA, Richard A, Thwaites M, Ailon J, Peters S, Dickson CT (2008) Cyclic and sleep-like spontaneous alternations of brain state under urethane anaesthesia. PLoS ONE 3:e2004
Cobb SR, Halasy K, Vida I, Nyiri G, Tamas G, Buhl EH, Somogyi P (1997) Synaptic effects of identified interneurons innervating both interneurons and pyramidal cells in the rat hippocampus. Neuroscience 79:629–648
Colgin LL (2015) Do slow and fast gamma rhythms correspond to distinct functional states in the hippocampal network? Brain Res 1621:309–315
Couey JJ, Witoelar A, Zhang S-J, Zheng K, Ye J, Dunn B, Czajkowski R, Moser M-B, Moser EI, Roudi Y, Witter MP (2013) Recurrent inhibitory circuitry as a mechanism for grid formation. Nat Neurosci 16:318–324

Crochet S, Chauvette S, Boucetta S, Timofeev I (2005) Modulation of synaptic transmission in neocortex by network activities. Eur J Neurosci 21:1030–1044

Csicsvari J, Jamieson B, Wise KD, Buzsáki G (2003) Mechanisms of gamma oscillations in the hippocampus of the behaving rat. Neuron 37:311–322

Cushman JD, Aharoni DB, Willers B, Ravassard P, Kees A, Vuong C, Popeney B, Arisaka K, Mehta MR (2013) Multisensory control of multimodal behavior: do the legs know what the tongue is doing? PLoS ONE 8:e80465

Danielson NB, Zaremba JD, Kaifosh P, Bowler J, Ladow M, Losonczy A (2016) Sublayer-specific coding dynamics during spatial navigation and learning in hippocampal area CA1. Neuron 91:652–665

DeFelipe J et al (2013) New insights into the classification and nomenclature of cortical GABAergic interneurons. Nat Rev Neurosci 14:202–216

Desai NS, Siegel JJ, Taylor W, Chitwood RA, Johnston D (2015) MATLAB-based automated patch-clamp system for awake behaving mice. J Neurophysiol 114:1331–1345

Diamantaki M, Frey M, Berens P, Preston-Ferrer P, Burgalossi A (2016a) Sparse activity of identified dentate granule cells during spatial exploration. Elife 5

Diamantaki M, Frey M, Preston-Ferrer P, Burgalossi A (2016b) Priming spatial activity by single-cell stimulation in the dentate gyrus of freely moving rats. Curr Biol 26:536–541

Dickson CT, Trepel C, Bland BH (1994) Extrinsic modulation of theta field activity in the entorhinal cortex of the anesthetized rat. Hippocampus 4:37–51

Dombeck DA, Khabbaz AN, Collman F, Adelman TL, Tank DW (2007) Imaging large-scale neural activity with cellular resolution in awake, mobile mice. Neuron 56:43–57

Dombeck DA, Harvey CD, Tian L, Looger LL, Tank DW (2010) Functional imaging of hippocampal place cells at cellular resolution during virtual navigation. Nat Neurosci 13:1433–1440

Domnisoru C, Kinkhabwala AA, Tank DW (2013) Membrane potential dynamics of grid cells. Nature 495:199–204

Doron G, von Heimendahl M, Schlattmann P, Houweling AR, Brecht M (2014) Spiking irregularity and frequency modulate the behavioral report of single-neuron stimulation. Neuron 81:653–663

Ego-Stengel V, Wilson MA (2007) Spatial selectivity and theta phase precession in CA1 interneurons. Hippocampus 17:161–174

English DF, Peyrache A, Stark E, Roux L, Vallentin D, Long MA, Buzsáki G (2014) Excitation and inhibition compete to control spiking during hippocampal ripples: intracellular study in behaving mice. J Neurosci 34:16509–16517

Epsztein J, Lee AK, Chorev E, Brecht M (2010) Impact of spikelets on hippocampal CA1 pyramidal cell activity during spatial exploration. Science 327:474–477

Epsztein J, Brecht M, Lee AK (2011) Intracellular determinants of hippocampal CA1 place and silent cell activity in a novel environment. Neuron 70:109–120

Fee MS (2000) Active stabilization of electrodes for intracellular recording in awake behaving animals. Neuron 27:461–468

Fenno LE et al (2014) Targeting cells with single vectors using multiple-feature boolean logic. Nat Methods 11:763–772

Fenton AA, Kao H-Y, Neymotin SA, Olypher A, Vayntrub Y, Lytton WW, Ludvig N (2008) Unmasking the CA1 ensemble place code by exposures to small and large environments: more place cells and multiple, irregularly arranged, and expanded place fields in the larger space. J Neurosci 28:11250–11262

Ferezou I, Bolea S, Petersen CCH (2006) Visualizing the cortical representation of whisker touch: voltage-sensitive dye imaging in freely moving mice. Neuron 50:617–629

Ferrante M, Tahvildari B, Duque A, Hadzipasic M, Salkoff D, Zagha EW, Hasselmo ME, McCormick DA (2017) Distinct functional groups emerge from the intrinsic properties of molecularly identified Entorhinal interneurons and principal cells. Cereb Cortex 27:3186–3207

Flusberg BA, Nimmerjahn A, Cocker ED, Mukamel EA, Barretto RPJ, Ko TH, Burns LD, Jung JC, Schnitzer MJ (2008) High-speed, miniaturized fluorescence microscopy in freely moving mice. Nat Methods 5:935–938

Fox SE, Ranck JB (1975) Localization and anatomical identification of theta and complex spike cells in dorsal hippocampal formation of rats. Exp Neurol 49:299–313

Fuchs EC, Neitz A, Pinna R, Melzer S, Caputi A, Monyer H (2016) Local and distant input controlling excitation in layer ii of the medial entorhinal cortex. Neuron 89:194–208

Fuentealba P, Begum R, Capogna M, Jinno S, Márton LF, Csicsvari J, Thomson A, Somogyi P, Klausberger T (2008) Ivy cells: a population of nitric-oxide-producing, slow-spiking GABAergic neurons and their involvement in hippocampal network activity. Neuron 57:917–929

Fuhrmann F, Justus D, Sosulina L, Kaneko H, Beutel T, Friedrichs D, Schoch S, Schwarz MK, Fuhrmann M, Remy S (2015) Locomotion, Theta oscillations, and the speed-correlated firing of hippocampal neurons are controlled by a medial septal Glutamatergic circuit. Neuron

Fuzik J, Zeisel A, Máté Z, Calvigioni D, Yanagawa Y, Szabó G, Linnarsson S, Harkany T (2016) Integration of electrophysiological recordings with single-cell RNA-seq data identifies neuronal subtypes. Nat Biotechnol 34:175–183

Gao P, Ploog BO, Zeigler HP (2003) Whisking as a "voluntary" response: operant control of whisking parameters and effects of whisker denervation. Somatosens Mot Res 20:179–189

Garcia S, Guarino D, Jaillet F, Jennings T, Pröpper R, Rautenberg PL, Rodgers CC, Sobolev A, Wachtler T, Yger P, Davison AP (2014) Neo: an object model for handling electrophysiology data in multiple formats. Front Neuroinform 8:10

Giocomo LM, Stensola T, Bonnevie T, Van Cauter T, Moser M-B, Moser EI (2014) Topography of head direction cells in medial entorhinal cortex. Curr Biol 24:252–262

Graves AR, Moore SJ, Bloss EB, Mensh BD, Kath WL, Spruston N (2012) Hippocampal pyramidal neurons comprise two distinct cell types that are countermodulated by metabotropic receptors. Neuron 76:776–789

Greenberg DS, Houweling AR, Kerr JN (2008) Population imaging of ongoing neuronal activity in the visual cortex of awake rats. Nat Neurosci 11:749–751

Grienberger C, Chen X, Konnerth A (2014) NMDA receptor-dependent multidendrite Ca(2+) spikes required for hippocampal burst firing in vivo. Neuron 81:1274–1281

Grosenick L, Marshel JH, Deisseroth K (2015) Closed-loop and activity-guided optogenetic control. Neuron 86:106–139

Guo ZV, Hires SA, Li N, O'Connor DH, Komiyama T, Ophir E, Huber D, Bonardi C, Morandell K, Gutnisky D, Peron S, Xu N, Cox J, Svoboda K (2014) Procedures for behavioral experiments in head-fixed mice. PLoS ONE 9:e88678

Guzowski JF, Timlin JA, Roysam B, McNaughton BL, Worley PF, Barnes CA (2005) Mapping behaviorally relevant neural circuits with immediate-early gene expression. Curr Opin Neurobiol 15:599–606

Hafting T, Fyhn M, Molden S, Moser M-B, Moser EI (2005) Microstructure of a spatial map in the entorhinal cortex. Nature 436:801–806

Hamilton DJ, Wheeler DW, White CM, Rees CL, Komendantov AO, Bergamino M, Ascoli GA (2016) Name-calling in the hippocampus (and beyond): coming to terms with neuron types and properties. Brain Inform

Hara K, Harris RA (2002) The anesthetic mechanism of urethane: the effects on neurotransmitter-gated ion channels. Anesth Analg 94:313–318

Hardcastle K, Maheswaranathan N, Ganguli S, Giocomo LM (2017) A multiplexed, heterogeneous, and adaptive code for navigation in medial entorhinal cortex. Neuron 94:375–387.e7

Hartley T, Lever C, Burgess N, O'Keefe J (2014) Space in the brain: how the hippocampal formation supports spatial cognition. Philos Trans R Soc Lond B Biol Sci 369:20120510

Harvey CD, Collman F, Dombeck DA, Tank DW (2009) Intracellular dynamics of hippocampal place cells during virtual navigation. Nature 461:941–946

Harvey CD, Coen P, Tank DW (2012) Choice-specific sequences in parietal cortex during a virtual-navigation decision task. Nature 484:62–68

Hasegawa T, Fujimoto H, Tashiro K, Nonomura M, Tsuchiya A, Watanabe D (2015) A wireless neural recording system with a precision motorized microdrive for freely behaving animals. Sci Rep 5:7853

Helmchen F, Fee MS, Tank DW, Denk W (2001) A miniature head-mounted two-photon microscope. High-resolution brain imaging in freely moving animals. Neuron 31:903–912
Helmchen F, Denk W, Kerr JND (2013) Miniaturization of two-photon microscopy for imaging in freely moving animals. Cold Spring Harb Protoc 2013:904–913
Helmstaedter M (2015) The mutual inspirations of machine learning and neuroscience. Neuron 86:25–28
Helmstaedter M, Briggman KL, Turaga SC, Jain V, Seung HS, Denk W (2013) Connectomic reconstruction of the inner plexiform layer in the mouse retina. Nature 500:168–174
Hemmings HC, Yan W, Westphalen RI, Ryan TA (2005) The general anesthetic isoflurane depresses synaptic vesicle exocytosis. Mol Pharmacol 67:1591–1599
Henze DA, Borhegyi Z, Csicsvari J, Mamiya A, Harris KD, Buzsáki G (2000) Intracellular features predicted by extracellular recordings in the hippocampus in vivo. J Neurophysiol 84:390–400
Herfst L, Burgalossi A, Haskic K, Tukker JJ, Schmidt M, Brecht M (2012) Friction-based stabilization of juxtacellular recordings in freely moving rats. J Neurophysiol 108:697–707
Heys JG, Rangarajan KV, Dombeck DA (2014) The functional micro-organization of grid cells revealed by cellular-resolution imaging. Neuron 84:1079–1090
Hölscher C, Schnee A, Dahmen H, Setia L, Mallot HA (2005) Rats are able to navigate in virtual environments. J Exp Biol 208:561–569
Houweling AR, Brecht M (2008) Behavioural report of single neuron stimulation in somatosensory cortex. Nature 451:65–68
Hulse BK, Moreaux LC, Lubenov EV, Siapas AG (2016) Membrane potential dynamics of CA1 pyramidal neurons during hippocampal ripples in awake mice. Neuron 89:800–813
Ishihara Y, Fukuda T (2016) Immunohistochemical investigation of the internal structure of the mouse subiculum. Neuroscience 337:242–266
Jacob P-Y, Poucet B, Liberge M, Save E, Sargolini F (2014) Vestibular control of entorhinal cortex activity in spatial navigation. Front Integr Neurosci 8:38
Jiang X, Wang G, Lee AJ, Stornetta RL, Zhu JJ (2013) The organization of two new cortical interneuronal circuits. Nat Neurosci 16:210–218
Jiang X, Shen S, Cadwell CR, Berens P, Sinz F, Ecker AS, Patel S, Tolias AS (2015) Principles of connectivity among morphologically defined cell types in adult neocortex. Science 350:aac9462
Jinno S, Klausberger T, Marton LF, Dalezios Y, Roberts JDB, Fuentealba P, Bushong EA, Henze D, Buzsáki G, Somogyi P (2007) Neuronal diversity in GABAergic long-range projections from the hippocampus. J Neurosci 27:8790–8804
Jonas E, Kording K (2015) Automatic discovery of cell types and microcircuitry from neural connectomics. Elife 4:e04250
Jouhanneau J-S, Kremkow J, Dorrn AL, Poulet JFA (2015) In vivo monosynaptic excitatory transmission between layer 2 cortical pyramidal neurons. Cell Rep 13:2098–2106
Jung MW, McNaughton BL (1993) Spatial selectivity of unit activity in the hippocampal granular layer. Hippocampus 3:165–182
Kale RP, Kouzani AZ, Walder K, Berk M, Tye SJ (2015) Evolution of optogenetic microdevices. Neurophotonics 2:31206
Kamondi A, Acsády L, Buzsáki G (1998) Dendritic spikes are enhanced by cooperative network activity in the intact hippocampus. J Neurosci 18:3919–3928
Kasthuri N et al (2015) Saturated reconstruction of a volume of neocortex. Cell 162:648–661
Katona L, Lapray D, Viney TJ, Oulhaj A, Borhegyi Z, Micklem BR, Klausberger T, Somogyi P (2014) Sleep and movement differentiates actions of two types of somatostatin-expressing GABAergic interneuron in rat hippocampus. Neuron 82:872–886
Kautzky M, Thurley K (2016) Estimation of self-motion duration and distance in rodents. R Soc Open Sci 3:160118
Kepecs A, Fishell G (2014) Interneuron cell types are fit to function. Nature 505:318–326
Kerlin AM, Andermann ML, Berezovskii VK, Reid RC (2010) Broadly tuned response properties of diverse inhibitory neuron subtypes in mouse visual cortex. Neuron 67:858–871

Kim EJ, Jacobs MW, Ito-Cole T, Callaway EM (2016) Improved monosynaptic neural circuit tracing using engineered rabies virus glycoproteins. Cell Rep 15(4):692–699

Kim JS, Greene MJ, Zlateski A, Lee K, Richardson M, Turaga SC, Purcaro M, Balkam M, Robinson A, Behabadi BF, Campos M, Denk W, Seung HS, EyeWirers (2014) Space-time wiring specificity supports direction selectivity in the retina. Nature 509:331–336

Kislin M, Mugantseva E, Molotkov D, Kulesskaya N, Khirug S, Kirilkin I, Pryazhnikov E, Kolikova J, Toptunov D, Yuryev M, Giniatullin R, Voikar V, Rivera C, Rauvala H, Khiroug L (2014) Flat-floored air-lifted platform: a new method for combining behavior with microscopy or electrophysiology on awake freely moving rodents. J Vis Exp:e51869

Kitai ST, Kocsis JD, Preston RJ, Sugimori M (1976) Monosynaptic inputs to caudate neurons identified by intracellular injection of horseradish peroxidase. Brain Res 109:601–606

Kitamura K, Judkewitz B, Kano M, Denk W, Häusser M (2008) Targeted patch-clamp recordings and single-cell electroporation of unlabeled neurons in vivo. Nat Methods 5:61–67

Kitamura T, Pignatelli M, Suh J, Kohara K, Yoshiki A, Abe K, Tonegawa S (2014) Island cells control temporal association memory. Science 343:896–901

Klausberger T, Somogyi P (2008) Neuronal diversity and temporal dynamics: the unity of hippocampal circuit operations. Science 321:53–57

Klausberger T, Magill PJ, Marton LF, Roberts JD, Cobden PM, Buzsáki G, Somogyi P (2003) Brain-state- and cell-type-specific firing of hippocampal interneurons in vivo. Nature 421:844–848

Klausberger T, Marton LF, Baude A, Roberts JD, Magill PJ, Somogyi P (2004) Spike timing of dendrite-targeting bistratified cells during hippocampal network oscillations in vivo. Nat Neurosci 7:41–47

Klausberger T, Marton LF, O'Neill J, Huck JHJ, Dalezios Y, Fuentealba P, Suen WY, Papp E, Kaneko T, Watanabe M, Csicsvari J, Somogyi P (2005) Complementary roles of cholecystokinin- and parvalbumin-expressing GABAergic neurons in hippocampal network oscillations. J Neurosci 25:9782–9793

Kodandaramaiah SB, Franzesi GT, Chow BY, Boyden ES, Forest CR (2012) Automated whole-cell patch-clamp electrophysiology of neurons in vivo. Nat Methods 9:585–587

Kohtala S, Theilmann W, Suomi T, Wigren H-K, Porkka-Heiskanen T, Elo LL, Rokka A, Rantamäki T (2016) Brief Isoflurane anesthesia produces prominent Phosphoproteomic changes in the adult mouse Hippocampus. ACS Chem Neurosci

Kropff E, Carmichael JE, Moser M-B, Moser EI (2015) Speed cells in the medial entorhinal cortex. Nature 523:419–424

Krupic J, Burgess N, O'Keefe J (2012) Neural representations of location composed of spatially periodic bands. Science 337:853–857

Kubie JL, Muller RU, Bostock E (1990) Spatial firing properties of hippocampal theta cells. J Neurosci 10:1110–1123

Lambolez B, Audinat E, Bochet P, Crépel F, Rossier J (1992) AMPA receptor subunits expressed by single purkinje cells. Neuron 9:247–258

Lampl I, Reichova I, Ferster D (1999) Synchronous membrane potential fluctuations in neurons of the cat visual cortex. Neuron 22:361–374

Langer D, Helmchen F (2012) Post hoc immunostaining of GABAergic neuronal subtypes following in vivo two-photon calcium imaging in mouse neocortex. Pflugers Arch 463:339–354

Lapray D, Lasztoczi B, Lagler M, Viney TJ, Katona L, Valenti O, Hartwich K, Borhegyi Z, Somogyi P, Klausberger T (2012) Behavior-dependent specialization of identified hippocampal interneurons. Nat Neurosci 15:1265–1271

Lasztóczi B, Klausberger T (2014) Layer-specific GABAergic control of distinct gamma oscillations in the CA1 hippocampus. Neuron 81:1126–1139

Lasztóczi B, Klausberger T (2016) Hippocampal place cells couple to three different gamma oscillations during place field traversal. Neuron 91:34–40

Lasztóczi B, Tukker JJ, Somogyi P, Klausberger T (2011) Terminal field and firing selectivity of cholecystokinin-expressing interneurons in the hippocampal CA3 area. J Neurosci 31:18073–18,093

Lee I, Rao G, Knierim JJ (2004) A double dissociation between hippocampal subfields: differential time course of CA3 and CA1 place cells for processing changed environments. Neuron 42:803–815

Lee AK, Manns ID, Sakmann B, Brecht M (2006) Whole-cell recordings in freely moving rats. Neuron 51:399–407

Lee AK, Epsztein J, Brecht M (2009) Head-anchored whole-cell recordings in freely moving rats. Nat Protoc 4:385–392

Lee D, Lin B-J, Lee AK (2012) Hippocampal place fields emerge upon single-cell manipulation of excitability during behavior. Science 337:849–853

Lee D, Shtengel G, Osborne JE, Lee AK (2014a) Anesthetized- and awake-patched whole-cell recordings in freely moving rats using UV-cured collar-based electrode stabilization. Nat Protoc 9:2784–2795

Lee S-H, Marchionni I, Bezaire M, Varga C, Danielson N, Lovett-Barron M, Losonczy A, Soltesz I (2014b) Parvalbumin-positive basket cells differentiate among hippocampal pyramidal cells. Neuron 82:1129–1144

Leitner FC, Melzer S, Lütcke H, Pinna R, Seeburg PH, Helmchen F, Monyer H (2016) Spatially segregated feedforward and feedback neurons support differential odor processing in the lateral entorhinal cortex. Nat Neurosci 19:935–944

Lever C, Burton S, O'Keefe J (2006) Rearing on hind legs, environmental novelty, and the hippocampal formation. Rev Neurosci 17:111–133

Lichtman JW, Pfister H, Shavit N (2014) The big data challenges of connectomics. Nat Neurosci 17:1448–1454

Lima SQ, Hromádka T, Znamenskiy P, Zador AM (2009) PINP: a new method of tagging neuronal populations for identification during in vivo electrophysiological recording. PLoS ONE 4:e6099

Lin MZ, Schnitzer MJ (2016) Genetically encoded indicators of neuronal activity. Nat Neurosci 19:1142–1153

Lithfous S, Dufour A, Després O (2013) Spatial navigation in normal aging and the prodromal stage of Alzheimer's disease: insights from imaging and behavioral studies. Ageing Res Rev 12:201–213

Long MA, Lee AK (2012) Intracellular recording in behaving animals. Curr Opin Neurobiol 22:34–44

Long MA, Jin DZ, Fee MS (2010) Support for a synaptic chain model of neuronal sequence generation. Nature 468:394–399

Looger LL, Griesbeck O (2012) Genetically encoded neural activity indicators. Curr Opin Neurobiol 22:18–23

Lovett-Barron M, Turi GF, Kaifosh P, Lee PH, Bolze F, Sun X-H, Nicoud J-F, Zemelman BV, Sternson SM, Losonczy A (2012) Regulation of neuronal input transformations by tunable dendritic inhibition. Nat Neurosci 15(423–430):S1–S3

Lovett-Barron M, Kaifosh P, Kheirbek MA, Danielson N, Zaremba JD, Reardon TR, Turi GF, Hen R, Zemelman BV, Losonczy A (2014) Dendritic inhibition in the hippocampus supports fear learning. Science 343:857–863

Lustig B, Wang Y, Pastalkova E (2016) Oscillatory patterns in hippocampus under light and deep isoflurane anesthesia closely mirror prominent brain states in awake animals. Hippocampus 26:102–109

Madisen L et al (2015) Transgenic mice for intersectional targeting of neural sensors and effectors with high specificity and performance. Neuron 85:942–958

Maier N, Tejero-Cantero A, Dorrn AL, Winterer J, Beed PS, Morris G, Kempter R, Poulet JFA, Leibold C, Schmitz D (2011) Coherent phasic excitation during hippocampal ripples. Neuron 72:137–152

Marblestone AH, Daugharthy ER, Kalhor R, Peikon ID, Kebschull JM, Shipman SL, Mishchenko Y, Lee JH, Dalrymple DA, Zamft BM, Kording KP, Boyden ES, Zador AM, Church GM (2014) Conneconomics: the economics of dense, large-scale, high-resolution neural Connectomics. bioRxiv:1214

Margrie TW, Brecht M, Sakmann B (2002) In vivo, low-resistance, whole-cell recordings from neurons in the anaesthetized and awake mammalian brain. Pflugers Arch 444:491–498

Margrie TW, Meyer AH, Caputi A, Monyer H, Hasan MT, Schaefer AT, Denk W, Brecht M (2003) Targeted whole-cell recordings in the mammalian brain in vivo. Neuron 39:911–918

Martina M, Schultz JH, Ehmke H, Monyer H, Jonas P (1998) Functional and molecular differences between voltage-gated K+ channels of fast-spiking interneurons and pyramidal neurons of rat hippocampus. J Neurosci 18:8111–8125

Maurer AP, Cowen SL, Burke SN, Barnes CA, McNaughton BL (2006) Phase precession in hippocampal interneurons showing strong functional coupling to individual pyramidal cells. J Neurosci 26:13485–13492

Melzer S, Michael M, Caputi A, Eliava M, Fuchs EC, Whittington MA, Monyer H (2012) Long-range-projecting GABAergic neurons modulate inhibition in hippocampus and entorhinal cortex. Science 335:1506–1510

Mikula S, Denk W (2015) High-resolution whole-brain staining for electron microscopic circuit reconstruction. Nat Methods 12:541–546

Minderer M, Harvey CD, Donato F, Moser EI (2016) Neuroscience: virtual reality explored. Nature 533:324–325

Mizrahi A, Crowley JC, Shtoyerman E, Katz LC (2004) High-resolution in vivo imaging of hippocampal dendrites and spines. J Neurosci 24:3147–3151

Mizuseki K, Diba K, Pastalkova E, Buzsáki G (2011) Hippocampal CA1 pyramidal cells form functionally distinct sublayers. Nat Neurosci Available at: http://www.ncbi.nlm.nih.gov/pubmed/21822270. Accessed 23 Aug 2011

Mizuseki K, Royer S, Diba K, Buzsáki G (2012) Activity dynamics and behavioral correlates of CA3 and CA1 hippocampal pyramidal neurons. Hippocampus 22:1659–1680

Monaco JD, Rao G, Roth ED, Knierim JJ (2014) Attentive scanning behavior drives one-trial potentiation of hippocampal place fields. Nat Neurosci 17:725–731

Moore JD, Deschênes M, Kurnikova A, Kleinfeld D (2014) Activation and measurement of free whisking in the lightly anesthetized rodent. Nat Protoc 9:1792–1802

Moroni F, Corradetti R, Casamenti F, Moneti G, Pepeu G (1981) The release of endogenous GABA and glutamate from the cerebral cortex in the rat. Naunyn Schmiedebergs Arch Pharmacol 316:235–239

Müller C, Remy S (2014) Dendritic inhibition mediated by O-LM and bistratified interneurons in the hippocampus. Front Synaptic Neurosci 6:23

Müller A, Kukley M, Stausberg P, Beck H, Müller W, Dietrich D (2005) Endogenous Ca2+ buffer concentration and Ca2+ microdomains in hippocampal neurons. J Neurosci 25:558–565

Muñoz W, Tremblay R, Rudy B (2014) Channelrhodopsin-assisted patching: in vivo recording of genetically and morphologically identified neurons throughout the brain. Cell Rep 9:2304–2316

Nashaat MA, Oraby H, Sachdev RNS, Winter Y, Larkum ME (2016) Air-Track: a real-world floating environment for active sensing in head-fixed mice. J Neurophysiol 116:1542–1553

Nassar M, Simonnet J, Lofredi R, Cohen I, Savary E, Yanagawa Y, Miles R, Fricker D (2015) Diversity and overlap of parvalbumin and somatostatin expressing interneurons in mouse presubiculum. Front Neural Circuits 9:20

Nassi JJ, Cepko CL, Born RT, Beier KT (2015) Neuroanatomy goes viral! Front Neuroanat 9:80

Niedworok CJ, Brown APY, Jorge Cardoso M, Osten P, Ourselin S, Modat M, Margrie TW (2016) aMAP is a validated pipeline for registration and segmentation of high-resolution mouse brain data. Nat Commun 7:11879

O'Connor DH, Huber D, Svoboda K (2009) Reverse engineering the mouse brain. Nature 461:923–929

O'Keefe J (1976) Place units in the hippocampus of the freely moving rat. Exp Neurol 51:78–109

O'Keefe J, Dostrovsky J (1971) The hippocampus as a spatial map. Preliminary evidence from unit activity in the freely-moving rat. Brain Res 34:171–175
O'Keefe J, Recce ML (1993) Phase relationship between hippocampal place units and the EEG theta rhythm. Hippocampus 3:317–330
Oberlaender M, Ramirez A, Bruno RM (2012) Sensory experience restructures thalamocortical axons during adulthood. Neuron 74:648–655
Ohki K, Chung S, Ch'ng YH, Kara P, Reid RC (2005) Functional imaging with cellular resolution reveals precise micro-architecture in visual cortex. Nature 433:597–603
Okaty BW, Sugino K, Nelson SB (2011) Cell type-specific transcriptomics in the brain. J Neurosci 31:6939–6943
Osten P, Margrie TW (2013) Mapping brain circuitry with a light microscope. Nat Methods 10:515–523
Packer AM, Russell LE, Dalgleish HWP, Häusser M (2015) Simultaneous all-optical manipulation and recording of neural circuit activity with cellular resolution in vivo. Nat Methods 12:140–146
Pagliardini S, Gosgnach S, Dickson CT (2013) Spontaneous sleep-like brain state alternations and breathing characteristics in urethane anesthetized mice. PLoS ONE 8:e70411
Pala A, Petersen CCH (2015) In vivo measurement of cell-type-specific synaptic connectivity and synaptic transmission in layer 2/3 mouse barrel cortex. Neuron 85:68–75
Park SI, Shin G, Banks A, McCall JG, Siuda ER, Schmidt MJ, Chung HU, Noh KN, Mun JG-H, Rhodes J, Bruchas MR, Rogers JA (2015) Ultraminiaturized photovoltaic and radio frequency powered optoelectronic systems for wireless optogenetics. J Neural Eng 12:56002
Pedreira C, Martinez J, Ison MJ, Quian Quiroga R (2012) How many neurons can we see with current spike sorting algorithms? J Neurosci Methods 211:58–65
Pinault D (1996) A novel single-cell staining procedure performed in vivo under electrophysiological control: morpho-functional features of juxtacellularly labeled thalamic cells and other central neurons with biocytin or Neurobiotin. J Neurosci Methods 65:113–136
Plaza SM, Scheffer LK, Chklovskii DB (2014) Toward large-scale connectome reconstructions. Curr Opin Neurobiol 25:201–210
Potez S, Larkum ME (2008) Effect of common anesthetics on dendritic properties in layer 5 neocortical pyramidal neurons. J Neurophysiol 99:1394–1407
Poulet JFA, Petersen CCH (2008) Internal brain state regulates membrane potential synchrony in barrel cortex of behaving mice. Nature 454:881–885
Preston-Ferrer P, Coletta S, Frey M, Burgalossi A (2016) Anatomical organization of presubicular head-direction circuits. Elife 5
Quilichini P, Sirota A, Buzsáki G (2010) Intrinsic circuit organization and theta-gamma oscillation dynamics in the entorhinal cortex of the rat. J Neurosci 30:11128–11142
Ragan T, Kadiri LR, Venkataraju KU, Bahlmann K, Sutin J, Taranda J, Arganda-Carreras I, Kim Y, Seung HS, Osten P (2012) Serial two-photon tomography for automated ex vivo mouse brain imaging. Nat Methods 9:255–258
Ramirez S, Liu X, Lin P-A, Suh J, Pignatelli M, Redondo RL, Ryan TJ, Tonegawa S (2013) Creating a false memory in the hippocampus. Science 341:387–391
Ramsden HL, Sürmeli G, McDonagh SG, Nolan MF (2015) Laminar and dorsoventral molecular organization of the medial entorhinal cortex revealed by large-scale anatomical analysis of gene expression. PLoS Comput Biol 11:e1004032
Rancz EA, Franks KM, Schwarz MK, Pichler B, Schaefer AT, Margrie TW (2011) Transfection via whole-cell recording in vivo: bridging single-cell physiology, genetics and connectomics. Nat Neurosci 14:527–532
Ravassard P, Kees A, Willers B, Ho D, Aharoni D, Cushman J, Aghajan ZM, Mehta MR (2013) Multisensory control of hippocampal spatiotemporal selectivity. Science 340:1342–1346
Ray S, Naumann R, Burgalossi A, Tang Q, Schmidt H, Brecht M (2014) Grid-layout and theta-modulation of layer 2 pyramidal neurons in medial entorhinal cortex. Science 343:891–896
Reijmers LG, Perkins BL, Matsuo N, Mayford M (2007) Localization of a stable neural correlate of associative memory. Science 317:1230–1233

Resch-Genger U, Grabolle M, Cavaliere-Jaricot S, Nitschke R, Nann T (2008) Quantum dots versus organic dyes as fluorescent labels. Nat Methods 5:763–775

Rich PD, Liaw H-P, Lee AK (2014) Place cells. Large environments reveal the statistical structure governing hippocampal representations. Science 345:814–817

Royer S, Zemelman BV, Losonczy A, Kim J, Chance F, Magee JC, Buzsáki G (2012) Control of timing, rate and bursts of hippocampal place cells by dendritic and somatic inhibition. Nat Neurosci 15:769–775

Russell NA, Horii A, Smith PF, Darlington CL, Bilkey DK (2006) Lesions of the vestibular system disrupt hippocampal theta rhythm in the rat. J Neurophysiol 96:4–14

Sanders H, Rennó-Costa C, Idiart M, Lisman J (2015) Grid cells and place cells: an integrated view of their navigational and memory function. Trends Neurosci 38:763–775

Sargolini F, Fyhn M, Hafting T, McNaughton BL, Witter MP, Moser M-B, Moser EI (2006) Conjunctive representation of position, direction, and velocity in entorhinal cortex. Science 312:758–762

Sawinski J, Wallace DJ, Greenberg DS, Grossmann S, Denk W, Kerr JND (2009) Visually evoked activity in cortical cells imaged in freely moving animals. Proc Natl Acad Sci U S A 106:19557–19562

Schmid LC, Mittag M, Poll S, Steffen J, Wagner J, Geis H-R, Schwarz I, Schmidt B, Schwarz MK, Remy S, Fuhrmann M (2016) Dysfunction of somatostatin-positive interneurons associated with memory deficits in an Alzheimer's disease model. Neuron 92:114–125

Schmidt-Hieber C, Häusser M (2013) Cellular mechanisms of spatial navigation in the medial entorhinal cortex. Nat Neurosci 16:325–331

Schwarz C, Hentschke H, Butovas S, Haiss F, Stüttgen MC, Gerdjikov TV, Bergner CG, Waiblinger C (2010) The head-fixed behaving rat—procedures and pitfalls. Somatosens Mot Res 27:131–148

Scott BB, Brody CD, Tank DW (2013) Cellular resolution functional imaging in behaving rats using voluntary head restraint. Neuron 80:371–384

Sejnowski TJ, Churchland PS, Movshon JA (2014) Putting big data to good use in neuroscience. Nat Neurosci 17:1440–1441

Seung HS, Sümbül U (2014) Neuronal cell types and connectivity: lessons from the retina. Neuron 83:1262–1272

Sharp PE (1996) Multiple spatial/behavioral correlates for cells in the rat postsubiculum: multiple regression analysis and comparison to other hippocampal areas. Cereb Cortex 6:238–259

Shoham S, O'Connor DH, Segev R (2006) How silent is the brain: is there a "dark matter" problem in neuroscience? J Comp Physiol A 192:777–784

Slomianka L, Amrein I, Knuesel I, Sørensen JC, Wolfer DP (2011) Hippocampal pyramidal cells: the reemergence of cortical lamination. Brain Struct Funct 216:301–317

Sofroniew NJ, Cohen JD, Lee AK, Svoboda K (2014) Natural whisker-guided behavior by head-fixed mice in tactile virtual reality. J Neurosci 34:9537–9550

Solstad T, Boccara CN, Kropff E, Moser M-B, Moser EI (2008) Representation of geometric borders in the entorhinal cortex. Science 322:1865–1868

Somogyi P, Katona L, Klausberger T, Lasztóczi B, Viney TJ (2014) Temporal redistribution of inhibition over neuronal subcellular domains underlies state-dependent rhythmic change of excitability in the hippocampus. Philos Trans R Soc Lond B Biol Sci 369:20120518

Stosiek C, Garaschuk O, Holthoff K, Konnerth A (2003) In vivo two-photon calcium imaging of neuronal networks. Proc Natl Acad Sci U S A 100:7319–7324

Suh J, Rivest AJ, Nakashiba T, Tominaga T, Tonegawa S (2011) Entorhinal cortex layer III input to the hippocampus is crucial for temporal association memory. Science 334:1415–1420

Sümbül U, Song S, McCulloch K, Becker M, Lin B, Sanes JR, Masland RH, Seung HS (2014) A genetic and computational approach to structurally classify neuronal types. Nat Commun 5:3512

Sun C, Kitamura T, Yamamoto J, Martin J, Pignatelli M, Kitch LJ, Schnitzer MJ, Tonegawa S (2015) Distinct speed dependence of entorhinal island and ocean cells, including respective grid cells. Proc Natl Acad Sci U S A 112:9466–9471

Swanson LW, Lichtman JW (2016) From Cajal to Connectome and beyond. Annu Rev Neurosci 39:197–216

Sylwestrak EL, Rajasethupathy P, Wright MA, Jaffe A, Deisseroth K (2016) Multiplexed intact-tissue transcriptional analysis at cellular resolution. Cell 164:792–804

Tang Q, Brecht M, Burgalossi A (2014a) Juxtacellular recording and morphological identification of single neurons in freely moving rats. Nat Protoc 9:2369–2381

Tang Q, Burgalossi A, Ebbesen CL, Ray S, Naumann R, Schmidt H, Spicher D, Brecht M (2014b) Pyramidal and stellate cell specificity of grid and border representations in layer 2 of medial entorhinal cortex. Neuron 84:1191–1197

Tang Q, Ebbesen CL, Sanguinetti-Scheck JI, Preston-Ferrer P, Gundlfinger A, Winterer J, Beed P, Ray S, Naumann R, Schmitz D, Brecht M, Burgalossi A (2015) Anatomical organization and spatiotemporal firing patterns of layer 3 neurons in the rat medial entorhinal cortex. J Neurosci 35:12346–12,354

Tang Q, Burgalossi A, Ebbesen CL, Sanguinetti-Scheck JI, Schmidt H, Tukker JJ, Naumann R, Ray S, Preston-Ferrer P, Schmitz D, Brecht M (2016) Functional architecture of the rat parasubiculum. J Neurosci 36:2289–2301

Tao C, Zhang G, Xiong Y, Zhou Y (2015) Functional dissection of synaptic circuits: in vivo patch-clamp recording in neuroscience. Front Neural Circuits 9:23

Tasic B et al (2016) Adult mouse cortical cell taxonomy revealed by single cell transcriptomics. Nat Neurosci 19:335–346

Taube JS (2007) The head direction signal: origins and sensory-motor integration. Annu Rev Neurosci 30

Taube JS, Muller RU, Ranck JBJ (1990) Head-direction cells recorded from the postsubiculum in freely moving rats. I. Description and quantitative analysis. J Neurosci 10:420–435

Teeters JL et al (2015) Neurodata without Borders: creating a common data format for neurophysiology. Neuron 88:629–634

Thurley K, Ayaz A (2017) Virtual reality systems for rodents. Curr Zool 63:109–119

Tonegawa S, Liu X, Ramirez S, Redondo R (2015) Memory engram cells have come of age. Neuron 87:918–931

Tsuno Y, Chapman GW, Hasselmo ME (2015) Rebound spiking properties of mouse medial entorhinal cortex neurons in vivo. Eur J Neurosci 42:2974–2984

Tukker JJ, Fuentealba P, Hartwich K, Somogyi P, Klausberger T (2007) Cell type-specific tuning of hippocampal interneuron firing during gamma oscillations in vivo. J Neurosci 27:8184–8189

Tukker JJ, Lasztóczi B, Katona L, Roberts JDB, Pissadaki EK, Dalezios Y, Márton L, Zhang L, Klausberger T, Somogyi P (2013) Distinct dendritic arborization and in vivo firing patterns of parvalbumin-expressing basket cells in the hippocampal area CA3. J Neurosci 33:6809–6825

Tukker JJ, Tang Q, Burgalossi A, Brecht M (2015) Head-directional tuning and theta modulation of anatomically identified neurons in the presubiculum. J Neurosci 35:15391–15395

Valero M, Cid E, Averkin RG, Aguilar J, Sanchez-Aguilera A, Viney TJ, Gomez-Dominguez D, Bellistri E, de la Prida LM (2015) Determinants of different deep and superficial CA1 pyramidal cell dynamics during sharp-wave ripples. Nat Neurosci 18:1281–1290

Varga C, Lee SY, Soltesz I (2010) Target-selective GABAergic control of entorhinal cortex output. Nat Neurosci 13:822–824

Varga C, Golshani P, Soltesz I (2012) Frequency-invariant temporal ordering of interneuronal discharges during hippocampal oscillations in awake mice. PNAS 109:E2726–E2734

Varga C, Oijala M, Lish J, Szabo GG, Bezaire M, Marchionni I, Golshani P, Soltesz I (2014) Functional fission of parvalbumin interneuron classes during fast network events. Elife 3

Vélez-Fort M, Rousseau CV, Niedworok CJ, Wickersham IR, Rancz EA, Brown APY, Strom M, Margrie TW (2014) The stimulus selectivity and connectivity of layer six principal cells reveals cortical microcircuits underlying visual processing. Neuron 83:1431–1443

Viney TJ, Lasztoczi B, Katona L, Crump MG, Tukker JJ, Klausberger T, Somogyi P (2013) Network state-dependent inhibition of identified hippocampal CA3 axo-axonic cells in vivo. Nat Neurosci 16:1802–1811

Vogelstein JT, Park Y, Ohyama T, Kerr RA, Truman JW, Priebe CE, Zlatic M (2014) Discovery of brainwide neural-behavioral maps via multiscale unsupervised structure learning. Science 344:386–392

Wang Y, Liu Y-Z, Wang S-Y, Wang Z (2016) In vivo whole-cell recording with high success rate in anaesthetized and awake mammalian brains. Mol Brain 9:86

Wertz A, Trenholm S, Yonehara K, Hillier D, Raics Z, Leinweber M, Szalay G, Ghanem A, Keller G, Rózsa B, Conzelmann K-K, Roska B (2015) Presynaptic networks. Single-cell-initiated monosynaptic tracing reveals layer-specific cortical network modules. Science 349:70–74

Westphalen RI, Hemmings HC (2006) Volatile anesthetic effects on glutamate versus GABA release from isolated rat cortical nerve terminals: 4-aminopyridine-evoked release. J Pharmacol Exp Ther 316:216–223

Wheeler DW, White CM, Rees CL, Komendantov AO, Hamilton DJ, Ascoli GA (2015) Hippocampome.org: a knowledge base of neuron types in the rodent hippocampus. Elife 4

Wiltschko AB, Johnson MJ, Iurilli G, Peterson RE, Katon JM, Pashkovski SL, Abraira VE, Adams RP, Datta SR (2015) Mapping sub-second structure in mouse behavior. Neuron 88:1121–1135

Winterer J, Maier N, Wozny C, Beed P, Breustedt J, Evangelista R, Peng Y, D'Albis T, Kempter R, Schmitz D (2017) Excitatory microcircuits within superficial layers of the medial entorhinal cortex. Cell Rep 19:1110–1116

Wolfe J, Houweling AR, Brecht M (2010) Sparse and powerful cortical spikes. Curr Opin Neurobiol 20:306–312

Wu F, Stark E, Ku P-C, Wise KD, Buzsáki G, Yoon E (2015) Monolithically integrated μLEDs on silicon neural probes for high-resolution optogenetic studies in behaving animals. Neuron 88:1136–1148

Ylinen A, Bragin A, Nadasdy Z, Jando G, Szabo I, Sik A, Buzsaki G (1995a) Sharp wave-associated high-frequency oscillation (200 Hz) in the intact hippocampus: network and intracellular mechanisms. J Neurosci 15:30–46

Ylinen A, Soltesz I, Bragin A, Penttonen M, Sik A, Buzsaki G (1995b) Intracellular correlates of hippocampal theta rhythm in identified pyramidal cells, granule cells, and basket cells. Hippocampus 5:78–90

Youngstrom IA, Strowbridge BW (2012) Visual landmarks facilitate rodent spatial navigation in virtual reality environments. Learn Mem 19:84–90

Zehl L, Jaillet F, Stoewer A, Grewe J, Sobolev A, Wachtler T, Brochier TG, Riehle A, Denker M, Grün S (2016) Handling metadata in a neurophysiology laboratory. Front Neuroinform 10:26

Zeisel A, Muñoz-Manchado AB, Codeluppi S, Lönnerberg P, La Manno G, Juréus A, Marques S, Munguba H, He L, Betsholtz C, Rolny C, Castelo-Branco G, Hjerling-Leffler J, Linnarsson S (2015) Brain structure. Cell types in the mouse cortex and hippocampus revealed by single-cell RNA-seq. Science 347:1138–1142

Zhu JJ, Connors BW (1999) Intrinsic firing patterns and whisker-evoked synaptic responses of neurons in the rat barrel cortex. J Neurophysiol 81:1171–1183

Ziv Y, Burns LD, Cocker ED, Hamel EO, Ghosh KK, Kitch LJ, El Gamal A, Schnitzer MJ (2013) Long-term dynamics of CA1 hippocampal place codes. Nat Neurosci 16:264–266

Ziv Y, Ghosh KK (2015) Miniature microscopes for large-scale imaging of neuronal activity in freely behaving rodents. Curr Opin Neurobiol 32:141–147

Spatial, Temporal, and Behavioral Correlates of Hippocampal Neuronal Activity: A Primer for Computational Analysis

Howard Eichenbaum

Abstract Creating useful models of the hippocampus will rely upon our ability to bridge between local circuitry and behavior. A critical intermediate between these levels is the functional activity of hippocampal principal neurons, the elements of neuronal information processing. This chapter provides an overview of the functional correlates of hippocampal neuronal activity, focusing on the nature of inputs these neurons receive; the broad range of sensory, behavioral, and spatial and temporal features of events captured by firing patterns of hippocampal neurons; and a framework for thinking about how the hippocampus organizes information from its inputs to support memory coding and retrieval.

Overview

Hippocampal neurons are extraordinarily interesting to observe in action. As animals perform a variety of natural or learned behaviors, hippocampal principal cells of areas CA1 and CA3, which otherwise are characterized by very low baseline firing rates, suddenly fire at rapid rates related to the current location of the animal, its ongoing behavior, specific salient stimuli, elapsed time, or some combination of these factors and the context of the behavioral situation. Unlike in many brain areas, specific sensory or behavioral correlates of neuronal activity are difficult to observe; in the hippocampus, it sometimes seems there are as many behavioral correlates as experimental paradigms in which they might be observed. The challenge is not to find correlates of neural activity in the hippocampus – it is to make sense of the broad range of sensory- and behavior-related firing properties observed.

Here I will provide an overview of the literature on spatial and behavioral correlates of hippocampal neural activity. This is a large literature, so this review will not be comprehensive. Rather, my aims are to sketch the breadth of the

H. Eichenbaum (✉)
Center for Memory and Brain, Boston University, Boston, MA, USA
e-mail: hbe@bu.edu

V. Cutsuridis et al. (eds.), *Hippocampal Microcircuits*, Springer Series in Computational Neuroscience, https://doi.org/10.1007/978-3-319-99103-0_10

correlates observed and to provide a framework for thinking about these properties and how they might be modeled. More detailed analyses and large lists of citations to the primary experimental literature are available in recent reviews (Eichenbaum et al. 1999; Eichenbaum 2004, 2007, 2014; Leutgeb et al. 2005a, b; McNaughton et al. 2007).

I will begin with a summary of the anatomy of the medial temporal lobe system in which the hippocampus is a central component. In all biological systems, function follows form, and the hippocampus is no exception. Understanding the functional properties of hippocampal neuronal activity should be helped considerably by an appreciation of the information contained in neural activity observed in areas that send inputs to the principal neurons of hippocampus. In this section I will argue that the hippocampus is a convergence site for highly processed information about space (the so-called "where" or dorsal stream of the cerebral cortex) and about objects (the "what" or ventral stream). From this perspective, the unsurprising outcome is that major correlates of hippocampal neural activity reflect both these kinds of information.

This will be followed by a discussion of the spatial coding features of hippocampal neural activity. These are the easiest to observe and the most commonly studied properties of hippocampal neural activity. While many hippocampal neurons fire associated with the current location of an animal, it should not be assumed that the hippocampus provides a map of space nor that the function of the hippocampus is navigation. The distinctions between place coding, map building, and navigation will be highlighted.

This will be followed by recent evidence that, when spatial location is controlled or held constant, hippocampal neurons encode the passage of time via neurons that fire specific, sequential moments in time during a structured interval. Observations of hippocampal "time cells" open a new dimension for organizing the temporal flow of experiences in memory.

Then I will consider the nonspatial and nontemporal firing properties of hippocampal neurons. It will be argued that hippocampal neurons do not reflect simple sensory perceptions or behavioral actions, but rather that sensory and behavioral events are also a major component of the information encoded by hippocampal neuronal activity.

A consensual general view is that the hippocampus does not so much encode the specific details of events (or places) but rather encodes a sufficient "gist" of events to generate some sort of index that points to where the details can be found in the cortical areas that provide the detailed inputs to the hippocampus and receive its outputs. Furthermore, it is believed that the hippocampus must also represent information about the spatial and temporal context in which events occurred, in order to select event representations that should be regenerated in the cortex to support remembering. Therefore I will also consider evidence that hippocampal neurons encode contextual information about where and when events occurred.

These considerations then will be combined in a framework I have offered called the "memory space" hypothesis of hippocampal neuronal representations. According to this view, hippocampal neurons encode events as associations among

stimuli and places; they represent episodes as sequences of events; and hippocampal ensembles represent networks of memories as linked events and episodes. Such a framework matches the functional role of the hippocampus in memory as described by a convergence of cognitive and neuroscience approaches.

The Data

Input/Output Circuitry and the Information Contained in Inputs to the Hippocampus

The hippocampus receives inputs from widespread areas of the neocortex and olfactory cortex that are relayed via the parahippocampal region, a set of highly interconnected cortical areas immediately surrounding the hippocampus (see section "Context," also Manns and Eichenbaum 2006). The purpose of this section is not to provide details on the anatomical circuitry of these inputs, but rather to emphasize the information they contain. Sensory information that enters the primary cortical areas subsequently passes through multiple secondary and tertiary stages of unimodal sensory processing, ultimately arriving in the parietal, retrosplenial, and temporal association areas. Similarly, motor and emotional information that are processed in early level cortical and subcortical areas pass into association areas of the prefrontal and limbic cortex. This large set of association areas provides the inputs to the parahippocampal region.

The cortical inputs to the parahippocampal region demonstrate a systematic organization but one that is unlike the punctate topographies that characterize the primary sensory and motor thalamocortical pathways (Suzuki and Amaral 1994; Burwell 2000; Manns and Eichenbaum 2006; Fig. 1). Association areas that process unimodal sensory information about qualities of objects, e.g., superior temporal and inferotemporal cortex, are sent primarily to one component of the parahippocampal region called the perirhinal cortex. By contrast, association areas that process polymodal spatial information, e.g., parietal and retrosplenial cortex, are sent primarily to another component of the parahippocampal region called the parahippocampal cortex in monkeys and the postrhinal cortex in rats. One view of this segregation of inputs is that information from the well-known "what" (ventral) stream of visual processing, as well as its counterparts in other sensory modalities, arrives in the perirhinal cortex, whereas information from the "where" (dorsal) stream arrives in the parahippocampal cortex (Eichenbaum et al. 2007). There are connections between the perirhinal cortex and parahippocampal cortex, but the "what" and "where" streams of processing remain largely segregated as they reach the parahippocampal region. Subsequently, the perirhinal and parahippocampal cortical areas project to the entorhinal cortex and, in doing so, maintain the segregation of "what" and "where" inputs to these areas. The lateral entorhinal area receives more cortical projections from the perirhinal cortex, whereas the medial

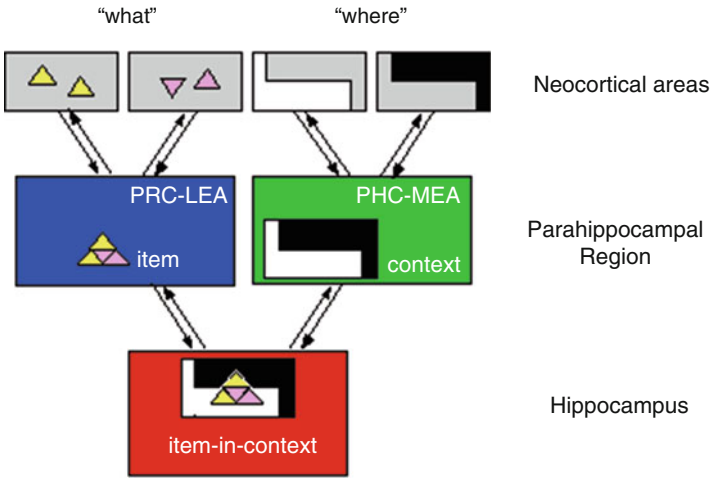

Fig. 1 Functional organization of the hippocampal memory system. Neocortical input regarding the object features ("what") converges in the perirhinal cortex (PRC) and lateral entorhinal area (LEA), whereas details about the location ("where") of objects converge in the parahippocampal cortex (PHC) and medial entorhinal area (MEA). These streams converge in the hippocampus which represents items in the context in which they were experienced. Reverse projections follow the same pathways back to the parahippocampal and neocortical regions. Back projections to the PHC-MEA may support recall or context, whereas back projections to the PHC-LEA may support recall of item associations. (From Eichenbaum et al. 2007)

entorhinal area receives more cortical projections from the parahippocampal cortex. There are also some connections between the perirhinal and parahippocampal cortices and between the lateral and medial entorhinal areas, but the "what" and "where" information mainly converge at the next stage, within the hippocampus.

The response properties of neurons in the parahippocampal region follow the functional differentiation suggested by the anatomy. Neurons in the perirhinal cortex of monkeys and rats respond to specific object stimuli, such as complex visual patterns and odors (Suzuki and Eichenbaum 2000; Eichenbaum 2000). In addition, many cells in the perirhinal cortex and lateral entorhinal area have selective responses to specific memory cues that are sustained through memory delays as animals perform short-term and working memory tasks. Also, many neurons in these areas show suppressed or enhanced responses to stimuli that are repeated, such as during the test phase of a short-term or working memory task (Brown and Xiang 1998). These findings are consistent with observations from functional imaging studies showing diminished activation to specific verbal or pictorial stimuli in the perirhinal cortex of humans (see Eichenbaum et al. 2007). These combined findings have led to the view that perirhinal cortex, perhaps along with the lateral entorhinal area, can support a sense of familiarity with specific stimuli, even in the absence of a contribution of the hippocampus (Eichenbaum et al. 1994; Brown and Aggleton 2001; Eichenbaum et al. 2007).

Neurons in parahippocampal cortex and medial entorhinal area, the regions that receive inputs from the "where" neocortical stream, respond to the spatial arrangement of stimuli (Wan et al. 1999; Fyhn et al. 2004; Hargreaves et al. 2005). Most prominently, neurons in the medial entorhinal area fire when an animal is in multiple places in the environment organized as regular array environmental locations (the so-called grid cells). Cells located more dorsally in the medial entorhinal area activate associated with more punctate locations within the grid, whereas cells located more ventrally fire associated with larger areas within the grid. Like hippocampal neurons (see below), grid cell activity can also reflect an animal's orientation and speed of movement, as well as contextual features (Sargolini et al. 2006; Lipton et al. 2007). In addition, recent evidence suggests that the medial entorhinal cortex also ends temporal context in rodents (Kraus et al. 2015). Notably, the closely associated parahippocampal cortex of humans is activated when subjects view spatial scenes or objects that generate associations with particular spatial contexts (Epstein and Kanwisher 1998; Bar and Aminoff 2003) and this area also encodes temporal context in humans (Hsieh et al. 2014). The combined observations from all these studies suggest a functional organization in which nonspatial object representation occurs in the perirhinal-lateral entorhinal "what" stream, spatial and perhaps other aspects of context are represented in the parahippocampal-medial entorhinal "where" and "when" stream, and that one critical role of the hippocampus is to associate objects with the spatial-temporal context in which they were experienced (Eichenbaum et al. 2007).

Spatial Firing Patterns of Hippocampal Neurons

Nearly all of our information on hippocampal neuronal firing patterns comes from data on CA1 and CA3 pyramidal cells in the dorsal hippocampus of rats and to a lesser extent, in mice, monkeys, and humans. There also exists substantial data on interneurons in the dorsal hippocampus – the firing patterns of these neurons correspond closely to the theta rhythm such that interneurons tend to burst at high rates locked to theta phase.

The most striking and prevalent pattern of firing in hippocampal pyramidal cells involves selective activation when a rat is in a particular location in its environment (see Muller 1996; Eichenbaum et al. 1999: for a more detailed reviews). These so-called place cells are typically observed by monitoring extracellularly recorded action potentials from principal cells in CA1 and CA3 of freely behaving rats. As the animal explores or merely traverses a large environment, one can readily observe dramatic increases in a place cell's firing rate when the rat arrives at a particular location, called the "place field" (Fig. 2). From a baseline of less than 1 spikes/sec, the firing rate can exceed 100 Hz, although during some passes through the place field, the cell may not fire at all. Typically a large fraction of cells (40–75%) have place fields in any environment, although the low baseline firing rates may result in many cells without place fields going undetected. Place fields vary in size from

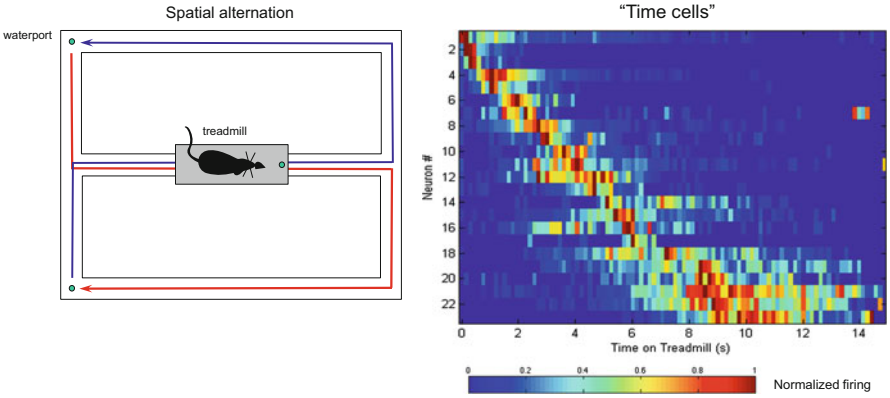

Fig. 2 Schematic overhead views of two types of apparatus and examples of location-specific activity of hippocampal place cells. (**a**) Eight-arm radial maze where the rat can obtain a food reward the first time it reaches the end of each arm. The figure includes bar graphs on either side of the maze arms showing firing rates of a place cell associated with inward (white bars) and outward (black bars) movements on each arm. This cell fires primarily as the animal moves inward on the NE arm. (From McNaughton et al. 1991). (**b**) Cylinder, with the location of the cue card indicated by a thickened part of the circle, in which rats continuously forage for food dropped at random locations on the floor. The firing pattern of a place cell is indicated by open pixels at loci associated with low firing rates and filled pixels at loci associated with high firing rates. (From Muller et al. 1987)

a few centimeters to half the size of an environment and are dispersed throughout the environment, although they may be concentrated at areas of particular salience (e.g., Hollup et al. 2001).

A major issue is what cues are driving the responses of place cells. Early studies showed that spatially specific activity can be dissociated from potential confounding influences of particular behaviors that might occur at different locations. For example, Olton et al. (1978) observed hippocampal cellular activity in rats performing the same inward and outward traversals on all arms of a radial maze and found that many hippocampal cells fired only when the rat was on a particular arm (Fig. 2a). Muller et al. (1987) equalized behavior throughout an environment by observing hippocampal cellular activity in rats foraging in random walks for food pellets randomly dispersed in a circular open field (Fig. 2b) and found location-specific activity evident in many of the event when behaviors and movement patterns were randomized.

Other studies have focused on the environmental cues that could drive spatially specific activity. Summarizing the early studies, O'Keefe (1979) defined place cells as neurons whose activity is not dependent on any particular stimulus, but rather reflects the presence and topography of multiple environmental cues. Whereas these early studies suggested that many place cells meet this criterion, more recent studies indicate that place cells are driven by relatively few proximal cues. O'Keefe and Burgess (1996) showed that the shape and locus of most place fields within a simple rectangular chamber are determined by the dimensions of, and spatial

relations between, only a few nearby walls of the environment. Several other recent studies have shown that place cells can encode subsets of the spatial cues and that these representations are not bound to other spatial representations in the same environment. Shapiro, Tanila, and colleagues (Shapiro et al. 1997; Tanila et al. 1997a, b, c) examined the responses of hippocampal cells to systematic manipulations of a large set of spatial cues. Different place cells encoded individual proximal and distant stimuli, combinations of proximal or distant stimuli, or relations between proximal and distant cues. The place fields of some cells were fully controlled by as little as a single cue within a very complex environment, and most cells were controlled by different subsets of the controlled cues.

Gothard and colleagues (1996a, b) found that when a particularly salient cue or enclosure within an open field is moved repeatedly and randomly, the spatial firing patterns of some cells become tied to that cue. When rats were trained to shuttle between a mobile starting box and a goal location defined by landmarks in an open field, some cells fired relative to the static environmental cues, but others fired relative to a landmark-defined goal site or in relation to the start box. When rats were trained to shuttle between a movable start-end box and goal site on a linear track, the anchor of the spatial representation of many cells switched between these two cues, depending on which was closer. Under these conditions the majority of the activated hippocampal cells did not exhibit location-specific activity that was associated with fixed environmental cues. Instead, their activity could be characterized as "spatial" only to the extent that they fired at specific distances from a particular stimulus or goal.

In addition, these and other studies have shown that place cells are not linked together to form a cohesive map of the environment. Tanila et al. (1997b) found that ensembles of simultaneously recorded place cells changed their firing patterns independently when distinct subsets of the cues presented at the same time, indicating that the spatial representation was not cohesive. In several cases where two cells had overlapping place fields associated with one configuration of the cues, each cell responded differently when the same cues were rearranged. This finding shows that each cell was controlled by a different subset of the cues at the same time and that their differential encodings are not due to shifts between two different spatial "reference frames" used by all cells at different times (Gothard et al. 1996b). Skaggs and McNaughton (1998) confirmed this finding by recording from a large number of place cells simultaneously in rats foraging randomly in two identical enclosures, between which they could move freely. Each hippocampal ensemble contained cells that had similar place fields and others that had distinct spatial firing patterns between the two enclosures. In this situation, some cells encoded the physical cues, whereas the activity of others at the same time reflected the knowledge that the two environments were distinct.

Combining the findings from all these studies, one can conclude that place fields reflect a collection of independent representations, each one encoding the place the animal occupies defined by a subset of cues. Spatial representations are not bound as coordinates within a systematic framework for the global topology, indicating that

hippocampal spatial codings are not organized as elements of a Cartesian "map." Rather, place cells seem to encode places where important events or stimuli occur.

Temporal Firing Properties of Hippocampal Neurons

There is considerable recent evidence that the hippocampus is involved in representing the flow of time, in parallel to its representation of space (Eichenbaum 2013, 2014), and indeed it has been suggested that bridging between successive events to link them in time may be a fundamental function of hippocampal circuitry (Rawlins 1985; Levy 1989; Wallenstein et al. 1998; Howard and Eichenbaum 2013). Consistent with this idea, an early study showed that ensemble activity patterns of CA1 neurons gradually change while rats sampled sequences of odors, and this signal of continuously evolving temporal context predicted success in remembering the odor sequence (Manns et al. 2007).

Several subsequent studies have identified hippocampal principal neurons that fire at particular moments in time of a temporally structured event, composing temporal maps of specific experiences. Across these studies, the location of the animal is held constant, or firing patterns associated with elapsed time are distinguished from those associated with spatial and behavioral variables, and the firing patterns of these cells are dependent on the critical temporal parameters that characterize the task. Because these properties parallel those of place cells in coding locations in spatially structured experiences, we called these neurons "time cells" (MacDonald et al. 2011), even though these neurons are the same cells that exhibit spatial firing specificity in other circumstances.

Time cells have now been observed in several experiments. The findings of these studies can be summarized as follows. Time cells have been observed in a range of behavioral conditions, including during delay periods in maze tasks in which rats alternate goals (Gill et al. 2011; Pastalkova et al. 2008; Kraus et al. 2013; Fig. 3), bridging temporal gaps between associated nonspatial cues (MacDonald et al. 2011), during the delay period in a nonspatial matching to sample task (MacDonald et al. 2013), and throughout trials in trace eyelid conditioning (Modi et al. 2014). Importantly, in some of these studies, the animal is immobilized and thus space plays no role in ongoing behavior or memory (MacDonald et al. 2013; Modi et al. 2014; Naya and Suzuki 2011). The findings of these studies establish a broad scope of temporally structured episodes in which the hippocampus encodes the temporal organization of specific experiences. Furthermore, some of the studies in animals have closely linked the emergence of time cells sequences to the encoding of specific memories and to subsequent memory accuracy (Modi et al. 2014; MacDonald et al. 2013), thus indicating a causal role of time cell firing patterns to memory performance. Also, the representation of temporally ordered sequences of events by the hippocampus extends to monkeys and humans. In monkeys, hippocampal

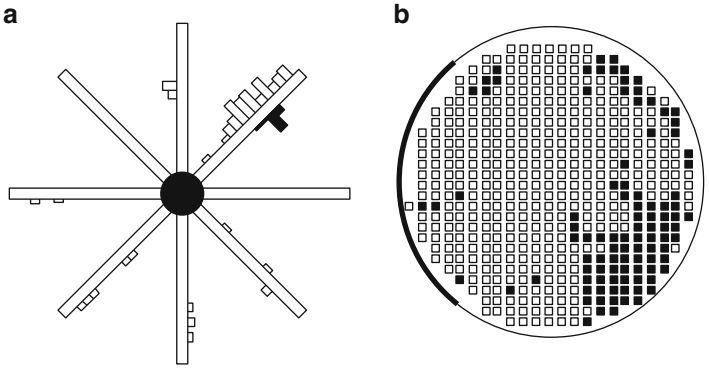

Fig. 3 Hippocampal time cells during the period when a rat runs in place while performing a spatial alternation task. Left: the spatial alternation task with treadmill in the center of the maze stem. Red and blue lines indicate alternate right-turn and left-turn paths. Right: ensemble firing rate mapping where each row represents the normalized average firing rate of a neuron (see cell numbers on Y-axis) over the 15 s treadmill run. Note that each cell fires during a specific moment of treadmill running and the entire period of running is filled with time-specific representations. (Adapted from Kraus et al. 2013)

neuronal activity signals elapsed time in a memory delay between associated objects (Naya and Suzuki 2011). In humans, hippocampal neurons fire in sequence associated with learning (Paz et al. 2010) and memory (Gelbard-Sagiv et al. 2008) of the flow of events experienced in movie clips.

The significance of prominent temporal representation as an aspect of nonspatial coding in the hippocampus is high in two ways. First, as introduced by Tulving (1983), episodic memories are defined by a temporal organization that embodies the temporal organization of events in personal experiences. We know that the hippocampus is critical to episodic memory and to memory for the temporal order of events, even when space is not relevant. Now the existence of time cells provides a mechanism by which the hippocampus organizes memories for events in time. Second, the existence of time cells offers a parallel temporal organizing mechanism to the spatial organizing mechanism offered by place cells. Therefore, the hippocampus could support representations of episodes by mapping objects and events within a framework of space and time, conferring upon those memories connections that reflect the spatial and temporal associations between distinct but related events embodied within a mapping by place and time cells (Eichenbaum 2013, 2014).

Nonspatial and Nontemporal Firing Properties of Hippocampal Neurons

According to O'Keefe (1979), true place cells fire whenever an animal is in the place field, regardless of its orientation or ongoing behavior. However, few hippocampal neurons meet this criterion because nearly all of them alter their activity associated with the animal's direction and behavior in most behavioral situations. Perhaps the only situation where large numbers of true place cells are observed is when animals forage by random walk through an environment (Fig. 2b), where behavior is held constant and the meaning of movement directions is homogeneous. In virtually any situation where movement directions are meaningfully different (e.g., in and out of a maze arm) or behaviors are differentiated throughout the environment, other factors dramatically influence spatial firing patterns, and in some situations where space is particularly irrelevant, some hippocampal neuronal activity can be closely linked to nonspatial stimuli and behaviors.

In many situations, spatially specific activity is influenced by meaningfully distinct movement directions. For example, in the radial maze task, where animals regularly run outward on each maze arm to obtain a reward then return to the central platform to initiate the next choice (Fig. 2a), outward and inward arm movements reflect meaningfully distinct behavioral episodes that occur repetitively. Correspondingly, hippocampal neurons reflect the relevant "directional structure" imposed by this protocol, and almost all place cells fire only during outward or inward journeys. Similarly, place cells are activated selectively during distinct approach or return episodes and from variable goal and start locations in open fields and linear tracks. Markus et al. (1995) directly compared the directionality of place cells under different task demands and found that place cells that were nondirectional when rats foraged randomly in an open field were directional when they systematically visited a small number of reward locations. Taken together, these findings emphasize that place cells exhibit movement-related firing patterns whenever particular movements are associated with meaningfully different events.

Other studies have demonstrated firing patterns of hippocampal neurons directly related to nonspatial, nontemporal stimulus, cognitive, and behavioral events. In rats and rabbits performing different classical conditioning tasks, a large fraction of hippocampal neurons fire strongly associated with the learned significance of stimuli and with learned responses. Hippocampal cells begin to fire early in training, prior to the appearance of the conditioned responses, and the responses of individual cells can be related to the timing of stimuli and conditioned responses. A large fraction of hippocampal neurons are also activated in animals performing a variety of instrumental learning tasks that involve discriminations among olfactory, visual, or auditory stimuli, and delayed matching and nonmatching to sample tasks that test recognition memory (see Eichenbaum et al. 1999). Different neurons are activated during virtually every moment of task performance, including during approach and stimulus sampling behaviors, discriminative responses, and consummatory behaviors (Fig. 4).

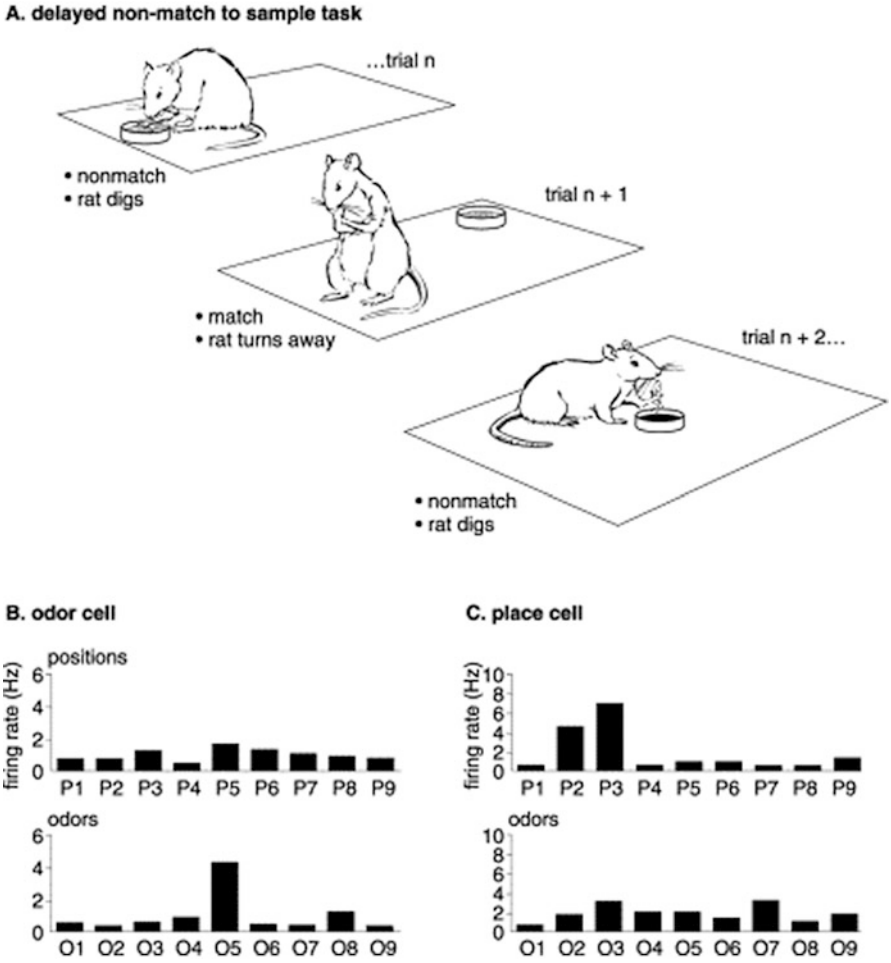

Fig. 4 Hippocampal neuronal firing patterns in rats performing an odor delayed nonmatch to sample task (Wood et al. 1999). (**a**) On each trial the rat is presented with one of nine odors at any of nine randomly selected locations. To obtain a buried reward, the rat must identify whether the odor is the same as (matches, trial n + 1) or differs from (nonmatches, trial n + 2) the odor presented on the previous trial. Panels **b** and **c** show the average firing rates of two cells associated with all the places and all the odors. (**b**) This cell fires selectively when the rat samples odor 5, and this cell does not fire differentially depending on where the trial was performed. (**c**) This cell fires selectively when the rat performs the trial at adjacent positions 2 and 3 and fires similarly associated with all the odors

Several recent studies suggest that some hippocampal neurons fire associated with specific stimulus, spatial, and action combinations, and their significance, and these findings show a remarkable range of information and combinations of information encoded by hippocampal neural activity. For example, Wirth et al. (2003) described hippocampal cells that change their responses to stimuli as animals

learn to make a particular spatially directed behavioral response to those stimuli. Moita et al. (2003) recently reported that place cells begin to fire to tone stimuli associated with shock when a rat occupies the cell's place field. Komorowski et al. (2009) showed that hippocampal neurons develop object-specific activity as animals acquire object-location associations. Similarly, after training on somatosensory or auditory discrimination tasks, hippocampal neurons encode tactile and auditory cues along with the locations where they were experienced and rewarded (Itskov et al. 2011, 2012; Vinnik et al. 2012). Leutgeb et al. (2005a, b) characterized hippocampal neurons as responding with changed firing rates when the rat occupied different small chambers within a constant large environment, but the same cells qualitatively changed firing patterns when the global environmental cues were altered. They suggested that specific events within an overall environment are encoded by a rate code within an overall consistent spatial representation. Rivard et al. (2004) described a class of place cells that fire when a rat is in proximity to a large object that occupies different positions in the environment (and even in multiple environments), as well as place cells whose activity is not influenced by the object, and yet others that fire only when the object is in a particular location. Similarly, Wood et al. (1999) described hippocampal neurons that fired associated with odorous stimuli, the location where they appeared in the environment as the animal explored them, or combinations of the odor and location (Fig. 4). In addition, the activity of some cells reflects the relevant cognitive demands of the task, for example, the match or nonmatch relationship between stimuli when a judgment between these is required. These firing patterns could also reflect reward expectancies associated with particular stimulus contingencies (Hok et al. 2007) also observed when rats discover a new goal location (Fyhn et al. 2002).

The nonspatial and nontemporal firing patterns of hippocampal neurons are as robust as spatial firing patterns, whenever the neural activity can be closely time-locked to critical sensory or behavioral events and the prevalence of spatial and nonspatial firing patterns is also comparable in studies where the incidence of both types of coding was evaluate (e.g., Wood et al. 1999). This combination of findings indicates that hippocampal neurons represent a broad variety of objects, places, and object-location conjunctions as well as actions taken toward those objects and their significance.

In addition, it is notable that hippocampal neurons represent sequences of events that compose entire behavioral episodes. As animals perform virtually all behavioral tasks, a series of hippocampal cells are sequentially active, consistent with the view that the hippocampus automatically encodes the flow of events in experience (Eichenbaum et al. 1999; Eichenbaum 2004, 2014). In addition, when rats traverse routes through space, the firing patterns of individual neurons are dependent on which neurons fired before and after, further suggesting sequence coding (Ferbinteanu and Shapiro 2003). Finally, sequences of spatial firing patterns produced during specific experiences are "replayed" during subsequent sleep, consistent with the binding of sequences of firing patterns (e.g., Louie and Wilson 2001), and firing sequences are replayed in anticipation of specific movement paths through space (Pfeiffer and Foster 2013, 2015).

Finally, both the spatial and nonspatial firing patterns of hippocampal neurons are as easily observed in behavioral tasks that do not depend upon the integrity of the hippocampus as they are in situations where the hippocampus is necessary for performance. For example, place cells are as readily observed in rats during random foraging or other spatial tasks without a memory demand, as they are in animals performing a hippocampal-dependent radial maze task. Similarly, nonspatial firing patterns were as robust and as prevalent in hippocampal cells recorded from animals performing classical conditioning or odor discrimination tasks where performance is not disrupted by hippocampal damage as in variants of the same task where hippocampal damage affects performance. Thus both nonspatial and spatial representations by hippocampal neurons are "automatic" in the sense that they arise regardless of whether task performance depends on hippocampal function.

Context

One view of hippocampal function is that the hippocampus represents the context in which specific events occur. What is meant by "context" is not clear, and whether its domain includes spatial and temporal as well as other aspects of the situation in which events occur is also not clear. The data suggests that all aspects of the background context in which specific events occur and when places are occupied can dramatically affect hippocampal neural activity. For example, the spatial firing patterns, and the extent to which firing is dependent on spatial orientation, are dramatically different when a rat forages randomly or produces repeated paths as it traverses an environment (Markus et al. 1995). Notably, as in most all experiments, some cells fire similarly in the two situational contexts, whereas others change dramatically – showing that the hippocampus represents both the commonalities and differences in the two contextually defined situations.

Seemingly subtle changes in environmental cues can also produce dramatic changes in the spatial firing patterns of hippocampal neurons. For example, changes in the background color or background odor of an environment can dramatically change the spatial firing patterns of individual hippocampal neurons (Anderson and Jeffery 2003). As in other studies, in this experiment some cells did not change for each contextual shift, whereas others did. What cues and the extent of situational change that causes alterations in firing patterns is not clear, but several recent studies have examined the dynamics of firing pattern changes when cues are gradually altered. For example, when the shape of an environment is gradually altered (Wills et al. 2005), or critical cues are gradually changed (Rotenberg and Muller 1997), most place cells do not alter their firing patterns initially, but at some level of change, dramatically alter their firing patterns. This sudden switch of firing patterns when a threshold of cue alteration is passed suggests an attractor state dynamic (not unlike that of many other brain areas) in which the contextual representation switches from pattern completion to pattern separation. Area CA3 demonstrates a particularly sharp discrimination gradient in making this switch (Leutgeb et al. 2004; Lee et

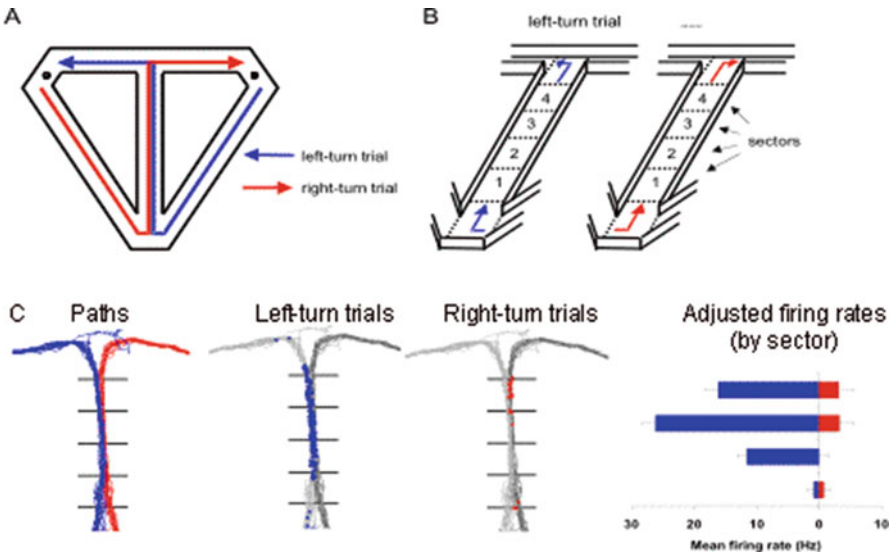

Fig. 5 Hippocampal neuronal activity as rats perform a delayed alternation task. (**a**) Schematic view of the modified T-maze. Rats performed a continuous alternation task in which they traversed the central stem of the apparatus on each trial and then alternated between left and right turns at the T-junction. Reinforcement for correct alternations was provided at water ports (small circles) on the end of each choice arm. The rat returned to the base of the stem via connecting arms and then traversed the central stem again on the next trial. For analysis of neural firing patterns, left turn (blue arrow) and right-turn (red arrow) trials were distinguished. Only trials that involved correct responses were included in the analyses. (**b**) Schematic of the stem of the T-maze indicating divisions of the central portion of the stem into the four sectors used in the data analyses (see below). (**c**) Example of a hippocampal cell that was active when the rat is traversing the central stem of the maze. This cell fired almost exclusively during left-turn trials. The paths taken by the animal are plotted in the left panel (blue, left-turn trial; red, right-turn trial). In the middle panels, the location of the rat when individual spikes occurred is indicated separately for left-turn trials (blue dots on light gray path) and right-turn trials (red dots on dark gray path). In the right panel, the mean firing rate of the cell for each sector (see **b** above) is shown separately for left-turn trials (blue) and right-turn trials (red)

al. 2004). It appears that hippocampal cell assemblies can rapidly switch between spatial representations as animals perform different tasks in the same environment (Fenton et al. 1998; Jackson and Redish 2007).

Several other recent studies have focused on changes in context defined by the behavioral demands of a task and the temporal contexts in which these demands are differentiated. In some of the most productive of these studies, animals traverse multiple overlapping paths such that the common places compose part of different overlapping routes. For example, in several of these studies, rats alternate left- and right-turn routes through a T-maze, where traversal of the stem of the maze is common to both paths (Fig. 5). In this and similar tasks, many hippocampal neurons have distinct firing patterns, even when the rat traverses the common stem depending on whether the rat is performing a left-turn or right-turn trial (Wood et

al. 2000; Frank et al. 2000; Ferbinteanu and Shapiro 2003; Ainge et al. 2007; Bower et al. 2005; Lee et al. 2006; Griffin et al. 2007; Robitsek et al. 2013). Importantly, some cells fire similarly as the rat performs both routes, indicating the hippocampus represents both the distinct paths and the common elements among them. A recent extension on these findings showed that when the alternation task is separated into distinct sample and choice phases, most hippocampal neurons have different spatial firing patterns on the distinct trial phases, and within that, some cells also differentiate the two routes within each phase (Griffin et al. 2007). These data show that different contextual conditions within a complex task are represented distinctly and are linked through representations of their common features by hippocampal neurons.

Additional recent data have shown global shifts in hippocampal firing patterns during the course of events over time, suggesting a representation of temporal context. In one study, as rats performed the T-maze alternation task for 100+ trials, ensembles of simultaneously recorded place fields gradually shifted forward along the maze (Lee et al. 2006). The gradual shifting of the overall spatial representation provided information that could distinguish between sequential trials along the same left-turn or right-turn paths.

In another study, rats were trained to alternate between two ends of a chamber where they sampled a sequence of odors and then were presented with two of the odors in the sequence and asked to judge their order (Fig. 6; Manns et al. 2007). In order to examine whether the firing patterns of hippocampal neurons differentiated the two spatial contexts in which odors were sampled and the temporal context in which odors were sampled within and between trials, small ensembles of hippocampal neurons were recorded around the time of odor sampling on each stimulus presentation in the sequence. The similarity of firing patterns of hippocampal ensembles was measured as the distance between n-dimensional population vectors wherein each dimension was the firing rate of each cell around the odor sampling period. Hippocampal neuronal ensembles differentiated the two sampling locations and gradually changed between odor sampling events, both within the stimulus sequence that composed each trial and across trials within a session. Moreover, the appearance of a substantial change in the contextual representation within trials predicted subsequent success in the judgment about the order of odors, whereas errors were marked by a lack of this temporal context signal. These data strongly suggest that hippocampal neural activity represents a combination of the spatial and temporal context of events both within specific experiences and across experiences over prolonged periods.

Finally, in a study directed at exploring hippocampal representations in context-dependent memory, McKenzie et al. (2014) characterized hippocampal neural activity in a task where rats learned multiple context-dependent object-reward associations. Analyses of single-neuron firing patterns revealed considerable variation in the types of nonspatial and spatial information encoded in hippocampal neural activity patterns, showing that hippocampal neuronal activity in complex tasks is "high dimensional" in the sense that hippocampal neurons exhibit considerable mixed selectivity to multiple relevant nonspatial and spatial dimensions that are

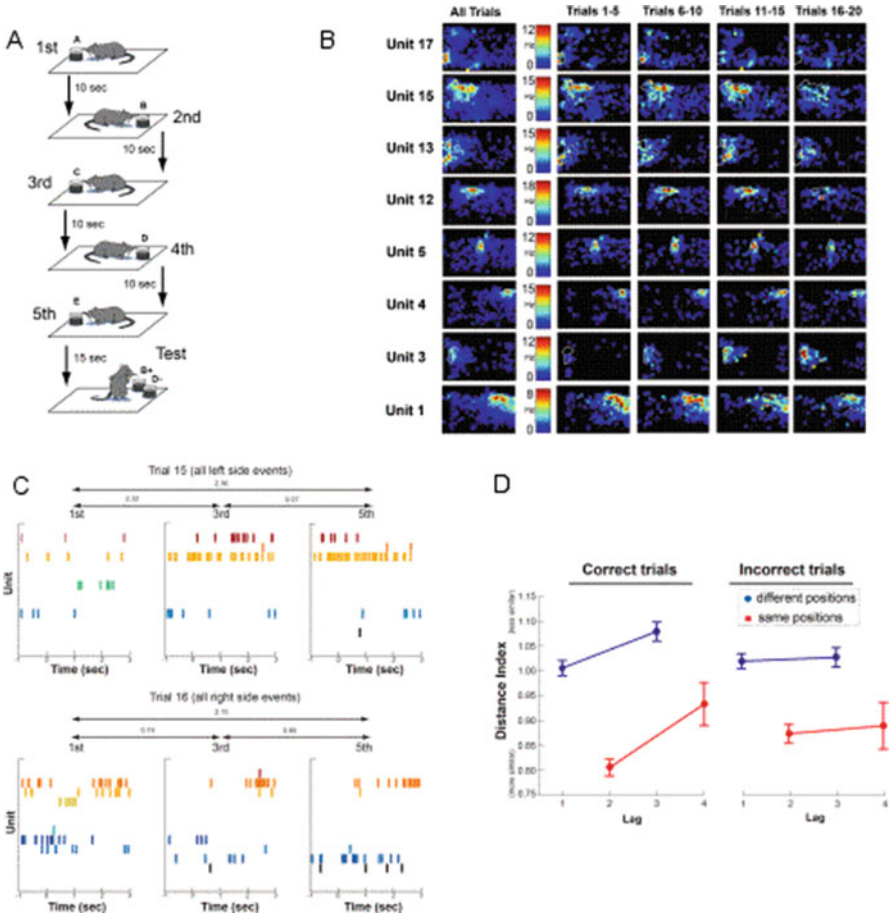

Fig. 6 Representation of temporal context supports memory for the order of a sequence of odors. (**a**). Schematic of the task. On each trial, rats alternated between left and right sides of the enclosure as they encountered a trial-unique sequence of five odors. Rats were then tested with a nonadjacent pair of the odors and were rewarded for selecting the odor that had appeared earlier in the sample sequence. (**b**). Examples of gradual changes in hippocampal place fields across a testing session. Example of hippocampal firing rates as a function of the rat's location in a rectangular testing enclosure for the 8 (out of 18) recorded place cells. The results are shown for the entire test session (leftmost column) and separately for blocks of five trials (rightmost four columns). Note that the firing rate of some cells increases, whereas that for others decreases through the session. (**c**). Example of changes in the pattern of hippocampal activity within a trial. The top row of graphs shows the first, third, and fifth events on trial 15 of this session. Because the rat alternated sides of the testing enclosure, these events all occurred on the left side of the enclosure. The bottom row shows the first, third, and fifth events on trial 16 of the same session. These events all occurred on the right side of the enclosure, and the difference in pattern of activity between the top row and bottom row illustrates the influence of location on the hippocampal ensemble response. The difference between events within a trial illustrates the effect of temporal context on the hippocampal ensemble, and the numbers above the double arrows show an index of the population firing rate distance for the indicated comparison. For both left and right side trials,

salient in a large range of memory tasks, as discussed above. In an effort to understand how these dimensions are organized in hippocampal networks, McKenzie et al. characterized the neural ensemble representations using a representational similarity analysis (RSA) that compared population vectors accumulated during each type of event defined as a particular object in a specific position associated with reward or non-reward value within one of two spatial contexts. The RSA generated correlation coefficients that characterized the similarity of ensemble firing patterns among all pairs of event types. Then a hierarchical clustering analysis was used to determine the pairs of events that were most similar, then iteratively, the combined pairs of events that were most similar, and so on. This analysis revealed a hierarchy of relations among events: Events that involved the different objects of the same value were lowest in the hierarchy and embedded within specific positions. Next, events that involved different values were embedded within positions. Next, events at each position within a context were embedded within each context. Finally, representations of events across contexts were anticorrelated. Thus, hippocampal ensemble represented the identity of the objects, their reward assignments, the positions within a context in which they were experienced, and the context in which they occurred and networked these representations to form a systematic "map" of relations between the different types of memories separated by the spatial context in which they occurred.

Summing Up: The Memory Space Hypothesis

What theoretical framework could capture the broad range of behavioral-related firing patterns of hippocampal neurons – and explain the role of these representations in hippocampal-dependent memory? Some have focused on the place cell phenomenon and its variants observed in areas that are outside of and connected with the hippocampus: head direction cells and grid cells. Combinations of these behavioral firing properties have been used to formulate schemes by which the hippocampus is used in navigation and path integration (e.g., McNaughton et al. 2007). Such narrow formulations fall short of matching the range of memory that relies on hippocampal processing (Squire et al. 2004; Eichenbaum et al. 2007; Eichenbaum 2014; Schiller et al. 2015). On the other hand, memory for routes does provide a good example of the kind of memory that depends on the hippocampus.

Fig. 6 (continued) the firing rate patterns become more different over the trial. (**d**). Similarity of ensemble responses according to temporal lag between odors encountered during the sample phase. Results from odors encountered in the same position (red) are plotted separately from odors encountered in different positions (blue). In addition, results from trials that were subsequently performed correctly are plotted separately from incorrect trials. A lower distance index corresponds to greater similarity of the population firing rates. Note steeper slopes of the lines, indicating greater change in the temporal context signal, on correct trials. (From Manns et al. 2007)

When we remember a spatially extended episode, one recalls a starting point, a series of landmarks and turns in the path one takes, turns examined with thoughts of where they would have led but then rejected, prospects of choices made, and finally what one discovered at the end of the route. Expanding on the example of spatial memories and adding an essential temporal organization component, we employ similar recollective processing to remember the twisting plot of a complex action thriller, the relationships and interactions among characters in a soap opera, and the scientific history and relationships among our own colleagues.

All of these examples highlight three central features in association prominent in the firing properties of hippocampal neurons and hippocampal-dependent memory. First, specific items, persons, and events are represented in the spatial and temporal context in which they occur. This is why spatial representations are both always prominent and strongly dependent on the objects and actions associated with locations. Second, representations of events are bound in sequences that compose distinct episodes. Such time binding explains the dependence of hippocampal representations on past and future events and supports the ability to remember the order of events in experiences. Third, event and episode representations are linked by common features of experience. These "nodal" events are reflected in the firing patterns of hippocampal neurons that are activated for a particular stimulus experienced in many different locations (Fig. 4b; Wood et al. 1999) or object features common to many stimuli (Hampson et al. 2004) or particular people presented in different scenarios (e.g., "Bill Clinton cells"; Kreiman et al. 2000). These nodal representations support our capacity to weave experiences into networks of memories. Remembering routes through the environment, action thrillers, soap operas, and collegial organizations are exceptionally vivid examples of each of these features of memory, and they reflect the fundamental features of declarative memory. The mission of modeling hippocampal function, in the view of this experimentalist, is to explain the mechanisms and structures of the hippocampal memory space and how it interacts with cortical areas to encode and generate the details of declarative memories.

Experimental Techniques

The state-of-the art method for recording the extracellular spike activity of hippocampal neurons involves the tetrode array, a set of independently driven electrodes, each composed of four twisted 12–13 micron-insulated wires gold plated at the exposed surface that is in contact with the brain tissue. Electrodes are connected to a headstage that typically includes a unity gain preamplifier for each wire used to decrease the impedance of the signal to be passed on. Signals are fed through a multiwire cable, often using a commutator to prevent cable twisting, to an A/D converter as the interface to a computer workstation, which digitizes the spike waveforms at high speed (e.g., 30 Khz).

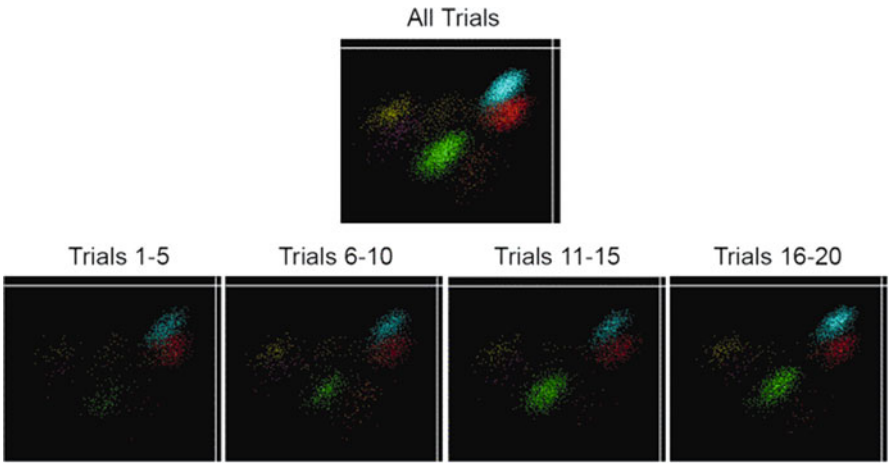

Fig. 7 Example data from one tetrode showing similar projections of spike waveform clusters across quartiles of a recording session in the test of memory for the order of a series of odors. Individual points correspond to neuronal spikes and are colored to represent the different neurons recorded on this tetrode. The Y-axis shows the amplitude of each spike as it was recorded on one wire of the tetrode, and the X-axis shows the amplitude of another wire from the same tetrode. The clusters are similar in each of the session quartiles, indicating that no tetrode movement occurred over the long recording session. (From Manns et al. 2007)

The close spacing of the four individual wires within each tetrode makes it likely that multiple wires will record the activity of a neuron whose cell body or axon is in proximity with the electrode tips. Each channel is likely to differ slightly in distance or area of contact with the neuron resulting in slightly differing waveforms of the action potential from each wire within a tetrode. Furthermore, when a tetrode is driven into a densely packed cell layer, such as found in the pyramidal cell layers of CA1 and CA3, wires are likely to record from several different cells, each characterized by a unique profile of action potential waveforms among the four wires within a tetrode. To isolate individual neurons, software programs compare the amplitude, width, and other parameters of spikes across wires within the tetrode, yielding distinct scatter plots of spike waveform clusters associated with different neurons for each parameter compared (Fig. 7). Each tetrode typically records the activity of up to approximately 6–8 isolatable cells, and tetrode arrays often have as many as 12–14 closely spaced electrodes, providing a realistic capability of simultaneous recording of 50–100+ neurons (Wilson and McNaughton 1993). Tetrodes perform well in recording from pyramidal cells and less well in recording interneurons, presumably because of their smaller cell body size, and success is rare in recording action potentials from dentate granule cells. Tetrodes are also suitable for recording extracellular local field potentials.

Once cells are isolated, spike trains are saved as lists of the time of arrival of spikes along with the onset times of behavioral parameters including task relevant stimuli and behaviors. In many experiments, the position of the animal's head is

also recorded at regular intervals (e.g., 30–60 s) by placing one or more lamps on the head stage and using a camera system to isolate the location of the lamps with the environment in an X-Y coordinate system. The firing rates of individual neurons are typically related to the onset or period of specific events by peri-event histograms (PETHs), and neuronal activity is usually considered related to a stimulus or event if the firing rate is reliably changed just after event onset compared to a baseline period before event onset, as tested with standard parametric statistical methods. Sometimes the selectivity of firing associated with different stimuli or events is characterized by comparing firing rates during specified event periods and testing for reliable differences between multiple repetitions of each different stimulus or event.

Spatial firing patterns are typically assessed by dividing the environment into a two-dimensional array of location pixels of 1–3 cm-sqr. Firing rate for each pixel is calculated as the number of spikes per second occupancy in the pixel. Often firing rates are smoothed by a weighted average of a target pixel and all surrounding pixels. Place fields are usually defined as a set of adjacent pixels that meet a firing rate criterion, e.g., above 1 Hz and 2 SD above the overall average firing rate. Similarity or difference in spatial firing patterns between conditions is typically measured by correlating activity among pixels in a pair of firing rate maps.

A major problem in comparing sensory-behavioral and spatial firing patterns of hippocampal neurons involves technical requirements for collecting data for each type of analysis. To collect multiple samples of recordings during well controlled behavioral events, which is required to assess the statistical reliability sensory-behavioral correlates, one needs to have several repetitions of each discrete event. By contrast, to collect spatial firing patterns independent of behavior, one needs to have the animal occupy all locations in the environment many times in constant or randomly changing behavioral patterns. These demands for data collection in behavioral and spatial characterizations are mutually exclusive and make it impossible to simultaneously determine sensory-behavioral and spatial correlates of activity.

Some of the best examples where both kinds of information have been obtained come from studies where the environment is “linearized,” that is, the animal moves along a narrow track that restricts its movements to one dimension and all locations are automatically occupied as the animal moves along a linear, rectangular, or circular track, and when specific behaviors or stimuli occur at particular locations that can be changed in some way relevant to the task under study. The continuous T-maze alternation task (Fig. 5a) is a particularly successful and productive example of such a protocol. Animals move throughout the maze every other trial, alternating left-turn and right-turn routes that overlap in the maze stem, and firing patterns associated with past or future locations and accuracy of decisions can readily be determined. Several variants on this task have provided opportunities to study many aspects of memory, movement, and decision processes.

The Future

The near future will surely bring continued investigation of potential differences in the spatial- and behavior-related firing patterns of neurons in different subfields and along the dorsal-ventral axis of the hippocampus as well as in the structures that send inputs into and receive the outputs of neurons in the hippocampus. Progress in providing sufficient information for constructing models of the functional microcircuitry of the hippocampus surely depends on characterizations of the major cell types in all the hippocampal subfields and areas to which they are connected. In addition, we have only begun to scratch the surface of characterizing the time series of firing patterns, particularly in relation to local rhythmic activity that can be recorded along with spikes.

Another dilemma that has to be resolved is how to combine the prevalence and ease of recording spatial firing patterns with the need to relate firing patterns to the kinds of learning and memory that are dependent on hippocampal function. Because it is so difficult to align electrodes to record from large numbers of neurons simultaneously, many of the best recording studies have maximized recording yield by minimizing the concurrent demands of the behavioral task. In many of these studies, the behavior is trivialized to asking the rat to merely find food scattered in the environment. Experimenters assume that learning occurs when this behavior is executed under conditions of novel environmental stimuli, but the protocol lacks any metric or evidence that learning has actually occurred or when it occurred. This strategy severely limits the extent and precision to which firing patterns can be linked to memory processes. Ultimately, methods must be found to maximize the recording yield while incorporating sufficient behavioral content to allow meaningful interpretation of the observed firing patterns.

Another challenge for the longer range future will be to isolate where within the hippocampus, particular sensory, behavioral, or spatial firing patterns arise. Because subfields and components of the hippocampal region are highly interconnected, it can be expected that firing patterns that reflect a specific aspect of memory processing will be projected to several other closely connected areas. In order to localize the origins of particular firing patterns, new advances will be required to record from specific hippocampal subfields while the activity in other subfields is silenced, and preferably the silencing can be reversible so that activity patterns can be compared in intact versus disconnected conditions.

The long range future of recording behavior-related firing patterns in the hippocampus is bright, despite the above-described challenges. Activity patterns of hippocampal neurons provide a crucial bridge between cellular plasticity phenomena, local and global circuitry, overt behavior, and cognition. This bridge will be required to show how intracellular processes and microcircuit connectivity leads to functional activity of the information processing units that generate behavior.

References

Ainge JA, Tamosiunaite M, Woergoetter F, Dudchencko PA (2007) Hippocampal CA1 place cells encode intended destination on a maze with multiple choice points. J Neurosci 27:9769–9779

Anderson MI, Jeffery KJ (2003) Heterogeneous modulation of place cell firing by changes in context. J Neurosci 23:8827–8835

Bar M, Aminoff E (2003) Cortical analysis of visual context. Neuron 38:347–358

Bower MR, Euston DR, McNaughton BL (2005) Sequential-context dependent hippocampal activity is not necessary to learn sequences with repeated elements. J Neurosci 15:1313–1323

Brown MW, Aggleton JP (2001) Recognition memory: what are the roles of the perirhinal cortex and hippocampus? Nat Rev Neuroscience 2:51–61

Brown MW, Xiang JZ (1998) Recognition memory: neuronal substrates of the judgment of prior occurrence. Prog Neurobiol 55:149–189

Burwell RD (2000) The parahippocampal region: corticocortical connectivity. Ann N Y Acad Sci 911:25–42

Eichenbaum H (2000) A cortical-hippocampal system for declarative memory. Nat Rev Neurosci 1:41–50

Eichenbaum H (2004) Hippocampus: cognitive processes and neural representations that underlie declarative memory. Neuron 44:109–120

Eichenbaum H (2013) Memory on time. Trends Cogn Sci 17:81–88

Eichenbaum H (2014) Time cells in the hippocampus: a new dimension for mapping memories. Nat Rev Neurosci 15:732–744

Eichenbaum H, Otto T, Cohen NJ (1994) Two functional components of the hippocampal memory system. Brain Behav Sci 17:449–518

Eichenbaum H, Dudchencko P, Wood E, Shapiro M, Tanila H (1999) The Hippocampus memory, and place cells: is it spatial memory or a memory space? Neuron 23:209–226

Eichenbaum H, Yonelinas AR, Ranganath C (2007) The medial temporal lobe and recognition memory. Annu Rev Neurosci 20:123–152

Epstein R, Kanwisher N (1998) A cortical representation of the local visual environment. Nature 392:598–601

Fenton AA, Wsierska M, Kaminsky Y, Bures J (1998) Both here and there: simultaneous expression of autonomous spatial memories in rats. PNAS USA 95:11493–11,498

Ferbinteanu J, Shapiro ML (2003) Prospective and retrospective memory coding in the hippocampus. Neuron 40:1227–1239

Frank L, Brown EN, Wilson M (2000) Trajectory encoding in the hippocampus and entorhinal cortex. Neuron 27:169–178

Fyhn M, Molden S, Hollup S, Moser M-B, Moser EI (2002) Hippocampal neurons responding to first-time dislocation of a target object. Neuron 35:555–566

Fyhn M, Molden S, Witter MP, Moser EI, Moser M-B (2004) Spatial representation in the entorhinal cortex. Science 305:1258–1264

Gelbard-Sagiv H, Mukamel R, Harel M, Malach R, Fried I (2008) Internally generated reactivation of single neurons in human hippocampus during free recall. Science 322:96–101

Gill PR, Mizumori SJ, Smith DM (2011) Hippocampal episode fields develop with learning. Hippocampus 21:1240–1249

Gothard KM, Skaggs WE, Moore KM, McNaughton BL (1996a) Binding of hippocampal CA1 neural activity to multiple reference frames in a landmark-based navigation task. J Neurosci 16:823–835

Gothard KM, Skaggs W, McNaughton BL (1996b) Dynamics of mismatch correction in the hippocampal ensemble code for space: interaction between path integration and environmental cues. J Neurosci 16:8027–8040

Griffin AL, Eichenbaum H, Hasselmo ME (2007) Spatial representations of hippocampal CA1 neurons are modulated by behavioral context in a hippocampus-dependent memory task. J Neurosci 27:2416–2423

Hampson RE, Pons TP, Stanford TR, Deadwyler SA (2004) Categorization in the monkey hippocampus: a possible mechanism for encoding information into memory. PNAS USA 101:3184–3189

Hargreaves EL, Rao G, Lee I, Knierim JJ (2005) Major dissociation between medial and lateral entorhinal input to dorsal hippocampus. Science 5729:1792–1794

Hok V, Lenck-Santini P-P, Roux S, Save E, Muller RU, Poucet B (2007) Goal-related activity in hippocampal place cells. J Neurosci 27:472–482

Hollup SA, Molden S, Donnett JG, Moser M-B, Moser EI (2001) Accumulation of hippocampal place fields at the goal location in an annular watermaze task. J Neurosci 21:1635–1644

Howard MW, Eichenbaum H (2013) The hippocampus, time, and memory across scales. J Exp Psychol Gen 142:1211–1230

Hsieh LT, Gruber MJ, Jenkins LJ, Ranganath C (2014) Hippocampal activity patterns carry information about objects in temporal context. Neuron 81:1165–1178

Itskov PM, Vinnik E, Diamond ME (2011) Hippocampal representation of touch-guided behavior in rats: persistent and independent traces of stimulus and reward location. PLoS One 6(1):e16462. https://doi.org/10.1371/journal.pone.0016462

Itskov PM, Vinnik E, Honey C, Schnupp J, Diamond ME (2012) Sound sensitivity of neurons in rat hippocampus during performance of a sound-guided task. J Neurophysiol 107:1822–1834

Jackson J, Redish AD (2007) Network dynamics of hippocampal cell assemblies resemble multiple spatial maps within single trials. Hippocampus 17(12):1209–1229

Komorowski RW, Manns JR, Eichenbaum H (2009) Robust conjunctive item-place coding by hippocampal neurons parallels learning what happens. J Neurosci 29:9918–9929

Kraus BJ, Robinson RJ II, White JA, Eichenbaum H, Hasselmo ME (2013) Hippocampal 'time cells': time versus path integration. Neuron 78:1090–1101

Kraus BJ, Brandon MP, Robinson RJ 2nd, Connerney MA, Hasselmo ME, Eichenbaum H (2015) During running in place, grid cells integrate elapsed time and distance run. Neuron 88:578–589

Kreiman G, Koch C, Fried I (2000) Category-specific visual responses of single neurons in the human medial temporal lobe. Nat Neurosci 3:946–953

Lee I, Yoganarasimha D, Rao G, Knierim JJ (2004) Comparison of population coherence of place cells in hippocampal subfields CA1 and CA3. Nature 430:456–459

Lee I, Griffin AL, Zilli EA, Eichenbaum H, Hasselmo M (2006) Gradual translocation of spatial correlates of neuronal firing in the hippocampus toward prospective reward locations. Neuron 51:539–650

Leutgeb S, Leutgeb JK, Treves A, Moser M-B, Moser EI (2004) Distinct ensemble codes in hippocampal areas CA3 and CA1. Science 305:1295–1298

Leutgeb S, Leutgeb JK, Barnes CA, Moser EI, McNaughton BL, Moser M-B (2005a) Independent codes for spatial and episodic memory in hippocampal neuronal ensembles. Science 309:619–623

Leutgeb S, Leutgeb JK, Moser M-B, Moser EI (2005b) Place cells, spatial maps, and the population code for memory. Curr Opin Neurobiol 15:1–9

Levy WB (1989) A Computational approach to hippocampal function. In: Hawkins RD, Bowers GH (eds) Computational models of learning in simple neural systems. Academic, San Diego, pp 243–305

Lipton PA, White J, Eichenbaum H (2007) Disambiguation of overlapping experiences by neurons the medial entorhinal cortex. J Neurosci 27:5787–5795

Louie K, Wilson MA (2001) Temporally structured replay of awake hippocampal ensemble activity during rapid eye movement sleep. Neuron 29:145–156

MacDonald CJ, Lepage KQ, Eden UT, Eichenbaum H (2011) Hippocampal "time cells" bridge the gap in memory for discontiguous events. Neuron 71:737–749

MacDonald CJ, Carrow S, Place R, Eichenbaum H (2013) Distinct hippocampal time cell sequences represent odor memories in immobilized rats. J Neurosci 33:14607–14,616

Manns JR, Eichenbaum H (2006) Evolution of the hippocampus. In: Kaas JH (ed) Evolution of nervous systems, vol 3. Academic, Oxford, pp 465–490

Manns JR, Howard M, Eichenbaum H (2007) Gradual changes in hippocampal activity support remembering the order of events. Neuron 56:530–540
Markus EJ, Qin Y-L, Leonard B, Skaggs WE, McNaughton BL, Barnes CA (1995) Interactions between location and task affect the spatial and directional firing of hippocampal neurons. J Neurosci 15:7079–7094
McKenzie S, Frank AJ, Kinsky NR, Porter B, Rivière PD, Eichenbaum H (2014) Hippocampal representation of related and opposing memories develop within distinct, hierarchically-organized neural schemas. Neuron 83:202–215
McNaughton BL, Chen L, Markus EJ (1991) "Dead reckoning", landmark learning, and the sense of direction: a neurophysiological and computational hypothesis. J Cogn Neurosci 3:190–202
McNaughton BL, Battaglia FP, Jensen O, Moser EI, Moser M-B (2007) Path integration and the neural basis of the 'cognitive map'. Nat Rev Neurosci 7:663–678
Modi MN, Dhawale AK, Bhalla US (2014) CA1 cell activity sequences emerge after reorganization of network correlation structure during associative learning. elife 3:e01982
Moita MA, Rosis S, Zhou Y, LeDoux JE, Blair HT (2003) Hippocampal place cells acquire location-specific responses to the conditioned stimulus during auditory fear conditioning. Neuron 37:485–497
Muller RU (1996) A quarter of a century of place cells. Neuron 17:813–822
Muller RU, Kubie JL, Ranck JB Jr (1987) Spatial firing patterns of hippocampal complex spike cells in a fixed environment. J Neurosci 7:1935–1950
Naya Y, Suzuki WA (2011) Integrating what and when across the primate medial temporal lobe. Science 333:773–776
O'Keefe JA (1979) A review of hippocampal place cells. Prog Neurobiol 13:419–439
O'Keefe J, Burgess N (1996) Geometric determinants of the place fields of hippocampal neurons. Nature 381:425–428
Olton DS, Branch M, Best PJ (1978) Spatial correlates hippocampal unit activity. Exp Neurol 58:387–409
Pastalkova E, Itskov V, Amarasingham A, Buzsaki G (2008) Internally generated cell assembly sequences in the rat hippocampus. Science 321(5894):1322–1327
Paz R, Gelbard-Sagiv H, Mukamel R, Harel M, Malach R, Fried I (2010) A neural substrate in the human hippocampus for linking successive events. Proc Natl Acad Sci U S A 107:6046–6051
Pfeiffer BE, Foster DJ (2013) Hippocampal place cell sequences depict future paths to remembered goals. Nature 497:74–79
Pfeiffer BE, Foster DJ (2015) Autoassociative dynamics in the generation of sequences of hippocampal place cells. Science 349:180–183
Rawlins JNP (1985) Associations across time: The hippocampus as a temporary memory store. Behav Brain Sci 8:479–496
Rivard B, Li Y, Lenck-Santini P-P, Poucet B, Muller RU (2004) Representation of objects in space by two classes of hippocampal pyramidal cells. J Gen Physiol 124:9–25
Robitsek JR, White J, Eichenbaum H (2013) Place cell activation predicts subsequent memory. Behav Brain Res 254:65–72
Rotenberg A, Muller RU (1997) Variable place-cell coupling to a continuously viewed stimulus: evidence that the hippocampus acts as a perceptual system. Philos Trans R Soc Lond B 352:1505–1513
Sargolini F, Fyhn M, Hafting T, McNaughton BL, Witter MP, Moser M-B, Moser EI (2006) Conjunctive representation of position, direction, and velocity in entorhinal cortex. Science 312:758–762
Schiller D, Eichenbaum H, Buffalo EA, Davachi L, Foster DJ, Leutgeb S, Ranganath C (2015) Memory and space: towards an understanding of the cognitive map. J Neurosci 35:13904–13,911
Shapiro ML, Tanila H, Eichenbaum H (1997) Cues that hippocampal place cells encode: Dynamic and hierarchical representation of local and distal stimuli. Hippocampus 7:624–642
Skaggs WE, McNaughton BL (1998) Spatial firing properties of hippocampal CA1 populations in an environment containing two visually identical regions. J Neurosci 18:8455–8466

Squire LR, Stark CE, Clark RE (2004) The medial temporal lobe. Annu Rev Neurosci 27:279–306
Suzuki WA, Amaral DG (1994) Perirhinal and parahippocampal cortices of the macaque monkey: cortical afferents. J Comp Neurol 350:497–533
Suzuki W, Eichenbaum H (2000) The neurophysiology of memory. Ann N Y Acad Sci 911:175–191
Tanila H, Shapiro M, Gallagher M, Eichenbaum H (1997a) Brain Aging: impaired coding of novel environmental cues. J Neurosci 17:5167–5174
Tanila H, Shapiro ML, Eichenbaum H (1997b) Discordance of spatial representation in ensembles of hippocampal place cells. Hippocampus 7:613–623
Tanila H, Sipila P, Shapiro M, Eichenbaum H (1997c) Brain aging: changes in the nature of information coding by the hippocampus. J Neurosci 17:5155–5166
Tulving E (1983) Elements of episodic memory. Oxford Univ Press, New York
Vinnik E, Antopolskiy S, Itskov PM, Diamond ME (2012) Auditory stimuli elicit hippocampal neuronal responses during sleep. Front Syst Neurosci 6:49
Wallenstein GV, Eichenbaum H, Hasselmo ME (1998) The hippocampus as an associator of discontiguous events. Trends Neurosci 21:315–365
Wan H, Aggleton JP, Brown MW (1999) Different contributions of the hippocampus and perirhinal cortex to recognition memory. J Neurosci 19:1142–1148
Wills TJ, Lever C, Cacucci F, Burgess N, O'Keefe J (2005) Attractor dynamics in the hippocampal representation of the local environment. Science 308:873–876
Wilson M, McNaughton BL (1993) Dynamics of the hippocampal ensemble code for space. Science 261:1055–1058
Wirth S, Yanike M, Frank LM, Smith AC, Brown EN, Suzuki WA (2003) Single neurons in the monkey hippocampus and learning of new associations. Science 300:1578–1581
Wood E, Dudchenko PA, Eichenbaum H (1999) The global record of memory in hippocampal neuronal activity. Nature 397:613–616
Wood E, Dudchenko P, Robitsek JR, Eichenbaum H (2000) Hippocampal neurons encode information about different types of memory episodes occurring in the same location. Neuron 27:623–633

Part II
Computational Analysis

Vassilis Cutsuridis and Bruce P. Graham

In the **Experimental Background** part, leading experimental neuroscientists discussed the morphological, physiological and molecular characteristics as well as the connectivity and synaptic properties of the various cell types found in the hippocampus. Behaviour-related ensemble activity patterns of morphologically identified neurons in anaesthetized and freely moving animals provided insights into the functions of the hippocampal areas. However, this accumulation of knowledge about the neural components (e.g. genes, molecules, synapses, dendrites, single neurons and networks) does not in itself provide conclusive insight into the computations performed in different hippocampal areas. Mathematical and computational modelling and analysis play an instrumental role in exploring these computations. They allow the synthesis of experimental data from different levels of complexity into a coherent picture of the system under study.

In this part, leading computational neuroscientists present models of the hippocampus at various levels of detail (molecular, synaptic, single cell and network). These models make use of the knowledge presented in the **Experimental Background** part to discuss the overall global function of hippocampal microcircuits (in areas CA1, CA3, dentate gyrus and entorhinal cortex). Synaptomics and connectomics models of hippocampal structures are initially discussed. Then, network models of memory, rhythm generation and spatial navigation are presented, followed by abstract and biophysical models of synaptic plasticity. Network models of hippocampal implicated disorders (epilepsy and schizophrenia) are then detailed, and how their network topologies, connectivities and activities change in these

V. Cutsuridis
School of Computer Science, University of Lincoln, Lincoln, UK
e-mail: vcutsuridis@lincoln.ac.uk

B. P. Graham
Department of Computing Science and Mathematics, University of Stirling, Stirling, UK
e-mail: b.graham@cs.stir.ac.uk

diseases are discussed. Finally, two chapters are dedicated to describing simulator environments of single neurons and networks currently used by computational neuroscientists in developing their models and modelling tools to parametrically constrain them.

In chapter "Systematic Data Mining of Hippocampal Synaptic Properties", Moradi and Ascoli describe a systematic approach to identify, interpret, extract, normalize, infer and finally model synaptic electrophysiology. First, they introduce the Hippocampome.org circuitry model, describe the relevant synaptic parameters and succinctly review the sources of experimental measurements. Then, they outline the conceptual organization of the available electrophysiological data, offer illustrations of proper and fuzzy empirical evidence and provide an interim summary of the ongoing literature mining effort. The implementation requirements in terms of data integration and simulation, namely, covariate analysis and uniform parameter normalization, inferential estimations of likely parameter ranges for missing data and computational models of synaptic amplitude, kinetics and plasticity, are then presented. With a closing part they provide a succinct outlook on future directions.

In chapter "Spatio-Temporal Patterns of Granule Cell Activity Revealed by a Large-Scale, Biologically Realistic Model of the Hippocampal Dentate Gyrus", Yu, Hendrickson, Song and Berger propose a computational framework able to integrate the majority of available, quantitative structural and functional information at various levels of organization to generate a large-scale, biologically realistic, neural network model with the goal of representing all of the major neurons and neuron types, and the synaptic connectivity, found in one hemisphere of the rat dentate gyrus. Detailed excitatory and inhibitory neuron models constructed using multi-compartment approaches (on the order of hundreds of compartments per neuron) are then geometrically arranged based on anatomical data to encompass the entire longitudinal extent of the hippocampus and finally synaptically connected using the topographical constraints describing the region. Through a series of simulations are performed which primarily explore the role of network architecture on the spatiotemporal patterns of activity generated by populations of granule cells in the dentate gyrus. The simulations show specifically that the topographical projection of axons between the entorhinal cortex and the dentate granule cell regions of the hippocampal formation acts as a spatial filter which organizes the postsynaptic population into subgroups of neurons that exhibit correlated firing expressed as spatiotemporal clusters of firing.

In chapter "A Model of Spatial Reach in LFP Recordings", Lindén, Tetzlaff, Łeski, Pettersen, Grün, Diesmann and Einevoll describe a model of LFP generation that considers how population geometry, single-cell features and population-level correlations determine the size of the region generating the LFP measured in the centre of a neuronal population. The model assumes passive dendrites and considers LFPs due to synaptic currents and the associated return currents. Discussions on how to model the spatial decay outside the active neuronal population which, in turn, may help to understand the relative LFP contributions from simultaneously active neuronal populations are also provided.

In chapter "Models of Rate and Phase Coding of Place Cells in Hippocampal Microcircuits", Cutsuridis presents four computer models of place cell rate and phase coding in hippocampal microcircuits in order to explore the mechanisms by which both coding schemes are generated and/or maintained in these microcircuits. Of crucial importance in these models is how theta-modulated inhibition interacts with synaptic plasticity in order to preserve the rate and phase coding properties of place cells in the CA1 microcircuits.

In chapter "A Model for Grid Firing and Theta-Nested Gamma Oscillations in Layer 2 of the Medial Entorhinal Cortex", Nolan presents a computational model of layer 2 of the entorhinal cortex. The model addresses the general question of whether layer 2 stellate cells and their indirect interactions through inhibitory interneurons are sufficient to account for grid firing or nested gamma oscillations.

In chapter "Computational Models of Grid Cell Firing", Bush and Schmidt-Hieber describe implementations of two classes of grid cell models – the oscillatory interference and the continuous attractor dynamics – alongside a hybrid model that incorporates the principal features of each. Discussions of the strengths and weaknesses of each model and the predictions they make for future experimental manipulations of the grid cell network in vivo are provided.

In chapter "Modeling Synaptic Plasticity in Hippocampus: A Calcium-Based Approach", Graupner and Brunel discuss a biologically plausible but simplified calcium-based model that provides links between stimulation protocols, calcium transients, protein signalling cascades and evoked synaptic changes. The model implements two opposing calcium-triggered pathways mediating increases of synaptic strength (LTP, i.e. protein kinase cascades) and decreases of synaptic strength (LTD, i.e. protein phosphatase cascades or G-protein cascades). The model accounts for a wide range of experimental plasticity outcomes in hippocampal cultures and hippocampal slices. Quantitative fitting of the experimental data allowed to predict differences in the underlying calcium dynamics between these different experimental systems. The model further predicted plasticity outcomes in response to more realistic activity patterns such as uncorrelated pre- and postsynaptic Poisson firing.

In chapter "Simplified Compartmental Models of CA1 Pyramidal Cells of Theta–Modulated Inhibition Effects on Spike Timing-Dependent Plasticity", Cutsuridis presents two simplified compartmental models of a CA1 pyramidal cell in order to investigate the role of theta-modulated inhibition on the shape, sign and magnitude of the spike-timing-dependent plasticity (STDP) kernel in its proximal dendrites.

In chapter "Factors Affecting STDP in the Dendrites of CA1 Pyramidal Cells", Saudargiene and Graham propose a biophysically complex microcircuit model of region CA1 in order to explore the synaptic plasticity outcomes at excitatory synapses on CA1 PC dendrites in response to experimentally used in vitro and behaviourally relevant in vivo stimulation patterns. The first study aimed to replicate the in vitro experiments of Wittenberg and Wang (2006) that demonstrated the importance of stimulus timing and repetition on plasticity outcomes. The second study aimed to study calcium-based plasticity in a spine head as a function of the

timing of synaptic stimulation relative to ongoing theta-modulated activity in the CA1 circuit.

In chapter "Computational Examination of Synaptic Plasticity and Metaplasticity in Hippocampal Dentate Granule Neurons", Shirrafiardekani and Moustafa present a nine-compartmental model of a granule cell to examine how STDP and metaplasticity contribute to the induction of homosynaptic LTP and concurrent heterosynaptic LTD, to investigate the role of noisy spontaneous activity in producing heterosynaptic LTD in the lateral perforant pathway (LPP) and to present the metaplasticity impact of the first medial HFS on synaptic plasticity produced by the second HFS.

In chapter "Genome-Wide Associations of Schizophrenia Studied with Computer Simulation", Neymotin, Sherif, Jung, Kabariti and Lytton using multiscale modelling explored changes in theta and gamma activity in hippocampal area CA3 in order to investigate how changes in ion channels at molecular scale will alter network activity. They showed how anomalies in brain waves can be correlated with explicit alterations in information ow (measured using information theory) and thereby could help explain alterations in cognitive function.

In chapter "Modelling Epileptic Activity in Hippocampal CA3", Sanjay and Krothapalli present an in silico model of the CA3 subfield of hippocampus to investigate the role of changes in neuronal connectivity in the epileptic activity generation in area CA3. They focus on the loss of dendritic inhibition leading to sprouting in pyramidal cell dendrites and increased pyramidal cell excitability, which in turn lead to epileptic activity generation.

In chapter "A Network Model Reveals That the Experimentally Observed Switch of the Granule Cell Phenotype During Epilepsy Can Maintain the Pattern Separation Function of the Dentate Gyrus", Hanuschkin, Yim and Wolfart discuss the development of a conductance-based network model of the dentate gyrus to investigate the experimentally constrained homeostatic adaptations of its intrinsic neuronal properties in order to restore its pattern separation ability if it is lost during epileptic excitability.

In chapter "Resources for Modeling in Computational Neuroscience", Birgiolas, Crook and Gerkin outline some of the most widely used software applications for simulating neural models at various levels of biological detail. They also describe resources that aid in reproducibility by allowing for model sharing and reusing, for portability of models across simulation platforms and for validation of models against experimental data.

In the final chapter (chapter "Experiment-Modelling Cycling with Populations of Multi-compartment Models: Application to Hippocampal Interneurons"), Sekulic and Skinner propose a cycling approach using experimental data as constraints for building populations of multi-compartment models (Sekulić et al. 2014). These models collectively capture a range of ion channel expression patterns that underlie cell-type appropriate model output. Constraints on model parameters variations, e.g. channel conductances, allow modelled cells to generate the desired output. The predicted intrinsic property balances for functional outputs of the neuronal cell types in question can then be examined with targeted experiments.

Systematic Data Mining of Hippocampal Synaptic Properties

Keivan Moradi and Giorgio A. Ascoli

Abstract Synaptic electrophysiology has been extensively investigated in the rodent hippocampal formation for several decades. The strength, duration, and plasticity of excitatory and inhibitory signals depend both on the presynaptic and postsynaptic neuron types and vary substantially among subregions (dentate gyrus, CA3, CA2, CA1, subiculum, and entorhinal cortex) and layers (e.g., oriens and radiatum). While certain connections are better characterized (e.g., the Schaffer collateral from CA3 pyramidal to CA1 pyramidal cells), the lack of a systematic accounting of published synaptic data prevents a comprehensive comparison across the whole circuit. Hippocampome.org, a knowledge base that identified over 100 neuron types based on morphological, electrophysiological, and molecular evidence, enables integration and dense coverage of the available synaptic data. Peters' Rule predicts more than 3000 "potential connections" among neuron types. Extensive literature mining revealed electrophysiological properties for approximately 50% of these potential synapses at neuron-type level in peer-reviewed publications. In these cases, we extract information about synaptic amplitude, kinetics, and, when available, short-term and long-term plasticity. Due to widely nonuniform experimental methods and conditions, these data must be normalized and modeled to enable meaningful quantifications. The resulting type-based organized and integrated data will facilitate large-scale data-driven simulations of the entire hippocampal formation.

Introduction

The mammalian hippocampus constitutes one of the most intensively studied neural systems. Abundant evidence crucially implicates the hippocampal formation in the consolidation and retrieval of episodic memories as well as in goal-oriented

K. Moradi · G. A. Ascoli (✉)
Krasnow Institute for Advanced Study, George Mason University, Fairfax, VA, USA
e-mail: ascoli@gmu.edu

V. Cutsuridis et al. (eds.), *Hippocampal Microcircuits*, Springer Series in Computational Neuroscience, https://doi.org/10.1007/978-3-319-99103-0_11

navigation. The basic organization of the hippocampal circuit has been known for over a century, and a wealth of information exists about the morphology, electrophysiology, and biochemistry of its neurons. Yet, a convincing explanation of the cognitive functions of the hippocampus in terms of detailed cellular and network mechanisms remains elusive.

Continuous growth in computing power makes it feasible to create a real-scale, real-time, biologically faithful simulations of hippocampus information processing at the level of individual spikes. Such a computational model could greatly accelerate progress toward a deep and comprehensive understanding of hippocampal function, further guiding experimental investigations. Designing a large-scale anatomically and electrophysiologically realistic neural network model of the hippocampus requires tight interactions with and proper support from an adequately populated and continuously updated database containing the definition of neuron types and their properties.

Since the advent of artificial neural networks, innumerable computational models of the hippocampal formation have been built. The vast majority of these models, however, greatly simplify the diversity of neuron types. Several models, for instance, are limited to the principal cell excitatory backbone of the circuit, finessing the inhibitory GABAergic connections. A complementary category of models includes the local principal cell and a subset of GABAergic interneurons (e.g., CA1 pyramidal cells, fast-spiking basket cells, bistratified cells, and oriens/lacunosum-moleculare cells) without including the entire extent of the hippocampal network. The few attempts at simulating real-scale hippocampal circuitry have been so far restricted to relatively data-richer subregions such as CA1 (Bezaire and Soltesz 2013) and DG (Schneider et al. 2012; Santhakumar et al. 2005) or had to greatly sacrifice biophysical accuracy and diversity (Scorcioni et al. 2008).

Given the considerable accumulation of data about hippocampal neuron types and their properties in the past two decades (e.g., Freund and Buzsaki 1996; Houser 2007; Klausberger 2009; Chamberland and Topolnik 2012; Somogyi and Klausberger 2005; Wester and McBain 2014; Canto and Witter 2012a, b), it is tempting to assume that a critical mass of information may now (or will soon) be available to draft a real-scale, biophysically and anatomically detailed neuron-level model of the complete rodent hippocampal formation, including dentate gyrus (DG); areas CA3, CA2, and CA1; subiculum; and entorhinal cortex. For example, more than 122 neuron types of the rodent hippocampus have been recently classified in terms of morphological patterns, electrophysiological characteristics, and molecular features (Wheeler et al. 2015).

Planning for such real-scale modeling efforts immediately reveals one particular informational bottleneck, namely, the methodical quantification of synaptic properties. The problem already becomes apparent at the simple numerical level: because synaptic signals vary with the identity of both pre- and postsynaptic neurons, a network with N neuron types contains of the order of up to N^2 distinct synaptic types. Moreover, while the properties of individual neurons can be investigated by traditional single-cell recording, interrogating specific synaptic types requires the much more challenging dual recording of identified neuronal pairs. As a result,

none of the available systematic reviews on hippocampal neurons is sufficiently comprehensive in terms of synaptic electrophysiology data to even remotely constraint real-scale models. Even in the most detailed modeling efforts to date (e.g., Santhakumar et al. 2005), the parameters quantifying synaptic electrophysiology (limited to a single table) are only loosely linked to the corresponding neuron types.

Some science historians believe that the theory of synapse has developed gradually over 18 centuries (Bennett 1999). In rodent hippocampus, the first synaptic signals were experimentally recorded starting in the late 1950s (Andersen 1959, 1960; Andersen et al. 1963; Kandel et al. 1961; Spencer and Kandel 1961). Since then countless papers have been published on hippocampal synaptic physiology, including seminal discoveries of most types of synaptic plasticity. Only a minute fraction of the publications that provide information about synaptic electrophysiology, however, are linkable to unequivocally identifiable neuron types. Nevertheless, in as much as we know no systematic literature mining effort has been organized to date for creating a database of model-ready synaptic parameters in the hippocampal formation similar to parallel projects for the neocortex (Markram et al. 2015). Thus we present a plan to create a comprehensive knowledge base of hippocampal synaptic electrophysiology for the modeling community.

Synaptic Informatics

The long-term goal of this project is to provide all necessary building blocks to create a real-scale spiking model of the rodent hippocampal formation. Although knowledge of neuron types abounds, a corresponding accounting of the electrophysiological properties of synapses is still missing. To generate biologically plausible and meaningful predictions from such a neuronal network model, it is essential to constrain the synaptic parameters based on existing experimental evidence or based on inferential knowledge if the required data are missing. This chapter describes a systematic approach to identify, interpret, extract, normalize, infer, and finally model synaptic electrophysiology.

The remaining of the chapter is organized as follows. The present section briefly introduces the Hippocampome.org circuitry model (section "Circuitry model"), describes the relevant synaptic parameters (section "Synaptic parameters"), and succinctly reviews the sources of experimental measurements (section "Sources of data"). The next section outlines the conceptual organization of the available electrophysiological data, offering illustrations of proper (section "Evidence proper") and fuzzy (section "Fuzzy evidence") empirical evidence and providing an interim summary of the ongoing literature mining effort (section "Integrated summary"). The following section describes the implementation requirements in terms of data integration and simulation, namely covariate analysis and uniform parameter normalization (section "Covariates and data normalization"), inferential estimations of likely parameter ranges for missing data (section "Inferential data"),

and computational models of synaptic amplitude, kinetics, and plasticity (section "Models of synapses"). The closing section provides a succinct outlook on future directions (section "Future directions").

Circuitry Model

The conceptual foundation of the envisioned real-scale simulation of hippocampal computation is grounded in the notion of neuron type (Bota and Swanson 2007). In this framework, the building blocks of the network are neuron types, and the synaptic circuitry can be described in terms of connectivity between neuron types. To map the synaptic properties of the hippocampal formation, we leverage the recent release of Hippocampome.org, a knowledge base of morphology, biomarkers, cellular electrophysiology, and connectivity of 122 hippocampal neuronal types in the rodent DG, areas CA3, CA2, CA1, subiculum, and entorhinal cortex (Wheeler et al. 2015).

If all the hippocampal neuron types were connected to each other, nearly 15,000 connection types (122×122) would exist. Anatomical constraints and circuit selectivity, however, considerably reduce the number of possible connections in the hippocampal formation. First and foremost, if the axons of one neuron type and the dendrites of another type are completely segregated in non-overlapping subregions and layers, the former cannot form a potential connection with the latter (Reimann et al. 2015). Connectivity of nearly 80% of the neuron type pairs in the hippocampus can be excluded on these grounds alone. More subtle rules of synaptic specificity further (if slightly) reduce the set of possible connected neuron type pairs: for instance, Interneuron Specific interneurons selectively target GABAergic neurons, whereas chandelier cells exclusively target the axonal initial segment of glutamatergic neurons.

Based on these considerations, the 122 cell types of Hippocampome.org give rise to 3289 potential synaptic types (Fig. 1), of which 1218 (37%) excitatory and 2071 (63%) inhibitory. Most of these potential connections occur within subregions: 261 (7%) in DG, 451 (14%) in CA3, 25 (< 1%) in CA2, 1065 (32%) in CA1, 8 (< 1%) in the subiculum, and 731 (22%) in the entorhinal cortex. Most (but not all) of the remaining 748 (23%) cross-regional projections are from the principal neurons (granule, pyramidal, and stellate cells). The vast majority of experiments reported in the scientific literature regarding synaptic physiology in the hippocampus are restricted to a tiny fraction of "famous" presynaptic/postsynaptic pairs, such as mossy fiber synapses from dentate granule cells to CA3 pyramidal cells and perisomatic synapses from fast-spiking basket cells to CA1 pyramidal cells. In order to constraint a real-scale model of the hippocampal formation, however, the synaptic parameters need to be estimated for all ~3289 potential connections.

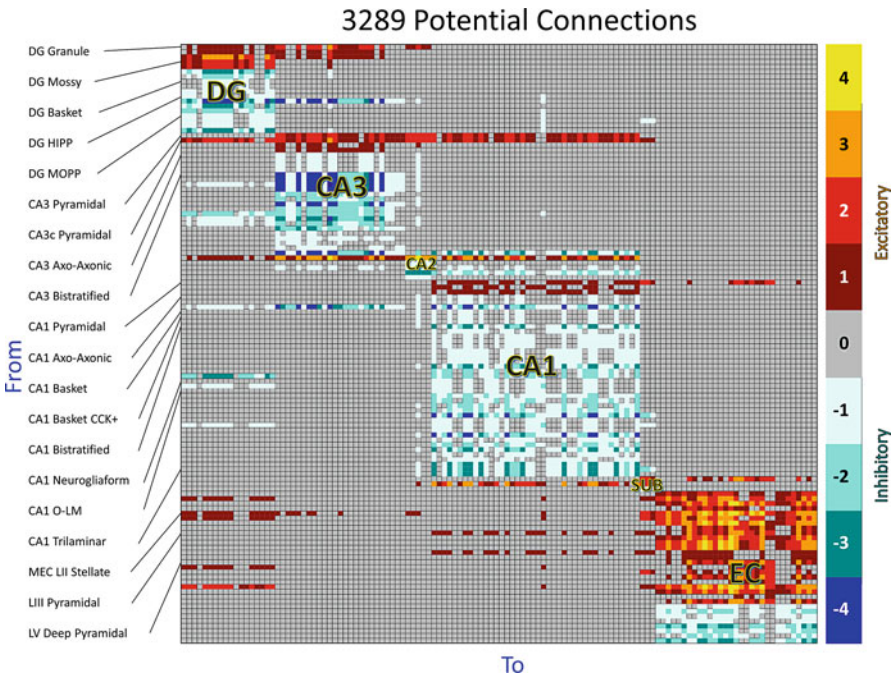

Fig. 1 Spatially co-located axons and dendrites form the backbone for potential circuit connectivity, identifying 3289 potential synaptic connections among 122 neuron types in the hippocampal formation. Rows and columns correspond to potential pre- and postsynaptic neuron types, respectively. Only a subset of the presynaptic neuron types is labeled for clarity of illustration. Colors represent the number of distinct anatomical parcels in which the axon of the presynaptic neuron type (red, excitatory; blue, inhibitory) and the dendrites of the postsynaptic neuron type in each pair are co-localized

Synaptic Parameters

Considering the large search domain and intended modeling application, we focus our data mining effort exclusively on phenomenological aspect of synaptic electrophysiology. In other words, we glean any and all essential evidence regarding the strength and time course of synaptic signals, as well as their temporal evolution. Consequently, we group available synaptic evidences as referring to amplitude, kinetics, and short-term and long-term plasticities.

Synaptic amplitude is typically measured by current-clamp or voltage-clamp methods, and the correspondingly reported voltage or current values depend on the specific holding potential. Thus, for modeling purposes, sufficient information must be extracted to allow conversion of these measurements into maximal synaptic conductance.

Synaptic kinetics characteristics are also quantified in a variety of ways. Many experimental studies report the 10–90% rise time and the half-height width (the

interval between two crossings of 50% maximal amplitude). In other cases, postsynaptic potentials or currents are fitted with alpha functions or with double or triple exponential functions, yielding well-defined rise and decay constants. Double and triple exponential time constants, however, cannot be analytically related to each other (Moradi et al. 2013). For the purpose of implementing simulations, kinetic data must be converted into uniformly defined parameters controlling charge transfer by numerical refitting (Baker et al. 2011; Moradi et al. 2012).

Synaptic plasticity refers to activity-dependent changes in synaptic amplitude and/or kinetic and is typically divided in short and long term depending on the duration of the effect. The former is usually reversible in the orders of seconds (Hennig 2013), although it can last up to minutes in hippocampal neurogliaform cells (Karayannis et al. 2010). Long-term synaptic plasticity, in contrast, might in principle be considered permanent, although it is most commonly studied for several hours (Lee et al. 2009; Bliss and Lomo 1973; Andersen et al. 1977).

Short-term plasticity may result in a decrease or increase of the synaptic signal (depressing and facilitating, respectively), or a combination thereof, depending on stimulation frequency and other experimental conditions. A simple paired-pulse ratio can be generally calculated whenever two successive synaptic signals are reported.

Long-term synaptic plasticity is more complex and diverse and includes the interplay of homeostatic and non-homeostatic modalities (Vitureira and Goda 2013). Homeostatic synaptic plasticity constitutes a negative feedback mechanism (Turrigiano 2012), whereas non-homeostatic plasticity consists of both potentiating and depressing phenomena that can be divided into Hebbian, anti-Hebbian, and non-Hebbian. Hebbian and anti-Hebbian plasticity are associative, that is, they depend on the correlated activity of the pre- and postsynaptic cells. Hebbian LTP, for instance, requires coupling of presynaptic firing with postsynaptic depolarization or firing (Le Roux et al. 2013; Perez et al. 2001; Ross and Soltesz 2001). In contrast, anti-Hebbian LTP requires coupling of presynaptic firing with postsynaptic hyperpolarization or quiescence (Le Duigou et al. 2015; Lamsa et al. 2007; Szabo et al. 2012; Le Roux et al. 2013; Nicholson and Kullmann 2014; Le Duigou and Kullmann 2011; Oren et al. 2009; Ali and Thomson 1998). In contrast, non-Hebbian plasticity is nonassociative, i.e., it occurs independent of postsynaptic firing or membrane potential; instead, it mostly depends on presynaptic firing rate (Urban and Barrionuevo 1996; Campanac et al. 2013; Maccaferri et al. 1998; Lei et al. 2003).

In a prominent type of long-term plasticity, spike-timing-dependent plasticity (STDP), the change in synaptic strength depends on the particular time difference between presynaptic and postsynaptic activity. The most commonly observed form of hippocampal STDP, especially in excitatory synapses, is asymmetric: presynaptic firing followed by postsynaptic firing (pre-post) leads to potentiation, whereas the reverse sequence of synaptic events (post-pre) leads to depression (Woodin et al. 2003; Dan and Poo 2006; Markram et al. 1997; Bi and Poo 1998; Astori et al. 2010). Inhibitory synapses have also been reported to display symmetric STDP in the hippocampus (Woodin et al. 2003), whereas both pre-post and post-pre firing

orders have similar plastic effects; even in these cases, however, the direction of the change still depends on the relative timing: potentiation occurs with shorter intervals and depression with longer ones.

Long-term synaptic plasticity is typically quantified by the temporal evolution of postsynaptic current (PSC), postsynaptic potentials (PSP), or field postsynaptic potentials (fPSP) upon synaptic stimulation with different frequencies and strengths. All long-term synaptic plasticity data from different modalities need to be translated into phenomenological parameters to be useful in computational modeling (see section "Models of synapses").

Sources of Data

Technologies to record synaptic signals have been available for several decades. For the key purpose of quantifying the synaptic parameters between pairs of identified neuron types, the most relevant approach is, unsurprisingly, *paired recording*. Direct synaptic signals can be measured from connected pairs of neurons either with intracellular electrodes (Dhillon and Jones 2000; Lacaille et al. 1987; Lacaille and Schwartzkroin 1988; Pawelzik et al. 2002, 2003; Scharfman 1994; Vida et al. 1998) or by patch clamp (Elfant et al. 2008; Geiger et al. 1997; Harney and Jones 2002; Hefft and Jonas 2005; Liu et al. 2014; Savanthrapadian et al. 2014; Szabadics and Soltesz 2009; Szabo et al. 2014; Williams et al. 2007). Either variant enables intracellular labeling of the recorded cells for post hoc morphological identification of neuron types. This approach also allows study of short- and long-term plasticity (Karayannis et al. 2010; Le Duigou et al. 2015). Paired recording can also be combined with extracellular stimulation to investigate the role of specific neuronal types in synaptic integration (Perea and Araque 2007; Miles et al. 1996; Buhl et al. 1994; Glickfeld and Scanziani 2006). Recent optimization of multiple (clustered) whole-cell recordings now makes it possible to measure synaptic signals between several neuron pairs simultaneously, thereby substantially speeding up detailed network analysis (Couey et al. 2013; Jiang et al. 2015).

A less technically challenging alternative to paired recording consists of extracellular stimulation combined with patch clamp and intracellular recording. Although this is a common method to study synaptic electrophysiology and long-term plasticity in the hippocampus (Jaffe and Johnston 1990; Maccaferri et al. 1998; Urban and Barrionuevo 1996), ascribing the presynaptic axons to a single neuronal type is often impossible (Empson and Heinemann 1995; Glickfeld and Scanziani 2006; Han et al. 1993; Hardie and Pearce 2006; Kelsch et al. 2014; Okazaki et al. 1999; Sik et al. 1997). The perforated or cell-attached variants are sometimes preferred to prevent cell dialysis, enabling stable patches for longer time (Yang and Dani 2014; Bi and Poo 1998; Woodin et al. 2003; Le Duigou et al. 2015). Combining extracellular stimulation with fPSP recording further reduces cell-to-cell resolution and essentially obliterates cell type specificity, but it may still provide general

information about long-term evolution of synaptic signals (Derrick and Martinez 1996; Schurmans et al. 1997).

Patch clamp or intracellular recording can also be combined with neurotransmitter uncaging to study synaptic signals. In particular, like many other electrophysiological techniques, two-photon glutamate and one-photon GABA uncaging methods have also been pioneered in the hippocampus (Lovett-Barron et al. 2012). Although laser-scanning photo-stimulation allows one to interrogate the connection of large numbers of cells with a single postsynaptic neuron, the identification of presynaptic neuronal types remains problematic (Beed et al. 2010, 2013; Bendels et al. 2008). Alternatively, optogenetic stimulation can also excite more or less homogeneous neuronal populations depending on the specificity of gene targeting (Kohara et al. 2014; Melzer et al. 2012; Cardin et al. 2010).

Synaptic electrophysiology can also be studied with voltage-sensitive dyes or calcium indicators as alternatives to patch clamp and intracellular recording. These methods are particularly useful to infer synaptic attenuation since the synaptic amplitude may be measured in the dendrites and in the soma within the same neuron. Two-photon calcium imaging, for example, has been used to investigate synaptic properties in combination with cell type-specific optical stimulation (Chiu et al. 2013) or paired patch-clamp recordings (Mullner et al. 2015). Still, application of these methods is generally limited because of the difficulty in unequivocally identifying the neuron types.

Synaptic signals can also be recorded without external stimulation (Ledri et al. 2011), as in the cases of spontaneous (Hajos and Mody 1997; Otis and Mody 1992) and miniature (Goswami et al. 2012; Kumar and Buckmaster 2006) events. Spontaneous events are synaptic responses to chance action potentials of presynaptic cells driven by intrinsic membrane properties and/or network activity. Miniature events, in contrast, are isolated in the presence of tetrodotoxin (TTX) to block action potential initiation and propagation, thus constituting even more "spontaneous" synaptic signals due to random neurotransmitter release. Therefore, they can be further utilized for the quantification of readily releasable pool size, a useful index to characterize short-term synaptic plasticity. Lastly, synaptic signals may also be induced by application of drugs like kainate (Gloveli et al. 2005; Whittington et al. 1995). Because the presynaptic neuron remains unknown in these methods, spontaneous events and pharmacological stimulation are of limited utility for the measurement of neuron pair-specific synaptic parameters.

Synaptic Electrophysiological Evidence

To ascribe a particular piece of synaptic electrophysiology evidence to a specific potential connection, it is necessary to assign a unique identity to both the presynaptic and postsynaptic neurons. In other words, sufficient morphological, electrophysiological, or molecular information must be available to unequivocally identify single pre- and postsynaptic neuron types. Using Hippocampome.org as the

reference framework for neuron types, we label all synaptic evidence that can be reasonably linked to a specific pair among the 3289 possible connections within the 122 × 122 connectivity matrix (Fig. 1) as "proper." When the available information is insufficient for such a determination, it is still usually possible to identify a limited subset of possible pre-/postsynaptic neuron type pairs for which the synaptic data are relevant. We call the synaptic evidence for those pairs "fuzzy." In other words, fuzzy evidence pertains to one among several pairs of neuronal types because either the presynaptic or postsynaptic neuronal descriptions, or both, match more than one Hippocampome.org neuron type.

Evidence Proper

As a first example of available synaptic information, we consider a case of evidence proper from paired recording. In a dual recording experiment among DG interneurons, both the pre- and postsynaptic cells were identified based on axonal and dendritic morphologies, biomarkers, and electrophysiological properties (Savanthrapadian et al. 2014). In particular, basket cells (BCs) and hilar commissural-associational pathway (HICAP) cells in this study were directly linkable to equivalent neuron types in Hippocampome.org. Both neuron types had dendrites spanning all layers of DG (hilus, granular, inner and outer molecular layer), but the axons of basket cells were only present in the granular layer, whereas the axons of HICAP cells only invaded the inner molecular layer. Furthermore, BCs were fast-spiking and expressed parvalbumin, whereas HICAP cells were regular firing and expressed CCK. Paired recordings provided a comprehensive battery of amplitude, kinetics, and short-term plasticity measurements for all four unidirectional synaptic pairs among these two neuron types. Furthermore, the fraction of connected neurons out of the number of tested pairs revealed specific estimates of connection probability: 25.9% for HICAP→HICAP (15:58), 10.7% for BC→BC (6:56), 16.3% for HICAP→BC (15:92), and 13.3% for BC→HICAP (6:45). It is important to note that, while paired recording allows computation of connection statistics, lack of connectivity cannot be inferred on the basis of absence of signals without strong assumptions on the number of neurons as well as their axonal and dendritic densities for each type (Song et al. 2005; Hellwig 2000; Sporns and Zwi 2004; Gerhard et al. 2011; Jiang et al. 2015).

Although electrophysiological evidence proper mostly comes from paired recording studies, the orderly circuit organization of the hippocampus may also aid univocal connection assignments. For instance, the synaptic signal from dentate granule cells to CA3 lucidum LAX interneurons (Toth and McBain 1998) was characterized simply based on single whole-cell patch clamp and extracellular stimulation (Maccaferri et al. 1998). The dentate granular layer or the CA3 lucidum layer was stimulated at low intensity in transverse hippocampal slices while recording excitatory postsynaptic currents (EPSCs) from CA3 interneurons located in the lucidum layer or at the border between the lucidum and radiatum

layers. The postsynaptic neuron type was identified based on its unique distributions of dendrites in the CA3 radiatum and lucidum layers (Fig. 2A1) and especially of axons in the CA3 lucidum layer (spilling in the adjacent pyramidal layers), which are different from those of other lucidum interneurons (hence the name LAX for "lucidum axon"). The assignment of the presynaptic identity to DG granule cells is less straightforward. Based on the presence of soma and axons in the dentate granular layer and CA3 lucidum, semilunar granule cells (Larimer and Strowbridge 2010; Williams et al. 2007), hilar ectopic granule cells (Marti-Subirana et al. 1986; McCloskey et al. 2006; Pierce et al. 2011; Scharfman et al. 2003; Scharfman and Pierce 2012), and CA3 granule cells (Szabadics et al. 2010) could all be alternative stimulus sources. Nevertheless, dentate granule cells can be confidently identified as the presynaptic type based on their sheer number relative to those much rarer neuronal populations, combined with specific pharmacological clues typical of the mossy fiber origin of the stimuli, such as the EPSC blockage by mGluR2

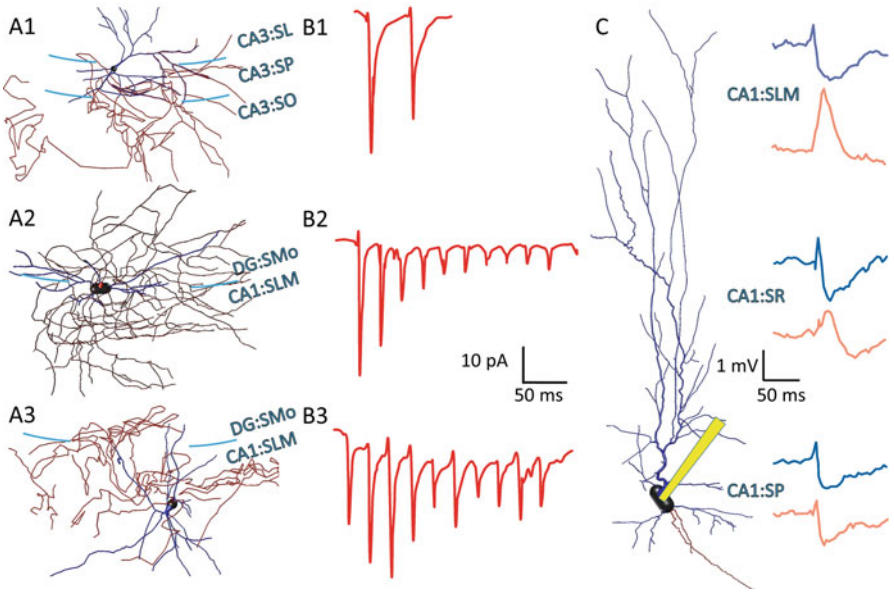

Fig. 2 Neuron types and synaptic signals. **A1**, CA3 lucidum LAX cells are identified by the presence of axons in CA3 pyramidal layer, both axon and dendrites in lucidum, and dendrites CA3 radiatum layer. **A2**, One of the CA1 neurogliaform types invades both the dentate gyrus outer molecular layer and the CA1 lacunosum-moleculare. **A3**, The other type of CA1 neurogliaform cells is limited to the lacunosum-moleculare layer only. **B1–B3**, somatic EPSCs corresponding to the three neuron types illustrated in panels A1–A3. **C**, CA1 pyramidal cells and somatic EPSPs recorded before (blue) and after (red) focal bicuculline application to different layers of CA1 (axons, red; dendrites, blue). A1 and B1 are adopted from Maccaferri et al. (1998); A2, A3, B2, and B3 from Price et al. (2005); and C from Empson and Heinemann (1995), all with permission. All morphologies are from NeuroMorpho.Org (Scorza et al. 2011; Cossart et al. 2006; Markwardt et al. 2011; Ascoli 2006; Ascoli et al. 2007)

agonists but not NMDA receptor antagonists. Synaptic amplitude and kinetics can be measured from numerous EPSC traces recorded in this study. Furthermore, paired-pulse facilitation was also reported in these synapses, thus revealing short-term synaptic plasticity as well (Fig. 2B1). Interestingly, this study also identifies the first known case of monosynaptic LTD between a hippocampal principal cell and an interneuron by high-frequency stimulation.

Fuzzy Evidence

As an example of fuzzy synaptic evidence, we consider the excitatory inputs to CA1 neurogliaform cells in the lacunosum-moleculare layer (Price et al. 2005). In horizontal hippocampal slices devoid of CA3 region, and in the presence of $GABA_A$ receptor blocker, extracellular lacunosum-moleculare stimulation elicits EPSCs in CA1 neurogliaform cells visually identified based on soma shape and size (Fig. 2B2-3). Assuming that only axons are activated by extracellular stimulation because of their lower threshold, all excitatory cells with axons in CA1 lacunosum-moleculare are potential presynaptic cells, including local neurons as well as projecting cells from entorhinal cortex, subiculum, thalamic nucleus reunions, and amygdala (Amaral and Witter 1995). Focusing on the hippocampal formation, these include entorhinal layer 3 pyramidal (Canto and Witter 2012b; Dickson et al. 1997; Germroth et al. 1991; Steward and Scoville 1976; Steward 1976; Tahvildari and Alonso 2005) and pyramidal-stellate neurons (Canto and Witter 2012a; Germroth et al. 1989; Gloveli et al. 1997; Andersen 2007; Steward and Scoville 1976; Steward 1976; Tahvildari and Alonso 2005; van der Linden and Lopes da Silva 1998), subicular CA1-projecting pyramidal neurons (Harris and Stewart 2001), and CA1 Cajal-Retzius cells (Anstotz et al. 2014; Quattrocolo and Maccaferri 2013, 2014). The grouped synaptic data also likely include recording from two morphologically distinct types of postsynaptic neurogliaform cells (Fig. 2 A2, 2A3). One of them, with soma located closer to the radiatum border, has axons and dendrites completely confined to the lacunosum-moleculare layer; the other type, with soma closer to the hippocampal fissure, has axons and dendrites crossing well into the outer molecular layer of DG. This second "projecting" variety of neurogliaform cells is considered a distinct neuron type in Hippocampome.org since it can both receive inputs from and send outputs to a portion of the circuit inaccessible to the "CA1-only" neurons. Thus, the synaptic evidence for this connection could be potentially ascribable to as many as eight distinct pre-/postsynaptic pairs (Table 1). When it comes to this kind of fuzzy evidence, the underlying assumptions need to be evaluated to assess the confidence of each assignment as (relatively) "high" or "low." Since entorhinal layer 3 pyramidal neurons are the principal cells of this projection, they are expected to have the highest density of excitatory axons in lacunosum-moleculare. Thus, the synaptic electrophysiology ascribed to these connections is marked as high confidence evidence in Table 1 and the rest as low confidence.

Table 1 Potential connections in an experiment in which the CA1 lacunosum-moleculare layer was stimulated extracellularly while recording from CA1 Neurogliaform cells

Presynaptic Neuron Types	Postsynaptic Neuron Types	Confidence
EC LIII Pyramidal	CA1 Neurogliaform	High
EC LIII Pyramidal-Stellate	CA1 Neurogliaform	Low
SUB CA1-Projecting Pyramidal	CA1 Neurogliaform	Low
CA1 Cajal-Retzius	CA1 Neurogliaform	Low
EC LIII Pyramidal	CA1 Neurogliaform Projecting	High
EC LIII Pyramidal-Stellate	CA1 Neurogliaform Projecting	Low
SUB CA1-Projecting Pyramidal	CA1 Neurogliaform Projecting	Low
CA1 Cajal-Retzius	CA1 Neurogliaform Projecting	Low

Cell type assignment confidence of fuzzy evidence in synaptic electrophysiology investigations may be boosted by enhancing the selectivity of excitation through the anatomical or pharmacological ablation of a parcel. As an example of such an approach, we consider again the extracellular stimulation of CA1 lacunosum-moleculare in horizontal hippocampal slices after surgical ablation of both CA3 and DG while recording intracellularly from the soma of CA1 pyramidal cells (Empson and Heinemann 1995). In the absence of any pharmacologic blockers, IPSPs were detected after EPSPs in the majority of cases, indicative of polysynaptic inhibition, with larger IPSP amplitudes closer to the stimulation site. The few observed cases of pure EPSPs had reversal potential (E_{rev}) of −40 mV, reflecting mixed contributions of multiple channels. Bath application of an AMPA/kainate receptor competitive antagonist (CNQX) reduced the IPSP amplitude. Focal application of $GABA_A$ antagonist (bicuculline) also affected IPSP amplitude but only when applied to the radiatum and pyramidal layers and not to lacunosum-moleculare (Fig. 2C). These results suggest that extracellular stimulation mainly activates excitatory cells with axons in CA1 lacunosum-moleculare (explaining the monosynaptic EPSPs). As in the previous example, entorhinal layer 3 pyramidal cells are assumed to be the main presynaptic excitatory type. The majority of (polysynaptic) IPSPs may thus be ascribed to inhibitory cells that have dendrites in CA1 lacunosum-moleculare and axons in the radiatum or pyramidal layers. The monosynaptic IPSPs, only observed in the presence of CNQX when the stimulation occurred close to the recording site, were elicited by inhibitory cells with axons in lacunosum-moleculare. Based on these assumptions, as many as 19 potential synaptic connections can be identified (Table 2). Similarly as in Table 1, only one of the four excitatory connections can be assigned with high confidence. Of the 15 low-confidence inhibitory connections, 6 are purely disynaptic, corresponding to presynaptic neuron types with dendrites in lacunosum-moleculare and axons in radiatum or pyramidale; 6 are purely monosynaptic, corresponding to presynaptic neuron types with axons in lacunosum-moleculare; and 3 could connect both mono- and disynaptically corresponding to neuron types with axons and dendrites in lacunosum-moleculare and axons in radiatum or pyramidale.

Table 2 Potential presynaptic neuron types in an experiment in which the CA1 lacunosum-moleculare layer was stimulated extracellularly while recording somatically from CA1 pyramidal cells (which constitute the postsynaptic neuron type in all cases)

Presynaptic neuron type	Confidence	Signal	Connectivity
EC LIII pyramidal (+)223111p	*High*	*Excitatory*	*Monosynaptic*
EC LIII pyramidal-stellate (+)223200p	Low	Excitatory	Monosynaptic
CA1 Cajal-Retzius (+)3000	Low	Excitatory	Monosynaptic
SUB CA1-projecting pyramidal (+)331p	Low	Excitatory	Monosynaptic
CA1 radial trilaminar (−)2333	Low	Inhibitory	Disynaptic
CA1 Schaffer collateral-assoc (−)2311	Low	Inhibitory	Disynaptic
CA1 axo-axonic (−)2232	Low	Inhibitory	Disynaptic
CA1 oriens/alveus (−)2233	Low	Inhibitory	Disynaptic
CA1 basket (−)2232	Low	Inhibitory	Disynaptic
CA1 basket CCK+ (−)2232	Low	Inhibitory	Disynaptic
CA1 LMR projecting (−)3300p	Low	Inhibitory	Either/both
CA1 LMR (−)3300	Low	Inhibitory	Either/both
CA1 quadrilaminar (−)3333	Low	Inhibitory	Either/both
CA1 perforant path-associated (−)3200p	Low	Inhibitory	Monosynaptic
CA1 neurogliaform projecting (−)3000p	Low	Inhibitory	Monosynaptic
CA1 neurogliaform (−)3000	Low	Inhibitory	Monosynaptic
CA1 back-projection (−)1133p	Low	Inhibitory	Monosynaptic
CA1 O-LM (−)1002	Low	Inhibitory	Monosynaptic
CA1 O-LMR (−)1102	Low	Inhibitory	Monosynaptic

Integrated Summary

Having illustrated the evidence-gathering approach, we can now evaluate the availability of synaptic information in the published literature. This assessment should only be considered a preliminary estimate at this time, since we have yet to conclude the data mining process.

We started the process from the original 466 papers included in v1.0 of Hippocampome.org, further mining the publications citing or referred to by these articles to find additional evidence. Publications from Hippocampome.org are already associated with specific neuron types, but may not contain synaptic electrophysiology data. Papers obtained from the cited references are purposefully selected based on the citation context as likely to contain synaptic electrophysiology data, but linking this information to morphologically defined neuron types is not always straightforward. When considering articles citing Hippocampome.org papers, both the availability of synaptic data and cell type linking are initially unknown.

In all three cases, papers undergo a two-stage evaluation process: triage and in-depth mining. Triage relies on the title, abstract, figures, and selected terms in the full text to assess whether the article might provide information about synaptic signals. Specifically, we leverage the "Vocabulary Highlighter" Firefox extension to identify efficiently the possibly presence of ∼400 (empirically selected) keywords.

This list includes a comprehensive collection of synaptic terms (such as "depolarization," "IPSP," "vesicle," and "facilitation") as well as (in different colors) other words referring to morphological concepts ("axon," "dendrite," "soma," etc.), hippocampal parcels (e.g., "CA3," "stratum oriens," or "hilus"), and other relevant information (species, cell types, electrophysiology, molecular marker, and more). Triage only takes a few minutes per paper and is designed to minimize false negatives: if we suspect that an article might possibly contain relevant data, it is marked for further processing.

In the second stage, the papers that passed the previous selection are studied in detail to find any data pertaining to synaptic electrophysiology. If no data are found, the paper is moved to the "excluded" group along with the triaged ones. Any evidence proper is annotated by associating the article identifier (typically PMID) with the identity of the presynaptic and postsynaptic neuron types. If fuzzy evidence is found, the annotation also includes a detailed explanation of the ambiguity and the explicit assumptions needed to link the presynaptic and postsynaptic neuron types. Lastly, the actual parameters regarding amplitude, kinetics, and short- and long-term plasticity are extracted along with the covariates affecting the synaptic signals. In order to maximize coverage and minimize redundancies, mining of papers in the pipeline is prioritized to give precedence to the connections with no available information to date.

Among 466 papers in Hippocampome.org, 348 were triaged or excluded upon in-depth reading. Of the remaining 118 with linkable synaptic evidence, 39 have already been mined, and 79 are currently in the pipeline. Furthermore, 149 new articles were identified through references and citations. Three of these were excluded, 37 were mined, and 109 are in the pipeline. Thus, a total of 615 publications have been evaluated so far: 76 were mined, 188 are in the pipeline, and 351 were excluded. In other words, evaluating the references and citations of 76 mined articles yielded 146 additional papers with synaptic data. Of the 351 excluded papers, 201 had no synaptic electrophysiology, 110 had no connectivity data, 35 were reviews or book chapters exclusively reporting secondhand information, 3 had only field potential electrophysiology, 1 pertained to an extra-hippocampal connection, and 1 was from a slice culture.

Of the 3289 potential connections in the hippocampal formation among the 122 neuron types of Hippocampome.org, only 167 could be firmly established and 72 could be refuted based on electrophysiological or histological evidence. Obviously no synaptic information can be found for the refuted connections. Of the validated connections, evidence proper was found for approximately half, while fuzzy evidence is available for almost all of the rest. The remaining ∼92.7% of the potential synapses remains "unknown," and any synaptic evidence for these connections can only be deemed fuzzy. Thus far, approximately 45% of potential connections could be linked to proper or fuzzy electrophysiological evidence, the vast majority of which (>90%) are low-confidence assignments (Fig. 3). For as many as 1862 pairs of potentially connected neuron types, we have not yet found synaptic evidence. Although we might be able to halve this amount through the completion of the ongoing literature mining, we still expect a substantial proportion

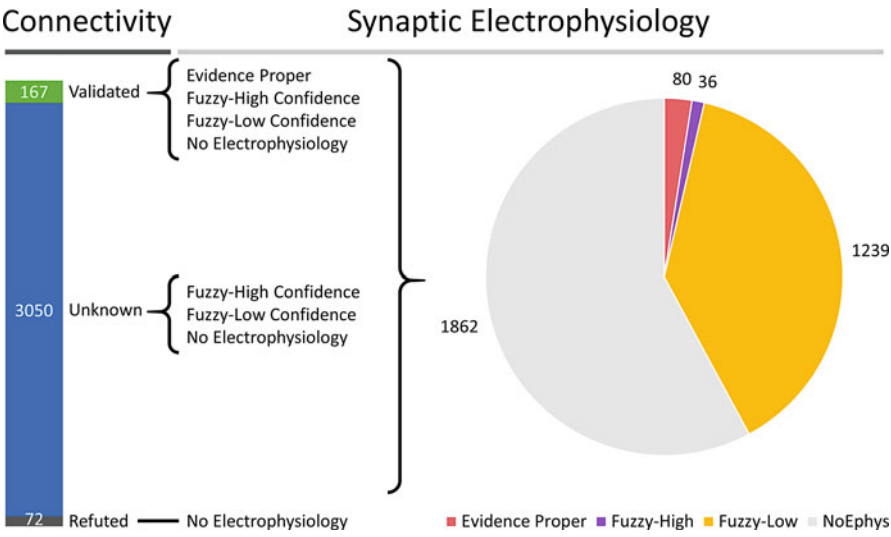

Fig. 3 Integrated summary. Of the 3289 potential connections in Hippocampome.org (left bar chart), 72 can be refuted based on available histological evidence. The remaining 3217 can be mapped into evidence proper (red), high-confidence fuzzy evidence (purple), low-confidence fuzzy evidence (yellow), and no electrophysiology (gray) groups (right pie chart)

of synaptic parameters to remain unknown as the corresponding experiments were never performed or published.

Implementation Requirements

In order to leverage the synaptic information gathered with the above-described strategy to aid implementation of a real-scale spiking neural network simulation of the hippocampal formation, several additional steps are necessary. First, the evidence collected with different experimental techniques under a variety of conditions must be normalized so as to be expressed within a uniform framework for all connections. Second, the missing data for the "unknown" connections has to be inferred based on patterns of similarities among the available data. Third and last, appropriate models of synaptic signals and plasticity need to be defined consistent with the collated knowledge.

Covariates and Data Normalization

Gleaning synaptic data from highly nonuniform sources makes data normalization both challenging and essential. Synaptic signals are strongly affected by the exper-

imental preparation, including the actual recording modality (voltage clamp vs. current clamp) and conditions, such as temperature and holding current or voltage, but also the stimulation technique, slice thickness and orientation, pharmacological cocktails and chemical compositions in the electrode and in the bathing solution, and the species, strain, age, and sex of the animal subject. Data normalization with respect to all these covariates is crucial to produce meaningful and reliable constraints for computational models. For instance, synaptic signals recorded at room temperature must be corrected with appropriate Q10 coefficients, if available. Most of the available synaptic data comes from young adult rodents (more than 2 weeks old); since synaptic amplitude tends to diminish with age, reasonable aging coefficients need to be applied when pooling non-age-matched data. When experiments are carried out in the presence of pharmacological agonists or antagonists of synaptic receptors or voltage-gated channels, which might potentiate or depress synaptic signals, such factors should be accounted and corrected for.

Inferential Data

In the absence of synaptic evidence for a connection, empirical rules or mathematical methods might be used to infer the missing information. For instance, the kinetics and amplitude of synaptic signals received by CA1 interneurons appear to be related to the laminar distribution of their axons (Cossart et al. 2006), and similar rules might apply to other subregions as suggested by the existence of an analogous phenomenon in primary visual neocortex (Dumitriu et al. 2007). Similarly, unitary synaptic amplitude correlates with the connection probability in the cortex (Jiang et al. 2015), so that one could be predicted if the other is known. In addition to these empirical observations, inferences can be derived directly from patterns of available data. We describe next one such an approach.

To a first approximation, synaptic properties can be considered as the product of distinct pre- and postsynaptic components. For example, the postsynaptic amplitude can be viewed as the result of local synaptic conductance followed by dendritic attenuation. Similarly, the dendritic filtering of the local postsynaptic current time constant would yield the observed somatic time course. Because both active and passive membrane properties depend on the location on the dendritic and axonal arbors, it is reasonable to assume that the specific pre- and postsynaptic characteristics of each neuron type vary depending on the layers and subregions their neurites invade. For example, DG granule cells would have distinct presynaptic properties for their axons in the hilus and in CA3 lucidum, relevant, respectively, for their connection to mossy cells and CA3 pyramidal neurons. Similarly, granule cells would also have distinct postsynaptic properties for their dendrites in the inner and outer molecular layer, relevant, respectively, for their connection from mossy cells and entorhinal layer 2 spiny stellate neurons.

If the hippocampal formation is represented as a list of distinct layers and subregions (such as inner and outer molecular layer, hilus, and CA3 lucidum), each neuron type can then be described with an axonal and a dendritic "vector," whose components correspond to distinct anatomical locations. Since Hippocampome.org divides the hippocampal formation in 26 such parcels, we can represent all neuron types with 26-dimensional axonal and dendritic vectors with non-zero values that represent the pre- and postsynaptic factors, respectively, corresponding to the parcels they invade. Although these putative parcel-specific pre- and postsynaptic factors are unknown for every neuron type, this formalism allows systematic farming of similarity patterns in the data using techniques borrowed from matrix algebra.

The set of all values for a given synaptic parameter, such as amplitude or the decay time constant, for the entire hippocampal circuit can be described with a 122×122 square matrix (where 122 is the number of neuron types in Hippocampome.org). The *ijth* entry of this matrix represents the value of the synaptic parameter corresponding to the connection from the *ith* (presynaptic) neuron type to the *jth* (postsynaptic) neuron type. This matrix can now be approximated by singular value decomposition (SVD) into the product of three matrices: a 122×26 matrix corresponding to the "presynaptic" factors of the 122 neuron types over the 26 parcels, a 26×26 diagonal matrix of singular values, and a 26×122 matrix corresponding to the "postsynaptic" factors of the 122 neuron types over the 26 parcels (Fig. 4). Even a small known sample of available data from each row and column of the original 122×122 synaptic matrix may be sufficient to estimate with high confidence the entries of the three decomposition matrices. Their product then yields a useful prediction of all missing values in the synaptic matrix. Several other similarly powerful methods exist for this classic *matrix completion* problem (Candès and Recht 2009; Chen et al. 2012; Mazumder et al. 2010). The key is that the missing synaptic values can be imputed based on the patterns of existing (though incomplete) data.

Models of Synapses

Even after massive literature mining, careful data normalization, and sophisticated inferential completion, a real-scale network model of the hippocampal formation must realistically contend with sparse knowledge of synaptic data about more than 3000 connection types. Several books and review articles offer a wealth of options for modeling synapses at different levels of detail (Dayan and Abbott 2001; Rothman 2015; Rothman and Silver 2014; Glyzin et al. 2013; De Schutter 2000, 2010; Feng 2004; Evans et al. 2004; Sterratt 2011; Wallisch 2014; Trappenberg 2010; Koch 1999), but the unavoidable sparsity of available constraints demands a delicate balance between an acceptable description of the data and a judicious minimization of the number of model parameters.

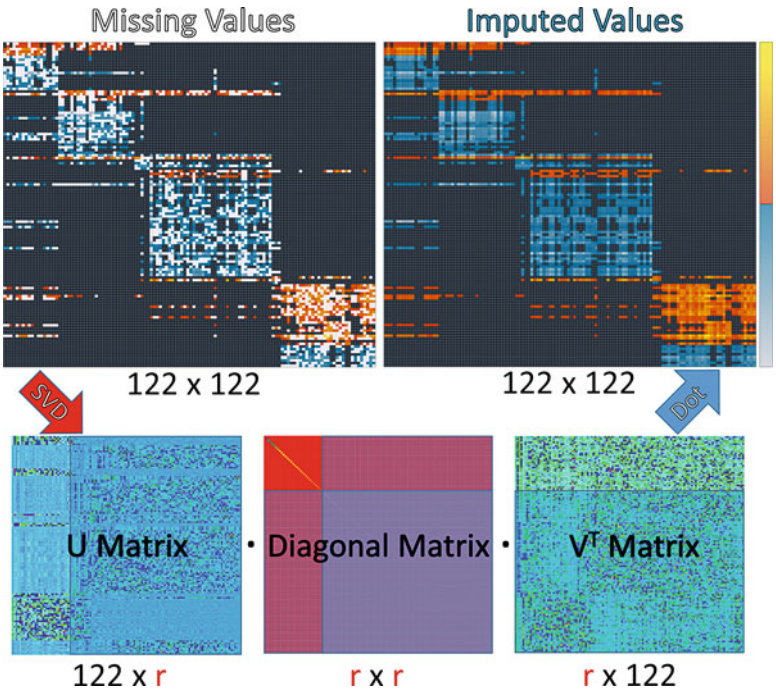

Fig. 4 Matrix completion. Incremental singular value decomposition (SVD) decomposes a connection matrix with missing values (pink cells) into U, D, and V matrices. The product of these matrices with an appropriate number of singular values (r) reconstructs the connection matrix with imputed values. Warm and cold colors in the connection matrix represent positive and negative synaptic values, respectively

In chemical ionotropic synapses, presynaptic neurotransmitter release leads to opening of ion channels on the postsynaptic membrane. Consequently, modeling synaptic signals involve both presynaptic and postsynaptic factors. Synaptic ion channels, similar to other ion channels, depend on gating and permeability. Complex models of permeability can account for calcium currents, ionic selectivity, and nonlinear current-voltage relationships (Coalson and Kurnikova 2005; Burger 2011; Eisenberg 1999, 2010, 2012; Hodgkin et al. 1949; Goldman 1943; Lewis 1979; Cooper et al. 1988; Chang et al. 1994; Jahr and Stevens 1987). Nevertheless, Ohm's law remains the simplest, most parsimonious, and most commonly adopted model:

$$I_{\text{syn}} = G_{\text{syn}}.\left(V_{\text{m}} - E_{\text{syn}}\right) \tag{1}$$

Where, I_{syn} is the synaptic current, G_{syn} is the synaptic conductance, V_{m} is the postsynaptic membrane potential, and E_{rev} is the reversal potential of the synaptic current, which under physiological conditions is typically close to 0 mV for excitatory synapses and to −70 mV or lower for inhibitory ones.

Channel gating actually involves modeling of G_{syn} as a function of time, presynaptic action potential time, and V_{m}. Synaptic amplitude, kinetics, and short-term and long-term synaptic plasticity can also all be described as multiplicative modifications of this function:

$$G_{\text{syn}} = G_{\text{max}}.P_o.P_{st}.w_{lt} \tag{2}$$

Where G_{max} is the baseline maximal synaptic conductance that defines amplitude, P_o is the time dependent open probability that defines channel kinetic, P_{st} is the release probability due to short-term plasticity, and w_{lt} is the synaptic weight coefficient due to long-term plasticity.

Models of synaptic gating range from single-exponential decay to complex biophysically detailed mechanisms involving several differential equations (Chapeau-Blondeau and Chambet 1995; Stiles et al. 1996; Stiles and Bartol 2001; Scimemi 2014). For instance, Markov kinetic processes have been used to describe postsynaptic receptor gating by chemical reactions (Clarke and Johnson 2008; Raghavachari and Lisman 2004; Patneau et al. 1992; Patneau and Mayer 1991) or simpler models (Destexhe et al. 1994a, b, 1995; Jahr and Stevens 1990).

Applications of these models in neural network simulations, however, are limited. In addition to their high computational costs, these models entail a larger number of tuning parameters than is possible to constrain with the limited experimental data available to date. Consequently, we next discuss simpler phenomenological models to represent synaptic electrophysiology that are consistent with existing data while optimizing model performance for real-scale hippocampal simulations.

For most purposes, synaptic amplitude can simply be defined in terms of maximal conductance (G_{max}):

$$G_{\text{max}} = N.d_{\text{syn}}.\gamma \tag{3}$$

Where N is the number of synaptic boutons, d_{syn} is the density of postsynaptic channels, and γ is the single channel conductance. Although G_{max} provides a useful approximation of synaptic amplitude, it is important to remember that the actual value also depends on stochastic neurotransmitter release probability, voltage-dependent and intracellular or extracellular ligand-dependent channel blockage, desensitization dynamics, and voltage-dependent postsynaptic gating. In NMDA receptors, for instance, Mg^{2+} block is both concentration- and voltage-dependent, which can be modeled with Boltzmann functions (Harsch and Robinson 2000; Kuner and Schoepfer 1996; Nowak et al. 1984; Mayer et al. 1984; Kim and Robinson 2011; Yang et al. 2010; Zhu and Auerbach 2001a) or Markov kinetics (Antonov and Johnson 1999; Nikolaev et al. 2012; Qian and Johnson 2006; Zhu and Auerbach 2001b). The voltage-dependent gating of NR1/2B subtype of NMDA receptors in hippocampal neurons can be modeled with Hodgkin-Huxley-like equations (Moradi et al. 2013) or Markov kinetics (Clarke and Johnson 2008).

Exponential functions are the most adopted phenomenological models of synaptic kinetics (Rothman and Silver 2014; Rothman 2015). These functions can often

describe synaptic kinetics with just one parameter. Specifically, when the time constant of synaptic activation (τ_a) is small enough to assume instant synaptic activation, the deactivation time constant (τ_d) is sufficient to describe synaptic kinetics as a single-exponential decay function:

$$P_o = \exp\left(-\Delta t/\tau_d\right), \qquad if\ t \geq t_{\text{pre}},\ \ \Delta t = t - t_{\text{pre}} \tag{4}$$

Conversely, if a synapse has similar activation and deactivation time constant ($\tau_a \approx \tau_d$), the one-parameter alpha function can model its kinetics:

$$P_o = \Delta t/\tau_a . \exp\left(1 - \Delta t/\tau_a\right) \tag{5}$$

Where τ_a is the time constant that controls peak time. When synapses do not meet the time constant requirements to employ the computationally fast and parametrically simple single-exponential or alpha functions, multiple-exponential functions are used to model different time courses (Rothman 2015). NMDA receptor kinetics at body temperature, for instance, is better described with triple-exponential functions (Moradi et al. 2013; Kim and Robinson 2011; Korinek et al. 2010; Hestrin et al. 1990; Spruston et al. 1995).

Short-term synaptic plasticity, a dynamic presynaptic factor that affects release probability, can be calculated "event based" whenever the synapse is stimulated (Varela et al. 1997; Fuhrmann et al. 2002; Tsodyks and Markram 1997; Tsodyks et al. 2000; Markram et al. 1998). Different variants of exponential functions can model the time-dependent evolution of short-term synaptic plasticity. In order to minimize the number of parameters, we assume synapses to be facilitating, depressing, or pseudo-linear. Two parameters are in principle required for modeling facilitation or depression: the facilitation amount, f, or depression fraction, d, and the corresponding decay time constants, τ_{stf} and τ_{std} (Morrison et al. 2008).

Spike-timing-dependent plasticity (STDP) is the most popular model of long-term plasticity in spiking neural networks (Markram et al. 2012; Morrison et al. 2008). In classic STDP, synapses are potentiated if the presynaptic neuron fires before the postsynaptic neuron or depressed otherwise (Markram et al. 1997; Bi and Poo 1998). Unlike short-term facilitation that is calculated based on presynaptic firing only, the degree of long-term change in synaptic potency (Δw_{lt}) depends on both presynaptic and postsynaptic firing times. Specifically, Δw_{lt} decreases with the time difference between the two firing events, which can be modeled by distinct potentiation and depression exponential decay functions with appropriate time constants and learning rates (τ_+, τ_-, L_+, and L_-, respectively). Using constant L values (additive rule), however, leads to a bimodal distribution of synaptic amplitudes (Song et al. 2000), which contrasts the unimodal distribution observed experimentally (Turrigiano et al. 1998; Song et al. 2005). Moreover, experimental studies suggest that potentiation is smaller in strong synapses compared to weak ones, while depression is not (van Rossum et al. 2000). Both of these problems can be solved by using L values that depend on synaptic weight (Gutig et al. 2003;

Morrison et al. 2007; Standage et al. 2007), which involves one additional parameter (Markram et al. 2012).

STDP also depends on stimulation frequency, whereby increasing stimulation leads to greater potentiation (Dudek and Bear 1993; Sjostrom et al. 2001; Froemke et al. 2006). In classic STDP models, however, when several presynaptic stimulations are coupled with one postsynaptic firing, only the most recent presynaptic spike potentiates the synapse, while all others depress it. Interestingly, this phenomenon can be accurately described with τ_+ and τ_- without adding extra parameters to the model by controlling potentiation through a "trace" of all presynaptic firings that can be computed as a single-exponential decay function of the presynaptic and postsynaptic firing times (Morrison et al. 2007). Even with all these modifications, STDP models still provide incorrect predictions of triplet or quadruplet spike pairing experiments. For instance, with symmetric timing, both pre-post-pre and post-pre-post protocols should produce the same degree of change in synaptic weight. Experimentally, however, although in pre-post-pre protocol potentiation and depression cancel each other out, post-pre-post protocol yields net potentiation (Bi and Wang 2002). Significant deviations from model prediction are observed with asymmetric timing protocols as well (Froemke and Dan 2002; Wang et al. 2005). Modifying potentiation with another postsynaptic firing trace solves this problem at the cost of an additional time constant (Pfister and Gerstner 2006).

Future Directions

Although suitable mathematical models exist when it comes to the phenomenological description of synaptic electrophysiology, the actual gathering of synaptic data needs to receive more attention by the neuroscience community. Specifically, ascribing synaptic data to specific cell types remains tremendously time consuming with existing experimental techniques. This process also requires a complete knowledge model of hippocampal cell types, such as the framework offered by Hippocampome.org, to provide a manageable data search domain.

Despite the plethora of up-and-coming optogenetic methods, the old-school, labor-intensive paired recording technique remains the most reliable method to gather synaptic data at cell type to cell type resolution. New clustered simultaneous recording techniques are rapidly improving the yield of synaptic data recording, enabling the recent mapping of the complete mice neocortical circuit in a single study, which led to discovering not only previously unknown cell types but also a novel rule-based theory of connectivity (Jiang et al. 2015). Expecting similar studies in the hippocampal formation makes a complete map of hippocampal synaptic electrophysiology linked to cell types a realistically achievable endeavor. Rapid advancements in genomics may also foster discoveries in connectomics, as specific genes might predict synaptic connectivity and cell typing (Kaufman et al. 2006; Varadan et al. 2006).

Acknowledgments This project is supported by grants R01NS39600 (NIH), MURI N00014–10–1-0198 (ONR), NAKFI (Keck), CENTEC (AFOSR), Robust Intelligence (NSF), and Northrop Grumman.

References

Ali AB, Thomson AM (1998) Facilitating pyramid to horizontal oriens-alveus interneurone inputs: dual intracellular recordings in slices of rat hippocampus. J Physiol 507(Pt 1):185–199

Amaral D, Witter M (1995) Hippocampal formation, Paxinos G., the rat nervous system, 2nd edn. Academic, San Diego

Andersen P (1959) Interhippocampal impulses. I. Origin, course and distribution in cat, rabbit and rat. Acta Physiol Scand 47:63–90. https://doi.org/10.1111/j.1748-1716.1960.tb01821.x

Andersen P (1960) Interhippocampal impulses. II. Apical dendritic activation of CAI neurons. Acta Physiol Scand 48:178–208. https://doi.org/10.1111/j.1748-1716.1960.tb01858.x

Andersen P (2007) The hippocampus book. In: Oxford. Oxford University Press, New York

Andersen P, Eccles JC, Loyning Y (1963) Recurrent inhibition in the hippocampus with identification of the inhibitory cell and its synapses. Nature 198:540–542

Andersen P, Sundberg SH, Sveen O, Wigstrom H (1977) Specific long-lasting potentiation of synaptic transmission in hippocampal slices. Nature 266(5604):736–737

Anstotz M, Cosgrove KE, Hack I, Mugnaini E, Maccaferri G, Lubke JH (2014) Morphology, input-output relations and synaptic connectivity of Cajal-Retzius cells in layer 1 of the developing neocortex of CXCR4-EGFP mice. Brain Struct Funct 219(6):2119–2139. https://doi.org/10.1007/s00429-013-0627-2

Antonov SM, Johnson JW (1999) Permeant ion regulation of N-methyl-D-aspartate receptor channel block by Mg(2+). Proc Natl Acad Sci U S A 96(25):14571–14576

Ascoli GA (2006) Mobilizing the base of neuroscience data: the case of neuronal morphologies. Nat Rev Neurosci 7(4):318–324. https://doi.org/10.1038/nrn1885

Ascoli GA, Donohue DE, Halavi M (2007) NeuroMorpho.Org: a central resource for neuronal morphologies. J Neurosci 27(35):9247–9251. https://doi.org/10.1523/JNEUROSCI.2055-07.2007

Astori S, Pawlak V, Kohr G (2010) Spike-timing-dependent plasticity in hippocampal CA3 neurons. J Physiol 588(Pt 22):4475–4488. https://doi.org/10.1113/jphysiol.2010.198366

Baker JL, Perez-Rosello T, Migliore M, Barrionuevo G, Ascoli GA (2011) A computer model of unitary responses from associational/commissural and perforant path synapses in hippocampal CA3 pyramidal cells. J Comput Neurosci 31(1):137–158. https://doi.org/10.1007/s10827-010-0304-x

Beed P, Bendels MH, Wiegand HF, Leibold C, Johenning FW, Schmitz D (2010) Analysis of excitatory microcircuitry in the medial entorhinal cortex reveals cell-type-specific differences. Neuron 68(6):1059–1066. https://doi.org/10.1016/j.neuron.2010.12.009

Beed P, Gundlfinger A, Schneiderbauer S, Song J, Bohm C, Burgalossi A et al (2013) Inhibitory gradient along the dorsoventral axis in the medial entorhinal cortex. Neuron 79(6):1197–1207. https://doi.org/10.1016/j.neuron.2013.06.038

Bendels MH, Beed P, Leibold C, Schmitz D, Johenning FW (2008) A novel control software that improves the experimental workflow of scanning photostimulation experiments. J Neurosci Methods 175(1):44–57. https://doi.org/10.1016/j.jneumeth.2008.08.010

Bennett MR (1999) The early history of the synapse: from Plato to Sherrington. Brain Res Bull 50(2):95–118

Bezaire MJ, Soltesz I (2013) Quantitative assessment of CA1 local circuits: knowledge base for interneuron-pyramidal cell connectivity. Hippocampus 23(9):751–785. https://doi.org/10.1002/hipo.22141

Bi GQ, Poo MM (1998) Synaptic modifications in cultured hippocampal neurons: dependence on spike timing, synaptic strength, and postsynaptic cell type. J Neurosci 18(24):10464–10472

Bi GQ, Wang HX (2002) Temporal asymmetry in spike timing-dependent synaptic plasticity. Physiol Behav 77(4–5):551–555

Bliss TV, Lomo T (1973) Long-lasting potentiation of synaptic transmission in the dentate area of the anaesthetized rabbit following stimulation of the perforant path. J Physiol 232(2):331–356

Bota M, Swanson LW (2007) The neuron classification problem. Brain Res Rev 56(1):79–88. https://doi.org/10.1016/j.brainresrev.2007.05.005

Buhl EH, Halasy K, Somogyi P (1994) Diverse sources of hippocampal unitary inhibitory postsynaptic potentials and the number of synaptic release sites. Nature 368(6474):823–828. https://doi.org/10.1038/368823a0

Burger M (2011) Inverse problems in ion channel modelling. Inverse Prob 27(8):083001

Campanac E, Gasselin C, Baude A, Rama S, Ankri N, Debanne D (2013) Enhanced intrinsic excitability in basket cells maintains excitatory-inhibitory balance in hippocampal circuits. Neuron 77(4):712–722. https://doi.org/10.1016/j.neuron.2012.12.020

Candès EJ, Recht B (2009) Exact matrix completion via convex optimization. Found Comput Math 9(6):717–772

Canto CB, Witter MP (2012a) Cellular properties of principal neurons in the rat entorhinal cortex. I. The lateral entorhinal cortex. *Hippocampus* 22(6):1256–1276. https://doi.org/10.1002/hipo.20997

Canto CB, Witter MP (2012b) Cellular properties of principal neurons in the rat entorhinal cortex. II. The medial entorhinal cortex. *Hippocampus* 22(6):1277–1299. https://doi.org/10.1002/hipo.20993

Cardin JA, Carlen M, Meletis K, Knoblich U, Zhang F, Deisseroth K et al (2010) Targeted optogenetic stimulation and recording of neurons in vivo using cell-type-specific expression of Channelrhodopsin-2. Nat Protoc 5(2):247–254. https://doi.org/10.1038/nprot.2009.228

Chamberland S, Topolnik L (2012) Inhibitory control of hippocampal inhibitory neurons. Front Neurosci 6:165. https://doi.org/10.3389/fnins.2012.00165

Chang H, Ciani S, Kidokoro Y (1994) Ion permeation properties of the glutamate receptor channel in cultured embryonic Drosophila myotubes. J Physiol 476(1):1–16

Chapeau-Blondeau F, Chambet N (1995) Synapse models for neural networks: from ion channel kinetics to multiplicative coefficient wij. Neural Comput 7(4):713–734

Chen C, He B, Yuan X (2012) Matrix completion via an alternating direction method. IMA J Numer Anal 32(1):227–245

Chiu CQ, Lur G, Morse TM, Carnevale NT, Ellis-Davies GC, Higley MJ (2013) Compartmentalization of GABAergic inhibition by dendritic spines. Science 340(6133):759–762. https://doi.org/10.1126/science.1234274

Clarke RJ, Johnson JW (2008) Voltage-dependent gating of NR1/2B NMDA receptors. J Physiol 586(Pt 23):5727–5741. https://doi.org/10.1113/jphysiol.2008.160622

Coalson RD, Kurnikova MG (2005) Poisson-Nernst-Planck theory approach to the calculation of current through biological ion channels. IEEE Trans Nanobioscience 4(1):81–93

Cooper KE, Gates PY, Eisenberg RS (1988) Surmounting barriers in ionic channels. Q Rev Biophys 21(3):331–364

Cossart R, Petanjek Z, Dumitriu D, Hirsch JC, Ben-Ari Y, Esclapez M et al (2006) Interneurons targeting similar layers receive synaptic inputs with similar kinetics. Hippocampus 16(4):408–420. https://doi.org/10.1002/hipo.20169

Couey JJ, Witoelar A, Zhang SJ, Zheng K, Ye J, Dunn B et al (2013) Recurrent inhibitory circuitry as a mechanism for grid formation. Nat Neurosci 16(3):318–324. https://doi.org/10.1038/nn.3310

Dan Y, Poo MM (2006) Spike timing-dependent plasticity: from synapse to perception. Physiol Rev 86(3):1033–1048. https://doi.org/10.1152/physrev.00030.2005

Dayan P, Abbott LF (2001) *Theoretical neuroscience: computational and mathematical modeling of neural systems* (computational neuroscience). Massachusetts Institute of Technology Press, Cambridge, MA

De Schutter E (2000) *Computational neuroscience: realistic modeling for experimentalists*. Boca Raton, CRC Press

De Schutter E (2010) *Computational modeling methods for neuroscientists* (computational neuroscience). MIT Press, Cambridge, MA

Derrick BE, Martinez JL Jr (1996) Associative, bidirectional modifications at the hippocampal mossy fibre-CA3 synapse. Nature 381(6581):429–434. https://doi.org/10.1038/381429a0

Destexhe A, Mainen ZF, Sejnowski TJ (1994a) An efficient method for computing synaptic conductances based on a kinetic model of receptor binding. Neural Comput 6(1):14–18

Destexhe A, Mainen ZF, Sejnowski TJ (1994b) Synthesis of models for excitable membranes, synaptic transmission and neuromodulation using a common kinetic formalism. J Comput Neurosci 1(3):195–230

Destexhe A, Mainen ZF, Sejnowski TJ (1995) Fast kinetic models for simulating AMPA, NMDA, GABA A and GABA B receptors. In: The neurobiology of computation. Springer, Boston, MA, pp 9–14

Dhillon A, Jones RS (2000) Laminar differences in recurrent excitatory transmission in the rat entorhinal cortex in vitro. Neuroscience 99(3):413–422

Dickson CT, Mena AR, Alonso A (1997) Electroresponsiveness of medial entorhinal cortex layer III neurons in vitro. Neuroscience 81(4):937–950

Dudek SM, Bear MF (1993) Bidirectional long-term modification of synaptic effectiveness in the adult and immature hippocampus. J Neurosci 13(7):2910–2918

Dumitriu D, Cossart R, Huang J, Yuste R (2007) Correlation between axonal morphologies and synaptic input kinetics of interneurons from mouse visual cortex. Cereb Cortex 17(1):81–91. https://doi.org/10.1093/cercor/bhj126

Eisenberg RS (1999) From structure to function in open ionic channels. J Membr Biol 171(1):1–24

Eisenberg, B. (2010) Crowded charges in ion channels. arXiv preprint arXiv:1009.1786

Eisenberg B (2012) A leading role for mathematics in the study of ionic solutions. SIAM News 45(9):11–12

Elfant D, Pal BZ, Emptage N, Capogna M (2008) Specific inhibitory synapses shift the balance from feedforward to feedback inhibition of hippocampal CA1 pyramidal cells. Eur J Neurosci 27(1):104–113. https://doi.org/10.1111/j.1460-9568.2007.06001.x

Empson RM, Heinemann U (1995) The perforant path projection to hippocampal area CA1 in the rat hippocampal-entorhinal cortex combined slice. J Physiol 484(Pt 3):707–720

Evans SM, Janson AM, Nyengaard JR (2004) Quantitative methods in neuroscience: a neuroanatomical approach. Oxford University Press, New York

Feng J (2004) Computational neuroscience: comprehensive approach (Chapman & Hall/CRC mathematical biology and medicine series). Chapman & Hall/CRC, Boca Raton

Freund TF, Buzsaki G (1996) Interneurons of the hippocampus. Hippocampus 6(4):347–470 doi:10.1002/(SICI)1098-1063(1996)6:4<347::AID-HIPO1>3.0.CO;2-I

Froemke RC, Dan Y (2002) Spike-timing-dependent synaptic modification induced by natural spike trains. Nature 416(6879):433–438. https://doi.org/10.1038/416433a

Froemke RC, Tsay IA, Raad M, Long JD, Dan Y (2006) Contribution of individual spikes in burst-induced long-term synaptic modification. J Neurophysiol 95(3):1620–1629. https://doi.org/10.1152/jn.00910.2005

Fuhrmann G, Segev I, Markram H, Tsodyks M (2002) Coding of temporal information by activity-dependent synapses. J Neurophysiol 87(1):140–148

Geiger JR, Lubke J, Roth A, Frotscher M, Jonas P (1997) Submillisecond AMPA receptor-mediated signaling at a principal neuron-interneuron synapse. Neuron 18(6):1009–1023

Gerhard F, Pipa G, Lima B, Neuenschwander S, Gerstner W (2011) Extraction of network topology from multi-electrode recordings: is there a small-world effect? Front Comput Neurosci 5:4. https://doi.org/10.3389/fncom.2011.00004

Germroth P, Schwerdtfeger WK, Buhl EH (1989) Morphology of identified entorhinal neurons projecting to the hippocampus. A light microscopical study combining retrograde tracing and intracellular injection. Neuroscience 30(3):683–691

Germroth P, Schwerdtfeger WK, Buhl EH (1991) Ultrastructure and aspects of functional organization of pyramidal and nonpyramidal entorhinal projection neurons contributing to the perforant path. J Comp Neurol 305(2):215–231. https://doi.org/10.1002/cne.903050205

Glickfeld LL, Scanziani M (2006) Distinct timing in the activity of cannabinoid-sensitive and cannabinoid-insensitive basket cells. Nat Neurosci 9(6):807–815. https://doi.org/10.1038/nn1688

Gloveli T, Schmitz D, Empson RM, Dugladze T, Heinemann U (1997) Morphological and electrophysiological characterization of layer III cells of the medial entorhinal cortex of the rat. Neuroscience 77(3):629–648

Gloveli T, Dugladze T, Saha S, Monyer H, Heinemann U, Traub RD et al (2005) Differential involvement of oriens/pyramidale interneurones in hippocampal network oscillations in vitro. J Physiol 562(Pt 1):131–147. https://doi.org/10.1113/jphysiol.2004.073007

Glyzin S, Kolesov AY, Rozov NK (2013) On a method for mathematical modeling of chemical synapses. Differ Equ 49(10):1193–1210

Goldman DE (1943) Potential, impedance, and rectification in membranes. J Gen Physiol 27(1):37–60

Goswami SP, Bucurenciu I, Jonas P (2012) Miniature IPSCs in hippocampal granule cells are triggered by voltage-gated Ca2+ channels via microdomain coupling. J Neurosci 32(41):14294–14304. https://doi.org/10.1523/JNEUROSCI.6104-11.2012

Gutig R, Aharonov R, Rotter S, Sompolinsky H (2003) Learning input correlations through nonlinear temporally asymmetric Hebbian plasticity. J Neurosci 23(9):3697–3714

Hajos N, Mody I (1997) Synaptic communication among hippocampal interneurons: properties of spontaneous IPSCs in morphologically identified cells. J Neurosci 17(21):8427–8442

Han ZS, Buhl EH, Lorinczi Z, Somogyi P (1993) A high degree of spatial selectivity in the axonal and dendritic domains of physiologically identified local-circuit neurons in the dentate gyrus of the rat hippocampus. Eur J Neurosci 5(5):395–410

Hardie JB, Pearce RA (2006) Active and passive membrane properties and intrinsic kinetics shape synaptic inhibition in hippocampal CA1 pyramidal neurons. J Neurosci 26(33):8559–8569. https://doi.org/10.1523/JNEUROSCI.0547-06.2006

Harney SC, Jones MV (2002) Pre- and postsynaptic properties of somatic and dendritic inhibition in dentate gyrus. Neuropharmacology 43(4):584–594

Harris E, Stewart M (2001) Propagation of synchronous epileptiform events from subiculum backward into area CA1 of rat brain slices. Brain Res 895(1–2):41–49

Harsch A, Robinson HP (2000) Postsynaptic variability of firing in rat cortical neurons: the roles of input synchronization and synaptic NMDA receptor conductance. J Neurosci 20(16):6181–6192

Hefft S, Jonas P (2005) Asynchronous GABA release generates long-lasting inhibition at a hippocampal interneuron-principal neuron synapse. Nat Neurosci 8(10):1319–1328. https://doi.org/10.1038/nn1542

Hellwig B (2000) A quantitative analysis of the local connectivity between pyramidal neurons in layers 2/3 of the rat visual cortex. Biol Cybern 82(2):111–121

Hennig MH (2013) Theoretical models of synaptic short term plasticity. Front Comput Neurosci 7:45. https://doi.org/10.3389/fncom.2013.00045

Hestrin S, Sah P, Nicoll RA (1990) Mechanisms generating the time course of dual component excitatory synaptic currents recorded in hippocampal slices. Neuron 5(3):247–253

Hodgkin A i, Huxley A, Katz B (1949) Ionic currents underlying activity in the giant axon of the squid. Arch Sci Physiol 3(2):129–150

Houser CR (2007) Interneurons of the dentate gyrus: an overview of cell types, terminal fields and neurochemical identity. Prog Brain Res 163:217–232. https://doi.org/10.1016/S0079-6123(07)63013-1

Jaffe D, Johnston D (1990) Induction of long-term potentiation at hippocampal mossy-fiber synapses follows a Hebbian rule. J Neurophysiol 64(3):948–960

Jahr CE, Stevens CF (1987) Glutamate activates multiple single channel conductances in hippocampal neurons. Nature 325(6104):522–525. https://doi.org/10.1038/325522a0

Jahr CE, Stevens CF (1990) A quantitative description of NMDA receptor-channel kinetic behavior. J Neurosci 10(6):1830–1837

Jiang X, Shen S, Cadwell CR, Berens P, Sinz F, Ecker AS et al (2015) Principles of connectivity among morphologically defined cell types in adult neocortex. Science 350(6264):aac9462. https://doi.org/10.1126/science.aac9462

Kandel ER, Spencer WA, Brinley FJ Jr (1961) Electrophysiology of hippocampal neurons. I. Sequential invasion and synaptic organization. J Neurophysiol 24:225–242

Karayannis T, Elfant D, Huerta-Ocampo I, Teki S, Scott RS, Rusakov DA et al (2010) Slow GABA transient and receptor desensitization shape synaptic responses evoked by hippocampal neurogliaform cells. J Neurosci 30(29):9898–9909. https://doi.org/10.1523/JNEUROSCI.5883-09.2010

Kaufman A, Dror G, Meilijson I, Ruppin E (2006) Gene expression of Caenorhabditis elegans neurons carries information on their synaptic connectivity. PLoS Comput Biol 2(12):e167–e167

Kelsch W, Li Z, Wieland S, Senkov O, Herb A, Gongrich C et al (2014) GluN2B-containing NMDA receptors promote glutamate synapse development in hippocampal interneurons. J Neurosci 34(48):16022–16030. https://doi.org/10.1523/JNEUROSCI.1210-14.2014

Kim NK, Robinson HP (2011) Effects of divalent cations on slow unblock of native NMDA receptors in mouse neocortical pyramidal neurons. Eur J Neurosci 34(2):199–212. https://doi.org/10.1111/j.1460-9568.2011.07768.x

Klausberger T (2009) GABAergic interneurons targeting dendrites of pyramidal cells in the CA1 area of the hippocampus. Eur J Neurosci 30(6):947–957. https://doi.org/10.1111/j.1460-9568.2009.06913.x

Koch C (1999) Biophysics of computation: information processing in single neurons (computational neuroscience). Oxford University Press, New York

Kohara K, Pignatelli M, Rivest AJ, Jung HY, Kitamura T, Suh J et al (2014) Cell type-specific genetic and optogenetic tools reveal hippocampal CA2 circuits. Nat Neurosci 17(2):269–279. https://doi.org/10.1038/nn.3614

Korinek M, Sedlacek M, Cais O, Dittert I, Vyklicky L Jr (2010) Temperature dependence of N-methyl-D-aspartate receptor channels and N-methyl-D-aspartate receptor excitatory postsynaptic currents. Neuroscience 165(3):736–748. https://doi.org/10.1016/j.neuroscience.2009.10.058

Kumar SS, Buckmaster PS (2006) Hyperexcitability, interneurons, and loss of GABAergic synapses in entorhinal cortex in a model of temporal lobe epilepsy. J Neurosci 26(17):4613–4623. https://doi.org/10.1523/JNEUROSCI.0064-06.2006

Kuner T, Schoepfer R (1996) Multiple structural elements determine subunit specificity of Mg2+ block in NMDA receptor channels. J Neurosci 16(11):3549–3558

Lacaille JC, Schwartzkroin PA (1988) Stratum lacunosum-moleculare interneurons of hippocampal CA1 region. I. Intracellular response characteristics, synaptic responses, and morphology. J Neurosci 8(4):1400–1410

Lacaille JC, Mueller AL, Kunkel DD, Schwartzkroin PA (1987) Local circuit interactions between oriens/alveus interneurons and CA1 pyramidal cells in hippocampal slices: electrophysiology and morphology. J Neurosci 7(7):1979–1993

Lamsa KP, Heeroma JH, Somogyi P, Rusakov DA, Kullmann DM (2007) Anti-Hebbian long-term potentiation in the hippocampal feedback inhibitory circuit. Science 315(5816):1262–1266. https://doi.org/10.1126/science.1137450

Larimer P, Strowbridge BW (2010) Representing information in cell assemblies: persistent activity mediated by semilunar granule cells. Nat Neurosci 13(2):213–222. https://doi.org/10.1038/nn.2458

Le Duigou C, Kullmann DM (2011) Group I mGluR agonist-evoked long-term potentiation in hippocampal oriens interneurons. J Neurosci 31(15):5777–5781. https://doi.org/10.1523/JNEUROSCI.6265-10.2011

Le Duigou C, Savary E, Kullmann DM, Miles R (2015) Induction of anti-Hebbian LTP in CA1 stratum Oriens interneurons: interactions between group I metabotropic glutamate receptors and M1 muscarinic receptors. J Neurosci 35(40):13542–13554. https://doi.org/10.1523/JNEUROSCI.0956-15.2015

Le Roux N, Cabezas C, Bohm UL, Poncer JC (2013) Input-specific learning rules at excitatory synapses onto hippocampal parvalbumin-expressing interneurons. J Physiol 591(Pt 7):1809–1822. https://doi.org/10.1113/jphysiol.2012.245852

Ledri M, Sorensen AT, Erdelyi F, Szabo G, Kokaia M (2011) Tuning afferent synapses of hippocampal interneurons by neuropeptide Y. Hippocampus 21(2):198–211. https://doi.org/10.1002/hipo.20740

Lee SJ, Escobedo-Lozoya Y, Szatmari EM, Yasuda R (2009) Activation of CaMKII in single dendritic spines during long-term potentiation. Nature 458(7236):299–304. https://doi.org/10.1038/nature07842

Lei S, Pelkey KA, Topolnik L, Congar P, Lacaille JC, McBain CJ (2003) Depolarization-induced long-term depression at hippocampal mossy fiber-CA3 pyramidal neuron synapses. J Neurosci 23(30):9786–9795

Lewis CA (1979) Ion-concentration dependence of the reversal potential and the single channel conductance of ion channels at the frog neuromuscular junction. J Physiol 286:417–445

Liu YC, Cheng JK, Lien CC (2014) Rapid dynamic changes of dendritic inhibition in the dentate gyrus by presynaptic activity patterns. J Neurosci 34(4):1344–1357. https://doi.org/10.1523/JNEUROSCI.2566-13.2014

Lovett-Barron M, Turi GF, Kaifosh P, Lee PH, Bolze F, Sun XH et al (2012) Regulation of neuronal input transformations by tunable dendritic inhibition. Nat Neurosci 15(3):423–430., S421-423. https://doi.org/10.1038/nn.3024

Maccaferri G, Toth K, McBain CJ (1998) Target-specific expression of presynaptic mossy fiber plasticity. Science 279(5355):1368–1370

Markram H, Lubke J, Frotscher M, Sakmann B (1997) Regulation of synaptic efficacy by coincidence of postsynaptic APs and EPSPs. Science 275(5297):213–215

Markram H, Wang Y, Tsodyks M (1998) Differential signaling via the same axon of neocortical pyramidal neurons. Proc Natl Acad Sci U S A 95(9):5323–5328

Markram H, Gerstner W, Sjostrom PJ (2012) Spike-timing-dependent plasticity: a comprehensive overview. Front Synaptic Neurosci 4:2. https://doi.org/10.3389/fnsyn.2012.00002

Markram H, Muller E, Ramaswamy S, Reimann MW, Abdellah M, Sanchez CA et al (2015) Reconstruction and simulation of neocortical microcircuitry. Cell 163(2):456–492. https://doi.org/10.1016/j.cell.2015.09.029

Markwardt SJ, Dieni CV, Wadiche JI, Overstreet-Wadiche L (2011) Ivy/neurogliaform interneurons coordinate activity in the neurogenic niche. Nat Neurosci 14(11):1407–1409. https://doi.org/10.1038/nn.2935

Marti-Subirana A, Soriano E, Garcia-Verdugo JM (1986) Morphological aspects of the ectopic granule-like cellular populations in the albino rat hippocampal formation: a Golgi study. J Anat 144:31–47

Mayer ML, Westbrook GL, Guthrie PB (1984) Voltage-dependent block by Mg2+ of NMDA responses in spinal cord neurones. Nature 309(5965):261–263

Mazumder R, Hastie T, Tibshirani R (2010) Spectral regularization algorithms for learning large incomplete matrices. J Mach Learn Res 11:2287–2322

McCloskey DP, Hintz TM, Pierce JP, Scharfman HE (2006) Stereological methods reveal the robust size and stability of ectopic hilar granule cells after pilocarpine-induced status epilepticus in the adult rat. Eur J Neurosci 24(8):2203–2210. https://doi.org/10.1111/j.1460-9568.2006.05101.x

Melzer S, Michael M, Caputi A, Eliava M, Fuchs EC, Whittington MA et al (2012) Long-range-projecting GABAergic neurons modulate inhibition in hippocampus and entorhinal cortex. Science 335(6075):1506–1510. https://doi.org/10.1126/science.1217139

Miles R, Toth K, Gulyas AI, Hajos N, Freund TF (1996) Differences between somatic and dendritic inhibition in the hippocampus. Neuron 16(4):815–823

Moradi K, Kaka G, Gharibzadeh S (2012) The role of passive normalization, voltage-gated channels and synaptic scaling in site-independence of somatic EPSP amplitude in CA1 pyramidal neurons. Neurosci Res 73(1):8–16

Moradi K, Moradi K, Ganjkhani M, Hajihasani M, Gharibzadeh S, Kaka G (2013) A fast model of voltage-dependent NMDA receptors. J Comput Neurosci 34(3):521–531. https://doi.org/10.1007/s10827-012-0434-4

Morrison A, Aertsen A, Diesmann M (2007) Spike-timing-dependent plasticity in balanced random networks. Neural Comput 19(6):1437–1467. https://doi.org/10.1162/neco.2007.19.6.1437

Morrison A, Diesmann M, Gerstner W (2008) Phenomenological models of synaptic plasticity based on spike timing. Biol Cybern 98(6):459–478. https://doi.org/10.1007/s00422-008-0233-1

Mullner FE, Wierenga CJ, Bonhoeffer T (2015) Precision of inhibition: dendritic inhibition by individual GABAergic synapses on hippocampal pyramidal cells is confined in space and time. Neuron 87(3):576–589. https://doi.org/10.1016/j.neuron.2015.07.003

Nicholson E, Kullmann DM (2014) Long-term potentiation in hippocampal oriens interneurons: postsynaptic induction, presynaptic expression and evaluation of candidate retrograde factors. Philos Trans R Soc Lond Ser B Biol Sci 369(1633):20130133. https://doi.org/10.1098/rstb.2013.0133

Nikolaev MV, Magazanik LG, Tikhonov DB (2012) Influence of external magnesium ions on the NMDA receptor channel block by different types of organic cations. Neuropharmacology 62(5–6):2078–2085. https://doi.org/10.1016/j.neuropharm.2011.12.029

Nowak L, Bregestovski P, Ascher P, Herbet A, Prochiantz A (1984) Magnesium gates glutamate-activated channels in mouse central neurones. Nature 307(5950):462–465

Okazaki MM, Molnar P, Nadler JV (1999) Recurrent mossy fiber pathway in rat dentate gyrus: synaptic currents evoked in presence and absence of seizure-induced growth. J Neurophysiol 81(4):1645–1660

Oren I, Nissen W, Kullmann DM, Somogyi P, Lamsa KP (2009) Role of ionotropic glutamate receptors in long-term potentiation in rat hippocampal CA1 oriens-lacunosum moleculare interneurons. J Neurosci 29(4):939–950. https://doi.org/10.1523/JNEUROSCI.3251-08.2009

Otis TS, Mody I (1992) Modulation of decay kinetics and frequency of GABAA receptor-mediated spontaneous inhibitory postsynaptic currents in hippocampal neurons. Neuroscience 49(1):13–32

Patneau DK, Mayer ML (1991) Kinetic analysis of interactions between kainate and AMPA: evidence for activation of a single receptor in mouse hippocampal neurons. Neuron 6(5):785–798

Patneau DK, Mayer ML, Jane DE, Watkins JC (1992) Activation and desensitization of AMPA/kainate receptors by novel derivatives of willardiine. J Neurosci 12(2):595–606

Pawelzik H, Hughes DI, Thomson AM (2002) Physiological and morphological diversity of immunocytochemically defined parvalbumin- and cholecystokinin-positive interneurones in CA1 of the adult rat hippocampus. J Comp Neurol 443(4):346–367

Pawelzik H, Hughes DI, Thomson AM (2003) Modulation of inhibitory autapses and synapses on rat CA1 interneurones by GABA(A) receptor ligands. J Physiol 546(Pt 3):701–716

Perea G, Araque A (2007) Astrocytes potentiate transmitter release at single hippocampal synapses. Science 317(5841):1083–1086. https://doi.org/10.1126/science.1144640

Perez Y, Morin F, Lacaille JC (2001) A hebbian form of long-term potentiation dependent on mGluR1a in hippocampal inhibitory interneurons. Proc Natl Acad Sci U S A 98(16):9401–9406. https://doi.org/10.1073/pnas.161493498

Pfister JP, Gerstner W (2006) Triplets of spikes in a model of spike timing-dependent plasticity. J Neurosci 26(38):9673–9682. https://doi.org/10.1523/JNEUROSCI.1425-06.2006

Pierce JP, McCloskey DP, Scharfman HE (2011) Morphometry of hilar ectopic granule cells in the rat. J Comp Neurol 519(6):1196–1218. https://doi.org/10.1002/cne.22568

Price CJ, Cauli B, Kovacs ER, Kulik A, Lambolez B, Shigemoto R et al (2005) Neurogliaform neurons form a novel inhibitory network in the hippocampal CA1 area. J Neurosci 25(29):6775–6786. https://doi.org/10.1523/JNEUROSCI.1135-05.2005

Qian A, Johnson JW (2006) Permeant ion effects on external Mg2+ block of NR1/2D NMDA receptors. J Neurosci 26(42):10899–10910. https://doi.org/10.1523/JNEUROSCI.3453-06.2006

Quattrocolo G, Maccaferri G (2013) Novel GABAergic circuits mediating excitation/inhibition of Cajal-Retzius cells in the developing hippocampus. J Neurosci 33(13):5486–5498. https://doi.org/10.1523/JNEUROSCI.5680-12.2013

Quattrocolo G, Maccaferri G (2014) Optogenetic activation of cajal-retzius cells reveals their glutamatergic output and a novel feedforward circuit in the developing mouse hippocampus. J Neurosci 34(39):13018–13032. https://doi.org/10.1523/JNEUROSCI.1407-14.2014

Raghavachari S, Lisman JE (2004) Properties of quantal transmission at CA1 synapses. J Neurophysiol 92(4):2456–2467. https://doi.org/10.1152/jn.00258.2004

Reimann MW, King JG, Muller EB, Ramaswamy S, Markram H (2015) An algorithm to predict the connectome of neural microcircuits. Front Comput Neurosci 9:120. https://doi.org/10.3389/fncom.2015.00120

Ross ST, Soltesz I (2001) Long-term plasticity in interneurons of the dentate gyrus. Proc Natl Acad Sci U S A 98(15):8874–8879. https://doi.org/10.1073/pnas.141042398

Rothman JS (2015) Modeling Synapses. In: Jaeger D, Jung R (eds) Encyclopedia of computational neuroscience. Springer New York, New York, NY, pp 1738–1750. https://doi.org/10.1007/978-1-4614-6675-8_240

Rothman JS, Silver RA (2014) Data-driven modeling of synaptic transmission and integration. Prog Mol Biol Transl Sci 123:305–350. https://doi.org/10.1016/B978-0-12-397897-4.00004-8

Santhakumar V, Aradi I, Soltesz I (2005) Role of mossy fiber sprouting and mossy cell loss in hyperexcitability: a network model of the dentate gyrus incorporating cell types and axonal topography. J Neurophysiol 93(1):437–453. https://doi.org/10.1152/jn.00777.2004

Savanthrapadian S, Meyer T, Elgueta C, Booker SA, Vida I, Bartos M (2014) Synaptic properties of SOM- and CCK-expressing cells in dentate gyrus interneuron networks. J Neurosci 34(24):8197–8209. https://doi.org/10.1523/JNEUROSCI.5433-13.2014

Scharfman HE (1994) Evidence from simultaneous intracellular recordings in rat hippocampal slices that area CA3 pyramidal cells innervate dentate hilar mossy cells. J Neurophysiol 72(5):2167–2180

Scharfman HE, Pierce JP (2012) New insights into the role of hilar ectopic granule cells in the dentate gyrus based on quantitative anatomic analysis and three-dimensional reconstruction. Epilepsia 53(Suppl 1):109–115. https://doi.org/10.1111/j.1528-1167.2012.03480.x

Scharfman HE, Sollas AE, Berger RE, Goodman JH, Pierce JP (2003) Perforant path activation of ectopic granule cells that are born after pilocarpine-induced seizures. Neuroscience 121(4):1017–1029

Schneider CJ, Bezaire M, Soltesz I (2012) Toward a full-scale computational model of the rat dentate gyrus. Front Neural Circuits 6:83. https://doi.org/10.3389/fncir.2012.00083

Schurmans S, Schiffmann SN, Gurden H, Lemaire M, Lipp HP, Schwam V et al (1997) Impaired long-term potentiation induction in dentate gyrus of calretinin-deficient mice. Proc Natl Acad Sci U S A 94(19):10415–10420

Scimemi A (2014) Plasticity of GABA transporters: an unconventional route to shape inhibitory synaptic transmission. Front Cell Neurosci 8:128. https://doi.org/10.3389/fncel.2014.00128

Scorcioni R, Hamilton DJ, Ascoli GA (2008) Self-sustaining non-repetitive activity in a large scale neuronal-level model of the hippocampal circuit. Neural Netw 21(8):1153–1163. https://doi.org/10.1016/j.neunet.2008.05.006

Scorza CA, Araujo BH, Leite LA, Torres LB, Otalora LF, Oliveira MS et al (2011) Morphological and electrophysiological properties of pyramidal-like neurons in the stratum oriens of Cornu ammonis 1 and Cornu ammonis 2 area of Proechimys. Neuroscience 177:252–268. https://doi.org/10.1016/j.neuroscience.2010.12.054

Sik A, Penttonen M, Buzsaki G (1997) Interneurons in the hippocampal dentate gyrus: an in vivo intracellular study. Eur J Neurosci 9(3):573–588

Sjostrom PJ, Turrigiano GG, Nelson SB (2001) Rate, timing, and cooperativity jointly determine cortical synaptic plasticity. Neuron 32(6):1149–1164

Somogyi P, Klausberger T (2005) Defined types of cortical interneurone structure space and spike timing in the hippocampus. J Physiol 562(Pt 1):9–26. https://doi.org/10.1113/jphysiol.2004.078915

Song S, Miller KD, Abbott LF (2000) Competitive Hebbian learning through spike-timing-dependent synaptic plasticity. Nat Neurosci 3(9):919–926. https://doi.org/10.1038/78829

Song S, Sjostrom PJ, Reigl M, Nelson S, Chklovskii DB (2005) Highly nonrandom features of synaptic connectivity in local cortical circuits. PLoS Biol 3(3):e68. https://doi.org/10.1371/journal.pbio.0030068

Spencer WA, Kandel ER (1961) Hippocampal neuron responses to selective activation of recurrent collaterals of hippocampofugal axons. Exp Neurol 4(2):149–161

Sporns O, Zwi JD (2004) The small world of the cerebral cortex. Neuroinformatics 2(2):145–162

Spruston N, Jonas P, Sakmann B (1995) Dendritic glutamate receptor channels in rat hippocampal CA3 and CA1 pyramidal neurons. J Physiol 482(Pt 2):325–352

Standage D, Jalil S, Trappenberg T (2007) Computational consequences of experimentally derived spike-time and weight dependent plasticity rules. Biol Cybern 96(6):615–623. https://doi.org/10.1007/s00422-007-0152-6

Sterratt D (2011) Principles of computational modelling in neuroscience. In: Cambridge. Cambridge University Press, New York

Steward O (1976) Topographic organization of the projections from the entorhinal area to the hippocampal formation of the rat. J Comp Neurol 167(3):285–314. https://doi.org/10.1002/cne.901670303

Steward O, Scoville SA (1976) Cells of origin of entorhinal cortical afferents to the hippocampus and fascia dentata of the rat. J Comp Neurol 169(3):347–370. https://doi.org/10.1002/cne.901690306

Stiles JR, Bartol TM (2001) Monte Carlo methods for simulating realistic synaptic microphysiology using MCell. Comput Neurosci Realistic Model Exp:87–127

Stiles JR, Van Helden D, Bartol TM Jr, Salpeter EE, Salpeter MM (1996) Miniature endplate current rise times less than 100 microseconds from improved dual recordings can be modeled with passive acetylcholine diffusion from a synaptic vesicle. Proc Natl Acad Sci U S A 93(12):5747–5752

Szabadics J, Soltesz I (2009) Functional specificity of mossy fiber innervation of GABAergic cells in the hippocampus. J Neurosci 29(13):4239–4251. https://doi.org/10.1523/JNEUROSCI.5390-08.2009

Szabadics J, Varga C, Brunner J, Chen K, Soltesz I (2010) Granule cells in the CA3 area. J Neurosci 30(24):8296–8307. https://doi.org/10.1523/JNEUROSCI.5602-09.2010

Szabo A, Somogyi J, Cauli B, Lambolez B, Somogyi P, Lamsa KP (2012) Calcium-permeable AMPA receptors provide a common mechanism for LTP in glutamatergic synapses of distinct hippocampal interneuron types. J Neurosci 32(19):6511–6516. https://doi.org/10.1523/JNEUROSCI.0206-12.2012

Szabo GG, Papp OI, Mate Z, Szabo G, Hajos N (2014) Anatomically heterogeneous populations of CB1 cannabinoid receptor-expressing interneurons in the CA3 region of the hippocampus show homogeneous input-output characteristics. Hippocampus 24(12):1506–1523. https://doi.org/10.1002/hipo.22330

Tahvildari B, Alonso A (2005) Morphological and electrophysiological properties of lateral entorhinal cortex layers II and III principal neurons. J Comp Neurol 491(2):123–140. https://doi.org/10.1002/cne.20706

Toth K, McBain CJ (1998) Afferent-specific innervation of two distinct AMPA receptor subtypes on single hippocampal interneurons. Nat Neurosci 1(7):572–578. https://doi.org/10.1038/2807

Trappenberg TP (2010) Fundamentals of computational neuroscience, 2nd edn. Oxford University Press, Oxford/New York

Tsodyks MV, Markram H (1997) The neural code between neocortical pyramidal neurons depends on neurotransmitter release probability. Proc Natl Acad Sci U S A 94(2):719–723

Tsodyks M, Uziel A, Markram H (2000) Synchrony generation in recurrent networks with frequency-dependent synapses. J Neurosci 20(1):RC50

Turrigiano G (2012) Homeostatic synaptic plasticity: local and global mechanisms for stabilizing neuronal function. Cold Spring Harb Perspect Biol 4(1):a005736. https://doi.org/10.1101/cshperspect.a005736

Turrigiano GG, Leslie KR, Desai NS, Rutherford LC, Nelson SB (1998) Activity-dependent scaling of quantal amplitude in neocortical neurons. Nature 391(6670):892–896. https://doi.org/10.1038/36103

Urban NN, Barrionuevo G (1996) Induction of hebbian and non-hebbian mossy fiber long-term potentiation by distinct patterns of high-frequency stimulation. J Neurosci 16(13):4293–4299

van der Linden S, Lopes da Silva FH (1998) Comparison of the electrophysiology and morphology of layers III and II neurons of the rat medial entorhinal cortex in vitro. Eur J Neurosci 10(4):1479–1489

van Rossum MC, Bi GQ, Turrigiano GG (2000) Stable Hebbian learning from spike timing-dependent plasticity. J Neurosci 20(23):8812–8821

Varadan V, Miller DM 3rd, Anastassiou D (2006) Computational inference of the molecular logic for synaptic connectivity in C. elegans. Bioinformatics 22(14):e497–e506. https://doi.org/10.1093/bioinformatics/btl224

Varela JA, Sen K, Gibson J, Fost J, Abbott LF, Nelson SB (1997) A quantitative description of short-term plasticity at excitatory synapses in layer 2/3 of rat primary visual cortex. J Neurosci 17(20):7926–7940

Vida I, Halasy K, Szinyei C, Somogyi P, Buhl EH (1998) Unitary IPSPs evoked by interneurons at the stratum radiatum-stratum lacunosum-moleculare border in the CA1 area of the rat hippocampus in vitro. J Physiol 506(Pt 3):755–773

Vitureira N, Goda Y (2013) The interplay between Hebbian and homeostatic synaptic plasticity. J Cell Biol 203(2):175–186. https://doi.org/10.1083/jcb.201306030

Wallisch P (2014) MATLAB for neuroscientists: an introduction to scientific computing in MATLAB, 2nd edn. Academic, Amsterdam

Wang HX, Gerkin RC, Nauen DW, Bi GQ (2005) Coactivation and timing-dependent integration of synaptic potentiation and depression. Nat Neurosci 8(2):187–193. https://doi.org/10.1038/nn1387

Wester JC, McBain CJ (2014) Behavioral state-dependent modulation of distinct interneuron subtypes and consequences for circuit function. Curr Opin Neurobiol 29:118–125. https://doi.org/10.1016/j.conb.2014.07.007

Wheeler DW, White CM, Rees CL, Komendantov AO, Hamilton DJ, Ascoli GA (2015) Hippocampome.org: a knowledge base of neuron types in the rodent hippocampus. Elife 4. https://doi.org/10.7554/eLife.09960

Whittington MA, Traub RD, Jefferys JG (1995) Synchronized oscillations in interneuron networks driven by metabotropic glutamate receptor activation. Nature 373(6515):612–615. https://doi.org/10.1038/373612a0

Williams PA, Larimer P, Gao Y, Strowbridge BW (2007) Semilunar granule cells: glutamatergic neurons in the rat dentate gyrus with axon collaterals in the inner molecular layer. J Neurosci 27(50):13756–13761. https://doi.org/10.1523/JNEUROSCI.4053-07.2007

Woodin MA, Ganguly K, Poo MM (2003) Coincident pre- and postsynaptic activity modifies GABAergic synapses by postsynaptic changes in Cl- transporter activity. Neuron 39(5):807–820

Yang K, Dani JA (2014) Dopamine D1 and D5 receptors modulate spike timing-dependent plasticity at medial perforant path to dentate granule cell synapses. J Neurosci 34(48):15888–15897. https://doi.org/10.1523/JNEUROSCI.2400-14.2014

Yang YC, Lee CH, Kuo CC (2010) Ionic flow enhances low-affinity binding: a revised mechanistic view into Mg2+ block of NMDA receptors. J Physiol 588(Pt 4):633–650. https://doi.org/10.1113/jphysiol.2009.178913

Zhu Y, Auerbach A (2001a) K(+) occupancy of the N-methyl-d-aspartate receptor channel probed by Mg(2+) block. J Gen Physiol 117(3):287–298

Zhu Y, Auerbach A (2001b) Na(+) occupancy and Mg(2+) block of the n-methyl-d-aspartate receptor channel. J Gen Physiol 117(3):275–286

Spatiotemporal Patterns of Granule Cell Activity Revealed by a Large-Scale, Biologically Realistic Model of the Hippocampal Dentate Gyrus

Gene J. Yu, Phillip J. Hendrickson, Dong Song, and Theodore W. Berger

Abstract Interest in the hippocampus has generated vast amounts of experimental data describing hippocampal properties, including anatomical, morphological, biophysical, and synaptic transmission levels of analysis. However, this wealth of structural and functional detail has not guaranteed insight into higher levels of system operation.

In this chapter, we propose a computational framework that can integrate the available, quantitative information at various levels of organization to construct a three-dimensional, large-scale, biologically realistic, spiking neuronal network model with the goal of representing all major neurons and neuron types, and the synaptic connectivity, found in the rat hippocampus. In this approach, detailed neuron models are constructed using a multi-compartment approach.

Simulations were performed to investigate the role of network architecture on the spatiotemporal patterns of activity generated by the dentate gyrus. The results show that the topographical projection of axons between the entorhinal cortex and the dentate granule cells organizes the postsynaptic population into subgroups of neurons that exhibit correlated firing expressed as spatiotemporal clusters of firing. These clusters may represent a potential "intermediate" level of hippocampal function. Furthermore, the effects of inhibitory and excitatory circuits, and their interactions, on the population granule cell response were explored using dentate basket cells and hilar mossy cells.

G. J. Yu (✉) · P. J. Hendrickson · D. Song · T. W. Berger
Department of Biomedical Engineering, Center for Neural Engineering, Viterbi School of Engineering, University of Southern California, Los Angeles, CA, USA
e-mail: geneyu@usc.edu; phendric@usc.edu; dsong@usc.edu; berger@usc.edu

V. Cutsuridis et al. (eds.), *Hippocampal Microcircuits*, Springer Series in Computational Neuroscience, https://doi.org/10.1007/978-3-319-99103-0_12

Overview

Comprehensive Computational Framework for Neural Systems

Possibly more than any other brain area, interest in the hippocampus has generated vast amounts of experimental data through the efforts of the neuroscience community. This has led to the accumulation of large amounts of quantitative information describing the properties of the hippocampus, including anatomical, morphological, biophysical, biochemical, and synaptic transmission levels of analysis. As with other brain areas, however, this wealth of structural and functional detail has not guaranteed insight into higher levels of system operation. The field continues, and rightfully so, to struggle to understand how all of the cellular and network properties of the hippocampus dynamically interact to produce the global functional properties of the larger system.

Multiple theories and hypotheses have been put forward to contextualize and interpret subsets of the huge amount of hippocampal data. These works have attempted to provide possible explanations for various behavioral and cognitive functions believed to be subserved by the hippocampus (Marr 1971; McNaughton and Morris 1987; Levy 1989; Treves and Rolls 1994; McClelland et al. 1995; Hasselmo 2005; Solstad et al. 2006; Myers and Scharfman 2011). Although these studies are highly admirable and have helped guide the field in its thinking about the cellular and network bases of hippocampal memory, they are limited by the narrow or partial scope of the quantitative experimental data on which they are based and by the multiple levels of neural organization that various models and theories must "reach over" to account for system/behavioral phenomena. There remain few computational frameworks (see Morgan and Soltesz 2010) that integrate at least a significant portion of the quantitative cellular and anatomical data of the hippocampus for its multiple subfields. As a consequence, there are no models to date that successfully integrate such data and extend those "lower-level" properties to putative explanations of "higher-level" function, be it at the system level or the cognitive and behavioral levels.

Hippocampal Architectural Constraints on Network Function

If there is any one brain structure that provides an opportunity for understanding integration from molecular to system neural function, it is the hippocampus. One basis for this argument has already been mentioned, namely, the large body of quantitative information already collected about its molecular, cellular, and network structure and function. The second basis is the nature and relative simplicity of the structural organization of the hippocampus.

There is a highly well-defined organization to the hippocampal formation consisting of a predominantly feedforward architecture wherein activity is propagated

from entorhinal cortex to the dentate gyrus, to the CA3/4 pyramidal zones, and finally to the CA1/2 pyramidal regions (Andersen et al. 1971; Swanson et al. 1978). The projections between each of the subfields exhibit unique organizational principles (e.g., targets and topography) (Swanson et al. 1978; Ishizuka et al. 1990; Freund and Buzsáki 1996; Dolorfo and Amaral 1998). These studies reveal a topographic projection between neural populations in that they are incomplete (in the sense that any one neuron within a subfield does not project to all neurons in the next subfield) and nonrandom nature of hippocampal connectivity. The topography describes the ordered structural connectivity of a neural system which organizes individual neurons into collections of neurons and offers a bridge between lower-level cellular dynamics and higher-level population dynamics.

General Framework of the Model

We are proposing a computational framework that is able to integrate the majority of available, quantitative structural and functional information at various levels of organization to generate a large-scale, biologically realistic, neuronal network model with the goal of representing all of the major neurons and neuron types, and the synaptic connectivity, found in one hemisphere of the rat hippocampus. In this approach, detailed neuron models are constructed using a multi-compartment approach (on the order of hundreds of compartments per neuron) which are then geometrically arranged based on anatomical data to encompass the entire longitudinal extent of the hippocampus and finally synaptically connected using the topographical constraints describing the region.

Using this framework, a series of simulations were performed which primarily explored the role of network architecture on the spatiotemporal patterns of activity generated by populations of granule cells in the dentate gyrus. The simulations involved pulse (all-or-none, spike-like) inputs from layer II cells of the entorhinal cortex and the spike-like granule cell and basket cell outputs from the dentate gyrus, with AMPA receptor channel-mediated excitatory synapses of granule cells and $GABA_A$ receptor channel-mediated inhibitory synapses of basket cells. The simulations in this chapter show specifically that the *topographical projection* of axons between the entorhinal cortex and the dentate granule cell regions of the hippocampal formation organizes the postsynaptic population into subgroups of neurons that exhibit correlated firing expressed as *spatiotemporal clusters* of firing. These findings strongly suggest that topography may act as a spatial filter whose functional characteristics are dependent on the three-dimensional properties of that topography. During this investigation, the effects of inhibitory and excitatory circuits, and their interactions, on the population granule cell response also were systematically explored by including study of feedforward and feedback inhibition and study of the hierarchical regulation of lower-level excitatory and inhibitory circuitry by dentate hilar mossy cells.

"Intermediate" Levels of System Function

One of the fundamental issues that has arisen in using our multi-level model of the hippocampus is that there is a need to identify what might be termed "intermediate" levels of hippocampal function. There are generally well-understood interpretations of "synaptic function" (presynaptic release, postsynaptic current and/or potential, etc.) and "cellular function" (metabolism, action potential generation, etc.). Although there are multiple possible definitions for each level of functionality, there is general agreement on what are the small number of possibilities in each case. But once "molecular," "synaptic," and "cellular functions" are accounted for, what is the definition of "multicellular" or "system" function, upon which there is generally little if any universal agreement? Even more difficult to address is the identification of levels of functions that lie between "cellular" or "multicellular" and behavioral or cognitive functions. Behavioral and inferred cognitive functions for the hippocampus have a theoretically rich and experimentally broad history (O'Keefe and Nadel 1978; Berger et al. 1986; Squire 1986; Berger and Bassett 1992; Cohen and Eichenbaum 1993; Nadel and Moscovitch 1997; Aggleton and Brown 1999). How hippocampal cognitive and behavioral functions derive from cellular and molecular dynamics remains a mystery.

For insights to be reached on this issue, we must identify levels of system or subsystem function that lie between the cellular and the behavioral. One of the main objectives in developing the large-scale model of the hippocampus described here was so that it would be possible to "observe" simulated spiking activity of large numbers of neurons simultaneously – the activity of many more neurons than had ever been observed previously, either computationally or experimentally. If there were regularities in granule cell firing that became apparent beyond the level of tens of neurons, i.e., beyond the levels typically used in previous studies identifying behavioral or cognitive population "correlates" of hippocampal cell activity (Berger et al. 1983, 2011; Berger and Weisz 1987; Eichenbaum et al. 1989; Hampson et al. 1999; Krupic et al. 2012; MacKenzie et al. 2014), such "regularities" in population firing of hippocampal neurons would indicate the existence of some kind of higher-level "structure" in the organization of the hippocampal system. The computational studies reviewed here have revealed one such an organizational structure: the "clusters" of granule cell firing revealed by the present analyses indicate cyclical, correlated levels of excitability distributed both in space and time throughout the rostro-caudal extent of the hippocampus in response to low levels of random entorhinal cortical activity. Because such correlated, clustering of granule cell firing is expressed to a low level of relatively even entorhinal input and does not require a radically, strong, and/or rhythmic bursting from entorhinal cortex, we believe the granule cell clusters represent a preferential space-time filtering by the dentate gyrus that constitutes a first-order level of processing by the multiple stages of hippocampal circuitry.

The Model

Though much data on the hippocampus exists, the search, quantification, and implementation of these data into a comprehensive model is problematic, considering the large variety of techniques that can be applied to characterize any particular hippocampal feature and the number of features that require investigation. Below, we review the experimental work that has been incorporated into this version of the model and the methods we used to extract and implement the results of those studies.

Anatomical Boundaries

Anatomical Description of the Hippocampus and Dentate Gyrus

The three-dimensional structure of the hippocampus resembles a curved cylinder (see Fig. 1) with a single homogeneous granule cell layer and a pyramidal cell layer that traditionally has been divided into four subsections (Lorente de Nó 1934; Ramón y Cajal 1968). A cross section of the hippocampus can reveal its principal internal structure in the form of two interlocking C-shapes. One of the structures is known as the dentate gyrus, and the other is known as the cornus ammonis (CA) which is commonly divided into four main subfields, the CA3/4 and the CA1/2.

The dentate gyrus is commonly divided into two blades, the upper and lower half of its C-shape. The suprapyramidal blade, also known as the enclosed or dorsal

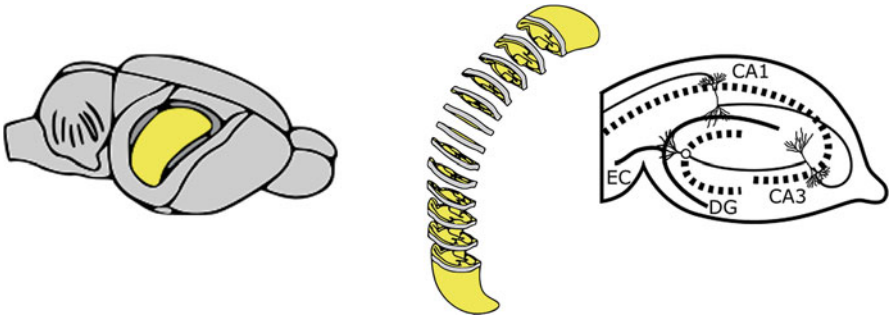

Fig. 1 Schematic representation of the rat hippocampus. (Left) Location of the hippocampus (yellow) relative to the rest of the rat brain (neocortex removed). (Middle) Depiction of how transverse slices typically are obtained relative to the septo-temporal axis of the hippocampus. (Right) The classical trisynaptic circuit of the hippocampus where the entorhinal cortex (EC) projects its inputs to the dentate gyrus (DG), the dentate projects to the CA3/4 regions, the CA3/4 projects to the CA1/2 regions, and the CA1 provides the output of the hippocampus to other cortical structures. Not shown here are entorhinal projections to the distal dendrites of CA3 (from layer II) and to the distal dendrites of CA1 (from layer III)

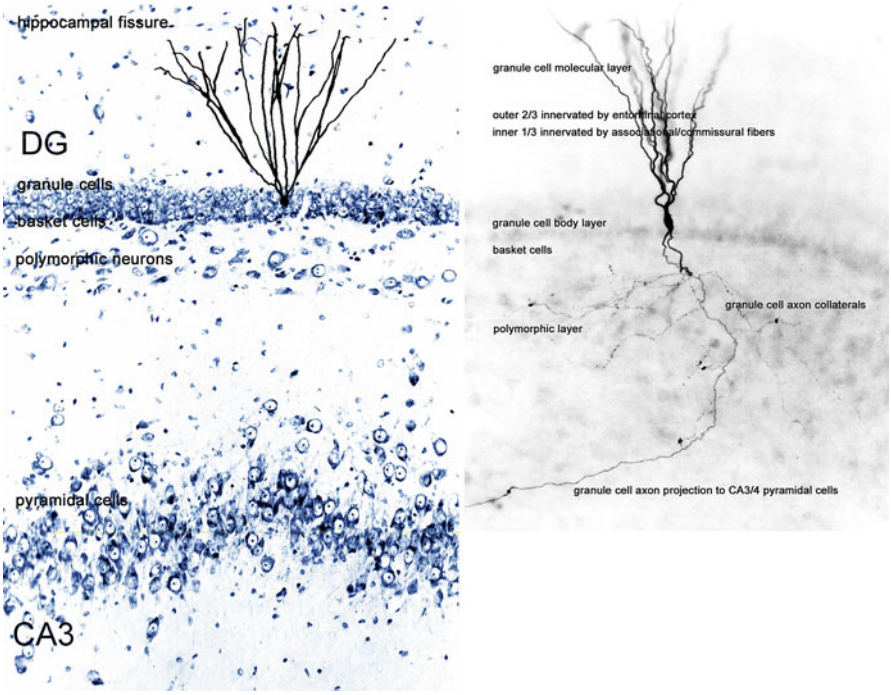

Fig. 2 Division of the dentate gyrus into the molecular, granule cell, and polymorphic layers. The molecular layer contains the dendrites of the granule cells. The densely packed cell bodies of the granule cells form the granule cell layer. The polymorphic layer is comprised of inhibitory and excitatory interneurons. Granule cell axons collateralize within the polymorphic layer to provide input to the interneurons. Granule cells also send axons through the polymorphic layer to synapse with CA3/4 pyramidal cells

blade, refers to the half of the dentate that is encapsulated by the CA regions. The remaining half is labeled the infrapyramidal blade, also known as the exposed or ventral blade, and the crest refers to the region where the infrapyramidal and suprapyramidal blades join. Furthermore, the dentate gyrus is divided into three layers. The outermost layer is the molecular layer, the middle layer is the granule cell layer, and the final layer is the hilus or the polymorphic layer (see Fig. 2).

The entorhinal cortex, which lies outside the hippocampus (but is formally defined as part of the hippocampal formation), contributes significantly to the input of the hippocampus. Layer II cells of the entorhinal cortex send axons to the outer two-thirds of the molecular layer of the dentate gyrus and synapse along the infra- and suprapyramidal blades as well as extend into and form synapses within the CA3 region (Hjorth-Simonsen and Jeune 1972; Yeckel and Berger 1990; Witter 2007). Layer III cells of the entorhinal project monosynaptically to the CA1/2 pyramidal cells (Yeckel and Berger 1995).

Formation of Anatomical Maps and Distribution of Neurons

Swanson et al. (1978) had developed a method to "unfold" the hippocampus to create two-dimensional, flattened representations of its various subfields (this flattened representation can extend to the entorhinal cortex as well) that still preserves well most of the relative anatomical geometry that exists in the original three-dimensional structure. Much of the data involving topography and the distributions of cellular populations is presented using such two-dimensional maps or, in some cases, along a one-dimensional axis. The axes describing the flattened maps can be used to easily project such two-dimensional data onto a proper three-dimensional hippocampal structure.

The work of Gaarskjaer (1978) was used in the model to create a more detailed anatomical map of the dentate gyrus due to its inclusion of both length measurements and granule cell body density measurements along the extents of both the suprapyramidal and infrapyramidal blades of the dentate gyrus. The basket cell distribution within the dentate has been less completely investigated, but ratios of granule cells and interneurons have been reported with septo-temporal and infra- and suprapyramidal differences. The granule cell/basket cell ratio in the suprapyramidal blade is approximately 100:1 at the septal end and approximately 150:1 at the temporal end, while the ratio in the infrapyramidal blade is 180:1 septally and 300:1 temporally (Seress and Pokorny 1981). The ratios were interpolated to provide a complete distribution of basket cell densities along the dentate gyrus. Buckmaster and Jongen-Rêlo (1999) reported the longitudinal distribution of mossy cells with the temporal pole having a density approximately ten times greater than that of the septal pole. The total number of the relevant neurons that are in the entorhinal-dentate system of the rat is listed in Table 1.

Multi-compartmental Neuron Models

The three main dentate neuron types that were included in the model were the granule cells, basket cells, and mossy cells. Granule cells are the principal neurons of the dentate gyrus and are situated with their somata in the granule cell layer. Their

Table 1 Cell numbers in the large-scale model

	Cell number
Lateral entorhinal cortex cells[a]	46,000
Medial entorhinal cortex cells[a]	66,000
Granule cells[a]	1,200,000
Basket cells[b]	4500
Mossy cells[c]	30,000

[a]Mulders et al. (1997); [b]Buckmaster and Dudek (1997); [c]Buckmaster and Jongen-Rêlo (1999)

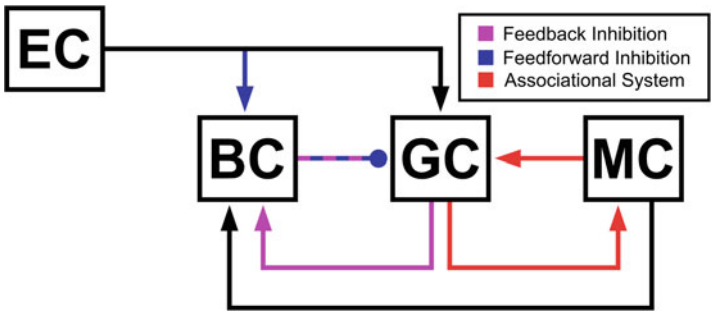

Fig. 3 Schematic of the neural circuits in the dentate gyrus model. The feedback inhibition circuit is formed by granule and basket cells. Feedforward inhibition is achieved by the entorhinal activation of basket cells. Mossy cells form the associational system and provide excitatory feedback to granule cells. Mossy cells also disynaptically inhibit granule cells by activating basket cells

apical dendrites extend into and span the molecular layer. Granule cells receive the majority of the entorhinal inputs which are excitatory. Their axons, while arborizing within the hilus, project a single primary axon, known as the mossy fiber, to cells in the CA3/4 regions.

Basket cells are interneurons within the granule cell layer that provide inhibitory input to granule cells (Gamrani et al. 1986). Many basket cells have apical dendrites that extend into the molecular layer from which they receive excitatory input from the entorhinal cortex and basal dendrites that arborize within the hilus from which they receive excitatory input from granule cells (Seress and Pokorny 1978; Ribak and Seress 1983; Zipp et al. 1989; Ribak et al. 1990; Acsády et al. 2000). Basket cell axons collateralize extensively in the granule cell layer and the innermost regions of the molecular layer where they form GABAergic synapses with granule cells, primarily on their cell bodies and the initial segments of their axons (Seress and Ribak 1983). Thus, synaptic arrangements exist that provide the basis for both feedforward and feedback inhibition (Fig. 3).

Mossy cells are hilar interneurons that contribute to the associational-commissural fibers that arise from both the ipsilateral and contralateral hippocampus (Zimmer 1971; Gottlieb and Cowan 1973; Berger et al. 1981). The dendrites of mossy cells are restricted to the hilus, but their axons collateralize extensively within the inner third of the molecular layer (Buckmaster et al. 1996; Ribak and Shapiro 2007). Mossy cells primarily serve an excitatory role by directly activating granule cells via glutamatergic synapses (Buckmaster et al. 1992; Soriano and Frotscher 1994; Ribak and Shapiro 2007). However, associational-commissural inputs have also been shown to activate inhibitory circuits within the dentate gyrus (Douglas et al. 1983; Scharfman et al. 1990; Scharfman 1995). These data indicate that mossy cells participate in both an excitatory and inhibitory capacity by monosynaptically exciting granule cells and disynaptically inhibiting granule cells

via other interneurons. In the present model, basket cells receive input from the mossy cells to provide the disynaptic inhibitory effect mediated by the mossy cells (Fig. 3).

Generation of Dendritic Morphologies

Neurons are commonly classified, in part, based on stereotypical morphological features that describe the branching of their dendrites. The diversity of morphological types has led many neuroscientists to investigate the functional role of different branching characteristics. The dendritic morphology of neurons has been shown to greatly influence several factors during input processing such as the propagation and attenuation of postsynaptic potentials and the linear or nonlinear integration of multiple inputs (Krueppel et al. 2011). Given this morphological diversity and its functional importance, the database NeuroMorpho.Org was used to obtain three-dimensional reconstructions of granule cell morphologies which were then used to generate the distributions of the relevant parameters using L-Measure (Rihn and Claiborne 1990; Ascoli et al. 2007; Scorcioni et al. 2008). The parameters were used by a software tool called L-NEURON to generate unique dendritic morphologies for each granule cell in the network (Ascoli and Krichmar 2000; see Hendrickson et al. 2015). The parameters provide the geometrical points at which a bifurcation can occur, the number of branches, their angles, etc. (see Table 2).

The dendritic morphology of basket cells and mossy cells varies as a function of cell location and the shape of the curvature of the hippocampus at that location. Due to the limited sample size of reconstructions, proper morphologies were not considered for these cell types. Due to the lack of information and to decrease

Table 2 Morphological parameters for granule cells

	Distribution	Mean/min	Std. dev./max
Soma diameter	Gaussian	9.0	2.0
Number of stems	Uniform	2	4
Stem initial diameter	Gaussian	1.51	0.39
Branching diameter	Gaussian	0.49	0.28
IBF branch length	Gaussian	10.7	8.4
Term. branch length	Gaussian	10.7	8.4
Daughter ratio	Uniform	1	2
Taper ratio	Gaussian	0.10	0.08
Rall power	Constant	1.5	–
Bifurcation amplitude	Gaussian	42	13
Tree elev. (narrow)	Gaussian	10	2
Tree elev. (medium)	Gaussian	42	2
Tree elev. (wide)	Gaussian	75	2

the computational load of the simulations, basket and mossy cells for this level of analysis were represented using a single somatic compartment.

Specification of Passive and Active Properties

The specification of morphology accounts for some of the passive propagation of electrical activity, i.e., the electrotonic response, but to create a complete model of the dendritic processing of granule cells, the parameters for passive properties needed to be augmented by active dendritic properties due to voltage-dependent channels also found in the dendritic regions (Krueppel et al. 2011).

The discretization of dendritic morphologies into compartments, the embedding of passive and active mechanisms into the compartments, and the simulation of the resulting model was performed using the NEURON simulation environment v7.3 and scripted using Python v2.8 (Carnevale and Hines 2006; Oliphant 2007; Hines et al. 2009). The passive and active properties can be set to match experimental data (see Fig. 4), much of which has been pioneered by previous groups. The works of these groups are the basis of our current neuron models (Yuen and Durand 1991; Aradi and Holmes 1999; Aradi and Soltesz 2002; Santhakumar et al. 2005). The active and passive properties used are summarized in Table 3. The resulting heterogeneous distribution of ion channel densities and the similarly heterogeneous nature of the morphologies then were able to closely approximate the electrophysiological responses of granule cells.

Topographic Connectivity

With the anatomical map and distribution of neurons within the map defined, the next step in completing the large-scale neural network was to connect the neuron models to each other. The connectivity methods used in this work are largely derived from the work of Patton and McNaughton (1995), who compiled an extensive amount of information concerning the connectivity of the dentate gyrus and described a method of distance-based probabilistic connectivity.

The present large-scale model makes a critical assumption about the function of axons in that it assumes that an axon acts merely as a propagator of action potentials from generation near the soma to the end of the terminal. Though studies exist that catalogue the role of axons in modulating synaptic transmission, the present model did not explicitly model axon morphologies and compartments. Rather, axons were functionally represented by incorporating the delay associated with the propagation of the action potential from the soma to the corresponding presynaptic terminal. This was calculated using the physical distance between the soma and the synapse and reported action potential propagation velocities.

Connectivity in the model was represented using probability distributions that were constrained by experimental data. The main concerns were, given the origin

Table 3 Distribution of passive and active properties in the neuron models

Mechanism	Granule cells					Basket cells	Mossy cells
	Soma	GCL	Inner third	Middle third	Outer third	Soma	Soma
C_m (μm/cm^2)	9.8	9.8	15.68	15.68	15.68	1.4	0.6
Ra (Ω-cm)	210	210	210	210	210	100	100
[a]Sodium (S/cm^2)	0.84	0.126	0.091	0.056	–	0.12	0.12
[a]Slow delayed rectifier K^+ (S/cm^2)	6e−3	6e−3	6e−3	6e−3	8e−3	–	–
[a]Fast delayed rectifier K^+ (S/cm^2)	0.036	9e−3	9e−3	2.25e−3	2.25e−3	0.013	5e−4
[b]A-type K^+ (S/cm^2)	0.108	–	–	–	–	1.5e−4	1e−5
[c]L-type Ca^{2+} (S/cm^2)	2.5e−3	7.5e−3	7.5e−3	5e−4	–	5.0e−3	6e−4
[c]N-type Ca^{2+} (S/cm^2)	7.35e−4	2.2e−3	7.35e−4	7.35e−4	7.35e−4	8.0e−4	8e−5
[c]T-type Ca^{2+} (S/cm^2)	7.4e−5	7.5e−5	2.5e−4	5e−4	1.0e−3	–	–
[a]Ca-dependent K^+ (S/cm^2)	1e−3	4e−4	2e−4	–	–	2.0e−6	0.016
[d]Ca- and V-dependent K^+ (S/cm^2)	1.2e−4	1.2e−4	2e−4	4.8e−4	4.8e−4	2.0e−4	0.0165
[a]Leak (S/cm^2)	2.9e−4	2.9e−4	4.6e−4	4.6e−4	4.6e−4	1.8e−3	1.1e−5
[c]Tau for decay of intracell. Ca^{2+} (ms)	10	10	10	10	10	10	10
[c]Steady-state intracell. Ca^{2+} (mM)	5.0e−6	5.0e−6	5.0e−6	5.0e−6	5.0e−6	5.0e−6	5.0e−6

The equations describing the channel dynamics were originally published in the following works: [a]Yuen and Durand (1991); [b]Warman et al. (1994); [c]Jaffe et al. (1994); and [d]De Schutter and Bower (1994). Reproduced from Hendrickson et al. 2016 with permission.

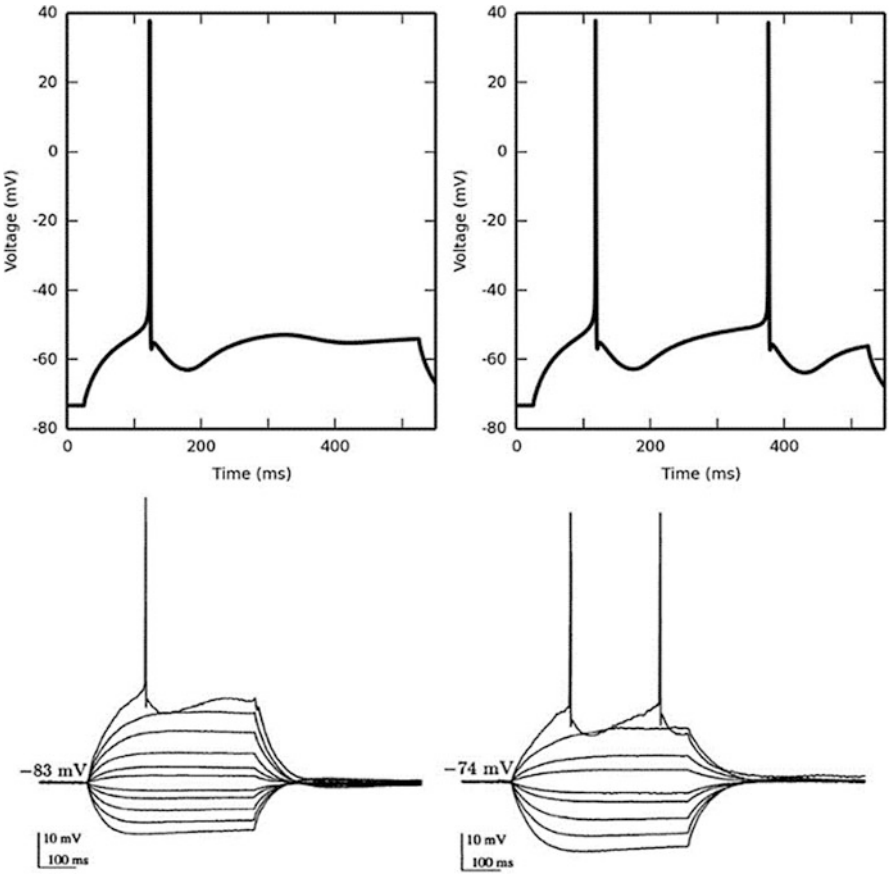

Fig. 4 Granule cell electrophysiology. Simulation results are on the top row. Experimental data are on the bottom row. (Top left) When current is injected at the soma, the granule cell responds by firing an action potential with a latency of approximately 100 ms. (Top right) When the current amplitude is just over the threshold required to elicit a second action potential, its latency is approximately 350 ms. This matches experimental data (bottom, reproduced from Spruston and Johnston 1992). Reproduced from Hendrickson et al. 2016 with permission.

of the axon, the postsynaptic region to which the axon is sent and, once the axon arrives at the postsynaptic region, the spatial distribution of the axon terminals. The next challenge after finding such data was the quantification of the work which was a nontrivial task due to the qualitative manner in which a majority of the works were presented. The key works that were used to constrain the projection from entorhinal cortex to dentate gyrus are detailed below.

Entorhinal-Dentate Topography

A major division of the entorhinal cortex is its separation into the medial and lateral regions. The projection of the axons from the entorhinal cortex to the hippocampus is termed the perforant path. An important topographical distinction between the medial and lateral entorhinal cortex is that upon reaching the dentate gyrus, the lateral perforant path terminates within the outer third of molecular layer and the medial perforant path terminates within the middle third (Hjorth-Simonsen and Jeune 1972; Witter 2007). This anatomical feature is preserved in the present model by limiting the respective connections to the appropriate regions of the granule cell morphologies.

A significant study by Dolorfo and Amaral (1998) was used to guide our models of the regional mappings from entorhinal cortex to the dentate gyrus. By injecting retrograde dye tracers in the dentate gyri of rats, the entorhinal origins of the cells projecting to those injection sites in the dentate were revealed. Injections were performed along the entire septo-temporal, or longitudinal, extent of the dentate, creating a thorough topographic map of the organization of entorhinal-dentate projections. Each injection was performed in a separate rat, and the result of the injection was presented as a grayscale heat map overlaid on a two-dimensional, flattened representation of the entorhinal cortex of the rat. The grayscale heat map represented the density of entorhinal neurons that projected to the injection site (Fig. 5).

Quantifying the data to use in the model proved a challenge due to the qualitative presentation of the results and the dissimilarity of brain shapes for each rat. To

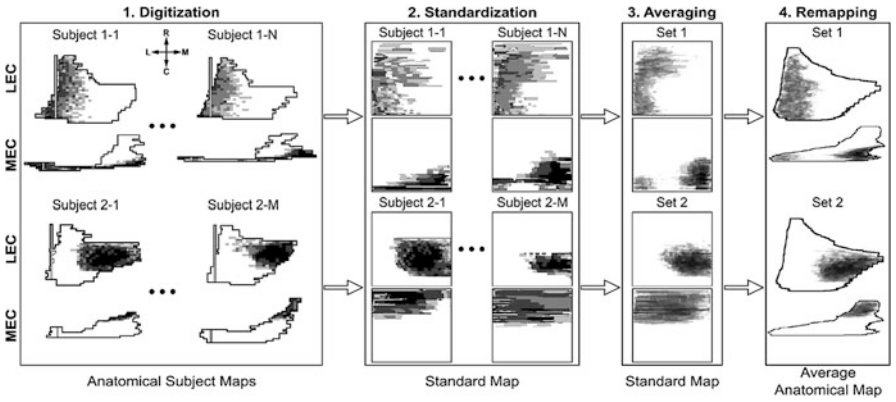

Fig. 5 Summary of the image-processing pipeline used to quantify the connectivity of entorhinal cortical projections to the dentate gyrus. Not all data are shown. (1) The data in the anatomical subject maps are digitized and grouped according to injection location. (2) The maps are projected onto a standard coordinate space. (3) The sets are averaged. (4) The averaged group data are projected onto an average anatomical map. The compass represents the rostro-caudal and mediolateral axes. Reproduced from Hendrickson et al. 2016 with permission.

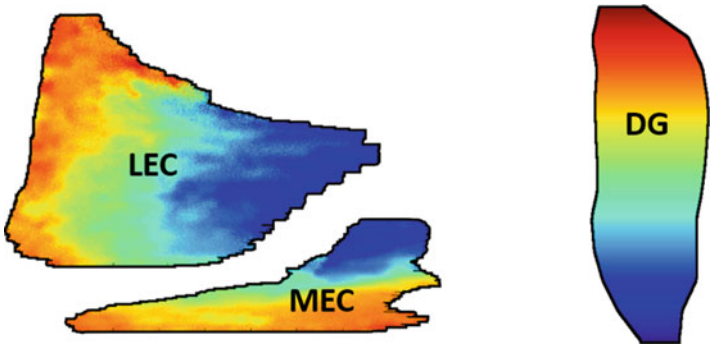

Fig. 6 Connectivity mapping from the lateral and medial entorhinal cortices (LEC and MEC) to the dentate gyrus (DG). Like colors between the entorhinal cortex and dentate gyrus correspond to the origin and destination of a projection, e.g., red entorhinal regions project to red dentate regions, blue entorhinal regions project to blue dentate regions, etc.

address this, a processing workflow was developed (Fig. 5). In the first step, the results of each injection were digitized, and the unique shape of the entorhinal cortex was extracted. Next, the individual entorhinal maps were transformed into a standard map, and the standardized maps were grouped based on the region of projection. The grouped, standardized maps were averaged, and the resulting averaged maps were transformed back to a representative entorhinal map that was created by calculating the average of all the entorhinal maps. The final grayscale heat maps were used to determine, given the origin of the neuron in the entorhinal cortex, the probabilistic location within the dentate gyrus to which the axon was connected. The final mapping depicts a mediolateral gradient in the lateral entorhinal cortex that projects along the longitudinal axis of the dentate gyrus. In the medial entorhinal cortex, there is a dorsoventral gradient that projects along the longitudinal axis of the dentate gyrus. A summary of the mapping is shown in Fig. 6.

The above study informed the regional mapping of the entorhinal-dentate projection, but it did not describe the morphology of the entorhinal axonal arbors. At the cellular level, Tamamaki and Nojyo (1993) produced some of the few reported single entorhinal neuron perforant path axon terminal field reconstructions. Based on their work, the septo-temporal extent of the axon terminals was constrained to be in the range of 1–1.5 mm. Given that the axon terminals cover the entire transverse extent of the dentate gyrus, the entorhinal axons in the model were represented using Gaussian distributions with a standard deviation 0.167 mm which corresponds to approximately 1 mm being covered within three standard deviations from the center of the axon terminal field. These distributions determined the connectivity between the entorhinal neurons and the granule cells, providing the basis for feedforward excitation in this system.

Topography Within the Dentate Gyrus

Upon identifying a neuron and filling it with dye, septo-temporal cross sections of the hippocampus can be made, and the total length of axon that exists in the cross sections can be quantified. Such experiments have yielded histograms of the total axon length of a neuron as a function of distance away from the cell body. The histograms were fitted to Gaussian functions to extract the standard deviations that parameterize the spatial distributions of axon terminal fields of dentate granule cells and basket cells. The septo-temporal and transverse standard deviations for granule cells were estimated to be 0.152 mm and 0.333 mm, respectively (Patton and McNaughton 1995; Buckmaster and Dudek 1999). The corresponding standard deviations for basket cells were estimated to be 0.215 and 0.150 mm (Han et al. 1993; Sík et al. 1997). The resulting two-dimensional Gaussian distributions described the probability of connectivity between granule cells and basket cells.

The associational system of the dentate gyrus is provided by the mossy cells, and their axons extend predominantly into the inner third of the molecular layer (Buckmaster et al. 1996; Ribak and Shapiro 2007). Mossy cell axon terminals contact both granule cell and basket cell dendrites within the inner third (Scharfman et al. 1990; Scharfman 1995). The longitudinal extent of the axon terminal field is dependent on the location of their soma with fields that span 7.5 and 1.5 mm for mossy cells located septally and temporally, respectively (Zimmer 1971; Hendrickson et al. 2015).

Conduction Velocity of Action Potentials

To account for the time delay between the generation of an action potential and its arrival at the presynaptic terminal where it triggers neurotransmitter release, conduction velocity values, taken from the literature, and the Euclidean distance between the neurons were used. For the entorhinal conduction delays, a bifurcation point was assigned at the crest of the dentate gyrus at a longitudinal location according to topographic rules described earlier. The distance between the perforation point and the postsynaptic neuron was used to calculate the delay. The conduction velocity was estimated to be 0.3 m/s (Andersen et al. 1978).

Synaptic Density

The inputs to a postsynaptic neuron for each possible presynaptic cell type were determined by calculating the pairwise distance between the postsynaptic neuron and all of the presynaptic neurons and computing the connection probability using an appropriate probability distribution. Inputs were randomly selected until a threshold number of inputs, determined by the convergence value for the presynaptic cell type, were satisfied. The convergence value denotes the number of afferent

connections that a postsynaptic neuron receives from a given presynaptic neuron type and was estimated by considering the number of synapses that was available for a presynaptic neuron type. The determination of the convergence is detailed below.

Granule Cell Synapse Counts

Hama et al. (1989) quantified the spine density of granule cells by performing analyses on electron microscopy images of the granule cell dendrites. Though Hama et al. did not separately quantify the synaptic density based on the location of the granule cells with respect to the suprapyramidal and infrapyramidal blades of the dentate gyrus, Desmond and Levy (1985) reported significant differences between the blades. However, the methodology of Hama et al. was preferred as they used higher resolution electron microscopy imaging to perform the counting rather than light microscopy. Using the ratio of the spine densities between the blades as reported by Desmond and Levy, the spine densities for the infrapyramidal blade based on the work of Hama et al. were estimated. Furthermore, Crain et al. (1973) were able to identify asymmetric synapses in only a certain proportion of spines in the distal and middle dendrites, signifying excitatory synapses presumably from perforant path input. Claiborne et al. (1990) characterized the dendritic lengths of axons that lie in the various strata. With a total mean length of 3,478 μm for suprapyramidal granule cells and 2,793 μm for infrapyramidal granule cells and a mean of 30% of the dendrites in the middle third of the molecular layer and 40% in the distal third, the mean numbers of synapses available for the lateral and medial perforant path were computed as 2,417 and 2,117 for suprapyramidal granule cells and 1,480 and 1,253 for infrapyramidal cells, respectively (Table 4).

Halasy and Somogyi (1993) reported that 7–8% of synapses on granule cell dendrites in the molecular layer are GABA-immunopositive and these dendritic synapses represent 75% of the inhibitory synapses on granule cells with the remaining 25% located in the granule cell layer. Given total spine counts of 8,695 and 5,533 for suprapyramidal and infrapyramidal granule cells, respectively, the number of inhibitory inputs in the molecular layer would be 652 and 415. This would then leave 217 and 138 synapses in the granule cell layer. Basket cells send their axon collaterals predominantly to the granule cell layer, but they are not the only interneurons to do so. Chandelier cells, not included in this study, are hilar cells that also provide inhibitory input to the granule cell layer (Soriano and Frotscher 1989; Buhl et al. 1994). Given the average number of boutons between basket cells and chandelier cells, 11,400 and 3,800, approximately 75% of the synapses in the granule cell layer should be dedicated for basket cell input (Sík et al. 1997). The convergence of basket cells onto granule cells should then be 174 and 110 for the suprapyramidal and infrapyramidal granule cells. However, parvalbumin-positive basket cells only make up 62% of the basket cell population, so the convergence is appropriately shifted to 108 and 68, respectively (Buckmaster and Dudek 1997).

Table 4 Spine density and spine counts in granule cells

Property	Reference	Suprapyramidal			Infrapyramidal		
		Inner	Middle	Outer	Inner	Middle	Outer
Proportion of asymmetric synapses	Crain et al. (1973)	0.89	0.89	0.86	–	–	–
Spine density (spines/μm)	Desmond and Levy (1985)	1.57	1.66	1.52	1.34	1.22	1.16
Number of spines	Hama et al. (1989)	3.36	2.28	2.02	2.87[a]	1.68[a]	1.54[a]
	–	3,506	2,379	2,810	2,405	1,408	1,720
Number of asymmetric synapses	–	3,120	2,117	2,417	2,140	1,253	1,480

[a]Estimated by calculating the supra- to infrapyramidal ratio from the Desmond and Levy (1985) data.

Mossy cells have been reported to create 30,000–40,000 synapses within the inner third of the molecular layer (Buckmaster et al. 1996). Assuming that mossy cells maximally form one synapse per granule cell and there are 30,000 mossy cells and 1,200,000 granule cells, then a granule cell would receive an average of 875 mossy cell inputs. This number is less than the estimated number of spines in the inner molecular layer for granule cells (Table 4), but the mossy cell connections that were being investigated originated from ipsilateral connections and do not consider commissural input from the contralateral hippocampus.

Basket Cell Synapse Counts

The total dendritic length of dentate basket cells has been reported to be 4,530 μm. Of this length, the basal dendrites receive input from the granule cells. The proportion of dendrite that lies in the molecular layer (apical dendrites) versus the hilus (basal dendrites) was estimated from measurements of surface area with an apical surface area of 7,600 μm^2 and a basal surface area of 2,200 μm^2 (Vida 2010). The synaptic density for the dentate basket cell was taken from an estimate made by Patton and McNaughton (1995) which was 1 synapse/μm. Another study reported that approximately 10% of synapses in CA1 basket cells are GABAergic (Gulyás et al. 1999). Using these data, the mean number of granule cell inputs for a basket cell was estimated to be 915. Assuming that the distribution of basket cell dendrites in the molecular layer was similar to that of granule cells, the number of lateral and medial entorhinal inputs for a basket cell was calculated to be 1,045 and 783, respectively. Similarly, the number of synapses in the inner third of the molecular layer was estimated to be 783. Considering that only a third of the inner molecular synapses of the granule cells were used for ipsilateral mossy cell connections, the same ratio was used for basket cells to estimate 260 mossy cell connections. Pyramidal basket cells also receive mossy cell input through its basal dendrites. Of the reported 2,700 synaptic contacts that mossy cells were found to make in the hilus, 60% was estimated to occur with inhibitory interneurons (Buckmaster et al. 1996; Wenzel et al. 1997). We assumed that all hilar interneurons have an equal probability of receiving a mossy cell input and that a hilar interneuron receives an average of two synaptic contacts from a single mossy cell (Buckmaster et al. 1996). Given a total hilar inhibitory interneuron population of 20,000 (Buckmaster and Jongen-Rêlo 1999), the estimated number of hilar mossy cell inputs to basket cells was 1,200. This would lead to a total number of mossy cell inputs to be 1,460.

Mossy Cell Synapse Counts

The present model only considers the granule cell input to mossy cells. Mossy cell excitation of other mossy cells and inhibitory inputs to mossy cells have yet to be included but are planned for future works. Acsády et al. (1998) reported that granule cells form synapses with 7–12 hilar mossy cells. Given a granule cell population of

Table 5 Parameters for AMPA synapses

	Granule cell	Basket cell	Mossy cell
Medial perforant path[a]			
g_{max} (μS)	1.17e−5	4.21e−6	–
τ_1 (ms)	1.05	1.05	–
τ_2 (ms)	5.75	5.75	–
Convergence	2,117/1,253	783	–
Lateral perforant path[a]			
g_{max} (μS)	1.50e−5	4.21e−6	–
τ_1 (ms)	1.05	1.05q	–
τ_2 (ms)	5.75	5.75	–
Convergence	2,417/1,480	1,045	–
Granule cell[b]			
g_{max} (μS)	–	1.13e−4	2.00e−5
τ_1 (ms)	–	0.1	0.3
τ_2 (ms)	–	0.49	0.6
Convergence	–	915	380
Mossy cell[c]			
g_{max} (μS)	1.17e−6	2.27e−5	–
τ_1 (ms)	1.05	1.05	–
τ_2 (ms)	5.75	0.49	–
Convergence	875	1,460	–

Presynaptic neurons are in the first column. Postsynaptic neurons are in the first row. The reversal potentials for AMPA synapses were 0 mV. The parameters for the postsynaptic potentials were optimized based on experimental data from the following papers: [a]Foster et al. (1991); [b]Geiger et al. (1997); and [c]Scharfman (1995). Convergence values for granule cells are divided into supra- and infrapyramidal blades (supra/infra).

1,200,000 and a mossy cell population of 30,000, the estimated number of granule cell inputs that a mossy cell receives was 380. A summary of the convergence values is listed in Table 5.

Synaptic Model

In the currently described large-scale network, synapses were the exclusive mechanism through which neuron-to-neuron communication was mediated. The synapse was phenomenologically and deterministically represented so, upon being triggered by an action potential, the synaptic conductance would follow a time course dictated by a double exponential function according to the Exp2Syn mechanism in NEURON.

Table 6 Parameters for $GABA_A$ synapses

	Granule cell	Basket cell	Mossy cell
Basket cell			
g_{max} (μS)	1.24e−3	–	–
$\tau_{1\,(}$ms)	0.1	–	–
τ_2 (ms)	12.35	–	–
Convergence	108/68	–	–

Presynaptic neurons are in the first column. Postsynaptic neurons are in the first row. The reversal potentials for GABA synapses were −75 mV. The parameters for the postsynaptic potentials were optimized based on experimental data (Buhl et al. 1995).

$$g(t) \propto e^{-t/\tau_2} - e^{-t/\tau_1}$$

Though NMDA is crucial to synaptic plasticity, synaptic function for this implementation of the model was limited to AMPA, which allowed a base response of the neural network to be expressed and focused on the analysis on the two properties in question: topography and inhibition. Inhibitory GABAergic synapses for the present model were restricted to the $GABA_A$ subtype and also were modeled using the Exp2Syn mechanism. The parameters of synapses between the various cell type pairs are summarized in Tables 5 and 6.

Simulation Results

Characterization of Baseline Dentate Response to Random Entorhinal Cortical Input

For our initial simulation study to characterize dentate granule cell responses to entorhinal input, the dentate network was driven using independent, identically distributed Poisson point processes which generated interstimulus intervals (ISIs) at a mean frequency of 3 Hz. The 3 Hz was chosen to represent a baseline of spontaneous activity for the entorhinal cortex. A Poisson process was used to generate ISIs that would perturb the synapses at a broad range of frequencies approximating a white noise input with which to investigate the entorhinal-dentate system. The resulting entorhinal activity was uncorrelated spatially and temporally. Once the inputs were generated, the same ISIs were used to perturb the network for all of the simulations that are described in this work.

The culmination of all of these steps resulted in the formation of a neural network approximating the entorhinal-dentate system of the hippocampus. Random, uncorrelated activity from the entorhinal cortex was projected to the dentate gyrus and spatially distributed according to experimentally established rules that

determine topographical connectivity. The activity was converted into postsynaptic potentials (PSPs) in the corresponding granule cells and basket cells based on the synaptic equations that determined the response. The PSPs were propagated through the dendritic morphologies, interacting with PSPs arising from other input timings and activating voltage-gated ion channels, resulting in a nonlinear transformation of the PSPs as they traveled toward, and were integrated at, the soma. Upon reaching a threshold, which was determined by the ion channel composition and density, the soma would generate an action potential which would activate neural circuits based on the local topography of the granule and basket cell axons and provoke a similar sequence of events from which large-scale population dynamics could be expressed in the form of spatiotemporal patterns of spiking. Initial simulations were performed at the full number of neurons in the entorhinal cortex and dentate gyrus (Table 1). To explore the various phenomena that were observed at the full-scale network, subsequent simulations were performed at a reduced scale with a tenth of the number of neurons to decrease the simulation times. Simulations performed at the reduced scale continued to exhibit the relevant phenomena seen at the full scale.

Simulations were performed on a computing cluster (hpc.usc.edu) using 125 dual quad-core 2.33 Ghz Intel-based nodes with 16 GB of RAM per node for a total of 1000 processor cores and 2 TB of RAM. The nodes were connected by a 10G Myrinet networking backbone. At full scale with 112,000 entorhinal cortex cells, 1,200,000 granule cells, and 4,000 basket cells with a simulation time of 4,000 ms, simulations required approximately 87 h to complete. Reduced scale simulations required approximately 9 h.

Spatiotemporal Clusters as an Emergent Property

The spiking activity of the network is depicted using raster plots with time on the x-axis. The entorhinal activity is sorted by cell ID which demonstrates the uncorrelated properties of its spatiotemporal firing pattern. For neurons in the dentate, the longitudinal location of a spike within the dentate is plotted on the y-axis. The basket cell activity is plotted similarly. The initial expectation was that spatiotemporally uncorrelated input from the entorhinal cortex would result in spatiotemporally uncorrelated output of granule cells. Contrary to that hypothesis, the dentate system responded with localized regions of spatially and temporally dense activity that were interspersed with periods of reduced activity. The dense activity spanned a spatial extent of 1–3 mm and persisted for approximately 50–75 ms with periods of reduced activity lasting 50–100 ms. Regions of dense activity were called “clusters” (Fig. 7).

The clustered activity was not a transient response but was the steady-state response after approximately 1 s of simulation had passed. The transient response was characterized by synchronized, oscillatory behavior (not shown). During this phase, the entire extent of the dentate gyrus alternated between periods of activity and inactivity before evolving into clustered activity which persisted indefinitely for

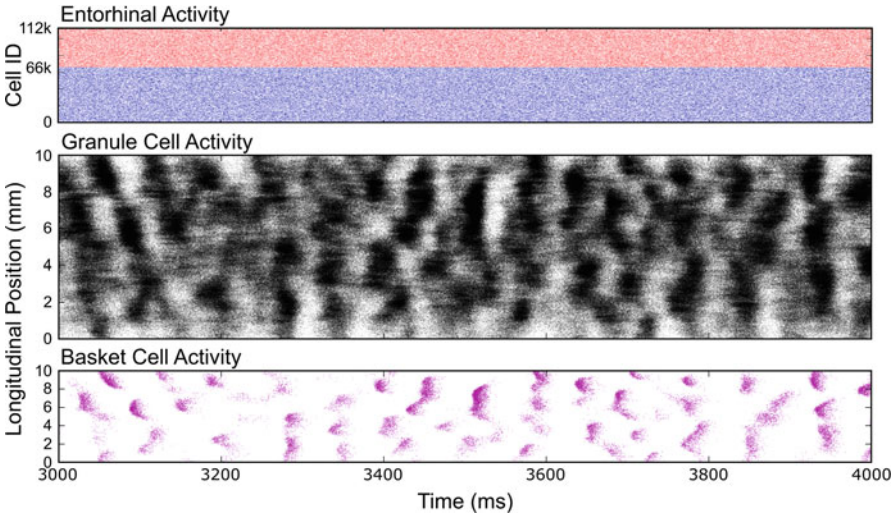

Fig. 7 Simulation result for topographically constrained entorhinal-dentate network with feedback inhibition at full scale with 1,200,000 granule cells. (Top) Entorhinal activity was generated by homogeneous Poisson process and was spatially and temporally uncorrelated. Medial entorhinal activity is in red and lateral entorhinal activity is in blue. (Middle) Granule cell activity displays spatiotemporal clustering with local regions of dense activity. (Bottom) Basket cell activity was also clustered, being driven, and activated in a feedback manner by granule cell activity

the rest of the simulation. Clusters persisted even after the network was scaled to one-tenth of the full scale (Fig. 9). The mean firing rate of the granule cells was 1.28 Hz.

A density-based clustering algorithm, DENCLUE 2.0 (Hinneburg and Gabriel 2007), was used to detect clusters for more in-depth characterization (Fig. 8). The mean number of spikes that contributed to each cluster in the reduced network was 156. Clusters had a mean temporal width of 18 ms and spatial extent of 0.90 mm. The mean density of the clusters was 12 spikes/ms•mm^2, and the intercentroid time between the clusters was 11 ms. Clusters were not formed due to bursts of spikes by individual granule cells. Rather, clusters were a result of increased population activity.

The clusters are an expression of a spatiotemporal correlation in the system. To test the robustness of this correlation, spatiotemporal correlation maps were computed in which the cross-correlations between cell pairs from the network were computed and the longitudinal distance between the cells was used to sort the correlations (Fig. 9). The spike times were sorted using a time bin of 5 ms, and the resolution of the cell distance was set to 0.05 mm. A uniform random sampling of 10,000 cells was performed, and the correlations were calculated with all unique cell pair combinations from this sampling. The resulting maps capture the average features of the clusters that are apparent visually and verify the existence of a

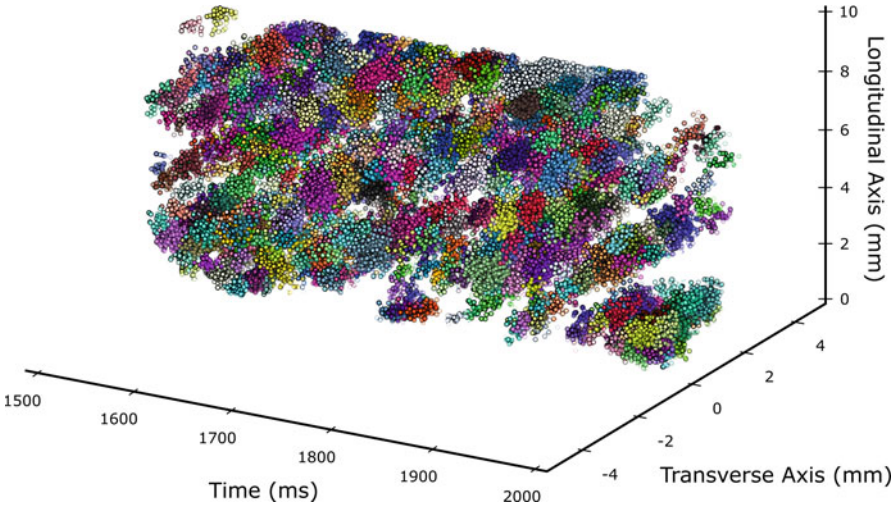

Fig. 8 DENCLUE analysis of granule cell-spiking activity which identifies clusters based on the local density. Each identified cluster is plotted with a separate color. The cluster analysis shows that clusters are organized by the transverse axis in addition to the longitudinal and temporal axes

spatiotemporal correlation in the dentate population which was not present in the entorhinal population.

Removal of Extrinsic and Intrinsic Sources of Inhibition

To identify the properties that were responsible for the spatiotemporal correlation, physiological components were successively removed until the clusters were substantially modified or no longer detected. The initial hypothesis was that the clusters were formed due to sources of inhibition. First, basket cells were considered as an extrinsic source of inhibition due to the inhibitory feedback they provide to granule cells. The dynamics of inhibition and spatial distribution of fibers should generally correspond to the inter-cluster timing and cluster size. The removal of basket cells from the network increased the level of background activity or "noise" in the system but changed the shape of clusters only subtly (Fig. 9). Next, an intrinsic source of inhibition was investigated, the afterhyperpolarization (AHP) of granule cells. The reduced spiking during the AHP could contribute to the reduced inter-cluster activity. The amplitude of the fast AHP of the granule cells was reduced by half, and the half-height width was reduced by one-third by removing the calcium-dependent potassium conductances (the small conductance calcium-activated potassium channel, SK, and the large conductance calcium-activated potassium channel, BK). In the absence of basket cell inhibition and the AHP, a greater amount of noise was present making clusters more difficult to detect visually, but the correlation maps continued to demonstrate the presence of a substantial

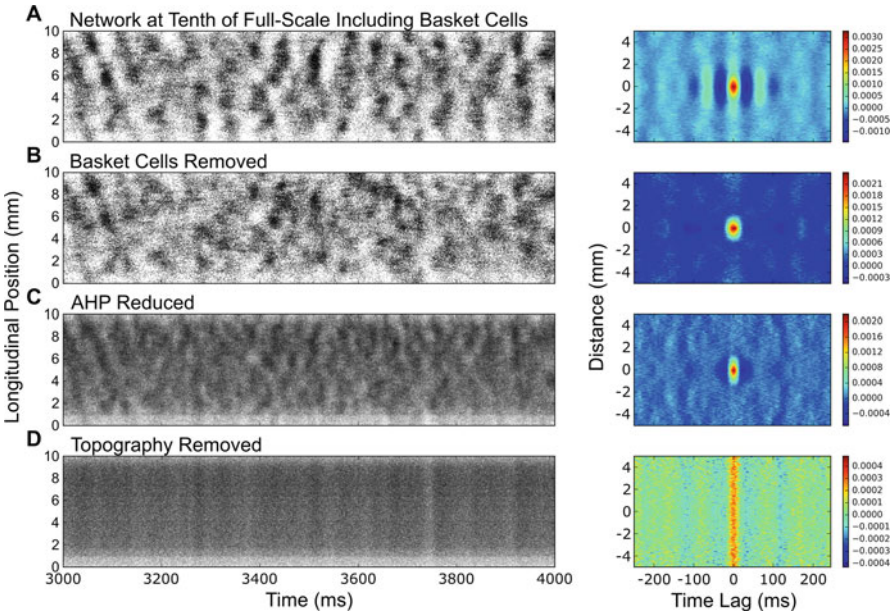

Fig. 9 Raster plots of activity from an entorhinal-dentate network at 1/10th of the full scale while cumulatively removing extrinsic and intrinsic sources of inhibition as well as topographical connectivity constraints. The corresponding correlation maps are to the right of each raster plot. (**a**) Clustered activity persists in a network that is scaled down. The correlation map exhibits spatial and temporal correlation that matches the size and extent of the dentate clusters. (**b**) Basket cells are removed as a source of extrinsic inhibition, but clustered activity remains. (**c**) Extrinsic and intrinsic sources of inhibition are eliminated by reducing the AHP amplitude and removing basket cells. Background activity increases, but clusters are still present. (**d**) In the absence of basket cells and AHP, entorhinal cortical cells and granule cells are randomly connected to eliminate topography. It is only after topographical connectivity constraints are removed that the clusters disappear

spatiotemporal correlation (Fig. 9). Both of these simulations indicated that clusters were not a result of neurobiological mechanisms that contribute to the inhibition of granule cell activity.

Topographic Connectivity as a Source of Spatial Correlation

The next simulation sought to eliminate topography. With topography, entorhinal cortical cells exhibited an axon terminal field that spanned a longitudinal extent of 1 mm, constraining their postsynaptic targets to granule cells within this extent. Topography was removed by using a random connectivity; entorhinal cortical cells were allowed to synapse with any dentate granule cell with equal probability. Each

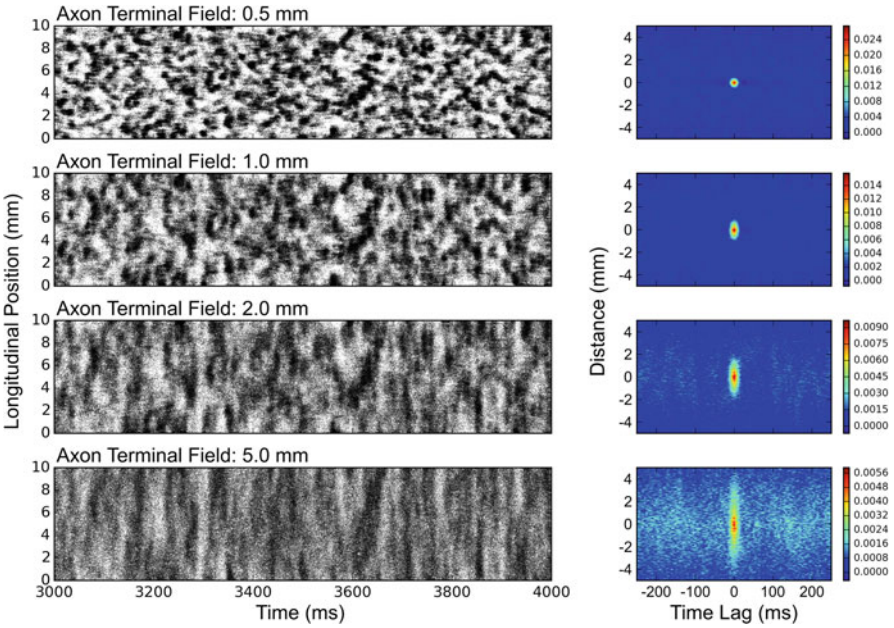

Fig. 10 Effect of increasing the axon terminal field extent in the septo-temporal direction. Raster plots of the granule cell activity are in the left column. Correlation maps are plotted on the right. As the terminal field extent is increased, the cluster size is increased, and this is further reflected by the expanding spatial extent of the correlation

neuron received the same number of connections as before, but the potential origin of the inputs was entirely random. The result of removing the topography of the entorhinal projection, in the absence of basket cells and a reduced AHP, was the elimination of clustered activity (Fig. 9). This result demonstrated that the spatial correlation and clusters are primarily dependent on the topography of the entorhinal-dentate system.

Given that both the spatial extent of the clusters and the span of the axon terminal field were approximately 1 mm, it was presumed that the axon terminal field could be acting as a spatial filter that controlled the spatial correlation in the population activity. To test this hypothesis, the axon terminal field of the entorhinal-dentate projection was varied from 0.5 to 5 mm (Fig. 10). Basket cells were not included in these simulations, and the granule cell models were restored to their original ion channel composition, i.e., amplitudes of AHPs were not reduced. The simulations verified that the extent of the axon terminal field determines the spatial extent of the clustered activity. However, the temporal extent of the clusters was not affected by the axon terminal field.

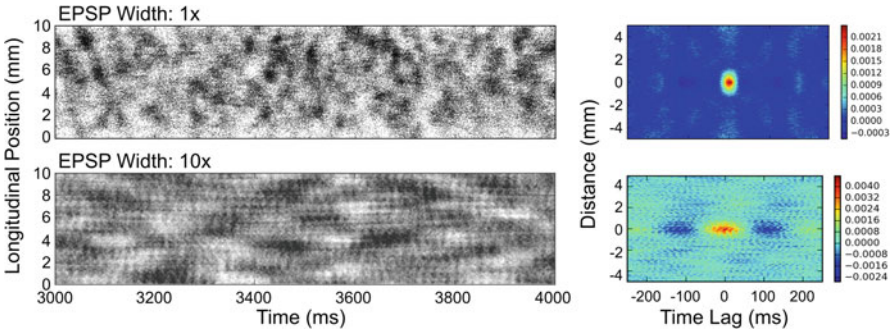

Fig. 11 Granule cell activity if the time course of the entorhinal-dentate EPSP is expanded. Fewer clusters were seen in the granule cell activity, but the temporal width of the clusters increased. This is also seen in the correlation map

Sources of Temporal Correlation

Though extrinsic and intrinsic sources of inhibition, i.e., basket cells and AHP, were not found to be the source of clusters, they were able to modulate the appearance of the clusters and the temporal aspect of the correlation maps (Fig. 9). In particular, they affected the regions of negative correlation that appeared on either sides of the positive correlation lobes. However, neither processes significantly changed the width of the lobes. We hypothesized that by changing the temporal properties of the EPSP, the temporal width of both the clusters and correlation could be manipulated. The second time constant τ_2 of the double exponential equation that describes the synaptic dynamics primarily influences the width of the resulting PSP. To extend the temporal width of the PSP, τ_2 was increased by a factor of 10. The first time constant τ_1 primarily affects the rise time of the PSP and was not manipulated for this simulation. In order to maintain similar levels of activity, the amplitude of the EPSP was altered such that its integral remained unchanged with respect to the original, experimentally based EPSP waveform. The population responded with wider but fewer clusters that appeared with a different spatiotemporal pattern than the control. The simulations verified that the temporal extent of the clusters and correlation were proportional to the temporal extent of the EPSP (Fig. 11).

Modulation of Clusters via Interneurons

The model of the dentate gyrus used in the present studies was comprehensive, particularly with respect to the morphologies of granule cells, topographic organization of perforant path fibers, biophysical properties of granule cell bodies and dendrites, relative numbers of granule cells and basket cell inhibitory interneurons, total numbers of neurons included in the model, and other prominent features known to be characteristic of the hippocampal entorhinal-dentate system in the

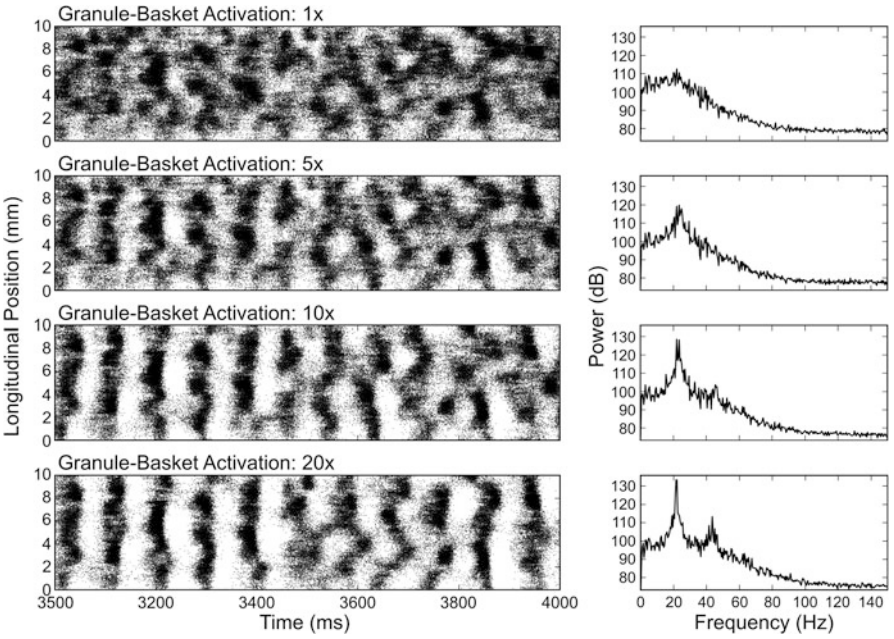

Fig. 12 Results of increasing the strength of feedback inhibition. As feedback inhibition increased, synchrony increased and oscillatory behavior became apparent. The Fourier transforms depict a strengthening of oscillation at 22 Hz. Reproduced from Hendrickson et al. 2016 with permission

rat. In addition, and relevant to the current volume, in the present model, we have investigated the role of basket cells forming feedforward and feedback inhibitory pathways and mossy cells contributing feedback from the hilus to granule cells and inhibitory interneurons (Hendrickson et al. 2015, 2016). Positive feedback was mediated by mossy cells which monosynaptically provided excitatory input to granule cells but also disynaptically provoked an inhibitory effect by activating basket cells.

The role of feedback inhibition was investigated by increasing the strength of basket cell activation by granule cells and observing the granule cell activity. As the coupling strength was increased, the clustered activity began to align temporally (Fig. 12). At higher coupling strengths, the aligned clusters became joined into a single vertical band, and the granule cell activity appeared as an oscillation between periods of activity and inactivity. The oscillation frequency of the synchronous activity was evaluated using Fourier analysis which exhibited a primary peak at 22 Hz and, at the higher coupling strengths, a resonant peak at 45 Hz.

Feedforward inhibition was investigated by increasing the strength of basket cell activation by entorhinal cortical cells and observing granule cell activity. Alone, feedforward inhibition acted to dampen activity and eventually ceased any granule cell activity from occurring at higher coupling strengths (figure not shown). The

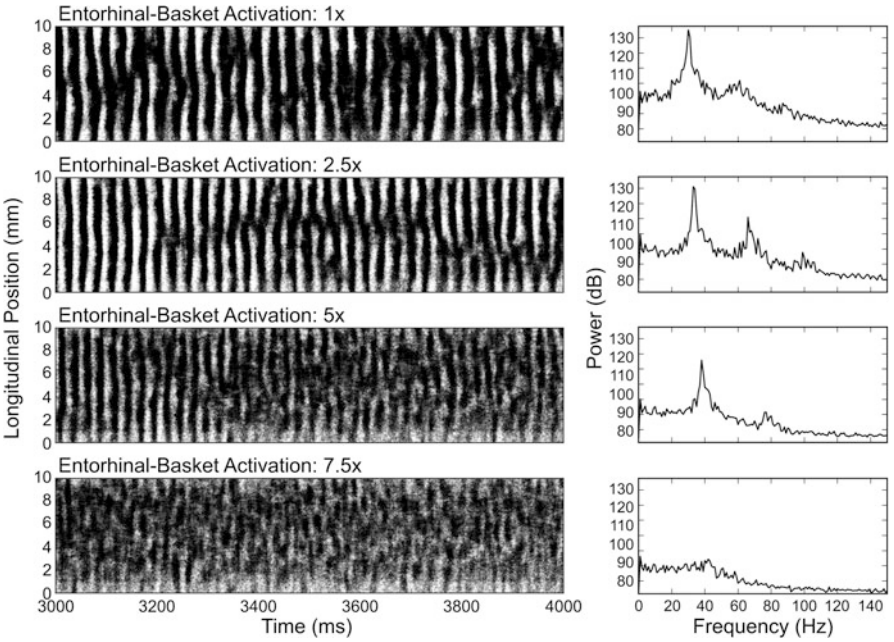

Fig. 13 Results of increasing the strength of feedforward inhibition while the network was in an oscillatory state due to feedback inhibition. As feedforward inhibition was increased, the oscillation frequency increased, but beyond a certain level, oscillatory activity was dampened, and the granule cells begin to exhibit clustered activity

interactions between feedforward and feedback inhibition then were explored (Fig. 13). The strength of feedback inhibition was set such that granule cells exhibited a 22 Hz oscillation. In this state, the entorhinal-basket cell coupling strength was steadily increased. At lower coupling strengths, the 22 Hz oscillation was shifted toward higher frequencies, but beyond a certain level, the peak oscillation was weakened and eventually eliminated, reverting to clustered activity.

Mossy cells were found to affect the shape of the clusters and the prevalence of excitatory activity in the network. Clusters were denser and started and terminated more sharply (Fig. 14). Larger clusters that spanned 4–6 mm of the longitudinal extent of the dentate also began to appear. The introduction of mossy cells further introduced a global oscillation dynamic in that the system would alternate between a period of strong and densely packed clusters and a period of weaker and more dispersed clusters. A Fourier analysis showed that the oscillation occurred in the low theta region in the range of 2–5 Hz. By manipulating the synaptic strength between the mossy-granule cell projection and the mossy-basket cell projection, the dentate network could be easily induced to enter an aberrant bursting state reminiscent of epileptic activity (Fig. 14). Changing the strengths by a factor of 2 was sufficient to elicit a bursting response during the strong cluster period. The results support both the “irritable mossy cell” hypothesis, which proposes a strengthened coupling

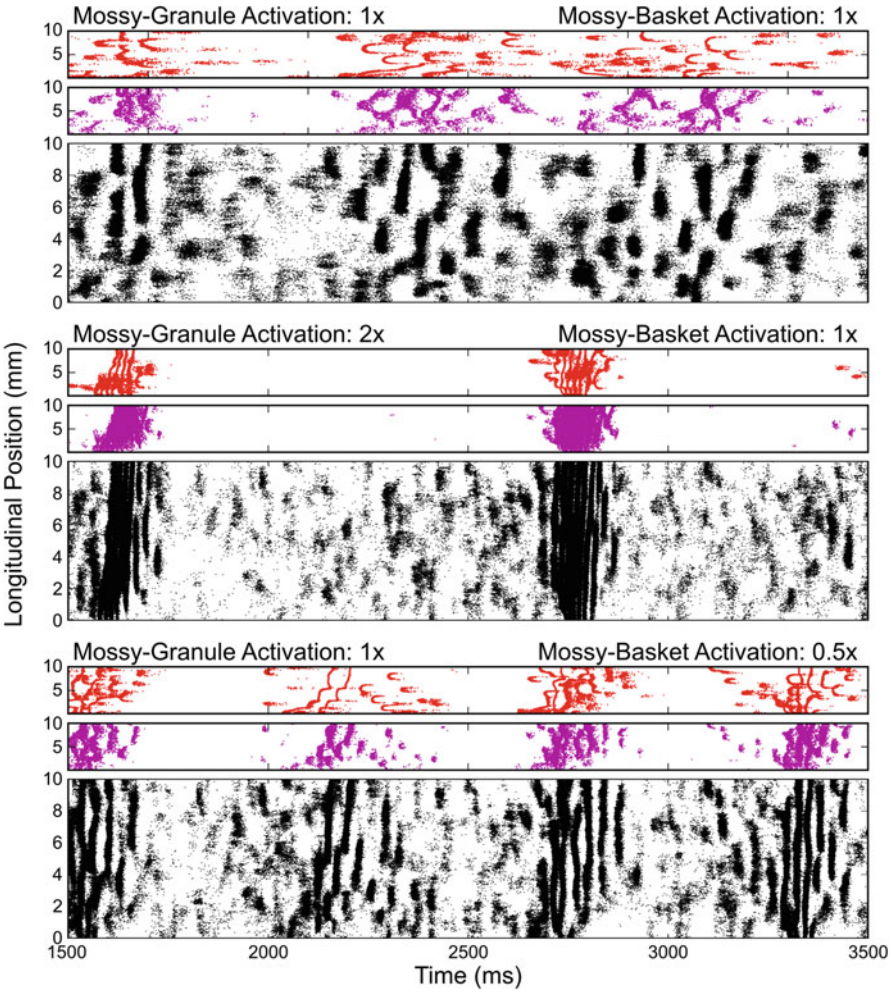

Fig. 14 Dentate activity in a network containing granule cells (black), basket cells (magenta), and mossy cells (red). A global oscillation is seen where the network responds with periods of strong and dense clusters and periods of weak and sparse clusters. When the strength of the mossy-granule cell synapses is increased, the strong cluster period exhibits epileptic activity. Similarly, when the strength of the mossy-basket cell synapses is decreased, the strong cluster period exhibits epileptic activity

between mossy cells and granule cells, and the "dormant basket cell" hypothesis, which proposes a weakened coupling between mossy cells and basket cells, that both explain a network level mechanism behind epilepsy (Santhakumar et al. 2000; Sloviter et al. 2003; Dyhrfjeld-Johnsen et al. 2007). Morgan and Soltesz (2010) developed a large-scale model of the dentate gyrus to investigate a biologically plausible mechanism by which the hyperexcitability seen in epilepsy could be

generated. Injury was simulated by adding granule cell-to-granule cell connections, a phenomenon called mossy fiber sprouting, and reducing the number of mossy cells in the network. Their study demonstrated that the formation of hub cells, highly connected granule cells with large numbers of incoming and outgoing connections, may explain hyperexcitability in epilepsy.

The relatively wide range of network parameters associated with the network tendency for high levels of excitability and epileptiform firing also demonstrates the difficulty in controlling a network as its complexity grows. Strictly from a modeling and simulation standpoint, this may be particularly troublesome given that computational studies of the hippocampus and other brain systems will increasingly seek to include greater and greater numbers of interconnects and neuron types to achieve biological completeness.

The additional hierarchical organization imposed by the mossy cells and basket cells resulted in a more unstable system which raises more questions on the role of hierarchies in a complex network and how stability is maintained in such systems. The investigations reviewed here lacked other key dentate interneurons such as chandelier, HICAP, HIPP, IS, and MOPP cells which, to complete the dentate network, will be included in future studies. Their inclusion will undoubtedly introduce many more sources of instability as the number of hierarchical circuit interactions grows, but understanding the intricacies of such a network will offer important insights into the conditions generating abnormal dentate system activity, as well as suggesting mechanisms behind disease states.

Discussion and Future Work

Spatiotemporal Clusters as a Higher Level of Functional Organization

The large-scale model introduced here offers one of the few insights into *in vivo* population dynamics by incorporating an anatomically derived connectivity and large numbers of detailed, biologically realistic neuron models. The emergence of spatially and temporally finite clusters in the spiking activity, indicative of a spatiotemporal correlation in the network, is a unique discovery that has yet to be validated experimentally but remains an hypothesis highly suggestive of how population activity could be organized at a higher level in the hippocampal dentate system. Topography, terminal field size, and synaptic communication are integral properties that underlie all neural systems and were found to significantly influence the shape of the clusters. The fundamental nature of topography, terminal fields, and synaptic transmission suggests that clusters could be found in many neural systems and that clusters may act as a basic unit of neuronal activity at the population level.

Though the correlation maps were able to be computed through averaging, the magnitude of the correlations was relatively low for all simulation cases. Clusters

could be visualized or detected only because of the scale of the network in terms of the geometry and the number of neurons. A network that is restricted in scale to that of a typical 400 μm hippocampal *in vitro* slice would not exhibit clustered activity because the spatial extent of the system would be insufficient to observe the spatial boundaries of a cluster which are approximately 1 mm. Without having constructed a network of the magnitude reported here, the number of observable spikes would not be sufficient to calculate the correlations. As described above, the clusters themselves are sparse, with an average of 156 spikes per cluster. This is not to suggest that the clusters represent a minor aspect of granule cell activity but rather to emphasize that the phenomena would otherwise be overlooked had a large-scale network not been constructed.

Propagation and Transformation of Clusters

By extending the model beyond the dentate gyrus and incorporating the CA3/4 and CA2/1 subfields, the propagation and transformation of the granule cell clusters will be investigated in future studies (Yu et al. 2015). Because the topography of the projections between each of the subfields is unique, multiple connectivity schemes will be tested and compared. The mossy fibers, which are composed of the axonal projection from the dentate granule cells to the CA3/4 pyramidal cells, originate from a large presynaptic population and have a low divergence on the postsynaptic population, i.e., each granule cell contacts 11–15 CA3 pyramidal cells (Acsády et al. 1998). Conversely, the entorhinal projections to CA3 (projections do not extend to CA4) have high divergence values similar to the entorhinal-dentate projection. Within the CA3 region, there is an extensive, widely diverging associational system. Finally, the Schaffer collaterals that describe the CA3/4 projection to CA1 contain axon terminal fields that span large portions of the CA1 subfield (Ishizuka et al. 1990). An implementation of the entorhinal-dentate-CA3 topography has already been constructed, and so many of these studies are already underway (Yu et al. 2014).

Behaviorally Relevant Inputs to the Hippocampus

In the current studies, entorhinal cortical activity has been represented using homogeneous Poisson processes based on white noise system identification principles, but this activity is nonphysiological. Toward implementing a behaviorally relevant input for the hippocampal neural network, the activity of grid cells in the medial entorhinal cortex (Hafting et al. 2005) is being modeled using experimentally based rate maps and heterogeneous Poisson processes (Yu et al. 2016). Using this input paradigm, the lower levels of hippocampal dynamics can be linked to an even higher-level function toward the behavioral level: the encoding of

spatial information. Using the network generated by our framework, the biological determinants of spatial encoding and spatial processing can be explored. The network model can also be used to explore spatial processing in the context of other proposed functions of the hippocampal subfields such as pattern separation and pattern completion.

Acknowledgments This work was supported by ONR Grant N00014-13-1-0211, NIBIB Grant P41 EB001978, and NIH Grant U01 GM104604. Computation for the work was supported by the University of Southern California Center for High-Performance Computing and Communications (www.usc.ed/hpcc).

References

Acsády L, Kamondi A, Sík A, Freund TF, Buzsáki G (1998) GABAergic cells are the major postsynaptic targets of mossy fibers in the rat hippocampus. J Neurosci 19:3386–3403

Acsády L, Katona I, Martínez-Guijarro FJ, Buzsáki G, Freund TF (2000) Unusual target selectivity of perisomatic inhibitory cells in the hilar region of the rat hippocampus. J Neurosci 20:6907–6919

Aggleton JP, Brown MW (1999) Episodic memory, amnesia, and the hippocampal-anterior thalamic axis. Behav Brain Sci 22:425–444

Andersen P, Bliss TVP, Skrede KK (1971) Lamellar organization of hippocampal excitatory pathways. Exp Brain Res 13:222–238

Andersen P, Silfvenius H, Sundberg SH, Sveen O, Wigström H (1978) Functional characteristics of unmyelinated fibres in the hippocampal cortex. Brain Res 144:11–18

Aradi I, Holmes WR (1999) Role of multiple calcium and calcium-dependent conductances in regulation of hippocampal dentate granule cell excitability. J Comput Neurosci 6:215–235

Aradi I, Soltesz I (2002) Modulation of network behaviour by changes in variance in interneuronal properties. J Phys 539:227–251

Ascoli GA, Krichmar JL (2000) L-neuron: a modeling tool for the efficient generation and parsimonious description of dendritic morphology. Neurocomputing 32-33:1003–1011

Ascoli GA, Donohue DE, Halavi M (2007) NeuroMorpho.Org: a central resource for neuronal morphologies. J Neurosci 27:9247–9251

Berger TW, Bassett JL (1992) System properties of the hippocampus. In: Gormezano I, Wasserman EA (eds) Learning and memory: the biological substrates. Lawrence Erlbaum, Hillsdale, pp 275–320

Berger TW, Weisz DJ (1987) Single unit analysis of hippocampal pyramidal and granule cells during classic conditioning of the rabbit nictitating membrane response. In: Gormezano I, Prokasy WF, Thompson RF (eds) Classical conditioning III: behavioral, neurophysiological and neurochemical studies in the rabbit. Lawrence Erlbaum, Hillsdale, pp 217–253

Berger TW, Semple-Rowland S, Bassett JL (1981) Hippocampal polymorph neurons are the cells of origin for ipsilateral association and commissural afferents to the dentate gyrus. Brain Res 215:329–336

Berger TW, Rinaldi P, Weisz DJ, Thompson RF (1983) Single unit analysis of different hippocampal cell types during classical conditioning of the rabbit nictitating membrane response. J Neurophysiol 50:1197–1219

Berger TW, Berry SD, Thompson RF (1986) Role of the hippocampus in classical conditioning of aversive and appetitive behaviors. In: Isaacson RL, Pribram KH (eds) The hippocampus, vol 4. Plenum, New York, pp 203–239

Berger TW, Hampson RE, Song D, Goonawardena A, Marmarelis VZ, Deadwyler SA (2011) A cortical neural prosthesis for restoring and enhancing memory. J Neural Eng 8:046017. https://doi.org/10.1088/1741-2560/8/4/046017

Buckmaster PS, Dudek FE (1997) Neuron loss, granule cell axon reorganization, and functional changes in the dentate gyrus of epileptic kainate-treated rats. J Comp Neurol 385:385–404

Buckmaster PS, Dudek FE (1999) In vivo intracellular analysis of granule cell axon reorganization in epileptic rats. J Neurophysiol 81:712–721

Buckmaster PS, Jongen-Rêlo AL (1999) Highly specific neuron loss preserves lateral inhibitory circuits in the dentate gyrus of kainite-induced epileptic rats. J Neurosci 19:9519–9529

Buckmaster PS, Strowbridge BW, Kunkel DD, Schmiege DL, Schwartzkroin PA (1992) Mossy cell axonal projections to the dentate gyrus molecular layer in the rat hippocampal slice. Hippocampus 2:349–362

Buckmaster PS, Wenzel HJ, Kunkel DD, Schwartzkroin PA (1996) Axon arbors and synaptic connections of hippocampal mossy cells in the rat in vivo. J Comp Neurol 366:271–292

Buhl EH, Halasy K, Somogyi P (1994) Diverse sources of hippocampal unitary inhibitory postsynaptic potentials and the number of synaptic release sites. Nature 368:823–828

Buhl EH, Cobb SR, Halasy K, Somogyi P (1995) Properties of unitary IPSPs evoked by anatomically identified basket cells in the rat hippocampus. Eur J Neurosci 7:1989–2004

Cajal SR (1968) The structure of the Ammon's horn. Charles C. Thomas, Springfield

Carnevale NT, Hines ML (2006) The NEURON book. Cambridge University Press, Cambridge

Claiborne BJ, Amaral DG, Cowan WM (1990) Quantitative, three-dimensional analysis of granule cell dendrites in the rat dentate gyrus. J Comp Neurol 302:206–219

Cohen NJ, Eichenbaum H (1993) Memory, amnesia and the hippocampal system. MIT Press, Cambridge

Crain B, Cotman C, Taylor D, Lynch G (1973) A quantitative electron microscopic study of synaptogenesis in the dentate gyrus of the rat. Brain Res 63:195–204

De Schutter E, Bower JM (1994) An active membrane model of the cerebellar Purkinje cell I. Simulation of current clamps in slice. J Neurophysiol 71:375–400

Desmond NL, Levy WB (1985) Granule cell dendritic spine density in the rat hippocampus varies with spine shape and location. Neurosci Lett 54:219–224

Dolorfo CL, Amaral DG (1998) Entorhinal cortex of the rat: topographic organization of the cells of origin of the perforant path projection to the dentate gyrus. J Comp Neurol 398:25–48

Douglas RM, McNaughton BL, Goddard GV (1983) Commissural inhibition and facilitation of granule cell discharge in fascia dentata. J Comp Neurol 219:285–294

Dyhrfjeld-Johnsen J, Santhakumar V, Morgan RJ, Huerta R, Tsimring L, Soltesz I (2007) Topological determinants of epileptogenesis in large-scale structural and functional models of the dentate gyrus derived from experimental data. J Neurophysol 97:1566–1587

Eichenbaum H, Wiener SI, Shapiro ML, Cohen NJ (1989) The organization of spatial coding in the hippocampus: a study of neural ensemble activity. J Neurosci 9:2764–2775

Foster TC, Barnes CA, Rao G, McNaughton BL (1991) Increase in perforant path quantal size in aged F-344 rats. Neurobiol Aging 12:441–448

Freund TF, Buzsáki G (1996) Interneurons of the hippocampus. Hippocampus 6:347–470

Gaarskjaer FB (1978) Organization of the mossy fiber system of the rat studied in extended hippocampi I: terminal area related to number of granule and pyramidal cells. J Comp Neurol 178:49–71

Gamrani H, Onteniente B, Seguela P, Geffard M, Calas A (1986) Gamma-aminobutyric acid-immunoreactivity in the rat hippocampus: a light and electron microscopic study with anti-GABA antibodies. Brain Res 364:30–38

Geiger JRP, Lübke J, Roth A, Frotscher M, Jonas P (1997) Submillisecond AMPA receptor-mediated signaling at a principal neuron-interneuron synapse. Neuron 18:1009–1023

Gottlieb DI, Cowan WM (1973) Autoradiographic studies of the commissural and ipsilateral association connection of the hippocampus and dentate gyrus of the rat. I. The commissural connections. J Comp Neurol 149:393–421

Gulyás AI, Megías M, Emri Z, Freund TF (1999) Total number and ratio of excitatory and inhibitory synapses converging onto single interneurons of different types in the CA1 area of the rat hippocampus. J Neurosci 19:10082–10097

Hafting T, Fyhn M, Molden S, Moser M-B, Moser EI (2005) Microstructure of a spatial map in the entorhinal cortex. Nature 436:801–806. https://doi.org/10.1038/nature03721

Halasy K, Somogyi P (1993) Distribution of GABAergic synapses and their targets in the dentate gyrus of rat: a quantitative immunoelectron microscopic analysis. J Hirnforsch 34:299–308

Hama K, Arii T, Kosaka T (1989) Three-dimensional morphometrical study of dendritic spines of the granule cell in the rat dentate gyrus with HVEM stereo images. J Electron Microsc Tech 12:80–87

Hampson RE, Simeral JD, Deadwyler SA (1999) Distribution of spatial and nonspatial information in dorsal hippocampus. Nature 402:610–614

Han ZS, Buhl EH, Lörinczi Z, Somogyi P (1993) A high degree of spatial selectivity in the axonal and dendritic domains of physiologically identified local-circuit neurons in the dentate gyrus of the rat hippocampus. Eur J Neurosci 5:395–410

Hasselmo ME (2005) What is the function of hippocampal theta rhythm?—linking behavioral data to phasic properties of field potential and unit recording data. Hippocampus 15:936–949. https://doi.org/10.1002/hipo.20116

Hendrickson PJ, Yu GJ, Song D, Berger TW (2015) Interactions between inhibitory interneurons and excitatory associational circuitry in determining spatio-temporal dynamics of hippocampal dentate granule cells: a large-scale computational study. Front Syst Neurosci 9. https://doi.org/10.3389/fnsys.2015.00155

Hendrickson PJ, Yu GJ, Song D, Berger TW (2016) A million-plus neuron model of the hippocampal dentate gyrus: critical role for topography in determining spatiotemporal network dynamics. IEEE Trans Biomed Eng 63:199–209

Hines ML, Davison AP, Muller E (2009) NEURON and Python. Front Neuroinform 28. https://doi.org/10.3389/neuro.11.001.2009

Hinneburg A, Gabriel H (2007) DENCLUE 2.0: fast clustering based on kernel density estimation. In Proceedings of the 7th international conference on advances in intelligent data analysis, Ljubljana, vol. 4723, pp 70–80

Hjorth-Simonsen A, Jeune B (1972) Origin and termination of the hippocampal perforant path in the rat studied by silver impregnation. J Comp Neurol 144:215–232

Ishizuka N, Weber J, Amaral DG (1990) Organization of intrahippocampal projections originating from CA3 pyramidal cells in the rat. J Comp Neurol. 295:580–623

Jaffe DB, Ross WN, Lisman JE, Lasser-Ross N, Miyakawa H, Johnston D (1994) A model for dendritic Ca^{2+} accumulation in hippocampal pyramidal neurons based on fluorescence imaging measurements. J Neurosci 71:1065–1077

Krueppel R, Remy S, Beck H (2011) Dendritic integration in hippocampal dentate granule cells. Neuron 71:512–528

Krupic J, Burgess N, O'Keefe J (2012) Neural representations of location composed of spatially periodic bands. Science 337:853–857

Levy WB (1989) A computational approach to hippocampal function. In: Psychology of learning and motivation. Elsevier, pp 243–305

Lorente de Nó R (1934) Studies on the structure of the cerebral cortex II: continuation of the study of the ammonic system. J Psychol Neurol 46:113–177

MacKenzie S, Frank AJ, Kinsky NR, Porter B, Riviére PD, Eichenbaum H (2014) Hippocampal representation of related and opposing memories develop within distinct, hierarchically organized neural schemas. Neuron 83:202–215

McClelland JL, McNaughton BL, O'Reilly RC (1995) Why there are complementary learning systems in the hippocampus and neocortex: insights from the successes and failures of connectionist models of learning and memory. Psychol Rev 102:419–457. https://doi.org/10.1037/0033-295x.102.3.419

McNaughton BL, Morris RGM (1987) Hippocampal synaptic enhancement and information storage within a distributed memory system. Trends Neurosci 10:408–415. https://doi.org/10.1016/0166-2236(87)90011-7
Marr D (1971) Simple memory: a theory for archicortex. Philos Trans R Soc Lond 262:23–81
Morgan RJ, Soltesz I (2010) Microcircuit model of the dentate gyrus in epilepsy. In: Cutsuridis V, Graham BP, Cobb S, Vida I (eds) Hippocampal microcircuits. Springer, New York, pp 495–525
Mulders WHAM, West MJ, Slomianka L (1997) Neuron numbers in the presubiculum, parasubiculum, and entorhinal area of the rat. J Comp Neurol 385:83–94
Myers CE, Scharfman HE (2011) Pattern separation in the dentate gyrus: a role for the CA3 backprojection. Hippocampus 21:1190–1215
Nadel L, Moscovitch M (1997) Memory consolidation, retrograde amnesia and the hippocampal complex. Curr Opin Neurobiol 7:217–227
O'Keefe J, Nadel L (1978) The Hippocampus as a cognitive map. Oxford University Press, London
Oliphant TE (2007) Python for scientific computing. Comput Sci Eng 9:10–20
Patton PE, McNaughton BL (1995) Connection matrix of the hippocampal formation: I. The dentate gyrus. Hippocampus 5:245–286
Ribak CE, Seress L (1983) Five types of basket cell in the hippocampal dentate gyrus: a combined Golgi and electron microscopic study. J Neurocytol 12:577–597
Ribak CE, Shapiro LA (2007) Ultrastructure and synaptic connectivity of cell types in the adult rat dentate gyrus. Prog Brain Res 163:155–166
Ribak CE, Nitsch R, Seress L (1990) Proportion of parvalbumin-positive basket cells in the GABAergic innervation of pyramidal and granule cells of the rat hippocampal formation. J Comp Neurol 300:449–461
Rihn LL, Claiborne BJ (1990) Dendritic growth and regression in rat dentate granule cells during late postnatal development. Dev Brain Res 54:115–124
Santhakumar V, Bender R, Frotscher M, Ross ST, Hollrigel GS, Toth Z, Soltesz I (2000) Granule cell hyperexcitability in the early post-traumatic rat dentate gyrus: the 'irritable mossy cell' hypothesis. J Physiol 524(Pt 1):117–134
Santhakumar V, Aradi I, Soltesz I (2005) Role of mossy fiber sprouting and mossy cell loss in hyperexcitability: a network model of the dentate gyrus incorporating cell types and axonal topography. J Neurophysiol 93:437–453
Scharfman HE (1995) Electrophysiological evidence that dentate hilar mossy cells are excitatory and innervate both granule cells and interneurons. J Neurophysiol 74:179–194
Scharfman HE, Kunkel DD, Schwartkroin PA (1990) Synaptic connections of dentate granule cells and hilar neurons: results of paired intracellular recordings and intracellular horseradish peroxidase injections. Neuroscience 37:693–707
Scorcioni R, Polavaram S, Ascoli GA (2008) L-measure: a web-accessible tool for the analysis, comparison and search of digital reconstructions of neuronal morphologies. Nat Protoc 3:866–876
Seress L, Pokorny J (1978) Structure of the granular layer of the rat dentate gyrus. A light microscopic and Golgi study. J Anat 133:181–195
Seress L, Pokorny J (1981) Structure of the granular layer of the rat dentate gyrus: a light microscopic and Golgi study. J Anat 133:181–195
Seress L, Ribak CE (1983) GABAergic cells in the dentate gyrus appear to be local circuit and projection neurons. Exp Brain Res 50:173–182
Sík A, Penttonen M, Buzsáki G (1997) Interneurons in the hippocampal dentate gyrus: an in vivo intracellular study. Eur J Neurosci 9:573–588
Sloviter RS, Zappone CA, Harvey BD, Bumanglag AV, Bender RA, Frotscher M (2003) 'Dormant basket cell' hypothesis revisited: relative vulnerabilities of dentate gyrus mossy cells and inhibitory interneurons after hippocampal status epilepticus in the rat. J Comp Neurol 459:44–76
Solstad T, Moser EI, Einevoll GT (2006) From grid cells to place cells: a mathematical model. Hippocampus 16:1026–1031. https://doi.org/10.1002/hipo.20244

Soriano E, Frotscher M (1989) A GABAergic axo-axonic cell in the fascia dentata controls the main excitatory hippocampal pathway. Brain Res 503:170–174
Soriano E, Frotscher M (1994) Mossy cells of the rat fascia dentate are glutamate-immunoreactive. Hippocampus 4:65–69
Spruston N, Johnston D (1992) Perforated patch-clamp analysis of the passive membrane properties of three classes of hippocampal neurons. J Neurophysiol 67:508–529. https://doi.org/10.1152/jn.1992.67.3.508
Squire LR (1986) Mechanisms of memory. Science 232:1612–1619
Swanson LW, Wyss JM, Cowan WM (1978) An autoradiographic study of the organization of intrahippocampal association pathways in the rat. J Comp Neurol 181:681–716
Tamamaki N, Nojyo Y (1993) Projection of the entorhinal layer II neurons in the rat as revealed by intracellular pressure-injection of neurobiotin. Hippocampus 3:471–480
Treves A, Rolls ET (1994) Computational analysis of the role of the hippocampus in memory. Hippocampus 4:374–391
Vida I (2010) Morphology of hippocampal neurons. In: Cutsuridis V, Graham BP, Cobb S, Vida I (eds) Hippocampal microcircuits. Springer, New York, pp 27–67
Warman EN, Durand DM, Yuen GLF (1994) Reconstruction of hippocampal CA1 pyramidal cell electrophysiology by computer simulation. J Neurosci 71:2033–2045
Wenzel HJ, Buckmaster PS, Anderson NL, Wenzel ME, Schwartzkroin PA (1997) Ultrastructural localization of neurotransmitter immunoreactivity in mossy cell axons and their synaptic targets in the rat dentate gyrus. Hippocampus 7:559–570
Witter MP (2007) The perforant path: projections from the entorhinal cortex to the dentate gyrus. Prog Brain Res 163:43–61
Yeckel MF, Berger TW (1990) Feedforward excitation of the hippocampus by entorhinal afferents: redefinition of the role of the trisynaptic pathway. Proc Natl Acad Sci USA 87:5832–5836
Yeckel MF, Berger TW (1995) Monosynaptic excitation of CA1 hippocampal pyramidal neurons by afferents from the entorhinal cortex. Hippocampus 5:108–114
Yu GJ, Song D, Berger TW (2014) Implementation of the excitatory entorhinal-dentate-CA3 topography in a large-scale computational model of the rat hippocampus. In: EMBC, 2014: 36th annual international conference of the IEEE Engineering in Medicine and Biology Society, Chicago. IEEE, pp 6581–6584
Yu GJ, Hendrickson PJ, Song D, Berger TW (2015) Topography-dependent spatio-temporal correlations in the entorhinal-dentate-CA3 circuit in a large-scale computational model of the rat hippocampus. In: EMBC, 2015: 37th annual international conference of the IEEE Engineering in Medicine and Biology Society, Milan. IEEE, pp 3965–3968
Yu GJ, Song D, Berger TW (2016). Place field detection using grid-based clustering in a large-scale computational model of the rat dentate gyrus. In: EMBC, 2016: 38th annual international conference of the IEEE Engineering in Medicine and Biology Society, Orlando. IEEE, pp 1405–1408
Yuen GLF, Durand DM (1991) Reconstruction of hippocampal granule cell electrophysiology by computer simulation. Neuroscience 41:411–423
Zimmer J (1971) Ipsilateral afferents to the commissural zone of the fascia dentata, demonstrated in decommissurated rats by silver impregnation. J Comp Neurol 142:393–416
Zipp F, Nitsch R, Soriano E, Frotscher M (1989) Entorhinal fibers form synaptic contacts on parvalbumin-immunoreactive neurons in the rat fascia dentata. Brain Res 495:161–166

A Model of Spatial Reach in LFP Recordings

Henrik Lindén, Tom Tetzlaff, Szymon Łęski, Klas H. Pettersen, Sonja Grün, Markus Diesmann, and Gaute T. Einevoll

Abstract The measurement of local field potentials (LFP), the low-frequency part of extracellularly recorded potentials, is one of the most commonly used methods for probing hippocampal and cortical activity in vivo. It offers the possibility to monitor the activity of many neurons close to the recording electrode simultaneously but has the limitation that it may be difficult to interpret and relate to the underlying neuronal activity. The recording electrode picks up activity from proximal neurons, but what about more distant neurons? An important piece of information for a correct interpretation of the LFP is to decide the size of the tissue that substantially contributes to the LFP, i.e., the *reach* of the LFP signal. In this chapter we present a simple model that describes how population geometry, spatial decay of single-

H. Lindén (✉)
Department of Neuroscience, University of Copenhagen, Copenhagen, Denmark
e-mail: hlinden@sund.ku.dk

T. Tetzlaff
Institute of Neuroscience and Medicine (INM-6) and Institute for Advanced Simulation (IAS-6) and JARA Institute Brain Structure-Function Relationships (INM-10), Jülich Research Centre, Jülich, Germany
e-mail: t.tetzlaff@fz-juelich.de

S. Łęski
Department of Neurophysiology, Nencki Institute of Experimental Biology of Polish Academy of Sciences, Warsaw, Poland

K. H. Pettersen
Letten Centre and GliaLab, Department of Molecular Medicine, Institute of Basic Medical Sciences, University of Oslo, Oslo, Norway
e-mail: klas.pettersen@gmail.com

S. Grün
Institute of Neuroscience and Medicine (INM-6) and Institute for Advanced Simulation (IAS-6) and JARA Institute Brain Structure-Function Relationships (INM-10), Jülich Research Centre, Jülich, Germany

Theoretical Systems Neurobiology, RWTH Aachen University, Aachen, Germany
e-mail: s.gruen@fz-juelich.de

V. Cutsuridis et al. (eds.), *Hippocampal Microcircuits*, Springer Series in Computational Neuroscience, https://doi.org/10.1007/978-3-319-99103-0_13

cell LFP contributions, and correlation between LFP sources determine the relation between LFP amplitude and population size and use it to study the spatial reach of the LFP. The model can also be used to study different frequency bands of the LFP separately as well as the spatial decay outside the active neuronal population.

Overview

What is the Model

The recording of electrical potentials with extracellular electrodes has for many decades been the work horse in in vivo studies of cortical and hippocampal function (Buzsáki et al., 2012). The high-frequency part ($\gtrsim$500 Hz), the multiunit activity (MUA), mainly reflects spiking in neurons surrounding the electrode contact. In contrast, the low-frequency part, the local field potential (LFP), is thought to mainly reflect synaptic inputs and their subthreshold dendritic processing (Einevoll et al., 2013b) (at least for LFP frequencies below, say, 100 Hz Schomburg et al. 2012).

In the context of hippocampal studies, the LFP has commonly been used to investigate characteristic oscillations at a wide range of frequencies: low-frequency theta oscillations ($\sim$5–10 Hz) (Buzsáki, 2002), gamma oscillations ($\sim$30–100 Hz) (Bragin et al., 1995), and very high-frequency "ripples" ($\sim$100–200 Hz) (Ylinen et al., 1995; Siapas and Wilson, 1998; Maier et al., 2011). When recorded across the hippocampal lamina, the LFP has also been used to extract current source densities (CSDs) (Brankack et al., 1993; Sirota et al., 2003; Buzsáki et al., 2012) and to estimate synaptic pathways into the hippocampus (Herreras et al., 2015). Further, the hippocampal LFP has been shown to encode spatial position, in analogy with the spiking of hippocampal place cells (Agarwal et al., 2014; Taxidis et al., 2015).

The LFP is, despite its name, a much less local measure of neural activity than spikes as the signal in general stems from populations of thousands or more neurons surrounding the electrode (Einevoll et al., 2013a). Thus while offering

M. Diesmann
Institute of Neuroscience and Medicine (INM-6) and Institute for Advanced Simulation (IAS-6) and JARA Institute Brain Structure-Function Relationships (INM-10), Jülich Research Centre, Jülich, Germany

Department of Psychiatry, Psychotherapy and Psychosomatics, Medical Faculty, and Department of Physics, Faculty 1, RWTH Aachen University, Aachen, Germany
e-mail: m.diesmann@fz-juelich.de

G. T. Einevoll
Faculty of Science and Technology, Norwegian University of Life Sciences, Ås, Norway

Department of Physics, University of Oslo, Oslo, Norway
e-mail: gaute.einevoll@nmbu.no

an attractive opportunity for monitoring population activity, the LFP also has a strong limitation: it can be difficult to interpret where the signal comes from and what it represents. Proper mathematical modeling and analysis is thus needed to properly infer the underlying neural activity from the signal (Einevoll et al., 2013b). A key aspect for a correct interpretation of the LFP is knowing the size of the region that generates it, i.e., knowing the spatial reach of the LFP. A number of experimental studies have addressed this issue (Liu and Newsome, 2006; Kreiman et al., 2006; Berens et al., 2008; Katzner et al., 2009; Xing et al., 2009; Kajikawa and Schroeder, 2011) but have come with contradictory evidence regarding the spatial reach, ranging from a few hundred micrometers (Katzner et al., 2009; Xing et al., 2009) to several millimeters (Kreiman et al., 2006). One possible explanation for this discrepancy is that the reach of the LFP is not a fixed quantity, but rather changes with experimental conditions as the neuronal network state changes due to behavioral context, stimulation, or level of anesthesia.

For spikes, i.e., the extracellular signatures of action potentials extracted from the MUA, the definition of spatial reach is rather straightforward. Since (1) the spike amplitude decays sharply with distance between the neuron and the recording electrode and (2) spikes of relevant neighboring neurons typically are nonoverlapping in time, it is natural to ask at which distance a spike becomes indiscernible from the background noise (Buzsáki, 2004; Pettersen and Einevoll, 2008). For LFPs the situation is quite different. Since the LFP is primarily generated by slower synaptic events, the contributions from different sources are overlapping in time resulting in a signal that is a sum over many contributions.

So what determines the reach of the LFP? Intuitively, the reach of the LFP is the result of two opposing scaling effects: as in the case of extracellular action potentials, the contribution from a single neuron to the LFP still decays with distance from the recording electrode (Lindén et al., 2010), but the number of potentially contributing neurons increases with distance. There is, however, also a third important factor that influences the LFP: whether the LFP contributions from separate neurons are correlated or not. Just like water waves from several sources may interfere constructively if they are synchronized, both the amplitude as well as the spatial reach of the LFP may be drastically changed depending on the level of correlation in the generating neuronal population (Lindén et al., 2011).

Questions Addressed

In this chapter we describe a compact model of LFP generation that encapsulates how population geometry, single-cell features, and population-level correlations determine the size of the region generating the LFP measured in the center of a neuronal population (Einevoll et al., 2013b). The model can also be used to model the spatial decay outside the active neuronal population which, in turn, may help to understand the relative LFP contributions from simultaneously active neuronal populations.

The present model assumes passive dendrites and considers LFPs due to synaptic currents and the associated return currents but could straightforwardly be extended to model, e.g., active subthreshold conductances (Ness et al., 2015).

Levels of Detail/Rationale

The spatial reach of the LFP is difficult to measure experimentally because it is in general difficult to precisely control or measure the neuronal activity that generates the signal. To complicate matters further, the LFP can in principle be composed of contributions from several local and distant populations that spread via volume conduction. Here we take an analytical approach to address the question of LFP reach for a situation where a single population dominates the signal and derive a model that relies on numerical simulations of synaptically activated neurons for certain components of the model. This approach has the advantage that we can fully control both the size and activity of the neuronal population. Specifically, in contrast to experiments, we can vary the size of the population to study the effects on the LFP.

The Model

Model Components

Let us consider an LFP measured in the center of a disclike neuronal population (Fig. 1). The size of the population is defined by the radius R. Each cell i in the population gives a contribution $\phi_i(t)$ to the population LFP $\phi(t) = \sum_i \phi_i(t)$. How does the amplitude of the LFP fluctuations (that we here quantify by the standard deviation σ) increase with the population radius R? As we will explain below, the answer to this question depends on three factors:

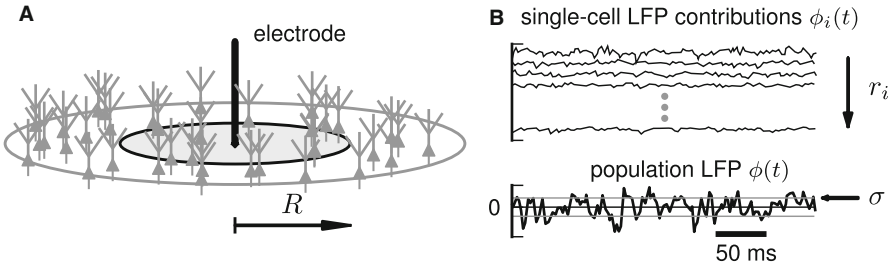

Fig. 1 Illustration of model setup. We study a model of the population LFP based on the spatial summation of single-neuron LFP contributions from many neurons. (**a**) An electrode is placed in the center of a disclike population, and by varying the radius R, we can investigate how the amplitude of the LFP increases with population radius. (**b**) Each neuron (ordered by their distance r_i from the recording electrode) gives a contribution $\phi_i(t)$ to the population LFP $\phi(t)$. The amplitude of the LFP is measured by the standard deviation σ of the LFP fluctuations over time. (Adapted with permission from Lindén et al. 2011)

1. The distance dependence of the amplitude of the single-neuron contributions $\phi_i(t)$ characterized by the shape function $F(r)$,
2. the number of neurons as a function of distance from the recording electrode, given by the population geometry,
3. the level of correlation between the LFP contributions from different neurons.

We will first turn to numerical simulations of single-cell LFP contributions generated by multi-compartment neuron models to find the shape functions $F(r)$ (point 1) and then derive an analytical expression for the LFP amplitude encapsulating all three factors above. Based on this we will give a precise definition of the reach of the LFP that we will test against full numerical population simulations and briefly describe how the model can be extended to study separate individual frequency components of the LFP (section "Results").

Single-Cell Shape Function

How does the amplitude of the LFP contribution from a cell depend on the distance to the recording electrode? To answer this question, we performed simulations of synaptically activated multi-compartment neuron models and computed the resulting LFP at the soma level for different radial distances to the electrode (Lindén et al., 2011). The LFP was calculated using the line-source formalism (Holt and Koch, 1999) as implemented in the software *LFPy* (http://lfpy.github.io) (Lindén et al., 2014), and the neurons were activated using uncorrelated spike trains. Results of these simulations are shown in Fig. 2.

We see that the amplitude typically decays as $\sim 1/r^2$ with distance r for distances further away than 200–300 μm from electrode (Fig. 2a, dashed line). This is consistent with the spatial decay of the electric potential generated by a current dipole. Closer to the electrode, the decay is less steep, roughly $\sim 1/r^{1/2}$. This is likely due to the dendritic extent of the neurons that typically is on the order of a few hundred micrometers.

This picture is very similar for neurons with different morphologies (Fig. 2a), but we see that the spatial decay changes somewhat for different synaptic input scenarios (Fig. 2b). The distance at which the decay changes slope from low to high is further away from the cell in the case of only apical input onto a pyramidal L5 neuron compared to when inputs are distributed basally or homogeneously over the whole cell. Because of the vertical extent of the pyramidal neuron (which is approximately 1200 μm), the synapses in this scenario are further away from the recording positions which also causes a lower amplitude of the LFP compared to basal input.

Based on these examples, we can formulate simplified expressions for the spatial decay $F(r)$ of the amplitude from a single-neuron LFP contribution (Einevoll et al., 2013a):

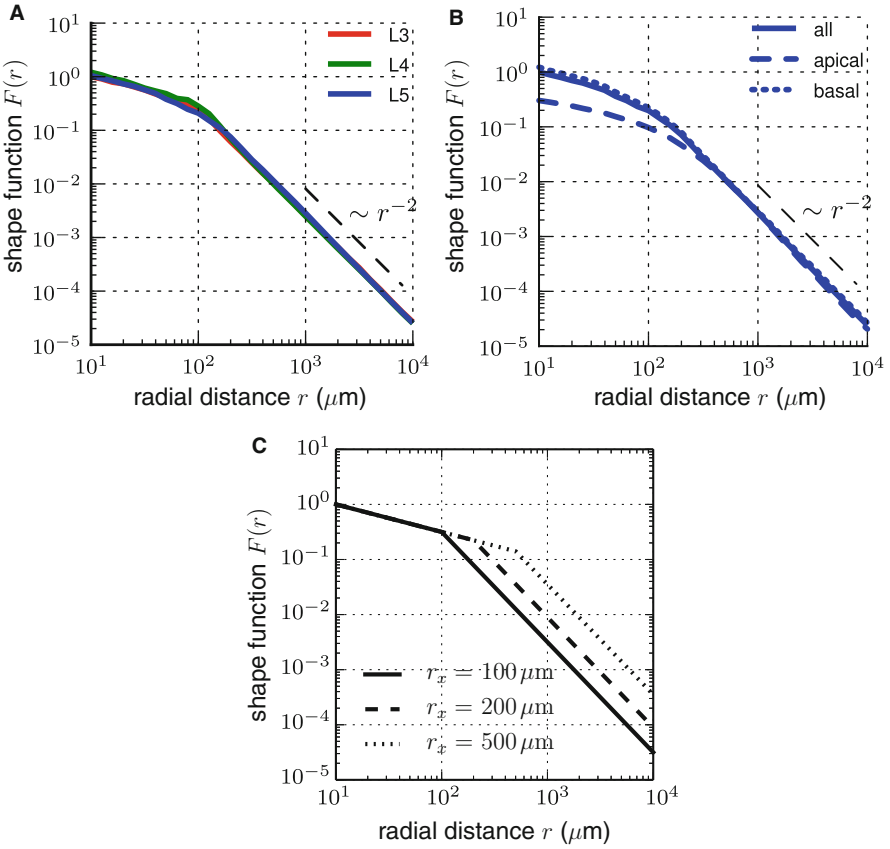

Fig. 2 Spatial decay of the LFP contribution from a single neuron. Multi-compartment neuron models were placed at different radial distances r away from a virtual recording electrode, and the LFP amplitude was computed at each distance. The distance dependence of the LFP amplitude is captured by the shape function $F(r)$ (see text). For further details of the simulation, we refer to Lindén et al. (2011). (**a**) Shape function for three types of cortical V1 neurons (layer 3 and layer 5 pyramidal neurons as well as a layer 4 stellate neuron). (**b**) Dependence of the shape function on the synaptic input region for the layer 5 pyramidal neuron. (**c**) Illustration of simplified shape function $F(r)$ given by Eq. 1 with $r_\epsilon = 10\,\mu$m and $F_0 = 1$ for three different values of the cutoff distance $r_x = [100,200,500]\,\mu$m (indicated by line style). ((**a**) and (**b**) adapted with permission from Lindén et al. 2011)

$$F(r) = \begin{cases} F_0 & r < r_\epsilon, \\ F_0 (r_\epsilon / r)^{1/2} & r_\epsilon < r \le r_x, \\ F_0 (r_\epsilon / r_x)^{1/2} (r_x / r)^2 & r \ge r_x, \end{cases} \tag{1}$$

where r_x is the *cutoff distance* where the decay changes slope and r_ϵ is a minimal radial distance introduced to avoid an unphysical divergence as r goes to zero. (This could represent, e.g., the distance to the cell closest to the electrode, but we leave this unspecified here.) For an illustration of this simplified shape function $F(r)$, see Fig. 2c.

Derivation of the Simplified Model

Let us now consider a population of neurons distributed in a disclike volume with radius R. How does the amplitude of compound LFP $\phi(t)$ measured in the center of the population depend on the population radius? In the following we will describe a simple analytical model that gives the answer to this question (Einevoll et al., 2013a).

First, let us assume that the contribution $\phi_i(t)$ from a neuron i can be decomposed into a temporal and spatial part:

$$\phi_i(t) = \xi_i(t)F(r_i) \tag{2}$$

where $\xi_i(t)$ is a time-dependent variable with zero mean and unit variance which describes the temporal fluctuations of the LFP contribution and $f(r_i)$ is the shape function described above.

For the disclike population considered here, the number of neurons at a specific distance r from the electrode is determined by:

$$N(r) = 2\pi r\rho \tag{3}$$

where ρ is the area density of neuronal LFP sources. If all LFP sources were *uncorrelated*, that is, $\mathrm{E}_t[\phi_i(t)\phi_j(t)] = 0$ for $i \neq j$ where $\mathrm{E}_t[\cdot]$ represents expectation value over time, the variance σ^2 of the LFP from cells at a particular distance would increase linearly with the number of LFP sources at that distance. In the continuum limit, the total LFP amplitude can be formulated as an integral (Lindén et al., 2011):

$$\sigma^2(R) = G_0(R) = \int_0^R dr\ N(r)F(r)^2 = \rho\int_0^R dr\ 2\pi r F(r)^2 \tag{4}$$

where we have made use of Eq. (3) above.

It is clear from this expression that the shape function $F(r)$ is the key factor determining the way the amplitude of the compound LFP increases with distance. In Fig. 3a, we show how the LFP amplitude $\sigma(R) = \sqrt{G_0(R)}$ increases with distance in the case of uncorrelated neuronal sources using the shape function defined in Eq. 1. We see from the plot that the LFP amplitude in this case quickly appears to saturate to a maximum value. It can be shown analytically (Lindén et al., 2011; Einevoll et al., 2013a) that when the spatial decay of neuronal sources decreases as $\sim 1/r^2$ or more steeply, the LFP amplitude indeed converges to a fixed values as $R \to \infty$. This convergence suggest an intuitive definition of the *reach of the LFP* as the population radius R^* at which the LFP amplitude $\sigma(R)$ has obtained a certain fraction α of the amplitude at infinite population size $\sigma(R \to \infty)$.

If, on the other hand, the LFP sources are completely *correlated*, i.e., $\mathrm{E}_t[\phi_i(t)\phi_j(t)] = E_t[\xi_i(t)\xi_j(t)]F_iF_j = F_iF_j$, the variance of the amplitude of

the compound LFP from cells at a particular distance increases as the square of the number of LFP sources at that distance, and we get (Lindén et al., 2011):

$$\sigma^2(R) = G_1(R) = \left(\int_0^R dr\ N(r)F(r)\right)^2 = \rho^2\left(\int_0^R dr\ 2\pi r F(r)\right)^2 \quad (5)$$

A more general expression valid for any level of correlation $c_\phi = \mathrm{E}_t[\phi_i(t)\phi_j(t)]$ between LFP sources is given by Lindén et al. (2011):

$$\sigma(R) = \sqrt{(1-c_\phi)G_0(R) + c_\phi G_1(R)}\,. \quad (6)$$

Here the terms for uncorrelated (Eq. 4) and correlated sources (Eq. 5) have been combined and are scaled by the correlation coefficient c_ϕ. Equation 6 can be computed by numerical integration of $G_0(R)$ and $G_1(R)$ for any shape function $F(r)$ and also for a numerically derived one as in Fig. 2. For the simplified shape function $F(r)$ given by Eq. 1, we may, however, even find analytical expressions for the results of the integrals in Eqs. 4 and 5 (Einevoll et al., 2013a):

$$G_0(R) = \begin{cases} F_0^2\rho\pi R^2 & R \le r_\epsilon, \\ F_0^2\rho\pi r_\epsilon(2R - r_\epsilon) & r_\epsilon \le R \le r_x, \\ F_0^2\rho\pi r_\epsilon(3r_x - r_\epsilon - r_x^3/R^2) & R \ge r_x, \end{cases} \quad (7)$$

$$G_1(R) = \begin{cases} F_0^2\rho^2\pi^2 R^4 & R \le r_\epsilon, \\ F_0^2\rho^2\frac{1}{9}\pi^2\left(r_\epsilon^2 - 4r_\epsilon^{1/2}R^{3/2}\right)^2 & r_\epsilon \le R \le r_x, \\ F_0^2\rho^2\frac{1}{9}\pi^2 r_\epsilon\left(r_\epsilon^{3/2} - (4 + 6\ln(R/r_x))r_x^{3/2}\right)^2 & R \ge r_x. \end{cases} \quad (8)$$

Frequency-Dependent Formulation of the Simplified Model

The simplified model outlined so far predicts the variance $\sigma^2 \sim \int df\ P(f)$ of the compound LFP, i.e., the integral of the LFP power spectrum $P(f)$. All frequency components are hence collapsed into a single measure. The model can however easily be reformulated to obtain a frequency-resolved version, resulting in the following expression for the power spectrum $P(f, R)$ of the compound LFP of a cell population of radius R, analogous to Eq. 6 (for details of the derivation, see Łęski et al. 2013):

$$P(f, R) = (1 - c_\phi(f))G_0(f, R) + c_\phi(f)G_1(f, R). \quad (9)$$

Here, $c_\phi(f)$ denotes the population-averaged coherence between single-cell LFP contributions. Analogous to Eqs. 4 and 5, the functions

$$G_0(f, R) = \int_0^R dr\ N(r)F(f, r)^2 \tag{10}$$

and

$$G_1(f, R) = \left(\int_0^R dr\ N(r)F(f, r) \right)^2 \tag{11}$$

are determined by the shape function $F(f, r)$ describing the dependence of the single-cell LFP amplitude at frequency f at the cell-electrode distance r and $N(r)$ giving the number of LFP sources at distance r (cf. Eq. 3 for a disclike population geometry). For the results shown in section "Frequency Dependence of LFP Power and Reach," we will use the phenomenological model of the shape function defined in Eq. 1. The frequency dependence of the shape function $F(f, r)$ results from introducing a frequency-dependent cutoff distance $r_x = r_x(f)$. This frequency dependence of the cutoff distance (Fig. 5a) is obtained by fitting $F(f, r)$ to the results of simulations of multi-compartment neurons stimulated by white-noise synaptic input, i.e., synaptic input with a flat power spectrum (same setup as explained in section "Single-Cell Shape Function"). The second source of frequency dependence in Eq. 9 is the LFP coherence $c_\phi(f)$. Again, the shape of $c_\phi(f)$ (Fig. 5b) is obtained from simulations of multi-compartment neurons fed by white, partially shared synaptic input (see section "Simulations with Multi-compartment Neuron Models").

Spatial Decay Outside the Neuronal Population

All the equations above apply to a scenario where the LFP electrode is placed in the center of the disclike population. The expressions for G_0 and G_1 can, however, also be extended to account for a situation where the electrode is placed at a distance X away from the center (Einevoll et al., 2013a):

$$\begin{aligned} G_0(R, X) &= \rho \int_{\{|\mathbf{r}| \le R\}} d^2r\ F(|\mathbf{r} - \mathbf{X}|)^2 \\ &= \rho \int_0^{2\pi} d\theta \int_0^R dr\ r\ F\left(\sqrt{(X - r\cos\theta)^2 + (r\sin\theta)^2}\right)^2, \end{aligned} \tag{12}$$

$$G_1(R, X) = \left(\rho \int\limits_{\{|\mathbf{r}| \le R\}} d^2r \; F(|\mathbf{r} - \mathbf{X}|)\right)^2$$
$$= \rho^2 \left(\int_0^{2\pi} d\theta \int_0^R dr \; r \; F\left(\sqrt{(X - r\cos\theta)^2 + (r\sin\theta)^2}\right)\right)^2. \quad (13)$$

Here, $\mathbf{r}$ denotes the position vectors of the LFP sources and $\mathbf{X}$ the vector $X\mathbf{e}_x$ with $\mathbf{e}_x$ being a unit vector in the x-direction.

Results

We will first go through some of the predictions of the simplified model derived above and then in the next section compare these predictions against numerical population simulations. Finally, we will briefly illustrate the spatial decay of the LFP outside the active population.

Analytical Predictions for Amplitude and Reach

The model equations above (Eqs. 4, 5 and 6) predict two qualitatively different scaling behaviors for uncorrelated and correlated neuronal activity, respectively. This is illustrated in Fig. 3a, b where the two components $\sqrt{G_0}$ and $\sqrt{G_1}$ are plotted separately for a population of radius 1 mm. In the case of uncorrelated activity, the amplitude $\sigma(R)$ of the compound LFP converges to a fixed value that would not increase even if the neuron population were infinitely sized (Fig. 3a, see also Lindén et al. 2011; Einevoll et al. 2013a). With the definition of spatial reach introduced above, as the population radius R^* where the LFP amplitude has obtained a fraction α of the infinite-size population, the LFP sources that are positioned within a radius R^* contributes a proportion α of the total LFP amplitude even if they are embedded in population with infinite size. In Lindén et al. (2011), and Einevoll et al. (2013a) we have used $\alpha = 0.95$ which is illustrated with a dashed line in Fig. 3a. In this case the spatial reach is small, roughly $\sim$200 μm.

In contrast, if the neuronal LFP sources were fully correlated, the amplitude increase with population radius is markedly different (Fig. 3b). In this case the LFP amplitude no longer converges to a fixed value. With the same definition of the spatial reach as in the uncorrelated case, the LFP now contains contributions from most of the neuronal population (>800 μm). Furthermore, the amplitude of the LFP is markedly higher.

For intermediate values of the correlation c_ϕ, the contributions from the two terms G_0 and G_1 are weighted according to Eq. 6 to give intermediate scaling behavior of the LFP amplitude compared to the uncorrelated or fully uncorrelated case

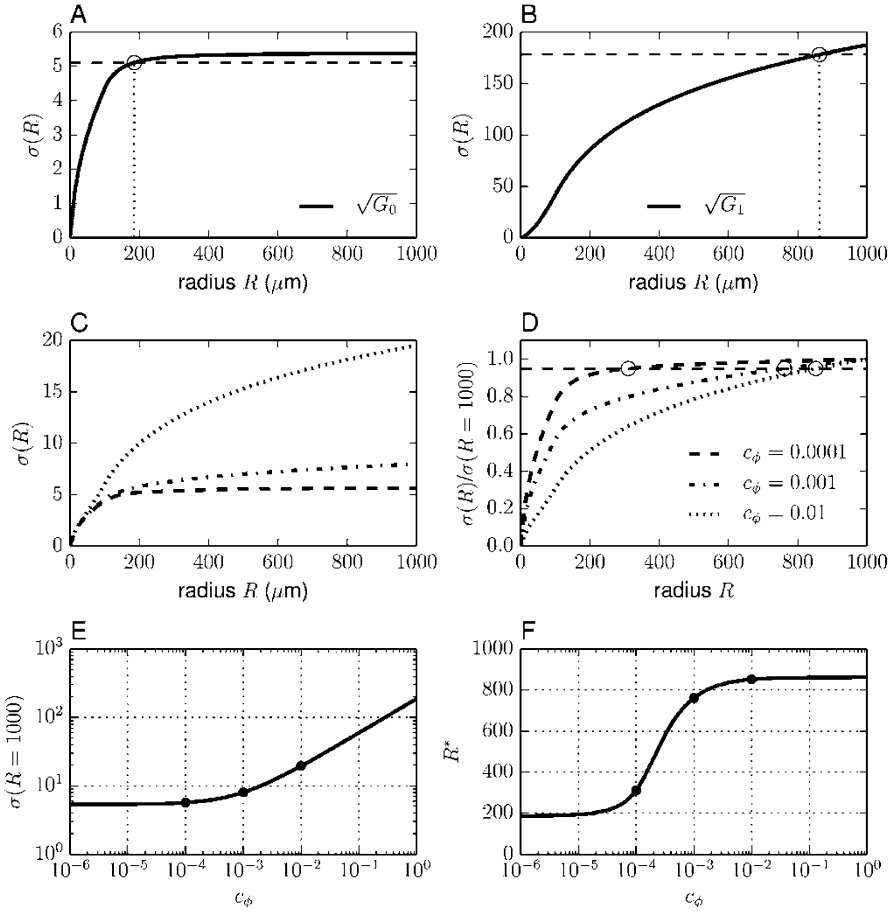

Fig. 3 Components of and results from the simplified model. Results of Eq. (6) using expressions for G_0 and G_1 given by Eqs.7 and 8 with area density $\rho = 10{,}000$ neurons/mm^2 derived using single-cell shape function $F(r)$ as defined in Eq. (1) with $r_\epsilon = 10\,\mu$m, $r_x = 100\,\mu$m and $F_0 = 1$. (**a**) When the LFP sources are uncorrelated, the amplitude $\sigma(R)$ of the compound signal is given by Eq. 4. In this case the amplitude converges to a fixed value for large R, and we here define the *spatial reach* of the LFP as the population radius R^* (dotted line) where the amplitude has obtained 95% of the maximum value (dashed line), here compared against the largest population radius considered in the study ($R = 1000\,\mu$m). (**b**) The amplitude $\sigma(R)$ in the case of fully *correlated* neuronal LFP sources, given by Eq. (5). (**c**) The LFP amplitude $\sigma(R)$ for intermediate levels of correlation c_ϕ (see legend in (**d**)). (**d**) Same as in (**c**), but normalized against the value at $R = 1000\,\mu$m. (**e**) LFP amplitude for population size $R = 1000\,\mu$m as a function of correlation level c_ϕ. (**f**) LFP reach R^* as a function of correlation level c_ϕ. Dots in (**e**) and (**f**) illustrate the examples shown in (**c**) and (**d**)

illustrated by three examples in Fig. 3c, d. As consequence, the LFP amplitude for large population radiuses becomes markedly higher as the correlation is increased (Fig. 3c). By normalizing the amplitude by that obtained for $R = 1000\,\mu$m, we show

in Fig. 3d how this affects the LFP reach: due to the larger increase in LFP amplitude with population radius, the spatial reach becomes larger with higher correlations.

In Fig. 3c, we plot the maximum LFP amplitude $\sigma(R = 1000\,\mu\text{m})$ for a wide range of correlations c_ϕ, and in Fig. 3d, the corresponding values for the LFP reach are shown. Already at low levels ($c_\phi =\sim 10^{-4}$), the correlations start to play a role in determining the LFP reach, and in the range between $\sim 10^{-4}$ and $\sim 10^{-2}$, there is a dramatic effect on the reach due to increasing correlation. Above this range ($\sim 10^{-2}$), the LFP is already getting substantial contributions from most of the population, and the reach does not increase further if the correlation level is increased. The amplitude $\sigma(R = 1000\,\mu\text{m})$, however, continues to increase up to the maximum correlation $c_\phi = 1$.

Simulations with Multi-compartment Neuron Models

The simplified LFP model described above neatly encapsulates the dependence of the LFP amplitude on the level of correlation between LFP contributions from different neurons in the population. In the above examples, we treated the level of correlation (c_ϕ) as a free parameter. In an experimental setting, however, the correlation between LFP sources depends on several factors, including (1) the correlation in synaptic input and (2) the spatial arrangement of dendrites and synaptic distributions on to the cells. As an example, one would expect larger LFP amplitude to be generated by synchronized input to spatially aligned cells with extended dendrites (in a so-called "open-field" arrangement) than asynchronous input on to spherically symmetric stellate cell (in so-called closed-field arrangements) (Mitzdorf, 1985; Lindén et al., 2010).

To test the predictions of the simplified model and to examine how the results depend on morphological features of the cells, we performed numerical simulations of populations of multi-compartment neuron models (Lindén et al., 2011) using digital reconstructions of V1 neurons from (Mainen and Sejnowski (1996)). We set up populations of 10,000 neurons in disclike populations of radius 1 mm (i.e., same scenario as in the model example above in Fig. 4) where correlations in the synaptic input could be systematically varied. This was done using a common pool of uncorrelated presynaptic spike trains with size N from which each neuron received n_{syn} spike trains. This generated a mean pair-wise correlation between the synaptic input to different cells of $c_\xi = n_{syn}/N$ (for details see Lindén et al. 2011). The resulting LFP was calculated using the line-source formalism (Holt and Koch, 1999; Lindén et al., 2014) for each cell separately, and the population LFP was then computed as a sum over contributions from cells within a specific radius R.

In Fig. 4a, b the results of such a simulation is shown for a population of pyramidal neurons activated by synapses distributed over the basal dendrites, for different levels of input correlation (indicated by line type). As predicted by the simplified model (Eq. 6), we see that the amplitude $\sigma(R)$ and the resulting LFP reach R^* are drastically changed by the correlation level. For this example, a change

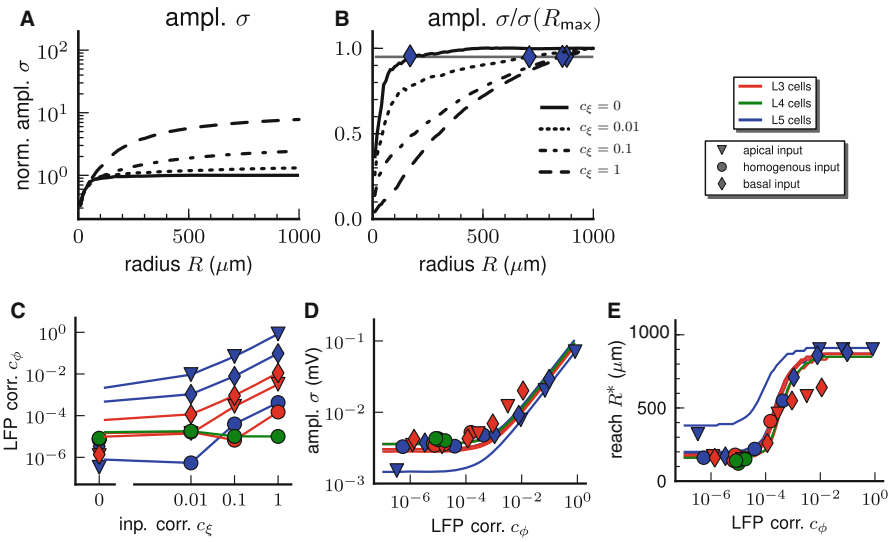

Fig. 4 Simulations of populations of multi-compartment neuron models. Results from the simplified model in Eq. 6 are compared with detailed numerical simulations of the LFP. Populations of 10,000 neurons were distributed in a disclike population with radius 1 mm^2 (layer 3 pyramidal neurons [red], layer 5 pyramidal neurons [blue], and layer 4 stellate neurons [green]). Neurons were synaptically activated using presynaptic spike trains from a common pool, and the degree of input correlation was varied by varying the pool size. The resulting LFP was computed using the line-source formalism (Holt and Koch, 1999). For details of the simulations we refer to Lindén et al. (2011). (**a**) LFP amplitude $\sigma(R)$ as a function of population radius R for a population of basally activated layer 5 pyramidal neurons. Line styles indicate the level of correlation between the incoming spike trains to different neurons (see inset in (**b**)). (**b**) Same as in (**a**), but normalized against the maximum value $\sigma(R = 1000\,\mu\text{m})$. (**c**) Resulting correlation c_ϕ between LFP contributions from different neurons in the population as a function of correlation c_ξ in incoming spike trains. Cell type and synaptic input region indicated by color and symbol (see inset). Lines show linear interpolation between numerical values (**d**) LFP amplitude $\sigma(R = 1000\,\mu\text{m})$ as a function of LFP correlation c_ϕ. (**e**) LFP reach R^* as a function of LFP correlation c_ϕ. In (**d**) and (**e**) lines show predictions from the simplified model (Eq. 6) using a numerically derived shape function $F(r)$ (as in Fig. 2) and symbols show numerical results for the LFP from population simulations. (Adapted with permission from Lindén et al. 2011)

between uncorrelation synaptic input $c_\xi = 0$ and fully correlated synaptic input $c_\xi = 1$ results in a change in spatial reach R^* of the LFP from small ($\sim$150 μm) to large ($\sim$800 μm) (Fig. 4b) accompanied by a tenfold increase in amplitude (Fig. 4a). For this example a correlation in synaptic input c_ξ in the range of [0,1] translates into a correlation between LFP contributions from different cells c_ϕ in the approximate range of [10^{-6},10^{-1}] (Fig. 4c). According to the simplified model (Fig. 3f), this range covers the whole range of values in which the LFP reach is markedly affected by the correlations. For asymmetric input onto large extended dendrites like in this example, the simplified model thus correctly predicts that a change in correlation due to changing network state as a result of, e.g., external activation would increase

the spatial reach of the LFP from very local (for uncorrelated activity) to very large, essentially capturing the whole neuronal population (for correlated synaptic input to all neurons).

To test how general the above findings are, we also performed population simulations of other synaptic input regions (homogeneously distributed or only onto apical dendrites) and other cell types (smaller layer 3 pyramidal neurons and more symmetrical layer 4 stellate neurons) (Lindén et al., 2011). We found that the same range of synaptic correlations c_ξ resulted in very different ranges of LFP contribution correlations c_ϕ (Fig. 4c). For homogeneously distributed synaptic input onto asymmetric dendrites, the induced LFP correlations c_ϕ were smaller than for asymmetric input (to either basal or apical dendrites, see symbols in Fig. 4c), and for symmetric neurons, a change in the synaptic correlations did not substantially change the resulting LFP correlation (Fig. 4c, green). As a consequence, the same level of synaptic correlation will result in very different LFP amplitude $\sigma(R = 1000\,\mu\text{m})$ (Fig. 4d) and LFP reach (Fig. 4e) for different cell types and spatial distribution of synapses. The simplified model can notably capture this effect when the resulting LFP correlation is extracted from the numerical simulation and used with Eq. 6 (see lines in Fig. 4d, e). Note, however, that the model predictions differ slightly between simulations since we here used a shape function extracted from numerical simulations (as in Fig. 2) rather than a common simplified shape function given by Eq. 1.

Frequency Dependence of LFP Power and Reach

The investigation of LFPs is often focused on specific frequency bands. Research on hippocampal LFP, for example, often focuses on extracellular potentials in the theta band (~5–10 Hz; for a review, see Buzsáki 2002), gamma band (~30–100 Hz; e.g., Bragin et al. 1995), or even higher frequencies characteristic of "ripples" (~100–200 Hz; see Maier et al. 2011 and references therein), as well as interactions between these components (cross-frequency coupling; see, e.g., Belluscio et al. 2012). In the neocortex, the tuning properties (Liu and Newsome, 2006; Berens et al., 2008) and information contents (Belitski et al., 2008; Mazzoni et al., 2011) of the LFP are frequency-dependent. To understand the biophysical origin of LFP components at different frequencies and to correctly interpret experimental findings, it is essential to know which neuron populations contribute to the different frequency modes picked up at the recording electrode or, in other words, what the spatial reach of these different LFP components is. In Łęski et al. (2013), we approached this problem by means of a simplified mathematical model (see section "Frequency-Dependent Formulation of the Simplified Model") combined with simulations of multi-compartment neurons with realistic morphologies. Here, we will briefly summarize the main results of this study.

The simplified model outlined in section "Derivation of the Simplified Model" highlights three key factors dominating the power and reach of the compound LFP:

(1) the single-cell shape function $F(r)$, (2) the population geometry captured by the number of cells (LFP sources) $N(r)$ at distance r from the recording electrode, and (3) the coherence (correlation) c_ϕ between the LFP contributions of different cells. In general, the factors (1) and (3) depend on the frequency f, i.e., $F(r) = F(f, r)$ and $c_\phi = c_\phi(f)$.

We have previously observed (Pettersen and Einevoll, 2008; Lindén et al., 2010) that intrinsic dendritic filtering leads to low-pass filtering of the LFP. In effect, the single-cell shape functions are different for different frequency bands of the LFP. As shown in Łęski et al. (2013), this can be modeled by replacing the frequency-independent function $F(r)$ in Eq. (1) with its frequency-resolved counterpart $F(f, r)$, where the dependence on the frequency is fully captured by a frequency-dependent cutoff distance $r_x(f)$ (see Fig. 2c and section "Frequency-Dependent Formulation of the Simplified Model"). The decrease of $r_x(f)$ with frequency f (Fig. 5a) is observed across a range of different cell morphologies and synaptic input distributions (see Fig. 4 in Łęski et al. 2013). It can be understood as a reduction of the dendritic electrotonic length constant with increasing frequency: For higher frequencies, the transition to the dipole (far-field) decay $\sim r^{-2}$ occurs at smaller distances than for the low frequencies (Pettersen et al., 2012).

The frequency dependence of the shape function $F(f, r)$ alone is not sufficient to correctly predict the compound LFP power spectrum. The additional required ingredient is the frequency dependence of the coherence $c_\phi(f)$ between individual single-cell LFP contributions. The ultimate source of correlations between single-cell LFPs (i.e., nonvanishing $c_\phi(f)$) is correlated synaptic input which may result from the dynamics of the presynaptic networks and/or overlap in presynaptic cell populations (shared-input correlations). Input correlations arising from the network dynamics are typically frequency-dependent, i.e., $c_\xi = c_\xi(f)$. Network dynamics leading to oscillations, for example, often results in an increased synaptic input coherence at the oscillation frequency (Tetzlaff et al., 2008). Shared synaptic input, on the other hand, gives rise to frequency-independent input correlations c_ξ (Tetzlaff et al., 2008).

A priori, it is not obvious how correlations $c_\xi(f)$ between synaptic inputs are transferred to correlations $c_\phi(f)$ between single-cell LFP contributions at a particular frequency f. In general, this correlation transfer is modulated by dendritic filtering and by the variability in synapse positions and cell morphologies. Even if the synaptic input currents at all synapses of two different cells are identical ($c_\xi = 1$), differences in synapse positions and cell morphologies lead to nonidentical transmembrane current distributions and, hence, different LFP contributions ($c_\phi < 1$). Similar to the procedure described in section "Simulations with Multi-compartment Neuron Models," we measured the frequency dependence of the correlation transfer $c_\xi \mapsto c_\phi(f)$ in simulations of multi-compartment neurons receiving partially shared, white synaptic input (i.e., frequency-independent c_ξ).

For pyramidal neurons, we observe that the LFP coherence $c_\phi(f)$ is largest at low frequencies and decays monotonously with increasing frequency (see example in Fig. 5b). This observation can be explained by the fact that at higher frequencies, the return currents are closer to the synapse positions, so that the effective

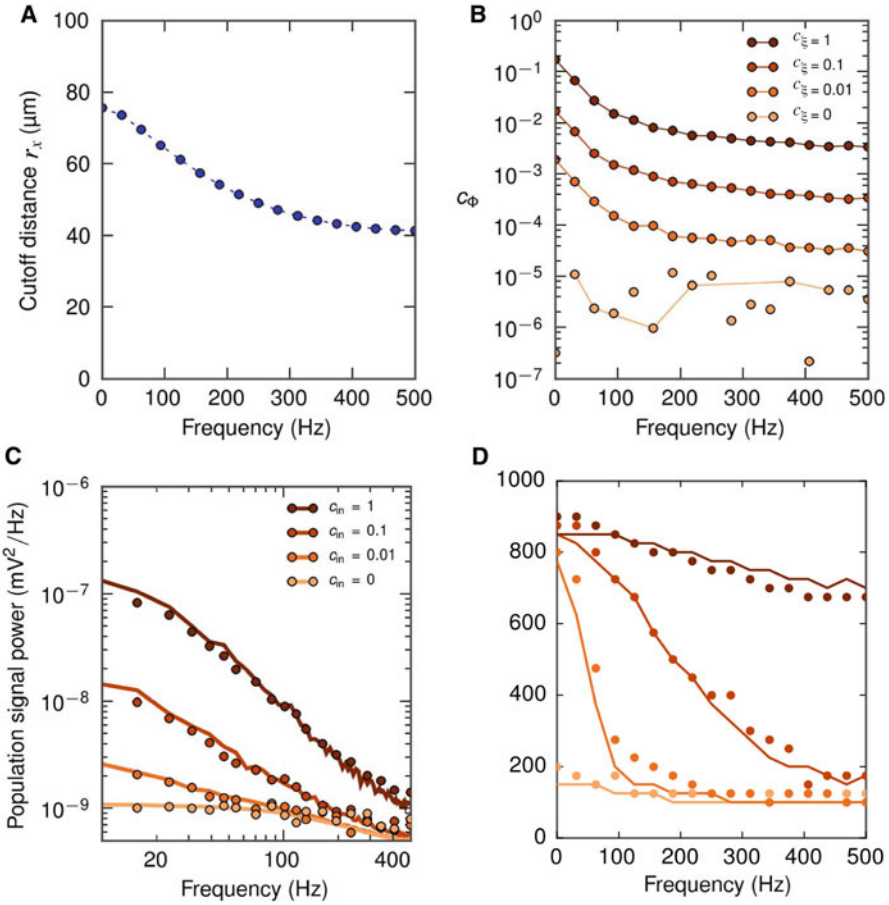

Fig. 5 Components and results of the frequency-resolved simplified model. (**a**) Frequency dependence of the cut-off distance r_x. (**b**) Frequency dependence of the population-averaged LFP coherence c_Φ for different input correlation levels c_ξ. (**c**) Power spectra of the total LFP in the center of a population of radius $R = 1000\,\mu$m. (**d**) Frequency dependence of the spatial reach. All panels show results for soma-level LFPs generated by cortical layer-5 pyramidal cells with white (frequency-independent) synaptic input to basal dendrites. Symbols in (**a**) and (**b**) depict results of multi-compartment-neuron simulations. Lines serve to guide the eye. Symbols not connected by lines indicate that the absolute value is plotted in place of spurious negative values. Lines and symbols in (**c**) and (**d**) show results of the simplified model (see section "Frequency-Dependent Formulation of the Simplified Model") and simulations for populations of multi-compartment neurons, respectively. (Adapted from Łęski et al. 2013)

current dipoles become shorter. For pyramidal neurons, the variability in dendrite orientation is largest at small spatial scales (e.g., within the basal bush). Hence, the high-frequency LFP components of individual neurons are decorrelated. At low frequencies, in contrast, the effective dipoles generated by synaptic input to pyramidal cells become larger and more aligned (parallel to the main cell axis).

For pyramidal cells, synaptic input correlations c_ξ are therefore more robustly transferred to LFP correlations c_ϕ at low frequencies than at high frequencies. For more symmetric stellate cells, the LFP correlations are typically much smaller (see Fig. 4c, green curve) and frequency-independent (Łęski et al., 2013).

Combining the frequency-dependent shape functions $F(f, r)$ and the LFP coherence $c_\phi(f)$ in the simplified model, Eq. (9) yields predictions for the power spectrum of the compound LFP (Fig. 5c) and the frequency dependence of the spatial reach (Fig. 5d). A comparison of the simplified-model predictions with the results of simulations of multi-compartment-neuron populations shows qualitative agreement for all investigated cell types and synapse distributions. In many cases, the predictions of the simplified model match the results of the simulations with multi-compartment models even quantitatively (compare dots and curves in Fig. 5c, d).

For pyramidal neurons, non-zero (frequency-independent) synaptic input correlations $c_\xi > 0$ can lead to a substantial amplification of the compound LFP power, in particular at low frequencies (Fig. 5c). The amplification of power at low frequencies results in a faster decay of the power spectrum. Note that this observation is compatible with findings showing larger EEG decay exponents during sleep as compared to awake states (Bédard et al., 2006). For vanishing input correlation $c_\xi = 0$, the frequency dependence of the reach is solely due to the frequency dependence of the cutoff distance $r_x(f)$. As a result, the frequency dependence of the reach is weak (Fig. 5d).

For nonvanishing input correlations $c_\xi > 0$, the compound LFP power and, hence, the LFP reach are more and more dominated by the frequency dependence of the LFP coherence $c_\phi(f)$. In the presence of intermediate input correlations $0 < c_\xi < 1$, the reach can exhibit a strong frequency dependence. For the example shown in Fig. 5d with $c_\xi = 0.01$, the reach can be as large as 800 μm at ∼0 Hz and drop to about 200 μm for frequencies above 100 Hz. For sufficiently large input correlations c_ξ, even the high-frequency LFP correlations c_ϕ become substantial (Fig. 5b). In consequence, the reach is close to the maximum population radius for all frequencies (cf. $c_\xi = 1$ in Fig. 5d).

Note that the results shown here were obtained for white synaptic input and frequency-independent (shared) input correlations c_ξ. In addition to the effects described here, the power and reach of the LFP at a particular frequency f are determined by the spectral properties of the synaptic input (e.g., resulting from the dynamics of presynaptic networks), in particular by the frequency dependence of $c_\xi(f)$. In general, our results suggest that the LFP power and reach are dominated by coherent frequency components. Due to the low-pass characteristics of the correlation transfer depicted in Fig. 5b, however, input components with non-zero coherence $c_\xi(f_1) = c^* > 0$ at some frequency f_1 will dominate components with the same level of coherence $c_\xi(f_2) = c^*$ at a higher frequency $f_2 > f_1$. Theta oscillations in the synaptic input, for example, would give rise to a larger LFP reach than gamma oscillations, even if the gamma coherence is as large as the coherence in the theta band.

Spatial Decay Outside the Neuronal Population

All the results shown so far have been for the situation where the LFP electrode is placed in the center of the neuronal population generating the LFP. Our simplified analytical formulas can, however, be extended to cover scenarios where the electrode is not in the center but some distance X away from the center position (see Eqs. 12 and 13). While we now return to the frequency-independent case and describe the total LFP amplitude σ as a sum over all frequencies, it should be noted that the spatial decay outside the population can in a similar manner as in Fig. 5 also be studied for different frequency components separately (for details and numerical results on this, we refer to Łęski et al. 2013).

In Fig. 6a we show how the LFP amplitude decays as a function of distance X for three different population sizes. For the case of *uncorrelated* LFP contributions, Eq. 6 gives that $\sigma(R, X) = \sqrt{G_0(R, X)}$ (solid lines), while the LFP from *completely correlated* LFP sources is given by $\sigma(R, X) = \sqrt{G_1(R, X)}$ (dotted lines).

For uncorrelated LFP sources, we see that there is a steep decay in LFP amplitude around the edge of the population. For all three population sizes plotted, the amplitude starts to decay around 200 μm from the edge of the population and has decreased to a fraction of ∼0.7 of the amplitude in the center of the population (Fig. 6a, solid lines) at the population boundary. When the electrode is moved away beyond the population boundary, the LFP amplitude decays quickly and has for all three population sizes decreased by a factor ten compared to the center amplitude within 250 μm from the population edge. Relative to the population radius, the spatial decay is however more steep for larger populations than for smaller ones, as seen in Fig. 6b.

For correlated LFP sources (Fig. 6a, b, dotted lines), the spatial falloff is less abrupt than for uncorrelated sources. In this case the LFP amplitude starts to decay considerably already for off-center positions close to the population center. Outside the population, the LFP extends further beyond the population edge than for uncorrelated activity (compared dotted and solid lines in Fig. 6a). This effect is more pronounced for larger populations than for smaller ones: while the amplitude decay for uncorrelated compared to correlated sources is very similar for a small population ($R = 250$ μm, Fig. 6a, black lines) outside the population, we see that the distance at which the amplitude has dropped to a fraction 0.1 of the center amplitude is increased for a population with radius $R = 1000$ μm to about 500 μm from the population boundary (Fig. 6a, green lines).

The simplified model formulated for off-center electrode positions (Eqs. 12 and 13) also allows us to examine how much crosstalk one would expect between neighboring populations, i.e., to which extent the LFP recorded in the center of one population would also contain contributions (or noise) from other neighboring neuronal populations. In Fig. 6c we show an example of such a situation with two neighboring populations with radius $R = 250$ μm that are positioned right next to each other. We assume that the two populations are uncorrelated with each other and

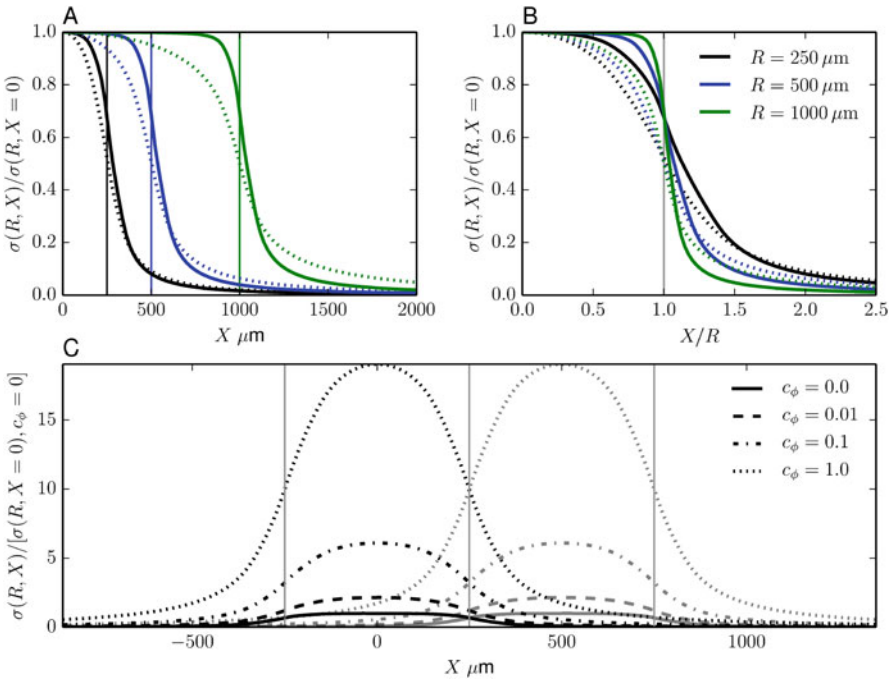

Fig. 6 Predictions for spatial decay outside the neuronal population. LFP amplitude $\sigma(R, X)$ at a distance X from the center of a population with radius R calculated from Eq. 6 using numerical integration of Eqs.12 and 13 with single-cell shape function $F(r)$ as defined in Eq. 1 for parameters $\rho = 10{,}000$ neurons/mm^2, $r_\epsilon = 10\,\mu$m, $r_x = 100\,\mu$m and $F_0 = 1$. (**a**) LFP amplitude $\sigma(R, X)$ for three different population sizes $R = [250{,}500{,}1000]\,\mu$m (indicated by color) for uncorrelated (solid lines) and correlated (dotted lines) LFP contributions. Curves have been normalized to the amplitude at the center of the population $\sigma(R, X = 0)$. (**b**) Same as in A with x-axis normalized by the population size R. (**c**) LFP amplitudes for two neighboring populations with radius $R = 250\,\mu$m centered at $X = 0$ and $X = 500\,\mu$m, respectively, for different levels of correlation c_ϕ (indicated by line style). Curves have been normalized to the LFP amplitude in the center of the population for uncorrelated LFP sources ($c_\phi = 0$). In all plots thin vertical lines represent the edge of the population

plot the LFP from each population separately. We see that the level of correlation between LFP sources in one population has a large effect on the overall amplitude of the LFP from that population as we would expect from our previous results on the LFP in the center of the population (see, e.g., Eq. 6 and Fig. 3e). This, however, also means that if the LFP sources within one population have a high degree of correlation, there is a large "spillover" to the neighboring population. In the example in Fig. 6c, we note that if we have one LFP electrode in the center of each population, the LFP generated by the *other* population may actually be larger than that from the local population, if the neighboring population is correlated, while the local population is uncorrelated. This, however, assumes that the overall activity in both populations is the same and that nothing else differs than the level of correlation

between LFP contributions within the populations. Since the overall LFP amplitude depends on several factors, such as synaptic strengths and activation rates, as well as synaptic placement (Lindén et al., 2011), a proper assessment of crosstalk would require a more detailed analysis. This is beyond the scope of this chapter, however.

Model Justification

Data for Model Components and Parameter Values

The simplified LFP model presented in this chapter is valid for a range of parameter values which are explicitly stated in the model formulation and does therefore not rely on specific choices of parameters. The model formulation was, however, made using a number of assumptions which we will list and discuss below.

Population geometry The presented formulation of the simplified model assumes a cylinder-like population geometry which seems like a good first approximation for several brain regions with a prominent layer structure as found both in the hippocampus and cortex. If the spatial reach is large enough, as the model predicts for a large area with correlated LFP sources, this assumed population geometry may be oversimplified. In the dentate gyrus, for example, the macroscopic curvature of the brain tissue creates large LFPs that are even larger *outside* the synaptically activated region that generates it (Fernandez-Ruiz et al., 2013). To model such brain regions, one would have to extend the model using a more realistic geometry (see below).

Spatially homogeneous LFP correlations When deriving the simplified model, we assumed that the LFP contribution from each cell can be decomposed into a temporal and spatial part (Eq. 2). As a consequence, the correlation between the LFP contributions from cells will be independent of the distance to the recording electrode, and we could therefore use a single parameter c_ϕ to represent the correlation for the entire population. Due to spatially distributed synapses and dendritic filtering (Lindén et al., 2011), we expect this assumption to not be valid under all circumstances. Indeed, when comparing with detailed population simulations, we saw some deviations that may be due to this assumption (see red markers in Fig. 4e). In the frequency-dependent model formulation (Eqs. 9, 10 and 11), we correspondingly assume the coherence to be spatially homogenous. While the model could be extended to include distant-dependent measures of correlation/coherence (see below), the simplified model performs quite well in comparison with the detailed numerical simulations also in the present form.

Definition of cells as individual LFP sources The model presented in this chapter views each cell as an individual LFP source, and the shape function $F(r)$ consequently describes the spatial decay of single-cell LFP contributions (Fig. 2). It would, however, be equally possible to formulate the model at the level of synapses,

so that the total LFP would be a sum over synaptic contributions, where different classes of synapses (based on, e.g., their spatial positioning on the dendrites) could be assigned different shape functions.

LFP calculations The LFP calculations in the detailed simulations were made assuming a linear, isotropic, homogenous, and ohmic extracellular medium which seems to be well-fulfilled for the frequencies studied here (Nunez and Srinivasan, 2006; Logothetis et al., 2007) (for further discussion, see Pettersen et al. 2012.) If warranted, however, other assumption about the extracellular medium could be accounted for in the biophysical forward-modeling scheme (Lindén et al., 2014) used to compute the shape function $F(r)$ and the LFP population correlation coefficient c_ϕ.

Passive dendritic conductances The present model assumes passive (RC) dendrites, but it can be extended to include active dendritic conductances. In particular, a recent study showed that the effect of subthreshold active conductances on the single-neuron LFP contribution, and thus the shape function $F(r)$, can be well described by means of so-called "quasi-active" linearization (Ness et al., 2015). Thus these active conductances can be included in the model without introducing any nonlinearity in the LFP generation, thus still allowing each frequency component to be treated independently in the model.

Successes and Limitations

The simplified model presented in this chapter encapsulates how the amplitude and reach of the LFP depends on three crucial factors: (1) the population geometry, (2) the spatial decay of single-neuron LFP contributions, and (3) the correlation between the LFP contributions from different cells. As the level of correlation between LFP sources depends on the state of the underlying network dynamic, our model demonstrates that the reach of the LFP is not a fixed quantity, but changes with the network state. Our model, thus, offers a putative explanation to the disparity between different experimental studies investigating the LFP reach, with estimates ranging from a few hundred micrometers (Katzner et al., 2009; Xing et al., 2009) to several millimeters (Kreiman et al., 2006).

The simplified model can straightforwardly be formulated in a frequency-specific manner that allows the investigation of different frequency bands of the LFP separately. The limited results shown here illustrate how frequency-specific spatial decay of single-cell contributions combined with frequency-specific coherence between LFP sources may lead to substantially larger spatial reach for low-frequency components of the LFP compared to higher frequencies. This directly influences the power spectrum of the LFP to have higher power at low compared to high frequencies.

The above results have focused on situations with the electrode placed in the center of the population at the depth of the somata, but the simplified model has proven equally applicable for other electrode positions; for example, see Lindén et al. (2011), and Łęski et al. (2013).

The Future

Model Extensions

The model presented in this chapter could be extended in several ways. As mentioned above a natural extension would be to adapt it for more realistic population geometries. This would be of particular interest for brain regions that have a clear macroscopic structure as, for instance, in the dentate gyrus. It has been shown by combined experimental and modeling work that for this particular system the curved shape of the cellular layers creates large amplitude LFPs that are due to the spatial summation of LFP contributions from different sites at the curved structure (Fernandez-Ruiz et al., 2013). To extend the model presented here to study such effects, one would have to replace Eq. 3 with a more appropriate expression and perform the analytical model derivation based on that. Alternatively, a numerical integration of Eqs. 4 and 5 using appropriate summation boundaries can also be done.

For some experimental setups, it may also be relevant to relax the assumption of homogeneous LFP correlations (see above) to include finer spatial structure of correlations. This could be important for capturing LFP correlations induced by spatially specific external inputs or for specific connectivity structures of the underlying neuronal circuits. This would make the integral expressions in Eqs. 4 and 5 more complicated; one can always use numerical summation of LFP sources to compute estimates of the spatial reach of the LFP.

New Uses of Model

The model presented in this chapter does not make any assumptions about the underlying neuronal network activity. In the multi-compartment simulations, we used random (Poissonian) spike trains to activate synapses and a simple common-input model to generate correlations between the input to different cells. Since LFP computed from the multi-compartment models with current-based synapses are linear with respect to the input level (see Lindén et al. 2011; Łęski et al. 2013), only the mean input correlation will affect the resulting LFP reach, while the synaptic rate will only affect the resulting LFP amplitude (through the constant F_0 in Eq. 1).

To use our model for a specific experimental setup, it would be possible to adapt our model to more closely match the hippocampal (or cortical) region of study. This could be done through the following steps:

1. By extracting the single-cell shape function $F(r)$ using reconstructed morphologies from the specific hippocampal (or cortical) area under study using a similar approach as in Fig. 2.
2. To use a more realistic model of spiking dynamics that would give a correlation structure in the synaptic inputs with, e.g., realistic oscillatory dynamics in frequency bands of interest. If these inputs then were used to activate multicompartment neuron models (similar to the setup illustrated in Fig. 4), the transfer from correlation between input spikes to correlation between LFP contributions could be estimated (as in Fig. 4c).
3. By setting the upper limit of population radius R according to known geometrical constraints in the region of study.

This could allow a detailed investigation of the LFP amplitude and the LFP reach for, e.g., theta compared to gamma oscillations.

Acknowledgements This work was done with financial support from the Danish Council for Independent Research and FP7 Marie Curie Actions – COFUND (grant id: DFF – 1330-00226), the European Union Seventh Framework Programme (FP7/2007-2013) under grant agreement 604102 (Human Brain Project, HBP) and grant agreement 269912 (BrainScaleS), the Helmholtz Association through the Helmholtz Portfolio Theme "Supercomputing and Modeling for the Human Brain" (SMHB), Jülich Aachen Research Alliance (JARA), and the Research Council of Norway (NFR, through ISP, NOTUR -NN4661K).

References

Agarwal G, Stevenson IH, Berényi A, Mizuseki K, Buzsáki G, Sommer FT (2014) Spatially distributed local fields in the hippocampus encode rat position. Science 344(6184):626–630

Bédard C, Kröger H, Destexhe A (2006) Does the $1/f$ frequency scaling of brain signals reflect self-organized critical states? Phys Rev Lett 97:118102

Belitski A, Gretton A, Magri C, Murayama Y, Montemurro MA, Logothetis NK, Panzeri S (2008) Low-frequency local field potentials and spikes in primary visual cortex convey independent visual information. J Neurosci 28(22):5696–5709

Belluscio MA, Mizuseki K, Schmidt R, Kempter R, Buzsáki G (2012) Cross-frequency phase-phase coupling between theta and gamma oscillations in the hippocampus. J Neurosci 32(2):423–435

Berens P, Keliris GA, Ecker AS, Logothetis NK, Tolias AS (2008) Comparing the feature selectivity of the gamma-band of the local field potential and the underlying spiking activity in primate visual cortex. Front Syst Neurosci 2:2

Bragin A, Jando G, Nadasdy Z, Hetke J, Wise K, Buzsáki G (1995) Gamma (40–100 Hz) oscillation in the hippocampus of the behaving rat. J Neurosci 15(1):47–60

Brankack J, Stewart M, Fox SE (1993) Current source density analysis of the hippocampal theta rhythm: associated sustained potentials and candidate synaptic generators. Brain Res 615: 310–327

Buzsáki G (2002) Theta oscillations in the hippocampus. Neuron 33(3):325–340

Buzsáki G (2004) Large-scale recording of neuronal ensembles. Nat Neurosci 7(5):446–451
Buzsáki G, Anastassiou C, Koch C (2012) The origin of extracellular fields and currents–EEG, ECoG, LFP and spikes. Nat Rev Neurosci 13:407–420
Einevoll GT, Lindén H, Tetzlaff T, Łęski S, Pettersen KH (2013a) Local field potentials: biophysical origin and analysis. In: Quiroga QR, Panzeri S (eds) Principles of neural coding. Taylor & Francis, CRC Press, Boca Raton
Einevoll GT, Kayser C, Logothetis N, Panzeri, S (2013b) Modelling and analysis of local field potentials for studying the function of cortical circuits. Nat Rev Neurosci 14:770–785
Fernandez-Ruiz A, Muñoz S, Sancho M, Makarova J, Makarov VA, Herreras O (2013) Cytoarchitectonic and dynamic origins of giant positive local field potentials in the dentate gyrus. J Neurosci 33(39):15518–15532
Herreras O, Makarova J, Makarov VA (2015) New uses of LFPs: pathway-specific threads obtained through spatial discrimination. Neuroscience 310:486–503
Holt GR, Koch C (1999) Electrical interactions via the extracellular potential near cell bodies. J Comp Neurol 6(2):169–184
Kajikawa Y, Schroeder CE (2011) How local is the local field potential? Neuron 72:847–858
Katzner S, Nauhaus I, Benucci A, Bonin V, Ringach DL, Carandini M (2009) Local origin of field potentials in visual cortex. Neuron 61:35–41
Kreiman G, Hung CP, Kraskov A, Quiroga RQ, Poggio T, DiCarlo JJ (2006). Object selectivity of local field potentials and spikes in the macaque inferior temporal cortex. Neuron 49:433–445
Łęski S, Lindén H, Pettersen KH, Einevoll GT (2013) Frequency dependence of signal power and spatial reach of the local field potential. PLoS Comput Biol 9(7):e1003137
Lindén H, Pettersen KH, Einevoll GT (2010). Intrinsic dendritic filtering gives low-pass power spectra of local field potentials. J Comp Neurol 29(3):423–444
Lindén H, Tetzlaff T, Potjans TC, Pettersen KH, Grün S, Diesmann M, Einevoll GT (2011) Modeling the spatial reach of the LFP. Neuron 72:859–872
Lindén H, Hagen E, Łęski S, Norheim ES, Pettersen KH, Einevoll GT (2014) LFPy: a tool for biophysical simulation of extracellular potentials generated by detailed model neurons. Front Neuroinform 7:41
Liu J, Newsome WT (2006) Local field potential in cortical area MT: stimulus tuning and behavioral correlations. J Neurosci 26(30):7779–7790
Logothetis NK, Kayser C, Oeltermann A (2007) In vivo measurement of cortical impedance spectrum in monkeys: implications for signal propagation. Neuron 55:809–823
Maier N, Tejero-Cantero A, Dorrn AL, Winterer J, Beed PS, Morris G, Kempter R, Poulet JF, Leibold C, Schmitz D (2011) Coherent phasic excitation during hippocampal ripples. Neuron 72:137–152
Mainen ZF, Sejnowski TJ (1996) Influence of dendritic structure on firing pattern in model neocortical neurons. Nature 382(6589):363–366
Mazzoni A, Brunel N, Cavallari S, Logothetis NK, Panzeri S (2011) Cortical dynamics during naturalistic sensory stimulations: experiments and models. J Physiol Paris 105(1–3):2–15
Mitzdorf U (1985) Current source-density method and application in cat cerebral cortex: investigation of evoked potentials and EEG phenomena. Physiol Rev 65(1):37–100
Ness TV, Remme MWH, Einevoll GT (2015) Active subthreshold dendritic conductances shape the local field potential. arXiv 1512.04293
Nunez PL, Srinivasan R (2006) Electric fields of the brain, 2nd edn. Oxford University Press, Inc., New York
Pettersen KH, Einevoll GT (2008) Amplitude variability and extracellular low-pass filtering of neuronal spikes. Biophys J 94(3):784–802
Pettersen KH, Lindén H, Dale AM, Einevoll GT (2012) Extracellular spikes and current-source density. In Brette R, Destexhe A (eds) Handbook of neural activity measurement. Cambridge University Press, Cambridge
Schomburg EW, Anastassiou CA, Buzsáki G, Koch C (2012) The spiking component of oscillatory extracellular potentials in the rat hippocampus. J Neurosci 32:11798–11811

Siapas AG, Wilson MA (1998) Coordinated interactions between hippocampal ripples and cortical spindles during slow-wave sleep. Neuron 21:1123–1112

Sirota A, Csicsvari J, Buhl D, Buzsáki G (2003) Communication between neocortex and hippocampus during sleep in rodents. Proc Natl Acad Sci USA 100:2065–2069

Taxidis J, Anastassiou CA, Diba K, Koch C (2015) Local field potentials encode place cell ensemble activation during hippocampal sharp wave ripples. Neuron 87(3):590–604

Tetzlaff T, Rotter S, Stark E, Abeles M, Aertsen A, Diesmann M (2008) Dependence of neuronal correlations on filter characteristics and marginal spike-train statistics. Neural Comput 20(9):2133–2184

Xing D, Yeh C-I, Shapley RM (2009) Spatial spread of the local field potential and its laminar variation in visual cortex. J Neurosci 29:11540–11549

Ylinen A, Bragin A, Nádasdy Z, Jandó G, Szabó I, Sik A, Buzsáki G (1995) Sharp wave-associated high-frequency oscillation (200 Hz) in the intact hippocampus: network and intracellular mechanisms. J Neurosci 15:30–46

Models of Rate and Phase Coding of Place Cells in Hippocampal Microcircuits

Vassilis Cutsuridis

Overview

Place cells are neurons that fire when the animal occupies a specific location within its environment (O'Keefe and Nadel 1978). As different place cells have different place fields (locations where they fire), they are thought to provide a cognitive map for the rat. Furthermore, place cells are speed-dependent oscillators, as their oscillation frequency is determined by the animal's traveling speed (Buzsaki 2011). Their firing rates and phases also change with respect to LFP theta (O'Keefe and Recce 1993; Johnson and Redish 2007; Skaggs et al. 1996; Wilson and McNaughton 1993). Theta oscillations (4–10 Hz) are observed during animal exploration and rapid eye movement sleep (Buzsaki 2002). During exploration (Fig. 1 top) hippocampal place cells' firing rate increases as the position of the rat in the place field increases, reaching a maximal value just after the middle of the place field and beyond this point it decreases again (Fig. 1 medium; Harris et al. 2002; Mehta et al. 2002). Place cells have also been shown to systematically shift their phase of firing to earlier phases of the theta rhythm as the animal transverses the place field (a phenomenon known as theta phase precession) (Fig. 1 bottom; O'Keefe and Recce 1993; Skaggs et al. 1996).

The goal of this chapter is to present computer models of place cell rate and phase coding in hippocampal microcircuits in order to explore the mechanisms by which both coding schemes are generated and/or maintained in these microcircuits. Of crucial importance is how theta-modulated inhibition interacts with synaptic plasticity in order to preserve the rate and phase coding properties of place cells in the CA1 microcircuits.

V. Cutsuridis (✉)
School of Computer Science, University of Lincoln, Lincoln, UK
e-mail: vcutsuridis@lincoln.ac.uk

V. Cutsuridis et al. (eds.), *Hippocampal Microcircuits*, Springer Series in Computational Neuroscience, https://doi.org/10.1007/978-3-319-99103-0_14

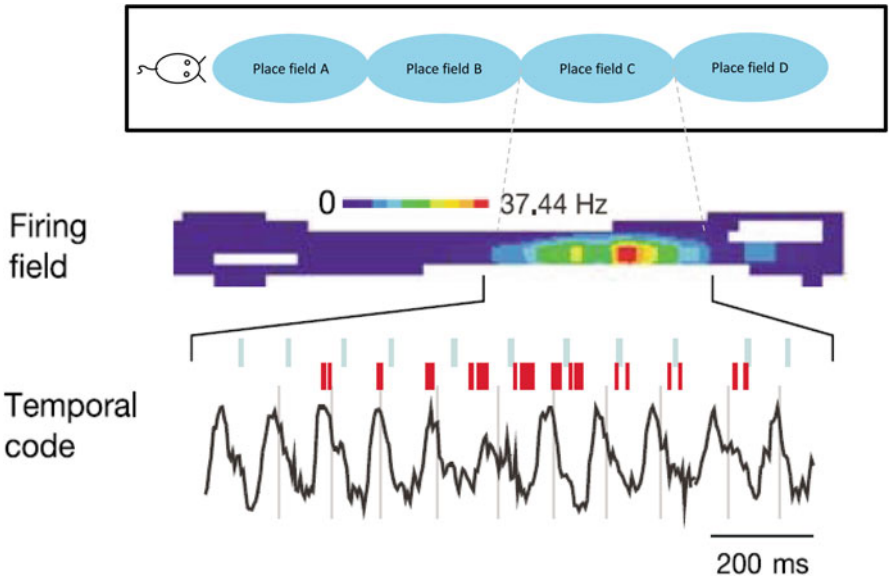

Fig. 1 (*Top*) A rat running along a linear track. Light blue filled ellipses represent the place fields of four pyramidal cells (place cells) in the network. Note their fields are nonoverlapping. The time the rat spends in each place field is equal to nine theta cycles, with each theta cycle lasting 250 ms, a total time of 2250 ms. (*Medium*) Firing rate of a place cell inside its place field (Skaggs et al. 1996; O'Keefe and Recce 1993). Firing rate is low in the beginning of the field, maximum just after the middle of the field and low in the end. (*Bottom*) Theta phase precession of a place cell's firing as the rat transverses the place field. As the rat transverses the place field, each place cell shifts its firing to earlier phases of the theta rhythm. (Skaggs et al. 1996; O'Keefe and Recce 1993)

The Model

A canonical CA1 microcircuit model (Cutsuridis and Hasselmo 2012) consisting of just four pyramidal cells (place cells) and six types of inhibitory interneurons: a BC, an AAC, a BSC, four IVYs, four NGLs and an OLM cell is presented (see Fig. 2). Hodgkin-Huxley mathematical formalism was used to describe the ionic and synaptic mechanisms of all cells (see APPENDIX).

Pyramidal Cells Each PC consisted of four compartments: an axon, a soma, a proximal dendrite and a distal dendrite. Active properties included a fast Na^+ current, a delayed K^+ rectifier current, a low-voltage-activated (LVA) L-type Ca^{2+} current, an A-type K^+ current, an h-current and a calcium-activated mAHP K^+ current (see the appendix for mathematical details of these currents). The conductance of the h-current was set to 0.005 mS/cm^2 at the soma, 0.01 mS/cm^2 at the proximal dendrite and 0.02 mS/cm^2 at the distal dendrite. No recurrent connections were assumed between PCs in the network.

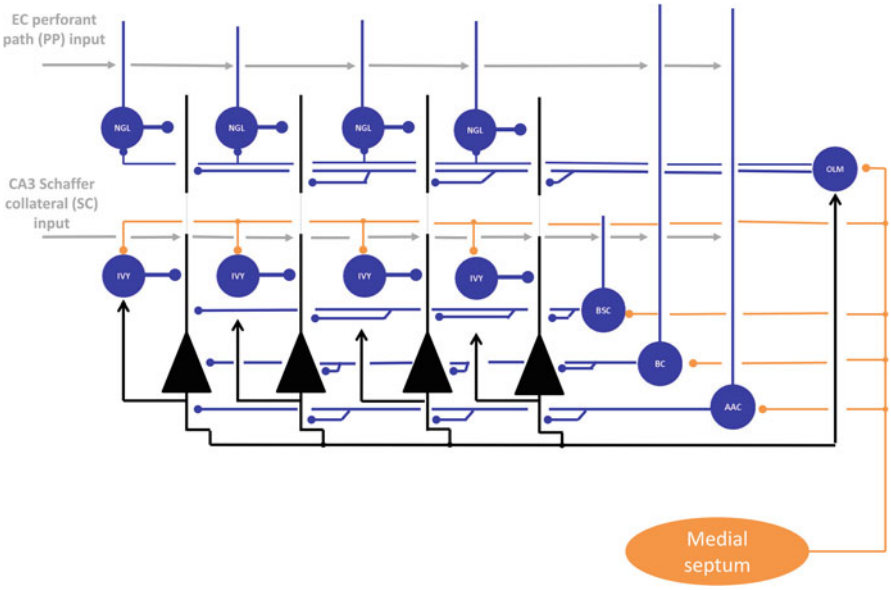

Fig. 2 Hippocampal CA1 microcircuit showing major cell types and their connectivity. Grey arrow lines: excitatory input connections. Black arrow lines: excitatory PC feedback connections. Blue filled circles: CA1 inhibitory connections. Orange filled circles: medial septal inhibitory connections. EC: entorhinal layer III perforant path (PP) input. SC: CA3 Schaffer collateral input. *AAC* axo-axonic cell; *BC* basket cell; *BSC* bistratified cell; *NGL* neurogliaform cell; *IVY* ivy cell; *OLM* oriens lacunosum-moleculare cell

Each PC received AMPA and NMDA excitation from the CA3 Schaffer collaterals and entorhinal cortex (EC) in their proximal and distal dendrites, respectively, and $GABA_A$ synaptic inhibition from BC cells to the soma, from AAC cells to the axon, from BSC and IVY cells to the proximal dendrite and from NGL and OLM cells to the distal dendrite.

Inhibitory Interneurons All inhibitory interneurons (INs) consisted of a single compartment (soma). Active properties of BC, AAC, BSC and IVY included a fast Na^+, a delayed rectifier K^+, a leakage and a type A K^+ currents (Cutsuridis et al. 2010; Cutsuridis and Hasselmo 2010). Active properties of the OLM cell included a fast Na^+ current, a delayed rectifier K^+ current, a persistent Na^+ current, a leakage current and an h-current (Cutsuridis and Hasselmo 2010; Kunec et al. 2005), whereas those of the NGL cell included a fast Na^+ current, a delayed rectifier K^+ current and a leakage current (see the appendix for mathematical details of these currents).

AAC and BC received excitatory inputs from the EC perforant path and the CA3 Schaffer collaterals and inhibition from the medial septum (MS). The BC received additional inhibition from the BSC. The BSC was excited by the CA3 Schaffer collateral input only, inhibited by the MS and the BC. Each IVY cell in the network

was recurrently excited by its companion PC. NGL cells were excited by the EC input only and inhibited by the OLM cell (Capogna 2011). The OLM cell received recurrent excitation from all PCs and feedforward inhibition from the MS.

Model Inputs The dynamics of the network were influenced by a number of external inputs. Excitatory inputs (spikes) to network cells originated from the EC and the CA3 Schaffer collaterals, whereas external inhibitory input originated from the MS. The EC input excited the distal dendrites of the PCs, whereas the CA3 input excited the proximal dendrites.

Each pyramidal cell in the network received a different set of EC and CA3 inputs (PC_1 was excited by EC_1 and $CA3_1$, PC_2 by EC_2 and $CA3_2$, PC_3 by EC_3 and $CA3_3$ and PC_4 by EC_4 and $CA3_4$). The proper order by which the EC and CA3 inputs were presented to each PC (EC_1 and $CA3_1$ first, followed by EC_2 and $CA3_2$, then by EC_3 and $CA3_3$ and finally by EC_4 and CA_4) was ensured (gated) by dopamine in the LM layer (see "Dopamine Modulation" section for details). The duration of each set of EC and CA3 inputs is 2250 ms, which corresponded to nine theta cycles, each theta cycle with duration of 250 ms. This was designed to match the average number of theta cycles within a place field reported in Maurer and McNaughton (2007). The presentation frequencies of the EC and CA3 inputs are set to 100 Hz (interspike interval (ISI) = 10 ms) and 50 Hz (ISI = 20 ms), respectively (Colgin et al. 2009).

Inhibitory MS inputs (spikes) were theta modulated. One MS input was tuned to near the peak of the extracellular theta (MS_{180}) (Borhegyi et al. 2004), whereas the other one to its trough (MS_{360}) (Dragoi et al. 1999). All network inhibitory interneurons except for the IVY and NGL cells were inhibited by the MS inputs (Borhegyi et al. 2004).

Presynaptic $GABA_B$ Inhibition A presynaptic $GABA_B$ inhibition that cyclically changed with respect to the external theta rhythm (Molyneaux and Hasselmo 2002) modulated the strength of Schaffer collateral input to the PC proximal synapses. This $GABA_B$ modulation was modelled with a 50% decrease in the CA3 input strength during the peak phase of each theta cycle and a return to its full strength during the trough phase of each theta cycle (Cutsuridis et al. 2010).

Synaptic Plasticity A mechanism for STDP in each PC dendrite was used to model plasticity effects. The mechanism had a modular structure consisting of three biochemical detectors: a potentiation (*P*) detector, a depression (*D*) detector and a veto (*V*) detector (Rubin et al. 2005). Each detector responded to the instantaneous calcium level and its time course in the dendrite. The potentiation (*P*) detector triggered LTP every time the calcium levels were above a high threshold (4 μM). The depression (*D*) detector detected calcium levels exceeding a low threshold level (0.6 μM). When the calcium levels remained above this threshold for a minimum time period, LTD was triggered. The veto (*V*) detector detected levels exceeding a mid-level threshold (2 μM) and triggered a veto to the *D* response. *P* and *D* compete to influence the plasticity variable W (see Eq. 48), which serves as a measure of the sign and magnitude of synaptic strength changes from the baseline.

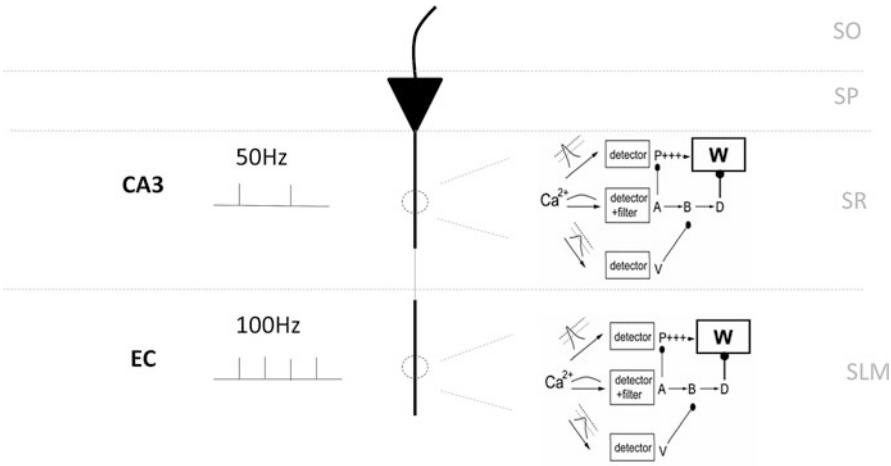

Fig. 3 Pyramidal (place) cell model with calcium detectors in distal and proximal dendrites. Synaptic plasticity at the dendritic synapses (circled regions) is governed by two model calcium detector systems. *P* potentiation detector, *A, B* intermediate elements, *D* depression detector activated by *B* and vetoed by *V*, *V* veto detector, *W* synaptic weight. *P* and *D* compete to influence the plasticity variable *W*, which serves as a measure of the sign and magnitude of synaptic strength changes from the baseline

Calcium entered the neuron through (1) voltage-gated calcium channels (VGCCs) and (2) NMDA channels located at each dendrite. Plasticity resulted from the synergistic action of these two calcium sources (NMDA and VGCC). A graphical schematic of the model pyramidal cell and its calcium detectors for STDP is shown in Fig. 3.

During the peak phases of theta, the AMPA and NMDA synaptic conductances in the proximal dendrite of the PCs were modelled as

$$g_{\text{syn}} = (w_{\text{s}} \cdot w + W) \cdot g_{\text{max}} \tag{1}$$

where w_{s} is the scaling factor (set to 0.5 for the present simulations) due to presynaptic $GABA_B$ inhibition, w is synaptic strength and W is given by Eq. (48). During the trough phases of theta, the $GABA_B$ inhibition was removed (i.e. $w_{\text{s}} = 1$), and the proximal AMPA and NMDA conductances were described as

$$g_{\text{syn}} = (w + W) \cdot g_{\text{max}} \tag{2}$$

During theta the AMPA and NMDA synaptic conductances in the distal dendrites of the pyramidal cells were described by

$$g_{\text{syn}} = (w + W) \cdot g_{\text{max}} \tag{3}$$

Dopamine Modulation In hippocampal microcircuits the primary targets of dopamine (DA) are the subiculum and region CA1 (Gasbarri et al. 1997). In CA1, the distal and proximal dendrites of pyramidal neurons are both targeted by the DAergic neurons (Cobb and Lawrence 2010). Previous studies have shown that when DA is applied to the bathing solution, the field EPSP (fEPSP) evoked by the EC temporoammonic (TA) pathway stimulation is depressed, whereas the fEPSP by the CA3 Schaffer collateral (SC) pathway stimulation remains unaltered (Otmakhova and Lisman 1999). Subsequent studies by Ito and Schuman (2007) demonstrated that DA acts as a gate on the direct cortical input to the CA1 PC distal dendrites, modulating the information flow and the synaptic plasticity in a frequency-dependent manner. During low-frequency stimulation, DA depresses the excitatory TA inputs to both CA1 pyramidal cells and NGL interneurons via presynaptic inhibition, whereas during high-frequency stimulation, DA potently facilitates the TA excitatory drive onto CA1 pyramidal neurons while diminishing the feedforward NGL inhibition to the distal PC dendrites.

Although we did not explicitly model the activity of DA cells, we assumed a tonic presence of DA and modelled effects of the tonic DA in the following way (see Eq. 50): when a pyramidal cell (place cell) was inside its place field, then high-frequency EC stimulation impinged on both NGL interneuron and the PC distal dendrite. During this high-frequency stimulation environment, the strength of the NGL inhibition to the PC distal dendrites was set to 1.1 ($w_{\text{ngl-to-pc}} = 1.1$), whereas the DA level was set to 0.73, thus reducing the inhibitory effect of the NGL cell to the PC distal dendrite and hence opening the gate. Dendritic spikes in the distal PC dendrites are evident, which propagate to the PC soma and generate action potentials. On the other hand, when a place cell was outside its place field, then both PC and NGL neurons received low-frequency EC and CA3 stimulations (1–3 spikes per theta cycle (Alonso and García-Austt 1987)). Although the strength of the NGL inhibition to PC distal dendrites remained unchanged, the modulation level of DA on the strength of the NGL inhibition was increased to 1 in order to simulate the closing of the gate by DA. The low-frequency stimulation then allowed the NGL to feedforwardly inhibit the PC distal dendrites, thus causing the PC to stop firing or at most fire one spike per theta cycle.

Results on Rate and Phase Coding of Place Cells in CA1 Microcircuit

Results on how place cell rate and phase coding can be supported by the sheer complexity of the CA1 microcircuit will be presented in this section. Out of a wide range of possible models, I present here four microcircuit models:

- Model with both pyramidal (place) and inhibitory cells stimulated tonically by non-precessing high-gamma EC and non-precessing low-gamma CA3 inputs.

- Model with tonic non-precessing high-gamma EC input exciting PC and IN distal dendrites, a non-precessing low-gamma CA3 input exciting IN proximal dendrites and a constant-rate phase-precessing low-gamma CA3 input exciting PC proximal dendrites.
- Model with tonic constant-rate non-phase-precessing high-gamma EC input exciting PC and IN distal dendrites, constant-rate phase-precessing low-gamma CA3 input exciting PC and IN proximal dendrites and constant-rate phase-precessing septal inhibition inhibiting all CA1 Ins.
- Model with tonic constant-rate non-phase-precessing high-gamma EC input exciting PC and IN distal dendrites, variable-rate (rate increased linearly from 25 to 50 Hz from the beginning to the middle of the place field and decreased linearly by the same amount from the middle to the end of the field) phase-precessing low-gamma CA3 input exciting PC and IN proximal dendrites, a constant-rate phase-precessing septal inhibition inhibiting all CA1 Ins and a suppressed constant-rate phase-precessing presynaptic $GABA_B$ inhibition.

Figure 4 provides a summary of a place cell firing rate in each theta cycle in each model.

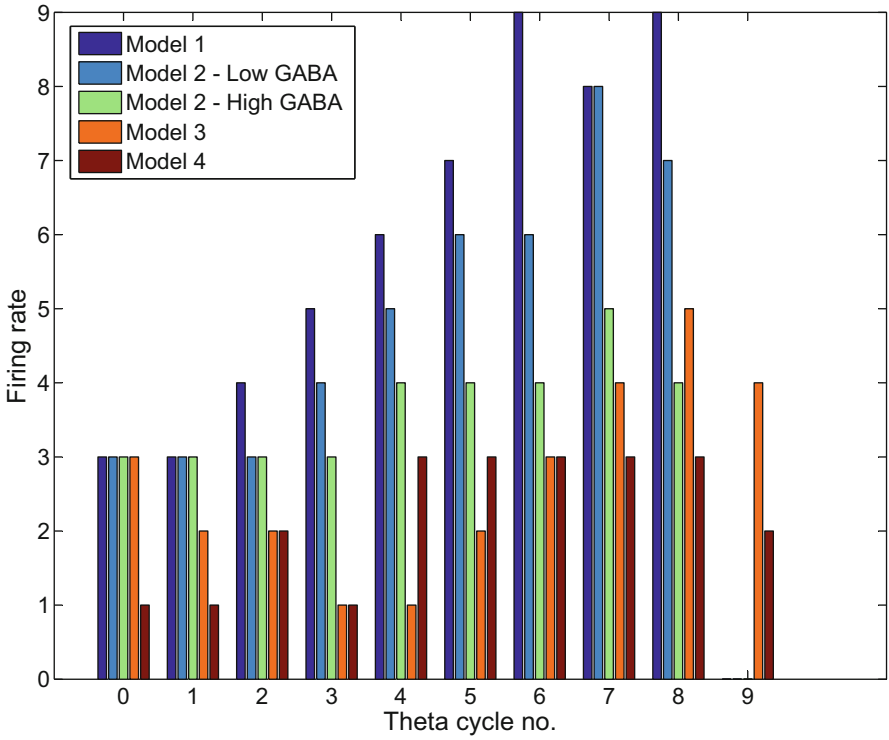

Fig. 4 Firing rate (number of spikes) of a pyramidal (place) cell as a function of theta cycle number for each of the four models

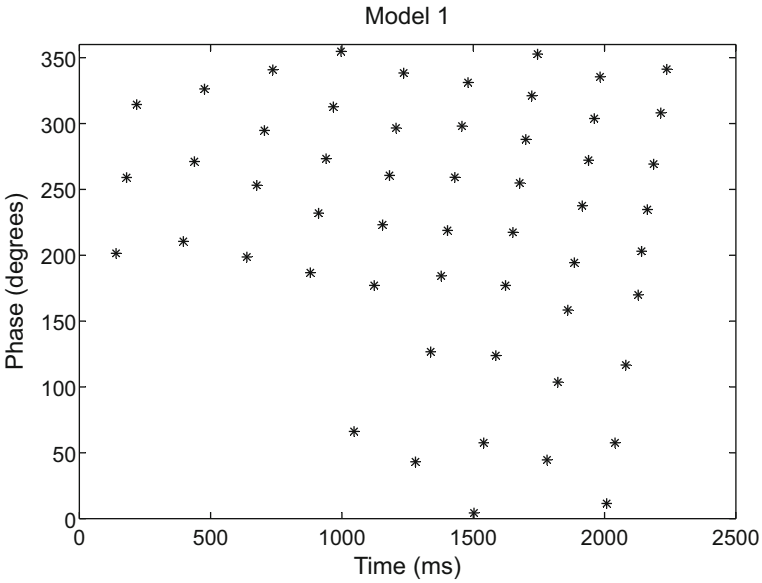

Fig. 5 Spike phase advancement of a place cell during a linear track running episode (*model 1*)

Model 1 This model attempted to answer the question of whether rate and phase coding of place cells can be generated by the CA1 microcircuit. In the model both pyramidal (place) and inhibitory cells were stimulated tonically by non-precessing high-gamma EC and non-precessing low-gamma CA3 inputs. We observe (see Fig. 5) that at the beginning of the place field (first theta cycle), the PC (place cell) fired its first spike near the trough of the external theta. As the rat approached the end of the place field (ninth theta cycle), the PC fired its first spike just after the peak of theta, having precessed almost 180°. This phase advancement was because of the constantly increasing synaptic strength of the proximal synapse, which allowed the PC to overcome the dendritic inhibition (BSC and IVY inhibition) and fire at earlier phases of the LFP theta. Despite these first-spike phase advancements, the remaining spikes in the train remained anchored to the end of each theta cycle. Furthermore, the rate of firing of each place cell increased at each theta cycle as the rat transversed the field. These observations come in disagreement with the experimentally observed evidence (O'Keefe and Recce 1993; Kamondi et al. 1998; Harris et al. 2002; Mehta et al. 2002; Skaggs et al. 1996), where the entire spike train and *not just the first-spike* theta phase precesses and the firing rate of place cells is initially low when the rat enters the place field, reaches its maximum rate as the rat approaches the middle of the field and decreases as the rat exits the field. Also in contrast to the experimental evidence (Klausberger and Somogyi 2008; Klausberger et al. 2003, 2004; Klausberger 2009; Somogyi and Klausberger 2005), the phase relationships of the INs with respect to the PCs and the LFP theta are disrupted.

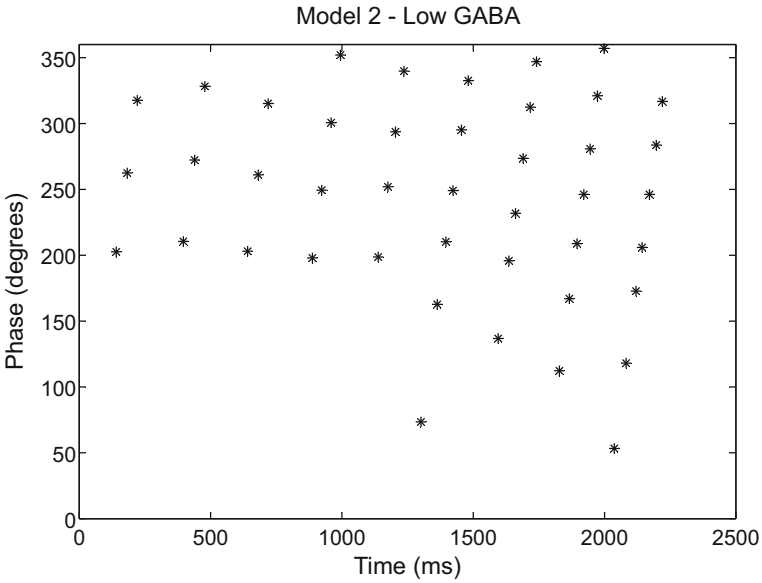

Fig. 6 Spike phase advancement of a place cell during a linear track running episode (*model 2 – low GABA*)

The following three models tackle the question of under what conditions could the rate and theta phase coding of CA1 place cells be maintained, but *not generated* by the CA1 microcircuit.

Model 2 In the model, tonic non-precessing high-gamma EC-PP input excited both CA1 PC and IN distal dendrites, whereas a non-precessing low-gamma CA3-SC input excited the IN proximal dendrites. PC proximal dendrites were excited by a constant-rate phase-precessing low-gamma CA3-SC input. This phase-precessing CA3-SC input was modelled to precess by approximately 40° in every subsequent theta cycle having precessed a full 360° by the ninth theta cycle (rat exits the place field). When the INs inhibition was low (see Fig. 6), then the place cell discharge pattern was identical to model 1. When the INs inhibition was high (see Fig. 7), then the place cell's discharge did not phase-precess and it was restricted to the trough of each theta cycle. Its firing rate remained constant in each theta cycle throughout the simulation. The firing phase relationships of pyramidal (place) cells and inhibitory interneurons with respect to the LFP theta were preserved (Klausberger and Somogyi 2008; Klausberger et al. 2003, 2004).

Model 3 In the model, tonic constant-rate non-phase-precessing high-gamma EC-PP input excited both CA1 PC and IN distal dendrites, whereas constant-rate phase-precessing low-gamma CA3-SC input excited both PC and IN proximal dendrites. Constant-rate phase-precessing septal inhibition inhibited all CA1 INs. CA3-SC and MS inputs were modelled to phase advanced by 40° in every theta cycle having

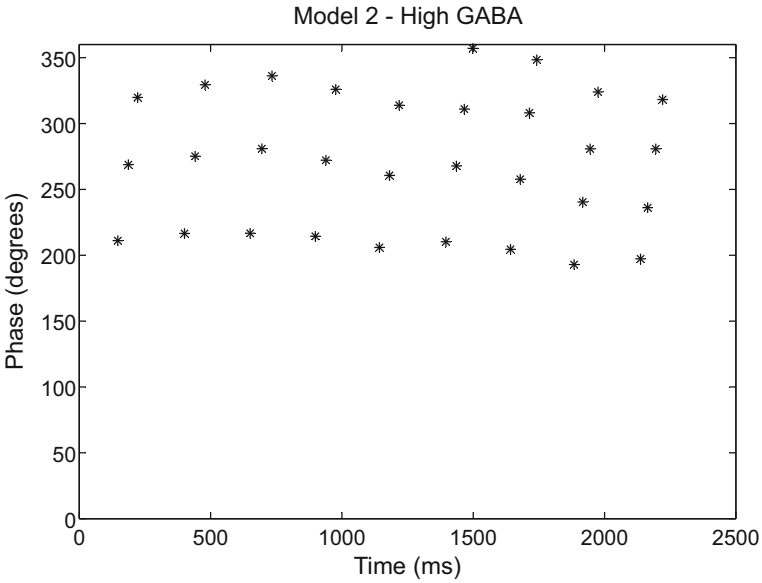

Fig. 7 Spike phase advancement of a place cell during a linear track running episode (*model 2 – high GABA*)

precessed a complete 360° by the end of the place field (ninth theta cycle). We observe that the PC firing precessed a full 360° by the end of the place field and so all INs (see Fig. 8). Phase relationships between the PCs and INs are also preserved due to the precessing of the septal inhibition. However, the firing rate of the PCs is not consistent with the experimental findings (Harris et al. 2002; Mehta et al. 2002). Their firing rate was high in the beginning of the field, low in the middle of the field and very high at the end of field. These firing rate inconsistencies were due to the nonlinear interaction of the inhibition and the calcium accumulation in the proximal PC dendrite, which caused the synaptic strength of the PC proximal synapse to increase with a high rate towards the end of the place field. In the first few theta cycles, inhibition is dominating, and the calcium level in the proximal dendrite is low (synapse is depressed). Thus, the proximal synaptic weight is decreasing (PC firing is low). In subsequent theta cycles, calcium level increases (synapses are potentiated) and inhibition is overcome, causing the PC firing rate to increase and thus PC to fire more spikes in every subsequent theta cycle.

Model 4 In the model, tonic constant-rate non-phase-precessing high-gamma EC-PP input excited both CA1 PC and IN distal dendrites, whereas *variable-rate* (rate increased linearly from 25 to 50 Hz from the beginning to the middle of the place field and decreased linearly by the same amount from the middle to the end of the field) phase-precessing low-gamma CA3-SC input excited both PC and IN proximal dendrites. Constant-rate phase-precessing septal inhibition inhibited all CA1 INs, whereas a constant-rate phase-precessing presynaptic $GABA_B$ inhibition

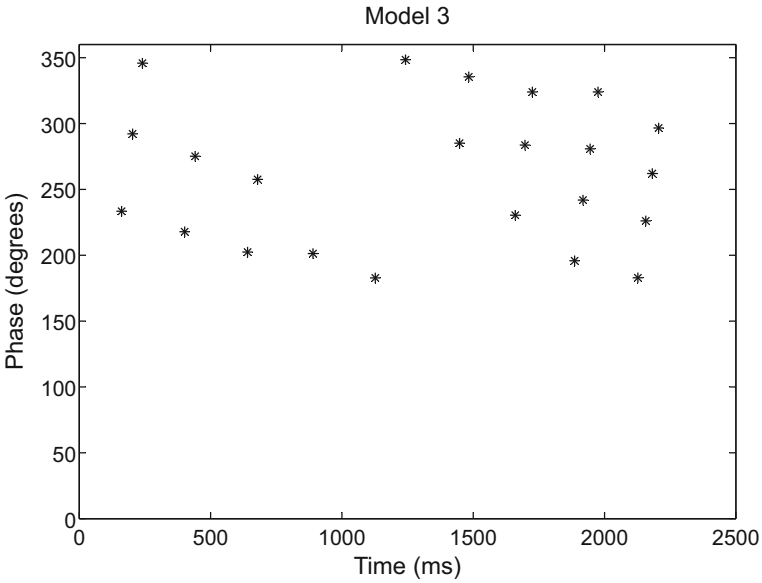

Fig. 8 Spike phase advancement of a place cell during a linear track running episode (*model 3)*

suppressed was also assumed. We observe (see Fig. 9) all of the experimentally observed characteristics of rate and phase coding of place cell firing: (1) the firing of the place cell starts at the trough of the external theta (beginning of the place field), (2) the firing of the place cell phase advances in every subsequent theta, (3) phase precession is almost 360° by the end of the place field (ninth theta cycle) and (4) the firing rate of the place cell increases as the rat transverses the field, peaks at about 200° and decreases as the rat approaches the end of the place field. The latter observation is due to the depressed throughout the simulation run (nine theta cycles) proximal PC synapse (data not shown), thus allowing the variable-rate and phase-precessed SC input to take charge of the firing of the CA1 place cell. The cell fired sparsely in the first 1 s of the trial run, after which its firing increased and phase precessed. In addition, the firing phase relationships between PCs and INs as they have been observed in the Klausberger studies (2003, 2004, 2008) are preserved (data not shown here, but see Fig. 12A in Cutsuridis and Hasselmo 2012). Thus, within these sets of parameters explored here, this model appears to most effectively match the experimental data.

Discussion and the Future

The main finding of the computer models presented in this chapter is that rate and phase coding of CA1 place cells are externally dictated by the CA3 Schaffer collateral inputs driving their proximal dendrites. In order for rate coding and phase

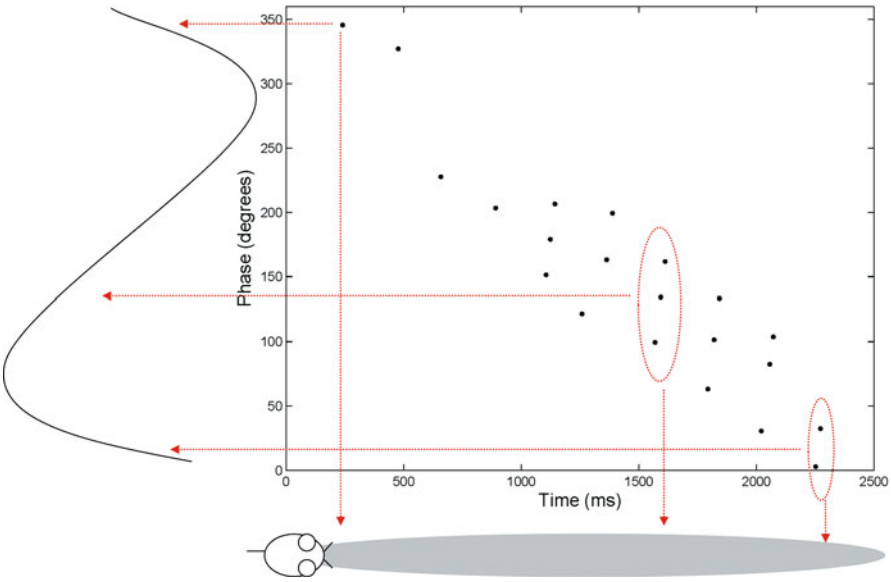

Fig. 9 Spike phase advancement of a place cell during a linear track running episode (*model 4*). The cell fired sparsely until 1 s into the trial, when an intense period of firing occurred, accompanied by phase precession

precession to be maintained by the internal CA1 architecture, then certain conditions need to be met. First, in order for the CA1 pyramidal cells (place cells) to phase precess to a full 360° as the rat reaches the end of the place field, then an excitatory precessing input (CA3 Schaffer collateral input) should drive not only the PCs but also the inhibitory interneurons causing them to also precess to earlier phases of the LFP theta. In addition, phase-precessing theta-modulated medial septal inhibitory inputs (MS_{180} and MS_{360}), inhibiting the CA1 inhibitory interneurons, are required to ensure that the between-phase relationships of the CA1 PCs and the inhibitory INs with respect to LFP theta are also maintained. These simulated findings are in line with the experimental evidence which has shown that layer 2 EC cells are phase precessing, but not the EC layer 3 cells (Mizuseki et al. 2009; Hafting et al. 2008). The EC layer 2 cells drive both the DG and CA3 excitatory cells, which in turn excite the proximal dendrites of the CA1 PCs, whereas the EC layer 3 cells excite only the distal dendrites of the CA1 PCs. Transient disruption of the CA3 input to CA1 PCs has been shown to cause a transient block of their phase precession dynamics (Zugaro et al. 2005). Therefore, our model assumption to model only the CA3 input as a phase-precessing input is consistent with the observed experimental findings. Other experimental evidence has shown that during spatial exploratory behaviour on a linear track, inhibitory interneurons also show phase precession dynamics (Ego-Stengel and Wilson 2007; Maurer et al. 2006). This finding supports our model assumption that also the CA1 inhibitory interneurons should be driven by the CA3 phase-precessing input causing them to phase precess.

Second, in order for the firing rate of CA1 place cells to increase as the rat moves through the place field reaching a maximum value just after the middle of the field, beyond which, it decreases again (Harris et al. 2002; Mehta et al. 2002), then (1) a variable-rate (linearly increasing from the start till the middle of the place field and linearly decreasing from the middle till the end of the field) low-gamma CA3 SC input must drive the CA1 PCs and INs; and (2) CA1 PC proximal synapses must be depressed, thus preventing the tendency due to synaptic potentiation PCs to increase their discharge activities in each theta cycle as the rat tranverses the field (see, e.g. Fig. 5 of model 1) and allowing the CA3 SC inputs to dictate their firing rates (see Fig. 9 of model 4).

Several extensions to model 4 deserve further consideration. One idea is to scale up the network to match the relative percentages of excitatory and inhibitory cells in CA1 (Vida 2010; Baude et al. 2007). Scaling up the model will allow it to circumvent the case of a single theta phase-precessing interneuron inhibiting pyramidal cells with place fields at different and overlapping locations, thus simultaneously inhibiting pyramidal cells that are at different stages (i.e. theta phases) of phase precession. In this case, a single theta phase-precessing interneuron may only correctly time only a few of its postsynaptic pyramidal cells. However, if our scaled up network consisted of, for example, 400 PCs and 24 inhibitory interneurons (i.e. less than 10% inhibition), with each set of 100 PCs and 6 INs representing a microcircuit coding for a spatial location, driven by EC and CA3 inputs presented at different but overlapping times, then the potentially simultaneous inhibition of PCs at different stages (i.e. theta phases) of phase precession maybe overcome.

Another idea is to test the robustness of the scaled up model. How would the firing patterns of CA1 interneurons and place cells change with more realistic, noisy, input coming from multiple EC and CA3 cells? How would random synaptic delays affect the results? How will the results scale with noise in connectivity parameters?

Appendix

CA1 Pyramidal Cell

The axonic (ax), somatic (s), proximal dendritic (pd) and distal dendritic (dd) compartments of the pyramidal neuron obey the following current balance equations:

$$C_{\mathrm{m}}\frac{\mathrm{d}V_{\mathrm{ax}}}{\mathrm{d}t} = I_{\mathrm{L}} + I_{\mathrm{Na,ax}} + I_{\mathrm{K,ax}} + I_{\mathrm{coup}} + I_{\mathrm{syn}} + I_{\mathrm{in}} \tag{4}$$

$$C_{\mathrm{m}}\frac{\mathrm{d}V_{\mathrm{s}}}{\mathrm{d}t} = I_{\mathrm{L}} + I_{\mathrm{Na,s}} + I_{K_{\mathrm{dr,s}}} + I_{\mathrm{A,s}} + I_{\mathrm{m,AHAP,s}} + I_{\mathrm{CaL,s}} + I_{\mathrm{h}} + I_{\mathrm{coup}} + I_{\mathrm{syn}} + I_{\mathrm{in}} \tag{5}$$

$$C_{\mathrm{m}}\frac{\mathrm{d}V_{\mathrm{pd}}}{\mathrm{d}t} = I_{\mathrm{L}} + I_{\mathrm{Na,d}} + I_{K_{\mathrm{dr,d}}} + I_{\mathrm{A,d}} + I_{\mathrm{CaL,d}} + I_{\mathrm{h}} + I_{\mathrm{coup}} + I_{\mathrm{syn}} + I_{\mathrm{in}} \tag{6}$$

$$C_{\mathrm{m}}\frac{\mathrm{d}V_{\mathrm{dd}}}{\mathrm{d}t} = I_{\mathrm{L}} + I_{\mathrm{Na,d}} + I_{K_{\mathrm{dr,d}}} + I_{\mathrm{A,d}} + I_{\mathrm{CaL,d}} + I_{\mathrm{h}} + I_{\mathrm{coup}} + I_{\mathrm{syn}} + I_{\mathrm{in}} \tag{7}$$

where I_{L} is the leak current, I_{Na} is the sodium current, I_{K} is the delayed rectifier potassium current, I_{A} is the type A potassium current, $I_{\mathrm{m,AHP}}$ is the medium Ca^{2+}-activated K^{+} after-hyperpolarization current, I_{CaL} is the L-type Ca^{2+} current, I_{h} is the h-current, I_{coup} is the electrical coupling between compartments, I_{in} is the injected current and I_{syn} is the synaptic current. Table 1 displays the ionic parameter values of the CA1 pyramidal cell.

The coupling currents for all compartments are

$$I_{\mathrm{coup}}^{\mathrm{axon}} = g_{\mathrm{axon,soma}} \cdot (V_{\mathrm{soma}} - V_{\mathrm{axon}}) \tag{8}$$

Table 1 Pyramidal cell parameter values. Units: g, mS/cm^2; C_{m}, μF/cm^2; V, mV; T, celcius

Name	Value	Name	Value
C_{m}	1	$g_{\mathrm{A,dend}}$	12
g_{L}	0.1	asap	0.001
V_{L}	−70	ζ_{p}	30
g_{coup}	1.125	inact	72
$g_{\mathrm{Na,soma}}$	30	inact_2	0.11
$g_{\mathrm{Na,axon}}$	100	inact_3	2
V_{Na}	60	inact_4	64
$g_{\mathrm{Na,dend}}$	30	inact_5	1
natt	0	$g_{\mathrm{K,dr,axon}}$	20
T	23	$g_{\mathrm{K,dr,soma}}$	14
$g_{\mathrm{A,soma}}$	7.5	$g_{\mathrm{K,dr,dend}}$	14
g_{mAHP}	25	V_{k}	−80
qhat	1	qma	0.00048
qmb	0.28	β_{s}	0.083
$g_{\mathrm{CaL,soma}}$	7	β_{d}	0.083
$g_{\mathrm{CaL,dend}}$	25	buff	0
V_{Ca}	140	nonc	6
Ca^{2+}	2	Ca_{τ}	1000
φ_s	0.1	s_1	0
φ_d	0.1	s_2	40
$\chi_{0,s}$	0.05	s_3	3.6
$\chi_{0,d}$	0.07	Mg^{2+}	2
κ	7		

$$I_{\text{coup}}^{\text{soma}} = g_{\text{soma,axon}} \cdot (V_{\text{axon}} - V_{\text{soma}}) + g_{\text{soma,dend}_{\text{prox}}} \cdot \left(V_{\text{pd}} - V_{\text{soma}}\right) \tag{9}$$

$$I_{\text{coup}}^{\text{dend}_{\text{prox}}} = g_{\text{soma,dend}_{\text{prox}}} \cdot \left(V_{\text{soma}} - V_{\text{pd}}\right) + g_{\text{dend}_{\text{dist}},\text{dend}_{\text{prox}}} \left(V_{\text{dd}} - V_{\text{pd}}\right) \tag{10}$$

$$I_{\text{coup}}^{\text{dend}_{\text{dist}}} = g_{\text{dend}_{\text{prox}},\text{dend}_{\text{dist}}} \left(V_{\text{pd}} - V_{\text{dd}}\right) \tag{11}$$

The leak current is described by

$$I_{\text{L}} = g_{\text{L}} \cdot (V - V_{\text{L}}) \tag{12}$$

where g_{L} is the leak conductance and V_{L} is the leak reversal potential.

The sodium current at the axon and soma is described by

$$I_{\text{Na}} = -g_{\text{Na}} \cdot M_{\text{Na}}^2 \cdot H_{\text{Na}} \cdot (V - V_{\text{Na}}) \tag{13}$$

where g_{Na} is the maximal conductance of the Na^+ current, M_{Na} and H_{Na} are the activation and inactivation constants and V_{Na} is the reversal potential of the Na^+ current. The activation and inactivation constants at the soma are given by

$$M_{\text{Na}} = \alpha_{\text{M}}(V) / (\alpha_{\text{M}}(V) + \beta_{\text{M}}(V))$$

$$\alpha_{\text{M}}(V) = 0.32 \cdot (-46.9 - V) / (\exp((-46.9 - V)/4.0) - 1.0)$$

$$\beta_{\text{M}}(V) = 0.28 \cdot (V + 19.9) / (\exp((V + 19.9)/5.0) - 1.0)$$

$$H'_{\text{Na}} = \alpha_{\text{H}}(V) - (\alpha_{\text{H}}(V) + \beta_{\text{H}}(V)) \cdot H_{\text{Na}}$$

$$\alpha_{\text{H}}(V) = 0.128 \cdot \exp((-43 - V)/18)$$

$$\beta_{\text{H}}(V) = 4/(1 + \exp((-20 - V)/5)$$

The sodium current at the dendrite is described by

$$I_{\text{Na,d}} = -g_{\text{Na,d}} \cdot M_{\text{Na,d}}^2 \cdot H_{\text{Na,d}} \cdot D_{\text{Na,d}} \cdot (V_{\text{d}} - V_{\text{Na}}) \tag{14}$$

where

$$M'_{\mathrm{Na,d}} = \left(M_{\infty_{\mathrm{Na,d}}} - M_{\mathrm{Na,d}}\right)/\tau_{M_{\mathrm{Na,d}}}$$

$$M_{\infty_{\mathrm{Na,d}}} = 1/\left(1 + \exp\left(\left(-V_{\mathrm{d}} - 40\right)/3\right)\right)$$

$$\tau_{M_{\mathrm{Na,d}}} = 0.1$$

$$H'_{\mathrm{Na,d}} = \left(H_{\infty_{\mathrm{Na,d}}} - H_{\mathrm{Na,d}}\right)/\tau_{H_{\mathrm{Na,d}}}$$

$$H_{\infty_{\mathrm{Na,d}}} = 1/\left(1 + \exp\left(\left(V_{\mathrm{d}} + 45\right)/3\right)\right)$$

$$\tau_{H_{\mathrm{Na,d}}} = 0.5$$

$$D'_{\mathrm{Na,d}} = \left(D_{\infty_{\mathrm{Na,d}}} - D_{\mathrm{Na,d}}\right)/\tau_{D_{\mathrm{Na,d}}}$$

$D_{\infty_{\mathrm{Na,d}}} = (1 + \mathrm{natt} \cdot \exp((V_{\mathrm{d}} + 60)/2)) / (1 + \exp((V_{\mathrm{d}} + 60)/2))$
$\tau_{D_{\mathrm{Na,d}}} = \max(0.1, (0.00333 \cdot \exp(0.0024 \cdot (V_{\mathrm{d}} + 60) \cdot Q))/$
$(1 + \exp(0.0012 \cdot (V_{\mathrm{d}} + 60) \cdot Q)))$

$$Q = 96480/(8.315 \cdot (273.16^{\circ} + T))$$

where T is the temperature in Celsius and *natt* is the Na^+ attenuation. The type A K^+ current at the soma and dendrite is given by

$$I_{K_{\mathrm{A,d}}} = -g_{K_{\mathrm{A,d}}} \cdot A_{\mathrm{d}} \cdot B_{\mathrm{d}} \cdot \left(V_{\mathrm{d}} - V_{\mathrm{K}}\right) \tag{15}$$

The activation and inactivation constants are given by

$$A'_{\mathrm{d}} = \left(A_{\infty_{\mathrm{d}}} - A_{\mathrm{d}}\right)/\tau_{A_{\mathrm{d}}}$$

$$A_{\infty_{\mathrm{d}}} = 1/\left(1 + A_{\alpha,\mathrm{d}}\right)$$

$$A_{\alpha,\mathrm{d}} = \exp\left(\mathrm{asap} \cdot \varsigma\left(V_{\mathrm{d}}\right) \cdot \left(V_{\mathrm{d}} + 1\right) \cdot Q\right)$$

$$A_{\beta,\mathrm{d}} = \exp\left(0.00039 \cdot Q \cdot \left(V_{\mathrm{d}} + 1\right) \cdot \varsigma_2\left(V_{\mathrm{d}}\right)\right)$$

$$\tau_{A_\mathrm{d}} = \max\left(A_{\beta,\mathrm{d}}/\left(\left(1 + A_{\alpha,\mathrm{d}}\right)\cdot QT\cdot 0.1\right), 0.1\right)$$

$$\varsigma\left(V_\mathrm{d}\right) = -1.5 - \left(1/\left(1 + \exp\left(\left(V_\mathrm{d} + \varsigma_\mathrm{p}\right)/5\right)\right)\right)$$

$$\varsigma_2\left(V_\mathrm{d}\right) = -1.8 - \left(1/\left(1 + \exp\left(\left(V_\mathrm{d} + 40\right)/5\right)\right)\right)$$

$$B'_\mathrm{d} = \left(B_{\infty_\mathrm{d}} - B_\mathrm{d}\right)/\tau_{B_\mathrm{d}}$$

$$B_{\infty_\mathrm{d}} = 0.3 + 0.7/\left(1 + \exp\left(\mathrm{inact}_2\cdot\left(V_\mathrm{s} + \mathrm{inact}\right)\cdot Q\right)\right)$$

$$\tau_{B_\mathrm{d}} = \kappa\cdot\max\left(\mathrm{inact}_3\cdot\left(V_\mathrm{s} + \mathrm{inact}_4\right), \mathrm{inact}_5\right)$$

The delayed rectifier K^+ current at the axon and soma is given by

$$I_{K_\mathrm{dr}} = -g_{K_\mathrm{dr}}\cdot N\cdot\left(V - V_\mathrm{K}\right) \tag{16}$$

where g_{Kds} is the maximal conductance. The activation constant, N, is given by

$$N' = \alpha_\mathrm{N}(V) - \left(\alpha_\mathrm{N}(V) + \beta_\mathrm{N}(V)\right)\cdot N$$

$$\alpha_\mathrm{N}(V) = 0.016\cdot\left(-24.9 - V\right)/\left(\exp\left(\left(-24.9 - V\right)/5\right) - 1\right)$$

$$\beta_\mathrm{N}(V) = 0.25\cdot\exp\left(-1 - 0.025\cdot V\right)$$

The delayed rectifier K^+ current at the dendrite is given by

$$I_{K_\mathrm{dr,d}} = -g_{K_\mathrm{dr,d}}\cdot N_\mathrm{d}^2\cdot\left(V_\mathrm{d} - V_\mathrm{K}\right) \tag{17}$$

where $g_{\mathrm{Kdr,d}}$ is the maximal conductance. The activation constant, N_d, is given by

$$N'_\mathrm{d} = \left(N_{\infty_\mathrm{d}} - N_\mathrm{d}\right)/\tau_{N_\mathrm{d}}$$

$$N_{\infty_\mathrm{d}} = 1/\left(1 + \exp\left(\left(-V_\mathrm{d} - 42\right)/2\right)\right.$$

$$\tau_{N_\mathrm{d}} = 2.2$$

The medium Ca^{2+}-activated K^+ after-hyperpolarization current at the soma is given by

$$I_{\mathrm{mAHP}} = -g_{\mathrm{mAHP}} \cdot Q_{\mathrm{m}} \cdot (V_{\mathrm{s}} - V_{\mathrm{K}}) \tag{18}$$

where g_{KmAHP} is the maximal conductance. The activation constant, Q_{m}, is given by

$$Q'_{\mathrm{m}} = \left(Q_{\mathrm{m}_\infty} - Q_{\mathrm{m}}\right) / \tau_{Q_{\mathrm{m}}}$$

$$Q_{\mathrm{m}_\infty} = \mathrm{qhat} \cdot Q_{\mathrm{m}_\alpha} \cdot \tau_{Q_{\mathrm{m}}}$$

$$Q_{\mathrm{m}_\alpha} = \mathrm{qma} \cdot \chi_{\mathrm{s}} / \left(0.001 \cdot \chi_{\mathrm{s}} + 0.18 \cdot \exp\left(-1.68 \cdot V_{\mathrm{s}} \cdot Q\right)\right)$$

$$Q_{\mathrm{m}_\beta} = \left(\mathrm{qmb} \cdot \exp\left(-0.022 \cdot V_{\mathrm{s}} \cdot Q\right)\right) / \left(\exp\left(-0.022 \cdot V_{\mathrm{s}} \cdot Q\right) + 0.001 \cdot \chi_{\mathrm{s}}\right)$$

$$\tau_{Q_{\mathrm{m}}} = 1 / \left(Q_{\mathrm{m}_\alpha} + Q_{\mathrm{m}_\beta}\right)$$

The h-current (Cutsuridis et al. 2010) at the soma and dendrite is described by

$$I_{\mathrm{h}} = -g_{\mathrm{h}} \cdot tt \cdot (V - E_{\mathrm{h}}) \tag{19}$$

$$\frac{\mathrm{d}tt}{\mathrm{d}t} = \frac{tt_\infty - tt}{\tau_{tt}}$$

$$tt_\infty = \frac{1}{1 + e^{-(V - V_{\mathrm{half}})/k_{\mathrm{l}}}}$$

$$\tau_{tt} = \frac{e^{0.0378 \cdot \varsigma \cdot \mathrm{gmt} \cdot (V - V_{\mathrm{halft}})}}{qtl \cdot q10^{(T-33)/10} \cdot a0t \cdot (1 + a_{tt})}$$

$$a_{tt} = e^{0.00378 \cdot \varsigma \cdot (V - V_{\mathrm{halft}})}$$

where g_{h} is the maximal conductance of the h-current and E_{h} is the reversal potential. The L-type Ca^{2+} current at the soma is described by

$$I_{\mathrm{CaL_s}} = -g_{\mathrm{CaL_s}} \cdot S_s \cdot g_{\mathrm{hk}}\left(V_{\mathrm{s}}, \chi_{\mathrm{s}}\right) \cdot \left(1 / \left(1 + \chi_{\mathrm{s}}\right)\right) \tag{20}$$

where $g_{\mathrm{CaL,s}}$ is the maximal conductance and

$$S'_{\mathrm{s}} = \left(S_{\infty_{\mathrm{s}}} - S_{\mathrm{s}}\right) / \tau_{s_{\mathrm{s}}}$$

$$S_{\infty_{\mathrm{s}}} = \alpha_{\mathrm{s}}\left(V_{\mathrm{s}}\right) / \left(\alpha_{\mathrm{a}}\left(V_{\mathrm{s}}\right) + \beta_{\mathrm{s}}\left(V_{\mathrm{s}}\right)\right)$$

$$\tau_{S_{\mathrm{s}}} = 1 / \left(5 \cdot \left(\alpha_{\mathrm{s}}\left(V_{\mathrm{s}}\right) + \beta_{\mathrm{s}}\left(V_{\mathrm{s}}\right)\right)\right)$$

$$\alpha_{\mathrm{s}}\left(V_{\mathrm{s}}\right) = -0.055 \cdot \left(V_{\mathrm{s}} + 27.01\right) / \left(\exp\left(\left(-V_{\mathrm{s}} - 27.01\right) / 3.8\right) - 1\right)$$

$$\beta_{\mathrm{s}}\left(V_{\mathrm{s}}\right) = 0.94 \cdot \exp\left(\left(-V_{\mathrm{s}} - 63.01\right) / 17\right)$$

$$xx = 0.0853 \cdot \left(273.16 + T\right) / 2$$

$$f(z) = (1 - z/2) \cdot f_2(z) + (z / (\exp(z) - 1)) \cdot f_3(z)$$

$$f_2(z) = H\left(0.0001 - |z|\right)$$

$$f_3(z) = H\left(|z| - 0.0001\right)$$

$$g_{\mathrm{hk}} = -xx \cdot \left(1 - \left(\left(\chi_{\mathrm{s}}/\mathrm{Ca}\right) \cdot \exp\left(V_{\mathrm{s}}/xx\right)\right)\right) \cdot f\left(V_{\mathrm{s}}/xx\right)$$

The Ca^{2+} concentrations in the soma and dendrites are given by

$$\chi'_{\mathrm{s}} = \varphi_{\mathrm{s}} \cdot I_{\mathrm{CaL_s}} - \left(\beta_{\mathrm{s}} \cdot \left(\chi_{\mathrm{s}} - \chi_{0,\mathrm{s}}\right)\right) + \left(\chi_{\mathrm{pd}} - \chi_{\mathrm{s}}\right) / \mathrm{Ca}_{\tau} - \left(\beta_{\mathrm{s}}/\mathrm{nonc}\right) \cdot \chi_{\mathrm{s}}^2 \tag{21}$$

$$\chi'_{\mathrm{pd}} = \varphi_{\mathrm{d}} \cdot \left(I_{\mathrm{CaL_d}} + I_{\mathrm{Ca,NMDA}}\right) - \beta_{\mathrm{d}} \cdot \left(\chi_{\mathrm{pd}} - \chi_{0,\mathrm{d}}\right) - \left(\beta_{\mathrm{d}}/\mathrm{nonc}\right) \cdot \chi_{\mathrm{pd}}^2 - \mathrm{buff} \cdot \chi_{\mathrm{pd}} \tag{22}$$

$$\chi'_{\mathrm{dd}} = \varphi_{\mathrm{d}} \cdot \left(I_{\mathrm{CaL_d}} + I_{\mathrm{Ca,NMDA}}\right) - \beta_{\mathrm{d}} \cdot \left(\chi_{\mathrm{dd}} - \chi_{0,\mathrm{d}}\right) - \left(\beta_{\mathrm{d}}/\mathrm{nonc}\right) \cdot \chi_{\mathrm{dd}}^2 - \mathrm{buf}f \cdot \chi_{\mathrm{dd}} \tag{23}$$

The L-type Ca^{2+} current at the dendrite is described by

$$I_{\mathrm{CaL_d}} = -g_{\mathrm{CaL_d}} \cdot S_{\mathrm{d}}^3 \cdot T_{\mathrm{d}} \cdot \left(V_{\mathrm{d}} - V_{\mathrm{Ca}}\right) \tag{24}$$

$$S'_{\mathrm{d}} = \left(S_{\infty_{\mathrm{d}}} - S_{\mathrm{d}}\right) / \tau_{s_{\mathrm{d}}}$$

$$S_{\infty_{\mathrm{d}}} = 1 / \left(1 + \exp\left(-V_{\mathrm{d}} - 37\right)\right)$$

$$\tau_{s_{\mathrm{d}}} = s_3 + s_1 / \left(1 + \exp\left(V_{\mathrm{d}} + s_2\right)\right)$$

$$T'_{\mathrm{d}} = \left(T_{\infty_{\mathrm{d}}} - T_{\mathrm{d}}\right) / \tau_{T_{\mathrm{d}}}$$

$$T_{\infty_{\mathrm{d}}} = 1 / \left(1 + \exp\left(\left(V_{\mathrm{d}} + 41\right) / 0.5\right)\right)$$

$$\tau_{T_{\mathrm{d}}} = 29$$

Basket, Axo-axonic, Bistratified and Ivy Cells

The membrane potential of the basket, axo-axonic, bistratified and ivy cell obeys the following equation:

$$C_{\mathrm{m}} \frac{\mathrm{d}V}{\mathrm{d}t} = I_{\mathrm{L}} + I_{\mathrm{Na}} + I_{K_{\mathrm{dr}}} + I_{\mathrm{A}} + I_{\mathrm{in}} + I_{\mathrm{syn}} \tag{25}$$

where C_{m} is the membrane capacitance, V is the membrane potential, I_{L} is the leak current, I_{Na} is the sodium current, I_{Kdr} is the fast delayed rectifier K^+ current, I_A is the A-type K^+ current and I_{syn} is the synaptic current.

The sodium current and its kinetics are described by

$$I_{\mathrm{Na}} = g_{\mathrm{Na}} m^3 h \left(V - E_{\mathrm{Na}}\right) \tag{26}$$

$$\frac{\mathrm{d}m}{\mathrm{d}t} = \alpha_{\mathrm{m}} \left(1 - m\right) - \beta_{\mathrm{m}} m$$

$$\alpha_{\mathrm{m}} = \frac{0.1 \left(V + 40\right)}{\left(1 - e^{(V+40)/10}\right)}$$

$$\beta_{\mathrm{m}} = 4 \cdot e^{(-(v+65)/18)}$$

$$\frac{\mathrm{d}h}{\mathrm{d}t} = \alpha_{\mathrm{h}}\,(1-h) - \beta_{\mathrm{h}} h$$

$$\alpha_{\mathrm{h}} = 0.07 \cdot e^{-(V+65)/20}$$

$$\beta_{\mathrm{h}} = \frac{1}{\left(1 + e^{-(V+35)/10}\right)}$$

The fast delayed rectifier K^+ current, I_{Kdr}, is given by

$$I_{\mathrm{Kdr}} = g_{\mathrm{Kdr}} n^4\,(V - E_{\mathrm{K}}) \tag{27}$$

$$\frac{\mathrm{d}n}{\mathrm{d}t} = \alpha_{\mathrm{n}}\,(1-n) - \beta_{\mathrm{n}} n$$

$$\alpha_{\mathrm{n}} = \frac{0.01\,(V+55)}{\left(1 - e^{-(V+55)/10}\right)}$$

$$\beta_{\mathrm{n}} = 0.125 e^{-(v+65)/80}$$

The A-type K^+ current, I_{A}, is described by

$$I_{\mathrm{A}} = g_{\mathrm{A}} ab\,(V - E_{\mathrm{k}}) \tag{28}$$

$$\frac{\mathrm{d}a}{\mathrm{d}t} = \alpha_{\mathrm{a}}\,(1-a) - \beta_{\mathrm{a}} a$$

$$\alpha_{\mathrm{a}} = \frac{0.02\,(13.1 - V)}{e^{\left(\frac{13.1-V}{10}\right)} - 1}$$

$$\beta_{\mathrm{a}} = \frac{0.0175\,(V - 40.1)}{e^{\left(\frac{V-40.1}{10}\right)} - 1}$$

$$\frac{\mathrm{d}b}{\mathrm{d}t} = \alpha_{\mathrm{b}}\,(1-b) - \beta_{\mathrm{b}} b$$

$$\alpha_{\mathrm{b}} = 0.0016 e^{\left(\frac{-13-V}{18}\right)}$$

Table 2 Inhibitory cell parameter values. Units: g, mS/cm^2; C_m, μF/cm^2; V, mV

Name	Value	Name	Value
C_m	1	$g_{K,dr}$	23
g_L	0.18	$g_{K,dr,OLM}$	36
V_L	−60	$V_{k,OLM}$	−77
g_{Na}	150	V_k	−90
$g_{Na,OLM}$	120	g_{NaP}	2.5
V_{Na}	55	g_h	1.5
$V_{Na,OLM}$	50	V_{NaP}	50
$g_{L,OLM}$	0.3	V_h	−20
$V_{L,OLM}$	−54.4	g_A	10

$$\beta_b = \frac{0.05}{1 + e^{\left(\frac{10.1-V}{5}\right)}}$$

The ionic parameter values are depicted in Table 2.

Neurogliaform Cell

The membrane potential of the neurogliaform cell obeys the following equation:

$$C_m \frac{dV}{dt} = I_L + I_{Na} + I_{K_{dr}} + I_{in} + I_{syn} \tag{29}$$

where C_m is the membrane capacitance, V is the membrane potential, I_L is the leak current, I_{Na} is the sodium current, I_{Kdr} is the fast delayed rectifier K^+ current and I_{syn} is the synaptic current.

The sodium current and its kinetics are described by

$$I_{Na} = g_{Na} m^3 h \, (V - E_{Na}) \tag{30}$$

$$\frac{dm}{dt} = \alpha_m \, (1 - m) - \beta_m m$$

$$\alpha_m = \frac{0.1 \, (V + 40)}{\left(1 - e^{(V+40)/10}\right)}$$

$$\beta_m = 4 \cdot e^{(-(v+65)/18)}$$

$$\frac{\mathrm{d}h}{\mathrm{d}t} = \alpha_{\mathrm{h}}\,(1-h) - \beta_{\mathrm{h}} h$$

$$\alpha_{\mathrm{h}} = 0.07 \cdot e^{-(V+65)/20}$$

$$\beta_{\mathrm{h}} = \frac{1}{\left(1 + e^{-(V+35)/10}\right)}$$

The fast delayed rectifier K^+ current, I_{Kdr}, is given by

$$I_{\mathrm{Kdr}} = g_{\mathrm{Kdr}} n^4\,(V - E_{\mathrm{K}}) \tag{31}$$

$$\frac{\mathrm{d}n}{\mathrm{d}t} = \alpha_{\mathrm{n}}\,(1-n) - \beta_{\mathrm{n}} n$$

$$\alpha_{\mathrm{n}} = \frac{0.01\,(V+55)}{\left(1 - e^{-(V+55)/10}\right)}$$

$$\beta_{\mathrm{n}} = 0.125 e^{-(v+65)/80}$$

The ionic parameter values are depicted in Table 2.

OLM Cell

The membrane potential of the OLM cell obeys the following equation:

$$C_{\mathrm{m}} \frac{\mathrm{d}V}{\mathrm{d}t} = I_{\mathrm{L}} + I_{\mathrm{Na}} + I_{K_{\mathrm{dr}}} + I_{\mathrm{NaP}} + I_{\mathrm{H}} + I_{\mathrm{syn}} + I_{\mathrm{in}} \tag{32}$$

where C_m is the membrane capacitance, V is the membrane potential, I_{L} is the leak current, I_{Na} is the sodium current, I_{Kdr} is the fast delayed rectifier K^+ current, I_{NaP} is the persistent sodium current, I_{h} is the h-current and I_{syn} is the synaptic current.

The sodium current and its kinetics are described by

$$I_{\mathrm{Na}} = g_{\mathrm{Na}} m^3 h\,(V - E_{\mathrm{Na}}) \tag{33}$$

$$\frac{\mathrm{d}m}{\mathrm{d}t} = \alpha_{\mathrm{m}}\,(1-\mathrm{m}) - \beta_{\mathrm{m}} m$$

$$\alpha_{\mathrm{m}} = \frac{0.1\,(V+40)}{\left(1-e^{(V+40)/10}\right)}$$

$$\beta_{\mathrm{m}} = 4\cdot e^{(-(v+65)/18)}$$

$$\frac{\mathrm{d}h}{\mathrm{d}t} = \alpha_{\mathrm{h}}\,(1-h) - \beta_{\mathrm{h}}h$$

$$\alpha_{\mathrm{h}} = 0.07\cdot e^{-(V+65)/20}$$

$$\beta_{\mathrm{h}} = \frac{1}{\left(1+e^{-(V+35)/10}\right)}$$

The fast delayed rectifier K^+ current, I_{Kdr}, is given by

$$I_{\mathrm{Kdr}} = g_{\mathrm{Kdr}}n^4\,(V-E_{\mathrm{K}}) \tag{34}$$

$$\frac{\mathrm{d}n}{\mathrm{d}t} = \alpha_{\mathrm{n}}\,(1-n) - \beta_{\mathrm{n}}n$$

$$\alpha_{\mathrm{n}} = \frac{0.01\,(V+55)}{\left(1-e^{-(V+55)/10}\right)}$$

$$\beta_{\mathrm{n}} = 0.125e^{-(v+65)/80}$$

The NaP current was assembled from the Kunec et al. (2005) studies and it was described by

$$I_{\mathrm{NaP}} = -g_{\mathrm{NaP}}\cdot m_{\mathrm{po}}\cdot\,(V-V_{\mathrm{Na}}) \tag{35}$$

$$\frac{\mathrm{d}m_{\mathrm{po}}}{\mathrm{d}t} = \alpha_{\mathrm{mpo}}(V)\left(1-m_{\mathrm{po}}\right) - \beta_{\mathrm{mpo}}(V)\cdot m_{\mathrm{po}}$$

$$\alpha_{\mathrm{mpo}} = \frac{1}{0.15\left(1+e^{-(V+38)/6.5}\right)}$$

$$\beta_{\mathrm{mpo}} = \frac{e^{-(V+38)/6.5}}{0.15\left(1+e^{-(V+38)/6.5}\right)}$$

Similarly, the h-current was assembled from Kunec et al. (2005) studies and it was described by

$$I_{\mathrm{h}} = -g_{\mathrm{h}} \left(0.65\lambda_{\mathrm{fo}} + 0.35\lambda_{\mathrm{so}}\right)\left(V - V_{\mathrm{h}}\right) \tag{36}$$

$$\frac{\mathrm{d}\lambda_{\mathrm{fo}}}{\mathrm{d}t} = \frac{\lambda_{\mathrm{f}\infty}(V) - \lambda_{\mathrm{fo}}}{\tau_{\lambda \mathrm{f}}(V)}$$

$$\lambda_{\mathrm{f}\infty}(V) = \frac{1}{\left(1 + e^{(V+79.2)/9.78}\right)}$$

$$\tau_{\lambda \mathrm{f}}(V) = \frac{0.51}{e^{(v-1.7)/10} + e^{-(V+340)/52}} + 1$$

$$\frac{\mathrm{d}\lambda_{so}}{\mathrm{d}t} = \frac{\lambda_{\mathrm{s}\infty}(V) - \lambda_{\mathrm{so}}}{\tau_{\lambda \mathrm{s}}(V)}$$

$$\lambda_{\mathrm{s}\infty}(V) = \frac{1}{\left(1 + e^{(V+2.83)/15.9}\right)^{58}}$$

$$\tau_{\lambda \mathrm{s}}(V) = \frac{5.6}{e^{(v-1.7)/14} + e^{-(V+260)/43}} + 1$$

The ionic parameter values are depicted in Table 2.

Input Spike Generator

The input spike generator simulating the CA3 Schaffer collateral, the EC perforant path and the MS inputs were described by

$$F_{\mathrm{pre}} = H\left(t - 1\right) \cdot \left(H\left(\sin\left(2\pi \cdot \left(t - 2\right)/T\right)\right) \cdot \left(1 - H\left(\sin\left(2\pi \cdot \left(t - 1\right)/T\right)\right)\right)\right) \tag{37}$$

where T is the period of oscillation and $H(\,)$ is the Heaviside function.

Input-to-Cell Synaptic Currents

The Ca^{2+}-NMDA, AMPA, $GABA_A$ and NMDA synaptic currents are given by

$$I_{\mathrm{Ca,NMDA}} = -g_{\mathrm{syn}} \cdot s_{\mathrm{NMDA}} \cdot m_{\mathrm{Ca,NMDA}} \cdot \left(V_{\mathrm{d}} - V_{\mathrm{Ca,NMDA}}\right) \tag{38}$$

$$I_{\mathrm{NMDA}} = -g_{\mathrm{syn}} \cdot s_{\mathrm{NMDA}} \cdot m_{\mathrm{NMDA}} \cdot \left(V_{\mathrm{d}} - V_{\mathrm{NMDA}}\right) \tag{39}$$

$$I_{\mathrm{AMPA}} = -g_{\mathrm{syn}} \cdot s_{\mathrm{AMPA}} \cdot \left(V_{\mathrm{d}} - V_{\mathrm{AMPA}}\right) \tag{40}$$

$$I_{\mathrm{GABA}} = -g_{\mathrm{syn}} \cdot s_{\mathrm{GABA}} \cdot \left(V_{\mathrm{d}} - V_{\mathrm{GABA}}\right) \tag{41}$$

where g_{syn} is the synaptic conductance expressed either by Eqs. (50) or (1–3) and

$$m_{\mathrm{NMDA}} = 1/\left(1 + 0.3 \cdot \mathrm{Mg} \cdot \exp\left(-0.062 \cdot V_{\mathrm{d}}\right)\right)$$

$$m_{\mathrm{Ca,NMDA}} = 1/\left(1 + 0.3 \cdot \mathrm{Mg} \cdot \exp\left(-0.124 \cdot V_{\mathrm{d}}\right)\right)$$

with $\mathrm{Mg}^{2+} = 2$ mM. The activation equations for AMPA, NMDA and $\mathrm{GABA_A}$ currents are

$$s_x = s_{x_{\mathrm{fast}}} + s_{x_{\mathrm{slow}}} + s_{x_{\mathrm{rise}}} \tag{42}$$

where x stands for AMPA, NMDA, GABA and

$$s'_{\mathrm{NMDA_{rise}}} = -20 \cdot \left(1 - s_{\mathrm{NMDA_{fast}}} - s_{\mathrm{NMDA_{slow}}}\right) \cdot F_{\mathrm{pre}} - (1/2) \cdot s_{\mathrm{NMDA_{rise}}}$$

$$s'_{\mathrm{NMDA_{fast}}} = 20 \cdot \left(0.527 - s_{\mathrm{NMDA_{fast}}}\right) \cdot F_{\mathrm{pre}} - (1/10) \cdot s_{\mathrm{NMDA_{fast}}}$$

$$s'_{\mathrm{NMDA_{slow}}} = 20 \cdot \left(0.473 - s_{\mathrm{NMDA_{slow}}}\right) \cdot F_{\mathrm{pre}} - (1/45) \cdot s_{\mathrm{NMDA_{slow}}}$$

$$s'_{\mathrm{AMPA_{rise}}} = -20 \cdot \left(1 - s_{\mathrm{AMPA_{fast}}} - s_{\mathrm{AMPA_{slow}}}\right) \cdot F_{\mathrm{pre}} - (1/0.58) \cdot s_{\mathrm{AMPA_{rise}}}$$

$$s'_{\mathrm{AMPA_{fast}}} = 20 \cdot \left(0.903 - s_{\mathrm{AMPA_{fast}}}\right) \cdot F_{\mathrm{pre}} - (1/7.6) \cdot s_{\mathrm{AMPA_{fast}}}$$

$$s'_{\mathrm{AMPA_{slow}}} = 20 \cdot \left(0.097 - s_{\mathrm{AMPA_{slow}}}\right) \cdot F_{\mathrm{pre}} - (1/25.69) \cdot s_{\mathrm{AMPA_{slow}}}$$

and

Table 3 Input-to-cell and cell-to-cell synaptic parameter values. Units: g, mS/cm^2; V, mV

Name	Value	Name	Value
$g_{\mathrm{Ca,NMDA}}$	25	$V_{\mathrm{Ca,NMDA}}$	140
g_{NMDA}	0.3	V_{NMDA}	0
g_{AMPA}	0.05	V_{AMPA}	0
g_{GABA}	0.05	V_{GABA}	−75

$$s'_{\mathrm{GABA_{rise}}} = -20 \cdot \left(1 - s_{\mathrm{GABA_{fast}}} - s_{\mathrm{GABA_{slow}}}\right) \cdot F_{\mathrm{pre}} - (1/1.18) \cdot s_{\mathrm{GABA_{rise}}}$$

$$s'_{\mathrm{GABA_{fast}}} = 20 \cdot \left(0.803 - s_{\mathrm{GABA_{fast}}}\right) \cdot F_{\mathrm{pre}} - (1/8.5) \cdot s_{\mathrm{GABA_{fast}}}$$

$$s'_{\mathrm{GABA_{slow}}} = 20 \cdot \left(0.197 - s_{\mathrm{GABA_{slow}}}\right) \cdot F_{\mathrm{pre}} - (1/30.01) \cdot s_{\mathrm{GABA_{slow}}}$$

where F_{pre} is the input spike generator simulating the CA3 Schaffer collateral, the EC perforant path and the MS inputs. The input-to-cell synaptic parameter values are displayed in Table 3.

Synaptic Plasticity Model

The calcium detector model is governed by the following six equations:

$$P' = \left(\varphi_{\mathrm{a}}\left(\chi_{\mathrm{d}}\right) - c_{\mathrm{p}} \cdot A \cdot P\right) / \tau_{\mathrm{p}} \tag{43}$$

$$V' = \left(\varphi_{\mathrm{b}}\left(\chi_{\mathrm{d}}\right) - V\right) / \tau_{\mathrm{V}} \tag{44}$$

$$A' = \left(\varphi_{\mathrm{c}}\left(\chi_{\mathrm{d}}\right) - A\right) / \tau_{\mathrm{A}} \tag{45}$$

$$B' = \left(\varphi_{\mathrm{e}}(A) - B - c_{\mathrm{d}} \cdot B \cdot V\right) / \tau_{\mathrm{B}} \tag{46}$$

$$D' = \left(\varphi_{\mathrm{d}}(B) - D\right) / \tau_{\mathrm{D}} \tag{47}$$

The change in the synaptic weight is governed by the following equation:

$$W' = \left(\alpha_{\mathrm{w}} / \left(1 + \exp\left(\left(P - a\right) / p_{\mathrm{a}}\right)\right) - \beta_{\mathrm{w}} / \left(1 + \left(\exp\left(\left(D - d\right) / p_{\mathrm{d}}\right)\right) - W\right) / \tau_{\mathrm{w}} \tag{48}$$

Table 4 Calcium detector model parameter values. Units: g, mS/cm^2; V, mV; α, 1/ms; β, 1/ms

Name	Value	Name	Value
c_p	5	num_b	1
τ_p	500	num_c	1
τ_v	10	num_d	1
τ_A	5	num_e	5
τ_B	40	CmHC	4
τ_D	250	CmHN	4
τ_w	500	CnHC	0.6
α_w	0.8	CnHN	3
β_w	0.6	θ_c	2
a	0.3	θ_d	2.6
p_a	−0.1	θ_e	0.55
d	0.05	σ_c	−0.05
p_d	−0.002	σ_d	−0.01

where P is the potentiation detector dynamics, V is the veto detector dynamics, D is the depression detector dynamics, A and B are the intermediate steps leading up to D and W is the readout variable (see Fig. 2). The Hill equations are

$$\varphi_a(x) = num_a \cdot \left((x/CmHC)^{CmHN}\right) / \left(1 + (x/CmHC)^{CmHN}\right)$$

$$\varphi_b(x) = num_b \cdot \left((x/CnHC)^{CnHN}\right) / \left(1 + (x/CnHC)^{CnHN}\right)$$

$$\varphi_c(x) = num_c / \left(1 + \exp\left((x - \theta_c)/\sigma_c\right)\right)$$

$$\varphi_d(x) = num_d / \left(1 + \exp\left((x - \theta_d)/\sigma_d\right)\right)$$

$$\varphi_e(x) = num_e / \left(1 + \exp\left((x - \theta_e)/\sigma_e\right)\right)$$

The calcium detector parameter values are displayed in Table 4.

Cell-to-Cell Synaptic Currents

The synaptic current is given by

$$I_{syn} = g_{syn} \cdot s \cdot (V - E_{rev}) \tag{49}$$

Table 5 Synaptic strength parameter values

Name	Value theta	Name	Value theta
$w_{\text{ec-to-pcAMPA}}$	$1.4 + W_3$	$w_{\text{aac-to-pc}}$	1.0
$w_{\text{ca3-to-pcAMPA}}$	$2.4 + W_1$	$w_{\text{bc-to-pc}}$	0.1
$w_{\text{ec-to-pcNMDA}}$	$1.4 + W_3$	$w_{\text{bc-to-bsc}}$	20
$w_{\text{ca3-to-pcNMDA}}$	$2.4 + W_1$	$w_{\text{bsc-to-pc}}$	0.3
$w_{\text{ec-to-aac}}$	0.9	$w_{\text{pc-to-bsc}}$	0
$w_{\text{ca3-to-aac}}$	0.8	$w_{\text{bsc-to-bc}}$	0.5
$w_{\text{ec-to-bc}}$	0.8	$w_{\text{olm-to-pc}}$	0.5
$w_{\text{ca3-to-bc}}$	0.8	$w_{\text{pc-to-olm}}$	1.1
$w_{\text{ca3-to-bsc}}$	2	$w_{\text{ivy-to-pc}}$	0.15
$w_{\text{sep360-to-aac}}$	10	$w_{\text{pc-to-ivy}}$	1
$w_{\text{sep360-to-bc}}$	10	$w_{\text{ec-to-ngl}}$	3
$w_{\text{sep180-to-bsc}}$	8	$w_{\text{ngl-to-pc}}$	0.8
$w_{\text{sep180-to-olm}}$	30	$w_{\text{bc-to-pc}}$	0.1

where g_{syn} is the synaptic conductance and E_{rev} is the reversal potential. The synaptic conductance is expressed by

$$g_{\text{syn}} = w \cdot DA \cdot g_{\max} \tag{50}$$

where $g_{\max}$ is the maximal synaptic conductance, DA is the dopamine level and w is the synaptic strength. The DA level is always 1 unless mentioned otherwise. The values of the synaptic strengths are given in Table 5. In the model three synaptic currents are included: AMPA, NMDA and GABA_{A}. The values of the synaptic parameters are displayed in Table 3. The gating variable, s, which represents the fraction of the open synaptic ion channels, obeys the following differential equation:

$$\frac{\mathrm{d}s}{\mathrm{d}t} = \alpha \cdot F\left(V_{\text{pre}}\right) \cdot (1 - s) - \beta \cdot s \tag{51}$$

where the normalized concentration of the postsynaptic transmitter-receptor complex, $F(V_{\text{pre}})$, is assumed to be an instantaneous and sigmoid functions of the presynaptic membrane potential

$$F\left(V_{\text{pre}}\right) = 1/\left(1 + e^{-\left(V_{\text{pre}} - \theta\right)/2}\right) \tag{52}$$

where $\theta = 0$ mV is high enough so that the transmitter release occurs only when the presynaptic cell emits a spike (Cutsuridis et al. 2007). The values of the channel opening and closing rates are displayed in Table 6.

Table 6 Cell-to-cell synaptic parameter values. Units: g, mS/cm^2; V, mV; α, 1/ms; β, 1/ms

Name	Value	Name	Value
α_{AAC2PC}	5	β_{AAC2PC}	0.01
α_{BC2PC}	5	β_{BC2PC}	0.015
α_{BSC2PC}	5	β_{BSC2PC}	0.01
α_{OLM2PC}	5	β_{OLM2PC}	0.01
α_{IVY2PC}	1	β_{IVY2PC}	0.0015
α_{BC2BC}	3.5	β_{BC2BC}	0.18
α_{BC2BSC}	3.5	β_{BC2BSC}	0.18
α_{BSC2BC}	3.5	β_{BSC2BC}	0.18
α_{NGL2PC}	5	β_{NGL2PC}	0.015
α_{PC2BC}	20	β_{PC2BC}	0.19
α_{PC2BSC}	20	β_{PC2BSC}	0.19
α_{PC2AAC}	20	β_{PC2AAC}	0.19
α_{PC2IVY}	20	β_{PC2IVY}	0.19
α_{PC2OLM}	20	β_{PC2OLM}	0.19
$\alpha_{OLM2NGL}$	5	$\beta_{OLM2NGL}$	0.01

Pyramidal Cell

Axonic (a) and somatic (s) compartments receive $GABA_A$ inhibition from axo-axonic and basket cells, respectively. The proximal dendritic (pd) compartment receives both AMPA and NMDA excitation from the CA3 Schaffer collateral input and $GABA_A$ inhibition from the bistratified and ivy cells. The distal dendritic (dd) compartment receives AMPA and NMDA excitation from the EC perforant path and $GABA_A$ inhibition from the neurogliaform and OLM cells. Both pd and dd AMPA and NMDA synapses are plastic and change according to the Eqs. (1), (2) and (3).

Axo-axonic and Basket Cells

The somatic (s) compartments of both axo-axonic and basket cells receive AMPA excitation from both the EC perforant and the CA3 Schaffer collateral paths. Axo-axonic cells receive also $GABA_A$ inhibition from the medial septal cells. Basket cells receive $GABA_A$ inhibition from the bistratified cells and the medial septal cells.

Bistratified Cells

The somatic (s) compartment of the bistratified cells receive s AMPA excitation only from the CA3 Schaffer collateral path and $GABA_A$ inhibition from the basket cells and the medial septal cells.

OLM, Neurogliaform and IVY Cells

The IVY cells receive recurrent AMPA excitation from the pyramidal cells and $GABA_A$ inhibition from the medial septal cells. The neurogliaform cells receive AMPA excitation from the EC perforant path and GABA inhibition from OLM cells, whereas the OLM cells receive AMPA excitation from the pyramidal cells and $GABA_A$ inhibition from the septum.

References

Alonso A, García-Austt E (1987) Neuronal sources of theta rhythm in the entorhinal cortex of the rat. II. Phase relations between unit discharges and theta field potentials. Exp Brain Res 67(3):502–509

Baude A, Bleasdale C, Dalezios Y, Somogyi P, Klausberger T (2007) Immunoreactivity for the GABAA receptor alpha1 subunit, somatostatin and Connexin36 distinguishes axoaxonic, basket, and bistratified interneurons of the rat hippocampus. Cerebral Cortex 17(9):2094–2107

Borhegyi Z, Varga V, Szilagyi N, Fabo D, Freund TF (2004) Phase segregation of medial septal GABAergic neurons during hippocampal theta activity. J Neurosci 24(39):8470–8479

Buzsaki G (2002) Theta oscillations in the hippocampus. Neuron 33(3):325–340

Buzsaki G (2011) Hippocampus. Scholarpedia 6(1):1468

Capogna M (2011) Neurogliaform cells and other interneurons of stratum lacunosum-moleculare gate entorhinal-hippocampal dialogue. J Physiol 589(9):1875–1883

Cobb S, Lawrence JJ (2010) Neuromodulation of hippocampal cells and circuits. In: Cutsuridis V et al (eds) Hippocampal Microcircuits: a Computational Modeller's Resource Book. Springer, New York, pp 187–246

Colgin LL, Denninger T, Fyhn M, Hafting T, Bonnevie T, Jensen O, Moser MB, Moser EI (2009) Frequency of gamma oscillations routes flow of information in the hippocampus. Nature 462(19):353–358

Cutsuridis V, Cobb S, Graham BP (2010) Encoding and retrieval in the hippocampal CA1 microcircuit model. Hippocampus 20(3):423–446

Cutsuridis V, Hasselmo M (2012) GABAergic modulation of gating, timing and theta phase precession of hippocampal neuronal activity during theta oscillations. Hippocampus 22:1597–1621

Cutsuridis V, Hasselmo M (2010) Dynamics and function of a CA1 model of the hippocampus during theta and ripples. In: Diamantaras K, Duch W, Iliadis LS (eds) ICANN 2010, Part I, LNCS 6352. Springer, Berlin/Heidelberg, pp 230–240

Cutsuridis V, Kahramanoglou I, Smyrnis N, Evdokimidis I, Perantonis S (2007) A Neural Variable Integrator Model of Decision Making in an Antisaccade Task. Neurocomputing 70(7–9):1390–1402

Dragoi G, Carpi D, Recce M, Csicsvari J, Buzsaki G (1999) Interactions between hippocampus and medial septum during sharp waves and theta oscillation in the behaving rat. J Neurosci 19(14):6191–6199

Ego-Stengel V, Wilson MA (2007) Spatial selectivity and theta phase precession in CA1 interneurons. Hippocampus 17(12):161–174

Gasbarri A, Sulli A, Packard MG (1997) The dopaminergic mesencephalic projections to the hippocampal formation in the rat. Prog Neuropsychopharmacol. Biol Psychiatry 21:1–22

Hafting T, Fynn M, Bonnevie T, Moser MB, Moser EI (2008) Hippocampus-independent phase precession in entorhinal grid cells. Nature 453(7199):1248–1252

Harris KD, Henze DA, Hirase H, Leinekugel Z, Dragoi G, Czurko A, Buzsaki G (2002) Spike train dynamics predicts theta-related phase precession in hippocampal pyramidal cells. Nature 417:738–741

Ito HT, Schuman EM (2007) Frequency-dependent gating of synaptic transmission and plasticity by dopamine. Front Neural Circuits 1(1):1–13

Johnson A, Redish AD (2007) Neural ensembles in CA3 transiently encode paths forward of the animal at a decision point. J Neurosci 27(45):12176–12189

Kamondi A, Acsady L, Wang XJ, Buzsaki G (1998) Theta oscillations in somata and dendrites of hippocampal pyramidal cells in vivo: activity-dependent phase precession of action potentials. Hippocampus 8:244–261

Klausberger T (2009) GABAergic interneurons targeting dendrites of pyramidal cells in the CA1 area of the hippocampus. Eur J Neurosci 30(6):947–957

Klausberger T, Magill PJ, Marton LF, David J, Roberts B, Cobden PM, Buzsaki G, Somogyi P (2003) Brain-state- and cell-type-specific firing of hippocampal interneurons in vivo. Nature 421:844–848

Klausberger T, Marton LF, Baude A, Roberts JD, Magill PJ, Somogyi P (2004) Spike timing of dendrite-targeting bistratified cells during hippocampal network oscillations in vivo. Nat Neurosci 7(1):41–47

Klausberger T, Somogyi P (2008) Neuronal diversity and temporal dynamics: the unity of hippocampal circuit operations. Science 321:53–57

Kunec S, Hasselmo M, Kopell N (2005) Encoding and retrieval in the CA3 region of the hippocampus: a model of theta-phase separation. J Neurophysiol 94(1):70–82

Maurer AP, Cowen SL, Burke SN, Barnes CA, McNaughton BL (2006) Phase precession in hippocampal interneurons showing strong functional coupling to individual pyramidal cells. J Neurosci 26(52):13,485–13,492

Maurer AP, McNaughton BL (2007) Network and intrinsic cellular mechanisms underlying theta phase precession of hippocampal neurons. TINS 30(7):325–333

Mehta MR, Lee AK, Wilson MA (2002) Role of experience and oscillations in transforming a rate code into a temporal code. Nature 417:741–746

Mizuseki K, Sirota A, Pastalkova E, Buzsaki G (2009) Theta oscillations provide temporal windows for local circuit computation in the entorhinal-hippocampal loop. Neuron 64:267–280

Molyneaux BJ, Hasselmo M (2002) $GABA_B$ presynaptic inhibition has an in vivo time constant sufficiently rapid to allow modulation at theta frequency. J Neurophys 87(3):1196–1205

O'Keefe J, Nadel L (1978) The Hippocampus as a Cognitive Map. Oxford University Press, London

O'Keefe J, Recce ML (1993) Phase relationship between hippocampal place units and the EEG theta rhythm. Hippocampus 3(3):317–330

Otmakhova NA, Lisman JE (1999) Dopamine selectively inhibits the direct cortical pathway to the CA1 hippocampal region. J Neurosci 19:1437–1445

Rubin JE, Gerkin RC, Bi GQ, Chow CC (2005) Calcium time course as signal for spike-timing-dependent plasticity. J Neurophysiol 93:2600–2613

Skaggs WE, McNaughton BL, Wilson MA, Barnes CA (1996) Theta phase precession in hippocampal neuronal populations and the compression of temporal sequences. Hippocampus 6:149–172

Somogyi P, Klausberger T (2005) Defined types of cortical interneurons structure space and spike timing in the hippocampus. J Physiol 562(1):9–26

Vida I (2010) Morphology of hippocampal neurons. In: Cutsuridis V et al (eds) Hippocampal microcircuits: A computational modeler's resource book. Springer, USA, pp 27–67

Wilson MA, McNaughton BL (1993) Dynamics of the hippocampal ensemble code for space. Science 261(5124):1055–1058

Zugaro MB, Monconduit L, Buzsaki G (2005) Spike phase precession persists after transient intrahippocampal perturbation. Nat Neurosci 8(1):67–71

A Model for Grid Firing and Theta-Nested Gamma Oscillations in Layer 2 of the Medial Entorhinal Cortex

Matt Nolan

Abstract Grid cell circuits in the superficial layers of the medial entorhinal cortex have become a focus of considerable experimental and theoretical attention as a model for investigating neural mechanisms of cognition. Together, grid firing and associated theta-nested gamma oscillations can be considered as a minimal set of phenomena which a satisfactory model of superficial entorhinal circuits should account for. The model presented here focuses on stellate cells in layer 2 (L2SCs) and their indirect interactions through inhibitory interneurons. In the model, L2SCs and inhibitory interneurons are represented as distinct excitatory and inhibitory cell populations. To enable investigation of network activity patterns as well as network computations, the model is implemented using spiking exponential integrate and fire neurons. The model demonstrates that indirect interactions between L2SCs mediated via inhibitory neurons are sufficient for emergence of grid firing and nested game oscillations.

Overview

What Is the Model

The medial entorhinal cortex (MEC) is a critical brain structure for spatial navigation and memory (Steffenach et al. 2005). Following the discovery of grid cells, it has become a focus of considerable experimental and theoretical attention as a model circuit for investigating neural mechanisms of cognition (Moser and Moser 2013). Grid cells are neurons that encode location through grid-like spatial firing fields (Fyhn et al. 2004; Hafting et al. 2005). Grid fields have been recorded from neurons in the MEC and adjacent parahippocampal structures (Boccara et al. 2010), with the highest proportion of grid cells in layer 2 of the MEC (Sargolini et al. 2006). During behaviors in which grid firing takes place, field potential oscillations

M. Nolan (✉)
Centre for Integrative Physiology, University of Edinburgh, Edinburgh, UK
e-mail: mattnolan@ed.ac.uk

V. Cutsuridis et al. (eds.), *Hippocampal Microcircuits*, Springer Series in Computational Neuroscience, https://doi.org/10.1007/978-3-319-99103-0_15

reflecting network activity in theta (6–12 Hz) and gamma (60–120 Hz) bands can also be recorded from layer 2 of the MEC (Chrobak and Buzsaki 1998; Colgin et al. 2009). The gamma band oscillations have amplitude that is modulated according to theta phase (Chrobak and Buzsaki 1998; Colgin et al. 2009). Thus, the gamma signal is largest at times close to the trough of theta and smallest around the peak of theta. Together, grid firing and theta-nested gamma oscillations can be considered as a minimal set of phenomena that a satisfactory model of layer 2 circuits should account for.

Within layer 2 of the MEC, there are two principle cell types. Layer 2 stellate cells (L2SCs), also previously called ocean cells, send axonal projections to the dentate gyrus and CA3 regions of the hippocampus and to deep layers of the MEC (Alonso and Klink 1993; Jones 1994; Klink and Alonso 1997; Pastoll et al. 2012; Sürmeli et al. 2015; Varga et al. 2010). Layer 2 pyramidal cells (L2PCs) send axonal projections to the CA1 region of the hippocampus (Alonso and Klink 1993; Kitamura et al. 2015; Klink and Alonso 1997; Sürmeli et al. 2015; Varga et al. 2010). Intermediate cell populations have also recently been identified, but their projections are unknown (Fuchs et al. 2016). L2SCs have been most extensively studied, and a good deal is known about their intrinsic electrophysiological properties (Pastoll et al. 2012). L2SCs and L2PCs can be distinguished at a molecular level by their respective expression of the proteins reelin and calbindin (Kitamura et al. 2014; Ray et al. 2014; Sürmeli et al. 2015; Varga et al. 2010). They are also distinguished by the activity of promoters that have been used to genetically identify each cell population using Cre driver lines (Fuchs et al. 2016; Kitamura et al. 2014; Sürmeli et al. 2015). L2SCs are unusual in comparison with many cortical excitatory neurons in that they do not appear to make direct local connections with one another (Couey et al. 2013; Dhillon and Jones 2000; Fuchs et al. 2016; Pastoll et al. 2013). Instead, they interact indirectly via local inhibitory interneurons. The model addresses the general question of whether L2SCs and their indirect interactions through inhibitory interneurons are sufficient to account for grid firing or nested gamma oscillations.

The model focuses on L2SCs and their indirect interactions through inhibitory interneurons (Pastoll et al. 2013). In the model, L2SCs and inhibitory interneurons are represented as distinct excitatory (E) and inhibitory (I) cell populations. To investigate consequences of indirect communication mediated via interneurons, in initial versions of the model, E cells are only allowed to synapse with I cells, and I cells are only allowed to synapse with E cells. To enable investigation of network activity patterns, as well as network computations, the model is implemented using spiking exponential integrate and fire neurons.

Questions Addressed

Development of the model was motivated by three specific questions. First, can excitatory-inhibitory (E-I) interactions between L2SCs and local interneurons account for grid firing patterns? Second, can E-I interactions account for theta-

nested gamma oscillations? Third, if grid firing and nested gamma oscillations share a common mechanism, then how are they related to one another?

Previously, models with continuous attractor network dynamics had been shown to account for grid firing (Burak and Fiete 2009; Fuhs and Touretzky 2006; Guanella et al. 2007). To do this, they were configured to generate a spatial code by integrating velocity inputs (McNaughton et al. 2006; Samsonovich and McNaughton 1997; Zhang 1996). Periodic spatial firing emerged either through cyclic movement of activity bumps in periodic networks with a toroidal structure (Guanella et al. 2007; Samsonovich and McNaughton 1997) or through competitive interactions between multiple activity bumps on an extended neural sheet (Burak and Fiete 2009; Fuhs and Touretzky 2006). However, these networks were either implemented with local excitatory interactions or with purely inhibitory cell populations. In contrast, our experimental investigations indicated that L2SCs, which are excitatory, are only able to interact indirectly via inhibitory interneurons (Pastoll et al. 2013). It was not immediately clear to us whether this connectivity would be able to support grid firing under physiologically plausible network configurations. Nevertheless, we suspected that if this is possible, then models based on this connectivity might lead to new mechanistic insights and predictions.

Many previous theoretical studies had also shown that E-I interactions could generate gamma oscillations (Tiesinga and Sejnowski 2009; Whittington et al. 2011). Our experimental data indicated that local optogenetic activation of layer 2 of the MEC is sufficient to generate nested gamma oscillations (Pastoll et al. 2013). However, it had not been shown that this observation could be accounted for by E-I models. More challengingly, it was not clear whether a single model based on E-I connectivity would be able to explain both grid firing and theta-nested gamma oscillations.

Level of Detail and Rationale

We chose to implement the model using exponential integrate and fire (EIF) neurons (Fourcaud-Trocme et al. 2003), with membrane and synaptic time constants approximating our experimental observations (Pastoll et al. 2013). We introduced separate populations of excitatory neurons, to simulate L2SCs, and inhibitory neurons, to simulate local interneurons. While previous studies had shown that grid firing could be accounted for in models based solely on firing rate equations, we wanted to approximate physiological membrane potential dynamics for two reasons. First, we reasoned that this would be required to account for gamma frequency oscillations. Second, we were concerned that attractor network models of grid firing may be sensitive to noise but that this may be overlooked in previous more abstract models, perhaps leading to overconfidence in the models' stability in physiological conditions. While we, and others, have previously implemented detailed ionic conductance-based models of L2SCs (Dodson et al. 2011; Dudman and Nolan 2009; Fransen et al. 2004; Garden et al. 2008), we did not use this level of detail in the

model for three reasons. First, our aim was to establish whether the general network architecture we had found experimentally could account for behaviorally relevant phenomena. Our findings would therefore be more robust if they did not require fine-tuning of ionic conductances. Second, while ionic mechanisms of L2SCs have received considerable experimental attention, and previous models can account for their subthreshold dynamics and spiking properties, we nevertheless still lack a basic understanding of their dendritic integrative mechanisms, and so more detailed models would at present be under constrained. Third, a more pragmatic issue is that we wished to simulate networks of several thousand cells and in later studies to systematically investigate the parameter space of these networks. Therefore, the shorter simulation time from use of EIF rather than more detailed models was a clear advantage.

The Model

Model Components and Parameters

Neurons

The model contains a population of inhibitory neurons and a population of excitatory neurons. Each neuron is implemented as an EIF unit, such that

$$C\frac{\partial V_{\mathrm{m}}}{\partial t} = g_{\mathrm{L}}\left(E_{\mathrm{L}} - V_{\mathrm{m}}\right) + g_{\mathrm{ahp}}\left(E_{\mathrm{ahp}} - V_{\mathrm{m}}\right) + g_{\mathrm{L}}\Delta_{\mathrm{T}}\exp\left(\frac{V_{\mathrm{m}} - V_{\mathrm{t}}}{\Delta_{\mathrm{T}}}\right) + \mathrm{I}_{\mathrm{syn}} + \mathrm{I}_{\mathrm{ext}} + \eta \quad (1)$$

where C is the membrane capacitance; V_{m} is the membrane potential; g_{L} and E_{L} are the leak conductance and its reversal potential; g_{ahp} and $\mathrm{E}_{\mathrm{ahp}}$ are the after hyperpolarization conductance and its reversal potential; Δ_{T} and V_{t} are constants that determine the sharpness of the action potential rise phase and its threshold for initiation; $\mathrm{I}_{\mathrm{syn}}$ is the local synaptic current; $\mathrm{I}_{\mathrm{ext}}$ is the externally applied current, which can include a theta-modulated input, a velocity input, and simulated inputs from place cells; and η is the noise current. The parameters for each type of neuron were chosen by hand to approximate the dynamics of the corresponding cell type observed during patch-clamp recordings in brain slices.

Internal Connectivity (Synapses)

The synaptic input to each neuron was modeled as the sum of several conductances.

$$\mathrm{I}_{\mathrm{syn}} = g_{\mathrm{GABA}}(t)\left(\mathrm{E}_{\mathrm{GABA_A}} - V_{\mathrm{m}}\right) + g_{\mathrm{AMPA}}(t)\left(\mathrm{E}_{\mathrm{AMPA}} - V_{\mathrm{m}}\right) + g_{\mathrm{NMDA}}(t)\left(\mathrm{E}_{\mathrm{NMDA}} - V_{\mathrm{m}}\right) \quad (2)$$

Synaptic connections from E to I cells are modeled as a sum of instantaneously activating and fast-decaying (g_{AMPA}) and slow-decaying (g_{NMDA}) conductances. While the peak NMDA component is only 2% of the peak AMPA conductance, its prolonged time course is important for maintenance of network states across the inhibitory phase of the theta cycle. Both AMPA and NMDA conductances are modeled as voltage-independent. We omit the known voltage dependence of NMDA conductances in part for simplicity and in part because it is the slow kinetics of NMDA conductances rather than their voltage dependence that is relevant to their primary role in the model, which is to maintain activity across the full theta cycle. Synaptic connections from I to E cells are modeled with a single (GABA) conductance with time course described by the difference between two exponentials, so as to give a rapid rise and slower decay. The GABA conductance has a reversal potential ($\mathrm{E_{GABA}}$) of −75 mV, whereas the AMPA and NMDA conductances have a reversal potential of 0 mV ($\mathrm{E_{AMPA}}$ and $\mathrm{E_{NMDA}}$).

Internal Connectivity (Topology)

Generation of attractor states and grid firing depends upon the structure of the E−I connectivity in the model. In network space, each population of neurons can be conceived of as being uniformly distributed across a sheet that is wrapped onto on a twisted torus. In our initial version of the model, the sheet of E cells has dimensions of 68 × 58, and the sheet of I cells has dimensions of 34 × 30. The normalized dimensions of the torus are 1 × 0.5sqrt(3) (cf. (Guanella et al. 2007)). The model can be connected so that E- > I connections are local and I- > E connections have a surround organization (I-surround configuration) or vice versa, so that I- > E connections are local and E- > I connections have a surround organization (E-surround configuration) (Pastoll et al. 2013).

For connections from E to I cells in the E-surround configuration,

$$W_{ij} = G_{\mathrm{exc}} \exp\left(\frac{-(d\,(i,\,j,\,C) - \mu_{\mathrm{exc}})^2}{2\sigma_{\mathrm{exc}}^2}\right) \tag{3}$$

$$d\,(i,\,j,\,C) = \left|u_i - u_j - Ce_p\right| \tag{4}$$

where W_{ij} is the AMPA (or NMDA) conductance of the connection from excitatory neuron i to inhibitory neuron j, G_{exc} is the maximal AMPA (or NMDA) conductance, d is the distance between neurons i and j on the network torus, μ_{exc} is the diameter of the connectivity ring, σ_{exc} is the width of the connectivity ring, u_i and u_j are vectors for the positions of neuron i and neuron j, C is an offset in the excitatory profile used to ensure translation of the activity bump in response to velocity inputs, and e_{p} is a unit vector oriented in the direction of the excitatory neuron's preferred movement direction.

For connections from I to E cells,

$$U_{ij} = G_{\text{inh}} \exp\left(\frac{-(d\,(i,\,j,\,C))^2}{2\sigma_{\text{inh}}^2}\right) \tag{5}$$

where U_{ij} is the GABA conductance of the connection from inhibitory neuron i to excitatory neuron j, G_{inh} is the maximal AMPA conductance, and other parameters are as for Eq. 3.

This topography can be implemented either through variation in the strength of connections as shown here or through variation in the probability of connections (Solanka et al. 2015). In our initial versions of the model, excitatory neurons make synaptic connections exclusively with inhibitory neurons, and inhibitory neurons make connections exclusively with excitatory neurons. Grid firing and gamma oscillations continue to be generated when E-E and I-I connections are added to the model, although their properties may be modified (Solanka et al. 2015).

External Inputs

The external input to the model I_{ext} is the sum of four components.

$$\mathrm{I}_{\text{ext}} = \mathrm{I}_{\text{const}}(t) + \mathrm{I}_{\theta}(t) + \mathrm{I}_{\text{vel}}(t) + \mathrm{I}_{\text{place}}(t) \tag{6}$$

A theta-modulated current (I_{θ}) input and a constant current input ($\mathrm{I}_{\text{const}}$) to E and I cells are used, respectively, to generate theta frequency activation of the network and to drive the network toward an active state. For the theta-modulated current,

$$I_{\theta}(t) = \frac{A_{\theta}}{2}\left(1 + \sin\left(2\pi f_{\theta} t + \phi_{\theta}\right)\right) \tag{7}$$

where A_{θ}, f_{θ}, and $\emptyset_{\theta}$, respectively, provide the amplitude, frequency, and phase of the theta oscillation.

A velocity-modulated input is used to drive bumps of activity around the network according to the simulated animal's speed and direction of movement. For a given neuron i,

$$\mathrm{I}_{\text{vel}}^{i}(t) = C_{\text{v}}\mathbf{v}(t) \cdot \mathbf{e}_{\text{p}}^{i} \tag{8}$$

$$C_{\text{v}} = \frac{N_{\text{x}}}{a\lambda_{\text{grid}}} \tag{9}$$

Here, C_{v} is the gain of the velocity input, N_{x} is the number of neurons through which the bump must travel so as to return to its starting position on the torus, a is the slope of the relationship between speed of movement of the bump and real-world

movement, and λ_{grid} is the grid field spacing. For simplicity, velocity-modulated inputs are tuned to one of four movement directions at 90 degrees from one another. Each neuron receives input tuned to only one of these directions. The mapping of the output from that neuron to cells in the other layer is shifted so that when the neuron becomes active, it moves the bump through the network in a direction appropriate for its input. The model can generate grid firing patterns when velocity-modulated inputs connected to either E or I cells (Pastoll et al. 2013).

Finally, E cells in the model receive input from place cells (I_{place}). In the simplest implementation, the summed place cell input to each neuron has spatial organization similar to the grid firing field of the E cell. In our initial implementation of the model, this input is active only every 10 s and acts to oppose drift in the grid representation that otherwise arises through intrinsic dynamics of the circuit (Pastoll et al. 2013). It is important to note that if this input were continuously active and were implemented with sufficiently strong connections, then it would be able to drive grid firing irrespective of the velocity integration mechanisms operating within the E-I circuit.

Noise Sources

Noise in the network (η) is simulated by injection into each neuron of independent Gaussian-distributed current, with zero mean and standard deviation (σ) typically in the range 0–300 pA. In the initial version of the model, σ was adjusted so that for each neuron, the resting fluctuations in its membrane potential had an amplitude of 2 mV (Pastoll et al. 2013). The level of intrinsic noise may be a critical functional parameter, as changing σ impacts grid firing patterns and emergence of gamma frequency network oscillations (Solanka et al. 2015).

Code for versions of the model used to generate data in Pastoll et al. (2013) is available from https://senselab.med.yale.edu/ModelDB/ShowModel.cshtml?model=150031. Code for versions of the model used to generate data in Solanka et al. (2015) is available from https://senselab.med.yale.edu/ModelDB/ShowModel.cshtml?model=183017. Additional code and documentation are available from https://github.com/MattNolanLab.

Limited Results

Network Attractor States and Grid Firing

In the absence of any place or velocity input, the network spontaneously generates an attractor state, which manifests as a bump of activity on the sheet of E cells (Fig. 1a). When movement is simulated by modulation of the velocity inputs, then the activity bump is moved around the sheet. Plotting the activity of individual neurons as a function of the simulated location produces grid firing fields (Fig.

Table 1 Biophysical and input properties of E and I cells

Property	Symbol (units)	Value (E cells)	Value (I cells)
Membrane capacitance	C (pF)	211.4	227.3
Leak conductance	g_L (nS)	22.73	22.73
Leak reversal potential	E_L (mV)	−68.5	−60
Maximal AHP conductance	g_{ahp_max} (nS)	5	22
AHP decay time constant	τ_{ahp} (ms)	10	7.5
AHP reversal potential	E_{ahp} (mV)	−80	−60
Action potential slope factor	Δ_T (mV)	0.4	0.4
Action potential threshold	V_t (mV)	−50	−45
Maximal GABA conductance	G_{inh} (nS)	2.12	–
GABA reversal potential	E_{GABA} (mV)	−75	–
GABA activation time constant	τ_{act_GABA} (ms)	0.1	–
GABA decay time constant	τ_{dec_GABA} (ms)	5	–
Maximal AMPA conductance	G_{AMPA} (pS)	–	355
AMPA reversal potential	E_{AMPA} (mV)	–	0
AMPA decay time constant	τ_{dec_AMPA} (ms)	–	1
Maximal NMDA conductance	G_{NMDA} (pS)	–	7.1
NMDA reversal potential	E_{NMDA} (mV)	–	0
NMDA time constant	τ_{dec_NMDA} (ms)	–	100
Constant input current	I_{const}	300	200
Theta current amplitude	A_θ	375	25
Theta current frequency	f_θ	8	8
Theta current phase offset	ϕ_θ	0	0

Properties are for the version of the model published in Pastoll et al. (2013). In later iterations of the model, some properties and their implementation are modified

1a). Because the bump velocity is linear as a function of movement speed, grid patterns are maintained across a range of running speeds corresponding to those of freely behaving animals. Thus, playing experimentally recorded trajectories into the model generates grid firing patterns in the activity of individual E cells.

The firing pattern generated by I cells depends on the configuration of the model (Pastoll et al. 2013). In the I-surround configuration, I cells also generate grid firing fields. In this configuration, the sheet of I cells contains a regular activity bump, with its maxima at a location in neural space corresponding to the position of the center of the activity bump on the E sheet. If the network is in the E-surround configuration, then the I cells have inverted grid firing fields (Fig. 1a). In this configuration, the sheet of I cells contains an inverted activity bump, with its minima at a location in neural space corresponding to the position of the center of the activity bump on the E sheet. The network continues to generate grid fields if the theta input is switched off (Pastoll et al. 2013). In contrast, if the intermittent place cell input is switched off, the grid pattern becomes smeared because of drift in the position of the activity bump.

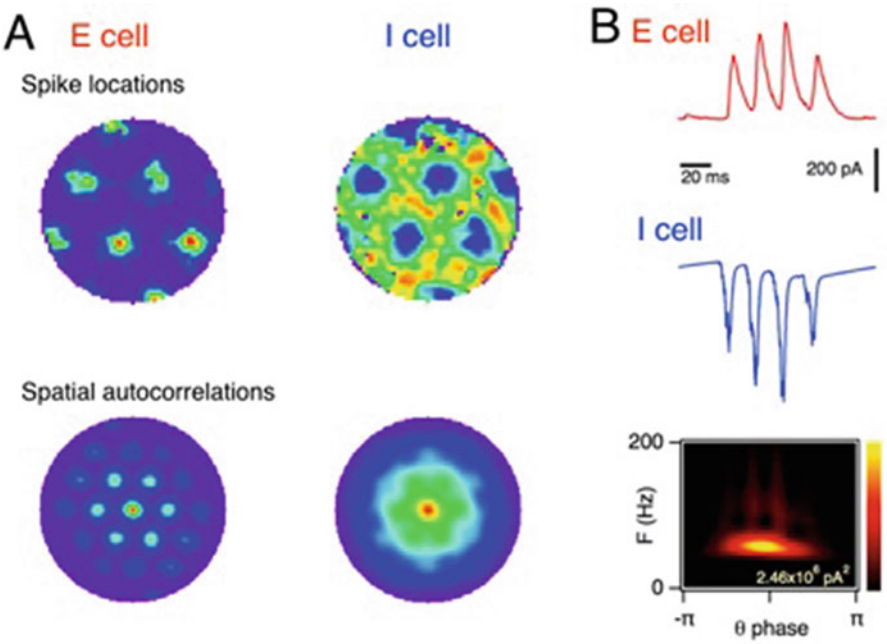

Fig. 1 Continuous E-I network attractors account for grid firing and theta-nested gamma oscillations. (**a**) Heat maps of firing of E cells (upper left) and I cells (upper right) as a function of location. The sixfold rotational symmetry shown in the spatial autocorrelation for the E cell (lower left) is a characteristic of grid firing. While the firing fields of I cells have an inverted grid-like organization, this symmetry appears to be absent from their spatial autocorrelation (lower right). (**b**) Inhibitory synaptic input to an E cell, excitatory synaptic input to an I cell, and spectrogram of the E cell membrane current for a single theta cycle. The network generates four cycles of gamma frequency activity during the theta cycle. (Data are from Pastoll et al. 2013)

Gamma Oscillations

Activation of the model leads to gamma frequency network oscillations in addition to generation of network attractor states (Fig. 1b). When the model receives theta frequency-modulated input, then the amplitude of the gamma oscillations becomes modulated according to the theta phase. The properties of these theta-nested gamma oscillations closely resemble observations made while recording from superficial layers of the MEC in behaving animals (cf. Chrobak and Buzsaki 1998). Each gamma cycle is initiated by spiking in a subset of E cells, resulting in rapid excitatory input to I cells. This triggers spiking of a majority of I cells at a relatively short latency from the E cell spikes. I cell spiking curtails any further activity of E cells within the gamma cycle. The next gamma cycle initiates as the inhibition decays. This corresponds to E-I gamma oscillations described in a number of other

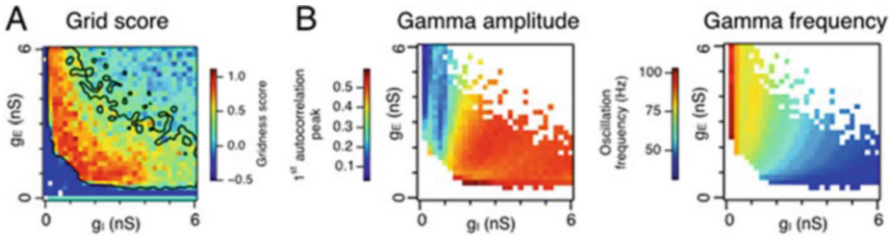

Fig. 2 Adjustment of recurrent connectivity enables tuning of gamma oscillations while maintaining grid firing. (**a**) Grid score as a function of the strength of recurrent excitatory (g_E) and inhibitory (g_I) connections. The black lines indicate regions where the gridness score is >0.5. The grid score is obtained by first calculating the spatial autocorrelation of the firing field, then rotating the autocorrelation in steps of 3 degrees, and for each rotation calculating a Pearson correlation coefficient with the original autocorrelation. The grid score is then calculated as the maximum values at 30-, 90-, and 150-degree rotation minus the minimum values at 60- and 120-degree rotation. (**b–c**) Amplitude of the first autocorrelation peak (**b**) and oscillation frequency (**c**) as a function of the strength of recurrent excitatory and inhibitory connections for networks in which the gridness score is >0.5. Results are from simulations of models in which intrinsic noise for each neuron has a standard deviation of 150 pA. (Data are from Solanka et al. 2015)

brain systems. Depending on the model parameters, the gamma oscillations can have frequency anywhere across the high gamma range (60–120 Hz) (Solanka et al. 2015) (Fig. 2).

Model Justification

Data for Model Components and Parameter Values

Neurons

The somatic integrative properties of L2SCs have been well studied with whole-cell and intracellular recordings in mouse and rat brain slices (reviewed in Pastoll et al. (2012)). Several key properties vary systematically according to the location of L2SCs along the dorsoventral axis of the MEC. For example, input resistance ranges from approximately 20 MΩ in dorsal neurons to approximately 80 MΩ in ventral neurons (Garden et al. 2008). Similarly, membrane time constants range from 6 ms dorsally to 15 ms ventrally (Garden et al. 2008). We set the parameter values of E cells so that the dynamics of synaptic integration approximate our experimental observations from more dorsally located stellate cells. Thus, the resting membrane potential is set at −68.5 mV, the spike threshold at −50 mV, and the average membrane time constant at 9.3 ms. Following an action potential, the membrane potential in the model resets to −68.5 mV. This is substantially more negative than the afterhyperpolarization observed experimentally but was required to obtain relatively slow spike rates observed experimentally within the constraints of the EIF

model. The model E cells also do not have resonant properties reported for L2SCs (Dickson et al. 2000; Giocomo et al. 2007; Nolan et al. 2007).

While the membrane properties of interneurons in L2 of the MEC are less well studied than those of L2SCs, our patch-clamp recordings in mouse brain slices indicated that fast-spiking interneurons in L2 have membrane properties similar to those in other brain areas (Pastoll et al. 2013). We therefore selected parameters to enable I cells to integrate synaptic input more rapidly than E cells and to fire at higher frequencies. Thus, the membrane potential is set at −60 mV, the spike threshold at −45 mV, and the average membrane time constant at 7.5 ms. The afterhyperpolarization conductance also had faster kinetics than that of the E cells and a less negative equilibrium potential.

Internal Connectivity (Synapses)

Voltage-clamp data describing conductances specifically for L2SC to interneuron or interneuron to L2SC connections is not currently available. We therefore based the kinetics of excitatory and inhibitory conductances on parameters used in existing models for other brain areas (e.g., Bartos et al. 2001). The strength of conductances was set so that the range of membrane potential changes associated with each input approximated our observations from simultaneous recordings from pairs of L2SCs and fast-spiking interneurons.

Internal Connectivity (Topology)

There is currently no data on the network-wide topology of connectivity in L2 of the MEC. The connectivity profiles that we selected – surround excitation/inhibition and local inhibition/excitation – instead came from theoretical considerations. In particular, we aimed for connectivity that would result in emergence of a single activity bump on the network sheet. Similarly, the twisted torus configuration of the two neural sheets was selected in order to achieve repeated firing fields with a grid-like organization (cf. Guanella et al. 2007). It is noteworthy that more recent modeling studies suggest that this type of network structure might emerge through spike timing-dependent plasticity processes operating during development of the circuit (Widloski and Fiete 2014).

External Inputs

Constant Current Because in brain slices L2SCs and fast-spiking interneurons are silent with negative resting membrane potentials (Pastoll et al. 2013), whereas in behaving animals these neurons have more depolarized membrane potentials and can fire action potentials (Domnisoru et al. 2013; Schmidt-Hieber and Hausser 2013), we reasoned that they must receive excitatory drive, which we simulate using

a constant offset current. This drive may arise from the hippocampus, as inactivation of the CA1 region reduces the firing rate of grid cells in layer 2 (Bonnevie et al. 2013). It is not clear whether this reflects a direct input to L2 or relay of synaptic signals via the deep layers of the MEC. Anatomical and optogenetic experiments demonstrate projections from CA1 and the subiculum to neurons in deep layers of the MEC (Sürmeli et al. 2015). There is evidence from transsynaptic tracing experiments that CA2 neurons project to L2SCs (Rowland et al. 2013), although we have not been able to find evidence for axons in L2 following labeling of neurons in CA2 (unpublished).

Theta-Modulated Current The membrane potential and spike firing of L2SCs and fast-spiking interneurons are modulated at theta frequency in behaving animals (Domnisoru et al. 2013; Schmidt-Hieber and Hausser 2013). In the model, we assume this is an externally imposed theta-driven oscillation. For example, it may originate from neurons in layer 3, which have strongly theta-modulated firing and are thought to project to layer 2 (Beed et al. 2010; Hafting et al. 2008; Mizuseki et al. 2009).

Velocity Signals The nature of the velocity signal required for models of path integration within the MEC is unclear. This is therefore a theoretical assumption of the model that requires experimental investigation. Recently characterized speed cells in the MEC may form a component of the velocity signal required for path integration (Kropff et al. 2015). It seems that the majority of head direction cells are unlikely to have appropriate firing properties to support path integration as head direction is often distinct from heading direction (Raudies et al. 2015). Thus, in the future, it will be important to identify heading direction cells and to establish whether they connect to grid cell networks.

Spatial Inputs We assume that spatial signals required to oppose drift in the grid representation arise from place cells in the hippocampus (cf. (Guanella et al. 2007)). Loss of grid firing following inactivation of CA1 neurons is consistent with an important role for hippocampal inputs (Bonnevie et al. 2013). As we mention above, hippocampal inputs to the MEC could be relayed via deep layers or may possibly project directly from CA2.

Noise Sources

Noise within the nervous system arises from stochastic ion channel gating and from the stochastic dynamics of neurotransmission (Faisal et al. 2008). In the model, these noise sources are not implemented directly, as this would add considerably to the computational resources required for simulation. Instead the standard deviation of a noisy current source was adjusted so that the membrane potential variability approximates that of in vivo recordings.

Selected Results

Common Mechanism for Grid Firing and Gamma Oscillations

The primary goal for the initial development of the model was to establish whether nested gamma oscillations and grid firing fields could arise from a shared synaptic mechanism (Pastoll et al. 2013). The model establishes in principle the feasibility of this idea (Fig. 1). Moreover, it does so using parameters that at a first pass are well constrained by biological data. The further successes of the model arise both from predictions resulting from exploration of its dynamics and from identification of key areas for which experimental data is at present lacking (Pastoll et al. 2013; Solanka et al. 2015).

Relationship Between E-I Strength, Network Computation, and Network Oscillations

A major goal for neuroscience is to establish mechanisms for cognitive phenomena and disorders. Many studies have associated cognitive measures with synaptic properties and with observations of network activity (Uhlhaas and Singer 2012). However, moving from observed correlations to convincing mechanistic explanations is challenging. The model takes a step in this direction by allowing exploration of the effects of systematic variation of synaptic and cellular parameters on gamma oscillations on the one hand and on path integration as a cognitive computation on the other (Solanka et al. 2015). We find that a wide range of excitatory and inhibitory synaptic strengths support grid firing and gamma oscillatory activity (Fig. 2). However, within this range, variation in excitatory or inhibitory synaptic strengths can be used to tune gamma frequency and power (Fig. 2b). This finding has two general implications. First, it suggests that gamma oscillations are not a reliable index of rate-coded computations, as grid firing is possible across a wide range of gamma frequency and power. Second, it suggests that fine-tuning of gamma by modulating local synaptic strength could be used to multiplex gamma coherence-based codes within rate code firing patterns generated by continuous attractor networks.

Assumptions About Connectivity

The assumptions required to generate the model highlight areas for further experimental and theoretical work. A key assumption is that the model at present is inspired solely by connectivity between stellate cells and interneurons in layer 2 of the MEC. The model neglects connectivity between L2SCs and pyramidal cells also found in layer 2 (Fuchs et al. 2016). It also does not include connectivity between L2SCs and neurons in other layers of the MEC (Beed et al. 2010; Sürmeli et al. 2015). In this context, recently discovered connections between L2SCs and

principle cells in layer 5b may be particularly important (Sürmeli et al. 2015). If the neurons in layer 5b that receive input from L2SCs are also part of deep layer circuits that project to stellate cells, then it may be important for future models to incorporate feedback loops operating across layers of the MEC.

A second key assumption is that the connections within the model that enable the emergence of attractor states and that cause translation of attractor bumps with movement are based on theoretical considerations and are not yet constrained by experimental data. This assumption applies to the local recurrent connections (both excitatory to inhibitory and inhibitory to excitatory), the velocity inputs, and the spatial inputs. It will be important for future experimental work to address the basis for these assumptions.

The Model Does Not Account for Theta Phase Precession

While the model successfully explains rate-coded grid firing and theta-nested gamma oscillations through a shared circuit mechanism, it does not yet account for the experimentally observed timing of grid cell firing relative to the theta rhythm. Thus, experimental data indicates that a subset of grid cells in layer 2 fire action potentials at phases of the theta rhythm that advance with movement through the cell's firing field (Hafting et al. 2008). This phase precession can be accounted for by models for grid firing based on oscillatory interference (O'Keefe and Burgess 2005) and by hybrid models that combine attractor networks with oscillatory interference mechanisms (Bush and Burgess 2014; Schmidt-Hieber and Hausser 2013). Phase precession has also been demonstrated in linear attractor network models of grid firing (Navratilova et al. 2012).

The Future

Model Extensions

Future development of the model will benefit from exploration of interactions between additional cell populations. Existing experimental data suggest two areas that could be explored. First, additional intra-layer mechanisms could be incorporated by addition of cell populations representing L2PCs and distinct interneuron populations found in L2 (Fuchs et al. 2016; Varga et al. 2010). Second, interlayer mechanisms could be incorporated, for example, to investigate interactions of L2SCs with cell populations in deeper layers (Sürmeli et al. 2015). An interesting study using a simpler model has recently shown that a network attractor containing structured connectivity required to generate grid firing patterns can in addition drive grid firing in a downstream attractor network that would not on its own generate grid firing (Tocker et al. 2015). While in this study the upstream attractor was

interpreted as corresponding to circuits in deep entorhinal layers, the discovery of connections from L2SCs to L5b suggests that a core attractor in L2 could equally entrain cells in deeper layers (Sürmeli et al. 2015). Exploration of extended versions of the model that account for this connectivity may generate predictions that enable these possibilities to be tested experimentally.

New Uses of Model

There are a number of questions for which the model, and its future extensions, may be useful:

1. How are spatial representations anchored to an environment? In the current version of the model, pre-configured place cell inputs are used to anchor representations to the environment. Future uses of the model might include investigation of how representations become anchored after entry into novel environments.
2. How are grid representations maintained across theta cycles? Neural inactivation during the positive phase of theta can destabilize the network attractor. In the model, slow NMDA conductances are used to sustain representations (Pastoll et al. 2013), while other studies have proposed roles for slow potassium conductances (Navratilova et al. 2012). The model may be used in the future to distinguish these and other possibilities.
3. How is theta phase precession generated? Related models suggest ways for generation of phase precession in continuous attractor networks (Navratilova et al. 2012). Future investigation will be required to establish how this can be achieved in E-I networks that generate gamma oscillatory activity and two-dimensional grid firing. A critical and as yet relatively unexplored goal is likely to be to establish how to do this efficiently using as few neurons as possible.

Finally, it may be that the principles established through models that focus on the MEC can be applied to other brain systems. Because of the robustness of spatial firing fields in the MEC, it is attractive as a potentially tractable system for understanding higher order cortical computations in general (Moser and Moser 2013). The model shows how populations of interacting inhibitory and excitatory neurons can integrate time-varying input signals, with the output expressed as a rate-coded population code. In principle, similar circuitry could implement this generic computation in other parts of the brain. In this case, the output would not be rate-coded grid fields but instead would reflect the nature of the information processed. It may be interesting in the future to establish whether such computations are carried out in a way that is consistent with the predictions of the model.

References

Alonso A, Klink R (1993) Differential electroresponsiveness of stellate and pyramidal-like cells of medial entorhinal cortex layer II. J Neurophysiol 70:128–143

Bartos M, Vida I, Frotscher M, Geiger JR, Jonas P (2001) Rapid signaling at inhibitory synapses in a dentate gyrus interneuron network. J Neurosci 21:2687–2698

Beed P, Bendels MH, Wiegand HF, Leibold C, Johenning FW, Schmitz D (2010) Analysis of excitatory microcircuitry in the medial entorhinal cortex reveals cell-type-specific differences. Neuron 68:1059–1066

Boccara CN, Sargolini F, Thoresen VH, Solstad T, Witter MP, Moser EI, Moser MB (2010) Grid cells in pre- and parasubiculum. Nat Neurosci 13:987–994

Bonnevie T, Dunn B, Fyhn M, Hafting T, Derdikman D, Kubie JL, Roudi Y, Moser EI, Moser MB (2013) Grid cells require excitatory drive from the hippocampus. Nat Neurosci 16:309–317

Burak Y, Fiete IR (2009) Accurate path integration in continuous attractor network models of grid cells. PLoS Comput Biol 5:e1000291

Bush D, Burgess N (2014) A hybrid oscillatory interference/continuous attractor network model of grid cell firing. J Neurosci 34:5065–5079

Chrobak JJ, Buzsaki G (1998) Gamma oscillations in the entorhinal cortex of the freely behaving rat. J Neurosci 18:388–398

Colgin LL, Denninger T, Fyhn M, Hafting T, Bonnevie T, Jensen O, Moser MB, Moser EI (2009) Frequency of gamma oscillations routes flow of information in the hippocampus. Nature 462:353–357

Couey JJ, Witoelar A, Zhang SJ, Zheng K, Ye J, Dunn B, Czajkowski R, Moser MB, Moser EI, Roudi Y et al (2013) Recurrent inhibitory circuitry as a mechanism for grid formation. Nat Neurosci 16:318–324

Dhillon A, Jones RS (2000) Laminar differences in recurrent excitatory transmission in the rat entorhinal cortex in vitro. Neuroscience 99:413–422

Dickson CT, Magistretti J, Shalinsky MH, Fransen E, Hasselmo ME, Alonso A (2000) Properties and role of I(h) in the pacing of subthreshold oscillations in entorhinal cortex layer II neurons. J Neurophysiol 83:2562–2579

Dodson PD, Pastoll H, Nolan MF (2011) Dorsal-ventral organization of theta-like activity intrinsic to entorhinal stellate neurons is mediated by differences in stochastic current fluctuations. J Physiol 589:2993–3008

Domnisoru C, Kinkhabwala AA, Tank DW (2013) Membrane potential dynamics of grid cells. Nature 495:199–204

Dudman JT, Nolan MF (2009) Stochastically gating ion channels enable patterned spike firing through activity-dependent modulation of spike probability. PLoS Comput Biol 5:e1000290

Faisal AA, Selen LP, Wolpert DM (2008) Noise in the nervous system. Nat Rev Neurosci 9:292–303

Fourcaud-Trocme N, Hansel D, van Vreeswijk C, Brunel N (2003) How spike generation mechanisms determine the neuronal response to fluctuating inputs. J Neurosci 23:11628–11640

Fransen E, Alonso AA, Dickson CT, Magistretti J, Hasselmo ME (2004) Ionic mechanisms in the generation of subthreshold oscillations and action potential clustering in entorhinal layer II stellate neurons. Hippocampus 14:368–384

Fuchs EC, Neitz A, Pinna R, Melzer S, Caputi A, Monyer H (2016) Local and distant input controlling excitation in layer II of the medial entorhinal cortex. Neuron 89:194–208

Fuhs MC, Touretzky DS (2006) A spin glass model of path integration in rat medial entorhinal cortex. J Neurosci 26:4266–4276

Fyhn M, Molden S, Witter MP, Moser EI, Moser MB (2004) Spatial representation in the entorhinal cortex. Science 305:1258–1264

Garden DL, Dodson PD, O'Donnell C, White MD, Nolan MF (2008) Tuning of synaptic integration in the medial entorhinal cortex to the organization of grid cell firing fields. Neuron 60:875–889

Giocomo LM, Zilli EA, Fransen E, Hasselmo ME (2007) Temporal frequency of subthreshold oscillations scales with entorhinal grid cell field spacing. Science 315:1719–1722

Guanella A, Kiper D, Verschure P (2007) A model of grid cells based on a twisted torus topology. Int J Neural Syst 17:231–240

Hafting T, Fyhn M, Bonnevie T, Moser MB, Moser EI (2008) Hippocampus-independent phase precession in entorhinal grid cells. Nature 453:1248–1252

Hafting T, Fyhn M, Molden S, Moser MB, Moser EI (2005) Microstructure of a spatial map in the entorhinal cortex. Nature 436:801–806

Jones RS (1994) Synaptic and intrinsic properties of neurons of origin of the perforant path in layer II of the rat entorhinal cortex in vitro. Hippocampus 4:335–353

Kitamura T, Macdonald CJ, Tonegawa S (2015) Entorhinal-hippocampal neuronal circuits bridge temporally discontiguous events. Learn Mem 22:438–443

Kitamura T, Pignatelli M, Suh J, Kohara K, Yoshiki A, Abe K, Tonegawa S (2014) Island cells control temporal association memory. Science 343:896–901

Klink R, Alonso A (1997) Morphological characteristics of layer II projection neurons in the rat medial entorhinal cortex. Hippocampus 7:571–583

Kropff E, Carmichael JE, Moser MB, Moser EI (2015) Speed cells in the medial entorhinal cortex. Nature 523:419–424

McNaughton BL, Battaglia FP, Jensen O, Moser EI, Moser MB (2006) Path integration and the neural basis of the 'cognitive map'. Nat Rev Neurosci 7:663–678

Mizuseki K, Sirota A, Pastalkova E, Buzsaki G (2009) Theta oscillations provide temporal windows for local circuit computation in the entorhinal-hippocampal loop. Neuron 64:267–280

Moser EI, Moser MB (2013) Grid cells and neural coding in high-end cortices. Neuron 80:765–774

Navratilova Z, Giocomo LM, Fellous JM, Hasselmo ME, McNaughton BL (2012) Phase precession and variable spatial scaling in a periodic attractor map model of medial entorhinal grid cells with realistic after-spike dynamics. Hippocampus 22:772–789

Nolan MF, Dudman JT, Dodson PD, Santoro B (2007) HCN1 channels control resting and active integrative properties of stellate cells from layer II of the entorhinal cortex. J Neurosci 27:12440–12451

O'Keefe J, Burgess N (2005) Dual phase and rate coding in hippocampal place cells: theoretical significance and relationship to entorhinal grid cells. Hippocampus 15:853–866

Pastoll H, Ramsden HL, Nolan MF (2012) Intrinsic electrophysiological properties of entorhinal cortex stellate cells and their contribution to grid cell firing fields. Front Neural Circuits 6:17

Pastoll H, Solanka L, van Rossum MC, Nolan MF (2013) Feedback inhibition enables theta-nested gamma oscillations and grid firing fields. Neuron 77:141–154

Raudies F, Brandon MP, Chapman GW, Hasselmo ME (2015) Head direction is coded more strongly than movement direction in a population of entorhinal neurons. Brain Res 1621:355–367

Ray S, Naumann R, Burgalossi A, Tang Q, Schmidt H, Brecht M (2014) Grid-layout and theta-modulation of layer 2 pyramidal neurons in medial entorhinal cortex. Science 343:891–896

Rowland DC, Weible AP, Wickersham IR, Wu H, Mayford M, Witter MP, Kentros CG (2013) Transgenically targeted rabies virus demonstrates a major monosynaptic projection from hippocampal area CA2 to medial entorhinal layer II neurons. J Neurosci 33:14889–14898

Samsonovich A, McNaughton BL (1997) Path integration and cognitive mapping in a continuous attractor neural network model. J Neurosci 17:5900–5920

Sargolini F, Fyhn M, Hafting T, McNaughton BL, Witter MP, Moser MB, Moser EI (2006) Conjunctive representation of position, direction, and velocity in entorhinal cortex. Science 312:758–762

Schmidt-Hieber C, Hausser M (2013) Cellular mechanisms of spatial navigation in the medial entorhinal cortex. Nat Neurosci 16:325–331

Solanka L, van Rossum MC, Nolan MF (2015) Noise promotes independent control of gamma oscillations and grid firing within recurrent attractor networks. elife 4:e06444

Steffenach HA, Witter M, Moser MB, Moser EI (2005) Spatial memory in the rat requires the dorsolateral band of the entorhinal cortex. Neuron 45:301–313

Sürmeli G, Marcu D-C, McClure C, Garden DLF, Pastoll H, Nolan MF (2015) Molecularly defined circuitry reveals input-output segregation in deep layers of the medial entorhinal cortex. Neuron 88(5):1040–1053

Tiesinga P, Sejnowski TJ (2009) Cortical enlightenment: are attentional gamma oscillations driven by ING or PING? Neuron 63:727–732

Tocker G, Barak O, Derdikman D (2015) Grid cells correlation structure suggests organized feedforward projections into superficial layers of the medial entorhinal cortex. Hippocampus 25:1599

Uhlhaas PJ, Singer W (2012) Neuronal dynamics and neuropsychiatric disorders: toward a translational paradigm for dysfunctional large-scale networks. Neuron 75:963–980

Varga C, Lee SY, Soltesz I (2010) Target-selective GABAergic control of entorhinal cortex output. Nat Neurosci 13:822–824

Whittington MA, Cunningham MO, LeBeau FE, Racca C, Traub RD (2011) Multiple origins of the cortical gamma rhythm. Dev Neurobiol 71:92–106

Widloski J, Fiete IR (2014) A model of grid cell development through spatial exploration and spike time-dependent plasticity. Neuron 83:481–495

Zhang K (1996) Representation of spatial orientation by the intrinsic dynamics of the head-direction cell ensemble: a theory. J Neurosci 16:2112–2126

Computational Models of Grid Cell Firing

Daniel Bush and Christoph Schmidt-Hieber

Abstract Grid cells in the medial entorhinal cortex (mEC) fire whenever the animal enters a regular triangular array of locations that cover its environment. Since their discovery, several models that can account for these remarkably regular spatial firing patterns have been proposed. These generally fall into one of three classes, generating grid cell firing patterns either by oscillatory interference, through continuous attractor dynamics, or as a result of spatially modulated input from a place cell population. Neural network simulations have been used to explore the implications and predictions made by each class of model, while subsequent experimental data have allowed their architecture to be refined. Here, we describe implementations of two classes of grid cell model – oscillatory interference and continuous attractor dynamics – alongside a hybrid model that incorporates the principal features of each. These models are intended to be both parsimonious and make testable predictions. We discuss the strengths and weaknesses of each model and the predictions they make for future experimental manipulations of the grid cell network in vivo.

Experimental Data

Grid cells recorded in freely moving rodents fire action potentials at multiple spatial locations. These firing fields form the vertices of a regular triangular array covering the whole environment of a navigating animal (Hafting et al. 2005; Fig. 1a). Grid cells were initially discovered in the superficial layers of rodent medial entorhinal

D. Bush (✉)
UCL Institute of Cognitive Neuroscience, London, UK

UCL Institute of Neurology, London, UK
e-mail: drdanielbush@gmail.com

C. Schmidt-Hieber (✉)
Institut Pasteur, Paris, France
e-mail: christoph.schmidt-hieber@pasteur.fr

V. Cutsuridis et al. (eds.), *Hippocampal Microcircuits*, Springer Series in Computational Neuroscience, https://doi.org/10.1007/978-3-319-99103-0_16

cortex (mEC; Hafting et al. 2005; Fyhn et al. 2008) but have since been identified in the pre- and para-subiculum (PreS and PaS; Boccara et al. 2010) and in the deeper layers of mEC, where their firing rate is often modulated by heading direction (Sargolini et al. 2006). Moreover, grid-like responses have been recorded in the parahippocampal cortices of the bat (Yartsev et al. 2011), human (Doeller et al. 2010; Jacobs et al. 2013) and non-human primate (Killian et al. 2012). In the rodent, grid cells are most often recorded in layer II of mEC (mECII), where they are likely comprised of both reelin-positive stellate (or 'ocean') cells, which form the majority of principal neurons in mECII (Gatome et al. 2010), and calbindin-positive (or 'island') pyramidal cells (Domnisoru et al. 2013; Kitamura et al. 2014; Ray et al. 2014; Sun et al. 2015).

Grid cell firing patterns can be characterised by their scale (i.e. the distance between adjacent firing fields), orientation (of one principal grid axis relative to an external cue) and the phase or spatial offset of their firing fields (Fig. 1a). Grid scale has been shown to increase in discrete steps along the dorsoventral axis of mEC (Fig. 1b; Barry et al. 2007; Stensola et al. 2012), and evidence suggests that grid cells which share a common scale form a single functional module (Stensola et al. 2012; Yoon et al. 2013). The scale, relative orientation and offset of grid firing patterns within each module are generally conserved across environments (Fyhn et al. 2007), aside from a transient expansion of grid scale in novel environments that returns to baseline with experience (Barry et al. 2012a). The spatial phases of individual grid cells are uniformly distributed across the environment but, importantly, the relative spatial phase of any two simultaneously recorded grid cells from the same module is also conserved across all environments visited by the animal (Fyhn et al. 2007; Yoon et al. 2013).

Principal cells and interneurons in the rodent entorhinal cortex and hippocampus are each modulated by a 5–12 Hz theta rhythm during movement (Vanderwolf 1969; O'Keefe and Nadel 1978). Both the power (Vanderwolf 1969; McFarland et al. 1975) and frequency (McFarland et al. 1975; Rivas et al. 1996; Jeewajee et al. 2008) of theta oscillations increase with running speed. Importantly, the majority of grid cells in layers II, V and VI of rodent mEC exhibit theta phase precession, firing spikes at progressively earlier phases of the ongoing movement-related theta rhythm as the grid firing field is traversed (Hafting et al. 2008; Reifenstein et al. 2012; Climer et al. 2013; Jeewajee et al. 2014; Reifenstein et al. 2014; Fig. 1c). This theta phase precession appears to be independent of input from the hippocampus (Hafting et al. 2008). Conversely, the majority of layer III grid cells exhibit theta phase locking, firing spikes at the trough of the ongoing theta rhythm throughout the firing field (Hafting et al. 2008; Climer et al. 2013). Interestingly, inactivation of the medial septum, which abolishes the theta rhythm, also impairs grid cell firing patterns while leaving head direction, border and place cell firing patterns unaffected (Brandon et al. 2011; Koenig et al. 2011).

Grid cell firing patterns, like those of place cells, remain stable for a limited period of time in the dark (Hafting et al. 2005). This, along with the fact that grid firing patterns are preserved across all environments visited by the animal, has led to the suggestion that grid cells perform path integration, updating their firing patterns

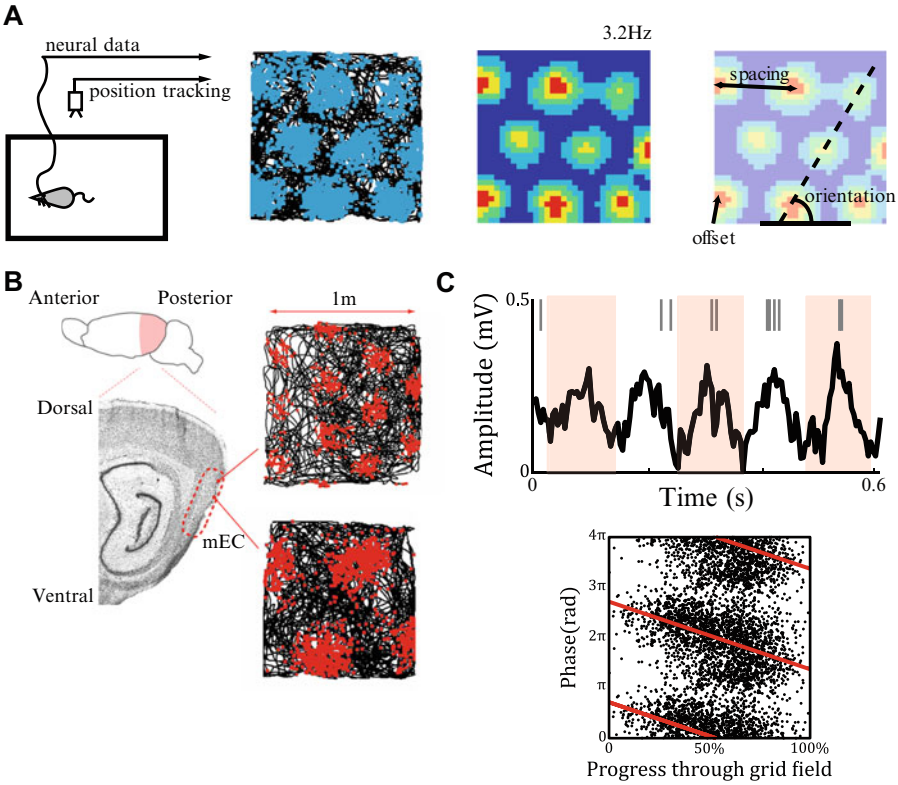

Fig. 1 Properties of grid cells. (**a**) The grid cell firing rate code. Left panel: schematic of single unit recording in the freely moving rodent. Middle left panel: the animal's path through the environment is indicated by the black line, and the locations at which action potentials were fired by a single neuron in rodent mEC are superimposed in blue. Middle right panel: firing rate map for the same mEC grid cell, with high firing rates indicated by hot colours and low firing rates by cold colours. Right panel: the firing pattern of this mEC grid cell can be characterised by its scale (the distance between any two adjacent firing fields), orientation (relative to some external cue) and offset or spatial 'phase' (relative to some arbitrary point in the environment; adapted from Bush et al. 2015). (**b**) Grid cells appear to be organised into discrete functional modules whose scale increases in discrete steps along the dorsoventral axis of mEC (adapted from Barry et al. 2007). (**c**) The grid cell temporal code. As the animal crosses a grid firing field, spikes are fired at successively earlier phases of the 5–12 Hz theta rhythm recorded from the local field potential (LFP), resulting in a negative circular-linear correlation (red line) between the theta phase of firing and progress through the grid field (adapted from Bush et al. 2015)

on the basis of self-motion information (Fuhs and Touretzky 2006; McNaughton et al. 2006). Indeed, grid cell firing patterns are abolished when self-motion signals are reduced by passive transport of the animal (Winter et al. 2015). However, grid firing patterns of individual cells are also stable between visits to an environment (Hafting et al. 2005; Fyhn et al. 2007), oriented to distal visual cues (Hafting et al. 2005), dependent on visual input (Chen et al. 2016; Pérez-Escobar et al. 2016) and

rescale parametrically in response to the reshaping of a familiar environment (Barry et al. 2007). This suggests that grid cell firing patterns become anchored to sensory cues with experience, analogous to the reset of a path integration system by sensory inputs to reduce integrated error where possible (Fuhs and Touretzky 2006; Evans et al. 2016). In addition, theoretical studies have demonstrated that the grid cell population provides a highly efficient code for location (Fiete et al. 2008) and may be used for goal-directed navigation (Bush et al. 2015; Stemmler et al. 2015).

Recent evidence suggests that sensory inputs to grid cells may be mediated by place and/or boundary cells (Langston et al. 2010; Wills et al. 2010; Bonnevie et al. 2013; Hardcastle et al. 2015; Evans et al. 2016). For example, stable grid cell firing patterns appear after stable head direction (HD), place and boundary cell responses during development and several days after rats leave the nest and actively explore their environment for the first time (Langston et al. 2010; Wills et al. 2010). Similarly, inactivating the hippocampus – and thus eliminating place cell inputs to mEC – impairs grid cell firing patterns (Bonnevie et al. 2013). Finally, it has been demonstrated that grid cell firing patterns drift coherently during excursions into the centre of an open-field environment and that this accumulated error is eliminated by contact with environmental boundaries (Hardcastle et al. 2015). This is complemented by the observation that environmental boundaries have a strong influence on the orientation and ellipticity of grid cell firing patterns (Derdikman et al. 2009; Krupic et al. 2015) that develops with experience (Stensola et al. 2015). Each of these effects is likely to be mediated by input from boundary cells (Barry et al. 2006; Savelli et al. 2008; Solstad et al. 2008; Lever et al. 2009).

The Models

Any computational model of grid cell firing patterns must account for the experimental data described above while remaining faithful to the known neurobiology of the medial entorhinal cortex. Ideally, such a model should replicate both the rate and temporal code exhibited by grid cells – that is, generate both a triangular lattice of spatial receptive fields and phase precession against an ongoing oscillation in the local field potential. In accordance with their hypothesised role in path integration, most models assume that the principal input to grid cells is a self-motion signal corresponding to the animal's velocity. However, to account for the stability of their firing patterns relative to the environment, grid cells must also receive environmental sensory inputs from place or boundary cells which may have an effect on those firing patterns. Finally, the stability of grid firing patterns relative to one another, and their modular organisation, also suggest that there are strong, local interactions between grid cells in mEC.

A number of grid cell models that can account for some or all of these properties have been proposed, each differing in how the animal's location is encoded, updated and decoded (reviewed by Giocomo et al. 2011; Zilli 2012). These models are not mutually exclusive, however, and the properties of grid cells may best be accounted

for by a 'hybrid' model that incorporates features from each class (Schmidt-Hieber and Häusser 2013; Bush and Burgess 2014). Grid cell models can be broadly divided into several principal classes. The first class are oscillatory interference (OI) models, which hypothesise that grid cell firing patterns are formed at the single-cell level by constructive interference (i.e. coincidence detection) among velocity-controlled oscillator (VCO) inputs (Burgess et al. 2005, 2007; Blair et al. 2008; Burgess 2008; Hasselmo 2008). The second class are continuous attractor network (CAN) models, which hypothesise that grid cell firing patterns are generated at the network level by local interactions characterised by a circular surround synaptic weight profile (Fuhs and Touretzky 2006; McNaughton et al. 2006; Guanella et al. 2007; Burak and Fiete 2009; Pastoll et al. 2013). Another class of models suggest that grid cell firing patterns arise at the single-cell level as a result of spatially modulated inputs from place cells, performing a process equivalent to principal component analysis (PCA) on the spatial representation provided by the hippocampus (Kropff and Treves 2008; Dordek et al. 2016). Finally, grid cell firing may emerge as a result of a self-organising learning process (Mhatre et al. 2012).

Here, we describe neural network models of two of these major classes of grid cell model, using either oscillatory interference or continuous attractor dynamics to generate grid firing patterns, alongside an appraisal of their strengths, weaknesses and relationship to experimental data. We then present a hybrid model that incorporates features of each class in order to account for a wider array of the known properties of grid cells. Finally, we provide suggestions for future experimental studies that will help to further refine the biological validity of grid cell models, and critical tests of each model.

The Oscillatory Interference Model

The oscillatory interference (OI) model was originally proposed to account for theta phase precession in place cells (O'Keefe and Recce 1993; Lengyel et al. 2003). This model proposes that grid firing patterns can be accounted for at the single-cell level by constructive interference between two or more oscillatory inputs (Burgess et al. 2005, 2007; Blair et al. 2008; Burgess 2008; Hasselmo 2008). In its simplest 1D form, one oscillator is assumed to have a constant baseline frequency, and the other 'velocity-controlled oscillator' (VCO) is assumed to have a frequency that varies linearly with the speed of movement (Equation 1; Burgess 2008). In rodents, the baseline frequency is generally assumed to be the 5–12 Hz movement-related theta oscillation (Vanderwolf 1969; O'Keefe and Nadel 1978; Burgess et al. 2007).

Input from these two signals generates grid cell membrane potential oscillations (MPOs) which are modulated by an 'envelope' frequency that is equal to the difference in baseline and VCO frequencies and a 'carrier' frequency that is equal to the mean of those two frequencies (Fig. 2a). The envelope corresponds to the grid cell rate code, being spatially periodic and approximately Gaussian or cosine tuned; while the carrier corresponds to the temporal code, being higher in frequency than

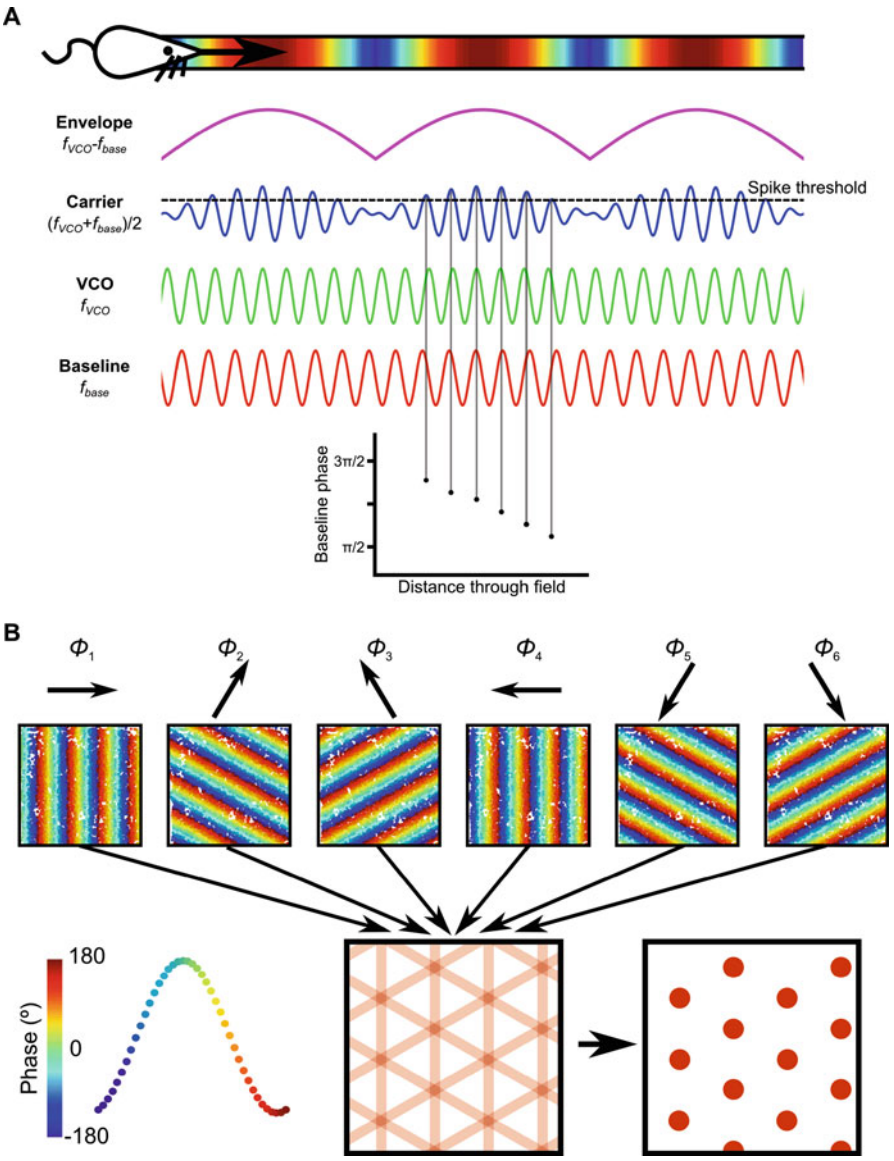

Fig. 2 The oscillatory interference model. (**a**) In 1D, consider a baseline oscillation with frequency f_{base} (red line) and a velocity-controlled oscillation (VCO) with a frequency f_{VCO} (green line) that varies linearly with movement speed. Constructive interference between these two oscillations generates a spatially periodic activity pattern with a carrier frequency (blue) equal to their mean frequency $(f_{\text{base}} + f_{\text{VCO}})/2$ and an envelope frequency (pink) equal to their difference in frequency $(f_{\text{VCO}} - f_{\text{base}})$. This activity pattern corresponds to spatially periodic, approximately Gaussian firing fields (top) within which spikes are fired at progressively earlier phases of the baseline oscillation (bottom), as observed in grid cells (following Blair et al. 2008).

the baseline oscillation and thus causing the grid cell to fire at progressively earlier phases of that baseline oscillation as the firing field is traversed (i.e. generating phase precession; Fig. 2a). The scale of the resultant grid firing pattern is controlled by the slope of the VCO movement speed/burst firing frequency relationship β, which determines how quickly the VCO and baseline oscillation move in and out of phase during movement.

$$\mathbf{v}_{\mathrm{VCO}}(t) = s(t)\cos\left(\varnothing(t) - \varnothing_{\mathrm{VCO}}\right)$$

$$f_{\mathrm{VCO}}(t) = f_{\mathrm{base}} + \beta \mathbf{v}_{\mathrm{VCO}}(t)$$

Equation 1 The relationship between VCO burst firing frequency and movement velocity. VCO burst firing frequency f_{VCO} deviates linearly from the baseline frequency f_{base} according to the component of movement velocity along the VCO's preferred direction $\mathbf{v}_{\mathrm{VCO}}$, which is dictated by the absolute speed s and direction $\varnothing$ of the animal's movement relative to the preferred direction of that VCO $\varnothing_{\mathrm{VCO}}$. The scale of the resultant grid firing pattern is dictated by the slope of the linear relationship between burst firing frequency and velocity, β.

The OI model can be extended to account for grid firing patterns in 2D by incorporating input from multiple VCOs whose burst firing frequencies vary linearly with movement speed along different preferred directions. Because distance is the time integral of velocity, and phase is the time integral of frequency, the phase of each VCO – if sampled at fixed intervals (i.e. at the peak or trough of the baseline oscillation) – encodes (periodic) displacement in its preferred direction (Fig. 2b). A grid cell that receives input from two or more VCOs whose preferred directions differ by multiples of 60° will exhibit a triangular array of firing fields at locations where those VCO inputs are in phase (Fig. 2b). The specific location or offset of those firing fields can be manipulated by adding a constant phase shift to one or more VCO inputs. Hence, the OI model proposes that each VCO performs path integration along different one-dimensional axes, while grid cells simply 'read-out' the activity of multiple VCO inputs by firing whenever they are in phase (Fig. 2b). Importantly, it is the phase *difference* between VCO and baseline oscillations that encodes location, and the baseline oscillation can therefore take any frequency value and need not be constant over time (Burgess 2008; Blair et al. 2014; Orchard 2015).

What is the source of these VCO inputs to grid cells? Early implementations of OI grid cell models suggested that spontaneous independent intrinsic oscillations in dendritic subunits, driven by animal velocity, may represent VCOs ('intrinsic

Fig. 2 (continued) (**b**) Velocity-controlled oscillators (VCOs) with different preferred firing directions $\varnothing_i$ encode periodic displacement along that direction in their firing phase. Combining input from two or more VCOs with preferred firing directions that differ by multiples of 60° can then account for the periodic firing fields exhibited by grid cells, which fire when their VCO inputs are in phase. (Adapted from Bush and Burgess 2014)

VCOs'; Burgess et al. 2007). This idea was inspired by the finding that mECII stellate cells can produce spontaneous somatic membrane potential oscillations in the theta frequency range (theta MPOs) when depolarised close to spike threshold (Alonso and Llinas 1989). Moreover, the frequency of these MPOs, along with several intrinsic membrane properties, shows a dorsal-ventral gradient (Giocomo et al. 2007; Garden et al. 2008) that mirrors the parallel anatomical gradient in grid spacing (Hafting et al. 2005). However, as biophysical modelling has revealed that dendritic intrinsic MPOs will rapidly phase lock (Remme et al. 2010), more recent OI model implementations assume that VCOs are represented by neurons projecting to grid cells that display velocity-dependent theta-modulated firing ('external VCOs'; Burgess 2008; Welday et al. 2011; Schmidt-Hieber and Häusser 2013; Bush and Burgess 2014).

How can we predict membrane potential V_m and spike rate from an OI model of grid cell firing? The simplest way is to analytically compute V_m for an OI model neuron that receives input from n VCOs with preferred firing directions that differ by multiples of 60°, each oscillating at frequency $f_{\mathrm{VCO},\,i}$ (see Equation 1) according to Equation 2.

$$V_\mathrm{m}(t) = \prod_{i=1}^{n} \left[\cos\left(2\pi f_\mathrm{base} t\right) + \cos\left(2\pi f_{\mathrm{VCO},i}(t) t\right) + \varphi_i\right]_+$$

Equation 2 Membrane potential of a grid cell simulated using the OI model. The membrane potential V_m of the simulated grid cell at time step t is dictated by the baseline frequency f_base, VCO burst firing frequency $f_{\mathrm{VCO},i}$ (see Equation 1) and spatial phase offset of the i^{th} VCO φ_i, with $[x]_+ = \max\{0, x\}$ (Burgess et al. 2007; Burgess 2008).

Figure 3a shows an example of the membrane potential V_m of a simulated grid cell in a 2D environment generated by two VCO inputs with preferred directions $\varnothing_{\mathrm{VCO},\,1} = 0^\circ$ and $\varnothing_{\mathrm{VCO},\,2} = 60^\circ$. Although two VCO inputs and a baseline oscillation are sufficient to produce a hexagonal grid, more circular firing fields that better approximate experimental recordings can be generated by six VCO inputs with preferred firing directions that differ by multiples of 60° (Burgess et al. 2007). This configuration is also necessary to produce omnidirectional phase precession in 2D, if the firing rate of VCOs is directionally tuned such that VCOs only fire spikes when movement velocity in their preferred direction is positive – i.e. when the running direction does not exceed $\varnothing_{\mathrm{VCO},\,i} \pm 90^\circ$ (Burgess 2008; Climer et al. 2013).

To obtain a more biophysically realistic estimate of grid cell activity, integrate-and-fire neurons (Welday et al. 2011; Bush and Burgess 2014) or detailed compartmental modelling (Schmidt-Hieber and Häusser 2013) have been employed. These implementations typically convert $f_{\mathrm{VCO},\,i}$, which is continuous in time, into discrete spike trains driving synaptic inputs to a model neuron. For example, discrete Poisson

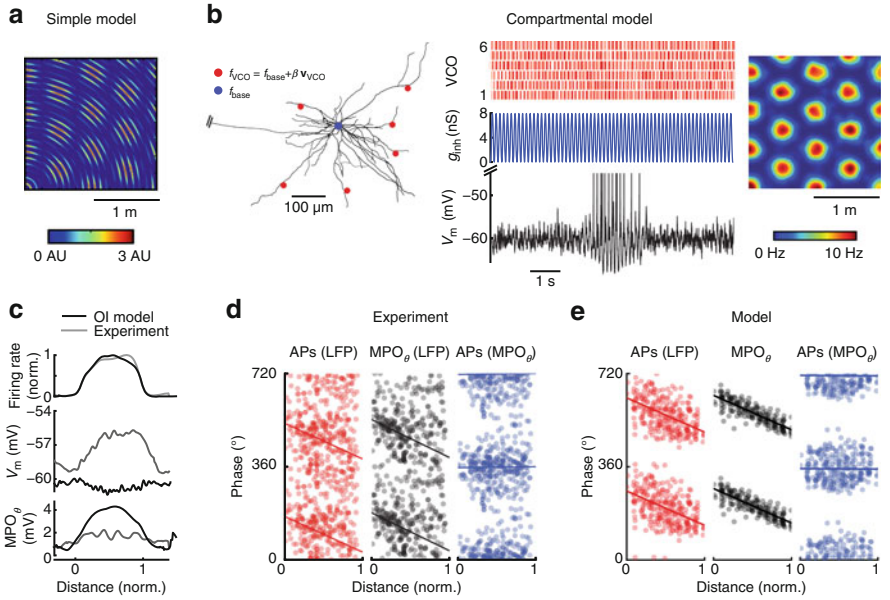

Fig. 3 Implementations of the oscillatory interference model. (**a**) In the simple implementation, following Equation 2, the membrane voltage V_m of a simulated grid cell is generated by 2 VCO inputs with preferred directions of $\varnothing_{VCO,1} = 0^\circ$ and $\varnothing_{VCO,2} = 60^\circ$. (**b**) In a more detailed implementation, Poissonian VCO spike trains, following Equation 3, are used as input to six excitatory synapses (red circles) located on the distal dendrites of a compartmental stellate cell model, while the baseline oscillation takes the form of an inhibitory conductance g_{inh} applied directly to the soma (blue circle). In both cases, the results shown here were generated by 90 linear runs with $s = 0.2\ ms^{-1}$ from the bottom left corner to the opposing boundaries of a 2 m sided square arena at angles spaced by 1°. For further details, see Schmidt-Hieber and Häusser (2013); code is available on ModelDB (accession number 150239). (**c**) Simulations demonstrate a discrepancy between the predictions of the OI model and whole-cell recordings of grid cell membrane potential in behaving animals (Schmidt-Hieber and Häusser 2013; Domnisoru et al. 2013). The OI model predicts no change in the average membrane voltage of a grid cell (middle panel) as the firing field is traversed (top panel) but does predict an increase in the amplitude of theta band membrane potential oscillations (MPO_θ) as VCO inputs become synchronised in the centre of the firing field (bottom panel). Conversely, experimental recordings indicate a sustained 'ramp' depolarisation that mirrors the change in firing rate within the grid field, but no change in the amplitude of theta band MPOs. (**d**) Simulations demonstrate that the predictions of the OI model are consistent with the properties of phase precession described by whole-cell recordings of grid cell membrane potential in behaving animals (Schmidt-Hieber and Häusser 2013; Domnisoru et al. 2013). The phases of action potentials (APs) with respect to LFP theta (left), theta band MPOs with respect to LFP theta (middle) and action potentials with respect to theta band MPOs (right) are plotted as a function of normalised position within firing fields of stellate cells recorded intracellularly in vivo. Action potentials show phase precession with respect to the LFP but are phase locked with MPOs. (**e**) The compartmental model correctly predicts the experimental observations. (Panels **d**–**e** adapted from Schmidt-Hieber and Häusser 2013)

spike trains can be generated by computing the firing probability $p_{\mathrm{VCO},i}$ for VCO_i according to Equation 3, where the time step Δt is chosen so that $p \ll 1$. Predictions for the membrane voltage V_m and spike rate from a detailed compartmental model are shown in Fig. 3b (adapted from Schmidt-Hieber and Häusser 2013). While an isolated single-cell OI model fails to reproduce the experimentally recorded membrane potential ramps during firing field crossings (Fig. 3c), it can account for the observed phase precession phenotype, with both action potentials and theta membrane potential oscillations showing phase precession with reference to LFP theta (Fig. 3d, e).

$$p_{\mathrm{VCO},i}\,(t, t + \Delta t) = \overline{r_{\mathrm{VCO}}}\left[\cos\left(2\pi f_{\mathrm{VCO},i}(t)t + \varphi_{\mathrm{VCO},i}\right) + 1\right]\Delta t$$

Equation 3 Simulated VCO spike train in the OI model of grid cell firing. The probability of an input spike in time step t is dictated by VCO mean firing frequency $\overline{r_{\mathrm{VCO}}}$, burst firing frequency $f_{\mathrm{VCO},i}$ (see Equation 1), the spatial phase of that VCO input $\varphi_{\mathrm{VCO},i}$ and length of the time step Δt. Firing probability is converted to input spikes by drawing a random number r from the interval [0, 1] for each time step. A spike is produced if $r \leq p$.

Critique of the Oscillatory Interference Model

The OI model accounts for both the rate and temporal firing patterns of grid cells – that is, it generates both hexagonally arranged firing fields and phase precession. In accordance with the OI model, grid cell burst firing frequency has been shown to increase with running speed (Jeewajee et al. 2008) and decrease in novel environments, when grid scale expands (Barry et al. 2012a; Wells et al. 2013). Moreover, cells with VCO-like properties have been identified in and around the entorhinal cortex (Welday et al. 2011); gridness scores correlate with spike train theta rhythmicity (Boccara et al. 2010); and grid cell firing patterns are impaired when theta power is reduced by inactivation of the medial septum (Brandon et al. 2011; Koenig et al. 2011) or when the influence of running speed on theta frequency is abolished by passive transport of the animal (Winter et al. 2015).

The OI model has recently been challenged by the finding that grid cell firing patterns in crawling bats exist in the absence of a continuous theta rhythm (Yartsev et al. 2011, but see Barry et al. 2012b). Similarly, continuous low-frequency oscillations are rarely observed in the human hippocampal formation during virtual navigation tasks (Ekstrom et al. 2005; Jacobs et al. 2013; Watrous et al. 2013). However, it is important to note that the OI model functions equally well with a baseline oscillation of any frequency, which need not be constant over time, as integrated displacement is encoded in the phase *difference* between baseline and VCO oscillations – irrespective of the absolute phase or frequency of

either oscillation (Burgess 2008; Blair et al. 2014; Orchard 2015). Indeed, several computational models of grid cells effectively make use of oscillatory interference with a baseline frequency of 0 Hz, in which case each VCO is equivalent to a non-oscillating 'stripe' or 'band' cell (Mhatre et al. 2012; Horiuchi and Moss 2015). Moreover, recent recordings from bats have revealed that, despite a lack of clear LFP rhythmicity, neurons still exhibit phase precession with respect to broadband low-frequency oscillations in the non-rhythmic LFP (Eliav et al. 2015). These data can be accounted for by an OI model with a baseline oscillation that varies dynamically over a wide range. Hence, the absence of any clear, sustained oscillatory activity in the LFP or grid cell spike train is not sufficient to disprove the OI model.

The OI model has also been criticised as being particularly susceptible to noise in the burst firing frequency of VCO inputs (Welinder et al. 2008). However, the phase precession of grid and place cell firing demonstrates that oscillations with the precise timing required to generate grid cell firing patterns by oscillatory interference do exist in the rodent hippocampal formation (O'Keefe and Recce 1993; Hafting et al. 2008). It is well known that grid firing patterns – like any hypothetical path integration system – will rapidly accrue error over time in the absence of sensory inputs (Hafting et al. 2005; Evans et al. 2016). Theoretical studies have demonstrated that input from place or boundary cells is sufficient to stabilise grid firing patterns in the face of phase noise (Bush and Burgess 2014). Similarly, the OI model has been criticised for relying on the preferred direction of VCO inputs to a grid cell being separated by multiples of 60°, but theoretical studies have shown that such inputs may be selected by a Hebbian learning mechanism during development as they most frequently co-occur in space (Burgess et al. 2007; Mhatre et al. 2012) and therefore offer optimal noise reduction (Burgess and Burgess 2014).

The OI model cannot, however, account for the relative stability of grid cell firing patterns within a module (Yoon et al. 2013). Oscillatory interference is a single-cell model and makes no comment on potential interactions between grid cells, while experimental evidence demonstrates that grid cell firing patterns from the same functional module are tightly coupled, responding coherently to changes in a familiar environment and maintaining their relative spatial phase between environments (Hafting et al. 2005; Barry et al. 2007; Fyhn et al. 2007; Stensola et al. 2012; Yoon et al. 2013). Organising VCO inputs into ring attractor circuits provides some stability between firing patterns of different grid cells (Blair et al. 2008) but overlooks the functional consequences of the known synaptic interactions between grid cells. Similarly, the observations of an in-field 'ramp' depolarisation in grid cell subthreshold membrane potentials, as well as the lack of increase in in-field theta amplitude, are not consistent with an OI model (Fig. 3c; Domnisoru et al. 2013; Schmidt-Hieber and Häusser 2013). Hence, some modification of the model or additional mechanism is required to account for both interactions between grid cells within each functional module, and the subthreshold membrane potential dynamics of grid cells recorded in vivo.

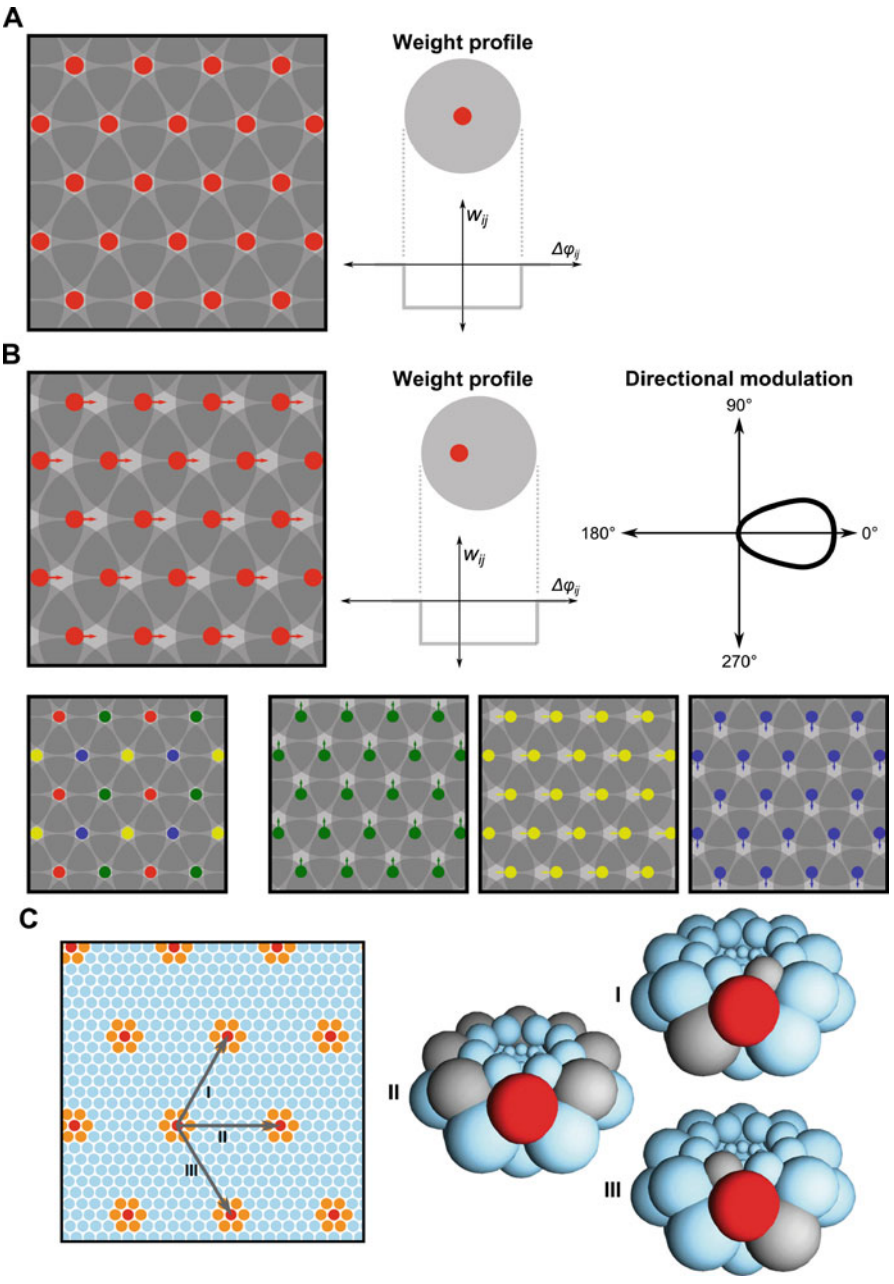

Fig. 4 The continuous attractor network model. (**a**) A sheet of topographically arranged neurons (left panel) are connected by disynaptic inhibitory projections with a circular surround profile (right panel), such that neurons which are proximate on the neural sheet inhibit each other. In the multiple bump CAN model, uniform excitatory input to such a network generates a grid firing

Continuous Attractor Network Models

Continuous attractor network (CAN) models were originally proposed to account for the properties of head direction (Zhang 1996) and place cells (Samsonovich and McNaughton 1997; Conklin and Eliasmith 2005). This class of model proposes that spatially modulated firing patterns can be accounted for by local, recurrent interactions among cells (Fuhs and Touretzky 2006; McNaughton et al. 2006; Guanella et al. 2007; Burak and Fiete 2009). The requisite recurrent connectivity is characterised by a circular, centre-surround synaptic weight profile on a topographically arranged sheet of neurons (Fig. 4a). In the case of grid cells, this implies that the strength of synaptic connections between cells decreases as a function of the distance between their firing fields (i.e. the difference in spatial phase). This establishes cooperation between grid cells with similar spatial phase, and competition between grid cells with different spatial phases (Fuhs and Touretzky 2006). Note that grid cells need not be topographically arranged in the actual brain, this formalism is introduced purely to aid visualisation (but see Heys et al. 2014; Naumann et al. 2015).

As direct recurrent excitatory connections between grid cell candidate neurons in mECII are sparse, recurrent connectivity in most CAN model implementations is mediated by disynaptic inhibition from interneurons, which have been shown to densely innervate mECII principal neurons (Dhillon and Jones 2000; Couey et al. 2013; Pastoll et al. 2013; Fuchs et al. 2016). Uniform excitatory input to such a network will generate one or more stable activity packets or 'bumps', and self-motion information can then be used to translate the position of this activity packet across the neural sheet in accordance with the animal's movement in the real world.

Fig. 4 (continued) pattern, as activity bump(s) form at the triangular array of inhibitory minima produced by close packing of the circular connectivity profile. In the single-bump CAN model, not illustrated here, a single activity bump forms at an arbitrary location on the neural sheet. Note that neurons need not be topographically arranged in the actual brain. (**b**) The location of the(se) activity bump(s) can be shifted by asymmetric interactions between grid cells. For example, if conjunctive grid cells, whose firing rate is modulated by movement direction, have recurrent inhibitory connections that are skewed along their preferred firing direction, then their activity will create inhibitory minima just ahead of the activity bump(s) in that direction on the neural sheet. The activity bump(s) will subsequently move across the neural sheet, tracking the animal's movement in the real world. A mixture of conjunctive grid cells with different preferred firing directions can therefore both establish and shift the grid firing pattern in any direction (following Burak and Fiete 2009). (**c**) To account for smooth changes in grid cell firing over large distances, a periodic continuous attractor network must adopt a twisted torus topology, such that movement along orientations that differ by multiples of 60° will return the activity bump to its original location on the sheet of cells once some integer number of grid scales have been travelled. Hence, if a grid cell is active at some location in the real world (red circle, left panel), then it will also be active at a fixed distance equal to the grid scale along any grid axis. Similarly, if an activity bump is located over some grid cell on a neural sheet that exhibits a twisted torus topology (red sphere, right panel), then movement of a fixed distance equal to the grid scale along any grid axis will return the activity bump to its original location (adapted from Bush et al. 2015)

The majority of CAN models suggest that the activity bump is shifted by asymmetric interactions between grid cells in the neural sheet. This can be achieved by rate-coded input from conjunctive grid × movement direction cells, which have also been identified in the deeper layers of mEC (Sargolini et al. 2006). If the recurrent inhibitory input from these conjunctive cells to other cells in the network is shifted along the axis of their preferred firing direction, then their firing will shift the activity bump in the movement direction (Fig. 4b).

In the case of a single activity bump, the network must exhibit a twisted torus topology, such that movement of a set distance in a direction corresponding to any multiple of 60° across the neural sheet will return it to its original position, thus accounting for the hexagonal symmetry of the grid firing pattern in the real world (Fig. 4c; Guanella et al. 2007; Pastoll et al. 2013). In the case of multiple bumps, the circular weight profile dictates that the location of activity bumps on the neural sheet exhibit sixfold symmetry through circular close packing. To ensure that activity bumps smoothly appear and disappear at the edges of the neural sheet, either periodic boundary conditions are imposed (which places constraints on the dimensions of the neural sheet), or alternatively the synaptic weights (Fuhs and Touretzky 2006) or feedforward synaptic inputs (Burak and Fiete 2009) are smoothly modulated to zero towards the edges of the neural sheet. Importantly, population activity is constrained by the synaptic connections between neurons such that grid cell firing patterns can only ever encode a single location at any time. Hence, grid cells in the continuous attractor network effectively perform path integration, tracking the animal's location by integrating self-motion signals.

An influential rate-based implementation of a multiple bump CAN model was proposed by Burak and Fiete (2009). In this model, each neuron i is arranged on a rectangular sheet and assigned one of four preferred directions ($\varnothing_i$=0°, 90°, 180°, or 270°). Typical sizes of the neuronal sheet range from 40 × 40 to 256 × 256 neurons – larger networks provide higher integration accuracy (Burak and Fiete 2009). The neuronal dynamics of each simulated grid cell are described by Equation 4, where r_i is the firing rate of neuron i, τ is the integration time constant, R_i are recurrent inputs and B_i are feedforward inputs. Recurrent inputs R_i are equal to the sum of all presynaptic firing rates r_j multiplied by the corresponding recurrent synaptic weights w_{ij}.

$$\tau \frac{\mathrm{d}r_i}{\mathrm{d}t} + r_i = [R_i + B_i]_+$$

$$R_i = \sum_j w_{ij} r_j$$

Equation 4 Firing rate dynamics of a grid cell simulated using the CAN model. The firing rate r_i of neuron i is dictated by the time constant τ, recurrent input R_i and feedforward inputs B_i, with $[x]_+ = \max\{0, x\}$. Recurrent inputs are equal to the sum of all presynaptic firing rates r_j multiplied by the corresponding recurrent synaptic weights w_{ij} (Burak and Fiete 2009).

The strength of recurrent inputs w_{ij} depends on the distance between the 2D positions $\mathbf{x}_i$ and $\mathbf{x}_j$ of pre- and postsynaptic neurons j and i on the neuronal sheet and is shifted by a vector $l\widehat{\mathbf{u}}_{\phi_j}$, where $\widehat{\mathbf{u}}_{\phi_j}$ is a unit vector in the preferred direction $\varnothing_j$ and l defines the amplitude of the shift (typically, a small number, e.g. two neurons; Equation 5). The dependence of this shift on $\varnothing_j$, the preferred direction of the presynaptic neuron, indicates that it is applied to the outgoing weights. The centre-surround synaptic weight matrix $\mathbf{W}_0$ classically takes the shape of a 'Mexican hat', with excitation dominating the centre and inhibition forming a brim in the periphery (Fuhs and Touretzky 2006). This can be generated as a difference of Gaussians (Equation 5), where a defines the amplitude and γ the width of the excitatory centre and κ determines the width of the inhibitory brim.

In the original implementation, the recurrent weight matrix was purely inhibitory (using $a = 1$). Interestingly, this implementation was suggested before detailed analysis of the functional connectivity in mECII revealed that direct excitatory recurrent connections between principal cells are sparse or lacking (Couey et al. 2013; Pastoll et al. 2013; Fuchs et al. 2016). Following more detailed analysis of the connectivity between mECII stellate cells, variations of the centre-surround connectivity matrix with steep edges that resemble a frying pan or 'Lincoln Hat' have also been used in CAN models (as illustrated in Fig. 4; Couey et al. 2013).

$$w_{ij} = f\left(\mathbf{x}_i - \mathbf{x}_j - l\widehat{\mathbf{u}}_{\phi_j}\right)$$

$$f(\mathbf{x}) = ae^{-\gamma|\mathbf{x}|^2} - e^{-\kappa|\mathbf{x}|^2}$$

Equation 5 Recurrent synaptic weight profile in the CAN model of grid cell firing. The strength of recurrent connectivity w_{ij} between presynaptic neuron j and postsynaptic neuron i is a function of the distance between their 2D locations $\mathbf{x}_i$ and $\mathbf{x}_j$ on the neural sheet and is skewed along the preferred direction $\varnothing_j$ of the presynaptic neuron according to the product of a constant l and unit vector in that direction $\widehat{\mathbf{u}}_{\phi_j}$. In canonical implementations of the CAN model, synaptic weights follow a 'Mexican hat' profile, consisting of excitatory projections to proximate neurons and inhibitory projections to more distant neurons on the neuronal sheet. This can be generated by a difference of Gaussian distributions, where a defines the amplitude of synaptic weights and γ and κ control the width of the excitatory and inhibitory components, respectively.

Finally, feedforward inputs in the CAN model B_i are modulated by the animal's running direction, as defined by Equation 6, where v is the animal's velocity and α determines the amplitude of the directional modulation of feedforward input. Hence, coupling of network activity to the animal's trajectory is realised through the combination of two mechanisms: a neuron receives more feedforward input if the animal is running in its preferred direction (Equation 6); and the outgoing weights of each neuron are shifted by a small number of neurons along that preferred direction (Equation 5). As a consequence, if the animal is running in a certain direction, neurons that prefer this direction (or components of this direction) will be

activated by their feedforward input and can then impose a shift in network activity towards their preferred direction. In contrast, neurons with preferred directions that point away from the running direction will receive less feedforward input, and their outgoing weights, which are shifted in the opposite direction, will be less effective. Importantly, attractor dynamics ensure that the firing rate of these cells may not be significantly modulated by running direction (Bonnevie et al. 2013), such that they would not be classed as conjunctive cells if recorded experimentally (Sargolini et al. 2006).

$$B_i = 1 + \alpha \widehat{\mathbf{u}}_{\phi_i} \cdot \mathbf{v}$$

Equation 6 Directionally modulated external input in the CAN model of grid cell firing. In order to shift the activity bump in concert with the animal's movement in the real world, external input to a simulated grid cell is modulated by the velocity of movement v multiplied by a unit vector $\widehat{\mathbf{u}}$ in the preferred direction $\varnothing_j$ of that grid cell and a positive constant α. The outgoing synaptic weight profile of each grid cell is also skewed along the preferred firing direction (Equation 5), creating an inhibitory minimum adjacent to the activity bump in that direction on the neural sheet.

The Burak and Fiete (2009) multiple bump CAN model shown in Fig. 5a is particularly efficient as it can be implemented as a convolutional neural network of rate-based or simple spiking neurons where, instead of computing the input to each neuron separately, network activity is convolved with the synaptic weight matrix in a single step. A more biophysically realistic single-bump implementation using separate layers of excitatory and inhibitory integrate-and-fire neurons has also been shown to produce theta-nested gamma oscillations in model grid cells (Pastoll et al. 2013). CANs consisting of detailed compartmental neurons have not yet been implemented, as simulating several minutes of grid cell firing in a network of >1000 model neurons is computationally prohibitive at this time. A simplified approach can be taken, however, where synaptic input rates are first derived from one of the rate-based model neurons and then fed into a single compartmental model neuron in a separate simulation (Schmidt-Hieber and Häusser 2013; Fig. 5b). For example, probabilities of firing for excitatory and inhibitory inputs can be derived from one of the rate-based model neurons (according to $P_{\text{exc}}(t, t + \Delta t) = f(B_i)\Delta t$ and $P_{\text{inh}}(t, t + \Delta t) = f(-R_i)\Delta t$, respectively) and used to generate Poisson input spike trains driving excitatory and inhibitory synaptic conductances in a compartmental model, similar to the approach described in Equation 3.

Critique of the Continuous Attractor Network Model

The CAN model can readily account for the modular organisation of grid cells (Barry et al. 2007; Stensola et al. 2012), and strong functional interactions between grid cells from within the same module in both 1D and 2D environments (Yoon

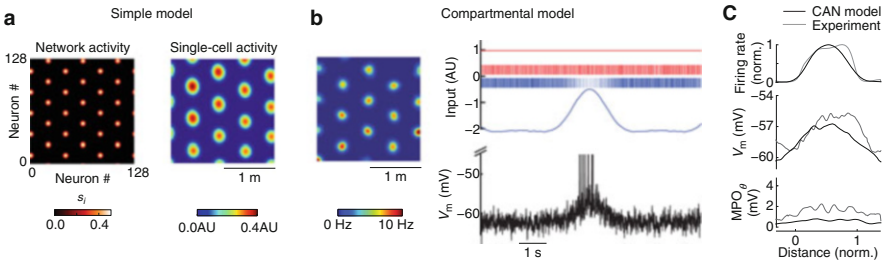

Fig. 5 Implementations of the continuous attractor network model. (**a**) In the simple implementation, 128^2 rate-based neurons are arranged on a neural sheet with periodic boundary conditions and Mexican hat connectivity as described by Equation 5. The left panel shows activity of each neuron in network space at a given moment in time. Note the periodic activity bumps that form spontaneously in the network. The right panel shows a colour-coded spatial map of the activity of an individual neuron averaged across time during simulated navigation within a square-shaped environment. (**b**) In a more detailed implementation, the probabilities of excitatory (red) and inhibitory (blue) input spikes in each time step are derived from the simple rate-based model in (A) and used to generate input to a compartmental stellate cell model. For further details see Schmidt-Hieber and Häusser (2013); code is available on ModelDB (accession number 150239). (**c**) Simulations demonstrate that the predictions of the CAN model closely match whole-cell recordings of grid cell membrane potential in behaving animals (Schmidt-Hieber and Häusser 2013; Domnisoru et al. 2013). The CAN model predicts a ramped depolarisation of the grid cell membrane voltage (V_m; middle panel) as the firing field is traversed (top panel), but no change in the amplitude of theta band membrane potential oscillations (MPO_θ) across the firing field. However, the CAN model does not account for the theta modulation or phase precession of grid cell firing (data not shown). Panels B-C adapted from Schmidt-Hieber and Häusser 2013

et al. 2013, 2016). For example, the coherent shift in firing field orientation (Hafting et al. 2005; Fyhn et al. 2007) and rescaling (Barry et al. 2007, 2012a; Stensola et al. 2012) of simultaneously recorded grid cells from the same module in 2D suggest that these are functionally coupled. In addition, instabilities in grid cell activity over time apparently correspond to drifts in a stable grid firing pattern relative to the environment, as opposed to corruption of the grid firing pattern itself, consistent with a CAN model (Hardcastle et al. 2015; Chen et al. 2016; Perez-Escobar et al., 2016).

The CAN model predicts the observed ramp depolarisation of grid cells in their firing field (Fig. 5c; Domnisoru et al. 2013; Schmidt-Hieber and Häusser 2013; Bush and Burgess 2014). Moreover, it has been demonstrated that stellate cells in mEC exhibit extensive recurrent inhibitory circuitry (Dhillon and Jones 2000; Couey et al. 2013; Fuchs et al. 2016) that is, in principle, sufficient to mediate continuous attractor dynamics (Burak and Fiete 2009; Pastoll et al. 2013; Shipston-Sharman et al. 2016). In addition, inhibitory inputs to stellate cells in mEC appear around the same time point during development as stable, adult-like grid cell firing patterns (Langston et al. 2010; Wills et al. 2010; Couey et al. 2013). Recent theoretical studies have demonstrated how this recurrent synaptic connectivity might be learned in an unsupervised manner (Widlowski and Fiete 2014), although it is also possible that some other mechanism is responsible for the initial generation of grid firing

patterns (McNaughton et al. 2006; Burgess et al. 2007; Kropff and Treves 2008; Bush and Burgess 2014; Dordek et al. 2016). Finally, cells with conjunctive grid × head direction responses, which are required to shift the activity bump in traditional CAN models, have been identified in the deeper layers of mEC (McNaughton et al. 2006; Sargolini et al. 2006; Navratilova et al. 2012). Similarly, the directionally modulated firing patterns exhibited by grid cells when excitatory drive to mEC is reduced by inactivation of the hippocampus are consistent with later CAN models (Bonnevie et al. 2013).

Implementations of CAN models with inhibitory disynaptic recurrent connectivity predict that silencing inhibitory interneurons in the mEC should eliminate grid cell firing patterns and that the same interneurons should exhibit spatially modulated firing patterns, as they are driven by input from grid cells (Pastoll et al. 2013; Bush and Burgess 2014). To date, it has been demonstrated that the firing patterns of parvalbumin-positive interneurons in mEC, which have strong, recurrent connections with grid cells, tend to show low spatial selectivity and gridness scores and that these interneurons receive input from grid cells with a wide range of spatial phases (Buetfering et al. 2014). This raises the question of whether they can support continuous attractor dynamics in the grid cell population. Nonetheless, several other classes of interneurons in the local circuits of mEC could be used to support continuous attractor dynamics, and further experiments are required to ascertain whether those neurons exhibit spatially modulated firing patterns or are necessary to support grid cell activity. Moreover, recent theoretical studies have demonstrated that adding spatially uncorrelated noise input to inhibitory neurons in a spiking CAN model (Pastoll et al. 2013) reduces spatial selectivity and impairs grid firing patterns in the interneuron population without compromising those in excitatory cells (Solanka et al. 2015).

Despite this wealth of evidence in support of attractor dynamics in grid cell firing patterns, very few CAN models of grid cell firing can account for theta modulation or phase precession. Those that do rely on subthreshold currents both to maintain the position of the activity bump between theta cycles (Pastoll et al. 2013) and to account for the temporal code of grid cell firing (Navratilova et al. 2012). This solution becomes problematic during periods when the animal is stationary, and grid cells are temporarily inactive or represent distant locations (Ólafsdóttir et al. 2016). As CAN models encode path integration information in the location of the activity bump, some mechanism must reinstantiate that activity bump in the same location within the network when the animal starts to move again and grid cell firing resumes. In familiar environments, theoretical studies have demonstrated that place or boundary cell input can eliminate drift of the attractor bump over time (Fuhs and Touretzky 2006; Guanella et al. 2007; Pastoll et al. 2013; Hardcastle et al. 2015). In novel environments, however, where the associations between grid, place and boundary cell responses have not been learned, there is no obvious solution to this problem.

It is also important to consider that grid firing patterns and phase precession may be functionally independent phenomena. For example, grid cells in layer III of the rodent mEC exhibit a triangular array of firing fields without phase precession,

spike times instead being phase locked to the trough of the ongoing theta oscillation (Hafting et al. 2008; Climer et al. 2013; Jeewajee et al. 2014). This raises the possibility that models of grid cell firing need not account for phase precession. However, these data also indicate that the firing of layer III grid cells follows that of layer II grid cells within each theta cycle, suggesting that they may inherit grid firing patterns from generative mechanisms in the more superficial layer (Hafting et al. 2008). In addition, there are – to date – no experimental manipulations that can eliminate grid cell phase precession without also eliminating grid firing patterns, indicating that the two phenomena may be co-dependent.

A Hybrid Grid Cell Model

The simulations and discussion above illustrate weaknesses in both the OI and CAN models – primarily, that the OI model fails to account for functional interactions between grid cell firing patterns or the subthreshold ramp depolarisation of grid cells in their firing fields and the CAN model fails to account for the phase precession of grid cell firing in the absence of an additional mechanism. In light of this, it is important to note that these two classes of grid cell model are not mutually exclusive – they each account for different properties of grid firing patterns using different mechanisms and can therefore be reconciled within a single 'hybrid' model (Burgess et al. 2007; Zilli 2012; Schmidt-Hieber and Häusser 2013; Bush and Burgess 2014). We now describe such a model, which makes use of continuous attractor dynamics to ensure relative stability among the firing patterns of grid cells from within the same module and produce subthreshold ramp depolarisation within firing fields, while oscillatory interference is used to shift the activity bump, generate phase precession and store path integration information in VCO phases between theta cycles and when the grid cell network is inactive.

In this implementation, grid cells are modelled as leaky integrate-and-fire neurons with a membrane time constant of $\tau_m = {}^{c_m}\!/_{g_m}$ (Equation 7). Simulated neurons integrate current input *I(t)* until the membrane potential V_m reaches a threshold V_t, at which point a spike is fired and the membrane potential is reset to V_{reset}.

$$\frac{dV_m}{dt} = \frac{1}{c_m}\left(I(t) - g_m\left(V_m - V_l\right)\right)$$

Equation 7 The leaky integrate-and-fire neuron model. The membrane potential V_m of a simulated neuron is dependent on the membrane capacitance c_m, membrane conductance g_m, applied current I and leak reversal potential V_l.

Grid cells receive synaptic input with fixed strength w_{VCO} from six populations of inhibitory VCOs that are arranged in ring attractor circuits (Blair et al. 2008; Welday et al. 2011; Bush and Burgess 2014). VCOs in each ring attractor circuit share a single preferred firing direction $\varnothing_{VCO}$ but differ in their initial phase φ_{VCO}.

To generate hexagonal grid-like firing patterns, the preferred firing directions of each VCO ring attractor circuit differ by multiples of 60°; and to produce evenly spaced grid fields, the initial phase of VCOs within each ring attractor circuit are uniformly distributed among N_{offset} values. To produce more realistic membrane dynamics in the grid cell population by increasing the number of inputs, N_{Vcopy} copies of each VCO input (i.e. combination of preferred firing direction and phase) are used.

The burst firing frequency of VCO inputs f_{VCO} increases linearly above a constant baseline oscillation frequency of f_{base}=8 Hz according to movement speed in the preferred direction (as described by Equation 1). Each VCO input produces an inhomogeneous, inhibitory Poissonian spike train only when movement speed in the preferred direction $\mathbf{v}_{\text{VCO}}$ is positive, with the probability $p(n, t)$ of firing n spikes in time step t described by Equation 8.

$$p\,(n,t) = \frac{\lambda_{\text{VCO}}^{n}(t)e^{-\lambda_{\text{VCO}}(t)}}{n!} H\,[\mathbf{v}_{\text{VCO}}]$$

$$\lambda_{\text{VCO}}(t) = \overline{r_{\text{VCO}}}\,(\cos\,(2\pi f_{\text{VCO}}(t)t + \varphi_{\text{VCO}}) + 1)\,\Delta t$$

Equation 8 Simulated VCO input spike train in the hybrid model of grid cell firing. The probability of a VCO input firing n spikes in time step t is dictated by the rate function λ_{VCO}, where $H[x] = 0$ for $x < 0$ and $H[x] = 1$ for $x \geq 0$. The rate function is, in turn, dictated by the mean VCO firing rate $\overline{r_{\text{VCO}}}$, burst firing frequency f_{VCO} (see Equation 1), spatial phase offset of that VCO input φ_{VCO} and length of the time step Δt.

Each grid cell in the hybrid network model is recurrently connected to a population of inhibitory interneurons that are also modelled as integrate-and-fire neurons according to Equation 7. All N_{Gcopy} grid cells that share a spatial phase send excitatory synapses with strength w_{GC} to a unique subpopulation of N_{Icopy} interneurons, which subsequently exhibit grid firing patterns with the same spatial phase. This interneuron subpopulation sends reciprocal projections with strength w_{INH} to the entire grid cell population with synaptic weights that are a cosine-tuned function of their difference in spatial phase to create a 'twisted torus' topology (Fig. 4c). Finally, to elicit firing, grid cells receive a tonic excitatory current $I_{\text{exc}}(t)$ that is drawn randomly from a Gaussian distribution with mean $\overline{I_{\text{exc}}}$ and standard deviation σ_{exc} at each time step.

Simulations of the hybrid model demonstrate that it can produce periodic, grid-like firing patterns in one- or two-dimensional environments (Fig. 6). In addition, theta phase precession of firing is observed as each grid field is traversed (Fig. 6b(v)). Moreover, the combination of rhythmic VCO input and recurrent inhibition can account for the experimentally observed pattern of subthreshold membrane potential dynamics (Domnisoru et al. 2013; Schmidt-Hieber and Häusser 2013). First, recurrent inhibition hyperpolarises grid cells outside of their firing fields, generating a slow, ramped depolarisation on entry to the firing field

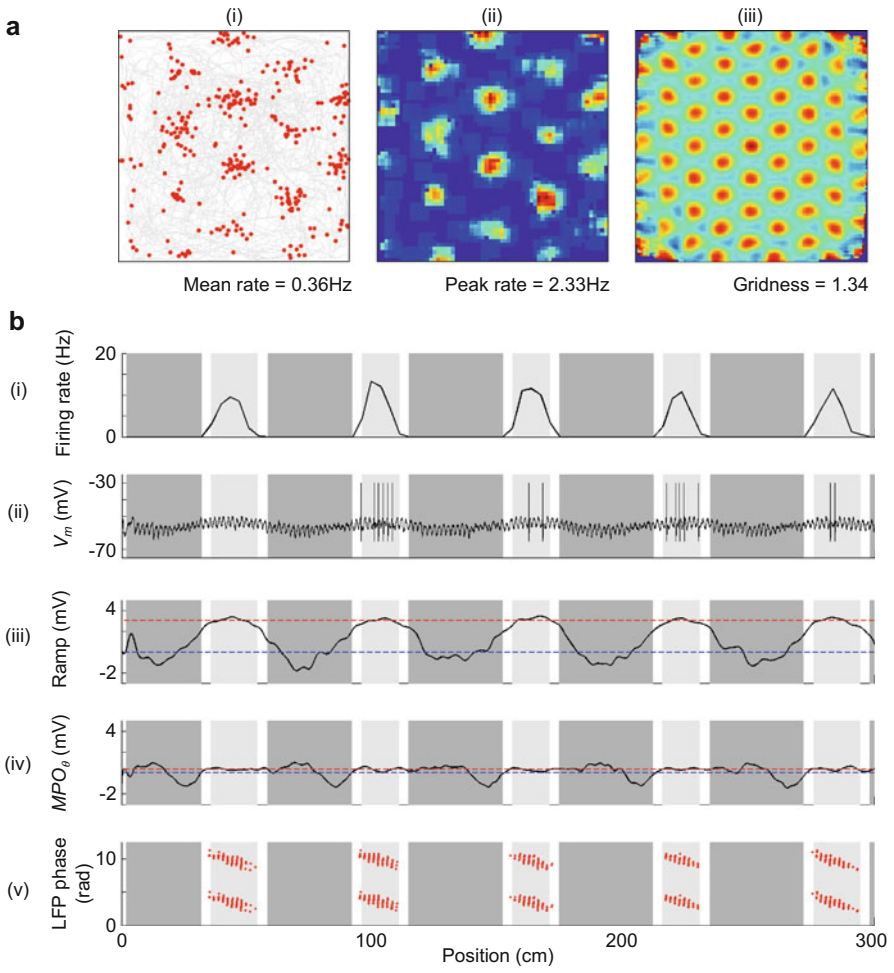

Fig. 6 A hybrid oscillatory interference (OI) and continuous attractor network (CAN) model (adapted from Bush and Burgess 2014). (**a**) Simulations of the hybrid OI/CAN model in a $1m^2$ 2D arena. VCO inputs determine the location of the activity bump and integrate movement over time, thereby shifting its location according to self-motion. Synaptic interactions between grid cells couple their firing patterns, providing relative stability. (i) Path taken by the animal (grey) and the location of spikes fired by a typical grid cell (red), (ii) smoothed firing rate map and (iii) smoothed spatial autocorrelation. (**b**) Simulations of the hybrid OI/CAN model on a 1D track. (i) Mean grid cell firing rate, (ii) membrane potential of a typical grid cell, (iii) mean low-frequency (<3 Hz) 'ramp' amplitude in the membrane potential, (iv) mean 5–11 Hz theta amplitude in the membrane potential and (v) phase of firing relative to LFP theta. In- (light grey background) and out-of-field (dark grey background) regions are used to compute mean ramp depolarisation and theta band MPO amplitude inside (red dashed line) and outside (blue dashed line) grid firing fields. The hybrid model predicts a ramped depolarisation of the grid cell membrane voltage as the firing field is traversed, and no change in the amplitude of membrane potential oscillations (MPO) across the firing field, in line with experimental data (Domnisoru and Tank 2013; Schmidt-Hieber and Häusser 2013)

(Fig. 6biii). Second, recurrent inhibition is theta modulated – as it is driven by active grid cells with theta-modulated firing – and so there is no significant difference in membrane potential theta amplitude in and out of the grid firing field, where subthreshold theta oscillations are driven by VCO inputs and recurrent inhibition, respectively (Fig. 6b(iv); see Bush and Burgess 2014, for more details).

Critique of the Hybrid Model

The hybrid model can account for a wide range of experimental data, including both the rate and temporal firing pattern of grid cells, the relative stability of grid cell firing patterns from the same module, and the subthreshold ramp depolarisation of grid cells inside the firing field. However, the hybrid model also exhibits some weaknesses. Firstly, it offers no explanation for the function of conjunctive cells in the deeper layers of mEC, or for the directional modulation of grid cell firing patterns when excitatory drive from the hippocampus is reduced, as the population activity bump is shifted by input from VCOs. It is possible that redundant mechanisms exist for path integration and both conjunctive cells or grid cells with directionally modulated input and VCOs are capable of updating grid cell firing during movement. Intriguingly, the majority of conjunctive cells do not show phase precession, suggesting that their firing patterns may be accounted for by a different mechanism (Climer et al. 2013). In its current form, then, the hybrid model predicts that silencing conjunctive cells should have no effect on grid firing patterns but that silencing VCO inputs should prevent the grid firing pattern from being updated during movement.

Secondly, the hybrid model – like all other CAN models – predicts that interneurons in circuits local to grid cell populations should exhibit spatially modulated firing patterns and that silencing those interneurons should impair grid firing patterns. As described above, it has been demonstrated that parvalbumin-positive inhibitory cells in mEC – which are strongly, recurrently connected to grid cells – show low spatial selectivity and low gridness scores and receive input from grid cells with a wide range of spatial phases (Buetfering et al. 2014). This suggests that this class of interneurons may not be able to support continuous attractor dynamics, although several other classes of interneurons exist in mEC and further experiments are required to ascertain their firing patterns and relationship to grid cell activity (Solanka et al. 2015). In addition, because grid cells in the hybrid model – unlike the majority of previous CAN models – exhibit phase precession, the interneurons that support continuous attractor dynamics should also exhibit phase precession (Bush and Burgess 2014). Whether interneurons in mEC exhibit this temporal code has yet to be established.

Finally, the hybrid model presented here also fails to account for sensory inputs to the grid cell network, which are likely to be important for reducing accumulated error during path integration (Fuhs and Touretzky 2006; Pastoll et al. 2013; Bush and Burgess 2014; Evans et al. 2016). Such inputs are straightforward to incorporate

into the model, however, by allowing the unsupervised learning of excitatory connections from place or boundary cells to grid cells. It is interesting to note that this spatially modulated input might, in familiar environments, be sufficient to produce a subthreshold ramp depolarisation in grid cells (Domnisoru et al. 2013; Schmidt-Hieber and Häusser 2013) and correlations in spike-timing at very short time lags between grid cells with similar spatial phases (Tocker et al. 2015).

The Future

Current experimental and theoretical data highlight several outstanding questions that are critical to the development of the next generation of grid cell models. First, both OI and CAN models assume that the primary function of grid cells is path integration and thus that grid firing patterns should primarily be accounted for by self-motion information. However, experimental evidence in support of this key assumption is currently lacking. Second, the effect of optogenetically silencing inhibitory interneurons in mEC on grid cell firing patterns should provide evidence either for or against the assumption, made by CAN models, that grid firing patterns are generated by recurrent inhibitory interactions between grid cells. Similarly, it would be of great interest to ascertain whether grid cells in other species, and in the rodent pre- and para-subiculum, exist within microcircuits of a similar structure or whether it is possible that independent mechanisms for generating grid firing patterns have evolved in disparate cortical and phylogenetic loci. Third, any mechanism that accounts for the existence of grid cell firing patterns must also provide some explanation for the sudden appearance of stable, adult-like grid cell responses in the rodent mEC during development. Fourth, optogenetic and juxtacellular recording techniques could shed light on the relationship between grid firing patterns in reelin-positive stellate (or 'ocean') cells and calbindin-positive pyramidal (or 'island') cells in mEC and how this relationship constrains the mechanism that generates grid firing patterns in each of these cell types across development.

Finally, most network-level models of grid cell firing assume that the individual rate-based or integrate-and-fire model neurons have uniform integrative properties and perform simple linear transformations of synaptic inputs into action potential output (Equation 4). However, grid cell candidate neurons in mEC express a rich repertoire of active nonlinear conductances, some of which are tuned to their functional grid cell properties (reviewed in Pastoll et al. 2012; Schmidt-Hieber and Häusser 2014; Schmidt-Hieber and Nolan 2017). Moreover, the functional distribution of synaptic inputs on the dendritic tree of grid cells may strongly affect how signals are integrated and transformed into action potential output. Imaging and electrophysiological studies suggest an important function for active dendritic conductances in the generation of place fields in CA1 (Lee et al. 2012; Bittner et al. 2015; Sheffield and Dombeck 2015). Similarly, active dendrites may improve the robustness and precision of the rate and temporal codes of grid cells, suggesting an

important role for nonlinear integration in the computation performed by grid cells (Schmidt-Hieber et al. 2017).

It is important to note that current experimental data also presents several challenges to all current models of grid cell firing patterns. First, distortions of the grid pattern close to environmental boundaries (Krupic et al. 2015; Stensola et al. 2015) present an issue to any model that accounts for grid cell firing patterns purely in terms of self-motion inputs, as it implies that an animal's perception of its own motion is perturbed by proximity to environmental boundaries. This issue might be solved by appealing to environmental sensory inputs to grid cells, which are likely to come from boundary cells (Evans et al. 2016; Hardcastle et al. 2015), but the question of why such inputs would actively distort the grid firing pattern, rather than simply reducing accumulated error, remain. It is possible that the observed grid field distortion offers a functional advantage, but if so, this has yet to be identified. Second, the stable differences in firing rate between different grid fields of a single cell are not accounted for by any of the models described above, although these differences may be important to encode contextual information and contribute to place cell remapping (Rolls et al. 2006; Andrzejak and Bicanski 2007; but see Fyhn et al. 2007). Finally, and most importantly, both OI and CAN models assume that self-motion input is readily available to the grid cell network and used to update grid firing patterns according to self-motion information. However, the overwhelming majority of single-cell responses in and around mEC encode head direction, not movement direction, even when those two signals differ significantly (Raudies et al. 2015). The importance of movement direction information is reinforced by the demonstration that phase precession follows body movement – rather than head direction – when rats travel backwards through place fields on a linear track (Cei et al. 2014). The origin of the movement direction signal that is clearly required to update grid cell firing patterns in this case, and during normal locomotion, has yet to be identified.

Acknowledgements The authors would like to thank Andrej Bicanski, Neil Burgess, Talfan Evans, Robin Hayman, Matt Nolan and Freyja Ólafsdóttir for helpful comments and discussion during the preparation of this chapter. This work was supported by a grant from the ERC (StG 678790 NEWRON to C.S.-H.).

Resources

A list of freely available code for various grid cell simulations is given below.

Burak and Fiete (2009) CAN simulations: http://clm.utexas.edu/fietelab/code.htm
Compilation of various grid cell model implementations by Eric Zilli (Zilli 2012): https://senselab.med.yale.edu/modeldb/showModel.cshtml?model=144006
Pastoll et al. (2013) CAN simulations: https://senselab.med.yale.edu/ModelDB/ShowModel.cshtml?model=150031

Schmidt-Hieber and Häusser (2013) compartmental model: https://senselab.med.yale.edu/modeldb/showModel.cshtml?model=150239

Solanka et al. (2015) CAN simulations: https://github.com/MattNolanLab/ei-attractor

Matlab code for hybrid model simulations presented in this chapter: https://senselab.med.yale.edu/ModelDB/ShowModel.cshtml?model=218085

References

Alonso A, Llinas RR (1989) Subthreshold Na^+-dependent theta-like rhythmicity in stellate cells of entorhinal cortex layer II. Nature 342:175–177

Andrzejak RG, Bicanski A (2007) Forming place cells through feedforward input from grid cells – a computational model. Soc Neurosci Abst 753:1

Barry C, Lever C, Hayman R, Hartley T, Burton S, O'Keefe J, Jeffery K, Burgess N (2006) The boundary vector cell model of place cell firing and spatial memory. Rev Neurosci 17:71–97

Barry C, Hayman R, Burgess N, Jeffery K (2007) Experience-dependent rescaling of entorhinal grids. Nat Neurosci 10:682–684

Barry C, Ginsberg LL, O'Keefe J, Burgess N (2012a) Grid cell firing patterns signal environmental novelty by expansion. PNAS 109:17687–17692

Barry C, Bush D, O'Keefe J, Burgess N (2012b) Models of grid cells and theta oscillations. Nature 488:E1

Bittner KC, Grienberger C, Vaidya SP, Milstein AD, Macklin JJ, Suh J, Tonegawa S, Magee JC (2015) Conjunctive input processing drives feature selectivity in hippocampal CA1 neurons. Nat Neurosci 18:1133–1142

Blair HT, Gupta K, Zhang K (2008) Conversion of a phase- to a rate-coded position signal by a three stage model of theta cells, place cells, and grid cells. Hippocampus 18:1239–1255

Blair HT, Wu D, Cong J (2014) Synchronization coding by ring attractors: a theoretical framework for oscillatory neurocomputing. Philos Trans R Soc Lond B 369:20120526

Boccara CN, Sargolini F, Thoresen VH, Solstad T, Witter MP, Moser EI, Moser MB (2010) Grid cells in pre- and parasubiculum. Nat Neurosci 13:987–994

Bonnevie T, Dunn B, Fyhn M, Hafting T, Derdikmann D, Kubie JL, Roudi Y, Moser EI, Moser M-B (2013) Grid cells require excitatory drive from the hippocampus. Nat Neurosci 16:309–317

Brandon MP, Bogaard AR, Libby CP, Connerney MA, Gupta K, Hasselmo ME (2011) Reduction of theta rhythm dissociates grid cell spatial periodicity from directional tuning. Science 332:595–599

Buetfering C, Allen K, Monyer H (2014) Parvalbumin interneurons provide grid cell–driven recurrent inhibition in the medial entorhinal cortex. Nat Neurosci 17:710–718

Burak Y, Fiete IR (2009) Accurate path integration in continuous attractor network models of grid cells. PLoS Comput Biol 5:e1000291

Burgess N, Barry C, Jeffery KJ, O'Keefe J (2005) A grid and place cell model of path integration utilizing phase precession versus theta. Computational cognitive neuroscience conference poster; Washington, DC: http://f1000.com/posters/browse/summary/225

Burgess N, Barry C, O'Keefe J (2007) An oscillatory interference model of grid cell firing. Hippocampus 17:801–812

Burgess N (2008) Grid cells and theta as oscillatory interference: theory and predictions. Hippocampus 18:1157–1174

Burgess CP, Burgess N (2014) Controlling phase noise in oscillatory interference models of grid cell firing. J Neurosci 34:6224–6232

Bush D, Burgess N (2014) A hybrid oscillatory interference/continuous attractor network model of grid cell firing. J Neurosci 34:5065–5079

Bush D, Barry C, Manson D, Burgess N (2015) Using grid cells for navigation. Neuron 87:507–520
Cei A, Girardeau G, Drieu C, El Kanbi K, Zugaro M (2014) Reversed theta sequences of hippocampal cell assemblies during backward travel. Nat Neurosci 17:719–724
Chen G, Manson D, Cacucci F, Wills TJ (2016) Absence of visual input results in the disruption of grid cell firing in the mouse. Curr Biol 26:2335
Climer JR, Newman EL, Hasselmo ME (2013) Phase coding by grid cells in unconstrained environments: two-dimensional phase precession. Eur J Neurosci 38:2526–2541
Conklin J, Eliasmith C (2005) An attractor network model of path integration in the rat. J Comput Neurosci 18:183–203
Couey JJ, Witoelar A, Zhang S-J, Zheng K, Ye J, Dunn B, Czajkowski R, Moser M-B, Moser EI, Roudi Y, Witter MP (2013) Recurrent inhibitory circuitry as a mechanism for grid formation. Nat Neurosci 16:318–324
Derdikman D, Whitlock JR, Tsao A, Fyhn M, Hafting T, Moser M-B, Moser EI (2009) Fragmentation of grid cell maps in multicompartment environment. Nat Neurosci 12:1325–1332
Dhillon A, Jones R (2000) Laminar differences in recurrent excitatory transmission in the rat entorhinal cortex in vitro. Neuroscience 99:413–422
Doeller CF, Barry C, Burgess N (2010) Evidence for grid cells in a human memory network. Nature 463:657–661
Dordek Y, Soudry D, Meir R, Derdikman D (2016) Extracting grid cell characteristics from place cell inputs using non-negative principal component analysis. elife 5:e10094
Domnisoru C, Kinkhabwala AA, Tank DW (2013) Membrane potential dynamics of grid cells. Nature 495:199–204
Eliav T, Geva-Sagiv M, Finkelstein A, Yartsev M, Rubin A, Las L, Ulanovksy N (2015) Synchronicity without rhythmicity in the hippocampal formation of behaving bats. Soc Neurosci Abstr 632:01
Ekstrom AD, Caplan JB, Shattuck K, Fried I, Kahana MJ (2005) Human hippocampal theta activity during virtual navigation. Hippocampus 15:881–889
Evans T, Bicanski A, Bush D, Burgess N (2016) How environment and self-motion combine in neural representations of space. J Physiol 594:6535
Fiete IR, Burak Y, Brookings T (2008) What grid cells convey about rat location. J Neurosci 28:6858–6871
Fuchs EC, Neitz A, Pinna R, Melzer S, Caputi A, Monyer H (2016) Local and distant input controlling excitation in layer II of the medial entorhinal cortex. Neuron 89:194–208
Fuhs MC, Touretzky DS (2006) A spin glass model of path integration in rat medial entorhinal cortex. J Neurosci 26:4266–4276
Fyhn M, Hafting T, Treves A, Moser M-B, Moser EI (2007) Hippocampal remapping and grid realignment in entorhinal cortex. Nature 446:190–194
Fyhn M, Hafting T, Witter MP, Moser EI, Moser MB (2008) Grid cells in mice. Hippocampus 18:1230–1238
Garden DLF, Dodson PD, O'Donnell C, White MD, Nolan MF (2008) Tuning of synaptic integration in the medial entorhinal cortex to the Organization of Grid Cell Firing Fields. Neuron 60:875–889
Gatome CW, Slomianka L, Lipp HP, Amrein I (2010) Number estimates of neuronal phenotypes in layer II of the medial entorhinal cortex of rat and mouse. Neuroscience 170:156–165
Giocomo LM, Zilli EA, Fransén E, Hasselmo ME (2007) Temporal frequency of subthreshold oscillations scales with entorhinal grid cell field spacing. Science 315:1719–1722
Giocomo LM, Moser M-B, Moser EI (2011) Computational models of grid cells. Neuron 71:589–603
Guanella A, Kiper D, Verschure P (2007) A model of grid cells based on a twisted torus topology. Int J Neural Syst 17:231–240
Hafting T, Fyhn M, Molden S, Moser MB, Moser EI (2005) Microstructure of a spatial map in the entorhinal cortex. Nature 436:801–806

Hafting T, Fyhn M, Bonnevie T, Moser MB, Moser EI (2008) Hippocampus-independent phase precession in entorhinal grid cells. Nature 453:1248–1252
Hardcastle K, Ganguli S, Giocomo LM (2015) Environmental boundaries as an error correction mechanism for grid cells. Neuron 86:1–13
Hasselmo ME (2008) Grid cell mechanisms and function: contributions of entorhinal persistent spiking and phase resetting. Hippocampus 18:1116–1126
Heys JG, Rangarajan KV, Dombeck DA (2014) The functional micro-organization of grid cells revealed by cellular-resolution imaging. Neuron 84:1079–1090
Horiuchi TK, Moss CF (2015) Grid cells in 3-D: reconciling data and models. Hippocampus 25:1489–1500
Jacobs J, Weidemann CT, Miller JF, Solway A, Burke JF, Wei X, Suthana N, Sperling MR, Sharan AD, Fried I, Kahana MJ (2013) Direct recordings of grid-like neuronal activity in human spatial navigation. Nat Neurosci 16:1188–1190
Jeewajee A, Barry C, O'Keefe J, Burgess N (2008) Grid cells and theta as oscillatory interference: electrophysiological data from freely-moving rats. Hippocampus 18:1175–1185
Jeewajee A, Barry C, Douchamps V, Manson D, Lever C, Burgess N (2014) Theta phase precession of grid and place cell firing in open environments. Philos Trans R Soc B 369:20120532
Killian NJ, Jutras MJ, Buffalo EA (2012) A map of visual space in the primate entorhinal cortex. Nature 491:761–764
Kitamura T, Pignatelli M, Suh J, Kohara K, Yoshiki A, Abe K, Tonegawa S (2014) Island cells control temporal association memory. Science 343:896–901
Koenig J, Linder AN, Leutgeb JK, Leutgeb S (2011) The spatial periodicity of grid cells is not sustained during reduced theta oscillations. Science 332:592–595
Kropff E, Treves A (2008) The emergence of grid cells: intelligent design or just adaptation? Hippocampus 18:1256–1269
Krupic J, Bauza M, Burton S, Barry C, O'Keefe J (2015) Grid cell symmetry is shaped by environmental geometry. Nature 518:232–235
Langston RF, Ainge JA, Couey JJ, Canto CB, Bjerknes TL, Witter MP, Moser EI, Moser MB (2010) Development of the spatial representation system in the rat. Science 328:1576–1580
Lee D, Lin BJ, Lee AK (2012) Hippocampal place fields emerge upon single-cell manipulation of excitability during behavior. Science 337:849–853
Lengyel M, Szatmáry Z, Érdi P (2003) Dynamically detuned oscillations account for the coupled rate and temporal code of place cell firing. Hippocampus 13:700–714
Lever C, Burton S, Jeewajee A, O'Keefe J, Burgess N (2009) Boundary vector cells in the subiculum of the hippocampal formation. J Neurosci 29:9771–9777
McFarland WL, Teitelbaum H, Hedges EK (1975) Relationship between hippocampal theta activity and running speed in the rat. J Comp Physiol Psychol 88:324–328
McNaughton BL, Battaglia FP, Jensen O, Moser EI, Moser MB (2006) Path integration and the neural basis of the cognitive map. Nat Rev Neurosci 7:663–678
Mhatre H, Gorchetchnikov A, Grossberg S (2012) Grid cell hexagonal patterns formed by fast self-organized learning within entorhinal cortex. Hippocampus 22:320–334
Naumann RK, Ray S, Prokop S, Las L, Heppner FL, Brecht M (2015) Conserved size and periodicity of pyramidal patches in layer 2 of medial/caudal entorhinal cortex. J Comp Neurol 524:783–806
Navratilova Z, Giocomo LM, Fellous JM, Hasselmo ME, McNaughton BL (2012) Phase precession and variable spatial scaling in a periodic attractor map model of medial entorhinal grid cells with realistic after-spike dynamics. Hippocampus 22:772–789
O'Keefe J, Nadel L (1978) The Hippocampus as a cognitive map. Oxford University Press, Oxford
O'Keefe J, Recce ML (1993) Phase relationship between hippocampal place units and the EEG theta rhythm. Hippocampus 3:317–330
Ólafsdóttir HF, Carpenter F, Barry C (2016) Coordinated grid and place cell replay during rest. Nat Neurosci 19:792–794
Orchard J (2015) Oscillator-interference models of path integration do not require theta oscillations. Neural Comput 27:548–560

Pastoll H, Ramsden H, Nolan MF (2012) Intrinsic electrophysiological properties of entorhinal cortex stellate cells and their contribution to grid firing fields. Front Neural Circuits 6:1–21

Pastoll H, Solanka L, van Rossum MCW, Nolan MF (2013) Feedback inhibition enables theta-nested gamma oscillations and grid firing fields. Neuron 77:141–154

Pérez-Escobar JA, Kornienko O, Latuske P, Kohler L, Allen K (2016) Visual landmarks sharpen grid cell metric and confer context specificity to neurons of the medial entorhinal cortex. elife 5: e16937

Raudies F, Brandon MP, Chapman GW, Hasselmo ME (2015) Head direction is coded more strongly than movement direction in a population of entorhinal neurons. Brain Res 1621:355–367

Ray S, Naumann R, Burgalossi A, Tang Q, Schmidt H, Brecht M (2014) Grid-layout and theta-modulation of layer 2 pyramidal neurons in medial entorhinal cortex. Science 343:891–896

Reifenstein ET, Kempter R, Schreiber S, Stemmler MB, Herz AV (2012) Grid cells in rat entorhinal cortex encode physical space with independent firing fields and phase precession at the single-trial level. PNAS 109:6301–6306

Reifenstein E, Stemmler M, Herz AVM, Kempter R, Schreiber S (2014) Movement dependence and layer specificity of entorhinal phase precession in two-dimensional environments. PLoS One 9:e100638

Remme MW, Lengyel M, Gutkin BS (2010) Democracy-independence trade-off in oscillating dendrites and its implications for grid cells. Neuron 66:429–437

Rivas J, Gaztelu JM, García-Austt E (1996) Changes in hippocampal cell discharge patterns and theta rhythm spectral properties as a function of walking velocity in the Guinea pig. Exp Brain Res 108:113–118

Rolls ET, Stringer SM, Elliot T (2006) Entorhinal cortex grid cells can map to hippocampal place cells by competitive learning. Netw Comput Neural Syst 447:447–465

Samsonovich A, McNaughton BL (1997) Path integration and cognitive mapping in a continuous attractor neural network model. J Neurosci 17:5900–5920

Sargolini F, Fyhn M, Hafting T, McNaughton BL, Witter MP, Moser MB, Moser EI (2006) Conjunctive representation of position, direction, and velocity in entorhinal cortex. Science 312:758–762

Savelli F, Yoganarasimha D, Knierim JJ (2008) Influence of boundary removal on the spatial representations of the medial entorhinal cortex. Hippocampus 18:1270–1282

Schmidt-Hieber C, Häusser M (2013) Cellular mechanisms of spatial navigation in the medial entorhinal cortex. Nat Neurosci 16:325–331

Schmidt-Hieber C, Häusser M (2014) How to build a grid cell. Philos Trans R Soc B 369:20120520

Schmidt-Hieber C, Toleikyte G, Aitchison L, Roth A, Clark BA, Branco T, Häusser M (2017) Active dendritic integration as a mechanism for robust and precise grid cell firing. Nat Neurosci 20:1114–1121

Schmidt-Hieber C, Nolan MF (2017) Synaptic integrative mechanisms for spatial cognition. Nat Neurosci 26:1483–1492

Sheffield ME, Dombeck DA (2015) Calcium transient prevalence across the dendritic arbour predicts place field properties. Nature 517:200–204

Shipston-Sharman O, Solanka L, Nolan MF (2016) Continuous attractor network models of grid cell firing based on excitatory–inhibitory interactions. J Physiol 594:6547.

Solanka L, van Rossum MCW, Nolan MF (2015) Noise promotes independent control of gamma oscillations and grid firing within a recurrent attractor network. elife 4:e06444

Solstad T, Boccara CN, Kropff E, Moser MB, Moser EI (2008) Representation of geometric borders in the entorhinal cortex. Science 322:1865–1868

Stemmler M, Mathis A, Herz AVM (2015) Connecting multiple spatial scales to decode the population activity of grid cells. Sci Adv 1:e1500816

Stensola H, Stensola T, Solstad T, Frøland K, Moser MB, Moser EI (2012) The entorhinal grid map is discretized. Nature 492:72–78

Stensola T, Stensola H, Moser M-B, Moser EI (2015) Shearing-induced asymmetry in entorhinal grid cells. Nature 518:207–212

Sun C, Kitamura T, Yamamoto J, Martin J, Pignatelli M, Kitch LJ, Schnitzer MJ, Tonegawa S (2015) Distinct speed dependence of entorhinal island and ocean cells, including respective grid cells. PNAS 112:9466–9471

Tocker G, Barak O, Derdikman D (2015) Grid cells correlation structure suggests organized feedforward projections into superficial layers of the medial entorhinal cortex. Hippocampus 25:1599–1613

Vanderwolf CH (1969) Hippocampal electrical activity and voluntary movement in the rat. EEG Clin Neurophysiol 26:407–418

Watrous AJ, Lee DJ, Izadi A, Gurkoff GG, Shahlaie K, Ekstrom AD (2013) A comparative study of human and rat hippocampal low-frequency oscillations during spatial navigation. Hippocampus 23:656–661

Welday AC, Shlifer IG, Bloom ML, Zhang K, Blair HT (2011) Cosine directional tuning of theta cell burst frequencies: evidence for spatial coding by oscillatory interference. J Neurosci 31:16157–16176

Welinder PE, Burak Y, Fiete IR (2008) Grid cells: the position code, neural network models of activity, and the problem of learning. Hippocampus 18:1283–1300

Wells CE, Amos DP, Jeewajee A, Douchamps V, Rodgers RJ, O'Keefe J, Burgess N, Lever C (2013) Novelty and anxiolytic drugs dissociate two components of hippocampal theta in behaving rats. J Neurosci 33:8650–8667

Widlowski J, Fiete IR (2014) A model of grid cell development through spatial exploration and spike time-dependent plasticity. Neuron 83:481–495

Wills TJ, Cacucci F, Burgess N, O'Keefe J (2010) Development of the hippocampal cognitive map in pre-weanling rats. Science 328:1573–1576

Winter SS, Mehlman ML, Clark BJ, Taube JS (2015) Passive transport disrupts grid signals in the Parahippocampal cortex. Curr Biol 25:2493–2502

Yartsev MM, Witter MP, Ulanovsky N (2011) Grid cells without theta oscillations in the entorhinal cortex of bats. Nature 479:103–107

Yoon K, Buice MA, Barry C, Hayman R, Burgess N, Fiete IR (2013) Specific evidence of low-dimensional continuous attractor dynamics in grid cells. Nat Neurosci 16:1077–1084

Yoon K, Lewallen S, Kinkhabwala AA, Tank DW, Fiete IR (2016) Grid cell responses in 1D environments assessed as slices through a 2D lattice. Neuron 89:1086–1099

Zhang K (1996) Representation of spatial orientation by the intrinsic dynamics of the head-direction cell ensemble: a theory. J Neurosci 16:2112–2126

Zilli EA (2012) Models of grid cell spatial firing published 2005–2011. Front Neural Circuits 6:16

Modeling Synaptic Plasticity in Hippocampus: A Calcium-Based Approach

Michael Graupner and Nicolas Brunel

Abstract Multiple stimulation protocols using firing rate and spike-timing correlations have been found to be effective in changing synaptic efficacy by inducing long-term potentiation or depression. In many of those protocols, increases in postsynaptic calcium concentration have been shown to play a crucial role. To which extent the plasticity outcome can be explained by the dynamics of the postsynaptic calcium alone remains unclear. Here, we discuss a minimal calcium-based model of a synapse in which potentiation and depression mechanisms are triggered by calcium. We illustrate that this model gives rise to a large diversity of spike timing-dependent plasticity curves, most of which have been observed experimentally in different systems. It accounts quantitatively for plasticity outcomes evoked by protocols involving patterns with variable spike timing and firing rate in hippocampus and neocortex. Furthermore, we use the model to predict memory decay times and plasticity in the presence of uncorrelated Poisson firing. The calcium model provides a mechanistic understanding of how various stimulation protocols provoke specific synaptic changes through the dynamics of calcium concentration and thresholds implementing in simplified fashion protein signaling cascades, leading to long-term potentiation and long-term depression.

M. Graupner (✉)
Laboratoire de Physiologie Cérébrale – UMR 8118, CNRS, Université Paris Descartes, Paris Cedex 06, France
e-mail: michael.graupner@parisdescartes.fr

N. Brunel
Departments of Neurobiology and Physics, Duke University, Durham, NC, USA
e-mail: nicolas.brunel@duke.edu

V. Cutsuridis et al. (eds.), *Hippocampal Microcircuits*, Springer Series in Computational Neuroscience, https://doi.org/10.1007/978-3-319-99103-0_17

Overview

Motivation for Including Biophysical Processes in Synaptic Plasticity Models

Activity-dependent, long-lasting changes in synaptic transmission efficacy (i.e., synaptic plasticity) underlie the functional reorganization of neuronal circuits, which in turn has been proposed as the biological substrate for learning and memory (Hebb, 1949). Long-term synaptic modifications have long been postulated to occur in response to the simultaneous activation of both pre- and postsynaptic neurons (Hebb, 1949). The first experiments on plasticity showed that a long-lasting increase in synaptic weight (long-term potentiation, LTP) could be induced by a repetitive high-frequency stimulation of the synaptic inputs (Bliss and Lømo, 1973), while a long-lasting decrease in synaptic weight (long-term depression, LTD) could be induced by a repetitive low-frequency stimulation (Dudek and Bear, 1993). More recent experiments provide evidence at the single-cell level that coincidence between afferent input with postsynaptic spiking evokes long-term modifications. In general, presynaptic input (onset of the excitatory postsynaptic potential – EPSP) occurring with little time difference to the postsynaptic action potential results in maximal synaptic modification, while no plasticity occurs if the temporal difference between both is large. In the hippocampus (Levy and Steward, 1983; Gustafsson et al., 1987; Magee and Johnston, 1997; Bi and Poo, 1998) an EPSP occurring repeatedly prior to the backpropagating action potential (pre-post pairing) typically evokes LTP, and the anti-causal order, i.e., an EPSP occurring repeatedly after the postsynaptic neuron spiked (post-pre pairing), typically leads to LTD. Such a temporal order of potentiation and depression occurrence is generally referred to as the "classical" spike-timing-dependent plasticity (STDP) rule.

Since the early STDP experiments, numerous studies in different brain regions and under varying experimental conditions have revealed a plethora of shapes of STDP curves. A second LTD window has been seen at large positive time differences between pre- and postsynaptic spike by a few studies in the hippocampus (Nishiyama et al., 2000; Wittenberg and Wang, 2006). In another form of STDP, the plasticity outcome does not depend on the order of the pre- and the postsynaptic spike but on the absolute value of the relative time difference alone (Egger et al., 1999; Wang et al., 2000; Wittenberg and Wang, 2006). Further studies investigating plasticity results in response to triplets and quadruplets of spikes have highlighted the nonlinearity of plasticity results (Bi and Wang, 2002; Froemke and Dan, 2002; Wang et al., 2005). These experiments have shown that whether the synapse gets potentiated or depressed in response to repetitive presentation of triplets or quadruplets of spikes cannot be deduced by adding linearly the changes emerging from pairs of spikes composing those activity patterns. These findings have led to phenomenological models which try to directly link spike patterns to the observed plasticity outcome (Sjöström et al., 2001; Froemke and Dan, 2002; Pfister and Gerstner, 2006; Clopath et al., 2010). Alternatively, it has been suggested that the link

between spike patterns and plasticity outcomes could arise naturally when taking into account biochemical intermediates such as the calcium concentration as the trigger of synaptic changes (Shouval et al., 2002, 2010; Graupner and Brunel, 2012). In that view, both firing rate and spike-timing-dependent plasticity are consequences of activity-dependent changes in the intracellular calcium concentration.

Here, we focus on the approach to link the calcium dynamics evoked by pre- and postsynaptic activity to observed plasticity outcomes. In particular, we will discuss a biologically plausible but simplified calcium-based model that provides links between stimulation protocols, calcium transients, protein signaling cascades, and evoked synaptic changes. The model implements in a schematic fashion two opposing calcium-triggered pathways mediating increases of synaptic strength (LTP; i.e., protein kinase cascades) and decreases of synaptic strength (LTD; i.e., protein phosphatase cascades or G-protein cascades). The model is shown to be able to account for a wide range of experimental plasticity outcomes in hippocampal cultures and hippocampal slices. Fitting this data quantitatively allows us to predict differences in the underlying calcium dynamics between these different experimental systems. The model allows us furthermore to predict plasticity outcomes in response to more realistic activity patterns than the periodic spike trains that are typically used in experiments. In particular, we present plasticity outcomes in response to uncorrelated pre- and postsynaptic Poisson firing.

Biophysical Underpinnings of Synaptic Plasticity at the Synapse

In glutamatergic synapses onto pyramidal cells in hippocampus and neocortex, synaptic activation leads to calcium entry in the postsynaptic terminal through N-methyl-D-aspartic acid receptor (NMDA-R)-channels (Koester and Sakmann, 1998; Kovalchuk et al., 2000; Yuste et al., 1999). Backpropagating action potentials (BPAPs) produce calcium influx through voltage-dependent calcium channels (VDCCs) (Jaffe et al., 1992; Majewska et al., 2000; Sabatini and Svoboda, 2000; Yuste and Denk, 1995). The induction of LTP at the hippocampal Schaffer collateral – CA1 neuron synapse necessitates activation of NMDA receptors (Collingridge et al., 1983; Bliss and Collingridge, 1993), while basal synaptic transmission and the maintenance of the potentiated state are not affected by NMDA blockade (Morris et al., 1986). The requirement of NMDA activation for LTP induction has also been identified between thick, tufted layer V pyramidal neurons in rat visual cortex (Artola and Singer, 1987; Bear et al., 1992; Markram et al., 1997; Sjöström et al., 2001), in layer IV to layer II/III pyramidal cell synapses in the somatosensory cortex (Castro-Alamancos et al., 1995; Feldman, 2000; Nevian and Sakmann, 2006), and in the lateral geniculate nucleus (Hahm et al., 1991; Mooney et al., 1993).

LTP induction evoked by STDP protocols also depends on the large calcium influx through NMDA-Rs in the hippocampus (Magee and Johnston, 1997) and the somatosensory cortex (Nevian and Sakmann, 2006). The induction of spike-timing-dependent LTD in visual and somatosensory cortex, however, is mediated by the

activation of presynaptic NMDA-Rs (Sjöström et al., 2003; Bender et al., 2006; Nevian and Sakmann, 2006). Nevian and Sakmann (2006) show in the somatosensory cortex that burst-pairing-induced LTD is independent of postsynaptic activation of NMDA-Rs, while the postsynaptic calcium influx through VDCCs is necessary for the induction of LTD. On the other hand, VDCC antagonists (nimodipine for L-type channels or Ni^{2+} for T-type channels) block spike-timing evoked LTP without any effect on baseline EPSPs in hippocampal slices (Magee and Johnston, 1997). In hippocampal cultures, (Bi and Poo, 1998) report that blocking L-type Ca^{2+} channels (by nimodipine) does not affect LTP induction by pre-post pairings but prevents LTD induction in response to post-pre pairings.

LTP and LTD rely on calcium influx through different channels, but both require postsynaptic calcium elevations (Lynch et al. 1983; Malenka et al. 1988; Neveu and Zucker 1996; Yang et al. 1999; Zucker 1999; Mizuno et al. 2001; Ismailov et al. 2004; Nevian and Sakmann 2006 – but see Nabavi et al. 2013). One of the main conclusions from those studies is that LTP is triggered by a brief increase of calcium with relatively high magnitude, whereas a prolonged modest rise of calcium reliably induces LTD. Neveu and Zucker (1996) show that the release of caged calcium by photolysis in hippocampal CA1 pyramidal cells is sufficient to evoke LTP and LTD and that concurrent presynaptic activity is not required. Nevian and Sakmann (2006) demonstrate that LTP and LTD are equally sensitive to fast (1,2-bis(o-aminophenoxy)ethane-N,N,N',N'-tetraacetic acid – BAPTA) and slow (ethylene glycol tetraacetic acid – EGTA) Ca^{2+} buffers loaded in the postsynaptic cell. They conclude that the calcium sensors that trigger the long-lasting synaptic changes respond to the global, volume-averaged increase in intracellular calcium concentration rather than to local calcium concentrations in microdomains. Note that cortical LTD involving the activation of metabotropic glutamate receptors (mGluRs) and retrograde signaling also requires postsynaptic calcium elevations (Nevian and Sakmann, 2006).

Modeling Approaches Using Calcium as the Plasticity Trigger

Calcium-based plasticity models determine the induced synaptic weight change based on the time course of the calcium transients triggered by pre- and postsynaptic spikes during specific stimulation protocols. The implementations differ in how activity patterns are translated into an intracellular calcium signal and how this signal is converted into a change in synaptic strength.

The Shouval et al. Model

Shouval et al. (2002) proposed a model in which the synaptic weight change is directly determined by the time course of the calcium transients triggered by pre-

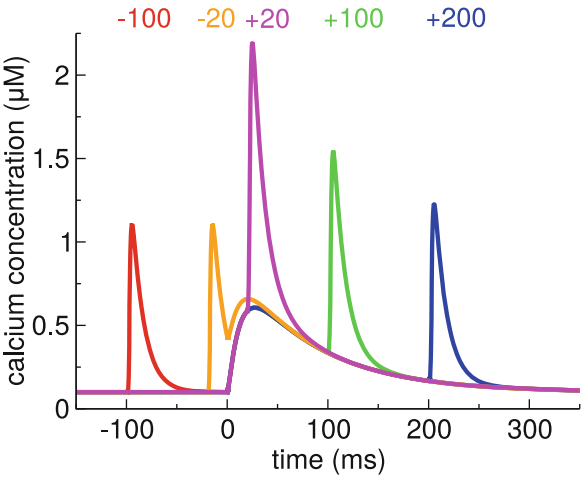

Fig. 1 Calcium dynamics in response to pairs of pre- and postsynaptic spikes for different Δts. Calcium transients for five different time differences (marked in the panel in ms) are shown. The transients are generated using the model for postsynaptic calcium and postsynaptic membrane potential dynamics presented in Graupner and Brunel (2007). The postsynaptic membrane potential is modeled using the Hodgkin-Huxley formalism in a single compartment. In the model, calcium influx is mediated by VDCCs (high-voltage activated L-type current) and voltage-dependent NMDA-Rs. The presynaptic spike occurs at $t = 0$ ms. The presynaptically evoked calcium amplitude is 0.6 μM, and the postsynaptic calcium amplitude is 1.2 μM (Sabatini et al., 2002). Note that the calcium amplitudes are the only parameters that are changed compared to Graupner and Brunel (2007). (Figure adapted from Graupner and Brunel 2010)

and postsynaptic spikes (Shouval et al., 2002; Cai et al., 2007). While this model readily accounts for LTD induction in response to post-pre pairs and for LTP in response to pre-post pairs, it leads to a second LTD window for pre-post pairs with large time differences, Δt, between pre- and postsynaptic spikes.

We start by discussing the properties of postsynaptic calcium transients evoked by pairs of spikes with different Δts. An isolated postsynaptic spike generates a short-lasting calcium transient due to opening of VDCCs induced by the depolarization through the BPAP (see $\Delta t = -100$ ms case in Fig. 1). Likewise, an isolated presynaptic spike generates a long-lasting calcium transient due to NMDA channel opening (Fig. 1). When the presynaptic spike is immediately followed by a postsynaptic spike, the strong depolarization by the BPAP increases drastically the voltage-dependent NMDA-R mediated calcium current due to removal of the magnesium block (Nowak et al. 1984; Jahr and Stevens 1990; magenta line in Fig. 1). This supralinear superposition of the two contributions at positive Δts generates a strong increase in the maximal amplitude and the integral of the calcium transients.

The induced synaptic weight change is then determined by the time course of the calcium transients (Shouval et al., 2002; Cai et al., 2007). The magnitude and sign of the resulting synaptic changes are based on the calcium control hypothesis (Fig. 2a)

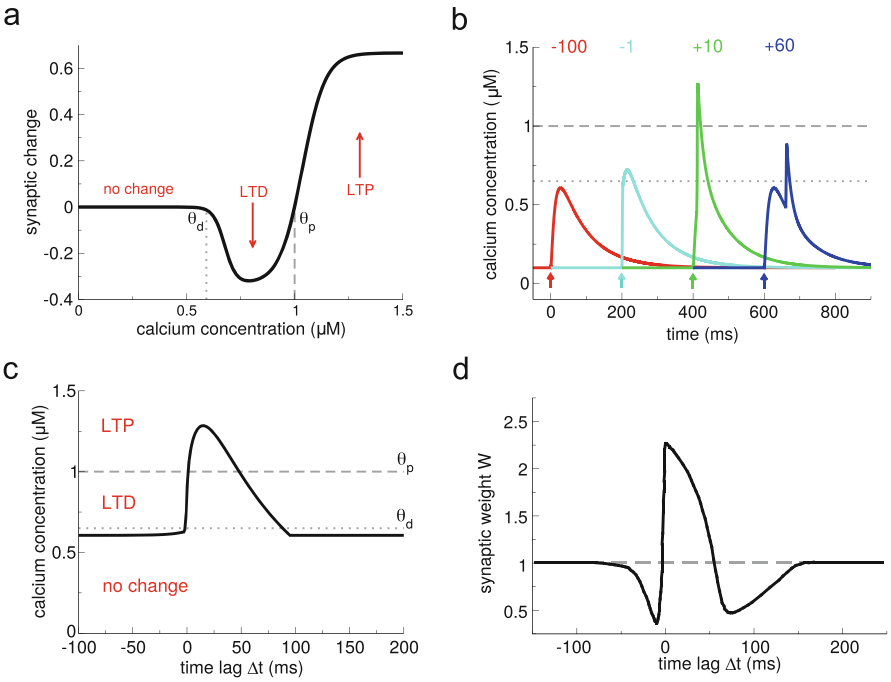

Fig. 2 Plasticity results based on calcium control hypothesis. (**a**) Calcium control hypothesis. The calcium control hypothesis posits that low calcium levels do not evoke any changes, intermediate calcium levels (between θ_d and θ_p) depress the synapse (leading to LTD), and high amplitude calcium transients (above θ_p) potentiate the synapse (leading to LTP). Note that depression and potentiation are not sudden events but occur with a calcium-dependent time constant, such that LTP induction is faster than LTD induction (see Shouval et al. 2002 for more details). (**b**) Calcium transients evoked by pairs of spikes and mediated exclusively by NMDA-Rs. In this plot, we use the model of Graupner and Brunel (2007), except that calcium influx occurs through NMDA-Rs only, i.e., there is no Ca^{2+} current mediated by VDCCs, as in Shouval et al. (2002). Otherwise, we use the same parameters as in Fig. 1, i.e., the presynaptically evoked Ca^{2+} amplitude is 0.6 μM. Calcium transients are shown for four different Δts (values given in the panel in ms). The timing of the presynaptic spike is indicated by an arrow for each particular Δt. The thresholds θ_d (dotted line) and θ_p (dashed line) from the calcium control hypothesis (see **a**) are chosen appropriately, that is, large Δt transients do not cross any threshold, short negative Δt transients cross θ_d, and short positive Δt transients cross θ_p. (**c**) Maximal calcium amplitude as a function of Δt, plotted together with the thresholds θ_d (dotted line) and θ_p (dashed line). (**d**) Plasticity outcomes in response to pairs of spikes. Pairs of spikes with short positive Δts evoke LTP. Pairs of spikes with short negative and with large positive Δts lead to LTD. Figure reproduced from Shouval et al. (2002). Note the large extent of the LTD range for short negative Δts as compared to **c**. The difference is due to the slow after-depolarizing tail of the BPAP used in Shouval et al. (2002). See text for more details. (Figure adapted from Graupner and Brunel 2010)

which is derived from experimental evidence showing that different calcium levels trigger different forms of synaptic plasticity (Zucker, 1999; Yang et al., 1999; Mizuno et al., 2001; Ismailov et al., 2004; Nevian and Sakmann, 2006). According to this hypothesis, no modification occurs when the calcium level is below a threshold θ_d which is larger than the resting concentration. If calcium resides in an intermediate calcium range, between θ_d and a second threshold $\theta_p > \theta_d$, the synaptic weight is decreased. Finally, if calcium increases above the second threshold, θ_p, the synaptic strength is potentiated (Fig. 2a).

This model explains to a large extent the spike-timing dependence of plasticity, as shown in Fig. 2, provided the maximal amplitude of the calcium transient for pre-post pairings at short Δt is larger than the potentiating threshold θ_p. Post-pre pairings evoke calcium transients which linearly superimpose and therefore yield moderate calcium elevations promoting LTD. Pre-post pairings result in supralinear superpositions of the calcium transients which attain high calcium levels required to evoke LTP. If Δt grows larger, the calcium transients pass again through a region of moderate levels inducing LTD (see Fig. 2c). Note that Shouval et al. (2002) assume the dominant source of calcium influx to be NMDA-Rs (compare Figs. 1a and 2b). They furthermore model the BPAPs with a slow after-depolarizing tail which increases the range of interaction between the postsynaptic spike and NMDA activation by the presynaptic action potential for $\Delta t < 0$. That interaction range defines the width of the LTD window in their model (compare LTD range in Fig. 2c without after-depolarizing tail, and the LTD range obtained in Shouval et al. 2002, reproduced in Fig. 2d).

Most STDP spike-pair experiments however have not found a "second LTD window" at large positive Δt (but see Nishiyama et al. 2000 and Wittenberg and Wang 2006). Shouval and Kalantzis (2005) show that stochastic properties of synaptic transmission can markedly reduce the LTD magnitude at positive time lags. The main idea is that the NMDA-mediated calcium transients at large positive Δts show a high level of relative fluctuations (high coefficient of variation) since the effective number of activated NMDA receptors is small. It is shown that a low number of NMDA-Rs ($\sim$10) gives rise to a sufficient amount of variability to average out the second LTD window (Shouval and Kalantzis, 2005).

Adding features such as short-term depression, stochastic transmitter release, and BPAP depression/facilitation to calcium-based models allows to reproduce spike-triplet data of hippocampal and visual cortex neurons (Cai et al., 2007). The nonlinearity of plasticity results between pre-post-pre and post-pre-post triplets is attributed in this model to the consecutive occurrence of either two presynaptic or two postsynaptic spikes, respectively. Depending on the recovery dynamics of neurotransmitter release, release probability and the depression/facilitation dynamics of BPAPs, two successive presynaptic spikes (in pre-post-pre triplets) and two successive postsynaptic spikes (in post-pre-post triplets) can generate markedly different calcium dynamics leading to different plasticity results. Models based on the calcium control hypothesis readily account for the frequency dependence of the plasticity (Shouval et al., 2002) and predict an optimal frequency for inducing LTP when the number of spikes in the stimulus is kept fixed (Kumar and Mehta, 2011).

The model described in this section has been surprisingly successful in reproducing experimental results about spike-timing dependent plasticity, given its simplicity. However, it leaves open the question of the mechanisms that translate a given calcium level into a particular synaptic change.

Models Including Biochemical Signaling Cascades Beyond Calcium

We now turn to models that include additional dynamical variables driven by the calcium concentration. These phenomenological variables can be seen as calcium-sensitive "detectors" mediating LTP and LTD (Karmarkar et al., 2002; Abarbanel et al., 2003; Rubin et al., 2005; Badoual et al., 2006). Such phenomenological detectors are assumed to represent biological signaling pathways in an abstract fashion.

Both Karmarkar et al. (2002) and Badoual et al. (2006) account for STDP using distinct but converging dynamical variables modeling calcium- and mGluR-activated pathways. In Badoual et al. (2006), an "LTP-mediating" enzyme is activated by large calcium transients. In contrast, LTD is evoked by the coincident activation of two enzymes, one activated by calcium and the other briefly activated by the presence of glutamate, potentially describing a mGluR-mediated signaling cascade. In turn, LTD occurs only when calcium is present at the time of the occurrence of the presynaptic spike, which is the case if the presynaptic spike is preceded by a BPAP. The model also accounts for plasticity results in response to pre-post-pre triplets in the visual cortex (Froemke and Dan, 2002). Karmarkar and Buonomano (2002) implement the calcium- and the mGluR pathway by assuming two functionally distinct calcium pools. In that view, calcium influx through VDCCs modulates the mGluR-mediated pathway leading to LTD induction, while calcium from NMDA-Rs is involved in LTP induction.

Abarbanel et al. (2003) propose a nonlinear competition between two calcium-sensitive detectors to evoke LTP/LTD, that is, phosphorylation and dephosphorylation processes which relate to the α-amino-3-hydroxyl-5-methyl-4-isoxazole-propionate receptor (AMPA-R, see next section) conductance. The half activation concentrations of the two opposing processes (described by Hill functions) are chosen well above the calcium amplitudes of single pre- or postsynaptic transients (Abarbanel et al., 2003). In consequence and similar to the results of Shouval et al. (2002), plasticity results in response to spike-pair stimulation yield LTD for short negative Δts, LTP for short positive Δts, and a further LTD window for large positive Δts (Abarbanel et al., 2003).

Rubin et al. (2005) propose a "detector" system based on pathways resembling the CaMKII kinase-phosphatase system (see Graupner and Brunel 2007), implementing three calcium-sensitive detectors ("P", "A", and "V"). In that model, high, short-lasting calcium levels evoke LTP by activating a detector promoting

the increase of synaptic weight ("P" in their model). Another detector builds up in response to low and prolonged calcium elevations (agent "A" and in turn "B") evoking LTD above a certain threshold. Importantly, intermediate calcium levels activate a "Veto" agent ("V") with a fast time constant providing fast tracking of the calcium transient. This veto mechanism suppresses the LTD induction pathway. The dynamics of the "veto" mechanism prevents in particular the appearance of LTD for large positive Δts in response to spike-pair stimulation (see Gerkin et al. 2010 for an in-depth review of the model).

Attention should be drawn to the fact that in all the models discussed so far, the time constant of the synaptic variable has to become essentially infinite at resting calcium concentration for the evoked synaptic changes not to decay after the presentation of the stimulation protocol. In the presence of noise and/or finite time constants, such models cannot maintain the evoked synaptic changes in a stable manner. This is in contrast to the model described in the next section, in which bistability leads naturally to maintenance of the evoked synaptic state.

A Minimal Calcium-Based Model

To get additional insights in the factors that govern the shape of STDP curves and the dependence of plasticity on other factors such as firing rates of pre- and postsynaptic neurons, spike patterns, and dendritic location, we recently developed and analyzed a simplified calcium-based rule (Graupner and Brunel, 2012). This simplification allowed us to compute analytically plasticity outcomes in response to standard protocols, as well as pre- and postsynaptic Poisson firing.

The model implements in a schematic fashion two opposing calcium-triggered pathways mediating increases of synaptic strength (LTP; i.e., protein kinase cascades) and decreases of synaptic strength (LTD; i.e., protein phosphatase cascades or G-protein coupled cascades). Both cascades are activated by calcium, and the resulting synaptic weight dynamics is described by

$$\tau\dot{\rho} = -\rho(1-\rho)(\rho_\star-\rho)-\gamma_d\rho\Theta[c(t)-\theta_d]+\gamma_p(1-\rho)\Theta[c(t)-\theta_p]+\text{Noise}(t). \quad (1)$$

τ is the time constant of synaptic efficacy changes happening on the order of seconds to minutes. The first term on the right-hand side describes the dynamics of the synaptic efficacy in the absence of pre- and postsynaptic activity. Here, we choose a cubic function of ρ that endows the synapse with two stable states at rest: one at $\rho = 0$, a DOWN state corresponding to low efficacy, and one at $\rho = 1$, an UP state corresponding to high efficacy. $\rho_\star = 0.5$ is the boundary of the basins of attraction of the two stable states. This bistable behavior is consistent with some experiments (Petersen et al., 1998; Bagal et al., 2005; O'Connor et al., 2005b) as well as some biochemically detailed models (Zhabotinsky, 2000; Graupner and Brunel, 2007). The next two terms in Eq. (1) describe calcium-dependent cascades leading to synaptic potentiation and depression, respectively. The synaptic efficacy variable

tends to increase, or decrease, when the instantaneous calcium concentration, $c(t)$, is above the potentiation (θ_p) or the depression threshold (θ_d), respectively (Θ denotes the Heaviside function, $\Theta[c-\theta]=0$ for $c<\theta$ and $\Theta[c-\theta]=1$ for $c\geq\theta$). The parameter γ_p (resp. γ_d) measures the rate of synaptic increase (resp. decrease) when the potentiation (resp. depression) threshold is exceeded.

The last term in Eq. (1) is an activity-dependent noise term, $Noise(t) = \sigma\sqrt{\tau}\sqrt{\Theta[c(t)-\min(\theta_d,\theta_p)]}\eta(t)$, where σ measures the amplitude of the noise, $\eta(t)$ is a Gaussian white noise process with unit variance, and the Θ function gives an activity dependence to noise (it is present whenever calcium is above the potentiation and/or depression threshold). This term accounts for activity-dependent fluctuations. See Fig. 3 and Graupner and Brunel (2012) for more details.

The postsynaptic calcium dynamics is described by

$$c(t) = \sum_i C_{\text{pre}} \exp\left(-\frac{t-t_i-D}{\tau_{Ca}}\right)\Theta\left(t-t_i-D\right) + \sum_j C_{\text{post}} \exp\left(-\frac{t-t_j}{\tau_{Ca}}\right)\Theta\left(t-t_j\right), \tag{2}$$

where c is the total calcium concentration, τ_{Ca} the calcium decay time constant, and C_{pre} and C_{post} the pre- and postsynaptically evoked calcium amplitudes (Fig. 3a). The sums run over all pre- and postsynaptic spikes occurring at times t_i and t_j, respectively. The time delay, D, between the presynaptic spike and the occurrence of the corresponding postsynaptic calcium transient accounts for the slow rise time of the NMDAR-mediated calcium influx.

The model is simple enough, so that the probabilities to induce LTP and LTD can be calculated analytically. The analytical results reproduce the model behavior under two assumptions: (i) single calcium transients induce small changes in the synaptic efficacy (Fig. 3c), and (ii) the depression and potentiation rates (γ_d and γ_p) are sufficiently large so that one can neglect the cubic term in Eq. (1) during synaptic stimulation (Fig. 3d, note the different scales for quadratic and double-well potentials). These assumptions reduce Eq. (1) to an Ornstein-Uhlenbeck process for which the potential of ρ during stimulation is quadratic with the minimum at $\bar{\rho}$ (Fig. 3b, d). This simplification allows to compute analytically the transition probabilities that the system will converge to the UP, $\mathcal{U}$, or the DOWN state, $\mathcal{D}$, using the Fokker-Planck formalism (Risken, 1996). The transitions induced by a particular plasticity protocol are largely determined by whether $\bar{\rho}$ is above or below the unstable fixed point $\rho_\star = 0.5$. LTP tends to be induced if $\bar{\rho} > \rho_\star$ (Fig. 3c, right), whereas LTD tends to be induced if $\bar{\rho} < \rho_\star$ (Fig. 3c, left). See Graupner and Brunel (2012) for details of the calculation.

We assume the synaptic strength is linearly related to ρ as $w = w_0 + \rho(w_1 - w_0)$, where w_0/w_1 is the synaptic strength of the DOWN/UP state. Synaptic strength as used here is typically measured in experiments as the excitatory postsynaptic potential (EPSP)/excitatory postsynaptic current (EPSC) amplitude, the initial EPSP

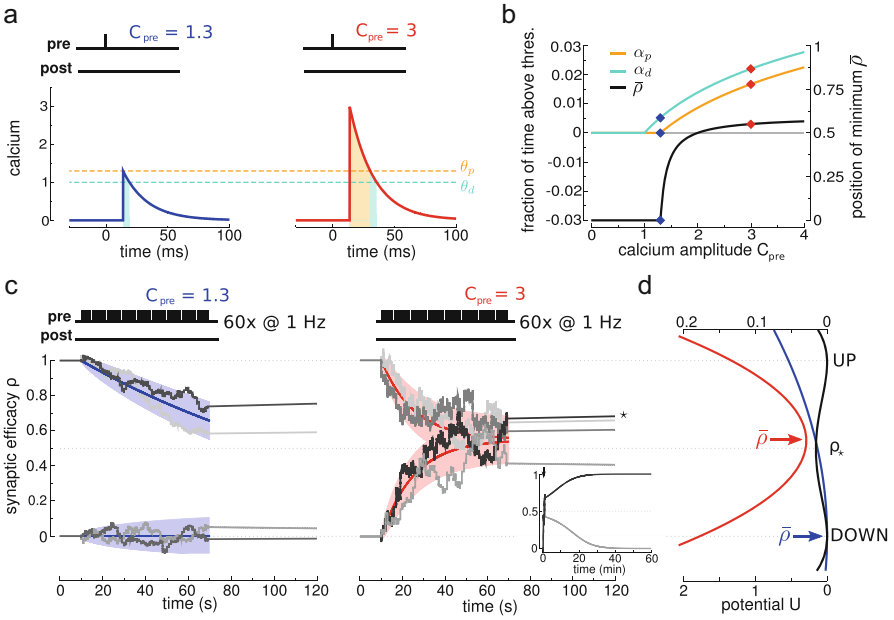

Fig. 3 Repeated calcium transients induce transitions between the two stable states of synaptic efficacy. (**a**) A presynaptic spike at time $t = 0$ ms induces a postsynaptic calcium transient of amplitude C_{pre} after a delay $D = 13.7$ ms. The two panels show transients with two different amplitudes, indicated on top of the panel. The times spent above the depression (turquoise) and the potentiation (orange) thresholds are indicated by shaded regions. (**b**) The higher the induced calcium transient, C_{pre}, the more time is spent above the depression (turquoise) and the potentiation (orange) thresholds (left-hand y-axis). Depression and potentiation together determine the average asymptotic value of synaptic efficacy, $\bar{\rho}$ (black, right-hand y-axis). The two examples from **a** are indicated by diamonds. (**c**) Repeated calcium transients of high amplitude can lead to a transition from the DOWN to the UP state. The dynamics of ρ is shown in response to 60 presynaptic spikes at 1 Hz inducing calcium transients of low (left-hand panel) and high (right-hand panel) amplitude. ρ resides initially in the UP or the DOWN state. Two instances of noise are shown for each initial condition (gray lines). A DOWN-to-UP transition occurs for the case marked with the star (right panel). The inset shows the temporal evolution of ρ on a longer time scale for the two cases starting at the DOWN state in the right-hand panel. The dynamics of the mean (colored line) and the standard deviation (shaded area) for the corresponding Ornstein-Uhlenbeck processes are depicted for each stimulation protocol and the two initial conditions. (**d**) During stimulation, the potential of the synaptic efficacy is approximately quadratic and has a single minimum at $\bar{\rho}$ (indicated by a colored arrow, shown for the two cases of **c**, bottom scale). In the absence of activity, the potential has two minima (black line, corresponding to two stable states, top scale). Note the different scales of the potential during (bottom) and in the absence (top) of synaptic activity (since $\gamma_p, \gamma_d \gg 1$, see text). (Adapted from Graupner and Brunel 2012)

slope, or the current in a 2 ms window at the peak of the EPSC. We assume that, before a stimulation protocol, a fraction β of the ensemble of stimulated synapses is in the DOWN state. The average initial synaptic strength is, therefore, equal to $\beta w_0 + [1 - \beta] w_1$. After the stimulation protocol, the average synaptic strength is

$w_0[(1-\mathcal{U})\beta+\mathcal{D}(1-\beta)]+w_1[\mathcal{U}\beta+(1-\mathcal{D})(1-\beta)]$, where $\mathcal{U}/\mathcal{D}$ are the probabilities of making a transition from the down to the up state/from the up to the down state, respectively. As in experiments, we consider the change in synaptic strength, α, as the ratio between the average synaptic strengths after and before the stimulation, i.e.,

$$\alpha = \frac{(1-\mathcal{U})\beta + \mathcal{D}(1-\beta) + b[\mathcal{U}\beta + (1-\mathcal{D})(1-\beta)]}{\beta + (1-\beta)b}, \tag{3}$$

with $b = w_1/w_0$. This change in synaptic strength can be computed analytically using the methods outlined above or using numerical simulations. Simulation results shown in Figs. 5 and 6 were obtained by simulating the model (Eq. (1)) 1,000 times with identical model parameters but different random number generator seeds for the Gaussian white noise process.

Fitting the Model to the Data

We explicitly fitted the above presented calcium-based model to experimental plasticity data obtained from synapses in hippocampal cultures (Wang et al., 2005) and slices (Wittenberg and Wang, 2006). A parameter set reproducing visual cortex plasticity data is furthermore provided in Graupner and Brunel (2012).

The stimulation protocol employed by Wittenberg and Wang (2006) explores plasticity at the Schaffer collateral – CA1 synapse for pre-post spike patterns with one or two postsynaptic spikes and for various number of spike pattern presentations. Pre- and postsynaptic spike pairings with one postsynaptic spike induce LTD only. LTP at positive values of Δt occurs when a burst of two spikes in close succession is combined with the presynaptic stimulation (as in the model by Kumar and Mehta 2011). Reducing the number of presentations of the pre-spike and post-burst pattern leaves LTP only (Wittenberg and Wang, 2006). Wang et al. (2005) induce pairs of spikes, triplets and quadruplets between neuron pairs with all patterns presented at 1 Hz for 60 times. Beyond the "classical STDP" curve obtained in response to pairs, the triplets and quadruplets uncover some nonlinearities underlying plasticity: (1) post-pre-post triplets induce LTP while pre-post-pre triplets induce little plasticity even though both patterns are comprised of the same spike pairings; (2) pre-post – post-pre quadruplets evoked no synaptic change, while post-pre – pre-post quadruplets evoked LTP (Wang et al., 2005).

Both hippocampal datasets provide the ideal test for the calcium-based model as the experimental conditions, and the synapse type can be assumed to be constant within each dataset. The only parameter which has been varied during each set of experiments is the activity patterns evoked in the pre- and postsynaptic neuron. In

Table 1 Parameters of the synapse model. The "hippocampal slices" and "cultures" parameters are obtained from fitting the synapse model to experimental data. Values in bold were fixed and were not allowed to be optimized by the fitting routine. The experimental external calcium concentrations is used to fit the respective data (Wittenberg and Wang, 2006; Wang et al., 2005); the external calcium concentration expected *in vivo* is given in brackets. The *in vivo* calcium amplitudes are derived using the estimated *in vivo* calcium concentration 1.5 mM and are given in brackets (Silver and Erecińska 1990, see text for more details). The right column shows the values of an example parameter set with balanced calcium amplitudes; other parameters are identical to the hippocampal slices dataset except for γ_p and β which were adjusted by hand to yield LTD at intermediate firing rates in Fig. 8c, f

Parameter	Hippocampal slices (Wittenberg and Wang, 2006)	Hippocampal cultures (Wang et al., 2005)	Balanced amplitudes example
$[Ca]_{ext}$ (mM)	2 (1.5)	3 (1.5)	–
τ_{Ca} (ms)	48.8373	11.9536	48.8373
C_{pre}	1 (0.75)	0.58156 (0.29078)	0.7
C_{post}	0.275865 (0.2069)	1.76444 (0.88222)	0.7
θ_d	**1**	**1**	1
θ_p	**1.3**	**1.3**	1.3
γ_d	313.0965	61.141	313.0965
γ_p	1645.59	113.6545	600
σ	9.1844	2.5654	9.1844
τ (sec)	688.355	33.7596	688.355
$\rho_\star$	**0.5**	**0.5**	0.5
D (ms)	18.8008	10	18.8008
β	**0.7**	**0.5**	0.5
b	5.28145	36.0263	5.28145

turn, the model should account for the observed plasticity outcomes in response to all employed stimulation protocols using the same parameter set accounting for the investigated synapse.

We defined the goodness of fit to the experimental data by a cost function which is the sum of all squared distances between data points and the analytical solution of the calcium-based model. We furthermore included two terms in the cost function which assured that synaptic changes induced by single calcium transients are small and that synaptic changes are slow compared to the calcium dynamics ($\tau \gg \tau_{Ca}$). We drew initial parameter values from a uniform distribution and use the Powell method of gradient descent to search the minimum of the cost function. The fit is repeated $>10^9$ times as the nonlinearities due to the calcium thresholding create a landscape with many local minima. The parameter set with the lowest cost function is used (Table 1). The 100 fit results with the lowest cost functions are shown in Fig. 4c (squares for the hippocampal slices and circles for the hippocampal cultures dataset) with respect to C_{pre} and C_{post}.

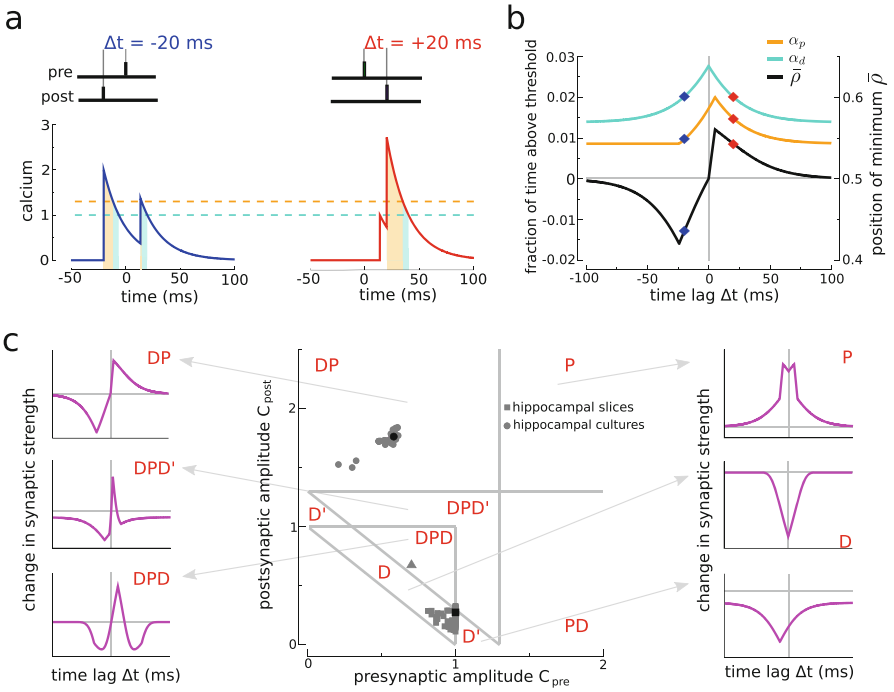

Fig. 4 Diversity of STDP curves in response to spike pair stimulation. (**a**), Compound calcium transients evoked by a pair of pre- and postsynaptic spikes for two values of Δt (indicated on top of the panels) for $C_{\text{pre}} = 1$ and $C_{\text{post}} = 2$. (**b**), Fraction of time spent above the depression (turquoise line) and potentiation thresholds (orange) and average asymptotic value of the synaptic efficacy ($\bar{\rho}$; black) as a function of Δt for the parameters of **a**. The two examples from **a** are indicated by diamonds in the same color. (**c**) The C_{pre}-C_{post} plane is shown for $\theta_d = 1$, $\theta_p = 1.3$. The seven regions of different possible STDP outcomes for spike-pair stimulation are indicated with respect to the occurrence of potentiation (P) and depression (D) along the Δt axis and illustrated in the left and right column of the panel. The gray squares and circles show outcomes from fitting the model to experimental data obtained in hippocampal slices (Wittenberg and Wang, 2006) and hippocampal cultures (Wang et al., 2005), respectively. The 100 best fit results obtained from randomly drawn initial conditions are shown for each of the two systems. The fit results used in Figs. 5, 6, 7 and 8 are shown as black symbols (see Table 1). Fits of the data from hippocampal slices lie in the D region, with small amplitudes of the presynaptically triggered calcium transient (Wang et al., 2005). Fits from hippocampal cultures lie in the DP region, with large amplitudes of the postsynaptically triggered calcium transient (Wang et al., 2005). Interestingly, all fits to the two different datasets yield comparable presynaptic calcium amplitudes. The location of the example parameter set with equal pre- and postsynaptic amplitudes (used in Fig. 8) is shown by the triangle (see Table 1). (Adapted from Graupner and Brunel 2012)

Model Results

Diversity of STDP Curves

We start by explaining how the model reproduces the "classical" STDP curve, that is, depression for post-pre and potentiation for pre-post pairs. Such a curve can be obtained when the potentiation threshold is larger than the depression threshold ($\theta_p > \theta_d$, consistent with O'Connor et al. 2005a); the amplitude of the postsynaptic calcium transient is larger than the potentiation threshold ($C_{\text{post}} > \theta_p$), and the amplitude of the presynaptic transient is smaller than the potentiation threshold ($C_{\text{pre}} < \theta_p$). In addition, we impose that pairs of spikes with a large time difference should not evoke efficacy changes. This is the case if potentiation and depression rates balance on average during the protocol (i.e., $\bar{\rho} = 0.5$). These conditions yield the "classical" STDP curve (Fig. 4b).

For large Δt, pre- and postsynaptic calcium transients do not interact, and contributions from potentiation (due to the postsynaptic spike) and depression (due to the postsynaptic spike and to the presynaptic spike if $C_{\text{pre}} > \theta_d$) cancel each other, leading to no synaptic changes on average. For short negative Δt, the presynaptically evoked calcium transient rises above the depression threshold. Consequently, depression increases, while potentiation remains constant, which brings the potential minimum closer to the DOWN state ($\bar{\rho} < 0.5$) leading to LTD induction (Fig. 4a, b). For short positive Δt, on the other hand, the postsynaptically evoked calcium transient rides on top of the presynaptic transient and increases activation of both depression and potentiation. This brings the potential minimum closer to the UP state ($\bar{\rho} > 0.5$) and in turn gives rise to potentiation, since the rate of potentiation is larger than the rate of depression ($\gamma_p > \gamma_d$, Fig. 4a, b). As observed in experiments, the transition from maximal potentiation to maximal depression occurs within a small range of time lags.

We now turn to discuss how STDP curves change when amplitudes of calcium transients or thresholds for potentiation and depression are varied. We find that a total of 10 qualitatively different STDP curves can be observed, D, D', DP, DPD, DPD', P, P', PD, PDP, and PDP', where D refers to depression and P to potentiation (see Fig. 4c side panels for some illustrations), depending on parameters. For example, in region D, depression occurs at all values of Δt, while region DPD means that when one increases Δt from large negative values, one first sees depression, then potentiation, and again depression. We impose no synaptic changes for large Δt (i.e., $\bar{\rho} = 0.5$) in regions where potentiation *and* depression are activated by individual calcium transients (P, DP, and PD). That requirement fixes the ratio γ_p/γ_d. A prime (e.g., D') means that in the corresponding region, potentiation and depression cannot be balanced for large Δt. This occurs when single calcium transients cross the depression but not the potentiation threshold (or vice versa). We furthermore choose γ_p and γ_d to yield both potentiation and depression in the DPD, PDP, DPD', and PDP' regions. For example, in the DPD' region, D' behavior can also be observed if γ_p is not large enough.

In Fig. 4c, these regions are plotted in the C_{pre}-C_{post} plane, for fixed values of the potentiation and depression thresholds ($\theta_p = 1.3, \theta_d = 1$). Starting from the already discussed DP region ("classical" STDP curve, top left corner of middle panel in Fig. 4c), we see that decreasing the amplitude of postsynaptic calcium transients leads to the DPD' and DPD regions, in which a second LTD window appears at positive Δt. Decreasing C_{pre} and C_{post} further so that their sum is below the potentiation threshold leads to the D and D' regions (depression occurs at all Δt). If both calcium transients are individually larger than the potentiation threshold, then only potentiation occurs (P region). Exchanging pre and post leads to an inversion of the curves along the Δt-axis – for example, $C_{\text{pre}} > \theta_p > C_{\text{post}}$ leads to a STDP curve that is inverted (PD) compared to the "classical" one (DP), as seen in some systems (Bell et al., 1997; Paille et al., 2013). Furthermore, a DPD curve occurs if both thresholds are crossed by interacting calcium transients only, a region originally described by Shouval et al. (2002).

The diversity of STDP curves emerges solely from a combination of linear superpositions of calcium transients from pre- and postsynaptic spikes, followed by the potentiation/depression threshold nonlinearities.

Dependence of Synaptic Plasticity on Spike Patterns

We demonstrate here that the model can quantitatively reproduce the data of Wittenberg and Wang (2006) from CA3-CA1 slices and of Wang et al. (2005) from hippocampal cultures. Our fit allows us to infer information about the calcium transients, and we illustrate that the model predicts that the postsynaptically evoked calcium transient is markedly different.

We find that all the results of the Wittenberg and Wang (2006) experiment can be reproduced by our model (see Fig. 5), provided the parameters of the model are such that it is located in the D region for single pairs of spikes at low frequency (Fig. 4). This naturally reproduces the results for the protocol in which the postsynaptic neuron emits a single spike (Fig. 5a, b). Adding a second postsynaptic spike with a short inter-spike interval between the two leads to a pronounced increase in the amplitude of the compound calcium trace (Fig. 5c), giving rise to LTP at short positive Δt (DPD curve), provided the potentiation rate γ_p is large enough (Fig. 5d). Interestingly, the model then produces a faster induction of LTP than LTD (as also seen in Froemke et al. 2006), which explains why only potentiation is seen when the duration of the protocol is reduced (Fig. 5e). The model parameters can be fitted quantitatively to the data of Wittenberg and Wang (2006) (see Table 1), yielding a reasonable fit between both. The model can then be used to predict the plasticity outcomes for arbitrary protocols in the same experimental setting. For example, we predict that adding a third spike in the burst would yield broader and stronger LTP at positive Δt and short negative Δt (Fig. 5f)

The fit of the model to the plasticity data from hippocampal slices (Wittenberg and Wang, 2006) yields a strong asymmetry between pre- and postsynaptically

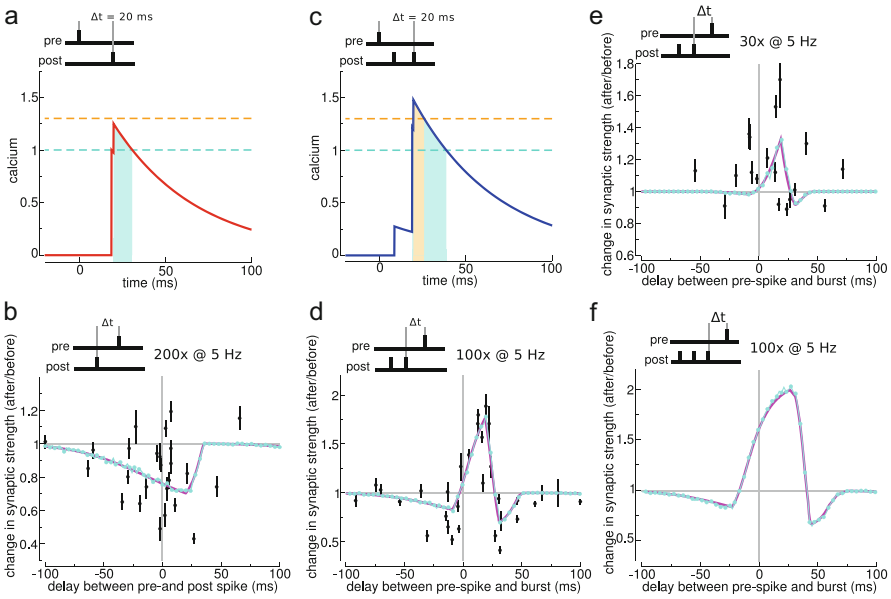

Fig. 5 Number of postsynaptic spikes and number of repetitions of the stimulation motif change qualitatively the STDP curve. (**a**) Compound calcium trace evoked by a spike-pair for $C_{\text{pre}} = 1$, $C_{\text{post}} = 0.276$, and $\Delta t = 20$ ms. For these parameter values, the calcium trace remains below the potentiation threshold ($\theta_p = 1.3$, $\theta_d = 1$). (**b**) For the parameters of **a**, spike-pair simulation induces synaptic depression for small positive and negative values of Δt. (**c**) Adding a postsynaptic spike, resulting in a postsynaptic burst with an inter-burst interval of 11.5 ms, leads to crossing of the potentiation threshold. (**d**) Pre-spike and post-burst stimulation results in a DPD curve. (**e**) Reducing the number of pre-spike, post-burst motif presentations from 100 to 30 turns the DPD curve into a PD curve exhibiting potentiation, with little depression at positive Δt. (**f**) Pre-spike and post-burst stimulation with three postsynaptic spikes amplify potentiation at short positive Δts. All data points are taken from plasticity experiments in hippocampal slices (mean ± SEM, Wittenberg and Wang 2006). Analytical results of changes in synaptic strength are shown in magenta, and simulation results in cyan. See Table 1 for parameters. (Adapted from Graupner and Brunel 2012)

induced calcium amplitudes with a small postsynaptic amplitude (see Table 1). In turn, the fit results gather in the lower part of the D region (see Fig. 4c). The size of C_{post} depends on the distance between θ_d and θ_p as adding a single postsynaptic spike moves the system from the D – for pre-post spike pairs – to the DPD region, for pre-spike and post-burst. In turn, choosing a larger difference between the two thresholds would yield more balanced calcium amplitudes.

We now demonstrate that our synapse model naturally reproduces nonlinearities of spike-triplet and quadruplet experiments, if calcium amplitudes of pre- and post-synaptically evoked transients have different amplitudes. In those experiments from hippocampal cultures, post-pre-post triplets and post-pre-pre-post quadruplets are shown to evoke LTP, while pre-post-pre triplets and pre-post-post-pre quadruplets induce no synaptic changes (or little potentiation, Wang et al. 2005).

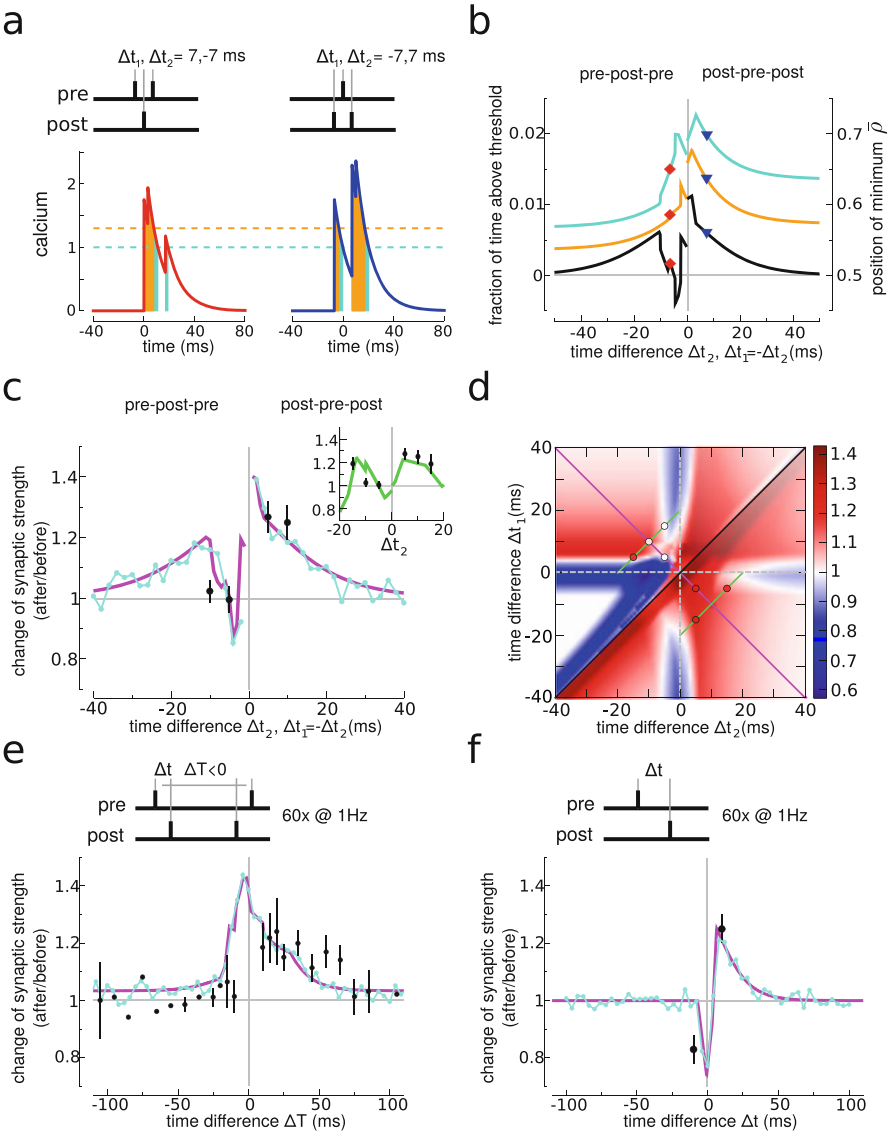

Fig. 6 Nonlinearities in response to spike-triplet and quadruplet stimulation in hippocampal cultures. (**a**) Calcium transients evoked by a pre-post-pre triplet (red line, $\Delta t_1 > 0$, $\Delta t_2 < 0$, see Wang et al. 2005 for the convention of Δt_1 and Δt_2) and a post-pre-post triplet (blue, $\Delta t_1 < 0$, $\Delta t_2 > 0$). Note the large calcium transients evoked by postsynaptic spikes ($C_{\text{post}} = 1.7644$, $C_{\text{pre}} = 0.5816$). (**b**) The fractions of time spent above the depression (turquoise) and the potentiation threshold (orange, left-hand y-axis) as well as position of the potential minimum, $\bar{\rho}$, (black, right-hand y-axis) are shown with respect to Δt_2 for the case of symmetrical spike triplets, i.e., $\Delta t_1 = -\Delta t_2$. The two examples from **a** are indicated by symbols in the same color. (**c**) The change in synaptic strength for symmetrical spike triplets ($\Delta t_1 = -\Delta t_2$) shows a clear imbalance: pre-post-pre triplets evoke no change or little potentiation, while post-pre-post triplets induce potentiation.

We fitted the synapse model to experimental plasticity results from protocols with spike-triplets and quadruplets (Fig. 6, Wang et al. 2005). The resulting parameter sets are located in the DP region (Fig. 4), consistent with the experimental results on pairs of spikes in hippocampal cultures (Bi and Poo, 1998; Wang et al., 2005) and in particular consistently yield a large postsynaptically evoked calcium amplitude, $C_{\text{post}} > C_{\text{pre}}$ (Fig. 6a). Consequently, post-pre-post triplets lead to stronger activation of potentiation compared to pre-post-pre triplets (Fig. 6b). Together with a potentiation rate that is larger than the depression rate ($\gamma_p > \gamma_d$), this creates an imbalance in plasticity outcomes between pre-post-pre and post-pre-post triplets (Fig. 6c, d). The model is also able to fit the quadruplet data (Fig. 6e), again due to the pronounced difference between pre- and postsynaptically evoked calcium transients. Finally, parameters that best fit triplet and quadruplet data also reproduce the pair data (Fig. 6f).

Plasticity in Physiological Conditions

The above studied deterministic spike patterns are at odds with experimentally recorded spike trains *in vivo*, which show a pronounced temporal variability. Furthermore, most of the *in vitro* experiments evoking synaptic changes use elevated extracellular calcium concentrations ($\geq$2 mM), while *in vivo* calcium levels are estimated to be around 1.5 mM or lower (Silver and Erecińska, 1990). We therefore turn to investigate the impact of reduced calcium entry due to the lower extracellular calcium concentration *in vivo* and of uncorrelated Poisson spike trains of pre- and postsynaptic neurons on synaptic plasticity (Figs. 7 and 8).

We first investigate the synaptic memory time constants in the presence of uncorrelated pre- and postsynaptic Poisson firing at various rates and for experimental

Fig. 6 (continued) The inset shows triplets with $\Delta t_1 = \Delta t_2 + 20$ ms for $-20 < \Delta t_2 < 0$ ms and $\Delta t_1 = \Delta t_2 - 20$ ms for $0 < \Delta t_2 < 20$ ms (see **d**). (**d**) The imbalance in plasticity outcomes between pre-post-pre and post-pre-post triplets becomes more apparent in the Δt_1 - Δt_2 plane. The color code depicts the change in synaptic strength as given by analytical results. Post-pre-post triplets evoke strong synaptic potentiation for small $|\Delta t_1|$ and $|\Delta t_2|$. The magenta and the green lines indicate the pairs of Δt_1, Δt_2 exemplified in **C** in the same color. The middle diagonal (black line) separates pre-post-pre (upper-left triangle) and post-pre-post triplets (lower right triangle). (**e**) In line with experiments, spike-quadruplet stimulation yields stronger potentiation for post-pre-pre-post quadruplets (convention: $\Delta T > 0$) as compared to pre-post-post-pre quadruplets ($\Delta T < 0$; $\Delta t = 5$ ms and -5 ms for pre-post and post-pre pairs, respectively). (**f**) Using the same parameter set as in **a**–**e**, the model reproduces the classical STDP curve (DP) in response to spike-pair stimulation as seen in experiments. All changes in synaptic strength are in response to the presentation of 60 motifs at 1 Hz. All data points in this figure are taken from Wang et al. (2005) (mean $\pm$ SEM, if multiple points are available). Analytical results of changes in synaptic strength are shown in magenta, and simulation results in cyan. The "hippocampal cultures" parameter set is used in this figure (see Table 1). (Adapted from Graupner and Brunel 2012)

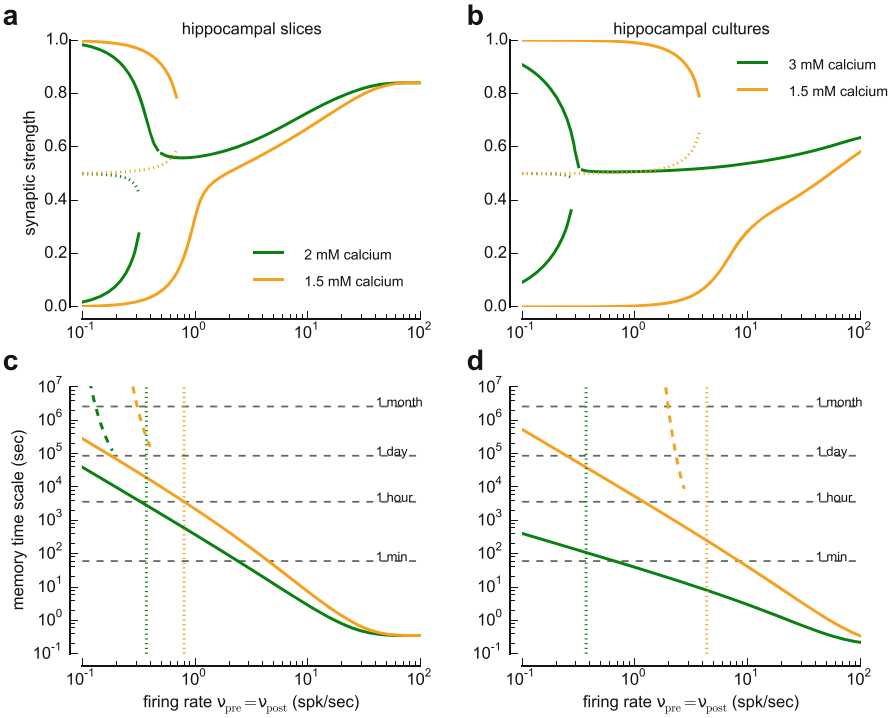

Fig. 7 Stable states and memory decay for a single bistable synapse in the presence of uncorrelated pre- and postsynaptic Poisson firing. (**a**, **b**) Steady states of synaptic efficacy as a function of firing rate for the *in vitro* (green) and the *in vivo* (orange) parameter sets accounting for hippocampal slices (**a**) and cultures (**b**) data. Stable states are shown by solid lines and unstable states by dotted lines. Synaptic efficacy is bistable at low rates and monostable at intermediate to high firing rates. (**c**, **d**) Single exponential decay time constant as a function of the firing rate for the *in vitro* (green) and the *in vivo* (orange) parameter sets for hippocampal slices (**c**) and cultures (**d**). The effective decay time is greatly extended at around and below the vertical lines which mark the appearance of the two stable states – bistability (compare panels **a** and **b**). The decay time in the bistable region can be predicted using Kramers escape rate (dashed line, see text for more details). The hippocampal slices parameter set is used in the left panels and the hippocampal cultures set in the right panels (see Table 1)

and *in vivo* external calcium concentrations (Higgins et al., 2014). Again, we use datasets that best fit plasticity data obtained in hippocampal slices (Wittenberg and Wang, 2006) and cultures (Wang et al., 2005). In those experiments, the extracellular calcium concentration was set to be 2 mM (Wittenberg and Wang, 2006) and 3 mM (Wang et al., 2005), which is significantly higher than the estimated *in vivo* concentration of about 1.5 mM (Silver and Erecińska, 1990). Here we assume that a decrease in extracellular calcium concentration leads to a proportional decrease in the calcium influx into the postsynaptic spine. Using this assumption, we can readily predict the effects of decreasing the extracellular calcium concentration on

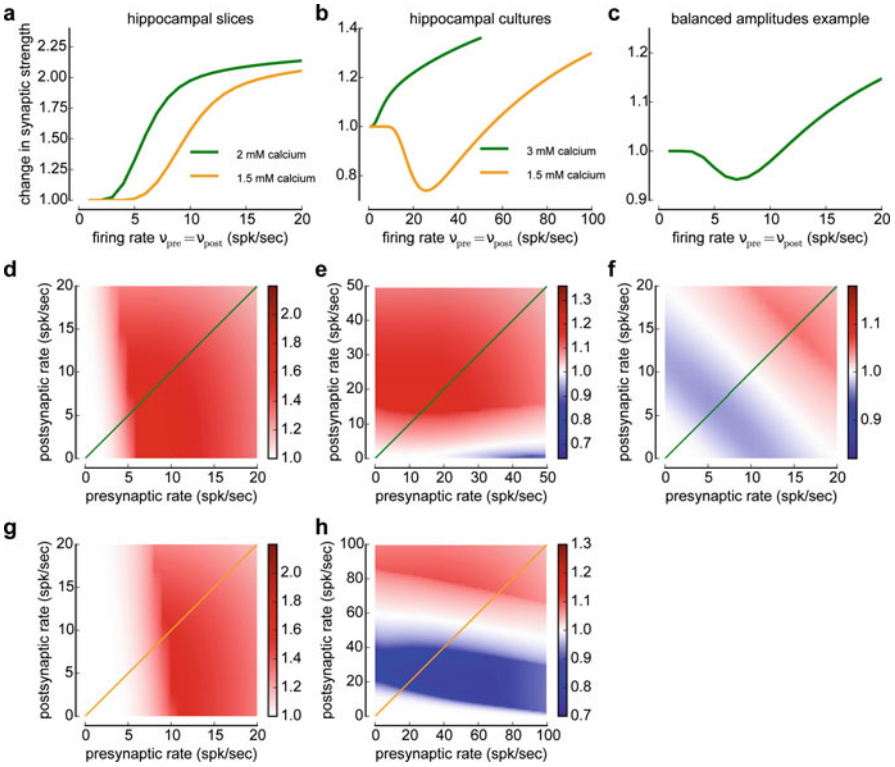

Fig. 8 Change in synaptic strength in response to pre- and postsynaptic Poisson firing. (**a**, **b**, **c**) The change in synaptic strength for pre- and postsynaptic Poisson firing at equal rates ($\nu_{\text{pre}} = \nu_{\text{post}}$) for the hippocampal slices (**a** external calcium concentration corresponding to *in vitro* condition, green; external calcium concentration corresponding to *in vivo* condition, orange), hippocampal cultures (**b**, *in vitro*, green; *in vivo*, orange), and the balanced amplitudes parameter sets (**c**, see Table 1). Analytical results of changes in synaptic strength are shown as derived in Graupner and Brunel (2012). (**d**–**h**) The change in synaptic strength (analytical results) in response to Poisson stimulation is shown for combinations of pre- and postsynaptic rates for the hippocampal slices (*in vitro*, **d**; *in vivo*, **g**), hippocampal cultures (*in vitro*, **e**; *in vivo*, **h**), and the balanced amplitudes parameter sets (**f**). The cases of equal pre- and postsynaptic firing rates depicted in panels **a**–**c** are illustrated by the green (*in vitro*) and orange (*in vivo*) lines. All changes are in response to a 10 s stimulation, i.e., total number of spikes varies with the firing rate

the plasticity rule in the calcium-based model by scaling the amplitudes of the pre- and postsynaptically evoked calcium transients according to the ratio of calcium concentrations, i.e., $1.5/2 = 0.75$ and $1.5/3 = 0.5$ for Wittenberg and Wang (2006) and Wang et al. (2005), respectively. Values of all parameters for both conditions are indicated in Table 1. We will refer to the parameters for the high external calcium concentration as to the *in vitro* dataset and to the parameters for the realistic calcium concentration (1.5 mM) as to the *in vivo* dataset.

To study the time scales of synaptic decay, we initialize the synaptic efficacy to 1 and investigate the time constant of decay of a bistable synapse (Eq. (1)) in the presence of an ongoing constant firing rate. There are two distinct regions of firing rates with respect to the stable states of synaptic efficacy. For sufficiently low rates, the synaptic efficacy has two stable states, one at high ("UP" state) and one at low ("DOWN" state) efficacy (Fig. 7a, b), and one unstable state separating the basins of attraction of the two stable states. There is a critical value of the rates at which the high or low efficacy minimum disappears through a saddle-node bifurcation (indicated by vertical lines in Fig. 7c, d). Beyond this rate, the synapse is no longer bistable, and synaptic efficacy has one stable state only (Fig. 7a, b). The transition from double-well to single-well regimes occurs at lower firing rates for the *in vitro* than the *in vivo* datasets due to the larger calcium amplitudes in the former.

In the monostable region, that is, for high firing rates, a fully potentiated synapse decays on average exponentially to the stable fixed point (Higgins et al., 2014). The time constant of this decay is much longer in the case of the *in vivo* data-set than in the *in vitro* data-set (compare green and blue lines in Fig. 7c, d, respectively). In the presence of two stable states at low firing rates, the decay of memory occurs only due to fluctuations that push the synaptic efficacy out of the UP state. The influence of the double-well potential on the dynamics of the synaptic efficacy traps synapses in the UP state leading to long dwell times before crossing the potential barrier and converging to the low efficacy state, effectively prolongating memory durations. The increase in memory decay time occurs at higher firing rates for the *in vivo* datasets and can be accurately predicted using Kramers escape rate for the mean first passage time across a potential barrier (dashed colored lines in Fig. 7c, d, Higgins et al. 2014).

We now turn to investigate synaptic plasticity in response to irregular pre- and postsynaptic firing. Increasing the rate of uncorrelated, Poisson firing in both pre- and postsynaptic neurons gives rise to two qualitatively different types of behaviors, depending on parameters. For hippocampal slice parameters (Fig. 8a) and the *in vitro* hippocampal culture dataset (Fig. 8b, green line), we observe a monotonically increasing synaptic change vs. firing rate curve: no change at low rates and potentiation at intermediate and high rates. In contrast, in the *in vivo* hippocampal cultures dataset, the curve exhibits three regions: no changes at low firing rates, depression at intermediate rates and potentiation at high rates, reminiscent of the Bienenstock-Cooper-Munro (BCM) curve (Bienenstock et al. 1982, Fig. 8b, orange line). In a balanced dataset in which $C_{\text{pre}} = C_{\text{post}}$, we observe a similar behavior provided γ_p is not too large (Fig. 8c).

We show in Fig. 8d–f how synaptic changes depend on any combination of pre- and postsynaptic firing rates. We see that in the case of different pre- and postsynaptic firing rates, plasticity depends mostly on the source of the largest calcium transient – presynaptic rate in the hippocampal slice dataset and postsynaptic rate in the hippocampal culture dataset. In a balanced dataset, plasticity depends on the sum of both pre- and postsynaptic rates, such that "iso-plasticity" lines are straight lines with -1 slope (Fig. 8f).

Discussion and Future Directions

The model presented here posits that synaptic changes are driven by calcium transients evoked by pre- and postsynaptic spikes through potentiation and depression thresholds that represent in a simplified fashion protein signaling cascades leading to LTP and LTD. In this model, plasticity outcomes can be computed analytically as a function of model parameters for deterministic as well as stochastic protocols. This feature allows us to fully characterize the behavior of the model in response to standard STDP protocols and show its ability to fit experimental data in different hippocampal preparations. Because of the properties of calcium transients, our synaptic learning rule (as is the experimental data) is naturally sensitive to both spike timing and firing rates of both pre- and postsynaptic neurons. The model illustrates that the calcium trace together with the nonlinear calcium-dependent activation of signaling cascades are potentially sufficient to explain the diversity and nonlinearity of plasticity outcomes.

One of the advantages of the simplicity of the model is the ability to fully characterize all the possible STDP curves that can be generated in the space of parameters of the model. In particular, we showed that six possible behaviors are possible if $\theta_d < \theta_p$: DP, P, PD, DPD, D, or no plasticity at all (see Fig. 4c), as two parameters are varied (C_{post} and C_{pre}; equivalently θ_d and θ_p can be varied to explore those regions, see Graupner and Brunel 2012). Interestingly, all these behaviors have been seen, either in different preparations or sometimes in the same preparations but by different groups or by the same group with different extracellular solutions. DP curves have been seen in hippocampal cultures (Bi and Poo, 1998) and cortical slices (Froemke and Dan, 2002); P curves have been observed in hippocampal cultures in the presence of dopamine (Zhang et al., 2009) as well as in CA3 recurrent collaterals in hippocampal slices (Mishra et al., 2016). PD curves have been observed in a cerebellar-like structure in the electric fish (Bell et al., 1997) and corticostriatal synapses with inhibition intact (Paille et al., 2013). DPD curves have been observed in CA3-CA1 connections in hippocampal slices (Nishiyama et al., 2000), but D curves were also observed in the same preparation (Wittenberg and Wang, 2006). This suggests that synapses in all these preparations may obey the same underlying mechanistic rule but be characterized by different parameters. This also opens the possibility of a new type of metaplasticity: by changing the size of the calcium transients (or the depression/potentiation thresholds), synapses might be able to qualitatively change the way they respond to specific spike timings.

The model in its most basic form yields plasticity for purely pre- or postsynaptic activity at sufficiently high frequencies. Synaptic plasticity has been reported to occur in various experimental preparations in protocols in which either the pre- or the postsynaptic pathways are silent. For instance, Kato et al. (2009) observed a VDCC-dependent LTP upon repetitive depolarization of a neuron, in the absence of presynaptic inputs. Tigaret et al. (2016) observed LTD for purely presynaptic stimulation. Note however that such a behavior could be prevented in the model through a frequency-dependent attenuation of the pre- or postsynaptically

induced calcium transients, modeling failure in neurotransmitter release, reduction in released neurotransmitter, or failure in backpropagating consecutive action potentials at high frequencies, respectively.

The model presented here is characterized by a linear summation of calcium transients induced by pre- and postsynaptic spikes. It therefore does not describe nonlinear summation due to the NMDA receptor voltage dependence, which has been observed in most calcium imaging studies of single dendritic spines (Yuste and Denk 1995; Koester and Sakmann 1998; Schiller et al. 1998; Nevian and Sakmann 2004, 2006; Harnett et al. 2012; but see Jia et al. 2014), and is a prominent feature of the Shouval et al. (2002) model. In spite of this lack of nonlinearity, we showed that the model can reproduce experimentally observed STDP curves, indicating that supralinearity per se is not crucial for the spike-timing dependence of plasticity. In Graupner and Brunel (2012), we also proposed a simple nonlinear extension of the model, which was shown to be able to reproduce qualitatively standard STDP curves, and the basic pharmacology of spike pair evoked STDP (see Section 3.1.2 of the supplementary information of Graupner and Brunel 2012). It will be a subject of future research to investigate systematically how such a nonlinearity affects the dependence of plasticity on spike timing and firing rate.

The model could be generalized in various directions. One of such directions is the implementation of a Bienenstock-Cooper-Munro (BCM)-like sliding threshold by introducing activity-dependent calcium amplitudes. For low calcium amplitudes, the synapse model exhibits only LTD in the physiological range of firing rates. Increasing the calcium amplitudes leads to the appearance of LTP at high frequencies, with a threshold between LTD and LTP that strongly depends on C_{pre} and C_{post} (see example in SI of Graupner and Brunel 2012). Therefore, adding an activity dependence to the model, such that calcium amplitudes decrease when firing rates increase, would naturally lead to a BCM-like rule. A similar behavior can be obtained if potentiation and depression thresholds increase with firing rates.

A second generalization would be to include the effects of various neuromodulators that are known to affect synaptic plasticity (Seol et al., 2007; Pawlak and Kerr, 2008; Zhang et al., 2009; He et al., 2015). One simple way of implementing neuromodulation would be to add neuromodulatory dependence to specific model parameters such as the thresholds or the plasticity rates. Focusing in particular on dopamine, experimental results of Zhang et al. (2009) (showing a change from DP to P in the presence of dopamine) could be reproduced by a decrease of both potentiation and depression thresholds when dopamine concentration is increased (see Fig. 4c). Such an implementation could potentially lead to a more biophysical grounding of reinforcement learning theories.

We showed that plasticity is dominated by either pre- or postsynaptic activity whenever the pre- or the postsynaptically induced calcium amplitude is much larger than the post- or presynaptic calcium amplitude, respectively. Correspondingly, equal pre- and postsynaptic calcium amplitudes entail equal contribution of pre- and post activity to plasticity changes. Depending on the calcium amplitude ratio, synaptic plasticity in different systems could implement rules mostly sensitive

to pre-, post-, or both activities and even shift sensitivity by changing calcium amplitude ratios in an activity-dependent manner.

In the model, each pre- or postsynaptic spike elicits a stereotypical calcium transient on the level of an individual synapse. In the intact brain, however, other factors such as the high-conductance state (Rudolph et al., 2005; Delgado et al., 2010), dendritic location (Froemke et al., 2005; Tsukada et al., 2005; Letzkus et al., 2006; Aihara et al., 2007), or inhibition (Müllner et al., 2015) – often blocked in *in vitro* studies – have been shown to influence the calcium dynamics in dendritic spines. In other words, the surrounding neural network shapes the local plasticity rule dynamically through setting the local depolarization level and through inhibitory inputs, in addition to the presynaptic spikes and BPAPs. Calcium-based plasticity models are a natural choice to take such influences into account and have been shown to capture the impact on inhibitory inputs on the dendritic location dependence of the STDP (Cutsuridis, 2011, 2012, 2013). More generally, they are well suited to incorporate network effects on synaptic plasticity (see e.g., Cutsuridis and Hasselmo 2012).

We have explored how the model responds to uncorrelated pre- and postsynaptic Poisson spike trains. Such patterns of activity represent one step toward more realistic spike trains compared to periodic spike trains, but they still lack some of the features of spike trains of hippocampal neurons *in vivo*. Spike trains of individual neurons are significantly different from homogeneous Poisson processes for several reasons: first, firing rates are modulated by both external variables such as spatial location but also by prominent population rhythms such as the theta rhythm; they also exhibit a pronounced refractory period. Second, spike trains of pairs of neurons often exhibit pronounced correlations, which can be due either to common inputs, or monosynaptic connections, or both. Extending the mathematical analysis of the model to such situations will be the subject of future studies.

Our model demonstrates that the levels of extracellular calcium concentrations should have a major impact on plasticity. A first prediction is that plasticity seen in standard STDP protocols should be greatly reduced (and even possibly vanish altogether) at physiological calcium concentrations, which are significantly lower than concentrations used in *in vitro* studies. While to our knowledge no study has explicitly compared plasticity results at different extracellular calcium concentration, comparisons between different studies using different extracellular concentrations seem to be consistent with this prediction. In hippocampal slices, a standard low-frequency STDP protocol produces LTD for all time differences with 2 mM extracellular calcium (Wittenberg and Wang, 2006), while it produces the standard STDP curve with 3 mM calcium (Campanac and Debanne, 2008). A second prediction is that induced synaptic changes should be much more stable in the face of ongoing pre- and postsynaptic activity. These results emphasize the need for experimental studies at physiological calcium concentrations $\sim$1.5 mM (Silver and Erecińska, 1990), unlike most published studies that used concentrations in the range 2$-$3 mM. Our predictions could be easily tested in slice experiments, by providing background activity at a specified rate after the plasticity-inducing protocol. Similar experiments have been performed in the developing Xenopus

retinotectal system *in vivo* (Zhou et al., 2003), where activity-induced modifications were shown to be erased by subsequent 10 min of spontaneous activity. Our model would predict that in hippocampal cultures, at 3 mM calcium, induced synaptic changes should disappear on a time scale of minutes, while at 1.5 mM calcium, they should be stable on a time scale of $\sim$1 h (at the background activity of $\sim$1 spk/sec).

To conclude, the synaptic learning rule described here provides a minimal biophysical framework to understand how firing patterns of pre- and postsynaptic neurons are translated into changes of synaptic efficacy, through the dynamics of the postsynaptic calcium concentration and calcium thresholds implementing biochemical signaling cascades in a simplified fashion. Its simplicity makes it an ideal candidate for investigating the effects of learning at the network level.

References

Abarbanel HDI, Gibb L, Huerta R, Rabinovich M (2003) Biophysical model of synaptic plasticity dynamics. Biol Cybern 89(3):214–26

Aihara T, Abiru Y, Yamazaki Y, Watanabe H, Fukushima Y, Tsukada M (2007) The relation between spike-timing dependent plasticity and Ca2+ dynamics in the hippocampal CA1 network. Neuroscience 145(1):80–87

Artola A, Singer W (1987) Long-term potentiation and NMDA receptors in rat visual cortex. Nature 330(6149):649–652

Badoual M, Zou Q, Davison AP, Rudolph M, Bal T, Frégnac Y, Destexhe A (2006) Biophysical and phenomenological models of multiple spike interactions in spike-timing dependent plasticity. Int J Neural Syst 16(2):79–97

Bagal AA, Kao JPY, Tang C-M, Thompson SM (2005) Long-term potentiation of exogenous glutamate responses at single dendritic spines. Proc Natl Acad Sci USA 102(40):14434–14439

Bear MF, Press WA, Connors BW (1992) Long-term potentiation in slices of kitten visual cortex and the effects of NMDA receptor blockade. J Neurophysiol 67(4):841–851

Bell C, Han V, Sugawara Y, Grant K (1997) Synaptic plasticity in a cerebellum-like structure depends on temporal order. Nature 387(6630):278–81

Bender VA, Bender KJ, Brasier DJ, Feldman DE (2006) Two coincidence detectors for spike timing-dependent plasticity in somatosensory cortex. J Neurosci 26(16):4166–4177

Bi G, Poo M (1998) Synaptic modifications in cultured hippocampal neurons: dependence on spike timing, synaptic strength, and postsynaptic cell type. J Neurosci 18(24):10464–10472

Bi GQ, Wang HX (2002) Temporal asymmetry in spike timing-dependent synaptic plasticity. Physiol Behav 77(4–5):551–555

Bienenstock EL, Cooper LN, Munro PW (1982) Theory for the development of neuron selectivity: orientation specificity and binocular interaction in visual cortex. J Neurosci 2(1):32–48

Bliss T, Collingridge G (1993) A synaptic model of memory: long-term potentiation in the hippocampus. Nature 361(6407):31–39

Bliss T, Lømo T (1973) Long-lasting potentiation of synaptic transmission in the dentate area of the anaesthetized rabbit following stimulation of the perforant path. J Physiol 232(2):331–356

Cai Y, Gavornik JP, Cooper LN, Yeung LC, Shouval HZ (2007) Effect of stochastic synaptic and dendritic dynamics on synaptic plasticity in visual cortex and hippocampus. J Neurophysiol 97(1):375–386

Campanac E, Debanne D (2008) Spike timing-dependent plasticity: a learning rule for dendritic integration in rat ca1 pyramidal neurons. J Physiol 586(3):779–793

Castro-Alamancos MA, Donoghue JP, Connors BW (1995) Different forms of synaptic plasticity in somatosensory and motor areas of the neocortex. J Neurosci 15(7 Pt 2):5324–5333

Clopath C, Büsing L, Vasilaki E, Gerstner W (2010) Connectivity reflects coding: a model of voltage-based STDP with homeostasis. Nat Neurosci 13(3):344–352
Collingridge GL, Kehl SJ, McLennan H (1983) Excitatory amino acids in synaptic transmission in the schaffer collateral-commissural pathway of the rat hippocampus. J Physiol 334:33–46
Cutsuridis V (2011) GABA inhibition modulates NMDA-R mediated spike timing dependent plasticity (STDP) in a biophysical model. Neural Netw 24(1):29–42
Cutsuridis V (2012) Bursts shape the NMDA-R mediated spike timing dependent plasticity curve: role of burst interspike interval and GABAergic inhibition. Cogn Neurody 6(5):421–441
Cutsuridis V (2013) Interaction of inhibition and triplets of excitatory spikes modulates the NMDA-R-mediated synaptic plasticity in a computational model of spike timing-dependent plasticity. Hippocampus 23(1):75–86
Cutsuridis V, Hasselmo M (2012) GABAergic contributions to gating, timing, and phase precession of hippocampal neuronal activity during theta oscillations. Hippocampus 22(7):1597–1621
Delgado JY, Gómez-González JF, Desai NS (2010) Pyramidal neuron conductance state gates spike-timing-dependent plasticity. J Neurosci 30(47):15713–15725
Dudek SM, Bear MF (1993) Bidirectional long-term modification of synaptic effectiveness in the adult and immature hippocampus. J Neurosci 13(7):2910–2918
Egger V, Feldmeyer D, Sakmann B (1999) Coincidence detection and changes of synaptic efficacy in spiny stellate neurons in rat barrel cortex. Nat Neurosci 2(12):1098–1105
Feldman DE (2000) Timing-based LTP and LTD at vertical inputs to layer II/III pyramidal cells in rat barrel cortex. Neuron 27(1):45–56
Froemke RC, Dan Y (2002) Spike-timing-dependent synaptic modification induced by natural spike trains. Nature 416(6879):433–438
Froemke R, Poo MM, Dan Y (2005) Spike-timing-dependent synaptic plasticity depends on dendritic location. Nature 434(7030):221–225
Froemke RC, Tsay IA, Raad M, Long JD, Dan Y (2006) Contribution of individual spikes in burst-induced long-term synaptic modification. J Neurophysiol 95(3):1620–1629
Gerkin RC, Bi G-Q, Rubin JE (2010) Hippocampal microcircuits: a computational modeler's resource book, vol 5. Springer series in computational neuroscience. Springer, New York
Graupner M, Brunel N (2007) STDP in a bistable synapse model based on CaMKII and associated signaling pathways. PLoS Comput Biol 3(11):2299–2323
Graupner M, Brunel N (2010) Mechanisms of induction and maintenance of spike-timing dependent plasticity in biophysical synapse models. Front Comput Neurosci 4: pii, 136
Graupner M, Brunel N (2012) Calcium-based plasticity model explains sensitivity of synaptic changes to spike pattern, rate, and dendritic location. Proc Natl Acad Sci USA 109(10):3991–3996
Gustafsson B, Wigström H, Abraham WC, Huang YY (1987) Long-term potentiation in the hippocampus using depolarizing current pulses as the conditioning stimulus to single volley synaptic potentials. J Neurosci 7(3):774–780
Hahm JO, Langdon RB, Sur M (1991) Disruption of retinogeniculate afferent segregation by antagonists to NMDA receptors. Nature 351(6327):568–570
Harnett MT, Makara JK, Spruston N, Kath WL, Magee JC (2012) Synaptic amplification by dendritic spines enhances input cooperativity. Nature 491(7425):599–602
He K, Huertas M, Hong SZ, Tie X, Hell JW, Shouval H, Kirkwood A (2015) Distinct eligibility traces for LTP and LTD in cortical synapses. Neuron 88:528–538
Hebb D (1949) The organization of behavior: a neurophsychological theory. Wiley, New York
Higgins D, Graupner M, Brunel N (2014) Memory maintenance in synapses with calcium-based plasticity in the presence of background activity. PLoS Comput Biol 10(10):e1003834
Ismailov I, Kalikulov D, Inoue T, Friedlander MJ (2004) The kinetic profile of intracellular calcium predicts long-term potentiation and long-term depression. J Neurosci 24(44):9847–9861
Jaffe DB, Johnston D, Lasser-Ross N, Lisman JE, Miyakawa H, Ross WN (1992) The spread of Na+ spikes determines the pattern of dendritic Ca2+ entry into hippocampal neurons. Nature 357(6375):244–246

Jahr C, Stevens C (1990) A quantitative description of NMDA receptor-channel kinetic behavior. J Neurosci 10(6):1830–1837

Jia H, Varga Z, Sakmann B, Konnerth A (2014) Linear integration of spine Ca2+ signals in layer 4 cortical neurons in vivo. Proc Natl Acad Sci USA 111:9277–9282

Karmarkar UR, Buonomano DV (2002) A model of spike-timing dependent plasticity: one or two coincidence detectors? J Neurophysiol 88(1):507–513

Karmarkar UR, Najarian MT, Buonomano DV (2002) Mechanisms and significance of spike-timing dependent plasticity. Biol Cybern 87(5–6):373–382

Kato HK, Watabe AM, Manabe T (2009) Non-Hebbian synaptic plasticity induced by repetitive postsynaptic action potentials. J Neurosci 29(36):11153–11160

Koester HJ, Sakmann B (1998) Calcium dynamics in single spines during coincident pre- and postsynaptic activity depend on relative timing of back-propagating action potentials and subthreshold excitatory postsynaptic potentials. Proc Natl Acad Sci USA 95(16):9596–9601

Kovalchuk Y, Eilers J, Lisman J, Konnerth A (2000) NMDA receptor-mediated subthreshold Ca(2+) signals in spines of hippocampal neurons. J Neurosci 20(5):1791–1799

Kumar A, Mehta MR (2011) Frequency-dependent changes in NMDAR-dependent synaptic plasticity. Front Comput Neurosci 5:38

Letzkus JJ, Kampa BM, Stuart GJ (2006) Learning rules for spike timing-dependent plasticity depend on dendritic synapse location. J Neurosci 26(41):10420–10429

Levy WB, Steward O (1983) Temporal contiguity requirements for long-term associative potentiation/depression in the hippocampus. Neuroscience 8(4):791–797

Lynch G, Larson J, Kelso S, Barrionuevo G, Schottler F (1983) Intracellular injections of EGTA block induction of hippocampal long-term potentiation. Nature 305(5936):719–721

Magee J, Johnston D (1997) A synaptically controlled, associative signal for Hebbian plasticity in hippocampal neurons. Science 275(5297):209–213

Majewska A, Brown E, Ross J, Yuste R (2000) Mechanisms of calcium decay kinetics in hippocampal spines: role of spine calcium pumps and calcium diffusion through the spine neck in biochemical compartmentalization. J Neurosci 20(5):1722–1734

Malenka RC, Kauer JA, Zucker RS, Nicoll RA (1988) Postsynaptic calcium is sufficient for potentiation of hippocampal synaptic transmission. Science 242(4875):81–84

Markram H, J. Lübke, Frotscher M, Sakmann B (1997) Regulation of synaptic efficacy by coincidence of postsynaptic APs and EPSPs. Science 275(5297):213–215

Mishra RK, Kim S, Guzman SJ, Jonas P (2016) Symmetric spike timing-dependent plasticity at CA3–CA3 synapses optimizes storage and recall in autoassociative networks. Nat Commun 7:11552

Mizuno T, Kanazawa I, Sakurai M (2001) Differential induction of LTP and LTD is not determined solely by instantaneous calcium concentration: an essential involvement of a temporal factor. Eur J Neurosci 14(4):701–708

Mooney R, Madison DV, Shatz CJ (1993) Enhancement of transmission at the developing retinogeniculate synapse. Neuron 10(5):815–825

Morris RG, Anderson E, Lynch GS, Baudry M (1986) Selective impairment of learning and blockade of long-term potentiation by an N-methyl-D-aspartate receptor antagonist, AP5. Nature 319(6056):774–776

Müllner FE, Wierenga CJ, Bonhoeffer T (2015) Precision of inhibition: dendritic inhibition by individual GABAergic synapses on hippocampal pyramidal cells is confined in space and time. Neuron 87(3):576–589

Nabavi S, Kessels HW, Alfonso S, Aow J, Fox R, Malinow R (2013) Metabotropic NMDA receptor function is required for NMDA receptor-dependent long-term depression. Proc Natl Acad Sci USA 110(10):4027–4032

Neveu D, Zucker RS (1996) Long-lasting potentiation and depression without presynaptic activity. J Neurophysiol 75(5):2157–2160

Nevian T, Sakmann B (2004) Single spine Ca2+ signals evoked by coincident EPSPs and back-propagating action potentials in spiny stellate cells of layer 4 in the juvenile rat somatosensory barrel cortex. J Neurosci 24(7):1689–1699

Nevian T, Sakmann B (2006) Spine Ca2+ signaling in spike-timing-dependent plasticity. J Neurosci 26(43):11001–11013
Nishiyama M, Hong K, Mikoshiba K, Poo MM, Kato K (2000) Calcium stores regulate the polarity and input specificity of synaptic modification. Nature 408(6812):584–588
Nowak L, Bregestovski P, Ascher P, Herbet A, Prochiantz A (1984) Magnesium gates glutamate-activated channels in mouse central neurones. Nature 307(5950):462–465
O'Connor DH, Wittenberg GM, Wang SS-H (2005) Dissection of bidirectional synaptic plasticity into saturable unidirectional processes. J Neurophysiol 94(2):1565–1573
O'Connor DH, Wittenberg GM, Wang SS-H (2005) Graded bidirectional synaptic plasticity is composed of switch-like unitary events. Proc Natl Acad Sci USA 102(27):9679–9684
Paille V, Fino E, Du K, Morera-Herreras T, Perez S, Kotaleski JH, Venance L (2013) GABAergic circuits control spike-timing-dependent plasticity. J Neurosci 33(22):9353–9363
Pawlak V, Kerr JND (2008) Dopamine receptor activation is required for corticostriatal spike-timing-dependent plasticity. J Neurosci 28(10):2435–2446
Petersen C, Malenka R, Nicoll R, Hopfield J (1998) All-or-none potentiation at CA3-CA1 synapses. Proc Natl Acad Sci USA 95(8):4732–4737
Pfister J-P, Gerstner W (2006) Triplets of spikes in a model of spike timing-dependent plasticity. J Neurosci 26(38):9673–9682
Risken H (1996) The Fokker-Planck equation, 2nd edn. Springer, Berlin/Heidelberg
Rubin JE, Gerkin RC, Bi G-Q, Chow CC (2005) Calcium time course as a signal for spike-timing-dependent plasticity. J Neurophysiol 93(5):2600–2613
Rudolph M, Pelletier JG, Paré D, Destexhe A (2005) Characterization of synaptic conductances and integrative properties during electrically induced EEG-activated states in neocortical neurons in vivo. J Neurophysiol 94(4):2805–2821
Sabatini B, Svoboda K (2000) Analysis of calcium channels in single spines using optical fluctuation analysis. Nature 408(6812):589–593
Sabatini BL, Oertner TG, Svoboda K (2002) The life cycle of Ca(2+) ions in dendritic spines. Neuron 33(3):439–452
Schiller J, Schiller Y, Clapham DE (1998) NMDA receptors amplify calcium influx into dendritic spines during associative pre- and postsynaptic activation. Nat Neurosci 1(2):114–118
Seol GH, Ziburkus J, Huang S, Song L, Kim IT, Takamiya K, Huganir RL, Lee H-K, Kirkwood A (2007) Neuromodulators control the polarity of spike-timing-dependent synaptic plasticity. Neuron 55(6):919–929
Shouval HZ, Kalantzis G (2005) Stochastic properties of synaptic transmission affect the shape of spike time-dependent plasticity curves. J Neurophysiol 93(2):1069–1073
Shouval HZ, Bear MF, Cooper LN (2002) A unified model of NMDA receptor-dependent bidirectional synaptic plasticity. Proc Natl Acad Sci USA 99(16):10831–10836
Shouval HZ, Wang SS-H, Wittenberg GM (2010) Spike timing dependent plasticity: a consequence of more fundamental learning rules. Front Comput Neurosci 4: pii, 19
Silver IA, Erecińska M (1990) Intracellular and extracellular changes of [Ca2+] in hypoxia and ischemia in rat brain in vivo. J Gen Physiol 95(5):837–866
Sjöström P, Turrigiano G, Nelson S (2001) Rate, timing, and cooperativity jointly determine cortical synaptic plasticity. Neuron 32(6):1149–1164
Sjöström PJ, Turrigiano GG, Nelson SB (2003) Neocortical LTD via coincident activation of presynaptic NMDA and cannabinoid receptors. Neuron 39(4):641–654
Tigaret CM, Olivo V, Sadowski JHLP, Ashby MC, Mellor JR (2016) Coordinated activation of distinct Ca(2+) sources and metabotropic glutamate receptors encodes Hebbian synaptic plasticity. Nat Commun 7:10289
Tsukada M, Aihara T, Kobayashi Y, Shimazaki H (2005) Spatial analysis of spike-timing-dependent LTP and LTD in the CA1 area of hippocampal slices using optical imaging. Hippocampus 15(1):104–109
Wang H-X, Gerkin RC, Nauen DW, Bi G-Q (2005) Coactivation and timing-dependent integration of synaptic potentiation and depression. Nat Neurosci 8(2):187–193

Wang SS, Denk W, Häusser M (2000) Coincidence detection in single dendritic spines mediated by calcium release. Nat Neurosci 3(12):1266–1273

Wittenberg GM, Wang SS-H (2006) Malleability of spike-timing-dependent plasticity at the CA3-CA1 synapse. J Neurosci 26(24):6610–6617

Yang S, Tang Y, Zucker R (1999) Selective induction of LTP and LTD by postsynaptic [Ca2+]i elevation. J Neurophysiol 81(2):781–787

Yuste R, Denk W (1995) Dendritic spines as basic functional units of neuronal integration. Nature 375(6533):682–684

Yuste R, Majewska A, Cash SS, Denk W (1999) Mechanisms of calcium influx into hippocampal spines: heterogeneity among spines, coincidence detection by NMDA receptors, and optical quantal analysis. J Neurosci 19(6):1976–1987

Zhabotinsky AM (2000) Bistability in the Ca(2+)/calmodulin-dependent protein kinase-phosphatase system. Biophys J 79(5):2211–2221

Zhang J-C, Lau P-M, Bi G-Q (2009) Gain in sensitivity and loss in temporal contrast of STDP by dopaminergic modulation at hippocampal synapses. Proc Natl Acad Sci USA 106(31):13028–13033

Zhou Q, Tao HW, Ming Poo M (2003) Reversal and stabilization of synaptic modifications in a developing visual system. Science 300(5627):1953–1957

Zucker RS (1999) Calcium- and activity-dependent synaptic plasticity. Curr Opin Neurobiol 9(3):305–313

Simplified Compartmental Models of CA1 Pyramidal Cells of Theta-Modulated Inhibition Effects on Spike Timing-Dependent Plasticity

Vassilis Cutsuridis

Overview

Spike timing-dependent plasticity (STDP) is a causal form of Hebb's law of synaptic plasticity, where the precise timing of the presynaptic and postsynaptic action potentials determines the sign and magnitude of synaptic modifications (Bell et al. 1997; Bi and Poo 1998; Magee and Johnston 1997; Markram et al. 1997; Debanne et al. 1998; Sjostrom et al. 2001; Yao and Dan 2001; Zhang et al. 1998). In their pioneering study, Bi and Poo (1998) showed that the shape of the STDP curve in the in vitro hippocampal network has an asymmetric shape with the largest LTP/LTD value at $\Delta\tau = t_{\text{post}} - t_{\text{pre}} = +/-10$ ms, respectively. New experimental evidence has shown that the STDP asymmetry can sometimes change with the target and the location of the synapse (Tzounopoulos et al. 2004; Froemke et al. 2005; Letzkus et al. 2006; Caporale and Dan 2009) and can be dynamically regulated by the activity of adjacent synapses (Harvey and Svoboda 2007; Caporale and Dan 2009) or by the action of neuromodulators (Seol et al. 2007; Caporale and Dan 2009). Nishiyama et al. (2000) reported that "... the profile of STDP induced in the hippocampal CA1 network with inhibitory interneurons is symmetrical for the relative timing of pre- and postsynaptic activation." Optical imaging studies in CA1 revealed that the shape of the STDP curve depends on the location on the stratum radiatum (SR) dendrite. A symmetric STDP profile was observed in the proximal-to-the-soma SR dendrite and an asymmetric STDP profile in the distal-to-the-soma one (Tsukada et al. 2005; Aihara et al. 2007). They suggested that this change in the shape of the STDP curve (i.e., from symmetry to asymmetry and vice versa) may be due to inhibition in the proximal SR dendrites (Tsukada et al. 2005). The functional consequences of such

V. Cutsuridis (✉)
School of Computer Science, University of Lincoln, Lincoln, UK
e-mail: vcutsuridis@lincoln.ac.uk

V. Cutsuridis et al. (eds.), *Hippocampal Microcircuits*, Springer Series in Computational Neuroscience, https://doi.org/10.1007/978-3-319-99103-0_18

a change in the STDP temporal kernel dynamics are of great importance in neural network dynamics. A symmetrical STDP profile with short temporal windows may serve as a coincidence detector between the incoming inputs and plays a functional role in heteroassociation of memories (Cutsuridis et al. 2010). On the other hand an asymmetric STDP profile with broad temporal windows may play a role in chunking of ordered items in sequence learning (Hayashi and Igarashi 2009).

Up-to-now very few studies (Cutsuridis 2010, 2011, 2012, 2013) have investigated the inhibitory factors (frequency, strength, timing, etc.) that are responsible for such a change in the shape in the STDP temporal kernel and the conditions under which a transition from asymmetrical STDP kernel to a symmetrical STDP kernel is possible. In this chapter, I will present two simplified compartmental models of CA1 pyramidal cells in order to investigate the role of theta-modulated inhibition on the shape, sign, and magnitude of the STDP kernel in CA1 pyramidal cell proximal dendrites.

The Model

CA1 Pyramidal Cell

A two-compartment (soma and dendrite) CA1 pyramidal cell model is presented (Fig. 1a). The somatic compartment contains the following ionic currents: a sodium (Na^+) current, a delayed rectifier K^+ current, an A-type K^+ current, a calcium-activated after-hyperpolarizing (AHP) K^+ current, and a HVA L-type CA^{2+} current. The dendritic compartment contains the following ionic currents: a sodium (Na^+) current, a delayed rectifier K^+ current, an A-type K^+ current, and a HVA L-type Ca^{2+} current. AMPA, NMDA, and $GABA_A$ synapses were present only in the dendrite.

In the model, calcium enters the neuron through (1) voltage-gated calcium channels (VGCCs) and (2) NMDA channels located at the SR dendrite. VGCCs are activated by the arrival of back-propagating action potentials (BPAPs) initiated in the soma by excitatory postsynaptic spikes. The NMDA channels are activated by the synergistic action of excitatory and inhibitory postsynaptic potentials and sufficient membrane potential depolarization due to the BPAP, which removes the magnesium block and allows calcium to enter the cell.

Plasticity is measured by a deterministic Ca^{2+} dynamics model (Bi and Rubin 2005; Rubin et al. 2005). The Ca^{2+} dynamics model consists of three detectors measuring the instantaneous calcium level and its time course in the dendrite and changes the strength of the synapse accordingly (Fig. 1b). Its detection system consists of (1) a potentiation detector (P), which detects calcium levels above a high threshold (4 μM) and triggers LTP; (2) a depression filter (D), which detects calcium levels that exceeds a low threshold level (0.6 μM) and triggers LTD; and

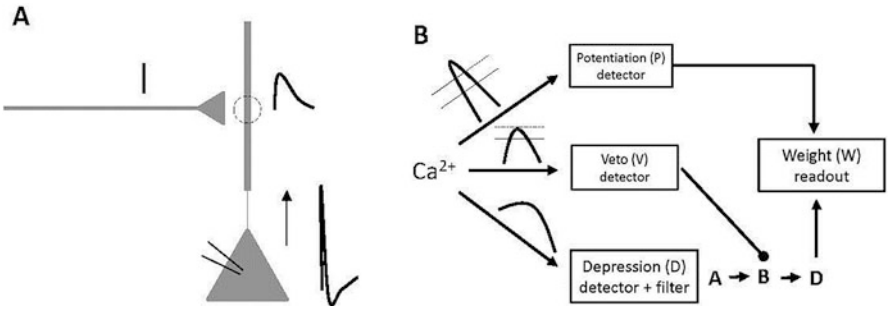

Fig. 1 (**a**) CA1 pyramidal cell. A presynaptic spike generates an EPSP at the dendrite which is paired with a back-propagating action potential generated by current stimulation of the soma. (**b**) Synaptic plasticity at the dendritic synapse (circled region) is governed by a model calcium detector system. P, potentiation detector; A, depression detector; B, Intermediate element; D, depression filter activated by B and vetoed by V; V, veto detector; W, synaptic weight. P and D compete to influence the plasticity variable W, which serves as a measure of the sign and magnitude of synaptic strength changes from the baseline

Table 1 Parameter values of all ionic and synaptic currents

Symbol	Value	Symbol	Value	Symbol	Value	Symbol	Value
g_L	0.1	g_{coup}	1.125	T	23	η	6
$g_{Na,s}$	30	$V_{AMPA,NMDA}$	0	$\Delta\tau$	Variable	ξ	0.001
$g_{Na,d}$	7	V_{GABA}	−75	$\Delta\tau_{GABA}$	Variable	λ	0
$g_{mAHP,s}$	25	V_{Na}	60	*Period*	300	$\overline{q}$	1
$g_{KA,s}$	75	V_{Ca}	140	ζ	72	s_1	0
$g_{KA,d}$	12	V_K	−80	ζ_2	0.11	s_2	40
$g_{Kdr,s}$	14	V_L	−70	ζ_3	2	s_3	3.6
$g_{Kdr,d}$	0.867	$V_{Ca,NMDA}$	140	ζ_4	64	$NMDA_{rate}$	2
g_{CaLs}	7	$\chi_{0,s}$	0.05	ζ_5	1	*ndf*	10
g_{CaLd}	25	$\chi_{0,d}$	0.07	φ_s	0.1	*nds*	45
g_{NMDA}	0.3	Ca_τ	1000	φ_d	0.1	*Buff*	0
g_{AMPA}	0.05	*Ca*	2	β_s	0.083	κ	7
$g_{Ca,NMDA}$	22	*Mg*	2	β_d	0.083	ζ_p	30
g_{GABA}	0	q_{mb}	0.28			q_{ma}	0.00048

(3) a veto detector (V), which detects levels exceeding a mid-level threshold (2 μM) and triggers a veto of the model's depression components.

The detailed mathematical formalism of the model and its detector system can be found in the Appendix. The parameters of all ionic and synaptic currents used in the model are listed in Table 1. The parameters of the calcium detector system are listed in Table 2.

Table 2 Parameters in the calcium detector equations

Symbol	Value	Symbol	Value	Symbol	Value	Symbol	Value
α_w	0.8	τ_A	500	θ_c	2	num_b	1
β_w	0.6	τ_B	5	θ_d	2.6	num_c	1
a	0.3	τ_C	10	θ_e	0.55	num_d	1
d	0.05	τ_D	250	σ_c	−0.05	num_e	5
p_a	−0.1	τ_E	40	σ_d	−0.01	C_mHC	4
p_d	−0.002	c_p	5	σ_e	−0.02	C_mHN	4
τ_W	500	c_d	4	num_a	10	C_nHC	0.6
						C_nHN	3

Inputs

Single Spike Inputs

To simulate the experimental spike-pair STDP protocol, two excitatory single spike inputs to the soma and the dendrite are generated by two spike generators. The dendritic spike generator is modelled as

$$F_{dend} = H\,(t-1)\cdot\left(H\left(\sin\left(2\pi\cdot(t-2)/T\right)\right)\cdot\left(1-H\left(\sin\left(2\pi\cdot(t-1)/T\right)\right)\right)\right) \tag{1}$$

where T is the period of oscillation and $H(\,)$ is the Heaviside function. The somatic spike generator is modelled as

$$\begin{aligned} F_{soma} = {} & H\,(t-1)\cdot\left(H\left(\sin\left(2\pi\cdot(t-2-\Delta\tau)/T\right)\right)\right. \\ & \left.\cdot\left(1-H\left(\sin\left(2\pi\cdot(t-1-\Delta\tau)/T\right)\right)\right)\right) \end{aligned} \tag{2}$$

where $\Delta\tau$ is the interval between the dendritic spike and the somatic spike. In all spike-pair (doublet) experiments, the pairing of the two excitatory inputs was repeated every 300 ms (3.5 Hz), typically for 5 s. The interstimulus interval $\Delta\tau$ between the pre- and postsynaptic spikes was variable ranging from −100 to 100 in increments of 10 ms, unless stated otherwise.

Excitatory Dendritic Bursts and Somatic Spikes

To simulate the experimental STDP protocol where a dendritic burst of spikes is paired with a somatic spike, two spike generators are used. The dendritic burst generator is modelled as

$$F_{burst}(t) = F_1(t) + F_2(t) + F_3(t) \tag{3}$$

where

$$F_1(t) = H\,(t-1)\cdot\left(H\left(\sin\left(2\pi\cdot(t-2)/T\right)\right)\cdot\left(1-H\left(\sin\left(2\pi\cdot(t-1)/T\right)\right)\right)\right),$$

$$F_2(t) = H\,(t-1)\cdot\left(H\left(\sin\left(2\pi\cdot(t-2-bISI)/T\right)\right)\cdot\left(1-H\left(\sin\left(2\pi\cdot(t-1-bISI\,)/T\right)\right)\right)\right)$$

and

$$F_3(t) = H\,(t-1)\cdot\left(H\left(\sin\left(2\pi\cdot(t-2-2\cdot bISI)/T\right)\right)\cdot\left(1-H\left(\sin\left(2\pi\cdot(t-1-2\cdot bISI)/T\right)\right)\right)\right)$$

where *bISI* is the interspike interval within a burst, T is the period of oscillation, and $H(\,)$ is the Heaviside function.

The somatic spike generator is modelled as

$$F_{spike}(t) = H\,(t-1)\cdot\left(H\left(\sin\left(2\pi\cdot(t-2-\Delta\tau)/T\right)\right)\cdot\left(1-H\left(\sin\left(2\pi\cdot(t-1-\Delta\tau)/T\right)\right)\right)\right) \tag{4}$$

where $\Delta\tau$ is the interval between the first spike of the burst and the somatic spike. In all experiments the pairing of the two excitatory inputs was repeated every 300 ms (3.5 Hz), typically for 5 s. The interstimulus interval $\Delta\tau$ between the dendritic and somatic stimuli was variable ranging from −180 ms to 180 ms in increments of 5 ms, unless stated otherwise.

Inhibitory Inputs

Inhibitory inputs to the dendrite are modelled as

$$F_{GABA}(t) = \sum_{i=1}^{11} F_{GABA_i}(t) \tag{5}$$

where

$$F_{GABA_i}(t) = -aa_i\cdot H\,(t-1)\cdot\Big(H\left(\sin\left(2\pi\cdot(t-2+offset-(i-1)\cdot\Delta\tau_{GABA})/T\right)\right)\cdot\left(1-H\left(\sin\left(2\pi\cdot(t-1+offset-(i-1)\cdot\Delta\tau_{GABA})/T\right)\right)\right)\Big)$$

where *offset* is the relative timing between the onset of the GABA spike train and the presynaptic (dendritic)-postsynaptic (somatic) interstimulus interval, $\Delta\tau_{GABA}$ is

the GABA interspike interval, and aa_i is either 1 or 0 depending on the duration of the interval between the dendritic and the somatic stimuli used.

Results

Model 1: Single Spikes Driving the Soma and Dendrite of CA1 Pyramidal Cell

Pairing of a Dendritic and a Somatic Spike in the Absence of Inhibition

When a presynaptic (dendritic) spike was paired with a postsynaptic (somatic) spike in the absence of inhibition then an asymmetric STDP kernel appeared with the largest LTP and LTD values at +5 ms and at −10 ms, respectively (Bi and Poo 1998). The saturated synaptic weight values (W_∞) as a function of the interstimulus interval, $\Delta\tau = t_{post} - t_{pre}$, are depicted in Fig. 2. $\Delta\tau$ is the interstimulus interval between the presynaptic dendritic spike and the postsynaptic somatic spike. For each $\Delta\tau$, the pre- and postsynaptic pairing was repeated every 300 ms (3.5 Hz) until saturation, typically for 5 s. W_∞ was measured as the saturated value of the readout variable W at $t = 5$ s. In the case where the saturated W oscillated between two values, W_∞ was the mean value of these two values. Simulations were performed with $\Delta\tau$ ranging from −100 ms to 100 ms in increments of 5 ms. The area of the LTP region ($\Delta\tau > 0$) is smaller than the area of the LTD region ($\Delta\tau < 0$), as

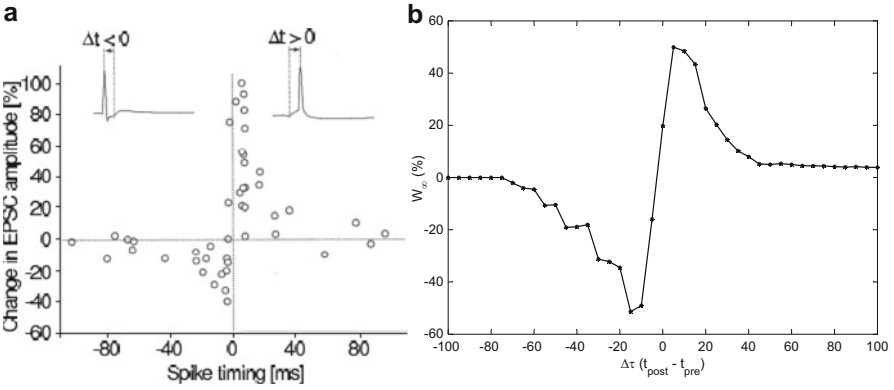

Fig. 2 (**a**) Experimentally observed STDP temporal kernel as a function of spiking timing. Spike timing was defined as the time interval between the onset of the EPSP and the peak of the postsynaptic action potential during each cycle of repetitive stimulation (reprinted with permission from Bi and Poo 1998). (**b**) Simulated STDP kernel from spike-pair simulations in the absence of $GABA_A$. W_∞ is the saturated value of the readout variable W (see Fig. 1) measured at the end of each simulation run multiplied by 100 (%). $\Delta\tau$ ($t_{post} - t_{pre}$) ranges from −100 ms to 100 ms in increments of 5 ms

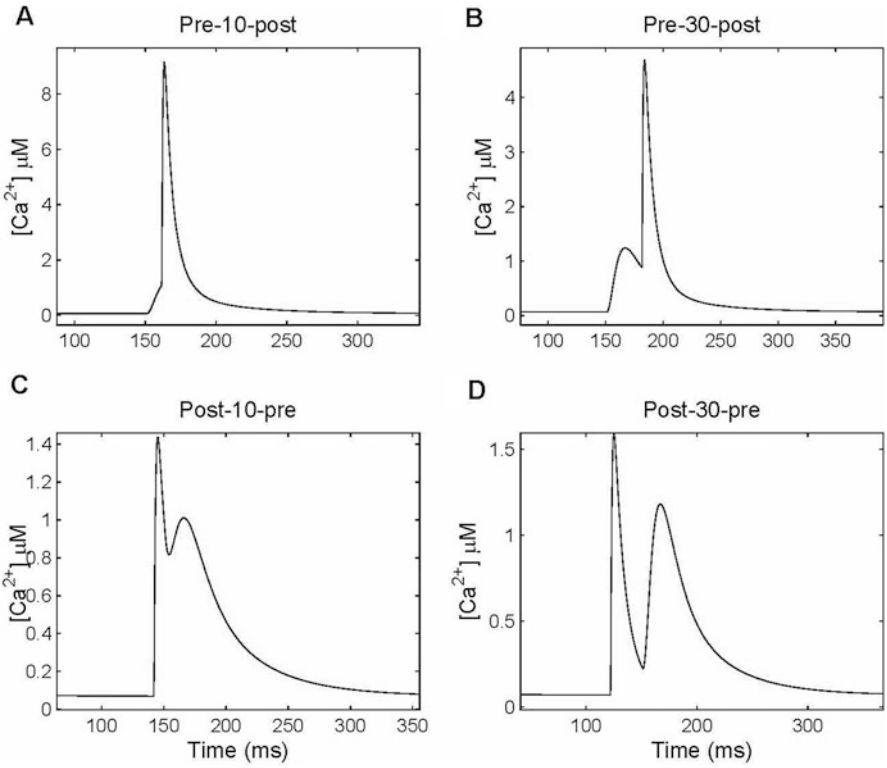

Fig. 3 Postsynaptic calcium time courses in the absence of inhibition. Times shown are measured relative to the onset of the stimulation experiments. (**a**) Pre-10-post case. (**b**) Pre-30-post case. (**c**) Post-10-pre case. (**d**) Post-30-pre case. (Reprinted with permission from Cutsuridis 2011)

it has been experimentally observed (Bi and Poo 1998). At interstimulus intervals $\Delta\tau > +40$ ms and $\Delta\tau < -70$ ms W_∞ approached zero.

In the paired pre-10-post-stimulation protocol, where a presynaptic (dendritic) stimulation was followed 10 ms later by a postsynaptic (somatic) stimulation, a large calcium influx through the NMDA channels is evident in the SR dendrite due to the removal of the magnesium block by the BPAP (Fig. 3a). In the pre-30-post scenario, 30 ms after the presynaptic (dendritic) stimulation a BPAP arrived at the dendrite causing removal of the magnesium block from the NMDA channels. By then though more and more NMDA channels were inactivated and hence the calcium influx were greatly reduced (compare peak calcium level in Fig. 3a, b). The peak calcium level continued to decrease as the pre-post interstimulus interval was lengthened.

In the post-10-pre scenario (see Fig. 3c), the calcium influx came through the VGCCs producing a slight amplitude increase in calcium influx almost immediately, followed by a second calcium with a lower peak. The valley that separated the two peaks was above the 0.6 μM threshold, but below the 2 μM threshold, which triggered the depression (D) detector, but not the veto (V) detector and

produced LTD. In the post-30-pre case, the two calcium level peaks were more distinguishable, because of the 30 ms delay between the post-stimulation and the pre-stimulation (see Fig. 3d). The valley that separated them dropped below the 0.6 μM threshold causing a much smaller LTD. The results summarized in this section have been published before in Cutsuridis 2010, 2011, 2012, and 2013.

Theta-Modulated Inhibitory Single Spikes Have a Minimal Effect on Shape of the Asymmetric STDP Curve

Experimental evidence has indicated that a symmetric STDP kernel is observed in the proximal-to-the-soma dendrites of CA1 pyramidal cells, whereas an asymmetric STDP kernel is observed in the distal-to-the-soma ones (Tsukada et al. 2005). In the same study authors suggested that inhibition maybe a factor of this kernel shape change (Tsukada et al. 2005). In this section and the next one I will present results of the effects of inhibition on the STDP kernel shape.

I first examined the effect of a single presynaptic (dendritic) GABA spike slid at different temporal delays with respect to the excitatory pre- (dendritic) and postsynaptic (somatic) stimulation (see insets of Fig. 4 for input presentation details). Both inhibitory and excitatory somatic and dendritic stimulations were repeated every 300 ms (3.5 Hz) for about 5 s. Figure 4 depicts the saturated synaptic weight values (W_∞) with respect to the interstimulus interval $\Delta\tau$ in the presence of a single GABA spike. As before, $\Delta\tau$ is the interstimulus interval between the

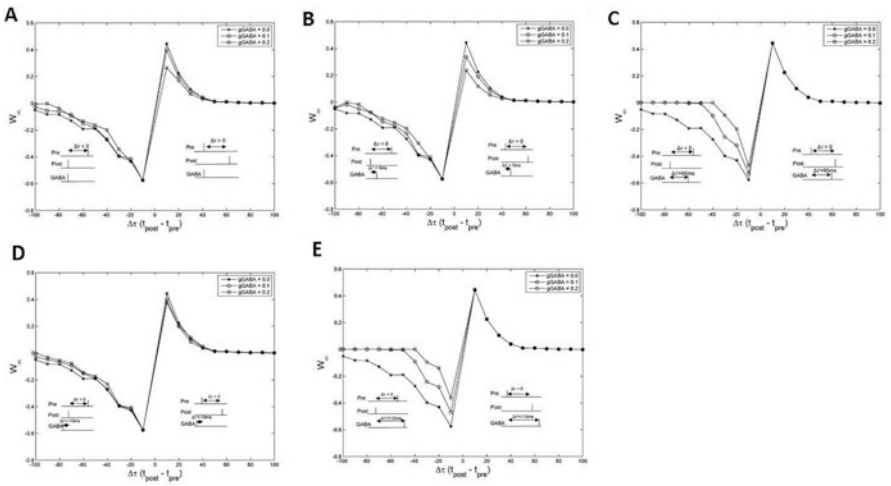

Fig. 4 Saturated synaptic weight values (W_∞) as a function of interstimulus interval $\Delta\tau = t_{post} - t_{pre}$ in the presence/absence of a single inhibitory spike of different strengths (reprinted with permission from Cutsuridis 2011). Δt is the time interval between the inhibitory spike and the excitatory spike pair. (**a**) $\Delta t = 0$ ms. (**b**) $\Delta t = 5$ ms. (**c**) $\Delta t = 95$ ms. (**d**) $\Delta t = -10$ ms. (**e**) $\Delta t = 110$ ms

presynaptic and postsynaptic stimulation. Simulations were performed with $\Delta\tau$ ranging from -100 to 100 in increments of 10 ms. An asymmetrical STDP kernel is shown with the largest LTP value at 10 ms and the largest LTD value at -10 ms. As the inhibitory strength (conductance) is increased ($g_{\mathrm{GABA}} = 0.1$ mS/cm^2 to 0.2 mS/cm^2), the STDP kernel shape is unaffected (asymmetry is preserved), but either the peak LTP or the peak LTD is reduced depending on temporal delay between the inhibitory spike and excitatory spike pair.

Frequency and Timing Effects of Theta-Modulated Inhibitory Bursts on the Shape of the STDP Curve

I next examined the effects of an inhibitory burst (spike train) at different interspike intervals (20 ms (50 Hz; low gamma) or 10 ms (100 Hz; high gamma)) (see Fig. 5). The inhibitory spike train was bounded by the onsets of the presynaptic (dendritic) and postsynaptic (somatic) excitatory spikes (i.e., no temporal delay (offset)). The excitatory pre- and postsynaptic spike pair and the inhibitory burst were repeated every 300 ms (3.5 Hz) for about 5 s. It is evident from Fig. 5 that the STDP kernel shape depends on the frequency and strength of inhibition. At low gamma (50 Hz) inhibition, the asymmetrical STDP kernel shape is preserved, but the peak LTP and LTD values are reduced as the strength (conductance) of inhibition increases (see Fig. 5a). At high gamma (100 Hz) inhibition, the STDP shape becomes symmetric without any LTD regions as the strength of inhibition is increased (see Fig. 5b).

Then I examined the effect of inhibition on the STDP kernel shape when inhibition is presented at various temporal delays (offsets) with respect to the excitatory spike pair. The desired, in line with the experimental evidence (Tsukada et al. 2005; Aihara et al. 2007) symmetric with a single LTP region and two LTD

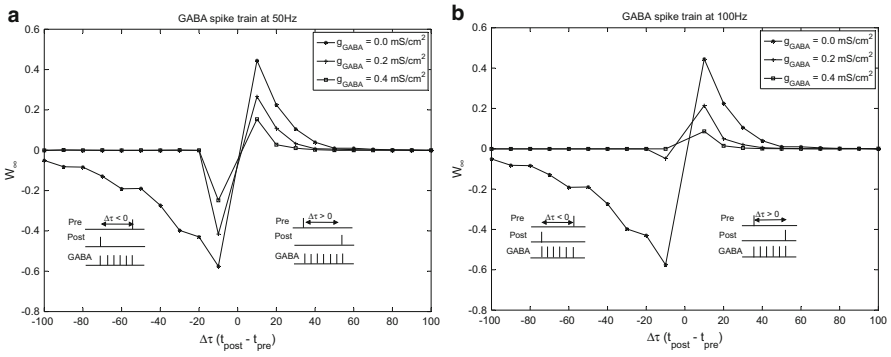

Fig. 5 Saturated synaptic weight values (W_∞) as a function of the interstimulus interval $\Delta\tau$. $\Delta\tau = t_{\mathrm{post}} - t_{\mathrm{pre}}$ and ranges from -100 to 100 in increments of 10 ms (reprinted with permission from Cutsuridis 2011). (**a**) A low gamma (50 Hz) inhibitory burst bounded by $\Delta\tau$. (**b**) A high gamma (100 Hz) inhibitory burst bounded by $\Delta\tau$

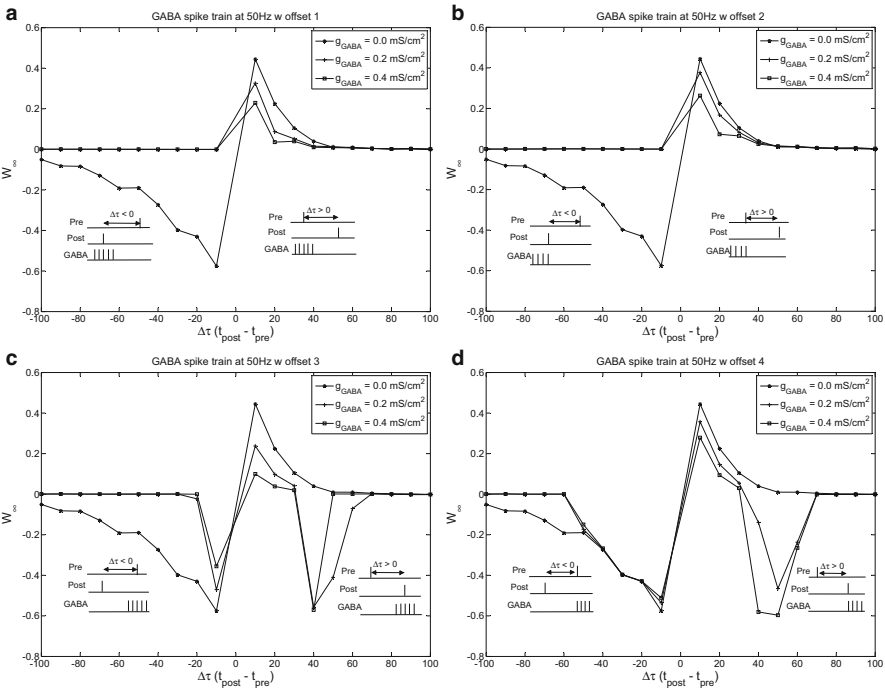

Fig. 6 (**a**)–(**d**) Saturated synaptic weight values (W_∞) as a function of $\Delta\tau$ in the presence of theta-modulated low gamma (50 Hz) burst with different temporal delays (offsets) and strengths. (Reprinted with permission from Cutsuridis 2011)

flanks, STDP kernel is evident only when the inhibitory burst (spike train) overlaps with (Fig. 6c) or is presented right after (Figs. 6d and 7d) the second spike of the excitatory pair. The maximum LTP value is at +10 ms, whereas the two LTD peaks are at −10 ms and + 50 ms, respectively.

Model 2: Interaction of Theta-Modulated Dendritic Bursts and Somatic Spikes in a CA1 Pyramidal Cell

Pairing of a Dendritic Burst and a Somatic Spike in the Absence of Inhibition

This stimulation protocol consisted of 16 sets of a dendritic burst and a somatic spike repeated every 300 ms (3.5 Hz) for about 5 s. The dendritic burst consisted of three spikes with variable interspike interval (ISI) (5 ms or 10 ms). Each pair was characterized by $\Delta\tau = t_{\text{postSpike}} - t_{\text{preBurst}}$, where t_{preBurst} is the first spike of the presynaptic (dendritic) burst and $t_{\text{postSpike}}$ is the time of postsynaptic (somatic)

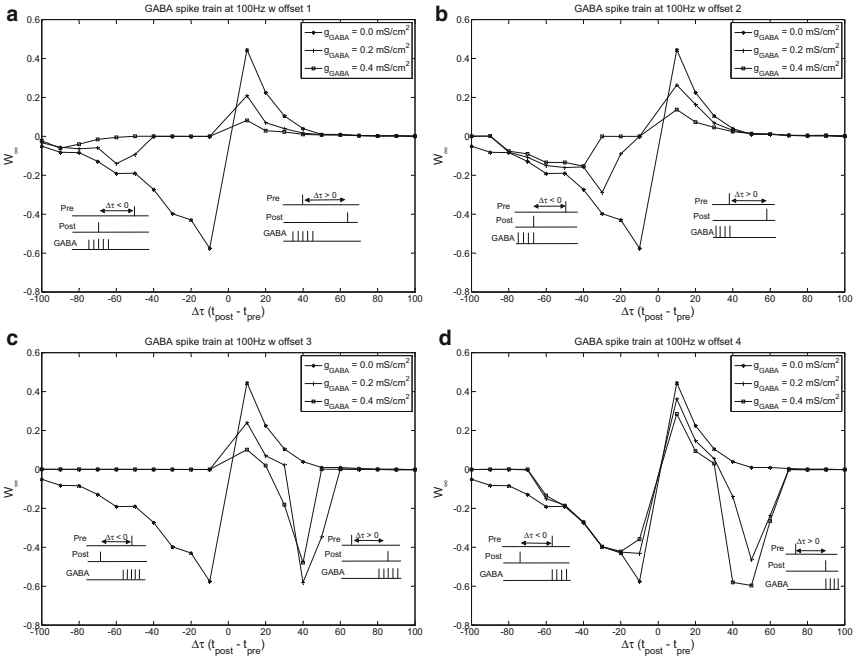

Fig. 7 (**a**)–(**d**) Saturated synaptic weight values (W_∞) as a function of $\Delta\tau$ in the presence of theta-modulated high gamma (100 Hz) burst with different temporal delays (offsets) and strengths. (Reprinted with permission from Cutsuridis 2011)

spike. $\Delta\tau$ was positive only when the dendritic burst preceded the somatic spike and negative when otherwise. The saturated synaptic weight values (W_∞) at the dendrite as a function of the interstimulus interval, $\Delta\tau = t_{\text{post}} - t_{\text{pre}}$, and burst interspike interval (bISI) are depicted in Fig. 8a. As before W_∞ is measured at the saturated value of the readout variable W at $t = 5$ s. When the saturated W is oscillating between two values, then W_∞ is the mean of these two values. Simulations were performed with $\Delta\tau$ ranging from -180 ms to 180 ms in increments of 5 ms. An asymmetric STDP kernel is shown with the largest LTP and LTD values at $+15$ ms and at -5 ms, respectively, when bISI is 5 ms. As bISI is increased to 10 ms, the shape of the STDP kernel remains asymmetric, but shifts to the right with the peak LTP value increased by 0.14 units and at $+40$ ms and the lowest LTP value increased by 0.1 units and set at 0 ms. The STDP curve levels off at 0.4 units and never decays back to zero even at $\Delta\tau = \pm 180$ ms. This is due to the repetition period of the pre-postsynaptic excitatory stimulation (every 300 ms), which allows the effects of the postsynaptic spike at $\Delta\tau > 150$ ms to interact with the effects of the presynaptic burst at the start of next pre-post excitatory stimulation.

In the preBurst-(40 ms)-postSpike case, the peak LTP value is larger when the bISI is 10 ms than when bISI is 5 ms (data not shown, but see Fig. 6b in Cutsuridis (2012)). This increase in potentiation is due to a larger amount of Ca^{2+} influx

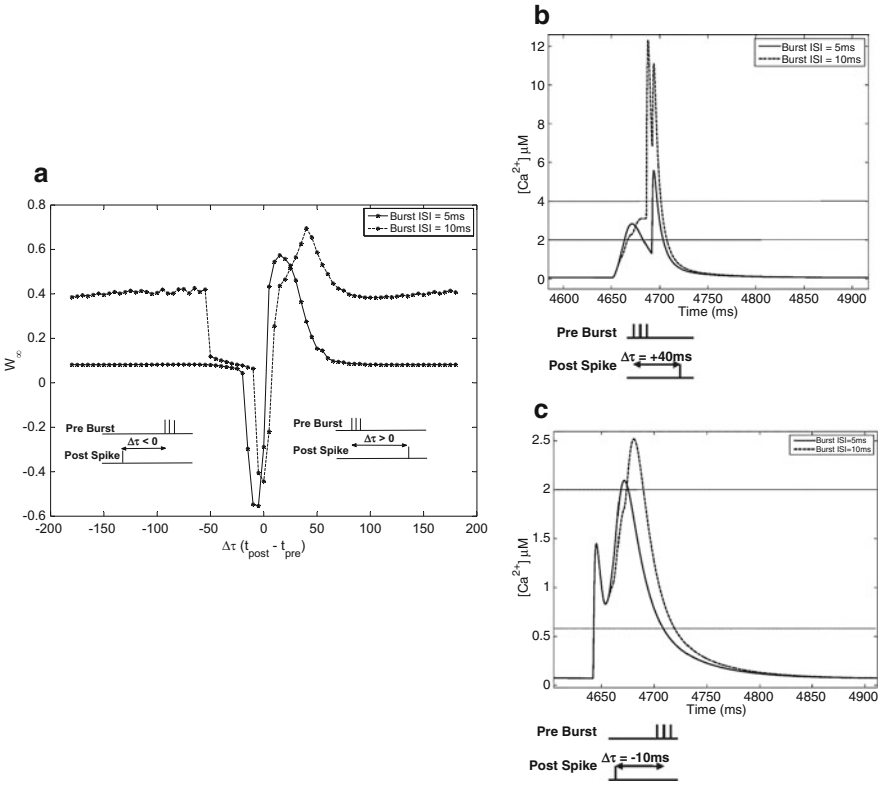

Fig. 8 (**a**) Simulated STDP temporal kernel as a function of burst interspike interval (burst ISI) in the absence of inhibition (reprinted with permission from Cutsuridis 2012). $\Delta\tau$ ($t_{\text{post}} - t_{\text{pre}}$) is the interstimulus interval between the first spike of the dendritic burst and the somatic spike. $\Delta\tau$ ranges from -180 ms to 180 ms in increments of 5 ms. (Inset-left) postSpike-preBurst scenario, where somatic single spike precedes the dendritic burst, comprised of three spikes, by $\Delta\tau$. $\Delta\tau$ takes values from -5 ms to -180 ms in increments of 5 ms. The pairing repeats every 300 ms for about 5 s. (Inset-right) preBurst-postSpike scenario, where a dendritic burst precedes the somatic spike by $\Delta\tau$. $\Delta\tau$ takes values from 0 ms to $+180$ ms in increments of 5 ms. The pairing repeats every 300 ms for about 5 s. (**b**) Bottom: Graphical representation of preBurst-($+40$ ms)-postSpike stimulation paradigm in the absence of inhibition (reprinted with permission from Cutsuridis 2012). Top: Time course of Ca^{2+} concentration (μM) as a function of burst interspike intervals (ISIs) (5 ms and 10 ms) in the absence of inhibition in the preBurst-($+40$ ms)-postSpike scenario (reprinted with permission from Cutsuridis 2012). (**c**) Bottom: Graphical representation of postSpike-(-10 ms)-preBurst stimulation paradigm in the absence of inhibition (reprinted with permission from Cutsuridis 2012). Top: Time course of Ca^{2+} concentration (μM) as a function of burst interspike intervals (ISIs) (5 ms and 10 ms) in the absence of inhibition in the postSpike-(-10 ms)-preBurst scenario. (Reprinted with permission from Cutsuridis 2012)

through the NMDA channel when bISI is 10 ms, thus allowing the time course of its concentration to stay above the potentiation (4 μM) and veto (2 μM) thresholds for a longer period of time (approximately 70 ms) (see Fig. 8b).

In the case of bISI at 5 ms, the calcium influx through the NMDA channel is greatly reduced, followed by a second calcium pulse with a higher peak 40 ms after the burst. The NMDA calcium pulse stays above the 2 μM veto threshold for a small period of time (approximately 10 ms) and subsequently decays to values below this threshold, thus triggering for 2–3 ms the depression (D) detector, which counteracts any previously triggered potentiation. The D response is very brief and it is followed by a calcium influx through the VGCC, which cause a second calcium pulse to peak above the 4 μM threshold, which re-potentiates the synapse and causes the synaptic weight to saturate to 0.27 units (data not shown, but see Fig. 6b in Cutsuridis (2012)).

In the postSpike-(−10 ms)-preBurst case, the calcium influx is greatly reduced due to a different time course than in the previous case. The first calcium spike comes from the VGCC and peaks under the 2 μM threshold, thus triggering the depression (D) detector (see Fig. 8c). The second calcium spike comes from the NMDA channels at the dendrite which opened by the dendritic burst. When bISI is 5 ms, the second calcium spike peaked and stayed above the 2 μM threshold for less than 5 ms and then decayed to zero. When bISI is 10 ms, the second calcium spike peaked at 2.5 μM and stayed above the 2 μM threshold for a longer period of time, thus triggering a larger veto response than before (data not shown). I remind the reader that the veto (V) response inhibits and counteracts the response of the depression (D) detector. Hence, the D response is larger in the 5 ms bISI case than in the 10 ms bISI one. Thus, the synaptic weight (W) will saturate to a more positive value when bISI is 10 ms than when bISI is 5 ms.

Pairing of a Dendritic Burst and a Somatic Spike in the Presence Inhibition: Effects of Inhibition Strength and Burst Interspike Interval

In this stimulation protocol, an inhibitory spike train with 10 ms (100 Hz) interspike interval, $\Delta\tau_{GABA}$, was repeated every 300 ms (3.5 Hz) for about 5 s (a total of 16 spike trains). Each inhibitory spike train was bounded by the onset and offset of the dendritic burst-somatic spike stimulation. As the strength of inhibition is increased, then the shape of the STDP kernel transitions from asymmetry to symmetry (see Fig. 9). When g_{GABA} is 0.1 mS/cm^2, then the shape of the STDP kernel resembles a Mexican hat consisting of a peak-positive phase at +10–15 ms when bISI is 5 ms and + 10 ms when bISI is 10 ms and two peak-negative regions at −5 ms and + 65 ms when bISI is 5 ms and at −5 ms and + 80 ms when bISI is 10 ms. As the strength of inhibition increases ($g_{GABA} = 0.2$ mS/cm^2), then the shape of the STDP kernel becomes fully symmetric with flat negative tails and a single positive region. When bISI is 5 ms, then the peak LTP value is slightly reduced as g_{GABA} is increased, but the peak LTD value remains unaffected (see Fig. 9a). Similarly, when bISI is 10 ms, then the peak LTP value is slightly reduced as g_{GABA} increases and is shifted rightward by about 15 ms. A similar reduction is observed for the peak LTD value when g_{GABA} increases (see Fig. 9b).

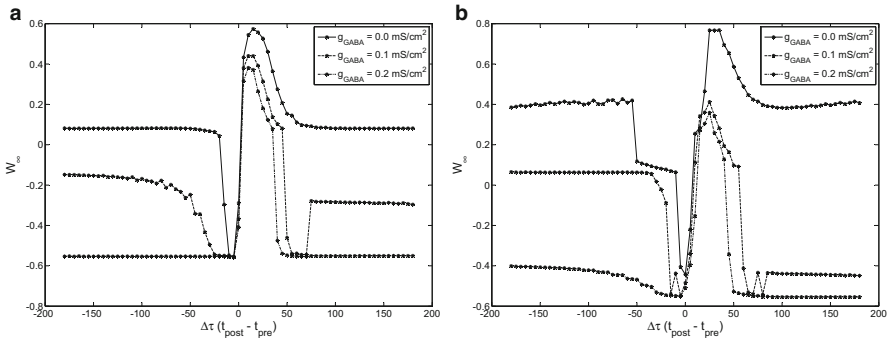

Fig. 9 Saturated synaptic weight (W_∞) values as a function of interstimulus time interval, $\Delta\tau = t_{\text{postSpike}} - t_{\text{preBurst}}$ (reprinted with permission from Cutsuridis 2012). $\Delta\tau$ ranges from -180 ms to 180 ms in increments of 5 ms. An 100 Hz GABA spike train is present within $\Delta\tau$. (**a**) Burst ISI is set to 5 ms. (**b**) Burst ISI is set to 10 ms

Discussion and the Future

The models presented in this chapter aimed to understand the conditions under which the sign, magnitude, and shape of the STDP temporal kernel change in the proximal-to-the-soma dendrites of CA1 pyramidal cells. Experimental evidence has shown that the profile of the STDP induced in the hippocampal CA1 network with inhibitory interneurons depends on the dendritic location and has a symmetric profile in the proximal-to-the-soma dendrite and an asymmetric one in the distal-to-the-soma one (Tsukada et al. 2005; Aihara et al. 2007). Further experimental evidence has shown that the switch between symmetrical and asymmetrical STDP operational modes is due to the presence of GABAergic inhibition in the proximal-to-the-soma dendrites (Tsukada et al. 2005). In the models, the dendrites were stimulated by either single spike or more complex (bursts) inputs. The parameters that varied in order to investigate the effects of inhibition on the STDP profile included input frequency (low gamma inhibition vs high gamma inhibition), strength of inhibition, and relative timing of inhibition with respect to the excitatory pre- and postsynaptic stimulation.

The central observation is that spike timing-dependent plasticity *indeed* undergoes a switch in its operational mode (asymmetry to symmetry), which is due to $GABA_A$ inhibition in the proximal-to-the-soma dendrite of a CA1 pyramidal cell, as it has been experimentally observed (Nishiyama et al. 2000; Tsukada et al. 2005; Aihara et al. 2007). In addition the models made further predictions:

- Theta-modulated inhibitory single spikes have a minimal effect on shape of the STDP curve.
- Burst ISI, strength (conductance value), frequency, and relative timing of theta-modulated inhibition with respect to theta-modulated excitatory spike pairs are the main factors for asymmetry-to-symmetry change in the shape of STDP curve in the dendrites of CA1 pyramidal cells.

- In contrast to experimental evidence (Tsukada et al. 2005; Aihara et al. 2007), the LTP peak value of the symmetric STDP curve is at ±10 ms, whereas the two LTD windows are at -10 ms and + 40 ms.

Several extensions to the basic idea of how inhibition affects the STDP profile resulting from a single event of a pre- and postsynaptic spike pairing deserve consideration. The dendritic trees of the CA1 pyramidal cells are extensive. An interesting idea is how STDP is dynamically regulated by adjacent synapses on the dendrites of CA1 pyramidal cells. Experimental evidence has shown that both distal and proximal SR dendrites receive excitatory inputs from CA3 cells as well as inhibitory inputs from local CA1 interneurons. An additional excitatory input drives the lacunosum-moleculare (LM) dendrites of the CA1 pyramidal neuron. Pairings of the SR and LM presynaptic excitatory and inhibitory inputs with the postsynaptic somatic activation will provide us with a more realistic picture of STDP in the SR dendrites.

Similarly, the same dendrites are also targeted by a number of neuromodulators such as acetylcholine or dopamine (Cobb and Lawrence 2010). Recent experimental evidence has shown that in the hippocampus, application of cholinergic agonists to slices in vitro facilitates LTP (Auerbach and Segal 1996; Blitzer et al. 1990). Shinoe et al. (2005) reported tetanic stimulation of hippocampal neurons in the presence of ACh-enhanced LTP. Similar facilitation is observed when medial septum is stimulated in vivo (Galey et al. 1994; Markevich et al. 1997). Differential effects of subtype-specific nicotinic AChR agonists have been reported in early and late hippocampal LTP (Kroker et al. 2011). The cholinergic drive to the hippocampus seems to be important in the control of the LTP induction threshold (Ovsepian et al. 2004; Boddeke et al. 1992). Sugisaki et al. (2011) showed that when spike-pair stimuli were applied during the muscarinic induction of a slow EPSP followed by repetitive stimulation in the stratum oriens, then an increase in ACh concentration following application of the cholinesterase inhibitor eserine resulted in LTP facilitation and abolition of LTD. Application of high ACh concentration completely suppressed STDP, LTP, and LTD. Application of atropine suppressed STDP.

Some of these issues are investigated by detailed compartmental models of CA1 pyramidal cells presented in next chapter by Saudargiene and Graham.

Appendix

The somatic (s) and dendritic (d) compartments of the pyramidal neuron obey the following current balance equations:

$$C_m \frac{dV_s}{dt} = I_L + I_{Na,s} + I_{K_{dr,s}} + I_{A,s} + I_{m,AHAP,s} + I_{CaL,s} + I_{coup} + I_{in} \cdot F_{post} \tag{6}$$

$$C_m \frac{dV_d}{dt} = I_L + I_{Na,d} + I_{K_{dr,d}} + I_{A,d} + I_{m,AHAP,d} + I_{CaL,d} + I_{coup} + I_{AMPA} + I_{NMDA} + I_{GABA} \quad (7)$$

where I_L is the leak current, I_{Na} is the sodium current, I_{Kdr} is the delayed rectifier potassium current, I_A is the type-A potassium current, $I_{m,AHP}$ is the medium Ca^{2+}-activated K^+ after-hyperpolarization current, I_{CaL} is the L-type Ca^{2+} current, I_{coup} is the electrical coupling between compartments, I_{in} is the injected current, I_{AMPA} is the AMPA current, I_{NMDA} is the NMDA current, and I_{GABA} is the GABA current.

The sodium current at the soma is described by

$$I_{Na,s} = -g_{Na,s} \cdot M_{Na,s}^2 \cdot H_{Na,s} \cdot (V_s - V_{Na}) \quad (8)$$

where $g_{Na,s}$ is the maximal conductance of the Na^+ current, $M_{Na,s}$ and $H_{Na,s}$ are the activation and inactivation constants, and V_{Na} is the reversal potential of the Na^+ current. The activation and inactivation constants at the soma are given by

$$M_{Na,s} = \alpha_{M,s}(V_s) / \left(\alpha_{M,s}(V_s) + \beta_{M,s}(V_s)\right)$$

$$\alpha_{M,s}(V_s) = 0.32 \cdot (-46.9 - V_s) / (\exp((-46.9 - V_s)/4.0) - 1.0)$$

$$\beta_{M,s}(V_s) = 0.28 \cdot (V_s + 19.9) / (\exp((V_s + 19.9)/5.0) - 1.0)$$

$$H'_{Na,s} = \alpha_{H,s}(V_s) - \left(\alpha_{H,s}(V_s) + \beta_{H,s}(V_s)\right) \cdot H_{Na,s}$$

$$\alpha_{H,s}(V_s) = 0.128 \cdot \exp((-43 - V_s)/18)$$

$$\beta_{H,s}(V_s) = 4/(1 + \exp((-20 - V_s)/5)$$

The sodium current at the dendrite is described by

$$I_{Na,d} = -g_{Na,d} \cdot M_{Na,d}^2 \cdot H_{Na,d} \cdot D_{Na,d} \cdot (V_d - V_{Na}) \quad (9)$$

where

$$M'_{Na,d} = \left(M_{\infty_{Na,d}} - M_{Na,d}\right)/\tau_{M_{Na,d}}$$

$$M_{\infty_{Na,d}} = 1/(1 + \exp((-V_d - 40)/3))$$

$$\tau_{M_{Na,d}} = \max(0.1, 0.05)$$

$$H'_{Na,d} = \left(H_{\infty_{Na,d}} - H_{Na,d}\right)/\tau_{H_{Na,d}}$$

$$H_{\infty_{Na,d}} = 1/\left(1 + \exp\left(\left(V_d + 45\right)/3\right)\right)$$

$$\tau_{H_{Na,d}} = 0.5$$

$$D'_{Na,d} = \left(D_{\infty_{Na,d}} - D_{Na,d}\right)/\tau_{D_{Na,d}}$$

$$\begin{aligned} D_{\infty_{Na,d}} &= \left(1 + \text{natt} \cdot \exp\left(\left(V_d + 60\right)/2\right)\right) / \left(1 + \exp\left(\left(V_d + 60\right)/2\right)\right) \tau_{D_{Na,d}} \\ &= \max\left(0.1, \left(0.00333 \cdot \exp\left(0.0024 \cdot \left(V_d + 60\right) \cdot Q\right)\right) / \left(1 + \exp\left(0.0012\right.\right.\right. \\ &\quad \left.\left.\left. \cdot \left(V_d + 60\right) \cdot Q\right)\right)\right) \end{aligned}$$

$$Q = 96480/\left(8.315 \cdot \left(273.16 + T\right)\right)$$

where T is the temperature in Celsius and *natt* is the Na^+ attenuation.

The type-A K^+ current at the soma is given by

$$I_{K_{A,s}} = -g_{K_{A,s}} \cdot A_s \cdot B_s \cdot \left(V_s - V_K\right) \tag{10}$$

where $g_{KA,s}$ is the maximal conductance, V_k is the reversal potential, and A_s and B_s are the activation and inactivation constants. The activation and inactivation constants are given by

$$A'_s = \left(A_{\infty_s} - A_s\right)/\tau_{A_s}$$

$$A_{\infty_s} = 1/\left(1 + A_{\alpha,s}\right)$$

$$A_{\alpha,s} = \exp\left(0.001 \cdot \sigma\left(V_s\right) \cdot \left(V_s - 11\right) \cdot Q\right)$$

$$\tau_{A_s} = \max\left(A_{\beta,s}/\left(\left(1 + A_{\alpha,s}\right) \cdot QT \cdot 0.05\right), 0.1\right)$$

$$A_{\beta,s} = \exp\left(0.00055 \cdot Q \cdot \left(V_s - 11\right) \cdot \sigma\left(V_s\right)\right)$$

$$\sigma\left(V_s\right) = -1.5 - \left(1/\left(1 + \exp\left(\left(V_s + \sigma_p\right)/5\right)\right)\right)$$

$$QT = 5^{((T-24)/10)}$$

$$B'_s = \left(B_{\infty_s} - B_s\right)/\tau_{B_s}$$

$$B_{\infty_s} = 0.3 + 0.7/\left(1 + \exp\left(0.02 \cdot \left(V_s + 63.5\right) \cdot Q\right)\right)$$

$$\tau_{B_s} = \kappa \cdot \max\left(0.11 \cdot \left(V_s + 62\right), 2\right)$$

The type-A K^+ current at the dendrite is given by

$$I_{K_{A,d}} = -g_{K_{A,d}} \cdot A_d \cdot B_d \cdot \left(V_d - V_K\right) \tag{11}$$

The activation and inactivation constants are given by

$$A'_d = \left(A_{\infty_d} - A_d\right) / \tau_{A_d}$$

$$A_{\infty_d} = 1 / \left(1 + A_{\alpha,d}\right)$$

$$A_{\alpha,d} = \exp\left(\text{asap} \cdot \sigma\left(V_d\right) \cdot \left(V_d + 1\right) \cdot Q\right)$$

$$A_{\beta,d} = \exp\left(0.00039 \cdot Q \cdot \left(V_d + 1\right) \cdot \sigma_2\left(V_d\right)\right)$$

$$\tau_{A_d} = \max\left(A_{\beta,d} / \left(\left(1 + A_{\alpha,d}\right) \cdot QT \cdot 0.1\right), 0.1\right)$$

$$\sigma\left(V_d\right) = -1.5 - \left(1 / \left(1 + \exp\left(\left(V_d + \sigma_p\right) / 5\right)\right)\right)$$

$$\sigma_2\left(V_d\right) = -1.8 - \left(1 / \left(1 + \exp\left(\left(V_d + 40\right) / 5\right)\right)\right)$$

$$B'_d = \left(B_{\infty_d} - B_d\right) / \tau_{B_d}$$

$$B_{\infty_d} = 0.3 + 0.7 / \left(1 + \exp\left(\text{inact}_2 \cdot \left(V_s + \text{inact}\right) \cdot Q\right)\right)$$

$$\tau_{B_d} = \kappa \cdot \max\left(\text{inact}_3 \cdot \left(V_s + \text{inact}_4\right), \text{inact}_5\right)$$

The delayed rectifier K^+ current at the soma is given by

$$I_{K_{dr,s}} = -g_{K_{dr,s}} \cdot N_s \cdot \left(V_s - V_K\right) \tag{12}$$

where $g_{Kdr,s}$ is the maximal conductance. The activation constant, N_s, is given by

$$N'_s = \alpha_{N_s}\left(V_s\right) - \left(\alpha_{N_s}\left(V_s\right) + \beta_{N_s}\left(V_s\right)\right) \cdot N_s$$

$$\alpha_{N_s}\left(V_s\right) = 0.016 \cdot \left(-24.9 - V_s\right) / \left(\exp\left(\left(-24.9 - V_s\right) / 5\right) - 1\right)$$

$$\beta_{N_s}\left(V_s\right) = 0.25 \cdot \exp\left(-1 - 0.025 \cdot V_s\right)$$

The delayed rectifier K^+ current at the dendrite is given by

$$I_{K_{dr,d}} = -g_{K_{dr,d}} \cdot N_d^2 \cdot \left(V_d - V_K\right) \tag{13}$$

where $g_{Kdr,d}$ is the maximal conductance. The activation constant, N_d, is given by

$$N_d' = \left(N_{\infty_d} - N_d\right) / \tau_{N_d}$$

$$N_{\infty_d} = 1 / \left(1 + \exp\left(\left(-V_d - 42\right) / 2\right)\right.$$

$$\tau_{N_d} = 2.2$$

The medium Ca^{2+}-activated K^+ after-hyperpolarization current is given by

$$I_{\mathrm{mAHP}} = -g_{\mathrm{mAHP}} \cdot Q_m \cdot \left(V_s - V_K\right) \tag{14}$$

where g_{KmAHP} is the maximal conductance. The activation constant, Q_m, isgiven by

$$Q_m' = \left(Q_{m_\infty} - Q_m\right) / \tau_{Q_m}$$

$$Q_{m_\infty} = \mathrm{qhat} \cdot Q_{m_\alpha} \cdot \tau_{Q_m}$$

$$Q_{m_\alpha} = qma \cdot \chi / \left(0.001 \cdot \chi + 0.18 \cdot \exp\left(-1.68 \cdot V_s \cdot Q\right)\right)$$

$$Q_{m_\beta} = \left(qmb \cdot \exp\left(-0.022 \cdot V_s \cdot Q\right)\right) / \left(\exp\left(-0.022 \cdot V_s \cdot Q\right) + 0.001 \cdot \chi\right)$$

$$\tau_{Q_m} = 1 / \left(Q_{m_\alpha} + Q_{m_\beta}\right)$$

The L-type Ca^{2+} current at the soma is described by

$$I_{CaL_s} = -g_{CaL_s} \cdot S_s \cdot g_{hk}\left(V_s, \chi_s\right) \cdot \left(1 / \left(1 + \chi_s\right)\right) \tag{15}$$

where $g_{CaL,s}$ is the maximal conductance and

$$S_s' = \left(S_{\infty_s} - S_s\right) / \tau_{s_s}$$

$$S_{\infty_s} = \alpha_s\left(V_s\right) / \left(\alpha_a\left(V_s\right) + \beta_s\left(V_s\right)\right)$$

$$\tau_{S_s} = 1 / \left(5 \cdot \left(\alpha_s\left(V_s\right) + \beta_s\left(V_s\right)\right)\right)$$

$$\alpha_s\left(V_s\right) = -0.055 \cdot \left(V_s + 27.01\right) / \left(\exp\left(\left(-V_s - 27.01\right) / 3.8\right) - 1\right)$$

$$\beta_s\left(V_s\right) = 0.94 \cdot \exp\left(\left(-V_s - 63.01\right) / 17\right)$$

$$xx = 0.0853 \cdot \left(273.16 + T\right) / 2$$

$$f\left(z\right) = \left(1 - z/2\right) \cdot f_2\left(z\right) + \left(z / \left(\exp\left(z\right) - 1\right)\right) \cdot f_3\left(z\right)$$

$$f_2\left(z\right) = H\left(0.0001 - |z|\right)$$

$$f_3(z) = H(|z| - 0.0001)$$

$$g_{hk} = -xx \cdot (1 - ((\chi_s/Ca) \cdot \exp(V_s/xx))) \cdot f(V_s/xx)$$

$$\chi_s' = \varphi_s \cdot I_{CaL_s} - \left(\beta_s \cdot \left(\chi_s - \chi_{0,s}\right)\right) + (\chi_d - \chi_s)/Ca_\tau - (\beta_s/nonc) \cdot \chi_s^2$$

$$\chi_d' = \varphi_d \cdot \left(I_{CaL_d} + I_{Ca,NMDA}\right) - \beta_d \cdot \left(\chi_d - \chi_{0,d}\right) - (\beta_d/nonc) \cdot \chi_d^2 - buff \cdot \chi_d$$

where χ_s and χ_d are the Ca^{2+} concentrations in the soma and dendrite, respectively. The L-type Ca^{2+} current at the dendrite is described by

$$I_{CaL_d} = -g_{CaL_d} \cdot S_d^3 \cdot T_d \cdot (V_d - V_{Ca}) \tag{16}$$

$$S_d' = \left(S_{\infty_d} - S_d\right)/\tau_{s_d}$$

$$S_{\infty_d} = 1/(1 + \exp(-V_d - 37))$$

$$\tau_{s_d} = s_3 + s_1/(1 + \exp(V_d + s_2))$$

$$T_d' = \left(T_{\infty_d} - T_d\right)/\tau_{T_d}$$

$$T_{\infty_d} = 1/(1 + \exp((V_d + 41)/0.5))$$

$$\tau_{T_d} = 29$$

The coupling constant for the compartment i is

$$I_{\text{coup}} = g_{\text{coup}} \cdot \left(V_j - V_i\right) \tag{17}$$

The Ca^{2+}-NMDA, AMPA, GABA-A, and NMDA synaptic currents are given by

$$I_{Ca,\text{NMDA}} = -g_{Ca,\text{NMDA}} \cdot s_{\text{NMDA}} \cdot m_{Ca,\text{NMDA}} \cdot \left(V_d - V_{Ca,\text{NMDA}}\right) \tag{18}$$

$$I_{\text{NMDA}} = -g_{\text{NMDA}} \cdot s_{\text{NMDA}} \cdot m_{\text{NMDA}} \cdot (V_d - V_{\text{NMDA}}) \tag{19}$$

$$I_{\text{AMPA}} = -g_{\text{AMPA}} \cdot s_{\text{AMPA}} \cdot (V_d - V_{\text{AMPA}}) \tag{20}$$

$$I_{\text{GABA}} = -g_{\text{GABA}} \cdot s_{\text{GABA}} \cdot (V_d - V_{\text{GABA}}) \tag{21}$$

where

$$m_{\text{NMDA}} = 1/\left(1 + 0.3 \cdot Mg \cdot \exp\left(-0.062 \cdot V_d\right)\right)$$

$$m_{Ca,\text{NMDA}} = 1/\left(1 + 0.3 \cdot Mg \cdot \exp\left(-0.124 \cdot V_d\right)\right)$$

with $Mg^{2+} = 2$ mM. The activation equations for AMPA, NMDA, and GABA-A currents are

$$s_x = s_{x_{\text{fast}}} + s_{x_{\text{slow}}} + s_{x_{\text{rise}}} \tag{22}$$

where x stands for AMPA, NMDA, and GABA and

$$s'_{NMDA_{rise}} = -20 \cdot \left(1 - s_{NMDA_{fast}} - s_{NMDA_{slow}}\right) \cdot F_{pre} - (1/NMDA_{rate}) \cdot s_{NMDA_{rise}}$$

$$s'_{NMDA_{fast}} = 20 \cdot \left(0.527 - s_{NMDA_{fast}}\right) \cdot F_{pre} - (1/ndf) \cdot s_{NMDA_{fast}}$$

$$s'_{NMDA_{slow}} = 20 \cdot \left(0.473 - s_{NMDA_{slow}}\right) \cdot F_{pre} - (1/nds) \cdot s_{NMDA_{slow}},$$

$$s'_{AMPA_{rise}} = -20 \cdot \left(1 - s_{AMPA_{fast}} - s_{AMPA_{slow}}\right) \cdot F_{pre} - (1/0.58) \cdot s_{AMPA_{rise}}$$

$$s'_{AMPA_{fast}} = 20 \cdot \left(0.903 - s_{AMPA_{fast}}\right) \cdot F_{pre} - (1/7.6) \cdot s_{AMPA_{fast}}$$

$$s'_{AMPA_{slow}} = 20 \cdot \left(0.097 - s_{AMPA_{slow}}\right) \cdot F_{pre} - (1/25.69) \cdot s_{AMPA_{slow}}$$

and

$$s'_{GABA_{rise}} = -20 \cdot \left(1 - s_{GABA_{fast}} - s_{GABA_{slow}}\right) \cdot F_{GABA} - (1/1.18) \cdot s_{GABA_{rise}}$$

$$s'_{GABA_{fast}} = 20 \cdot \left(0.803 - s_{GABA_{fast}}\right) \cdot F_{GABA} - (1/8.5) \cdot s_{GABA_{fast}}$$

$$s'_{GABA_{slow}} = 20 \cdot \left(0.197 - s_{GABA_{slow}}\right) \cdot F_{GABA} - (1/30.01) \cdot s_{GABA_{slow}}$$

The calcium detector model is governed by the following six equations:

$$P' = \left(\varphi_a\left(\chi_d\right) - c_p \cdot A \cdot P\right)/\tau_p \tag{23}$$

$$V' = \left(\varphi_b\left(\chi_d\right) - V\right)/\tau_V \tag{24}$$

$$A' = \left(\varphi_c\left(\chi_d\right) - A\right)/\tau_A \tag{25}$$

$$B' = \left(\varphi_e(A) - B - c_d \cdot B \cdot V\right)/\tau_B \tag{26}$$

$$D' = \left(\varphi_d(B) - D\right)/\tau_D \tag{27}$$

$$W' = \left(\alpha_w / \left(1 + \exp\left(\left(P - a\right) / p_a\right)\right) - \beta_w / \left(1 + \left(\exp\left(\left(D - d\right) / p_d\right)\right) - W\right) / \tau_w \tag{28}$$

where P is the potentiation detector dynamics, V is the veto detector dynamics, D is the depression detector dynamics, A and B are the intermediate steps leading up to D, and W is the readout variable (see Fig. 1b). The Hill equations are

$$\phi_a\left(x\right) = num_a \cdot \left(\left(x/\mathrm{CmHC}\right)^{\mathrm{CmHN}}\right) / \left(1 + \left(x/\mathrm{CmHC}\right)^{\mathrm{CmHN}}\right) \tag{29}$$

$$\phi_b\left(x\right) = num_b \cdot \left(\left(x/\mathrm{CnHC}\right)^{\mathrm{CnHN}}\right) / \left(1 + \left(x/\mathrm{CnHC}\right)^{\mathrm{CnHN}}\right) \tag{30}$$

$$\phi_c\left(x\right) = num_c / \left(1 + \exp\left(\left(x - \theta_c\right) / \sigma_c\right)\right) \tag{31}$$

$$\phi_d\left(x\right) = num_d / \left(1 + \exp\left(\left(x - \theta_d\right) / \sigma_d\right)\right) \tag{32}$$

References

Aihara T, Abiru Y, Yamazaki Y, Watanabe H, Fukushima Y, Tsukada M (2007) The relation between spike-timing dependent plasticity and Ca^{2+} dynamics in the hippocampal CA1 network. Neuroscience 145:80–87

Auerbach JM, Segal M (1996) Muscarinic receptors mediating depression and long-term potentiation in rat hippocampus. J Physiol 492(Pt 2):479–493

Bell CC, Han VZ, Sugawara Y, Grant K (1997) Synaptic plasticity in a cerebellum-like structure depends on temporal order. Nature 387:278–281

Bi GQ, Poo MM (1998) Synaptic modifications in cultured hippocampal neurons: dependence on spike timing, synaptic strength, and postsynaptic cell type. J Neurosci 18:10464–10472

Bi GQ, Rubin J (2005) Timing in synaptic plasticity: from detection to integration. TINS 28(5):222–228

Blitzer RD, Gil O, Landau EM (1990) Cholinergic stimulation enhances longterm potentiation in the CA1 region of rat hippocampus. Neurosci Lett 119:207–210

Boddeke EW, Enz A, Shapiro G (1992) SDZ ENS 163, a selective muscarinic M1 receptor agonist, facilitates the induction of long-term potentiation in rat hippocampal slices. Eur J Pharmacol 222:21–25

Caporale N, Dan Y (2009) Spike timing dependent plasticity: a Hebbian learning rule. Annu Rev Neurosci 31:25–46

Cobb S, Lawrence JJ (2010) Neuromodulation of hippocampal cells and circuits. In: Cutsuridis V et al (eds) Hippocampal microcircuits: a computational Modeller's resource book, vol V. Springer, New York, pp 187–246

Cutsuridis V (2010) Action potential bursts modulate the NMDA-R mediated spike timing dependent plasticity in a biophysical model, Lecture notes in computer science (LNCS), vol 6352. Springer-Verlag, Berlin/Heidelberg, pp 107–116

Cutsuridis V (2011) GABA inhibition modulates NMDA-R mediated spike timing dependent plasticity (STDP) in a biophysical model. *Neural Netw* 24(1):29–42

Cutsuridis V (2012) Bursts shape the NMDA-R mediated spike timing dependent plasticity curve: role of burst interspike interval and GABA inhibition. Cogn Neurodyn 6(5):421–441

Cutsuridis V (2013) Interaction of inhibition and triplets of excitatory spikes modulates the NMDA-R mediated synaptic plasticity in a computational model of spike timing dependent plasticity. Hippocampus 23(1):75–86

Cutsuridis V, Cobb S, Graham BP (2010) Encoding and retrieval in the hippocampal CA1 microcircuit model. *Hippocampus* 20(3):423–446

Debanne D, Gahwiler BH, Thompson SM (1998) Long-term synaptic plasticity between pairs of individual CA3 pyramidal cells in rat hippocampal slice cultures. *J Physiol* 507:237–247

Froemke RC, Poo MM, Dan Y (2005) Spike-timing-dependent synaptic plasticity depends on dendritic location. *Nature* 434(7030):221–225

Galey D, Destrade C, Jaffard R (1994) Relationships between septo-hippocampal cholinergic activation and the improvement of long-term retention produced by medial septal electrical stimulation in two inbred strains of mice. Behav Brain Res 60:183–189

Harvey CD, Svoboda K (2007) Locally dynamic synaptic learning rules in pyramidal neuron dendrites. *Nature* 450(7173):1195–1200

Hayashi H, Igarashi J (2009) LTD windows of the STDP learning rule and synaptic connections having a large transmission delay enable robust sequence learning amid background noise. *Cogn Neurodyn* 3:119–130

Kroker KS, Rast G, Rosenbrock H (2011) Differential effects of subtype-specific nicotinic acetylcholine receptor agonists on early and late hippocampal LTP. Eur J Pharmacol 671(1–3):26–32

Letzkus JJ, Kampa BM, Stuart GJ (2006) Learning rules for spike timing-dependent plasticity depend on dendritic synapse location. *J Neurosci* 26(41):10,420–10,429

Magee JC, Johnston D (1997) A synaptically controlled, associative signal for hebbian plasticity in hippocampal neurons. *Science* 275:209–213

Markevich V, Scorsa AM, Dawe GS, Stephenson JD (1997) Cholinergic facilitation and inhibition of long-term potentiation of CA1 in the urethane-anaesthetized rats. Brain Res 754:95–102

Markram H, Luebke J, Frotscher M, Sakmann B (1997) Regulation of synaptic efficacy by coincidence of postsynaptic APs and EPSPs. *Science* 275:213–215

Nishiyama M, Hong K, Mikoshiba K, Poo MM, Kato K (2000) Calcium stores regulate the polarity and input specificity of synaptic modification. *Nature* 408:584–588

Ovsepian SV, Anwyl R, Rowan MJ (2004) Endogenous acetylcholine lowers the threshold for long-term potentiation induction in the CA1 area through muscarinic receptor activation: in vivo study. Eur J Neurosci 20:1267–1275

Rubin JE, Gerkin RC, Bi GQ, Chow CC (2005) Calcium time course as a signal for spike-timing-dependent plasticity. *J Neurophysiol* 93:2600–2613

Seol GH, Ziburkus J, Huang SY, Song L, Kim IT, Takamiya K, Huganir RL, Lee HK, Kirkwood A (2007) Neuromodulators control the polarity of spike-timing-dependent synaptic plasticity. *Neuron* 55(6):919–929

Shinoe T, Matsui M, Taketo MM, Manabe T (2005) Modulation of synaptic plasticity by physiological activation of M1 muscarinic acetylcholine receptors in the mouse hippocampus. J Neurosci 25:11194–11200

Sjostrom PJ, Turrigiano GG, Nelson SB (2001) Rate, timing, and cooperativity jointly determine cortical synaptic plasticity. *Neuron* 32:1149–1164

Sugisaki E, Fukushima Y, Tsukada M, Aihara T (2011) Cholinergic modulation on spike timing-dependent plasticity in hippocampal CA1 network. Neuroscience 192:91–101

Tsukada M, Aihara T, Kobayashi Y, Shimazaki H (2005) Spatial analysis of spike-timing-dependent LTP and LTD in the CA1 area of hippocampal slices using optical imaging. *Hippocampus* 15:104–109

Tzounopoulos T, Kim Y, Oertel D, Trussell LO (2004) Cell-specific, spike timing-dependent plasticities in the dorsal cochlear nucleus. *Nat Neurosci* 7(7):719–725

Yao H, Dan Y (2001) Stimulus timing-dependent plasticity in cortical processing of orientation. *Neuron* 32:315–323

Zhang LI, Tao HW, Holt CE, Harris WA, Poo M (1998) A critical window for cooperation and competition among developing retinotectal synapses. *Nature* 395:37–44

Factors Affecting STDP in the Dendrites of CA1 Pyramidal Cells

Ausra Saudargiene and Bruce P. Graham

Abstract Synaptic spike-time-dependent plasticity (STDP) is a function of the membrane depolarisation at the synapse, which is determined not only by somatic spiking activity in the postsynaptic cell but also by the synaptic site in the dendrites (distance from the cell body) and other local synaptic activities, particularly at inhibitory synapses. These factors can result in spatio-temporal gradients of STDP in a single neuron. In a pair of modelling studies (Saudargiene A, Graham BP, Biosystems 130:37–50, 2015; Saudargiene A, et al., Hippocampus 25(2):208–218, 2015), we have examined these effects for inputs onto synaptic spines at different locations in the complex apical dendrites of a CA1 pyramidal cell. The first study (Saudargiene A, Graham BP, Biosystems 130:37–50, 2015) examines the temporal signal requirements for inducing long-term potentiation (LTP) or long-term depression (LTD) at a synapse on a spine located at different locations in the dendrites. It is also determined how dendritic inhibition can alter these signalling requirements. The second study (Saudargiene A, et al., Hippocampus 25(2):208–218, 2015) moves on to explore more physiological situations involving theta and gamma rhythms in the hippocampus.

Overview

In simple terms, synaptic plasticity is a function of coincident presynaptic and postsynaptic activity. A now vast volume of experimental and modelling work has been aimed at discovering the plasticity 'rules' that determine the likely change in synaptic strength for different patterns of pre- and postsynaptic activity. One family

A. Saudargiene
Laboratory of Biophysics and Bioinformatics, Neuroscience Institute, Lithuanian University of Health Sciences, Kaunas, Lithuania
e-mail: ausra.saudargiene@lsmuni.lt

B. P. Graham (✉)
Division of Computing Science & Mathematics, University of Stirling, Stirling, UK
e-mail: b.graham@cs.stir.ac.uk

V. Cutsuridis et al. (eds.), *Hippocampal Microcircuits*, Springer Series in Computational Neuroscience, https://doi.org/10.1007/978-3-319-99103-0_19

of such rules is written in terms of the relative timing of pre- and postsynaptic spikes and is known as spike-time-dependent plasticity (STDP; see Graupner and Brunel, this volume). Many factors can contribute to the same spiking patterns yielding different STDP rules at different synaptic pathways (Buchanan and Mellor 2010). A key factor is the depolarisation state of the postsynaptic neuron at the synaptic site, which strongly influences calcium influx at the synapse and consequently the plasticity outcome (Graham et al. 2014; Hardie and Spruston 2009; Sjöström et al. 2008). In addition to somatic spiking activity in the postsynaptic cell, the depolarisation state at the synapse is affected by the synaptic site in the dendrites (distance from the cell body) and other local synaptic activities, particularly at inhibitory synapses (Bar-Ilan et al. 2013). Neuromodulatory signals may also influence transmitter release at synapses and the local postsynaptic membrane excitability (Hasselmo et al. 2002b). These factors can result in spatio-temporal gradients of STDP in a single neuron. In a pair of modelling studies (Saudargiene and Graham 2015; Saudargiene et al. 2015), we have examined these effects for inputs onto synaptic spines at different locations in the complex apical dendrites of a CA1 pyramidal cell.

The first study (Saudargiene and Graham 2015) examines the temporal signal requirements for inducing long-term potentiation (LTP) or long-term depression (LTD) at a synapse on a spine located at different locations in the dendrites. It is also determined how dendritic inhibition can alter these signalling requirements. The classic form of STDP is that a postsynaptic spike occurring in a short time window (a few tens of milliseconds) after a presynaptic spike can contribute to LTP at that synapse, whereas if the postsynaptic spike occurs a short time before the presynaptic spike, then LTD may result (Markram et al. 1997; Bi and Poo 1998, 2001). The actual plasticity outcome for a synapse depends on the frequency of pre- and postsynaptic spike pairing, the duration of such pairing and spike bursting in the postsynaptic cell (Mizuno et al. 2001; Nishiyama et al. 2000; Wittenberg and Wang 2006; Buchanan and Mellor 2010). The location of the synapse on the dendritic tree also determines the plasticity outcome (Golding et al. 2002; Froemke et al. 2005, 2010; Letzkus et al. 2006; Sjöström and Häusser 2006; Sjöström et al. 2008). In dendritic regions close to the soma, somatic back-propagating action potentials provide the strong postsynaptic depolarisation necessary for induction of synaptic modifications (Bi and Poo 2001; Wittenberg and Wang 2006). In more distal dendrites, local dendritic regenerative spikes might drive synaptic modifications (Magee and Johnston 1997; Golding et al. 2002; Froemke et al. 2005; Remy and Spruston 2007) even in the absence of somatic spiking.

Thus, synapses undergo changes according to local rather than global synaptic plasticity rules (Letzkus et al. 2006; Sjöström and Häusser 2006). Further, even at a particular dendritic location, the plasticity rule can be altered dynamically by local synaptic input, particularly inhibition, and neuromodulatory inputs. Specific patterns of inhibition are rarely controlled in experiments, with inhibition either blocked or allowed to be the result of unmeasured activity in local circuit interneurons. Nonetheless, it has been shown that inhibition can contribute to the emergence of a causal LTD window for a postsynaptic spike following a moderate time after a

presynaptic spike (Tsukada et al. 2005). Most knowledge of the potential influence of inhibition on plasticity comes from computational modelling studies (Bar-Ilan et al. 2013; Cutsuridis 2011, 2012), such as the ones presented in this chapter.

The first study concentrates on experimentally used stimulation protocols. The second study (Saudargiene et al. 2015) moves on to explore more physiological situations involving theta and gamma rhythms in the hippocampus. In a series of experimental and modelling studies, Hasselmo and colleagues (Hasselmo et al. 2002a, b; Hyman et al. 2003; Judge and Hasselmo 2004; Manns et al. 2007; Molyneaux and Hasselmo 2002; Wyble et al. 2000; Zilli and Hasselmo 2006) have shown that plasticity of Schaffer collateral synapses from hippocampal CA3 PCs onto CA1 PCs waxes and wanes between a propensity for LTP and a propensity for LTD on different phases of the CA1 theta rhythm and that this can correspond to a temporal distinction between memory encoding and retrieval. It is known that inhibition onto CA1 PCs also varies across a theta cycle, with perisomatic and apical dendritic inhibition being strongest on opposite phases of theta (Klausberger et al. 2003, 2004). Using a detailed spiking neuron model of the CA1 microcircuit, it has been demonstrated that this rhythmic variation in inhibition can determine memory encoding and retrieval during theta (Cutsuridis et al. 2010). The study presented here incorporates a more detailed PC model (Poirazi et al. 2003) and a spine head calcium-based plasticity model (Graupner and Brunel 2012) into this microcircuit to take these findings further towards biophysical realism.

The Model

Model Details

A detailed multicompartmental model of a CA1 pyramidal cell (Poirazi et al. 2003) was embedded in a model of the CA1 pyramidal neuron microcircuit (Cutsuridis et al. 2010) containing major input pathways from entorhinal cortex (EC) and Schaffer collaterals and spatially specific inhibition from oriens lacunosum-moleculare (OLM) and bistratified (BS), basket (B) and axo-axonic (AA) inhibitory interneurons (Fig. 1).

CA1 Microcircuit

CA3 Schaffer collateral synaptic inputs and EC inputs activate AMPA synapses, formed on the stratum radiatum (SR) and stratum lacunosum-moleculare (SLM) dendrites of the CA1 pyramidal neuron, respectively. Bistratified interneurons inhibit the SR dendrites, and OLM cells provide inhibition to SLM dendrites via GABAA and GABAB synapses. Basket cell-driven GABAA synapses inhibit the soma of the CA1 pyramidal cell. Axo-axonic cells drive GABAA synapses on

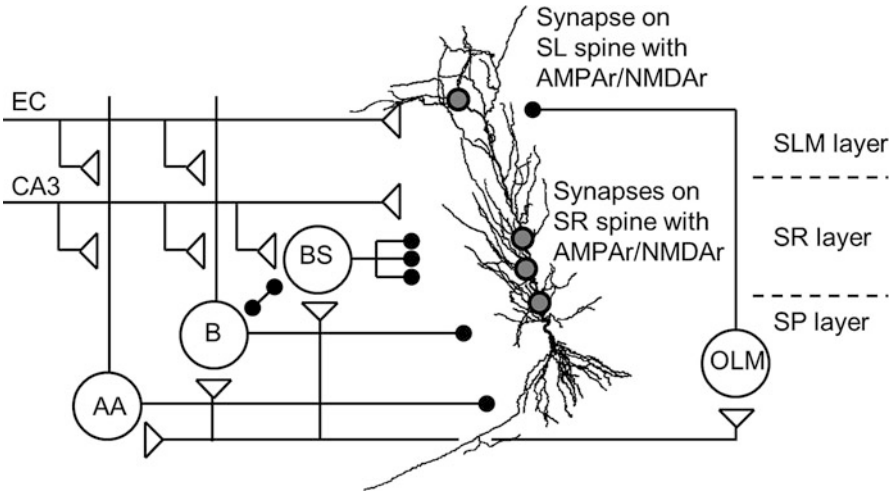

Fig. 1 CA1 microcircuit. Compartmental model of a CA1 pyramidal neuron (Poirazi et al. 2003) with the added AMPA/NMDA synapses on SLM spine and SR spines is embedded in a microcircuit consisting of oriens lacunosum-moleculare (OLM) and bistratified (BS), basket (B) and axo-axonic (AA) inhibitory interneurons (Cutsuridis et al. 2010). Synaptic inputs come from entorhinal cortex (EC) and CA3 region. CA1 stratum lacunosum-moleculare (SLM), stratum radiatum (SR) and stratum pyramidale (SP) layers are shown schematically (Redrawn with permission from Saudargiene et al. (2015), Fig. 1. Copyright Wiley)

the axon of the CA1 pyramidal neuron. Bistratified, basket and axo-axonic cells are activated by the CA3 Schaffer collateral synaptic inputs and somatic action potentials of the CA1 pyramidal neuron. Basket and axo-axonic cells receive also EC inputs. Basket and bistratified cells inhibit each other. OLM cells receive excitatory input from the CA1 pyramidal neuron. The full details of the microcircuit model, including details of the interneuron models, are given in Cutsuridis et al. (2010).

Pyramidal Cell Model

CA1 pyramidal cell model (Poirazi et al. 2003) consists of 183 compartments and includes a leak current, somatic/axonic and dendritic Hodgkin-Huxley-type sodium and potassium currents, proximal and distal A-type potassium currents, m-type potassium current, a mixed conductance hyperpolarisation-activated h-current, LVA T-type calcium current, somatic and dendritic HVA R-type currents, somatic and dendritic HVA L-type currents, two types of Ca^{2+}-dependent potassium currents (a slow AHP current and a medium AHP current) and a persistent sodium current.

Full details of the pyramidal neuron model are given in Poirazi et al. (2003). Spines were added at specific locations to create the postsynaptic compartments for excitatory synapses subject to plasticity (Fig. 1).

Synaptic Plasticity

Synaptic plasticity is examined in proximal, medial and distal spines, formed on the apical SR dendrites and in the spine on the SLM apical dendrite of the CA1 pyramidal cell. The spines have AMPA and NMDA receptor-gated channels. Spine head diameter and length equal 0.5 μm, and spine neck diameter is 0.2 μm and length 1 μm. Spines contain the same ion channels as their parent dendrites. However, calcium109 channels were not inserted in the SLM spine as there is a lack of knowledge of the calcium levels observed in spines on distal apical dendrites during dendritic spike induction. Details of synaptic dynamics and calcium transients are given in the Appendix.

The two studies used different calcium-driven models of synaptic plasticity. The first study used a biophysically detailed model of the plasticity signalling pathways. This was replaced by a simple phenomenological model (Graupner and Brunel 2012) in the second study to make the simulations computationally feasible. Details of these models are given in the Appendix.

Study 1

The first study (Saudargiene and Graham 2015) sought to replicate hippocampal slice experiments (Wittenberg and Wang 2006) by applying the experimental pre- and postsynaptic stimulation protocols to the CA1 pyramidal cell and examining the plasticity outcome for a synapse on a spine head at different locations in the apical dendrites.

Synaptic Plasticity Model

A biophysically realistic, calcium-driven plasticity model was used to generate STDP curves.

The model of synaptic plasticity is based on molecular pathways of LTP and LTD induction, involving activation of Ca^{2+}/calmodulin-dependent protein kinase II (CaMKII) (Graupner and Brunel 2007) and protein phosphatase 2 (PP2A) (Pi and Lisman 2008), and the interaction of CaMKII and PP2A that leads to the AMPA receptor phosphorylation or dephosphorylation (Fig. 2) underlying LTP and LTD (Lisman et al. 1997). These pathways are driven by the intracellular calcium signal in spines of the CA1 pyramidal neuron model.

CaMKII is responsible for LTP induction: calcium binds to calmodulin and so activates CaMKII, resulting in AMPAr phosphorylation and synaptic strengthening. As CaMKII activity becomes high, the autophosphorylation process enables CaMKII to retain activity even in the absence of calcium-bound calmodulin. Protein phosphatase inhibitor-1 (I1) and type 1 protein phosphatase (PP1) chains control the rate of dephosphorylation of phosphorylated CaMKII subunits and enable a synapse

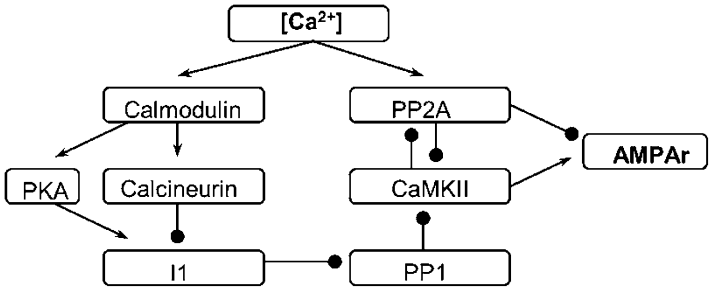

Fig. 2 Protein signalling cascades governing AMPAr changes (⟶ denotes activation; ⟶● denotes inhibition). (Reproduced with permission from Saudargiene and Graham (2015), Fig. 2. Copyright Elsevier)

to act like a binary switch. CaMKII dynamics is described by a complex bistable model consisting of a large set of differential equations (Graupner and Brunel 2007).

In the LTD induction pathway, phosphatase PP2A is dephosphorylated by calcium and being in its active form inhibits CaMKII, dephosphorylates AMPAr and leads to LTD. PP2A is bistable, and a high level of active PP2A triggers autodephosphorylation of PP2A and allows PP2A to stay activated for resting calcium concentrations. PP2A activity is described by a single differential equation (Pi and Lisman 2008). In addition, CaMKII and PP2A mutually inhibit each other. If CaMKII wins over PP2A, AMPAr is potentiated, and it is depressed if PP2A activity overwhelms CaMKII.

Stimulation Protocols

Calcium transients are obtained by two different stimulation protocols (Fig. 3) applied to induce synaptic modifications at SR and SLM synapses:

1. A presynaptic action potential at the SR spines close to the soma is paired with a burst-like doublet of somatic action potentials or a single action potential, following the experimental protocol of Wittenberg and Wang (2006); postsynaptic action potentials in doublets are spaced 10 ms apart.
2. A presynaptic action potential at a distal SLM spine is paired with a dendritic spike, as in Golding et al. (2002).

The temporal difference T between the presynaptic action potential and the first (or second for a doublet) postsynaptic action potential is varied from −100 ms up to 100 ms. Causal presynaptic-postsynaptic pairings correspond to positive T, and negative T denotes anti-causal postsynaptic-presynaptic pairings. Somatic action potentials and dendritic spikes are induced by postsynaptic depolarisation generated by two somatic and one dendritic artificial excitatory synapses, respectively, modelled with double exponential functions (Eq. 1).

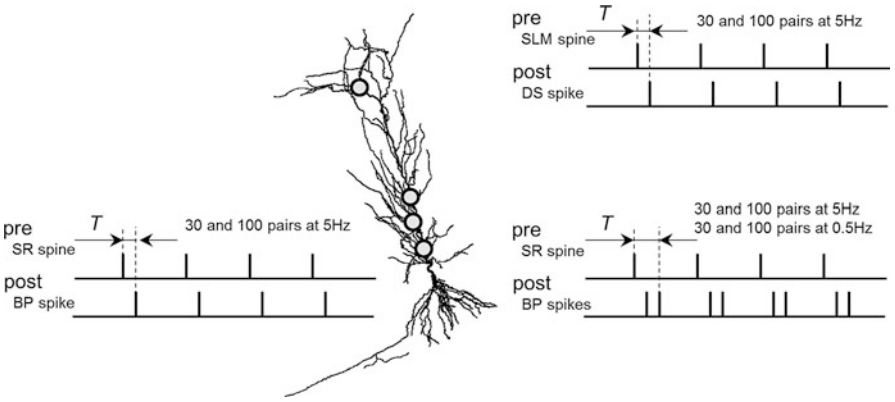

Fig. 3 Stimulation protocol of the CA1 pyramidal neuron used to analyse the influence of dendritic synapse location on plasticity. At the SR spines, a presynaptic action potential is paired with a burst-like doublet of back-propagating (BP) somatic action potentials or a single action potential; postsynaptic action potentials in doublets are spaced 10 ms apart. At a SLM spine, a presynaptic action potential is paired with a dendritic spike (DS). Stimulation protocols are presented 100 and 30 times at 5 Hz and 0.5 Hz. Temporal difference T between the presynaptic action potential and the postsynaptic action potential is varied from -100 ms up to 100 ms

Stimulation protocols are applied 30 and 100 times at 5 Hz and at 0.5 Hz, as per Wittenberg and Wang (2006).

To make the simulations computationally feasible, the pyramidal cell with synaptic inputs was simulated in NEURON, and a single epoch of pre-post stimulation was given, and the resultant spine head calcium transient was recorded. This was then fed in multiple times (to simulate a complete experiment) to a separate, computationally efficient implementation (in C++) of the plasticity model.

Results

Temporal Effects

If the presynaptic action potential precedes the second postsynaptic spike by $T = 10$ ms, the depolarisation provided by the back-propagating spikes in the proximal SR region (Fig. 4a, black solid line) together with the presynaptically released glutamate opens NMDAr-gated channels, and the calcium concentration in the SR spine reaches a high level of 3.8 μM (Fig. 4b, solid line). One hundred such causal pairings at 5 Hz result in CaMKII phosphorylation and PP2A inhibition and lead to AMPAr potentiation (Fig. 4c, solid line). If the temporal order of the pairings is reversed, the presynaptic action potential follows the second postsynaptic action potential. For $T = -10$ ms, the depolarisation provided by the back-propagating spikes in the SR region decreases by the time NMDAr is activated (Fig. 4a, dashed line); therefore the peak calcium concentration is low, approximately 1.2 μM

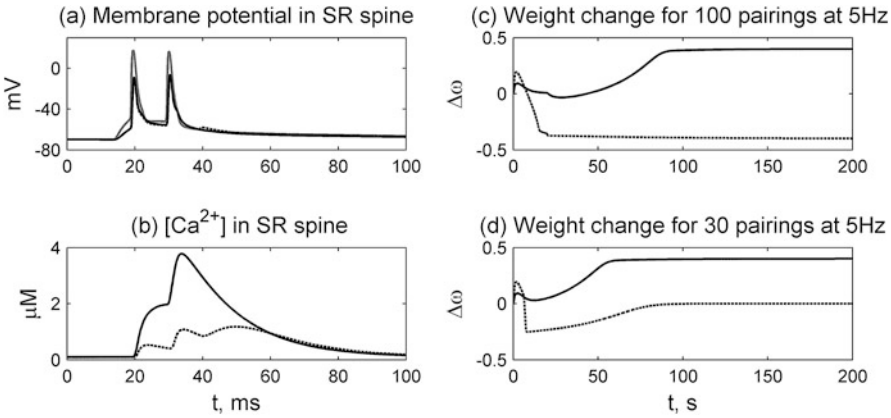

Fig. 4 (**a** and **b**) Membrane potential and calcium concentration in a proximal SR spine during a single pre-post pairing. (**a**) Membrane potential in spine (black solid line, $T = 10$ ms; black dashed line, $T = -10$ ms) and in soma (grey line). The postsynaptic action potentials are generated at 20 and 30 ms (two-spike burst, doublet; second postsynaptic action potential is used as a reference point for T definition). Presynaptic action potential is induced at 20 ms when $T = 10$ ms or at 40 ms when $T = -10$ ms. (**b**) Calcium concentration in spine (solid line, $T = 10$ ms; dashed line, $T = -10$ ms). (**c**, **d**) AMPAr weight changes in a proximal SR spine after 20 s of stimulation with 100 pairings (**c**) and 6 s of stimulation with 30 pairings (**d**) at 5 Hz of 1 presynaptic and 2 postsynaptic action potentials, followed by 180 s of presynaptic and postsynaptic inactivity of a CA1 pyramidal neuron (**c**) solid line, $T = 10$ ms; AMPAr is potentiated; dashed line, $T = -10$ ms; AMPAr is depressed after 100 pairings of stimulation; (**d**) solid line, $T = 10$ ms; AMPAr is potentiated; dashed line, $T = -10$ ms: AMPAr remains at a basal level after 30 pairings of stimulation). (Reproduced with permission from Saudargiene and Graham (2015), Figs. 3 and 4c,f. Copyright Elsevier)

(Fig. 4b, dashed line). This weak calcium signal is not sufficient to phosphorylate CaMKII but activates PP2A and leads to AMPAr depression (Fig. 4c, dashed line). LTP still occurs with only 30 causal pairings with $T = 10$ ms (Fig. 4d, solid line). However, 30 anti-causal pairings fail to induce LTD and leave the synapse unmodified (Fig. 4d, dashed line), as the calcium signal is not sufficient to activate PP2A.

Synaptic weight changes and peak calcium concentrations in the proximal SR spine for temporal difference T values [−100 ms, 100 ms] are presented in Fig. 5a, b. High peak calcium concentrations above 2.5 μM are observed for causal pairings at 5 Hz, specifically for the positive T window from 0 ms up to 20 ms (Fig. 5a), and result in AMPAr potentiation (Fig. 5b, black line). Lower calcium concentrations below 2.5 μM and above 1 μM lead to AMPAr depression: LTD is obtained for anti-causal pairings within the T interval [−50 ms,-10 ms] and for causal pairings within the T interval [30 ms, 50 ms]. AMPAr stays at its basal level if the peak calcium concentration is low. The sombrero-shaped curve of synaptic modifications, however, is obtained only if the stimulation consists of 100 pairings at 5 Hz. Thirty

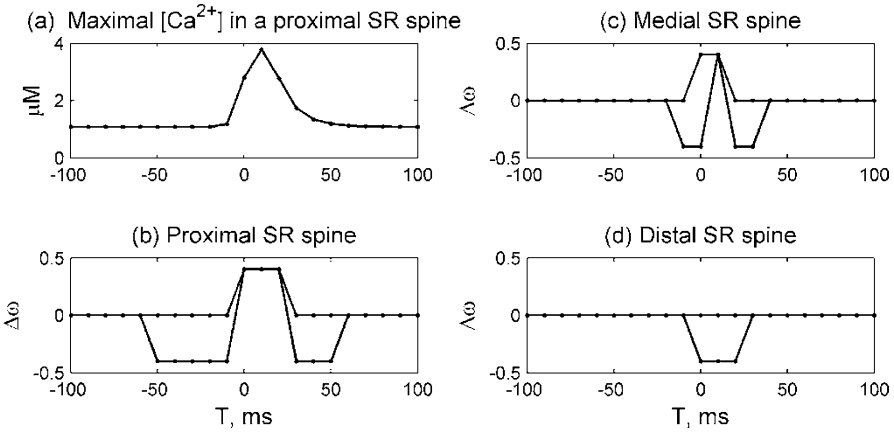

Fig. 5 (**a**) Peak calcium concentration in a proximal SR spine. (**b–d**) Synaptic weight change in the proximal, medial and distal SR synapses as a function of T, temporal difference between the presynaptic and a second postsynaptic action potential, after 100 pairings (black line) and 30 pairings (grey line) at 5 Hz, followed by 400 s of presynaptic and postsynaptic inactivity. Proximal SR spine is located 94 μm from the soma, medial SR spine is located 121 μm from the soma, and distal SR spine is located 157 μm from the soma (Reproduced with permission from Saudargiene and Graham (2015), Figs. 5a and 7a–c. Copyright Elsevier)

pairings at 5 Hz abolishes LTD and results in a potentiation-only plasticity rule (Fig. 5b, grey line).

In contrast, decreasing the frequency of stimulation to 0.5 Hz leads to a depression-only learning rule for both 30 and 100 pairings (not shown). Similarly, a single postsynaptic action potential, paired with a presynaptic action potential 100 times at 5 Hz, evokes depression, and 30 such pairings fail to induce synaptic changes as the calcium influx is reduced.

These simulation results show that the weight change curve is not a simple function of peak calcium but also depends on temporal factors such as the number of repetitions, pattern of postsynaptic activity and frequency of the pairing protocol.

Spatial Effects

The medial SR synapse, having the same synaptic strength as the proximal SR synapse, undergoes LTP for causal pairings and LTD for anti-causal and causal pairings within very narrow T intervals (Fig. 5c, black line). The decreased temporal width of the STDP curve is due to the fact that the back-propagating spike reaches the medial SR spine with a lower amplitude and results in reduced calcium influx both for anti-causal and causal pairings. Calcium levels at long, causal T are no longer sufficient to generate a causal LTD window. The distal SR spine receives even weaker depolarisation by the back-propagating spike; therefore calcium levels are not sufficient to induce synaptic changes for anti-causal pairings, and only LTD is observed within a limited T interval [0 ms, 20 ms] for 100 pairings (Fig. 5d, black line).

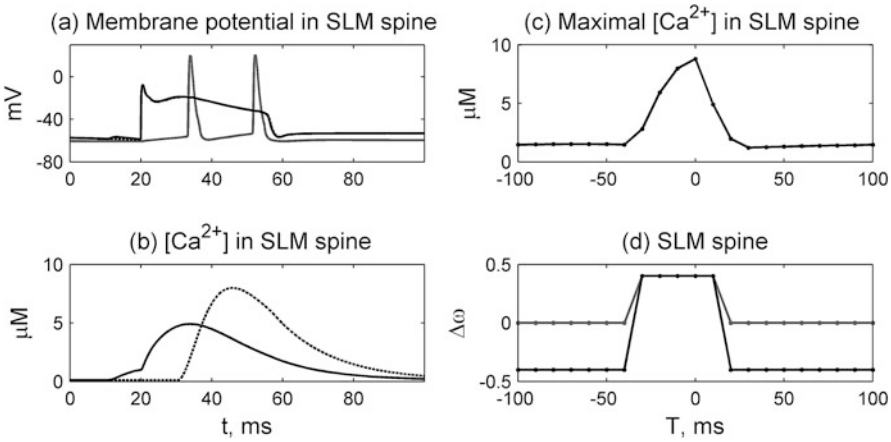

Fig. 6 (**a** and **b**) Membrane potential and calcium concentration in a SLM spine. (**a**) Membrane potential in spine (black solid line, $T = 10$ ms; black dashed line, $T = -10$ ms) and in soma (grey line). The presynaptic action potential is induced at 10 ms (black solid line, $T = 10$ ms) or at 30 ms (black dashed line, $T = -10$ ms), and the postsynaptic dendritic spike is induced at 20 ms by suprathreshold dendritic current injection. (**b**) Calcium concentration in spine (solid line, $T = 10$ ms; dashed line, $T = -10$ ms). (**c**, **d**)Synaptic modifications in a SLM spine evoked by pairing a presynaptic action potential with a dendritic spike at 5 Hz. (**c**) Peak calcium concentration in spine as a function of T. (**d**) Synaptic weight change as a function of T, temporal difference between the presynaptic action potential and the onset of dendritic spike, after 100 pairings (black line) and 30 pairings (grey line), followed by 400 s of presynaptic and postsynaptic inactivity. The postsynaptic dendritic spike is induced by suprathreshold dendritic current injection. (Reproduced with permission from Saudargiene and Graham (2015), Figs. 8 and 9. Copyright Elsevier)

Excitatory synapses in distal SLM dendrites of a CA1 pyramidal neuron are largely influenced by local dendritic regenerative action potentials but not much by somatic action potentials, as these fail to invade distal dendritic regions (Golding et al. 2002; Froemke et al. 2005; Letzkus et al. 2006). Changes at the synapse on a distal SLM spine thus are modelled by pairing a local dendritic spike as a source of postsynaptic depolarisation with the presynaptic action potential at varying temporal difference T values. The dendritic spike is induced by suprathreshold dendritic current injection. This spike consists of a sodium spike followed by a high-amplitude calcium spike (Fig. 6a) that provides depolarisation for NMDAr-gated channels even when anti-causal pairings are applied (Fig. 6b). Causal pairings at $T = 10$ ms induce high calcium influx and cause LTP (Fig. 6a, b, black solid lines; Fig. 6d, $T = 10$ ms). However, larger temporal difference T values in the interval [20 ms, 100 ms] lead to LTD as the postsynaptic sodium spike is not strong enough to effectively open NMDAr-gated channels and the subsequent calcium spike arrives too late, but moderate depolarisation at the postsynaptic site is provided by a dendritic spike of the preceding pre- and postsynaptic spike pair. Consequently, the synapse is weakened for 100 pairings and remains unmodified for 30 pairings at 5 Hz in the T interval [20 ms, 100 ms] (Fig. 6d, black and grey lines, respectively).

For anti-causal pairings and $T = -10$ ms, NMDAr-gated channels are strongly depolarised by the dendritic calcium spike, calcium levels rises to 7.8 μM (Fig. 6a, b, black dashed lines), and 100 and 30 such pairings at 5 Hz lead to LTP. Synaptic weight changes and peak calcium concentration in the SLM spine for temporal difference T values are shown in Fig. 6c, d. Peak calcium concentration is high for negative T and leads to LTP in a wide T interval [−30 ms, 10 ms] and to LTD in the T intervals [−100 ms, −40 ms] and [20 ms, 100 ms] for 100 pairings at 5 Hz. Decreasing the number of pairings to 30 abolishes LTD and results in a LTP-only synaptic plasticity rule.

These results show that synapses in distal SLM dendritic regions of the CA1 pyramidal neuron are potentiated if activated shortly before or during the induction of a long-lasting dendritic spike and depressed if triggered once the dendritic membrane potential has returned to the moderately depolarised level for anti-causal and causal pairings. The temporal order of the pre- and local postsynaptic events is neglected. Timing requirements for LTP are not as strict as for the plasticity rule of excitatory synapses in the SR proximal dendritic region which shows a sharp transition from LTD to LTP at 0 ms and has a narrow LTP window (Fig. 5b).

Effects of Inhibition

Pyramidal neurons in hippocampal CA1 regions are inhibited by spatially targeted perisomatic and dendritic inhibitory inputs (Klausberger et al. 2003; Cutsuridis et al. 2010). Specifically, basket interneurons provide perisomatic inhibition, while dendritic inhibition is induced by bistratified and OLM interneurons.

To reveal the influence of the perisomatic inhibition on the plasticity in SR synapses, the pyramidal neuron is inhibited by a basket cell. This interneuron is activated by somatic spiking of the pyramidal cell (PC) (Cutsuridis et al. 2010), inhibits the soma of the pyramidal neuron and prevents the generation of the second action potential in the two-spike burst. As a result of the reduced PC somatic spiking activity, the membrane potential at the SR synapse location and calcium concentration in the SR spine are considerably reduced for pre-post and post-pre pairing protocols.

The synapse is not modified if the presynaptic action potential arrives once the inhibition is already triggered for anti-causal pairings. The basket interneuron not only blocks a second postsynaptic action potential but effectively hyperpolarises the soma for the tens of milliseconds, prevents depolarisation of a proximal SR spine by a single back-propagating spike and thus reduces calcium influx through NMDAr-gated channels. The synapse is depressed if the presynaptic activation shortly precedes the somatic inhibition for 100 pairings (Fig. 7a, black line). However, 30 pairings do not induce synaptic modifications (Fig. 7a, grey line). Synaptic changes under the influence of a basket interneuron resemble the results obtained applying a single postsynaptic action potential, as only LTD is induced. Thus, perisomatic inhibition, mediated by basket interneurons, refines excitatory synaptic modifications by terminating somatic burst firing, limiting calcium influx into proximal spines, and leads to depression of the synapse if it is causally

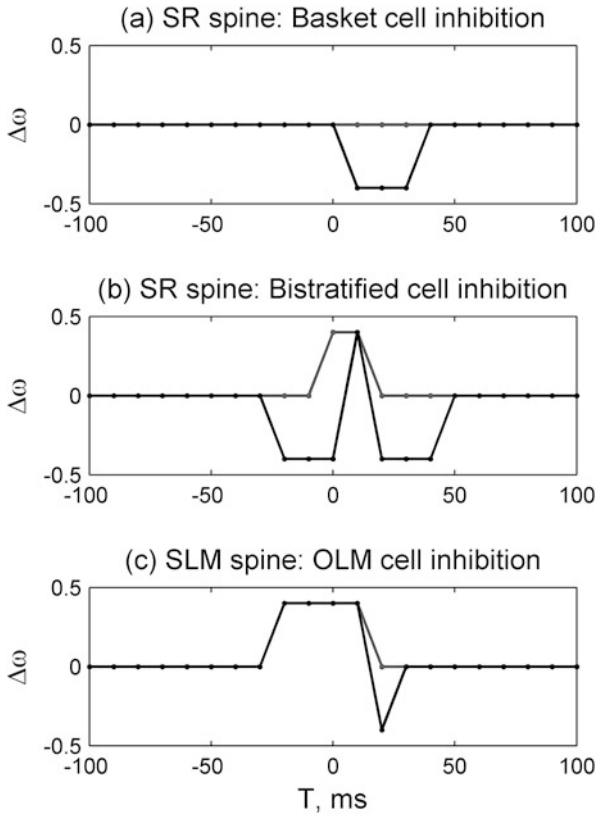

Fig. 7 Synaptic modifications in a proximal SR synapse evoked by pairing a presynaptic action potential with a doublet of postsynaptic action potentials at 5 Hz under the inhibitory effect of a basket cell and bistratified cell (**a** and **b**) and synaptic modifications in a SLM spine evoked by pairing a presynaptic action potential with a dendritic spike at 5 Hz under the inhibitory effect of an OLM cell (**c**). Proximal SR spine is located 94 μm from the soma; distal SLM spine is located 413 μm from the soma. (**a**) Synaptic weight change in the proximal SR spine as a function of T, temporal difference between the presynaptic action potential and a dummy second postsynaptic spike (not generated due to inhibition) after 100 pairings (black line) and 30 pairings (grey line) at 5 Hz, followed by 400 s of presynaptic and postsynaptic inactivity. Soma of the CA1 pyramidal neuron is inhibited by a basket cell that is activated by the first somatic action potential of the pyramidal neuron. (**b**) Synaptic weight change in the proximal SR spine; SR dendritic membrane potential of the CA1 pyramidal neuron is inhibited by a bistratified cell that is activated by the same CA3 input as the SR synapse. (**c**) Synaptic weight change in the SLM spine as a function of T, temporal difference between the presynaptic action potential and the onset of dendritic spike, after 100 pairings (black line) and 30 pairings (grey line). The postsynaptic dendritic spike is induced by suprathreshold dendritic current injection. SLM dendritic region of a pyramidal neuron is inhibited by an OLM cell triggered by the somatic action potentials of the pyramidal cell with approximately a 25 ms delay after the onset of the dendritic spike (Reproduced with permission from Saudargiene and Graham (2015), Figs. 11b, 13c, 15b. Copyright Elsevier)

activated within a narrow temporal window over many repetitions. Synapses remain unmodified for short stimulation protocols.

Inhibition of the SR dendrites is provided by bistratified interneurons receiving the same CA3 inputs that also stimulate excitatory synapses on SR dendrites (Cutsuridis et al. 2010). In this study, the bistratified neuron is triggered by the same presynaptic CA3 input that activates the SR synapse.

Dendritic inhibition impairs back-propagation of somatic action potentials and consequently the membrane potential at the proximal SR synapse, and the calcium concentration in the SR spine is reduced. Causal pairing with increasing T leads to LTD within the T interval [20 ms; 40 ms] (Fig. 7b, positive T). However, the membrane potential at the synapse and the calcium concentration are only slightly affected by inhibition for anti-causal pairings as the bistratified cell is activated too late to effectively inhibit the back-propagating action potentials. Thus the acausal LTD window with 100 pairings is retained but is narrower than with no inhibition (Fig. 7b, black solid line, negative T). In summary, the shape of the STDP curve remains symmetrical for 100 pairings, but the causal LTP window is narrowed, and the causal LTD side window is consequently left shifted towards smaller values of T, compared with no inhibition (Fig. 7b, black line; compare with Fig. 5b, black line). Short stimulation of 30 pairings abolishes LTD and leads to LTP in a temporal window [0; 20 ms] (Fig.7b, grey line).

The distal SLM dendrites are affected by inhibition that is triggered by OLM cells (Cutsuridis et al. 2010). In the model, OLM interneurons are activated by the CA1 pyramidal neuron somatic action potential induced by the SLM dendritic spike approximately 25 ms after its onset. Thus OLM inhibition reduces depolarisation at the synapse location, and calcium levels in the SLM spine with a 25 ms delay in respect to the postsynaptic activity (dendritic spike). Due to the delayed OLM cell activation, calcium concentration is slightly affected within the T interval [−20 ms; 20 ms], and it is decreased for the remaining T values. Synaptic depression is abolished for anti-causal pairings, and synaptic potentiation is observed within the T interval [−20 ms; 10 ms] for long (100 pairings) stimulation (Fig. 7c, black line). Short (30 pairings) stimulation leads to synaptic strengthening within the T interval [−20 ms; 10 ms], and no synaptic modification for the remaining T values (Fig. 7c, grey line), which is very similar to when no inhibition, is present (Fig. 6d, grey line). Thus, OLM inhibition removes LTD at acausal and long causal time intervals, without causing much effect on LTP at shorter acausal or any causal time intervals, when it is activated in response to a SLM dendritic spike.

Study 2

The second study explored the behavioural scenario of pattern storage during theta/gamma activity (Hasselmo et al. 2002a, b; Cutsuridis et al. 2010). In this case the pyramidal cell was driven by continuous theta/gamma-modulated excitatory activity (with accompanying temporally and spatially varying inhibition) for a large

number of theta cycles, with the synapse of interest being activated at different phases of theta in different modelling experiments.

Synaptic Plasticity Model

To be able to run relatively long simulations in NEURON, a simpler but still calcium-based model of synaptic plasticity (Graupner and Brunel 2012 and this volume) was used to determine the plasticity outcome (LTP or LTD) at the end of an experiment. Changes in synaptic weight are represented by the state transitions of the synaptic efficacy variable ρ and are driven by the intracellular calcium concentration in the spine. Synaptic efficacy variable ρ describes the competition of kinases and phosphatases in an abstract way and represents a model of the binary synapse: ρ can reside in two stable states, so-called DOWN and UP states. Transition from the DOWN state to the UP state is triggered by high intracellular calcium concentration levels and is considered as potentiation of the synapse. Transition from the UP state to the DOWN state is induced by low prolonged calcium signals and is regarded as depression of the synapse.

Synaptic plasticity is examined in a single spine of the CA1 pyramidal cell. This spine is formed on a medial SR apical dendrite and has AMPA and NMDA receptor-gated channels. AMPA synaptic conductance is 3nS if a synapse is activated on the retrieval phase and reduced to 1.2 nS, if it is activated on the encoding (storage) phase, this way capturing the suppression of the strength of Schaffer collateral synaptic transmission during a half-theta cycle (Hasselmo et al. 2002a). Initially, synaptic efficacy variable ρ is set to the DOWN or to the UP state, to represent either an initially unpotentiated or a potentiated synapse, respectively. Transitions from the DOWN to the UP or from the UP to the DOWN states are regarded as changes in synaptic weight.

Network Stimulation

Cell populations in CA3 and EC exhibit gamma frequency (around 40 Hz) activity, with average population activity waxing and waning at the slower theta frequency. EC III theta is largely out of phase with CA3 theta (Mizuseki et al. 2009). We model synaptic input during the theta retrieval phase as being strong CA3 input only, represented by 20 CA3 inputs on two successive gamma cycles. Input on the encoding theta phase consists of strong EC input on two successive gamma cycles in combination with weak CA3 inputs on the same gamma cycles (but delayed by 9 ms on average, modelling the direct versus trisynaptic loop delay (Leung et al. 1995). These ‘bursts’ of two reliable inputs represent the likely synaptic outcome of the theta burst protocol that is commonly required to induce LTP (Hyman et al. 2003). Cyclical changes during theta in the strength of synaptic input from the CA3 Schaffer collateral pathway (Wyble et al. 2000; Molyneaux and Hasselmo 2002) are

modelled as a reduction of the AMPA synaptic weight during the theta trough. Theta frequency is taken to be 4 Hz, and gamma frequency is 40 Hz.

Theta Retrieval/Encoding Phases

The combination of excitatory and inhibitory inputs results in the following scenario. The CA1 pyramidal neuron is driven by spatially focussed patterns of excitation and inhibition depending on the phase of theta. During the encoding phase, EC inputs arrive at the apical SLM dendrites, and CA3 inputs arrive at SR dendrites. EC inputs are strong enough to induce local dendritic spikes and cause somatic spiking, whereas CA3 inputs are weak in this phase. However, axo-axonic (AA) and and basket (B) interneurons receive activation from EC and CA3 inputs and inhibit the axon and soma of the pyramidal neuron preventing its spiking. During the retrieval phase, EC inputs are weak or absent, and CA3 inputs are strong to induce somatic spiking as AA and B cells are inactive. The apical dendrites are inhibited by bistratified (BS) and OLM cells in this phase.

In the simulations, theta-modulated inputs from CA3 and EC were applied in a consistent pattern for 16 theta cycles (4 s). During these cycles, the inputs to the CA3 synapse on the SR spine were applied either during the encoding or retrieval phase of theta, depending on the experiment being performed. The following simulation protocols of the pyramidal neuron were applied, based on the encoding/retrieval hypothesis (Hasselmo et al. 2002a; Cutsuridis et al. 2010):

1. Weak CA3 inputs and EC inputs in encoding phase and strong CA3 inputs in retrieval phase: Schaffer collateral synapse (on SR spine) is active in encoding phase. This is a full implementation of the hypothesised encoding phase.
2. Weak CA3 inputs and EC inputs in encoding phase and strong CA3 inputs in retrieval phase: Schaffer collateral synapse is active in retrieval phase. This is a full implementation of the hypothesised retrieval phase.

Results

Encoding Phase

The first simulation protocol is a full implementation of the hypothesised encoding phase of theta. Figure 8, left column, shows the raster plots of the CA3 and EC inputs, somatic membrane potentials, SR spine head calcium concentration and the induced transitions of the synaptic efficacy variable ρ in the spine for 16 theta cycles in this protocol. In the encoding phases (0–0.125 s, 0.250 s–0.375 s, 0.500 s–0.625 s, 0.750 s–0.875 s, 1.000–1.125 s, etc.), the Schaffer collateral pathway on the SR spine is active, and weak CA3 inputs (Fig. 8b, grey dots) are paired with the EC inputs (Fig. 8a) and induce dendritic spikes. However, perisomatic inhibition provided by AA and B interneurons prevents somatic spiking during this phase (Fig. 8c). Activation of NMDAr on the SR spine, paired with the strong postsynaptic

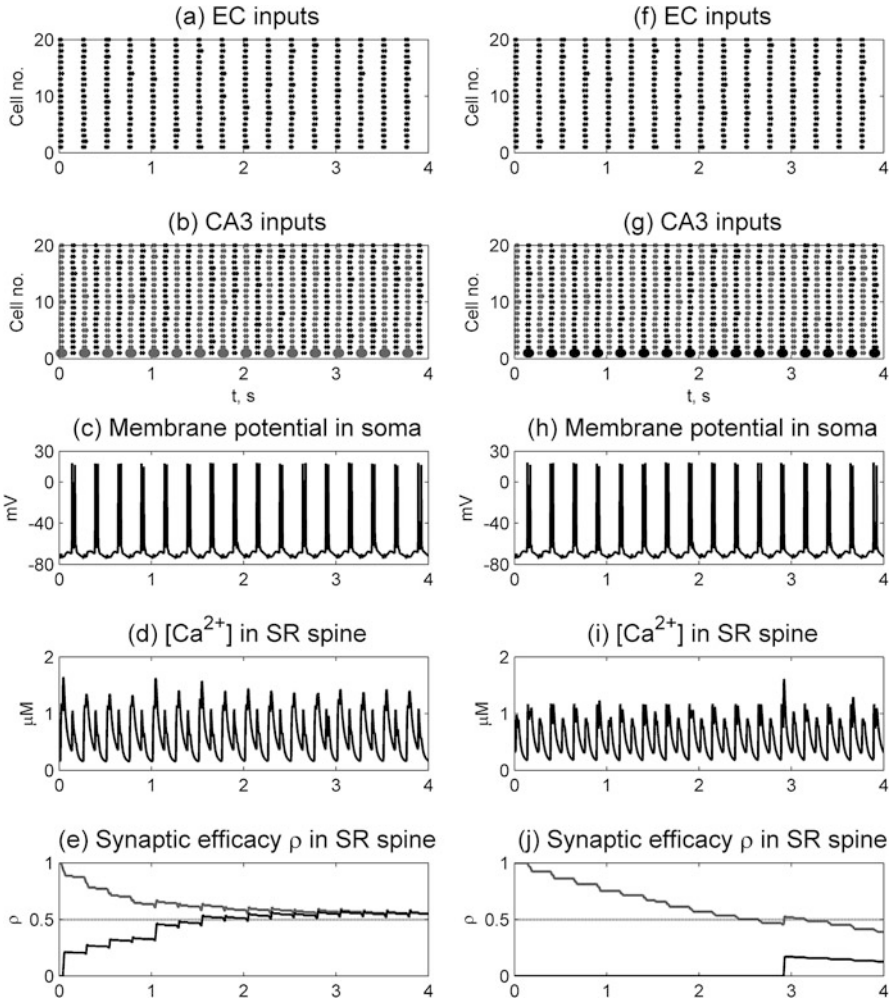

Fig. 8 Regional membrane potential and spine calcium concentration in CA1 PC for simulation protocols 1 (encoding, left column) and 2 (retrieval, right column). Medial SR spine is located 144 μm from the soma. (**a** and **f**) EC inputs are active on encoding phase. CA3 inputs are active in (**b**) encoding phase (weak, grey dots) and on (**g**) retrieval phase (strong, black dots). (**c** and **f**) Membrane potential in soma. (**d** and **i**) Calcium concentration in exemplar SR spine. (**e** and **j**) Synaptic efficacy ρ in SR spine (initially in DOWN state—black line; initially in UP state, grey line): (**e**) LTP is induced; (**j**) LTD is induced. (Reproduced with permission from Saudargiene et al. (2015), Figs. 2 and 3. Copyright Wiley)

depolarisation (dendritic spikes), produces high prolonged calcium transients during the encoding phases, rising up to 1.6 μM (Fig. 8d). In the retrieval phases (0.125 s–0.250 s, 0.375–0.500 s, 0.625 s–0.500 s, 0.875 s–1 s, 1.125–1.250 s, etc.), EC inputs are absent, but strong CA3 inputs (Fig. 8b, black dots) alone are sufficient to induce

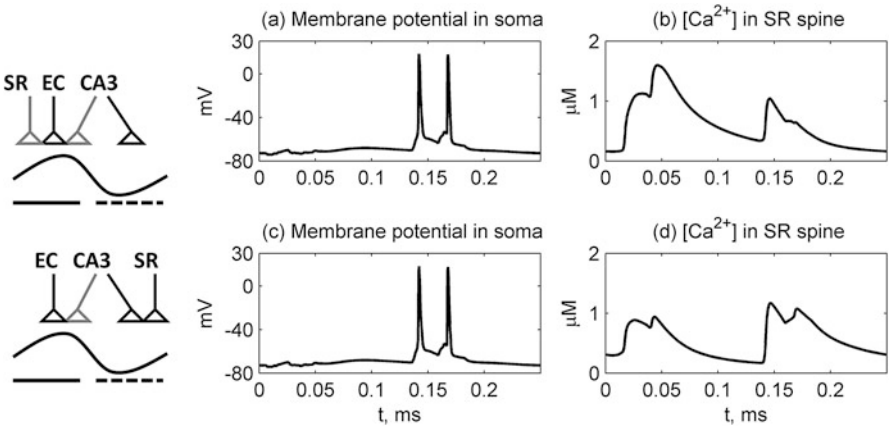

Fig. 9 Regional membrane potential and spine calcium concentration in CA1 PC from a single theta cycle for the two simulation protocols: top row is protocol 1; bottom row is protocol 2. Left-hand side, schematics of each protocol—triangles indicate which theta half-cycle the EC, CA3 and exemplar SR spine inputs are active, with first half-cycle being the encoding phase and second half-cycle is the retrieval phase (grey indicates weak input); solid horizontal line indicates the presence of perisomatic inhibition, and dashed horizontal line is dendritic inhibition. Columns: (**a**–**c**) membrane potential in soma, (**b**–**d**) calcium concentration in exemplar SR spine (Reproduced with permission from Saudargiene et al. (2015), Fig. 4, rows 1, 2. Copyright Wiley)

somatic spiking (Fig. 8c). However, calcium levels in the SR spine do not reach the heights of the encoding phases (Fig. 8d) as the SR dendritic region is inhibited by BS interneurons, and, in addition, spine NMDAr are almost closed as no additional spine inputs are assumed during this retrieval phase. This difference in calcium transients is more clearly seen in the details of a single theta cycle (0–0.250 s), shown in Fig. 9 (top row).

The high calcium transients in the SR spine during the encoding phase, induced by the combined CA3 and EC inputs, lead to a transition of the synaptic efficacy variable ρ from the DOWN state to the UP state (Fig. 8e, black line) and prevent its transition from the UP state to the DOWN state (Fig. 8e, grey line). So an unpotentiated synapse will undergo LTP induction, and an already potentiated synapse will remain so. Thus the PC's association with this CA3 input will be increased due to its co-occurrence with the EC inputs, as per the hypothesis.

Retrieval Phase

The second simulation protocol is a full implementation of the hypothesised retrieval phase, and the results are presented in Fig. 8, right column, and Fig. 9, bottom row. The Schaffer collateral pathway on the test SR spine is now active on the retrieval phase. In the encoding phase, weak CA3 inputs are again paired with the EC inputs (Fig. 8f, g, grey dots) and induce dendritic spikes. However, as there is no synaptic input to the spine on this phase, calcium currents are mediated by voltage-sensitive calcium channels (VSCC) alone, as the NMDAr are closed.

Therefore spine calcium levels remain low, approximately 0.9 μM (Fig. 8i). Somatic spiking is prevented by perisomatic inhibition (Fig. 8h).

In the retrieval phase, strong CA3 inputs (Fig. 8g, black dots) again cause somatic spiking (Fig. 8h). Although the SR spine is depolarised by the back-propagating spike and the synapse on this SR spine is activated (NMDAr are open), the resulting calcium concentration typically rises only slightly above 1.1 μM as the SR dendritic region is inhibited by bistratified interneurons and the EC inputs are silent. In addition, the SLM dendritic region is inhibited by OLM cells. For clarity, Fig. 9c, 9d shows membrane potential and calcium levels in the SR spine for one encoding-retrieval cycle (0–0.250 s).

The low-calcium concentrations seen by the SR spine during this protocol provoke the transition of the synaptic efficacy variable ρ from the UP state to the DOWN state (Fig. 8j, grey line), but are not sufficient to cause transition from the DOWN state to the UP state (Fig. 8j, black line), and thus LTD induction is promoted, particularly during the retrieval phase. Note that the spine head calcium does reach the LTP threshold (set at 1.3 μM) a couple of times (at around 3 s in this simulation), and so ρ starting in the DOWN state does increase, but does not get near the level required to trigger LTP. SR activity contributes to CA1 PC spiking and thus retrieval of previously encoded inputs but may be subject to depression if not reinforced during subsequent encoding phases, leading to reversal of prior learning (Hasselmo et al. 2002a).

Model Justification

Model Components

The model components are based on well-established and previously published models:

1. CA1 microcircuit architecture (Cutsuridis et al. 2010)
2. CA1 pyramidal cell model (Poirazi et al. 2003)
3. CA1 interneuron models (Cutsuridis et al. 2010)
4. Synaptic plasticity models (Graupner and Brunel 2007, 2012; Pi and Lisman 2008)

Rather than repeat all the details of the complex models here, the reader is referred to these papers and chapters in this volume (Graupner and Brunel) and also its first edition (Graham et al. 2010; Poirazi and Pissadaki 2010). Details of the plasticity models are given in the Appendix.

The motivation behind our modelling was to extend the CA1 microcircuit model of Cutsuridis et al. (2010) by (1) increasing the spatial complexity of dendritic synapse distributions by using a detailed compartmental model of a CA1 pyramidal cell based on a real cell's morphology and (2) using more biophysically realistic synaptic plasticity based on continuous spine head calcium concentrations.

Simulation Configurations

The intent of the work presented here was to increase the biophysical realism of models exploring synaptic plasticity outcomes at excitatory synapses on CA1 PC dendrites in response to experimentally used in vitro and behaviourally relevant in vivo stimulation patterns.

The first study was aimed at replicating the in vitro experiments of Wittenberg and Wang (2006) that demonstrated the importance of stimulus timing and repetition on plasticity outcomes. As a consequence, model parameters, in particular synaptic weights and spine head calcium transients, were tuned by hand to achieve the appropriate outcomes. This was readily achieved without going beyond the known physiological bounds of these quantities.

The second study looked at pattern storage and recall over theta cycles, with the aim of increasing the biophysical realism of the established model of Cutsuridis et al. (2010), which instantiated the hypothesis developed by Hasselmo and co-workers (2002a) in a network of spiking neurons. The main advance presented here is to study calcium-based plasticity in a spine head as a function of the timing of synaptic stimulation relative to ongoing theta-modulated activity in the CA1 circuit. As in the first study, hand tuning was sufficient to achieve a physiologically reasonable model that did indeed support the hypothesis of separate encoding and retrieval phases during theta activity.

The Future

As indicated above, in both studies, it was possible to hand-tune the models to replicate the experimental data and satisfy the theta storage/recall hypothesis. In addition, the first study makes predictions about the effects of synaptic location in the dendrites and spatially targeted inhibition on synaptic plasticity, as defined by STDP curves.

These results could be extended in a number of ways. Given sufficient computing resources and time, automated explorations of the parameter space could be carried out to explore the robustness of the derived STDP curves. This should include variations in synaptic position in a dendritic layer and strengths of inhibition. We predict that the results will be independent of within-layer synaptic location but may require tuning of spine head calcium transients as a function of position. Such tuning could be implemented by variations in spine head size and calcium buffering.

The theta activity simulated here corresponds to high levels of the neuromodulator acetylcholine in the network (Hasselmo et al. 2002b). This neuromodulation is not modelled explicitly, but its effects are implicit in the model parameters, including synaptic strengths and cellular membrane properties. It would be interesting to redefine the parameters to a low acetylcholine state to give greater insight into the contribution of such neuromodulation to the situations explored here.

Many details are still simplified in these models, including subcellular, cellular and network properties. Membrane properties of all cell types in the CA1 circuit are not fully known. Many known cell types are not included in the microcircuit model. Active properties of spine heads are particularly important here as they strongly determine the relationship between synaptic activity and plasticity. As such details become available from experimental data, the models can be refined and retested. A major advance would be a truly generalizable model of synaptic plasticity that gives insight into the 'learning rules' employed at different synaptic connections under physiological conditions. Experimentally, being able to visualise individual synaptic activity and measure changes in synaptic strength in awake, behaving animals is an ideal that still awaits realisation.

These modelling studies represent just one stage on a continuing journey towards understanding the neural basis of learning and memory in the brain. Increasingly complex, biophysically based models of cortical circuitry are being developed and can be simulated on supercomputers (e.g. Markram et al. 2015). However, simplified models are still required to enable simulations of behaviourally relevant time periods (seconds to minutes). An ideal is the development of closed-loop models of whole animal behaviour. For example, this CA1 microcircuit model could be at the centre of a model of a rat or mouse undertaking a spatial navigation or choice selection task. Current models have needed many further simplifications to achieve this, typically using rate-based models of neural activity rather than detailed spiking in individual neurons (Hasselmo et al. 2002b; Strösslin et al. 2005), but computing power and techniques are becoming sufficient to create more realistic models of cognitive behaviour based on the biophysics of neurons and their synaptic plasticity. Hybrid models involving combinations of rate-based population-level activity with the spiking of individual neurons and combinations of hardware-based (Furber and Temple 2007; Rast et al. 2011; Pfeil et al. 2013) and software-based simulation will allow this to be achieved.

Appendix

Detailed Biochemical Model of STDP

STDP model is described by the following set of equations. Parameter definitions and values are presented in Table A1.

Concentration of calcium-calmodulin complex (Graupner and Brunel 2007):

$$\mathrm{CaM} = \frac{\mathrm{CaM_{Tot}}}{1 + \frac{K_4}{[\mathrm{Ca}^{2+}]} + \frac{K_3K_4}{[\mathrm{Ca}^{2+}]^2} + \frac{K_2K_3K_4}{[\mathrm{Ca}^{2+}]^3} + \frac{K_1K_2K_3K_4}{[\mathrm{Ca}^{2+}]^4}}. \tag{A.1}$$

Table A.1 Parameters of the STDP model

Parameter	Value	Units	Definition and reference
CaMKII			
K_{PKA}	0.175	μM	PKA half activity concentration; defines the LTP threshold; adjusted
k_{PP2A}	0.14	s^{-1}	Rate of CaMKII subunit dephosphorylation by PP2A; adjusted
k_{PP1}	6000	s^{-1}	Maximal rate of CaMKII subunit dephosphorylation by PP1 (Graupner and Brunel 2007)
K_M	0.4	μM	Michaelis-Menten constant of CaMKII subunit dephosphorylation (Graupner and Brunel 2007)
K_1	0.1	μM	Dissociation constant to calcium binding to calmodulin (Graupner and Brunel 2007)
K_2	0.025	μM	Dissociation constant to calcium binding to calmodulin (Graupner and Brunel 2007)
K_3	0.32	μM	Dissociation constant to calcium binding to calmodulin (Graupner and Brunel 2007)
K_4	0.4	μM	Dissociation constant to calcium binding to calmodulin (Graupner and Brunel 2007)
K_5	0.1	μM	Dissociation constant between dephosphorylated CaMKII subunit and calmodulin (Graupner and Brunel 2007)
k_6	6	s^{-1}	Rate of CaMKII subunit autophosphorylation; calmodulin is bound to the two interacting and not phosphorylated CaMKII subunits (Graupner and Brunel 2007)
k_7	6	s^{-1}	Rate of CaMKII subunit autophosphorylation; calmodulin is bound to the phosphorylated CaMKII subunit and to the CaMKII subunit to be phosphorylated; or phosphorylated CaMKII subunit is calmodulin-free, and the CaMKII subunit to be phosphorylated is bound with calmodulin (Graupner and Brunel 2007)
k_{PP1}	500	$(s\ \mu M)^{-1}$	I1P, PP1 association rate (Graupner and Brunel 2007)
$k_{\_PP1}$	0.1	s^{-1}	I1P, PP1 dissociation rate (Graupner and Brunel 2007)
n_{CaN}	3	–	Calcineurin Hill coefficient (Graupner and Brunel 2007)
k^0_{CaN}	0.1	s^{-1}	Calcineurin base activity (Graupner and Brunel 2007)
k_{CaN}	18	s^{-1}	Maximum calcium-calmodulin-dependent calcineurin activity (Graupner and Brunel 2007)
K_{CaN}	0.053	μM	Calcineurin half-activation concentration (Graupner and Brunel 2007)
n_{PKA}	8	–	PKA Hill coefficient (Graupner and Brunel 2007)
k^0_{PKA}	0.00359	s^{-1}	PKA base activity (Graupner and Brunel 2007)
k_{PKA}	100	s^{-1}	Maximum calcium-calmodulin-dependent PKA activity (Graupner and Brunel 2007)
$PP1_{Tot}$	0.2	μM	Total PP1 concentration (Graupner and Brunel 2007)
$CaMKII_{Tot}$	33.3	μM	Total CaMKII concentration (Graupner and Brunel 2007)
CaM_{Tot}	0.1	μM	Total calmodulin concentration (Graupner and Brunel 2007)
$I1_{Tot}$	1	μM	Total I1 concentration (Graupner and Brunel 2007)

(continued)

Table A.1 (continued)

Parameter	Value	Units	Definition and reference
PP2A			
K_m	1.95	μM	Dissociation constant for calcium, defines the LTD threshold; adjusted
K_{m11}	15	μM	Michaelis-Menten constant for PP2A autodephosphorylation; adjusted
K_{m12}	1	μM	Michaelis-Menten constant for PP2A phosphorylation (Pi and Lisman 2008)
k_{11}	0.05	s^{-1}	Rate constant of PP2A autodephosphorylation; adjusted
k_{12}	0.0026	s^{-1}	Rate constant of PP2A phosphorylation by CaMKII, adjusted
k_{13}	0.025	s^{-1}	Rate constant of PP2A basal activity; adjusted
k_{14}	2	s^{-1}	Rate constant of calcium-dependent PP2A dephosphorylation; adjusted
$CaMKII_0$	71.4	μM	Basal concentration of phosphorylated CaMKII subunits; adjusted
$PP2A_0$	0.0425	μM	Basal concentration dephosphorylated PP2A; adjusted
$PP2A_{Tot}$	20	μM	Total concentration PP2A (Pi and Lisman 2008)
AMPAr			
c_1	0.054	–	Scaling constant; adjusted
c_2	0.520	–	Scaling constant; adjusted
c_3	1.014	s^{-1}	Rate constant independent from CaMKII activity; adjusted
c_4	1	s^{-1}	Rate constant independent from PP2A activity; adjusted
AMPA	1	–	Normalised total concentration of AMPAr (Pi and Lisman 2008)

Reproduced with permission from Saudargiene and Graham (2015), Table A1 Copyright Elsevier

PKA activity (Graupner and Brunel 2007):

$$v_{\mathrm{PKA}} = k^{\mathrm{o}}_{\mathrm{PKA}} + \frac{k_{\mathrm{PKA}}}{1 + \left(\frac{K_{\mathrm{PKA}}}{\mathrm{CaM}}\right)^{n_{\mathrm{PKA}}}}. \tag{A.2}$$

Calcineurin activity (Graupner and Brunel 2007):

$$v_{\mathrm{CaN}} = k^{\mathrm{o}}_{\mathrm{CaN}} + \frac{k_{\mathrm{CaN}}}{1 + \left(\frac{K_{\mathrm{CaN}}}{\mathrm{CaM}}\right)^{n_{\mathrm{CaN}}}}. \tag{A.3}$$

Concentration of active PP1 (Graupner and Brunel 2007):

$$\frac{\mathrm{d}}{\mathrm{d}t}\mathrm{PP1} = -k_{\mathrm{PP1}}\mathrm{I1P}\cdot\mathrm{PP1} + k_{\mathrm{PP1}}\left(\mathrm{PP1_{Tot}} - \mathrm{PP1}\right). \tag{A.4}$$

Concentration of active I1P (Graupner and Brunel 2007):

$$\frac{\mathrm{d}}{\mathrm{d}t}\mathrm{I1P} = -k_{\mathrm{PP1}}\mathrm{I1P}\cdot\mathrm{PP1} + k_{\mathrm{PP1}}\left(\mathrm{PP1_{Tot}} - \mathrm{PP1}\right) + v_{\mathrm{PKA}}\mathrm{I1P_{Tot}} - v_{\mathrm{CaN}}\mathrm{I1P}. \tag{A.5}$$

Probability that CaMKII subunit binds with calcium-calmodulin complex (Graupner and Brunel 2007):

$$\gamma = \frac{\mathrm{CaM}}{K_5 + \mathrm{CaM}}. \tag{A.6}$$

Rate of CaMKII subunit dephosphorylation (a modified equation from Graupner and Brunel (2007)):

$$k_D = \frac{k_{\mathrm{PP1}}\mathrm{PP1} + k_{\mathrm{PP2}A}\mathrm{PP2A}}{K_M + \mathrm{CaMKII}}. \tag{A.7}$$

Concentrations of CaMKII with different numbers of phosphorylated subunits (Graupner and Brunel 2007):

$$\frac{\mathrm{d}}{\mathrm{d}t}S_0 = -6k_6\gamma^2 S_0 + k_D S_1, \tag{A.8}$$

$$\frac{\mathrm{d}}{\mathrm{d}t}S_1 = 6k_6\gamma^2 S_0 - 4k_6\gamma^2 S_1 - k_7\gamma S_1 - k_D S_1 + 2k_D\left(S_2 + S_3 + S_4\right), \tag{A.9}$$

$$\frac{\mathrm{d}}{\mathrm{d}t}S_2 = k_6\gamma^2 S_1 + k_7\gamma S_1 - 3k_6\gamma^2 S_2 - k_7\gamma S_2 - 2k_D S_2 + k_D\left(2S_5 + S_6 + S_7\right), \tag{A.10}$$

$$\frac{\mathrm{d}}{\mathrm{d}t}S_3 = 2k_6\gamma^2 S_1 - 2k_6\gamma^2 S_3 - 2k_7\gamma S_3 - 2k_D S_3 + k_D\left(S_5 + S_6 + S_7 + 3S_8\right), \tag{A.11}$$

$$\frac{\mathrm{d}}{\mathrm{d}t}S_4 = k_6\gamma^2 S_1 - 2k_6\gamma^2 S_4 - 2k_7\gamma S_4 - 2k_D S_4 + k_D\left(S_6 + S_7\right), \tag{A.12}$$

$$\frac{\mathrm{d}}{\mathrm{d}t}S_5 = k_6\gamma^2 S_2 + k_7\gamma^2\left(S_2 + S_3\right) - 2k_6\gamma^2 S_5 - k_7\gamma S_5 - 3k_D S_5 + k_D\left(2S_9 + S_{10}\right), \tag{A.13}$$

$$\frac{\mathrm{d}}{\mathrm{d}t}S_6 = k_6\gamma^2\left(S_2 + S_3\right) + 2k_7\gamma S_4 - k_6\gamma^2 S_6 - 2k_7\gamma S_6 - 3k_D S_6 + k_D\left(S_9 + S_{10} + 2S_{11}\right), \tag{A.14}$$

$$\frac{\mathrm{d}}{\mathrm{d}t}S_7 = k_6\gamma^2\left(S_2 + S_4\right) + k_7\gamma S_3 - k_6\gamma^2 S_7 - 2k_7\gamma S_7 - 3k_D S_7 + k_D\left(S_9 + S_{10} + 2S_{11}\right), \tag{A.15}$$

$$\frac{\mathrm{d}}{\mathrm{d}t}S_8 = k_6\gamma^2 S_3 - 3k_7\gamma S_8 - 3k_D S_8 + k_D S_{10}, \tag{A.16}$$

$$\frac{\mathrm{d}}{\mathrm{d}t}S_9 = k_6\gamma^2 S_5 + k_7\gamma\,(S_5 + S_6 + S_7) - 2k_6\gamma^2 S_9 - 2k_7\gamma S_9 - 4k_D S_9 + 2k_D S_{12}, \tag{A.17}$$

$$\frac{\mathrm{d}}{\mathrm{d}t}S_{10} = k_6\gamma^2\,(S_5 + S_6) + k_7\gamma\,(S_7 + 3S_8) - 2k_7\gamma^2 S_{10} - 4k_D S_{10} + 2k_D S_{12}, \tag{A.18}$$

$$\frac{\mathrm{d}}{\mathrm{d}t}S_{11} = k_6\gamma^2 S_7 + k_7\gamma S_6 - 2k_7\gamma S_{11} - 4k_D S_{11} + 2k_D S_{12}, \tag{A.19}$$

$$\frac{\mathrm{d}}{\mathrm{d}t}S_{12} = k_6\gamma^2 S_9 + k_7\gamma\,(S_9 + 2S_{10} + 2S_{11}) - k_7\gamma S_{12} - 5k_D S_{12} + 6k_D S_{13}, \tag{A.20}$$

$$\frac{\mathrm{d}}{\mathrm{d}t}S_{13} = k_7\gamma S_{12} - 6k_D S_{13}. \tag{A.21}$$

Concentration of phosphorylated CaMKII subunits (Graupner and Brunel 2007):

$$\begin{aligned}\mathrm{CaMKII} = {} & S_1 + 2\,(S_2 + S_3 + S_4) + 5\,(S_5 + S_6 + S_7 + S_8) \\ & + 4\,(S_9 + S_{10} + S_{11}) + 5S_{12} + 6S_{13}.\end{aligned} \tag{A.22}$$

Concentration of dephosphorylated PP2A (a modified equation from Pi and Lisman (2008)):

$$\begin{aligned}\tfrac{\mathrm{d}}{\mathrm{d}t}\mathrm{PP2A} = {} & k_{11}\frac{\mathrm{PP2A_{Tot}} - \mathrm{PP2A}}{K_{m11} + \mathrm{PP2A}_{Tot} - \mathrm{PP2A}}\mathrm{PP2A} - \\ & - k_{12}\frac{\mathrm{PP2A}}{K_{m12} + \mathrm{PP2A}}\,(\mathrm{CaMKII} + \mathrm{CaMKII_0}) + \\ & + k_{13}\mathrm{PP2A_0} + k_{14}\frac{\left[\mathrm{Ca^{2+}}\right]^3}{K_m^3 + \left[\mathrm{Ca^{2+}}\right]^3}\,(\mathrm{PP2A_{Tot}} - \mathrm{PP2A})\,.\end{aligned} \tag{A.23}$$

Rate of AMPAr phosphorylation (Pi and Lisman 2008):

$$k_{\mathrm{AMPA}} = c_1\mathrm{CaMKII} + c_2. \tag{A.24}$$

Rate of AMPAr dephosphorylation (Pi and Lisman 2008):

Table A.2 Parameters of the STDP model

Parameter	Value	Units	Definition and reference
θ_d	1	μM	LTD threshold (adjusted)
θ_p	1.3	μM	LTP threshold (adjusted)
γ_d	300	–	Rate of decrease in ρ (adjusted)
γ_p	1600	–	Rate of increase in ρ (adjusted)
τ	100	s	Time constant of ρ changes (Graupner and Brunel 2012)
ρ_*	0.5	–	Unstable ρ state (Graupner and Brunel 2012)

Reproduced with permission from Saudargiene et al. (2015), Table A2. Copyright Wiley

$$k_{\mathrm{AMPA}} = c_3 \mathrm{PP2A} + c_4. \tag{A.25}$$

Concentration of active AMPAr (Pi and Lisman 2008):

$$\frac{\mathrm{d}}{\mathrm{d}t}\mathrm{AMPA} = k_{\mathrm{AMPA}}\left(\mathrm{AMPA}_{\mathrm{Tot}} - \mathrm{AMPA}\right) - k_{-\mathrm{AMPA}}\mathrm{AMPA}. \tag{A.26}$$

Phenomenological Model of STDP

Synaptic efficacy variable ρ is described by a first-order differential equation (Graupner and Brunel 2012):

$$\begin{aligned}\tau\frac{\mathrm{d}\rho}{\mathrm{d}t} = &-\rho\left(1-\rho\right)\left(\rho_* - \rho\right) + \gamma_p\left(1-\rho\right)\Theta\left[c(t) - \theta_p\right] \\ &- \gamma_d\rho\Theta\left[c(t) - \theta_d\right] + \mathrm{Noise}(t),\end{aligned} \tag{A.27}$$

where $c(t)$ is the instantaneous calcium concentration, Θ denotes the Heaviside function and all the remaining parameters and their values are presented in Table A2. Noise term Noise(t) is not implemented.

Synaptic Conductances

Study 1 (Detailed Biochemical Model of STDP Used)

AMPA, GABA-A and GABA-B synaptic conductances are modelled as a double exponential function:

$$g_{\mathrm{syn}} = \overline{g}_{\mathrm{syn}}\left(e^{-(t-t_{\mathrm{pre}})/\tau_{\mathrm{fall}}} - e^{-(t-t_{\mathrm{pre}})/\tau_{\mathrm{rise}}}\right), \tag{A.28}$$

where τ_{rise} is the rising time constant, τ_{fall} is the decay time constant, $\overline{g}_{\text{syn}}$ is a peak synaptic conductance and t_{pre} is the time of the synapse activation. Time constants, peak synaptic conductances and reversal potentials are presented in Tables A3 and A4.

Kinetic model of the NMDAr-gated channel is described by the activation and deactivation reactions for Mg-bound and Mg-free channel states (Vargas-Caballero and Robinson 2004; Erreger et al. 2005).

Mg-bound NMDAr channel states are given:

$$\frac{\mathrm{d}}{\mathrm{d}t} R_{\text{Mg}} = k_{\text{off}} R_{A\text{Mg}} - 2k_{\text{on}} R_{\text{Mg}}, \tag{A.29}$$

$$\frac{\mathrm{d}}{\mathrm{d}t} R_{A\text{Mg}} = 2k_{\text{on}} R_{\text{Mg}} + 2k_{\text{of}\,f} R_{A2\text{Mg}} - (k_{\text{on}} + k_{\text{off}})\, R_{A\text{Mg}}, \tag{A.30}$$

$$\begin{aligned} \tfrac{\mathrm{d}}{\mathrm{d}t} R_{A2\text{Mg}} = {} & k_{\text{on}} R_{A\text{Mg}} + k_{f\,\text{off}} R_{A2f\text{Mg}} + k_{s\,\text{off}} R_{A2s\text{Mg}} \\ & - \left(2k_{\text{off}} + k_{f\,\text{on}} + k_{s\,\text{on}}\right) R_{A2\text{Mg}}, \end{aligned} \tag{A.31}$$

$$\frac{\mathrm{d}}{\mathrm{d}t} R_{A2f\text{Mg}} = k_{f\,\text{on}} R_{A2\text{Mg}} + k_{s\,\text{off}} R_{O\text{Mg}} - \left(k_{f\,\text{off}} + k_{s\,\text{on}}\right) R_{A2f\text{Mg}}, \tag{A.32}$$

$$\frac{\mathrm{d}}{\mathrm{d}t} R_{A2s\text{Mg}} = k_{s\,\text{on}} R_{A2\text{Mg}} + k_{f\,\text{off}} R_{O\text{Mg}} - \left(k_{s\,\text{off}} + k_{f\,\text{on}}\right) R_{A2s\text{Mg}}, \tag{A.33}$$

$$\begin{aligned} \tfrac{\mathrm{d}}{\mathrm{d}t} R_{O\text{Mg}} = {} & k_{s\,\text{on}} R_{A2f\text{Mg}} + k_{f\,\text{on}} R_{A2s\text{Mg}} + k_{\text{Mg}\,\text{on}} R_O - \\ & \left(k_{s\,\text{off}} + k_{f\,\text{off}} + k_{\text{Mg}\,\text{off}}\right) R_{O\text{Mg}}. \end{aligned} \tag{A.34}$$

Mg-free NMDAr channel states are expressed:

$$\frac{\mathrm{d}}{\mathrm{d}t} R = k_{\text{off}} R_A - 2k_{\text{on}} R, \tag{A.35}$$

$$\frac{\mathrm{d}}{\mathrm{d}t} R_A = 2k_{\text{on}} R + 2k_{\text{off}} R_{A2} - (k_{\text{on}} + k_{\text{off}})\, R_A, \tag{A.36}$$

$$\frac{\mathrm{d}}{\mathrm{d}t} R_{A2} = k_{\text{on}} R_A + k_{f\,\text{off}} R_{A2f} + k_{s\,\text{off}} R_{A2s} - \left(2k_{\text{off}} + k_{f\,\text{on}} + k_{s\,\text{on}}\right) R_{A2}, \tag{A.37}$$

$$\frac{\mathrm{d}}{\mathrm{d}t} R_{A2f} = k_{f\,\text{on}} R_{A2} + k_{s\,\text{off}} R_O - \left(k_{f\,\text{off}} + k_{s\,\text{on}}\right) R_{A2f}, \tag{A.38}$$

$$\frac{\mathrm{d}}{\mathrm{d}t} R_{A2s} = k_{s\,\text{on}} R_{A2} + k_{f\,\text{off}} R_O - \left(k_{s\,\text{off}} + k_{f\,\text{on}}\right) R_{A2s}. \tag{A.39}$$

Conducting open state of the NMDAr is equal:

$$\frac{\mathrm{d}}{\mathrm{d}t} R_O = k_{s\,\mathrm{on}} R_{A2f} + k_{f\,\mathrm{on}} R_{A2s} + k_{\mathrm{Mgoff}} R_{O\,\mathrm{Mg}} - \left(k_{s\,\mathrm{off}} + k_{f\,\mathrm{off}} + k_{\mathrm{Mgon}}\right) R_O . \tag{A.40}$$

Calcium current through open NMDAr-gated channel is described:

$$I_{\mathrm{Ca}} = 0.06\, \overline{g}_{\mathrm{NMDA}} R_O \left(V - E_{\mathrm{Ca}}\right). \tag{A.41}$$

Parameter values and definitions are presented in Table A5.

Study 2 (Phenomenological Model of STDP Used)

AMPA, GABA-A and GABA-B synaptic conductances are modelled as in Eq. A.28.

The NMDAr-mediated synaptic response is expressed:

$$g_{\mathrm{syn}} = \overline{g}_{\mathrm{syn}} \frac{e^{-(t-t_{\mathrm{pre}})/\tau_{\mathrm{fall}}} - e^{-(t-t_{\mathrm{pre}})/\tau_{\mathrm{rise}}}}{1 + \mu \left[\mathrm{Mg}^{2+}\right] e^{-\gamma V}}, \tag{A.42}$$

where τ_{rise} is the rising time constant, τ_{fall} is the decay time constant, $\overline{g}_{\mathrm{syn}}$ is a peak synaptic conductance, t_{pre} is the time of the synapse activation and $[\mathrm{Mg}^{2+}] = 1$ mM is Mg concentration, $\mu = 0.33$/mM, $\gamma = 0.08$/mV.

Time constants, peak synaptic conductance and reversal potential of AMPA, GABA-A, GABA-B and NMDA synapse are given in Tables A6 and A7.

Calcium Concentration

Calcium concentration in a spine is modelled as (Badoual et al. 2006):

$$\frac{\mathrm{d}}{\mathrm{d}t}\left[Ca^{2+}\right] = -\frac{I_{\mathrm{Ca}}}{2Fd \times 18} + \frac{\left(\left[\mathrm{Ca}^{2+}\right]_{\infty} - \left[\mathrm{Ca}^{2+}\right]\right)}{\tau_{\mathrm{Ca}}}, \tag{A.43}$$

where $[\mathrm{Ca}^{2+}]$ is the calcium concentration in a spine, I_{Ca} is the calcium current, F is the Faraday constant, $d = 0.1$ μm is the depth of dendritic shell and $\tau_{\mathrm{Ca}} = 15$ ms is the time constant of calcium concentration decay (Badoual et al. 2006). Factor 18 reflects the influence of the endogenous buffers (Badoual et al. 2006).

Network Parameters

Study 1 (Detailed Biochemical Model of STDP)

Table A.3 Time constants, reversal potential and peak synaptic conductance of AMPA, GABA-A and GABA-B synapses and two somatic and one SLM dendritic excitatory synapses used to induce doublets of somatic action potentials and a dendritic spike in the CA1 pyramidal neuron model

Synapse	Rising time constant τ_{rise}, *ms*	Decay time constant τ_{fall}, *ms*	Reversal potential, *mV*
AMPA	0.5	3	0
GABA-A	1	8	−75
GABA-B	35	100	−75
Excitatory somatic slow	4	5	0
Excitatory somatic fast	0.2	2	0
Excitatory SLM dendritic	0.2	0.5	0

Reproduced with permission from Saudargiene and Graham (2015), Table A1. Copyright Elsevier

Table A.4 Peak synaptic conductances (nS for AMPA, GABA-A, GABA-B, nS/cm^2 for NMDA) (type of postsynaptic receptor is indicated in parentheses)

Presynaptic	Postsynaptic			
	CA1 pyramidal neuron PC	BC	BSC	OLM
EC	2.2 (AMPA)	–	–	–
	65 (NMDA)			
CA3	2.2 (AMPA)	–	5 (AMPA)	–
	13 (strong AMPA)			
	65 (NMDA)			
BC	500 (GABA-A)	–	–	–
BSC	10 (strong GABA-A)	–	–	–
	1 (strong GABA-B)			
	5 (weak GABA-A)			
	0.5 (weak GABA-B)			
OLM	50 (GABA-A)	–	–	–
	10 (GABA-B)			
CA1 pyramidal neuron PC	–	100 (AMPA)	–	10 (AMPA)
–	20 (excitatory somatic slow)	–	–	–
–	20 (excitatory somatic fast)	–	–	–
–	500 (excitatory SLM dendritic)	–	–	–

Reproduced with permission from Saudargiene and Graham (2015), Table A2. Copyright Elsevier

Table A.5 Parameters of NMDAr channel kinetic model

Parameter	Value	Units	Definition and reference
k_{on}	31.6 *Glu*	$(\text{s}\ \mu\text{M})^{-1}$	Rate, dependent on presynaptic glutamate concentration *Glu* (Erreger et al. 2005); glutamate concentration is modelled as a pulse of 1 mM amplitude and 1 ms duration
k_{off}	1010	s^{-1}	Rate constant (Erreger et al. 2005)
k_{f_on}	3140	s^{-1}	Rate constant (Erreger et al. 2005)
k_{f_off}	174	s^{-1}	Rate constant (Erreger et al. 2005)
k_{s_on0}	230	s^{-1}	Rate constant (Erreger et al. 2005)
k_{s_off}	178	s^{-1}	Rate constant (Erreger et al. 2005)
$k_{\text{Mg\_on}}$	$0.610\ e^{(-V/17)}$	$(\text{s}\ \mu\text{M})^{-1}$	Rate of Mg^{2+} binding, dependent on membrane potential V (Vargas-Caballero and Robinson 2004)
$k_{\text{Mg\_off}}$	$5400\ e^{(-V/47)}$	s^{-1}	Rate of Mg^{2+} unbinding, dependent on membrane potential V (Vargas-Caballero and Robinson 2004)
k_{s_on}	$k_{s\_\text{on0}} e^{(V+/47)}$	s^{-1}	Rate, dependent on membrane potential V
$\overline{g}_{\text{NMDA}}$	65	nS/cm^2	Peak NMDA synaptic conductance (adjusted)
E_{Ca}	140	mV	Ca^{2+} reversal potential

Study 2 (Phenomenological Model of STDP)

Table A.6 Time constants, reversal potential and peak synaptic conductance of NMDA, AMPA, GABA-A and GABA-B synapses

Synapse	Rising time constant τ_{rise}, *ms*	Decay time constant τ_{fall}, *ms*	Reversal potential, *mV*
NMDA	3	100	0
AMPA	0.5	3	0
GABA-A	1	8	−75
GABA-B	35	100	−75

Table A.7 Peak synaptic conductances (nS)

Presynaptic	Postsynaptic				
	CA1 pyramidal neuron	BSC	B	AA	OLM
CA3	Synapse on a SR spine				
	0.05 (NMDA)				
	1.2 (AMPA, encoding phase)				
	3 (AMPA, retrieval phase)				
CA3	40(AMPA, encoding phase)	1 (AMPA)	0.05 (AMPA)	0.02 (AMPA)	–
	100(AMPA, retrieval phase)				

(continued)

Table A.7 (continued)

Presynaptic	Postsynaptic				
EC	80 (AMPA)	–	2.5 (AMPA)	2.5 (AMPA)	–
BSC	4(GABA-A)	–	10 (GABA-A)	–	–
	0.1 (GABA-B)				
B	100 (GABA-A)	50 (GABA-A)	–	–	–
AA	40 (GABA-A)	–	–	–	–
OLM	20(GABA-A)	–	–	–	–
	20 (GABA-B)				
CA1 pyramidal neuron	–	0.5(AMPA)	0.5 (AMPA)	1(AMPA)	1 (AMPA)

Type of the postsynaptic receptor is indicated in parentheses (Reproduced with permission from Saudargiene et al. (2015), Table A1. Copyright Wiley)

References

Badoual M, Zou Q, Davison AP, Rudolph M, Bal T, Frégnac Y, Destexhe A (2006) Biophysical and phenomenological models of multiple spike interactions in spike-timing dependent plasticity. Int J Neural Syst 16(2):79–97

Bar-Ilan L, Gidon A, Segev I (2013) The role of dendritic inhibition in shaping the plasticity of excitatory synapses. Front Neural Circuits 6(118):1–13

Bi GQ, Poo MM (1998) Synaptic modifications in cultured Hippocampal neurons: dependence on spike timing, synaptic strength, and postsynaptic cell type. J Neurosci 18:10464–10472

Bi GQ, Poo MM (2001) Synaptic modification by correlated activity: Hebb's postulate revisited. Annu Rev Neurosci 24:139–166

Buchanan KA, Mellor JR (2010) The activity requirements for spike timing dependent plasticity in the hippocampus. Front Synaptic Neurosci 2(11):1–5

Cutsuridis V (2011) GABA inhibition modulates NMDA-R mediated spike timing dependent plasticity (STDP) in a biophysical model. Neural Netw 24(1):29–42

Cutsuridis V (2012) Bursts shape the NMDA-R mediated spike timing dependent plasticity curve: role of burst interspike interval and GABAergic inhibition. Cogn Neurodyn 6(5):421–441

Cutsuridis V, Cobb S, Graham BP (2010) Encoding and retrieval in a model of the hippocampal CA1 microcircuit. Hippocampus 20(3):423–446

Erreger K, Dravid SM, Banke TG, Wyllie DJ, Traynelis SF (2005) Subunit-specific gating controls rat NR1/NR2A and NR1/NR2B NMDA channel kinetics and synaptic signalling profiles. J Physiol 563(2):345–358

Froemke RC, Poo MM, Dan Y (2005) Spike-timing-dependent synaptic plasticity depends on dendritic location. Nature 434(7034):221–225

Froemke RC, Letzkus JJ, Kampa BM, Hang GB, Stuart GJ (2010) Dendritic synapse location and neocortical spike-timing dependent plasticity. Front Synaptic Neurosci 2(29):1–14

Furber S, Temple S (2007) Neural systems engineering. J R Soc Interface 4:193–206

Golding NL, Staff NP, Spruston N (2002) Dendritic spikes as a mechanism for cooperative long-term potentiation. Nature 418(6895):326–331

Graham BP, Cutsuridis V, Hunter R (2010) Associative memory models of hippocampal areas CA1 and CA3. In: Cutsuridis V et al (ed) Hippocampal microcircuits, Springer Series in Computational Neuroscience 5 (first edition)

Graham BP, Saudargiene A, Cobb S (2014) Spine head calcium as a measure of summed postsynaptic activity for driving synaptic plasticity. Neural Comput 26:2194–2222

Graupner M, Brunel N (2007) STDP in a bistable synapse model based on CaMKII and associated signaling pathways. PLoS Computat Biol 3(11):e221

Graupner M, Brunel N (2012) Calcium-based plasticity model explains sensitivity of synaptic changes to spike pattern, rate, and dendritic location. Proc Natl Acad Sci U S A 109:3991–3996

Hardie J, Spruston N (2009) Synaptic depolarization is more effective than back-propagating action potentials during induction of associative long-term potentiation in hippocampal pyramidal neurons. J Neurosci 29:3233–3241

Hasselmo M, Bodelon C, Wyble B (2002a) A proposed function of the hippocampal theta rhythm: separate phases of encoding and retrieval of prior learning. Neural Comput 14:793–817

Hasselmo ME, Hay J, Ilyn M, Gorchetchnikov A (2002b) Neuromodulation, theta rhythm and rat spatial navigation. Neural Netw 15:689–707

Hyman JM, Wyble BP, Goyal V, Rossi CA, Hasselmo ME (2003) Stimulation in hippocampal region CA1 in behaving rates yields long-term potentiation when delivered to the peak of theta and long-term depression when delivered to the trough. J Neurosci 23:11725–11731

Judge SJ, Hasselmo ME (2004) Theta rhythmic stimulation of stratum lacunosum-moleculare in rat hippocampus contributes to associative LTP at a phase offset in stratum radiatum. J Neurophysiol 92:1615–1624

Klausberger T, Magill PJ, Marton LF, David J, Roberts B, Cobden PM, Buzsaki G, Somogyi P (2003) Brain-state and cell-type-specific firing of hippocampal interneurons in vivo. Nature 421:844–848

Klausberger T, Marton LF, Baude A, Roberts JD, Magill PJ, Somogyi P (2004) Spike timing of dendrite-targeting bistratified cells during hippocampal network oscillations in vivo. Nat Neurosci 7:41–47

Letzkus JJ, Kampa BM, Stuart GJ (2006) Learning rules for spike timing dependent plasticity depend on dendritic synapse location. J Neurosci 26(41):10420–10429

Leung LS, Roth L, Canning KJ (1995) Entorhinal inputs to hippocampal CA1 and dentate gyrus in the rat: a current-source-density study. J Neurophysiol 73:2392–2403

Lisman J, Malenka RC, Nicoll RA, Malinow R (1997) Learning mechanisms: the case for CaM-KII. Science 276:2001–2002

Magee JC, Johnston DA (1997) Synaptically controlled, associative signal for Hebbian plasticity in hippocampal neurons. Science 275(5297):209–213

Manns JR, Zilli EA, Ong KC, Hasselmo ME, Eichenbaum H (2007) Hippocampal CA1 spiking during encoding and retrieval: Relation to theta phase. Neurobiol Learn Mem 87:9–20

Markram H, Lübke J, Frotscher M, Sakmann B (1997) Regulation of synaptic efficacy by coincidence of postsynaptic APs and EPSPs. Science 275:213–215

Markram H et al (2015) Reconstruction and simulation of neocortical microcircuitry. Cell 163(2):456–492

Mizuno T, Kanazawa I, Sakurai M (2001) Differential induction of LTP and LTD is not determined solely by instanteneous calcium concentration: an essential involvement of a temporal factor. Eur J Neurosci 14(4):701–708

Mizuseki K, Sirota A, Pastalkova E, Buzsaki G (2009) Theta oscillations provide temporal windows for local circuit computation in the entorhinal-hippocampal loop. Neuron 64:267–280

Molyneaux BJ, Hasselmo ME (2002) GABAB presynaptic inhibition has an in vivo time constant sufficiently rapid to allow modulation at theta frequency. J Neurophysiol 87:1196–1205

Nishiyama M, Hong K, Mikoshiba K, Poo MM, Kato K (2000) Calcium stores regulate the polarity and input specificity of synaptic modification. Nature 408:584–588

Pfeil T, Grübl A, Jeltsch S, Müller E, Müller P, Petrovici MA, Schmuker M, Brüderle D, Schemmel J, Meier K (2013) Six networks on a universal neuromorphic computing substrate. Front Neurosci 7(11)

Pi HJ, Lisman JE (2008) Coupled phosphatase and kinase switches produce the tristability required for long-term potentiation and long-term depression. J Neurosci 28(49):13132–13138

Poirazi P, Pissadaki E (2010) The making of a detailed CA1 pyramidal neuron model. In: Cutsuridis V et al (ed) Hippocampal Microcircuits, Springer Series in Computational Neuroscience 5 (first edition)

Poirazi P, Brannon T, Mel BW (2003) Arithmetic of subthreshold synaptic summation in a model CA1 pyramidal cell. Neuron 37:977–987

Rast A, Galluppi F, Davies S, Plana L, Patterson C, Sharp T, Lester D, Furber S (2011) Concurrent heterogeneous neural model simulation on real-time neuromimetic hardware. Neural Netw 24:961–978

Remy S, Spruston N (2007) Dendritic spikes induce single-burst long term potentiation. Proc Natl Acad Sci U S A 104:17192–17197

Saudargiene A, Graham BP (2015) Inhibitory control of site-specific synaptic plasticity in a model CA1 pyramidal neuron. Biosystems 130:37–50

Saudargiene A, Cobb S, Graham BP (2015) A computational study on plasticity during theta cycles at schaffer collateral synapses on CA1 pyramidal cells in the hippocampus. Hippocampus 25(2):208–218

Sjöström PJ, Häusser M (2006) A cooperative switch determines the sign of synaptic plasticity in distal dendrites of neocortical pyramidal neurons. Neuron 51(2):227–238

Sjöström PJ, Rancz EA, Roth A, Häusser M (2008) Dendritic excitability and synaptic plasticity. Physiol Rev 88(2):769–840

Strösslin T, Sheynikhovich D, Chavarriaga R, Gerstner W (2005) Robust self-localisation and navigation based on hippocampal place cells. Neural Netw 18:1125–1140

Tsukada M, Aihara T, Kobayashi Y, Shimazaki H (2005) Spatial analysis of spike timing-dependent LTP and LTD in the CA1 area of hippocampal slices using optical imaging. Hippocampus 15(1):104–109

Vargas-Caballero M, Robinson HP (2004) Fast and slow voltage-dependent dynamics of magnesium block in the NMDA receptor: the asymmetric trapping block model. J Neurosci 24(27):6171–6180

Wittenberg GM, Wang SS (2006) Malleability of spike-timing-dependent plasticity at the CA3–CA1 synapse. J Neurosci 26:6610–6617

Wyble BP, Linster C, Hasselmo ME (2000) Size of CA1-evoked synaptic potentials is related to theta rhythm phase in rat hippocampus. J Neurophysiol 83:2138–2144

Zilli EA, Hasselmo ME (2006) An analysis of the mean theta phase of population activity in a model of hippocampal region CA1. Network 7:277–297

Computational Examination of Synaptic Plasticity and Metaplasticity in Hippocampal Dentate Granule Neurons

Azam Shirrafiardekani, Jörg Frauendiener, Ahmed A. Moustafa, and Lubica Benuskova

Abstract Long-term potentiation (LTP) and long-term depression (LTD) are two forms of long-lasting synaptic plasticity. To protect synaptic weights from extreme increase or decrease, neurons need to regulate their activities; this phenomenon is called homeostatic plasticity. The induction of homosynaptic plasticity by high-frequency stimulation (HFS) increases the strength of synaptic weights dramatically which makes a neuron loses balance. However, heterosynaptic plasticity keeps the synaptic weights away from the extreme increase and brings them into a stable range. Therefore, neurons need both homosynaptic and heterosynaptic plasticity to regulate their synaptic weights. In most previous studies of spike-timing-dependent plasticity (STDP) models, postsynaptic spikes are treated as all-or-none events; however, in this study, we calculate the voltage of the postsynaptic spikes instead of counting the number of spikes. Further, we incorporate a modified model of

The original version of this chapter was revised: two of the chapter authors were inadvertently missed in the authors list which has been added now. The correction to this chapter is available at https://doi.org/10.1007/978-3-319-99103-0_27

A. Shirrafiardekani (✉)
Department of Computer Science, University of Otago, Dunedin, New Zealand
e-mail: ashirrafi@cs.otago.ac.nz

J. Frauendiener
Mathematics & Statistics, University of Otago, New Zealand
e-mail: joerg.frauendiener@otago.ac.nz

A. A. Moustafa
School of Social Sciences and Psychology & Marcs Institute for Brain and Behaviour, Western Sydney University, Sydney, NSW, Australia
e-mail: A.Moustafa@westernsydney.edu.au

L. Benuskova
Department of Applied Informatics, Faculty of Mathematics, Physics and Informatics, Comenius University, Bratislava, Slovakia
e-mail: lubica@ii.fmph.uniba.sk

V. Cutsuridis et al. (eds.), *Hippocampal Microcircuits*, Springer Series in Computational Neuroscience, https://doi.org/10.1007/978-3-319-99103-0_20

metaplasticity based on the voltage of the spike rather than the spike count. To model synaptic plasticity of dentate granule cells, we used computational simulations and employed STDP rules accompanied with metaplasticity model and noisy spontaneous activity to address these questions; firstly, could our plasticity and metaplasticity models produce homosynaptic LTP in one pathway and heterosynaptic LTD in the neighbouring pathway? Secondly, does the magnitude of spontaneous activity after stimulation determine the level of heterosynaptic LTD? Thirdly, when two stimulations with the same frequency are applied to the same synapse at different time interval, will both stimulations produce the same level of synaptic plasticity? Our result shows that employing STDP and metaplasticity rules based on the voltage of the spikes accompanied with noisy spontaneous activity could replicate homosynaptic LTP in the stimulated pathway and heterosynaptic LTD in the non-stimulated neighbouring pathway of the dentate granule cell, as shown experimentally (Abraham WC, Mason-Parker SE, Bear MF, Webb S, Tate WP, Proc Natl Acad Sci 98(19):10924–10929, 2001; Abraham WC, Logan B, Wolff A, Benuskova L, J Neurophysiol 98(2):1048–1051, 2007).

Introduction

Neural stem cells have a capacity of generating new neurons. This phenomenon is called neurogenesis. Hippocampal dentate granule is one of a few areas in the brain that could reproduce the adult neurogenesis (Barker et al. 2011). According to the new studies, synaptic plasticity of adult-born dentate granule cells is highly involved in the process of learning and memory formation Snyder et al. (2001). Therefore, for further investigation of synaptic plasticity in the adult dentate granule cell, our work is concentrated in this specific cell type of the hippocampus. The ability of synapses to change their efficacy in respond to activity is called synaptic plasticity. There are two forms of long-lasting synaptic plasticity, long-term potentiation (LTP) and long-term depression (LTD). Bliss and LØmo were the first to observe LTP in the dentate gyrus in anaesthetized rabbits (Bliss and Cooke 2011). Following that Douglas and Goddard in 1975 found that high-frequency stimulation (HFS) could reproduce longer and stronger LTP. LTP and LTD could occur simultaneously in the neighbouring pathways of the dentate granule cells (Douglas and Goddard 1975). A mechanism in which a synapse is activated by presynaptic stimulation is called homosynaptic plasticity. However, when activations of other synapses cause synaptic plasticity at inactivated synapse, heterosynaptic plasticity occurs. In dentate granule neurons, both forms of homo- and heterosynaptic plasticity are required for the modulation of synaptic plasticity. There are some activities of the brain that put the neurons in the unstable condition; therefore, to stabilize the synaptic plasticity and control synaptic weights, neurons use a mechanism called homeostatic plasticity (Watt and Desai 2010). For example, homosynaptic plasticity extremely increases the synaptic weights, while heterosynaptic plasticity could modify the affected synapse by returning the synaptic weights to balance (Chistiakova et al. 2014). Heterosynaptic LTD of the dentate granule cells for the

first time was observed in vivo in 1979. To produce longer homosynaptic LTP in the hippocampus, heterosynaptic plasticity needs to be induced. Experimental studies from dentate granule cells reveal that homosynaptic LTP in the activated synapse is accompanied by heterosynaptic LTD in the inactivated ones (Foy 2001). Another mechanism that might be involved in the regulation of synaptic plasticity is metaplasticity. Metaplasticity is a form of homeostatic plasticity, in which the previous activity of the neuron regulates further synaptic plasticity. More precisely, if the induction of specific stimulation causes synaptic plasticity in a synapse, with the induction of the same stimulation at the same synapse only a few minutes later, the same amplitude of synaptic plasticity will not be produced (Morrison 2012). This mechanism modifies the firing rate of the neuron and prevents the synaptic weights from excessive growth (Yger and Gilson 2015). Metaplasticity can also be classified as homosynaptic and heterosynaptic metaplasticity. In homosynaptic metaplasticity induction, synaptic plasticity is modified by the previous activity at the same synapse. However, in heterosynaptic metaplasticity, synaptic plasticity is modified by the previous activity from other synapses (Abraham et al. 2001).

Experimental studies from Levy and Steward in 1983 revealed that besides the frequency of presynaptic activity, the precise timing between pre- and postsynaptic spikes is also crucial for the LTP induction. This mechanism is called spike-timing-dependent plasticity (STDP). In this work, we have used computer simulation to test that which of the above mechanisms might be involved on the induction of synaptic plasticity. Noisy spontaneous activity is a background activity of the brain. Bienenstock, Cooper and Munro (BCM) was the first plasticity rule that took into account the role of this activity. However, in this work, we show that the frequency of noisy spontaneous activity determines the amplitude of LTP and LTD. Therefore, it will be a critical factor for our plasticity model as well. Although, in most STDP models, the postsynaptic spike count is calculated for induction of synaptic plasticity, in our STDP model, the postsynaptic voltage is calculated for induction of synaptic plasticity, because some evidence from experimental studies show that the average of postsynaptic voltage is significant for induction of synaptic plasticity rather than the spike count.

In this work, our modified metaplasticity model is also based on the postsynaptic voltage because we think synaptic plasticity can be produced if the average of postsynaptic voltage is bigger than the threshold. Furthermore, in this model of metaplasticity, only one factor either potentiation or depression is needed to be controlled by model.

In this work, we used nine-compartmental model of granule cell accompanied with STDP and metaplasticity mechanisms with noisy spontaneous activity to address the following questions:

1. With our model, could we replicate homosynaptic LTP in the tetanized pathway and concurrent heterosynaptic LTD in the neighbouring non-tetanized pathway?
2. Could the frequency of noisy spontaneous activity determine the magnitude of heterosynaptic LTD?

3. Does the metaplasticity of the first stimulation impact on the level of synaptic plasticity caused by the second HFS?

To answer the above questions and test our metaplasticity and plasticity models, we use experimental studies by Abraham et al. (2001) and Abraham et al. (2007).

In the first simulation, we replicated the data from Abraham et al. (2001), when HFS is applied to the medial perforant pathway (MPP). The aim of this simulation is to examine our plasticity and metaplasticity models on induction of homosynaptic LTP and concurrent heterosynaptic LTD.

In the second simulation, we replicated the data from Abraham et al. (2007), when HFS is applied to the medial pathway and simultaneous spontaneous activity is switched off in the lateral perforant pathway (LPP) only during the medial HFS. The goal of this simulation was to examine the role of noisy spontaneous activity in producing heterosynaptic LTD in the lateral perforant pathway (LPP).

In the third simulation, we also replicated the data from Abraham et al. (2007), when two HFS with the same patterns are applied to the medial pathway and simultaneous lateral spontaneous activity is switched off only during the first medial HFS. The aim of this simulation is to examine the metaplasticity impact of the first medial HFS on synaptic plasticity produced by the second HFS. In this work, we show that with our STDP and metaplasticity models based on the voltage of the postsynaptic spikes accompanied with noisy spontaneous activity, our model can replicate experimental studies by Abraham et al. (2001) and Abraham et al. (2007), while the granule cell model is a realistic nine-compartmental model.

In the first section of the chapter, we will describe relevant experimental studies. After that, we will describe our novel model and explain how it relates to experimental data presented in the first section.

Review of In Vivo Experimental Studies that We Model

In this section we will briefly review two in vivo experimental studies from Abraham et al. (2001) and Abraham et al. (2007). In Abraham et al. (2001), the role of sliding modification threshold from the BCM rule in homosynaptic LTP and heterosynaptic LTD of the awake rats was examined. The first goal of experimental studies by Abraham et al. (2007) was to examine the role of spontaneous activity in heterosynaptic plasticity LTD of the anaesthetized rats. And the second goal was to examine the metaplastic effect of the first stimulation on the synaptic plasticity produced by the second stimulation.

Description for Experimental Studies by Abraham et al. (2001)

In Abraham et al. (2001) various experiments have been conducted to investigate synaptic plasticity in the dentate granule cells, but we only describe one part of

their experimental studies, when only one specific pattern of HFS was applied to the medial pathway.

Adult male Sprague-Dawley rats (400–550 g) were prepared and chronically implanted with stimulating and recording electrodes (Abraham and Goddard 1983). Activation of the medial and lateral perforant path fibres by stimulating an electrode evokes field excitatory postsynaptic potentials (fEPSPs) within the dentate granule hilus (McNaughton and Barnes 1977). After surgery, animals were put into the recording chamber, and an experimental procedure was started, while animals were awake (Abraham et al. 2001). According to Abraham et al. (2001), following the stability of fEPSPs baseline, different patterns of HFS were applied to the medial pathway. As we only describe one of the experiments, we examine the effect of one pattern of HFS. As can be seen from Fig. 2, the first HFS pattern was 400 Hz delta-burst stimulation (DBS) with 30-s interburst intervals repeated ten times, applied to the medial pathway. Delta-burst stimulation as a train within one burst is delivered at the delta frequency of 1 Hz. After applying HFS, the field EPSP slope is expressed as a percentage change from the average baseline value prior to injection. The percent change of data was presented as mean ± SEM (Abraham et al. 1985).

The aim of this paper was to examine the homosynaptic LTP and heterosynaptic LTD within the two neighbouring pathways of the granule cells with sliding modification threshold using the BCM rule. As can be seen from Fig. 3, before applying HFS, both medial and lateral pathways are quite stable. When the first HFS was applied to the medial pathway, the percentage of the average of fEPSP slope increased by (37 ± 5%) which means homosynaptic LTP occurred in this pathway. However, in the lateral pathway, the percentage of the average of fEPSP slope simultaneously decreased by (30 ± 5%), which means heterosynaptic LTD occurred in this pathway.

Description of Experimental Studies by Abraham et al. (2007)

The first experimental condition from Abraham et al. (2007) investigates the role of spontaneous activity in heterosynaptic LTD of dentate granule cell. The second experimental condition examines the metaplasticity impact of the previous plasticity on synaptic plasticity produced by the second stimulation at different time intervals. All experiments from Abraham et al. (2007) are examined with two control and procaine groups. In the procaine group, the lateral pathway will be blocked during the first medial HFS. However, in the control group, both pathways are open during the whole experiments (Fig. 1).

In this procedure, the first adult male Sprague-Dawley rats (2–4 mo) were anaesthetized with urethan. Then, stimulating electrodes were implemented to the medial and lateral pathway by stereotaxic method. Recording electrodes were also implemented to the dentate hilus to record the extracellular field potential (Christie and Abraham 1992). After about 30 min that both pathways became stable, HFS was applied to the medial pathway, and simultaneously PBS or procaine was injected to

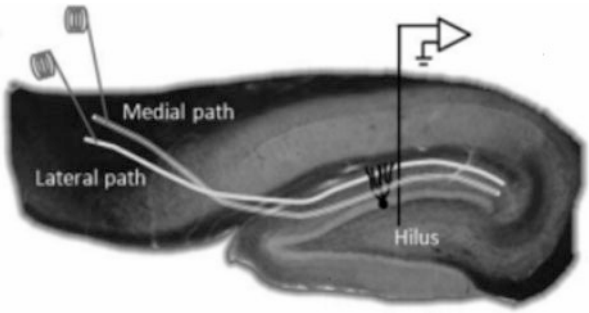

Fig. 1 Position of the stimulating (far left, end of medial and lateral paths) and recording (centre right) electrodes in the rat hippocampus. (Source: Bowden et al. 2012)

Fig. 2 Schematic illustration of the 400 Hz delta-burst stimulation (DBS) of HFS consists of five trains at 1 Hz, while each train contains ten spikes at 400 Hz. Bursts are repeated ten times at every 30-s. (Source Shirrafiardekani et al. 2017)

the lateral pathway. As can be seen from Fig. 4, in this experiment, HFS consists of 400 Hz DBS (delta-burst stimulation) with 60-s interburst intervals repeated ten times. After injecting HFS, the percentage change of the average of fEPSP slope was calculated from the baseline for both medial and lateral path responses, and all data were demonstrated as means ±SE (Figs. 2 and 3).

Examining the synaptic plasticity and metaplasticity in the dentate granule cell in vivo is more accurate than in vitro (like slice). The reason of that is because of the level of spontaneous activity. Unlike in vivo, the degree of spontaneous activity in slice is zero.

The first aim of experimental studies by Abraham et al. (2007) was to examine the impact of the spontaneous activity on heterosynaptic plasticity LTD in the dentate granule cell. As we explained before, all the experimental studies from Abraham et al. (2007) are tested with two control and procaine groups. In the procaine group, when the first pattern of HFS (Fig. 4) was applied to the medial pathway, simultaneously either procaine or PBS was injected to the lateral pathway to block the spontaneous activity in this pathway. As can be seen from Fig. 6 (black circle), procaine also blocked the response evoked by the test pulses which firstly caused a large "depression" in this pathway that is considered to be artefact. After a few minutes that procaine washed out, the magnitude of fEPSP slope was decreased to $(-5 \pm 8\%\ n = 6)$ in the lateral pathway. However, blocking the spontaneous activity in the lateral pathway did not affect the synaptic plasticity in the medial pathway.

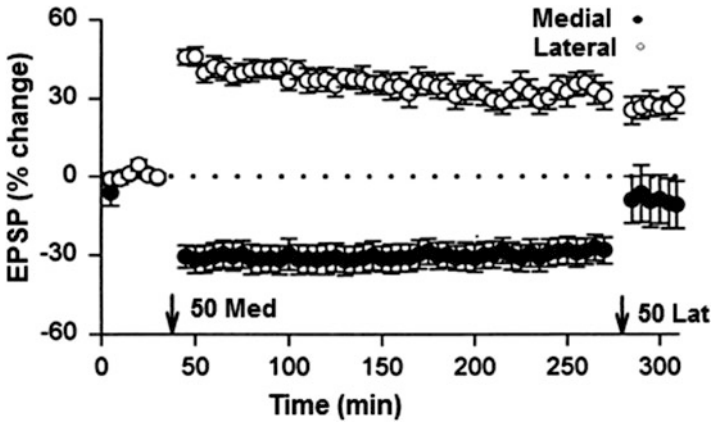

Fig. 3 The percentage of changes of synaptic weights in medial and lateral pathways is calculated by the field excitatory postsynaptic potential (fEPSP). 50 Med is the first HFS (400 Hz delta-burst stimulation (DBS) with 30-s interburst intervals repeated ten times) applied to the medial pathway. The percentage of the average change of synaptic weights in the medial pathway is shown with unfilled circles, and the percentage of the average change of synaptic weights in the lateral pathway is shown with filled circles. With applying the first HFS to the medial pathway, ($37 \pm 5\%$) LTP is observed in this pathway, and ($30 \pm 5\%$) LTD is observed in the lateral pathway. (Source: Abraham et al. 2001)

Fig. 4 Schematic illustration of the 400 Hz delta-burst stimulation (DBS) of HFS consists of five trains at 1 Hz, while each train contains ten spikes at 400 Hz. Bursts are repeated ten times at every 60-s. (Source Shirrafiardekani et al. 2017)

Therefore, the percentage of the average of fEPSP slope raised by ($37 \pm 5\%$, $n = 7$) which caused homosynaptic LTP in this pathway (Fig. 5 white circle). However, with applying the first medial HFS in the control group, the magnitude of fEPSP slope decreased by ($24 \pm 3\%$, $n = 7$) in the lateral pathway (Fig. 6 white circle), while the magnitude of fEPSP slope increased by ($37 \pm 5\%$, $n = 7$) in the medial pathway. Comparing the results from procaine group and control group in the lateral pathway reveals the requirement of spontaneous activity for heterosynaptic LTD in the granule cell.

The purpose of the second experimental condition of Abraham et al. (2007) was to investigate the role of metaplasticity from the first stimulation on synaptic

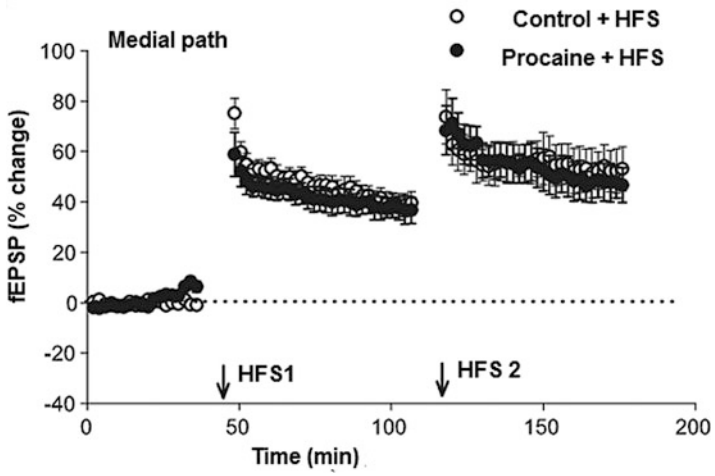

Fig. 5 The percentage of changes of synaptic fEPSP slope for the medial pathway in the control group (unfilled circle) and for the procaine group (filled circle) is shown. When the first HFS was applied to the medial pathway, simultaneously lateral pathway will be blocked by procaine to block the degree of spontaneous activity. With applying the first medial HFS, the fEPSP slope increased by ($37 \pm 5\%$, $n = 7$) in the medial pathway, but when the second HFS was applied, it causes no larger LTP in this pathway for both procaine and control groups. (Source: Abraham et al. 2007)

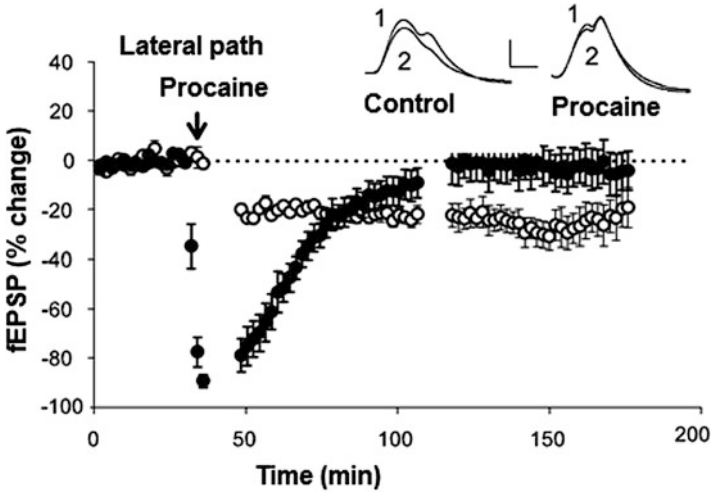

Fig. 6 The average change in the slope of fEPSP in the lateral pathway in the control group (unfilled circles) and the procaine group (filled circle). With applying the first medial HFS, procaine was injected to the lateral pathway to block the lateral spontaneous activity. Therefore, LTD was inhibited in this group. The reason why we see depression (filled circles) is that procaine also inhibits the response evoked by the test pulses. However, in the control group, fEPSP slope decreased by ($24 \pm 3\%$, $n = 7$). When the second medial HFS was applied, no further LTD was observed in neither of groups. (Source: Abraham et al. 2007)

plasticity produced by the second stimulation. Therefore, a few minutes after applying the first medial HFS, the second HFS with the same pattern as the first one was applied to the medial pathway.

As can be seen from Fig. 5, in both procaine and control groups, although LTP occurred in the second HFS, no further increase in the average of fEPSP slope was observed in this pathway. However, when the second medial HFS was applied, although LTD was observed in the control group, no further LTD occurred in this pathway (Fig. 6 white circle). The same results were observed in the procaine group, when the second medial HFS was applied, and no further LTD was observed in the lateral pathway in this group (Fig. 6 black circle).

These results prove that the metaplasticity impact of the previous plasticity does not let the second HFS to reproduce the same level of plasticity as the first HFS.

Model Overview

Mathematical and computational neuroscientists benefit from a variety of numerical and analytical techniques for examining different mechanisms that might be involved in the processing information in the nervous system. Therefore, with employing a variety of mathematical and computational tools, it will be possible for scientists to propose different hypotheses and evaluate new aspects of the experimental studies (Ulinski 1999). In this section we introduce some plasticity rules, and then we describe the compartmental model of neuron and plasticity and metaplasticity rules that we have employed to examine the synaptic plasticity in the granule cells. In this work we have simulated the experimental studies of Abraham et al. (2001) and Abraham et al. (2007). Using simulations and employing STDP and metaplasticity models based on the voltage accompanied with reduced compartmental model of neuron and noisy spontaneous activity, we addressed three questions; the first question was: Could our model replicate homosynaptic LTD in the triggered MPP and heterosynaptic LTD in the neighbouring inactivated LPP of the dentate granule cell? With this question in mind, we will test the plasticity model. The second question that we addressed was: Does the frequency of spontaneous activity impact the level of heterosynaptic plasticity LTD? The purpose of this question was to investigate the role of frequency of spontaneous activity on the synaptic plasticity. The third question we addressed was: When two high-frequency stimulations (HFS) with the same pattern at different times are applied to the synaptic pathway, do they both produce the same level of synaptic plasticity in our model? The aim of this question is to examine our metaplasticity model.

Modelling the Dentate Granule Cells

There are two computational models for implementing the dentate granule cells: realistic and simplified models. In the realistic models, biological details such as

cellular mechanism with different concentrations of ion channels are described (DAngelo et al. 2013). However, in the simplified models, the biological details are not described as much as the realistic models. Because only specific properties of the neural dynamics are desired, these models do not need to be more detailed. Multi-compartmental model of the neuron is an example of a realistic model, and integrate-and-fire model is known as simplified model of neuron (Izhikevich 2004).

The dendritic tree of the dentate granule cells consists of four parts: the granule cell layer dendrites (GCLD), the proximal (PD), the middle (MD) and distal (DD) dendrites. The proximal dendrite (PD) receives inputs from commissural. The middle dendrite (MD) receives inputs from the medial entorhinal cortex, and the distal dendrite (DD) receives inputs from the lateral entorhinal cortex (Andersen et al. 2006). The entorhinal cortex transfers inputs via medial perforant pathway (MPP) to the MD of the granule cells, while lateral perforant pathway (LPP) of the entorhinal cortex transfers inputs to the DD of the granule cells (Scharfman 2011).

As the length and the size of dendritic tree (or axon) increases, the amount of inputs that will be received by each branch might be different. Therefore, to describe complicated structure of the dendrites (or axons), it is important to use a compartmental model. When each dendrite (or axon) is divided into smaller compartments, each compartment will have its own radius, length and voltage that can be formulated by ordinary differential equations (Sterratt et al. 2011). Desmond and Levy in 1982 were the first to introduce the full-morphology compartmental model of the dentate granule cells (Desmond and Levy 1982). Since then, the reduced compartmental model with four ion channels was introduced by Yuen and Durand in 1991, but this model could not describe some important properties of the granule cells (Yuen and Durand 1991). A reduced 60-compartmental model with nine types of ion channels was extended by Aradi and Holmes in 1999. Aradi and Holmes' model could explain varieties of experimental studies quite well (Tejada et al. 2014). This model has 2 dendrites, while each dendrite has 14 compartments. It also has one compartment for soma and an axon with 31 compartments (Aradi and Holmes 1999). Our dentate granule cell model is based on a reduced compartmental model of Aradi and Holmes (1999) which is implemented in *Neuron* by Santhakumar et al. (2005). We first downloaded simulation files from the *ModelDB* database at (http://senselab.med.yale.edu/modeldb/, accession No. 51781). Because we did not want to produce the propagation of action potential, we did not include the axon into the model. To reduce the simulation time, our model has only nine compartments: One compartment for soma and four compartments for each dendrite, and each dendrite has 150 excitatory synapses.

Our granule cell model has seven ion channels: fast sodium (Na), fast delayed rectifier potassium (fKDR), slow delayed rectifier potassium (sKDR), A-type potassium (KA) and large conductance T-type (TCa), Ntype (NCa) and L-type (LCa) calcium channels from Aradi and Holmes (1999). The GC files can be downloaded from the *ModelDB* at http://senselab.med.yale.edu/modeldb/, accession No. 51781.

Table 1 Parameter values of all compartments of GC model

Parameters	Distal	Middle	Proximal	Granule cell	Soma
C_m (μF/cm^2)	1.6	1.6	1.6	1	1
g_{Na} (S/cm^2)	0	0.008	0.013	0.018	0.12
$g_{fK_{DR}}$ (S/cm^2)	0.001	0.001	0.004	0.004	0.16
$g_{sK_{DR}}$ (S/cm^2)	0.008	0.006	0.006	0.006	0.006
g_{Na} (S/cm^2)	0	0	0	0	0.012
$g_{T\mathrm{Ca}}$ (S/cm^2)	0.001	0.005	2.5×10^{-4}	7.5×10^{-5}	3.7×10^{-5}
$g_{N\mathrm{Ca}}$(S/cm^2)	0.001	0.001	0.001	0.003	0.002
$g_{L\mathrm{Ca}}$ (S/cm^2)	0	0.0005	0.0075	0.0075	0.005
E_{Na}(mV)	45	45	45	45	45
E_K (mV)	−90	−90	−90	−90	−90
E_l(mV)	−75	−75	−75	−75	−75
E_{Ca} (mV)	130	130	130	130	130
τ_{rise} (ms)	0.2	0.2	0.2	0.2	0.2
τ_{decay}(ms)	2.5	2.5	2.5	2.5	2.5

Source: Santhakumar et al. (2005)

Table 2 Parameter values for individual compartments

Parameters	DD	MD	PD	GCLD	Soma
R_a (Ωcm^2)	210	210	210	210	210
L (μm)	150	150	150	150	16.8
φ (μm)	3	3	3	3	16.8

Source: Santhakumar et al. (2005)

The following equations describe the membrane current density at each compartment with unit $^{\mathrm{mA}}/_{\mathrm{cm}^2}$. All the parameter values and units are taken from (Santhakumar et al. 2005) and demonstrated in Tables 1 and 2.

Fast Sodium Current

The equations for $I_{Na,\,i}$ current at compartment i are:

$$I_{Na,i} = G_{Na,i}\,(V_i - E_{Na}) \tag{1}$$
$$G_{Na,i} = g_{Na,i} {m_i}^3 h_i$$

where V_i is a membrane potential, i is the number of compartment, $g_{Na,\,i}$ is the maximum conductance of the sodium channel and E_{Na} is the reverse potential. Variable m_i is dimensionless sodium activation gate, and h_i is dimensionless inactivation gate (see Eqs. 9, 10, 11,12 and 13 from Appendix (rate function)).

Fast and Slow Delayed Rectifier Potassium Currents

The equations for fK_{DR} current at the compartment i are:

$$I_{fK_{DR,i}} = G_{fK_{DR,i}} (V_i - E_K) \tag{2}$$

$$G_{fK_{DR,i}} = g_{fK_{DR,i}} n_{f,i}^4$$

where V_i is a membrane potential, i is the number of compartment, $g_{fK_{DR,i}}$ is the maximum conductance of the fast delayed rectifier potassium and E_K is the reverse potential. Variable $n_{f,i}$ is dimensionless fast potassium activation gate (see Eqs. 9, 14 and 15 from Appendix (rate functions)).

The equations for sK_{DR} current at the compartment i are:

$$I_{sK_{DR,i}} = G_{sK_{DR,i}} (V_i - E_K) \tag{3}$$

$$G_{sK_{DR,i}} = g_{sK_{DR,i}} n_{s,i}^4$$

where V_i is a membrane potential, I is the number of compartment, $g_{sK_{DR,i}}$ is the maximum conductance of the slow delayed rectifier potassium and E_K is the reverse potential. Variable $n_{s,i}$ is dimensionless slow potassium activation gate (see Eqs. 9, 16 and 17 from Appendix (rate functions)).

A-Type Potassium Current

The equations for A-type potassium current at the compartment i are:

$$I_{K_A,i} = G_{K_A,i} (V_i - E_K) \tag{4}$$

$$G_{K_A,i} = g_{K_A,i} k_i l_i$$

where V_i is a membrane potential, i is the number of compartment, $g_{K_A,i}$ is the maximum conductance of the A-type potassium and E_K is the reverse potential. Variable k_i is dimensionless A-type potassium activation gate, and l_i is dimensionless A-type potassium inactivation gate (see Eqs. 9, 18, 19, 20 and 21 from Appendix (rate functions)).

Calcium Channels

T-, N- and L-type voltage-gated calcium channels are specified for dentate granule cell. The rate of change of the intracellular calcium concentration at compartment i was given by:

$$\frac{d[Ca^{2+}]_i}{dt} = B_i \left(I_{TCa,i} + I_{NCa,i} + I_{LCa,i} \right) - \frac{[Ca^{2+}]_i - [Ca^{2+}]_0}{\tau} \tag{5}$$

where $B_i \frac{5.2\times10^{-6}}{Ad}$ is unit of $mol/c.m^3$ for a shell of surface area A and thickness d (0.2 μm), $\tau = 10$ ms was the calcium removal rate and $[Ca^{2+}]_0 = 70$ nM was the resting calcium concentration (Aradi and Holmes 1999).

The equations for calcium channels at the compartment i were:

$$I_{TCa,i} = G_{TCa,i}\,(V_i - E_{Ca}) \tag{6}$$

$$G_{TCa,i} = g_{TCa,i} a_i^2 b_i$$

$$I_{NCa,i} = G_{NCa,i}\,(V_i - E_{Ca}) \tag{7}$$

$$G_{NCa,i} = g_{NCa,i} c_i^2 d_i$$

$$I_{LCa,i} = G_{LCa,i}\,(V_i - E_{Ca}) \tag{8}$$

$$G_{LCa,i} = g_{LCa,i} e_i^2$$

where V_i is a membrane potential, i represents the number of the compartment and $g_{TCa,\,i}$, $g_{NCa,\,i}$ *and* $g_{LCa,\,i}$ are the maximum conductance of T-, N- and L-type calcium, respectively. E_{Ca} is the reverse potential. Variables a_i and b_i are dimensionless T-type calcium activation and inactivation gates, respectively. Variables c_i and d_i are dimensionless N-type calcium activation and inactivation gates, respectively. Variable e_i is dimensionless L-type calcium activation gates (see Eqs. A.9, A.22, A.23, A.24, A.25, A.26, A.27, A.28, A.29, A.30 and A.31 from Appendix (rate functions)).

Neural Plasticity Models

A variety of plasticity models have been created within the last few decades; each of them has tried to model new features of synaptic plasticity with more details. In this section we describe three models of synaptic plasticity called Hebb rules, Bienenstock, Cooper and Munro (BCM) rules and spike-timing-dependent plasticity (STDP) rule. We also describe plasticity models we incorporated in our simulation studies.

Hebbian Plasticity Rule

Donald Hebb was the first one who introduced the plasticity models. He discovered that the correlation between pre- and postsynaptic activities makes a stronger connectivity between neurons. Homosynaptic LTP can be described with the Hebbian plasticity model, but this model is unable to explain the synaptic depression (Bush et al. 2010).

$$\frac{dw_{ij}}{dt} = \alpha . v_i u_j \tag{9}$$

where w_{ij} is the synaptic weight between presynaptic v_i and postsynaptic u_j, u_j is the jth presynaptic activity, v_i is the ith postsynaptic activity and α is a learning rule. Implementation of the model shows that synaptic weights increase extremely as no boundary was defined for the synaptic weight in this model (Yger and Gilson 2015).

BCM Rule

BCM rule was another classic model of synaptic plasticity based on experimental studies from the visual cortex, and it was the first model that took into account the role of spontaneous activity. In the BCM model, a concept is introduced to determine the direction of synaptic plasticity called sliding modification threshold or θ_m. Sliding modification threshold is a non-linear function of the time average of postsynaptic activity. BCM rule (Bienenstock et al. 1982; Cooper et al. 2004) can be formulated according to the following equations:

$$\varnothing\left(v(t), \theta_m\left(t\right)\right) = v(t)\left(v(t) - \theta_m(t)\right) \tag{10}$$

$$v(t) = \sum u(t)w(t) \tag{11}$$

$$\frac{\mathrm{d}w}{\mathrm{d}t} = \eta \varnothing u \tag{12}$$

where $v(t)$ is the average of postsynaptic activity over time, $u(t)$ is the presynaptic activity over time, $w(t)$ is the synaptic weight over time, $\varnothing$ is the synaptic modification function and η is the modification rate (Fig. 7). When postsynaptic activity is less than θ_m and above the baseline, synaptic weight decreases which shows LTD has occurred. While when postsynaptic activity is bigger than θ_m and below the baseline, synaptic weight increases which shows LTD has occurred (Jedlicka 2002). To investigate synaptic plasticity of the single dentate granule cell, we employed mechanism called nearest-neighbour spike-timing-dependent plasticity (STDP) and metaplasticity rules accompanied with the brain background activity called noisy spontaneous activity. The selected neuron model in this investigation is a nine-compartmental model of the granule cell (Santhakumar et al. 2005) (Fig. 8).

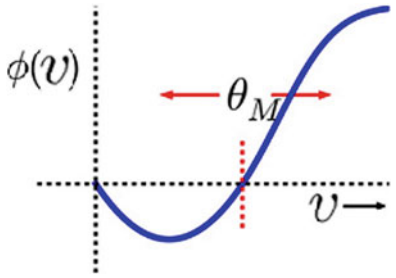

Fig. 7 v is a postsynaptic activity, and θ_m is a modification threshold. $\Phi(v)$ is a BCM function which shows the synaptic changes. (Source: http://www.scholarpedia.org/article/BCM/)

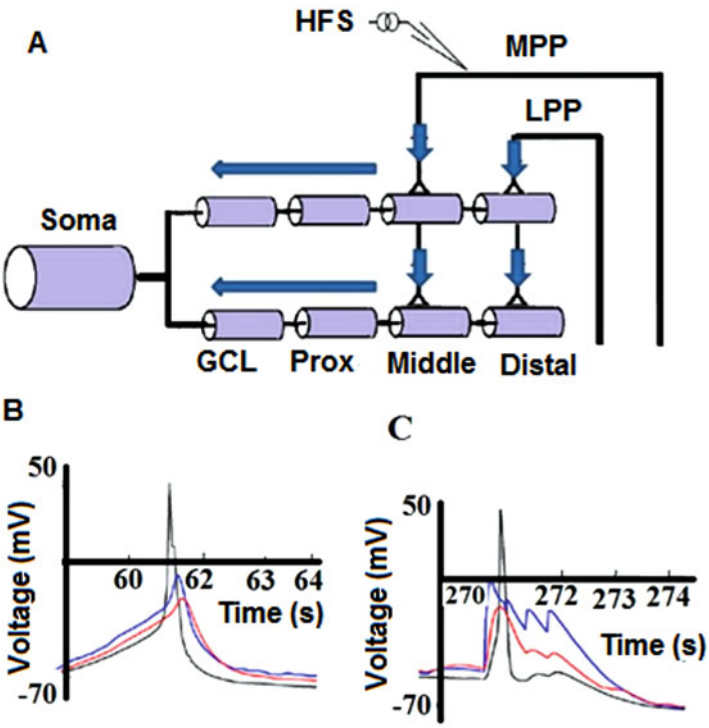

Fig. 8 (**a**) is a 9-compartmental model of the dentate granule cell, which has 2 dendrites with 300 excitatory synapses (each dendrite has 150 synapses). Each dendrite consists of four compartments, and soma has one compartment. This model does not have an axon. The lateral perforant pathway (LPP) relays presynaptic inputs from the entorhinal cortex to the distal part of the dendrites, and medial perforant pathway (MPP) relays presynaptic inputs from the entorhinal cortex to the middle parts of the dendrites. Lines showing LPP and MPP pathways are only for illustration, because input spikes are delivered directly to synapses in our model. Filled arrows show the flow of input activities and empty arrows the direction of backpropagating action potential. Currents flow through the axial resistance between compartments. (**b**) Somatic action potential (the biggest spike) and backpropagation of action potential plus EPSPs from MPP (the smallest spike) and LPP (the medium spike) before HFS. (**c**) Somatic membrane potential (the biggest spike) and backpropagation of action potential plus EPSPs from MPP (the smallest spike) and LPP (the medium spike) during HFS. (Source: Shirrafiardekani et al. 2017)

The STDP Rule

Several experimental studies from different areas of the brain suggest that precise timing between pre- and postsynaptic activity is one of the key factors that is involved in the synaptic plasticity processing. It has also shown experimentally that excitatory synapses from different circuits follow the STDP rules. Repeated presynaptic spikes that precede postsynaptic spikes within a certain time window produce LTP; however, if repeated presynaptic spikes follow postsynaptic spikes

within a certain time window, LTD occurs (Sjöström and Gerstner 2010). Classical spike pair-based STDP is one of the STDP models which propose how pre- and postsynaptic spikes interact together. This model that is based on experimental studies by Lin et al. (2006) indicates that delivering pre- and postsynaptic activities to the granule cell in order, pre-post or post-pre, causes STDP with two exponential windows. Pairing the presynaptic spike with the following postsynaptic spike in the specific time window causes LTP, and pairing the presynaptic spike with the proceeding postsynaptic spike in the specific time window causes LTD (Lin et al. 2006). The following equations show the classical spike pair-based STDP:

$$\Delta w_+ = P \exp\left(-\frac{\Delta t}{\tau_p}\right) \text{ if } \Delta t > 0 \tag{13}$$

$$\Delta w_- = D \exp\left(-\frac{\Delta t}{\tau_d}\right) \text{ if } \Delta t < 0 \tag{14}$$

where $\Delta t = t_{\text{post}} - t_{\text{pre}}$ is the time difference between the incoming time of postsynaptic spike and the outcoming time of presynaptic spike. τ_p is the decay constant for the LTP window, and τ_d is the decay constant for the LTD window. P is the amplitude for potentiation value, and D is the amplitude for depression parameter. All-to-all interaction and nearest-neighbour interaction are two ways to implement the spike pair-based STDP model. In the all-to-all interaction, each presynaptic spike pairs with all postsynaptic spikes, and each postsynaptic spike pairs with all presynaptic spikes (Fig. 9a). However, in the nearest-neighbour interaction, each presynaptic spike pairs only with two postsynaptic spikes: the

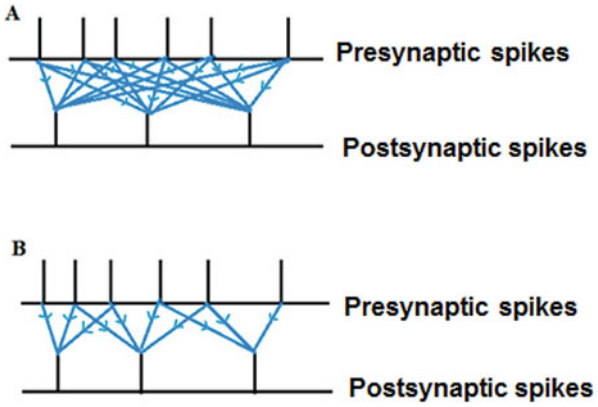

Fig. 9 (**a**) Interaction of pre- and postsynaptic spikes with all-in-all interaction. In this interaction each presynaptic spike pairs with all postsynaptic spikes. (**b**) The nearest-neighbour interaction. In this interaction, each postsynaptic spike pairs only with the two most closely precedes presynaptic spikes: and each presynaptic spike pairs only with the most closely follows postsynaptic spikes. (Source: Shirrafiardekani et al. 2017)

postsynaptic spike that most closely precedes the given presynaptic spike and the postsynaptic spike that most closely follows the given presynaptic spike (Van Rossum et al. 2000); see Fig. 9b. Our STDP implementation is based on spike pair-based nearest-neighbour STDP which is formulated by the following equation:

$$\Delta w\,(t+\Delta t) = w(t)\,(1+\Delta w_{+}+\Delta w_{-}) \tag{15}$$

Synaptic weight updates when the second postsynaptic spike in the nearest neighbours is detected.

Metaplasticity Models

In this section we first introduce two metaplasticity models, Benuskova and Abraham rule and Clopath metaplasticity model, and then will describe the metaplasticity model that we have used in our simulations.

Benuskova and Abraham Rule

According to investigations by Izhikevich and Desai (2003), there is a correlation between the nearest-neighbour STDP model and BCM rule. They suggested that the sliding modification threshold (θ_m) from the BCM rule is equal to the following equation:

$$\theta_m = \frac{\frac{P}{\tau_d}+\frac{D}{\tau_p}}{P+D} \tag{16}$$

where P and D are potentiation and depression values from Eqs. 13 and 14 and $\tau_p$and τ_d are decay constants for LTP and LTD windows from the STDP rule (see Eqs. 13 and 14). In their idea the value of θ_m is fixed which means P and D are fixed as well. However, in the Benuskova and Abraham model, the value of sliding modification threshold is not fixed, and it is equal to the average of postsynaptic activity or $\langle c(t)\rangle$. According to this theory, the average of postsynaptic activity is calculated by the following equation:

$$\langle c(t)\rangle = \frac{c_0}{\tau_m}\int_{-\infty}^{t} c\left(t'\right)\exp\left(-\frac{\left(t-t'\right)}{\tau_m}\right)\mathrm{d}t' \tag{17}$$

where c_0 is a scaling constant, τ_m is a time constant and $c(t)$ is a postsynaptic spike count with time. When there is a postsynaptic spike at time t, $c(t) = 1$, and when there is no postsynaptic spike, $c(t) = 0$.

The following equations show how the relation between the average of postsynaptic activity and amplitude of potentiation and depression values is calculated:

$$P = \frac{P(0)}{\langle c(t) \rangle} \text{ and } D = D(0)\, \langle c(t) \rangle \tag{18}$$

Here, $\langle c(t) \rangle$ is an average of postsynaptic activity; $P(0)$ and $D(0)$ are the initial amplitudes for P and D. According to this idea when the average of postsynaptic activity is high, less LTP will be induced, but it is more likely to induce LTD (Benuskova and Abraham 2007).

Clopath Metaplasticity Model

Basically, in the Clopath et al. (2010) metaplasticity model, the potentiation and depression factors are introduced differently. While the potentiation factor (A_{LTP}) is defined as a fixed value, the depression factor ($A_{\text{LTD}}(u^{=})$) is introduced as a function based on a homeostatic variable, which is equivalent with the average of postsynaptic activity from Benuskova and Abraham rule (Clopath et al. 2010):

$$A_{\text{LTD}}\left(\bar{\bar{u}}\right) = A_{\text{LTD}}\, \frac{\bar{\bar{u}}^{2}}{u_{\text{ref}}^{2}} \tag{19}$$

where u_{ref}^{2} is a constant value and $\bar{\bar{u}}^{2}$ is a homeostatic variable which is dependent on a low-pass filter of the average of postsynaptic potential or $\bar{u}_{-}$.

They calculated the spikes are based on the average of postsynaptic potential. Therefore, in their model, at each time step, they have treated the spikes as the continuous events.

$$\tau_x \frac{\mathrm{d}x}{\mathrm{d}t} = -x(t) + X(t) \tag{20}$$

when a presynaptic spike is coming, $X(t) = 1$ and 0 otherwise and τ_x is the decay time constant. In their model $\bar{u}_{-}$ is calculated by:

$$\tau_{-} \frac{\mathrm{d}\bar{u}_{-}}{\mathrm{d}t} = -\bar{u}_{-}(t) + u(t) \tag{21}$$

where $u(t)$ is the postsynaptic membrane potential and τ_{-} is the time decay constant. Therefore, synaptic weights are calculated as follows:

$$\frac{\mathrm{d}w^{-}}{\mathrm{d}t} = -A_{-}\, (\bar{u})\, X(t)\, (u_{-}(t) - \theta_{-}) \text{ if } w > w_{\min} \tag{22}$$

$$\frac{\mathrm{d}w^{+}}{\mathrm{d}t} = -A_{+} x(t)\, (u - \theta_{+}) \text{ if } w < w_{\max} \tag{23}$$

where u is the membrane potential, θ_- and θ_+ are adjustable parameters and A_+ and A_- are potentiation and depression factors.

Metaplasticity Model Used in This Work

As we explained in Clopath et al.'s metaplasticity model, only depression factor depends on the average of postsynaptic activity, while potentiation factor is fixed. We incorporated their idea to test our metaplasticity model with only depression factor being depended on the average of postsynaptic activity. Therefore, we ran our simulation, while our metaplasticity model was from the following equations:

$$P(t) = P(0) \text{ and } D(t) = 1.5D(0)\,\langle c(t)\rangle \tag{24}$$

where $P(0)$ and $D(0)$ are initial values for potentiation and depression factors, $\langle c(t)\rangle$ is the average of postsynaptic activity and 1.5 is the scaling constant value (Shirrafiardekani et al. 2017).

We also extended their idea to test our model considering the depression factor as a fixed value and potentiation factor being depended on the average of postsynaptic activity. Therefore, we ran our simulation, while our metaplasticity model was from the following equations:

$$P(t) = \frac{0.75P(0)}{\langle c(t)\rangle} \text{ and } D(t) = D(0) \tag{25}$$

where $P(0)$ and $D(0)$ are initial values for potentiation and depression factors, $\langle c(t)\rangle$ is the average of postsynaptic activity and 0.75 is the scaling constant value. Surprisingly, running the simulations with both metaplasticity models did not show the significant difference in our results. Therefore, we concluded that if only one of the potentiation or depression factors is being dependent on the average of postsynaptic activity, it will be sufficient to produce synaptic plasticity (Shirrafiardekani et al. 2017).

As we explained in the last section, the average postsynaptic activity from Abraham and Benuskova rule is based on counting the number of spikes (see Eq. 17). This means they have treated the spikes as all-or-nothing events. However, in our model, the postsynaptic voltage is calculated rather than a postsynaptic spike count. Therefore, the average postsynaptic activity is calculated by the difference between the postsynaptic voltage and resting potential at the soma which is shown by the following equations:

$$\langle c(t)\rangle_\tau = \frac{c_0}{\tau}\int_{-\infty}^{t}\left(V\left(t'\right) - V_{\text{rest}}\right)^2 \exp\left(-\frac{\left(t-t'\right)}{\tau}\right) \mathrm{d}t' \tag{26}$$

where $\langle c(t)\rangle$ is calculated numerically. The scaling constant c_0 is equal to 0.0025 $1/\text{mV}^2$. $(V(t') - V_{\text{rest}})^2$ is the difference between the postsynaptic voltage and resting potential at the soma, and V_{rest} is the initial resting potential and equal

to −75 mV. By taking the second power of this difference, we ensure that $\langle c(t) \rangle \geq 0$ (Shirrafiardekani et al. 2017).

Modelling Spontaneous Presynaptic Activity and HFS

Spontaneous activity (background activity) is not based on the external stimulation. It is a consequence of interaction between the neural networks and electrophysiological properties of the single neuron (Herz et al. 2006). In our model, simulated granule cells receive the presynaptic noisy spontaneous activity via the LPP and MPP from the entorhinal cortex. In this work, we have used the Poisson process model to generate the random Poisson spike train along the MPP and LPP (Fellous et al. 2003). In all of our simulations, we have chosen the frequency of presynaptic spontaneous activity to be less than 10 HZ (Gloveli et al. 1997), and the interspike interval (ISI) of spiking activity is generated according to the following equation:

$$\mathrm{ISI} = (1 - n)\,\mathrm{ISI}_0 + \mathrm{neg}\,(-n\mathrm{ISI}_0) \tag{27}$$

where n is noise with $0 < n < 1$, "negexp(−x)" is the negative exponential distribution and it is equal to homogeneous Poisson distribution with probability of the next spike occurring after time "ISI." ISI_0 is the initial value, and in this work, it is equal to 125 ms. With $n = 0$, $\mathrm{ISI} = \mathrm{ISI}_0$ shows spiking activity periodically. With $0 < n < 1$, the spiking activity is quasi-periodic. The value of noise has been chosen by $n = 0.02$ in our model.

As we discussed above, HFS was the other source of inputs that granule cell neuron has received. In the first simulation based on experimental studies by Abraham et al. (2001), 400 Hz DBS at 30-s intervals was applied to the MPP. In the second simulation based on experimental studies by Abraham et al. (2007), the same patterns of HFS as the first one but at 60-s intervals were applied to the MPP. In all simulations, presynaptic spontaneous activity is along with HFS, except those where it is deliberately blocked.

Simulation and Integration Methods for the Model

To calculate the percentage of changes of LTP and LTD, we have implemented the STDP and metaplasticity rules in the *Neuron* environment and included into the granule cell model. Thus, the complete set of our simulation files is available for download from the *ModelDB* database (accession number 185350): http://senselab.med.yale.edu/modeldb/.

The integration method that we have used in our simulations is the Crank-Nicolson integration. We used this method as we have to deal with some non-linear equations which need to be solved by iteration with small time steps (Hines and Carnevale 1997). In all of our simulations, we have chosen the time step $\mathrm{d}t = 0.2$ ms.

The Plasticity Parameters Obtained for the Model

Although numerous parameters are involved in the synaptic plasticity mechanism, in our work, we found these five parameters; τ_p, τ_d, initial synaptic weights and frequency of medial and lateral noisy spontaneous activity are quite critical for our plasticity model in the dentate granule cell. Parameters are obtained manually, and we have changed the values until to achieve a right match with experimental studies. Because looking for a right value of parameters and adjusting them to match with experimental studies consume a lot of time and energy, it is reasonable to find those ones that are highly involved in synaptic plasticity process. Finding the correct values is also very important because wrong values cause inaccurate results. To find the mentioned parameters and test our plasticity and metaplasticity models, we used experimental studies by Abraham et al. (2001). Therefore, we calculated the magnitude of LTP and LTD as a function of changing the values of parameters,τ_p, τ_d,initial synaptic weights and frequency of medial and lateral noisy spontaneous activity. With analysing all these functions, we found that with our plasticity and metaplasticity models, the parameter values from Table 3 could reproduce homosynaptic LTP and concurrent heterosynaptic LTD from the experimental studies quite well.

Model Justification

As we mentioned from the method section, our granule cell model had nine compartments, one for soma and four for each dendrite. According to "Description for experimental studies by Abraham et al. (2001)" the granule cell model from Aradi and Holmes (1999) consists of 29 compartments (14 compartments for dendrites and one compartment for soma). We simulated our model with both 9 compartments and 29 compartments and observed the same plasticity results (Shirrafiardekani et al. 2017). Therefore, to reduce the simulation time, our compartmental model has only nine compartments.

Our model also has two ion channels less than Aradi and Holmes' (1999) model.

Our results with the lack of calcium-voltage-dependent potassium (BK) and small conductance calcium-dependent potassium (SK) channels (Aradi and Holmes 1999) did not show significant difference when these two channels were included

Table 3 Parameter values for optimal match with the experimental data (Shirrafiardekani et al. 2017)

$D(0)$	$P(0)$	τ_p	τ_d	Initial weight	Medial frequency	Lateral frequency	α	τ
0.001	0.004	95 ms	25 ms	0.65 (nS)	2.9 Hz	6.8 Hz	0.2500	60 s

to the model. Therefore at least our model shows synaptic plasticity the same as experimental studies without needing these two ion channels.

First Simulation Study Based on Abraham et al. (2001) and Testing the Synaptic Plasticity Model

In this section, we have employed STDP rules from Eqs. 13, 14 and 15 and metaplasticity model from Eq. 25 accompanied by nine-compartmental model of dentate granule cell and noisy spontaneous activity to test our plasticity model with the first part of experimental studies by Abraham et al. (2001).

In this simulation, our plasticity parameters are taken from Table 3. As we explained in experimental part, when the first HFS pattern was applied to the MPP, synaptic weights increased by (37 $\pm$ 5%) in this pathway, and homosynaptic LTP occurred. However, in the LPP, heterosynaptic plasticity occurred simultaneously, and synaptic weights decreased by (30 $\pm$ 5%) in this pathway (see Fig. 3, experimental section). In our simulation, HFS pattern was the same as in Fig. 2 in the experimental section. After starting simulation, it takes a couple of second for both average of synaptic weights in MPP and LPP to get stable and stay at baseline level. As can be seen from Fig. 10, both synaptic weights get almost no change until the coming of the first burst of HFS. When HFS is applied to the medial pathway, as a result of STDP combined with the metaplasticity rule, synaptic weights increase

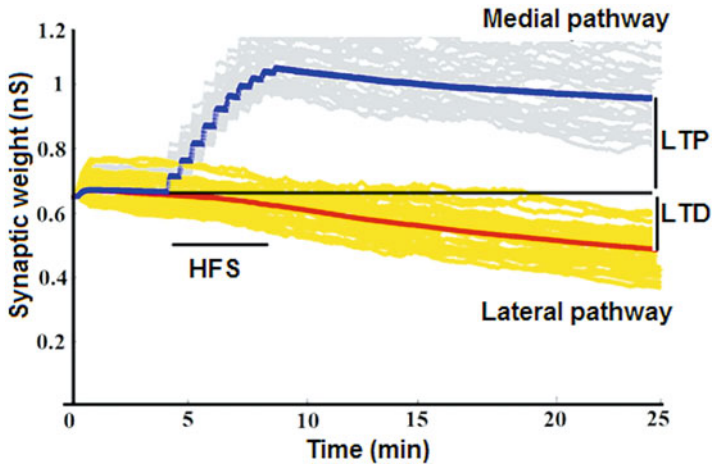

Fig. 10 The thick trace over the baseline shows the average weight of medial synapses, and the thick trace under the baseline corresponds to the average weight of lateral synapses. Narrow traces around the thick ones (over the baseline) are for individual medial synapses, and narrow traces around the thick ones (under the baseline) are for individual lateral synapses. Before medial HFS, both synaptic pathways are stable. During HFS, synaptic weights increase in the medial pathway and decrease in the lateral pathway. In this run, we observe +37% LTP in the medial pathway and −27% LTD in the lateral pathway. (Source Shirrafiardekani et al. 2017) (Fig. 12)

in the medial pathway, and we could observe approximately 37% homosynaptic LTP. However, in the lateral pathways, simultaneously LTD occurred, and we could observe approximately – 25% LTD from the baseline. Comparing our results shows a good consistency with the results from experimental studies (Shirrafiardekani et al. 2017).

Second Simulation Study Based on Abraham et al. (2007) and Examining the Role of Spontaneous Activity

In this section we replicate the first part of experimental studies from Abraham et al. (2007), when only one HFS is applied to the medial pathway and simultaneously spontaneous activity is blocked in the lateral pathway during the HFS (procaine group). The aim of this study is to investigate the requirement of noisy spontaneous activity for induction of heterosynaptic LTD. In our simulation to replicate the procaine inhibition of spontaneous activity, we switched lateral spontaneous activity off during the first medial HFS, while at the end of HFS, we switched the lateral activity on with different values of frequency. As can be seen from Fig. 6 in the experimental studies section, after injecting procaine, it takes sometimes for it to be washed out. Therefore, during this time, procaine reduces the frequency of spontaneous activity. According to that, we introduced a new parameter called lateral frequency after HFS (LAH) to demonstrate the frequency of lateral activity after HFS. The percentage of synaptic weights in the MPP and LPP as a function of lateral spontaneous frequency after HFS (LAH) is shown in Table 4 while the plasticity parameters are taken from Table 3. As can be seen in Fig. 11, the fluctuation of synaptic weight as a function of LAH in the medial pathway is very slow. But in the lateral pathway, as the frequency increases, synaptic weights increase as well. That means when the frequency of LAH is low, we observe less LTD. This can be explained by the BCM rule as well. When the level of input activity is low, the sliding modification threshold shifts very little to the left which shows the less amount of LTD. According to Table 4, when the level of LAH is 3.5 HZ, only -6% LTD was observed in the LPP. However, in real experiments $-10 \pm 6\%$ LTD was also observed. This shows that even after injecting procaine to the lateral pathway, still small amount of LTD can be observed in this pathway. Therefore, we concluded that to explain the procaine inhibition in our model, the frequency of lateral spontaneous activity after HFS should be less than 4 Hz to get almost no LTD in the lateral pathway (Shirrafiardekani et al. 2017).

Third Simulation Based on Abraham et al. (2007) for Testing the Metaplasticity Model

The aim of this section is to test our metaplasticity model with the data from Abraham et al. (2007). As we explained above, Abraham et al. (2007) have conducted their experiment with two different groups, control and procaine. In the

Table 4 Percentage of LTP and LTD as a function of frequency of lateral activity after HFS

LAH (Hz)	LTP %	LTD %	Firing rate (Hz)
6.5	54	−22.2	1.4
6.2	52	−20	1.2
5.8	55.5	−18.6	1.34
5.5	54.5	−15	1.1
5	58.3	−12	1
4.7	60	−11	1.3
4.5	58.5	−9	1.3
4	58.5	−8	1
3.7	59.5	−7	1.1
3.5	60	−6	0.9

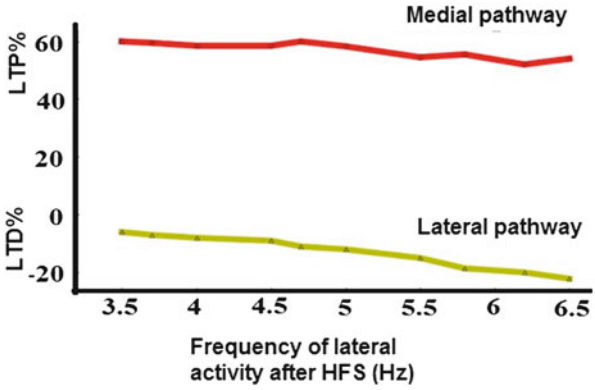

Fig. 11 The line contained with squares shows the amplitude of LTP as a function of lateral frequency after HFS (LAH), and the line contained with triangles shows the amplitude of LTD as a function of lateral activity after HFS (LAH) (Shirrafiardekani et al. 2017)

experimental studies in the control group, when the first medial HFS was applied, synaptic weight increased by (37 ± 5) % in the medial pathway. As the second medial HFS was applied, as a result of metaplasticity, no further LTP was observed in this pathway (Fig. 5 experimental section). As can be seen from Fig. 6, during the first medial HFS, synaptic weights depressed by (24 ± 3%) in the lateral pathway. When the second medial HFS was induced, as a result of metaplasticity, no further LTD occurred in this pathway.

In the computational model, our simulations are conducted for both procaine and control groups with the plasticity parameters taken from Table 3. For both groups, we have used two separate figures to demonstrate the amplitude of the average synaptic plasticity in the MPP and LPP. In the control group, a few seconds after starting simulations, both averages of medial and lateral synaptic weights become stable. When the first HFS (see Fig. 13a) was applied to the MPP as a result of STDP and metaplasticity models accompanied with noisy spontaneous activity, the average of synaptic weights increases in this pathway, and we could observe 45% homosynaptic LTP. When the second medial HFS was applied a few minutes after the first one, the average of synaptic weights increases, but as a result of metaplasticity, we could observe only 9% more LTP from the second HFS (see Fig. 13a). However, in the lateral pathway, when the first medial HFS was applied,

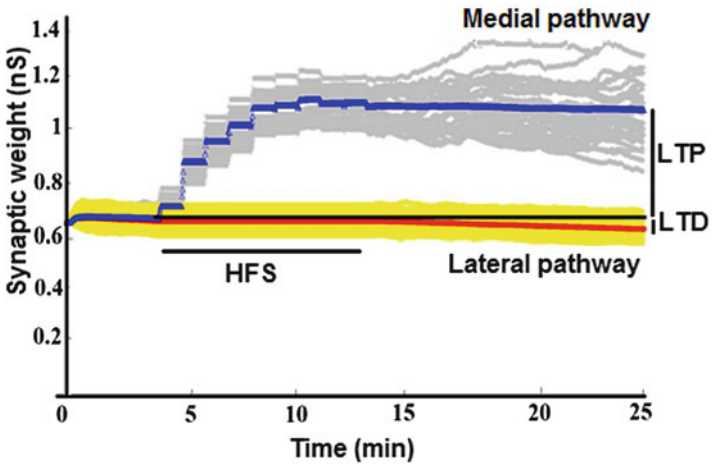

Fig. 12 The thick curve above the baseline is the average of medial synaptic weights, and the narrow curves around the thick ones (above the baseline) are synaptic weights from 150 medial synapses. Thick curve under the baseline is the average of lateral synaptic weights, and narrow curves around the thick ones (under the baseline) are lateral synaptic weights. As the HFS starts at the medial pathway, synaptic weights increase in this pathway. However, almost no LTD happens in the lateral pathway as we switch the lateral activity off during HFS (Shirrafiardekani et al. 2017)

simultaneously synaptic weights depressed in this pathway, and we could observe -27% heterosynaptic LTD in this pathway. When the second medial HFS was applied, although synaptic weight decreases in the lateral pathway, as a result of metaplasticity, we could observe only -12% more LTD in this pathway (see Fig. 13b). In the procaine group from the experimental studies, as the first medial HFS was applied, simultaneously procaine was injected to the lateral pathway to block the lateral spontaneous activity; after the procaine was washed out $-10 \pm 6\%$, LTD was observed in this pathway. With applying the second medial HFS, as a metaplasticity effect of the first HFS, no further LTD was observed in the LPP (Fig. 6). In our computational model, we switched the lateral activity off during the first medial HFS, and then we switched it on after the HFS with lower lateral frequency as before HFS. Because we think it will take a few minutes for procaine to be washed out; therefore, the frequency of lateral pathway after HFS is lower than before HFS. Thus, with our model, we observed -6% LTD. When the second medial HFS was applied, as a result of metaplasticity, we observed only -4% more LTD in the lateral pathway (see Fig. 14b). These results show that previous plasticity from the first HFS affects on synaptic plasticity generated by the second HFS and causes metaplasticity; therefore, the same amount of LTP and LTD cannot be observed by the second HFS (Morrison 2012). This experiment can be explained with the BCM rule; after the first medial HFS, medial pathway will be highly activated which increases the threshold and makes further LTP more difficult. This interpretation is also valid for further LTD induction. Comparing results from our simulations with

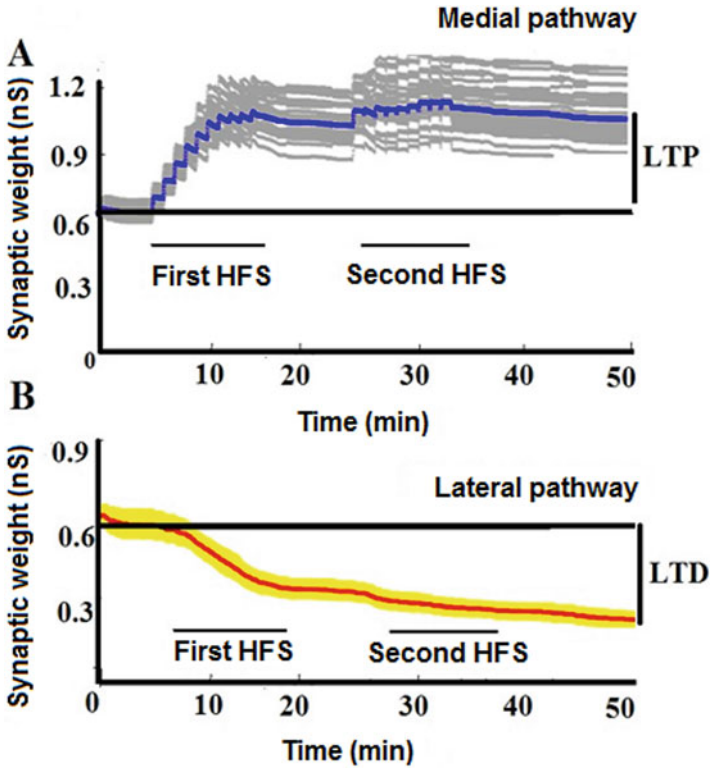

Fig. 13 (**a**) The average of medial synaptic weights is shown by thick curve above the baseline, and the individual medial synaptic weights are shown by narrow curves around the thick ones. During the first HFS, the average of synaptic weights increases up to 45% in the medial pathway. After applying the second HFS, the synaptic weight increases slightly, and additional 9% LTP is observed. (**b**) The average of lateral synaptic weights is shown by thick curve under the baseline, and the individual medial synaptic weights are shown by narrow curves around the thick ones. After the first HFS, average synaptic weights depress in the lateral pathway by about −27%. After the second HFS, average synaptic weight decreases by only additional −12%. (Source Shirrafiardekani et al. 2017)

the experimental studies shows also a good match with the model data and shows that our metaplasticity model could reproduce the experimental studies quite well (Shirrafiardekani et al. 2017).

Discussion

The main purpose of this work was to show that our model could reproduce synaptic plasticity and metaplasticity across a range of experimental conditions. To achieve this, we used computational modelling and employed reduced nine-compartmental

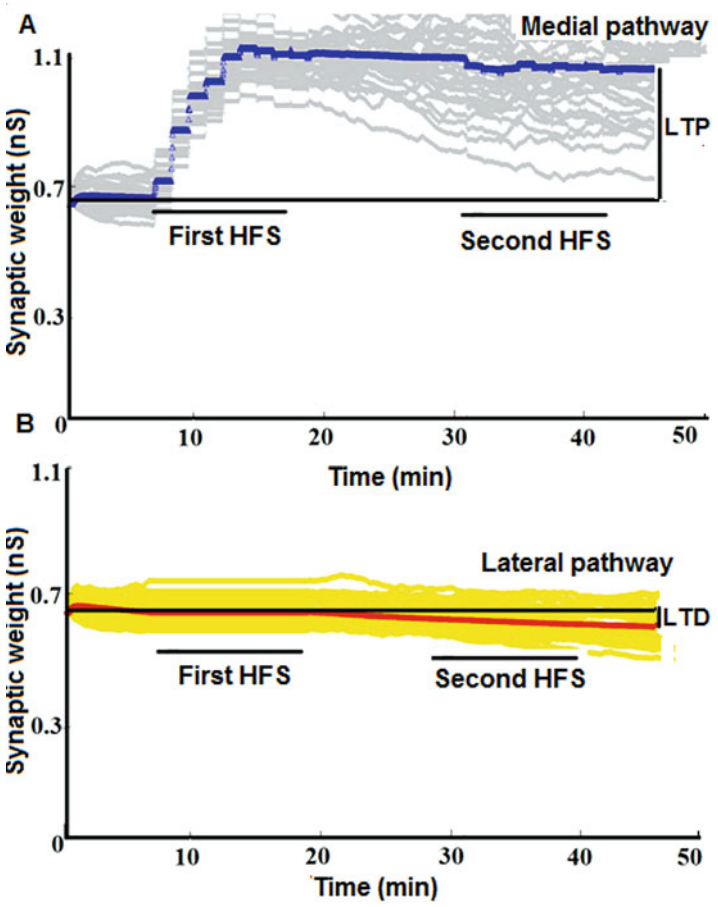

Fig. 14 Results for two medial HFS and later spontaneous activity off during the first HFS. (**a**) Thick curve above the baseline is the average of medial synaptic weights, and narrow curves around the thick ones are the individual medial synaptic weights from 150 synapses. During the first HFS, the average of synaptic weights increases in the medial pathway but not much further increases in synaptic weights during the second HFS occurs. (**b**) Thick curve under the baseline shows the average of lateral synaptic weights, and narrow curves around the thick ones show the individual lateral weights from 150 synapses. In the lateral pathway as the lateral activity is off during the first HFS, no LTD happens, while after the first HFS, as lateral activity switches on with low frequency, hardly any LTD occurs during and after the second HFS (Shirrafiardekani et al. 2017)

model of dentate granule cell with paired-based nearest-neighbours STDP and metaplasticity model based on the voltage accompanied with noisy spontaneous activity. Our reduced nine-compartmental model with one compartment for soma and four compartments for each dendrite was introduced by Aradi and Holmes (1999) and implemented in *Neuron* by Santhakumar et al. (2005). With our simulations, we assessed all the compartments and concluded that all of them are

required for synaptic plasticity induction. We also assessed the necessity of nine ion channels from Aradi and Holmes (1999) to replicate synaptic plasticity. We found out that at least with our model, only seven ion channels are required for reproducing synaptic plasticity. In this work, STDP and metaplasticity rules are based on Eqs. 13, 14, 15 and 25, such that all 300 synapses are affected by these rules. To test our model, we used two experimental studies from Abraham et al. (2001) and Abraham et al. (2007). The aim of the first simulation was to reproduce data from experimental studies by Abraham et al. (2001). With our model we could reproduce homosynaptic LTP in the medial pathway and concurrent heterosynaptic LTD in the non-tetanized lateral pathway.

Our second and third simulations were based on experimental studies by Abraham et al. (2007). The aim of our second simulation was to test the effect of procaine inhibition on heterosynaptic LTD. For this purpose, during the first medial HFS, we switched the lateral spontaneous activity off; therefore, no LTD was observed in this pathway. This result showed that the presence of noisy spontaneous activity is critical for LTD induction. After HFS, a parameter called LAH was introduced (lateral frequency after HFS) to show the effect of procaine inhibition. When the frequency of LAH was reducing, the magnitude of LTD was reducing as well. Therefore, we concluded that the level of frequency of spontaneous activity after HFS impacts on the magnitude of heterosynaptic LTD in the lateral pathway.

The goal of the third simulation was to examine our metaplasticity model. With our model we examined two control and procaine groups. Our simulations from the control group indicated that after inducing the second HFS, although small amount of LTP and LTD observed in both pathways, the same level of synaptic plasticity caused by the first HFS was not occurred by the second HFS in either of pathways. In the procaine group, the lateral activity was switched off during the first medial HFS, while, after that, it was switched on again with lower frequency. After inducing the second medial HFS, synaptic weight increased in the medial pathway, but the same level of LTP that occurred by the first HFS was not occurred by the second HFS. In the lateral pathway also, small amount of LTD was observed after the second medial HFS, but the magnitude of LTD produced by the second HFS was less than the magnitude of LTD produced by the first HFS (Shirrafiardekani et al. 2017).

Model Limitations and Strength

With our plasticity and metaplasticity rules, accompanied with noisy spontaneous activity and nine-compartmental model of dentate granule cell, we could replicate homosynaptic LTP in the MPP and heterosynaptic LTD in the LPP in the first simulation. Also our results show a good consistency with real experimental studies by Abraham et al. (2001). Our second and third simulations were based on experimental studies by Abraham et al. (2007). In the first experiments, we showed that the level of noisy spontaneous activity after HFS determined the magnitude of heterosynaptic LTD in the lateral pathway.

In the third simulation, we showed when two HFS apply to the same synapse with a few minutes time difference, the same level of LTP and LTD will not occur with the second stimulation (metaplasticity). This results also were in a good consistency with real experimental studies. One of the highlights of this work was finding good parameters that could make a reasonable match between our model simulations and a variety of the range of experimental studies. It is also interesting that in all simulations, we have used the same parameters in Table 3; however, in other computational studies for each experiment, parameters need to be changed. In many computational studies, the role of spontaneous activity is neglected; however, in our work, spontaneous activity is critical for induction of heterosynaptic plasticity.

Although most plasticity models are investigated from CA1 circuits, our work was based on synaptic plasticity of the dentate granule cell. In the Benuskova and Abraham metaplasticity rule, both potentiation and depression factors from plasticity rules depend on the average postsynaptic activity. However, our simulations show either potentiation or depression factor being dependent on average postsynaptic spikes is enough to reproduce homosynaptic LTP and heterosynaptic LTD. In our pair-based STDP model, we have used a more realistic model to calculate the voltage of the postsynaptic spikes. In this model, spikes are considered as continuous events rather than treat them as all-or-no events. As we mentioned in the last section, the frequency of spontaneous activity has not been recorded in the reviewed experimental studies; however, in this work, we could find parameter values for frequency of lateral spontaneous activity (6.8 Hz) and frequency of medial spontaneous activity (2.9 Hz) which are in agreement with experimental studies by Gloveli et al. (1997). To simulate the dentate granule cell model, we only added two synapses to the model, while thousands of synapses of the granule cell are involved in the synaptic plasticity mechanism. In our simulations we did not include the axon to the model; however, in real neurons, the backpropagation of action potential is also part of the spike. It will be more realistic to add the axon to the model. In this work we only modelled the excitatory synapses, while inhibitory synapses also produce synaptic plasticity. Our plasticity and metaplasticity models are only examined with a simulated granule cell, and they have not been tested with other dentate gyrus cells like mossy cells and basket cells.

Future Directions

Investigation by Zheng et al. (2014) shows that the duration of action potential (AP) has an important role on STDP rule; therefore they included AP into the STDP model and called their new model dSTDP. It will be worthwhile to test our model with the new dSTDP model and see the amplitude of synaptic plasticity. We only tested our detailed plasticity model with a single granule cell. If we want to test our detail model with the large number of networks, simulation will get too complicated, but for the future work, we are interested to simulate our detailed model with the small network. As we mentioned before, this work was limited to the granule cell;

in the extension work, we will examine our plasticity model with other hippocampal cells if in vivo LTP and LTD data are available. Our plasticity model is only tested with three experimental studies; in the further work, we will test our model with other real experimental studies.

In this work all the synapses were excitatory; in the further work, we will test our model with inhibitory synapses as well. As we explained in the method section, our granule cell model does not have an axon, to include the property of backpropagation of action potential from the axon to the postsynaptic activity; it is worthwhile to add the axon to the model. Our granule cell model has only two dendrites, but the real granule cell has many. In the further work, to propose a more realistic model of granule cell, it is important to include more than two dendrites to the model (Shirrafiardekani et al. 2017).

Appendix

Integration Method of Crank-Nicolson

The Crank-Nicolson method or the central difference is a finite difference method with the accuracy of the second order in time, which was developed by Crank and Nicolson. The error oscillation of this method decays with time; therefore the solution is stable and safe for most solutions. The Crank-Nicolson method is a combination of the backward and forward Euler methods. It is equivalent to advancing by one-half step using backward Euler and then advancing by one-half step using forward Euler. The global error for this method is proportional to the square of the step size (Hines and Carnevale 1997).

By considering the forward Euler method as:

$$\frac{y_{n+1} - y_n}{\Delta t} = f\,(t_n, y_n) \tag{A.1}$$

and the backward Euler method as:

$$\frac{y_{n+1} - y_n}{\Delta t} = f\,(t_{n+1}, y_{n+1}) \tag{A.2}$$

Therefor the Crank-Nicolson method can be calculated as:

$$\frac{y_{n+1} - y_n}{\Delta t} = \frac{f\,(t_n, y_n) + f\,(t_{n+1}, y_{n+1})}{2} \tag{A.3}$$

The RC Circuit

With injecting the current into the circuit, the membrane potential changes. Therefore, Kirchhoff's current law indicates that the total current entering into the junction is equal to the total current leaving the junction. The summation of the membrane current Ia and injected current I_e is equal to the summation of the capacitance current $I_c a$ and ionic current $I_i a$. a is the curved surface area of the cylinder (Sterratt et al. 2011).

$$Ia + I_e = I_c a + I_i a \tag{A.4}$$

The following equation shows the ionic current flows through the resistor:

$$I_i a = \frac{V - E_m}{\frac{R_m}{a}} \tag{A.5}$$

where $\frac{R_m}{a}$ is the membrane resistance and E_m is the equilibrium potential of the membrane. According to the following equation, the capacitive current is proportional to the rate of change of the voltage:

$$I_c a = C_m a \frac{\mathrm{d}V}{\mathrm{d}t} \tag{A.6}$$

The membrane capacitance is $C_m a$. If we suppose that the circuit is isolated, then Ia is zero. With substituting the I_i and I_c in Eq. 4, we have:

$$C_m \frac{\mathrm{d}V}{\mathrm{d}t} = \frac{E_m + V}{R_m} + \frac{I_e}{a} \tag{A.7}$$

This is the first-order ordinary differential equation (ODE) for the membrane potential V with units from Table 5 (Sterratt et al. 2011).

Multi-compartmental Models

Multi-compartmental models are useful techniques to model dendritic trees of the neuron. In this model, dendritic tree breaks up into the small compartment. With considering each compartment as a cylinder with a length l and a diameter d, the surface area will be equal to $a = \pi dl$ (Ermentrout and Terman 2010). Current flows through each compartment into the membrane capacitance and the membrane resistance. It also flows through intracellular and extracellular of the membrane and can be modelled by axial resistances. The extracellular resistance can be considered zero. R_a is the specific axial resistance with units Ω cm, and the axial resistance

Table 5 Passive quantities

Quantity	Description	Typical units	Relationships
d	Diameter of neurite	μm	
l	Length of compartment	μm	
R_m	Specific membrane resistance	Ωcm^2	
C_m	Specific membrane capacitance	μFcm^{-2}	
R_a	Specific axial resistance	Ωcm	
r_m	Membrane resistance per inverse unit length	Ωcm	$r_m = \frac{R_m}{\pi d}$
c_m	Membrane capacitance per unit length	μFcm^{-1}	$c_m = C_m \pi d$
r_a	Axial resistance per unit length	$\Omega / \mathrm{cm}^{-1}$	$r_a = \frac{4R_a}{\pi d^2}$
V	Membrane potential	mV	
E_m	Leakage reversal potential due to different ions	mV	
I	Membrane current density	μAcm^{-2}	
I_e	Injected current	nA	
I_c	Capacitive current density	nA/cm^2	
I_i	Ionic current density	mA/cm^2	

of the cylindrical compartment is $4R_a\, l/\pi d^2$ in which $\pi d^2/4$ is a cross-sectional area. j is the number of compartment, and V_j is the membrane potential in the j the compartment, and $I_{e,j}$ is the injected current into the compartment j. The membrane current I_j is equal to the sum of the leftwards and rightwards axial currents. Therefore, according to Ohm's law:

$$I_j a = \frac{V_{j+1} - V_j}{4R_a l / \pi d^2} + \frac{V_{j-1} - V_j}{4R_a l / \pi d^2} \tag{A.8}$$

where $I_j a$ is a current, and according Kirchhoff's current law:

$$I_{c,j} a + I_{i,j} a = I_j a + I_{e,j} \tag{A.9}$$

$$I_{c,j} a + I_{i,j} a = \frac{V_{j+1} - V_j}{4R_a l / \pi d^2} + \frac{V_{j-1} - V_j}{4R_a l / \pi d^2} + I_{e,j} \tag{A.10}$$

The following equations are similar to Eq. 10 for a patch of membrane with two extra equations which describe the flowing current through two compartments $j-1$ and $j+1$:

$$\pi d l C_m \frac{\mathrm{d}V_j}{\mathrm{d}t} = \frac{E_m - V_j}{R_m / \pi d l} + \frac{V_{j+1} - V_j}{4R_a l / \pi d^2} + \frac{V_{j-1} - V_j}{4R_a l / \pi d^2} + I_{e,j} \tag{A.11}$$

Where a is the surface area of the cylinder.

$$C_m \frac{\mathrm{d}V_j}{\mathrm{d}t} = \frac{E_m - V_j}{R_m} + \frac{d}{4R_a}\left(\frac{V_{j+1} - V_j}{l^2} + \frac{V_{j-1} - V_j}{l^2}\right) + \frac{I_{e,j}}{\pi dl} \tag{A.12}$$

This equation is the fundamental equation for the compartmental model (Sterratt et al. 2011).

Rate Functions for Nine-Compartmental Models of GC

Activation and inactivation gates at compartment i are formulated as:

$$\frac{\mathrm{d}z_i}{\mathrm{d}t} = \alpha_{z_{ii}} - \left(\alpha_{z_i} + \beta_{z_i}\right) z_i \tag{A.13}$$

$$\left(z_i : m_i, h_i, n_{f,i}, n_{s,i}, k_i, l_i, a_i, b_i, c_i, d_i, e_i, r_i, q_i\right)$$

variable z_i represents m_i, h_i, $n_{f,i}$, $n_{s,i}$, k_i, l_i, a_i, b_i, c_i, d_i, e_i, r_i *and* q_i ion-gating variables. Rate functions at compartment i determine the transition between open and closed states of the ion channels. The following equations show the rate functions at compartment *i* (Aradi and Holmes 1999):

$$\alpha_{m,i}(V) = \frac{-0.3\,(V_i - 25)}{\left[\exp\left(\frac{V_i - 25}{-5}\right) - 1\right]} \tag{A.14}$$

$$\beta_{m,i}(V) = \frac{0.3\,(V_i - 53)}{\left[\exp\left(\frac{V_i - 53}{5}\right) - 1\right]} \tag{A.15}$$

$$\alpha_{h,i}(V) = \frac{0.23}{\exp\left(\frac{V_i - 3}{20}\right)} \tag{A.16}$$

$$\beta_{h,i}(V) = \frac{3.33}{\left[\exp\left(\frac{V_i - 55.5}{-10}\right) + 1\right]} \tag{A.17}$$

$$\alpha_{n_f,i}(V) = \frac{-0.07\,(V_i - 47)}{\left[\exp\left(\frac{V_i - 47}{-6}\right) - 1\right]} \tag{A.18}$$

$$\beta_{n_f,i}(V) = \frac{0.264}{\exp\left(\frac{V_i - 22}{40}\right)} \tag{A.19}$$

$$\alpha_{n_s,i}(V) = \frac{-0.028\,(V_i - 35)}{\left[\exp\left(\frac{V_i-35}{-6}\right) - 1\right]} \tag{A.20}$$

$$\beta_{n_s,i}(V) = \frac{0.1056}{\exp\left(\frac{V_i-10}{40}\right)} \tag{A.21}$$

$$\alpha_{k,i}(V) = \frac{-0.05\,(V_i + 25)}{\left[\exp\left(\frac{V_i+25}{-5}\right) - 1\right]} \tag{A.22}$$

$$\beta_{k,i}(V) = \frac{0.1\,(V_i + 15)}{\left[\exp\left(\frac{V_i+15}{8}\right) - 1\right]} \tag{A.23}$$

$$\alpha_{l,i}(V) = \frac{0.00015}{\exp\left(\frac{V_i+13}{15}\right)} \tag{A.24}$$

$$\beta_{l,i}(V) = \frac{0.06}{\left[\exp\left(\frac{V_i+68}{-12}\right) + 1\right]} \tag{A.25}$$

$$\alpha_{a,i}(V) = \frac{0.2\,(19.26 - V_i)}{\left[\exp\left(\frac{19.26-V_i}{10}\right) - 1\right]} \tag{A.26}$$

$$\beta_{a,i}(V) = 0.009\ \exp\left(\frac{-V_i}{22.03}\right) \tag{A.27}$$

$$\alpha_{b,i}(V) = 10^{-6} \exp\left(\frac{-V_i}{16.26}\right) \tag{A.28}$$

$$\beta_{b,i}(V) = \frac{1}{\left[\exp\left(\frac{29.76-V_i}{10}\right) + 1\right]} \tag{A.29}$$

$$\alpha_{c,i}(V) = \frac{0.19\,(19.88 - V_i)}{\left[\exp\left(\frac{19.88-V}{10}\right) - 1\right]} \tag{A.30}$$

$$\beta_{c,i}(V) = 0.046\ \exp\left(\frac{-V_i}{20.76}\right) \tag{A.31}$$

$$\alpha_{d,i}(V) = 1.6 \times 10^{-4} \exp\left(\frac{-V_i}{148.4}\right) \tag{A.32}$$

$$\beta_{d,i}(V) = \frac{1}{\left[\exp\left(\frac{39-V_i}{10}\right) + 1\right]} \tag{A.33}$$

$$\alpha_{e,i}(V) = \frac{15.69\ (81.5 - V_i)}{\left[\exp\left(\frac{81.5-V_i}{10}\right) - 1\right]} \tag{A.34}$$

$$\beta_{e,i}(V) = 0.29\ \exp\left(\frac{-V_i}{10.86}\right) \tag{A.35}$$

References

Abraham W, Goddard GV (1983) Asymmetric relationships between homosynaptic long-term potentiation and heterosynaptic long-term depression. Nature (London) 305:717–719

Abraham WC, Bliss TVP, Goddard GV (1985) International review of neurobiology. J Physiol 363:335–349

Abraham WC, Mason-Parker SE, Bear MF, Webb S, Tate WP (2001) Heterosynaptic metaplasticity in the hippocampus in vivo: a BCM-like modifiable threshold for LTP. Proc Natl Acad Sci 98(19):10924–10929

Abraham WC, Logan B, Wolff A, Benuskova L (2007) Heterosynaptic LTD in the dentate gyrus of anesthetized rat requires homosynaptic activity. J Neurophysiol 98(2):1048–1051

Andersen P, Morris R, Amaral D, Bliss T, O'Keefe J (2006) The hippocampus book. Oxford University Press, New York

Aradi I, Holmes WR (1999) Role of multiple calcium and calcium-dependent conductances in regulation of hippocampal dentate granule cell excitability. J Comput Neurosci 6(3):215–235

Barker JM, Boonstra R, Wojtowicz JM (2011) From pattern to purpose: how comparative studies contribute to understanding the function of adult neurogenesis. Eur J Neurosci 34(6):963–977

Benuskova L, Abraham WC (2007) STDP rule endowed with the BCM sliding threshold accounts for hippocampal heterosynaptic plasticity. J Comput Neurosci 22(2):129–133

Bienenstock EL, Cooper LN, Munro PW (1982) Theory for the development of neuron selectivity: orientation specificity and binocular interaction in visual cortex. J Neurosci 2(1):32–48

Bliss TV, Cooke SF (2011) Long-term potentiation and long-term depression: a clinical perspective. Clinics 66:3–17

Bowden JB, Abraham WC, Harris KM (2012) Differential effects of strain, circadian cycle, and stimulation pattern on LTP and concurrent LTD in the dentate gyrus of freely moving rats. Hippocampus 22(6):1363–1370

Bush D, Philippides A, Husbands P, O'Shea M (2010) Reconciling the STDP and BCM models of synaptic plasticity in a spiking recurrent neural network. Neural Comput 22(8):2059–2085

Chistiakova M, Bannon NM, Bazhenov M, Volgushev M (2014) Heterosynaptic plasticity multiple mechanisms and multiple roles. Neuroscientist, 1073858414529829

Christie BR, Abraham WC (1992) Priming of associative long-term depression by theta frequency synaptic activity. Neuron 8:79–84

Clopath C, Büsing L, Vasilaki E, Gerstner W (2010) Connectivity reflects coding: a model of voltage-based STDP with homeostasis. Nat Neurosci 13(3):344–352

Cooper LN, Intrator N, Blais BS, Shouval HZ (2004) *Theory of cortical plasticity*, volume 150. World Scientific Singapore

DAngelo E, Solinas S, Garrido J, Casellato C, Pedrocchi A, Mapelli J, Gandol D, Prestori F (2013) Realistic modeling of neurons and networks: towards brain simulation. Funct Neurol 28(3):153

Desmond NL, Levy WB (1982) A quantitative anatomical study of the granule cell dendritic fields of the rat dentate gyrus using a novel probabilistic method. J Comp Neurol 212:131–145

Douglas RM, Goddard GV (1975) Long-term potentiation of the perforant path-granule cell synapse in the rat hippocampus. Brain Res 86(2):205–215

Ermentrout GB, Terman DH (2010) Mathematical foundations of neuroscience. Springer

Fellous J-M, Rudolph M, Destexhe A, Sejnowski TJ (2003) Synaptic background noise controls the input/output characteristics of single cells in an in vitro model of in vivo activity. Neuroscience 122(3):811–829

Foy M (2001) Long-term depression (Hippocampus)

Gloveli T, Schmitz D, Empson RM, Heinemann U (1997) Frequency dependent information flow from the entorhinal cortex to the hippocampus. J Neurophysiol 78(6):3444–3449

Herz AV, Gollisch T, Machens CK, Jaeger D (2006) Modeling single neuron dynamics and computations: a balance of detail and abstraction. Science 314(5796):80–85

Hines ML, Carnevale NT (1997) The NEURON simulation environment. Neural Comput 9(6):1179–1209

Izhikevich EM (2004) Which model to use for cortical spiking neurons? IEEE Trans Neural Netw 15(5):1063–1070

Izhikevich EM, Desai NS (2003) Relating stdp to bcm. Neural Comput 15(7):1511–1523

Jedlicka P (2002) Synaptic plasticity, metaplasticity and BCM theory. Bratisl Lek Listy 103(4/5):137–143

Lin Y-W, Yang H-W, Wang H-J, Gong C-L, Chiu T-H, Min M-Y (2006) Spike-timing-dependent plasticity at resting and conditioned lateral perforant path synapses on granule cells in the dentate gyrus: different roles of N-methyld-aspartate and group I metabotropic glutamate receptors. Eur J Neurosci 23(9):2362–2374

McNaughton BL, Barnes CA (1977) J Comp Neurol 175:439–454

Morrison D (2012) Metaplasticity: A new frontier in the neural representation of memory. University of British Columbia's Undergraduate Journal of Psychology, 1

Santhakumar V, Aradi I, Soltesz I (2005) Role of mossy fiber sprouting and mossy cell loss in hyperexcitability: a network model of the dentate gyrus incorporating cell types and axonal topography. J Neurophysiol 93(1):437–453

Scharfman HE (2011) *The dentate gyrus: a comprehensive guide to structure, function, and clinical implications: a comprehensive guide to structure, function, and clinical implications*, Volume 163. Elsevier

Shirrafiardekani A, Benuskova L, Frauendiener J (2017) A voltage based metaplasticity rule applied to the model hippocampal granule cell accounts for homeostatic heterosynaptic plasticity. J Neural Plast 5018563.vl (Under Review)

Sjöström PJ, Gerstner W (2010) Spike-timing dependent plasticity. Scholarpedia J 5:1362. https://doi.org/10.4249/scholarpedia.1362

Snyder J, Kee N, Wojtowicz J (2001) Effects of adult neurogenesis on synaptic plasticity in the rat dentate gyrus. J Neurophysiol 85(6):2423–2431

Sterratt D, Graham B, Gillies A, Willshaw D (2011) Principles of computational modelling in neuroscience. Cambridge University Press

Tejada J, Garcia-Cairasco N, Roque AC (2014) Combined role of seizure-induced dendritic morphology alterations and spine loss in newborn granule cells with mossy fiber sprouting on the hyperexcitability of a computer model of the dentate gyrus. PLoS Comput Biol 10(5):e1003601. https://doi.org/10.1371/journal.pcbi.1003601

Ulinski PS (1999) Neural mechanisms underlying the analysis of moving visual stimuli. In: Models of cortical circuits. Springer, 283–399

Van Rossum MC, Bi GQ, Turrigiano GG (2000) Stable Hebbian learning from spike timing-dependent plasticity. J Neurosci 20(23):8812–8821

Watt AJ, Desai NS (2010). Homeostatic plasticity and STDP: keeping a neurons cool in a fluctuating world. *Spike-timing dependent plasticity*,

Yger P, Gilson M (2015) Models of metaplasticity: a review of concepts. Front Comput Neurosci 9:138

Yuen GL, Durand D (1991) Reconstruction of hippocampal granule cell electro-physiology by computer simulation. Neuroscience 41:411–423

Zheng Y, Schwabe L, Plotkin JL (2014) Location-dependent dendritic computation in a modeled striatal projection neuron. In: International conference on artificial neural networks. Springer, 741–748

Genome-Wide Associations of Schizophrenia Studied with Computer Simulation

Samuel A. Neymotin, Nathan S. Kline, Mohamed A. Sherif, Jeeyune Q. Jung, Joseph J. Kabariti, and William W. Lytton

Schizophrenia: Clinical Pathways of Disorder

A recent genome-wide association study (GWAS) demonstrated 108 association loci that are associated with development of schizophrenia (Schizophrenia Working Group, 2014). These are just the sites that can be implicated using the statistical power conferred by current data. It is expected that many more sites will be uncovered as new studies use larger numbers of cases and controls. The number of likely associated loci is uncertain, but one estimate suggests it may be in the thousands International Schizophrenia Consortium and Others et al. (2009). For any given patient, only a small subset of these locations will show mutations. The

S. A. Neymotin (✉)
Department of Neuroscience, Brown University, Providence, RI, USA
e-mail: samuel_neymotin@brown.edu

N. S. Kline
Institute for Psychiatric Research, Orangeburg, NY, USA

M. A. Sherif
Yale University, New Haven, CT, USA

VA Connecticut Healthcare System, West Haven, CT, USA

Department Physiology and Pharmacology, SUNY Downstate, Brooklyn, NY, USA

J. Q. Jung · J. J. Kabariti
Department Physiology and Pharmacology, SUNY Downstate, Brooklyn, NY, USA

W. W. Lytton
Department Neurology, Kings County Hospital Center, Brooklyn, NY, USA

Department Physiology and Pharmacology, SUNY Downstate, Brooklyn, NY, USA

V. Cutsuridis et al. (eds.), *Hippocampal Microcircuits*, Springer Series in Computational Neuroscience, https://doi.org/10.1007/978-3-319-99103-0_21

clinical pathway hypothesis for polygenic diseases predicts that the various sites of damage associated with a given disease reflect sets of mutationally damaged genes that together produce the disease (we will use the term *clinical pathway* so as to distinguish it from the traditional definition of a *pathway* as a biochemical sequence) (Sullivan, 2012). What is a clinical pathway? This term remains weakly defined and will differ between diseases and even within a single disease. For example, multiple clinical pathways in schizophrenia may well involve (1) developmental sequences, (2) intracellular cascade sequences such as second-messenger cascades in neurons, (3) genetic activation sequences or RNA transcriptional control sequences, (4) immunological and scavenging pathways (e.g., synapse and cell elimination in schizophrenia Sullivan 2012), and (5) pathways of dynamical physiological interactions that together provide physiological activity.

Schizophrenia is triggered by insults and anomalies that act at various times of life. Susceptibility at each of these stages of pathological influence would be expected to be associated with a different clinical pathway or set of clinical pathways. One clinical pathway would confer susceptibility to the perinatal insult that is believed to predispose to the disease. Subsequently, there is a likelihood of a clinical pathway involving synaptic pruning in late adolescence (Sekar et al., 2016). This may be the same or different from a clinical pathway that confers susceptibility in response to external stress, an important factor in the onset of clinical disease (Tost and Meyer, 2012). Finally, there will be one or more clinical pathways that produce the various signs and symptoms of schizophrenia – cognitive disorder, positive symptoms such as hallucinations, and negative symptoms of social withdrawal.

Given this complexity, it is expected that multiple pathway "hits," with various hits within each involved pathway, determine the clusters of clinical manifestations that make it difficult to clearly define schizophrenia or to define clinical subtypes (Rajiv et al., 2013). The welter of schizophrenia definitions, and the mix of symptoms, has led the US National Institute of Mental Health to move away from symptom-based disease definition in favor of future biomarker-based diagnosis (Insel et al., 2010). In this context, one notes the genetic overlap with other disorders that feature particular symptoms of schizophrenia: bipolar disorder in which one may have hallucinations and autism whose characteristic feature is social withdrawal (Sullivan, 2012). At some schizophrenia-associated loci, a more damaging mutation will produce one of these other disorders, rather than a more severe form of schizophrenia.

In this chapter, we discuss our explorations of alterations in theta and gamma activity in hippocampal area CA3, using multiscale modeling to show how changes in ion channels at molecular scale will alter network activity. We then show how anomalies in brain waves can be correlated with explicit alterations in information flow (measured using information theory) and thereby could help explain alterations in cognitive function.

I_h and NMDA: Clinical Pathway Partners?

We focus here on two identified genomic/proteomic factors that we have studied through physiological simulation: I_h channels and NMDA receptors (Neymotin et al., 2011b, 2013, 2016). We propose that these mutations will be part of the same clinical pathway involved in generating oscillations (a potential biomarker) and in producing the cognitive dysfunction hypothesized to be an underlying disorder in schizophrenia (Nicolas et al., 2013). I_h current is mediated by hyperpolarization-activated cyclic nucleotide-gated (HCN) channels. A putative mutation in the HCN1 gene (5p21) is near one of the 108 loci implicated in schizophrenia (Schizophrenia Working Group, 2014). The other implicated mutation that we study here is in the GRIN2A gene (glutamate ionotropic NMDA-type receptor subunit 2A on 16p13), a subunit that forms part of the ionotropic NMDA-type glutamatergic receptor (NMDAR). Changes in either the NMDAR synaptic current or in I_h will alter cortical oscillations. Of course, additional factors will also be expected to be involved in this clinical pathway, altering cortical oscillations. For example, basket cells are reduced in schizophrenia (David et al., 2012). These cells play an important role in generating fast oscillations through PING (pyramidal-interneuron network gamma) and ING (interneuron network gamma) mechanisms (Cobb et al., 1995; Lytton and Sejnowski, 1991).

A recent set of observations indicates that patients diagnosed with schizophrenia have increased spontaneous and driven gamma (30–80 Hz) compared to controls (Hirano, 2015). Other studies have shown differences in gamma activation between patients and controls performing complicated recognition tasks (Uhlhaas et al., 2008; Uhlhaas and Singer, 2010). These changes in gamma are similar to what is seen in animal models of schizophrenia (Lazarewicz, 2010; Lee et al., 2014). Animal models also show a reduction in theta power (6–10 Hz with different ranges by species). We focused on these two physiological markers, using alterations in gamma or in theta-gamma balance as an indicator of pathology in our simulations. Network oscillation anomalies are also implicated in the genesis and expression of many other neurological and psychiatric disorders, including the epilepsies (Lytton, 2008) and mild cognitive impairment (Moretti et al., 2013; de Haan et al., 2012).

The **HCN** ion channel, providing current I_h, is a voltage-gated channel involved in maintaining resting potential, augmenting subthreshold resonance, and providing depolarization with activation (Accili et al., 2002; Chen et al., 2001; Santoro and Baram, 2003; Zemankovics et al., 2010; Dyhrfjeld-Johnsen et al., 2008, 2009; Poolos et al., 2002). HCN has four defined isoforms (HCN1–HCN4); HCN1 and HCN2 are the dominant forms in neurons. HCN1 is implicated in schizophrenia. Inhomogeneous isoform distributions of the HCN channel lead to differential expression and modulation of I_h in different cell types (Accili et al., 2002; Aponte et al., 2006; Bender et al., 2001; Santoro and Baram, 2003). Neurotransmitters from different brain areas and local neuromodulators provide multiple pathways for regulating I_h (Hagiwara and Irisawa, 1989). Multiple functions, multiple types, and multiple routes for modulation make HCN a complex control point in the circuit.

HCN channels are unusual in terms of their behavior compared to other voltage- and ligand-sensitive membrane channels. The HCN-associated current is called an *anomalous rectifier* because it is activated by neuronal membrane hyperpolarization (hence I_h), rather than by the depolarization that is typical for most voltage-gated ion channels. I_h is also unusual in having an intermediate reversal potential (-30 to -40 mV).

The focus of much literature on **NMDAR** has been on the role that it plays in plasticity, specifically on long-term potentiation. In that context, NMDAR serves an adjunctive role by signaling, via calcium levels, an activity level which is then translated into altered synaptic strength (Lisman and Raghavachari, 2006; Yafell et al., 2007). A separate, but likely related, aspect of NMDAs role is as a synaptic receptor and ionotropic channel that complements AMPA in excitatory activation of a postsynaptic cell (Chover et al., 2001; Hasselmo and Bower, 1992; Hasselmo, 2005). NMDAR is voltage-dependent via a Mg^{+2} blockade that is relieved by postsynaptic depolarization. It shows permeability to both Ca^{2+} and Na^{+} so that activation provides a local depolarization, as well as Ca^{2+} signaling of postsynaptic cascades. These direct ionotropic effects provide a postsynaptic activation that is complementary to the more rapid, earlier, and less prolonged excitatory postsynaptic potentials due to AMPA. This complementarity can be viewed as dynamically providing the network with a second matrix of connectivity (Chover et al., 2001). Prior to the evidence from GWAS, the psychotomimetic effects of NMDA blockade with drugs such as phencyclidine (PCP) and ketamine had already suggested that NMDARs might play an important role in schizophrenia and other psychotic disorders.

Network Simulation

Oscillation generation involves interactions among inhibitory cells (ING) and between inhibitory cells and pyramidal cells (PING) (Börgers and Kopell, 2003). As in other brain regions, I_h is present in all cell types in the hippocampus. In our network simulations, we model pyramidal cells (PYR), basket cells (BAS), and oriens lacunosum-moleculare (OLM) cells. Interneurons in our network are driven by oscillatory output from the medial septum. Our network consisted of 800 five-compartment PYR cells, 200 one-compartment BAS cells, and 200 one-compartment OLM cells (Fig. 1) (Neymotin et al., 2013). The model contained 152,000 synapses, with baseline activity maintained by providing background white-noise external inputs. Basket cells synapsed on somata of both pyramidal and other basket cells. OLM cells synapsed on pyramidal cell apical dendrites. Connectivity was determined by connection densities so that specific connectivity in a given network was random. Parameters were based on the literature where available, as well as on previous computer models (Cutsuridis et al., 2010; Neymotin et al., 2011b; Tort et al., 2007; Wang, 2002; Wang and Buzsaki, 1996; White et al., 2000).

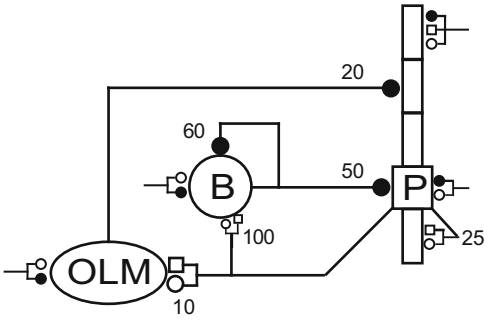

Fig. 1 Schematic representation of the network. Each symbol represents a population: 800 pyramidal cells (P, PYR), 200 basket cells (B, BAS), and 200 oriens lacunosum-moleculare (OLM) cells. Convergence values (number of inputs for an individual synapse) are shown near synapses: $GABA_A$ receptors (filled circles), AMPA receptors (open circles), and NMDA receptors (open squares). External stimulation from other areas was modeled by synaptic bombardment (synapses with truncated lines)

The basic simulation produces robust theta and gamma activity (Fig. 2), measured from an LFP (top) generated from the pyramidal cells (spikes in red in raster plot at bottom). The interplay among the BAS cells produced robust ING (Buzsáki and Wang, 2012; Lytton and Sejnowski, 1991; White et al., 2000), visualizable in the raster by noting the strong rapid synchrony among the BAS cells in green (see also Fig. 3 from Neymotin et al. 2013). Theta oscillation was augmented by oscillatory driving from the medial septum via the OLM (blue) and basket cells (green). Theta was still present in the absence of medial septum drive (Neymotin et al., 2011b).

HCN Effects on I_h

Through its non-zero conductance and a relatively depolarized reversal potential (E_h of −40 to −30), I_h contributes to neuronal resting membrane potential (RMP). Because of this, increase in I_h produced depolarization, leading to increased cell firing. Depolarization also increased the driving force for inhibition and decreased the driving force for excitation. Paradoxically however, EPSP strength *increased* with increasing I_h due to a boosting effect through partial activation of sodium currents.

Control of I_h by the second messenger cAMP could permit I_h to function as a control point for hippocampal oscillations. Differential activation of cAMP in different cell populations would then allow I_h to have different effects depending on this modulatory activation pattern. We hypothesized that I_h control on different populations would produce specific gamma or theta frequency shifts and changes in power. We look first at effects on the BAS cells, which we predicted would give strong gamma control, since BAS activity is associated with production of gamma

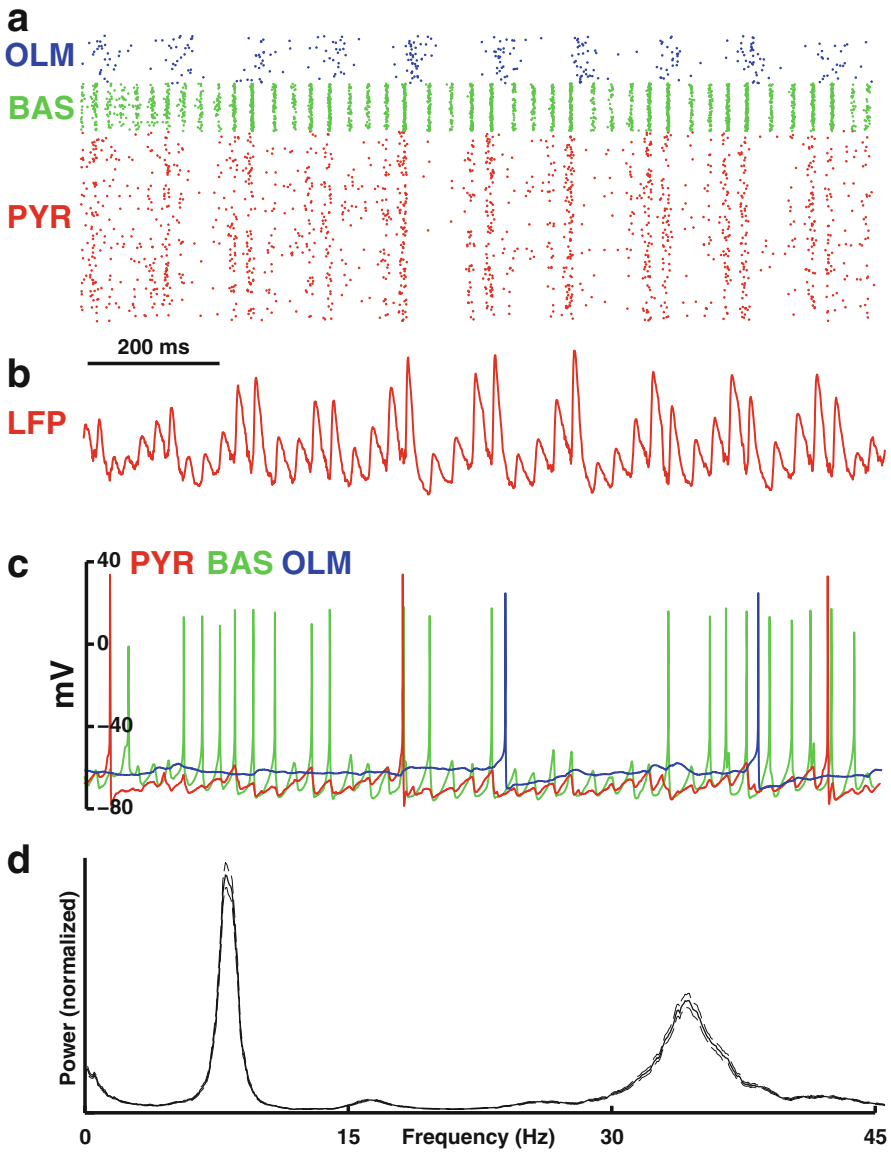

Fig. 2 Network generates theta and gamma activity. Raster plot (bottom) shows firing times of individual cells – note the strong gamma in the green BAS cells (∼8 cycles in 200 ms) and theta from the blue OLM cells (∼2 cycles in 200 ms). Spectrum from local field potential (LFP, red at top) generated by PYR cells. (Adapted from Neymotin et al. 2013)

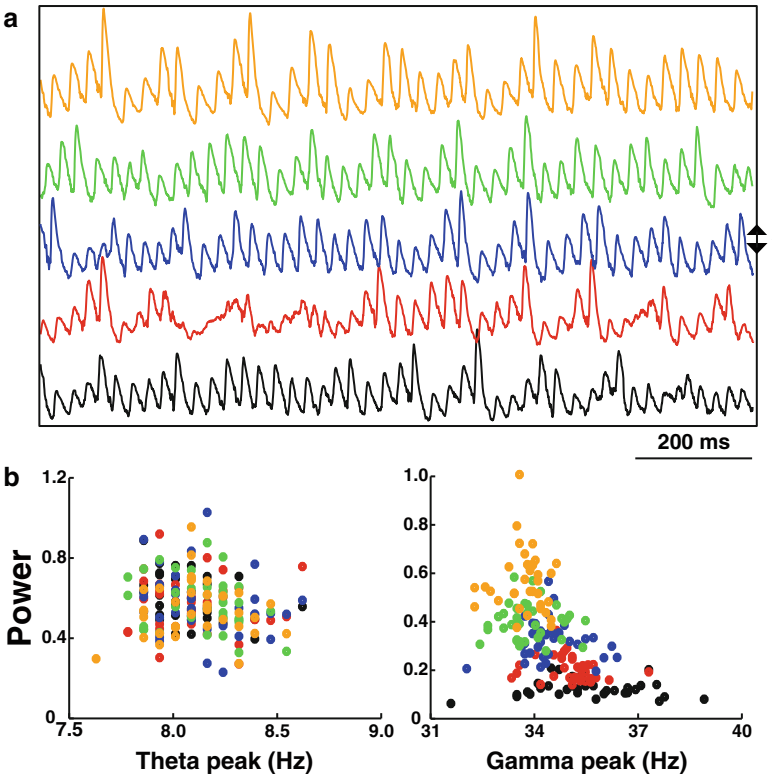

Fig. 3 Gamma power increases with I_h increase in basket (BAS) cells. (**a**) Local field potentials (LFPs) from one simulation show fast frequency power increasing with increasing BAS I_h. Center shows scatter plots of theta and gamma peak frequency and power (arbitrary units) – each point from a single simulation with different random activation and wiring. Bottom shows the average power spectrum across simulations bounded by standard error of the mean (SEM). n = 180 simulations; (Adapted from Neymotin et al. 2013)

through both ING and PING. The simulations confirmed this effect on gamma and showed inconsistent effects on theta with different randomized networks (Fig. 3; networks are randomized with different white-noise drive and different specific wiring). With increased I_h the amplitude of gamma increased (Fig. 3, top: green, orange LFPs). With decreased I_h, gamma amplitude was reduced (red, black LFPs). The scatter plots at center of Fig. 3 demonstrate the variability in network dynamic effects due to different random seeds. The average power spectra (Fig. 3, bottom) demonstrated the overall effect on gamma. Increased gamma with increased I_h can be explained as a consequence of the increased IPSP amplitude which will tend to augment ING effects particularly, producing greater cooperativity among the BAS cells (Carlos, 1999). These increased IPSPs also increased the gamma period.

Alteration of I_h in OLM did not produce regular-tending effects (Fig. 4 top). Change of OLM I_h in either direction tended to abolish theta – note near-zero values

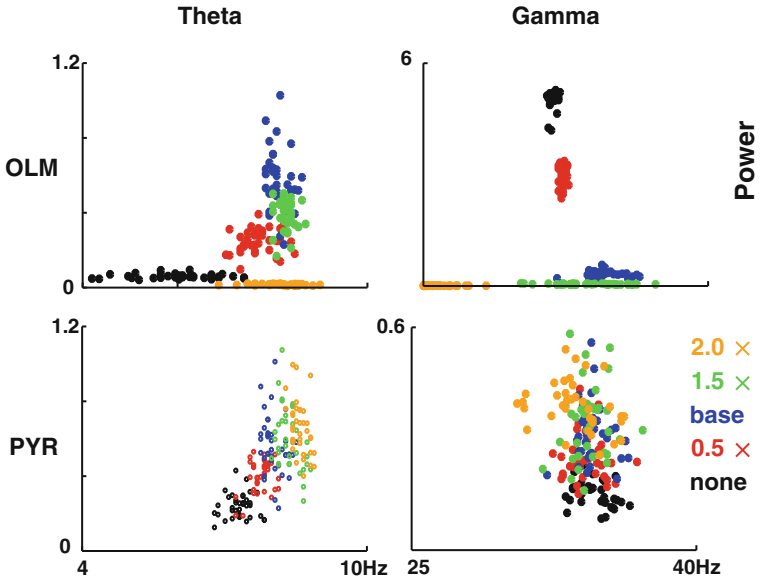

Fig. 4 Changes in theta and gamma power and frequency with alteration in OLM and PYR I_h. Alterations in OLM in either direction tended to wipe out theta. Increased OLM I_h also reduced gamma while decreased produced a high gamma state (note y-axis up to 6 in upper right panel). Increased PYR I_h produced relatively isolated effect on theta – increasing theta power and frequency with little effect on gamma. (Adapted from Neymotin et al. 2013)

for 2× (orange) and 0× (black) at upper left. Reduced OLM I_h gave extremely high gamma – 0× (black) and 0.5× (red) at upper right (note maximum y-axis value here). I_h increase in PYR produced augmentation of theta power with a slight shift to higher frequency and little change in gamma (Fig. 4 bottom). This effect was mediated by increased PYR firing driving OLM firing. From Figs. 3 and 4, we see that BAS I_h could be a control point for gamma, while PYR I_h could function as a control point for theta modulation. Manipulating both PYR and BAS I_h together produced augmentation of both theta and gamma power in tandem (Fig. 5). This was associated with an increase in theta frequency with a decrease in gamma frequency. Alteration of I_h at all three sites (PYR, BAS, OLM) gave a pattern of change similar to that of OLM alone (not shown).

Pyramidal cell I_h control of theta with basket cell I_h control of gamma suggested that simultaneous control could be achieved through comodulation of I_h in both of these cell types. This could occur either through similar control mechanisms or through more complex modulation utilizing different second messengers, different isoform second-messenger sensitivity, or neuromodulators with differing downstream effects. Cyclic adenosine monophosphate (cAMP) selectively modulates HCN2 (Wahl-Schott and Biel, 2009; Zong et al., 2012), and p38 mitogen-activated protein kinase (MAP kinase) modulates HCN1 (Nicholas et al., 2006). We note here that this type of complex comodulation control mechanisms would provide many

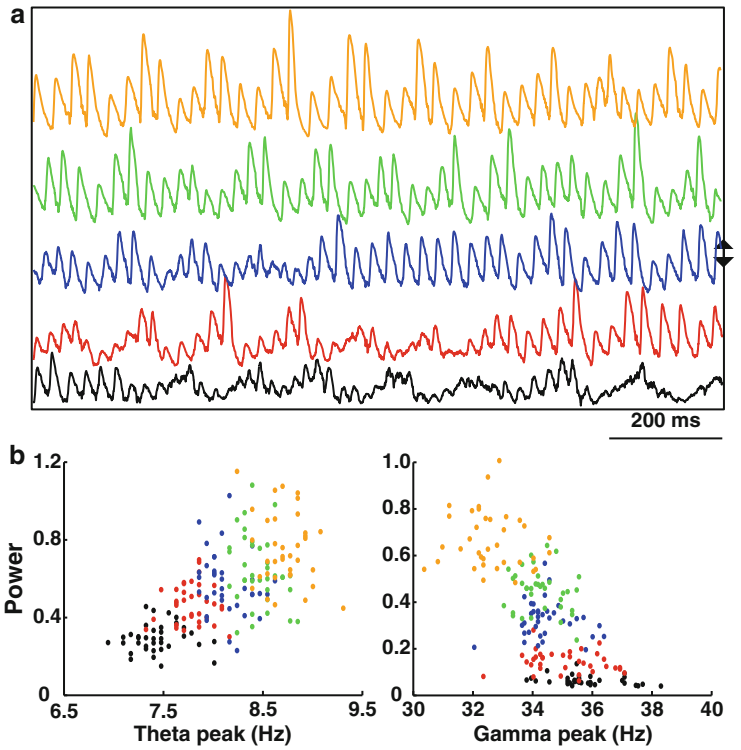

Fig. 5 Changes in theta and gamma power and frequency with simultaneous alteration in PYR and BAS I_h. Augmentation at these two sites increased power in both frequency bands while increasing theta and decreasing gamma frequency

points of vulnerability along a clinical pathway, points that could be detected in the clinical population via GWAS.

Simultaneous increase of I_h at both PYR and BAS locations produced power increases in both theta and gamma (Fig. 5). Power increases and frequency shifts seen with comodulation were similar to those produced by modulation of each independently – compare with Fig. 4 for effects on theta (lower left) and Fig. 3 for effects on gamma (arrow in Fig. 3). Relatively little cross interference was seen, not surprising in that each locus of control showed such specific effects on one frequency band, with little effect on the other. This independence was confirmed by independently altering PYR and BAS I_h (Fig. 6). There was practically no influence of BAS I_h on theta (left panel): power gradually increased with increased PYR I_h along y direction with almost no alteration with changed BAS I_h (x-axis). There was however some influence of PYR I_h on gamma (center panel): high gamma required PYR I_h at or above baseline. Some effect here is expected because PYR contributes to gamma via the PING mechanism as well as by modulation of gamma by theta. This modulation of gamma by theta was measured using cross-frequency

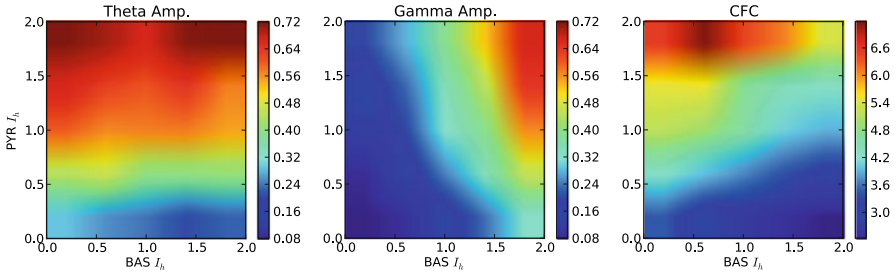

Fig. 6 Changes in theta and gamma power (z-axis color code) as function of BAS I_h augmentation (x-axis; $0\times - 2\times$ baseline values as before) and PYR I_h augmentation (y-axis; $0\times - 2\times$ baseline). Third panel shows strength of influence of theta on gamma at different values using cross-frequency coherence (CFC)

coherence (CFC; right panel): high modulation of gamma was seen with the high theta associated with high PYR I_h. The influence of BAS I_h on CFC was more subtle, with the strongest modulation seen at relatively low values of BAS I_h. With high values of BAS I_h, the powerful gamma is high at all times and is unmodulated. Modulation of spiking by gamma and of gamma by theta has been suggested as a mechanism of item separation for short-term memory (Lisman and Idiart, 1995).

GRIN2A Effects on NMDA

GRIN2A encodes the NR2A subunit of the NMDA receptor. A mutation in this subunit could potentially alter one or more attributes of this synaptic channel, including conductance, Mg^{+2} responsivity, and Zn^{+2} sensitivity (Cull-Candy et al., 2001). For these simulations, we assumed that the mutation would reduce NMDA conductance and examined how decreased NMDA conductance would change network properties. As shown in Fig. 1, NMDARs are located at each of the three cell locations in the circuit (squares). Reducing NMDA conductance at each location produces different effects on theta and gamma waves: $\downarrow\theta\downarrow\gamma$ at PYR, $\uparrow\theta\downarrow\gamma$ at BAS, and $\downarrow\theta\uparrow\gamma$ at OLM locations (Fig. 7). Combinations of block at two or more locations generally produced the $\downarrow\theta\downarrow\gamma$ pattern of PYR blockage (Neymotin et al., 2011b). As noted above, both animal model and human studies of schizophrenia show gamma increase, and animal models also show theta decrease. We therefore predict that schizophrenia-associated mutations in GRIN2A would primarily reduce the conductance for OLM NMDAR, producing this increased gamma and decreased theta. This further predicts that one or both of the OLM NMDAR NR2 wild-type isoforms would be NR2A. This could be tested in vitro using the characteristic effects of TPEN (a zinc chelator) on NR2A-containing NMDARs (Cull-Candy et al., 2001). An alternative hypothesis would be that gamma increase could be produced by a GRIN2A-based NR2A conductance *increase* at one of the other two sites, BAS or PYR.

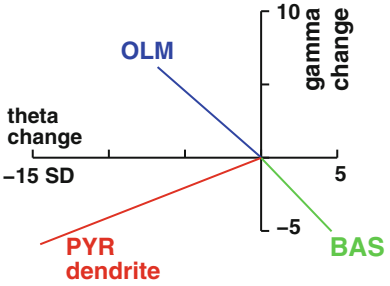

Fig. 7 Changes in theta and gamma power with NMDA conductance reduction at three locations. OLM NMDA block increases gamma and decreases theta. PYR dendrite NMDA block produces decrease in both bands. BAS NMDA block produces reduction in gamma and increase in theta. Axes are in units of standard deviation from the mean compared to control based on 25 different simulations with different seeds. (Adapted from Fig 6 of Neymotin et al. 2011b)

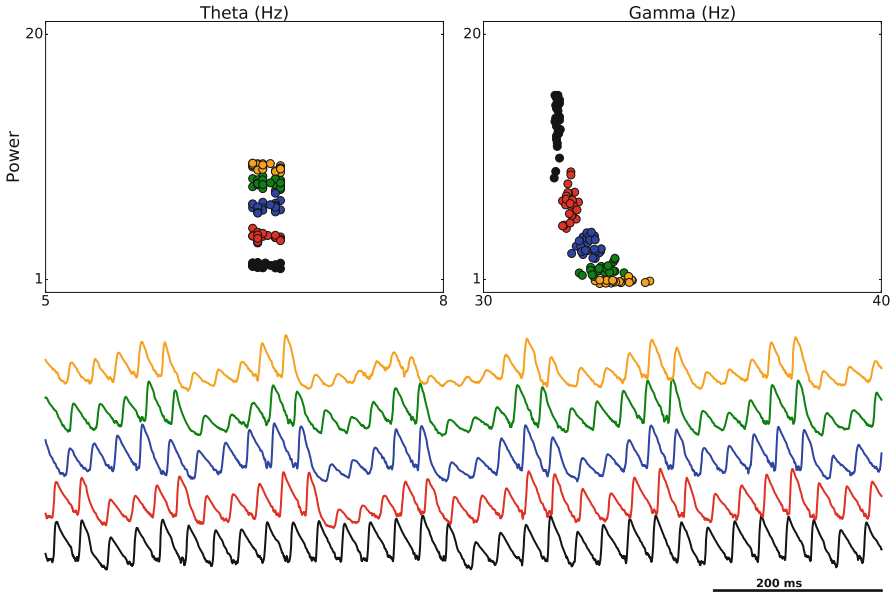

Fig. 8 Shift in theta and gamma power as a function of OLM NMDAR decreased conduction from orange (high conductance, wild type) to lower conductance values in sequence: green, blue, red, black. Decreased conductance here leads to greater gamma. Note that *y* scale (power) in these panels differ from those in prior figures due to a different algorithm having been used to calculate LFP

Gradual reduction of OLM NMDA conductance produced gradual augmentation of gamma with decrement in theta power, associated with a slight shift of gamma peak frequency (Fig. 8). Note that the increase in gamma seen here occurs with *decreased* NMDAR conductance, opposed to the direction of effect of I_h, where

increased gamma was seen with increased I_h conductance in BAS (Fig. 3). With OLM NMDAR conductance decrease, we have a single location which alters both gamma and theta in tandem – increasing gamma and reducing theta. By contrast, when changing I_h we found that one location, BAS I_h, primarily controlled gamma, while another locations, PYR I_h, controlled theta (Fig. 6).

Information Flow-Through

In addition to assessing the effects on frequency, we evaluated how alterations in dynamics would change the ability of our CA3 network to accurately convey signals. This is important because it starts to make the connection between dynamics – the study of how neurons and networks are active over time through spiking and oscillations – and *information*, in the Shannon information theoretic sense (Claude and Warren, 1949). Shannon information theory is concerned with abstract symbols and signals rather than with the meaning, if any, of a symbol or signal. However, in the quest to examine correlation and causality between neurodynamics and cognitive representations, information theory does represent an important first step. This connection is particularly relevant to schizophrenia, whose manifestations include alterations in thought processing, changes in cognition and sensory processing, and difficulties in distinguishing external stimuli from internal activations – hallucinations.

It is currently believed that the pathology of schizophrenia involves a *cognitive core* that underlies the more obvious positive symptoms (e.g., hallucinations and delusions) and negative symptoms (e.g., social withdrawal) (Silverstein et al., 2006; Uhlhaas et al., 2006b,c). The difficulty in cognitive coordination associated with schizophrenia can be shown by assessing the patient's ability to identify a complex object, a gestalt. Gestalt perception requires *binding* many individual aspects of a scene, pulling them together to see an object – for example, the camouflaged animal in Fig. 9 (Uhlhaas and Silverstein, 2005). Gestalt perception requires coordination of activity across multiple areas of cortex, all the more so when a perception is multisensory rather than just visual. This *neural coordination* is postulated to underlie the *cognitive coordination* required for gestalt perception. Neural coordination is thought to be mediated by ensemble formation by matching of firing through oscillations in gamma and beta bands (Dumenko, 2002; Fries et al., 2007; Lisman and Idiart, 1995; Uhlhaas et al., 2006a). Therefore, schizophrenia illustrates a disorder where one can start to make connections between neural and cognitive processing and between the dynamics of oscillations, the flow of information, attribution of meaning, and coordination of perception.

Technical aside We used normalized transfer entropy (nTE) to measure the influence of synaptic inputs on spiking outputs, providing our information theoretic measure of information flow-through. The nTE algorithm allows us to determine how much signal, coming in as postsynaptic potentials (PSPs), comes out of the cell

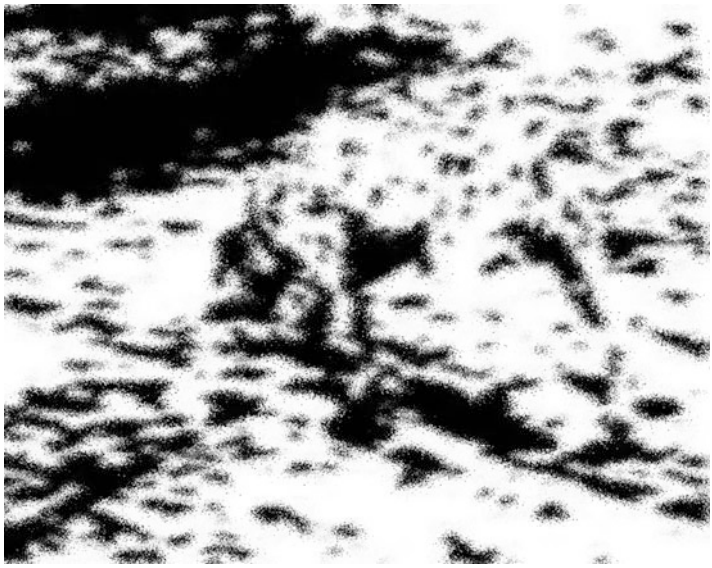

Fig. 9 There is a dog hidden in this picture. If you're having difficulty finding it search internet images "gestalt dog speckle" for a guided tour of this and related gestalt images

as a lagged spike output. A single cell, with a Poisson input and identical lagged output (incoming EPSP reliably triggers a spike), provides full input/output information transfer – a loss-less communication line. In this case, nTE would be high, although it would not be 1.0 due both to the statistical nature of the measure and of its normalization. By contrast, two identical Poisson spike trains with no lag would have nTE near 0 – previous input does not predict output at all – any effects of spike train structure on history will be subtracted out by the algorithm. When a cell is embedded within a network, in the present case within the CA3 network, the network itself interferes with the information that flows from external inputs (local afferents) through the network to outputs (local efferents). We measured information flow cell-by-cell from external inputs (the drive) onto an individual pyramidal cell, with output the spiking of that cell. We then average these to get *network nTE* (Fig. 10). This results in low nTE values that are nonetheless significant, as can be shown by assessing the change in nTE while gradually connecting up a network, starting from independent individual cells with no effect on one another (Neymotin et al., 2011a).

Reduced OLM NMDAR conductance is associated not only with higher gamma but also with reduced information flow-through (Fig. 10). A correlation between dynamics and information capacity here is not unexpected – increased gamma is an indicator of increased activity structure – spiking in the network will be more constrained by the oscillations such that individual cell spike firing will occur with a higher probability at the peak of the cycle. This increased constraint is necessarily associated with a reduction in the ability of firing to follow inputs that come in at arbitrary times, a decrease in the number of possible states of the network, and

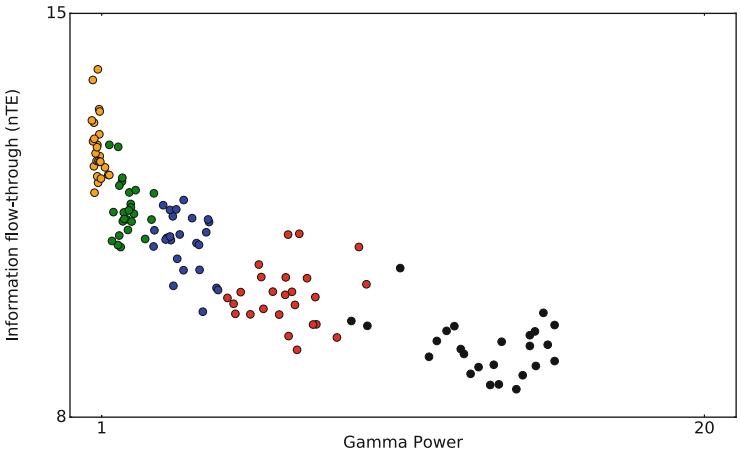

Fig. 10 Shift in gamma power (x-axis) and information flow through the network as a function of OLM NMDAR conduction from orange (high, wild type) to lower values in sequence: green, blue, red, black. As gamma increases information flow-through measured by nTE decreases

a decrease in network entropy. Borrowing a clinical term from schizophrenia, we can characterize this reduced entropy as *increased stereotypy*. This suggests that a reduction in variability of information flow, and information processing, in the gamma-bound network would be associated with a rigidity of thought and reduction of behavioral responsivity to changing circumstances. The thought patterns and behavior of patients suffering from schizophrenia do show this combination of reduced gestalt perceptual ability, decreased flexibility of thought (e.g., in paranoia), and stereotypic patterns of behavior.

Conclusions

While only including a bare sketch of the scales circled in Fig. 11, our basic multiscale model of CA3 was used to provide connections from the molecular scale of genomics, proteomics, and pharmacology to observations at the high levels of cognition and behavior. This is a "bare sketch" insofar as much detail has been omitted, even at the scales of focus – notably in the use of five-compartment models for the pyramidal cells, leaving out the complexity of ion channel distribution across the dendritic tree and the complexities of dendritic signal alterations. This particular simplification can be explained by the limitations of knowledge and the limitations of computer power. Considering HCN, there is evidence for a difference in density at different locations in the pyramidal dendritic tree, possibly associated with differential distribution of HCN1 and HCN2; however, the details of this distribution are not fully described. With regard to computational load, the use of random background inputs and random specific wiring based on wiring densities between

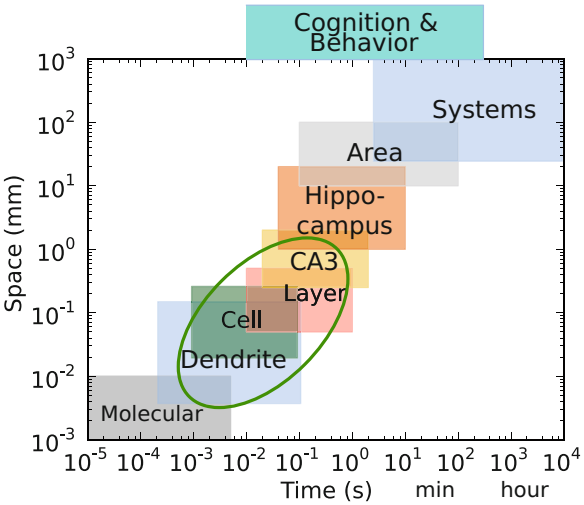

Fig. 11 Scales for multiscale modeling. We have focused on the scale from dendrite to local circuit (green circle) but have reached downward to the level of molecules (synaptic receptor and ion channel populations) and upward to the levels of information and cognition. One key aspect of the multiscale brain is the great overlap across levels. An example is the wiring complexity (network scale) of projections from dentate gyrus and entorhinal cortex which show layer scale organization which directly impacts dendritic and cell processing due to the projection of dendrite across layers

populations requires that we run multiple simulations to confirm the robustness and consistency of any result, therefore requiring that even these relatively simple simulations be run on high performance computing (HPC) platforms (Lytton et al., 2016).

Despite these many limitations, we are able to elaborate and extend existing general concepts that connect channel alterations to cell and network physiology and connect network physiology to cognitive disorders of schizophrenia, allowing us to make specific predictions that would not be possible without representing each scale with needed detail. Rather than considering the minimum detail that is needed to represent the overall phenomenon,we ask what details are needed at each scale in order to be able to represent system queries (clinical tests) or system inputs (pharmacological, electrical, behavioral treatments) at these many scales.

We predict that the HCN and GRIN2 mutations suggested for schizophrenia are involved in the same clinical pathway and that the abnormalities in this clinical pathway produce alterations in oscillations and in deficits in cognitive coordination. We specifically suggest that the GRIN2A-associated mutations associated with schizophrenia would produce *decreased* conductance for NMDARs on oriens lacunosum-moleculare (OLM) cells and that HCN1 mutations would involved *increased* conductance for I_h on basket (BAS) cells and possibly on pyramidal cells as well. These alterations would be associated with augmented gamma activity in CA3 and reduced nTE from mossy fibers input to Schaffer collateral output.

References

Accili EA, Proenza C, Baruscotti M, DiFrancesco D (2002) From funny current to HCN channels: 20 years of excitation. Physiology 17(1):32–37

Aponte Y, Lien CC, Reisinger E, Jonas P (2006) Hyperpolarization-activated cation channels in fast-spiking interneurons of rat hippocampus. J Physiol 574(1):229–243

Bender RA, Brewster A, Santoro B, Ludwig A, Hofmann F, Biel M, Baram TZ et al (2001) Differential and age-dependent expression of hyperpolarization-activated, cyclic nucleotide-gated cation channel isoforms 1–4 suggests evolving roles in the developing rat hippocampus. Neuroscience 106(4):689–698

Börgers C, Kopell N (2003) Synchronization in networks of excitatory and inhibitory neurons with sparse, random connectivity. Neural Comput 15(3):509–538

Brody CD (1999) Correlations without synchrony. Neural Comput 11(7):1537–1551

Buzsáki G, Wang XJ (2012) Mechanisms of gamma oscillations. Annu Rev Neurosci 35:203–225

Chen S, Wang J, Siegelbaum SA (2001) Properties of hyperpolarization-activated pacemaker current defined by coassembly of HCN1 and HCN2 subunits and basal modulation by cyclic nucleotide. J Gen Physiol 117(5):491–504

Chover J, Haberly L, Lytton WW (2001) Alternating dominance of NMDA and AMPA for learning and recall: a computer model. Neuroreport 12:2503–2507

Cobb SR, Buhl EH, Halasy K, Paulsen O, Somogyi P (1995) Synchronization of neuronal activity in hippocampus by individual GABAergic interneurons. Nature 378:75–78

Cull-Candy S, Brickley S, Farrant M (2001) NMDA receptor subunits: diversity, development and disease. Curr Opin Neurobiol 11(3):327–335

Cutsuridis V, Graham B, Cobb S, Vida I (2010) Hippocampal microcircuits: a computational modeler's resource book, vol 5. Springer, New York

de Haan W, van der Flier WM, Wang H, Van Mieghem PFA, Scheltens P, Stam CJ (2012) Disruption of functional brain networks in alzheimer's disease: what can we learn from graph spectral analysis of resting-state magnetoencephalography? Brain Connect 2(2):45–55

Dumenko VN (2002) Functional significance of high-frequency components of brain electrical activity in the processes of gestalt formation. Zh Vyssh Nerv Deiat Im I P Pavlova 52:539–550

Dyhrfjeld-Johnsen J, Morgan RJ, Földy C, Soltesz I (2008) Upregulated H-Current in hyperexcitable CA1 dendrites after febrile seizures. Front Cell Neurosci 2:2

Dyhrfjeld-Johnsen J, Morgan RJ, Soltesz I (2009) Double trouble? potential for hyperexcitability following both channelopathic up-and downregulation of Ih in epilepsy. Front Neurosci 3(1):25

Franck N, Duboc C, Sundby C, Amado I, Wykes T, Demily C, Launay C, Le Roy V, Bloch P, Willard D et al (2013) Specific vs general cognitive remediation for executive functioning in schizophrenia: a multicenter randomized trial. Schizophr Res 147:68–74

Fries P, Nikolic D, Singer W (2007) The gamma cycle. Trends Neurosci 30:309–316

Schizophrenia Working Group (2014) Biological insights from 108 schizophrenia-associated genetic loci. Nature 511:421–427

Hagiwara N, Irisawa H (1989) Modulation by intracellular Ca2+ of the hyperpolarization-activated inward current in rabbit single sino-atrial node cells. J Physiol 409(1):121–141

Hasselmo M (2005) Expecting the unexpected: modeling of neuromodulation. Neuron 46:526–528

Hasselmo ME, Bower JM (1992) Cholinergic suppression specific to intrinsic not afferent fiber synapses in rat piriform (olfactory) cortex. J Neurophysiol 67:1222–1229

Hirano Y, Oribe N, Kanba S, Onitsuka T, Nestor PG, Spencer KM (2015) Spontaneous gamma activity in schizophrenia. JAMA Psychiat 72:813–821

Insel T, Cuthbert B, Garvey M, Heinssen R, Pine DS, Quinn K, Sanislow C, Wang P (2010) Research domain criteria (RDoC): toward a new classification framework for research on mental disorders. Am J Psychiatry 167(7):748

International Schizophrenia Consortium and Others et al (2009) Common polygenic variation contributes to risk of schizophrenia and bipolar disorder. Nature 460(7256):748. Nature Publishing Group

Lazarewicz MT, Ehrlichman RS, Maxwell CR, Gandal MJ, Finkel LH, Siegel SJ (2010) Ketamine modulates theta and gamma oscillations. J Cogn Neurosci 22(7):1452–1464

Lee H, Dvorak D, Fenton AA (2014) Targeting neural synchrony deficits is sufficient to improve cognition in a schizophrenia-related neurodevelopmental model. Front Psychiat 5:15

Lewis DA, Curley AA, Glausier JR, Volk DW (2012) Cortical parvalbumin interneurons and cognitive dysfunction in schizophrenia. Trends Neurosci 35(1):57–67

Lisman J, Raghavachari S (2006) A unified model of the presynaptic and postsynaptic changes during LTP at CA1 synapses. Sci STKE 2006(356):re11. American Association for the Advancement of Science

Lisman JE, Idiart MAP (1995) Storage of 7 ± 2 short-term memories in oscillatory subcycles. Science 267:1512–1515

Lytton WW (2008) Computer modelling of epilepsy. Nat Rev Neurosci 9:626–637

Lytton WW, Sejnowski TJ (1991) Simulations of cortical pyramidal neurons synchronized by inhibitory interneurons. J Neurophysiol 66(3):1059–1079

Lytton WW, Seidenstein AH, Dura-Bernal S, McDougal RA, Schürmann F, Hines ML (2016) Simulation neurotechnologies for advancing brain research: parallelizing large networks in NEURON. Neural Comput 28(10):2063–2090. MIT Press

Moretti DV, Paternicò D, Binetti G, Zanetti O, Frisoni GB (2013) EEG upper/low alpha frequency power ratio relates to temporo-parietal brain atrophy and memory performances in mild cognitive impairment. Front Aging Neurosci 5:63

Neymotin SA, Hilscher MM, Moulin TC, Skolnick Y, Lazarewicz MT, Lytton WW (2013) Ih tunes theta/gamma oscillations and cross-frequency coupling in an in silico CA3 model. PLoS One 8:e76285

Neymotin SA, Jacobs KM, Fenton AA, Lytton WW (2011a) Synaptic information transfer in computer models of neocortical columns. J Comput Neurosci 30(1):69–84

Neymotin SA, Lazarewicz MT, Sherif M, Contreras D, Finkel LH, Lytton WW (2011b) Ketamine disrupts theta modulation of gamma in a computer model of hippocampus. J Neurosci 31(32):11733–11743

Neymotin SA, McDougal RA, Bulanova AS, Zeki M, Lakatos P, Terman D, Hines ML, Lytton WW (2016) Calcium regulation of HCN channels supports persistent activity in a multiscale model of neocortex. Neurosci 316(1):344–366

Poolos NP, Migliore M, Johnston D (2002) Pharmacological upregulation of h-channels reduces the excitability of pyramidal neuron dendrites. Nat Neurosci 5(8):767–774

Poolos NP, Bullis JB, Roth MK (2006) Modulation of h-channels in hippocampal pyramidal neurons by p38 mitogen-activated protein kinase. J Neurosci 26(30):7995–8003

Santoro B, Baram TZ (2003) The multiple personalities of h-channels. Trends Neurosci 26(10):550–554

Sekar A, Bialas AR, Rivera H, Davis A, Hammond TR, Kamitaki N, Tooley K, Presumey J, Baum M et al Schizophrenia risk from complex variation of complement component 4. Nature 530:177–183 (2016)

Serulle Y, Zhang S, Ninan I, Puzzo D, McCarthy M, Khatri L, Arancio O, Ziff EB (2007) A GLuR1-cGKII interaction regulates ampa receptor trafficking. Neuron 56:670–688

Shannon CE, Weaver W (1949) The mathematical theory of communication. U Illinois Press, Urbana

Silverstein SM, Hatashita-Wong M, Schenkel LS, Wilkniss S, Kovács I, Fehér A, Smith T, Goicochea C, Uhlhaas P, Carpiniello K, Savitz A (2006) Reduced top-down influences in contour detection in schizophrenia. Cogn Neuropsychiatry 11:112–132

Sullivan PF (2012) Puzzling over schizophrenia: schizophrenia as a pathway disease. Nat Med 18:210–211

Tandon R, Gaebel W, Barch DM, Bustillo J, Gur RE, Heckers S, Malaspina D, Owen MJ, Schultz S, Tsuang M et al (2013) Definition and description of schizophrenia in the DSM-5. Schizophr Res 150:3–10

Tort AB, Rotstein HG, Dugladze T, Gloveli T, Kopell NJ (2007) On the formation of gamma-coherent cell assemblies by oriens lacunosum-moleculare interneurons in the hippocampus. Proc Nat Acad Sci 104:13490–13495

Tost H, Meyer-Lindenberg A (2012) Puzzling over schizophrenia: schizophrenia, social environment and the brain. Nat Med 18:211–213

Uhlhaas PJ, Silverstein SM (2005) Perceptual organization in schizophrenia spectrum disorders: empirical research and theoretical implications. Psychol Bull 131:618–632

Uhlhaas PJ, Singer W (2010) Abnormal neural oscillations and synchrony in schizophrenia. Nat Rev Neurosci 11(2):100–113

Uhlhaas PJ, Linden DE, Singer W, Haenschel C, Lindner M, Maurer K, and Rodriguez E. (2006a) Dysfunctional long-range coordination of neural activity during gestalt perception in schizophrenia. J Neurosci 26:8168–8175

Uhlhaas PJ, Phillips WA, Mitchell G, Silverstein SM (2006b) Perceptual grouping in disorganized schizophrenia. Psychiatry Res 145:105–117

Uhlhaas PJ, Phillips WA, Schenkel LS, Silverstein SM (2006c) Theory of mind and perceptual context-processing in schizophrenia. Cogn Neuropsychiatry 11:416–436

Uhlhaas PJ, Haenschel C, Nikolić D, Singer W (2008) The role of oscillations and synchrony in cortical networks and their putative relevance for the pathophysiology of schizophrenia. Schizophr Bull 34(5):927–943

Wahl-Schott C, Biel M (2009) HCN channels: structure, cellular regulation and physiological function. Cel Mol Life Sci 66(3):470–494

Wang XJ (2002) Pacemaker neurons for the theta rhythm and their synchronization in the septohippocampal reciprocal loop. J Neurophysiol 87(2):889–900

Wang XJ, Buzsaki G (1996) Gamma oscillation by synaptic inhibition in a hippocampal interneuronal network model. J Neurosci 16(20):6402–6413

White JA, Banks MI, Pearce RA, Kopell NJ (2000) Networks of interneurons with fast and slow γ-aminobutyric acid type A (GABAA) kinetics provide substrate for mixed gamma-theta rhythm. Proc Nat Acad Sci 97(14):8128–8133

Zemankovics R, Káli S, Paulsen O, Freund TF, N Hájos (2010) Differences in subthreshold resonance of hippocampal pyramidal cells and interneurons: the role of h-current and passive membrane characteristics. J Physiol 588(12):2109–2132

Zong X, Krause S, Chen CC, J Krüger, Gruner C, Cao-Ehlker X, Fenske S, Wahl-Schott C, Biel M (2012) Regulation of hyperpolarization-activated cyclic nucleotide-gated (HCN) channel activity by cCMP. J Biol Chem 287(32):26506–26512

Modelling Epileptic Activity in Hippocampal CA3

Sanjay M. and Srinivasa B. Krothapalli

Abstract This chapter is about developing a computational model of the mechanism of epileptic activity generation in the hippocampal CA3 subfield, a very well-known area that initiates it presumably due to high recurrent connectivity between its constituent neurons, specifically, epileptic activity due to degeneration of OLM interneurons. The model consists of 800 pyramidal neurons, 200 basket and 200 OLM interneurons. The degeneration of OLM interneurons primarily leads to reduced dendritic inhibition on pyramidal neurons. What this leads to is a cascade of network changes including chemical changes as validated by published literature. The biophysical features of the model are explained, and how these changes lead to epileptic activity is described and modelled. Such a proposed model would help to investigate if the progression to epileptic activity generation can be contained at some stage. This could imply a therapeutic strategy for validation using further experimental studies, hence the relevance of the model.

Overview

Epilepsy is a neurodegenerative disorder with a variety of aetiologies, generally arising due to altered balance between excitatory and inhibitory interactions in a neuronal network (Dudek and Staley 2007). Temporal lobe epilepsy (TLE) is a

The original version of this chapter was revised: corresponding author's affiliation was corrected. The correction to this chapter is available at https://doi.org/10.1007/978-3-319-99103-0_26

Sanjay M.
Neurophysiology Unit, Department of Neurological Sciences, Christian Medical College, Vellore, Tamil Nadu, India

Department of Bioengineering, Christian Medical College, Vellore, Tamil Nadu, India

Department of Electrical Engineering, National Institute of Technology Calicut, Kattangal, Kerala, India

S. B. Krothapalli (✉)
Neurophysiology Unit, Department of Neurological Sciences, Christian Medical College, Vellore, India
e-mail: srinivas@cmcvellore.ac.in

V. Cutsuridis et al. (eds.), *Hippocampal Microcircuits*, Springer Series in Computational Neuroscience, https://doi.org/10.1007/978-3-319-99103-0_22

common type of epilepsy named after the brain area of origin – the temporal lobe structures of the brain. The hippocampus and entorhinal cortices of the temporal lobe are reported to be two independent originators of epileptic activity (Lytton et al. 2005). The mechanisms of epileptogenesis including that for temporal lobe structures are still not fully understood. Various experimental studies using animal models have attempted to study its generation, route of spread, severity, activity patterns, etc. Experimental methods, viz. electrical stimulation, enhanced potassium in artificial cerebrospinal fluid (aCSF) (Dzhala and Staley 2003; Id Bihi et al. 2005), zero magnesium in aCSF (Barbarosie and Avoli 1997; Whittington et al. 1995), adding chemical convulsants (e.g. bicuculline) to aCSF (Stoop and Pralong 2000), in vivo intraperitoneal administration of pilocarpine (Dinocourt et al. 2003; Cymerblit-Sabba and Schiller 2012) etc., induce epileptic activity through different mechanisms that are not exactly known. All these studies are performed to mimic pathological states similar to that observed in human epileptic patients, with a view to understand the underlying mechanisms better with an ultimate aim to develop therapeutic methods.

The advancements in the field of computational neuroscience have tremendously helped in unravelling the detailed functions of nervous system right from channel mechanisms to systems level. Simulating the normal function at molecular, cellular, network, and systems levels helps further to understand the mechanisms of pathological states including epilepsy. This will enable us to tailor drugs to restore normal function. It can also help us to understand the action of current antiepileptic drugs on specific channels regarding its efficacy and limitation.

This chapter focusses on development of an in silico model of epileptic activity generation in the highly vulnerable CA3 subfield of hippocampus. This subfield is known to have a low threshold to initiate epileptic activity which then spreads to other connected areas. This propensity of CA3 subfield to become epileptic is thought to be due to its high degree of recurrent connections between the neurons, especially the pyramidal cells (Witter 2007). Compared to experimental studies on CA3 subfield, computational studies involving biophysically detailed CA3 models have been very few.

Specifically in this study, the role of *changes in neuronal connectivity in* hippocampal CA3 subfield in generation of epileptiform activity was investigated. Consistent with experimental observations in pilocarpine models (Cossart et al. 2001; Dinocourt et al. 2003; Cymerblit-Sabba and Schiller 2012) and clinical observations (Mora et al. 2009; Furman 2013), this study focusses on *loss of dendritic inhibition* as a cause of epileptic activity generation. This altered inhibition was reported to lead to sprouting in pyramidal cell dendrites (McAllister 2000; Ren et al. 2014), leading to increased reception of excitatory external inputs mainly from the entorhinal cortex. The increased pyramidal cell excitability causes potentiation of synaptic mechanisms and also suppresses other inhibitory inputs in the network leading to generation of an experimentally comparable epileptic pattern. From a baseline network generating theta-modulated gamma oscillations, stepwise changes in neuronal connectivity and synaptic mechanisms are performed to generate epileptic activity.

The Model

The biophysical model of CA3 neuronal network described in this chapter (Sanjay et al. 2015) was adopted from the ModelDB of Neuron software (Neymotin et al. 2011). The full source code of this model is available in the ModelDB (Accession No. 139421). Additional connectivities as described in Sanjay et al. (2015) were added as per published anatomical data. After establishing the normal baseline network activity, systematic network changes were simulated to explore how (1) reduced connectivity from OLM to pyramidal cells alone influences overall network activity, (2) changes in external inputs received by pyramidal neurons alter the network activity and (3) changes in connectivity between all the neurons affect the overall network activity. This in silico model of CA3 subfield is available in the ModelDB (https://senselab.med.yale.edu/ModelDB, Accession No. 186768).

The following sub-sections first describe the features of the normal baseline network model that generates theta-modulated gamma oscillations.

Cell Types and Currents

Pyramidal Cells

A pyramidal neuron has a pyramid-shaped cell body or soma with two distinct classes of dendrites – apical and basal. There is a single axon for sending the signal along and transmission to the connected neurons. The pyramidal neurons of CA3 subfield of hippocampus have varying morphologies within the subfield. The high degree of recurrent connections between the pyramidal cells is a particular feature of hippocampal CA3 subfield. This recurrent connectivity is thought to play a significant role in enhancing the neuronal excitability in this subfield and even leading to pathological state-like epilepsy.

The network had 800 pyramidal cells each with 5 compartments – 1 somatic compartment, 3 apical dendritic compartments and 1 basal dendritic compartment. In order to get a stable baseline activity, a current of −50 pA is injected in this cell model. This injected current substitutes for the absence of external inputs that were not exclusively modelled. The pyramidal cell contained leak current, transient sodium current I_{Na}, delayed rectifier current $I_{K\text{-}DR}$, A-type potassium current $I_{K\text{-}A}$ and hyperpolarization-activated current I_h. The leak currents, I_{Na} and $I_{K\text{-}DR}$, were for action potential generation and $I_{K\text{-}A}$ for rapid inactivation.

Basket Cells

A basket cell is an inhibitory neuron, the dendrites of which make a basket-like shape around the cell body. They are placed close to the somatic regions of the pyramidal neurons and connected to the somatic and perisomatic regions of the

pyramidal cell. The proximity of basket cells to pyramidal cells leads to their easier excitation due to the drive from the pyramidal neurons. Their close proximity and projection to soma control pyramidal cells' hyperexcitability. The feedback interactions from pyramidal to basket cell and back generated the gamma frequency oscillations of about 35 Hz in a normally connected network. These oscillations are important in learning and memory, encoding and retrieval (Colgin and Moser 2010). There were 200 basket cells in the network, each simulated as a one-compartment model. The basket cells contained leak current, transient sodium current I_{Na} and delayed rectifier potassium current $I_{K\text{-}DR}$.

OLM Interneurons

The oriens-lacunosum moleculare (OLM) inhibitory interneurons have their anatomical presentation extending from stratum oriens to the stratum lacunosum-moleculare in the hippocampus and their axons synapse onto the distal apical dendrites of the pyramidal cells. The feedback interactions from pyramidal to OLM cells and back generate the theta oscillations of about 4–8 Hz in a normally connected network. The theta oscillations play a significant role in spatial navigation and motor behaviour (Colgin and Moser 2010).

The model network contained 200 one-compartment OLM interneurons. Apart from leak currents, I_{Na} and $I_{K\text{-}DR}$, the OLM interneurons contained calcium-activated potassium current $I_{K\text{-}Ca}$, high-threshold calcium current I_L, hyperpolarization-activated current I_h and intracellular calcium dynamics. $I_{K\text{-}Ca}$ allowed long-lasting inactivation after bursting, I_L augmented bursting and activated $I_{K\text{-}Ca}$, and I_h allowed bursting.

All the current types were based on the published work by Tort et al. (2007). The selection of these currents and synaptic and connectivity parameters established the normal baseline activity of the CA3 network.

Neuronal Connectivity and Synaptic Mechanisms

The interconnectivity of neurons in a network is a significant factor that determines its overall activity. This section describes the connectivity of different neurons in the model network (Fig. 1), the synaptic mechanisms involved, the number of neurons synapsing on each type (convergence) and external inputs to these neurons.

The pyramidal neurons in the model are recurrently connected similar to anatomical observation (Witter 2007; Amaral 1993). A pyramidal cell receives excitatory inputs through AMPA and NMDA receptors from 25 other pyramidal cells at their basal dendritic compartment. The pyramidal cell excites the basket cells and OLM interneurons through both AMPA and NMDA receptors. A single pyramidal neuron receives inhibitory inputs from 50 basket cells at the soma and 20 OLM interneurons at the middle apical dendritic compartment, both through

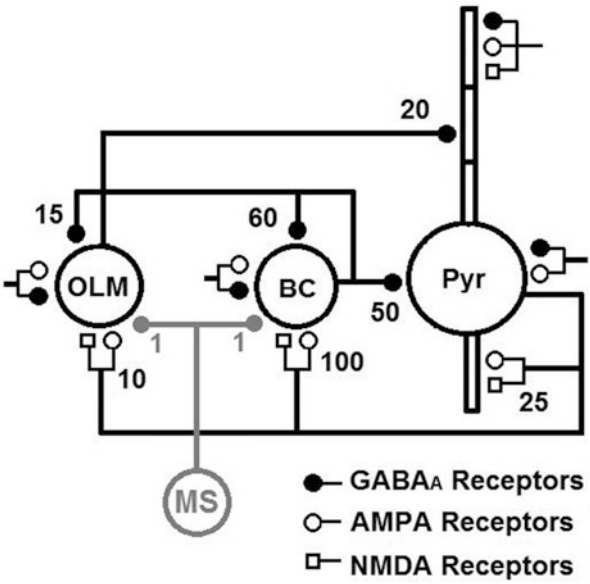

Fig. 1 Schematic network with 800 pyramidal cells (Pyr), 200 basket cells (BC), 200 OLM interneurons. The number of inputs for an individual synapse (convergence) is shown near synapses. Synapses with truncated lines – external random inputs. MS medial septum inputs

$GABA_A$ receptors. External random inputs are received by the pyramidal cells at their somatic compartment through AMPA and $GABA_A$ receptors. Similar inputs are received at the distal most apical dendritic compartment through AMPA, NMDA and $GABA_A$ receptors. These inputs at apical dendrites mainly simulate the inputs received from the entorhinal cortex.

The basket cells are recurrently connected, similar to pyramidal cells. A single basket cell receives inhibitory inputs through $GABA_A$ receptors from 60 other basket cells and excitatory inputs through AMPA and NMDA receptors from 100 pyramidal cells. The basket cells somatically inhibit pyramidal cells through $GABA_A$ synapses. An additional connection from basket cells to OLM interneurons was added to the model through $GABA_A$ synapses based on anatomical information (Cobb et al. 1997). External random inputs are received by basket cells through AMPA and $GABA_A$ receptors.

The OLM interneurons inhibit pyramidal cell dendrites and synapse through $GABA_A$ receptors in the middle compartment of the apical dendrite. An OLM interneuron receives excitatory inputs through AMPA and NMDA receptors from 10 pyramidal cells and inhibitory inputs through $GABA_A$ receptors from 15 basket cells. External random inputs are received by OLM interneurons through AMPA and $GABA_A$ receptors.

Altogether there are 155,000 synapses in the model. The basket cells and OLM interneurons receive $GABA_A$ergic inhibitory inputs from the medial septum (MS) which acts as a pacemaker (Stewart and Fox 1990; Dragoi et al. 1999; Borhegyi et al. 2004). Its effect on inhibitory cells is modelled as a rhythmic input received every 150 ms.

Proposed Mechanism of Epileptic Activity Generation

A step-by-step approach was taken to study how decreased connectivity from OLM interneurons to pyramidal cells leads to hyperexcitability, a characteristic of epileptic activity in the network. Three scenarios are given below:

1. Reducing the OLM interneuron to pyramidal cell connectivity alone, without any other changes in the network
2. Proportionate increment of external excitatory input received by the pyramidal cells in addition to first scenario
3. Changes in synaptic strength simulated at all the synapses in the network

The network activity was considered epileptic when (i) there is total disruption of baseline theta-modulated gamma activity; (ii) the constituent cells show high rate of firing, especially firing rate of pyramidal cells close to 5 Hz (consistent with experimental observations (Ziburkus et al. 2006)); and (iii) the spiking pattern in local field potential record was similar to an experimental ictal condition (10–20 ictal spikes per second (Isaev et al. 2007; Cymerblit-Sabba and Schiller 2012)).

Scenario 1

In the first scenario (Fig. 2), the weight of connection from OLM interneurons to pyramidal cells was reduced in steps from the baseline 100% to 80%, 60%, 40%, 20%, 10%, 5% and 0% (total loss). This was done to understand the influence of dendritic inhibition by OLM interneurons in the network and specifically if this change alone could lead to hyperexcitability in the network.

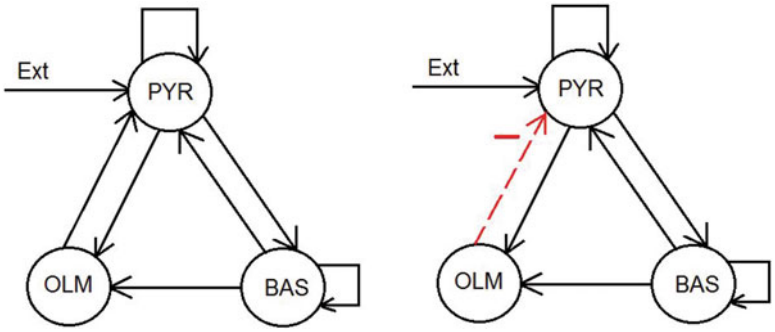

Fig. 2 Reduced schematic diagram showing normal baseline connectivity (left) and reduction in OLM to pyramidal cell connectivity alone (right). PYR pyramidal cell, BAS basket cell, OLM oriens-lacunosum moleculare interneuron, Ext external input

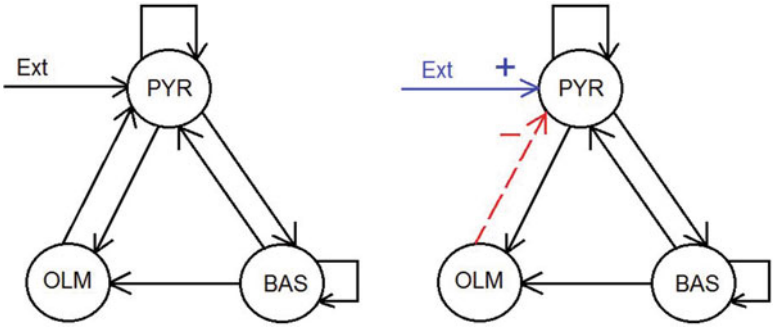

Fig. 3 Reduced schematic diagram. Left shows normal baseline connectivity. Right shows reduction (red arrow) in OLM-pyramidal connectivity along with increase (blue arrow) in external excitatory inputs. PYR pyramidal cell, BAS basket cell, OLM oriens-lacunosum moleculare interneuron, Ext external input

Scenario 2

In the second scenario (Fig. 3), along with reduction in dendritic inhibition provided by OLM interneurons, a proportionate increment of external excitatory inputs received by the pyramidal cells at their distal dendritic compartment was simulated. These excitatory inputs are mainly received from the entorhinal cortex. The OLM interneuron to pyramidal cell connectivity is reduced in steps from the baseline 100% to 80%, 60%, 40% 20%, 10%, 5% and 0% (total loss of this connectivity). Concurrently, the reception of external inputs at the distal dendritic compartment of pyramidal cells was increased from baseline 100% to 120%, 140%, 160%, 180%, 190%, 195% and 200%, respectively.

Scenario 3

In this scenario (Fig. 4), with reduction in dendritic inhibition and corresponding increase in reception of external excitatory inputs by pyramidal cells, the synaptic strengths between the different neuron types were altered in a stepwise manner. The extent of changes in synaptic strengths was assumed arbitrarily and modelled since there were no quantitative information available from experimental or anatomical studies to show exactly *how much* change in synaptic strength in vivo or in vitro predisposes the hippocampal neuronal network towards epilepsy. When the dendritic inhibition was reduced, the following changes were assumed to occur and simulated accordingly (Fig. 4).

- The excitability of pyramidal cells increases due to increased reception of external excitatory inputs at their distal dendritic compartment.
- The enhanced excitability of pyramidal cells strengthens the communication between them due to their recurrent connections. The overall excitatory output from the pyramidal cell population increases which drives the connected cells.

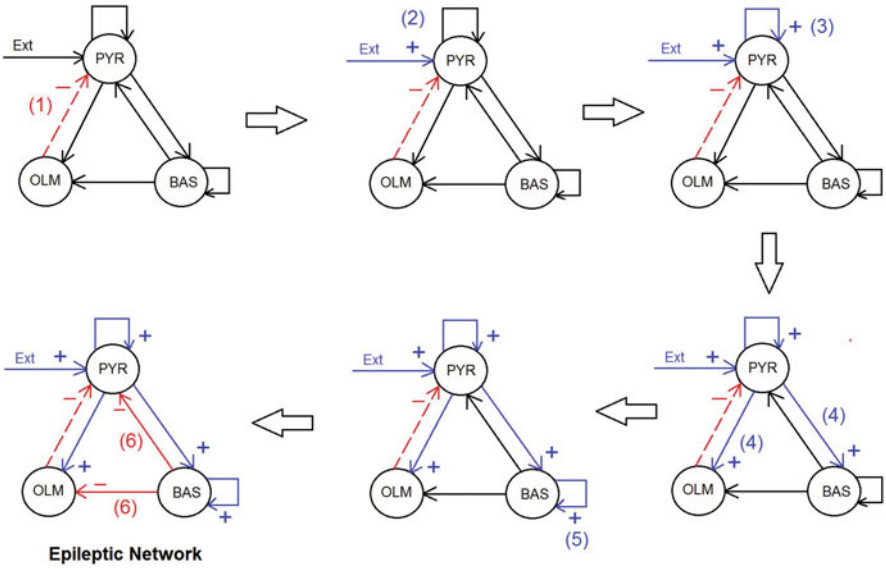

Fig. 4 Stepwise simulation of network connectivity changes leading to epileptic activity generation in a CA3 network. Blue arrows with '+' sign show strengthened synaptic responses, red arrows with '−' sign show weakened synaptic responses. The dashed arrow from OLM to pyramidal cell shows the input condition – reduced dendritic inhibition. The number in parenthesis shows the sequence of network changes. PYR pyramidal cell, BAS basket cell, OLM oriens-lacunosum moleculare interneuron, Ext external input

- The basket cells and OLM interneurons are strongly excited by the pyramidal cells.
- The recurrent inhibition between basket cells is increased, and this further disinhibits the pyramidal cells.
- The increased activity of pyramidal cells drives OLM interneurons, but the reduced connectivity from them to the pyramidal cells prevents increased dendritic inhibition of pyramidal cells.
- The increased reception of external excitatory inputs by the pyramidal cells simulates the sprouting and formation of spines in their distal apical dendrites, as reported in the literature (McAllister 2000).

Based on these proposed changes in the network, two representative conditions are shown – reduction of OLM to pyramidal cell connectivity to (1) 50% (50% impairment of dendritic inhibition) (Fig. 5a) and (2) 30% (70% impairment of dendritic inhibition) (Fig. 5b) of the baseline along with changes in strength of connectivity between the other neurons.

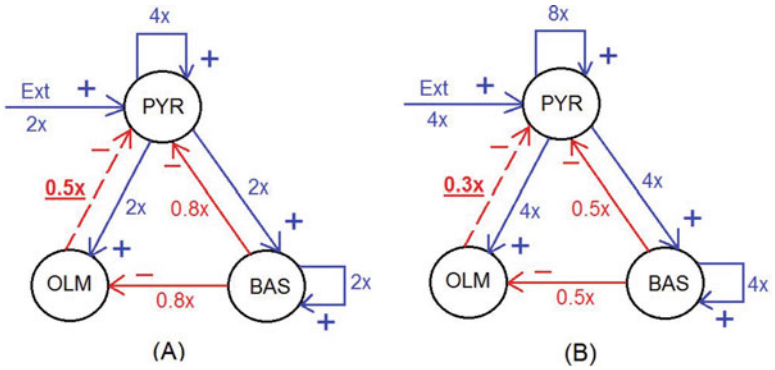

Fig. 5 Network connectivity changes when dendritic inhibition was reduced to 50% (0.5x) of the baseline (**a**) and 30% (0.3x) of the baseline (**b**). Blue arrows with '+' sign show strengthened synaptic responses; red arrows with '−' sign show weakened synaptic responses. The dashed arrow from OLM to pyramidal cell shows the input condition – reduced dendritic inhibition. PYR pyramidal cell, OLM oriens-lacunosum moleculare interneuron, BAS basket ell, Ext external input

With reduction in OLM to pyramidal cell connectivity to 50% of the baseline (50% impairment), the following connectivity changes were simulated. *Compared to the baseline normal levels*:

- External excitatory inputs as received by the pyramidal cells doubled.
- Pyramidal cell to pyramidal cell recurrent connectivity strengthened by four times.
- Pyramidal cell to OLM interneuron interactions strengthened twice.
- Pyramidal cell to basket cells interactions strengthened twice.
- Basket to basket interactions strengthened twice.
- Basket cell to pyramidal cell inhibition reduced to 80% of baseline.
- Basket cell to OLM interneuron inhibition reduced to 80% of baseline.

With reduction in OLM to pyramidal cell connectivity to 30% of the baseline (70% impairment), the following connectivity changes were simulated. *Compared to baseline normal levels*:

- External excitatory inputs received by the pyramidal cells increased by four times.
- Pyramidal cell to pyramidal cell recurrent connectivity strengthened by eight times.
- Pyramidal cell to OLM interneuron interactions strengthened by four times.
- Pyramidal cell to basket cell interactions strengthened by four times.
- Basket to basket interactions strengthened by four times.
- Basket cell to pyramidal cell inhibition reduced to 50% of baseline.
- Basket cell to OLM interneuron inhibition reduced to 50% of baseline.

Simulations and Analysis

The simulations were run on a quad core 2.66 GHz Linux-based 64-bit system using the Neuron simulator with Python Interpreter (Hines et al. 2009; Carnevale and Hines 2006). A single simulation (5s, 1200 neurons) with a time step of 0.1 ms took about 5 min to run. More than 500 simulations have been done for this study. The output of the simulations including the individual cell firing patterns and local field potentials was saved as text files. The data were imported to the software pClamp v.10 (Molecular Devices Inc., USA) for analysis. Analysis of the data included average firing frequency of each type of neuron, synchronous activity between the neuron types, changes in firing rates of individual cell types, theta and gamma frequencies and their power.

Results

Baseline Activity Generation

The normal baseline activity of the network obtained as the local field potential (LFP) is a combined response of pyramidal-OLM interneuron interaction generating theta oscillations and pyramidal-basket cell interaction generating gamma oscillations (Fig. 6). The medial septal inputs inhibited the activity of OLM interneurons and basket cells, the effect being more pronounced on OLM interneurons because of greater excitatory drive received by basket cells from the pyramidal cells. The baseline theta-modulated gamma oscillations had a theta component of 6.7 Hz and gamma component of 33 Hz. The average firing rates were 2.36 ± 0.024 Hz for pyramidal cells, 16.05 ± 0.15 Hz for basket cells and 0.96 ± 0.027 Hz for OLM interneurons. The powers of the theta and gamma components, respectively, were 5.35 mV^2/Hz and 2.55 mV^2/Hz.

Scenario 1: Reducing the Dendritic Inhibition Alone

The stepwise reduction of OLM interneuron to pyramidal cell connectivity alone increased the firing rates of all individual cell types. Specifically, at 5% OLM-pyramidal cell connectivity – the firing of all three cell types significantly increased.

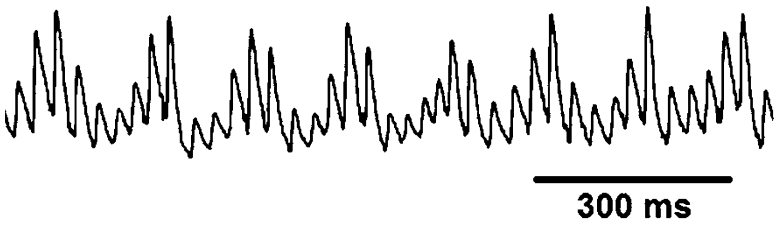

Fig. 6 Baseline activity – theta-modulated gamma oscillations simulated as local field potential

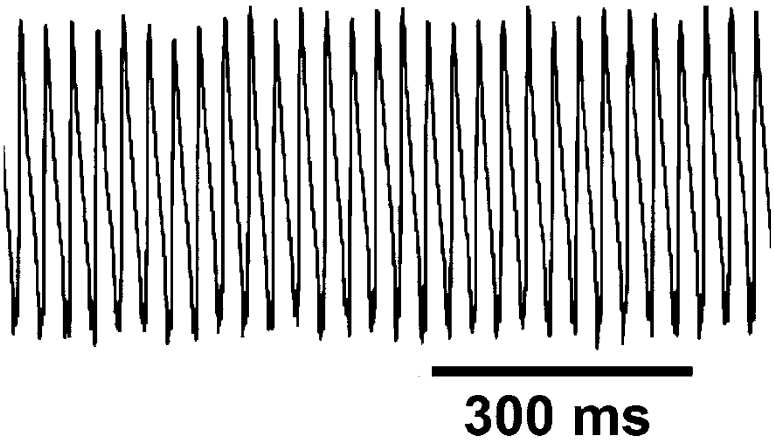

Fig. 7 The simulated local field potential record, with total impairment of dendritic inhibition of pyramidal cells. The theta oscillations have disappeared, and only the gamma component of about 33 Hz remains

The firing rate of pyramidal and basket cells almost doubled at 0% OLM (pyramidal cell connectivity): 2.36 ± 0.02 Hz at baseline to 4.19 ± 0.04 Hz for pyramidal cells and 16.05 ± 0.15 Hz to 30.98 ± 0.07 Hz for basket cells. The firing rate of OLM interneurons increased by almost three times, from 0.96 ± 0.03 Hz to 2.7 ± 0.03 Hz.

A fairly constant theta and gamma frequencies of 6.7 and 33 Hz were maintained till the OLM-pyramidal cell connectivity was reduced to 5%. At total lack of this connectivity, theta oscillations disappeared with only the gamma component remaining in the local field potential record (Fig. 7). The powers of theta and gamma oscillations changed in inverse fashion. While theta power reduced from 5.35 mV^2/Hz at baseline to 0.95 mV^2/Hz at 5% OLM-pyramidal cell connectivity and then to 0 at 0% connectivity, the gamma power increased from 2.55 to 8.7 mV^2/Hz.

Scenario 2: Increasing External Dendritic Inputs to Pyramidal Cells Along with Decrease in Dendritic Inhibition

With reduction in OLM-pyramidal cell connectivity from baseline 100% to 80%, 60%, 40%, 20%, 10%, 5% and 0%, the external inputs received were increased, respectively, from 100% to 120%, 140%, 160%, 180%, 190%, 195% and 200%. All the cell types showed increased firing with this change in connectivity. At 0% OLM-pyramidal cell connectivity and 200% reception of external excitatory inputs, the firing rates were 6.14 ± 0.05 Hz for pyramidal cells, 24.26 ± 0.44 Hz for basket cells and 4.98 ± 0.035 Hz for OLM interneurons.

The theta frequency remained at 6.7 Hz till the OLM-pyramidal connectivity was reduced to 5%, due to the medial septum inputs. The theta frequency is reduced to

0 when there was total lack of this connectivity. The gamma frequency remained fairly constant around 33 Hz till the connectivity was reduced to 10%. On further reduction of OLM-pyramidal connectivity to 0%, this frequency increased to about 39 Hz. The theta power reduced from 5.35 mV^2/Hz to 0 at total lack of dendritic inhibition, while gamma power increased to a significant level at 10% OLM-pyramidal cell connectivity and sharply dropped to 1.3 mV^2/Hz when there was total lack of dendritic inhibition.

It was observed that the rhythmic oscillatory pattern of baseline theta-modulated gamma activity (LFP) was noticeably disturbed at 10% OLM-pyramidal cell connectivity. Hence, a special condition was tested by increasing the external inputs to pyramidal cells by about 15 times the baseline (8 times over the already set increment of 1.9 times (190%)) (Fig. 8, top). In this condition the basket cells entered a state of *depolarization block*, i.e. not being able to fire action potentials due to excessive excitation from pyramidal cells. The local field potential showed a characteristic epileptic activity (Fig. 8, bottom) which started 1.45 s after the start of the simulation. This epileptic pattern was comparable to published experimental results (Cymerblit-Sabba and Yitzhak Schiller (J Neurophysiol 107:1718–1730, 2012, Fig. 2, p. 1721 – Ictal Phase-I); Isaev et al. (Hippocampus 17:210–219, 2007, Fig. 6B-b (left panel), p. 216)).

The firing rates of cells were 10.45 ± 0.1 Hz, 44.2 ± 0.24 Hz and 11.52 ± 0.07 Hz for pyramidal cells, basket cells and OLM interneurons, respectively, before the depolarization block of basket cells. These further increased to 19.09 ± 0.09 Hz for pyramidal cells and 18.56 ± 0.03 Hz for OLM interneurons after depolarization block.

Scenario 3: Changes in Connectivity at All the Synapses

Two conditions were described in this scenario: reduction of OLM to pyramidal cell connectivity to 50% (50% impaired dendritic inhibition) and then to 30% (70% impaired dendritic inhibition).

At 50% OLM to pyramidal cell connectivity along with the changes in connectivity across all synapses, the firing rates for pyramidal, basket and OLM cells changed from baseline values to 1.93 ± 0.02 Hz, 10.58 ± 0.24 Hz and 3.52 ± 0.03 Hz, respectively. The theta and gamma frequencies were 6.8 Hz and 34.9 Hz, respectively, and their powers 0.4 mv^2/Hz and 0.36 mv^2/Hz, respectively. There was a disruption in baseline theta-modulated gamma oscillations due to reduced synchrony of basket cells with other neurons in the network, but this did not lead to epileptic activity.

At 30% OLM to pyramidal cell connectivity (70% impaired dendritic inhibition), with changes in connectivity between other neurons, the basket cells entered *depolarization block*, and a pattern characteristic of epileptic activity (ictal tonic) was seen in the local field potential record (Fig. 9). This pattern commenced 1.3 s after the start of the simulations and was comparable to published experimental results (Isaev et al. 2007; Cymerblit-Sabba and Schiller 2012). The firing rates of

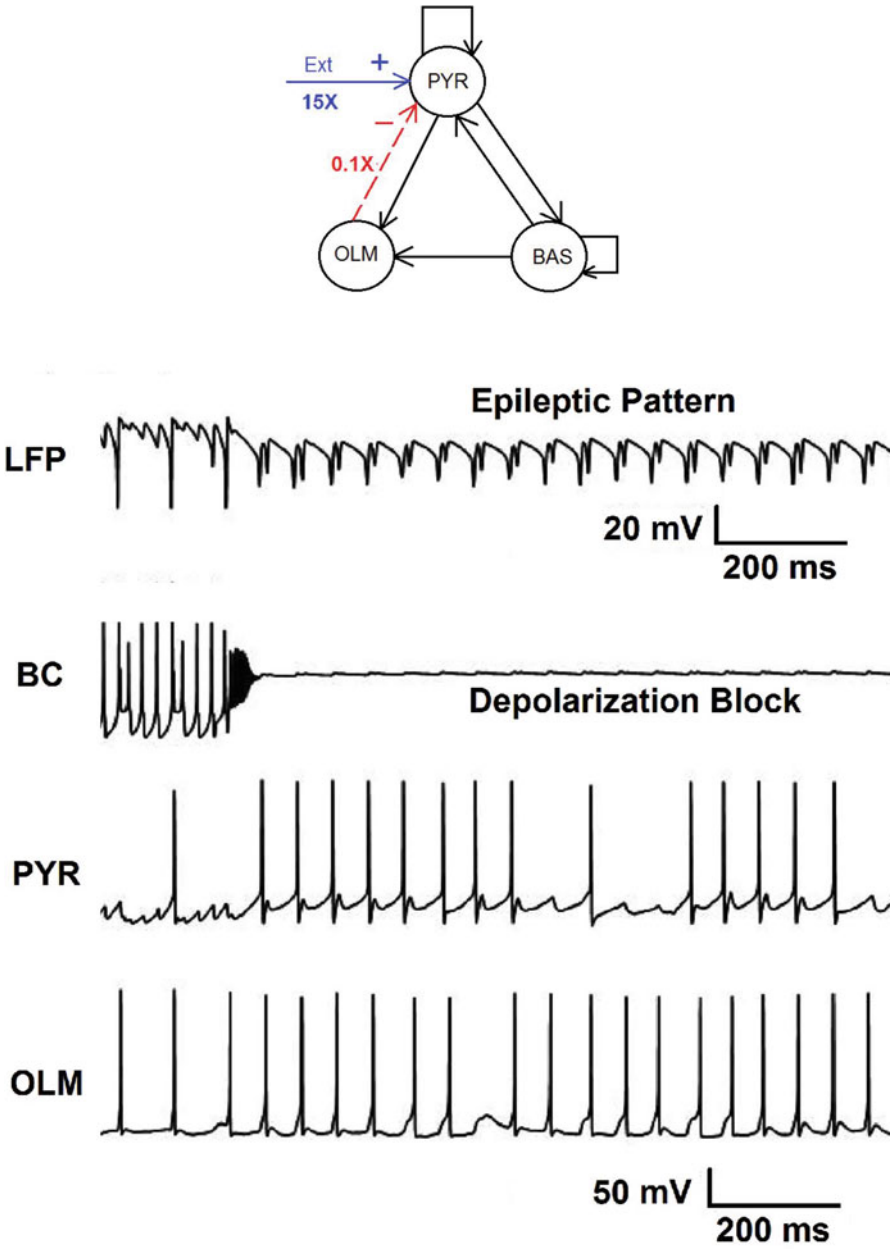

Fig. 8 Top: network schematic diagram showing the condition that generated epileptiform activity; 0.1X–10% baseline connectivity (90% impaired inhibition) and 15X–15 times increase in reception of external excitatory inputs by pyramidal cells. Bottom: simulated epileptic activity seen in the local field potential (LFP) record along with individual cell firing patterns. The depolarization block of basket cells leads to epileptic activity as shown in the LFP

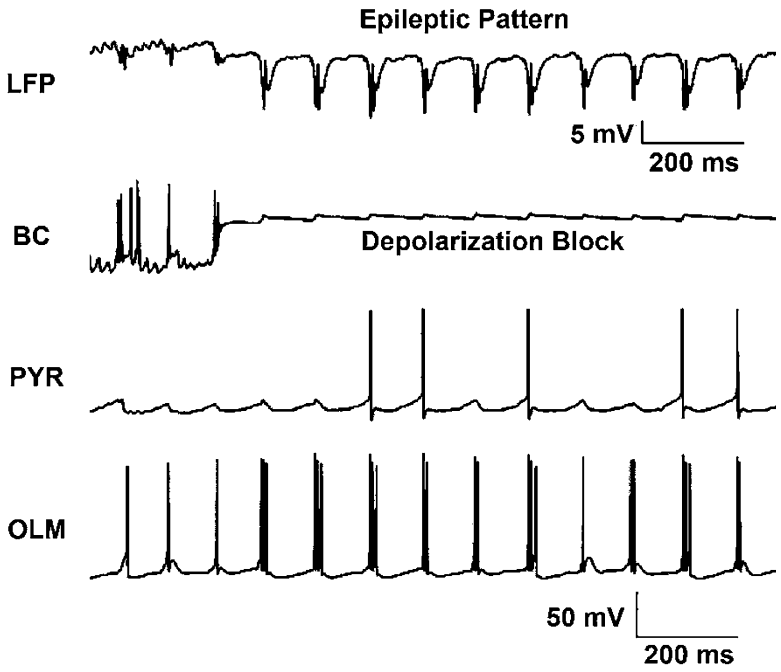

Fig. 9 Simulated epileptic activity due to 70% impaired dendritic inhibition seen in the local field potential (LFP) record along with individual cell firing patterns. The depolarization block of basket cells may be particularly noted after which the LFP shows epileptic activity

the cell types before the depolarization block of basket cells were 3.14 ± 0.06 Hz for pyramidal cells, 13.9 ± 0.39 Hz for basket cells and 11.6 ± 0.11 Hz for OLM interneurons. The theta and gamma frequency components were 10 Hz and 32.7 Hz, respectively, and their powers 0.175 mv^2/Hz and 0.0075 mv^2/Hz, respectively. The firing rates of pyramidal and OLM cells more than doubled to 7.17 ± 0.03 Hz and 23.8 ± 0.05 Hz after the depolarization block of basket cells. The theta frequency remained at 10 Hz, while its power increased to 5.4 mv^2/Hz. The gamma power component was zero since basket cell was not firing.

The results show that the depolarization block of basket cells led to epileptic activity as seen from the LFP record. This was observed in two scenarios: in scenario 2, when the 90% of dendritic inhibition was impaired and reception of external inputs by pyramidal cells increased to about 15 times the baseline, and scenario 3, when there was 70% impairment in dendritic inhibition and simultaneous changes in connectivity strengths between all the neurons in the network. The scenario 2 indicates that epileptiform activity could occur due to high external input reception in a neuronal network with significantly impaired inhibition. These 'high' inputs could be visual (flashes of bright light), auditory (loud sounds), etc. The third scenario indicates synaptic changes that could occur slowly over a period of time

due to impaired inhibition in a neuronal network, contributed even by secondary reasons like brain injuries.

Model Justification

The Baseline Normal Network

In this study, an in silico model of CA3 subfield of hippocampus with necessary modifications was used to investigate what changes in this model network leads to epileptiform activity generation when there is impaired dendritic inhibition of pyramidal neurons. The baseline activity of the network, viz. theta-modulated gamma oscillations, was simulated first. The theta oscillations are significant in spatial navigation and motor behaviour and gamma oscillations in learning, memory encoding and retrieval. Experimental observations show that they co-occur in synchrony in field potential records even though originating from different cell assemblies independently (Colgin and Moser 2010).

After standardizing the model with the generation of baseline normal activity, stepwise reduction of OLM interneuron to pyramidal cell connectivity was done to simulate impairment of dendritic inhibition. As mentioned earlier, this type of structural changes have been observed in human subjects (Mora et al. 2009; Furman 2013) and also in animal models that led to epileptic activity (intraperitoneal administration of pilocarpine, Dinocourt et al. 2003; Cymerblit-Sabba and Schiller 2012).

Simulating Epileptic Activity Generation: The Three Scenarios

The three scenarios that were simulated in this study were systematic approaches to understand the extent of network changes (excitatory-inhibitory balance) required to generate a characteristic epileptic activity. There was no quantitative information from published data regarding *how much* the synaptic strength changes are required to cause a pathological situation. Hence, linear or proportionate changes in synaptic strengths were assumed and simulated.

In the first scenario, dendritic inhibition to the pyramidal cells alone was decreased by reducing the synaptic strength from OLM interneurons to pyramidal cells, without making any other changes in the network. This was to study in isolation the contribution of this connectivity in maintaining the normal activity of the network and to understand if this reduction alone could make the network hyperexcitable. The results showed that this impaired connectivity did not lead to epileptic activity per se but noticeably altered the baseline network activity, blocking theta oscillations (Fig. 7).

In the second scenario, the reception of external excitatory inputs was increased by increasing the synaptic weights for these inputs at the distal dendritic compartment of pyramidal cells, as a consequence of reduction in dendritic inhibition. The fact that the external excitatory input reception increases is justified by studies showing dendritic sprouting with spine formation when inhibitory responses in those segments are reduced (McAllister 2000). For simulations, a linear and inverse change in the connectivities was assumed. For example, when dendritic inhibition was reduced by 40%, the reception of external inputs was increased by 40%. This was a simplified assumption again as there are no experimental data available as to how much of these changes occur in a realistic network.

As in the first scenario, the combination of these two changes alone did not lead to epileptic activity generation. An additional strong external excitatory input was further required to make the network epileptic, that too only at high impairment of dendritic inhibition (90% impairment, 10% OLM-pyramidal cell connectivity). The main source of these inputs is the entorhinal cortex that receives inputs from other cortical areas (Amaral 1993; Witter 2007). Hence, excessive inputs such as light flashes (visual) or large sounds (auditory) might potentially trigger hyperactivity in the vulnerable hippocampus (Manganotti et al. 1998; Seddigh et al. 1999).

The third scenario simulates an intuitively more realistic situation, whereby changes in synaptic strengths of one set of connections in a neuronal network lead to further changes in a cascade, ultimately leading to pathological state. As mentioned earlier, the extent of changes in synaptic strengths in this scenario was a simplified model assumption due to lack of quantitative experimental or anatomical data. For example, a two-time increment in external excitatory inputs received by pyramidal cells was assumed to strengthen the communication between pyramidal cells by four times through their recurrent connections. At 70% impairment in dendritic inhibition, the network showed epileptic activity generation that is comparable with experimental observations (Cymerblit-Sabba and Schiller 2012; Isaev et al. 2007).

The epileptiform activity was generated in the network due to depolarization block of basket cells which compromised the residual inhibitory responses of the network (somatic inhibition of pyramidal cells) as well. In all the three scenarios, the OLM interneurons and basket cells received rhythmic medial septal inputs every 150 ms that paced theta oscillations in the baseline network. It is observed that the theta rhythm was resilient to partial network changes, probably due to the strong pacing by medial septal inputs.

The enhanced neuronal activity and potentiation of network activity have been observed in different studies on epilepsy. Experimental studies showing enhancement of synaptic strength leading to epileptic activity in temporal lobe including hippocampus have been described by Leite et al. (2005). Similarly, McAllister (2000) has described the enhancement of activity in neuronal networks due to sprouting at dendrites which could lead to epileptic activity generation. The contribution of enhanced neuronal connectivity (long-term potentiation) leading to epileptic activity in human central nervous system has been discussed by Cooke and Bliss (2006). Hence, the generation of epileptic activity could be an effect of gross network changes in the brain rather than at those at specific connections.

Depolarization Block of Basket Cells

In this study, the depolarization block of basket cells is the contributing factor that caused epileptic activity generation due to excessive excitatory drive from pyramidal cells. Karlocai et al. (2014) mention few reasons why this could be possible. One is their perisomatic organization which facilitates their faster activation due to enhanced pyramidal cell firing. Second, the synaptic inputs received by them are high due to recurrently connected pyramidal cells. Third is the absence of K^+ channel-mediated hyperpolarizing currents and M-currents. The group observed depolarization block of basket cells in three epileptogenic treatments – high extracellular potassium, zero magnesium and addition of 4-amino-pyridine in hippocampal CA3 subfield. The firing rates of pyramidal cells and interneurons in the network increased in all these methods leading to depolarization block of basket cells due to their high excitation. After the depolarization block, pyramidal cells and the dendrite-inhibiting interneurons continued firing. Similarly, many other studies also showed inactivation of basket cells and other interneurons in pathological states (Bikson et al. 2003; Sloviter et al. 2003; Ziburkus et al. 2006; Zhang and Buckmaster 2009; Curley and Lewis 2012).

Successes and Limitations of the Model

This study used a computational model of CA3 network successfully generating baseline theta-modulated gamma oscillations (Neymotin et al. 2011). Computational models of CA3 have been fewer in number, compared to CA1 subfield, though CA3 is the originator of epileptic activity as shown in many experimental studies (Stoop and Pralong 2000; Lytton et al. 2005). The less number of CA3 models is presumably due to the highly heterogeneous connectivity patterns as well as the lack of exact information on its biophysical parameters. The three neuron types in this model have biophysical parameters comparable to those in other model neurons displaying normal physiology.

Many studies have been conducted to understand how excitation-inhibition imbalance in neuronal networks leads to abnormal pathologically implicated activity patterns (Wittner et al. 2005; El-Hassar et al. 2007). This work shows that inhibitory activity is compromised in the network. It also demonstrated and proposed a quantitative extent of impairment of dendritic inhibition (threshold of connectivity changes, 70% as in scenario 3) as well as a set of changes in synaptic connectivities that made the network hyperexcitable. The simulated hyperactivity in the network was comparable to experimental observations. It is also worth noting from the model results that the network was able to withstand the stable activity till a significant extent of neurodegeneration occurred. This also indicates the resilience of brain networks to insults that could predispose them to pathological conditions.

This work is not devoid of limitations as in the case of other computer models. The exact mechanisms of epileptogenesis are not yet fully known. Hence, many assumptions and simplifications had to be made. The three model neurons in the network had highly reduced anatomical features, though necessary biophysics have been added. Only two main inhibitory mechanisms have been considered – somatic and dendritic through two contributing neurons, the basket cells and OLM interneurons, respectively. Other interneurons that are part of CA3 network in vivo have not been included in the model. The extent of changes in synaptic weights was a model assumption due to lack of related information from published anatomical and experimental studies.

The Future

This computational model could be further expanded by including more neuron types, alternate connectivity patterns, different number of each neuron types, receptors and biochemistry to more realistically replicate anatomical details. Since hippocampal CA3 subfield plays a significant role in learning, memory encoding and retrieval, cognitive processes, and spatial navigation, the changes in the network could potentially lead to impairment of these processes in an affected individual. After adding additional relevant biophysical parameters, the resilience of the updated model to alterations of normal baseline activity leading to pathological states could be tested.

Experimental studies could be planned to quantify the extent of impairment of dendritic inhibition that can lead to epileptic activity. Another interesting set of studies could help to understand how network modifications alter their oscillatory behaviour in pathological conditions. A significant but challenging step for the future would be devising methods for controlling epileptic activity generation. Therapies designed to restore excitatory-inhibitory balance are particularly promising in reducing pathological dynamics. The computational studies should be combined with future experiments to advance our present understanding and develop therapeutic strategies for neurodegenerative disorders.

Appendix: Additional Model Information

Information on the Various Parameters Considered for Baseline Model

The model mentioned in this chapter is primarily based on a published model of CA3 neuron and hence adapted mainly from Neymotin et al. 2011 and Neymotin et al. 2013. The various information to build the model have been considered from

Table A.1 Parameters for modelling background random activity

Cell type	Section	Synapse	Type	τ_1(ms)	τ_2 (ms)	Conductance (nS)
Pyramidal	Dendrite	AMPA	Excitatory	0.05	5.3	0.05
Pyramidal	Dendrite	NMDA	Excitatory	15	150	6.5
Pyramidal	Dendrite	$GABA_A$	Inhibitory	0.07	9.1	0.012
Pyramidal	Soma	AMPA	Excitatory	0.05	5.3	0.05
Pyramidal	Soma	$GABA_A$	Inhibitory	0.07	9.1	0.012
Basket	Soma	AMPA	Excitatory	0.05	5.3	0.02
Basket	Soma	$GABA_A$	Inhibitory	0.07	9.1	0.2
OLM	Soma	AMPA	Excitatory	0.05	5.3	0.0625
OLM	Soma	$GABA_A$	Inhibitory	0.07	9.1	0.2

These parameters are based on publications (Neymotin et al. 2011, 2013; Destexhe et al. 2003)

Table A.2 Synaptic parameters for neuronal connectivity in the model

Presynaptic	Postsynaptic	Receptor	Type	τ_1(ms)	τ_2 (ms)	Conductance (nS)
Pyramidal	Pyramidal	AMPA	Excitatory	0.05	5.3	0.02
Pyramidal	Pyramidal	NMDA	Excitatory	15	150	0.004
Pyramidal	Basket	AMPA	Excitatory	0.05	5.3	0.36
Pyramidal	Basket	NMDA	Excitatory	15	150	1.38
Pyramidal	OLM	AMPA	Excitatory	0.05	5.3	0.36
Pyramidal	OLM	NMDA	Excitatory	15	150	0.7
Basket	Pyramidal	$GABA_A$	Inhibitory	0.07	9.1	0.72
Basket	Basket	$GABA_A$	Inhibitory	0.07	9.1	4.5
*Basket	OLM	$GABA_A$	Inhibitory	0.07	9.1	0.0288
OLM	Pyramidal	$GABA_A$	Inhibitory	0.2	20	72
Medial septum	Basket	$GABA_A$	Inhibitory	20	40	1.6
Medial septum	OLM	$GABA_A$	Inhibitory	20	40	1.6

the experimental and computational studies by Stewart and Fox (1990), White et al. (2000), Destexhe et al. (2003), Gloveli et al. (2005), Tort et al. (2007), Hangya et al. (2009), Stacey et al. (2009), and Neymotin et al. (2011). Modifications as mentioned in Sanjay et al*. (2015) are incorporated.

Specifically, the studies by White et al. (2000) and Gloveli et al. (2005) emphasize the importance of pyramidal-OLM interneuron connectivity in generating theta oscillations and pyramidal-basket cell connectivity in generating gamma oscillations and modulating gamma component by the theta component as observed experimentally.

References

Amaral DG (1993) Emerging principles of intrinsic hippocampal organization. Curr Opin Neurobiol 3:225–229

Barbarosie M, Avoli M (1997) CA3-driven hippocampal-entorhinal loop controls rather than sustains *in vitro* limbic seizures. J Neurosci 17(23):9308–9314

Bikson M, Hahn PJ, Fox JE, Jefferys JGR (2003) Depolarization block of neurons during maintenance of electrographic seizures. J Neurophysiol 90:2402–2408

Borhegyi Z, Varga V, Szilágyi N, Fabo D, Freund TF (2004) Phase segregation of medial septal GABAergic neurons during hippocampal theta activity. J Neurosci 24(39):8470–8479

Carnevale NT, Hines ML (2006) The NEURON book. Cambridge University Press, Cambridge

Cobb SR, Halasy K, Vida KI, Nyiri G, Tamas G, Buhl EH, Somogyi P (1997) Synaptic effects of identified interneurons innervating both interneurons and pyramidal cells in the rat hippocampus. Neuroscience 79(3):629–648

Colgin LL, Moser EI (2010) Gamma oscillations in the hippocampus. Physiology 25:319–329

Cooke SF, Bliss TVP (2006) Plasticity in the human central nervous system. Brain 129:1659–1673

Cossart R, Dinocourt C, Hirsch JC, Merchan-Perez A, De Felipe J, Ben-Ari Y, Esclapez M, Bernard C (2001) Dendritic but not somatic GABAergic inhibition is decreased in experimental epilepsy. Nat Neurosci 4(1):52–62

Curley AA, Lewis DA (2012) Cortical basket cell dysfunction in schizophrenia. J Physiol 590(4):715–724

Cymerblit-Sabba A, Schiller Y (2012) Development of hypersynchrony in the cortical network during chemoconvulsant-induced epileptic seizures in vivo. J Neurophysiol 107:1718–1730

Destexhe A, Rudolph M, Paré D (2003) The high-conductance state of neocortical neurons in vivo. Nat Rev Neurosci 4:739–751

Dinocourt C, Petanjek Z, Freund TF, Ben-Ari Y, Esclapez M (2003) Loss of interneurons innervating pyramidal cell dendrites and axon initial segments in the CA1 region of the hippocampus following pilocarpine-induced seizures. J Comp Neurol 459:407–425

Dragoi G, Carpi D, Recce M, Csicsvari J, Buzsáki G (1999) Interactions between hippocampus and medial septum during sharp waves and theta oscillation in the behaving rat. J Neurosci 19(14):6190–6199

Dudek EF, Staley KJ (2007) How does the balance of excitation and inhibition shift during epileptogenesis? Epilepsy Curr 7(3):86–88

Dzhala VI, Staley KJ (2003) Transition from interictal to ictal activity in limbic networks *in vitro*. J Neurosci 23(21):7873–7880

El-Hassar L, Milh M, Wendling F, Ferrand N, Esclapez M, Bernard C (2007) Cell domain-dependent changes in the glutamatergic and GABAergic drives during epileptogenesis in the Rat CA1 region. J Physiol 578(Pt 1):193–211

Furman M (2013) Seizure initiation and propagation in the pilocarpine rat model of temporal lobe epilepsy. J Neurosci 33(42):16409–16411

Gloveli T, Dugladze T, Rotstein HG, Traub RD, Monyer H, Heinemann U, Whittington MA, Kopell NJ (2005) Orthogonal arrangement of rhythm-generating microcircuits in the hippocampus. PNAS 102(37):13295–13300

Hangya B, Borhegyi Z, Szilagyi N, Freund T, Varga V (2009) GABAergic neurons of the medial septum lead the hippocampal network during theta activity. J Neurosci 29:8094–8102

Hines ML, Davison AP, Muller E (2009) NEURON and Python. Front Neuroinform 3:2009

Id Bihi R, Jefferys JGR, Vreugdenhil M (2005) The role of extracellular potassium in the epileptogenic transformation of recurrent GABAergic inhibition. Epilepsia 46(Suppl. 5):64–71

Isaev D, Isaeva E, Khazipov R, Holmes GL (2007) Shunting and hyperpolarizing GABAergic inhibition in the high-potassium model of ictogenesis in the developing rat hippocampus. Hippocampus 17(3):210–219

Karlocai MR, Kohus Z, Kali S, Ulbert I, Szabo G, Mate Z, Freund TF, Gulyas AI (2014) Physiological sharp wave-ripples and interictal events in vitro: what's the difference? Brain 137:463–485

Leite JP, Neder L, Arisi GA, Carlotti CG Jr, Assirati A, Moreira E (2005) Plasticity, synaptic strength, and epilepsy: what can we learn from ultrastructural data? Epilepsia 46(Suppl. 5):134–141

Lytton WW, Orman R, Stewart M (2005) Computer simulation of epilepsy: implications for seizure spread and behavioral dysfunction. Epilepsy Behav 7(3):336–344

Manganotti P, Miniussi C, Santorum E, Tinazzi M, Bonato C, Marzi CA, Fiaschi A, Bernardina DB, Zanette G (1998) Influence of somatosensory input on paroxysmal activity in benign rolandic epilepsy with 'extreme somatosensory evoked potentials'. Brain 121:647–658

McAllister KA (2000) Cellular and molecular mechanisms of dendritic growth. Cereb Cortex 10:963–973

Mora GN, Bramanti P, Osculati F, Chakir A, Nicolato E, Marzola P, Sbarbati A, Fabene PF (2009) Does pilocarpine-induced epilepsy in adult rats require status epilepticus? PLoS One 4(6):e5759

Neymotin SA, Lazarewicz MT, Sherif M, Contreras D, Finkel LH, Lytton WW (2011) Ketamine disrupts theta modulation of gamma in a computer model of hippocampus. J Neurosci 31(32):11733–11743

Neymotin SA, Hilscher MM, Moulin TC, Skolnick Y, Lazarewicz MT et al (2013) Ih tunes Theta/gamma oscillations and cross-frequency coupling in an in silico CA3 model. PLoS One 8(10):e76285. https://doi.org/10.1371/journal.pone.0076285

Ren, Ye-Jun Shi, Qin-Chi Lu, Pei-Ji Liang, Pu-Ming Zhang (2014) The role of the entorhinal cortex in epileptiform activities of the hippocampus. Theor Biol Med Model 11:14

Sanjay M, Neymotin SA, Krothapalli SB (2015) Impaired dendritic inhibition leads to epileptic activity in a computer model of CA3. Hippocampus 25:1336–1350

Seddigh S, Thomke F, Vogt TH (1999) Complex partial seizures provoked by photic stimulation. J Neurol Neurosurg Psychiatry 66:801–802

Sloviter RS, Zappone CA, Harvey BD, Bumanglag AV, Bender RA, Frotscher M (2003) "Dormant basket cell" hypothesis revisited: relative vulnerabilities of dentate gyrus mossy cells and inhibitory interneurons after hippocampal status epilepticus in the rat. J Comp Neurol 459(1):44–76

Stacey W, Lazarewicz M, Litt B (2009) Synaptic noise and physiological coupling generate high-frequency oscillations in a hippocampal computational model. J Neurophysiol 102:2342–2357

Stewart M, Fox SE (1990) Do septal neurons pace the hippocampal theta rhythm? Trends Neurosci 13:163–168

Stoop R, Pralong E (2000) Functional connections and epileptic spread between hippocampus, entorhinal cortex and amygdala in a modified horizontal slice preparation of the rat brain. Eur J Neurosci 12:3651–3663

Tort AB, Rotstein HG, Dugladze T, Gloveli T, Kopell NJ (2007) On the formation of gamma-coherent cell assemblies by oriens lacunosum moleculare interneurons in the hippocampus. Proc Natl Acad Sci U S A 104:13490–13495

White J, Banks MI, Pearce R, Kopell N (2000) Networks of interneurons with fast and slow γ-aminobutyric acid type A (GABAA) kinetics provide substrate for mixed gamma-theta rhythm. Proc Natl Acad Sci 97:8128–8133

Whittington MA, Traub RD, Jefferys JGR (1995) Erosion of inhibition contributes to the progression of low magnesium bursts in rat hippocampal slices. J Physiol 486(3):723–734

Witter MP (2007) Intrinsic and extrinsic wiring of CA3: implications for connectional heterogeneity. Learn Mem 14:705–713

Wittner L, Eross L, Czirják S, Halász P, Freund TF, Maglóczky Z (2005) Surviving CA1 pyramidal cells receive intact perisomatic inhibitory input in the human epileptic hippocampus. Brain 128:138–152

Zhang W, Buckmaster PS (2009) Dysfunction of the dentate basket cell circuit in a rat model of temporal lobe epilepsy. J Neurosci 29(24):7846–7856

Ziburkus J, Cressman JR, Barreto E, Schiff SJ (2006) Interneuron and pyramidal cell interplay during in vitro seizure-like events. J Neurophysiol 95:3948–3954

A Network Model Reveals That the Experimentally Observed Switch of the Granule Cell Phenotype During Epilepsy Can Maintain the Pattern Separation Function of the Dentate Gyrus

Alexander Hanuschkin, Man Yi Yim, and Jakob Wolfart

Overview

What Is the Model?

The model is a conductance-based neural network model of the brain circuit thought to be involved in pattern separation during hippocampal memory acquisition: the dentate gyrus (DG). In this chapter we explain the concepts of pattern separation and how it was tested in our model. Our hypothesis is that experimentally constrained homeostatic adaptations of intrinsic neuronal properties can restore the pattern separation ability of the DG network, if it was lost during epileptic excitability (Stegen et al. 2009; Young et al. 2009; Yim et al. 2015).

What Is Pattern Separation?

One definition of a pattern is spatial, based on cell identities (i.e., an active cell population is a pattern) and is usually employed without the temporal dimension.

A. Hanuschkin
Optophysiology Lab, Department of Biology, University of Freiburg, Freiburg, Germany

M. Y. Yim
Center for Theoretical and Computational Neuroscience and Department of Neuroscience, The University of Texas at Austin, Austin, TX, USA
e-mail: manyi.yim@utexas.edu

J. Wolfart (✉)
Medizinische Hochschule Brandenburg Theodor Fontane, Neuruppin, Germany

Oscar Langendorff Institute of Physiology, University of Rostock, Rostock, Germany
e-mail: jakob.wolfart@mhb-fontane.de

V. Cutsuridis et al. (eds.), *Hippocampal Microcircuits*, Springer Series in Computational Neuroscience, https://doi.org/10.1007/978-3-319-99103-0_23

Alternatively, a pattern can be defined as a set of action potentials (APs) or excitatory postsynaptic potentials (EPSPs) with specific time intervals. Obviously, the physiological situation is a combination of the two definitions.

Theoreticians who studied pattern separation in the brain often focused on the DG of the hippocampal formation and mostly used the above spatial definition of patterns (Marr 1969, 1971; Mittenthal 1974; Torioka 1978; Gibson et al. 1991; Treves and Rolls 1992; O'Reilly and McClelland 1994). They defined pattern separation as the process of making two similar (overlapping, parallel) patterns more distinguishable (non-overlapping, orthogonal), while they are transmitted from an upstream cell layer to a downstream cell layer. This computational process is also called orthogonalization, while the opposite is pattern completion, sometimes called pattern convergence (Santoro 2013). Although pattern separation is defined as an interregional phenomenon, we adopt a simplified description such as "the DG performs pattern separation," implicitly adding "with the input pattern from the upstream layer." To quantify pattern separation or completion, the percent pattern overlap of two output patterns can be calculated as a function of overlap of the respective input patterns. If the ratio of output pattern overlap to input pattern overlap is smaller than 1, i.e., the outputs are less similar than the inputs, the network performs pattern separation (Fig. 1a).

What Is the Experimental Evidence that Pattern Separation Occurs in the DG?

In behavioral studies, the ability to discriminate small spatial changes is called behavioral pattern separation; a more precise term is behavioral discrimination (Santoro 2013). An example of such a task would be that the shape of a box, in which a rat has to orientate, is modified in small steps. Experiments that combined behavioral tests with selective lesions to hippocampal substructures suggest that the DG is particularly needed, when very similar spatial cues have to be differentiated during hippocampal memory acquisition (Fig. 1b) (Gilbert et al. 2001; Goodrich-Hunsaker et al. 2008; Kesner 2013). When DG cells are recorded in vivo during a behavioral discrimination task, they are more effective than CA3 cells in decorrelating neuronal activity representing very similar shapes (Fig. 1c) (Leutgeb et al. 2007). The above explained (computational) pattern separation is seen as the mechanism underlying behavioral discrimination. However, it should be noted that different forms of behavioral discrimination exist and that some do not depend on the DG (Gilbert and Kesner 2002, 2006; Potvin et al. 2009; Santoro 2013). In summary, although the precise relationship between behavioral discrimination and computational pattern separation is not clarified in all details, the discussed and other evidence (Fig. 1d) (McHugh et al. 2007; Bakker et al. 2008; Moser et al. 2008) points to the DG as an ideal candidate to perform pattern separation with the input it receives.

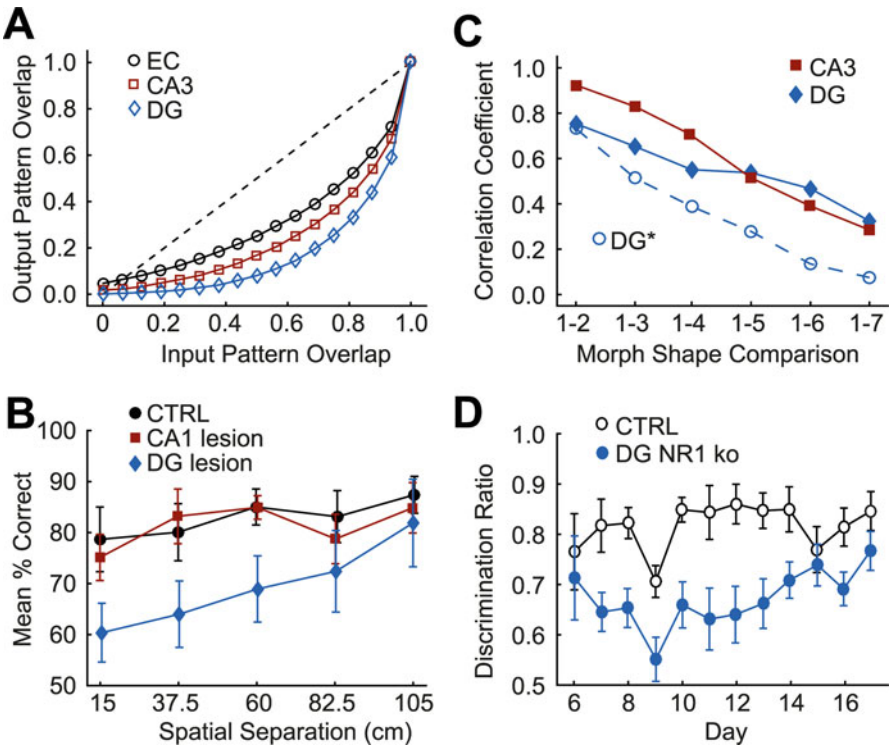

Fig. 1 Previous studies on the role of the DG in pattern separation. (**a**) Results from a statistical model adapted from Figure 8 in O'Reilly and McClelland (1994) comparing the overlap of two output patterns as a function of the two respective input patterns. The lower the function is below the line of equality (dashed), the better is the pattern separation. All models perform pattern separation because the processing is split in different stages; however, the DG is best suited for this task. (**b**) Results from a behavioral experiment adapted from Figure 2B in Gilbert et al. (2001). In a delayed-match-to-sample-for-spatial-location-task, rats with DG lesion (but not with CA1 lesion) experience particular problems to distinguish small spatial differences (DG lesion: smaller correlation coefficient) indicating a crucial role of the DG pattern separation. (**c**) Results from behavioral experiments, combined with in vivo single unit DG recordings, modified from Figure 3A in Leutgeb et al. (2007). Rats are trained to compare boxes (the shape of which is increasingly different from left to right on x-axis), while correlation of place cell firing of CA3 and DG cells is measured (y-axis). In similar surroundings correlation is higher than in dissimilar boxes. However, DG cells show a specific drop in correlation in the region of very similar shapes compared to CA3 cells. DG*, The dashed line with empty circles is derived from Figure 4B in Myers and Scharfman (2009) which simulated this experiment in a DG network model with patterns defined as spatial cell population activity (Adapted with permission from the authors). (**d**) Results adapted from Figure 4F in McHugh et al. (2007). Genetic deletion of postsynaptic NMDA receptors (which are important for LTP-dependent learning) specifically in GCs leads to decreases in behavioral discrimination ability

Biological Constraints for Pattern Separation

During the transmission of a pattern from one brain area to another, two factors are crucial for the degree of pattern separation. The most important factor for the degree of pattern separation is the *activity level* in the output layer; if it is too high, pattern separation is severely hampered (Torioka and Ikeda 1988, 1990; Gibson et al. 1991; O'Reilly and McClelland 1994). In the DG, the output is generated from granule cells (GCs) via their axons, the mossy fibers (MFs), to the dendrites of pyramidal cells in the CA3 region. Thus, for pattern separation to be successfully performed by the DG, the ratio of activated to silent GCs has to remain low. This is known as *sparse coding* and is a general coding strategy of the brain which can but does not have to be related to pattern separation (Vinje and Gallant 2000; Hahnloser et al. 2002; Olshausen and Field 2004). The activity level in the output layer can be kept down by different mechanisms. *Local inhibition* is one such mechanism (Torioka 1978). In the DG this is realized via strong inhibitory feedback which might implement winner-take-all mechanisms among GCs (O'Reilly and McClelland 1994; Lawrence and McBain 2003; de Almeida et al. 2009; Jinde et al. 2012). Another possibility to reduce the number of activated GCs is to keep the *intrinsic excitability* of GCs low, and this is precisely the basis of the present model: the excitability of GCs is kept low via activity-dependent intrinsic plasticity (Stegen et al. 2009, 2012; Young et al. 2009; Kirchheim et al. 2013). Consistent with sparse GC activation during hippocampus-dependent learning, in vivo recordings in the DG rarely discovered spiking GCs (Jung and McNaughton 1993; Leutgeb et al. 2007), and retrospective analysis found only few activity-labeled GCs (Chawla et al. 2005). Other factors which improve pattern separation but are dispensable are sources of variability, like the stochastic nature of transmitter release (Gibson et al. 1991).

The other important constraining factor is *anatomical*. A small output layer population has a reduced capacity to represent patterns, compared to a big population, i.e., it is easier to keep two patterns non-overlapping in the big cell population (Torioka 1978; O'Reilly and McClelland 1994). Additionally, the interlayer connectivity can be convergent or divergent: a divergence factor larger than 1 means that (on average) every neuron of the input layer connects to more than 1 cell of the output layer. The DG receives its excitatory input from entorhinal cortex (EC) layer II cells which project via their perforant path (PP) axons to the dendrites of GCs. The number of EC layer II cells vs. GCs is approximately 110,000 vs. 1,200,000 in rats and 660,000 vs. 18,000,000 in humans (Amaral and Lavenex 2006), suggesting considerable divergence from EC to DG, although it should be noted that the real connectivity cannot be inferred via cell numbers alone. In summary, a pattern separation function can be obtained in two different manners: either by activating more different cells or by activating less overlapping cells. It turns out the latter is biologically more probable and also computationally more efficient.

Behavioral Context of Pattern Separation and Completion

The real-life importance of pattern separation becomes evident when considering that a neuronal pattern encodes for a food location – space is the main information processed in this context (Kesner et al. 2000). Clearly the animal has to be able to distinguish similar environments (pattern separation). However, if only partial information on the food location is available, the full memory of the location has to be recovered, i.e., pattern completion must also occur in hippocampus-dependent learning and retrieval. Thus, a major question in the field is: how can two clearly competing tasks be achieved in one brain area? Mainly inspired by connectivity, a division of labor was suggested with the DG achieving sparse coding and pattern separation and CA3 as an autoassociative network performing pattern completion (McNaughton and Morris 1987; Treves and Rolls 1992).

Epilepsy and the Dentate Gyrus

As discussed above, the activity level of GCs is an important factor of the DG's performance in pattern separation. Therefore *epilepsy* with massive seizure activity invading the DG should be disastrous for the above proposed capacities. On the other hand, we observed that the GC excitability was reduced during temporal lobe epilepsy (TLE) in humans (Stegen et al. 2009) as well as in an animal model of TLE (Young et al. 2009). To explain TLE: the affected patients experience partial memory and consciousness impairments due to focal seizures in the hippocampal formation; the mechanisms underlying TLE are unclear (Spencer 2002; Bonilha et al. 2007). Due to its anatomical and physiological properties, the DG has been implicated as a "filter" or "gate" to the hippocampus which could be of major importance for the spread of epileptic seizures (Heinemann et al. 1992; Lothman et al. 1992; Hsu 2007; Krook-Magnuson et al. 2015). Some of the mechanisms proposed to underlie TLE are based on anatomical changes such as the backsprouting of GC MFs resulting in recurrent excitation of GCs (Tauck and Nadler 1985; Nadler 2003; Buckmaster 2012; Artinian et al. 2015). The MF sprouting scenario inspired several modeling studies showing that recurrent excitatory connections can produce runaway excitation in the DG network (Santhakumar et al. 2005; Morgan and Soltesz 2008; Schneider et al. 2012). Another view supported by experimental evidence is that the seizure activity is already present in the EC and fed into the DG via elevated PP input (Spencer and Spencer 1994; Kobayashi et al. 2003; Bonilha et al. 2007). Furthermore, there are many genetic and acquired ion channel changes which potentially contribute to the seizure-prone network in one way or another (Hoffman 1995; Waxman 2001; Kullmann and Waxman 2010; Wolfart and Laker 2015; Köhling and Wolfart 2016).

Goals of Our Model

In the present study, we modified a previously designed model of the DG circuit (Santhakumar et al. 2005). In particular, we implemented a quantifiable spatiotemporal pattern separation task as well as experimentally determined ion channels changes of GCs in TLE (Young et al. 2009; Yim et al. 2015) in order to address the questions formulated in the following section.

Questions Addressed

While it is well accepted that ion channel expression controls the functional phenotype of isolated neurons, the intrinsic cellular details are usually not considered when studying the computation of entire neuronal networks. In contrast, large-scale neuronal networks are typically built with only a few detailed but stereotypical cell type models or even only with point neurons and yet successfully reproduce a wide range of physiological activity patterns (Koch 1999; Dayan and Abbott 2001; Izhikevich 2007; Rolls 2010). Thus, in most studies, intrinsic properties are either not implemented, or they are considered uniform and stable. Therefore a first, general question we address in the present study is:

How plausible is it that cell type-specific intrinsic plasticity controls the function of local neuronal networks?

Secondly, from the perspective of epilepsy research (Stegen et al. 2009; Young et al. 2009), we ask:

Why is it that during TLE, GCs from sclerotic hippocampi exhibit these abnormally high "leak" conductances?

Theoretically, an elevated resting conductance (i.e., reduced input resistance) renders the neuron's voltage responses (V) less responsive to excitatory current input (I) as predicted by Ohm's law ($V = R \times I$). Therefore, one explanation for the intrinsic plasticity observed during TLE is that it insures cell survival in conditions of enhanced excitotoxicity which is indeed one likely factor (Kirchheim et al. 2013). Here we focus on an additional hypothesis which combines the former two questions:

Are these leak channel adaptations – at least theoretically – in a position to homeostatically adjust the performance of the DG network in separating spatiotemporal patterns?

Level of Detail and Rationale

It was necessary to use a conductance-based model in order to directly implement the experimental observed cell type-specific rescaling. Abstract neuron models with reduced dynamics (e.g., Myers and Scharfman 2009, 2011) might be used after the development of a faithful theory of how to implement cell type-specific rescaling.

Theoretical studies on pattern separation have stressed the importance of output activity, interlayer connectivity, and local inhibition (see section "What Is the Model?"). Hence, realistic GC properties and strong inhibitory feedback are needed in order to reproduce a low activity level of GCs. Furthermore, realistic interlayer connectivity and spatiotemporal input pattern from EC to DG are important. Since there is no theoretical hint that the absolute network size would influence pattern separation function, a small network size with reduced model complexity should be sufficient for a proof of principle. The previously published conductance-based network model of the DG (Santhakumar et al. 2005) fulfills the major requirements as a basic model for our purposes, with slight modifications and extension described in the following.

The Model

Model Components

As in the original study, the DG model consists of biophysically relatively realistic multicompartmental models of the principal cell types of the DG (see Overview in Fig. 2a): excitatory GCs, inhibitory basket cells (BCs), excitatory mossy cells (MCs), and hilar neurons with axon distributed in the PP termination zone (HIPP cells or HCs in Fig. 2a). These cell types and characteristics were carefully elaborated in the original study (Santhakumar et al. 2005). All cells contain a variety of voltage-dependent sodium, potassium, calcium, and unspecific leak channels. We modified the DG model on two levels: synaptic weights and intrinsic changes in GCs (Tables 1 and 2).

The GC model (within the DG model) was originally developed by Aradi and Holmes (1999) which itself was mainly based on data from Yuen and Durand (1991) (Table 2). We added two additional conductances to this GC model. According to our experimental data from the intrahippocampal kainate injection mouse model of TLE, an inward rectifier potassium conductance (Kir) and a tonic $GABA_A$ chloride conductance (sensitive to picrotoxin and bicuculline) are upregulated in GCs of the seizure-experienced hippocampus (Young et al. 2009). Thus, two different GC phenotypes exist in control vs. epileptic animals: control GCs with

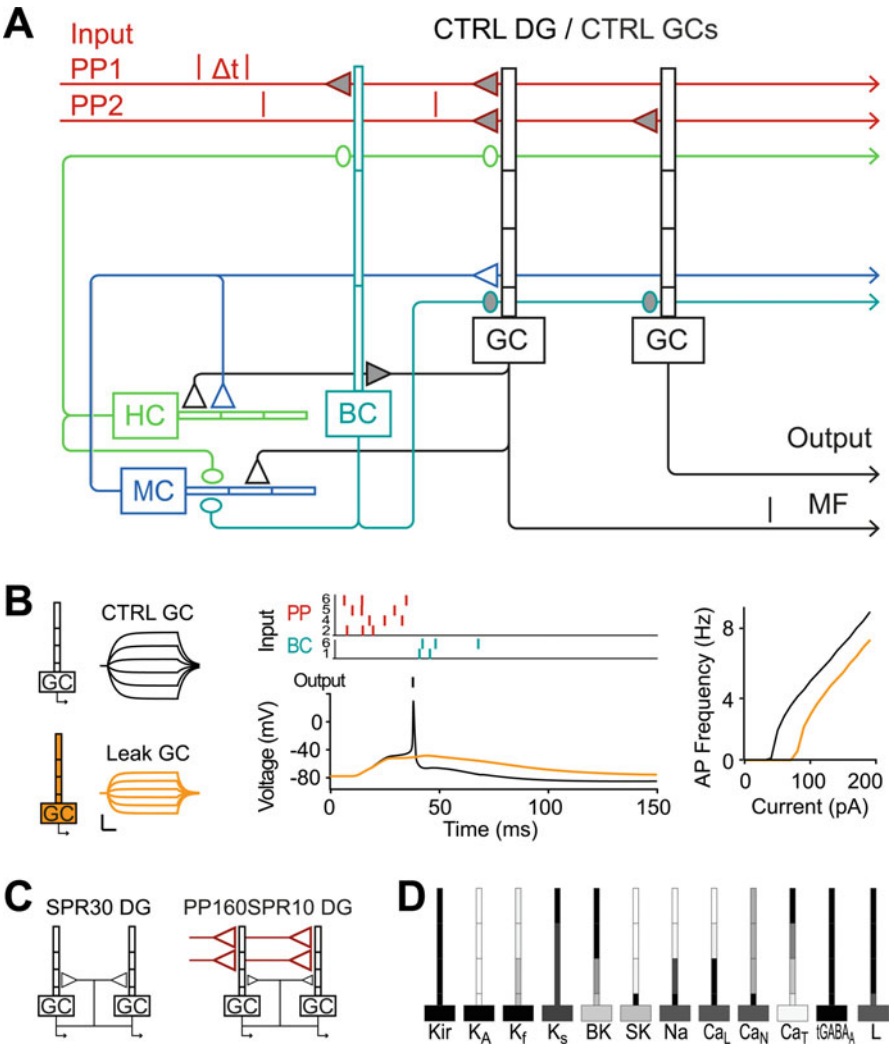

Fig. 2 Scheme of DG network model with focus on the intrinsic properties of GCs (Yim et al. 2015). (**a**) Control situation with basic wiring and GC properties (CTRL DG/CTRL GCs). Besides GCs, basket cells (BC), HIPP cells (HC), and Mossy cells (MC) were modeled. Perforant path (PP) inputs to GCs and GC action potential (AP) output via mossy fibers (MF) are symbolized with vertical tics. Only one of two modeled GC dendrites is displayed. Round arrow heads indicate inhibitory connections and triangular arrow heads excitatory connections. Locations of synaptic weight changes vs. Santhakumar et al. (2005) are grayed. (**b**) The two modeled GC phenotypes: CTRL GCs (black) and Leak GCs (orange) with increased Kir channel and tonic $GABA_A$ channel conductances. The latter leads to smaller subthreshold voltage responses (left traces, scale bars 1 mV, 100 ms) and lower likelihood to fire APs, despite identical input from PP and BCs (middle panel). Right panel, AP frequency vs. injected current: the gain of Leak GCs is moderately lowered. (**c**) The changes in connectivity and synaptic weights to simulate CTRL vs. epileptic: "SPR30 DG," recurrent excitation via sprouted MFs from GCs to GCs, and "PP160SPR10 DG," combination of increased PP input and weak MF sprouting. (**d**) Subcellular distribution of conductance density for each channel type of the GC model. The relative density is symbolized as gray values between maximum black = 1 and minimum white = 0. For further abbreviations see text

Table 1 Parameters of the network model during control condition

From (row)/to (column)	GC	BC	MC	HIPP
PP				
Connectivity (%)	20 (CC)	20* (CC)		
Weight (nS)	2.0*	1.0*	–*	–
Delay (ms)	3	3		
GC				
Connectivity (%)	Sprouted	16.7†	6.7	50
Weight (nS)	2.0	14.1*	0.2	0.5
Delay (ms)	0.8	0.8	1.5	1.5
BC				
Connectivity (%)	20	33.3	20†	
Weight (nS)	4.8*	7.6	1.5	–
Delay (ms)	0.85	0.8	1.5	
MC				
Connectivity (%)	40	16.7	20	33.3
Weight (nS)	0.3	0.3	0.5	0.2
Delay (ms)	3	3	2	3
HIPP				
Connectivity (%)	32	66.7	26.7	
Weight (nS)	0.5	0.5	1.5†	–
Delay (ms)	1.6	1.6	1	

Explanations: CC, convergent connection (each postsynaptic cell receives the same number of presynaptic afferents); all other connections are divergent (postsynaptic cell can have different numbers of presynaptic afferents). Values marked with * were modified from the original model. Entries marked with † differed between Santhakumar et al. (2005) and their ModelDB script. If the two types of neurons have no connection, the corresponding field is marked with –

an input resistance of around 420 MΩ (CTRL GCs) and leaky GCs with an input resistance of about 260 MΩ (~60% of CTRL, Leak GC). To simulate these phenotypes appropriately, we incorporated Kir and tonic $GABA_A$ as additional "leak" conductances into the GC model and scaled them to approximate the experimentally determined subthreshold and spiking phenotype (Fig. 2b). It should be noted that physiologists use the term "leak" channel not necessarily meaning that the native channel displays an absolutely linear current-voltage relationship across the whole voltage range. For example, Kir2 channels are here called "leak channels" because they are constitutively open at resting potential (Stanfield et al. 2002). When the membrane is strongly depolarized, the channels are blocked by intracellular magnesium, hence the name.

To probe network function, we added in particular the option to pass increasingly different spatiotemporal input patterns (IPs) as synaptic input to GCs (Figs. 2a, b and 3a). Otherwise we adopted the connection probabilities and connectivity

Table 2 Overview of distributed conductance mechanisms modeled in DG GCs in Yim et al. (2015). Channel distributions are visualized in Fig. 2d

Channel or mechanism name	NEURON mod file names and references	Experimental methods of source reference
Inward rectifier K^+ (Kir) channel	**Kir.mod** (Yim et al. 2015)	Human, DG GCs, acute slice, patch clamp, RT (Stegen et al. 2012)
Fast inactivating voltage-gated K^+ (A-type Kv) channel	**Ka.mod** (Yim et al. 2015) **bgka.mod** (Santhakumar et al. 2005; Dyhrfjeld-Johnsen et al. 2007; Morgan et al. 2007; Morgan and Soltesz 2008) **borgka.mod** (Migliore et al. 1995)	Guinea pig, dissociated CA3 (Traub et al. 1991) and CA1 pyramidal cells, patch clamp, RT (Kay and Wong 1987; Numann et al. 1987)
Fast delayed rectifier Kv (Kf) channel	**I_Kf** in **Ichan2.mod** (Santhakumar et al. 2005; Dyhrfjeld-Johnsen et al. 2007; Morgan et al. 2007; Morgan and Soltesz 2008; Yim et al. 2015) **Original model** (Aradi and Holmes 1999; Aradi and Soltesz 2002)	Rat, acute slice, DG GCs, sharp electrodes, 37 °C (Yuen and Durand 1991)
Slow delayed rectifier Kv (Ks) channel	**I_Ks** in **Ichan2.mod** (Santhakumar et al. 2005; Dyhrfjeld-Johnsen et al. 2007; Morgan et al. 2007; Morgan and Soltesz 2008; Yim et al. 2015) **Original model** (Aradi and Holmes 1999)	See above (Yuen and Durand 1991)
Big conductance Ca^{2+}-activated K^+ (BK) channel	**BK.mod** (Yim et al. 2015) **CaBK.mod** (Santhakumar et al. 2005) **Cagk.mod** (Migliore et al. 1995) Note bug fix (Dyhrfjeld-Johnsen et al. 2007; Morgan et al. 2007; Morgan and Soltesz 2008)	Rat, skeletal muscle single channels recorded in artificial lipid bilayers, RT (Moczydlowski and Latorre 1983)
Small conductance Ca^{2+}-activated K^+ (SK) channel	**SK.mod** (Yim et al. 2015) **gskch.mod**, note error in rate dynamics implementation (Aradi and Holmes 1999; Santhakumar et al. 2005)	See above (Yuen and Durand 1991)
Voltage-gated Na + (Nav) channel	**I_Na** in **Ichan2.mod** (Dyhrfjeld-Johnsen et al. 2007; Morgan et al. 2007; Morgan and Soltesz 2008; Yim et al. 2015) **Original model** (Aradi and Soltesz 2002)	See above (Yuen and Durand 1991)

Long-lasting voltage-activated Ca^{2+} (L-type Cav) channels	**CaL.mod** (Yim et al. 2015) **Original model** (Aradi and Holmes 1999)	Rat, acute slice, CA1 pyramidal cells, sharp electrodes, calcium imaging, 30 °C (Jaffe et al. 1992, 1994)
Neural (N-type) Cav channels	**CaN.mod** (Yim et al. 2015) **Original model** (Aradi and Holmes 1999)	See above (Jaffe et al. 1992, 1994)
Transient (T-type) Cav channels	**CaT.mod** (Yim et al. 2015) **Original model** (Aradi and Holmes 1999)	See above (Jaffe et al. 1992, 1994)
Tonic $GABA_A$ receptor Cl^- channel	**I_GABAA** in **Ichan2.mod** (Yim et al. 2015)	
Local Ca^{2+} accumulation	**ccanl.mod** (Yim et al. 2015), note bug fix by Ted Carnevale (2015, pers. comm.), (Santhakumar et al. 2005; Dyhrfjeld-Johnsen et al. 2007; Morgan et al. 2007; Morgan and Soltesz 2008)	Theory (Aradi and Holmes 1999)
Unspecific leak conductance	In **Ichan2.mod** (Santhakumar et al. 2005; Dyhrfjeld-Johnsen et al. 2007; Morgan et al. 2007; Morgan and Soltesz 2008; Yim et al. 2015)	

Explanations: RT, room temperature (~20–22 °C); *sharp electrode* recordings, cell is penetrated with high-resistance glass electrodes filled with KCl solution (low seal, high leakage); *patch-clamp* recordings (high seal, low leakage), glass electrode filled with "intracellular" solution which determines reversal potentials; *acute slice* preparation, brain tissue cut with vibratome, neurons preserved with dendrites; *dissociated cell* preparations, cells are mechanically and chemically dissociated from slice and remain as ball-like cell bodies in solution (can be cultured over weeks, potentially with changing properties)

strengths of the local network with a ring structure from the original study, except slight modifications to accomplish sparse coding (see section "Parameters" and Yim et al. 2015 for details). After each simulation the similarity of all pairs of IPs was computed vs. the similarity of the respective GC output patterns (OPs, Fig. 3a). A total of 13 IPs were presented in turn to the network with decreasing overlap from IP1 to 7. IP1 and IP8 are not overlapping. Each PP input line could transmit three excitatory events, evoking EPSPs in one time window. To obtain sparse GC activation as required for pattern separation (see section "What Is the Model?") and as observed *in vivo* (Jung and McNaughton 1993), we reduced the strength of PP input synapses to GCs (and BCs) to 10% of the original model.

In addition to this control DG network connectivity (CTRL DG), various forms of epileptic hyperexcitability were simulated (Figs. 2c and, 3b, c, e). Backsprouting of MF, leading to recurrent excitation of GCs, is a proposed TLE seizure mechanism (see section "What Is the Model?"), and MF sprouting is also present in the TLE animal model (Suzuki et al. 1997) in which we recorded the GC properties. Therefore we used MF sprouting to render the network epileptic (Fig. 2c, SPR30 DG), similar to the original model (Santhakumar et al. 2005). Another mechanism thought to underlie hyperexcitability in TLE is the elevated synaptic input strength from PP to GCs (see section "What Is the Model?"). Therefore we increased PP synaptic weight up to 160% (PP160) of our CTRL DG condition (Fig. 2c).

In order to quantify the pattern separation performance, a similarity score was defined as the average Pearson correlation coefficient of the low-pass filtered spike trains over all PPs (and GCs) in the model. These correlations were computed within a 200 ms time window, consistent with the physiologically relevant oscillatory activities in the hippocampus (Lisman et al. 2005; Rangel et al. 2013). The method also corrects for rate dependence through baseline subtraction and normalization. The ratio between the amount of similarity between two OPs and the similarity between the two respective IPs was then used to compare the pattern separation ability of the DG network (Fig. 3a, right panel).

Parameters

As mentioned above, most of the parameters were inherited from the original model (Santhakumar et al. 2005), and details of the added connectivity and conductances can be found in Yim et al. (2015) and Tables 1 and 2. As the intrinsic properties of GCs are in focus here, we provide an additional table in which the experimental origins of the GC ion channel model parameters of our model are listed (Table 2; see also Fig. 2d for spatial channel distribution).

Limited Results

Under control conditions, i.e., with control network connectivity in the DG (CTRL DG, Fig. 2a) and control intrinsic properties of GCs (CTRL GCs, Fig. 2b), the DG network model separates patterns well: the PP input pattern similarity is always greater than the GC output similarity (Fig. 3a, right panel). Note also the sparse GCs activity generated by the PP input to the DG network (Yim et al. 2015).

Implementing 30% MF sprouting (Spr30 DG) forces the DG network to massive seizure-like hyperexcitation in response to PP input: all GCs of the network are driven to long barrages of APs (Fig. 3b, left panel). With 30% sprouting, the DG fails the pattern separation task completely (Fig. 3b, right panel). The output similarity is always higher than the input similarity, i.e., in the area of pattern completion. Implementing leaky GCs in this network to test their influence on pattern separation, a dichotomous effect is observed: the network falls silent (not shown), or seizures remain (Fig. 3b, right panel inset, orange Leak GCs), i.e., leaky GCs cannot restore pattern separation in this network with heavy recurrent excitation.

As justified above and below (sections "What Is the Model?" and "Data for Model Components and Parameter Value"), we designed a mixed epileptic condition with PP-GC input strength increased to 160%, together with 10% sprouting (PP160Spr10 DG, Fig. 3c, left panel). In this epileptic network, CTRL GCs also show a seizure-like level of activity, and the DG does not separate the patterns for small input similarities (Fig. 3c, right panel). For higher input similarities, the network does perform pattern separation but not nearly as good as the CTRL DG. Thus, with a more realistic epilepsy scenario of increased EC input combined with mild MF sprouting, DG-mediated pattern separation is degraded but not abolished. Introducing now the experimentally observed leaky GC phenotype into the more realistic epileptic DG network (PP160Spr10 DG/Leak GCs, Fig. 3d), the sparse GC activity is restored (Fig. 3d, left panel). Importantly, the pattern separation ability of the epileptic DG network is improved to CTRL DG levels with leaky GCs (Fig. 3, right panel). We scanned the parameter space with respect to different levels of MF sprouting and PP input strength and basically found that the effect of leaky GCs on pattern separation is robust in most situations (Fig. 3e). These simulations indicate that the intrinsic adaptations observed in GCs could restore or ameliorate the pattern separation ability of the DG (Yim et al. 2015).

Model Justification

Data for Model Components and Parameter Values

If not mentioned otherwise, data and parameter values were as in the original model (Santhakumar et al. 2005). The DG connectivity of our model is summarized in Table 1. As mentioned above (section "Model Components"), we added Kir and

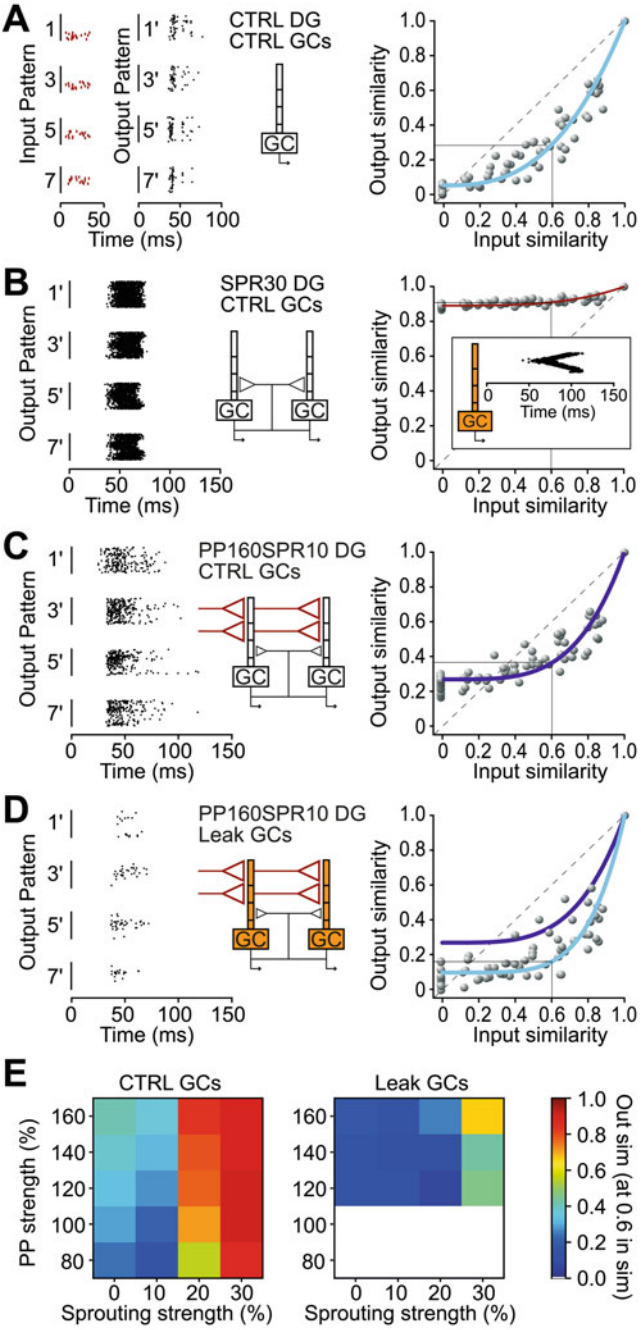

Fig. 3 Pattern separation in DG network under different forms of epileptic hyperexcitation with and without leaky GCs (Modified from Yim et al. (2015)). (**a**) Left panels show 4 of 13

$GABA_A$ channel mechanisms (Table 2) to reproduce the leaky GC phenotype. This phenotype was described in numerous studies, not only in TLE animal model (Young et al. 2009; Kirchheim et al. 2013) but also in TLE patients (Stegen et al. 2009; Stegen et al. 2012). Although more than one type of potassium channel plays a role in the increased leak conductance (Young et al. 2009), the identification of a strong contribution of the Kir channel (subfamily Kir2) to the leaky GC phenotype was revealed via several methods: (i) pharmacology (Stegen et al. 2009, 2012; Young et al. 2009), (ii) biophysical characteristics of the isolated currents (Stegen et al. 2009; Young et al. 2009), (iii) immunocytochemistry (Young et al. 2009), and (iv) single-cell reverse transcriptase polymerase chain reaction (supplementary methods in Kirchheim et al. 2013). Note that neither the leaky GC phenotype nor the presence of Kir channels has been reported in studies using the systemic pilocarpine rat epilepsy model which displays less or no hippocampal sclerosis (see discussion in Young et al. 2009; Wolfart and Laker 2015) although one pilocarpine study did report leaky GCs (Mehranfard et al. 2014). The data of our and other labs clearly show that Kir channels are important for GCs not only in the pathological but also in the physiological situation (Mongiat et al. 2009; Stegen et al. 2009, 2012; Young et al. 2009).

So-called tonic $GABA_A$ receptor-mediated chloride currents are known to exist in GCs, and the underlying subunits are under discussion (Peng et al. 2002; Stell et al. 2003; Farrant and Nusser 2005; Zhang et al. 2007; Glykys et al. 2008). We identified an augmented $GABA_A$ component in leaky GCs via its picrotoxin and bicuculline-sensitivity but did not further investigate the molecular $GABA_A$ subunits (Young et al. 2009). Note that with respect to the relatively negative resting potential of GCs, the reversal potential of the tonic $GABA_A$ chloride current is depolarized although it is not known though how depolarized it really is (Farrant

Fig. 3 (continued) input patterns (IPs 1, 3, 5, and 7) with increasing spatiotemporal difference and respective output patterns (OPs 1′, 3′, 5′, and 7′) under control conditions, i.e., with control connectivity (CTRL DG) and control GC properties (CTRL GCs). Right panel shows similarity scores between IPs and those of OPs fitted by a shifted power law. Data below dashed line indicate pattern separation. (**b**) Same as in **a** (input not shown) but with epileptic 30% MF sprouting (SPR30 DG). With same input patterns as in **a**, seizure-like hyperexcitation occurs. Right graph shows devastating effect on pattern separation performance. Leak GCs (inset orange) cannot restore pattern separation in this situation (more graphs in Yim et al. 2015). (**c**) Same as in **a** (input not shown) but with increased PP weights and 10% MF sprouting (PP160SPR10 DG). In this epileptic situation, pattern separation is degraded but not abolished. (**d**) Same as **c** but with Leak GCs. Despite epileptic wiring and input, the DG pattern separation abilities are restored with Leak GCs (light blue line). Line for CTRL GC as in **c** (dark purple). (**e**) Scan of parameter space for simulations as in **a**–**d** with different strengths of MF sprouting and PP input. The color-coded pattern separation performance was measured as output similarity at 0.6 input similarity (right scale). With combination of Leak GCs and PP80–100, similarity score cannot be computed (white area). In many conditions of epileptic hyperexcitation, the DG with CTRL GCs fails to separate patterns (left panel, red colors). In contrast, with Leak GCs pattern separation was restored under most conditions (right panel, blue colors) suggesting that amelioration of pattern separation via Leak GCs is robust

and Nusser 2005; Pathak et al. 2007; Chiang et al. 2012). The effects of the leaky GCs are not much affected by the reversal potential of $GABA_A$ conductance as long as it is shunting and depolarizing.

So it appears that the $GABA_A$ leak fulfills the role of adding a depolarizing force to the increased Kir conductance in the epilepsy-related leaky GC phenotype, such that the excitability of GCs is reduced but their resting potential is not made too negative (which would be the case if Kir would be elevated alone). To ensure a cell type-specific resting potential is of critical importance: many metabolic functions depend on a constant resting potential. In this context it is interesting to note that in human GCs, the TLE-associated increase of a depolarizing shunt is not mediated via a tonic $GABA_A$ conductance but by an enhanced hyperpolarization-activated current (I_H), mediated by hyperpolarization-activated nucleotide-gated (HCN) channels (Stegen et al. 2012). This difference is likely due to the more severe, time compressed progress of the epileptic disease in the animal model although species difference cannot be ruled out at this point. In rodent GCs, the I_H plays a minor role, but it does contribute to the increased resting conductance (Young et al. 2009). As in rodent GCs, the Kir leak was prominent in GCs of TLE patients (Stegen et al. 2012).

As mentioned above (section "What Is the Model?"), we implemented two mechanisms to create seizure-like activity in the DG network. The MF sprouting hypothesis is quite popular although its functional impact is still controversial (Scharfman et al. 2003; Buckmaster 2012; Heng et al. 2013). In contrast, it is quite certain that TLE is associated with an increased PP input from EC to GCs (Spencer 2002; Kobayashi et al. 2003; Bonilha et al. 2007). Therefore, we implemented an epileptic condition in our network model in which increased PP input was combined with mild MF sprouting.

Since the precise strength of PP inputs is not known (Amaral and Lavenex 2006) and hippocampal memory impairment in TLE patients is also gradual (Cashdollar et al. 2009; Coras et al. 2014), we carefully investigated the regime where increased PP input introduced gradual perturbations and calibrated our model input. For our control condition, the baseline PP strength of the original model was lowered to obtain a physiologically more realistic EPSP summation in GCs (McNaughton et al. 1981) and the low activity that GCs likely possess in vivo (Jung and McNaughton 1993; Leutgeb et al. 2007).

Successes and Limitations

The influence of topological changes on DG network activity and the generation of seizure-like activity pattern have been investigated in several DG network models (Santhakumar et al. 2005; Dyhrfjeld-Johnsen et al. 2007; Morgan and Soltesz 2008). Similarly, multiple modeling studies examined the impact of intrinsic (non-synaptic) properties in DG cell types on network activity (Howard et al. 2007; Thomas et al. 2009; 2010; Winkels et al. 2009; Thomas and Petrou 2013; Yu et al. 2013) and

morphological changes (Tejada et al. 2012; Tejada and Roque 2014). These studies show that epilepsy-related activity pattern can be generated by varying model parameters that influence either local connectivity or neuronal excitability.

We hypothesized that due to the importance of sparse coding (section "What Is the Model?"), it is very likely that intrinsic changes could also have an influence on DG network function. Consistent with this hypothesis, our model shows that only by intrinsic ion channel adaptations in one cell type, even a topologically changed DG network can homeostatically assure sparseness of GC output and thereby dynamically maintain the proposed DG function. Notably, this was achieved by tightly constraining GC conductance parameters to experimentally observed adaptations from "epileptic" tissue (Stegen et al. 2009, 2012; Young et al. 2009). However, there are clear limitations in the ability of leaky GCs to rescue the pattern separation ability of the DG: if the network activity is rendered all-or-none by strong recurrent connectivity, meaningful pattern processing is basically eliminated: all patterns are either transferred as identical or not transferred at all.

Our model belongs to the group of deterministic approaches which has been often used to investigate the control of seizure activity (Tejada et al. 2013). While no common framework for this kind of models exists, we decided to use the open-source NEURON simulator (Hines and Carnevale 1997) because it is widely used for multicompartmental models (Brette et al. 2007; Carnevale and Hines 2008), offers low-threshold interface to parallel computing resources (Sivagnanam et al. 2013), and has an extensive database of models (ModelDB: https://senselab.med.yale.edu/) which is publicly available. Publishing the simulation code makes model and result verification feasible. A possible handicap is that implementation errors might be inherited to the offspring models (De Schutter 2014). We marked differences between published values and model implementation (see Table 1 and Yim et al. 2015) and made our model available on ModelDB (https://senselab.med.yale.edu/ModelDB/ShowModel.cshtml?model=185355) with commented channel mechanisms. Further limitations of our approach are discussed below with the possible extensions.

The Future

Model Extensions

Even though we added conductance mechanisms to GCs, the GC model and the other cell type models could be made more realistic if they would be grounded on more specific experimental data. It is not satisfying that many of the channel models are based on data from different species, recorded with different recording techniques at different temperatures (Table 2). With respect to the latter, it should be noted that the compensation of temperature differences was not always implemented consistently in published channel models. Some of these inconsistencies may be due

to reusing the same channel model without or with only slightly adjusted parameters for different cell types in offspring models (De Schutter 2014). This approach has another potential problem: although it might be feasible to reproduce firing patterns by tuning conductance densities alone (Almog and Korngreen 2016), in reality the same channels could function in a completely different manner in an alternative cell type (Wolfart and Roeper 2002; Wolfart et al. 2005; Marder and Goaillard 2006). Besides augmenting the existing channel models, an extension to our model would be to implement other mechanisms which are subject to epilepsy-related modification; many homeostatic and pathologic channel changes have been reported from different cell types and models (Stegen et al. 2012; Kirchheim et al. 2013; Artinian et al. 2015; Meier et al. 2015; for review see Wolfart and Laker 2015). All these alterations could be sorted for cell types and pathologies and implemented for free interaction into the model.

Within a given cell type, we have not implemented biophysical variability in our current model. Neurons of the same type can exhibit differences in their ion channel repertoire which in some cases lead to considerable heterogeneity in the functional phenotype whereas in other cases not (Marder and Goaillard 2006; Marder and Taylor 2011). This heterogeneity obviously influences neuronal spiking dynamics (Yim et al. 2013; Ly 2015) and network functions (Mejias and Longtin 2012; Bernacchia and Wang 2013) and may enhance information processing (Padmanabhan and Urban 2010). Also the morphology of DG cell types is variable which alone can create a wealth of functional phenotypes (Mainen and Sejnowski 1996) which may even specifically affect pattern separation (Chavlis et al. 2017). As the cellular morphology can change during epilepsy, more precise morphologies should be implemented in the model, ideally based on detailed cell reconstructions (Young et al. 2009; Tejada and Roque 2014). Alternatively, synthetic morphologies could be adapted with new automatic tools (Schneider et al. 2014).

The network size of the model used here has a scale down factor of ∼2000:1 (Santhakumar et al. 2005). While the model offers the appropriate level of detail for testing our hypothesis (see section "Model Components"), it might be interesting to reproduce our results with a larger size and complexity of the DG network. Conductance-based DG network models with reduced scale down value and even full-scale models already exist (Dyhrfjeld-Johnsen et al. 2007; Morgan and Soltesz 2008; Schneider et al. 2012; Hendrickson et al. 2016). Ideally, more detailed models should incorporate the precise functional connectivity and its changes during epilepsy (Ewell and Jones 2010). Ultimately, such DG models will have to be included in a larger simulation, in terms of anatomy, i.e., including the entire entorhinal-hippocampal loop (Jones 1993; Spencer and Spencer 1994), as well as including associated functions like memory acquisition and retrieval (Franzius et al. 2007). Finally, the internal and external oscillations in the theta and gamma frequency range, which control much of the hippocampal activity in vivo (Chrobak et al. 2000; Lisman et al. 2005), could be considered in a complete network model of the hippocampal formation.

New Uses of the Model

Previous studies have tested the effect of sodium channel manipulations across all DG cell types on seizure spread in the network (Thomas et al. 2009, 2010; Thomas and Petrou 2013). Others have also tested seizure spread with channel manipulation in specific DG cell types (Artinian et al. 2015). A new use of our model could be to test DG network function with further *cell type-specific ion channel modulations*. Ultimately, if the link between pattern separation and an elaborated DG network model and behavioral discrimination can be firmly established, such simulations could help to predict behavioral consequences after pharmacological and gene therapy interventions.

In addition, the influence of particular DG *cell types* (as a whole) on pattern separation could be tested in more detail. For example, analytical models suggested a positive influence of local inhibition on pattern separation performance (Torioka 1978; Gibson et al. 1991; O'Reilly and McClelland 1994). On the other hand, in an abstract deterministic DG model, the influence of inhibitory BCs on pattern separation was not prominent (Myers and Scharfman 2009, 2011). This effect and other indirect influences, e.g., via MC (Nakazawa 2017) activation of interneurons which inhibit GCs (Jinde et al. 2012), could be tested in our model.

Adult neurogenesis is known from two brain regions, and the DG is one of them. Behavioral experiments have suggested that neurogenesis (the addition of newborn GCs) supports behavioral pattern separation (Clelland et al. 2009; Sahay et al. 2011; Nakashiba et al. 2012; Tronel et al. 2012; Dery et al. 2013). Consistently, computational studies stated that neurogenesis enhances pattern separation (Aimone et al. 2009, 2010). Remember that in this context the term "pattern separation" is used for different forms of behavioral discrimination and the term "pattern completion" is used for behavioral memory recall (section "What Is the Model?"). Some experimental studies proposed that only the immature GCs are involved in pattern separation but not the mature ones (Alme et al. 2010) or mature GCs even mediate memory recall (Nakashiba et al. 2012) which in turn had also been attributed to adult-born GCs (Kee et al. 2007) or GCs in general (Deng et al. 2013). Thus for a while, some confusion existed about the role of GC neurogenesis in behavioral pattern separation.

One problem for the hypothesis that neurogenesis supports pattern separation is immediately obvious to those who know how highly excitable immature GCs are (Schmidt-Hieber et al. 2004; Bischofberger 2007); how can cells which respond to almost every tiny input with APs – and even show increased long-term synaptic potentiation (Schmidt-Hieber et al. 2004) – contribute to pattern separation? As discussed above (section "What Is the Model?"), pattern separation crucially depends on sparse activation of GCs (Finnegan and Becker 2015). Even when taking into account the fewer PP synapses contacting adult-born GCs, there is a period when they are much more easily activated than their mature counterparts during memory formation (Bischofberger 2007; Kee et al. 2007).

The solution for the neurogenesis puzzle in DG pattern separation may lie in a secondary effect of immature GCs on mature GCs: apparently newborn GCs inhibit old GCs via interneurons (Marin-Burgin et al. 2012; Drew et al. 2016). If this turns out to be the case in vivo, the whole picture is consistent again. Alternatively or additionally, GC neurogenesis may have a more sophisticated role in hippocampal memory processing than to simply support mature GCs in pattern separation. Adult-born GCs appear to be particularly likely to be activated by PP input in a specific time window a couple of weeks after birth and thereby "time-stamp" memories improving their resolution (Becker 2005; Bischofberger 2007; Alme et al. 2010; Aimone et al. 2011; Rangel et al. 2013). In any case, our model is perfectly suitable for future studies on the role of GC neurogenesis in DG pattern separation.

Suggested Experiments

Obviously, the most direct experiment to test our hypothesis would be to combine behavioral discrimination experiments with a selective modification of the intrinsic properties of GCs. For the latter, one possibility would be the generation of a GC-selective transgene construct (McHugh et al. 2007; Krook-Magnuson et al. 2015), preferably graded in both directions, gain and loss of function for Kir and $GABA_A$ channels. Other methods like viral GC transfection (Ahmed et al. 2004) and intracerebral delivery of drugs could also allow modulation of the channels in vivo. The precise effect on the GCs excitability would have to be titrated such that it is in the range of the TLE-related GC phenotype (Stegen et al. 2009; Young et al. 2009). The prediction would be that behavioral discrimination is sensitive to the degree of GC leak channel expression accompanied by the reduced input resistance and excitability. In addition, epileptic animals could be tested. If these would show reduced behavioral discrimination capacities, elevating leak channel expression in GCs should be able to improve these capacities again.

Independently of the precise channel identity, any manipulation of the activity level of GCs should interfere with behavioral discrimination capabilities. One approach would be indirectly manipulating the GC activity in vivo to influence behavioral discrimination. For example, an indirect reduction of GC activity presumably occurs after genetic ablation of MC function, and these animals are indeed impaired in behavioral discrimination (Jinde et al. 2012). Another method to achieve selective manipulation of GCs in vivo is via optogenetic activation of light-sensitive ion channels genetically introduced into GCs (Drew et al. 2016; Krook-Magnuson et al. 2015). Boosting the activity level of GCs during the task would then be expected to weaken behavioral discrimination, while decreasing GC activity in impaired animals could improve performance.

Acknowledgments This work was supported by grants of the Deutsche Forschungsgemeinschaft (DFG) to JW (SFB780/C2, WO1563/1-1). AH was supported by the Bernstein Award Computational Neuroscience (to Ilka Diester).

References

Ahmed BY, Chakravarthy S, Eggers R, Hermens WT, Zhang JY, Niclou SP, Levelt C, Sablitzky F, Anderson PN, Lieberman AR, Verhaagen J (2004) Efficient delivery of Cre-recombinase to neurons in vivo and stable transduction of neurons using adeno-associated and lentiviral vectors. BMC Neurosci 5:4

Aimone JB, Wiles J, Gage FH (2009) Computational influence of adult neurogenesis on memory encoding. Neuron 61:187–202

Aimone JB, Deng W, Gage FH (2010) Adult neurogenesis: integrating theories and separating functions. Trends Cogn Sci 14:325–337

Aimone JB, Deng W, Gage FH (2011) Resolving new memories: a critical look at the dentate gyrus, adult neurogenesis, and pattern separation. Neuron 70:589–596

Alme CB, Buzzetti RA, Marrone DF, Leutgeb JK, Chawla MK, Schaner MJ, Bohanick JD, Khoboko T, Leutgeb S, Moser EI, Moser MB, McNaughton BL, Barnes CA (2010) Hippocampal granule cells opt for early retirement. Hippocampus 20:1109–1123

Almog M, Korngreen A (2016) Is realistic neuronal modeling realistic? J Neurophysiol 116:2180–2209

Amaral DG, Lavenex P (2006) Hippocampal neuroanatomy. In: Andersen P, Morris RG, Amaral DG, Bliss T, O'Keefe J (eds) The hippocampus book. Oxford University Press, Oxford, New York, pp 37–114

Aradi I, Holmes WR (1999) Role of multiple calcium and calcium-dependent conductances in regulation of hippocampal dentate granule cell excitability. J Comput Neurosci 6:215–235

Aradi I, Soltesz I (2002) Modulation of network behaviour by changes in variance in interneuronal properties. J Physiol 538:227–251

Artinian J, Peret A, Mircheva Y, Marti G, Crepel V (2015) Impaired neuronal operation through aberrant intrinsic plasticity in epilepsy. Ann Neurol 77:592–606

Bakker A, Kirwan CB, Miller M, Stark CE (2008) Pattern separation in the human hippocampal CA3 and dentate gyrus. Science 319:1640–1642

Becker S (2005) A computational principle for hippocampal learning and neurogenesis. Hippocampus 15:722–738

Bernacchia A, Wang XJ (2013) Decorrelation by recurrent inhibition in heterogeneous neural circuits. Neural Comput 25:1732–1767

Bischofberger J (2007) Young and excitable: new neurons in memory networks. Nat Neurosci 10:273–275

Bonilha L, Yasuda CL, Rorden C, Li LM, Tedeschi H, de Oliveira E, Cendes F (2007) Does resection of the medial temporal lobe improve the outcome of temporal lobe epilepsy surgery? Epilepsia 48:571–578

Brette R et al (2007) Simulation of networks of spiking neurons: a review of tools and strategies. J Comput Neurosci 23:349–398

Buckmaster PS (2012) Mossy fiber sprouting in the dentate gyrus. Jasper's basic mechanisms of the epilepsies [Internet]

Carnevale NT, Hines ML (2008) The NEURON simulation environment in epilepsy research. In: Soltesz I, Staley K (eds) Computational neuroscience in epilepsy. Elsevier, London, pp 18–33

Cashdollar N, Malecki U, Rugg-Gunn FJ, Duncan JS, Lavie N, Duzel E (2009) Hippocampus-dependent and -independent theta-networks of active maintenance. Proc Natl Acad Sci U S A 106:20493–20498

Chavlis S, Petrantonakis PC, Poirazi P (2017) Dendrites of DG granule cells contribute to pattern separation by controlling sparsity. Hippocampus 27:89–110

Chawla MK, Guzowski JF, Ramirez-Amaya V, Lipa P, Hoffman KL, Marriott LK, Worley PF, McNaughton BL, Barnes CA (2005) Sparse, environmentally selective expression of Arc RNA in the upper blade of the rodent fascia dentata by brief spatial experience. Hippocampus 15:579–586

Chiang PH, Wu PY, Kuo TW, Liu YC, Chan CF, Chien TC, Cheng JK, Huang YY, Chiu CD, Lien CC (2012) GABA is depolarizing in hippocampal dentate granule cells of the adolescent and adult rats. J Neurosci 32:62–67

Chrobak JJ, Lorincz A, Buzsaki G (2000) Physiological patterns in the hippocampo-entorhinal cortex system. Hippocampus 10:457–465

Clelland CD, Choi M, Romberg C, Clemenson GD Jr, Fragniere A, Tyers P, Jessberger S, Saksida LM, Barker RA, Gage FH, Bussey TJ (2009) A functional role for adult hippocampal neurogenesis in spatial pattern separation. Science 325:210–213

Coras R, Pauli E, Li J, Schwarz M, Rossler K, Buchfelder M, Hamer H, Stefan H, Blumcke I (2014) Differential influence of hippocampal subfields to memory formation: insights from patients with temporal pole epilepsy. Brain 137:1945

Dayan P, Abbott LF (2001) Theoretical neuroscience. MIT Press, Cambridge/London

de Almeida L, Idiart M, Lisman JE (2009) The input-output transformation of the hippocampal granule cells: from grid cells to place fields. J Neurosci 29:7504–7512

De Schutter E (2014) The dangers of plug-and-play simulation using shared models. Neuroinformatics 12:227–228

Deng W, Mayford M, Gage FH (2013) Selection of distinct populations of dentate granule cells in response to inputs as a mechanism for pattern separation in mice. eLife 2:e00312

Dery N, Pilgrim M, Gibala M, Gillen J, Wojtowicz JM, Macqueen G, Becker S (2013) Adult hippocampal neurogenesis reduces memory interference in humans: opposing effects of aerobic exercise and depression. Front Neurosci 7:66

Drew LJ, Kheirbek MA, Luna VM, Denny CA, Cloidt MA, Wu MV, Jain S, Scharfman HE, Hen R (2016) Activation of local inhibitory circuits in the dentate gyrus by adult-born neurons. Hippocampus 26:763–778

Dyhrfjeld-Johnsen J, Santhakumar V, Morgan RJ, Huerta R, Tsimring L, Soltesz I (2007) Topological determinants of epileptogenesis in large-scale structural and functional models of the dentate gyrus derived from experimental data. J Neurophysiol 97:1566–1587

Ewell LA, Jones MV (2010) Frequency-tuned distribution of inhibition in the dentate gyrus. J Neurosci 30:12597–12607

Farrant M, Nusser Z (2005) Variations on an inhibitory theme: phasic and tonic activation of GABA(A) receptors. Nat Rev Neurosci 6:215–229

Finnegan R, Becker S (2015) Neurogenesis paradoxically decreases both pattern separation and memory interference. Front Syst Neurosci 9:136

Franzius M, Sprekeler H, Wiskott L (2007) Slowness and sparseness lead to place, head-direction, and spatial-view cells. PLoS Comput Biol 3:e166

Gibson WG, Robinson J, Bennett MR (1991) Probabilistic secretion of quanta in the central nervous system: granule cell synaptic control of pattern separation and activity regulation. Philos Trans R Soc Lond Ser B Biol Sci 332:199–220

Gilbert PE, Kesner RP (2002) The amygdala but not the hippocampus is involved in pattern separation based on reward value. Neurobiol Learn Mem 77:338–353

Gilbert PE, Kesner RP (2006) The role of the dorsal CA3 hippocampal subregion in spatial working memory and pattern separation. Behav Brain Res 169:142–149

Gilbert PE, Kesner RP, Lee I (2001) Dissociating hippocampal subregions: double dissociation between dentate gyrus and CA1. Hippocampus 11:626–636

Glykys J, Mann EO, Mody I (2008) Which GABA(A) receptor subunits are necessary for tonic inhibition in the hippocampus? J Neurosci 28:1421–1426

Goodrich-Hunsaker NJ, Hunsaker MR, Kesner RP (2008) The interactions and dissociations of the dorsal hippocampus subregions: how the dentate gyrus, CA3, and CA1 process spatial information. Behav Neurosci 122:16–26

Hahnloser RH, Kozhevnikov AA, Fee MS (2002) An ultra-sparse code underlies the generation of neural sequences in a songbird. Nature 419:65–70

Heinemann U, Beck H, Dreier JP, Ficker E, Stabel J, Zhang CL (1992) The dentate gyrus as a regulated gate for the propagation of epileptiform activity. Epilepsy Res Suppl 7:273–280

Hendrickson PJ, Yu GJ, Song D, Berger TW (2016) A million-plus neuron model of the hippocampal dentate gyrus: critical role for topography in determining spatiotemporal network dynamics. IEEE Trans Biomed Eng 63:199–209

Heng K, Haney MM, Buckmaster PS (2013) High-dose rapamycin blocks mossy fiber sprouting but not seizures in a mouse model of temporal lobe epilepsy. Epilepsia 54:1535–1541

Hines ML, Carnevale NT (1997) The NEURON simulation environment. Neural Comput 9:1179–1209

Hoffman EP (1995) Voltage-gated ion channelopathies: inherited disorders caused by abnormal sodium, chloride, and calcium regulation in skeletal muscle. Annu Rev Med 46:431–441

Howard AL, Neu A, Morgan RJ, Echegoyen JC, Soltesz I (2007) Opposing modifications in intrinsic currents and synaptic inputs in post-traumatic mossy cells: evidence for single-cell homeostasis in a hyperexcitable network. J Neurophysiol 97:2394–2409

Hsu D (2007) The dentate gyrus as a filter or gate: a look back and a look ahead. Prog Brain Res 163:601–613

Izhikevich EM (2007) Dynamical systems in neuroscience: the geometry of excitability and bursting. MIT Press, Cambridge

Jaffe DB, Johnston D, Lasser-Ross N, Lisman JE, Miyakawa H, Ross WN (1992) The spread of Na+ spikes determines the pattern of dendritic Ca2+ entry into hippocampal neurons. Nature 357:244–246

Jaffe DB, Ross WN, Lisman JE, Lasser-Ross N, Miyakawa H, Johnston D (1994) A model for dendritic Ca2+ accumulation in hippocampal pyramidal neurons based on fluorescence imaging measurements. J Neurophysiol 71:1065–1077

Jinde S, Zsiros V, Jiang Z, Nakao K, Pickel J, Kohno K, Belforte JE, Nakazawa K (2012) Hilar mossy cell degeneration causes transient dentate granule cell hyperexcitability and impaired pattern separation. Neuron 76:1189–1200

Jones RS (1993) Entorhinal-hippocampal connections: a speculative view of their function. Trends Neurosci 16:58–64

Jung MW, McNaughton BL (1993) Spatial selectivity of unit activity in the hippocampal granular layer. Hippocampus 3:165–182

Kay AR, Wong RK (1987) Calcium current activation kinetics in isolated pyramidal neurones of the Ca1 region of the mature guinea-pig hippocampus. J Physiol 392:603–616

Kee N, Teixeira CM, Wang AH, Frankland PW (2007) Preferential incorporation of adult-generated granule cells into spatial memory networks in the dentate gyrus. Nat Neurosci 10:355–362

Kesner RP (2013) An analysis of the dentate gyrus function. Behav Brain Res 254:1–7

Kesner RP, Gilbert PE, Wallenstein GV (2000) Testing neural network models of memory with behavioral experiments. Curr Opin Neurobiol 10:260–265

Kirchheim F, Tinnes S, Haas CA, Stegen M, Wolfart J (2013) Regulation of action potential delays via voltage-gated potassium Kv1.1 channels in dentate granule cells during hippocampal epilepsy. Front Cell Neurosci 7:248

Kobayashi M, Wen X, Buckmaster PS (2003) Reduced inhibition and increased output of layer II neurons in the medial entorhinal cortex in a model of temporal lobe epilepsy. J Neurosci 23:8471–8479

Koch C (1999) Biophysics of computation: information processing in single neurons. Oxford University Press, New York

Köhling R, Wolfart J (2016) Potassium channels in epilepsy. Cold Spring Harb Perspect Med 6:a022871

Krook-Magnuson E, Armstrong C, Bui A, Lew S, Oijala M, Soltesz I (2015) In vivo evaluation of the dentate gate theory in epilepsy. J Physiol 593:2379–2388

Kullmann DM, Waxman SG (2010) Neurological channelopathies: new insights into disease mechanisms and ion channel function. J Physiol 588:1823–1827

Lawrence JJ, McBain CJ (2003) Interneuron diversity series: containing the detonation–feedforward inhibition in the CA3 hippocampus. Trends Neurosci 26:631–640

Leutgeb JK, Leutgeb S, Moser MB, Moser EI (2007) Pattern separation in the dentate gyrus and CA3 of the hippocampus. Science 315:961–966
Lisman JE, Talamini LM, Raffone A (2005) Recall of memory sequences by interaction of the dentate and CA3: a revised model of the phase precession. Neural Netw 18:1191–1201
Lothman EW, Stringer JL, Bertram EH (1992) The dentate gyrus as a control point for seizures in the hippocampus and beyond. Epilepsy Res Suppl 7:301–313
Ly C (2015) Firing rate dynamics in recurrent spiking neural networks with intrinsic and network heterogeneity. J Comput Neurosci 39:311–327
Mainen ZF, Sejnowski TJ (1996) Influence of dendritic structure on firing pattern in model neocortical neurons. Nature 382:363–366
Marder E, Goaillard JM (2006) Variability, compensation and homeostasis in neuron and network function. Nat Rev Neurosci 7:563–574
Marder E, Taylor AL (2011) Multiple models to capture the variability in biological neurons and networks. Nat Neurosci 14:133–138
Marin-Burgin A, Mongiat LA, Pardi MB, Schinder AF (2012) Unique processing during a period of high excitation/inhibition balance in adult-born neurons. Science 335:1238–1242
Marr D (1969) A theory of cerebellar cortex. J Physiol 202:437–470
Marr D (1971) Simple memory: a theory for archicortex. Philos Trans R Soc Lond Ser B Biol Sci 262:23–81
McHugh TJ, Jones MW, Quinn JJ, Balthasar N, Coppari R, Elmquist JK, Lowell BB, Fanselow MS, Wilson MA, Tonegawa S (2007) Dentate gyrus NMDA receptors mediate rapid pattern separation in the hippocampal network. Science 317:94–99
McNaughton BL, Morris J (1987) Hippocampal synaptic enhancement and information storage within in a distributed memory system. Trends Neurosci 10:408–414
McNaughton BL, Barnes CA, Andersen P (1981) Synaptic efficacy and EPSP summation in granule cells of rat fascia dentata studied in vitro. J Neurophysiol 46:952–966
Mehranfard N, Gholamipour-Badie H, Motamedi F, Janahmadi M, Naderi N (2014) Occurrence of two types of granule cells with different excitability in rat dentate gyrus granule cell layer following pilocarpine-induced status epilepticus. Annu Res Rev Biol 4:3707–3715
Meier JC, Semtner M, Wolfart J (2015) Homeostasis of neuronal excitability via synaptic and intrinsic inhibitory mechanisms. In: Boison D, Masino SA (eds) Homeostatic control of brain function. Oxford University Press, Oxford
Mejias JF, Longtin A (2012) Optimal heterogeneity for coding in spiking neural networks. Phys Rev Lett 108:228102
Migliore M, Cook EP, Jaffe DB, Turner DA, Johnston D (1995) Computer simulations of morphologically reconstructed CA3 hippocampal neurons. J Neurophysiol 73:1157–1168
Mittenthal JE (1974) Reliability of pattern separation by the cerebellar mossy fiber–granule cell system. Kybernetik 16:93–101
Moczydlowski E, Latorre R (1983) Gating kinetics of Ca2+-activated K+ channels from rat muscle incorporated into planar lipid bilayers. Evidence for two voltage-dependent Ca2+ binding reactions. J Gen Physiol 82:511–542
Mongiat LA, Esposito MS, Lombardi G, Schinder AF (2009) Reliable activation of immature neurons in the adult hippocampus. PLoS One 4:e5320
Morgan RJ, Soltesz I (2008) Nonrandom connectivity of the epileptic dentate gyrus predicts a major role for neuronal hubs in seizures. Proc Natl Acad Sci U S A 105:6179–6184
Morgan RJ, Santhakumar V, Soltesz I (2007) Modeling the dentate gyrus. Prog Brain Res 163:639–658
Moser EI, Kropff E, Moser MB (2008) Place cells, grid cells, and the brain's spatial representation system. Annu Rev Neurosci 31:69–89
Myers CE, Scharfman HE (2009) A role for hilar cells in pattern separation in the dentate gyrus: a computational approach. Hippocampus 19:321–337
Myers CE, Scharfman HE (2011) Pattern separation in the dentate gyrus: a role for the CA3 backprojection. Hippocampus 21:1190–1215

Nadler JV (2003) The recurrent mossy fiber pathway of the epileptic brain. Neurochem Res 28:1649–1658

Nakashiba T, Cushman JD, Pelkey KA, Renaudineau S, Buhl DL, McHugh TJ, Rodriguez Barrera V, Chittajallu R, Iwamoto KS, McBain CJ, Fanselow MS, Tonegawa S (2012) Young dentate granule cells mediate pattern separation, whereas old granule cells facilitate pattern completion. Cell 149:188–201

Nakazawa K (2017) Dentate mossy cell and pattern separation. Neuron 93:465–467

Numann RE, Wadman WJ, Wong RK (1987) Outward currents of single hippocampal cells obtained from the adult guinea-pig. J Physiol 393:331–353

O'Reilly RC, McClelland JL (1994) Hippocampal conjunctive encoding, storage, and recall: avoiding a trade-off. Hippocampus 4:661–682

Olshausen BA, Field DJ (2004) Sparse coding of sensory inputs. Curr Opin Neurobiol 14:481–487

Padmanabhan K, Urban NN (2010) Intrinsic biophysical diversity decorrelates neuronal firing while increasing information content. Nat Neurosci 13:1276–1282

Pathak HR, Weissinger F, Terunuma M, Carlson GC, Hsu FC, Moss SJ, Coulter DA (2007) Disrupted dentate granule cell chloride regulation enhances synaptic excitability during development of temporal lobe epilepsy. J Neurosci 27:14012–14022

Peng Z, Hauer B, Mihalek RM, Homanics GE, Sieghart W, Olsen RW, Houser CR (2002) GABA(A) receptor changes in delta subunit-deficient mice: altered expression of alpha4 and gamma2 subunits in the forebrain. J Comp Neurol 446:179–197

Potvin O, Dore FY, Goulet S (2009) Lesions of the dorsal subiculum and the dorsal hippocampus impaired pattern separation in a task using distinct and overlapping visual stimuli. Neurobiol Learn Mem 91:287–297

Rangel LM, Quinn LK, Chiba AA, Gage FH, Aimone JB (2013) A hypothesis for temporal coding of young and mature granule cells. Front Neurosci 7:75

Rolls ET (2010) A computational theory of episodic memory formation in the hippocampus. Behav Brain Res 215:180–196

Sahay A, Scobie KN, Hill AS, OCarroll CM, Kheirbek MA, Burghardt NS, Fenton AA, Dranovsky A, Hen R (2011) Increasing adult hippocampal neurogenesis is sufficient to improve pattern separation. Nature 472:466–470

Santhakumar V, Aradi I, Soltesz I (2005) Role of mossy fiber sprouting and mossy cell loss in hyperexcitability: a network model of the dentate gyrus incorporating cell types and axonal topography. J Neurophysiol 93:437–453

Santoro A (2013) Reassessing pattern separation in the dentate gyrus. Front Behav Neurosci 7:96

Scharfman HE, Sollas AL, Berger RE, Goodman JH (2003) Electrophysiological evidence of monosynaptic excitatory transmission between granule cells after seizure-induced mossy fiber sprouting. J Neurophysiol 90:2536–2547

Schmidt-Hieber C, Jonas P, Bischofberger J (2004) Enhanced synaptic plasticity in newly generated granule cells of the adult hippocampus. Nature 429:184–187

Schneider CJ, Bezaire M, Soltesz I (2012) Toward a full-scale computational model of the rat dentate gyrus. Front Neural Circuits 6:83

Schneider CJ, Cuntz H, Soltesz I (2014) Linking macroscopic with microscopic neuroanatomy using synthetic neuronal populations. PLoS Comput Biol 10:e1003921

Sivagnanam S, Majumdar A, Yoshimoto K, Astakhov V, Bandrowski A, Martone ME, Carnevale NT (2013) Introducing the neuroscience gateway. In: CEUR workshop proceedings, CEUR-WSorg, 2013, vol 993

Spencer SS (2002) Neural networks in human epilepsy: evidence of and implications for treatment. Epilepsia 43:219–227

Spencer SS, Spencer DD (1994) Entorhinal-hippocampal interactions in medial temporal lobe epilepsy. Epilepsia 35:721–727

Stanfield PR, Nakajima S, Nakajima Y (2002) Constitutively active and G-protein coupled inward rectifier K+ channels: Kir2.0 and Kir3.0. Rev Physiol Biochem Pharmacol 145:47–179

Stegen M, Young CC, Haas CA, Zentner J, Wolfart J (2009) Increased leak conductance in dentate gyrus granule cells of temporal lobe epilepsy patients with Ammon's horn sclerosis. Epilepsia 50:646–653

Stegen M, Kirchheim F, Hanuschkin A, Staszewski O, Veh RW, Wolfart J (2012) Adaptive intrinsic plasticity in human dentate gyrus granule cells during temporal lobe epilepsy. Cereb Cortex 22:2087–2101

Stell BM, Brickley SG, Tang CY, Farrant M, Mody I (2003) Neuroactive steroids reduce neuronal excitability by selectively enhancing tonic inhibition mediated by delta subunit-containing GABAA receptors. Proc Natl Acad Sci U S A 100:14439–14444

Suzuki F, Makiura Y, Guilhem D, Sorensen JC, Onteniente B (1997) Correlated axonal sprouting and dendritic spine formation during kainate-induced neuronal morphogenesis in the dentate gyrus of adult mice. Exp Neurol 145:203–213

Tauck DL, Nadler JV (1985) Evidence of functional mossy fiber sprouting in hippocampal formation of kainic acid-treated rats. J Neurosci 5:1016–1022

Tejada J, Roque AC (2014) Computational models of dentate gyrus with epilepsy-induced morphological alterations in granule cells. EpilepsyBehav: E&B 38:63–70

Tejada J, Arisi GM, Garcia-Cairasco N, Roque AC (2012) Morphological alterations in newly born dentate gyrus granule cells that emerge after status epilepticus contribute to make them less excitable. PLoS One 7:e40726

Tejada J, Costa KM, Bertti P, Garcia-Cairasco N (2013) The epilepsies: complex challenges needing complex solutions. Epilepsy Behav: E&B 26:212–228

Thomas EA, Petrou S (2013) Network-specific mechanisms may explain the paradoxical effects of carbamazepine and phenytoin. Epilepsia 54:1195–1202

Thomas EA, Reid CA, Berkovic SF, Petrou S (2009) Prediction by modeling that epilepsy may be caused by very small functional changes in ion channels. Arch Neurol 66:1225–1232

Thomas EA, Reid CA, Petrou S (2010) Mossy fiber sprouting interacts with sodium channel mutations to increase dentate gyrus excitability. Epilepsia 51:136–145

Torioka T (1978) Pattern separability and the effect of the number of connections in a random neural net with inhibitory connections. Biol Cybern 31:27–35

Torioka T, Ikeda N (1988) Pattern separating functioning of two-layered random nerve nets with feedforward inhibitory connections. IEEE Trans Syst Man Cybern 18:358–366

Torioka T, Ikeda N (1990) Consideration on pattern-separating function in a generalized random-nerve net consisting of two layers. IEEE Trans Syst Man Cybern 20:619–627

Traub RD, Wong RK, Miles R, Michelson H (1991) A model of a CA3 hippocampal pyramidal neuron incorporating voltage-clamp data on intrinsic conductances. J Neurophysiol 66:635–650

Treves A, Rolls ET (1992) Computational constraints suggest the need for two distinct input systems to the hippocampal CA3 network. Hippocampus 2:189–199

Tronel S, Belnoue L, Grosjean N, Revest JM, Piazza PV, Koehl M, Abrous DN (2012) Adult-born neurons are necessary for extended contextual discrimination. Hippocampus 22:292–298

Vinje WE, Gallant JL (2000) Sparse coding and decorrelation in primary visual cortex during natural vision. Science 287:1273–1276

Waxman SG (2001) Transcriptional channelopathies: an emerging class of disorders. Nat Rev Neurosci 2:652–659

Winkels R, Jedlicka P, Weise FK, Schultz C, Deller T, Schwarzacher SW (2009) Reduced excitability in the dentate gyrus network of betaIV-spectrin mutant mice in vivo. Hippocampus 19:677–686

Wolfart J, Laker D (2015) Homeostasis or channelopathy? Acquired cell type-specific ion channel changes in temporal lobe epilepsy and their antiepileptic potential. Front Physiol 6:168

Wolfart J, Roeper J (2002) Selective coupling of T-type calcium channels to SK potassium channels prevents intrinsic bursting in dopaminergic midbrain neurons. J Neurosci 22:3404–3413

Wolfart J, Debay D, Le Masson G, Destexhe A, Bal T (2005) Synaptic background activity controls spike transfer from thalamus to cortex. Nat Neurosci 8:1760–1767

Yim MY, Aertsen A, Rotter S (2013) Impact of intrinsic biophysical diversity on the activity of spiking neurons. Phys Rev E 87:1–5

Yim MY, Hanuschkin A, Wolfart J (2015) Intrinsic rescaling of granule cells restores pattern separation ability of a dentate gyrus network model during epileptic hyperexcitability. Hippocampus 25:297–308

Young CC, Stegen M, Bernard R, Muller M, Bischofberger J, Veh RW, Haas CA, Wolfart J (2009) Upregulation of inward rectifier K+ (Kir2) channels in dentate gyrus granule cells in temporal lobe epilepsy. J Physiol 587:4213–4233

Yu J, Proddutur A, Elgammal FS, Ito T, Santhakumar V (2013) Status epilepticus enhances tonic GABA currents and depolarizes GABA reversal potential in dentate fast-spiking basket cells. J Neurophysiol 109:1746–1763

Yuen GL, Durand D (1991) Reconstruction of hippocampal granule cell electrophysiology by computer simulation. Neuroscience 41:411–423

Zhang N, Wei W, Mody I, Houser CR (2007) Altered localization of GABA(A) receptor subunits on dentate granule cell dendrites influences tonic and phasic inhibition in a mouse model of epilepsy. J Neurosci 27:7520–7531

Resources for Modeling in Computational Neuroscience

Justas Birgiolas, Sharon M. Crook, and Richard C. Gerkin

Abstract Computational models of the nervous system help researchers discover principles of brain operation and form/function relationships. They can provide a framework for understanding empirical data and serve as an experimental platform to test concepts and intuitions. In practice, the effective use of theoretical, computational, and information theoretic approaches requires an ongoing cycle of experiments, data analysis, modeling studies, and model-generated predictions that are tested by further empirical work. This cycle requires that computational scientists be able to build on the work of others. In this chapter, we provide an overview of simulation tools and resources for creating computational models of hippocampal function. First, we outline some of the most widely used software applications for simulating models at various levels of biological detail. We also describe resources that aid in reproducibility by allowing for model sharing and reuse, for portability of models across simulation platforms, and for validation of models against experimental data.

Introduction

The complexity of the nervous system implies that intuitive approaches will not suffice for discovering the principles of brain operation and form/function relationships. Computational approaches help researchers discover these principles and make sense of empirical data and can serve as an experimental platform to test

J. Birgiolas · R. C. Gerkin (✉)
School of Life Sciences, Arizona State University, Tempe, AZ, USA
e-mail: justas@asu.edu; rgerkin@asu.edu

S. M. Crook
School of Mathematical and Statistical Sciences, School of Life Sciences, Arizona State University, Tempe, AZ, USA
e-mail: sharon.crook@asu.edu

V. Cutsuridis et al. (eds.), *Hippocampal Microcircuits*, Springer Series in Computational Neuroscience, https://doi.org/10.1007/978-3-319-99103-0_24

concepts and intuitions. In practice, the effective use of theoretical, computational, and information theoretic approaches requires an ongoing cycle of experiments, data analysis, modeling studies, and model-generated predictions that are tested by further empirical work.

This cycle—a modern implementation of the scientific method—also requires model reproducibility; that is, computational scientists must be able to build on the work of others. In this chapter, we provide an overview of simulation tools and resources for creating computational models of hippocampal function. First, we outline some of the most widely used software applications for simulating models at various levels of biological detail. We also describe resources that aid in reproducibility by allowing for model sharing and reuse, for portability of models across simulation platforms, and for validation of models against experimental data.

Simulators and Programming Languages

One of the first decisions that many computational neuroscientists wishing to model a neural system face is the trade-off between the level of detail in individual cell models and the number of cells in the network being modeled. The cell or component detail can vary from abstract point neurons like perceptrons (Rosenblatt 1958) or leaky integrate and fire (LIF) neurons (Lapicque 1907) to multi-compartment, morphologically detailed, and biophysically realistic models that model the stochastic kinetics of individual ion channels. Meanwhile, the network scale can range from "networks" consisting of single cells with multiple synaptic inputs to networks modeling entire brains (Markram 2006; Eliasmith et al. 2012). A modeler must choose a combination of component detail and network size that is expected to provide insight into a scientific question while being within the computational budget defined by the resources available to the modeler (Fig. 1). Optimization of this tractability/detail trade-off may be different for different computational problems (Brette et al. 2007). Thus, to facilitate the creation of models with different trade-offs, several simulator software packages have been developed. For example, widely used simulators like NEURON and GENESIS (Wilson et al. 1989) have specialized features and optimizations for simulating biophysically detailed neuronal models, while NEST (Gewaltig and Diesmann 2007) and Brian (Goodman and Brette 2009) favor simpler cells but provide specialized features for defining the network connectivity patterns and spike propagation between the cells. Other simulators and packages further specialize in other niche areas of model development or analysis. In the following sections, we survey the most widely used simulators and programming languages.

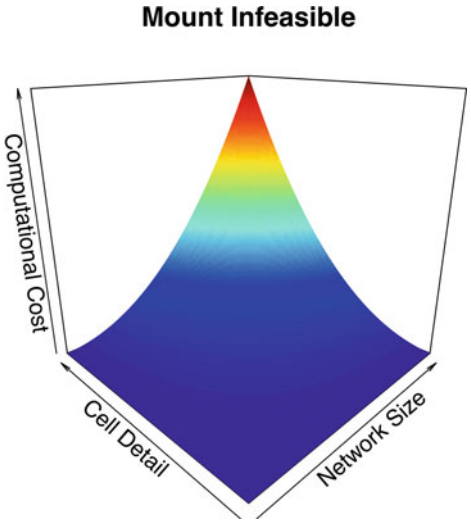

Fig. 1 The combination of increased cell detail with increased network size results in a rapidly growing computational cost of simulations. Simulations with the largest number of cells, each with the highest level of detail, sit on top of "Mount Infeasible." In order to remain within a computational budget, a modeler must make a trade-off between the desired network size and cell detail

Widely Used Simulators

In the following section, we review the most widely used simulators. All of these simulators are mature and well documented and have large user bases with many examples or tutorials available on the simulator websites and on the Internet in general.

NEURON

Primary strengths	Detailed cell and microcircuit specification cluster/MPI support
Installation	http://neuron.yale.edu/neuron/download
Documentation	http://neuron.yale.edu/neuron/docs https://neuron.yale.edu/neuron/static/new_doc/index.html *The NEURON book* (Carnevale and Hines 2006)
Forum	https://www.neuron.yale.edu/phpBB/
Models	https://senselab.med.yale.edu/ModelDB/ModelList.cshtml?id=1882
Platforms	MacOS, Windows, Linux

The NEURON simulator allows users to define ion channel and synapse dynamics in terms of differential equations (.mod files), reaction-diffusion systems, or electric circuits. The channel dynamics can be placed on membrane sections that can be subdivided into iso-potential compartments. The sections can be connected together to form dendritic or axonal branches of the neuronal model. To build network models, cell sections can have synapses, which can send action potentials to other cell

sections. Inputs like current and voltage clamps can be attached to cell sections, and state variables like membrane potential can be read, saved, and plotted as outputs.

The most common channel, cell, and network specifications can be performed via the GUI. However, all aspects of the model and simulation control can be specified via the simulator's HOC/NMODL language or with Python (Hines et al. 2008). NEURON supports both fixed time step and variable time step (CVODE) integration methods. To facilitate large network simulations, the simulator supports parallel multiprocessor and cluster programming via the Message Passing Interface (MPI). Each cell and synapse, with corresponding equations, can be assigned to an MPI node and executed in parallel. This allows large-scale simulation of networks consisting of cells with detailed morphology. See, for example, Migliore et al. (2014).

NEST

Primary strengths	Large-scale network connectivity specification cluster/MPI support
Installation	http://www.nest-simulator.org/installation/ http://www.nest-simulator.org/introduction-to-pynest/
Documentation	http://nest-simulator.org/documentation/
Forum	http://mail.nest-initiative.org/cgi-bin/mailman/listinfo/nest_user https://github.com/nest/nest-simulator/issues
Models	http://www.nest-simulator.org/publications/?sort=search&type=nest_simulated https://senselab.med.yale.edu/ModelDB/ModelList.cshtml?id=2832&allsimu=true
Platforms	MacOS, Linux, Solaris, Windows (via Linux Virtual Machine)

The NEST simulator (Gewaltig and Diesmann 2007) favors simpler, pre-defined, point (or few-compartment) neuron models and focuses on advanced network connectivity specification between those cells. In NEURON, every connection must specify the source synapse and the target cell section, while in NEST, cell connectivity can be specified with abstract rules. Cells can be grouped into layers of various shapes, and different probability distributions can be specified to connect the cells in those layers. Similarly, the synapse parameters that connect those cells can be defined to follow various probability distributions. Like the NEURON simulator, various inputs can be added to the network, and state variables can be read and plotted as output. The focus on network connectivity allows users to rapidly experiment with different network architectures and cell connectivity patterns. Models can be specified in Python (Eppler et al. 2007) or using a native simulator language. NEST has native parallel hardware support via MPI. The combination of simpler cells, ease of specifying network architecture, and optimizations of parallel hardware have allowed NEST to simulate some of the largest spiking neural networks (Kunkel et al. 2014).

XPP

Primary strength	Differential equation/dynamical system behavior analysis
Installation	http://www.math.pitt.edu/~bard/xpp/xpp.html
Documentation	http://www.math.pitt.edu/~bard/xpp/help/xpphelp.html http://www.math.pitt.edu/~bard/bardware/tut/start.html *Simulating, Analyzing, and Animating Dynamical Systems: A Guide to XPPAUT for Researchers and Students* (Ermentrout 2002)
Forum	https://mailman.ucsd.edu/mailman/listinfo/xppaut-l
Models	https://senselab.med.yale.edu/ModelDB/ModelList.cshtml?id=33977&allsimu=true
Platforms	MacOS, Windows, Linux, iOS

XPP (Ermentrout 2002) is a dynamical systems analysis tool that has been very useful to neuroscience researchers. The tool allows the user to define systems of differential equations and provides a rich set of features to analyze the behavior of those systems. For example, the Hodgkin-Huxley equations can be specified in plain text, and the user can select parameter values bound to the GUI slider controls. The sliders can be adjusted, and a plot of the membrane potential versus time is automatically refreshed, elucidating the effect of different parameter values. The tool also allows plotting of nullclines, vector fields, Poincaré maps, and phase-space plots. Additionally, the AUTO feature allows plotting of bifurcation diagrams and exploring the stability of branch points. Finally, a curve fitter based on the Levenberg-Marquardt algorithm is available.

Brian

Primary strengths	Rapid prototyping with XPP-like equation specification Python is native simulator language GPU-accelerated model fitting
Installation	http://brian2.readthedocs.io/en/latest/introduction/install.html
Documentation	https://brian2.readthedocs.io/
Forum	http://groups.google.com/group/briansupport
Models	https://senselab.med.yale.edu/ModelDB/ModelList.cshtml?id=113733
Platforms	MacOS, Windows, Linux

The Brian simulator (Goodman and Brette 2009) can be viewed as a hybrid of the intuitive equation editing of XPP with the network support of NEST. Like in XPP, differential equations for individual neurons and synapses can be entered as plain text. Similar to NEST, Brian enables the management of those cells and synapses with groups and allows connectivity to be specified algorithmically. Unlike NEST and XPP, Brian does not have a separate native simulator language; instead it is implemented as a Python library (Goodman and Brette 2008). This can reduce the learning curve for initial use of the simulator and allows for using popular Python

analysis and plotting packages directly. Support for parallel hardware is available for Brian simulations. For example, parameter searches for neuron models can be parallelized in a cluster environment via MPI or with the help of CUDA-based graphics processing units (GPUs).

Other Simulators and Tools

PCSIM—A Parallel neural Circuit SIMulator (http://www.lsm.tugraz.at/pcsim)
Similar to NEST, PCSIM (Pecevski et al. 2009) favors single-compartment or abstract pre-defined neuron models to define and simulate large neural networks. The simulator is implemented in C++, but Python is used as the main interface. Supports parallel multi-threaded and cluster, via MPI, execution.

Platforms: Linux, others via Linux Virtual Machine.

GENESIS (http://genesis-sim.org)
GENESIS (Wilson et al. 1989) is a simulator with functionality similar to NEURON. Historically, GENESIS was of similar popularity as NEURON; however, in recent years, its use has waned. Many important models implemented in GENESIS are still available on ModelDB.

Platforms: Linux, MacOS, Windows with Cygwin.

MOOSE (https://moose.ncbs.res.in)
The MOOSE simulator (Dudani et al. 2009) is a successor to GENESIS. Many of the original features of GENESIS have been implemented using modern programming techniques, and the simulator has a modern GUI as well as a Python interface. MOOSE allows the user to define arbitrary multi-scale models. Models can be assembled by defining and connecting reaction-diffusion models, single- and multi-compartment neurons, synapses, and networks. The simulator features deterministic and stochastic solvers and can import NeuroML, GENESIS, and NeuroMorpho.org files.

Platforms: Linux, MacOS, Windows (via Linux Virtual Machine).

PSICS—Parallel Stochastic Ion Channel Simulator (http://psics.org)
PSICS (Cannon et al. 2010) allows modeling of stochastic ion channel behavior on morphologically detailed cells. Cell morphology can be imported, and channels can be placed either individually or algorithmically following a distribution.

Platforms: Linux, MacOS, Windows.

MCell—Monte Carlo Cell (http://mcell.org)
MCell (Stiles and Bartol 2001) together with the companion tool CellBlender leverages the popular 3D modeling tool, Blender, to create detailed 3D models of cells and simulate the movement and interaction of molecules using optimized Monte Carlo algorithms.

Platforms: Linux, MacOS, Windows.

STEPS—STochastic Engine for Pathway Simulation (http://steps.sourceforge.net)
STEPS (Hepburn et al. 2012) is a set of Python modules for exact simulations of stochastic reaction-diffusion systems within arbitrary 3D geometry. Also supports local membrane potentials and voltage-gated ion channels.

Platforms: Linux, MacOS, Windows.

MUSIC—Multi-Simulation Coordinator (http://software.incf.org/software/music)
MUSIC (Djurfeldt et al. 2010) is a C++ library that streamlines the building of hybrid models that take advantages of different simulators by implementing a communication protocol that can pass messages between the simulators. The simulators can run in separate processes and communicate with each other via the interface defined by MUSIC.

Platforms: Linux.

Programming Languages

Below, we review the most popular programing languages and their strengths for model development.

MATLAB is a programming language developed by MathWorks, which has been commercially developed and features detailed documentation and a large user base. Many computational neuroscience models in MATLAB are available on ModelDB; however, most simulators do not have a MATLAB interface. The language syntax is optimized for matrix operations, and there are packages available for signal analysis and visualization. MATLAB also has packages for interfacing with other programming languages like Python and C++.

Python is an open-source scripting language that is designed to be easy to learn and extend. It has many scientific libraries available for signal processing and visualization. Many simulators have Python interfaces available, making Python a good choice as a language for both model definition and analysis. One downside of Python is that it is a scripted, dynamically typed language. This can impact performance in computationally intensive applications. To alleviate this, the Cython project (http://cython.org) allows for programming in Python but with the performance and type-checking benefits of compilation (Behnel et al. 2011). Simulators such as Brian utilize Cython to produce native Python simulations that run nearly as fast as their counterparts in pure C code.

The iPython project (Pérez and Granger 2007) allows users to create interactive notebooks that can be used to share code blocks and analysis results with others. This has been extended to Jupyter (http://jupyter.org) which is not specific to Python.

C++ is a popular object-oriented version of the C programming language, which generally is used when computational efficiency is critical. One downside of C++

is that it is a low-level, compiled language. This means that in order to achieve the highest performance, tedious and error-prone techniques of memory management and pointer arithmetic must be utilized. Because maintaining a large C++ project can be costly in terms of productivity, it is not uncommon to see software that is mostly developed in a more forgiving language (e.g., Python) with selected code areas optimized with C++.

Simulator-Independent Languages

Models created using a general programming language or using a specific simulator are often not usable by researchers using different simulators or languages without a lengthy conversion process. Because there is a significant overlap in functionality of some simulators, projects to standardize model specification have arisen to address the problem of model reuse. The two main efforts are NeuroML, a declarative XML model description language, and PyNN, a procedural Python-based library for model specification. Modelers are strongly encouraged to describe most or at least portions of their models using such a simulator-independent language (SIL). One of the main benefits of doing so is that, once implemented, the toolchain of each SIL can be used to convert the model into the language of a specific simulator. Another is that the ability to determine the structure of the model, and its parameters make it straightforward to programmatically manipulate models without specific knowledge of the implementation details. This effectively makes models expressed using SILs more useful to a wider audience than the same models implemented in a simulator specific or a general programming language.

NeuroML (https://neuroml.org)
NeuroML is a declarative simulator-independent model specification language that uses a standardized XML schema to describe neural models (Crook et al. 2007; Gleeson et al. 2010). The language can specify ion channel and synapse dynamics, abstract point neurons, morphologically detailed cells, and large networks. The channel dynamics can be described by either reusing one of the numerous existing formalisms such as the Hodgkin-Huxley-type conductance-based channel kinetics or via the Low Entropy Model Specification (Cannon et al. 2014) language when arbitrary dynamics are required.

Models can be specified in NeuroML as an XML file via a text editor or using an editor with a GUI. neuroConstruct (Gleeson et al. 2007) is an application that allows for the construction of NeuroML files and features an interface to visualize 3D cells and networks. Once a model is specified, the pyNeuroML or jNeuroML ((Vella et al. 2014) https://github.com/NeuroML) tools can be used to convert NeuroML files to simulator- specific code that can be executed on a target simulator. The currently supported simulators are NEURON, GENESIS, MOOSE, XPP, as well as Brian, NEST, and others through PyNN. The tools also can export models to C, MATLAB, NineML, SpineML, VHDL, and LEMS languages.

PyNN (http://neuralensemble.org/trac/PyNN)
PyNN is a set of Python libraries that allows simulator-independent model specification procedurally via Python code (Davison et al. 2007). The library features a set of pre-defined neuron models and synapses and provides methods for defining cell placement and connectivity rules. With a single line of code, the PyNN model can then be directed to run on a supported simulator (currently NEURON, NEST, PCSIM, or Brian). Similarly, PyNN models can be executed on neuromorphic hardware; models that are supported by the target hardware can be run on either the BrainScaleS (Schemmel et al. 2010) or the SpiNNaker (Furber et al. 2013) platforms.

Simulators vs. Programming Languages

We have made a distinction between dedicated simulators and general programming languages. Simulators generally include optimized integrators, abstractions for easier definition of neural concepts or equations, input and output mechanisms, and plotting and visualization features. Popular programming languages like MATLAB, Python, Java, or C++ tend to have a large pool of skilled workers and generally have libraries that can be used in modeling and analysis work. However, the development teams of the popular simulators have invested considerable resources into building, testing, debugging, and optimizing the simulation infrastructure. Re-implementing that functionality in custom code takes considerable time, decreasing productivity. More importantly, it would be difficult to reuse parts of previously built models, and a nontrivial amount of time might be spent ensuring the re-implemented models work correctly. Similarly, models that are easier to quickly reuse (e.g., copy and paste) in a popular simulator are more likely to be reused and cited. While using a simulator to define the model is a large part of model building, analysis of the model simulation data often is performed using a general programming language.

A major component of simulator productivity comes from the documentation and example models available to new users. The more widely used simulators tend to have extensive documentation, large forums or mailing list archives, and many tutorials and examples. Similarly, widely used programming languages have large documentation and forum bases and also have mature integrated development environments (IDEs) that make it easy to efficiently write, organize, debug, and refactor code, as well as measure performance. To estimate the use of different simulators within the computational neuroscience community, we counted the number of models encoded in a particular simulator language that are available in the ModelDB (Hines et al. 2004) database and the number of citations of the publication describing the simulator on Google Scholar. Similarly, for programming languages, we estimated their popularity by counting the number of models using them in ModelDB, the number of job postings listing them on the global job postings aggregator Indeed.com, and the number of questions tagged on the popular programming question and answer site StackOverflow.com.

Simulator	Models	Citations
NEURON	537	1,836
XPP	90	1,266
GENESIS	38	1,114
NEST	7	492
Brian	36	309
MCell	2	259
NeuroML	5	206
neuroConstruct	6	139
Emergent	3	96
STEPS	5	64
CalC	8	59
SNNAP	21	55
PSICS	1	45
Nengo	2	42

	Models	Job Postings	Questions
MATLAB	258	5,145	63,870
Python	118	28,552	622,485
C or C++ prog	106	27,330	466,669
Java	11	53,528	1,127,259
FORTRAN	10	550	6,545
Mathematica	5	139	39,683
R	4	10,098	150,598

Fig. 2 Popular simulators and programming languages used in computational neuroscience models. Left: The number of models available on ModelDB for a given simulator and the Google Scholar citation count for the simulator's corresponding publication. Right: The number of models on ModelDB implemented in a given programming language, the number of Indeed.com job postings seeking candidates with experience in that language, and the number of questions on StackOverflow.com tagged with that language

As shown in Fig. 2, these results suggest that NEURON, XPP, GENESIS, NEST, and Brian are the most widely used simulators, while MATLAB, Python, and C++ are the most popular programming languages within the computational neuroscience community. Python is the second most popular programming language; however, many simulators and other resources have Python-based interfaces. These include NEURON, NEST, Brian, NeuroML, neuroConstruct, PCSIM, and Nengo (Stewart et al. 2009). These interfaces allow a user to define and set up the simulator model using the Python language and in many cases bypass the native simulator language, making Python a unique language that can be used for both model definition and model result analysis.

Finally, if no single simulator can meet a research need, but a combination of several simulators could, a tool like MUSIC (Djurfeldt et al. 2010) can be used to obtain the benefits of multiple simulators. For example, a model implemented in NEST was used to send and receive spike data to and from a model implemented in MOOSE with the MUSIC library acting as the orchestrating middleware to facilitate the communication (Djurfeldt et al. 2010).

Running, Fitting, Testing, and Visualizing Models

Data-driven model development requires fitting models to experimental data. Additional challenges arise in visualizing simulation results and validating models against more extensive simulation experiments that mimic multiple experimental paradigms. Here, we describe resources to aid in these steps. For an overview, see Fig. 3.

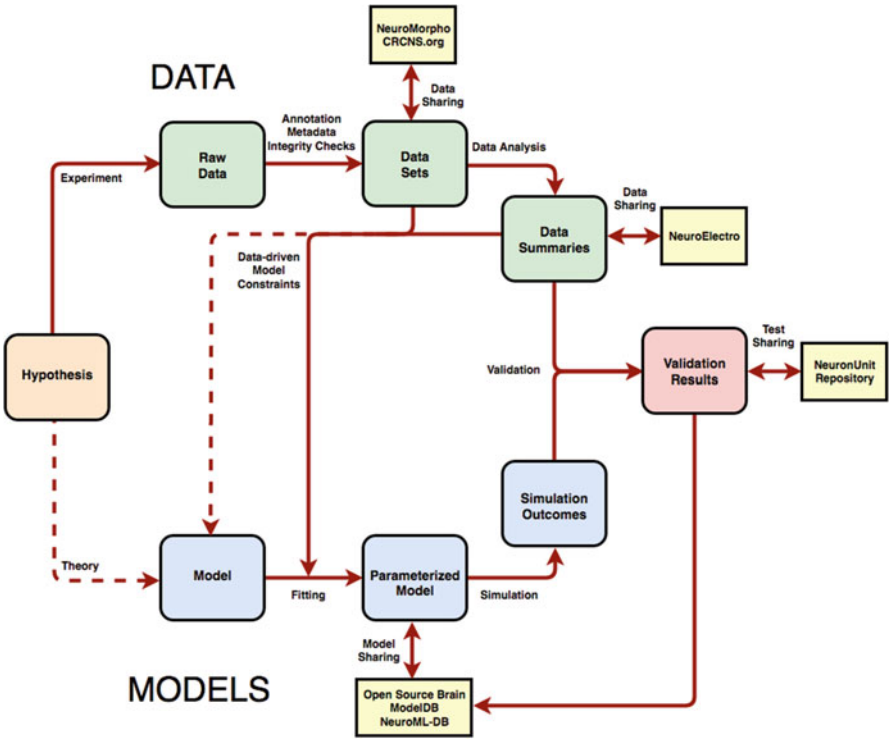

Fig. 3 Overview of the development of data-driven models including model fitting, model sharing, and model validation. Experimental data are shared through open-source resources. Typically, published results form the basis of the model, and additional open-source data or data from new experiments are used to constrain model parameters during the model fitting process. Once the basic properties have been established, computational models and results are shared through model sharing resources. Model validation is performed to compare multiple models by testing how well simulation outcomes match additional experimental results. The validation framework that makes use of tests of individual properties also can be used during the fitting process

Running Models

All of the simulators discussed above execute their models on the CPU. As models in neuroscience become more complex, computational efficiency is increasingly important. To decrease simulation time, simulations can be parallelized across several CPUs on a single machine, a cluster of machines, or a high-performance MPI server cluster. Increasingly, there are resources for running models remotely such as the Neuroscience Gateway Portal (NSG, http://nsgportal.org). The NSG Portal is funded by the US National Science Foundation and provides free supercomputer access to neuroscience researchers. After requesting an account, data and models can be uploaded through a website for execution on supercomputers at the University of California San Diego or the University of Texas Austin. NSG

supports models written in Python, as well as the following simulators: Brian, NEST, NEURON, PGENESIS, PyNN, and FreeSurfer. The availability of such resources can be used to execute parallelized NeuroML models obtained from OpenSourceBrain.org (Gleeson et al. 2015). For example, a NeuroML model can be converted to parallel NEURON using the NetPyNE library ((Dura-Bernal et al. 2016); https://github.com/neurosim-lab/netpyne) and then executed at the NSG Portal.

Hardware Acceleration: Graphics Processing Units and Neuromorphic Hardware

Parallelization also can be achieved locally via utilization of off-the-shelf graphic cards or specialized hardware. Generally, the more customized the hardware for a specific model, the faster it will run. The customization can range from taking advantage of the parallel processing cores of modern graphics cards to custom digital, or even analog, application-specific integrated chips (ASIC). The disadvantage of customized hardware is reduced flexibility. Models have to be coded in a specific fashion and usually have to be mindful of the specific hardware limitations.

Graphics processing units (GPUs) that have general programming capabilities via languages like NVidia CUDA or OpenCL have hundreds or thousands of cores that can execute sets of instructions in parallel. If those computations are independent from each other, the performance gains compared to serial execution can be several orders of magnitude. One such "embarrassingly parallel" application in computational neuroscience is model parameter fitting. For example, the Brian simulator has a feature to perform model fitting to electrophysiology data that can result in 60-fold performance improvement (Goodman and Brette 2008) using GPUs versus single processor execution.

Similarly, since many neural network models involve integrating hundreds or thousands of mostly independent differential equations, they too can benefit from the parallel execution on GPUs. For example, the GeNN framework can generate arbitrary neuron model code that executes on a CUDA GPU and results in up to 200-fold performance improvement over a single CPU core (Yavuz et al. 2016). A similar approach taken by NeMO simulated 40,000 Izhikevich neurons (Izhikevich 2004) with 1000 synapses each in real time (Fidjeland et al. 2009).

Field-programmable gate arrays (FPGAs) are special purpose-integrated circuits that have thousands of logic blocks that can be programmed to implement arbitrary logic circuits. They are usually programmed using a hardware description language like VHDL or Verilog. Because FPGAs are inherently parallel, speed gains can be substantial. For example, using an FPGA board, Cheung et al. (2012) simulated a network composed of 64,000 Izhikevich neurons, with 1000 synapses each at 2.5 times the biological real time.

SpiNNaker is a microprocessor that has been specially designed for simulating spiking neural networks. Each chip is composed of 20 ARM cores and can simulate the activity of about 1000 arbitrary point neurons in real time (Khan et al. 2008). The chips can be joined into larger boards, and the boards can be stacked to accommodate large-scale neural networks. With the help of PyNN (Davison et al. 2007), models compatible with SpiNNaker can be seamlessly executed on a cluster or on the SpiNNaker platform.

TrueNorth is a neuromorphic chip developed by IBM. One chip features one million modified-LIF (Cassidy et al. 2013) neurons, with up to 256 synapses each (Merolla et al. 2014). Just like SpiNNaker, these chips can be tilled in boards, and boards can be stacked. In a performance test utilizing all the neurons on the chip and random connectivity, the chip performed 500–1500 times faster than a single CPU and 20–60 times faster than a 32-host Blue Gene cluster (Cassidy et al. 2014).

BrainScaleS is an analog hardware platform that features naturally stochastic adaptive exponential (AdEx) neurons that can each have 10K synapses (Schemmel et al. 2010). Because the neurons are based on an analog circuit, the chip is very fast. For example, a simulation of 200K neurons, with 40M synapses, ran 10,000 times faster than biological real time (Schemmel et al. 2012). Similar to SpiNNaker, PyNN models that are supported by the platform can be executed on BrainScaleS. A web interface is available that allows uploading of PyNN models to be executed on one of the Human Brain Project's BrainScaleS hardware units.

The Human Brain Project Neuromorphic Computing Platform provides HBP researchers and affiliates with access to the HBP neuromorphic hardware chips: the analog BrainScaleS and the digital SpiNNaker. BrainScaleS models run 1000–10,000 times faster than real time, while SpiNNaker models run at biological real time. Similar to the NSG Portal, models implemented with PyNN and supported by the two hardware platforms can be uploaded via a web interface (or via Python interface) and executed on one of the platforms. Submitting jobs requires an HBP Collaboratory account, which can be requested online.

Visualizing Models and Results

Many simulators that emerged before Python became popular implemented their own plotting and visualization functionalities. More recently developed simulators (e.g., Brian, NEST) delegate plotting functionalities to specialized Python visualization libraries.

NEURON features built-in 2D and 3D plotting capabilities. The 2D plots allow visualization of any simulation variable (e.g., membrane potentials, currents) and spike trains. The 3D plot functionality allows visualization of 3D morphology of cells. Animations are also possible.

XPP's default view shows a plot of the main integration variable versus time. The UI also features three slider controls that can be assigned to modify the value of a specific parameter. The sliders can then be dragged, and an updated version

of the plotted variable is immediately displayed. The AUTO sub-package can plot bifurcation diagrams. Many other custom plots including phase planes can be selected through the menu items.

neuroConstruct (http://neuroconstruct.org) is able to construct or load cell morphologies and network models in 3D (Gleeson et al. 2007). The full model can be viewed in 3D, and individual sections can be selected so that their properties can be inspected and modified. neuroConstruct can generate NeuroML for the resulting model, as well as simulation code for a variety of simulators, and simulation results can be displayed within the neuroConstruct user interface.

Geppetto (http://geppetto.org) is a web-based visualization and simulation platform (Idili et al. 2011). The software is a web application that connects to a backend simulator and provides a web-browser-based simulator user interface that shows interactive 3D morphology and 2D plots. The 3D plot allows selection of segments and inspection of their properties. The 2D plots can include variable versus time plots and connectivity matrix widgets. Geppetto is used by OpenSourceBrain to allow in-browser visualization of uploaded NeuroML models, while the OpenWorm Project (http://www.openworm.org) uses the platform to display a 3D model of *C. elegans* movement (Szigeti et al. 2014). Geppetto also supports the visualization of electrophysiology data traces from Neurodata without Borders (NwB) files (Teeters et al. 2015).

Fitting Models

Once the initial model has been implemented, researchers can use various optimization tools to tune the model parameter values to fit experimental data. There is a wide range of optimization algorithms available; see (2008) for review. The tools described below utilize algorithms that are best suited for neuronal model fitting.

NEURON has a built-in curve fitter that provides a GUI to specify the parameter values for an arbitrary algebraic expression to fit against imported datasets. Similarly, the Multiple Run Fitter (MRF) feature can be used to fit one or more NEURON model variable values under different experimental conditions such as different levels of current injection (Carnevale 2007). The curve fitter and the MRF both use the PRAXIS algorithm (Brent 2013) to perform the optimization and can be parallelized with MPI. Similar to NEURON, **XPP** features a curve fitter that will optimize the XPP model parameter values to fit a specified dataset using the Levenberg-Marquardt algorithm (Ermentrout 2002).

The **Brian** simulator has a model fitter to fit against experimental spike time data. Parallelization is supported both via MPI and also notably via CUDA GPUs. In the GPU case, the speedup versus a single CPU can be up to 60 fold (Goodman and Brette 2009).

Neurofitter (Van Geit et al. 2007) and **Optimizer** (Friedrich et al. 2014) are software packages that can be used with simulators to fit model parameters to experimental data. Neurofitter uses XML files to set the optimization parameters,

and Optimizer has a GUI for this task. Both tools feature a range of optimization algorithms including evolutionary and simulated annealing algorithms. Neurofitter supports parallelization via MPI. The **BluePyOpt** library performs similar functions and provides additional visualization features and support for parallel hardware (Van Geit et al. 2016).

Python libraries specializing in optimization also can be used for model fitting, which can be used if a simulator has a Python interface. Two popular libraries with a wide range of algorithms are **scipy.optimize** (Jones et al. 2001) and **NLopt** (Johnson 2014). NLopt is notable for a range of derivative-free optimization algorithms. The parameter sweeps for both libraries can be parallelized using MPI with the help of the **mpi4py** library (Dalcín et al. 2005).

Finding Models

There are many computational neuroscience models publicly available to researchers. For this reason, it might be more productive to find a previously built model and reuse it in its entirety or with some modifications. In some cases, combining multiple different models could also yield productive results. For example, several models of particular ion channel currents can be combined to yield a cell with a particular behavior. In addition to the web resources listed above for finding models written for the most widely used simulators, there are several resources dedicated to model sharing and collaborative development.

ModelDB (https://senselab.med.yale.edu/ModelDB)
ModelDB (Hines et al. 2004) is a repository of models that have been published in scientific journals. It is one of the largest repositories, featuring over 1000 models covering a wide range of simulators and programming languages. It has a robust search engine, browsing and model viewing capabilities, and an online model submission system.

OpenSourceBrain (http://opensourcebrain.org)
OpenSourceBrain (OSB) is the flagship model repository for NeuroML models that fosters collaboration (Gleeson et al. 2015). The website allows creation of accounts for laboratories, researchers, and projects and allows browsing and searching of these models. Multiple researchers can then coordinate model development using version control systems and show the results of automated tests via the Travis system. OSB also has several features specific for NeuroML models. Models can be marked to reflect how well their specific, auto-converted, simulator versions match the original version. NeuroML models that specify morphology can be interactively visualized via the web-based visualization and simulation platform Geppetto. As with all NeuroML models, entire models or selected model components like individual channels or cells can be converted to one of the supported simulator formats and executed on the target simulator using the pyNeuroML or jNeuroML tools or with NetPyNE.

NeuroML-DB (http://neuroml-db.org)
NeuroML-DB (Crook and Dietrich 2014) is a database of NeuroML models that features a semantic search engine (Birgiolas et al. 2015). NeuroML models of ion channels, cells, and networks can be searched and downloaded directly from the site. The search engine will return direct keyword results as well as results semantically related (via the Neuroscience Information Framework ontology) to the original query. For example, searching for a cell will also return any ion channels that such cell contains, as well as models of networks that contain the target cell. Combination searches are possible too, for example, searching for the neurotransmitter glutamate and hippocampus will return all glutamatergic hippocampal cells.

Model Validation

One obligatory step of the scientific method is checking the output of the model (the hypothesis) against the experimental data. Too frequently, this is done informally, selectively, and without consideration for continuous improvement of the model. Part of the past challenge has been the lack of an infrastructure for model validation, beyond selecting a figure from the experimental literature and determining whether a model can produce something that is qualitatively similar as determined by eye.

SciUnit (Omar et al. 2014); http://sciunit.scidash.org) was developed to address this problem, turning data-driven model validation into a process that looks more like unit testing (Sarma et al. 2016), a process that is both essential to and ubiquitous in professional software development. The idea is to write a series of "tests," each of which encodes a quantitative summary of some experimental data, and then require each model or version of a model to take these tests, producing a score that summarizes model-data agreement. SciUnit specifies an interface to make this process reliable and to insure that models and tests are paired appropriately. **NeuronUnit** (http://neuronunit.scidash.org) is a library based on SciUnit that facilitates this process specifically for neuron and ion channel models. It provides a wide range of tests related to the properties of models that mimic electrophysiological measures and can automatically pull data from external sources like those described in the next section, to parameterize each test with the data relevant to the neuron or ion channel being modeled. Models expressed in NeuroML can be validated directly using any NeuroML-compatible simulator; other models require only a small Python wrapper giving access to the model functionality (e.g., inject current, run the simulation, etc.) that the tests must access in order to compute the result.

Testing models in this way achieves several important goals: (1) model performance can be evaluated on a continuous basis during development or even after publication as new data come to light; (2) different models across labs and

institutions can use a common set of tests to evaluate models; and (3) the process for validation is transparent and open source.

Resources for Experimental Data

It has become easier than ever to locate high-quality experimental data that can be used to constrain model parameters or assess simulation outcomes through validation. Previously, the state of the art was to identify specific journal articles and use the subset of data reported therein or contact the authors directly for additional data. Now, much of this same data is available in public databases that make it quite easy to locate experiment files, waveforms, or summary statistics for a wide variety of cell types and brain areas. Here, we discuss key experimental data resources for each of several modalities.

Cell and Ion Channel Properties

There are several resources providing data specific to neurons and their electrophysiological, anatomical, or histological properties. For example, detailed anatomical reconstructions of neurons, and statistical properties of their neurites, can be found on **NeuroMorpho** (Ascoli et al. 2007). Currently, over 2000 reconstructions are available from hippocampus alone, spanning all of the major anatomical subdivisions. The Allen Institute's **Big Neuron** project aims to use state-of-the-art techniques to reconstruct a far larger number of neurons and make these reconstructions available.

Alternatively, the **Cell Centered Database** (Martone et al. 2003) focuses on images from light and electron microscopy, with excellent coverage of hippocampal areas; although the data is largely nonquantitative, the images cover a wider range of cell types including glial cells, which have become increasingly appreciated in modeling work.

Electrophysiological properties of neurons, especially measurements typically reported in journal article tables such as input resistance, action potential height and width, and rheobase, are curated in the **NeuroElectro Project** (Tripathy et al. 2014). NeuroElectro contains over 1000 electrophysiological values from the CA1 pyramidal cell alone, and several hundred more from other hippocampal cell types.

The SenseLab at Yale has several databases, including **NeuronDB** and **CellPropDB**, (Crasto et al. 2007), which contain mostly qualitative reports on the ionic currents and neurotransmitters associated with different neuron types, including their distribution across the dendritic tree.

More quantitative information on ion channels, including the dynamics needed for modeling, is available at **Channelpedia** (Ranjan et al. 2011), a resource produced by the Blue Brain Project. Recently two more large single neuron experimental data resources have become available, both containing data produced using

a standardized workflow to reduce heterogeneity across experiments. The **Allen Cell Types Database** (ACTD), a product of the Allen Institute for Brain Science, contains electrophysiology, anatomy, and gene expression data for dozens of cell types across mouse visual cortex. While it does not contain any physiological data about hippocampal neurons, it is comprehensive across cortical layers, including those both afferent and efferent to hippocampal neurons. The Blue Brain Project has a similar resource, also limited to neocortex, called **Digital Reconstruction of Neocortical Microcircuitry** (DRNM, (Markram et al. 2015)), with electrophysiological, anatomical, and microcircuit connectivity data about neurons.

Systems Physiology

The resources above mostly focus on data obtained in brain slices or sections, with a focus on single or small groups of neurons. The corresponding recordings are usually obtained via patch clamp or sharp electrodes. For researchers interested in larger ensembles of neurons and/or recordings in intact organisms, the **Collaborative Research in Computational Neuroscience** (Teeters and Sommer 2009) website hosts nearly 100 separate datasets, collected by a variety of investigators and contributed to the site, spanning several brain areas and animal models. Like, the ACTD and DRNM, these datasets usually contain most or all of the raw physiology data, which for recording with large arrays can be tens of GB in size. Documentation is provided by the contributors. CRCNS hosts six datasets corresponding to hippocampal recordings, all from the lab of Dr. Gyorgy Buzsáki.

Systems Anatomy

For those interested in the connectivity of brain areas, there exist several resources, each focusing on different scales of connectivity. The DRNM has abundant data on synaptic connectivity (probability, strength, and dynamics of synapses between neurons), but this is limited to the neocortex. There are other major projects in development to provide large public resources for hippocampal data. Hippocampome.org (Wheeler et al. 2015) provides extensive anatomical, histological, connectivity, and electrophysiological data about hippocampal cell types. Compared with NeuroElectro, Hippocampome.org utilizes a much finer division of cell types, reporting electrophysiological properties for 122 distinct hippocampal cell types. The Human Brain Project also is working on a rodent hippocampal data portal, although the public-facing component of this project is still in development.

For longer range connectivity, The **Brain Architecture Management System** (BAMS; (Bota et al. 2005)) contains neural connectivity information across species that has been manually curated from the existing research literature. For those modeling the primate brain, **CoCoMac** (Bakker et al. 2012) contains records of tracing studies in the macaque.

For an even more wider view of connectivity, **The Human Connectome Project** (Van Essen et al. 2013) is a large-scale effort to map complete structural and functional neural connections in vivo in individual humans. Similarly, **Brain Map** (Laird et al. 2005) consists of a database and related software to search published functional and structural human neuroimaging experiments.

Integration

There are also several useful uber databases that help integrate these resources, allow them to be more easily searched, and link out to still more resources. **NeuroLex** (Larson and Martone 2013) provides a platform for community annotation of neuron types on the basis of anatomical, histological, and electrophysiological properties. It is an excellent first place to start when one has a particular neuron or group of neurons in mind. Some of the resources listed above use the NeuroLex nomenclature and even the internal identification numbers to index their own neuron data.

Lastly, the **Neuroscience Information Framework** (NIF, (Marenco et al. 2010; Cachat et al. 2012)) provides tools for searching across many of these databases. The success of this search mechanism is based in part on their development of domain-specific ontologies for neuroscience that link related concepts. For example, in NIF, the search query "CA1 pyramidal cell" returns a number of database records including links to relevant research literature, gene expression data, ion channel information, and hits from BioNumbers (Milo et al. 2010), a compendium of random quantitative facts extracted from the research literature. A useful example of the latter: the approximate number of AMPA receptors opened by a single vesicle in the dendrites of CA1 pyramidal neurons.

Outlook

Increasingly, computational models are being used by experimentalists to understand complex neurophysiological data. Similarly, theoreticians use models to investigate general principles underlying neural computation. A wide array of available resources and tools allow for more rapid creation, simulation, visualization, and validation of data-driven models.

As models become more complex, model reproducibility, transparency, and reuse become even more important to the success of the scientific method. Current efforts toward model sharing databases, simulator-independent languages, and tools for model validation play a vital role in addressing these issues. The range of tools and resources for computational modeling is constantly expanding. In addition, publicly available experimental data that can be used to constrain models are more comprehensive, covering a broader range of scales, datatypes, and experimental paradigms.

Experimental data resource	Web location	Data type
Allen Cell Types Database	http://celltypes.brain-map.org	Anatomy, electrophysiology, gene expression
Brain Architecture Management System	http://bams2.bams1.org	Neural connectivity
Big Neuron	https://alleninstitute.org/bigneuron	Anatomical reconstructions
Brain Map	http://brainmap.org	Functional and structural neuroimaging experiments
Cell Centered Database	http://ccdb.ucsd.edu	Cell images
Channelpedia	http://channelpedia.net	Channel information and models
CoCoMac	http://cocomac.g-node.org	Tracing studies from Macaque
CRCNS	http://crcns.org	Electrophysiology data
Digital Reconstruction of Neocortical Microcircuitry	https://bbp.epfl.ch/nmc-portal	Anatomy, electrophysiology, microcircuitry
Hippocampome	http://hippocampome.org	Anatomy, histology, electrophysiology, microcircuitry
Human Connectome Project	http://humanconnectomeproject.org	Structural and functional connectivity
NeuroElectro	http://neuroelectro.org	Electrophysiological properties
NeuroLex	http://neurolex.org	Ontological information
NeuroMorpho	http://neuromorpho.org	Anatomical reconstructions
NeuronDB/CellPropDB	http://senselab.med.yale.edu/NeuronDB	Channels/neurotransmitters
Neuroscience Information Framework	http://neuinfo.org	Federated database across neuroscience

Acknowledgments This work was supported in part by the National Institute on Deafness and Other Communication Disorders and the National Institute of Biomedical Imaging and Bioengineering of the National Institutes of Health under award numbers 1F31DC016811 to JB and R01MH106674 to SMC and R01EB021711 to RCG. The content is solely the responsibility of the authors and does not necessarily represent the official views of the National Institutes of Health.

References

Ascoli GA, Donohue DE, Halavi M (2007) NeuroMorpho.Org: a central resource for neuronal morphologies. J Neurosci 27:9247–9251. https://doi.org/10.1523/JNEUROSCI.2055-07.2007

Bakker R, Wachtler T, Diesmann M (2012) CoCoMac 2.0 and the future of tract-tracing databases. Front Neuroinform 6:30. https://doi.org/10.3389/fninf.2012.00030

Behnel S, Bradshaw R, Citro C, Dalcin L, Seljebotn DS, Smith K (2011) Cython: the best of both worlds. Comput Sci Eng 13:31–39

Birgiolas J, Dietrich SW, Crook S, Rajadesingan A, Zhang C, Penchala SV, Addepalli V (2015) Ontology-assisted keyword search for NeuroML models. ACM, New York, p 37

Bota M, Dong H-W, Swanson LW (2005) Brain architecture management system. Neuroinformatics 3:15–47. https://doi.org/10.1385/NI:3:1:015

Brent RP (2013) Algorithms for minimization without derivatives. Courier Corporation, North Chelmsford

Brette R, Rudolph M, Carnevale T, Hines M, Beeman D, Bower JM, Diesmann M, Morrison A, Goodman PH, Harris FC Jr (2007) Simulation of networks of spiking neurons: a review of tools and strategies. J Comput Neurosci 23:349–398

Cachat J, Bandrowski A, Grethe JS, Gupta A, Astakhov V, Imam F, Larson SD, Martone ME (2012) A survey of the neuroscience resource landscape: perspectives from the neuroscience information framework. Int Rev Neurobiol 103:39–68. https://doi.org/10.1016/B978-0-12-388408-4.00003-4

Cannon RC, O'Donnell C, Nolan MF (2010) Stochastic ion channel gating in dendritic neurons: morphology dependence and probabilistic synaptic activation of dendritic spikes. PLoS Comput Biol 6:e1000886

Cannon RC, Gleeson P, Crook S, Ganapathy G, Marin B, Piasini E, Silver RA (2014) LEMS: a language for expressing complex biological models in concise and hierarchical form and its use in underpinning NeuroML 2. Front Neuroinform 8:79

Carnevale T (2007) Neuron simulation environment. Scholarpedia 2:1378

Carnevale NT, Hines ML (2006) The NEURON book. Cambridge University Press, Cambridge

Cassidy AS, Merolla P, Arthur JV, Esser SK, Jackson B, Alvarez-Icaza R, Datta P, Sawada J, Wong TM, Feldman V (2013) Cognitive computing building block: a versatile and efficient digital neuron model for neurosynaptic cores. In: Proceedings of the international joint conference on neural networks (IJCNN 2013). IEEE, Piscataway, pp 1–10

Cassidy AS, Alvarez-Icaza R, Akopyan F, Sawada J, Arthur JV, Merolla PA, Datta P, Tallada MG, Taba B, Andreopoulos A (2014) Real-time scalable cortical computing at 46 giga-synaptic OPS/watt with. In: Proceedings of the international conference for high performance computing, networking, storage and analysis. IEEE, Piscataway, pp 27–38

Cheung K, Schultz SR, Luk W (2012) A large-scale spiking neural network accelerator for FPGA systems. In: Proceedings of the 22nd international conference on artificial neural networks and machine learning – volume part I. Springer, Berlin/Heidelberg, pp 113–120

Crasto CJ, Marenco LN, Liu N, Morse TM, Cheung K-H, Lai PC, Bahl G, Masiar P, Lam HYK, Lim E, Chen H, Nadkarni P, Migliore M, Miller PL, Shepherd GM (2007) SenseLab: new developments in disseminating neuroscience information. Brief Bioinform 8:150–162. https://doi.org/10.1093/bib/bbm018

Crook SM, Dietrich S (2014) Model exchange with the NeuroML model database. BMC Neurosci 15:1

Crook S, Gleeson P, Howell F, Svitak J, Silver RA (2007) MorphML: level 1 of the NeuroML standards for neuronal morphology data and model specification. Neuroinformatics 5:96–104

Dalcín L, Paz R, Storti M (2005) MPI for Python. J Parallel Distrib Comput 65:1108–1115

Davison AP, Brüderle D, Eppler J, Kremkow J, Muller E, Pecevski D, Perrinet L, Yger P (2007) PyNN: a common Interface for neuronal network simulators. Front Neuroinform 2:11–11

Djurfeldt M, Hjorth J, Eppler JM, Dudani N, Helias M, Potjans TC, Bhalla US, Diesmann M, Kotaleski JH, Ekeberg Ö (2010) Run-time interoperability between neuronal network simulators based on the MUSIC framework. Neuroinformatics 8:43–60

Dudani N, Ray S, George S, Bhalla US (2009) Multiscale modeling and interoperability in MOOSE. BMC Neurosci 10:1

Dura-Bernal S, Suter BA, Neymotin SA, Kerr CC, Quintana A, Gleeson P, Shepherd GMG, Lytton W (2016) NetPyNE: a Python package for NEURON to facilitate development and parallel simulation of biological neuronal networks. BMC Neurosci 17:P105

Eliasmith C, Stewart TC, Choo X, Bekolay T, DeWolf T, Tang Y, Tang C, Rasmussen D (2012) A large-scale model of the functioning brain. Science 338:1202–1205

Eppler JM, Helias M, Muller E, Diesmann M, Gewaltig MO (2007) PyNEST: a convenient Interface to the NEST simulator. Front Neuroinform 2:12–12

Ermentrout B (2002) Simulating, analyzing, and animating dynamical systems: a guide to XPPAUT for researchers and students. SIAM, Philadelphia

Fidjeland AK, Roesch EB, Shanahan MP, Luk W (2009) NeMo: a platform for neural modelling of spiking neurons using GPUs. In: 20th IEEE international conference on application-specific systems, architectures and processors, 2009. IEEE, Piscataway, pp 137–144

Friedrich P, Vella M, Gulyás AI, Freund TF, Káli S (2014) A flexible, interactive software tool for fitting the parameters of neuronal models. Front Neuroinform 8:63

Furber SB, Lester DR, Plana LA, Garside JD, Painkras E, Temple S, Brown AD (2013) Overview of the SpiNNaker system architecture. IEEE Trans Comput 62:2454–2467

Gewaltig M-O, Diesmann M (2007) NEST (neural simulation tool). Scholarpedia 2:1430

Gleeson P, Steuber V, Silver RA (2007) neuroConstruct: a tool for modeling networks of neurons in 3D space. Neuron 54:219–235

Gleeson P, Crook S, Cannon RC, Hines ML, Billings GO, Farinella M, Morse TM, Davison AP, Ray S, Bhalla US (2010) NeuroML: a language for describing data driven models of neurons and networks with a high degree of biological detail. PLoS Comput Biol 6:e1000815

Gleeson P, Silver A, Cantarelli M (2015) Open source brain. In: Jaeger D, Jung R (eds) Encyclopedia of computational neuroscience. Springer, New York, pp 2153–2156

Goodman D, Brette R (2008) Brian: a simulator for spiking neural networks in Python. BMC Neurosci 9:1–2

Goodman DFM, Brette R (2009) The brian simulator. Front Neurosci 3:26

Hepburn I, Chen W, Wils S, De Schutter E (2012) STEPS: efficient simulation of stochastic reaction–diffusion models in realistic morphologies. BMC Syst Biol 6:36

Hines ML, Morse T, Migliore M, Carnevale NT, Shepherd GM (2004) ModelDB: a database to support computational neuroscience. J Comput Neurosci 17:7–11. https://doi.org/10.1023/B:JCNS.0000023869.22017.2e

Hines ML, Davison AP, Muller E (2008) NEURON and Python. Front Neuroinform 3:1–1

Idili G, Cantarelli M, Buibas M, Busbice T, Coggan J, Grove C, Khayrulin S, Palyanov A, Larson S (2011) Managing complexity in multi-algorithm. In: Multi-scale Biological simulations: an integrated software engineering and Neuroinformatics approach. Front Neuroinform. Conference Abstract: 4th INCF Congress of Neuroinformatics. https://doi.org/10.3389/conf.fninf.2011.08.00112

Izhikevich EM (2004) Which model to use for cortical spiking neurons? IEEE Trans Neural Netw 15:1063–1070. https://doi.org/10.1109/TNN.2004.832719

Johnson SG (2014) The NLopt nonlinear-optimization package. http://ab-initio.mit.edu/nlopt

Jones E, Oliphant T, Peterson P (2001) SciPy: Open source scientific tools for Python. http://www.scipy.org

Khan MM, Lester DR, Plana LA, Rast A, Jin X, Painkras E, Furber SB (2008) SpiNNaker: mapping neural networks onto a massively-parallel chip multiprocessor. In: Proceedings of the international joint conference on neural networks (IJCNN 2008). IEEE, Piscataway, pp 2849–2856

Kunkel S, Schmidt M, Eppler JM, Plesser HE, Masumoto G, Igarashi J, Ishii S, Fukai T, Morrison A, Diesmann M (2014) Spiking network simulation code for petascale computers. Front Neuroinform 8:78

Laird AR, Lancaster JJ, Fox PT (2005) BrainMap. Neuroinformatics 3:65–77. https://doi.org/10.1385/NI:3:1:065

Lapicque L (1907) Recherches quantitatives sur l'excitation électrique des nerfs traitée comme une polarisation. J Physiol Pathol Gen 9:620–635

Larson SD, Martone ME (2013) NeuroLex.org: an online framework for neuroscience knowledge. Front. Neuroinformatics 7:18. https://doi.org/10.3389/fninf.2013.00018

Marenco L, Wang R, Shepherd GM, Miller PL (2010) The NIF DISCO framework: facilitating automated integration of neuroscience content on the web. Neuroinformatics 8:101–112. https://doi.org/10.1007/s12021-010-9068-8

Markram H (2006) The blue brain project. Nat Rev Neurosci 7:153–160. https://doi.org/10.1038/nrn1848

Markram H, Muller E, Ramaswamy S, Reimann MW, Abdellah M, Sanchez CA, Ailamaki A, Alonso-Nanclares L, Antille N, Arsever S, Kahou GAA, Berger TK, Bilgili A, Buncic N, Chalimourda A, Chindemi G, Courcol J-D, Delalondre F, Delattre V, Druckmann S, Dumusc R, Dynes J, Eilemann S, Gal E, Gevaert ME, Ghobril J-P, Gidon A, Graham JW, Gupta A, Haenel V, Hay E, Heinis T, Hernando JB, Hines M, Kanari L, Keller D, Kenyon J, Khazen G, Kim Y, King JG, Kisvarday Z, Kumbhar P, Lasserre S, Le Bé J-V, Magalhães BRC, Merchán-Pérez A, Meystre J, Morrice BR, Muller J, Muñoz-Céspedes A, Muralidhar S, Muthurasa K, Nachbaur D, Newton TH, Nolte M, Ovcharenko A, Palacios J, Pastor L, Perin R, Ranjan R, Riachi I, Rodríguez J-R, Riquelme JL, Rössert C, Sfyrakis K, Shi Y, Shillcock JC, Silberberg G, Silva R, Tauheed F, Telefont M, Toledo-Rodriguez M, Tränkler T, Van Geit W, Díaz JV, Walker R, Wang Y, Zaninetta SM, DeFelipe J, Hill SL, Segev I, Schürmann F (2015) Reconstruction and simulation of neocortical microcircuitry. Cell 163:456–492. https://doi.org/10.1016/j.cell.2015.09.029

Martone ME, Zhang S, Gupta A, Qian X, He H, Price DL, Wong M, Santini S, Ellisman MH (2003) The cell-centered database: a database for multiscale structural and protein localization data from light and electron microscopy. Neuroinformatics 1:379–395. https://doi.org/10.1385/NI:1:4:379

Merolla PA, Arthur JV, Alvarez-Icaza R, Cassidy AS, Sawada J, Akopyan F, Jackson BL, Imam N, Guo C, Nakamura Y (2014) A million spiking-neuron integrated circuit with a scalable communication network and interface. Science 345:668–673

Migliore M, Cavarretta F, Hines ML, Shepherd GM (2014) Distributed organization of a brain microcircuit analyzed by three-dimensional modeling: the olfactory bulb. Front Comput Neurosci 8:50

Milo R, Jorgensen P, Moran U, Weber G, Springer M (2010) BioNumbers—the database of key numbers in molecular and cell biology. Nucleic Acids Res 38:D750–D753. https://doi.org/10.1093/nar/gkp889

Omar C, Aldrich J, Gerkin RC (2014) Collaborative infrastructure for test-driven scientific model validation. In: Companion proceedings of the 36th international conference on software engineering. ACM, New York, pp 524–527

Pecevski D, Natschläger T, Schuch K (2009) PCSIM: a parallel simulation environment for neural circuits fully integrated with Python. Front Neuroinform 3:11

Pérez F, Granger BE (2007) IPython: a system for interactive scientific computing. Comput Sci Eng 9:21–29

Ranjan R, Khazen G, Gambazzi L, Ramaswamy S, Hill SL, Schürmann F, Markram H (2011) Channelpedia: an integrative and interactive database for ion channels. Front Neuroinform 5:36. https://doi.org/10.3389/fninf.2011.00036

Rosenblatt F (1958) The perceptron: a probabilistic model for information storage and organization in the brain. Psychol Rev 65:386

Sarma GP, Jacobs TW, Watts MD, Ghayoomie SV, Larson SD, Gerkin RC (2016) Unit testing, model validation, and biological simulation. F1000Research 5:1946. https://doi.org/10.12688/f1000research.9315.1

Schemmel J, Briiderle D, Griibl A, Hock M, Meier K, Millner S (2010) A wafer-scale neuromorphic hardware system for large-scale neural modeling. In: Proceedings of 2010 IEEE international symposium on circuits and systems (ISCAS). IEEE, Piscataway, pp 1947–1950

Schemmel J, Grübl A, Hartmann S, Kononov A, Mayr C, Meier K, Millner S, Partzsch J, Schiefer S, Scholze S (2012) Live demonstration: a scaled-down version of the brainscales wafer-scale neuromorphic system. In: Proceedings of 2012 IEEE international symposium on circuits and systems (ISCAS). IEEE, Piscataway, pp 702–702

Stewart TC, Tripp B, Eliasmith C (2009) Python scripting in the Nengo simulator. Front Neuroinform 3:7

Stiles JR, Bartol TM (2001) Monte Carlo methods for simulating realistic synaptic microphysiology using MCell. In: De Schutter E (ed) Computational neuroscience: realistic modeling for experimentalists. CRC Press, Boca Raton, pp 87–127

Szigeti B, Gleeson P, Vella M, Khayrulin S, Palyanov A, Hokanson J, Currie M, Cantarelli M, Idili G, Larson S (2014) OpenWorm: an open-science approach to modeling Caenorhabditis elegans. Front Comput Neurosci 8:137

Teeters JL, Sommer FT (2009) CRCNS.ORG: a repository of high-quality data sets and tools for computational neuroscience. BMC Neurosci 10:1–1. https://doi.org/10.1186/1471-2202-10-S1-S6

Teeters JL, Godfrey K, Young R, Dang C, Friedsam C, Wark B, Asari H, Peron S, Li N, Peyrache A, Denisov G, Siegle JH, Olsen SR, Martin C, Chun M, Tripathy S, Blanche TJ, Harris K, Buzsáki G, Koch C, Meister M, Svoboda K, Sommer FT (2015) Neurodata without Borders: creating a common data format for neurophysiology. Neuron 88:629–634. https://doi.org/10.1016/j.neuron.2015.10.025

Tripathy SJ, Savitskaya J, Burton SD, Urban NN, Gerkin RC (2014) NeuroElectro: a window to the world's neuron electrophysiology data. Front Neuroinform 8:40. https://doi.org/10.3389/fninf.2014.00040

Van Essen DC, Smith SM, Barch DM, Behrens TEJ, Yacoub E, Ugurbil K (2013) The WU-Minn human connectome project: an overview. NeuroImage 80:62–79. https://doi.org/10.1016/j.neuroimage.2013.05.041

Van Geit W, Achard P, De Schutter E (2007) Neurofitter: a parameter tuning package for a wide range of electrophysiological neuron models. BMC Neurosci 8:1

Van Geit W, De Schutter E, Achard P (2008) Automated neuron model optimization techniques: a review. Biol Cybern 99:241–251

Van Geit W, Gevaert M, Chindemi G, Rössert C, Courcol J-D, Muller EB, Schürmann F, Segev I, Markram H (2016) BluePyOpt: leveraging open source software and cloud infrastructure to optimise model parameters in neuroscience. Front Neuroinform 10. https://doi.org/10.3389/fninf.2016.00017

Vella M, Cannon RC, Crook S, Davison AP, Ganapathy G, Robinson HPC, Silver RA, Gleeson P (2014) libNeuroML and PyLEMS: using Python to combine procedural and declarative modeling approaches in computational neuroscience. Front Neuroinform 8:38

Wheeler DW, White CM, Rees CL, Komendantov AO, Hamilton DJ, Ascoli GA (2015) Hippocampome.org: a knowledge base of neuron types in the rodent hippocampus. eLife. https://doi.org/10.7554/eLife.09960

Wilson MA, Bhalla US, Uhley JD, Bower JM (1989) GENESIS: a system for simulating neural networks. In: Touretzky D (ed) Advances in neural information processing systems, vol 1. Morgan Kaufmann Publishers Inc, San Francisco, pp 485–492

Yavuz E, Turner J, Nowotny T (2016) GeNN: a code generation framework for accelerated brain simulations. Sci Rep 6:18854

Experiment-Modelling Cycling with Populations of Multi-compartment Models: Application to Hippocampal Interneurons

Vladislav Sekulić and Frances K. Skinner

Abstract Understanding how neurons operate involves investigating how their complements of ion channels interact dynamically along the extent of their somatodendritic trees to produce spiking output appropriate to the cell type in question. This can be approached using experiments where individual ion channel activity is manipulated. However, a large body of experimental and theoretical work has demonstrated that a single neuron may dynamically alter its intrinsic ion channel expression profile in order to maintain output that is required for it to perform its functional role within the network that it is embedded. To appreciate this, a clear sense of the cellular functional role would be required, and this is not usually known. More typically, cellular output for an identified cell type can be characterized and captured in models with different complements of intrinsic properties. In this chapter we propose a cycling approach using experimental data as constraints for building populations of multi-compartment models with a range of ion channel expression patterns that underlie cell-type appropriate model output. These populations or databases can be analyzed to develop predictions regarding the intrinsic property balances for the cell type in question and for the proposed function. Predicted balances and functions can be examined experimentally.

V. Sekulić
Krembil Research Institute, University Health Network, Toronto, ON, Canada

Department of Physiology, University of Toronto, Toronto, ON, Canada
e-mail: vlad.sekulic@utoronto.ca

F. K. Skinner (✉)
Krembil Research Institute, University Health Network, Toronto, ON, Canada

Departments of Medicine (Neurology) and Physiology, University of Toronto, Toronto, ON, Canada
e-mail: frances.skinner@uhnresearch.ca; frances.skinner@utoronto.ca

V. Cutsuridis et al. (eds.), *Hippocampal Microcircuits*, Springer Series in Computational Neuroscience, https://doi.org/10.1007/978-3-319-99103-0_25

Overview

Understanding how neurons operate involves investigating how the activity of their complements of ion channels interact dynamically along the extent of their somatodendritic trees to produce spiking output that is idiosyncratic to the neuronal cell type in question. This can be approached using experiments, where individual ion channel activity is manipulated using pharmacological, genetic, and other techniques. However, a large body of experimental and theoretical work has demonstrated that a single neuron may dynamically alter its intrinsic ion channel expression profile in order to maintain output that is required for it to perform its functional role within the network it is embedded in (Marder and Goaillard 2006). In fact, any given neuron from an apparently homogeneous population may nevertheless exhibit strikingly different levels of expression of individual ion channels at any given time, as measured by current or conductance densities, that nevertheless produce spiking output that is appropriate to that cell type, if known (Schulz et al. 2006; Swensen and Bean 2005; MacLean et al. 2003). To understand how cell-type-specific spiking output arises as a function of intrinsic properties, ideally one would investigate the range of homeostatic tuning rules of a given neuronal type (O'Leary et al. 2013). However, a clear sense of the cellular functional role would be required, which is not usually known. More typically, cellular output for an identified cell type can be characterized and captured in models with different complements of intrinsic properties.

In this chapter we outline a computational modelling approach to investigate how the intrinsic properties of neurons, in this case inhibitory interneurons of the hippocampus, give rise to output. We have proposed a cycling approach using experimental data as constraints for building populations of multi-compartment models (Sekulić et al. 2014). These models collectively capture a range of ion channel expression patterns that underlie cell-type appropriate model output. Constraints on co-regulations of model parameters, such as channel conductances, that give rise to the appropriate output can also be found. Further, these populations or databases can be analyzed to develop predictions regarding the balances of intrinsic properties for functional outputs of the neuronal cell type in question. The predicted balances can then be examined with targeted experiments.

From Hand-Tuned to Populations of Conductance-Based Models

Computational modelling methods are well poised to study how intrinsic properties, such as ion channel kinetics and conductance densities, interact to produce neuronal output (Koch and Segev 1998; Dayan and Abbott 2001). The Hodgkin-Huxley formalism provides a biophysical description of ion channel activity, allowing for the direct incorporation of electrophysiological data in constraining model parameters (Hodgkin and Huxley 1952). Thus, Hodgkin-Huxley or conductance-

based computational modelling (Skinner 2006) provides a platform for assessing the contribution of individual ionic currents to neuronal activity (Foster et al. 1993; Golowasch et al. 1992). Furthermore, dendritic expression of voltage-gated ion channels in different neuronal cell types interacts with synaptic inputs to generate nonlinear computational properties of dendrites that go beyond passive integration (London and Häusser 2005; Narayanan and Johnston 2012; Lai and Jan 2006; Johnston and Narayanan 2008). Thus, the use of multi-compartment models that are based on cable theory is required to develop insight into the interplay of electrophysiology and morphology (Rall 2009; Niebur 2008; Segev and London 2000; Mainen and Sejnowski 1996). Traditionally, models with ion channel parameters that are manually tuned to experimental data have been built and used. However, due to the inherent variability in ion channel expression levels in biological neurons, in addition to the inadequacy of using averaged electrophysiological measurements for constraining these hand-tuned models (Golowasch et al. 2002), alternative approaches are needed.

Constructing populations or databases of models has been an increasingly widely used method for robustly exploring variability in parameters of conductance-based models (Marder and Taylor 2011). In general, these methods perform a search of the space of conductance-based model parameter values (Van Geit et al. 2008). Such techniques span a range of search methods, from coarsely sampling the entirety of the parameter search space (Prinz et al. 2003; Günay et al. 2008) to the use of evolutionary algorithms that stochastically traverse the search space to find models that optimally match some fitness criteria (Keren et al. 2005; Druckmann et al. 2007). Each method has its share of benefits and drawbacks. Coarse-grained search methods, for instance, perform a uniform and exhaustive sampling of the entire parameter space yet are computationally expensive. Evolutionary algorithm approaches, on the other hand, are more efficient in that they do not perform an exhaustive search. However, they may be prone to converging on local minima and thus miss regions of the parameter space that also contain appropriate models.

The Experiment-Modelling Cycling Approach

The motivation for generating populations of conductance-based models is typically to answer the question: given a set of experimental data (e.g., voltage traces), what combinations of model parameters can give rise to output that captures the features of the experimental dataset? In other words, the goal is to obtain an appropriate population of models that best represent a neuronal cell type in terms of electrophysiological outputs. In most cases, studies using these approaches aim to find a set of optimal models to capture some predetermined electrophysiological features of interest, such as Ca^{2+} spikes triggered by back-propagating action potentials in L5b pyramidal cells (Hay et al. 2011) or general spiking characteristics of accommodating vs fast-spiking interneurons in somatosensory cortex (Druckmann et al. 2007). However, any modelling approach tends to be under-constrained in terms of the range of experimental recordings available, with the resulting models

incompletely capturing the entirety of the character of a neuronal cell type. The question therefore arises of how to use population-based modelling to address unknown physiological properties of interest while simultaneously allowing for the results of such work to be incorporated back into the models.

The approach we have proposed is a general methodology for how to incorporate population modelling techniques in the course of investigating particular physiological questions of neurons. Named the *experiment-modelling cycling approach*, we propose from the outset that the goal of population-based modelling is not to find optimal models per se but rather to develop a database of models in such a way that a specific physiological question is addressed. There are four general steps to this approach (Fig. 1): (i) develop a starting or reference model with acquired experimental data to constrain the model parameters, and design the database so that its analysis in subsequent steps can provide information pertaining to the physiological question; (ii) build the database of models and find subset(s) of models that best characterize the experimental data; (iii) perform model analysis to determine constraints on parameters, including co-regulations between parameters, of the model subset(s) in (ii); (iv) apply analysis for the question of interest, determine limitations of the models, and formulate new physiological questions that then lead back to a new cycle starting with step (i). We note that this is a

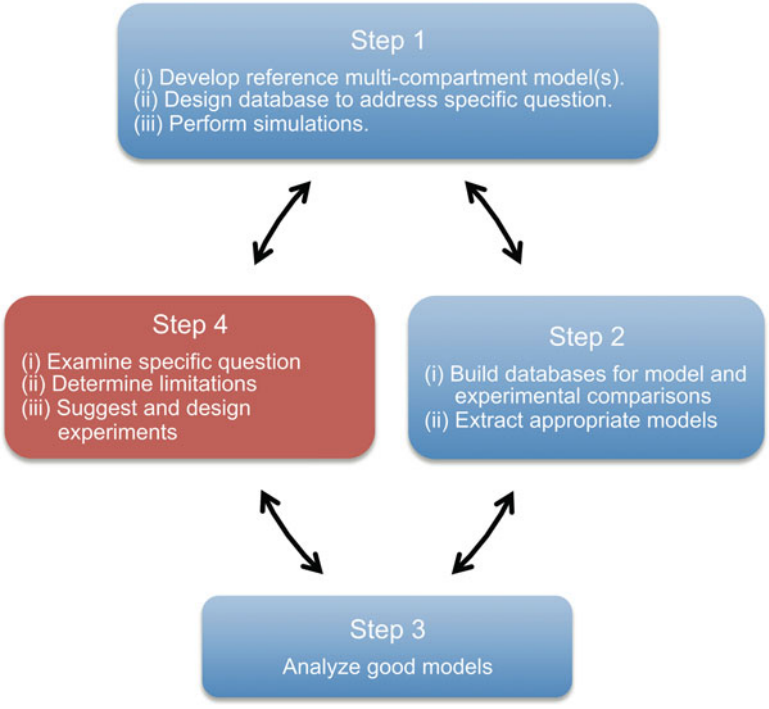

Fig. 1 The experiment-modelling cycling approach. Schematic highlighting the bidirectional methodological links between stages in the approach. (Figure adapted from Sekulić et al. 2014)

cyclical approach in that models are never considered to be "complete." Instead, the simulations as well as database development and analysis, in light of specific physiological questions, lead to parameter constraints for the models which then result in new experiments to address follow-up questions. The back-and-forth cycling between experiments and models thus leads to continual refinement of the model relative to the biological cell – as expressed collectively by a model database and the parameter constraints extracted from the database – as well as guidance for further experiments.

We have applied this approach to hippocampal interneurons, specifically the oriens-lacunosum/moleculare (O-LM) cell in the CA1 region of mammalian hippocampus (Sekulić et al. 2014). The O-LM cell plays an important role in information flow, neuronal rhythms, and synaptic plasticity in CA1 (Bartos et al. 2011; Leão et al. 2012; Perez et al. 2001; Matt et al. 2011). O-LM cell somata and dendrites are located in the stratum oriens layer, with their dense axonal arborizations projecting to the lacunosum/moleculare layer. The principal axonal targets of O-LM cells are the distal dendrites of local pyramidal neurons and are thus ideally located to influence the efficacy of perforant path input (Sik et al. 1995; Freund and Buzsáki 1996). O-LM cells possess a variety of voltage-gated ion channels across their somatodendritic tree. One feature of O-LM cells is the "sag" response to hyperpolarizing current steps, indicative of the presence of the nonselective, hyperpolarization-activated mixed cation current, or I_h (Maccaferri and McBain 1996). I_h contributes to the spontaneous firing of O-LM cells in vitro, and may allow them to contribute to the generation of population theta activities (Rotstein et al. 2005). However, it is unknown whether I_h is present in the dendrites of O-LM cells. This is an important question to consider as the integrative properties of the dendritic tree in response to synaptic input are likely modulated by dendritic I_h. Therefore, understanding the functional role of O-LM cells in in vivo network contexts requires elucidating the question of whether they express dendritic I_h. Unfortunately, performing non-somatic recordings on specific cell types is a difficult endeavor in rats and is particularly challenging in mice. Although multi-compartment O-LM cell models that capture salient features of experimental data have been developed (Saraga et al. 2003; Lawrence et al. 2006a; Skinner and Saraga 2010), they only include somatically located I_h. Thus, the question of localization of dendritic I_h in O-LM cells is ideally suited to an experiment-modelling cycling approach using model databases.

We present here the work we performed in addressing this question (Sekulić et al. 2014), using the experiment-modelling cycling approach. Briefly, we adapted previously developed multi-compartment models of an O-LM cell (Lawrence et al. 2006a; Skinner and Saraga 2010) and used them as reference models for building a database of O-LM models. The database was designed to address whether I_h is likely to be present in O-LM cell dendrites. We used experimental recordings from O-LM cells to rank and extract a subset of O-LM models that best represented the experimental dataset of O-LM cell output (Lawrence et al. 2006b). We then analyzed the resulting population using techniques for the visualization of high-dimensional parameter spaces as well as examining conductance density histograms. We found three co-regulatory conductance balances, two of which were

dependent on the presence of dendritic I_h. Full details pertaining to the model development, justification, and results are presented below, including the next steps performed to initiate a new "cycle" of experiment-modelling investigations.

Model Details and Justification

Reference Multi-compartment O-LM Model

The reference model used in this work was adapted from previous multi-compartment models of O-LM cells that were constrained by current-clamp experimental data (Lawrence et al. 2006b; Skinner and Saraga 2010). The reference model included nine voltage-gated ionic conductances which are known to be expressed in O-LM cells and was hand-tuned to experimental recordings. The currents included are the Hodgkin and Huxley fast sodium current (Nad/Nas, with somatic and dendritic treated separately), fast and slow delayed rectifier potassium currents (Kdrf and Kdrs, respectively), the transient or A-type potassium current (KA), the L- and T-type calcium currents (CaL and CaT, respectively), the calcium-activated mixed cation current (AHP), the hyperpolarization-activated mixed cation current (H), and the M current (M). Full details on the mathematical form of the model are described in Lawrence et al. (2006a) and Skinner and Saraga (2010).

Experimental Data for Constraining the Model Database

The set of recordings used in the experiment-modelling cycling approach described here consisted of those obtained during somatic whole-cell current-clamp conditions of O-LM cells in a previous work (Lawrence et al. 2006b). The cells were maintained at approximately -60 mV, which resulted in a membrane potential of approximately -73.8 mV after junction potential correction of -13.8 mV. To maintain the cells at -60 mV, a small negative bias or holding current was applied through the recording pipette (-8.0 ± 4.0 pA, $n = 11$). Depending on experimental protocol, an additional depolarizing ($+90$ pA) or hyperpolarizing (-90 pA) step would then be applied for a duration of 1 s. The experimental recordings used in this model database work consisted of ten identified O-LM cells in total, with traces including ± 90 pA current steps chosen for each cell, resulting in a dataset of 56 total experimental traces.

There was substantial variability in the experimental voltage waveform recordings (Fig. 2a). For instance, the depolarizing current step protocol results in O-LM cells with varying firing frequencies. Similarly, in response to a -90pA current step, variability was observed in the peak hyperpolarization of V_m, time course of the sag response, and presence and number of post-inhibitory rebound spikes after cessation of the current step. It is clear just from examination of the variability in experimentally observed outputs that using single, hand-tuned models is inadequate

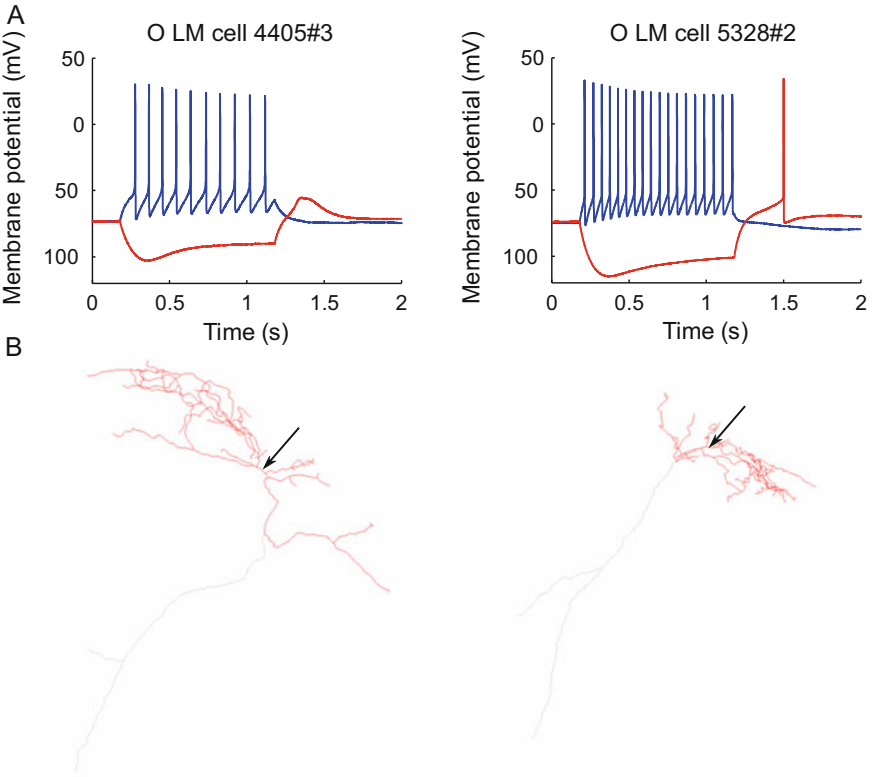

Fig. 2 Example experimental data and model morphologies used in database construction. (**a**) Experimental data showing somatic voltage responses to +90 pA (blue) and −90 pA (red) 1 s-long current-clamp steps for two separate O-LM cells (Adapted from Sekulić et al. 2014). (**b**) 2D projections of morphology 1 (left) and morphology 2 (right) as displayed in the NEURON simulation environment. Somatodendritic compartments are shown in red with axons in gray. Arrows denote locations of cell bodies; axons are truncated in the models. Morphologies are from different cells than the ones from which recordings were obtained in (**a**)

to capture the variability inherent in biological neurons and that a population of models is needed to capture the range of responses observed.

Passive Properties and Compartmentalization

The recordings used in the construction of the model database described here were obtained from a different experimental dataset (Lawrence et al. 2006b) than the one used to constrain the original reference O-LM multi-compartment model (Lawrence et al. 2006a). We did not have access to the morphologies from which the electrophysiological traces were extracted, thus leading to discrepancies between the passive membrane properties in the reference model morphologies and those of

the unknown underlying morphologies from the experimental dataset. In order to be able to use the recordings to constrain the voltage-gated channel conductances, we refitted the passive membrane properties in the reference model to reproduce the transient membrane responses observed in the experimental dataset. This was done by averaging 50 voltage-clamp seal tests from each O-LM cell in the dataset, which corresponded to the capacitative current elicited in response to a −5 mV step away from a −74 mV holding potential.

The reference O-LM model included two different morphological reconstructions (Fig. 2b). For each of the two morphologies, an appropriate number of compartments were determined to maintain the spatiotemporal accuracy of simulations. This was done using the fraction of the frequency-dependent length constant at 100 Hz, or λ_{100} (Hines and Carnevale 2001), and was determined by fitting the passive properties of the model to the experimental O-LM seal test recordings using the principal axis (PRAXIS) optimization procedure in the NEURON simulation environment. The passive properties fitted in this way consisted of the specific membrane resistivity (R_m), specific membrane capacitance (C_m), the leak reversal potential (E_L), and the potassium leak conductance (g_{KL}). The fitting was continued until the error value for the model did not change appreciably, thus indicating that the model output was being simulated with sufficient accuracy. Intracellular resistivity (R_a) is known to vary from 50 to 400 Ωcm in neurons (Holmes 2010). However, allowing R_a to vary in addition to R_m leads to nonuniqueness in obtained values since the two properties are interrelated, for instance, in determining the dendritic length constant, λ (Rall et al. 1992). As a result, independently verifying R_a is required in order to not introduce inappropriate estimates in the fitting of R_m; however, this is a difficult measurement to make (Rall et al. 1992), and no reported values are available for O-LM cells. We therefore decided to keep R_a fixed at 300 Ωcm since this is in the upper range of reported R_a values, pertaining mostly to mammalian neurons. In contrast, marine invertebrate neurons exhibit a threefold increase in concentration of charge carriers in axoplasm, leading to much lower measured R_a values (Rall et al. 1992). The resulting passive properties as well as λ_{100} fraction, number of compartments, input resistance, and resulting membrane time constant (τ_M) for each morphology are shown in Table 1.

Table 1 Passive membrane properties and number of compartments after passive property fitting procedure

Property	Model morphology 1	Model morphology 2
R_a (Ω · cm)	300	300
C_m (μF/cm^2)	0.96857	0.9
R_m (Ω · cm^2)	59,156	39,038
E_L (mV)	−73.588	−73.8424
g_{KL} (S/cm^2)	9.9005×10^{-10}	1.0015×10^{-9}
λ_{100} fraction	0.0101	0.00465
Number of compartments	1291	2413
Input resistance (MΩ)	474	530
Membrane time constant, τ_M (ms)	57	66

Establishing Model Parameter Ranges

The values that the maximum conductance densities ($\overline{g}$) for the various ion channels were allowed to be assigned were determined on a case-by-case basis depending on what was previously known about that ion channel type and specifically about its presence and somatodendritic densities in the O-LM cell. Table 2 lists the final maximum conductance density values used in the model database construction, including the references consulted. The possible parameter values were chosen so as to balance the coverage of plausible maximum conductance density values while limiting computational burden. Therefore, each conductance was allowed a range of 3–5 different possible values spanning the lowest and highest maximum conductance density values reported in literature – or calculated from reported current density values – with approximately uniform spacing in-between the values. For H, because no current or conductance density values were available for O-LM cells, we initially chose a range of values appropriate to the pyramidal cell literature ("version 1"). Subsequent simulations showed that these values were too high, as total inward current from H caused high firing rates for almost any combination of conductances, leading to rejection of most models. Therefore, we lowered the range of allowable $\overline{g}_h$ ("version 2") so that the highest value was the previous lowest value. This resulted in a much larger set of acceptable model outputs and is thus a prediction of possible H maximum conductance densities in O-LM cells (see Discussion).

Generating Model Outputs Using High-Performance Computing

The coarse-grained parameter search method used here relies on systematically varying all of the parameters and generating model output for each possible combination of parameters (Van Geit et al. 2008; Günay et al. 2009). By varying the maximum conductance densities of the various currents in the O-LM model, of which there are ten (treating Nas and Nad separately – see Table 2), as well as the distribution of H in somatic only versus somatodendritic compartments (2 options) and, finally, the morphology of the model used (2 options), there were a total of 933,120 possible models. Considering that experiments for both −90 pA and + 90 pA current injections needed to be applied to each model, this resulted in 1,866,240 total simulations that potentially needed to be evaluated. Therefore, the use of high-performance computing (HPC) was required. For this work, the SciNet HPC supercomputer cluster was used for generating the model outputs. The SciNet General Purpose Computing (GPC) cluster consists of 3780 nodes with 8 cores each (Loken et al. 2010). Each simulation required approximately 3–5 minutes of simulation time, of which eight could be running simultaneously per cluster node (one per core). The maximum allowable runtime on a single cluster node was 48 h. We were typically able to allocate 12–24 nodes to run simulations at any given

Table 2 Summary of maximum conductance density values used in the construction of the model database

Channel types	Maximum conductance density values, $\overline{g}$ (pS/μm^2)	Compartmental locations	References
Nas	60, 107, 220	Soma	Martina et al. (2000) and Lien et al. (2002)
Nad	70, 117, 230	Dendrites, axon	Martina et al. (2000) and Lien et al. (2002)
Kdrf	6, 95, 215, 506	Soma, dendrites, axon	Skinner and Saraga (2010), Martina et al. (2000) and Lien et al. (2002)
Kdrs	2.3, 42, 92, 222	Soma, dendrites, axon	Skinner and Saraga (2010), Martina et al. (2000) and Lien et al. (2002)
KA	2.5, 32, 72, 169	Soma, dendrites	Lawrence et al. (2006a), Skinner and Saraga (2010), Martina et al. (2000) and Lien et al. (2002)
H (version 1)	0.5, 16, 53, 90	Soma only or soma and dendrites	Saraga et al. (2003), Magee (1998), Martina et al. (2000), Lien et al. (2002), Angelo et al. (2007), Berger et al. (2001) and Kole et al. (2006)
H (version 2)	0.02, 0.05, 0.1, 0.3, 0.5	Soma only or soma and dendrites	Same as version 1 (above)
CaL	12.5, 25, 30	Dendrites	Skinner and Saraga (2010), Traub et al. (1994) and Destexhe et al. (2003)
CaT	1.25, 2.5, 5	Dendrites	Skinner and Saraga (2010), Traub et al. (1994) and Destexhe et al. (2003)
AHP	2.75, 5.5, 11	Dendrites	Skinner and Saraga (2010)
M	0.375, 0.75, 1.5	Soma, dendrites	Lawrence et al. (2006a)

The third column shows the model compartments where the conductance was distributed. In all cases, distributions were uniform within the specified compartments. The References column indicates the literature used to determine the range of plausible maximum conductance densities

time, depending on the overall cluster usage and the fluctuating priority for our compute jobs. The total compute time required for the work reported here, including the fitting of holding current and several iterations of database development, was approximately 107 core years. Being able to handle all of the model simulations required significant software automation. We implemented three tools to facilitate the management of simulation execution: (1) a script to generate the command-line invocations for all of the models; (2) fully automated NEURON code to evaluate the output of each model; (3) an efficient system for finding missing models that may have resulted from jobs that exceeded their time limit and were thus terminated by the SciNet job scheduler.

Pruning the Population: Removal of Models with Inappropriate Resting V_m

The membrane potential of each O-LM cell was held at a fixed voltage to ensure consistency in the state of activation of the voltage-gated ion channels present in the membrane relative to action potential threshold. This was accomplished by dynamically varying the amount of bias current or holding current which was injected prior to, and concurrently with, the subsequent ± 90 pA hyperpolarizing or depolarizing current injection step in order to maintain a V_{m} of approximately -74 mV prior to the current injection step. However, we found that many models would exhibit premature action potential firing before reaching an experimentally appropriate bias current, whereas others would need too much positive bias current, relative to experimental values, to drive them to fire. Since these models did not contain appropriate O-LM cell characteristics, they were discarded. By following this procedure, 609,143 out of a total of 933,120 models were found to be inadequate, with 323,977 models being considered acceptable and retained for further analysis of conductance density balances.

Ranking of Models According to Goodness of Fit to Experimental Data

Once model outputs were obtained, they were imported into PANDORA's Toolbox, a MATLAB toolbox for the statistical analysis of experimental and model voltage traces (Günay et al. 2009). We chose 11 electrophysiological measures for the -90 pA and 92 for the $+90$ pA experimental current-clamp traces (Table 3).

To obtain an aggregate measure of the "closeness" or error between a model and experimental trace, we used a ranking function provided by PANDORA that calculated the normalized Euclidean distance between models in the provided model database and a single experimental trace, as per Eq. 1 (Günay et al. 2009):

Table 3 Subset of electrophysiological measurements used to rank models

Measure	Description	Average ± standard deviation
IniSpontPotAvg (−, +)	The average V_m value for the duration of the spontaneous (prior to current injection) period.	−74.1 ± 0.6 mV
PulsePotMin (−)	The minimum value of V_m obtained during the current injection period, i.e., the minimum membrane voltage induced by the hyperpolarization	−113.9 ± 3.7 mV
PulsePotMinTime (−)	The time at which the minimum of V_m occurred during the current injection period	166.8 ± 54.7 ms
PulsePotSag (−)	The amount of sag (in mV) exhibited by the trace as a result of the hyperpolarization. This is a measure of the depolarizing effects of the I_h current	14.2 ± 3.1 mV
PulsePotTau (−)	The time constant for fitting an exponential curve to the decay of the hyperpolarization-induced sag	47.4 ± 8.0 ms
PulseSpikeRate (+)	Firing frequency during the current injection period	22.2 ± 3.0 Hz
PulseSpikeRateISI (+)	Mean inter-spike interval (ISI) between spikes during the current injection period	29.5 ± 7.0 ms
PulseSpikeAmplitudeMean (+)	The mean amplitude of the spikes during the current injection period. Amplitude was calculated by taking the difference in spike height from the V_m at spike initiation	62.2 ± 6.8 mV
PulseSpikeFallTimeMean (+)	The time a spike takes to fall from its peak back to the spike initiation point, averaged across all spikes in the current injection period	1.5 ± 0.5 ms
PulseSpikeHalfVmMean (+)	V_m equal to half of the spike height, averaged across all spikes in the current injection period	−20.9 ± 2.4 mV
PulseSpikeInitVmMean (+)	V_m of spike threshold, averaged across all spikes in the current injection period. Calculated by finding the point of maximum curvature in the V-$^{dV}/_{dt}$ phase plane. (PANDORA supports additional methods for spike initiation detection)	−52.0 ± 1.6 mV
PulseSpikeMaxVmSlopeMean (+)	Maximum slope or first-order derivative of V_m during a spike	133.4 ± 29.5 mV

Names, descriptions, and values for a subset of the electrophysiological measurements extracted from the ±90 pA current-clamp simulations. The same measurements were extracted from the ±90 pA current-clamp experimental traces. The (−) and (+) symbols after each measure name denote whether the measure was applied to the −90pA or + 90 pA stimulus traces, respectively. The reported values consist of averages of the measures across all experimental voltage traces as well as the standard deviation of the measures within the *experimental* dataset. For full list of measures, see Sekulić et al. (2014)

$$d_{x,y} = \sum_{i=1}^{N} \frac{|x_i - y_i|}{N\sigma_i}, \tag{1}$$

where x_i and y_i represent the ith measure, out of N total measures or features, of the model and experimental traces, respectively, σ_i is the standard deviation of the measure in the experimental database, and $d_{x,y}$ is the Euclidean distance between model trace x and experimental trace y. The importance of the σ_i normalization term is to penalize models whose measures differ significantly when those measures are tightly constrained in the experimental database – that is, when σ_i is small. On the other hand, models with measures that vary significantly in the experimental database – that is, when σ_i is large – will not be penalized by the distance calculation if they differ significantly from the experimental measure, y_i. Effectively, the equation calculates the standard score, or z-score, of all of the model's measures against the experimental measures. The resulting distance value, $d_{x,y}$, represents how close of a match a model trace is to an experimental trace. Larger $d_{x,y}$ values correspond to models that are "further away" from the experimental trace, whereas lower $d_{x,y}$ values correspond to models that are "closer" or better matches for the experimental trace. Note that this corresponds to the distance between individual model and experimental traces. Distance values of per-model traces against all experimental traces were then summed and normalized by the number of experimental traces (Eq. 2):

$$d_x = \frac{1}{N_y} \sum_{y} d_{x,y}, \tag{2}$$

where $d_{x,y}$ is the distance of model trace x against experimental trace y, N_y is the total number of experimental traces, and d_x is the distance of model trace x against all of the experimental data traces. The total distance d_x was normalized by the number of experimental traces N_y so that distances between databases with different N_y could be meaningfully compared to one another.

To obtain a subset of models that captured the output characteristics of O-LM cells as exemplified by the experimental dataset, we ranked the models according to their goodness of fit to the experimental dataset. This consisted in sorting the Euclidean distance values, d_x, for all models, x, from low to high values, such that highly ranked models had low distance values, and poorly ranked models had high distance values (Fig. 3a). Voltage responses to ±90 pA current steps illustrated that a highly ranked (Fig. 3a, red arrow) O-LM cell model (Fig. 3b) better represented O-LM cell properties than a poorly ranked (Fig. 3a, black arrow) O-LM cell model (Fig. 3c). Furthermore, from comparing the model outputs with example experimental data (Fig. 2a), it is apparent that the highly ranked models (Fig. 3b) better represented the empirical set of physiological O-LM cell recordings (Fig. 2a), as compared to lower-ranked ones (Fig. 3c). Thus, highly ranked models seemed to capture important intrinsic properties of O-LM cells that the poorly ranked models did not.

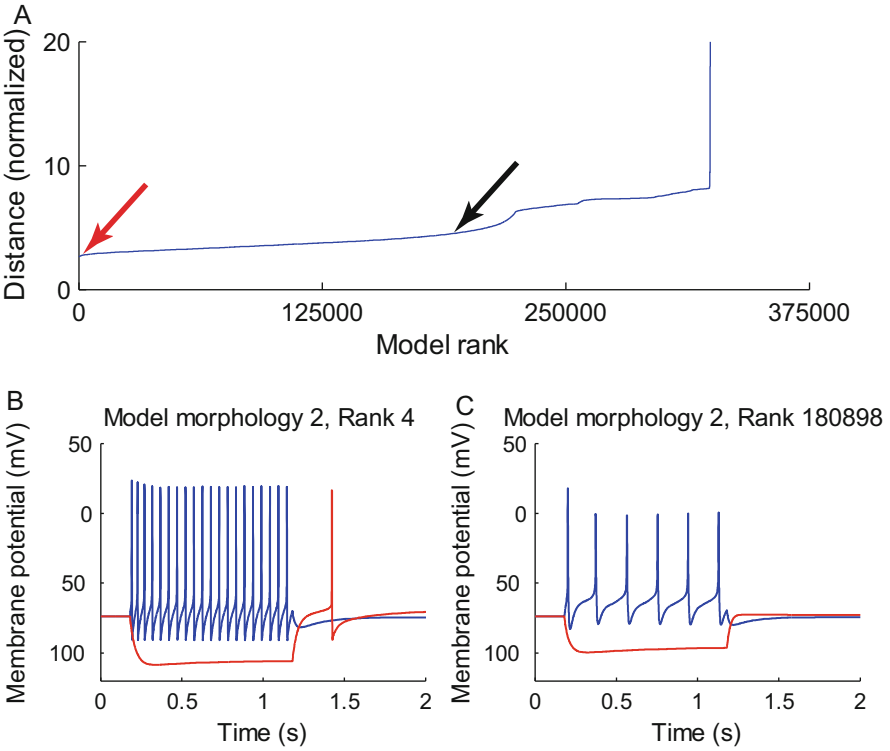

Fig. 3 Ranking of O-LM models against experimental data. (**a**) The ranking of models against O-LM cell experimental recordings shows a gradual decrease of the goodness of fit of a given model as the rank of the model becomes poorer, i.e., as the distance values increase. Hyperpolarizing and depolarizing voltage responses of two representative models, a highly ranked one (**b**, red arrow in **a**) and poorly ranked one (**c**, black arrow in **a**), are shown for comparison purposes. (Figure adapted from Sekulić et al. 2014)

Although it was clear that highly ranked models were better representations of O-LM cells than poorly ranked models, it was not immediately obvious where a cutoff point was to be applied to distinguish between them. This was because the distance metric considered all features and ranked models in a continuous or graded fashion. A principled cutoff criterion was therefore needed to extract appropriate models. We first considered determining a cutoff point from the distance measure itself, noting that the distance measure incorporated consideration of a multitude of electrophysiological features. We referred to this cutoff point as the *general* criterion. This was done by plotting the slopes of the distance measure with respect to the model rank, which is equivalent to the difference of distances between adjacent models in the ranking. Using the built-in MATLAB function *diff*, the first-order derivative of d_x was calculated to compare the rate of change of d_x as a function of the model rank. In order to test whether there were morphology-

specific differences in the ranking of the O-LM models, the models using each of the two reconstructed O-LM cell morphologies were ranked and analyzed separately. After plotting the slopes for models of both morphologies, it was clear that the distance values changed rapidly in the first few thousand highly ranked models, after which they increased at a relatively constant rate (Fig. 4a, horizontal dashed line). Eventually, the distance values of the ranked models for both morphologies started changing again at a more rapid rate. We therefore set the point at which the ranked models started to rapidly increase their distance values as the cutoff (Fig. 4a, vertical dashed line). For models of morphology 1, this resulted in the first 60,000 highly ranked models counting as appropriate O-LM cell representations (Fig. 4a); likewise, for models of morphology 2, the first 90,000 highly ranked models were incorporated into the ensemble of appropriate O-LM cell representations (not shown). This total set of 150,000 models was considered the *general subset* of appropriate O-LM models.

To assess the validity of the general criterion, we additionally considered a more restricted criterion in order to check whether the conductance density balances found in the two subsets would overlap. For this, we chose representative electrophysiological measures for both the depolarizing and hyperpolarizing current step voltage traces. We used the firing frequency of the models during the current injection step as a representative measure of depolarizing current step traces and the time constant of the hyperpolarization-induced sag response as a representative measure of hyperpolarizing current step traces (Fig. 4b–d). When comparing the firing frequencies of the highly ranked models for both morphologies, we noticed that relatively early on in the ranking, some models exhibited behavior which we termed "failure-to-fire." These models were characterized by a combination of conductance densities that prevented the model cell from firing more than one or two action potentials during the +90 pA current injection step (Fig. 4c). Since none of the experimental O-LM cell voltage traces had an observed instance of this failure-to-fire behavior, we deemed models that possessed this characteristic to be potentially inappropriate O-LM cell representations and set the restricted cutoff at the rank prior to the first failure-to-fire model. In the case of models of morphology 1, the first failure-to-fire model occurred at rank 13,613 (Fig. 4b), whereas for models of morphology 2, the first failure-to-fire model was found at rank 19,245 (not shown). The resulting set of 32,856 models (13,612 + 19,244 models without failure-to-fire behavior) was considered one candidate for a restricted subset of appropriate O-LM models as determined by the firing frequency measure.

For the representative measure of the hyperpolarizing traces, the time constant of the sag response, we plotted the sag time constants as a function of model rank (Fig. 4d) and compared them to the sag time constants exhibited in the experimental dataset, by plotting the histogram of sag time constants for the latter (Fig. 4e). We observed that the sag time constants for the highly ranked models of either morphology exhibited appropriate values for the first tens of thousands of highly ranked models – as determined by being within the range observed in the physiological O-LM cells (Fig. 4e). However, at a certain point, the sag time constants became markedly lower and fell outside the range of those observed in

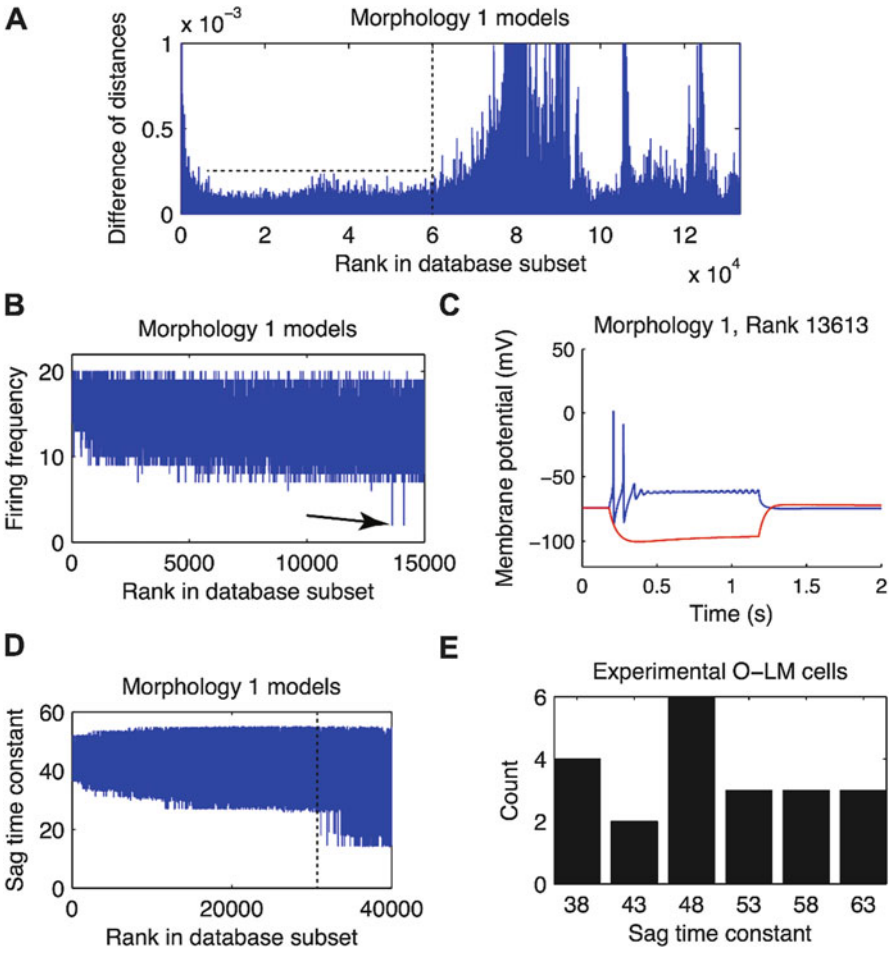

Fig. 4 Extracting subsets of appropriate O-LM models from the database. (**a**) Plot showing the general subset cutoff determined by visual examination of the derivative of the distance metric with respect to the model ranking in the database. Vertical dashed line shows cutoff point. (**b**) The firing frequency plotted as a function of model rank demonstrates one restricted subset of O-LM models. The arrow points to the first failure-to-fire model, thus marking the cutoff point for this restricted subset. (**c**) The voltage traces of the failure-to-fire model shown in (**b**). (**d**) The time constant of the hyperpolarization-induced sag plotted as a function of model rank. The vertical dashed line shows the point in the ranking at which the time constant starts to deviate from the experimentally observed time constants. (**e**) Histogram of hyperpolarization-induced sag time constants within the experimental O-LM cell dataset. (Figure adapted from Sekulić et al. 2014)

the physiological O-LM cells (Fig. 4d, dashed line). We marked the approximate rank at which the models started exhibiting inappropriate time constants as another restricted cutoff point. This point was much further down the ranking of models than the restricted cutoff point for the firing frequency criterion, however (compare

the location of arrow in Fig. 4b and dashed line in Fig. 4d along the x-axis; data for models of morphology 2 was similar and is not shown). Therefore, we only considered the cutoff point determined by analyzing the firing frequency behavior as forming the *restricted subset* of appropriate O-LM models to be used as a comparison to the more general subset determined by the difference of distance metric.

Ordering of Conductances According to Influence on Model Outputs

Once the general and restricted subsets of appropriate O-LM models were determined, we examined the conductance density space of the models in each highly ranked subset. For this, we generated conductance histograms. These plots consisted of histograms of the number of highly ranked models contained in each subset of appropriate O-LM models that possessed any combination of conductance density values for the two ion channel conductances being considered. In order to avoid having to consider the exhaustive set of possible conductance histogram plots, we used clutter-based dimension reordering (CBDR), or dimensional stacking, an algorithm for the visualization of high-dimensional data in two dimensions, as a way to constrain which conductances were considered (Taylor et al. 2006; Peng et al. 2004). See Fig. 5 for a dimensional stack image of the subset of ranked models extracted using the general cutoff criterion. The ordering of the parameters in a given "stack" is important in determining sensitivity of model outputs to parameter changes. An optimal stack can be found where the models are organized in the image such that highly ranked models cluster together more tightly than poorly ranked models. In this case, the high-order parameters (conductance densities and distributions) in the stack reflected those conductances whose changes in value were associated with changes in model ranking, or goodness of fit to experimental data. On the other hand, low-order parameters were those for which changes in their values could be made and yet the ranking of the models would not be appreciably affected. Therefore, high-order parameters were those to which the model distances were most sensitive and therefore were the likeliest to demonstrate compensatory balances with each other. To determine this, the high-order parameters were used to construct conductance histograms. However, although the first-order parameters in the dimensional stack images were clearly to be considered the highest-order and the fifth-order parameters were clearly to be considered the lowest-order, it was not entirely clear whether the third- and fourth-order parameters should be considered high-order or low-order. Therefore, for the conductance histograms, third- and fourth-order parameters were also used in order to check whether they showed correlations with other conductances. Most high-order parameters, especially of the first- and second-orders, were largely shared between the database subsets corresponding to the two morphologies in both the general and restricted subsets.

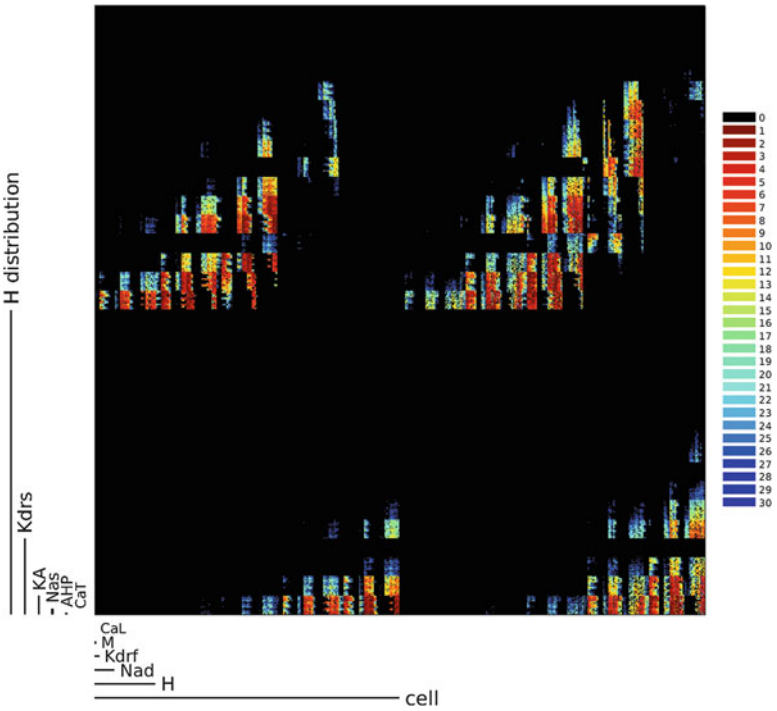

Fig. 5 Dimensional stack image of the highly ranked O-LM models in the general database subset. Each colored point in the image corresponds to a model in the subset; black regions correspond to models that are not included in the subset. See results of main text for description of general database subset. The ranking of models is reflected in the color, from highest-ranked (red end of spectrum) to lowest-ranked (blue end of spectrum) of the subset of highly ranked models. Numbered bins, each containing an equal amount of models (except bin 0, black), are shown to the right of the image. The axes show the ordering of model parameters as obtained by the clutter-based dimension reordering (CBDR) algorithm (Taylor et al. 2006). The parameters include the maximum conductance densities of all voltage-gated ion channels in the model as well as the "cell" parameter which refers to the morphology of the model (one of two possibilities) and the H distribution parameter, of which there are two possibilities (soma only vs soma and dendrites). The vertical and horizontal lines in the axes show the region of models in the image for which the maximum conductance density labelled in that particular axis is uniform in value. Thus, lower-order conductances (small lines, e.g., CaT and CaL) are those for which the maximum conductance density values can change without affecting the ranking of the models, as reflected in the regions of similarly colored models that nevertheless possess different values of those conductances. In all cases, the maximum conductance density values for each axis increase away from the origin in the bottom left-hand corner

We could thus eliminate the low-order parameters from further consideration, as they did not seem to affect the behavior of the models as exercised by the particular depolarizing and hyperpolarizing current injection step protocols used. The high-order parameters were Nad, KA, H, Kdrf, and Kdrs, whereas the low-order parameters were Nas, M, AHP, CaL, and CaT. We proceeded to compute the

correlation histograms for all pairwise combinations of the high-order parameters as determined by CBDR analysis, in addition to one parameter that straddled the boundary between high- and low-order parameters, AHP, that provided a check. The AHP conductance was found to not show any clear interaction with any of the higher-order parameters, which served as confirmation that AHP, and all lower-order parameters, could be discounted from further analysis.

Verifying Passive Properties Fitting

After the models were ranked against the experimental data as described above, it was important to verify that the passive properties of the models would not appreciably change if refitted using the active conductances exhibited by highly ranked models. This is because active conductances play a role in the current/voltage dynamics of the experimental protocol used in fitting the passive properties. It was thus conceivable that a model with the initial (reference) values of maximum conductance densities may have resulted in a different fit of the passive properties than if the maximum conductance densities of its ion channel models were allowed to vary. To determine this, two highly ranked models of each model morphology were taken from the database subset of appropriate O-LM models. In particular, the most highly ranked model of each morphology with somatodendritic H was found and used to refit the passive properties. This is because H in both somatic and dendritic compartments cover a much greater surface of the cell's membrane and can therefore more strongly affect the model's membrane response to the passive properties experimental protocol. The two models obtained were rank 1 from the morphology 1-specific subset of the general database and rank 3 from the morphology 2-specific subset of the general database. The parameters for these two models are shown in Table 4. The same protocol described for the fitting of passive properties to experimental data, above, was used in refitting the passive properties using these two models. After the fitting procedure was completed, the passive membrane properties of the two models were compared to those obtained from the reference model. Table 5 shows the refit passive properties of the highly ranked morphology 1 and morphology 2 models. Note that the passive properties did not seem to vary appreciably as compared to the originally fit values in Table 1. To verify that the differences in passive properties did not significantly affect the model behavior, the voltage traces of the two highly ranked models before and after fitting of the passive properties were compared (Fig. 6). The voltage responses were found to be very similar regardless of whether the original or refit passive properties were used. Therefore, it was determined that the passive properties obtained by fitting the reference model against the experimental data were adequate for the ensemble of models subsequently obtained and that it was not necessary to re-evaluate the simulations using the newly fit passive properties.

Table 4 Model parameters for the two highest-ranked per-morphology models with somatodendritic H

Channel type	Maximum conductance density ($\overline{g}$) values for model morphology 1, rank 1 (pS/μm^2)	Maximum conductance density ($\overline{g}$) values for model morphology 2, rank 3 (pS/μm^2)
Nad	117	230
Nas	220	107
Kdrf	215	506
Kdrs	2.3	2.3
KA	2.5	32
H (soma + dendrites)	0.02	0.02
CaL	50	25
CaT	5	2.5
AHP	5.5	11
M	0.375	0.75

Table 5 Refit passive properties for the highly ranked morphology 1 and morphology 2 models

Passive properties	Refit values for model morphology 1, rank 1	Refit values for model morphology 2, rank 3
R_a ($\Omega \cdot$ cm)	300	300
C_m (μF/cm^2)	0.96857	0.9
R_m ($\Omega \cdot$ cm^2)	61,117	40,397
E_L (mV)	-71.4	-68.7
g_{KL} (S/cm^2)	9.9137×10^{-10}	9.9256×10^{-10}

Compare with the values fitted prior to the construction of the model database, in Table 1

Results

We found three categories of relationships between high-order conductances, similar to that found in previous work in an ensemble of model neurons of the crustacean stomatogastric ganglion network (Smolinski and Prinz 2009). Using similar terminology, we found that conductances showed either (1) no clear interaction, (2) a local peak or preference of conductance density values, or (3) a co-regulation. The first two cases were not deemed to be of interest in terms of uncovering putative conductance density balances. In the case of no clear interaction, any change in the maximum conductance density of one or the other conductance had no effect on the resulting models' goodness of fit as measured by the number of highly ranked models contained within the general or restricted subsets of appropriate O-LM models and that possessed those conductance density values (Fig. 7a). For the second case of local preference, more models in the highly ranked general or restricted subsets of appropriate O-LM models exhibited one particular combination of conductance density values, with tapering-off numbers of models exhibiting

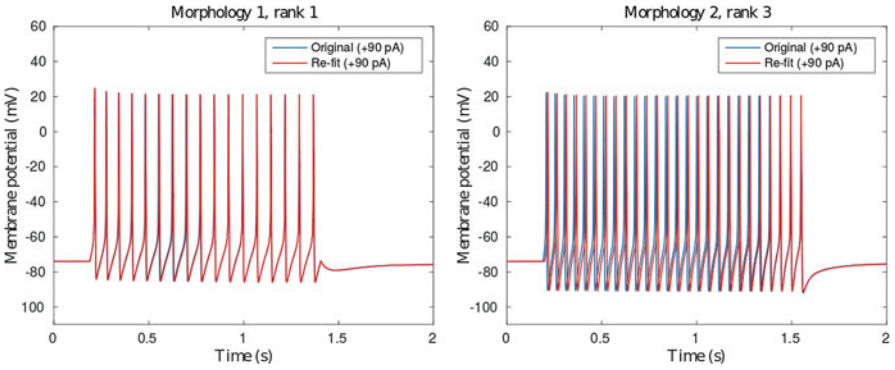

Fig. 6 Voltage traces of highly ranked models corresponding to original and refit passive properties. The blue and red traces show the model responses to +90 pA current injection with, respectively, the original and the refit passive properties, for the models with morphology 1, rank 1 (left), and morphology 2, rank 3 (right). The voltage responses are very similar regardless of whether the original or refit passive properties were used

nearby combinations of conductance density values (Fig. 7b). In this case, although there was a clear preference for a particular value of one or both conductances, the two conductances did not interact in a meaningful way. The third category of relationships, that of co-ordinated regulation or co-regulatory balance, was exhibited by a characteristic "ridge" in the correlation plots of the two conductances in question. Of all the examined pairwise combination of conductances, we only found three co-regulatory balances. Intriguingly, these three co-regulations were equally present in both the general as well as the restricted subsets of appropriate O-LM models. An example of two conductance histogram plots for the same two conductances, with one plot obtained from the general subset and the other from the restricted subset, and showing similar co-regulatory "ridges" can be seen in Fig. 8a, b.

The first co-regulatory balance observed was that between Kdrf and Na_d in the case of all models of both morphologies (Fig. 8a, b). This indicates that Nad is balanced against Kdrf: when maximum conductance densities of one of these conductances is increased or decreased, the maximum conductance densities of the other is also increased or decreased in a corresponding fashion in order to maintain physiological O-LM cell output. The remaining two co-regulations were only observed in those models that had H distributed in their dendrites – that of H and Kdrs as well as H and KA (Fig. 8c–f). In this case, inward H was co-regulated against outward Kdrs as well as KA such that increases of H occurred with increases of Kdrs or KA. For models that expressed H in the somatic compartments only, there was no co-regulatory balance found between H and either Kdrs and KA (Fig. 8c, e). On the other hand, models with H uniformly distributed across all somatic and dendritic compartments exhibited these co-regulations (Fig. 8d, f). In all cases, there

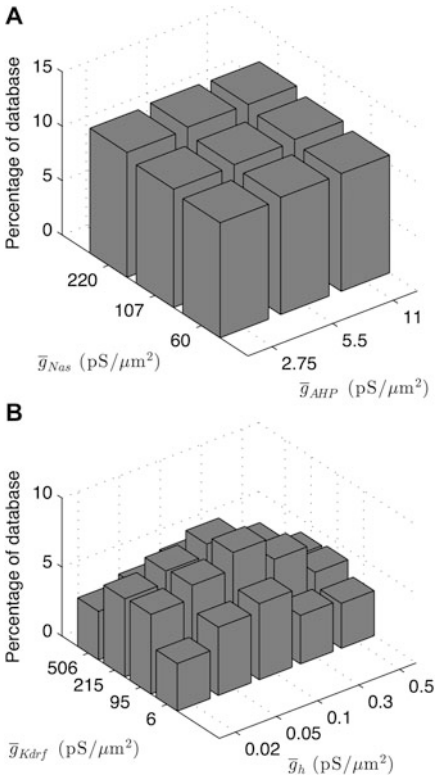

Fig. 7 Conductance histograms showing either no clear interaction or local preference. Pairwise conductance histogram plots show the number of highly ranked models from the general subset, expressed as a percentage of the general subset of O-LM models, which possess the parameter values for the two given combinations of ion channel maximum conductance densities shown on the x- and y-axes. (**a**) Conductance histogram plot for Nas ($\overline{g}_{Nas}$) and AHP ($\overline{g}_{AHP}$), demonstrating no clear interaction. (**b**) Conductance histogram plot demonstrating a local preference between Kdrf ($\overline{g}_{Kdrf}$) and H ($\overline{g}_{h}$). Note the peak in the middle of the conductance density range for both conductances. (Figure adapted from Sekulić et al. 2014)

were no specific differences in the patterns of co-regulations found for morphology 1 and 2, suggesting that the co-regulations were not dependent on morphological details.

One of the motivating questions for this work was the possibility of expression of dendritic H in O-LM cell models. Accordingly, the presence or absence of dendritic H was included as a parameter in the model database that we constructed. We found that there was an approximately equal number of models in the resulting subsets of appropriate O-LM models that expressed somatic H only and that expressed somatodendritic H with a uniform dendritic distribution. Although this showed that it was possible for O-LM models to include dendritic H and also be considered appropriate representations of O-LM cells, it did not lead to a clear prediction of whether dendritic H was likely to be expressed in biological O-LM cells or not. However, this led us to further investigate the question of dendritic H more fully, which we did in subsequent work that leveraged the model database (Sekulić et al. 2015; see Discussion).

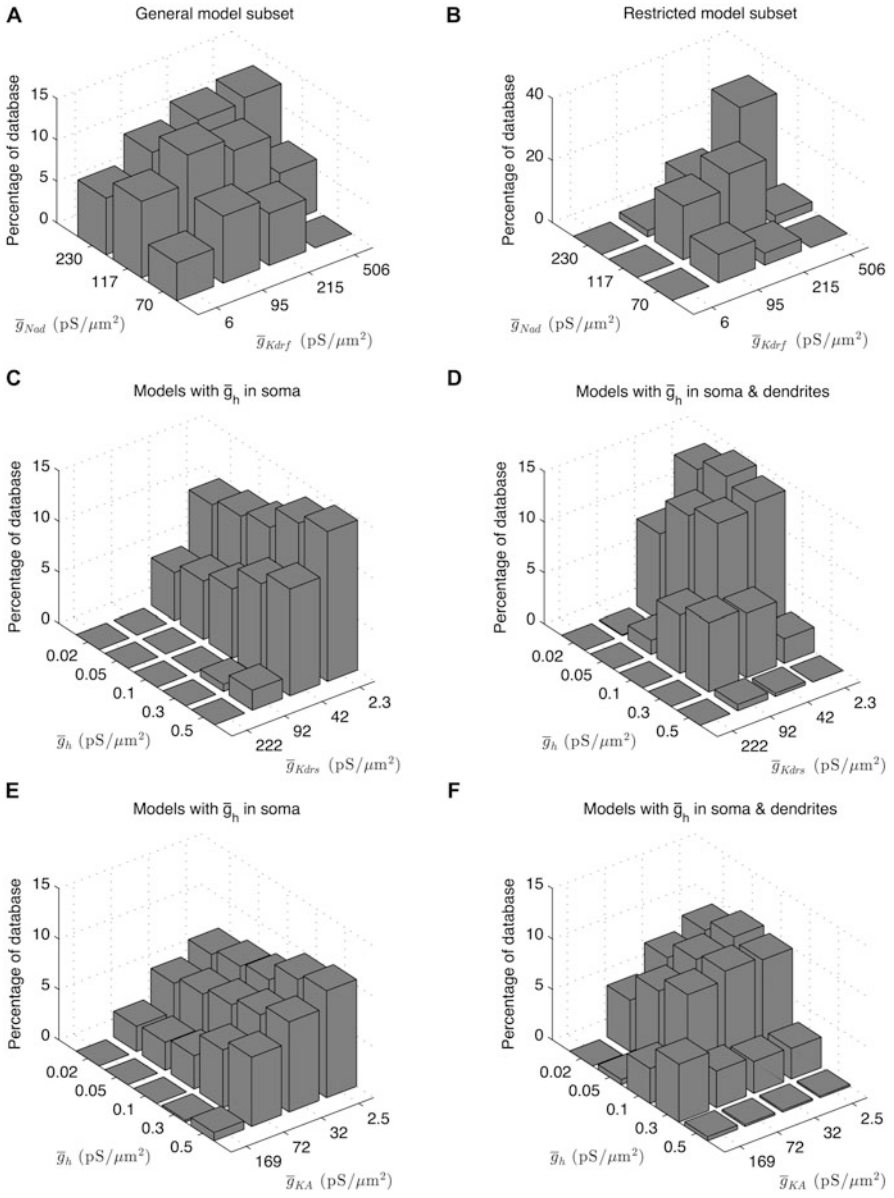

Fig. 8 Conductance histograms for co-regulatory balances in the highly ranked model database subsets. Histograms for pairwise conductance density values show three co-regulations between four of the nine active conductances present in the highly ranked model subsets. Nad ($\overline{g}_{Nad}$) is co-regulated with Kdrf ($\overline{g}_{Kdrf}$) as seen in both the general (**a**) and restricted (**b**) database subsets. H ($\overline{g}_h$) is co-regulated with both Kdrs ($\overline{g}_{Kdrs}$) and KA ($\overline{g}_{KA}$), as seen by the characteristic ridge in (**d**) and (**f**). These co-regulations are only present in the subset of models with H distributed uniformly across the somatic and dendritic compartments (**d** and **f**) and not the models with H distributed within the soma only (**c** and **e**). (Figure adapted from Sekulić et al. 2014)

Discussion and Future Work

Extending the Model Database

In this chapter, we described our work on the development of a database of O-LM cell models with varying parameter values that captured O-LM cell electrophysiological features and led to predictions regarding ion channel conductance density co-regulations. However, model limitations are always present relative to the biology.

One limitation is the question of the composition of time- and voltage-independent ionic conductances, or leak conductances, in O-LM cells. Leak channels have been incorporated in almost all Hodgkin-Huxley-based compartmental models since Hodgkin and Huxley's own pioneering work (Hodgkin and Huxley 1952). Initially, the leak conductance was introduced in computational models as a general or "catch-all" conductance to account for the permeability of the membrane at rest to K^+ and Cl^- ions. Over time, a wide variety of two-pore domain potassium channels underlying leak conductances have been identified in central nervous system (CNS) neurons, for instance, TWIK, TREK, TASK, and others (Enyedi and Czirják 2010). Some of these channel types have been identified specifically in hippocampal interneurons. In particular, a TASK-like (TWIK-Related Acid-Sensitive K^+ Channel) has been found in a subpopulation of horizontal interneurons in stratum oriens in CA1, whose electrophysiological profiles resemble that of O-LM cells (Talley et al. 2001; Torborg et al. 2006). TASK-like channels have been proposed to provide a shunting effect during modulation of I_h in pyramidal cell computational models (Migliore and Migliore 2012). Given the expression of I_h and possibly TASK-like conductances in O-LM cells, investigating the computational effect of TASK-like channels in O-LM cells is necessary to further elucidate O-LM cell activity in functional contexts. Although the O-LM models used in our work incorporated both "generic" leak as well as a leak conductance that follows a K^+ reversal potential, future work would ideally investigate the possibility of the expression of specific two-pore-domain K^+ channel types in O-LM cells, of which there may be several.

Further limitations in the models involve the kinetics of H. We found here that even with the highly ranked models in the database, the "sag" characteristic of H channel activation was far less pronounced than that in the experimental dataset used to constrain the models. One possible explanation was that either the kinetics of the mathematical model for H, or the dendritic distribution of H in the models, were not appropriate with respect to the particular O-LM cells from which the experimental data was obtained. Accordingly, in a subsequent study, we developed a more general mathematical representation of the time constant of activation of H and examined the possibility of the presence of nonuniform distributions of H (Sekulić et al. 2015). Using four of the top-ranked models in the database developed here, as well as experimental traces of responses to hyperpolarizing current-clamp stimuli, we fitted both the H time constant and a scaling factor for

determining nonuniformity in dendritic H distributions. We found that we could obtain better fits for the sag response in all four models used. Interestingly, we observed a morphology-related trend in nonuniform distributions of H in that, regardless of distribution, the total membrane conductance for the H current was conserved on a per-morphology basis. A similar result was found in a mixed modelling and experimental study in cerebellar Purkinje neuron dendrites, where total H was conserved regardless of dendritic distribution (Angelo et al. 2007). That study proposed that the electrotonically compact dendrites of Purkinje cells was a factor in allowing for this flexibility in dendritic distributions. Since O-LM cells also contain electrotonically compact dendrites, as opposed to those in pyramidal neurons, it is not surprising that a similar constraint on total membrane H would be observed. However, the constraints on dendritic H distribution may change provided additional information regarding dendritic organization of synaptic inputs onto O-LM cells, which are yet to be determined. Ultimately, the experiment-modelling cycling approach utilized here allowed us to find aspects of the output of highly ranked models that were not well fit to the experimental data, thus pointing out specific deficiencies in the reference model. We thus focused on the kinetics and distributions of H in a targeted way during subsequent modelling, leading to predictions. In particular, we found that experiment-modelling cycling to further assess kinetics and distributions of H using multi-compartment modelling needs to be done using electrophysiological recordings and morphological reconstructions obtained from the same O-LM cells. Most importantly, this ability of the model database approach to highlight model parameters and behavior that cannot be properly matched to experimental data is seen as a strength. Since no combination of parameter values can result in models that capture these features, these deficiencies in model outputs simply show what *particular* underlying biophysical features are as yet insufficiently understood and thus improperly modelled. This then leads to the natural formulation of precise follow-up questions for experimental investigation and further model database formation and analysis, as per the experiment-cycling approach.

Critical Issues in Population Modelling

Building databases of models may be done in several ways, each having its own advantages and disadvantages. The method of database construction used here is characterized by coarse-grained examination of the parameter space, also known as the "brute-force" method (Prinz et al. 2003, 2004; Günay et al. 2009). The major advantage of this approach is that the entire parameter space may be sampled, and, provided that the steps between parameters are not too large, all of the regions of the parameter space with models conforming to features or characteristics of interest may be found. The major disadvantage of this approach is the trade-off between the coarse nature of parameter changes and computational requirements. If the grid is too widely spaced, then important regions of the parameter space may be missed.

On the other hand, if the grid is too finely spaced, evaluating every combination of parameters in a model will be prohibitively expensive. A balance between the two can be achieved with several iterations of database construction. For instance, in this work we described a "version 1" of the database with a larger $\overline{g}_h$ range initially taken from pyramidal cell literature that was then changed to a narrower and lower range of values with "version 2." Importantly, the amount of computational burden – whether through fine-grained parameter values or multiple iterations of database construction – is likely to be commensurate with the lack of experimental constraints in the model parameters. An alternative is to use multi-objective evolutionary algorithm approaches (MOEAs) where a genetic algorithm is utilized to stochastically traverse the parameter space. This is done by both "mutating" or randomly changing the values of some of the model parameters during each iteration, as well as performing "crossover" operations where the models that conform to desired features or characteristics – the objective function – have a subset of their parameter values interchanged so as to introduce variation in the models. These approaches have met with success in finding sets of conductance-based multi-compartment models that conform to experimental constraints (Druckmann et al. 2007; Hay et al. 2011). An advantage of this approach is that it does not require traversal of the entire parameter space, like with coarse-grid approaches. On the other hand, due to the "greedy" nature of genetic algorithms, meaning that they quickly converge to optimal models, there is a risk of getting trapped in local minima, where models cannot be further improved in the immediate locale of the parameter space, thus missing other acceptable models found elsewhere in the space. Some specialized techniques have been applied to avoid local minima, for instance, using simulated annealing to allow for uphill traversal in the objective function gradient so as to escape the minima (Ingber 1993). Another technique is to run several iterations of the genetic algorithm, each starting in different regions of the parameter space. However, the more comprehensively the parameter space is explored using these techniques, the more these approaches resemble the brute-force method, chiefly via the incurring of increased computational burden. One possible reconciliation of these two approaches may be in the application of a hybrid method where an initial step of a brute-force search is performed using a coarse-grid parameter space. Then, regions of the parameter space that seem promising with respect to an objective function can be further traversed with a genetic algorithm to find a larger range of models, with finer variability in their parameter values, within each local minimum identified in the initial brute-force search.

An important issue in parameter space traversal and database construction is the *goal* of such approaches. In our approach, the goal is not to find optimal models, per se. It is in fact advantageous to find as many regions of the parameter space as possible that contain models that address a specific physiological question, rather than a potentially small subset of models that best optimize an objective function, as the former can be more illustrative regarding the underlying dynamics of the model and hence biological system. For instance, in the work related to the model database described here, the physiological question under consideration was whether H could be present in O-LM cell dendrites or not (Sekulić et al. 2014).

We found that both combinations were possible, given the right balance of H against two other conductances, that of KA and Kdrs, as per the conductance co-regulations found (Fig. 7). This resulted in one full experiment-modelling "cycle" (Fig. 1). Once the database was built, it could be leveraged in multiple ways to create further cycles. For instance, we subsequently used the database to show that the dendritic distributions of H could vary in O-LM cells, as long as total H conductance across the membrane was maintained (Sekulić et al. 2015). This led to a specific experimental protocol that was implemented in the lab of Dr. J. J. Lawrence, the results of which will inform the next cycle of an entirely new database, to be constructed in the near future. Crucially, once a cycle has determined a possible "answer" to a physiological question, the parameters in the model corresponding to that investigation can be fixed or constrained significantly. Thus, there is a trade-off between considering variability in the model parameters as capturing inherent biological variability and considering the model parameter ranges as simply reflective of how unconstrained the experimental data for those parameters are.

Another important issue to consider in the context of building a population of models is the source and form of constraints from experimental data. This includes sources of experimental data, i.e., what protocols should be used to generate data that best constrain population modelling (Druckmann et al. 2011). But also, the output features of the models, and the inclusion criteria for appropriate versus inappropriate models, vary tremendously depending on what is known about the cell type in question. For instance, the stomatogastric ganglion preparation (STG) is in the favorable position of having its network and circuit dynamics fairly well understood, so that the roles of any individual cell are more or less clearly delineated (Marder and Bucher 2007). This makes it easier to develop objective functions for populations of models for those cells. On the other hand, in vertebrate systems, including hippocampus, there is much less known about the functional output and role of any given cell in a circuit. This is starting to change, however, with optogenetic studies that are beginning to tease apart contributions of individual cell types, including those of inhibitory interneurons, to both network function and behavior (Leão et al. 2012; Lovett-Barron et al. 2014; Kvitsiani et al. 2013; Pi et al. 2013; Royer et al. 2012). However, important limitations in inferring conclusions regarding underlying circuit behavior using acute optogenetic manipulations remain (Otchy et al. 2015).

Despite advances afforded by more precise experimental manipulations in vitro and in vivo, a very real possibility exists that one will not fully understand the functional role of a cell type of interest in the local network it is embedded from the outset. This may impede database modelling of that cell type insofar as lack of knowledge of its expected output may lead to difficulties in assessing good models in the parameter space traversal. However, experimental investigations to examine the intrinsic properties of the cells in order to develop a database of models that collectively match the range of in vitro current- and voltage-clamp experimental data are still possible and desirable. In particular, such work can provide needed predictions or hypotheses of *possible* roles of cell types. This can be done both by

giving insight into how the conductance density balances uncovered may lead to the intrinsic properties observed in vitro, as well as using the population of models to simulate in vivo-like conditions that may provide hints as to the possible ways the cell type may contribute to circuit functioning. Moving forward, we hope that population modelling in the spirit of what we have suggested in this chapter will become a new standard for fruitful work in using conductance-based computational models to inform experiments and clarify intrinsic and functional properties of the various neuronal cell types in the CNS.

Glossary

CA1 A subfield in the mammalian hippocampus, referring to "Cornu Ammonis 1," or the first region in "Amun's horns," a name for the hippocampus coined by de Garengeot in the mid-eighteenth century.

O-LM Oriens/lacunosum-moleculare; the abbreviation of a type of interneuron in hippocampal CA1/CA3 with soma in stratum oriens and axons projecting to stratum lacunosum/moleculare.

CBDR Clutter-based dimension reordering is a technique for the visualization of high-dimensional parameter spaces in 2D (Taylor et al. 2006; Peng et al. 2004).

PANDORA's toolbox An open-source MATLAB toolbox that provides an object-oriented framework for assembling and manipulating databases of electrophysiological data, whether from computational models or experiment.

References

Angelo K, London M, Christensen SR, Häusser M (2007) Local and global effects of I_h distribution in dendrites of mammalian neurons. J Neurosci 27:8643–8653

Bartos M, Alle H, Vida I (2011) Role of microcircuit structure and input integration in hippocampal interneuron recruitment and plasticity. Neuropharmacology 60:730–739

Berger T, Larkum ME, Lüscher HR (2001) High I_h channel density in the distal apical dendrite of layer V pyramidal cells increases bidirectional attenuation of EPSPs. J Neurophysiol 85:855–868

Dayan P, Abbott LF (eds) (2001) Theoretical neuroscience. MIT Press, Cambridge, MA

Destexhe A, Rudolph M, Paré D (2003) The high-conductance state of neocortical neurons *in vivo*. Nat Rev Neurosci 4:739–751

Druckmann S, Banitt Y, Gidon A, Schurman F, Markram H et al (2007) A novel multiple objective optimization framework for constraining conductance-based neuron models by experimental data. Front Neurosci 1:7–18

Druckmann S, Berger TK, Schürmann F, Hill S, Markram H, Segev I (2011) Effective stimuli for constructing reliable neuron models. PLoS Comput Biol 7(8):e1002133

Enyedi P, Czirják G (2010) Molecular background of leak K^+ currents: two-pore domain potassium channels. Physiol Rev 90:559–605

Foster WR, Ungar LH, Schwaber JS (1993) Significance of conductances in Hodgkin-Huxley models. J Neurophysiol 70(6):2502–2518

Freund TF, Buzsáki G (1996) Interneurons of the hippocampus. Hippocampus 6:347–470
Golowasch J, Buchholtz F, Epstein IR, Marder E (1992) Contribution of individual ionic currents to activity of a model stomatogastric ganglion neuron. J Neuro-Oncol 67(2):341–349
Golowasch J, Goldman MS, Abbott LF, Marder E (2002) Failure of averaging in the construction of a conductance-based neuron model. J Neurophysiol 87:1129–1131
Günay C, Edgerton JR, Jaeger D (2008) Channel density distributions explain spiking variability in the globus pallidus: a combined physiology and computer simulation database approach. J Neurosci 28:7476–7491
Günay C, Edgerton JR, Li S, Sangrey T, Prinz AA et al (2009) Database analysis of simulated and recorded electrophysiological datasets with PANDORA's Toolbox. Neuroinformatics 7:93–111
Hay E, Hill S, Schürmann F, Markram H, Segev I (2011) Models of neocortical layer 5b pyramidal cells capturing a wide range of dendritic and perisomatic active properties. PLoS Comput Biol 7(7):e1002107
Hines ML, Carnevale NT (2001) NEURON: a tool for neuroscientists. Neuroscientist 7:123–135
Hodgkin AL, Huxley AF (1952) A quantitative description of membrane current and its application to conduction and excitation in nerve. J Physiol 117:500–544
Holmes WR (2010) Passive cable modeling. In: De Schutter E (ed) Computational modeling methods for neuroscientists. MIT Press, Cambridge, MA
Ingber L (1993) Simulated annealing: practice versus theory. Math Comput Model 18(11):29–57
Johnston D, Narayanan R (2008) Active dendrites: colorful wings of the mysterious butterflies. Trends Neurosci 32(6):309–316
Keren N, Peled N, Korngreen A (2005) Constraining compartmental models using multiple voltage recordings and genetic algorithms. J Neurophysiol 94:3730–3742
Koch C, Segev I (eds) (1998) Methods in neuronal modeling. MIT Press, Cambridge, MA
Kole MHP, Hallermann S, Stuart GJ (2006) Single I_h channels in pyramidal neuron dendrites: properties, distribution, and impact on action potential output. J Neurosci 26:1677–1687
Kvitsiani D, Ranade S, Hangya B, Taniguchi H, Huang JZ, Kepecs A (2013) Distinct behavioural and network correlates of two interneuron types in prefrontal cortex. Nature 498:363–366
Lai HC, Jan LY (2006) The distribution and targeting of neuronal voltage-gated ion channels. Nat Rev Neurosci 7:548–562
Lawrence JJ, Saraga F, Churchill JF, Statland JM, Travis KE et al (2006a) Somatodendritic Kv7/KCNQ/M channels control interspike interval in hippocampal interneurons. J Neurosci 26:12325–12338
Lawrence JJ, Statland JM, Grinspan ZM, McBain CJ (2006b) Cell type-specific dependence of muscarinic signalling in mouse hippocampal stratum oriens interneurons. J Physiol 570:595–610
Leão RNR, Mikulović SS, Leão KEK, Munguba HH, Gezelius HH et al (2012) OLM interneurons differentially modulate CA3 and entorhinal inputs to hippocampal CA1 neurons. Nat Neurosci 15:1524–1530
Lien CC, Martina M, Schultz JH, Ehmke H, Jonas P (2002) Gating, modulation and subunit composition of voltage-gated K^+ channels in dendritic inhibitory interneurones of rat hippocampus. J Physiol 538:405–419
Loken C, Gruner D, Groer L, Peltier R, Bunn N et al (2010) SciNet: lessons learned from building a power-efficient top-20 system and data centre. J Phys Conf Ser 256:012026
London M, Häusser M (2005) Dendritic computation. Annu Rev Neurosci 28:503–532
Lovett-Barron M, Kaifosh P, Kheirbek MA, Danielson N, Zaremba JD et al (2014) Dendritic inhibition in the hippocampus supports fear learning. Science 343:857–863
Maccaferri G, McBain CJ (1996) The hyperpolarization-activated current (Ih) and its contribution to pacemaker activity in rat CA1 hippocampal stratum oriens-alveus interneurones. J Physiol 497:119–130
MacLean JN, Zhang Y, Johnson BR, Harris-Warrick RM (2003) Activity-independent homeostasis in rhythmically active neurons. Neuron 37:109–120
Magee JC (1998) Dendritic hyperpolarization-activated currents modify the integrative properties of hippocampal CA1 pyramidal neurons. J Neurosci 18:7613–7624

Mainen Z, Sejnowski TJ (1996) Influence of dendritic structure on firing pattern in model neocortical neurons. Nature 382:363–366
Marder E, Bucher D (2007) Understanding circuit dynamics using the stomatogastric nervous system of lobsters and crabs. Annu Rev Physiol 69:291–316
Marder E, Goaillard JM (2006) Variability, compensation and homeostasis in neuron and network function. Nat Rev Neurosci 7:536–574
Marder E, Taylor AL (2011) Multiple models to capture the variability in biological neurons and networks. Nat Neurosci 14(2):133–138
Martina M, Vida I, Jonas P (2000) Distal initiation and active propagation of action potentials in interneuron dendrites. Science 287:295–300
Matt L, Michalakis S, Hofmann F, Hammelmann V, Ludwig A et al (2011) HCN2 channels in local inhibitory interneurons constrain LTP in the hippocampal direct perforant path. Cell Mol Life Sci 68:125–137
Migliore M, Migliore R (2012) Know your current Ih: interaction with a shunting current explains the puzzling effects of its pharmacological or pathological modulations. PLoS One 7(5):e36867
Narayanan R, Johnston D (2012) Functional maps within a single neuron. J Neurophysiol 108:2343–2351
Niebur E (2008) Neuronal cable theory. Scholarpedia 3(5):2674
O'Leary T, Williams AH, Caplan JS, Marder E (2013) Correlations in ion channel expression emerge from homeostatic tuning rules. Proc Natl Acad Sci U S A 110(28):E2645–E2654
Otchy TM, Wolff SBE, Rhee JY, Pehlevan C, Kawai R et al (2015) Acute off-target effects of neural circuit manipulations. Nature 528:348–363
Peng W, Ward MO, Rundensteiner EA (2004) Clutter reduction in multi-dimensional data visualization using dimensional reordering. In: Keahey A (ed) Proceedings of the IEEE symposium on information visualization 2004. Austin, TX, pp 89–96
Perez Y, Morin F, Lacaille JC (2001) A hebbian form of long-term potentiation dependent on mGluR1a in hippocampal inhibitory interneurons. Proc Natl Acad Sci U S A 98:9401–9406
Pi HJ, Hangya B, Kvitsiani D, Sanders JI, Huang ZJ, Kepecs A (2013) Cortical interneurons that specialize in disinhibitory control. Nature 503:521–524
Prinz AA, Billimora CP, Marder E (2003) Alternative to hand-tuning conductance-based models: construction and analysis of databases of model neurons. J Neurophysiol 90:3998–4015
Prinz AA, Bucher D, Marder E (2004) Similar network activity from disparate circuit parameters. Nat Neurosci 7(12):1345–1352
Rall W (2009) Rall model. Scholarpedia 4(4):1369
Rall W, Burke RE, Holmes WR, Jack JJB, Redman SJ, Segev I (1992) Matching dendritic neuron models to experimental data. Phys Rev 72(4):S159–S186
Rotstein HG, Pervouchine DD, Acker CD, Gillies MJ, White JA et al (2005) Slow and fast inhibition and an H-current interact to create a theta rhythm in a model of CA1 interneuron network. J Neurophysiol 94:1509–1518
Royer S, Zemelman BV, Losonczy A, Kim J, Chance F, Magee JC, Buzsáki G (2012) Control of timing, rate and bursts of hippocampal place cells by dendritic and somatic inhibition. Nat Neurosci 15:769–775
Saraga F, Wu CP, Zhang L, Skinner FK (2003) Active dendrites and spike propagation in multi-compartment models of oriens-lacunosum/moleculare hippocampal interneurons. J Physiol 552(3):673–689
Schulz DJ, Goaillard JM, Marder E (2006) Variable channel expression in identified single and electrically coupled neurons in different animals. Nat Neurosci 9:356–362
Segev I, London M (2000) Untangling dendrites with quantitative models. Science 290:744–750
Sekulić V, Lawrence JJ, Skinner FK (2014) Using multi-compartment ensemble modeling as an investigative tool of spatially distributed biophysical balances: application to hippocampal oriens-lacunosum/moleculare (O-LM) cells. PLoS One 9(10):e106567
Sekulić V, Chen TC, Lawrence JJ, Skinner FK (2015) Dendritic distributions of I_h channels in experimentally-derived multi-compartment models of oriens-lacunosum/moleculare (O-LM) hippocampal interneurons. Front Syn Neurosci 7(2):1–15

Sik A, Penttonen M, Ylinen A, Buzsáki G (1995) Hippocampal CA1 interneurons: an in vivo intracellular labeling study. J Neurosci 15:6651–6665

Skinner FK (2006) Conductance-based models. Scholarpedia 1(11):1408

Skinner FK, Saraga F (2010) Single neuron models: interneurons. In: Hippocampal microcircuits: a computational Modeler's resource book. Springer, New York, pp 399–422

Smolinski TG, Prinz AA (2009) Computational intelligence in modeling of biological neurons: a case study of an invertebrate pacemaker neuron. IEEE Proc Intl Jt Conf Neural Netw:2964–2970

Swensen AM, Bean BP (2005) Robustness of burst firing in dissociated purkinje neurons with acute or long-term reductions in sodium conductance. J Neurosci 25:3509–3520

Talley EM, Solorzano G, Lei Q, Kim D, Bayliss DA (2001) CNS distribution of members of the two-pore-domain (KCNK) potassium channel family. J Neurosci 21:7491–7505

Taylor AL, Hickey TJ, Prinz AA, Marder E (2006) Structure and visualization of high-dimensional conductance spaces. J Neurophysiol 96:891–905

Torborg CL, Berg AP, Jeffries BW, Bayliss DA, McBain CJ (2006) TASK-like conductances are present within hippocampal CA1 stratum oriens interneuron subpopulations. J Neurosci 26:7362–7367

Traub RD, Jefferys JGR, Miles R, Whittington MA, Tóth K (1994) A branching dendritic model of a rodent CA3 pyramidal neuron. J Physiol 481:79–95

Van Geit W, De Schutter E, Achard P (2008) Automated neuron model optimization techniques: a review. Biol Cybern 99:241–251

Correction to: Modelling Epileptic Activity in Hippocampal CA3

Sanjay M. and Srinivasa B. Krothapalli

Correction to:
Chapter 22 in: V. Cutsuridis et al. (eds.), *Hippocampal Microcircuits*, Springer Series in Computational Neuroscience,
https://doi.org/10.1007/978-3-319-99103-0_22

In the original version of this chapter the corresponding author Srinivasa B. Krothapalli's affiliation was incorrectly mentioned as Department of Electrical Engineering, National Institute of Technology Calicut, Kattangal, Kerala, India. The affiliation is now corrected as 'Neurophysiology Unit, Department of Neurological Sciences, Christian Medical College, Vellore, India'. The same has been updated in Contributors list in the FM.

The updated version of this chapter can be found at
https://doi.org/10.1007/978-3-319-99103-0_22

V. Cutsuridis et al. (eds.), *Hippocampal Microcircuits, Springer Series*
in Computational Neuroscience, https://doi.org/10.1007/978-3-319-99103-0_26

Correction to: Computational Examination of Synaptic Plasticity and Metaplasticity in Hippocampal Dentate Granule Neurons

Azam Shirrafiardekani, Jörg Frauendiener, Ahmed A. Moustafa, and Lubica Benuskova

Correction to:
Chapter 20 in: V. Cutsuridis et al. (eds.), *Hippocampal Microcircuits*, Springer Series in Computational Neuroscience, https://doi.org/10.1007/978-3-319-99103-0_20

In the original version of this chapter, two of the chapter authors were inadvertently missed to be added in the authors list. The authors' names Jörg Frauendiener, and Lubica Benuskova have now been added in chapter 20.

The updated version of this chapter can be found at
https://doi.org/10.1007/978-3-319-99103-0_20

V. Cutsuridis et al. (eds.), *Hippocampal Microcircuits*, Springer Series in Computational Neuroscience, https://doi.org/10.1007/978-3-319-99103-0_27

Index

V. Cutsuridis et al. (eds.), *Hippocampal Microcircuits*, Springer Series in Computational Neuroscience, https://doi.org/10.1007/978-3-319-99103-0

I

J

T

U